THIN FILMS AND NANOSTRUCTURES

PHYSICO-CHEMICAL PHENOMENA IN THIN FILMS AND AT SOLID SURFACES

edited by
Leonid I. Trakhtenberg
Sheng H. Lin
Olusegun J. Ilegbusi

Lam Research Ex. 1035 - Page 1
Lam Research Corp. v. Inpria Corp.
IPR2024-00033 - U.S. Patent No. 9,823,564

Contents

Chapter 1. Introduction
L.I. Trakhtenberg, S.H. Lin, and O.J. Ilegbusi 1

Part 1. Theoretical Approaches to the Study of the Processes in Films and on Surfaces

Chapter 2. Conventional Theory of Multi-Phonon Electron Transitions
M.A. Kozhushner

1. Introduction. 9
2. Born–Oppenheimer's Adiabatic Approach 11
3. General Expression for Transition Probability in Unit of Time. . . . 13
4. Influence of Changes of Equilibrium Positions and Frequencies . . . 15
5. Calculation of Multi-Phonon Transition Probability in Unit of Time 18
6. Local Vibrations. Method of Density Matrix 24
7. Electron Transfer in Polar Medium 28
8. Adiabatic Transitions 30
9. Conclusions 33

References 34

Chapter 3. Contemporary Theory of Electrons Tunneling in Condensed Matter
M.A. Kozhushner

1. Introduction. 37
2. Amplitude of Electron Tunneling Transfer 38
3. Influence of Crystal Medium on Electron Tunneling 44
4. Multiple Tunneling Scattering and Bridge Effect 48
5. Violation of Born–Oppenheimer's Approach in Electron Tunneling Transfer 54
6. Conclusions 63

References 64

Lam Research Ex. 1035 - Page 2
Lam Research Corp. v. Inpria Corp.
IPR2024-00033 - U.S. Patent No. 9,823,564

Chapter 4. *Ab Initio* Calculations of Electronic Transitions and Photoabsorption and Photoluminescence Spectra of Silica and Germania Nanoparticles
A.M. Mebel, A.S. Zyubin, M. Hayashi, and S.H. Lin

1. Introduction . . . 68
2. Theoretical Approach and Methods . . . 72
   2.1. Model Clusters and Geometry Optimization . . . 72
   2.2. Calculations of Excitation Energies . . . 75
   2.3. Calculations of Vibronic Spectra . . . 81
3. Photoluminescence Properties of Point Defects in SiO_2 . . . 83
   3.1. Red and Near Infrared Photoluminescence Bands in Silica Nanostructures . . . 83
   3.2. PL Properties of the Silanone and Dioxasilyrane Point Defects . . . 89
   3.3. Photoabsorption and Photoluminescence of the $[AlO_4]^0$ Defect in SiO_2 . . . 95
4. Optical Properties of Point Defects in GeO_2 . . . 99
   4.1. Photoluminescence of Oxygen-Containing Surface Defects in Germanium Oxides . . . 99
      4.1.1. NBO or –O–Ge≡ Defect . . . 99
      4.1.2. Peroxy Radical or –O–O–Ge≡ Defect . . . 103
      4.1.3. $O_2Ge=$ Defect . . . 104
      4.1.4. O = Ge = Defect . . . 107
   4.2. Photoluminescence of Oxygen-Deficient Defects in Germanium Oxides . . . 108
      4.2.1. Surface E′-Center, or –Ge≡ Defect . . . 109
      4.2.2. Combination of the –Ge≡ Defect with an Oxygen Vacancy, E′–OV . . . 112
5. Summary and Outlook . . . 113
6. Discussion Topics and Questions on Concepts . . . 115

References . . . 116

Chapter 5. Density Matrix Treatments of Ultrafast Radiationless Transitions
S.H. Lin, K.K. Liang, M. Hayashi, and A.M. Mebel

1. Introduction . . . 122
2. Density Matrix and Liouville Equation . . . 123
   2.1. Definition of Density Matrix . . . 123
   2.2. Dynamics of Isolated Systems . . . 126

Lam Research Ex. 1035 - Page 3
Lam Research Corp. v. Inpria Corp.
IPR2024-00033 - U.S. Patent No. 9,823,564

3. Dynamics of a System Embedded in Heat Bath 132
3.1. Reduced Density Matrix and its Equation of Motion 134
3.2. Generalized Master Equations 136
3.3. Ultrafast Non-Adiabatic Dynamics of Molecular Systems . . 138
3.4. Single-Vibronic-Level and Thermal Average Rate Constant 142
4. Density Matrix Method and Spectroscopies 147
4.1. Steady State Spectroscopy 147
4.2. Pump–Probe Experiments 151
5. An Example — Interfacial Electron Transfer in Organic Solar Cells 156
5.1. Experimental Results and Theoretical Analysis 157
5.2. Remarks 172
6. Summary 172
Appendix A. $G_{v_j}(t)$ for Displaced–Distorted Oscillator 173
Appendix B. Derivation of the TCF for the Band-Shape Function . . . 177
References 180

Chapter 6. Ultrafast Radiationless Transitions
M. Hayashi, A.M. Mebel, and S.H. Lin

1. Introduction 184
2. Theoretical Approach and Methods 185
2.1. Non-Adiabatic Processes 186
2.2. Rate Constants 190
2.3. Radiationless Transitions 193
2.3.1. Internal Conversion (IC) 194
2.3.2. Intersystem Crossing (ISC) 195
3. Photo-Induced Electronic Transfer and Photo-Induced Energy Transfer 199
3.1. General Consideration 199
3.2. Photo-Induced Electron Transfer 200
3.3. Photo-Induced Energy Transfer 201
4. Applications 204
4.1. Pump–Probe Time-Resolved Stimulated Emission Spectra . . 204
4.1.1. Relaxation and Coherence Dynamics 205
4.1.2. A Model of Vibrational Relaxation and Dephasing . 206
4.1.3. A Single Harmonic Displaced Oscillator Mode System 208
4.2. Bacterial Photosynthetic RCs 211
4.2.1. Vibrational Coherence and Relaxation in Photosynthetic Reaction Centers 212

Lam Research Ex. 1035 - Page 4
Lam Research Corp. v. Inpria Corp.
IPR2024-00033 - U.S. Patent No. 9,823,564

4.2.2. Rapid Electron Transfer in Photosynthetic Reaction Centers . . . 214
4.2.3. Vibronic Coherence in Photosynthetic Reaction Center . . . 215
5. Summary . . . 219
References . . . 222

Part 2. Physico-Chemical Processes at the Surface of Solids

Chapter 7. Point Defects on the Silica Surface: Structure and Reactivity
V.A. Radzig

1. Introduction . . . 233
2. Methods for Creation of Defects on Silica Surface . . . 236
   2.1. Preparation of the Thermo-Activated Silica (TSi) Samples . . . 236
   2.2. Preparation of the Mechano-Activated Silica Samples (MSi) 237
   2.3. Preparation of the "Reactive Silica" (RSi) Samples . . . 238
   2.4. Structure and Concentration of Paramagnetic and Diamagnetic Point Defects on Activated Silica Surface . . . 239
3. Quantum-Chemical Calculations . . . 240
4. Chemical Modification of the Surface Defects . . . 243
   4.1. Preparation of ≡Si-O* Radicals: The System (≡Si* + N_2O) . 244
   4.2. Mutual Transformations of the $(\equiv Si\text{-}O)_2Si$: (SC) and $(\equiv Si\text{-}O)_2Si = O$ (SG) Groups . . . 248
   4.3. Si = O Bond Strength in the $(\equiv Si\text{-}O)_2Si = O$ Group . . . 248
   4.4. Microcalorimetry of the Processes at the SiO_2 and GeO_2 Surfaces . . . 252
5. Interrelation Between the EPR Parameters of the Silicon-Centered Paramagnetic Sites and Their Spatial Structure: Results of Quantum-Chemical Calculations . . . 253
6. Silicon-Centered Paramagnetic Centers (PCs) in SiO_2 . . . 260
   6.1. PC $(\equiv Si_\beta\text{-}O)_3Si_\alpha^\bullet$ on the Surface and in the Bulk of Silica . . 260
   6.2. PC $(\equiv Si_\beta\text{-}O)_2Si_\alpha^\bullet\text{-}r$, Where r = H(D), OH(OD), NH_2, and $CH_3(CD_3)$ . . . 264
   6.3. Stretching Vibration Frequencies of the Si-H Bonds in the Hydrogenation Products of Silicon-Centered PCs . . . 269
   6.4. Optical Characteristics of the Silicon-Centered PCs . . . 270
7. Paramagnetic Centers $\equiv Si\text{-}O^\bullet$ on the Silica Surface (Non-Bridging Oxygen Center) . . . 275
8. The $(\equiv Si\text{-}O)_3Si\text{-}O\text{-}O^*$ Radicals: Structure and Reactivity . . . 279
9. Diamagnetic Point Defects on Silica Surface . . . 281

Lam Research Ex. 1035 - Page 5
Lam Research Corp. v. Inpria Corp.
IPR2024-00033 - U.S. Patent No. 9,823,564

9.1. $(\equiv Si\text{-}O\text{-})_2Si<O_2>Si(\text{-}O\text{-}Si\equiv)_2$ Groups (Strained Rings, SRs) on the Silica Surface 282
9.2. Diamagnetic Sites Containing Two-fold Coordinated Silicon Atoms $(\equiv Si\text{-}O\text{-})_2Si$: (SC): Identification of SC Structure . . . 285
9.2.1. Identification of the Site Structure 285
9.3. Products of High-Temperature Hydration of RSi Samples. . 288
9.4. Optical Parameters of SC 290
9.5. The Mechanism of Singlet–Triplet Conversion of SC 291
9.6. Silanone Groups $(\equiv Si\text{-}O)_2Si=O$ on Silica Surface 292
9.7. Dioxasilyrane Groups $((\equiv Si\text{-}O)_2Si<O_2)$. 296
9.8. Reactivity of the $>Si<O_2$ Groups Toward the Polar X-H ($X = OH, NH_2, OCH_3$) Molecules. 305
10. Inhomogenity of Physico-Chemical Properties of Surface Defects . 309
11. Impurity Centers in Quartz Glass: Carbon in the Silica Structure . 314
11.1. $\equiv Si\text{-}^{\bullet}CH_2$, $(\equiv Si\text{-})_2^{\bullet}CH$, and $(\equiv Si\text{-})_3C^{\bullet}$ Radicals 314
11.2. Reactivity of the $(\equiv Si\text{-})_3C^{\bullet}$ Radicals Toward H_2 Molecules . 317
11.3. Increase in the Concentration of Paramagnetic Centers Upon the Thermo Oxidizing Treatment of the RSi Samples. 317
12. Nitrogen in Silica 319
12.1. PCs $(\equiv Si\text{-}O)_2Si^*(NH_2)$, $(\equiv Si\text{-}O)_2Si^*\text{-}N(Si\equiv)_2$, $(\equiv Si\text{-}O)_2(HO)Si\text{-}N^*H$, and $\equiv Si\text{-}N^*\text{-}Si\equiv$ 320
12.2. Reactions of $\equiv Si\text{-}N^*\text{-}H$ and $\equiv Si\text{-}N^*\text{-}Si\equiv$ PC with H_2 (D_2) . 324
12.3. On the Strengths of Si-O and Si-N Bonds in Vitreous Silica 328
13. Surface and Near-Surface Defects in Silica 329
14. Design of Intermediates with Desired Structure on Silica Surface 330
15. Conclusions 335
16. Questionnaire. 339
References 340

Chapter 8. Atomic-Molecular Kinetic Theory of Physico-Chemical Processes in Condensed Phase and Interfaces
Y.K. Tovbin

1. Introduction. 349
2. Gas–Solid Processes 352
2.1. Gas–Solid Interface 352
2.1.1. Gas Phase. 352
2.1.2. Solid 353
2.1.3. Subsurface Region of a Solid 354
2.1.4. Adsorption 354

Lam Research Ex. 1035 - Page 6
Lam Research Corp. v. Inpria Corp.
IPR2024-00033 - U.S. Patent No. 9,823,564

2.1.5. Effect of Adsorbed Particles on the State of a Surface . . . 356
2.1.6. Absorption . . . 356
2.1.7. Particle Mobility . . . 357
2.2. Lattice-Gas Model and Elementary Processes . . . 357
2.2.1. Elementary Processes and their Models . . . 359
2.2.2. Surface Mobility . . . 362
2.3. Lateral Interactions . . . 363
2.4. Quasi-Particle Description of Elementary Rates . . . 264
2.4.1. One-Site Reactions . . . 365
2.4.2. Two-Site Reactions . . . 368
3. Kinetic Equations for Multistage Processes in Condensed Phase . . . 370
3.1. Hamiltonian . . . 371
3.2. Master Equation . . . 372
3.3. Probabilities of Elementary Reactions . . . 375
3.4. Kinetic Equations . . . 378
3.5. Reaction Rates . . . 380
3.6. Hierarchy of the Kinetic Equations . . . 382
3.7. Two-Dimensional Model . . . 384
3.8. Point-Like Models of a Reaction . . . 387
3.8.1. Restricted Mobility of the Reactants . . . 388
3.8.2. Rapid Mobility of Reactants . . . 390
3.9. Different Mobilities of Reactants . . . 390
4. Surface Processes . . . 391
4.1. Physical Adsorption and Chemisorption . . . 392
4.2. Adsorption and Thermodesorption Spectra . . . 395
4.3. Multistage Processes . . . 399
4.4. Islands and Two-Dimensional Phases . . . 402
4.5. Self-Consistency of the Lattice-Gas model . . . 404
4.6. Surface Diffusion . . . 409
5. Solid Phase Processes in Solid–Gas Systems . . . 412
5.1. Interface States . . . 412
5.2. Diffusion Through Solids . . . 414
5.3. Phase Transitions and Topochemical Processes . . . 418
6. Physico-Chemical Mechanics Problems . . . 419
6.1. Rates of Elementary Stages at Solid Deformations . . . 419
6.2. Hydrogen–Palladium System . . . 421
6.3. Effective Potential . . . 422
6.4. Mechanical and Transport Properties of the Pd–H_2 System . . . 423
6.4.1. Effect of Lattice Deformation on the Properties of Membranes . . . 426

Lam Research Ex. 1035 - Page 7
Lam Research Corp. v. Inpria Corp.
IPR2024-00033 - U.S. Patent No. 9,823,564

7. Numerical Dynamics Investigations 427
7.1. Cellular Automata Technique 427
7.2. Monte-Carlo Technique 429
7.2.1. Adsorption Processes and Surface Reactions 429
7.2.2. Surface Diffusion and Phase Formation 431
7.2.3. Crystal Growth 433
7.2.4. Complex Processes 434
7.3. Correlation Between Monte-Carlo Simulations and Kinetic Theory 435
8. Summary and Perspectives 438
Appendix A. Equilibrium Distributions of Particles on Heterogeneous Lattices in Condensed Phases 441
Appendix B. Lowering the Dimension of a System of Equations in the Quasi-Chemical Approximation 448
Problems 451
References 452

Part 3. Formation and Physico-Chemical Properties of the Films

Chapter 9. Integrated Approach to Dielectric Film Growth Modeling: Growth Mechanisms and Kinetics
A.A. Bagatur'yants, M.A. Deminskii, A.A. Knizhnik, B.V. Potapkin, and S.Y. Umanskii

1. Introduction. 468
2. Quantum-Chemical Modeling 470
3. Gas-Surface Reactions Proceeding via a Strongly Adsorbed Precursor 471
3.1. Description of the Model 471
3.2. Master Equation and Macroscopic Rate Constants. 472
3.3. Macroscopic Rate Constant of a Barrierless Adsorption–Desorption Reaction 477
4. Simulation Methods 479
4.1. Molecular Dynamics 479
4.1.1. Equation of Motion 480
4.1.2. Energy Functional for MD 481
4.2. Monte Carlo Method 483
4.3. Kinetic Monte Carlo Method 483
4.4. Lattice and Dynamic Versions of Kinetic Monte Carlo 485

Lam Research Ex. 1035 - Page 8
Lam Research Corp. v. Inpria Corp.
IPR2024-00033 - U.S. Patent No. 9,823,564

4.5. Kinetic Monte Carlo Method with Dynamic Relaxation (KMC-DR) . . . 486
4.6. Reactor Modeling of Thin-Film Deposition . . . 488
5. Modeling of the Deposition of Thin Dielectric Films . . . 493
5.1. Molecular Dynamics Modeling of Precursor Interaction with Surface . . . 493
5.2. Kinetic Mechanism of Zirconium and Hafnium Oxide Film Deposition . . . 494
5.3. Reduction of the Kinetic Mechanism of $Zr(Hf)O_2$ Film Growth . . . 502
5.4. Kinetic Monte Carlo and Molecular Dynamics Modeling of ZrO_2 Film Roughness in an ALD Process . . . 503
5.5. Modeling of the ZrO_2 Film Composition Using the Monte Carlo Method . . . 508
5.6. Modeling of the Si/ZrO_2 Interface Structure Using the KMC-DR Method . . . 512
6. Conclusions and Outlook . . . 516
Questions and Problems . . . 516
References . . . 517

Chapter 10. Vapor Deposited Composite Films Consisting of Dielectric Matrix with Metal/Semiconductor Nanoparticles
G.N. Gerasimov, and L.I. Trakhtenberg

1. Introduction . . . 524
2. Features of Metal and Semiconductor Nanoparticles . . . 526
2.1. Metal Nanocrystals . . . 526
2.2. Semiconductor Nanocrystals . . . 531
3. Methods of Preparation and Structure of Nanocomposite Films . . . 536
3.1. M/SC Nanoparticle Deposition on a Surface of Dielectric Substrate . . . 537
3.2. Co-Deposition of M/SC and A Dielectric Material . . . 544
4. Physico-Chemical Properties of Nanocomposite Films . . . 554
4.1. Conductivity and Photoconductivity . . . 554
4.2. Sensor Properties . . . 557
4.3. Dielectric Properties . . . 562
4.4. Catalytic Activity . . . 566
5. Conclusion . . . 571
Acknowledgments . . . 574
References . . . 574

Lam Research Ex. 1035 - Page 9
Lam Research Corp. v. Inpria Corp.
IPR2024-00033 - U.S. Patent No. 9,823,564

Chapter 11. Transport and Magnetic Properties of Nanogranular Metals
B.A. Aronzon, S.V. Kapelnitsky, and A.S. Lagutin

1. Introduction. 582
2. Production of Nanocomposite Films 585
3. Structure of Granular Metals (Nanocomposites) 589
4. Magnetic Properties of Granular Magnetic Metals 595
   - 4.1. General Statements and Magnetization at Low Temperatures. 597
   - 4.2. Magnetization at High Temperatures (Paramagnetic Region). 599
   - 4.3. Magnetization of Granular Ferromagnetic Metals with Non-Spherical Granules 601
   - 4.4. A Relaxation of Magnetization and Nanocomposite as Cluster Spin Glass.. 604
5. Magnetotransport Properties of the Granular Metals. 607
   - 5.1. Conductivity Dependence on a Metal Granules Fraction: The Percolation Threshold 608
   - 5.2. Temperature Dependence of Conductivity 612
   - 5.3. Magnetoresistance: Field Dependence of the Conductivity. . 614
   - 5.4. Hall Effect 621
6. Quantum-Size Effects in Granular Metals Near the Percolation Threshold 627
7. Conclusions 631
8. Questions for Readers. 632

References 633

Chapter 12. Organized Organic Thin Films: Structure, Phase Transitions and Chemical Reactions
S. Trakhtenberg

1. Introduction. 640
2. Preparation and Structure of Langmuir–Blodgett Films. 645
   - 2.1. Langmuir Monolayers 646
   - 2.2. Film Transfer 648
   - 2.3. Structure of Langmuir–Blodgett Films. 649
3. Temperature-Induced Phase Transitions in Langmuir–Blodgett Films. 650
   - 3.1. Order–Disorder Transitions 651
   - 3.2. Effect of Phase Transitions on the Reactivity of Langmuir–Blodgett Films 652
4. Self-Assembled Films 654

Lam Research Ex. 1035 - Page 10
Lam Research Corp. v. Inpria Corp.
IPR2024-00033 - U.S. Patent No. 9,823,564

4.1. Covalently Bonded Silane Monolayers 655
4.2. Stability of Self-Assembled Silane Films 656
4.3. Self-Assembled Silane Multilayers 657
5. Conclusions 659
Acknowledgments 661
References 661

Chapter 13. Non-Catalytic Photo-Induced Immobilization Processes in Polymer Films
S. Trakhtenberg, A.S. Cannon, and J.C. Warner

1. Introduction 666
2. Photo-Induced Processes in Natural Polymers–DNA 671
3. Photopolymers and Photoresists Containing DNA Bases 676
4. Light-Induced Immobilization of Crosslinkable Photoresists 679
5. Reverse Processes 687
6. Conclusions 690
Acknowledgments 691
References 691

Chapter 14. Formation of Unconventional Compounds and Catalysts in Magnesium-Containing Organic Films
V.V. Smirnov, L.A. Tyurina, and I.P. Beletskaya

1. Introduction: Reactions in the Films Obtained by Co-Condensation of Metal Vapor with Organic Compounds 697
2. Synthesis of Magnesium-Containing Films by Co-Condensation of Reagents 701
3. Synthesis of RMg_4X Compounds in Thin Films of Co-Condensates 703
4. Mechanism of the Processes in Organic Magnesium-Containing Films and the Nature of the Magic Number Four 705
5. Competition Between the Aggregation of Magnesium Atoms and the Generation of Radicals in Mg–RX Films 710
6. Structure and Reactivity of Unconventional Organomagnesium Compounds Obtained in Co-Condensate Films 712
7. Catalytic Reactions in Mg–RH Films 714
8. Synthesis of Catalysts in Multicomponent Films Containing Magnesium and a Transition Metal 717
9. Conclusions 719
References 720

Lam Research Ex. 1035 - Page 11
Lam Research Corp. v. Inpria Corp.
IPR2024-00033 - U.S. Patent No. 9,823,564

Chapter 15. Charge Effects in Catalysis by Nanostructured Metals
S.A. Gurevich, V.M. Kozhevin, I.N. Yassievich, D.A. Yavsin, T.N. Rostovshchikova, and V.V. Smirnov

1. Introduction. . . . 726
2. Catalyst Fabrication and Structural Properties 729
   2.1. Catalyst Fabrication by Laser Electrodispersion of Metals. . 729
   2.2. Structural Properties of the Catalyst Coatings 732
3. Charge State of Metallic Nanostructures 735
4. Effect of Nanoparticle Charging on the Catalytic Properties. 741
   4.1. Analytical Estimates. . . . 742
   4.2. Experimental Results and Discussion. . . . 744
5. Summary. . . . 750

References 752

Chapter 16. Synthesis of Crystalline C–N Thin Films
H. Song, and O.J. Ilegbusi

1. Introduction. . . . 756
2. Synthesis 758
3. Theoretical Models. . . . 761
   3.1. Thermodynamic Models. . . . 761
   3.2. Molecular Dynamics Simulation 765
   3.3. Thermal Spike Model. . . . 766
4. Characterization. . . . 770
   4.1. Microstructure: XRD and TEM 770
   4.2. Chemical State: EELS and XPS 771
   4.3. Composition: AES and RBS. . . . 773
5. Potential Applications of CN Films 774
6. Closure 774

Acknowledgment 775
Questions 775
References 775

Subject Index 779

Recent Volumes In This Series 783

Lam Research Ex. 1035 - Page 12
Lam Research Corp. v. Inpria Corp.
IPR2024-00033 - U.S. Patent No. 9,823,564

Chapter 1
Introduction

L.I. Trakhtenberg[a], S.H. Lin[b], and O.J. Ilegbusi[c]

[a]*Karpov Institute of Physical Chemistry, 10, Vorotsovo Pole Str., Moscow, 105064, Russia and Semenov Institute of Chemical Physics, Russian Academy of Sciences, ul. Kosygina 4, Moscow, 119991, Russia*
[b]*Institute of Atomic and Molecular Sciences, Academia Sinica, P.O. Box 23-166, Taipei 106, Taiwan and Division of Mechanics, Research Center for Applied Sciences, Academia Sinica, Taipei 115, Taiwan*
[c]*Department of Mechanical, Materials and Aerospace Engineering, University of Central Florida, Orlando, FL 32816, USA*

Thin film processing and interfacial phenomena are currently of intense interest due to their fundamental and practical significance. Fundamentally, they pose a number of scientific and thought-provoking problems and issues to be addressed. Thin film materials possess unique performance attributes that make them useful for a variety of applications. Some properties of these substances (for example, spectral properties) cut across dimensional scales, ranging from atomic to macroscopic states. By the same token, other film properties (for example, kinetic, catalytic, and sensor properties) may differ qualitatively, and bear no relationship to the original material. This feature is most evident in nanocomposite films where, in addition to film thickness and composition, the dimension of nanoclusters also plays significant role in determining the film properties. Many physico-chemical characteristics of the films are dependent on cluster size. As an example, for CdS-clusters, the radiation lifetime corresponding to the allowable transition from the first excited state changes from tens to units of nanoseconds, and the melting point changes from 400 to 1600°C. The size of clusters correspondingly changes from molecular to macroscopic dimensions.

A major application of this scientific field is in the production of novel nanocomposite materials with unique characteristics. By changing the processing conditions and chemical composition of the film, it is possible to affect its structure and consequently, its physico-chemical properties. Therefore the key to a successful production of such important materials, specifically, nanostructural films of predetermined optical, magnetic, dielectric,

THIN FILMS AND NANOSTRUCTURES, vol. 34
ISSN 1079-4050
DOI: 10.1016/S1079-4050(06)34001-X
© 2007 by Elsevier Inc.
All rights reserved.

Lam Research Ex. 1035 - Page 13
Lam Research Corp. v. Inpria Corp.
IPR2024-00033 - U.S. Patent No. 9,823,564

photovoltaic and sensor properties, is to establish the fundamental dependence on the synthesis conditions, of the film structure and its properties.

This volume focuses on the variety of phenomena associated with the above-mentioned systems. The discussion has both experimental and theoretical components. It is desirable to consider all these processes within the framework of a unified theoretical approach. Such an approach is possible because the most important physico-chemical phenomena in such media are accompanied by the rearrangement of intra- and inter-molecular coordinates and consequently, a surrounding molecular ensemble. Some powerful mathematical tools are presented for such processes describing the theory of radiationless multi-vibrational transitions. Thus, the first part of the volume addresses the following issues:

- radiationless transitions, such as electron- and photo-induced transfer;
- *ab initio* methods for calculating potential energy surfaces for excited electronic states, electronic and vibronic spectra, rates of radiationless transitions, and examples of their application to molecular and condensed phase systems;
- density matrix method for theoretical study of ultrafast radiationless transitions; and
- some approaches to the study of femto-second time-resolved spectra.

The above issues are addressed in the book because of numerous newly published results since the publication of the well-known surveys on the theory of radiationless transitions. Therefore, along with a description of the traditional approaches to the theory of radiationless transitions (Chapter 2), these effects are discussed starting from the pioneering to contemporary studies (Chapter 3).

The different methods for calculating the rate constant of radiationless multi-vibrational electron transitions are among the issues considered in Chapter 2. The discussion starts from the pioneering works of Pekar, Huang Kun and Rhys, Lax, Krivoglaz, Kubo and Toyozawa. The concept of reorganization energy is introduced in the description of the high-temperature limit of the rate constant – the Marcus formula. Application of the theory to electron transfer reactions in polar media is also considered.

Chapter 3 describes radiationless transitions in the tunneling electron transfers in multi-electron systems. The following are examined within the framework of electron Green's function approach: the dependence on distance, the influence of crystalline media, and the effect of intermediate particles on the tunneling transfer. It is demonstrated that the Born–Oppenheimer approximation for the wave function is invalid for long-distance tunneling.

Lam Research Ex. 1035 - Page 14
Lam Research Corp. v. Inpria Corp.
IPR2024-00033 - U.S. Patent No. 9,823,564

The calculation of rate constants of radiationless transitions should be based on first principles and *ab initio* potential energy surfaces. These issues are addressed in Chapter 4, where modern methods of *ab initio* calculations of excited electronic states are described along with theoretical prediction of vibronic spectra. The latter includes geometry optimization using accurate *ab initio* methods, calculation of vibrational frequencies and normal modes for the ground and excited electronic states, and computation of transition dipole moments, vibrational overlap integrals, and Franck-Condon factors. Chapter 4 also discusses applications of these theoretical methods to the prediction and assignment of photoabsorption and photoluminescence spectra for silica and germania nanomaterials.

The next two chapters are devoted to ultrafast radiationless transitions. In Chapter 5, the generalized linear response theory is used to treat the non-equilibrium dynamics of molecular systems. This method, based on the density matrix method, can also be used to calculate the transient spectroscopic signals that are often monitored experimentally. As an application of the method, the authors present the study of the interfacial photo-induced electron transfer in dye-sensitized solar cell as observed by transient absorption spectroscopy. Chapter 6 uses the density matrix method to discuss important processes that occur in the bacterial photosynthetic reaction center, which has congested electronic structure within ~200–1500 cm^{-1} and weak interactions between these electronic states. Therefore, this biological system is an ideal system to examine theoretical models (memory effect, coherence effect, vibrational relaxation, etc.) and techniques (generalized linear response theory, Forster–Dexter theory, Marcus theory, internal conversion theory, etc.) for treating ultrafast radiationless transition phenomena.

The second part of the book considers a variety of surface phenomena, most of which are accompanied by media reorganization. Chapter 7 provides a description of the physico-chemical processes that occur on the surface of a very important material – silica. Indeed, from one hand, a set of practically important reactions occurs on the silica surface. From another hand, this surface could be considered as a model, and the experimental data obtained for such a model system can be compared with the theoretical results and used for planning new experiments. The subjects discussed in this chapter include the methods of generating point defects, quantum-chemical modeling of the properties (optical, IR, and ESR) of point defects on silica surface, inhomogeneity of physico-chemical properties of the point defects stabilized on silica surface, comparison of spectral properties of the surface and bulk defects in silica, mechanisms of point defect rearrangement, and design of the reactive intermediates with desired structure on silica surface. The structure, spectral, dia- and paramagnetic characteristics of point defects will also be considered.

Lam Research Ex. 1035 - Page 15
Lam Research Corp. v. Inpria Corp.
IPR2024-00033 - U.S. Patent No. 9,823,564

Chapter 8 provides a unified view of the different kinetic problems in condensed phases on the basis of the lattice–gas model. This approach extends the famous Eyring's theory of absolute reaction rates to a wide range of elementary stages including adsorption, desorption, catalytic reactions, diffusion, surface and bulk reconstruction, etc., taking into consideration the non-ideal behavior of the medium. The Master equation is used to generate the kinetic equations for local concentrations and pair correlation functions. The many-particle problem and closing procedure for kinetic equations are discussed. Application to various surface and gas–solid interface processes is also considered.

The third part of the book focuses on the methods of synthesizing thin films (chemical vapor deposition, Langmuir–Blodgett, vacuum magnetron sputtering, laser electrodispersion), film characteristics, and associated phenomena including growth mechanisms, chemical reaction spectral characteristics, and thermodynamic, optical, electrical, magnetic, transport and sensor properties.

Chapter 9 provides a bridge between the second and third parts of the book. It is concerned with the theoretical methods currently used for describing the epitaxial growth of dielectric and semiconductor thin films on the surface. The multi-scale approach to film growth modeling is outlined, including *ab initio* calculations of the main gas-phase and surface reactions, estimation of the rate constants using transition state or Rice–Ramsperger–Kassel–Marcus (RRKM) theory, and kinetic modeling using the kinetic Monte Carlo (KMC) method or formal chemical kinetics. The KMC method is supplemented with a dynamic relaxation procedure (KMC-DR) in situations requiring the modeling of irregular growth (defect or amorphous films). Specific technical details of KMC and KMC-DR methods are discussed. Examples of specific applications of multi-scale techniques are also discussed.

Chapter 10 deals with composite films synthesized by the physical vapor deposition method. These films consist of dielectric matrix containing metal or semiconductor (M/SC) nanoparticles. The film structure is considered and discussed in relation to the mechanism of their formation. Some models of nucleation and growth of M/SC nanoparticles in dielectric matrix are presented. The properties of films including dark and photo-induced conductivity, conductometric sensor properties, dielectric characteristics, and catalytic activity as well as their dependence on film structure are discussed. There is special focus on the physical and chemical effects caused by the interaction of M/SC nanoparticles with the environment and charge transfer between nanoparticles in the matrix.

Chapter 11 provides a state-of-the-art description of the physical properties of granular metals or nanocomposites (metallic grains embedded in

Lam Research Ex. 1035 - Page 16
Lam Research Corp. v. Inpria Corp.
IPR2024-00033 - U.S. Patent No. 9,823,564

insulator matrix). The description focuses on magnetic granular metals due to renewed interest in these materials in spintronics and the wide array of possible applications. Chapter 12 describes various types of organized organic thin films. Both self-assembly and Langmuir–Blodgett techniques of preparing mono- and multi-layer films are presented. Structure, stability, and phase transitions in the films are discussed. The effect of film structure on their chemical reactions with gas-phase species is discussed. Existing and potential applications of organized organic thin films are also presented. Photopolymers containing thymine or a DNA base are described in Chapter 13. The historical account as well as the current state of research on the mechanisms of thymine photodimerization and its reversal in various media is provided. The synthetic thymine-containing polymers and their photo-immobilization are described in the context of Flory's theory of network formation.

Chapter 14 describes low-temperature synthesis of metal-containing films, an original and promising field of organometallic chemistry. A classical Grignard reaction in Mg–RX films turned out to yield novel compounds of composition RMg_nX. The use of cluster Grignard reagents and their hydrid analogues considerably extends the range of objects and processes in the chemistry of organomagnesium compounds, and makes it possible to observe catalytic transformations of hydrocarbons. Chapter 15 deals with the properties of nanostructured catalysts composed of nearly monodispersive and amorphous metal (Cu, Ni, and Pd) nanoparticles, which are produced by laser electrodispersion technique. Experimental data show unusually high (up to 10^5 product mole/metal mole/h) catalytic activity of these structures measured in several chlorohydrocarbon conversions (Cu, Ni) and hydrogenation (Ni, Pd) reactions. The enhanced catalytic activity of these structures is related to the appearance of specific charge state of the system of particles, which originates from thermally activated inter-particle or particle-to-support tunnel electron transitions. The mechanism of tunnel electron transfer from charged metal nanoparticle to the chemisorbed reagent molecule is examined, and it is shown that nanoparticle charging may result in substantial reduction of the reaction activation energy. Estimates made on this basis are in good agreement with the experimental results.

Chapter 16 deals with the relationship between processing, structure, and properties of CN films. Such films potentially are believed to have attractive properties derived largely from their short covalent bonding. The status of current research on CN films is reviewed and the most widely used experimental techniques employed to produce them are presented. The theoretical models often used to optimize the processing are then described. Next, microstructural characterization of CN films are discussed followed by a discussion on the effect of processing and structure on film properties.

Lam Research Ex. 1035 - Page 17
Lam Research Corp. v. Inpria Corp.
IPR2024-00033 - U.S. Patent No. 9,823,564

Finally, the prospects for practical application of CN films are summarized at the end of the chapter.

It is desirable to describe the above phenomena on the basis of the theoretical approaches considered in the first part of the book wherever possible. Indeed, reorganization of media and reagents occurs at all stages starting from film formation (Chapter 9) to the associated phenomena. This reorganization is particularly evident at phase transitions (for example, Chapter 12) in which the phenomenon involves a change in the position of lattice atoms and molecules. Therefore, phase transitions should be studied on the basis of the theory of radiationless transitions. Media rearrangement coupled with the reagent transformation largely determines the absolute value and temperature dependence of the rate constants and other characteristics of the processes considered.

The material in some of the chapters in the book is presented at two levels of complexity. The first part briefly describes established and widely available information. Non-specialists with physico-chemical background, who wish to familiarize themselves with the subject matter, may use this part. The second part presents the material at a higher academic level with emphasis on recent research developments in the field. Existing and potential applications of the processes and phenomena are considered, and future research plans are identified. Questions are included at the end of some chapters to further reinforce the material discussed.

Lam Research Ex. 1035 - Page 18
Lam Research Corp. v. Inpria Corp.
IPR2024-00033 - U.S. Patent No. 9,823,564

Chapter 2

Conventional Theory of Multi-Phonon Electron Transitions

M.A. Kozhushner

Semenov Institute of Chemical Physics, Russian Academy of Sciences, ul. Kosygina 4, Moscow 119991, Russia

1. Introduction 9
2. Born–Oppenheimer's Adiabatic Approach 11
3. General Expression for Transition Probability in Unit of Time 13
4. Influence of Changes of Equilibrium Positions and Frequencies. 15
5. Calculation of Multi-Phonon Transition Probability in Unit of Time. 18
6. Local Vibrations. Method of Density Matrix 24
7. Electron Transfer in Polar Medium 28
8. Adiabatic Transitions 30
9. Conclusions 33
References 34

The theory of the multi-vibrational electron transitions based on the adiabatic representation for the wave functions of the initial and final states is the subject of this chapter. Then, the matrix element for radiationless multi-vibrational electron transition is the product of the electron matrix element and the nuclear element. The presented theory is devoted to the calculation of the nuclear component of the transition probability. The different calculation methods developed in the pioneer works of S.I. Pekar, Huang Kun and A. Rhys, M. Lax, R. Kubo and Y. Toyozawa will be described including the operator method, the method of the moments, and density matrix method. In the description of the high-temperature limit of the general formula for the rate constant, specifically Marcus's formula, the concept of reorganization energy is introduced. The application of the theory to electron transfer reactions in polar media is described. Finally, the adiabatic transitions are discussed.

1. Introduction

The large broadening of the absorption lines of F-centers and its dependence on the temperature was observed in the thirties of the previous century. Such

THIN FILMS AND NANOSTRUCTURES, vol. 34
ISSN 1079-4050
DOI: 10.1016/S1079-4050(06)34002-1

© 2007 by Elsevier Inc.
All rights reserved.

Lam Research Ex. 1035 - Page 19
Lam Research Corp. v. Inpria Corp.
IPR2024-00033 - U.S. Patent No. 9,823,564

dependence proves the strong interaction of the electron in F-center with crystal lattice. The received experimental regularities stimulated the development of the electron transitions theory that takes into account the influence of electron upon the lattice environment. Such theory, taking into account the change of equilibrium position of number of oscillation modes bounded with electron system, has started to develop from the fundamental works of Pekar [1] and Kun and Rhys [2] published in 1950. It is this change of equilibrium position that can bring about a change in the populations of many vibration modes [3]. Besides, it is also possible to change the vibration modes frequencies [4]. In the works described in Refs. [1, 2], the transitions between the electron states localized at the impurity centers in crystals, and the vibration modes of the crystal optical phonons at the same frequencies were considered. Then, the general method for calculation of the rate constant of the multi-phonon transition at the phonon branches with the arbitrary frequency dispersion was developed in the articles of Refs. [5, 6]. During electron transition, it is possible to change the system of normal coordinates that is particularly characteristic of the localized vibration modes. The method for the calculation of transition probability for such general case was elaborated in the work [7]. It permits to obtain the expression for the rate constant if the matrix of transition from the initial normal coordinates to final ones is known.

The electron transition probability depends strongly on overlapping of the phonon wave functions of the initial and final states. This overlapping depends on, first, the initial excitation levels of the oscillators and, second, the energy transmitted to vibration modes. As a rule, the system in initial state is in equilibrium position; therefore, the initial vibration levels, i.e. the initial populations, are defined by the temperature. The transmitted energy is equal to the difference of the electron energies in the initial and final states. The goal of the theory is the calculation of the dependence of transition probability on the temperature and the transmitted energy.

The theory of multi-oscillator electron transitions developed in the works [1, 2, 5–7] is based on the Born–Oppenheimer's adiabatic approach where the electron and nuclear variables are divided. Therefore, the matrix element describing the transition is a product of the electron and oscillator matrix elements. The oscillator matrix element depends only on overlapping of the initial and final vibration wave functions and does not depend on the electron transition type. The basic assumptions of the adiabatic approach and the approximate oscillator terms of the nuclear subsystem are considered in the following section. Then, in the subsequent sections, it will be shown that many vibrations take part in the transition due to relative change of the vibration system in the initial and final states. This change is defined by the following factors: the displacement of the equilibrium positions in the

Lam Research Ex. 1035 - Page 20
Lam Research Corp. v. Inpria Corp.
IPR2024-00033 - U.S. Patent No. 9,823,564

vibration modes, the shift of the frequencies, the change of the normal vibration coordinates at the transition, or all these factors together. The different methods of calculation of the vibration multiplier in the expression for the transition probability will be considered, and the general expression for it will be obtained for the case of big energy liberation in the phonon system.

2. Born–Oppenheimer's Adiabatic Approach

The total Hamiltonian of the electron–nuclear system is described as:

$$\hat{H} = \hat{T}_e + V_e(r) + V_{eR}(r, R) + V_R(R) + \hat{T}_R \tag{1}$$

where $\hat{T}_e$ and T_R are the operators of the electron and nuclei kinetic energies, respectively; $V_e(r)$, $V_{eR}(r, R)$ and $V_R(R)$ are the potential energies of the electron–electron, electron–nuclei and nuclei–nuclei interactions, respectively. The values r and R denote the whole of electron and nuclear coordinates. According to the adiabatic approach, the eigen function of the system has the form:

$$\Psi_\mu(r; R) = \psi_\mu(r; R)\chi^\mu(R). \tag{2}$$

Here, the electron wave function $\psi_\mu(r; R)$ is the eigen function of Hamiltonian

$$\hat{H}_e(r; R) = \hat{T}_e + V_e(r) + V_{eR}(r, R) + V_R(R). \tag{3}$$

There is no operator of differentiation on R in Hamiltonian (3), and hence these coordinates are the parameters. The wave function $\psi_\mu(r; R)$ obeys the following Schrödinger equation

$$\hat{H}_e(r; R)\psi_\mu(r; R) = E_\mu(R)\psi_\mu(r; R). \tag{4}$$

The index μ numbers the electron states and $E_\mu(R)$ is the μ's electron term of the system.

Nuclear Hamiltonian for μ's electron term

$$\hat{H}_n^\mu = \hat{T}_R + E_\mu(R)$$

corresponds to nuclear wave function $\chi^\mu(R)$. The eigen energy of the electron subsystem $E_\mu(R)$ from Eq. (4) plays the role of the potential energy of the nuclear subsystem. The point R_μ in the multi-dimensional space R, where $E_\mu(R)$ has the minimum $E_\mu^{\min}$, corresponds to the equilibrium position of the nuclear system for μ's electron state. Usually, the electron term $E_\mu(R)$ near the minimum is the quadratic form of the deflection of nuclear

Lam Research Ex. 1035 - Page 21
Lam Research Corp. v. Inpria Corp.
IPR2024-00033 - U.S. Patent No. 9,823,564

coordinates from the equilibrium position,

$$E_\mu(R) = E_\mu^{\min} + \sum_{i,k}^{N} \frac{1}{2} k_{is}^{\mu} (R_i - R_{i,\min}^{\mu})(R_k - R_{k,\min}^{\mu}),$$

where the summation is made on the coordinates of N nuclei of the system. As a result, nuclear Hamiltonian is also expressed in the quadratic form:

$$\hat{H}_{\mathrm{n}}^{\mu} = E_\mu^{\min} - \hbar^2 \sum_n \frac{1}{2M_n} \frac{\partial^2}{\partial R_n^2} + \sum_{i,k}^{N} \frac{1}{2} k_{is}^{\mu} (R_i - R_{i,\min}^{\mu})(R_k - R_{k,\min}^{\mu}). \quad (5)$$

This expression can be reduced to the diagonal form; then, the resulting Hamiltonian $\hat{H}_{\mathrm{n}}^{\mu}$ will be the sum of the oscillator Hamiltonians with normal coordinates q_s^{μ}. The eigen energy of the system is the sum of the energies of the independent oscillators,

$$E_{\mu,\{n_s\}} = E_{\mu,\min} + \sum_s \hbar\omega_s^{\mu} \left(n_s + \frac{1}{2} \right). \quad (6)$$

The values ω_s^{μ}, n_s are the frequency and the level number of s's oscillator of μ's term, respectively. The nuclear wave function in the expression (2) is the product

$$\chi^{\mu}(R) = \prod_s \chi_{n_s}^{\mu}(q_s). \quad (7)$$

Here, $\chi_{n_s}^{\mu}(q_s)$ is the wave function of the s's mode corresponding to the energy $\hbar\omega_s^{\mu}(n_s + 1/2)$.

Let us discuss here the electron transitions in a condensed medium; then, the multi-dimensional space R includes both the coordinates of the molecules where the electron states are localized (the centers of localization) and the coordinates of the particles of the surrounding medium. Therefore, the index s in product (7) numbers all these modes.

Note that the expression of potential energy of local vibration as a quadratic polynomial (see Eq. (5)) is valid for small deflection from the equilibrium position. In other words, the energy of the local oscillator should be much smaller than the energy of dissociation on corresponding coordinates. But for the delocalized crystal vibrations, i.e. phonons, the quadratic expression of the potential energy is always valid because the deflections of the nuclei from the equilibrium position are small at any energy of a phonon. Anharmonic terms in Hamiltonian of the crystal vibrations do not give the noticeable contribution in the energy of the crystal, but they are important in the kinetic processes, for example, in the thermal conduction.

Lam Research Ex. 1035 - Page 22
Lam Research Corp. v. Inpria Corp.
IPR2024-00033 - U.S. Patent No. 9,823,564

3. General Expression for Transition Probability in Unit of Time

The nuclear wave functions $\chi^{\mu}_{n_s}(q_s)$, corresponding to different electronic terms, i.e. for different μ, are not orthogonal with each other, $\langle\chi^{\mu}_{n_s}|\chi^{\nu}_{n'_s}\rangle \neq 0$ at $\mu \neq \nu$ for any n_s and n'_s. It is this non-orthogonality that is the principal reason for the population change in many modes of the vibration system (multi-phonon transition), as it was first noticed by Frenkel' [3].

Generally speaking, the adiabatic wave function (2) is not a stationary one because it is not the eigen function of total Hamiltonian of the system (1). In reality, the electron wave function $\psi_{\mu}(r; R)$ depends on R and so the differential operator $\hat{T}_{\mathrm{R}}$ acts not only on $\chi^{\mu}(R)$, but also on $\psi_{\mu}(r; R)$. It results in appearance of non-adiabatic correction operator in the basis of functions (2)

$$\hat{H}_{\mathrm{na}} = -\sum_i \left[\frac{1}{M_i}\frac{\partial\psi(r;R)}{\partial R_i}\frac{\partial\chi(R)}{\partial R_i} + \frac{1}{2M_i}\chi(R)\frac{\partial^2\psi(r;R)}{\partial R_i^3}\right]. \tag{8}$$

The operator (8) may be the cause of non-adiabatic transitions between initial and final adiabatic electron terms. These terms are denoted sometimes as diabatic ones since the interactions between these terms do not take into account the definition of the terms. The reason of the transitions between diabatic terms may not only be operator (8), but any interaction operator V that also does not take into account definition of the terms. For the optic transitions, V is the interaction of the electrons with the alternating electromagnetic field; for the radiationless transitions between the electron states localized on one center, V is the non-adiabatic interaction (8). In the case of donor–acceptor tunneling electron transition at long distance, the interaction V causing the transition is the tunneling operator, V_{tun}, the definition of which is given in Chapter 3. Considered below in general is the inter-center electron transfer.

It is assumed that the system in initial state is in the statistic equilibrium. According to the "gold rule", the rate constant of the electron–nuclear transition is

$$W_{\mathrm{if}} = \frac{2\pi}{\hbar}|V_{\mathrm{if}}|^2 A v_{n_s^{\mathrm{i}}}\left\{\sum_{n_p^{\mathrm{f}}}\prod_{s,p}\langle n_s^{\mathrm{i}}|n_p^{\mathrm{f}}\rangle^2\delta\left(E_{\mathrm{i\,min}} - E_{\mathrm{f\,min}} + \sum_s \hbar\omega_s^{\mathrm{i}}\left(n_s^{\mathrm{i}} + \frac{1}{2}\right)\right.\right.$$
$$\left.\left. - \sum_p \hbar\omega_p^{\mathrm{f}}\left(n_p^{\mathrm{f}} + \frac{1}{2}\right)\right)\right\}. \tag{9}$$

Lam Research Ex. 1035 - Page 23
Lam Research Corp. v. Inpria Corp.
IPR2024-00033 - U.S. Patent No. 9,823,564

Here, $Av_{n_s^i}$ denotes statistic averaging on the initial equilibrium populations of the vibration modes, and it is introduced with the designation

$$\langle n_s^i | n_p^f \rangle \equiv \langle \chi_{n_s}^i(q_s^i) | \chi_{n_p}^f(q_p^f) \rangle. \tag{9a}$$

At the optic transition (absorption or radiation of the electromagnetic wave with frequency Ω_0), it should put in the value $\Delta E + \hbar\Omega_0$ to δ-function in the expression (9) instead of the difference of electron energies:

$$\Delta E = E_{\text{i min}} - E_{\text{f min}}. \tag{9b}$$

The space–energy scheme of the transition in the one-mode case is represented on Figure 2.1.

The expression (9) for the non-adiabatic transition probability is correct, naturally, if the phonon spectrum is quasi-continuous one. Moreover, use of Fermi's "gold rule" or the first order of the perturbation theory on V_{if} is correct, if the following inequality is realized.

$$|V_{\text{if}}| << \Delta E_{\text{eff}}. \tag{10}$$

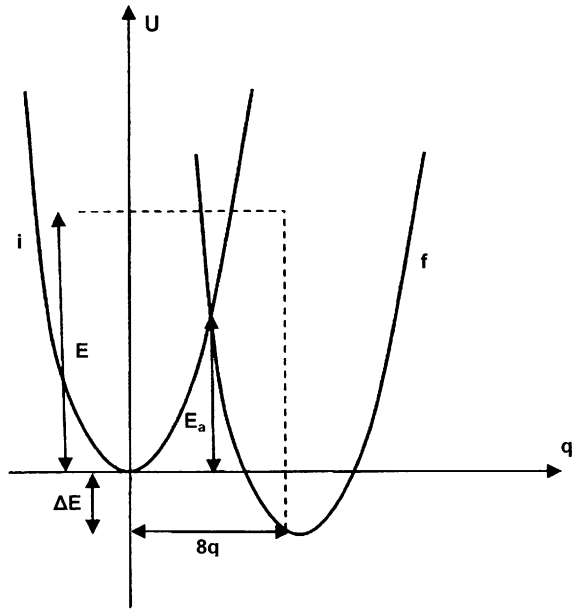


Fig. 2.1. The energy scheme of one-oscillator model. The indexes i, f denote initial and final vibration terms. It shows the reorganization energy E_r, the transferred energy (reaction heat) ΔE, and the activation energy E_a (see formula (30) in the text).

Lam Research Ex. 1035 - Page 24
Lam Research Corp. v. Inpria Corp.
IPR2024-00033 - U.S. Patent No. 9,823,564

Here, ΔE_{eff} is the typical energy scale where the rate constant W_{if} may be substantially varied, i.e.

$$\frac{d|\ln W_{\text{if}}|}{d\,\Delta E} << \frac{1}{|V_{\text{if}}|}. \tag{10a}$$

The goal of the theory of multi-phonon transitions is to calculate the rate constant (9) and to determine its dependence on the energy defect ΔE and the temperature T. This problem was resolved for the first time in the works described in Refs. [1, 2] for the case of Einstein's crystal, i.e. all phonons participating in the electron transition have the same frequency ω. It took into account only the shift of the equilibrium positions, and the result was obtained by straight calculation of the number of distributions of the energy ΔE on the phonon modes.

Generally, the following three cases are possible.

(1) The system of normal coordinates in the initial state q_s^{i} does not coincide with the one in the final state q_p^{f}.
(2) The frequencies of the vibration modes are different in the initial and final states even at coincidence of the normal coordinates.
(3) The equilibrium positions in the vibration modes are shifted in the final state relative to the initial ones.

It is these changes in the vibration system due to which the multi-vibration transitions are possible, which are considered below in this chapter.

4. Influence of Changes of Equilibrium Positions and Frequencies

Let us examine the multi-phonon electron transitions when the change of large number of the medium vibration modes takes place. The set of normal phonon modes can be changed only at the strong local disturbance of the lattice symmetry near the electron center. Such disturbance is usually very small and its influence on the rate constant is negligible as compared to the influence of the shift of the equilibrium positions. The medium polarization change denotes, in particular, the shift of equilibrium positions of the phonon coordinates. But in the case of the local modes, for example, molecular vibrations or vibrations of a solvation sphere, the change of set of normal modes should be taken into account since disturbing the geometry of center at electron transitions is a sufficiently frequent phenomenon.

Lam Research Ex. 1035 - Page 25
Lam Research Corp. v. Inpria Corp.
IPR2024-00033 - U.S. Patent No. 9,823,564

One will start with the study of influence of the shift in the phonon equilibrium positions and the change of the phonon frequencies on the rate constant $W_{if}(\Delta E, T)$ (Eq. (9)). On changing the location of a center electron state, the distances between the equilibrium positions of only a small number of crystal particles near the center change simultaneously. Let us prove it in the case of electron transfer from one center to another. Then, the shift of the distance between the crystal particles is stimulated by the change of Coulomb field. Let us find the change of the distance between adjacent particles, $\delta \boldsymbol{R}_i = \delta(\boldsymbol{R}_i - (\boldsymbol{R}_i + \boldsymbol{d}))$, where $\boldsymbol{d}$ is the lattice vector. If $R_i \gg d$, then $\delta \boldsymbol{R}_i \sim \nabla \boldsymbol{F}_i \boldsymbol{d}$, where $\boldsymbol{F}_i$ is the addition force acting on the crystal particle at the point $\boldsymbol{R}_i$. This force in the atomic crystals, for example, the noble gas crystal, is a polarization force; thus, $\boldsymbol{F}_{ia} \sim R_i^{-5}$. $\boldsymbol{F}_i \sim R_i^{-3}$ in molecular crystals with dipole molecules. In ionic crystals, the change of distance $\boldsymbol{a}$ between two ions in i-th crystal cell $\delta \boldsymbol{R}_i$ is proportional to $\nabla \boldsymbol{F}_{i0}$, $\delta \boldsymbol{R}_i \sim \nabla \boldsymbol{F}_{i0}\ \boldsymbol{a}$, where $\boldsymbol{F}_{i0} \sim R_i^{-2}$.

The change of the equilibrium position of the phonon mode dimensionless coordinate with wave vector $\boldsymbol{k}$ induced by the displacement of lattice particles in this case can be written as [8]:

$$\delta \vec{q}_{\vec{k}} = \sqrt{\frac{M\omega_k}{\hbar}} \frac{1}{\sqrt{N}} \sum_i \delta \vec{R}_i \, e^{i\vec{k}\vec{R}_i}. \tag{11}$$

Here, M is the reduced mass for the optic oscillation in the cell, or the mass of crystal cell for the acoustic phonons; ω_k the mode frequency; and N the number of cells in the macro-crystal. It is easy to see that the sum in Eq. (11) converges for all types of the displacements $\delta \boldsymbol{R}_i$ due to the rapid decrease in $\delta \vec{R}_i$ with the increasing distance from the center R_i. Therefore, the lattice particles located near the center only give the real contribution to the sum. The number N is very large, so the displacement $\delta \vec{q}_{\vec{k}}$ for each mode is very small. Then, one may take into account the first few terms only in the expansion of the final phonon wave function on displacement δq:

$$\chi_n(q_f) \equiv \chi_n(q_i + \delta q_i) = \chi_n(q_i) + \frac{\partial \chi_n(q_i)}{\partial q_i} \delta q_i + \frac{1}{2} \frac{\partial^2 \chi_n(q_i)}{\partial q_i^2} (\delta q_i)^2 + \cdots. \tag{12}$$

Using the known expressions for the oscillator wave function to find the phonon matrix elements $\langle n^{\mathrm{i}} | n^{\mathrm{f}} \rangle$ in the expression (9), one ought to keep only such matrix elements that when squared have a smallness $\sim 1/N$. These are the ones where $n^{\mathrm{f}} = n^{\mathrm{i}}$, $n^{\mathrm{f}} = n^{\mathrm{i}} \pm 1$ (the remainder matrix elements give

Lam Research Ex. 1035 - Page 26
Lam Research Corp. v. Inpria Corp.
IPR2024-00033 - U.S. Patent No. 9,823,564

the smallness of the greater order of $1/N$):

$$\begin{gathered}\langle\chi_{n_q}(q^{\mathrm{i}})|\chi_{n_q}(q^{\mathrm{f}})\rangle = 1 - \tfrac{(\delta q)^2}{2}\left(n_q + \tfrac{1}{2}\right),\\ \langle\chi_{n_q}(q^{\mathrm{i}})|\chi_{n_q+1}(q^{\mathrm{f}})\rangle = \delta q\sqrt{\tfrac{n_q}{2}},\\ \langle\chi_{n_q}(q^{\mathrm{i}})|\chi_{n_q-1}(q^{\mathrm{f}})\rangle = -\delta q\sqrt{\tfrac{n_q+1}{2}}.\end{gathered} \tag{12a}$$

Then, the summation of the squared matrix elements on the modes in the expression (9) gives the finite value since the mode number is equal to N and the squared matrix element (Eq. (12)) is proportional to $1/N$ owing to Eq. (11).

Let us consider the result of the phonon frequencies shift at the transition. This shift is caused by the local change of the interaction between the lattice particles. Then, the shift of frequency of each mode may be written as [4]:

$$\delta\omega_q = \omega_q \frac{B_q}{N} \tag{13}$$

where B_q is the numerical coefficient. An oscillator wave function $\chi_n(q)$ depends on the frequency ω through the dimensionless coordinates q, $\chi_n(q) \equiv \chi_n(\sqrt{M\omega/\hbar}x_q)$, where x_q is the dimensional vibration coordinate. Then, expanding $\chi_n(q^{\mathrm{f}}) \equiv \chi_n(\sqrt{M(\omega_i + \delta\omega_i)/\hbar}x_q)$ on the small value $\delta\omega_i$ and using the expression (13) one can find:

$$\chi_n(q^{\mathrm{f}}) = \chi_n(q^{\mathrm{i}}) + \frac{\partial\chi_n(q^{\mathrm{i}})}{\partial q^{\mathrm{i}}}\frac{1}{2}q^{\mathrm{i}}\frac{B_q}{N}. \tag{13a}$$

Now, it is easy to see that the frequency shift may influence only the diagonal matrix elements $\langle n^{\mathrm{i}}|n^{\mathrm{f}}\rangle$ similarly to the expansion (12), since the squared non-diagonal elements $\sim N^{-2}$,

$$\langle\chi_n(q^{\mathrm{i}})|\chi_n(q^{\mathrm{f}})\rangle = 1 - \frac{B_q}{4}\frac{1}{N}. \tag{13b}$$

Then, it should write in the first equality (12a)

$$\langle\chi_{n_q}(q^{\mathrm{i}})|\chi_{n_q}(q^{\mathrm{f}})\rangle = 1 - \left[\frac{(\delta q)^2}{2} + \frac{B_q}{4N}\right]\left(n_q + \frac{1}{2}\right). \tag{14}$$

If one takes into account the frequency amendment (13) in the δ-function of energy in the expression (9) (this amendment contains the difference of the frequencies in the argument of δ-function), then instead of ΔE the following expression should be substituted:

$$\tilde{\Delta}E = \Delta E - \frac{1}{N}\sum_q B_q\hbar\omega_q\left(n_q + \frac{1}{2}\right). \tag{15}$$

Lam Research Ex. 1035 - Page 27
Lam Research Corp. v. Inpria Corp.
IPR2024-00033 - U.S. Patent No. 9,823,564

Just the energy $\tilde{\Delta}E$ is compensated by the change of the quanta number in the different modes at the electron transition.

5. Calculation of Multi-Phonon Transition Probability in Unit of Time

As stated above, expression (9) for the rate constant of transition in Einstein's crystal was first calculated analytically by the method of the straight search in the pioneer works of Pekar [1] and Kun and Rhys [2]. Their analytic expression remains till now the unique exact expression for multi-phonon transition probability in the time unit. Then, there appeared different methods that permit to derive the integral expressions for the rate constant in the general case of the phonon frequencies dispersion: the operator calculation method [5], the method of generating polynomial [6], and the method of density matrix [7]. The detailed consideration of these methods was made in the Perlin's review [9].

Let us design the scheme of the probability calculation according to Lax [5]. Note, the frequency shift was not taken into account in this work. It will be done here by the substitution of the expressions (14) and (15) in the corresponding matrix elements and δ-function of energy. Using the integral representation of δ-function, the expression (9) may be written as:

$$W = \frac{|V_{\mathrm{if}}|^2}{\hbar} \int_{-\infty}^{\infty} dt\, I_{\mathrm{if}}(t), \tag{16}$$

where

$$I_{\mathrm{if}}(t) = A v_{n_{\mathrm{i}}} \left\{ \sum_{\{n_{\mathrm{f}}\}} \exp\left\{ \frac{i}{\hbar} [\hat{H}_{\mathrm{i}}(q) - \hat{H}_{\mathrm{f}}(q) + \Delta E]t \right\} |\langle n_{\mathrm{i}} | n_{\mathrm{f}} \rangle|^2 \right\}. \tag{17}$$

It may obtain after the simple operator transformation (see the works [5, 9])

$$I_{\mathrm{if}}(t) = A v_{n_{\mathrm{i}}} \left\{ \langle n_{\mathrm{i}}| \exp\left\{ \frac{i}{\hbar} [\hat{H}_{\mathrm{i}}(q) - \hat{H}_{\mathrm{f}}(q) + \Delta E]t \right\} |n_{\mathrm{i}}\rangle \right\}. \tag{17a}$$

The difference of the operators in the exponent (17a)

$$H_{\mathrm{i}}(q) - H_{\mathrm{f}}(q) = \sum_s \frac{\hbar\omega_s}{2} [(\delta q_s)^2 + 2 q_s \delta q_s] \tag{18}$$

is not diagonal in relation to the wave functions $|n_s\rangle$. Then, the expression (18) in the different points of time does not commute with each other. The technique of the time-sequenced operators [10,11] is used for the calculation

Lam Research Ex. 1035 - Page 28
Lam Research Corp. v. Inpria Corp.
IPR2024-00033 - U.S. Patent No. 9,823,564

of the integral in the formula (16). Besides, averaging on n_i in the expression (17a) denotes that n_i in the resulting expression should be replaced by the equilibrium values $\bar{n}_i$ at temperature T

$$\bar{n}_i = \frac{1}{e^{\hbar\omega_i kT} - 1}, \quad \bar{n}_i + \frac{1}{2} = \coth\left(\frac{\hbar\omega_i}{2kT}\right). \tag{19}$$

It is necessary to consider only the matrix elements (12a), (14) and the formula (15) at the integral calculations in the expression (17a). As a result, the integral expression for the transition probability in the unit of time is obtained, where the displacements of the phonon equilibrium positions and frequencies are taken into account simultaneously (see the detailed derivation but without the frequencies shift in Refs. [5, 8]):

$$W(\Delta E, T) = \frac{|V_{12}|^2}{\hbar^2} \int_{-\infty}^{\infty} dt\, I(t) \exp\left\{-\frac{it}{\hbar}\tilde{\Delta}E\right\}, \tag{20}$$

where

$$I(t) = e^{-\tilde{B}/4} \exp\left\{\frac{1}{2}\sum_s (\delta q_s)^2 \frac{\cosh((\hbar\omega_s/2kT) + i\omega_s t) - \cosh(\hbar\omega_s/2kT)}{\sinh(\hbar\omega_s/2kT)}\right\}, \tag{20a}$$

$$\tilde{\Delta}E = \Delta E - \frac{1}{N}\sum_s B_s \hbar\omega_s \coth\left(\frac{\hbar\omega_s}{2kT}\right). \tag{20b}$$

The integral in the expression (20) can be calculated exactly only in the absence of the frequency dispersion of the phonons, i.e. for Einstein's model of the crystal $\omega_s = \bar{\omega}$. Then, the expression for the rate constant of multi-phonon transition results from the formula (20):

$$W(\Delta E, T) = \frac{2\pi|V_{if}|^2}{\hbar^2\bar{\omega}} e^{-(\tilde{B}/4)} \exp\left\{-\frac{E_r}{\hbar\bar{\omega}}\coth\left(\frac{\hbar\bar{\omega}}{2kT}\right) + \frac{\tilde{\Delta}E}{2kT}\right\} \times I_{\tilde{\Delta}E/\hbar\bar{\omega}}\left(\frac{E_r}{\hbar\bar{\omega}\ \sinh(\hbar\bar{\omega}/2kT)}\right). \tag{21}$$

Here, $\tilde{\Delta}E$ is given in the expression (15) with the equal frequencies $\omega_s = \bar{\omega}$,

$$\tilde{B} = \frac{1}{N}\sum_s B_s \tag{21a}$$

Lam Research Ex. 1035 - Page 29
Lam Research Corp. v. Inpria Corp.
IPR2024-00033 - U.S. Patent No. 9,823,564

and $I_n(z)$ is Bessel function from the image argument. The value E_r is defined as

$$E_r = \frac{1}{2}\sum_s \hbar\omega_s(\delta q_s)^2, \tag{22}$$

and is called the reorganization energy. This term was introduced by Marcus [12], and its sense is sufficiently transparent. The reorganization energy is the potential energy in all modes of the initial state at the coordinates equal to the equilibrium positions in the modes of the final states. It may see on the one-mode model. The oscillator potential energy is $1/2Kx^2$, where the elasticity constant $K = M\omega^2$ and dimensionless coordinate $q = \sqrt{(M\omega/\hbar)}x$. Then, the resulting expression is similar to (32) but for one mode only (see Fig. 2.1). The total reorganization energy is the sum of corresponding energies in all modes.

The formula (21) coincides with the expression for the transition probability derived in works [1] and [2], if to neglect the frequency shift, i.e. to put $B_s = 0$ and $\Delta E = p\hbar\bar{\omega}$, where p is the integer. It should be noted that if the only one oscillator participates in the transition, the same expression (21) is valid without the frequency shift. It can be checked by the straight calculation of the matrix element $\langle\chi_{n_i}(q^i)|\big|\chi_{n_f}(q^f)\rangle$. It is this coincidence of the expressions for the probability that permits to model the multi-phonon transition by the transition with only one effective oscillator at the same values E_r and ΔE (see Fig. 2.1). The transition rate constant (21) as a function of $\Delta E = p\hbar\bar{\omega}$ is the set of equidistant "lines", i.e. the narrow curves. The envelope of the set is the asymmetric bell-shaped curve (see Fig. 2.2). Each such "line" is broadened by some stochastic process in order to tell about the rate constant. Of course, taking into account the phonon frequency dispersion makes this envelope curve continuous one but its form remains the same (21) at the reasonable choice of the frequency $\bar{\omega}$ that is near to the mean frequency of phonons giving the main contribution to the value (20a).

Let us consider now some important limits of the general formula (20), and one will assume below that the reorganization energy E_r is large, $E_r >> \hbar\omega$, where ω is the typical frequency giving the main contribution to the reorganization energy (22). The condition $E_r >> \hbar\omega$ is usually called as the condition of large energy liberation. It denotes the number of modes much bigger than unity where the equilibrium positions are strongly shifted at the transition. To obtain the approximate analytic expression for $W(\tilde{\Delta}E, T)$, calculate the frequency moments M_i of the function (20),

$$M_i = \int_{-\infty}^{+\infty} d\Omega\ \ \Omega^i W(\Omega; T), \qquad i = 0, 1, 2, \ldots;\ \ \Omega = \frac{\tilde{\Delta}E}{\hbar} \tag{23}$$

Lam Research Ex. 1035 - Page 30
Lam Research Corp. v. Inpria Corp.
IPR2024-00033 - U.S. Patent No. 9,823,564

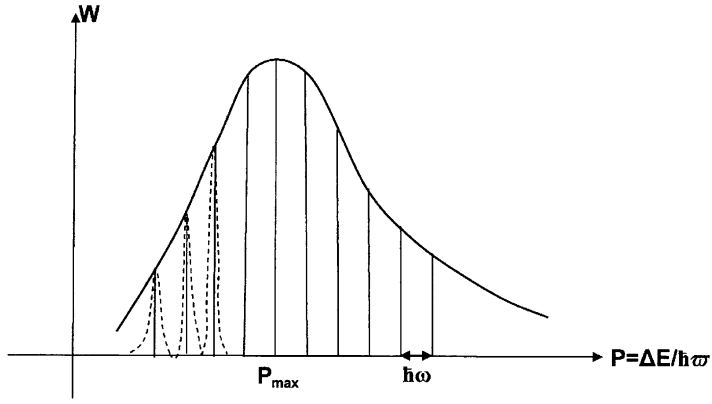


Fig. 2.2. The dependence of the rate constant for the charge transfer reactions W on the transferred energy (reaction heat) $\Delta E = p(\hbar\omega)$. The dotted lines show the function $W(\Delta E)$ at given p. The firm line is the enveloping curve of the dotted lines for different values of p.

The integral in the expression (20) is Fourier-transform of function I(t) (20a). If to return this Fourier-transform, i.e. to express $I(t)$ through $I(\Omega)$, it is easy to find the expressions for the frequency moments

$$M_i = \frac{2\pi|V_{\text{if}}|^2}{\hbar}\frac{\partial_i I(t)}{(\partial t)^i}|_{\,t=0} \tag{24}$$

that permits to simply calculate the moments M_i.

Then, comparing the moments (24) with the moments of Gauss curve $\varphi(\Omega)$,

$$\varphi(\Omega) \sim \exp\left\{-\frac{(\Omega-\bar{\Omega})^2}{2\sigma}\right\}, \tag{25}$$

one may see that $W(\Omega) \sim \varphi(\Omega)$ with good accuracy, if $\bar{\Omega} = M_1/M_0$ and the dispersion of Gauss curve (25) σ is equal to second moment relative $\bar{\Omega}$, $\sigma = (M_2/M_0) - (M_1/M_0)^2$. Third moment of the symmetric Gauss curve (25) relative mean frequency $\bar{\Omega}$ is equal to 0; it does not equal 0 for the asymmetric function $W(\Omega)$ but is much smaller than $\sigma^{3/2}$, i.e. the asymmetry of $W(\Omega)$ is small. It permits to consider the function $W(\Omega)$ as a Gauss curve where

$$\sigma = \frac{1}{2}\sum_s (\hbar\omega_s)^2(\delta q_s)^2 \coth\left(\frac{\hbar\omega_s}{2kT}\right), \tag{25a}$$

Lam Research Ex. 1035 - Page 31
Lam Research Corp. v. Inpria Corp.
IPR2024-00033 - U.S. Patent No. 9,823,564

and

$$W = \frac{|V_{\text{if}}|^2 \exp\{-\tilde{B}/4\}}{\hbar\sqrt{2\pi\sigma}} \exp\left\{\frac{(\tilde{\Delta}E - E_{\text{r}})^2}{2\sigma}\right\}, \tag{26}$$

$$\tilde{\Delta}E = \Delta E - \frac{1}{N}\sum_q B_q \hbar\omega_q \coth\left(\frac{\hbar\omega_q}{2kT}\right). \tag{27}$$

The last formula follows from Eqs. (15) and (19).

Consider the expressions for the transition probability at high and low temperatures. Let us start from the case of high temperature

$$\frac{\hbar\omega}{kT} << 1. \tag{28}$$

Then, the resulting expression for the rate constant deduced from the formulas (26) and (25a) is

$$W(\tilde{\Delta}E, T) = \frac{|V_{\text{if}}|^2 \exp\{-\tilde{B}/4\}}{2\hbar\sqrt{\pi E_{\text{r}} kT}} \exp\left\{-\frac{(E_{\text{r}} - \tilde{\Delta}E)^2}{4E_{\text{r}}kT}\right\} \tag{29}$$

where it follows from (27) and (28)

$$\tilde{\Delta}E = \Delta E - 2\tilde{B}kT. \tag{29a}$$

Note the inequality (28) corresponds to the high population of the crystal modes,

$$\bar{n}_s \approx \frac{kT}{\hbar\omega_s} >> 1,$$

i.e. the crystal modes may be considered as classical ones. Therefore, the transition in these modes is the classic thermally activated transition; Plank constant is present in expression (29) since the electron transition is a quantum one. On placing the expression (27a) in formula (29), one sees that the maximum of the transition probability as a function of ΔE shifts with temperature increasing [2,4] to the right or left of the axis ΔE depending on the sign of the value $\tilde{B}$ (21a). So, the shift of maximum of the rate constant on ΔE with temperature is explained by the shift of the phonon frequencies as a result of transition. The thermal activation energy (neglecting the frequency shift, $\tilde{B} = 0$)

$$E_{\text{a}} = \frac{(\Delta E - E_{\text{r}})^2}{4E_{\text{r}}kT} \tag{30}$$

Lam Research Ex. 1035 - Page 32
Lam Research Corp. v. Inpria Corp.
IPR2024-00033 - U.S. Patent No. 9,823,564

may be treated easily in the model of one effective mode (see Fig. 2.1), namely E_a is the difference of two energies: the energy where the terms are crossing and the minimum of initial term $E_{i\,min}$. It corresponds to the classic picture – the electron transition can occur only when the classic vibration system is excited until the energy E_a.

Note, the activation energy E_a decreases with the ΔE increase, if $E_r > \Delta E$. It is the manifestation of Polyany–Semenov general rule: the activation energy is lowered with the growth of the reaction heat ΔE. The activation energy in the electron transition reactions becomes 0 at $E_r = \Delta E$ (see Eq. (30)), but then E_a increases with the growth of ΔE. The electron transition in the electro-chemical reactions takes place in the region of the drastic potential drop. So, one may change ΔE by changing the bias. Then, one may really observe the activation energy behavior corresponding to formula (29) [13].

Let us consider now the transitions at low temperature. At first, one will investigate the case when the optical phonons only participate in the transition when the rate constant is described by the expression (21). It is assumed the temperature is so low that:

$$\frac{\hbar\bar{\omega}}{kT} >> 1, \quad \frac{E_r}{\hbar\bar{\omega}} >> \exp\left\{\frac{\hbar\bar{\omega}}{kT}\right\}. \tag{31}$$

As it follows from these inequalities, the argument of Bessel's function in the expression (21) is very small, and $\coth(\hbar\bar{\omega}/2kT) \approx 1$. The resulting formula can be deduced, if we take into account that $\tilde{\Delta}E/\hbar\bar{\omega} = p$, where p is integer and $I_p(x) = I_{-p}(x)$ [14],

$$W(\tilde{\Delta}E, T) = \frac{2\pi|V_{if}|^2}{\hbar^2\bar{\omega}} e^{-\tilde{B}/4} \times \left\{ \begin{array}{ll} \frac{e^{-E_r/\hbar\omega}}{p!}\left(\frac{E_r}{\hbar\bar{\omega}}\right)^p, & p>0 \\ \frac{e^{-E_r/\hbar\omega}}{p!}\left(\frac{E_r}{\hbar\bar{\omega}}\right)^p e^{\tilde{\Delta}E/kT}, & p<0 \end{array} \right\}. \tag{32}$$

The ground states of the vibration modes are only populated at low temperatures. If the energy is liberated in the transition, i.e. $p>0$, the transition occurs without activation, but when $E_{f\,min} > E_{i\,min}$, i.e. $p<0$, the activation energy $E_a = |\tilde{\Delta}E| = -\tilde{\Delta}E$.

The quite another temperature dependence of the rate constant at helium temperatures is resulted in the case when the principal contribution to dispersion σ in formula (25a) gives the acoustic phonons. Their frequencies lie in the interval $[0, \omega_D]$, where ω_D is Debye's frequency. Even if $\hbar\omega_D >> kT$, it exists always in the range of such low frequencies that $\hbar\omega < kT$. It is these phonons that give the contribution depending on the temperature in the dispersion σ [15]. One assumes that the displacements of the equilibrium positions of phonon modes δq_s do not depend on frequency. Then, the calculation of the rate constant gives at low temperatures, $\hbar\omega_D > kT$,

Lam Research Ex. 1035 - Page 33
Lam Research Corp. v. Inpria Corp.
IPR2024-00033 - U.S. Patent No. 9,823,564

the expression [15]:

$$\ln W_{\mathrm{if}}(T) = \ln W_{\mathrm{if}}(0) + C_6 T^6, \tag{33}$$

where C_6 is a constant depending on the characteristics of the medium and the particle undergoing the transition. It is this temperature dependence of the rate constant of the tunneling transition of hydrogen atom in hydrogenium molecule crystals that was observed experimentally in the work [16]. The reorganization of medium plays the leading role in the transition process, and the mass transferred does not influence the temperature dependence of the rate constant. At the tunneling of a light atomic particle, it may apply the same considerations as in electron tunneling, in particular, the adiabatic approach for the wave function. The temperature dependence is defined by the reorganization of the crystal phonons bounded with motion of this particle.

In the conclusion of this section, the electron transition in Condon's approach was examined, i.e. the dependence of electronic matrix element V_{if} on the vibration coordinates was neglected. Generally speaking, this dependence is always rather weak, so we should consider only the few first terms in the expansion

$$V_{\mathrm{if}}(q) = \sum_n \left.\frac{\partial_n V_{\mathrm{if}}(q)}{\partial q^n}\right|_{q=q_0} \frac{1}{n!}(q - q_0)^n,$$

where q_0 is the equilibrium position of the mode. It means taking this dependence into account will result in the birth or death of a few phonons that is much smaller than the total number of modes

$$N_{\mathrm{c}} \approx \frac{E_{\mathrm{r}}}{\hbar\bar{\omega}} >> 1,$$

where the populations change at the transition. Therefore, taking into account the dependence on phonons $V_{\mathrm{if}}(q)$ does not practically change the results (20) and (21). The spillover of Condon's approach at the calculation of the rate constant of a radiationless transition in one center was performed by Krivoglaz [17] by using the method of generating polynomial.

6. Local Vibrations. Method of Density Matrix

In the sections above, we have considered only the phonons where the maximal change of population in each mode is unity (see Eqs. (12) and (14)).

Lam Research Ex. 1035 - Page 34
Lam Research Corp. v. Inpria Corp.
IPR2024-00033 - U.S. Patent No. 9,823,564

But if we examine the localized near the donor or the acceptor crystal vibrations or intra-molecular vibrations, the electron transition may induce much larger changes in such modes. It may be the substantial shifts of the equilibrium positions, the frequencies, or at last, the change of the set of normal modes due to violation of the space structure of the centers. The local vibrations at electron transitions between the atomic centers in the polar medium are the oscillations of the rigid solvation spheres near the centers. Such vibrations are denoted by the inner-sphere vibrations in contrast to the outer-sphere vibrations of the medium. The expressions for the rate constant cited above are based on the smallness of the shift of the equilibrium position or the frequency in each mode (see Eqs. (11) and (13)). They may be useless for the case of local vibrations that are, as a rule, high-frequency ones. The general formal approach to the description of the electron transitions in such systems based on the method of density function was developed by Kubo and Toyozawa [7] within the bounds of the conception of the harmonic vibrations in the initial and final states.

The definition of the density matrix $\rho(\lambda)$ for the system with Hamiltonian $\hat{H}_{\mathrm{n}}$ is

$$\rho_{H_{\mathrm{n}}}(\lambda) = e^{-\lambda \hat{H}_{\mathrm{n}}} \tag{34}$$

where $\lambda = 1/kT$ in the statistical equilibrium. The formula (17a) can be expressed via density matrix, if we take into account the averaging on the equilibrium initial vibrations:

$$I_{\mathrm{if}}(t) = \frac{\mathrm{Tr}[\rho_{H_{\mathrm{f}}}(-it/\hbar)\rho_{H_{\mathrm{i}}}((1/kT) + (it/\hbar))]}{\mathrm{Tr}[\rho_{H_{\mathrm{i}}}(1/kT)]} e^{i(\Delta E/\hbar)t}. \tag{35}$$

It is convenient to convert to the coordinate representation of the density matrix of the vibration system to take into account the possible change of the set of normal coordinates. The Hamiltonian of the harmonic vibration system in the initial and final states may be expressed in the form:

$$\hat{H}_{\mathrm{i,f}} = \frac{1}{2}\left(\vec{X}\hat{\Omega}^2_{\mathrm{i,f}}\vec{X} - \hbar^2 \frac{\partial^2}{\partial \vec{X}^2}\right). \tag{36}$$

Here, $\vec{X}$ is the $3K$-dimensional vector consisting of K 3-dimensional vectors $\vec{x}_s = \sqrt{M_s}(\vec{R}_s - \vec{R}^0_s)$, where $s = 1, 2, 3, \ldots K$ numbers the nuclei in the system of the local vibrations, M_s is the mass of sth nucleus, $(\vec{R}_s - \vec{R}^0_s)$ is the vector of deviation from the equilibrium position $\vec{R}^0_s$, $\hat{\Omega}^2_{\mathrm{i,f}}$ are the frequency tensors of second rank in the initial and final states. Let us introduce such unitary operators $\hat{S}_{\mathrm{i,f}}$ that transformations $\vec{X} = \hat{S}_{\mathrm{i,f}}\vec{Y}$ reduce the quadratic

Lam Research Ex. 1035 - Page 35
Lam Research Corp. v. Inpria Corp.
IPR2024-00033 - U.S. Patent No. 9,823,564

forms (36) to diagonal ones:

$$\hat{H}_{\mathrm{i,f}} = \frac{1}{2}\sum_{s=1}^{3K}\left[(\omega_{\mathrm{i,f}}^{s})^2 y_s^2 - \hbar^2\frac{\partial^2}{\partial y_s^2}\right], \tag{36a}$$

where $(\omega_{\mathrm{i,f}}^{s})^2$ are the elements of the diagonal tensors of second rank

$$\hat{\omega}_{\mathrm{i,f}}^2 = \hat{S}^{-1}\hat{\Omega}_{\mathrm{i,f}}^2\hat{S}. \tag{36b}$$

The density matrix of one-dimensional oscillator in the coordinate representation is expressed as [18]:

$$\rho(y,y';\lambda) = \left(\frac{\omega}{2\pi\hbar\ \sinh(\lambda\cdot\hbar\omega)}\right)^{1/2}\exp\left\{-\frac{\omega}{4\hbar}\left[(y+y')^2\tanh\left(\frac{\lambda}{2}\hbar\omega\right)\right.\right.$$
$$\left.\left.+(y-y')^2\coth\left(\frac{\lambda}{2}\hbar\omega\right)\right]\right\} \tag{37}$$

One may obtain now (see [7]) the general expression of the density matrix of multi-dimensional system that is invariant to relation of the unitary transformation $\hat{S}$:

$$\rho_{\mathrm{i,f}}(\vec{X},\vec{X}';\lambda) = [\det(2\pi\hbar\hat{\Omega}_{\mathrm{i,f}}^{-1}\ \sinh(\hat{\Omega}\lambda))]^{-1/2}$$
$$\times\exp\left\{-\frac{1}{4\hbar}\left[(\vec{X}+\vec{X}')\hat{\Omega}_{\mathrm{i,f}}\ \tanh\left(\frac{\hbar\hat{\Omega}_{\mathrm{i,f}}\lambda}{2}\right)\right.\right.$$
$$\left.\left.\times(\vec{X}+\vec{X}')+(\vec{X}-\vec{X}')\hat{\Omega}_{\mathrm{i,f}}\coth\left(\frac{\hbar\hat{\Omega}_{\mathrm{i,f}}\lambda}{2}\right)(\vec{X}-\vec{X}')\right]\right\} \tag{38}$$

This formula should be substituted in expression (34), which then results in:

$$I_{\mathrm{if}}(t) = e^{i(\Delta E/\hbar)t}\det\left[2\ \sinh\frac{\hbar\hat{\Omega}_i}{2kT}\right]\iint d\vec{X}\ d\vec{X}'\rho_{\mathrm{i}}\left(\vec{X}-\vec{X}_{\mathrm{i}},\vec{X}'-\vec{X}_{\mathrm{i}};\frac{1}{kT}+\frac{it}{\hbar}\right)$$
$$\times\rho_{\mathrm{f}}\left(\vec{X}-\vec{X}_{\mathrm{f}},\vec{X}'-\vec{X}_{\mathrm{f}};-\frac{it}{\hbar}\right). \tag{39}$$

The difference of the equilibrium positions $\vec{X}_{\mathrm{i}}$ and $\vec{X}_{\mathrm{f}}$ in the initial and final states is specifically underlined here. The integral in expression (39) is the counterpart of the operation of trace in formula (35), and it can be integrated analytically due to the forms on $\vec{X}$ and $\vec{X}'$ in the exponent of the expression (38), which are the quadratic ones.

Lam Research Ex. 1035 - Page 36
Lam Research Corp. v. Inpria Corp.
IPR2024-00033 - U.S. Patent No. 9,823,564

Finally, after long transformation (see the articles in Refs. [7] and [8]), the resulting expression for the rate constant is:

$$W(\Delta E, T) = \frac{|V_{\mathrm{if}}|^2}{\hbar^2} \int dt\, e^{-f(t,T)}, \tag{40}$$

where

$$f(t,T) = i\frac{\Delta E}{\hbar}t + \vec{\Delta}\hat{\Theta}_{\mathrm{i}}[\hbar(\hat{\Theta}_{\mathrm{i}} + \hat{\Theta}_{\mathrm{f}})]^{-1}\hat{\Theta}_{\mathrm{f}}\vec{\Delta} + \frac{1}{2}Sp\ln\left\{2\left(\sinh\frac{\hbar\hat{\Omega}_{\mathrm{i}}}{2kT}\right)^2\hat{\Omega}_{\mathrm{i}}^{-1}\sinh\left(\frac{\hbar\hat{\Omega}_{\mathrm{i}}}{kT} + i\hat{\Omega}_{\mathrm{i}}t\right) \times (\hat{\Theta}_{\mathrm{i}} + \hat{\Theta}_{\mathrm{f}})(\hat{\Phi}_{\mathrm{i}} + \hat{\Phi}_{\mathrm{f}})\hat{\Omega}_{\mathrm{f}}^{-1}\sinh(-i\hat{\Omega}_{\mathrm{f}}t)\right\}. \tag{41}$$

Here, the following terms are introduced:

$$\vec{\Delta} = \vec{X}_{\mathrm{f}} - \vec{X}_{\mathrm{i}}. \tag{42}$$

$$\hat{\Theta}_{\mathrm{i}} = \hat{\Omega}_{\mathrm{i}}\tanh\left(\frac{\hbar\hat{\Omega}_{\mathrm{i}}}{2kT} + i\frac{\hat{\Omega}_{\mathrm{i}}}{2}t\right); \quad \hat{\Theta}_{\mathrm{f}} = -\hat{\Omega}_{\mathrm{f}}\tanh\left(i\frac{\hat{\Omega}_{\mathrm{f}}}{2}t\right), \tag{42a}$$

$$\hat{\Phi}_{\mathrm{i}} = \hat{\Omega}_{\mathrm{i}}\coth\left(\frac{\hbar\hat{\Omega}_{\mathrm{i}}}{2kT} + i\frac{\hat{\Omega}_{\mathrm{i}}}{2}t\right), \quad \hat{\Phi}_{\mathrm{f}} = -\hat{\Omega}_{\mathrm{f}}\coth\left(i\frac{\hat{\Omega}_{\mathrm{f}}}{2}t\right). \tag{42b}$$

Naturally, the expression for the rate constant (40) with $f(t)$ defined by (6.10) coincides with the expressions (16) and (17), if the phonons only participate in the transition and the change of the set of normal modes should not be taken into account.

The complicated function (41) may be used for calculation of the rate constant, if the tensors $\hat{\Omega}_{\mathrm{i}}$ and $\hat{\Omega}_{\mathrm{f}}$ are known. So, the number of the reorganizing local vibrations should be small in order to calculate the change of the geometry and the force constants at electron transition. The potential energy of the vibration localized near acceptor may decline on the parabolic form, if the energy ΔE transmitted in the local vibration is sufficiently large. Then, the formulas (40) and (41) are useless, and it is necessary to simpliciter calculate the matrix elements $\langle\psi(q_{\mathrm{i}})|\psi(q_{\mathrm{f}})\rangle$ in the expression (9).

The energy ΔE is distributed among both the local modes and the medium modes. Then, while calculating the total transition probability, one should consider the different ways of the energy distribution on the inner-sphere

Lam Research Ex. 1035 - Page 37
Lam Research Corp. v. Inpria Corp.
IPR2024-00033 - U.S. Patent No. 9,823,564

and outer-sphere degrees of freedom

$$W_{\mathrm{if}}(\Delta E, T) = \frac{2\pi}{\hbar^2} |V_{\mathrm{if}}|^2 \int d\Omega_1 I_{\mathrm{loc}}(\Omega_1) I_{\mathrm{med}} \left(\frac{\Delta E}{\hbar} - \Omega_1 \right). \tag{43}$$

Here, the energies $\hbar\Omega_1$ and $\Delta E - \hbar\Omega_1$ are distributed on the inner-sphere and outer-sphere vibrations correspondingly, and

$$I(\Omega) = \int \mathrm{d}t \, I(t) \tag{44}$$

where the function $I_{\mathrm{loc}}(t)$ is given by the expression (20a) and $I_{\mathrm{med}}(t)$ is the exponent $\exp\{f(t, T)\}$, $f(t, T)$ given by the formula (41).

7. Electron Transfer in Polar Medium

The electron transfer in polar medium is characterized by, first, the strong interactions of the donor and acceptor ions with the polar medium and, second, the large reorganization energy of the medium. First, the medium outer-sphere polarization energy at the purely classic examination of electron transfer was considered by Marcus [12]. Then, Levich, Dogonadze and Kuznetsov with their collaborators have applied the quantum approach to multi-vibration transitions, considered in the above sections of this chapter, to the description of the reactions of electron transfer [19–23]. The polar liquids were described in these works by the set of oscillators that permits to apply the theory of multi-phonon transition to the electron transfer in liquids. The division of the degrees of freedom on the outer-sphere phonons describing the classic polarization and the intra-sphere local vibrations was well defined. The contribution of last ones is given by the expressions (40) and (41). The outer-sphere contribution is described by the expression (20), or by (29) at high temperature.

For the closed description of the electron transfer in polar medium, it is necessary to express the reorganization energy in the formula (27) via the characteristics of polar media (it is assumed that the high-temperature approach can be always applied to the outer-sphere degrees of freedom). It was done in the works [12, 19, 23], and most consistently in the work of Ovchinnikov and Ovchinnikova [24] where the frequency dependence of the medium dielectric permittivity $\varepsilon(\omega)$ is taken into account exactly, but the spatial dispersion was neglected.

The interaction of the charge system of the donor (or acceptor) with the linear dielectric medium is described in the form

$$V_{\mathrm{i,f}} = \iint d\vec{r} \, d\vec{r}' \rho_{\mathrm{i,f}}(\vec{r}) \frac{(\vec{r} - \vec{r}')}{\left|\vec{r} - \vec{r}'\right|^3} \vec{P}(\vec{r}'). \tag{45}$$

Lam Research Ex. 1035 - Page 38
Lam Research Corp. v. Inpria Corp.
IPR2024-00033 - U.S. Patent No. 9,823,564

Here, $\rho_{i,f}(\vec{r})$ is the charge density in donor or acceptor and $\vec{P}(\vec{r}')$ is the density of the medium polarization. This interaction changes the directions of the medium dipoles in the same way as the interaction of donor and acceptor with a crystal results in the shift of the equilibrium positions of phonons.

The resulting expression for $I(\Delta E, t)$ in the homogenous polar medium is similar to expression (20a); the sum on the modes is replaced by the sum on the frequencies

$$I_{\text{pol}}(\Delta E, t) = \exp\left\{\frac{1}{8\pi^2\hbar}\int d\vec{r}\,[\Delta\vec{D}(\vec{r})]^2 \int \frac{\varepsilon''(\omega)}{\omega^2\left|\varepsilon(\omega)\right|^2} \times \frac{\cosh\left(\frac{\hbar\omega}{2kT} - i\omega t\right) - \cosh\left(\frac{\hbar\omega}{2kT}\right)}{\sinh\left(\frac{\hbar\omega}{2kT}\right)}\, d\omega - i\frac{\Delta E}{\hbar}t\right\} \tag{46}$$

Here, $\varepsilon''(\omega)$ is the image part of the dielectric permittivity $\varepsilon(\omega)$, and $\Delta\vec{D}(\vec{r})$ is the difference of the values of electrostatic induction in the initial and final states; this difference is caused by the electron transfer:

$$\Delta\vec{D}(\vec{r}) = \varepsilon_0 q_e\left[\frac{\vec{r}-\vec{R}_i}{\left|\vec{r}-\vec{R}_i\right|^3} - \frac{\vec{r}-\vec{R}_f}{\left|\vec{r}-\vec{R}_f\right|^3}\right]. \tag{47}$$

In this formula, $\varepsilon_0 = \varepsilon(0)$ is the static permittivity, q_e is the electron charge, $\vec{R}_{i,f}$ are the donor and acceptor coordinates.

The expression

$$\frac{1}{8\pi^2}\int d\vec{r}\,[\Delta\vec{D}(\vec{r})]^2 = E_{\text{r stat}}, \tag{48}$$

is the reorganization energy of the polar medium in the static limit. Firstly the value $E_{\text{r stat}}$ was introduced by Marcus [12]. As a rule, $E_{\text{r stat}} \gg kT$ for room temperatures. It is similar to the criterion of the large energy liberation. Then, $W_{\text{if}}(\Delta E, T)$ has a Gaussian form. The parameters of it may be found by calculation of the moments (see formulas (24) and (25)), or via the calculation by the steepest descent method of the integral in (20) with $I_{\text{pol}}(\Delta E, t)$ from the formula (46). The resulting expression is:

$$W_{\text{if}}(\Delta E, T) = \frac{|V_{\text{if}}|^2}{\hbar\sqrt{\pi g(T)}} e^{-(E_r^{\text{pol}} - \Delta E)^2/g(T)} \tag{49}$$

where E_r^{pol} is the total reorganization energy of the polar medium,

$$E_r^{\text{pol}} = E_{\text{r stat}}\int d\omega\, \frac{\varepsilon''(\omega)}{\omega\left|\varepsilon(\omega)\right|^2}, \tag{50}$$

Lam Research Ex. 1035 - Page 39
Lam Research Corp. v. Inpria Corp.
IPR2024-00033 - U.S. Patent No. 9,823,564

and function $g(T)$ is

$$g(T) = 2E_{\text{r stat}} \int d\omega \, \frac{\varepsilon''(\omega)}{\left|\varepsilon(\omega)\right|^2} \coth\left(\frac{\hbar\omega}{2kT}\right). \tag{51}$$

At high temperatures, $\hbar\omega/kT \ll 1$; it is valid to approximate equality $\coth(\hbar\omega/2kT) \approx 2kT/\hbar\omega$, and the resulting expression for the rate constant of electron transfer in polar medium will be the expression (29), where E_r is given by the expressions (50) and (48).

The integral in the expression (48) for $E_{\text{r stat}}$ diverges near R_i and R_f. Naturally, the down limits in the integration are radii of the solvation spheres near the donor and acceptor (r_i and r_f). If the donor and acceptor are the atomic ions, $r_i \approx r_f$. The radius r_i at room temperature is approximately, on the order of value, equal to the mean distance between the molecules of polar medium. At such distances, one need to take into account the space dispersion of the dielectric permittivity [25,26], i.e. to examine $\varepsilon(\vec{k}, 0)$. As a rule, $\varepsilon(\vec{k}, 0) < \varepsilon_0$, i.e. the true $E_{\text{r stat}}$ is smaller than in expression (48).

Note, $E_{\text{r stat}}$ depends on the inter-center distance $R_{if} = |\boldsymbol{R}_i - \boldsymbol{R}_f|$ according to formulas (47) and (48). But usually, this dependence is purely a formal one since the part of $E_{\text{r stat}}$ depending on R_{if} is proportional to $(r_i/R_{if})^2 \ll 1$.

The theory of electron transfer in polar media is considered in detail in Kuznetsov's book [13] where numerous references on the different problems are cited. It should be noted that the tunneling transfer of protons accompanied by the reorganization of the vibration degrees of freedom may be examined in the same way as the electron transfer. The theory of this phenomenon is investigated in details in the monograph of Gol'danskii, Trakhtenberg and Flerov [28], and also in Ref. [13].

8. Adiabatic Transitions

Now, the non-adiabatic electron transitions is examined only when electron matrix element $|V_{if}|$ is small (see the criterion (10) and (10a)). It is the criterion of applicability of the perturbation theory on $|V_{if}|$, but it is not the criterion of applicability of the concept of non-adiabatic transition between two crossing diabatic terms. As it is known (see, for example, ref. [5]) the true image of terms is changed on taking into account the interaction V. Denote two terms without inter-term interaction as $E_i(R)$ and $E_f(R)$, where R is the generalized nuclear coordinate. If the crystal phonons (or the outer-sphere variables in a polar medium) only participate in the transition, then $E_i(R)$ and $E_f(R)$ are the parabolic terms independent of the value of shift of

Lam Research Ex. 1035 - Page 40
Lam Research Corp. v. Inpria Corp.
IPR2024-00033 - U.S. Patent No. 9,823,564

the equilibrium positions and the reorganization energy. The exact terms $E^{ex}_{1,f}(R)$while taking into account the interaction V are described by the expressions

$$E^{ex}_{1,2}(R) = \frac{E_i(R) + E_f(R)}{2} \pm \sqrt{\frac{[E_i(R) - E_f(R)]^2}{4} + V^2_{if}}. \quad (52)$$

The terms $E^{ex}_{1,2}(R)$ at the point R^* of crossing of the terms $E_i(R)$ and $E_f(R)$ differ by the value $2|V_{if}|$,

$$E^{ex}_{1,2}(R^*) = E(R^*) \pm |V_{if}|. \quad (53)$$

The new image of the terms is shown in Figure 2.3.

The combined lower term $E^{ex}_2(R)$ corresponds to the initial electron state (the electron is localized near the donor) at coordinates near the point of minimum R_i where $|E_i(R) - E_f(R)| >> |V_{if}|$, and in the same way, term $E^{ex}_2(R)$ corresponds to the final state (the electron is localized near the acceptor) near the minimum R_f. Near the point R^*, the term $E^{ex}_2(R)$ corresponds to some mixture of the states i and f, i.e. electron is spread on the donor–acceptor pair in this region of coordinate R. But, far from the point R^* where$|E_1(R) - E_2(R)| >> |V_{if}|$, it is not necessary to consider the change of the structure of terms. At low temperature when $\exp(-E_a/kT) << 1$, E_a is the activation energy (30), the expression (32) for the transition probability is valid. The system in the initial state is placed near minimum R_i and the pure quantum transition to the final state occurs near minimum R_f.

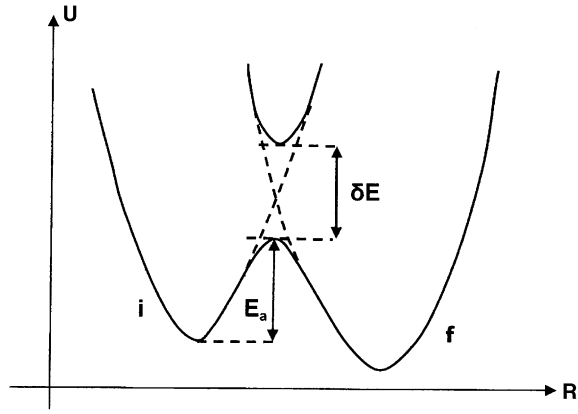


Fig. 2.3. The adiabatic terms of a system as functions of the generalized coordinate R. The dotted lines denote the crossing diabatic terms in the region of strong influence of the inter-term interaction. The indexes i and f denote the regions of the initial and final states.

Lam Research Ex. 1035 - Page 41
Lam Research Corp. v. Inpria Corp.
IPR2024-00033 - U.S. Patent No. 9,823,564

But it is quite another picture at high temperatures when, in accordance with (29), the transition occurs at the thermal excitation of the system in initial state to the activation energy E_a that is the energy of terms crossing. The terms splitting δE plays a very essential role in these circumstances. If

$$\delta E = 2|V_{if}| \ll kT, \tag{54}$$

then splitting does not practically occur at thermal excitation, and the rate constant is described by expression (27). However, if

$$\delta E = 2|V_{if}| > kT, \tag{54a}$$

the subsequent thermal excitation on the higher term $E_1^{ex}(R)$ after being mounted to the region near R^* in the lower term $E_2^{ex}(R^*)$ is hampered, the system will be dropped in the minimum f with much larger probability. It means that it is the case of the classic adiabatic reaction of electron transfer, and R is the collective reaction coordinate. The rate constant W_{if} may be found by, for example, the approach of the transition state theory (TST), and it is in the simplest "one-dimensional" case:

$$W_{if} = k_{tr}\frac{\bar{\omega}}{2\pi}\exp\left\{-\frac{E_a^{ex}}{kT}\right\}. \tag{55}$$

Here, $\bar{\omega}$ is the frequency of vibration along the coordinate R, or in another words, the mean effective frequency of the phonons in the initial state, and k_{tr} is the so-called transmission coefficient. The activation energy in the adiabatic reaction E_a^{ex} is smaller than E_a:

$$E_a^{ex} = E_a - |V_{if}|. \tag{56}$$

The transmission coefficient $k_{tr} = 1$ in TST approach, but $k_{tr} < 1$ in reality. It can be obtained in the more exact approach of Kramers equation [27]. The detailed account of the theory of adiabatic reactions of electron transfer in polar media may be found in the already mentioned Kuznetsov's monograph [13].

It was examined in this chapter that in the standard situation the system is in equilibrium in the initial state; therefore, the result of averaging out the populations of the oscillator levels in this state is their replacement with their equilibrium values (see the determination (19)). But very frequently the electron photo-transfer is studied where the initial state is the excited state of donor. The electron matrix element V_{if} increases exponentially with the growth of the tunneling electron energy (see Chapter 3). So, it is possible that the transfer probability in unit of time becomes bigger than the inverse time of the vibration relaxation in the donor excited state. Then, the transfer occurs from the electron's excited state with the non-relaxed or partly relaxed vibration populations. The high temperature rate constant of the

Lam Research Ex. 1035 - Page 42
Lam Research Corp. v. Inpria Corp.
IPR2024-00033 - U.S. Patent No. 9,823,564

electron transfer in this case depends on the rate of approach of the system on the initial excited term to the point of crossing with the final term, and its temperature dependence may noticeably differ from Arrenius's exponent [29–32].

9. Conclusions

The theory of multi-phonon electron transitions due to non-adiabatic interaction between the electron terms is expounded in this chapter. The participation of the large number of the vibration degrees of freedom in the transition is caused by the non-orthogonality of the oscillator wave function in the initial and final states. This non-orthogonality may be connected with the following factors: the shift of the equilibrium positions of the oscillations, the change of the frequencies in the transition, and the change of the set of normal coordinates of the vibration system.

For the transition description, the phonon system may be replaced by one effective vibration mode. We obtained the expressions for the transition probability as a function of the temperature and the difference of electron energies, and the most important parameter that defined this dependence is reorganization energy of the vibration system. The transition probability, or the rate constant, has the form of thermo-activation exponent at high temperatures.

The electron transfer in polar media is described by the general theory where the reorganization energy is expressed via dielectric characteristics of the medium. The strong interaction between the terms results in the transition of the adiabatic one over the activation barrier.

Some important problems of the theory of multi-phonon electron transition were not touched upon in this chapter. These are, first, the calculation of the expression for the electron matrix element at the tunneling transfer, second, the influence of medium on the electron matrix element, and, finally, the investigation of the applicability of Born–Oppenheimer approach in the electron tunneling transfer. These issues will be considered in the next chapter.

The following questions are posed for the fixation of the chapter content.

1. Why is the electron transition a multi-phonon transition? Name the main reason.
2. Why does the rate constant depend on the temperature?
3. What is the reorganization energy and what is its physical sense?
4. What are the intra-sphere and outer-sphere degrees of freedom?

Lam Research Ex. 1035 - Page 43
Lam Research Corp. v. Inpria Corp.
IPR2024-00033 - U.S. Patent No. 9,823,564

5. How does the activation energy depend of the electron energies difference?
6. What change of the temperature results in the non-adiabatic electron transition change over to adiabatic one?

References

1. S. I. Pekar, J. Exp. Theor. Phys. **20** (1950) 510.
2. H. Kun, A. Rhys, Proc. R. Soc. **A204** (1950) 406.
3. Ya. I. Frenkel', Phys. Rev. **37** (1931) 17.
4. T. Muto, Prog. Theor. Phys. (Japan) **4** (1949) 181.
5. M. Lax, J. Chem. Phys. **20** (1952) 1752.
6. S. I. Pekar, M. A. Krivoglaz, Works Inst. Phys. Ukraine Acad. Sci. **4** (1953) 37.
7. R. Kubo, Y. Toyozawa, Prog. Theor. Phys. (Japan) **13** (1955) 160.
8. J. M. Ziman, Principles of the Theory of Solids, Cambridge University Press, London, 1964.
9. Yu. E. Perlin, Russ. Phys. Rev. **53** (1963) 553.
10. F. Dyson, Phys. Rev. **75** (1949) 486, 1736.
11. R. P. Feynman, Phys. Rev. **84** (1951) 108.
12. R. Marcus, J. Phys. Chem. **24** (1956) 966, 979; R. Marcus, J. Phys. Chem. **26** (1957) 867; R. Marcus, Disc. Far. Soc. **29** (1960) 21.
13. A. M. Kuznetsov, Charge Transfer in Physics, Chemistry and Biology, Gordon and Breach, NY, 1995.
14. M. A. Lavrent'ev, B. V. Shabat, Methods of the Theory of Functions of Complex Variables, Nauka, Moscow, 1965.
15. G. K. Ivanov, M. A. Kozhushner, L. I. Trakhtenberg, J. Chem. Phys. **113** (2000) 1992.
16. T. Kumada, K. Komaguchi, Y. Aratono, T. Miyazaki, Chem. Phys. Lett. **261** (1996) 463.
17. M. A. Krivoglaz, J. Exp. Theor. Phys. **25** (1953) 191.
18. K. Husimi, Proc. Phys. Math. Soc. Japan **22** (1940) 406.
19. V. G. Levich, R. R. Dogonadze, Dokl. Phys. Chem. **124** (1959) 123; V. G. Levich, R. R. Dogonadze, Dokl. Phys. Chem. **133** (1960) 158.
20. R. R. Dogonadze, Dokl. Phys. Chem. **133** (1960) 258.
21. R. R. Dogonadze, Yu. A. Chizmadzhev, Dokl. Phys. Chem. **144** (1962) 1077.
22. R. R. Dogonaze, A. M. Kuznetsov, Yu. A. Chizmadzhev, Russ. J. Phys. Chem. **38** (1964) 1195.
23. R. R. Dogonaze, A. M. Kuznetsov, Electrochemistry **3** (1967) 1324.

Lam Research Ex. 1035 - Page 44
Lam Research Corp. v. Inpria Corp.
IPR2024-00033 - U.S. Patent No. 9,823,564

24. A. A. Ovchinnikov, M. Ya. Ovchinnikova, J. Exp. Theor. Phys. **56** (1969) 1278.
25. R. R. Dogonadze, A. A. Kornyshev, Phys. Status Solidi **B53** (1972) 439.
26. A. A. Kornyshev, M. A. Vorotyntsev, H. Nielsen, J. Ulstrup, J. Chem. Soc., Faraday Trans. **78** (1982) 217.
27. P. Hänggi, P. Talkner, M. Borkovec, Reaction-Rate Theory: Fifty Years After Kramers, Rev. Mod. Phys. **62** (1990) 251.
28. V. I. Gol'danskii, L. I. Trakhtenberg, V. N. Flerov, Tunneling Phenomena in Chemical Physics, Gordon and Breach, NY, 1989.
29. I. M. Bystriak, G. I. Likhtenshtein, A. I. Kotel'nikov, Kh. O. Khanovskii, K. Hideg, Russ. J. Phys. Chem. **60** (1986) 2796.
30. M. V. Koz'menko, M. G. Kuz'min, Chem. Phys. Rep. **4** (1985) 794.
31. J. Jortner, Biochim. Biophys. Acta **594** (1980) 193.
32. A. M. Kuznetsov, J. Ulstrup, Biochim. Biophys. Acta **636** (1981) 50.

Lam Research Ex. 1035 - Page 45
Lam Research Corp. v. Inpria Corp.
IPR2024-00033 - U.S. Patent No. 9,823,564

Chapter 3

Contemporary Theory of Electrons Tunneling in Condensed Matter

M.A. Kozhushner

Semenov Institute of Chemical Physics, Russian Academy of Sciences, ul. Kosygina 4, Moscow, 119991, Russia

1. Introduction 37
2. Amplitude of Electron Tunneling Transfer 38
3. Influence of Crystal Medium on Electron Tunneling. 44
4. Multiple Tunneling Scattering and Bridge Effect 48
5. Violation of Born–Oppenheimer's Approach in Electron Tunneling Transfer 54
6. Conclusions 63
References 64

In this chapter, a description is provided on how to determine the electron component of the transition amplitude (electron tunneling amplitude) for multielectron systems. The electron Green's function determines the distance dependence of the electron matrix element. The influence of crystal media on Green's function is examined. The effect of the intermediate particles on electron tunneling will be considered within the framework of electron sub-barrier scattering to adequately describe the bridge effect. The multiparticle (electron + nuclei) Green's function approach for describing electron–nuclei transition indicates that the Born–Oppenheimer representation of the wave function is invalid in tunneling over long distances. In the high temperature limit, it results in the dependence of the electron tunneling exponent and the reorganization energy on the tunneling distance.

1. Introduction

The issues of the electron transfer theory that should be resolved to make this theory sufficiently complete and closed was formulated in the conclusion of the previous chapter. These issues were concerned with the methods of the calculation of the electron matrix element and the spillover of Born–Oppenheimer approach. It is these problems that will be examined in this chapter.

THIN FILMS AND NANOSTRUCTURES, vol. 34
ISSN 1079-4050
DOI: 10.1016/S1079-4050(06)34003-3

© 2007 by Elsevier Inc.
All rights reserved.

Lam Research Ex. 1035 - Page 46
Lam Research Corp. v. Inpria Corp.
IPR2024-00033 - U.S. Patent No. 9,823,564

The strict expression for the electron matrix element V_{if} in the tunneling electron transfer is derived in Section 2. Electron Green's function at the negative energy of bound electron in this expression denotes the exponential dependence of the matrix element on the donor–acceptor distance. It is shown in Section 3 that the influence of crystal medium on the matrix element V_{if} is reduced to its influence on Green's function. The bound electron level is positioned on the forbidden crystal energy band, and the exponent in Green's function depends on two values: (1) the energy distance between the level and the minimum of the conductivity band or the maximum of the valence band, (2) the width of these bands. The modulo of the negative exponent decreases and V_{if} increases when this energy distance decreases. The bridge effect, i.e. the influence of the intermediate particles of disordered media or a molecular chain between the donor and the acceptor on the value of V_{if} is described in Section 4. This influence is interpreted as multiple scattering of the tunneling electron on these intermediate particles. It results in a decrease in the modulo of the exponent, i.e. in exponential increase of V_{if} with number of the particles. In conclusion, it is shown in Section 5 that the adiabatic Born–Oppenheimer's approach in the description of the wave function of an electron–nuclear system becomes invalid in the far asymptotics of the wave function on the electron coordinates. As a result, the tunneling exponent begins to depend on the temperature at tunneling on the long distances, and the effective reorganization energy in the vibration system depends on the distance. In referring to formulas of Chapter 2, the cipher 2 will be put before the number of the formula.

2. Amplitude of Electron Tunneling Transfer

The value and form of the electron interaction V that defines the dependence of the transfer probability on the donor–acceptor distance were not elaborated in the previous chapter. As it was pointed out, the electron transfer at the large distance r_{DA} exceeding the magnitude of a donor and acceptor occurs via the tunneling mechanism. In this section, the expression for the matrix element V_{if} will be deduced. Tunneling of a particle including, naturally, an electron denotes particle transfer under a potential barrier that is higher than the electron energy [1]. The amplitude of the tunneling transition is denoted by the exponentially small value of the wave function in the underbarrier region. This classically inaccessible region is named asymptotic underbarrier region. It is learned the electron transfer takes place from one localized state (on the donor) to another localized state (on the acceptor).

Lam Research Ex. 1035 - Page 47
Lam Research Corp. v. Inpria Corp.
IPR2024-00033 - U.S. Patent No. 9,823,564

The term "tunneling transition" may be applied to this case, if the acceptor is placed in the asymptotic underbarrier region of the wave function of the initial state on the donor, and vice versa, the donor is placed in the asymptotic region of the acceptor. It will be shown that the amplitude of such tunneling transition is denoted by the values of the donor and acceptor wave functions in the corresponding asymptotic regions near the acceptor and donor, out of the main region of electron localization (MREL) [2–4].

In the beginning, let us examine for simplicity the one electron center-donor. The interaction of the donor with tunneling electron can be described by the sum of the short-range potential $U_D^S(\vec{r})$ and Coulomb attractive potential $V_D(r) = -1/r$ where r is the distance from the donor center (here and below in this chapter it is used the atomic units). It means that far from the donor, the donor-positive ion interacts with the electron, so the donor is neutral in the initial state. The total donor potential is

$$U_D(\vec{r}) = U_D^S(\vec{r}) + V_D(r). \tag{1}$$

Note, Coulomb's interaction of the electron with the donor "ion residue" may be picked out at $r > r_0$ only where r_0 is the radius of the ion residue, but such division of the total potential proves convenient at all values of the radius r.

Hamiltonian $\hat{H}$ of the system which contains the electron + the donor ion residue is written down in the form:

$$\begin{aligned} \hat{H} &= \hat{H}_0 + U_D^S(\vec{r}) \\ \hat{H}_0 &= \hat{T} + V_D(r) \end{aligned} \tag{2}$$

where $\hat{T}$ is the operator of the kinetic energy. The initial state with energy E and the wave function $\psi_D(\mathbf{r}; E)$ is the eigenstate of Hamiltonian $\hat{H}$. The asymptotic of $\psi_D(\mathbf{r}; E)$ at $r >> r_0$ where r_0 is the range of the potential $U_D^S(\vec{r})$ will be investigated using Lippman–Schwinger equation that is the integral analog of Schrödinger differential equation [5].

Schrödinger equation corresponding to Hamiltonian $\hat{H}$ for the wave function $\psi_D(\mathbf{r}; E)$ of the initial state of electron on the donor

$$[\hat{T} + U_D^S(\vec{r}) + V_D(r)]\Psi_D(\vec{r}; E) = E\Psi_D(\vec{r}; E) \tag{3}$$

may be rewritten taking into account definition (2) as

$$\Psi_D(\vec{r}; E) = (E - \hat{H}_0)^{-1} U_D^S \Psi_D. \tag{4}$$

The operator $(E - \hat{H}_0)^{-1}$ is by definition Green's function of electron with the energy ' for Hamiltonian $\hat{H}_0$ with potential V [5]

$$(E - \hat{H}_0)^{-1} \equiv G_V(\vec{r}, \vec{r}'; E).$$

Lam Research Ex. 1035 - Page 48
Lam Research Corp. v. Inpria Corp.
IPR2024-00033 - U.S. Patent No. 9,823,564

The action of this operator on a function denotes the integration of this function with the kernel $G_V(\vec{r},\vec{r}';E)$, and Eq. (4) may be rewritten in the canonical form of Lippman–Schwinger equation [5]:

$$\Psi_D(\vec{r};E) = \int d\vec{r}\,' G_{V_D}(\vec{r},\vec{r}';E) U_D^S(\vec{r}')\Psi_D(\vec{r}';E). \tag{5}$$

The analytic expression for Green's function is known for a few important forms of potential $V(r)$, particularly, for Coulomb's potential [6]. If the donor is the negative ion, the potential $V(r) = 0$ at $r > r_0$. Then, Green's function of free particle G_0 should be substituted in Eq. (5). For the case of $E < 0$

$$G_0(\vec{r},\vec{r}';E) = -\frac{1}{2\pi|\vec{r}-\vec{r}'|}\exp\{-\kappa|\vec{r}-\vec{r}'|\} \tag{6}$$

where

$$\kappa = \sqrt{2|E|}. \tag{7}$$

The integral Eq. (5) gives the opportunity to calculate the asymptotics of wave function $\Psi^a(\vec{r};E) = \Psi(\vec{r};E)\big|_{r\gg r_0}$, i.e. need for the calculation of electron matrix element at tunneling transition. The latest quantum-chemical methods permit us to find the wave function in MREL only, but not in the asymptotic region. The wave function is calculated with the help of minimization of the energy function. The relative accuracy of the determination of the ground state energy in multielectron systems, atoms or molecules, does not exceed 10^{-3}. As the asymptotics of the bound state wave function is always exponentially small, $\Psi^a(\vec{r};E)\sim\exp\{-\kappa r\}$ [7], the relative contribution of the asymptotics to the energy is of the order $\exp\{-2\kappa r\}$, and this contribution is smaller than the accuracy of the energy determination, $\exp\{-2\kappa r\} < 10^{-3}$, already at not great distances. At typical bound energy $|E| \cong 0.18$ ($|E| \cong 5\,\text{eV}$) the value $\kappa(|E|) \cong 0.6$, and the above inequality is satisfied already at $r > 6$ ($r > 3\,\text{Å}$). It means that the wave function at these distances does not give the controlled contribution to the energy, and therefore it cannot be calculated via quantum-chemistry method.

The integration in the right side of Eq. (5) occurs on the MREL $r' < r_0$ where potential $U_D^S(\vec{r}')$ is not zero and the wave function $\Psi(\vec{r}';E)$ may be calculated with good accuracy. Then Eq. (5) may serve as a quantitative determination of the asymptotics at $r > r_0$,

$$\Psi_D^a(\vec{r};E)\big|_{r>r_0} = \int d\vec{r}\,' G_{V_D}(\vec{r},\vec{r}';E) U_D^S(\vec{r}')\Psi_D(\vec{r}';E), \tag{8}$$

since all values in the integrand can be calculated with good accuracy.

Lam Research Ex. 1035 - Page 49
Lam Research Corp. v. Inpria Corp.
IPR2024-00033 - U.S. Patent No. 9,823,564

The general property of Green's functions $G_{V_D}(\vec{r},\vec{r}';E)$ at $E<0$ for any potential V_D, obeying the condition $|V_D|<|E|$, is its exponential decay with the distance $|\vec{r}-\vec{r}'|$ (see, e.g., the expression (6), Green's function for Coulomb potential [6], and its general quasi-classic expression [4]). It is not difficult to see in the expression (8) the asymptotic that decays exponentially agrees with the general theorem [6]. The expression (8) gives the correct value of the exponent and permits us to determine the pre-exponential factor with the accuracy of the calculation of the wave function in MREL.

Let the electron–acceptor interaction be described by the short-range potential $U_A^S(\vec{r}-\vec{r}_A)$ where $\vec{r}_A$ is the center of acceptor coordinate. It is supposed that the wave function of the electron bound state on the acceptor with energy E, $\Psi_A(\vec{r}-\vec{r}_A;E)$, is an exact one, i.e. it is considered not only $U_A^S(\vec{r}-\vec{r}_A)$ but the donor–electron interaction also. Then, the exact value of the matrix element of the electron donor–acceptor transfer is equal [1]:

$$V_{if}=\left\langle \Psi_D^a(\vec{r};E)\middle|U_A(\vec{r}-\vec{r}_A)\middle|\Psi_A(\vec{r}-\vec{r}_A;E)\right\rangle. \tag{9}$$

The integration in Eq. (9) occurs near the acceptor, i.e. in the asymptotic region of the donor wave function. Therefore, the asymptotics $\Psi_D^a(\vec{r};E)$ is substituted in the matrix element (9) instead of the wave function $\Psi_D(\vec{r};E)$. The value of the matrix element V_{if} is proportional to $\exp\{-\kappa r_{DA}\}$ due to the exponential decay of $\Psi_D^a(\vec{r};E)$. The evaluation of the correction to the wave function $\Psi_A(\vec{r}-\vec{r}_A;E)$ due to the interaction with the donor obviously shows that it is also proportional to $\exp\{-\kappa r_{DA}\}<<1$.

Therefore, to calculate v_{if} to the first order of the value $\exp\{-\kappa r_{DA}\}$, it should substitute the wave function $\Psi_A(\vec{r}-\vec{r}_A;E)$ in the expression (9) defined on the potential $U_A(\vec{r}-\vec{r}_A)$ only, and the same designation is kept for this function. If the acceptor without electron is a single charged positive ion, the potential of acceptor contains Coulomb's potential $V_A(\vec{r}-\vec{r}_A)=-1/|\vec{r}-\vec{r}_A|$ similar to the donor (see the expression (1)). This long-range potential should be included along with $V_D(\vec{r})$ in the Hamiltonian $\hat{H}_0$ for the definition of Green's function. Then, substituting the function (8) in the expression (9) gives the expression for the electron matrix element of the tunneling transition in the final form:

$$V_{if}=\iint d\vec{r}'d\vec{r}\,\Psi_D(\vec{r}';E)U_D^S(\vec{r}')G_{V_D+V_A}(\vec{r}',\vec{r};E)U_A^S(\vec{r})\Psi_A(\vec{r};E). \tag{10}$$

Naturally, this expression is symmetric on the donor and acceptor coordinates. The general form of the total Coulomb's potential is

$$V_D+V_A=-\left(\frac{Z_D}{\varepsilon_0 r}+\frac{Z_A}{\varepsilon_0|\vec{r}-\vec{r}_A|}\right), \tag{11}$$

Lam Research Ex. 1035 - Page 50
Lam Research Corp. v. Inpria Corp.
IPR2024-00033 - U.S. Patent No. 9,823,564

Z_D, Z_A are the charges of the donor and acceptor ions, and ε_0 is the static dielectric permittivity of the medium where the tunneling electron transition occurs.

Let us examine Green's function for long-range potential $V(\boldsymbol{r})$ in more details. In the general case, the different multipole potentials in addition to Coulomb's potentials of the donor and the acceptor may be included in the Hamiltonian (2) to the definition of Green's function. These multipole potentials are non-zero in the asymptotic region only, but in MREL they are a part of the short-range potentials $U^S_{D,A}(\vec{r})$. In the asymptotic region the values $|V_D|, |V_A| << |E|$, and their inequalities permit us to calculate the Green's function by the quasi-classic method [4,8]. The general expression of Green's function may be expressed in this case as

$$G_V(\vec{r},\vec{r}';E) = A(\vec{r},\vec{r}';E)\exp\{-S(\vec{r},\vec{r}';E)\}. \tag{12}$$

Here, $S(\vec{r},\vec{r}';E)$ is the classic action along the trajectory of the electron motion with the "turned" energy in the "turned" potential, $V_{\text{turn}}(\boldsymbol{r}) = -V(\boldsymbol{r})$, $E_{\text{turn}} = -E$. If the inequality $E_{\text{turn}} > V_{\text{turn}}(\boldsymbol{r})$ takes place in the asymptotic region, then the classic motion is possible there, and one may use the classic expression of the action:

$$S(\vec{r},\vec{r}';E) = \int_{\vec{r}'}^{\vec{r}} d\vec{l}\sqrt{2(E_{\text{turn}} - V_{\text{turn}}(\vec{l}))}, \tag{13}$$

where the integration is carried out along the trajectory that joined two points $\boldsymbol{r}$ and $\boldsymbol{r}'$ on the motion of the particle with energy E_{turn} in potential $V_{\text{turn}}(\boldsymbol{r})$. The coefficient $A(\vec{r},\vec{r}';E)$ in Eq. (12) is expressed in the following form:

$$A(\vec{r},\vec{r}';E) = \frac{1}{4\pi}\left[\frac{D(\vec{r},\vec{r}';E)}{(V(\vec{r})-E)(V(\vec{r}')-E)}\right]^{1/2} \tag{14}$$

where $D(\vec{r},\vec{r}';E)$ is the determinant of 4th rank consisting of the first and second derivatives of the action $S(\vec{r},\vec{r}';E)$ on $\vec{r}$ and $\vec{r}'$ [8]. A computational program to calculate Green's function (12) is presented in Ref. [4].

It should be noted that the expression (11) for Coulomb's potential is only valid in the asymptotic region, far from the donor and acceptor. At the small distance from the charge, the dielectric permittivity does not weaken the electric field. Therefore the approximate expression for Green's function in this case can be obtained by combining its exact expression in Coulomb's field [6] and the quasi-classic approach [2,4]:

$$G_V(\vec{r},\vec{r}';E) \approx g(r_{DA},E)\sum_{lm,l'm'}\varphi_{D;lm}(\vec{r}',E)\varphi_{A;l'm'}(\vec{r}-\vec{r}_A,E). \tag{15}$$

Lam Research Ex. 1035 - Page 51
Lam Research Corp. v. Inpria Corp.
IPR2024-00033 - U.S. Patent No. 9,823,564

One uses the following designations in (15):

$$g(r_{DA}, E) = -\frac{1}{r_{DA}}(\kappa r_{DA})^{(Z_D+Z_A)/\varepsilon_0\kappa}\exp\{-\kappa r_{DA}\}, \tag{16}$$

$$\varphi_{D,A;lm}(\vec{\rho}) = Y_{lm}\left(\frac{\vec{\rho}}{\rho}\right)\frac{\Gamma(l+1-\kappa^{-1})}{(2l+1)!}(2\kappa\rho)^l\exp\{-\kappa\rho(1\pm\cos\ \theta)\} \times F(l+1-\kappa^{-1}, 2l+2, 2\kappa\rho). \tag{17}$$

The sign "+" in the function (17) is related to the donor, and "–" to the acceptor; the angle θ is counted on the axis Z that is directed along the vector $\boldsymbol{r}_{DA}$; $F(l+1-\kappa,\ 2l+2;\ 2\kappa\rho)$ is the degenerate hypergeometric function. The expressions (15), (16) and (17) should be substituted in the integral (10) to calculate the matrix element V_{if} .

Hitherto the one-electron model of the donor and acceptor has been used. If to consider them as real many-electron systems, the structure of the expression (10) will remain as the previous one, but integrals will be addedto the degrees of freedom of other electrons [3]. Now, $\Psi_{D,A} \equiv \Psi_{D,A}(\{r_{N_{D,A}}\})$ where $\{r_{N_{D,A}}\}$ denotes the whole of the degrees of freedom of all electrons of the donor or the acceptor. Besides, it should introduce the wave functions of the ion residue both of the donor and of the acceptor, $\Phi_{D,v_D}(\{r_{N_D-1}\})$ and $\Phi_{A,v_A}(\{r_{N_A-1}\})$, where $v_{D,A}$ are the sets of quantum numbers of the corresponding states. As a rule, the donor ion residues ensue after the electron transfer in the ground state just as the acceptor ion residue before the reaction, and then one will omit the indexes $v_{D,A}$ below. The short-range potentials depend now on all variables, $U^S_{D,A} \equiv U^S_{D,A}(\vec{r}, \{r_{N_{D,A}-1}\})$. Since one-electron transfer is examined, the Green's function remains as it was before the one-electron one. The expression for the tunneling matrix element in the many-electron case is described in the form:

$$V_{if} = g(r_{DA}, E)\sum_{lm,l'm'} Q^{lm}_D Q^{l'm'}_A \tag{18}$$

where the function $g(r_{DA}, E)$ is defined by the formula (16), and the values $Q^{lm}_{D,A}$ are expressed by the following:

$$Q^{lm}_{D,A} = \int d\{r_{N_{D,A}-1}\} \times \int d\vec{r}\,\Psi_{D,A}(\{r_{N_{D,A}}\})U^S_{D,A}(\vec{r}, \{r_{N_{D,A}-1}\})\Phi_{D,A}(\{r_{N_{D,A}-1}\})\varphi_{D,A;lm}(\vec{r}). \tag{19}$$

Here, the functions $\varphi_{D,A;lm}(\vec{r})$ are presented in expression (17).

So, if the wave functions $\psi_{D,A}$ and $\Phi_{D,A}$ are known after some quantum-chemical calculation, the integrals (19) give the possibility to find the matrix element V_{if}. The values $Q_{D,A}$ are equal at the order of values to the tunneling

Lam Research Ex. 1035 - Page 52
Lam Research Corp. v. Inpria Corp.
IPR2024-00033 - U.S. Patent No. 9,823,564

electron bound energy E. Then, the simple approximate expression for the electron tunneling matrix element V_{if} may be introduced:

$$\left|V_{if}\right| \cong E^2(\kappa r_{DA})^{2/\varepsilon_0\kappa}\frac{\exp\{-\kappa r_{DA}\}}{r_{DA}}. \tag{20}$$

The influence of the medium on the dielectric permittivity only becomes apparent when it weakens the Coulomb's field. But as it will be shown in the following sections, the medium's influence on V_{if} is much stronger where the crystal and electron structures of the medium play a role. Besides, it was supposed in deducing the expression for V_{if} that the electron bound energies E on the donor and acceptor are equal, or in other words, the energy transmitted to the vibrations, $\Delta E \ll E$, changes the function $\exp\{-\kappa r_{DA}\}$ very weakly at the replacement of E in $E \pm \Delta E$. The influence of the energy defect ΔE on the matrix element V_{if} and the connection of the electron and nuclei degrees of freedom at electron transfer will be examined in Section 5 of this chapter.

3. Influence of Crystal Medium on Electron Tunneling

The electron tunneling matrix element was examined in the preceding section without taking into account the influence of the media where the donor and acceptor are placed. The dielectric constant ε_0 was only considered. As it will be seen that the influence of media changes considerably the exponential dependence of the main factor of Green's function $g(r_{DA})$ (16), hence the matrix element V_{if} (10), on the distance r_{DA}. As regards expressions (17) that are included in Green's function, the values of these functions near the donor and acceptor are important only since the short-range potentials $U^S_{D,A}(\vec{r})$ are the factors in the integrand in the matrix element (10). The functions (17) near the donor and acceptor do not change practically due to the action of media.

Let us examine the structure of expression (16). The influence of the dielectric medium constant ε_0 affects the factor aroused from the long-range Coulomb's field of the donor and acceptor charges, $(\kappa r_{DA})^{(Z_D+Z_A)/\varepsilon_0\kappa}$. But the influence of medium on the second, exponential factor in $g(r_{DA})$ is not yet examined. Note, the expression $-(1/r_{DA})\exp\{-\kappa r_{DA}\}$ differs from the Green's function of a free electron $G_0(\vec{r}_D, \vec{r}'_A; E)$ by the numeric factor $1/2\pi$ only (see formula (6)). Therefore it will be considered that the influence of the medium on Green's function of a free electron does not interact with the donor and the acceptor.

First a crystal insulator will be examined where the electron bound energy levels on the donor and acceptor lie in the forbidden zone (see Figure 3.1).

Lam Research Ex. 1035 - Page 53
Lam Research Corp. v. Inpria Corp.
IPR2024-00033 - U.S. Patent No. 9,823,564

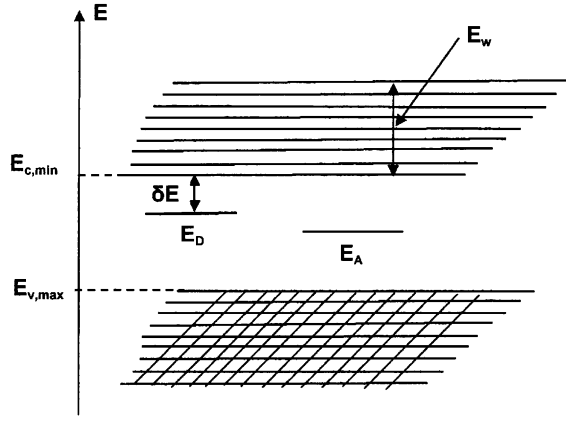


Fig. 3.1. The location of the donor and acceptor levels relatively to the crystal energy bands. The levels of valence band are shaded to underline their occupation, the levels of conductivity band are empty. The conductivity band width E_w and the value δE (see formula (23) in the text) are shown.

Naturally, it is suggested that the concentrations of the free carriers, i.e. electrons in the conductivity band and holes in the valence band, are epsilon squared. In another case, electrons from the conductivity band will be captured by the acceptor, or holes from the valence band will get annihilated by the electron on the donor. Then, the tunneling transition becomes impossible because either the acceptor level becomes populated or the donor level is emptied.

The Green's function of electron in a crystal has the following spectral representation [9,10]:

$$G(\vec{r},\vec{r}';E)=\sum_{\vec{k},s}\frac{\psi^{s}_{\vec{k}}(\vec{r})\psi^{s*}_{\vec{k}}(\vec{r}')}{E-\varepsilon_{s}(\vec{k})}-\sum_{\vec{k},t}\frac{\psi^{t*}_{\vec{k}}(\vec{r})\psi^{t}_{\vec{k}}(\vec{r}')}{E-\varepsilon_{t}(\vec{k})} \tag{21}$$

Here $\psi^{v}_{\vec{k}}(\vec{r})$ is the wave function of the electron state with quasi-momentum $\vec{k}$ and energy $\varepsilon_v(\vec{k})$ in vth band. The summation in the first summand in the right part occurs on all quasi-moments $\vec{k}$ of Brillouin's zone corresponding to states in all s non-populated energy conduction bands. The sign * denotes the complex conjugation. The summation in second summand occurs on all states in all t populated valence bands, i.e. on the non-populated states of holfes in the empty hole bands. Naturally, the summation corresponds to the integration on $d\vec{k}$ in the large crystal.

The physical sense of the electron and hole parts of Green's function in expression (21) is quite obvious. Green's function $G(\vec{r},\vec{r}';E)$ is the propagator of the electron motion from point $\vec{r}'$ near the donor to point $\vec{r}$ near the

Lam Research Ex. 1035 - Page 54
Lam Research Corp. v. Inpria Corp.
IPR2024-00033 - U.S. Patent No. 9,823,564

acceptor. The electron may pass virtually from the donor on one of the empty states of the conduction band and move in this state until it is captured by the acceptor. The first sum is the sum on these virtual ways. But there is another virtual way of electron transfer from the donor to the acceptor: an electron from the occupied valence band passes to the acceptor, and the resulting hole in the valence band moves to the donor and annihilates with donor electron. The sum on these ways makes the hole part of Green's function. This is the second item in the expression (21).

The electron wave functions $\psi^s_{\vec{k}}(\vec{r})$ are Bloch's functions normalized on the volume Ω of the crystal:

$$\psi^s_{\vec{k}}(\vec{r}) = \frac{1}{\sqrt{\Omega}} e^{i\vec{k}\vec{r}} u^s_{\vec{k}}(\vec{r}), \tag{22}$$

where $u^s_{\vec{k}}(\vec{r})$ is the real periodic function normalized on the volume of the crystal elementary cell and is the smooth function of $\vec{k}$. The essential influence on the value of the sums in expression (21) and their dependence on $|\vec{r} - \vec{r}'|$ exert the analytic form of the functions $\varepsilon_{s,t}(\vec{k})$. If energy E is close to the energy minimum of the lowest conduction band $\varepsilon_{\min}$,

$$\delta_E = \varepsilon_{\min} E << E_w, \tag{23}$$

(E_w is the width of this band), the biggest contribution to the first, electron, sum in expression (21) makes the states with the energies near this minimum with corresponding quasi-momentum $\vec{k}_0$, $\varepsilon_{\min} = \varepsilon(\vec{k}_0)$. One may represent the band energy near the minimum by:

$$\varepsilon(\vec{k}_0) \cong \varepsilon_{\min} + \frac{(\vec{k} - \vec{k}_0)^2}{2m^*_e}. \tag{24}$$

For simplicity, the effective mass m^*_e was considered as the isotropic one. Note that the effective mass m^*_e in atomic units derives from the relation between the genuine effective mass and the electron mass. The electron contribution in Green's function (21), taking into account definitions (22) and (24), is equal to

$$G_e(\vec{r}, \vec{r}'; E) = -\frac{(m^*_e)^2}{2\pi|\vec{r} - \vec{r}'|} u_{k_0}(\vec{r}) u_{k_0}(\vec{r}') \exp\left\{-\sqrt{2m^*_e \delta_E}|\vec{r} - \vec{r}'|\right\}. \tag{25}$$

The contribution of the hole band is described by the similar formula with the hole effective mass m^*_h, and the energy difference in (25) is $\delta_E = E - \varepsilon_{\max}$ where $\varepsilon_{\max}$ is the maximum energy of the highest valence band $\delta E << E_w, E_w$ is its width of the valence band.

If inequality (23) is violated, the exponential decay of Green's function on the distance $|\vec{r} - \vec{r}'|$ remains, of course, but the coefficient before this distance in the exponent is increased. The value of this coefficient depends on

Lam Research Ex. 1035 - Page 55
Lam Research Corp. v. Inpria Corp.
IPR2024-00033 - U.S. Patent No. 9,823,564

δ_E and the analytic function $\varepsilon(\vec{k})$ in the whole band, but not on the effective mass. All states of the band contribute to Green's function, not only the states near the minimum of the conductance band or the maximum of the valence band. Then, in a general case, it should be known that $\varepsilon(\vec{k})$ for the energy bands are the nearest ones to the energy level E for the calculation of the exponent in the expression (25).

A new method of calculating the exponent was presented in article [11]. Instead of the two-step calculation of the exponent – first calculating the band structures $\varepsilon_{s,t}(\vec{k})$ and then the integral in expression (21) – Ref. [11] proposes to find the momentum $\vec{k}$ corresponding to a given energy E. When the energy E lies in the forbidden zone, the corresponding momentum proves to be image $i\vec{k}(E)$. The wave function with electron energy in the forbidden zone decays as $\exp\{-\vec{k}(E)\vec{r}\}$, and then Green's function is proportional to $\exp\{-\vec{k}(E)|\vec{r}-\vec{r}'|\}$. This method is simpler, but in essence one should, as before, know the exact analytic dependencies $\varepsilon_{s,t}(\vec{k})$ to find the complex value $\vec{k}(E)$ since one needs to continue analytically the functions $\varepsilon_{s,t}(\vec{k})$ in the complex plane k far from the real axis, if the energy E is far from the band levels.

If the expression (25) is accepted then, to calculate V_{if}, it should be substituted in expression (18). The new function is $g_c(r_{DA}, E)$ instead of $g(r_{DA}, E)$,

$$g_c(r_{DA}, E) = -\frac{(m*)^2}{r_{DA}}(\tilde{\kappa} r_{DA})^{2/\varepsilon_0 \tilde{\kappa}} \exp\{-\tilde{\kappa} r_{DA}\} \tag{26}$$

where

$$\tilde{\kappa} = \sqrt{2m* \delta_e}. \tag{26a}$$

In the same way, one should substitute $Q_{D,A}$ in expression (19) by the new function $Q^c_{D,A}$ where the periodic parts of Bloch's function $u_{k_0}(\vec{r})$ (see definition (22)) are added to the integrand in Eq. (19):

$$Q^{c,lm}_{D,A} = \int d\{r_{N_{D,A}-1}\}$$
$$\times \int d\vec{r}\, \Psi_{D,A}(\{r_{N_{D,A}}\}) U^S_{D,A}(\vec{r}, \{r_{N_{D,A}-1}\}) \Phi_{D,A}(\{r_{N_{D,A}-1}\}) \varphi_{D,A;lm}(\vec{r}) u_{k_0}(\vec{r}). \tag{27}$$

So, the expression for the matrix element for the electron tunneling transfer in a crystal medium has the former form (see Eq. (18)), and the crystal influence is reduced to the strong change in the tunneling exponent (compare expressions (26) and (16)) and, besides, to some changes in the pre-exponential factor (compare expressions (19) and (27)).

Lam Research Ex. 1035 - Page 56
Lam Research Corp. v. Inpria Corp.
IPR2024-00033 - U.S. Patent No. 9,823,564

4. Multiple Tunneling Scattering and Bridge Effect

A medium where electron transfer occurs is mostly a disordered one – either a liquid in electrochemical reactions or bio-oligomers in biologic objects etc. Generally speaking, formula (21) is suitable for any media, but it is impossible at present to calculate the wave functions in the expression (21) accurately so that it may calculate Green's function sufficiently and reliably. For the calculation of electron Green's function in such systems, a new method of multiple sub-barrier scattering was suggested in the works [12–16].

Let us first examine the influence of one intermediate particle (an atom or molecule) on electron Green's function, and let the center of this particle be placed at point $\boldsymbol{R}_1$ (see Figure 3.2). It can then be shown as [9,14]

$$G(\vec{r},\vec{r}';E) = G_0(\vec{r}-\vec{r}';E) + G(\vec{r}-\vec{R}_1;E)t_{R_1}(E,\theta;\Omega)G_0(\vec{R}_1-\vec{r}';E) \quad (28)$$

where $t_{R_1}(E,\theta;\Omega)$ is the electron scattering operator on the intermediate particle, θ is the angle between the vectors $\vec{r}-\vec{R}_1$ and $\vec{R}_1-\vec{r}'$, and Ω is the set of angles between these vectors and the coordinate axes bound with the center, if it is a molecule. This expression has a simple physical sense. The electron may arrive at point $\vec{r}'$ from point $\vec{r}$ by two ways namely, either by free movement (first summand in expression (28) or by moving from point $\vec{r}$ to the scattering center at point $\vec{R}_1$, scattering and moving to point $\vec{r}'$.

In the case of positive electron energy, the scattering operator

$$t(E,\theta;\Omega) = -2\pi\alpha(E,\theta;\Omega),$$

where $\alpha(E,\ \theta;\ \Omega)$, is the amplitude of electron scattering at the center. At $E<0$, i.e. at tunneling, the operator $t(E,\ \theta;\ \Omega)$, or $t(k,\ \theta;\ \Omega)$ in another variable where k is the electron momentum, is the analytic continuation of the function t(k, θ; Ω) at real k to the image axis in the complex plane k (see Refs. [1,9]). If the electron momentum is image one, its energy $E = k^2/2 < 0$. To make such analytic continuation it is necessary to know the analytic

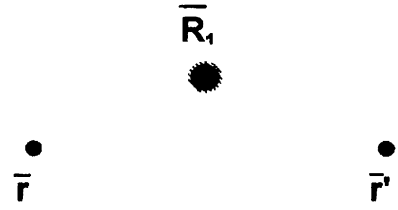


Fig. 3.2. The position of the intermediate particle-scatter with coordinate $\mathbf{R}_1$ in relation to points $\mathbf{r}$ and $\mathbf{r}'$.

Lam Research Ex. 1035 - Page 57
Lam Research Corp. v. Inpria Corp.
IPR2024-00033 - U.S. Patent No. 9,823,564

form of the scattering amplitude for the energies ε when $\varepsilon \leq |E|$. Such data for the amplitude of scattering at the real atomic or molecular centers are lacking now.

The variation-asymptotic method for the calculation of scattering operator $t(E, \theta; \Omega)$ at $E<0$ was proposed in works [12,13]. Its kernel is presented in the following. The distortion of the asymptotics of the donor wave function near the intermediate article, i.e. scattering center, may be found if one first introduces the correcting varied function φ_{var} and then minimizes the amendment to the total energy of the system (the donor + the scattering center) due to the electron interaction with electron–nuclear system of the scattering center. Both the Coulomb's interaction and the exchange one are taken into account strictly at this variation. The wave function of the electron state localized on the donor becomes known after calculation of φ_{var} in two MREL's (see Section 2), one near the donor and the other near the scatterer. Then, the asymptotics of the wave function at any point $\vec{r}$ may be found using the formula similar to (8) but with integration on two MREL. In result, one obtains the expression (28), and the operator $t(E, \theta; \Omega)$ is expressed as the integral where the integrand includes the function $\varphi_{var}(\boldsymbol{r}-\boldsymbol{R}_1)$ (see the works [12–14] where the detailed deduction is given).

In the frame of the simplest Hartry–Fock's approximation, the variation calculation of the scattering operator $t(E, \theta)$ for a few atoms has been made in the articles [12–14]. However, the variation scheme permits taking into account the different configurations in the wave function of the united system of electron and the scatterer. The general form of the scattering operator $t(E, \theta; \Omega)$ is [9,13,14]

$$t(E, \theta; \Omega) = \frac{a(\theta; \Omega)}{E - E_0} + t_{pot}(E, \theta; \Omega) \tag{29}$$

where E_0 is the energy of the electron bound on the scatterer. The first summand in Eq. (29) is the so-called pole term and the second summand is the potential part of the scattering operator. At $t_{pot} < 0$, the effective attraction of electron to the center takes place. The existence of the bound states means that $t_{pot} < 0$. The positive value of t_{pot} corresponds to the effective repulsion of electron from the center. The energy and the angle dependencies of the scattering operator for a few atoms calculated in Refs. [12–14] are presented in Figure 3.3. Note the strongly increasing $|t_{pot}(E, \theta)|$ when energy modulo $|E|$ increases for all investigated cases. It is bound by the effective growth of the exchange interaction at lowering of the electron energy, i.e. at increasing $|E|$.

So, the influence of one intermediate particle on Green's function and hence on V_{if} is given by expressions (28) and (10). If the donor, the scatterer and the acceptor lie on one straight line, the exponential factor

Lam Research Ex. 1035 - Page 58
Lam Research Corp. v. Inpria Corp.
IPR2024-00033 - U.S. Patent No. 9,823,564

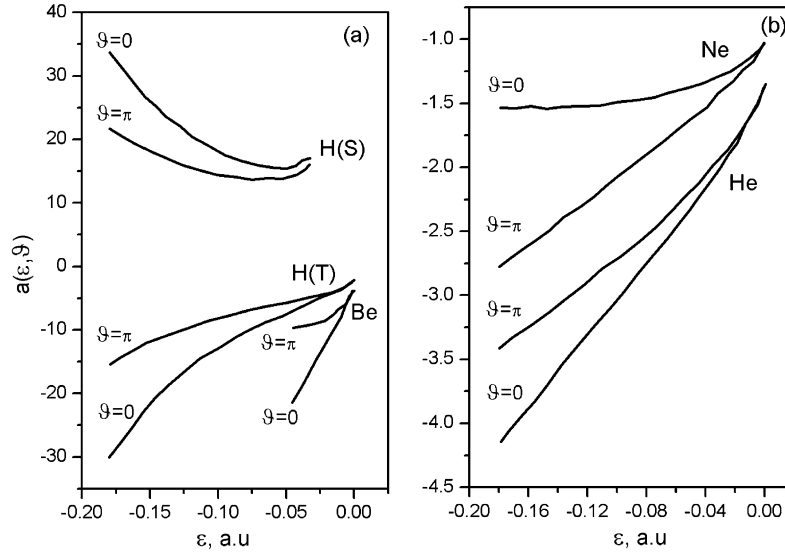


Fig. 3.3. The energy dependence of the amplitude of sub-barrier scattering $a(\varepsilon, \vartheta) = -t(\varepsilon, \vartheta)/2\pi$ at two scattering angles $\vartheta = 0$, and, $\vartheta = \pi$ for (a) singlet and triplet scattering off the hydrogen atom, beryllium atom and (b) helium and neon atoms.

$\exp\{-\kappa|\vec{r}_D - \vec{r}_A|\}$ is the same for both summands in formula (28). The second summand corresponding to the influence of the scatterer will be bigger than the first one at the fulfillment of the inequality

$$\left|\frac{t(E,0)}{2\pi}\right| > \frac{|\vec{r}_1 - \vec{r}_D||\vec{r}_A - \vec{r}_1|}{|\vec{r}_A - \vec{r}_D|} \tag{30}$$

(see definition (6)). The evaluations of the value $\left|\mathrm{t(E,\,0)}/2\pi\right|$ at the typical tunneling energies $E \approx -6\,\mathrm{eV}$ (see also Figure 3.3) show that the inequality (30) is fulfilled at $|\vec{r}_A - \vec{r}_D| \leq 50$ ($\sim 25\,\text{Å}$).

The molecular chain is frequently placed between the donor and the acceptor, and it may cause V_{if} increase very strongly. Such increase in the probability of tunneling transfer due to intermediate particles, or the bridge, is named bridge effect in the scientific literature [17]. This effect is particularly noticeable in the reactions in electron transfer in biologic systems [17,18] where the intermediate protein fragments serve as a bridge. Such fragments may be represented as a chain of molecular centers scattering the tunneling electron, and the bridge effect is the consequence of multiple electron scattering.

Let us deduce the general expression for the amplitude of the tunneling transition, i.e. the electron matrix element, in the presence of multiple

Lam Research Ex. 1035 - Page 59
Lam Research Corp. v. Inpria Corp.
IPR2024-00033 - U.S. Patent No. 9,823,564

scattering centers. It is supposed that the distance between any mth and nth centers $r_{mn} > \rho_{m,n}$, ρ_m is the characteristic radius of the region near the center where the correction function $\varphi_{\text{var}}(\boldsymbol{r} - \boldsymbol{r}_m)$ is noticeably different from zero. So, the correction functions of different centers do not overlap one another. It is convenient to represent the scattering operator t_n (29) on nth center in the form

$$\hat{t}_n(E, \theta; \boldsymbol{r}) = t_n(E, \theta)\delta(\boldsymbol{r} - \boldsymbol{r}_n).$$

The expression (28) for Green's function at one nth scattering center may be rewritten as:

$$G(\boldsymbol{r}, \boldsymbol{r}'; \varepsilon) = G_0(\boldsymbol{r}, \boldsymbol{r}'; \varepsilon) + \int d\boldsymbol{R} G_0(\boldsymbol{r}, \boldsymbol{R}; \varepsilon)\hat{t}_n(E, \theta; \boldsymbol{R})G_0(\boldsymbol{R}, \boldsymbol{r}'; \varepsilon). \tag{31}$$

As it was shown in article [19], the total operator of scattering in the system of N centers $\hat{T}$ is represented by the sum

$$\hat{T} = \sum_{n=1}^{N} \hat{T}_n \tag{32}$$

where the operators $\hat{T}_n$ are the resolutions of the system of the linear equations

$$\begin{aligned} \hat{T}_1 &= \hat{t}_1 + \sum_{i \neq 1} \hat{t}_1 G_0(\boldsymbol{r}_1, \boldsymbol{r}_i)\hat{T}_i \\ &\vdots \\ \hat{T}_N &= \hat{t}_2 + \sum_{i \neq N} \hat{t}_N G_0(\mathbf{r}_N, \mathbf{r}_i)\hat{T}_i \end{aligned} \tag{33}$$

It follows from these equations that the operators $\hat{T}_n$, $\hat{T}$ depend on two coordinates $\hat{T}(E, \boldsymbol{R}, \boldsymbol{R}')$ and Green's function is expressed in the form

$$G(\mathbf{r}, \mathbf{r}'; E) = G_0(\mathbf{r}, \mathbf{r}'; E) + \iint d\mathbf{R} d\mathbf{R}' G_0(\mathbf{r}, \mathbf{R}; E)\hat{T}(E; \mathbf{R}, \mathbf{R}')G_0(\mathbf{R}, \mathbf{r}', E). \tag{34}$$

The operators $\hat{t}_n(E, \theta, \mathbf{r}_n)$ are always situated between Green's functions $G_0(\boldsymbol{r}_s, \boldsymbol{r}_n; E)$ and $G_0(\boldsymbol{r}_n, \boldsymbol{r}_p; E)$ in the expressions for any $\hat{T}_i$, and θ is the angle between the vectors $\boldsymbol{r}_n - \boldsymbol{r}_s$ and $\boldsymbol{r}_p - \boldsymbol{r}_n$, where $\boldsymbol{r}_s$, $\boldsymbol{r}_p$ are the coordinates of the centers or $\mathbf{r}$, $\mathbf{r}'$. Therefore the operators $\hat{t}_n(E, \theta; r_n)$ and $\hat{t}_m(E, \theta; r_m)$ do not commute in general case when the angle dependence should be taken into account, since the angle θ changes when these operators are permuted. It is not difficult to see that only two angles θ, $\theta = 0$ and $\theta = \pi$, will appear in the scattering operators $\hat{t}_n(E, \theta; r_n)$ in the case of the linear chain. Therefore it is necessary to watch on the sequence of operators

Lam Research Ex. 1035 - Page 60
Lam Research Corp. v. Inpria Corp.
IPR2024-00033 - U.S. Patent No. 9,823,564

$\hat{t}_n(E, \theta; r_n)$ at the resolution of system (33) and to take it into account in the computer program [14].

The operators and Green's functions in the system of equations (33) should be taken at the energy of electron tunneling E_t, so the energy value in the total scattering operator will be E_t, $\hat{T}(E_t, \mathbf{R}, \mathbf{R}')$. Then, the general expression for the function $g_{\text{tot}}(r_{DA}, E)$ that should be substituted into Eq. (15) has the following form:

$$g_{\text{tot}}(r_{DA}, E_t) = g(r_{DA}, E_t)[1 + B(E_t; \boldsymbol{r}_{DA})], \tag{35}$$

where $g(r_{DA}, E_t)$ is described by the formula (16). The value $B(\varepsilon; \boldsymbol{r}_{DA})$ denotes the increasing coefficient due to the bridge of the scatterers.

Results of the numerical calculations [14,15] show that the value grows exponentially with the number of the centers N in the chain, or with the distance $\boldsymbol{r}_{DA} \approx Nd$ where d is the adjacent centers' separation,

$$B(\varepsilon; r_{DA}) = \exp\{\beta(\varepsilon, d)\mathrm{N}\}, \tag{36}$$

$\beta(\varepsilon, d) > 0$. Then, the exponential part of the tunneling transition amplitude is equal to

$$g_{\text{tot}}(r_{DA}, E_t) = -\frac{1}{r_{DA}}(\kappa r_{DA})^{(Z_D+Z_A)/\varepsilon_0\kappa}\exp\{-\alpha(E_t, d)r_{DA}\}. \tag{37}$$

The coefficient $\alpha(E_t, d)$ in the exponent,

$$\alpha(E_t, d) = \kappa - \frac{\beta(E_t, d)}{d}. \tag{38}$$

The analytic expression for $\beta(E_t; \boldsymbol{r}_{DA})$ via the value of operator $t(E_t, \vartheta)$ may be found, if the following inequality is fulfilled:

$$tG(\mathbf{R}_i, \mathbf{R}_{i+1}; \varepsilon) = \frac{t}{2\pi d}\exp(-\kappa d) \ll 1, \tag{39}$$

but it is considered that $t/2\pi d \geq 1$, since it is the term of the noticeable influence of the bridge. Inequality (39) is valid in the case where the tunneling energy E_t is far from the energy band of bound electron states on the chain [14–16]. Then it results in

$$\beta(E_t, d) = \ln\left[1 + \left|\frac{t(E_t, 0)}{(2\pi d)}\right|\right]. \tag{40}$$

The genuine criterion of the appreciable influence of the bridge on tunneling results from the equalities (40) and (36), i.e. $\mathrm{B}(\varepsilon, d) > 1$, if:

$$\frac{t(\varepsilon, 0)}{2\pi d} > \frac{1}{N}. \tag{41}$$

Lam Research Ex. 1035 - Page 61
Lam Research Corp. v. Inpria Corp.
IPR2024-00033 - U.S. Patent No. 9,823,564

This inequality is fulfilled with a large advantage in an overwhelming majority of cases, and the bridge effect is exponentially large (see Figure 3.3).

Let us now examine the chain of the similar centers in the case where the electron tunneling energy E_t is close to the bound energy E_0 of electron on one center (if it is), and consequently, the pole part of scattering operator is vastly more than potential one, $\alpha/(E_t - E_0) >> t_{\text{pot}}(E)$ (the angle dependence is omitted). The energy E_0 splits in the band of the energies of the bound states on the chain. If d is sufficiently large, so the inequality (39) is fulfilled for $t_{\text{pot}}(E_0)$, then the energy band is:

$$E_k = E_0 - V\cos\left(\pi d\frac{k}{(N+1)d}\right), \quad k = 1, 2, 3, \ldots, N \tag{42}$$

where the hopping integral V is expressed via the parameters of the pole part of the scattering operator (see (29)),

$$V = \left(\frac{a}{d}\right)\exp\{-\sqrt{2E_0}d\}. \tag{43}$$

If the tunneling energy E_t lies below the band but close to its minimum, $\delta_E = (E_0 - V) - E_t << V$, Green's function $G(\vec{r}, \vec{r}'; E)$ may be obtained according to formula (21) where the energy levels and the wave functions of the band states are only used [20]. Then, the resulting expression is:

$$G_e(\vec{r}, \vec{r}'; E) = -\frac{(m_e^*)^2}{2\pi|\vec{r} - \vec{r}'|}\varphi(\vec{r} - \vec{r}_1)\varphi(\vec{r}' - \vec{r}_N)\exp\{-\sqrt{2m_e^*\delta_E}|\vec{r} - \vec{r}'|\}. \tag{44}$$

Here, it is supposed that coordinates $\vec{r}$ and $\vec{r}'$ are near the ends of the chain, $\varphi(\vec{r} - \vec{r}_1)$ and $\varphi(\vec{r}' - \vec{r}_N)$ are the wave functions of the bound state at the first and last centers, and the effective mass is

$$m_e^* = (d^2V)^{-1} = (ad)^{-1}\exp\{\sqrt{2E_0}d\}. \tag{45}$$

Due to the bridge effect the value of coefficient $\alpha(E_t, d)$ (38) in the exponent of function $g_{\text{tot}}(r_{DA}, E_t)$ (39) may occur very small, so the matrix element V_{if} remains sufficiently large that the inequality (54a) of Chapter 2 is fulfilled on the significant distances r_{DA}. Then the transition becomes adiabatic even for the electron transfer over considerable distances. Really, the expression for V_{if} may be rewritten, taking into account the formulas (10), (15), (37) and (38), in the form

$$V_{if} \cong \exp\{-\alpha r_{DA}\} \tag{46}$$

where V_0 is of order 1. It follows from inequality (54a) of Chapter 2 that donor–acceptor electron transfer is adiabatic for all values $r_{DA} < r_{DA}^c$

Lam Research Ex. 1035 - Page 62
Lam Research Corp. v. Inpria Corp.
IPR2024-00033 - U.S. Patent No. 9,823,564

where

$$r_{DA}^{c} = \frac{1}{\alpha} \ln \frac{V_0}{2kT}. \tag{46a}$$

The transfer rate constant does not depend on r_{DA} when $r_{DA} < r_{DA}^{c}$ (see formula (55) of Chapter 2). The coefficient α at electron tunneling with the energy $E_t \approx -5\,\text{eV}$ (0.185 a.e.) along the polyene chain was measured in work [21], and it turned out $\alpha = 0.12$. Taking into account that the atomic unit of energy is equal to $\sim 3 \times 10^5$ K, one obtains the formula (46a) $r_{DA}^{c} \approx 28$ Å at the room temperature. So, the boundary value r_{DA}^{c} between the adiabatic and non-adiabatic processes is considerably shifted to the larger values due to bridge effect.

The influence of the molecules of an irregular medium, for example water, on the electron matrix element V_{if} may be examined just the same way. Using Eqs. (33) and (34) one can find electron Green's function by taking into account sub-barrier scattering on the water molecules between the donor and the acceptor. The chain of $N = r_{DA}/d$ molecules, where d is the mean intermolecule distance, makes the leading contribution to the bridge effect. The scattering operator of the molecule H_2O $t_{H_2O}(E, \theta; \Omega)$ depends on the molecule orientation angles Ω. The characteristic time of the electron motion ($\tau_e \sim r_{DA}/\kappa$) is much shorter than the time of the water molecule reorientation. Therefore the rate constant of the electron transfer $W \sim |V_{if}|^2$ should be averaged on all molecule orientations.

So, the different methods of calculating electron Green's function have been considered in the Sections 3 and 4. The most general method is the use of the spectral expansion of Green's function (see formula (21)), but it demands the knowledge of the electron energy spectrum and the wave functions of a media. These data are usually known for the crystals, but they are inaccessible in the case of an irregular media or the intermediate molecular chain. In these cases, the multiple sub-barrier scattering method gives an adequate description of the bridge effect.

5. Violation of Born–Oppenheimer's Approach in Electron Tunneling Transfer

The consideration of the reactions of the electron tunneling transfer was until now based on Born–Oppenheimer's adiabatic approach (see Section 2 of Chapter 2) that was used for the description of the wave functions of the initial and final states. The electron tunneling interaction $\hat{V}$ results in the non-adiabatic transition between these states, if the matrix element V_{if}

Lam Research Ex. 1035 - Page 63
Lam Research Corp. v. Inpria Corp.
IPR2024-00033 - U.S. Patent No. 9,823,564

satisfies to the inequality (54) of Chapter 2. But it will be shown in this section that Born–Oppenheimer's adiabatic approach is violated even for one term, without taking into account the interaction with another term, if the asymptotics of the wave function is examined [1]. The wave function of a system cannot be expressed in this case as the product of the electron wave function and nuclear one.

Let us use the method of calculating the asymptotics of the wave function from Section 2, but for the united electron-vibration system. For simplicity, the donor and the acceptor are presented below as the one-electron centers with the vibration degrees of freedom. Hamiltonian of the donor system in this case is

$$\hat{H}_i = \hat{H}_e(\vec{r}) + \hat{H}_{iv}(\{q\}) + V_i(\vec{r}) + U_i(\vec{r}, \{q\}). \tag{47}$$

Here, $\hat{H}_e(\vec{r})$ is Hamiltonian of a free electron, $V_i(\vec{r})$ is Coulomb's interaction of the electron with the donor ion residue, $\hat{H}_{iv}(\{q\})$ is Hamiltonian of the vibration subsystem depending on the set of the vibration coordinates $\{q\}$ that corresponds to the movement of nuclei without taking into account the interaction of the electron with the vibrations. The short-range (on $\vec{r}$) potential $U_i(\vec{r}, \{q\})$ describes the electron interaction with the donor ion residue and with the nuclear oscillations. The wave function of the system donor + electron may be represented in MREL in the adiabatic approach (see Section 2 of Chapter 2):

$$\Psi_D(\vec{r}, \{q\}; E_i) = \psi_D(\vec{r}) \prod_s \chi_{n_s^i}(q_s) \tag{48}$$

where the weak parametric dependence of the electron wave function Ψ_D on q is omitted and $\chi_{n_s}(q_s)$ is the wave function of sth vibration mode corresponding to the level n_s. The energy E_i is the sum of the bound energy of the electron on the donor E_D and the vibration energy of the system when the electron is bound to the donor

$$E_i = E_D + E_{vi} = E_D + \sum_s \hbar\omega_s \left(n_s^i + \frac{1}{2} \right). \tag{49}$$

The asymptotics of the wave function (48) at $r \in$ AR (AR is the asymptotic region, out of MREL) may be expressed similarly to formula (8):

$$\Psi_D^a(\vec{r}, \{q\}; E_i)\big|_{r \in AO} = \iint d\vec{r}' d\{q'\} G_{V_i + \hat{H}_e + \hat{H}_v}(\vec{r}, \vec{r}'; \{q\}, \{q'\}; E_i) \times U_i(\vec{r}', \{q'\}) \psi_D(\vec{r}') \prod_s \chi_{n_s}(q_s'). \tag{50}$$

Lam Research Ex. 1035 - Page 64
Lam Research Corp. v. Inpria Corp.
IPR2024-00033 - U.S. Patent No. 9,823,564

One may use the spectral representation [9] to find Green's function in expression (50) (see and compare the definition (21)):

$$G_{\hat{H}(\{\rho\})}(\{\rho\},\{\rho'\};E)=\sum_{v}\frac{\psi_v(\{\rho\})\psi_v*(\{\rho'\})}{E-\varepsilon_v-i\delta}. \tag{51}$$

Here, $\Psi_v(\{\rho\})$ is the eigen function of Hamiltonian $\hat{H}(\{\rho\})$ with the eigen energy ε_v and the summation occurs on all states including the integration on the continuous spectra, δ is the infinitesimal defining the rule of the pole bypass in expression (51).

Hamiltonian $\hat{H}(\{\rho\})$ in the considered case is

$$\hat{H}(\{\rho\})\equiv\hat{H}_e(\vec{r})+V_i(r)+\hat{H}_{iv}(\{q\}) \tag{52}$$

where Hamiltonian of the electron in Coulomb's field, $\hat{H}_{\text{coul}}(\vec{r})=\hat{H}_e(\vec{r})+V_i(r)$, commutes with vibration Hamiltonian $\hat{H}_{iv}(\{q\})$. Then, the eigen function of Hamiltonian $\hat{H}(\{\rho\})$ that should be substituted in formula (51) should have the form:

$$\psi_v(\vec{r},\{q\};\varepsilon_v)\equiv\psi_{\mu,\text{coul}}(\vec{r};\varepsilon_\mu)\prod_s\chi_{n_s}(q_s-\delta q_s). \tag{53}$$

In the expression (53), $\psi_{\mu,\text{coul}}(\vec{r};\varepsilon_\mu)$ is the eigen function of Hamiltonian $\hat{H}_{\text{coul}}(\vec{r})$ and $\chi_{n_s}(q_s-\delta q_s)$ is the wave function of sth mode of the system without electron. Note that the potential of the electron interaction with the vibrations $U_i(\vec{r},\{q\})$ does not include in Hamiltonian $\hat{H}(\{\rho\})$, therefore the equilibrium position of the vibration mode is shifted to the value δq_s with respect to one in the system with electron (48). It is supposed that the vibrations are the phonons of the media, and the shift of the equilibrium positions are only taken into consideration. The possible shift of the frequencies may be easily taken into account by the corresponding changes in the phonon energy (see Chapter 2, formulas (20b), (27) and (27a)). The set of quantum numbers in (51) is $v\equiv(\mu,\{n_s\})$, and the corresponding energies are

$$\varepsilon_v=\varepsilon_\mu+\sum_s\hbar\omega_s\left(n_s+\frac{1}{2}\right). \tag{54}$$

Then, after substitution of the definitions (53) and (54) in formula (51) one obtains:

$$\begin{aligned}G_{V_i+\hat{H}_e+\hat{H}_v}(\vec{r},\vec{r}';\{q\},\{q'\};E_i)=&\sum_{\{n_s\}}G_{\hat{H}_{\text{coul}}}\left(\vec{r},\vec{r}';E_i-\sum_s\hbar\omega_s\left(n_s+\frac{1}{2}\right)\right)\\&\times\prod_s\chi_{n_s}(q_s-\delta q_s)\chi_{n_s}(q'_s-\delta q_s).\end{aligned} \tag{55}$$

Lam Research Ex. 1035 - Page 65
Lam Research Corp. v. Inpria Corp.
IPR2024-00033 - U.S. Patent No. 9,823,564

The asymptotics of the donor wave function may be calculated now, if to substitute the function (55) in formula (50) and to take into account the expressions (15)–(17) for electron Green's function in Coulomb's field. The influence of the acceptor Coulomb's field is meanwhile excluded from these expressions since the asymptotics of the one-center wave function is considered now:

$$\Psi_D^a(\vec{r},\{q\};E_i) = -A_D\frac{1}{r}(\kappa r)^{Z_D/\varepsilon_0\kappa} \times \sum_{\{n_s'\}}\exp\left\{-\sqrt{2\left|\left[E_D+E_{vi}-\sum_s\hbar\omega_s\left(n_s'+\frac{1}{2}\right)\right]\right|}r\right\} \cdot\prod_s\chi_{n_s'}(q_s-\delta q_s)\left\langle\chi_{n_s'}(q_s'-\delta q_s)\middle|\chi_{n_s}(q_s')\right\rangle. \tag{56}$$

The coefficient A_D is defined as

$$A_D=\sum_{lm}\int d\vec{r}\,'\varphi_{D;lm}(\vec{r}\,',E)U_i(\vec{r}\,')\psi_D(\vec{r}\,'), \tag{57}$$

where $\varphi_{D;lm}(\vec{r}\,',E)$ is defined by the formula (17). The weak dependence of potential $U_i(\vec{r}\,',\{q'\})$ on vibration coordinates q_s' is not taken into account in the matrix elements on these coordinates (see similar approach in Chapter 2, the paragraph after formula (31)).

It is not difficult to see the asymptotics of the wave functions $\Psi_D^a(\vec{r},\{q\};E_i)\big|_{r\in AO}$ (56) that are not represented, generally speaking, by the product of the wave functions of the electron and nuclear coordinates, contrary to the wave function in MREL (48). The contributions of the different vibration modes in the asymptotics (56) change with changes in the electron coordinates. So, Born–Oppenheimer's approach is really violated in the asymptotics of the wave function [2]. Such violation has also been revealed in article [22].

The deviation from the adiabatic approach in the asymptotics is particularly remarkable when the energy $|E_D|$ is small and comparable with the reorganization energy in the vibration system E_{rD} at the transition from the neutral donor to the positive ion. Such smallness of $|E_D|$ is possible, if the donor electron level in a crystal (see Section 3) lies near the conductivity or valence bands (compare with expression (23)), and δ_E plays the role of E_D.

However, if $|E_D| >> E_{rD}$, the adiabatic approach proves valid even at a sufficiently large distance r. This inequality permits us to expand the exponent in formula (56) on the small value $E_{rD}/|E_D|$. Then, the exponent

Lam Research Ex. 1035 - Page 66
Lam Research Corp. v. Inpria Corp.
IPR2024-00033 - U.S. Patent No. 9,823,564

(with an accuracy of the first order) is equal to

$$-\sqrt{2|E_D|}r + \sqrt{2|E_D|}\frac{E_{rD}}{2|E_D|}r.$$

The second term can be neglected for the values of r when

$$r < \frac{\sqrt{2|E_D|}}{E_{rD}}, \tag{58}$$

and therefore the exponential function in formula (56) may be taken out from the sign of sum on $\{n_s\}$. Then, the equation

$$\sum_{n_s} \chi_{n_s}(q_s - \delta q_s)\chi_{n_s}(q'_s - \delta q_s) = \delta(q_s - q'_s).$$

is valid for each sth mode because this equation is the definition of the completeness of the system of the oscillator eigen functions. It results that the standard adiabatic expression with divided electron and nuclear variables is valid for the asymptotics until the inequality (58) is fulfilled:

$$\Psi_D^a(\vec{r}, \{q\}; E_D + \sum_s \hbar\omega_s(n_{s+1/2}))\Big|_{r\in AO} = -A_D\frac{1}{r}(\kappa r)^{Z_D/\varepsilon_0\kappa}\exp\{-\sqrt{2|E_D|}r\} \times \prod_s \chi_{n_s}(q_s). \tag{59}$$

The amplitude of electron tunneling transfer with simultaneous change of the vibrations in the case of the non-adiabatic asymptotics (56) may be found, if to substitute the expression (56) instead of Ψ_D^a to the definition (9) and the acceptor wave function in the matrix element (9) should be its total expression

$$\Psi_A(\vec{r}, \{q\}; E_f) = \psi_A(\vec{r}; E_A)\prod_s \chi_{n_s^f}(q_s - \delta_A q_s). \tag{60}$$

Here $\delta_A q_s$ is the shift of the equilibrium position in sth mode resulting at the electron transfer from the donor to the acceptor. The total energy E_f of the system in the final state is

$$E_f = E_A + E_{vf} = E_A + \sum_s \hbar\omega_s\left(n_s^f + \frac{1}{2}\right). \tag{61}$$

Besides, Coulomb's field of the acceptor should be taken into account in Green's function (55) and, hence, in the asymptotics of donor wave function Ψ_D^a (56) (see the formulas (15)–(17)).

Lam Research Ex. 1035 - Page 67
Lam Research Corp. v. Inpria Corp.
IPR2024-00033 - U.S. Patent No. 9,823,564

The rate constant of the electron tunneling transfer is then calculated on the standard formula (see expression (9) of Chapter 2):

$$W_{if} = 2\pi A v_{\{n_s^i\}} \{V_{if}^2 \delta(E_i - E_f)\} \tag{62}$$

where V_{if} is defined by formula (9), $\Psi_D^a(\vec{r}, \{q\}; E_i)$ – by formulas (56) and (57), $\Psi_A(\vec{r}, \{q\}; E_f)$ – by formula (60). The initial and final energies E_i and E_f are given by expressions (49) and (61) correspondingly. It results in:

$$\begin{aligned} W_{if} = {} & 2\pi |A_D A_A|^2 \frac{1}{r^2} (\kappa r_{DA})^{2(Z_D+Z_A)/\varepsilon_0\kappa} \\ & \times A v_{n_s^i} \prod_s \sum_{\{n_s'\}} \int d\varepsilon \delta \left(\varepsilon - E_{vi} + \sum_s \hbar\omega_s \left(n_s' + \frac{1}{2} \right) \right) \\ & \times \exp\{-2\sqrt{2|E_D + \varepsilon|} r_{DA} \left| \left\langle \chi_{n_s^i}(q_s') \middle| \chi_{n_s'}(q_s' - \delta q_s) \right\rangle \right|^2 \\ & \times \sum_{n_s^f} \left| \left\langle \chi_{n_s'}(q_s - \delta q_s) \middle| \chi_{n_s^f}(q_s - \delta_A q_s) \right\rangle \right|^2 \delta(E_{vf} - \Delta E - E_{vi}). \end{aligned} \tag{63}$$

Here, $\Delta E = E_D - E_A$ is the heat of the reaction of electron transfer (see formula (9b) of Chapter 2), and the value A_A is defined by the expression similar to expression (57) for A_D.

Let us analyze and simplify the expression (63). The multiphonon transitions occur near the donor and the acceptor in the processes of tearing off the electron from the donor and the capture of electron by the acceptor (see the corresponding sums of the squared matrix elements in expression (63)). Since the distance r_{DA} is large, much bigger than the interparticle distance in the media, one may neglect the correlation between the modes of which the populations are changed near the donor and the same near the acceptor [23]. It means the populations of the different modes are changed near the donor and the acceptor, i.e. at averaging on n_s^i in expression (63), simultaneous independent averaging on the populations n_s' of the modes in the matrix elements $\langle \chi_{n_s'}(q_s - \delta q_s) | \chi_{n_s^f}(q_s - \delta_A q_s) \rangle$ occurs.

The expression (63) may then be rewritten as

$$W_{if} = B(r_{DA}) \int d\varepsilon \, \exp\{-2r_{DA}\sqrt{2|E_D + \varepsilon|}\} f_D(T, -\varepsilon) f_A(T, \Delta E + \varepsilon). \tag{64}$$

The designation is introduced here:

$$B(r_{DA}) = 2\pi |A_D A_A|^2 \frac{1}{r^2} (\kappa r_{DA})^{2(Z_D+Z_A)/\varepsilon_0\kappa} \tag{65}$$

Lam Research Ex. 1035 - Page 68
Lam Research Corp. v. Inpria Corp.
IPR2024-00033 - U.S. Patent No. 9,823,564

$$f_D(T,-\varepsilon) = Av_{n_s^i}\left\{\sum_{n_s'} |\langle\chi_{n_s^i}(q_s')|\chi_{n_s'}(q_s'-\delta q_s)\rangle|^2\delta \left(\varepsilon - E_{vi} + \sum_s \hbar\omega_s\left(n_s' + \frac{1}{2}\right)\right)\right\}, \tag{66}$$

$$f_A(T,\Delta E+\varepsilon) = Av_{n_s'}\left\{\sum_{n_s^f} |\langle\chi_{n_s'}(q_s-\delta q_s)|\chi_{n_s^f}(q_s-\delta_A q_s)\rangle|^2\delta(E_{vf}-\Delta E-\varepsilon)\right\}. \tag{67}$$

Due to the weak dependence of $B(r_{DA})$ on ε, the definition $\kappa = \sqrt{2|E_D|}$ is retained in formula (65) instead of $\kappa = \sqrt{2|E_D+\varepsilon|}$, therefore the value $B(r_{DA})$ may be taken out from the sign of the integral on ε in expression (64).

Note, the structure of expressions (66) and (67) is absolutely similar to the structure of the phonon part of the expression (9) of Chapter 2 for the rate constant of the multiphonon transition. The energy difference $-\varepsilon$ between the energies of the intermediate phonon system and initial one in function $f_D(T, -\varepsilon)$ and the energy difference $\Delta E+\varepsilon$ of the energies of the final phonon system and intermediate one in function $f_A(T, \Delta E+\varepsilon)$ play the role of ΔE, i.e. the difference of the final and initial energies, in formula (9) of Chapter 2. Let us examine the most widespread case of high temperatures and large reorganization energies on the donor and the acceptor (see inequalities (23) of Chapter 2). Then, the functions f_D and f_A that should be substituted in expression (64) have the form (see formula (27) of Chapter 2):

$$\begin{aligned} f_D(T,-\varepsilon) &= \tfrac{1}{4\pi^{3/2}\sqrt{E_{rD}kT}}\exp\left\{-\tfrac{(E_{rD}+\varepsilon)^2}{4E_{rD}kT}\right\}, \\ f_A(T,\Delta E+\varepsilon) &= \tfrac{1}{4\pi^{3/2}\sqrt{E_{rA}kT}}\exp\left\{-\tfrac{(E_{rA}-\Delta E-\varepsilon)^2}{4E_{rA}kT}\right\}. \end{aligned} \tag{68}$$

The values E_{rD} and E_{rA} are the reorganization energies at the ionization of the donor and at the electron capture by the acceptor.

Since all factors in the integrand (64) depend exponentially on ε, the integral may be easily calculated by the method of speediest descent, or the method of stationary phase [24]. The stationary point ε^* can be found from the equation

$$\frac{d}{d\varepsilon^*}\left\{-2\sqrt{2|E_D|-\varepsilon^*}r_{DA} - \frac{(E_{rD}+\varepsilon^*)^2}{4E_{rD}kT} - \frac{(E_{rA}-\Delta E-\varepsilon^*)^2}{4E_{rA}kT}\right\} = 0. \tag{69}$$

Lam Research Ex. 1035 - Page 69
Lam Research Corp. v. Inpria Corp.
IPR2024-00033 - U.S. Patent No. 9,823,564

The expression for the rate constant ensues after the sufficiently simple algebraic transformation:

$$W_{if} = C\ \exp\{-2\sqrt{2(|E_D| - \varepsilon^*)}r_{DA}\}\exp\left\{-\frac{(E_r - \Delta E)^2}{4E_r kT}\right\}$$
$$\exp\left\{-\frac{E_r}{4E_{rD}E_{rA}kT}\left(\varepsilon^* + \frac{E_{rD}\Delta E}{E_r}\right)^2\right\}, \tag{70}$$

where coefficient C weakly depends on both r_{DA} and the energy characteristics of the system, and

$$E_r = E_{rD} + E_{rA}. \tag{71}$$

The exponent determining the dependence of the rate constant on the distance of tunneling is, generally speaking, the function of the temperature, of the reaction heat ΔE and of the donor and acceptor reorganization energies, as it follows from Eqs. (69) and (70). The electron tunneling transfer in organic glasses was studied in work [25]. The experimental situation was the following. The γ-radiation induces the ionization in the glass, then the free electron are captured by the intrinsic traps. After that, the captured electrons start to tunnel from the traps (donors specially placed in the glass) to the different molecules (acceptors) with the controlled concentration. The coefficient κ in the exponent κr_{DA} was found from the dependence of the logarithm of the rate constant on the concentration. It was discovered that the dependence of k on the type of acceptor for the same donor cannot be explained by the theory where the electron and nuclear variables are divided as in Chapter 2. But such dependence follows from formula (70) since the change of the type of acceptor designs the change of E_{rA} and ΔE.

The physical sense of the condition of the violation of the adiabatic approach in the representation of the wave functions can be easily understood if we expand the exponent in the expression (64) on ε and turn to the usual units:

$$2r\frac{1}{\hbar}\sqrt{2m(|E_D| - \varepsilon)} \approx 2r\frac{1}{\hbar}\sqrt{2m|E_D|} - \frac{\varepsilon}{\hbar}\frac{r}{\sqrt{2|E_D|/m}}. \tag{72}$$

Let us take into account that the characteristic value of $\varepsilon \sim E_{rD}$, and the second factor in the last summand of expression (72) is time τ of the classic motion of an electron with energy $|E_D|$ on distance r. Then, if it fulfills the condition

$$\frac{\tau E_{rD}}{\hbar} \geq 1, \tag{73}$$

Lam Research Ex. 1035 - Page 70
Lam Research Corp. v. Inpria Corp.
IPR2024-00033 - U.S. Patent No. 9,823,564

second summand in formula (72) is not small. Therefore, the adiabatic representation of the wave function is violated on such distance from MREL that the time of classic flight of electron is larger than the inverse frequency corresponding to the reorganization energy at the electron tearing off the electron.

If r_{DA} is not too large, namely,

$$r_{DA} << \frac{\sqrt{2|E_D|}\Delta E}{2E_{rA}kT}, \tag{74}$$

the stationary point ε^* after the resolution of equation (69) is the following one: $\varepsilon^* = -E_{rD}\Delta E/E_r$. This value converts third exponent in expression (70) to 0. Besides, one may neglect the value ε^* in the first exponent due to inequality (74). Then, the expression for the rate constant ensues in the standard form (see (29) of Chapter 2):

$$W_{if} \cong CExp\{-2\sqrt{2|E_D|}r_{DA}\}\exp\left\{-\frac{(E_r - \Delta E)^2}{4E_r kT}\right\}, \tag{75}$$

where E_r from expression (71) proves to be the total reorganization energy. This expression has the simple physical sense: the phonon modes that participate in the transition near the donor and the acceptor are different (see the discussion above), therefore the total reorganization energy should be the sum of the reorganization energies connected with the donor and the acceptor.

The general expression for the rate constant (70) transforms to expression (75) at $\Delta E = 0$, if the following limitation on the tunneling distance r_{DA} is realized:

$$r_{DA} << \sqrt{\frac{2|E_D|}{E_r kT}}. \tag{74a}$$

As it was shown above, the condition of validity of usual Born–Oppenheimer's approach (see wave function (59)) is the inequality (58) which practically coincides with inequality

$$\frac{\tau E_{rD}}{\hbar} << 1 \tag{76}$$

that is strongly opposite to the condition of violation of the adiabatic approach (73).

At the classical description of the nuclear degrees of freedom (it is the classical approach that is used in the theory of electron transfer in polar media (see Chapter 2, Section 5)), the fulfillment of criterion (73) results in the following. Instead of one effective oscillator (see Chapter 2) where the equilibrium position is shifted at the transition, it should now introduce two

Lam Research Ex. 1035 - Page 71
Lam Research Corp. v. Inpria Corp.
IPR2024-00033 - U.S. Patent No. 9,823,564

oscillators with the different reorganization energies. Then the energy of electron tunneling depends on the value of the coordinates of these oscillators, at which the transition occurs. Such dependence results in the dependence of the activation energy on the distance r_{DA}. Such classical approach to the electron tunneling is described in detail in works [26,27].

6. Conclusions

So, the description of the theory of electron tunneling transfer is logically accomplished in this chapter – it describes the methods of calculation of the electron matrix element, whereas the methods of calculation and the form of the vibration part of the transition probability was represented in Chapter 2. Besides, in Chapter 3 the procedure of the calculation of the rate constant of tunneling transfer in the conditions of the violation of Born–Oppenheimer's approach is examined. The basic results of this chapter may be formulated as follows.

The formula for the electron matrix element V_{if} at the tunneling transfer is strongly realized where it is given the exact expression for the pre-exponential factor. The exponent is defined by the electron energy.

The influence of the insulator crystal media on the matrix element V_{if} is reduced to taking into account the dependence of Green's function on the position of the electron energy level in relation to the crystal electron energy bands. The calculation of Green's function is carried out using of its spectral representation. If the level of the bound electron is close to the minimum of the conductivity band or to the maximum of the valence band, the value of the tunneling exponent decreases noticeably.

The bridge effect, i.e. the influence of the intermediate particles of an irregular media or of a molecular chain between the donor and the acceptor on the value of matrix element V_{if} has been investigated This influence is described as the multiple scattering of the tunneling electron on these intermediate particles. The amplitude of electron sub-barrier scattering on one particle strongly increased with lowering of the tunneling energy that resulted in appreciable decrease in the modulo of exponent in Green's function, i.e. in the exponential growth of V_{if} with increase in the number of scattering particles. It is shown that in the description of the wave function of an electron–nuclear system, the Born–Oppenheimer's adiabatic approach is violated in the far asymptotics of the wave function on the electron coordinate. It results in the following effects: the tunneling exponent starts to depend on the temperature and the reorganization energy of the vibration system depends on the donor–acceptor distance at the far tunneling transfer.

Lam Research Ex. 1035 - Page 72
Lam Research Corp. v. Inpria Corp.
IPR2024-00033 - U.S. Patent No. 9,823,564

The answers to the following questions will help the readers to better understand the contents of the chapter.

1. What is Green's function of a particle?
2. What is the asymptotics of a wave function and how it is calculated?
3. What is the accuracy parameter in the calculation of the tunneling electron matrix element?
4. What is the spectral representation of Green's function?
5. How does electron Green's function in a crystal change at the change of the electron energy in the forbidden zone?
6. When is the approach of effective mass in the band suitable in the calculation of electron Green's function?
7. What is the criterion of the applicability of the adiabatic approach for the description of the asymptotics of the wave function of an electron–nuclear system?
8. What are the expressions for the donor and acceptor reorganization energies at the electron transfer in polar media?

References

1. L. D. Landau, E. M. Lifshits, Quantum Mechanics, GIFML, Moscow, 1963.
2. G. K. Ivanov, M. A. Kozhushner, Phys. Solid State **20** (1978) 9.
3. G. K. Ivanov, M. A. Kozhushner, Chem. Phys. **170** (1993) 303.
4. G. K. Ivanov, M. A. Kozhushner, Phys. Lett. **A188** (1994) 361; K. Ya. Burshtein, G. K. Ivanov, M. A. Kozhushner, V. S. Posvyanskii, J. Exp. Theor. Phys. **109** (1996) 63.
5. M. L. Goldberger, K. M. Watson, Collision theory, Wiley, New York, 1964.
6. L. Hostler, R. H. Pratt, Phys. Rev. Lett. **10** (1963) 469.
7. E. L. Slagi, E. H. Wichman, J. Math. Phys. **3** (1962) 946.
8. R. Balian, C. Bloch, Ann. Phys. (N.Y.) **63** (1971) 592.
9. A. I. Baz', B. Ya. Zel'dovich, A. M. Perelomov, Scattering, Reactions Decays in Non-Relativistic Quantum Mechanics, Nauka, Moscow, 1971.
10. A. A. Abrikosov, L. P. Gor'kov, I. E. Dzialoshinskii, Methods of Quantum Theory of Field in Statistical Physics, FML, Moscow, 1962.
11. J. Tomphor, O. F. Sankey, Phys. Rev. **B65** (2002) 245105.
12. M. A. Kozhushner, R. R. Muriasov, Doklady Phys. Chem. **372** (2000) 628.

Lam Research Ex. 1035 - Page 73
Lam Research Corp. v. Inpria Corp.
IPR2024-00033 - U.S. Patent No. 9,823,564

13. M. A. Kozhushner, R. R. Muriasov, Chem. Phys. **24** (2005) 22.
14. D. I. Bolgov, M. A. Kozhushner, R. R. Muriasov, V. S. Posvianskii, J. Chem. Phys. **119** (2003) 3871.
15. D. I. Bolgov, M. A. Kozhushner, R. R. Muriasov, V. S. Posvianskii, Electrochemistry **39** (2003) 81.
16. M. A. Kozhushner, V. S. Posvyanskii, I. I. Oleynik, Chem. Phys. **319** (2005) 368.
17. E. G. Petrov, Physics of Charge Transfer in Bio-Systems, Naukova dumka, Kiev, 1984.
18. J. M. Klein, P. L. McEuen, J. E. Bowen Katari, R. Roth, A. P. Alivisatos, Appl. Phys. Lett. **68** (1996) 2574.
19. F. I. Dalidchik, G. K. Ivanov, J. Appl. Spectrosc. **13** (1970) 363.
20. L. N. Christoforov, V. N. Kharkyanen, Phys. Stat. Sol. **B116** (1983) 415.
21. X. D. Cui, A. Primak, X. Zarate, J. Tomphor, O. F. Sankey, J. Phys. Chem. **B106** (2002) 8609.
22. D. N. Beratan, J. J. Hopfield, J. Chem. Phys. **81** (1984) 5753.
23. M. A. Kozhushner, Phys. Solid State **13** (1971) 2601.
24. M. A. Lavrent'ev, B. V. Shabat, Methods of Theory of Functions of Complex Variable, Nauka, Moscow, 1965.
25. J. R. Miller, J. Chem. Phys. **56** (1972) 5173.
26. A. I. Burshtein, G. K. Ivanov, M. A. Kozhushner, Chem. Phys. Rep. **1** (1982) 195.
27. A. I. Burshtein, G. K. Ivanov, M. A. Kozhushner, Chem. Phys. Lett. **84** (1981) 135.

Lam Research Ex. 1035 - Page 74
Lam Research Corp. v. Inpria Corp.
IPR2024-00033 - U.S. Patent No. 9,823,564

Chapter 4

Ab Initio Calculations of Electronic Transitions and Photoabsorption and Photoluminescence Spectra of Silica and Germania Nanoparticles

A.M. Mebel[a], A.S. Zyubin[b,c], M. Hayashi[d], and S.H. Lin[c]

[a]*Department of Chemistry and Biochemistry, Florida International University, Miami, FL 33199, USA*
[b]*Institute of Problems of Chemical Physics, Russian Academy of Sciences, Chernogolovka, Moscow Region 142432, Russia*
[c]*Institute of Atomic and Molecular Sciences, Academia Sinica, P.O. Box 23-166, Taipei 106, Taiwan*
[d]*Center for Condensed Matter Sciences, National Taiwan University, Taipei 106, Taiwan*

1. Introduction 68
2. Theoretical Approach and Methods 72
   2.1. Model Clusters and Geometry Optimization 72
   2.2. Calculations of Excitation Energies 75
   2.3. Calculations of Vibronic Spectra 81
3. Photoluminescence Properties of Point Defects in SiO_2 83
   3.1. Red and Near Infrared Photoluminescence Bands in Silica Nanostructures . 83
   3.2. PL Properties of the Silanone and Dioxasilyrane Point Defects 89
   3.3. Photoabsorption and Photoluminescence of the $[AlO_4]^0$ Defect in SiO_2 . . . 95
4. Optical Properties of Point Defects in GeO_2 99
   4.1. Photoluminescence of Oxygen-Containing Surface Defects in Germanium Oxides 99
   4.2. Photoluminescence of Oxygen-Deficient Defects in Germanium Oxides . . . 108
5. Summary and Outlook 113
6. Discussion Topics and Questions on Concepts 115
References 116

Ab initio and density functional calculations of potential energy surfaces for the ground and excited electronic states of model clusters simulating various point defects, impurities, and their combinations in nanosized silica and germania materials are reported. The accurate geometric and electronic structures of these clusters, calculated photoabsorption and photoluminescence (PL) energies, and predicted absorption and PL spectra are obtained. Our calculations reproduced the experimental excitation energy (1.9–2.0 eV)

THIN FILMS AND NANOSTRUCTURES, vol. 34
ISSN 1079-4050
DOI: 10.1016/S1079-4050(06)34004-5

© 2007 by Elsevier Inc.
All rights reserved.

Lam Research Ex. 1035 - Page 75
Lam Research Corp. v. Inpria Corp.
IPR2024-00033 - U.S. Patent No. 9,823,564

for the non-bridging oxygen (NBO) defect in SiO_2. The combined defects with oxygen vacancy (OV) in the first coordination sphere of NBO are shown to be unstable, but more distant OVs can coexist with NBO. The variety of the red PL bands observed experimentally at 1.1–1.9 eV has been assigned in terms of different arrangements of NBO and OV in the combined defects. The silanone and dioxasilyrane defects were found to be plausible candidates for green and red light-emitters. The PL band corresponding to the $[AlO_4]^0$ defect is predicted to contain few bands between 1.5 and 1.0 eV and in the range of 0.7–0.2 eV. In the –O–Ge≡ (NBO), –OO–Ge≡ (peroxy radical), O = Ge = , and (O_2)Ge = defects in GeO_2 nanomaterials, UV-photoabsorption is shown to be accompanied by red or IR PL. The surface E′-center, $–GeX_3$, and combined E′–OV, $X_3Ge–GeX_2$, defects are demonstrated to produce photoabsorption bands between 4 and 6 eV. The $–GeX_3$ defect is able to generate several PL bands in the UV (~3 eV) and IR (1.2–1.4 and 0.5–0.6 eV) spectral ranges, whereas the $X_3Ge–GeX_2$ defect gives a red/orange PL band at 2.0–2.1 eV.

1. Introduction

Novel nanomaterials based on crystalline and vitreous modifications of SiO_2 and GeO_2, including silica nanoparticles and mesoporous molecular sieves (MSs), germanosilicate glasses, and pure germanium oxides, play a central role in optoelectronic technologies, metal-oxide semiconductor devices, Si/SiO_2 superlattices, optical fibers, and phase-grating patterns [1–12]. Silica- and germania-based nanoscale materials exhibit great catalytic, adsorption, and photophysical properties [6] and are expected to play a vital role as both interconnect and act as functional components in future micro- and mesoscopic electronic and optical devices. Because of their potential broad applications, the synthesis and study of SiO_2 and GeO_2 nanomaterials is a cornerstone of modern nanoscience and technology. The goal of experimental material science is to develop new materials with properties desirable for particular applications. However, this goal is often difficult and expensive to attain unless scientists achieve a clear understanding of basic relationships between the microscopic structure of materials at the atomic/molecular level and their macroscopic properties. In this view, the role of theoretical chemistry is to elucidate these relationships through reliable and accurate calculations of the electronic structure of nanomaterials.

The particular property we are concerned with in this chapter is the ability of silica and germania nanostructures to absorb UV or visible light giving rise to visible or IR photoluminescence (PL). In bulk, SiO_2 and GeO_2 are

Lam Research Ex. 1035 - Page 76
Lam Research Corp. v. Inpria Corp.
IPR2024-00033 - U.S. Patent No. 9,823,564

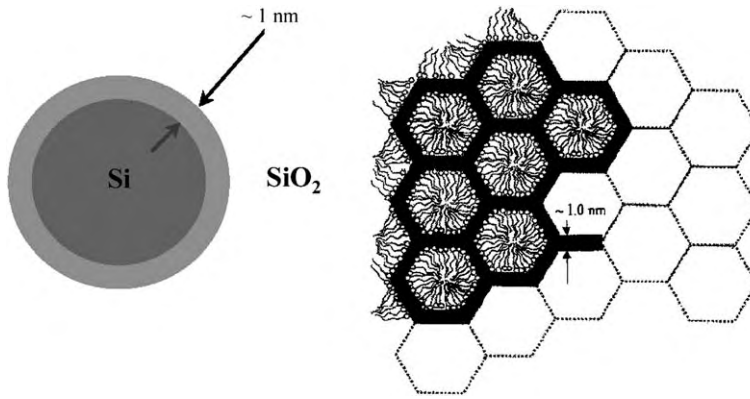


Fig. 4.1. Schematic structure of a silicon nanoparticle with a thin SiO_2 passivating layer and of mesoporous silica (MCM-41 material).

insulators and can absorb light only in the ultraviolet spectral region. However, the presence of point defects can enable them to absorb and emit lower frequency photons. In nanomaterials, due to a large surface-to-volume ratio, a variety of structural defects (mainly broken bonds and local violations of stoichiometry) can be much more abundant than in the bulk resulting in dramatic changes of optical properties.

For example, recent studies of thermally treated silica-based nanomaterials, including the MSs MCM-41 and Si/SiO_2 nanoparticles, which contain oxide fragments of ~1 nm thickness (see Figure 4.1), revealed a presence of several types of structural defects and their combinations [13–18]. These defects are able to emit light with optical excitations, giving rise to a diversity of the PL bands spread over the entire visible and near-infrared ranges, which is extremely important for future applications. It has been suggested that the PL from MSs originates from non-bridging oxygens (NBOs) (red bands), hydrogen-related defects (green bands), and some water and organic impurities (blue bands) [15,16]. However, the actual nature of the emitting centers in SiO_2 and in combined Si/SiO_2 materials including oxidized silicon nanocrystals and porous silicon with passivating oxide layers [19,20] still remains controversial. Various theories have been put forward which suggest that the PL properties are determined by light-emitters located either inside silicon nanoscales or on the Si/SiO_2 interface [3–5] and that the observed diversity of the PL spectra is in part due to the quantum confinement effect. Another important factor is recognized to be the role of various point defects and impurities that are able to emit light in the visible range [21–27]. Numerous defects are typical for silica nanoparticles and MSs, such as NBOs, oxygen vacancies (OV), the surface E′-center (–Si≡),

Lam Research Ex. 1035 - Page 77
Lam Research Corp. v. Inpria Corp.
IPR2024-00033 - U.S. Patent No. 9,823,564

the silanone group (O = Si =), the peroxy linkage (≡Si–O–O–Si≡), the dioxasilyrane (= SiO_2), the two-coordinated silicon (= Si:), the double OVs (≡Si–Si–Si≡), etc. These defects and their combinations exhibit different absorption and PL properties and may be responsible for the visible PL of silica nanoscales in different energy ranges. The generation of SiO_2 defects in experiment, their characterization by various experimental techniques and by theoretical quantum-chemical analysis are also described by Radzig in Chapter 7 of this book.

Optical properties of Ge-related defects in germanosilicate glasses and pure germanium oxides have also attracted significant attention due to their potential applications in combined GeO_2/SiO_2 systems [28, 29], and have been investigated both experimentally [11, 12, 30–38] and theoretically [39–44]. For example, bulk quantity GeO_2 nanowires with a diameter of ~50–120 nm with remarkable PL properties have been synthesized [12]. The structure of these nanomaterials is quartz-like and the chemical composition is close to $GeO_{1.75}$ (substoichiometric GeO_2). On photoexcitation at 5.6 eV, the nanowires emit stable and very bright blue light in the range between 2 and 3 eV with the peak position at 2.56 eV. The PL intensity for the nanowires [12] has been found to be more than an order of magnitude higher than that for GeO_2 nanopowders [35, 36]. The PL apparently originates as a result of electronic transitions at one or more point defects, but the nature of the emitting centers is unknown. It has been proposed [12] that the PL is related to OVs, but the photon energy used for photoexcitation was substantially lower than the energy required for exciting an OV in GeO_2 (~7 eV) [43]. The PL band observed for nanowires is rather broad and may have a multi-source origin; at least several defects may contribute to its formation.

Apparently, a variety of different structures or point defects can coexist in nanoscale Si/SiO_2 and Ge/GeO_2 materials, which are able to emit visible and near infrared PL. In some nanostructures (nanoparticles, nanowires, nanofibers, mesoporous materials, or ultrathin layers) synthesized under certain conditions particular point defects or their combinations can be more favorable that the others and the large concentration of defects of a certain type may determine optical properties of the material. Therefore, it is crucial to understand electronic transitions inherent to each defect (or their combination), and thus to establish a solid relationship between the structure of the material and its electronic spectra. By now, systematic information has been accumulated about point defects in silica. Quantum chemical modeling has made significant contribution to interpretation and understanding of structure and photoabsorption properties of these defects [21, 45, 46]. On the other hand, theoretical modeling of PL properties, which accompany the light absorption, is a more challenging task because they are related to geometric relaxation of defect structures in excited electronic

Lam Research Ex. 1035 - Page 78
Lam Research Corp. v. Inpria Corp.
IPR2024-00033 - U.S. Patent No. 9,823,564

states. Consequently, only scarce theoretical data are currently available to interpret PL spectra of silica and GeO_2 nanoscale materials.

Ab initio and density functional (DFT) calculations represent a powerful tool for theoretical investigations of electronic properties, such as electronic transition energies, transition dipole moments, geometry relaxation due to electronic excitation, and vibrational properties including vibrational frequencies, IR and Raman intensities, normal modes, coupling between electronic and vibrational motions (vibronic coupling), as well as radiationless relaxation of excited electronic states (internal conversion, IC and intersystem crossing, ISC). The properties of nanoparticles obtained from the quantum chemical calculations can be applied to predict their optical properties, such as absorption, luminescence, and various non-linear optical properties. In this chapter, we describe *ab initio* and DFT calculations of various defects in SiO_2- and GeO_2-based nanomaterials, in order to characterize their structural, electronic, and vibrational properties and to predict their spectroscopic properties using vibronic theory. Theoretical calculations allow us to establish the structure/optical properties correlation, and should eventually help researchers to suggest novel nanostructures with desirable optical properties.

In the ongoing research in our groups, we investigate the most common defects in AO_2 (A = Si and Ge), including NBOs, the surface E′-center (–A≡), the O = A = group, the peroxy linkage (≡A–O–O–A≡), the = AO_2 defect, the single and double OVs (≡A–A≡ and ≡A–A–A≡), the protonated A–O–A bridge, the most common impurities like Al and Ti, as well as combinations of two or more different defects. We predict accurate geometric and electronic structures of nanosized silica and GeO_2 clusters containing different point defects, impurities, and their combinations. Next, we calculate electronic excitation energies for the structures containing these defects and optimize their geometries in excited states. The results of the *ab initio* and DFT calculations are then used to assign or predict absorption and PL spectra related to various defects in GeO_2- and SiO_2-based nanoparticles.

Absorption of light in many cases can lead to significant structural transformations in nanoparticles resulting in large Stokes shifts, which can reach up to several eV. Therefore, the interpretation of PL bands and understanding which point defect is the source of each particular PL band detected in experiment is a very difficult task. In order to achieve this goal, it is necessary to obtain a detailed information concerning structural transformations of local defects after their electronic excitation by visible or UV light. Such information is useful not only for the purposes of interpretation and assignment, but also for understanding the mechanisms and the role of point defects in degradation of SiO_2- and GeO_2-based electronic devices.

Lam Research Ex. 1035 - Page 79
Lam Research Corp. v. Inpria Corp.
IPR2024-00033 - U.S. Patent No. 9,823,564

The quantum chemical modeling is a very useful supplement to spectroscopic experimental methods for investigation of properties of point defects, however, until recently it was used mainly for calculations of vertical excitation energies. The modeling of structural transformation in excited electronic states is still a rather complicated task, which requires state-of-the-art quantum chemical calculations. In this chapter, we first describe theoretical methods applied in *ab initio* and vibronic theory calculations and then demonstrate their applications in theoretical studies of various point defects in silica and germania.

2. Theoretical Approach and Methods

In this section, we discuss theoretical methods, which can be applied for calculations of photoabsorption and PL spectra of silica and germania nanoparticles. We start with the choice of model cluster simulating these materials and point defects in them and consider methods for geometry optimization in the ground and excited electronic states (Subsection 2.1). This is followed by the description of more advanced quantum chemical methods for accurate calculations of excitation energies (Subsection 2.2) and the section is completed by the discussion on the theoretical procedure used for predicting vibronic spectra associated with point defects (Subsection 2.3).

2.1. Model Clusters and Geometry Optimization

The most stable forms of bulk SiO_2 are constructed from vertex-sharing SiO_4 tetrahedrons (Figure 4.2) forming a continuous three-dimensional network. The Si–O–Si angles are flexible and can have a variety of values from 125° to 180° (144° for the α-quartz). The torsion angles are also non-rigid, which results in the diversity of SiO_2 polymorphs [47]. On the other hand, the SiO_4 tetrahedrons conserve their shape with Si–O distances and O–Si–O angles of ~1.61 Å and 109.5°, respectively [47, 48]. One can imagine the modification of the silica network as a rotation of vertex-sharing rigid tetrahedrons leading to substantial shifts of oxygen atoms, while the positions of Si atoms remain nearly unchanged. In quartz-like GeO_2, as in SiO_2, bonding has a local character, and the influence of a point defect on the electronic redistribution is limited to its nearest neighborhood. In the adjacent layers around the defect, the perturbation of electronic density is usually small. This allows us to treat electronic transitions in such defects using cluster models, which were discussed and widely used earlier [39–46, 49–55]. A model cluster usually

Lam Research Ex. 1035 - Page 80
Lam Research Corp. v. Inpria Corp.
IPR2024-00033 - U.S. Patent No. 9,823,564

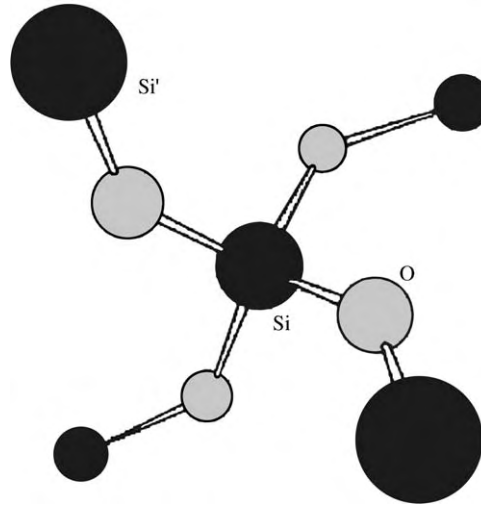


Fig. 4.2. Model $Si(OX)_4$ cluster ($X = OSiH_3$) simulating the defect-less bulk silica structure.

includes the atoms directly involved in the electronic redistribution (the active region) and their nearest neighborhood. In order to avoid the appearance of artificial transitions originated from broken boundary bonds connecting the cluster with the rest of the bulk, hydrogen atoms are usually added to terminate these bonds. It was demonstrated that, in order to properly reproduce the electronic structure and relative energies of excited states, it is sufficient to take into account the defect itself and the oxygen atoms directly linked to it, for instance, the O–AO_3, O = AO_2, or AO_2 fragments for the O–A≡, O = A<, or A< point defects, respectively. Normally, surface point defects, such as the NBO, peroxy radical, surface E′-center, or two-coordinated Si or Ge do not cause substantial distortion of the network. For model clusters simulating such systems, full geometry optimization can be usually carried out. Various orientations of boundary groups corresponding to different local minima in these clusters only weakly influence the electronic excitation energies, and, to simplify the calculations of excited electronic states, it is convenient to use the most symmetric structure corresponding to the local symmetry of the defect.

Alternatively, defects containing an oxygen vacancy (OV) can significantly deform the network, mainly due to mechanical distortions of the defect and its surrounding fragment. In order to simulate both network relaxation caused by the defect and its incorporation into the bulk in such systems, one needs to use larger model clusters that include at least one additional layer of bonds surrounding the defect. The atomic coordinates inside the model

Lam Research Ex. 1035 - Page 81
Lam Research Corp. v. Inpria Corp.
IPR2024-00033 - U.S. Patent No. 9,823,564

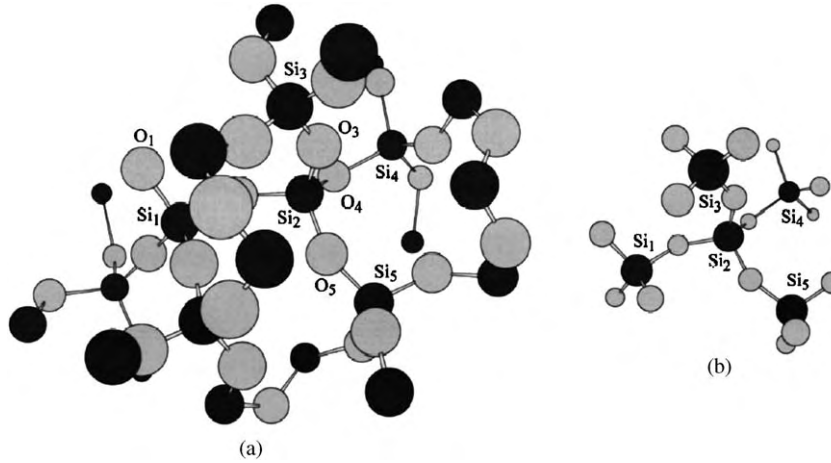


Fig. 4.3. Typical model cluster for simulating oxygen vacancies (a) and its high-level ONIOM fragment (b).

cluster should be optimized to simulate relaxation of the neighborhood, while the positions of the boundary atoms should be kept frozen in order to mimic the situation where the defect is embedded into the bulk. The positions of boundary atom can be determined from larger defect-less clusters or taken from the crystallographic data (such as those for α-quartz).

Density functional B3LYP calculations with the standard 6-31G* basis set of SiO_2 model clusters provide a good agreement with experimental data for bulk silica. However, because of large cluster sizes (Figure 4.3a) it is not feasible to use this level of theory for the whole cluster. Therefore, we used the ONIOM method [56], which gives an opportunity to treat various parts of large systems at different levels of theory. Within this approach, the model clusters were separated into two layers, inner and outer. The inner layer is calculated using a high level of theory, including the defect area with its nearest neighborhood, and contains 5 Si and 12–15 O atoms (Figure 4.3b), while the remaining atoms of the cluster constitute the outer layer and are treated by a low-level calculation. The inner part was handled at the B3LYP/6-31G* level and the semiempirical PM3 approach was employed for the outer layer [57–59]. The PM3 method provides quite reasonable structural parameters for the SiO_2 and GeO_2 networks [55], better than the results of Hartree-Fock (HF) calculations (see Table 4.1). We have tested this ONIOM (B3LYP/6-31G*:PM3) approach for calculations of a model $Si(OX)_4$ cluster ($X = SiH_3$ represents the outer layer) and obtained the geometrical parameters in good agreement with those from the B3LYP/6-31G* calculations for the whole cluster (Table 4.1).

Lam Research Ex. 1035 - Page 82
Lam Research Corp. v. Inpria Corp.
IPR2024-00033 - U.S. Patent No. 9,823,564

Table 4.1. Inter-atomic distances R(A–B) (in Å) for model $Si(OX)_4$ (X = SiH_3) cluster calculated by different theoretical methods

Method	R(Si–Si′)	R(Si–O)	R(O–Si′)
ONIOM[a]	2.98	1.63	1.66
B3LYP/6-31G*	3.12	1.63	1.66
B3LYP/mixed[b]	3.08	1.64	1.71
HF/6-31G*	3.31	1.64	1.67
PM3	3.01	1.67	1.67
Exp. (α-quartz)	3.01, 3.09	1.61	1.61

[a]B3LYP/6-31G *for SiO_4; PM3 for X.
[b]6-31G *for SiO_4; 6-31G for X.

Each particular two-layer combination of the ONIOM method (like B3LYP/6-31G*:PM3 or MP2/6-31G*:PM3) was first tested and calibrated for particular defect types. For example, the density functional B3LYP approach appeared to be unreliable for geometry optimization of silica clusters containing the $[AlO_4]^0$ impurity defect [60, 61]. Therefore, in ONIOM calculations of such clusters we chose to use the MP2:PM3 combination, which gave clusters' geometries in good agreement with those obtained by more sophisticated multi-reference complete active space self consistent field (CASSCF) calculations. Basis sets for *ab initio* and DFT calculations also have to be chosen with special care because calculations without polarization *d* functions usually lead to overestimation of Si–O bond lengths and Si–O–Si bond angles, significant overestimation of the Si–Si distances in silica clusters, and therefore may give poor results. Geometries of excited electronic states can be optimized employing the CASSCF [62, 63], TD-DFT [64], or symmetry-adapted clusters configuration interaction (SAC-CI) [65–68] methods, or using partial optimization of critical geometric parameters using more accurate levels of theory – the details for each particular case are described in the subsequent sections.

2.2. Calculations of Excitation Energies

Various *ab initio* and density functional methods available in commercial quantum chemistry program packages, such as GAUSSIAN 03, MOLPRO, ACES II, and DALTON, can be employed for calculations of excitation energies. The most reliable approaches based on multi-reference configuration interaction with single and double excitations (MRDCI [69] and internally contracted MRCI [70, 71]) or complete active space perturbation theory to the 2nd order (CASPT2 [72]) are very demanding computationally

Lam Research Ex. 1035 - Page 83
Lam Research Corp. v. Inpria Corp.
IPR2024-00033 - U.S. Patent No. 9,823,564

and can be used in present only for small systems containing up to 20–30 active electrons and for few electronic states in each symmetry subgroup. The treatment of high-lying excitations within these approaches is problematic even for small model molecules. The coupled clusters based approaches (such as SAC-CI or equation-of-motion coupled clusters with single and double excitations EOM-CCSD [73, 74]) are applicable for a wider set of excited electronic states but their use in present is still limited to middle-sized closed-shell systems or small open-shell ones.

In recent years, the time-dependent density functional response theory (TD-DFT) has become a broadly applied tool for excited state calculations [53, 64, 75–78]. This approach allows one to treat much larger systems as compared to those that can be computed by the methods mentioned above and in many cases provides quite reasonable results. However, due to the incorrect asymptotic behavior of the DFT exchange-correlation potentials [79–81], the accuracy of TD-DFT excitation energies depends on the type of the considered electronic transition. Normally, TD-DFT performs satisfactorily for localized transitions with relatively low excitation energies (~2–5 eV), but for high-lying excited states involving delocalized electron distributions and, in particular, for Rydberg states, TD-DFT tends to underestimate transition energies by up to 1–2 eV.

To test the accuracy of this method dealing with excitation energy calculations of various defects in SiO_2, we compared the TD-B3LYP results with those obtained with higher level *ab initio* calculations and from experimental data (see Table 4.2) [59, 82]. The excitation energies calculated with the TD-B3LYP/6-31 + G* approach closely (within 0.2 eV) match those measured experimentally when electronic transitions involve localized orbitals, such as the lone pairs of bridging and NBO atoms, LP_{BO} and LP_{NBO}, in the O–SiX_3 clusters as well as π^*_{OO} and σ^*_{OO} in X_2SiO_2. However, the performance of the TD-B3LYP/6-31 + G* approach is much worse for transitions involving orbitals with a significant diffuse (Rydberg) character. For instance, the TD-B3LYP method underestimates the higher level MRDCI and experimentally obtained excitation energies by 1–1.5 eV for the transitions to both Si lone pairs (LP_{Si}) in the –SiX_3 and SiX_2 clusters and the Si–Si antibonding σ^* orbital in X_3Si–SiX_3. Even more underestimated excitation energies are found from the calculations of both the π^*_{OO}–σ^*_{OO} transition in the $X_3SiOOSiX_3$ cluster (peroxide bridge defect) and the Rydberg LP_{BO}–R_{Si} transition in the $X_3SiOSiX_3$ cluster (silica band-to-band transition [83]). Similar conclusions about the performance of TD-DFT for excited states of point defects in silica were obtained in a detailed study by Raghavachari et al. [53]. Therefore, the application of the higher level *ab initio* CASPT2, MRCI, EOM-CCSD, or SAC-CI methods is essential to provide more reliable excitation energies.

Lam Research Ex. 1035 - Page 84
Lam Research Corp. v. Inpria Corp.
IPR2024-00033 - U.S. Patent No. 9,823,564

Table 4.2. Vertical excitation energies (in eV) for different defects in SiO_2

Cluster	Transition character	TD-B3LYP	EOM-CCSD	MRDCI	Exp.
–O–SiX_3	LP_{BO}–LP_{NBO} (D_0–D_2)	2.00[a]		2.18[b,c]	2.0[d]
–O–SiX_3	σ_{SiO}–LP_{NBO}	5.27[b]		6.14[b,c]	~4.8[d]
X_2SiO_2	π^*_{OO}–σ^*_{OO} (S_0–S_1)	3.19[a]	3.33[a,e]	3.02[b,e]	~3.0[e]
X_2SiO_2	π'^*_{OO}–σ^*_{OO} (S_0–S_2)[f]	5.03[a]	5.27[a,e]	5.15[b,e]	~5.0[e]
$X_2Si=O$	π'_{Si-O}–LP_{Si} (S_0–S_1)[g]	5.09[a]	5.70[a,e]	5.75[b,e]	~5.6[e]
$X_2Si=O$	π_{Si-O}–LP_{Si} (S_0–S_2)[g]	5.45[a]	6.02[a,e]	5.73[b,e]	
–SiX_3	LP_{BO}–LP_{Si} (D_0–D_1)[g]	5.04[b]		6.21[b,h]	~6.2[d]
SiX_2	LP_{Si}–LP_{Si} (S_0–S_1)[g]	4.63[b]		5.62[b,e]	~5.0[d]
X_3Si–SiX_3	σ_{SiSi}–σ^*_{SiSi} (S_0–S_1)[g]	6.08[b]		7.47[b,e]	~7.6[d]
$X_3SiOOSiX_3$	π^*_{OO}–σ^*_{OO} (S_0–S_1)[g]	4.99[a]		6.84[b,e]	
$X_3SiOSiX_3$	LP_{BO}–R_{Si}[g,i]	6.94[a]		8.80[b,e]	~8.9[j]

[a]Calculated with $X = OSiH_3$.
[b]Calculated with $X = OH$.
[c]From Ref. [46].
[d]From Ref. [45].
[e]From Ref. [52].
[f]π' orbital is placed in the SiO_2 plane.
[g]Excited state wavefunction has a significant contribution from diffuse (Rydberg) orbitals.
[h]From Ref. [50].
[i]R – Rydberg electronic state.
[j]From Ref. [83].

Another alternative is the outer valence Green functions (OVGF) method based on the electron propagator theory [84–87]. The OVGF approach is designed for calculations of electron binding energies, i.e., ionization potentials (IP) or electron affinities (EA) related to various electrons in atoms and molecules. For the transitions involving the highest occupied or lowest unoccupied molecular orbitals (HOMO or LUMO), we proposed using OVGF to evaluate a set of excitation energies combining IP and EA values for neutral and charged systems [88,89]. For instance, using the first ionization potential for a neutral system and EA values for the corresponding positive ion one can estimate excitation energies EE^0(HOMO,J) for the transitions from HOMO to the empty orbital J as a difference between the IP and EA:

$$EE^0(\mathrm{HOMO,J}) = IP^0(\mathrm{HOMO}) - EA^+(\mathrm{J}) \tag{1}$$

or for a system with the charge N:

$$EE^N(\mathrm{HOMO,J}) = IP^N(\mathrm{HOMO}) - EA^{N+1}(\mathrm{J}) \tag{1a}$$

where IP^N denotes ionization potential for the N-charged system and EA^{N+1} for electron affinity for the system with the charge $N+1$. For a

Lam Research Ex. 1035 - Page 85
Lam Research Corp. v. Inpria Corp.
IPR2024-00033 - U.S. Patent No. 9,823,564

closed-shell neutral system, the $EA^+(J)$ values for β and α spin correspond to singlet–singlet and singlet–triplet excitations, respectively. It should be noted that applications of Eq. (1) to lower lying occupied orbitals would give less accurate results, since $EA^+(J)$ values in the OVGF method are calculated for the system with an electron removed from HOMO. If the basis set contains suitable diffuse functions, one can apply this approach to evaluate excitation energies for transitions from HOMO to high-lying Rydberg states.

Another type of transitions where OVGF can be readily applied corresponds to excitations in open-shell systems with electron transferring from doubly occupied orbitals to the singly occupied molecular orbital (SOMO). The excitation energies for such transitions can be evaluated using IPs of the corresponding anion:

$$EE^0(I, SOMO) = IP^{-1}(I) - IP^{-1}(HOMO) \quad (2)$$

or for system with the charge N:

$$EE^N(I, SOMO) = IP^{N-1}(I) - IP^{N-1}(HOMO) \quad (2a)$$

Here, EE^N(I,SOMO) is excitation energy for the transition of an electron from the doubly occupied orbital I to SOMO in the N-charged radical, while $IP^{N-1}(I)$ and IP^{N-1}(HOMO) for IPs from orbital I and HOMO in the closed-shell system with one additional electron.

While testing the performance of the TD-DFT and OVGF methods, we looked at molecules with different types of electronic transitions. As an example of systems with electronic excitations occurring to a localized molecular orbital, we considered radicals containing a single-bonded O atom, which are related to the NBO defect in SiO_2 and GeO_2 (see Table 4.3). Here, the lowest in energy excitations take place from doubly occupied MOs to SOMO with the dominant character of a lone pair of the single-coordinated oxygen atom, LP (O_1). For most systems tested, the excitation energies calculated with B3LYP, CASPT2, MRDCI, and OVGF theoretical approaches are in good agreement with each other and with available experimental data. However, we have found a few alarming discrepancies. For instance, at all levels of theory used here (Table 4.3), the lowest in energy electronic excitation in the $O^\bullet$–OH and $O^\bullet$–OCH_3 radicals, ~1.1 eV, occurs from the antibonding π'^*(OO) orbital located in the molecular plane with the main contribution from the terminal oxygen (the $^2A'$ electronic state), while the second excitation is much higher in energy, 5.5–6 eV, and takes place from the π(OO) orbital lying in the perpendicular plane ($^2A''$ state). Similar results were obtained for the $O^\bullet$–$OSi(OH)_3$ system using the CASPT2 and OVGF methods; however, at the TD-B3LYP level the character of the excited states significantly differs.

Lam Research Ex. 1035 - Page 86
Lam Research Corp. v. Inpria Corp.
IPR2024-00033 - U.S. Patent No. 9,823,564

Table 4.3. Excitation energies (in eV) for transitions from doubly occupied MOs to the singly occupied orbital of oxygen in systems with single-bonded O atom

System	Transition from	TD-B3LYP	CASPT2	MRDCI	OVGF	Exp.
$O^{\bullet}$–H	OH-bond	4.33	4.36		4.35	4.05
$O^{\bullet}$–OH	π'^{*}(OO)	1.13 $1^2A'$	1.08 $1^2A'$[a]		1.06 $1^2A'$	~1[a]
$O^{\bullet}$–OH	π(OO)	6.10 $2^2A''$	6.16 $2^2A''$[a]		6.36 $2^2A''$	~6[a]
$O^{\bullet}$–OCH_3	π'^{*}(OO)	1.12 $1^2A'$	1.12 $1^2A'$[a]		1.08 $1^2A'$	–
$O^{\bullet}$–OCH_3	π(OO)	5.19 $2^2A''$	5.40 $2^2A''$[a]		5.48 $2^2A''$	5.4[a]
$O^{\bullet}$–$OSi(OH)_3$	π'^{*}(OO)	0.79 $1^2A'$	0.71 $1^2A'$[a]		0.69 $1^2A'$	
$O^{\bullet}$–$OSi(OH)_3$	π(OO)	6.28 $6^2A''$	5.49 $2^2A''$[a]		5.41 $2^2A''$	
$O^{\bullet}$–$OSi(OH)_3$	σ(OO)		6.39[a] $2^2A'$[a]		6.40 $2^2A'$	
$O^{\bullet}$–$OSi(OH)_3$	π′(OO)		6.83[a] $3^2A'$[a]		6.49 $3^2A'$	
$O^{\bullet}$–$OSi(OH)_3$	LP(OH)	4.16 $2^2A''$	7.59[a] $3^2A''$[a]		6.25 $3^2A''$	
$O^{\bullet}$–$OSi(OH)_3$	LP(OH) $^2A''$	4.83, 5.17				
$O^{\bullet}$–$OSi(OH)_3$	LP(OH) $^2A'$	4.98, 5.88				
$O^{\bullet}$–$Si(OH)_3$	π(O)	0.45 $1^2A'$	0.24 $1^2A'$[a]	0.04[b]	0.20 $1^2A'$	
		$f = 1.0 \times 10^{-4}$	$f = 7.7 \times 10^{-6}$	$f = 3.0 \times 10^{-6}$		
$O^{\bullet}$–$Si(OH)_3$	σ(SiO)	5.17 $5^2A'$	2.02 $2^2A'$[a]	2.18[b,c]	2.07 $2^2A'$	~4.8[d]
		$f = 6.0 \times 10^{-3}$	$f = 5.6 \times 10^{-4}$	$f = 4.0 \times 10^{-4}$		
$O^{\bullet}$–$Si(OH)_3$	LP(OH)	2.05 $2^2A'$	4.08 $2^2A''$[a]	6.14[b,c]	3.75 $2^2A''$	~2.0[d]
		$f = 1.0 \times 10^{-3}$	$f = 5.2 \times 10^{-2}$	$f = 2.0 \times 10^{-3}$		
$O^{\bullet}$–$Si(OH)_3$	LP(OH)	2.62 $2^2A''$	5.02 $3^2A'$[a]		4.99 $3^2A'$	
		$f = 7.0 \times 10^{-3}$	$f = 3.5 \times 10^{-2}$			
$O^{\bullet}$–$Si(OH)_3$	LP(OH)	3.36 $3^2A''$			4.63 $3^2A''$	
		$f = 6.0 \times 10^{-3}$				
$O^{\bullet}$–$Si(OH)_3$	σ(SiOH),	4.09 $4^2A'$				
	σ(SiO)	$f = 5.0 \times 10^{-3}$				
$O^{\bullet}$–$Si(OSiH_3)_3$	π(O)	0.28			0.11	
$O^{\bullet}$–$Si(OSiH_3)_3$	σ(SiO)	5.39			2.07	
$O^{\bullet}$–$Si(OSiH_3)_3$	LP(O_b), H	2.00			3.84	
$O^{\bullet}$–$Si(OSiH_3)_3$	LP(O_b), H	2.58, 2.81			3.99	
$O^{\bullet}$–$Si(OSiH_3)_3$	LP(O_b), H	3.05–3.45			4.41	
$O^{\bullet}$–$Si(OSiH_3)_3$	LP(O_b), H	4.42–5.09			4.66	

[a] From Ref. [90].
[b] From Ref. [46].
[c] The character of the transition is not given.
[d] From Ref. [21].

Another example concerns $O^{\bullet}$–SiX_3 clusters simulating NBO in bulk SiO_2. While all the methods used give the energy of the second excitation close to 2 eV, within the CASPT2 and OVGF approaches this transition originates from the orbital mainly of the σ(Si–O) character, but at the TD-DFT level the excitation occurs predominantly from lone pairs of bridging O_b atoms in the nearest neighborhood of NBO (Table 4.3). At TD-DFT, the σ(Si–O)→LP(NBO) excitation lies rather high in energy, 5.1–5.4 eV for various clusters. While both approaches predict a smaller oscillator strength for the 2 eV transition as compared to the 5 eV one, at the B3LYP level the difference is not as large as at CASPT2 (Table 4.3). The σ(Si–O)→LP(NBO)

Lam Research Ex. 1035 - Page 87
Lam Research Corp. v. Inpria Corp.
IPR2024-00033 - U.S. Patent No. 9,823,564

excitation at TD-DFT lies rather high in energy (~5.4 eV for the largest $O^{\bullet}$–$Si(OSiH_3)_3$ cluster). TD-DFT calculations additionally produce a set of electronic states between 2 and 5 eV corresponding to transitions from MOs combined of $LP(O_b)$ of terminal OH or $OSiH_3$ groups. Thus, although the calculated energies of the ~2 eV transition are similar, its assignment from the TD-DFT calculations significantly differs from that for supposedly more accurate CASPT2. A possible reason for this discrepancy could be misinterpretation of complicated multi-determinant wave functions. $LP(O_b)$ indeed contributes in the molecular orbital giving rise to the $\sigma(Si–O) \rightarrow LP(NBO)$ transition as does the $\sigma(Si–O)$ orbital in the $LP(O_b) \rightarrow LP(NBO)$ excitation but these contributions are relatively small. Although the TD-DFT assignment of the ~2 eV transition agrees with the tentative assignment made by experimentalists [21], the CASPT2 [90] and OVGF assignments seem to be better justified. One could argue that the $\sigma(Si–O) \rightarrow LP(NBO)$ excitation should cause a significant variation of the Si–O bond length and, accordingly, a large Stokes shift. However, this is not the case; the Stokes shift is small (0.1 eV) for the NBO-related 2.0 eV transition in silica. This can be explained by the fact that in the excited state, terminal O and Si atoms bear significant opposite charges and are subjected to additional donor–acceptor interaction compensating for the removal of an electron from the $\sigma(Si–O)$ bond. As a result, the change of the Si–O distance in the excited state calculated at the CASPT2 level is small.

In the $^{\bullet}Si(OX)_3$ cluster, which simulates a surface E′-center in bulk silica, two lowest in energy electronic transitions occur from MOs combined of oxygen lone pairs to the singly occupied sp^3-hybrid-type orbital of Si. In this case, the TD-B3LYP result (4.66 eV) underestimates the experimental value by ~1.5 eV, while the OVGF excitation energy (6.36 eV) is close to the MRDCI value (6.21 eV) and experimental data (6.2 eV).

Thus, the TD-DFT method can significantly underestimate excitation energies not only for diffuse Rydberg states, but also for electronic states involving transitions between MOs localized in different, remote from each other, spatial regions, for example, charge-transfer excitations. The most probable reason for the deviations is incorrect asymptotic behavior of DFT exchange-correlation functionals. In many cases where TD-DFT is unreliable, excitation energies can be evaluated by the OVGF approach, for which the accuracy is determined by its accuracy for calculations of electron binding energies. Since the computational demands for OVGF calculations are similar to those of the MP2 method, the OVGF method can be applied for calculations of electronic excitation energies for rather large clusters simulating nanoparticles. For the excitations with predominantly single-determinant wave functions, the performance of the OVGF method is satisfactory, with the deviations of calculated energies from experiment or

Lam Research Ex. 1035 - Page 88
Lam Research Corp. v. Inpria Corp.
IPR2024-00033 - U.S. Patent No. 9,823,564

higher level theoretical results in the range of 0.2–0.3 eV for transitions involving valence and low-lying Rydberg MOs and of 0.1–0.2 eV for high-lying Rydberg states. However, for excited states with multi-reference wave functions or for transitions involving complicated multiple bonds, the OVGF approach is less reliable and in some cases the errors can be as high as 0.5–1 eV. Thus, both TD-DFT and OVGF approaches are not universal and should be carefully tested for each group of molecules or radicals and for specific electronic excitations before they are used.

In summary, a variety of *ab initio* and DFT methods can be applied for different types of model clusters. A comparison of the results of different methods with available experimental data should be carried out and, based on this comparison, a proper theoretical procedure should be chosen for each particular type of point defect in SiO_2 and GeO_2.

2.3. Calculations of Vibronic Spectra

The *ab initio* and DFT calculations of the ground and excited potential energy surfaces (PESs) for model clusters simulating point defects in nanoparticles lay foundation for theoretical prediction of their spectroscopic and dynamic properties, such as vibronic spectra for symmetry-allowed and symmetry-forbidden electronic transitions, vibronic and non-adiabatic coupling between different electronic states, and rate constants for radiationless transitions, such as IC and ISC. For instance, modern *ab initio* programs can generate normal modes as a result of analytical or numerical Hessian calculations in the form of the displacement matrix $|L|$ connecting the vector of the mass-weighted Cartesian coordinates $\boldsymbol{q}$ with the vector of normal coordinates $\boldsymbol{Q}$:

$$\boldsymbol{Q} = |L| \cdot \boldsymbol{q} \text{ or } Q_k = \sum_{i=1}^{3n} l_{ik} \cdot q_i, \text{ for } k = 1, \ldots, 3n-6 \tag{3}$$

For an excited state,

$$\boldsymbol{Q} = \left|L'\right| \cdot \boldsymbol{q} + \Delta\boldsymbol{Q} = \left|L'\right| \cdot |L|^{-1} \cdot \boldsymbol{Q} + \Delta\boldsymbol{Q} \tag{4}$$

where

$$\Delta\boldsymbol{Q} = |L| \cdot \Delta\boldsymbol{q} \tag{5}$$

Since matrix $|L|$ is unitary, Eq. (4) can be written as

$$\boldsymbol{Q} = \left|L'\right| \cdot |L|^{\mathrm{T}} \cdot \boldsymbol{Q} + \Delta\boldsymbol{Q} = |C| \cdot \boldsymbol{Q} + \Delta\boldsymbol{Q} \tag{6}$$

where $|C|$ is a Duschinsky matrix.

Lam Research Ex. 1035 - Page 89
Lam Research Corp. v. Inpria Corp.
IPR2024-00033 - U.S. Patent No. 9,823,564

Assuming that the PESs are harmonic, the vibrational overlap integral is defined as

$$I_{nn'} = \langle \Theta_n(Q) | \Theta_{n'}(Q') \rangle = \int dQ \Theta_n(Q) \Theta_{n'}(Q') \tag{7}$$

and the Franck–Condon factor for the $\{n\} \rightarrow \{n'\}$ transition is $|I_{nn'}|^2$. Using harmonic approximation, in which vibrational wavefunctions are represented by Hermite polynomials, one can derive general equations [91–93] to compute vibronic spectra for polyatomic systems through calculations of transition dipole moments and Franck–Condon factors from the PESs of the ground and excited states taking into account displacement, distortion, and rotation of normal modes in excited electronic states. Two simplest cases most important for practical applications are those of displaced and distorted normal modes. For instance, when a normal mode is displaced but is not distorted, Franck–Condon factors are given by

$$|I_{a0bn'}|^2 = \frac{S^{n'}}{n'!} e^{-S} \tag{8}$$

where $S = \frac{1}{2}\beta\Delta Q^2 = \frac{1}{2} \cdot \frac{\omega}{\hbar}\Delta Q^2$ is a dimensionless Huang-Rhys factor and ω is a vibrational frequency. Obviously, the maximal Franck–Condon factor is found for $n' = [S]$, the integer part of S. This means that the larger the displacement of the normal mode, the greater n' for the most intense vibronic transition. On the other hand, if vertical excitation energy is higher than adiabatic excitation energy, displaced vibrations are excited after absorption of a photon.

When a normal mode is distorted but is not displaced, then, according to the selection rules, vibronic transitions with odd n', $a0 \rightarrow bn'$, are forbidden. For even n', Franck–Condon factors are expressed as follows:

$$\left|I_{a0b0'}\right|^2 = \left[\frac{4\omega\omega'}{(\omega+\omega')^2}\right]^{1/2} \tag{9}$$

$$\left|I_{a0b2'}\right|^2 = \frac{\sqrt{\omega\omega'}(\omega'-\omega)^2}{(\omega+\omega')^3} \tag{10}$$

$$\left|I_{a0b4'}\right|^2 = \frac{3}{4}\frac{\sqrt{\omega\omega'}}{(\omega+\omega')}\left(\frac{\omega'-\omega}{\omega+\omega'}\right)^4 \tag{11}$$

$|I_{a0bn'}|^2$rapidly decreases with n':

$$\frac{\left|I_{a0b2'}\right|^2}{\left|I_{a0b0'}\right|^2} = \frac{(\omega'-\omega)^2}{2(\omega'+\omega)^2} \text{ and } \frac{\left|I_{a0b4'}\right|^2}{\left|I_{a0b0'}\right|^2} = \frac{3}{8}\left(\frac{\omega'-\omega}{\omega'+\omega}\right)^4. \tag{12}$$

Lam Research Ex. 1035 - Page 90
Lam Research Corp. v. Inpria Corp.
IPR2024-00033 - U.S. Patent No. 9,823,564

As a result, vibronic spectra are less influenced by normal mode distortion than by displacement.

We have also derived equations for optical absorption and radiationless transitions with displaced-distorted-rotated harmonic potential surfaces including the temperature effect [93], which is evaluated using the correlation function method for computing absorption coefficients, and developed a procedure for calculating symmetry-forbidden vibronic spectra using vibronic coupling. Our theoretical approach can be utilized to compute vibronic absorption and emission spectra for model clusters simulating point defects in nanoscale silica and GeO_2, and the calculated spectral bands can be directly compared with those observed experimentally. Meanwhile, for the qualitative assignment or prediction of vibronic spectra, *ab initio* calculations of geometry relaxation in excited states provide important information about normal mode displacements. Taking into account the fact that these displacements exhibit the largest influence on the shape of vibronic spectra and on the appearance of vibrational progressions, the knowledge of the ground and excited state PESs (in terms of equilibrium geometries, vibrational frequencies, and normal modes) is critical even for the qualitative spectral assignment.

3. Photoluminescence Properties of Point Defects in SiO_2

This section is devoted to the results of *ab initio* and DFT calculations of PL properties of a variety of point defects in silica nanomaterials, including NBO atoms and their combinations with OVs (Subsection 3.1), silanone and dioxasilyrane defects (Subsection 3.2), and Al impurity (Subsection 3.3). We demonstrate that the aforementioned defects can give rise to various IR and visible red and green PL bands.

3.1. Red and Near Infrared Photoluminescence Bands in Silica Nanostructures

In order to assign the red and near infrared PL spectra observed experimentally for heat-pretreated MSs and silica nanoparticles (shown in Figure 4.4), we considered model clusters with various combinations of two types of the point defects, NBO and OV, with OV located 2–5 layers of Si–O bonds away from NBO [57–59]. In our calculations, we used much larger clusters as compared to those in the previous studies, the defect areas were surrounded by at least two layers of Si–O bonds (Figure 4.5), and only

Lam Research Ex. 1035 - Page 91
Lam Research Corp. v. Inpria Corp.
IPR2024-00033 - U.S. Patent No. 9,823,564

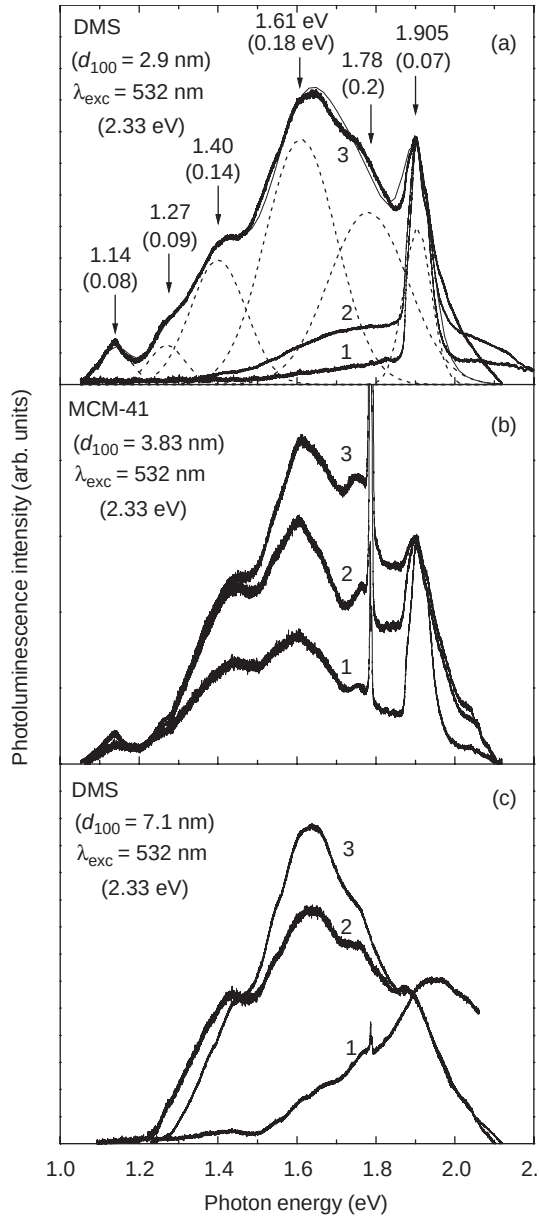


Fig. 4.4. PL spectra for mesoporous silica measured with $\lambda_{EXC} = 532\,nm$ (2.33 eV) at room temperature in air: (a) disordered mesoporous silica, DMS (the pore size $d_{100} = 2.9\,nm$); (b) MCM-41 ($d_{100} = 3.83\,nm$); and (c) DMS ($d_{100} = 7.1\,nm$); heat-pretreatment temperature $T_{ht} = 300\,K$ (curves 1), 873 K (curves 2), and 1173 K (curves 3).

Lam Research Ex. 1035 - Page 92
Lam Research Corp. v. Inpria Corp.
IPR2024-00033 - U.S. Patent No. 9,823,564

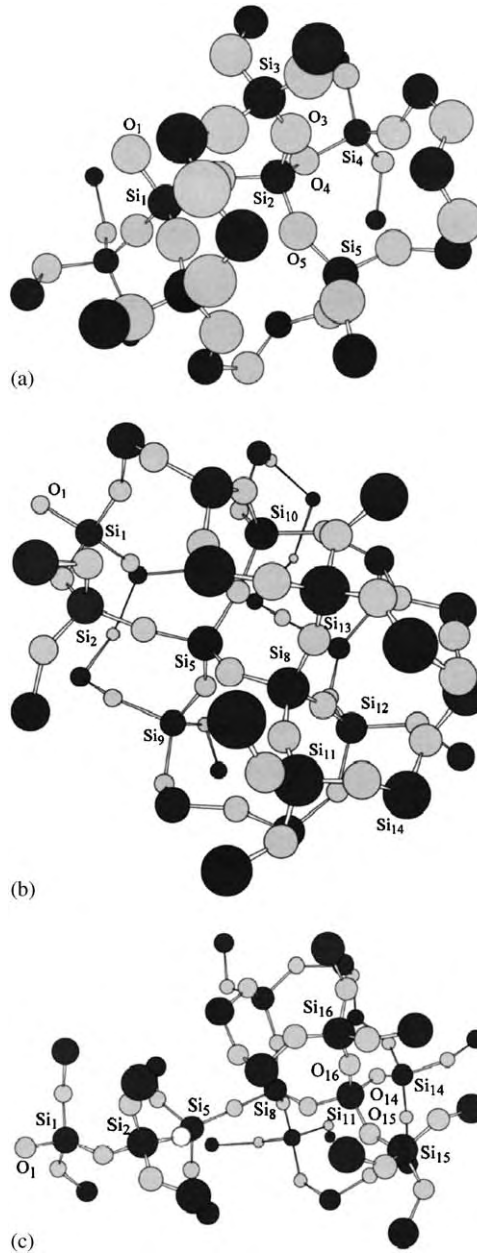


Fig. 4.5. Model clusters used for simulating OVs in the second (a), third and fourth (b), and fifth (c) layers from the NBO defect. Terminal H atoms are not shown.

Lam Research Ex. 1035 - Page 93
Lam Research Corp. v. Inpria Corp.
IPR2024-00033 - U.S. Patent No. 9,823,564

boundary Si atoms were kept frozen as the most rigidly incorporated into the network. The boundary Si coordinates were taken from the experimental data for α-quartz, whereas the coordinates of inner Si, all O, and terminal H atoms were optimized to mimic the possibility of rotations of oxygen atoms and shifts of silicon atoms due to the local defects. Such clusters include up to 50–60 heavy atoms (Si and O). The cluster size was ~1 nm, similar to the wall thickness in MSs. The atomic coordinates optimized by the ONIOM method for large clusters were used to construct smaller clusters designed for calculations of excited states (Figure 4.6). The boundary bonds in the smaller clusters were terminated by H atoms placed along the missing Si–O bonds.

The computed vertical excitation energy, E_{EXC}, for the lowest in energy electronic transition in the clusters containing only NBO but no OV, 1.9–2.0 eV, is close to the experimental value of 2.0 eV [21] and to the previous *ab initio* result for a similar cluster, 2.18 eV, obtained by the multireference configuration interaction method [46]. Also, our calculations show that OVs are not likely to occur in the first layer since, on geometry optimization, the NBO atom inserts into the neighboring Si–Si bond without a barrier, restoring the Si–O–Si bridge and resulting in the formation of the E′ defect. Alternatively, more remote OVs remain stable. As a result, two lowest excited states exist in OV-bearing clusters, one of which is similar to that for the isolated NBO defect without OV and another corresponds to the transition from the Si–Si bond to NBO (Si–Si → NBO). A single OV in the second layer gives E_{EXC}(Si–Si → NBO) in the range of 1.7–1.8 eV which are lower than E_{EXC}(LP → NBO) ranging from 2.1 to 2.2 eV (Table 4.4). If OV appears in the third layer, the E_{EXC} for the two types of electronic states are comparable (1.93–2.10 eV for Si–Si → NBO and 1.89–1.94 eV for LP → NBO).

The PL energy, E_{PL}, can be estimated as a transition from the excited state at its equilibrium geometry to the ground state. For OV-less clusters the excited state geometry relaxation is small, resulting in a moderate Stokes shift ~0.1 eV [21], so E_{PL} is only slightly lower than E_{EXC}. However, if the transition occurs from the Si–Si bond, its length (Table 4.5) significantly changes compared to that in the ground electronic state (2.34 Å). We scanned PESs of the clusters along the Si–Si distance and used a parabolic fit to evaluate PL energies (Table 4.5). Our calculations showed that the 1.905 peak is due to the NBO defect, while the presence of OV can shift this peak to the red, and different NBO–OV combinations are responsible for a number of PL bands between 1 and 2 eV. This allowed us to assign the experimental spectra. According to the calculations, both excitation and PL energies E_{EXC} and E_{PL} oscillate when OV is shifted from one layer to another. For instance, E_{PL} values are higher for the third (1.27–1.62 eV) and

Lam Research Ex. 1035 - Page 94
Lam Research Corp. v. Inpria Corp.
IPR2024-00033 - U.S. Patent No. 9,823,564

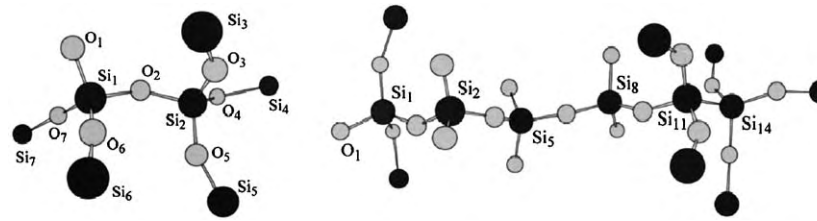


Fig. 4.6. Model cluster used for calculations of excited electronic states in SiO_2 clusters containing the combined NBO/OV defect: (a) OV in the second layer from NBO in the positions of O_3, O_4, and O_5 atoms; (b) OV in the fifth layer from NBO.

Table 4.4. Calculated lowest vertical excitation energies E_{EXC} (in eV) and oscillator strengths (f) for clusters with various NBO–OV combinations

Vacancy positions	E_{EXC}	$f \times 1000$	E_{EXC}	$f \times 1000$
None	1.96	2.5	2.14	3.1
O_3, 2nd layer, Fig. 4.5a	1.69*	1.0	2.11	0.6
O_4, 2nd layer, Fig. 4.5a	1.77*	0.2	2.16	0.0
O_5, 2nd layer, Fig. 4.5a	1.68*	0.5	2.18	1.0
O_4 and O_5, Fig. 4.5a	0.94*	3.7	2.04	1.9
O_3 and O_4, Fig. 4.5a	1.10*	6.1	2.21	0.3
O_3 and O_5, Fig. 4.5a	1.18*	6.7	2.17	0.2
O_3–O_5, Fig. 4.5a	1.13*, 1.19*	3.0, 4.9	2.22	0.1
O_8, 3rd layer, Fig. 4.5b	1.89	1.6	2.10*	3.3
O_9, 3rd layer, Fig. 4.5b	1.89	0.8	1.93*	0.1
O_{10}, 3rd layer, Fig. 4.5b	1.94	0.7	1.96*	0.1
O_{11}, 4th layer, Fig. 4.5b	1.65*	0.1	1.90	1.2
O_{12}, 4th layer, Fig. 4.5b	1.90*	2.8	1.96	0.5
O_{13}, 4th layer, Fig. 4.5b	1.56*	0.1	1.90	1.0
O_{14}, 5th layer, Fig. 4.5c	1.99	1.6	2.00*	0.02
O_{15}, 5th layer, Fig. 4.5c	1.99	0.8	2.49*	0.01
O_{16}, 5th layer, Fig. 4.5c	1.99	0.9	2.60*	0.002

*marks the Si–Si → NBO transitions.

the fifth (1.67–2.19 eV) layers than for the second (1.04–1.43 eV) and the fourth (1.14–1.31 eV) layers from NBO, respectively. The oscillator strengths f generally decrease for more distant NBO–OV combinations but show significant variations for OVs in the same layer. Apparently, both distance and mutual orientation of NBO and OV are relevant to this behavior. Moreover, variations of the R(Si–Si) distance also causes substantial changes. The most probable origin of such behavior is the character of overlap between the ground and excited wavefunctions, which is formed

Lam Research Ex. 1035 - Page 95
Lam Research Corp. v. Inpria Corp.
IPR2024-00033 - U.S. Patent No. 9,823,564

Table 4.5. Distances (in Å) between NBO (O_1) and oxygen atom to be removed to create OV (O_{OV}), Si–Si bond lengths (in Å) optimized for the excited electronic states corresponding to the Si–Si → NBO transition, PL energies E_{PL} (NBO → Si–Si) (in eV), and oscillator strengths f for clusters with single OVs in various positions

O_{OV}	O_3, 2nd l–r	O_4, 2nd l–r	O_5, 2nd l–r	O_8, 3rd l–r	O_9, 3rd l–r	O_{10}, 3rd l–r
$R(O_1–O_{OV})$	4.2	4.8	5.2	7.5	6.4	5.9
R(Si–Si)	2.68	2.56	2.60	2.56	2.70	2.58
E_{PL}	1.04	1.43	1.27	1.54	1.27	1.62
$f \times 1000$	0.9	4.9	1.6	4.7	0.03	0.1
O_{OV}	O_{11}, 4th l–r	O_{12}, 4th l–r	O_{13}, 4th l–r	O_{14}, 5th l–r	O_{15}, 5th l–r	O_{16}, 5th l–r
$R(O_1–O_{OV})$	10.2	9.4	9.4	12.8	11.6	11.9
R(Si–Si)	2.60	2.70	2.62	2.52	2.57	2.61
E_{PL}	1.21	1.31	1.14	1.67	2.19	2.16
$f \times 1000$	0.1	1.7	0.1	0.003	0.006	0.001

mainly by their oscillating tails at the link between NBO and OV. In the absence of a "wire" connecting these defects the calculated f value is zero. For OV in the second layer the oscillator strengths are comparable with that for the regular NBO transition (the 1.905 peak). For the third and the fourth layers they become smaller by about an order of magnitude, and for the fifth layer their fall continues. One can expect that for more distant NBO–OV combinations the f values will be negligible.

Summarizing, we have demonstrated that our ONIOM (B3LYP/6-31G*: PM3) calculations are able to provide reasonably accurate geometries for the SiO_2 clusters and time-dependent B3LYP calculations reproduce the experimental excitation energy of the NBO defect. The structures with OV in the first coordination sphere of NBO are shown to be unstable with respect to the insertion of the under-coordinated O atom into the neighboring Si–Si bond. The more distant OVs are able to coexist with NBO and their appearance leads to a decrease of the vertical excitation energy E_{EXC} at NBO to 1.7–1.8 eV. A presence of double and triple OVs further shifts E_{EXC} to 1.0–1.2 eV. Different orientations of the vacancies result in E_{EXC} variations within the range 0.1–0.2 eV. The excitation leads to significant elongation of the Si–Si bond at OV. As a result, E_{PL} should be much lower than E_{EXC}. Therefore, double and triple OVs will result in E_{PL} below 1 eV and the experimentally observed effect is only caused by single OVs. The variety of the observed red PL bands is rationalized in terms of different arrangements of NBO and OV mainly in the third and the fourth layers of O atoms around NBO, when the two defects are separated by 0.6–1.0 nm. Unfortunately, because of the large cluster size we were able to calculate PL

Lam Research Ex. 1035 - Page 96
Lam Research Corp. v. Inpria Corp.
IPR2024-00033 - U.S. Patent No. 9,823,564

properties of the NBO/OV combination defects only at the DFT level. Although the agreement with experiment is encouraging, it is still desirable to confirm these results in future by more sophisticated methods.

3.2. PL Properties of the Silanone and Dioxasilyrane Point Defects

The PL energies calculated at the most accurate CASPT2 level [82] for the largest $(OSiH_3)_2Si=O$ (Figure 4.7a) model cluster simulating the silanone defect are ~2.31 eV and ~1.6 eV for the $S_2 \rightarrow S_0$ and $S_1 \rightarrow S_0$ transitions, respectively. As seen from Table 4.6, the oscillator strengths for the $S_0 \rightarrow S_1$ and $S_0 \rightarrow S_2$ transitions are similar, indicating that both S_1 and S_2 excited states are equally probable following photoexcitation. The S_1 and S_2 states are expected to decay radiatively, being responsible for the red and green PL bands, respectively. The $S_2 \rightarrow S_1$ emission is much less probable because of different symmetry properties of the excited state wavefunctions; the singly occupied π_{Si-O} orbital for the S_1 state lies in the $O_b'O_bSi=O$ plane, but it is perpendicular to this plane for the S_2 state. As a consequence of a small value of the transition dipole moment, the corresponding oscillator strength calculated with the CASSCF level at the S_2 equilibrium geometry is negligibly small (~0.0002). A radiationless IC between S_2 and S_1 states is also expected to be insignificant, because the equilibrium structures for the two states are similar, so the overlap of the corresponding vibronic wavefunctions will be small.

The electronic excitation of the $X_2Si=O$ cluster leads to both out-of-plane distortion of the $O_b'O_bSi=O$ fragment and change of the $Si=O$ bond length (Figure 4.7b), resulting in the activation of the $Si=O$ stretching and out-of-plane bending vibrations for the $S_2 \rightarrow S_0$ transition. The calculated B3LYP frequencies of these vibrations are ~1300 and ~360 cm^{-1}, respectively. Therefore, one can expect to see a superposition of two vibrational progressions in the PL spectra, but due to inhomogeneity of a solid specimen the small spacing can be essentially blurred and only the higher frequency progression would appear. Indeed, the green PL bands with 1200–1450 cm^{-1} vibrational progressions were observed experimentally with 6.4 eV excitation of silica nanoparticles and MSs [13–15]. The presence of the second, lower frequency vibration may be responsible for the apparent small shifts of the band maximum and variations of the vibrational spacing in different specimens.

The optimized geometries of $X_2Si(O_2)$ clusters are presented in Figure 4.7c. The calculated frequency of the O–O stretching vibrations are in the range of 665–680 cm^{-1} and 609–629 cm^{-1} at the B3LYP and BLYP levels, respectively. On vertical excitation of dioxasilyrane into the S_2 (2^1A_1)

Lam Research Ex. 1035 - Page 97
Lam Research Corp. v. Inpria Corp.
IPR2024-00033 - U.S. Patent No. 9,823,564

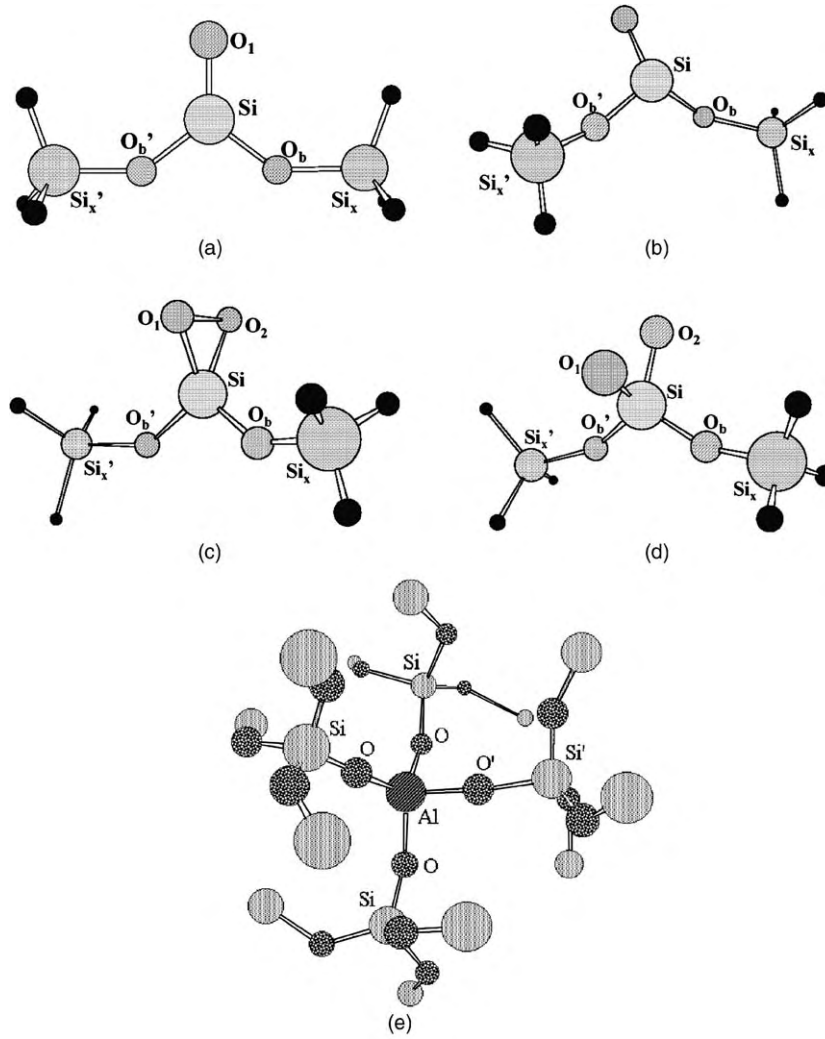


Fig. 4.7. Model clusters used for simulating silanone and dioxasilyrane point defects and Al impurity atom ($[AlO_4]^0$ defect) in SiO_2: (a) silanone, $X_2Si = O$, in the ground electronic state; (b) $X_2Si = O$ in excited electronic states; (c) dioxasilyrane, $X_2Si(O_2)$, in the ground electronic state; (d) $X_2Si(O_2)$ in excited electronic states; and (e) $Al(OSiX_3)_4$.

electronic states, a total of five excited states (1^1B_2, 2^1A_1, 1^1A_2, 3^1A_1, and 1^1B_1) are involved in the radiative and radiationless decay into the ground state (Figure 4.8a). The energies of the 1^1B_2, 1^1A_2, and 2^1A_1 states approach (within 0.6 eV) the ground state energy with an increase of the O–Si–O angle

Lam Research Ex. 1035 - Page 98
Lam Research Corp. v. Inpria Corp.
IPR2024-00033 - U.S. Patent No. 9,823,564

Table 4.6. Excitation energies E_{EXC} (in eV) and oscillator strengths f for the lowest two excited states of the $X_2Si = O$ cluster calculated at various levels of theory with X = OH and $OSiH_3$

X	Geometry[a]	Basis set	Method	$2^1A'$: E_{EXC}, f	$1^1A''$: E_{EXC}, f
OH	Ground state	6-31 + G*	EOM-CCSD	6.02[b]	5.82[b]
OH	Ground state	6-31 + G*	CASPT2	5.82, 0.059	5.84
OH	Ground state	6-31 + G*	EOM-CCSD	6.04	5.84
OH	Ground state	6-31 + G*	TD-B3LYP	5.55, 0.038	5.30, 0.021
$OSiH_3$	Ground state	6-31 + G*	EOM-CCSD	6.02[b]	5.70[b]
$OSiH_3$	Ground state	6-31 + G*	EOM-CCSD	5.95	5.65
$OSiH_3$	Ground state	6-31 + G*	TD-B3LYP	5.45, 0.018	5.09, 0.032
$OSiH_3$	Ground state	6-31 + G*	CASPT2	5.70, 0.056	5.59
OH	Triplet state	6-31 + G*	CASPT2	2.05, 0.005	0.81
OH	Triplet state	6-31 + G*	EOM-CCSD	2.34	1.06
OH	Triplet state	6-31 + G*	TD-B3LYP	2.16, 0.006	0.94, 0.000
$OSiH_3$	Triplet state	6-31 + G*	TD-B3LYP	1.91, 0.004	1.12, 0.001
$OSiH_3$	$1^1A''$ state	6-31 + G*	TD-B3LYP	2.36, 0.005	1.58, 0.001
$OSiH_3$	$2^1A'$ state	6-31 + G*	TD-B3LYP	2.42, 0.007	1.65, 0.002
$OSiH_3$	$2^1A'$ state	6-31 + G*	EOM-CCSD	2.60	1.82
$OSiH_3$	$2^1A'$ state	6-31 + G*	CASPT2	2.31, 0.012	1.63, 0.0007[c]

[a]Calculations of E_{EXC} were performed at the cluster geometry optimized in the electronic state shown in this column.

[b]From Ref. [52]; symmetry type of the electronic state was not given.

[c]Computed using the transition dipole moment calculated at the CASSCF level.

from 60° to 100°. Therefore, these excited states are expected to decay into the ground state (1^1A_1) either through IC or by emitting light in the infrared range. As seen from Figure 4.8a, the 1^1B_1 and 3^1A_1 states can decay radiatively producing visible PL bands. If the dioxasilyrane defect is excited into the S_1 (1^1B_2) state, the most probable scenario is the radiationless decay (IC) since the difference in energies between the 1^1B_2 and 1^1A_1 states after geometry relaxation reaches only 0.28 eV.The second excited singlet state 2^1A_1 may decay into the ground state by a cascade IC mechanism because of the $2^1A_1/3^1A_1$ and $2^1A_1/1^1A_2$ intersections. On the other hand, the 3^1A_1 state populated through the $2^1A_1/3^1A_1$ intersection can decay into the ground state radiatively. By contrast, the 3^1A_1 state may first relax into the 1^1B_1 state through the $3^1A_1/1^1B_1$ intersection at the O–Si–O angle equal to 88° and then decay with light emission ($1^1B_1 \rightarrow 1^1A_1$).

In order to obtain more accurate PL energies for the 3^1A_1 and 1^1B_1 states, the larger $(OSiH_3)_2Si(O_2)$ model cluster was used, with the refined singlet excited state geometry (Figure 4.7d). According to the potential energy profiles shown in Figure 4.8a, equilibrium structures of the two states are expected to be similar. Therefore, only the 3^1A_1 state was partially

Lam Research Ex. 1035 - Page 99
Lam Research Corp. v. Inpria Corp.
IPR2024-00033 - U.S. Patent No. 9,823,564

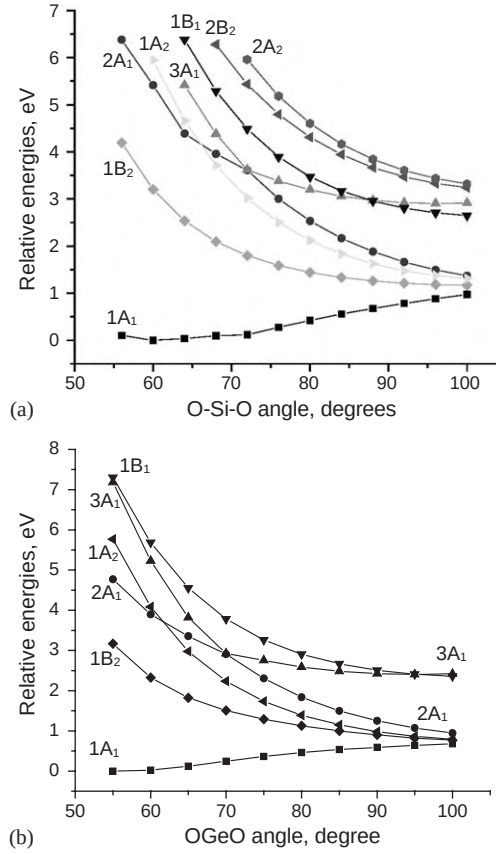


Fig. 4.8. Potential energy curves for the lowest excited states of the $X_2Si(O_2)$ (a) and $X_2Ge(O_2)$ (b) defects as functions of the OSiO and OGeO angles, respectively.

optimized varying two parameters, the O–Si distance and O–Si–O angle. The optimization was performed at the TD-B3LYP and CASPT2 levels starting from the fully optimized geometry of the triplet $^3B_2$ state. The resulting CASPT2 geometry of the 3^1A_1 state is similar to that of the triplet $^3B_2$ structure. As seen from Table 4.7, the CASPT2 excitation energies of the 1^1B_1 and 3^1A_1 states calculated at the excited state minimum (PL energies) are 2.13 and 2.32 eV, respectively, for the TD-B3LYP optimized geometry and 1.72 and 2.05 eV for the CASPT2 geometry. Hence, we conclude that the $1^1B_1 \rightarrow 1^1A_1$ transition can produce a red PL band and the $3^1A_1 \rightarrow 1^1A_1$ transition can contribute to the green PL band with an origin at 2.05–2.3 eV. Due to a big difference in equilibrium geometry for the 3^1A_1 and 1^1A_1

Lam Research Ex. 1035 - Page 100
Lam Research Corp. v. Inpria Corp.
IPR2024-00033 - U.S. Patent No. 9,823,564

Table 4.7. Excitation energies (in eV) for transitions into the lowest excited states in the X_2SiO_2 cluster ($X = OSiH_3$) calculated at the optimized geometry of the $3^1A'$ electronic state using TD-B3LYP, EOM-CCSD, and CASPT2 methods

State	TD-B3LYP[a]	EOM-CCSD[a]	CASPT2[a]	CASPT2[b]
1^1B_2	0.16	0.51	0.56	0.28
1^1A_2	0.84	0.94	0.89	0.44
2^1A_1	1.50	2.28	1.18	0.59
1^1B_1	1.51	2.80	2.13	1.72
3^1A_1	2.43	4.16	2.32	2.05
2^1B_2	1.60	4.80	3.00	2.47
2^1A_2	1.85	4.78	3.16	2.55
2^1B_1	2.84	5.39	3.69	3.22

[a]At the TD-B3LYP optimized geometry.
[b]At the CASPT2 optimized geometry.

states, the $3^1A_1 \rightarrow 1^1A_1$ transitions should result in a broad PL band (Franck–Condon envelope) with progression spacing of 610–630 cm^{-1}, which is due to the O–O stretching vibrations. According to calculated oscillator strengths, the most probable channels for the radiative decay of 3^1A_1 are the $3^1A_1 \rightarrow 1^1A_1$ transition giving rise to a green PL and $3^1A_1 \rightarrow 1^1B_2$ producing a red PL band.

Let us compare the calculated PL energies with experimental data observed in different silicon oxides. The PL energy ($S_2 \rightarrow S_0$) of 2.31 eV calculated with the most accurate CASPT2 level for the largest $(OSiH_3)_2Si=O$ model cluster closely matches the peak position of the experimental green PL band observed for silica- and silicon-based nanoscale materials [13–15, 22–25]. However, the excitation sources applied differed in various experiments. To excite the green PL from silicon-based nanoscale materials, ~3.5 eV photons were typically used, the energy of which closely corresponds to the direct bandgap transitions in Si, whereas the PL from silica-based nanoscale materials was observed with much higher excitation (4.66 and 6.4 eV). Because the excitation energy for the $(OSiH_3)_2Si=O$ groups is found to be ~5.7 eV [52], which is in good agreement with the calculation results presented here, one can conclude that the direct excitation of these species can only be realized in silica specimens with 6.4 eV photons. Nevertheless, they might be excited in silicon nanoscale materials by an indirect process.

The green PL from nanoscale silica excited with 6.4 eV photons is peaked at ~2.35 eV [13], so it is close to the PL energy calculated for the $(OSiH_3)_2Si=O$ groups. This PL is known to show the vibrational progression with spacings of ~630 and 1200–1450 cm^{-1}, which were initially assigned to the bending vibrations of Si–H and Si–H– –O–Si, respectively

Lam Research Ex. 1035 - Page 101
Lam Research Corp. v. Inpria Corp.
IPR2024-00033 - U.S. Patent No. 9,823,564

[13–15]. However, the latter frequency is also consistent with that of the Si = O stretching vibrations (1300 cm^{-1}). The silanone group is not expected to be stable with respect to hydration at ambient temperatures, since the calculated barrier for the exothermic $=Si=O+H_2O \rightarrow =Si(OH)_2$ reaction is low, only 6 kcal/mol [54]. Since the green PL from nanoscale silica is observed even for specimens containing the high concentration of adsorbed water, the $(OSiH_3)_2Si=O$ groups are unlikely to contribute to the light emission process from the initial heat-untreated materials, unless one assumes a two-photon excitation mechanism suggested by Zhou and Head [54]. In this mechanism, the $=Si(OH)_2$ groups are dehydrated presumably by energy provided by the incident photon source to produce a large concentration of silanone groups and these metastable $=Si=O$ groups would then be excited by additional photons to produce PL. Heat pretreatment can also produce the silanone defects within the dehydration process, $=Si(OH)_2 \rightarrow =Si=O+H_2O$, with the activation energy of ~50 kcal/mole [54]. Since no additional PL bands in the green range arise with heat pretreatment procedure in air [13–15], one can expect that the concentration of such species should be relatively small. Thus, despite the fact that the $(OSiH_3)_2Si=O$ groups could be excited with 6.4 eV photons and can contribute in the observed green PL bands, the silanone defect apparently is not the only species involved in the green PL emission process from silica nanoscale materials.

The $X_2Si(O_2)$ groups can contribute to the green PL band with an origin at 2.05–2.3 eV. The vertical excitation energy of the S_2 (2^1A_1) state is ~5 eV. Therefore, the $X_2Si(O_2)$ species are unlikely to contribute to the green PL from silicon nanoscale materials excited by ~3.5 eV photons. The calculated frequency of the O–O stretching vibrations, which ranges from 610 to 630 cm^{-1}, supports this conclusion as well. The green PL from porous silicon is only observed for oxygen-free untreated specimens, for which the FTIR spectra show the strong absorption bands near the 2100 and 664 cm^{-1} [22]. These bands were assigned to the stretching and bending vibrations of $Si–H_n$ ($n = 1–3$). After exposure to air, the PL is red-shifted and saturated in the orange range near 2.1 eV.Thus, the $X_2Si(O_2)$ groups may contribute to the orange PL from porous silicon but the mechanism of the PL excitation should involve some indirect process.

The absorption of 4.66 and 6.4 eV photons can excite the PL from $X_2Si(O_2)$ species in silica nanoscale materials. The vertical excitation energy of the S_2 (2^1A_1) state, ~5 eV, is only slightly higher than 4.66 eV, whereas both 2^1A_1 and 3^1A_1 states have adiabatic excitation energies significantly lower than this value. This means that Franck–Condon factors for vibronic transitions in the available energy range have non-zero values and absorption of a 4.66 eV photon can excite the system into the S_2 state. The

Lam Research Ex. 1035 - Page 102
Lam Research Corp. v. Inpria Corp.
IPR2024-00033 - U.S. Patent No. 9,823,564

calculated frequency of the O–O stretching vibrations is close to that for the experimentally observed progression spacing in the green PL from these materials [13–15]. Thus, the dioxasilyrane defect can be considered as a potential light emitter in the green spectral range. The reaction mechanism of this defect on the silica surface with water as well as with other molecules is described in detail by Radzig in Chapter 7 of this book.

In summary, the silanone and dioxasilyrane defects in silicon oxides are found to be possible candidates for green and red light-emitters. In silanone, two lowest excited singlet states are found to be degenerate with vertical excitation energies ($S_0 \rightarrow S_1$ and $S_0 \rightarrow S_2$) of ~5.7 eV and similar oscillator strengths. Due to a significant geometry relaxation in the excited states, the corresponding PL is calculated to appear at 2.3 and 1.6 eV. Additional broadening of the PL bands can be due to an involvement of the ground state $= Si = O$ stretching and bending vibrations with frequencies of ~1300 and ~360 cm^{-1}, respectively. The vertical excitation energies in dioxasilyrane are calculated as ~3.0 eV for S_1 (1^1B_2) and ~5.0 eV for S_2 (2^1A_1). The excitation initiates a rupture of the O–O bond and the de-excitation process drives through the activation of O–O stretching vibrations in the ground state (610–630 cm^{-1}). After the system is excited into the S_2 state five electronic states, 1^1B_2, 2^1A_1, 1^1A_2, 3^1A_1, and 1^1B_1, can be involved in the radiationless and radiative relaxation. The radiative $3^1A_1 \rightarrow 1^1A_1$ transition contributes to PL in the range from 2.05 to 2.3 eV, while the $3^1A_1 \rightarrow 1^1B_2$ and $1^1B_1 \rightarrow 1^1A_1$ transitions can produce red PL bands at 1.7–1.8 eV.

3.3. Photoabsorption and Photoluminescence of the $[AlO_4]^0$ Defect in SiO_2

The calculations of excitation energies for the $[AlO_4]^0$ defect (Figure 4.7e) were carried out using two model clusters, $Al(OSiH_3)_4$ and $Al(OH)_4$ [60]. In the ground electronic state, the unpaired electron is localized on one of the oxygen atoms and this particular atom exhibits a weaker bonding to Al than the other Os with the corresponding O′–Al and O′–Si′ bond lengths of 1.98 and 1.79 Å, respectively, whereas the interatomic distances for the other O atoms (with a low spin density) are shorter, 1.73–1.74 Å for Al–O and 1.62–1.63 Å for Si–O bonds. The Al–Si (3.24–3.33 Å) and Al–Si′ (3.56 Å) distances are also not equal. The calculated transition energies are close for both model systems, especially for lower excited states. The first excited state formed by the HOMO → SOMO transition, where the unpaired electron remains localized on one O atom, is only slightly higher in energy than the ground state. The next six transitions to the 3^2A–8^2A states, which involve delocalization of the unpaired electron on the lone pairs of the other O

Lam Research Ex. 1035 - Page 103
Lam Research Corp. v. Inpria Corp.
IPR2024-00033 - U.S. Patent No. 9,823,564

Table 4.8. Excitation energies (E_{ex}, in eV) and oscillator strengths (f) for vertical excitations in the model C_1-symmetric $Al(OH)_4$ and $Al(OSiH_3)_4$ clusters calculated at various levels of theory

State	System				
	$Al(OH)_4$, C_1			$Al(OSiH_3)_4$, C_1	
	TD-B3LYP E_{ex}, f	EOM-CCSD E_{ex}, f	OVGF E_{ex}	TD-B3LYP E_{ex}, f	OVGF E_{ex}
2^2A	0.32, 0.0004	0.34, 0.0001	0.34	0.43, 0.0023	0.37
3^2A	0.45, 0.0025	2.28, 0.0007	1.63	0.51, 0.0035	1.72
4^2A	0.99, 0.0056	2.68, 0.0067	2.09	0.84, 0.0057	1.97
5^2A	1.27, 0.0023	2.77, 0.0169	2.19	1.03, 0.0029	2.03
6^2A	1.48, 0.0056	3.02, 0.0154	2.48	1.08, 0.0037	2.24
7^2A	1.72, 0.0250	3.36, 0.0091	2.74	1.32, 0.0300	2.23
8^2A	1.90, 0.0052	3.60, 0.0014	2.95	1.39, 0.0560	2.43

atoms around the Al center exhibit excitation energies ranging from 1.72 to 2.43 eV at the OVGF level (Table 4.8). These margins for the $Al(OSiH_3)_4$ cluster are narrower than those obtained for $Al(OH)_4$, 1.63–2.95 eV.Taking into account that the OVGF approach underestimates the excitation energies by 0.2–0.3 eV, one can expect that the energies of vertical excitations to the 3^2A–8^2A states at the $[AlO_4]^0$ center are shifted by this value with respect to the OVGF data and are distributed in the range of 2.0–2.7 eV.TD-DFT calculations of the oscillator strengths f demonstrate that they do not change significantly when the model $Al(OH)_4$ cluster is replaced by $Al(OSiH_3)_4$ (Table 4.8). For the smaller C_s-symmetric $Al(OH)_4$ cluster, the oscillator strengths were computed also at the EOM-CCSD and state-averaged CASSCF levels and the two methods show similar trends; the oscillator strengths are rather small and peak for the $3^2A''$ state. According to the most reliable EOM-CCSD data for the $Al(OH)_4$ system with a non-symmetric C_1 geometry, all the excitations should have low oscillator strength ($f < 0.01$), except for the 5^2A and 6^2A states, which exhibit the highest f values of ~0.02 (Table 4.8). Therefore, a maximum in the absorption spectrum due to the $[AlO_4]^0$ center in SiO_2 should occur in the 2.2–2.5 eV range.

We evaluated geometry relaxation in the lowest five excited electronic states and the Stokes shift values employing the C_s-symmetric $Al(OH)_4$ model cluster. Geometric parameters for various electronic states were optimized at the CASSCF level and the resulting bond lengths, bond angles, and torsional angles are presented in Table 4.9. The optimized structures of the two lowest $1^2A''$ and $1^2A'$ states with the hole localized on the O′ center are

Lam Research Ex. 1035 - Page 104
Lam Research Corp. v. Inpria Corp.
IPR2024-00033 - U.S. Patent No. 9,823,564

Table 4.9. Interatomic distances R (in Å), bond and torsional angles (degrees) for the lowest excited states of the C_s-symmetric $Al(OH)_4$ model system calculated at the CASSCF level

	$1^2A''$	$2^2A''$	$3^2A''$	$1^2A'$	$2^2A'$	$3^2A'$
R(AlO′)	2.063	1.828	1.818	2.171	1.714	1.711
R(AlO″)	1.736	1.827	1.705	1.744	1.716	1.719
R(AlO)	1.714	1.736	1.839	1.704	1.848	1.823
∠O′AlO″	99.6	101.6	106.6	85.3	116.2	119.0
∠O′AlO	93.1	109.8	108.1	100.6	112.3	106.4
OAlO′O″[a]	122.9	116.1	125.3	121.2	125.8	119.4
R(O′H)	0.964	0.953	0.953	0.958	0.944	0.940
R(O″H)	0.967	0.953	0.942	0.967	0.943	0.960
R(OH)	0.947	0.946	0.950	0.947	0.950	0.950
∠AlO′H	106.0	116.8	118.8	174.9	126.1	145.8
∠AlO″H	124.4	116.8	128.7	123.8	126.1	152.8
∠AlOH	124.4	125.7	121.3	122.9	144.5	115.8
HOAlO′[a]	160.3	180.0	26.3	185.2	123.2	110.5

[a]Torsional angle.

similar; the Al–O′ distance is significantly longer than Al–O″ and Al–O. This result qualitatively agrees with the ground state geometric parameters optimized for the large model cluster (Figure 4.7e) using the ONIOM method. In the 3^2A–8^2A states, the hole is redistributed among lone pairs of the O and O″ atoms resulting in weakening of the Al–O″ and Al–O bonds, whereas the Al–O′ distance significantly shortens to 1.71–1.83 Å (Table 4.9). Such a large geometry relaxation in the excited states causes substantial Stokes shifts, which were estimated by OVGF and MRCI calculations of the excitation energies for several low-lying states at their optimized structures. Geometry optimization of the $1^2A'$ state reverses the order of the $1^2A'$ and $1^2A''$ relative energies; at the $1^2A'$ geometry the energy of $1^2A''$ is higher than that of $1^2A'$ but difference is small, 0.03–0.04 eV. In this case, the $1^2A'$ optimized structure corresponds to a local minimum on the ground state potential energy surface and the $1^2A'' \rightarrow 1^2A'$ excitation triggers isomerization of the AlO_4 fragment. The energies of the other excited states remain higher than that of $1^2A''$ after optimization, so that they can undergo a radiation decay giving rise to PL. At the $2^2A''$ optimized geometry only the ground state lies below $2^2A''$, and the $2^2A''-1^2A''$ energy difference is small, ~0.3 eV both at the OVGF and MRCI + Q levels of theory (Table 4.10). Hence, the $2^2A''$ state can produce a PL band in the IR range. The energy of the $2^2A'$ state at its optimized geometry is higher than those of $1^2A'$ and $2^2A''$ at the same geometry, and therefore three PL bands can be produced due to the $2^2A' \rightarrow 1^2A''$ (0.78–0.88 eV), $2^2A' \rightarrow 1^2A'$ (0.02–0.23 eV), and $2^2A' \rightarrow 2^2A''$ (~0.54 eV) de-excitations (Table 4.10). According to the

Lam Research Ex. 1035 - Page 105
Lam Research Corp. v. Inpria Corp.
IPR2024-00033 - U.S. Patent No. 9,823,564

Table 4.10. PL energies (in eV) and oscillator strengths (f) of the $2^2A''$–$3^2A'$ excited electronic states of the C_s-symmetric $Al(OH)_4$ model cluster simulating the $[AlO_4]^0$ center in SiO_2[a]

Geometry[b]	Method	$1^2A''$	$1^2A'$	$2^2A''$	$2^2A'$	$3^2A''$
$2^2A''$	OVGF	0.31	−0.19[c]	0.0	−0.57[c]	−1.05[c]
	MRCI[d] $f(2^2A'')$[e]	0.36 (0.29) 0.0336		0.0		
$2^2A'$	OVGF	0.88	0.23	0.54	0.0	−0.73[c]
	MRCI[d] $f(2^2A')$[e]	0.93 (0.98) 0.0056	0.05 (0.02) 0.00006	0.35 (0.59) 0.0032	0.0	
$3^2A''$	OVGF	0.62	0.17	0.19	−0.63[c]	0.0
	MRCI[d] $f(3^2A'')$[f]	0.72 (0.71) 0.0336	0.32 (0.27) 0.0072	0.30 (0.33) 0.0240		0.0
$3^2A'$	OVGF	1.51	0.76	0.91	0.58	0.26
	MRCI[d] $f(3^2A')$[f]	1.55 (1.38) 0.0062	0.61 (0.58) 0.0130	1.38 (0.90) 0.0048	0.25 (0.29) 0.0012	0.40 (0.51) 0.0012

[a]Calculated at the OVGF and MRCI levels at the optimized geometries of the states shown in the left column.

[b]Electronic states for which the geometries were optimized.

[c]Negative number indicates that the electronic state in the corresponding column caption lies higher in energy than the electronic state for which the structure was optimized, i.e., this is not a PL energy.

[d]MRCI calculations used starting CASSCF wavefunctions from state-average calculations with equal weight for all ground and excited states. The numbers in parentheses show Davidson-corrected MRCI + Q energies.

[e]Oscillator strength is obtained from state-averaged CASSCF calculations including four electronic states, two $^2A'$ and two $^2A''$.

[f]Oscillator strength is obtained from state-averaged CASSCF calculations including six electronic states, three $^2A'$ and three $^2A''$.

Lam Research Ex. 1035 - Page 106
Lam Research Corp. v. Inpria Corp.
IPR2024-00033 - U.S. Patent No. 9,823,564

oscillator strengths calculated at the CASSCF level, the $2^2A' \rightarrow 1^2A''$ band should be the most intense of the three. The $3^2A''$ state at its optimized structure lies at 0.62–0.71, 0.17, and 0.19–0.33 eV higher in energy than the $1^2A''$, $1^2A'$, and $2^2A''$ states at this geometry, respectively, and also can give rise to three PL bands. Finally, de-excitation of the $3^2A'$ state is able to form five PL bands with the energies ranging from 1.5 to 0.3 eV (Table 4.10). As a rule, the oscillator strengths do not differ significantly (the only exception is the extremely weak $2^2A' \rightarrow 1^2A'$ transition), so one can expect an appearance of nearly all the lines discussed above in the PL spectra due to the $[AlO_4]^0$ defect, unless some of the excited states decay in a radiationless manner through IC. The redistribution of the electron hole among oxygen atoms of the $[AlO_4]^0$ center causes significant Stokes shifts of 1.1–1.7 eV, at least for the excitations up to the $3^2A''$ fifth excited state. Summarizing, our results show that the $[AlO_4]^0$ defect can produce a complex PL band containing several lines, including a few lines between 1.5 and 1.0 eV and a larger number of more intense lines in the range of 0.7–0.2 eV.

4. Optical Properties of Point Defects in GeO_2

In this section, we consider optical properties of two types of point defects in germania, oxygen-containing surface defects (Subsection 4.1) and oxygen-deficient defects (Subsection 4.2). Both photoabsorption and PL energies are calculated for these structures with the goal to assign available experimental data for GeO_2 nanomaterials.

4.1. Photoluminescence of Oxygen-Containing Surface Defects in Germanium Oxides

A variety of surface point defects in GeO_2 may exist that are related to a specific local environment of oxygen atoms. Here, we investigate most typical oxygen-containing defects occurring on surfaces of nanoparticles, such as NBO, peroxy radical group, as well as $O_2Ge=$ (silanone-like) and $O=Ge=$ (dioxasilyrane-like) defects, and compare their properties with the analogous defects in SiO_2.

4.1.1. NBO or –O–Ge≡ Defect

The calculated photoabsorption bands for a model cluster simulating NBO in GeO_2 (Figure 4.9) are located in three energy ranges, ~1.7–1.9 eV ($2^2A'$),

Lam Research Ex. 1035 - Page 107
Lam Research Corp. v. Inpria Corp.
IPR2024-00033 - U.S. Patent No. 9,823,564

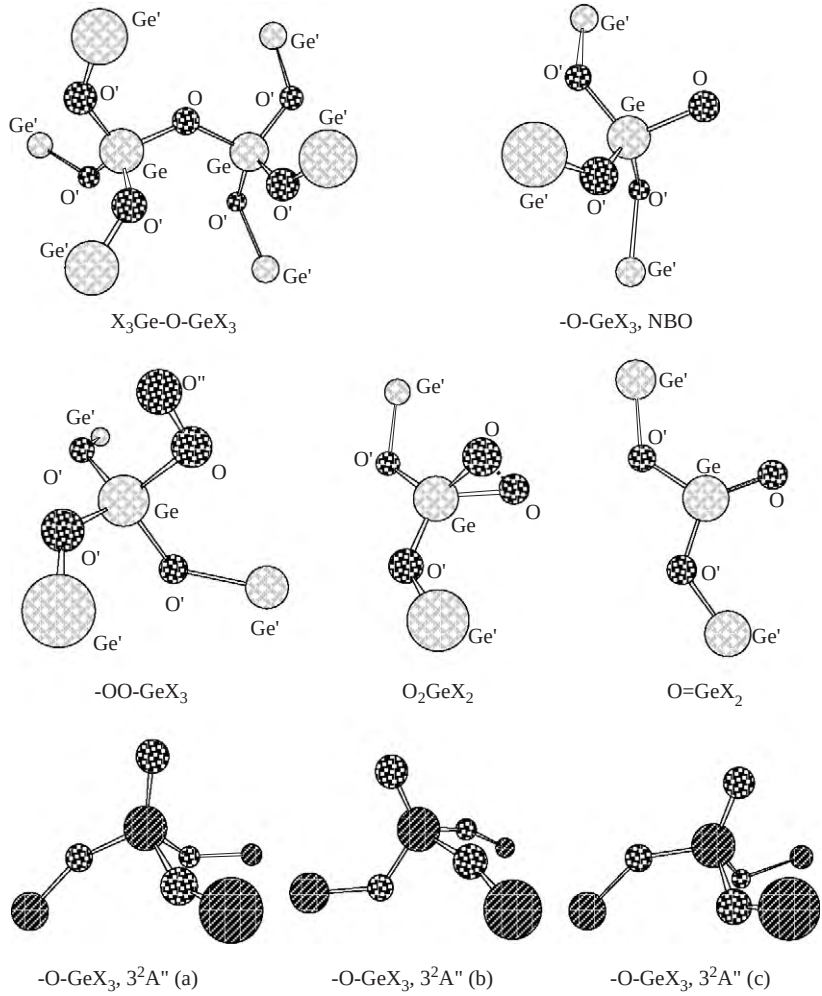


Fig. 4.9. Model clusters used for simulating oxygen-containing point defects in GeO_2. Terminal H atoms are not shown.

~3.8–4.0 eV (weak, $2^2A''$), and around 5 eV (more intense, $3^2A''$–$4^2A''$) [94]. In the third group, the most probable excitation is $4^2A' \leftarrow 1^2A''$, if the ground state is $1^2A''$, or $3^2A' \leftarrow 1^2A'$ if $1^2A'$ is the ground state ($1^2A''$ and $1^2A'$ are close in energy). As compared to NBO in SiO_2, the NBO-related bands in GeO_2 are slightly red-shifted. In all excited states considered, the electron transfer proceeds to SOMO, which is mostly composed of the lone pair of the

Lam Research Ex. 1035 - Page 108
Lam Research Corp. v. Inpria Corp.
IPR2024-00033 - U.S. Patent No. 9,823,564

NBO atom. In the $2^2A'$ state, an electron is transferred mainly from the Ge–O bond but weakening of the σ-component of this bond is compensated by strengthening of the π-component, and the defect in geometry remains approximately the same as that in the ground state. In the higher $2^2A''$–$4^2A'$ states, an electron is removed from the orbitals constructed mainly from the lone pairs of bridging O′ atoms. The appearance of the hole in this region leads to the bond weakening between the central Ge and the corresponding O′ atoms; simultaneously, the Ge–O bond for the NBO becomes stronger, and the O–Ge–O′ angles increase. As a result, the geometry relaxation for these states is substantial and the Stokes shifts are significant.

Geometry optimization for the $4^2A''$ state was not successful because, during the optimization process, the system arrives to a region where the energy difference between the $4^2A''$ and $3^2A''$ states is extremely small (~0.001 eV). This indicates that the two surfaces cross in this region and, as the geometry continues to relax, the system passes from the $4^2A''$ PES to $3^2A''$. Since the intersection has two slopes, one can expect that two different local minima for the $3^2A''$ state can exist in its vicinity. Indeed, we found two additional local minima on the $3^2A''$ surface, which differ by the orientation of the O–GeO′group (see Figure 4.9). In structure (b), the O–Ge bond is directed towards the Ge' atom located in the symmetry plane, while in structure (c) this bond is oriented in the opposite direction. Structure (b) is formed if we continue to follow the energy descent from the $4^2A''$ PES straight after the intersection, while structure (c) is obtained when the slope direction is changed. Therefore, if the system is photoexcited to the $4^2A''$ state, the formation of configuration (b) is more probable than the formation of (c). As compared to the local minimum (a) in the $3^2A''$ state optimized starting from the initial ground state geometry, the (c) and (b) structures, respectively lie ~0.2 and 0.5 eV lower in energy. When photoexcitation occurs to the $3^2A''$ state, we can expect the system to initially relax to structure (a), but, if barriers separating (a) from (b) and (c) are not too high and the available energy is sufficient to overcome them, the geometry relaxation can continue to form the most stable structure (b).

PL transitions from the $2^2A''$ state produce two low-energy bands at ~0.3 and 0.5 eV with small oscillator strengths (Table 4.11). The Stokes shift in this case exceeds 3 eV. For the $3^2A''$ state three different local minima were found depending on the starting geometry. For structure (a), the most probable transition with an energy of 1.8–2.0 eV occurs to the $1^2A''$ state. The $3^2A''(a) \rightarrow 1^2A'$ de-excitation has a similar energy but a lower oscillator strength. The transitions to $2^2A'$ and $2^2A''$ exhibit low energies and f values (Table 4.11). For the most stable $3^2A''$ structure (b), de-excitation energies and oscillator strengths are similar to those for (a). However, due to substantial differences in O–Ge′ distances, relative stabilities of various A′

Lam Research Ex. 1035 - Page 109
Lam Research Corp. v. Inpria Corp.
IPR2024-00033 - U.S. Patent No. 9,823,564

Table 4.11. De-excitation energies (in eV) and oscillator strengths (given after commas) for the lowest doublet states[a] of the $-OGeX_3$ model cluster ($X = OGeH_3$) calculated[b] at the excited state optimized geometries

	Method	$1^2A''$	$1^2A'$	$2^2A'$	$2^2A''$	$3^2A''$	$3^2A'$
$4^2A'$	SAC-CI	−2.19, 0.0219	−2.13, 0.0052	−0.83, 0.0200	−1.26, **0.0874**	−0.95, 0.0110	−0.36, 0.0140
	OVGF	−2.36	−2.33	−0.74	−1.12	−0.82	−0.27
	CASSCF(15, 13)	−2.89, 0.0153	−2.79, 0.0063	−1.25, **0.0747**	−1.67, **0.0540**	−1.44, 0.0210	−0.57, 0.0119
	MRCI(13, 13)[c]	−2.90 (−2.88)	−2.86 (−2.82)	**−1.12** (**−1.10**)	**−1.59** (**−1.59**)	−1.29 (−1.31)	−0.57 (−0.59)
$3^2A'$	SAC-CI	−1.49, 0.0026	−1.38, 0.0098	−0.47, 0.0062	−0.84, **0.0685**	0.53	
	OVGF	−1.82	−1.72	−0.49	−0.79	0.37	
	CASSCF(13, 12)	−2.78, 0.0001	−2.69, 0.0020	−1.02, 0.0116	−1.28, **0.1024**		
	MRCI(13/12)[c]	−2.18 (−2.07)	−2.10 (−1.98)	−0.55 (−0.44)	**−1.04** (**−0.99**)		
$3^2A''$ (a)	SAC-CI	−1.32, **0.0675**	−1.34, 0.0149	−0.10, 0.0051	−0.89, 0.0064		0.38
	OVGF	−1.78	−1.72	−0.26	−0.87		0.46
	CASSCF(17, 15)	−1.97, **0.0540**	−2.25, 0.0135	0.38, 0.0089	−1.06, 0.0013		1.12
	MRCI (17, 12)[c]	**−1.98** (**−1.97**)	−2.05 (−1.98)	−0.20 (−0.13)	−0.91 (−0.87)		
$3^2A''$ (b)	SAC-CI	−0.73, **0.0382**	−0.41, 0.0019	0.49	−0.14, 0.0044		0.74
	OVGF	−0.79	−0.72	0.60	−0.26		0.68
	CASSCF(17, 14)	−1.27, **0.0099**	−1.66, 0.0013	0.23	−0.43, 0.0005		1.96
	MRCI(17, 12)[c]	**−1.89** (**−2.02**)	−1.44 (−1.40)	0.45 (0.48)	−0.65 (−0.70)		
$3^2A''$ (c)	SAC-CI	−1.48, 0.0094	−1.99, 0.0068	−0.89, **0.0105**	−0.13, **0.0099**		−0.39, 0.0044
	OVGF	−1.63	−1.53	−0.75	−0.85		0.03
	CASSCF(17, 14)	−2.01, 0.0009	−2.55, 0.006	−0.59, 0.0002	−0.60, **0.0355**		0.24, 10^{-5}
	MRCI(17/12)[c]	−2.32 (−2.35)	−2.84 (−2.84)	−0.93 (−0.93)	**−0.73** (**−0.77**)		−0.50 (−0.65)
$2^2A''$	SAC-CI	−0.15, 0.0004	0.14, **0.0015**				
	OVGF	−0.27	−0.16	1.09			
	CASSCF(13, 12)	−0.41, 2×10^{-5}	−1.40, **0.0170**	0.56			
	MRCI(13, 12)[c]	0.31 (−0.29)	**−0.62** (**−0.52**)	1.25 (1.33)			
$2^2A'$	SAC-CI	−1.50, 0.0002	−1.56, 0.0001				
	OVGF	−1.60	−1.56				
	CASSCF(19, 15)	−1.77, 7×10^{-6}	−1.67, 6×10^{-5}				
	MRCI(19, 13)[c]	−1.84 (−1.78)	−1.81 (−1.71)				

[a]De-excitations occur from the states shown in the left column to the states shown in the first row. Numbers in bold refer to the transitions most significant for PL.

[b]All calculations were carried out with the LanL2-DZP basis set for Ge and 6-31G* for O and H augmented with diffuse s and p functions on the O atom with exponents of 0.08 and 0.03.

[c]Numbers in parentheses include Davidson's corrections for quadruple excitations.

Lam Research Ex. 1035 - Page 110
Lam Research Corp. v. Inpria Corp.
IPR2024-00033 - U.S. Patent No. 9,823,564

and A″ states are shifted, and the transitions to $1^2A'$ and $2^2A''$ have lower energies than those in the case of (a) (Table 4.11). For structure (c), the A′ and A″ energies are shifted in the opposite direction, and the $1^2A'$ state is lower than $1^2A''$ resulting in the $3^2A'' \rightarrow 1^2A'$ transition energy of ~2.8 eV. The most probable transition from (c) occurs to the $2^2A''$ state and has energy of 0.7–0.8 eV.

The $3^2A'$ state can be de-excited to four low-lying states. At the MRCI level, the energies of these transitions range from 0.4–0.5 to 2.0–2.1 eV, and the $3^2A' \rightarrow 2^2A''$ de-excitation with an energy of ~1 eV has the largest oscillator strength. The *f* values for the transitions with energies of ~2 eV are much lower (Table 4.11), so the de-excitation process is likely to proceed mainly to $2^2A''$ (~90%) and $2^2A'$ (~10%). Therefore, one can expect the most intense PL bands at ~1.0 and 0.5–0.3 eV with weak satellite bands at 1.8–2.0 eV (the transitions of $2^2A'$ and $3^2A'$ to $1^2A'$ and $1^2A''$). At the $4^2A'$ optimized geometry, six electronic states have lower energies, and the transitions to the $2^2A'$ and $2^2A''$ states with energies of ~1.1 and 1.6 eV have highest intensities. The intermediate $2^2A'$ and $2^2A''$ states can be further de-excited by emitting photons with energies of 1.7–1.8 and 0.5–0.6 eV. The transitions from $4^2A'$ to $1^2A'$ and $1^2A''$ exhibit much lower *f* values and the corresponding PL band at 2.8–2.9 eV should be weak. The transitions to the $3^2A'$ and $3^2A''$ states also have low oscillator strengths.

We conclude that NBO defects in GeO_2 are able to absorb light in the visible red (the D_2 state, 1.7–1.9 eV) and UV energy ranges (D_3–D_7, the most intense band at 4.6–4.9 eV). PL originated from the red D_2 absorption band should occur with a small Stokes shift of only ~0.1 eV. De-excitation of the D_3–D_7 states should proceed with significant geometric relaxation and large Stokes shifts, mainly through intermediate states, thus forming several PL bands in the same energy region as the D_2-related PL and also with low energies, in the IR spectral range. Only a small fraction of electronic transitions from the D_7–D_4 levels will occur directly to the ground state forming a weak PL band at 2.7–2.9 eV.

4.1.2. Peroxy Radical or –O–O–Ge≡ Defect

The –O–O–Ge≡ groups can be formed by oxidation of surface E′-centers (–Ge≡ defects) on air. The structure and properties of these defects in SiO_2 and GeO_2 are similar. In the ground $1^2A''$ electronic state of –O–O–Ge≡, the O–O fragment forms a single bond with the surface Si or Ge atom (Figure 4.9). The unpaired electron is located predominantly at the terminal O atom, but the corresponding SOMO has a substantial π^*_{OO} antibonding

Lam Research Ex. 1035 - Page 111
Lam Research Corp. v. Inpria Corp.
IPR2024-00033 - U.S. Patent No. 9,823,564

character. In the first excited $1^2A'$ state, the unpaired electron is located at a similar in-plane (A′) MO, and the transition energy is low, 0.6–0.7 eV.The next six doublet excited states are formed by electronic transitions to SOMO from the lower in energy doubly occupied MOs, which either have a predominantly O–O bonding character or are composed of lone pairs of bridging O atoms. The most intense transitions in this group are $2^2A'' \leftarrow 1^2A''$ and $4^2A' \leftarrow 1^2A''$ with energies of ~6.0 and ~7.6 eV, respectively, while the other excitations exhibit much smaller oscillator strengths. These results are in qualitative agreement with the observed optical adsorption bands for the peroxy defect in SiO_2 [95,96], where two rather intense peaks at 5.4 and 7.6 eV were assigned to the peroxy radical fragment.

CASSCF geometry optimization for the $2^2A''$–$4^2A'$ states leads to destruction of the O–O fragment because these states are formed by occupation of the O–O antibonding MO. The resulting decomposition products are the O atom with different orientations of the doubly occupied p-AO and the –O–Ge≡ (NBO) defect in the ground state (for the excitations up to $3^2A''$ and $3^2A'$) or in the $2^2A'$ excited state (for $4^2A''$ and $4^2A'$). For the $2^2A''$–$3^2A'$ and $4^2A''$ states, the potential energy profile along the O–O distance is repulsive, while the $4^2A'$ state geometry is optimized to a weakly bound O…O–Ge≡ complex with the O–O distance of ~2 Å and the O–O–Ge angle close to linear. The electronic structure of this configuration can be interpreted as a donor–acceptor complex between the $2^2A'$ excited state of NBO (donor) and the O atom in the $^1\Delta$ state (acceptor). PL energies evaluated for this complex at the CASSCF level are ~1 eV and lower, with very small oscillator strengths; the most probable de-excitation is $4^2A' \rightarrow 3^2A'$ ($f = 8 \times 10^{-6}$) to be followed by a further decay of the $3^2A'$ state. Hence, luminescence from the excited peroxy radicals is not expected to be significant.

4.1.3. $O_2Ge=$ Defect

In the ground singlet electronic state, the $O_2Ge=$ defect contains an O_2Ge triangular group with the O–Ge–O angle of ~55° (Figure 4.9). This triangle is significantly strained and lower energy electronic excitations lead to destruction of the weakest O–O bond. Five lowest excited states (1^1B_2 (S_1), 2^1A_1 (S_2), 1^1A_2, 1^1B_1, and 3^1A_1) at the ground state geometry are formed by electronic transitions from the occupied MOs with predominantly O–O contributions (similar to π^*_{OO}, π_{OO}, and σ_{OO} MOs in O_2^{2-}) to the LUMO of b_1 symmetry (with an antibonding σ^*_{OO} character). Due to a local character of the excitations, the properties of these states are not very sensitive to the cluster size (Table 4.12) and are similar for $O_2Ge=$ and $O_2Si=$. The state that seems to be most suitable to contribute to the observed PL band [12] is

Lam Research Ex. 1035 - Page 112
Lam Research Corp. v. Inpria Corp.
IPR2024-00033 - U.S. Patent No. 9,823,564

Table 4.12. Excitation energies (in eV) and oscillator strengths (given after commas) for the lowest singlet states of the O_2GeX_2 and $O = GeX_2$ model clusters[a]

$O_2Ge(OGeH_3)_2$, S_0	1^1B_2	2^1A_1	1^1A_2	1^1B_1	3^1A_1
CIS/B4	3.94, 0.0003	5.30, 0.0016	7.64, 0.0000	7.84, 0.0379	
TD-B3LYP/B4	3.37, 0.0011	4.74, 0.0031	4.44, 0.0000	5.56, 0.0018	
EOM-CCSD/B3	3.76	5.41	5.66	6.67	7.88
EOM-CCSD/B5	3.69	5.32	5.46	6.47	7.49
$O_2Ge(OH)_2$, S_0	1^1B_1	2^1A_1	1^1A_2	1^1B_2	3^1A_1
EOM-CCSD/B5	3.68	5.38	5.31	6.52	8.41
CASPT2/B5	3.56	5.27	6.13	7.79	7.61
MRCI/B5	3.91 (3.78)	5.60 (5.42)	6.50 (6.36)	8.40 (8.10)	7.76 (7.50)
$O_2Ge(OGeH_3)_2$, S_2	1^1B_2	1^1A_2	2^1A_1	3^1A_1	1^1B_1
CIS/B4	0.44, 0.0001	0.96, 0.0000	1.55, 0.0000		1.75, 0.0287
TD-B3LYP/B4	0.42, 0.0008	0.17, 0.0000	0.56, 0.0006	1.75, 0.0011	0.69, 0.0001
EOM-CCSD/B5	0.30	0.49	1.82	3.14	2.15
MRCI/B1a//CAS, S_2				2.04 (1.96)	
$O_2Ge(OH)_2$, S_2	1^1B_2	1^1A_2	2^1A_1	3^1A_1	1^1B_1
EOM-CCSD/B5	0.29	0.48	1.89	3.08	2.26
CASPT2/B5	0.16	0.17	0.29	1.80	1.82
MRCI/B5	0.26 (0.22)	0.28 (0.23)	0.34 (0.20)	2.03 (1.91)	2.08 (1.93)
$O = Ge(OGeH_3)_2$, S_0	1^1B_2	1^1B_1	1^1A_2	2^1A_1	2^1A_2
CIS/B4	6.32, 0.0770	6.32, 0.0320	6.94, 0.0000	7.42, 0.0034	8.07, 0.0000
TD-B3LYP/B4	4.44, 0.0430	4.69, 0.0850	5.40, 0.0000	5.77, 0.0160	5.68, 0.0000
EOM-CCSD/B3	5.21	5.40	5.78	6.48	6.90
EOM-CCSD/B5	5.03	5.24	5.84	6.39	6.52
EOM-CCSD/B1b	5.03	5.23	5.88	6.44	6.59
SAC-CI/B1b	5.05, 0.0481	5.28, 0.0378	5.95, 0.0000	6.51, 0.0029	6.98, 0.0000
$O = Ge(OH)_2$, S_0	1^1B_2	1^1B_1	1^1A_2	2^1A_1	2^1A_2
EOM-CCSD/B5	4.96	5.19	5.85	6.50	7.19
CASPT2/B5	4.52	4.72		6.32	
MRCI/B5	5.18 (4.89)	5.39 (5.10)		7.08 (6.74)	
$O = Ge(OGeH_3)_2$, S_2	$1^1A''$	$2^1A'$	$3^1A'$	$2^1A''$	$3^1A''$
CIS/B4	1.94, 0.0034	2.32, 0.0095	4.78, 0.2051	6.10, 0.0653	6.47, 0.0097
TD-B3LYP/B4	1.18, 0.0020	1.65, 0.0023	3.50, 0.0347	3.37, 0.0359	3.72, 0.0244
EOM-CCSD/B5	1.42	1.94	4.36	4.52	–
EOM-CCSD/B1b//CAS, S_1	1.13	1.68	4.15	4.30	4.85

(*Continued*)

Lam Research Ex. 1035 - Page 113
Lam Research Corp. v. Inpria Corp.
IPR2024-00033 - U.S. Patent No. 9,823,564

Table 4.12. (*Continued*)

$O=Ge(OGeH_3)_2$, S_2	$1^1A''$	$2^1A'$	$3^1A'$	$2^1A''$	$3^1A''$
MRCI/B1b//CAS, S_1	0.82 (1.11)				
EOM-CCSD/B1b//CAS, S_2	1.25	1.78	4.41	4.80	5.16
MRCI/B1a//CAS, S_2		1.76 (1.67)			
$O=Ge(OH)_2$, S_2	$1^1A''$	$2^1A'$	$3^1A'$	$2^1A''$	$3^1A''$
EOM-CCSD/B5	1.33	1.90	4.57	4.99	
CASPT2/B5	1.04	1.63			
MRCI/B5	1.07 (1.08)	1.90 (1.72)			

[a]The following basis sets were used in the calculations: B1 – LanL2-DZP basis set for Ge and 6-31G* for O and H; B1a – B1 augmented with diffuse s and p functions on O with exponents of 0.08 and 0.03; B1b – B1a with additional s and p functions on Ge with the exponent of 0.03; B2 – 6-311+G* for Ge and 6-31G* for O and H; B3 – aug-cc-pVDZ; B4 – 6-311+G*; B5 – aug-cc-pVTZ for Ge, 6-31+G* for O, and 6-31G for H. The following active spaces were used in CASPT2 and MRCI calculations: for $O_2Ge(OH)_2$, (16,13) at the CASSCF stage and (16,11) for CASPT2 and MRCI stages, where core orbitals include 2s AO of oxygen atoms; for $O=Ge(OH)_2$, (14,14) (CASSCF) and (14,11) (CASPT2 and MRCI) with only actual core orbitals treated as the core. For MRCI, the numbers in parentheses include Davidson's corrections for quadruple excitations.

2^1A_1; it lies in the proper energy range and has a perceivable oscillator strength (Table 4.12). On the other hand, the energy of the 1^1B_2 state is too low and that of 1^1B_1 is too high, while 1^1A_2 has a suitable energy but the $1^1A_2 \leftarrow 1^1A_1$ transition is symmetry forbidden. The geometry of the lowest excited singlet states can be initially approximated by the structure of the T_1 triplet $^3B_2$ state. In this state, the O–O bond breaks apart, which leads to a significant increase of the O–O distance and O–Ge–O bond angle, while the variations of all other geometrical parameters are small. To refine these two critical variables, we scanned PESs for several singlet excited states along the O–Ge–O angle. The calculations were carried out at the CASPT2 level for the small model $O_2Ge(OH)_2$ cluster. The computed profiles of the singlet PESs are shown in Figure 4.8b. On vertical excitation of the ground state $O_2Ge=$ fragment to S_2 (2^1A_1), a total of five excited electronic states (additionally, 1^1A_2, 3^1A_1, and 1^1B_1) can participate in the radiative and radiationless decay into the ground state. When the O–Ge–O angle increases from 50° to 100°, the energies of the 1^1B_2, 1^1A_2, and 2^1A_1 states come close (within 0.5 eV) to the ground state energy. Therefore, these excited states would decay to 1^1A_1 either through IC or by emitting light in the IR region. As seen in Figure 4.8b, at O–Ge–O = 70°, the 2^1A_1 and 3^1A_1 states can cross or avoid crossing. The 1^1B_1 and 3^1A_1 states can decay

Lam Research Ex. 1035 - Page 114
Lam Research Corp. v. Inpria Corp.
IPR2024-00033 - U.S. Patent No. 9,823,564

radiatively producing visible PL bands. Three other states will transform to 1^1A_1 through radiationless decay (IC) since the energy differences between them and 1^1A_1 are small after geometry relaxation (Figure 4.8b and Table 4.12). The second excited singlet state 2^1A_1 may undergo a cascade IC into the ground state via the 2^1A_1–3^1A_1 and 2^1A_1–1^1A_2 intersections by the $2^1A_1(3^1A_1) \rightarrow 1^1A_2 \rightarrow 1^1B_2 \rightarrow 1^1A_1$ mechanism. On the other hand, 3^1A_1 produced through the 2^1A_1–3^1A_1 intersection can emit a photon and thus decay to the ground state forming a PL band. Alternatively, the $3^1A_1 \rightarrow 1^1B_1$ IC is possible via the intersection at O–Ge–O of ~95° and then 1^1B_1 can decay radiatively ($1^1B_1 \rightarrow 1^1A_1$). The 1^1B_1 and 3^1A_1 states have very close energies and their PL bands should be similar. The S_2–S_0 energy gap at the 3^1A_1 equilibrium geometry, which corresponds to the peak position of the PL band due to de-excitation of S_2, is ~2 eV at the most reliable MRCI level both for the smaller (X = OH) and larger (X = $OGeH_3$) model clusters. Therefore, the 5.5–6.5 eV photoexcitation of the $O_2Ge=$ point defect can result in a PL band peaked at ~2 eV.Because only the O–Ge–O angle changes significantly after the $S_0 \rightarrow S_2$ de-excitation, the PL band can exhibit a vibrational progression with spacing of ~600 cm^{-1}, which is the frequency of the O–Ge–O vibration in the ground state calculated at the B3LYP level.

4.1.4. O = Ge = Defect

In the ground electronic state of the O = Ge = defect, the O = GeO_2 fragment has a planar structure with local C_{2v} symmetry (Figure 4.9). As for silanone, the first two excited singlet states S_1 and S_2 are formed by electronic transitions from two HOMOs to the LUMO, which predominantly consists of the lone pair of the Ge atom, LP_{Ge}. Both HOMOs are mainly composed of the oxygen lone pairs and exhibit a perceptible π-type Ge–O bonding character (π_{Ge-O}). One of these orbitals lies in the OGeO′O′ plane and the other is perpendicular to it. When the HOMO → LUMO electronic transition takes place, an out-of-plane distortion (pyramidalization) of the O = GeO'_2 fragment reduces the cluster symmetry from C_{2v} to C_s. Since the compositions of the two HOMOs (A′ and A″ in C_s symmetry) are similar, one can expect that the energies of the S_1 and S_2 electronic states should be close. Indeed, at all theoretical levels used here, the S_1-S_2 differences are in the range of 0.1–0.2 eV (Table 4.12). The calculated S_1 and S_2 excitation energies for the O = Ge = defect are ~1 eV lower as compared to those in silanone. The most probable reason for the reduction of these excitation energies is a weaker bonding character of HOMO and HOMO−1 for O = Ge in comparison with those for O = Si. Electronic transitions to the

Lam Research Ex. 1035 - Page 115
Lam Research Corp. v. Inpria Corp.
IPR2024-00033 - U.S. Patent No. 9,823,564

three higher states with energies of 5.9–6.5 eV exhibit very small or zero (for symmetry-forbidden cases) *f* values (Table 4.12), and we do not consider their geometry relaxation here. These states are formed by electronic transitions from oxygen lone pairs (all three bridging O atoms give nearly equal contributions) to a Rydberg orbital distributed at Ge and O atoms. In this case, Stokes shifts are not anticipated to be very significant.

Next, we performed TD-B3LYP, EOM-CCSD, and CASPT2 calculations of the S_1 and S_2 excited states in the vicinity of their equilibrium structures. The optimal geometry of these states was initially approximated by the optimized structure of the triplet T_1 state. The Ge = O double bond is elongated in the triplet state, being transformed into a single bond. Additionally, the $O = GeO'_2$ fragment loses its planarity, while the Ge–O′–Ge′ bridges remain nearly unchanged. This geometry was refined for S_1 and S_2 states at the EOM-CCSD level by scanning PES along the O = Ge bond length and the O = Ge(O′O′) dihedral angle with 0.05 Å and 5° steps, respectively, and by using the parabolic approximation to determine the minimum position. The other geometric parameters were kept frozen at constant values optimized for the triplet state. The optimized parameters for the S_1, S_2, and T_1 states are found to be close. Also, full geometry optimization of these states using analytical gradients at the CASSCF level gives similar geometric parameters for the excited states; however, the excited state geometries differ significantly from the ground state structure. Vertical transition energies calculated at the S_2 and S_1 optimized geometries are lower as compared to the corresponding values for O = Si = (~2.31 and ~1.6 eV); they are 1.7–1.6 eV for S_2 and 1.1–1.0 eV for S_1 at the most accurate Davidson-corrected MRCI, CASPT2, and EOM-CCSD levels. Vibrational progressions, which can be observed in these PL bands are expected to be more complicated than for the case of $O_2Ge =$, because two geometric parameters, the O–Ge distance and the $O–GeO'_2$ torsion angle, significantly change and both corresponding vibrations (960 and 240 cm^{-1} at the B3LYP level) can contribute to these progressions.

4.2. Photoluminescence of Oxygen-Deficient Defects in Germanium Oxides

In substoichiometric germanium oxides, GeO_{2-x}, the insufficiency of oxygen atoms can result in the formation of oxygen-deficient defects. The most typical of these defects is the so-called E′-center (–Ge≡) defect, which can also be combined with OV located in its nearest neighborhood. The E′-center and the E′–OV combination exhibit peculiar optical properties considered in this subsection.

Lam Research Ex. 1035 - Page 116
Lam Research Corp. v. Inpria Corp.
IPR2024-00033 - U.S. Patent No. 9,823,564

4.2.1. Surface E′-Center, or –Ge≡ Defect

The threefold-coordinated Ge atom is connected with the rest of the bulk by three Ge–O–Ge bridges with approximately the same geometrical characteristics (Ge–O and Ge–Ge distances) as in the cluster modeling the defectless region of the bulk (Figure 4.10). The unpaired electron from the broken Ge–O bond is located at SOMO, which is close in composition to a Ge lone pair. The lowest in energy electronic transitions proceed to this half-filled orbital from underlying MOs composed mainly from lone pairs of the nearest oxygen atoms [97]. Another group of excitations is related to the transitions of the unpaired electron from SOMO to an empty MO on the Ge atom with a predominantly Rydberg character. Similarly to the excitations in the :Si< and :Ge< defects, one can expect in this case moderate geometry relaxation and a relatively small Stokes shift. In contrast, for the first group of transitions the reorganization of Ge–O–Ge bridges involved in the excitation should be significant. The calculations of vertical excitation energies at the ground state geometry show that this defect should have two noticeable absorption bands at 4.7–5.3 eV and 6.2–6.4 eV (Table 4.13).

The character of geometry relaxation in excited states depended on the location of the electron hole; the bonds formed by the hole-bearing atoms were weakened. For instance, the $2^2A'$ excited state is produced by the transfer of an electron to SOMO from the orbital constructed mainly by symmetrical combination of lone pairs located at the O″ atoms (lying beyond the symmetry plane, Figure 4.10), and the hole located at these centers leads to elongation of the Ge–O″ bond. In the $4^2A'$ state, three O atoms are involved in the excitation, and all the Ge–O′ and Ge–O″ bonds are elongated, but the changes are smaller as compared to the previous case. The weakening of the Ge–O bonds simultaneously leads to an increase of the corresponding Ge–Ge′ and Ge–Ge″ distances and a decrease of the O–Ge–O angles. Similar changes take place in the $3^2A''$ state, but the hole distribution is less symmetrical – the contributions from the O′ atom are larger, and the alterations of the Ge–O′ and O′–Ge″ bonds are more significant. In contrast, the $1^2A''$ state at the ground state geometry is formed by electronic transfer from anti-symmetric combinations of lone pairs located at the single O′ atom (placed within the symmetry plane), and geometry optimization leads to a cleavage of the Ge–O′ bond (Figure 4.10). Actually, the system is transformed to a combination of the :Ge< and –O–Ge≡ defects in their ground states. With this optimized geometry, the $1^2A''$ state has a lower energy than that of $1^2A'$, and PL cannot occur; apparently, thermal activation is required to convert the system into its initial state. However, due to low oscillator strength for the $1^2A' \rightarrow 1^2A''$ excitation, a direct formation of the $1^2A''$ state on absorption of light has a very low probability.

Lam Research Ex. 1035 - Page 117
Lam Research Corp. v. Inpria Corp.
IPR2024-00033 - U.S. Patent No. 9,823,564

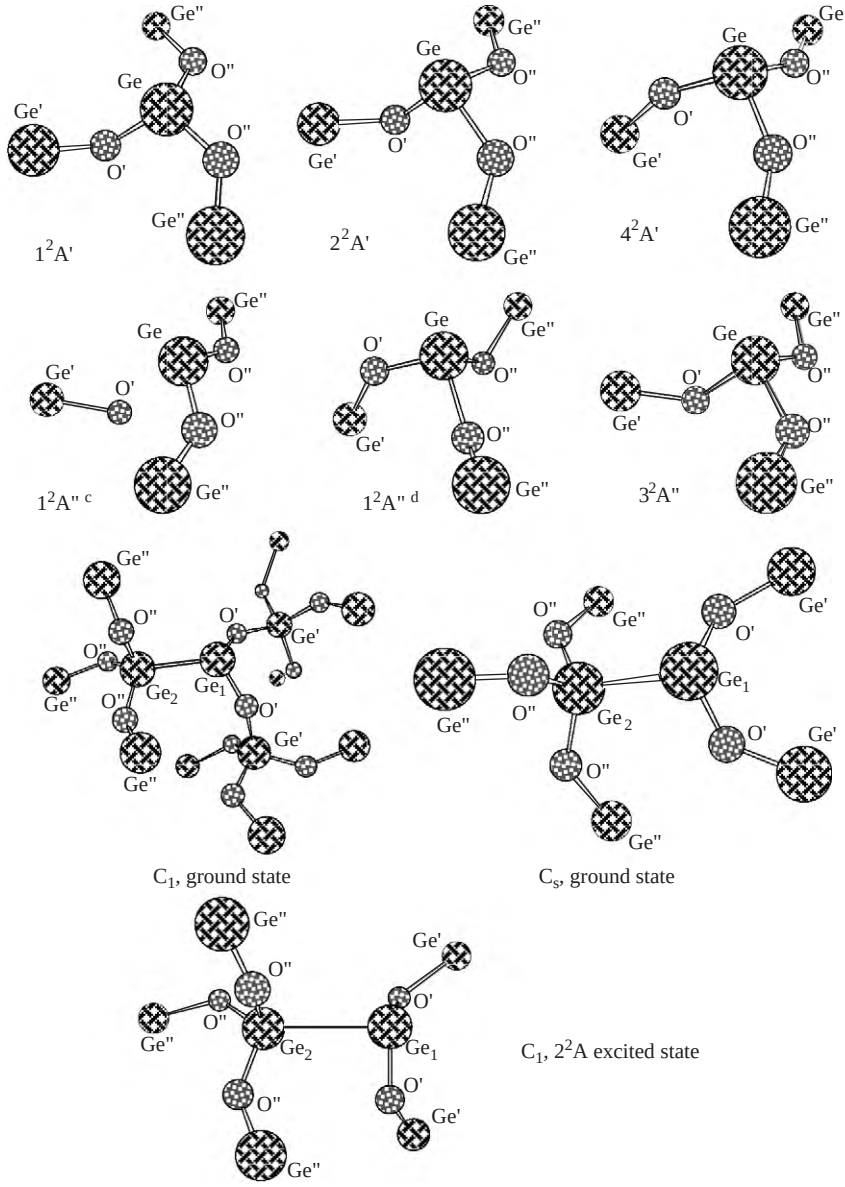


Fig. 4.10. Model clusters used for simulation of the –Ge≡ defect (E′) and the combined –Ge≡ and oxygen vacancy defect (E′–OV). Terminal H atoms are not shown.

Lam Research Ex. 1035 - Page 118
Lam Research Corp. v. Inpria Corp.
IPR2024-00033 - U.S. Patent No. 9,823,564

Table 4.13. Vertical excitation energies (in eV) and oscillator strengths for the lowest doublet states of the $-GeX_3$ and $X_2Ge-GeX_3$ ($X = OGeH_3$) model clusters[a]

GeX_3	$1^2A''$	$2^2A''$	$2^2A'$	$3^2A'$	$3^2A''$	$4^2A'$
SAC-CI′/B2a	4.72, 0.0001	4.97, 0.0353	5.36, 0.0503	5.49, 0.0113	6.12, 0.0001	6.41, 0.0532
SAC-CI′/B1a	4.69, 0.0004	4.91, 0.0328	5.31, 0.0514	5.44, 0.0058	6.01, 0.0001	6.26, 0.0477
SAC-CI′/B1b	4.68, 0.0004	4.87, 0.0324	5.32, 0.0552	5.41, 0.0055	6.01, 0.0001	6.22, 0.0467
MCSCF/B1a	4.43, 0.0001	4.67, 0.0180	5.17, 0.0368	5.26, 0.0129	6.02, 0.0030	6.26, 0.0805
MRCI/B1a[b]	4.63 (4.51)	4.88 (4.73)	5.43 (5.29)	5.58 (5.44)	6.12 (5.90)	6.37 (6.20)
B3LYP/B2a	3.23, 0.0006	3.39, 0.0189	3.75, 0.0222	3.84, 0.0075	4.18, 0.0006	4.44, 0.0013
$X_2Ge-GeX_3$[c]	2^2A ($2^2A'$)	3^2A ($1^2A''$)	4^2A ($2^2A''$)	5^2A ($3^2A''$)	6^2A ($3^2A'$)	7^2A ($4^2A'$)
SAC-CI′/B1a, C_s	3.87, 0.1017	4.37, 0.0001	4.95, 0.0677	5.25, 0.0005	5.49, 0.0329	5.90, 0.0385
SAC-CI′/B1a, C_1	3.60, 0.0511	4.45, 0.0002	4.98, 0.0365	5.31, 0.0058	5.43[d], 0.054	5.47, 0.0084
CASSCF/B1a, C_1	4.30, 0.0118	4.99, 0.0135	5.10, 0.1976	5.34, 0.1261		
MRCI/B1a[b] C_1	4.15 (4.02)	5.08 (5.03)	4.98 (4.83)	5.32 (5.23)		

[a]The B1a basis set is LanL2DZ + d (Ge) and 6-31G* (O, H) augmented with diffuse functions s (0.03, 0.01) and p (0.02) on Ge atoms. The B1b basis set is B1a + s, p (0.08) on O atoms. The B2a basis set is 6-311 + G* on Ge and 6-31G* on O and H.

[b]The values in parenthesis are calculated at the MRCI + Q level, with Davidson's corrections for quadruple excitations.

[c]Electronic terms given in parentheses denote corresponding states within C_s-symmetry.

[d]Significant contributions of double excitations (0.2 and higher) are present.

Geometry relaxation of the $3^2A'$ state leads to a decrease of the energy gap between $2^2A'$ and $3^2A'$ and eventual crossing of the PESs of these two states. Therefore, as the geometry continues to relax, the system passes from the $3^2A'$ PES to $2^2A'$. Since the PES crossing has two slopes, one can expect that two different local minima for the $2^2A'$ state can exist in its vicinity. Therefore, we have performed geometry optimization for the $2^2A'$ state starting from two structures lying on different slopes of the crossing. However, in both cases we obtained the same minimum as in optimization starting from the ground state geometry. A similar behavior is found for the $2^2A''$ state, which crosses with the $1^2A''$ surface. In this case, however, in the vicinity of the crossing point the hole is distributed between two O″ atoms, and optimization from the slopes of the crossing vicinity leads to another minimum (denoted by the superscript d in Figure 4.10) as compared to the optimization result starting from the ground state geometry (denoted by c): in the former case, the Ge–O′ bond is conserved but the Ge–O″ and O″–Ge″ bonds are weakened (Figure 4.10).

Two PL bands can be expected for the $4^2A'$ state, at ~3.3 eV (transition to the ground state) and ~1.2–1.4 eV (transitions to $1^2A'$, $2^2A'$, $2^2A''$). The probabilities of the $4^2A' \rightarrow 3^2A'$ and $4^2A' \rightarrow 3^2A''$ processes are much lower (see oscillator strengths in Table 4.14). De-excitation of the $3^2A''$ state can result in three PL bands, at ~3.0, 1.3, and 0.5 eV, but the first one has a low oscillator strength and should be weak (Table 4.14). The $2^2A' \rightarrow 1^2A''$ de-excitation energy

Lam Research Ex. 1035 - Page 119
Lam Research Corp. v. Inpria Corp.
IPR2024-00033 - U.S. Patent No. 9,823,564

Table 4.14. De-excitation energies (in eV) and oscillator strengths calculated at the equilibrium structures of excited states of the GeX_3 ($X = OGeH_3$) point defect[a]

		$1^2A'$	$1^2A''$	$2^2A'$	$2^2A''$	$3^2A''$	$3^2A'$
$4^2A'$	SAC-CI′	3.39, 0.0458	1.44, 0.0324	1.32, 0.0911	1.24, 0.0842	0.43, 0.0026	0.35, 0.0062
	CASSCF	3.32, 0.0532	1.54, 0.0172	1.44, 0.0628	1.26, 0.0526	0.44, 0.0005	0.35, 0.0034
	MRCI[b]	3.33 (3.27)	1.43 (1.37)	1.31 (1.26)	1.19 (1.16)	0.37 (0.35)	0.27 (0.25)
$3^2A''$	SAC-CI′	2.79, 0.0027	1.07, 0.0392	0.55, 0.0219	0.39, 0.0108		0.10, 0.0020
	CASSCF	3.00, 0.0020	1.34, 0.0233	0.63, 0.0106	0.59, 0.0063		0.27, 0.0040
	MRCI[b]	3.03 (2.94)	1.27 (1.20)	0.53 (0.48)	0.51 (0.48)		0.26 (0.23)
$2^2A'$	SAC-CI′	1.76, 0.0020	0.48, 0.0562		0.04, 0.0002		
	CASSCF	1.58, 0.0057	0.65, 0.0467				
	MRCI[b]	1.66 (1.65)	0.58 (0.56)				
$1^2A''$	SAC-CI′	1.11, 0.0004					
	CASSCF	0.81, 0.0005					
	MRCI[b]	0.96 (0.99)					

[a]The basis set used in all calculations was B1a: LanL2DZ + d (Ge) and 6-31G* (O, H) augmented with diffuse functions s (0.03, 0.01) and p (0.02) on Ge atoms. The emission occurs from the electronic states shown in the left column to the states specified in the first row of the table.

[b]The values in parenthesis are calculated with Davidson-corrected MRCI + Q energies.

is calculated to be in the range of 0.5–0.6 eV, the $2^2A' \rightarrow 1^2A'$ transition has a higher energy (~1.6 eV), but much lower oscillator strength. Finally, $1^2A''^d \rightarrow 1^2A'$ PL has a very low oscillator strength and an energy of ~1 eV (Table 4.14).

In summary, upon excitation of the –Ge≡ defect with the PE energy up to 6–7 eV one can expect two PA bands at 4.7–5.4 and 6.2 eV and three broad PL bands in the ranges of 3.0–3.3, 1.2–1.4, and 0.5–0.6 eV, possibly with a weak satellite near 1 eV.

4.2.2. Combination of the –Ge≡ Defect with an Oxygen Vacancy, E′–OV

Electronic structure of the ground state for the E′–OV defect (Figure 4.10) is similar to that of the E′ defect, but with the Ge–Ge bond replacing a Ge–O–Ge bridge. As in the –Ge≡ defect, SOMO is formed mainly by the orbitals from the threefold-coordinated Ge atom. The much shorter Ge_1–Ge_2 bond length as compared to the Ge–Ge distance in Ge–O–Ge bridges mainly leads to variations of valence angles, whereas the Ge–O distances are similar for both defects and do not differ substantially from the corresponding values in the defect-less structures. Thus, the shortening of the Ge–Ge distance at the OV is compensated mainly by rotations of GeO_4 fragments in the vicinity of the defect and does not lead to significant changes of rigid geometric parameters.

For excited electronic states, the difference between the $–GeX_3$ and $X_3Ge–GeX_2$ defects is more substantial. For the latter system, the Ge–Ge

Lam Research Ex. 1035 - Page 120
Lam Research Corp. v. Inpria Corp.
IPR2024-00033 - U.S. Patent No. 9,823,564

bond, lone pairs of oxygen atoms from the Ge_1–O′–Ge bridges, and lone pairs with significant contributions of Rydberg-type orbitals from the Ge_1 center (Figure 4.10) all participate in the formation of the lowest excited states. The first excited 2^2A state of the $X_3Ge–GeX_2$ defect corresponds to the electronic transition from the Ge_1–Ge_2 bond to SOMO, which is formed mainly by contributions of the s- and p_z-AOs of the Ge_1 center. In the 3^2A state, the electron donation again proceeds from the Ge–Ge bond, but with an additional contribution from lone pairs of O′, and the accepting orbital is LUMO that is formed mostly from the p_y- and s-AOs of the Ge_1 center. The next several states are formed mainly by transitions from O′ lone pairs to SOMO, but contributions from the Ge–Ge bond and LUMO are also noticeable. The absorption spectrum for the E′–OV system should include a relatively narrow band near 4 eV and a more diffuse and intense band around 5 eV (Table 4.13).

Geometry relaxation was investigated for the states from 2^2A to 5^2A. On geometry optimization, a stationary point was obtained only for the 2^2A state (see Figure 4.10). In this state, geometry relaxation leads mainly to a cleavage of the Ge–Ge bond, whereas all other geometric parameters of the 1^2A and 2^2A states do not differ significantly. In the 3^2A–5^2A states, in the process of geometry optimization PES cross with those of the lower states, and the system gradually descends to the 2^2A state. This means that the 3^2A–5^2A states will be transformed into 2^2A through a cascade of ICs in a radiationless manner, and one can expect only the $2^2A \rightarrow 1^2A$ PL process originating from these states. The corresponding PL energy calculated at the 2^2A optimized geometry is ~2.0–2.1 eV.So, after photoexcitation in the energy range of 4–5 eV, the $X_3Ge–GeX_2$ defect is able to produce a red/orange PL band in the range of 2.0–2.1 eV.

Among all points defects in GeO_2 considered so far, including oxygen-bearing and oxygen-deficient defects described in Section 4, no intense PL band was found in the blue spectral region of 2.5–2.7 eV, and, assuming that the accuracy of our calculations is better than 0.3–0.5 eV, these defects are not likely to contribute to the intense blue PL observed for GeO_2 nanowires [12]. The quest for the structural features responsible for that PL thus needs to be continued. Currently, optical properties of single and double OVs are under investigation in our groups, and preliminary results for divacancy seem hopeful.

5. Summary and Outlook

We have performed *ab initio* and DFT calculations of model clusters simulating various point defects, impurities, and their combinations in

Lam Research Ex. 1035 - Page 121
Lam Research Corp. v. Inpria Corp.
IPR2024-00033 - U.S. Patent No. 9,823,564

nanosized silica and germania materials. The size and shape of the model clusters were chosen to correctly reproduce the structural motives of the corresponding bulk materials containing defects. We obtained their accurate geometric and electronic structures, calculated photoabsorption and PL energies, and predicted the absorption and PL spectra using PESs for the ground and excited electronic states generated by *ab initio* and DFT calculations.

Our calculations provide reasonably accurate geometries for the SiO_2 clusters and reproduce the experimental excitation energy (1.9–2.0 eV) of the NBO defect. The combined defects with OV in the first coordination sphere of NBO are shown to be unstable with respect to insertion of the undercoordinated O atom into the neighboring Si–Si bond. The more distant OVs are shown to be able to coexist with NBO and their appearance leads to a decrease of the vertical excitation energy at NBO to 1.7–1.8 eV.A presence of double and triple OVs further shifts the excitation energies to 1.0–1.2 eV.The excitation leads to significant elongation of the Si–Si bond at OV and, as a result, PL energies are much lower than E_{EXC}. The variety of the red PL bands observed experimentally has been rationalized in terms of different arrangements of NBO and OV in the combined defect, mainly in the third and the fourth layers of O atoms around NBO, when the two defects are separated by 0.6–1.0 nm.We have also investigated PL properties of silanone, $=Si=O$, and dioxasilyrane, $=Si(O_2)$, and the impurity $[AlO_4]^0$ defect in silica. The silanone and dioxasilyrane defects were found to be possible candidates for green and red light-emitters. The PL band corresponding to the $[AlO_4]^0$ defect was predicted to be multi-component with few bands between 1.5 and 1.0 eV and a more numerous group of electronic transitions in the range of 0.7–0.2 eV.

In a search of emitting centers responsible for the intense blue PL observed in GeO_2 nanowires, we calculated optical properties of –O–Ge≡ (NBO), –OO–Ge≡ (peroxy radical), O = Ge = , and $(O_2)Ge=$ defects in germanium oxides. The results showed that the excited states of these defects normally exhibit strong geometry relaxation leading to large Stokes shifts and, as a result, UV-photoabsorption is accompanied by red or IR PL. We have also studied oxygen-deficient surface E′-center, $–GeX_3$, and combined E′–OV, $X_3Ge–GeX_2$, defects in substoichiometric germanium oxides. Both of them were shown to give rise to photoabsorption bands between 4 and 6 eV.The $–GeX_3$ defect is able to generate several PL bands in the UV (~3 eV) and IR (1.2–1.4 and 0.5–0.6 eV) spectral ranges, whereas the $X_3Ge–GeX_2$ defect gives only one red/orange PL band at 2.0–2.1 eV.No intense PL band was found in the blue spectral region of 2.5–2.7 eV.Thus, none of the defects considered so far are likely to contribute to the blue PL bands and the studies of the origin of these bands need to be continued.

Lam Research Ex. 1035 - Page 122
Lam Research Corp. v. Inpria Corp.
IPR2024-00033 - U.S. Patent No. 9,823,564

Remarkable optical properties of silica and germania nanomaterials are often related to a large difference between the energies of absorbed and emitted photons, i.e., to the Stokes shift. PL (vertical emission) energy is determined by the energy difference between an excited and the ground state PESs at the equilibrium structure of the excited state. The larger geometry relaxation in the excited electronic state, the larger the difference between the absorption and emission energies, which determines the Stokes shift. Point defects in GeO_2 and SiO_2, for which one can expect a significant Stokes shift, include (in addition to the defects considered in this chapter) OVs (= A–A =) and divacancies (= A–A–A =), peroxide bridges (= A–O–O–A =), different combinations of NBO, E′-centers, and OVs, etc. These defects are the best candidates for emitting centers responsible for the PL spectra observed experimentally so far. On the other hand, theoretical calculations of electronic transitions characteristic for particular defects in SiO_2 and GeO_2 will allow us to suggest novel nanostructures with desirable optical properties, which can have potential broad applications in optoelectronic technologies, and to provide guidelines to materials scientists for their synthesis. Our predictions directly connect the composition and geometrical structure of nanosized objects with a variety of their optical properties and therefore will render their guided synthesis more efficient and less costly.

6. Discussion Topics and Questions on Concepts

1. Why optical (photoabsorption and PL) properties of SiO_2 and GeO_2 nanomaterials can dramatically differ from the properties of bulk silica and germania?
2. What is the role of point defects in optical properties of silica and germania nanomaterials?
3. Discuss the structure and composition of the most typical point defects in SiO_2 and GeO_2.
4. Why the absorption and luminescence spectra of SiO_2 and GeO_2 nanomaterials can be drastically different from one another both in terms of maximum wavelength and band shape? What is the origin of large Stokes shifts in these materials?
5. Why the properties of point defects in silica and germania can be simulated using quantum chemical calculations of model clusters of a finite size? Describe the requirements for model clusters to be suitable for such simulations.
6. What is the essence of the ONIOM method for geometry optimization of model clusters and why this method is convenient for calculations of large SiO_2 and GeO_2 clusters?

Lam Research Ex. 1035 - Page 123
Lam Research Corp. v. Inpria Corp.
IPR2024-00033 - U.S. Patent No. 9,823,564

7. Describe the advantages and drawbacks of various theoretical methods that can be used for calculations of excitation energies for model SiO_2 and GeO_2 clusters.
8. For what types of electronic states the use of TD-DFT and OVGF methods to compute excitation energies is appropriate and when these methods are not expected to provide accurate results?
9. Compare the photoabsorption and PL properties of NBO in SiO_2 with those of the NBO–OV combination defects. How the presence of OVs affects the PL bands?
10. Discuss common features and differences in optical properties of analogous point defects in silica and germania nanomaterials.

References

1. J. F. Conley, P. M. Lenahan, Appl. Phys. Lett. **62** (1993) 40.
2. K. Hess, B. Tuttle, F. Register, D. K. Ferry, Appl. Phys. Lett. **75** (1999) 3147.
3. L. Tsybeskov, G. F. Grom, P. M. Fauchet, J. P. McCaffrey, J. M. Baribeau, G. I. Sproule, D. J. Lockwood, Appl. Phys. Lett. **75** (1999) 2265.
4. G. F. Grom, D. J. Lockwood, J. P. McCaffrey, H. J. Labbe, P. M. Fauchet, B. White, J. Diener, D. Kovalev, F. Koch, L. Tsybeskov, Nature **407** (2000) 358.
5. L. Pavesi, L. Dal Negro, C. Mazzoleni, G. Franzo, F. Priolo, Nature **408** (2000) 440.
6. A. Monnier, F. Schuth, Q. Huo, D. Kumar, D. Margolese, R. S. Maxwell, G. D. Stucky, M. Krishnamurty, P. Petroff, A. Firouzi, M. Janicke, B. F. Chmelka, Science **261** (1993) 1299.
7. C. T. Kresge, M. E. Leonowicz, W. J. Roth, J. C. Vartuli, J. S. Beck, Nature **359** (1992) 710.
8. D. L. Williams, S. T. Davey, R. Kashyap, J. R. Armitage, B. J. Ansile, Electron. Lett. **28** (1992) 369.
9. R. M. Atkins, V. Mizrahi, Electron. Lett. **28** (1992) 1743.
10. V. Mizrahi, R. M. Atkins, Electron. Lett. **28** (1992) 2210.
11. X. C. Wu, W. H. Song, K. Y. Wang, T. Hu, B. Zhao, Y. P. Sun, J. J. Du, Chem. Phys. Lett. **336** (2001) 53.
12. X. C. Wu, W. H. Song, B. Zhao, Y. P. Sun, J. J. Du, Chem. Phys. Lett. **349** (2001) 210.
13. Yu. D. Glinka, S. H. Lin, Y.-T. Chen, Appl. Phys. Lett. **75** (1999) 778.

Lam Research Ex. 1035 - Page 124
Lam Research Corp. v. Inpria Corp.
IPR2024-00033 - U.S. Patent No. 9,823,564

14. Yu. D. Glinka, S. H. Lin, Y.-T. Chen, Phys. Rev. B **62** (2000) 4733.
15. Yu. D. Glinka, S. H. Lin, L.-P. Hwang, Y.-T. Chen, J. Phys. Chem. B **104** (2000) 8652.
16. Yu. D. Glinka, S. H. Lin, L.-P. Hwang, Y.-T. Chen, Appl. Phys. Lett. **77** (2000) 3968.
17. Yu. D. Glinka, S. H. Lin, L.-P. Hwang, Y.-T. Chen, N. H. Tolk, Phys. Rev. B **64** (2001) 085421.
18. Yu. D. Glinka, S. H. Lin, Y.-T. Chen, Phys. Rev. B **66** (2002) 035404.
19. W. L. Wilson, P. F. Szajowski, L. E. Brus, Science **262** (1993) 1242.
20. L. E. Brus, P. F. Szajowski, W. L. Wilson, T. D. Harris, S. Schuppler, P. H. Citrin, J. Am. Chem. Soc. **117** (1995) 2915.
21. L. Skuja, J. Non-Cryst. Solids **179** (1994) 51.
22. M. V. Wolkin, J. Jorne, P. M. Fauchet, G. Allan, C. Delerue, Phys. Rev. Lett. **82** (1999) 197.
23. B. Zou, J. Wang, C. Liu, J. Z. Zhang, M. A. El-Sayed, Phys. Rev. B **62** (2000) 16595.
24. A. N. Trukhin, M. Goldberg, J. Jansons, H.-J. Fitting, I. A. Tale, J. Non-Cryst. Solids **223** (1998) 114.
25. J. L. Gole, D. A. Dixon, Phys. Rev. B **57** (1998) 12002.
26. K. Tanimura, C. Itoh, N. Itoh, J. Phys. C **21** (1988) 1869.
27. M. A. S. Kalceff, Phys. Rev. B **57** (1998) 5674.
28. C. M. Lieber, Solid State Commun **107** (1998) 607.
29. J. Hu, T. W. Odom, C. M. Lieber, Acc. Chem. Res. **32** (1999) 435.
30. L. N. Skuja, A. N. Streletsky, A. B. Pakovich, Solid State Commun. **50** (1984) 1069.
31. G. W. Arnold, IEEE Trans. Nucl. Sci. **20** (1973) 220.
32. A. J. Cohen, H. L. Smith, J. Phys. Chem. Solids **7** (1958) 301.
33. H. Imai, K. Arai, H. Imagawa, H. Hosono, Y. Abe, Phys. Rev. B **38** (1988) 12772.
34. H. Hosono, Y. Abe, D. L. Kinser, R. A. Weeks, K. Muta, H. Kawazoe, Phys. Rev. B **46** (1992) 11145.
35. Y. Maeda, Phys. Rev. B **51** (1995) 1658.
36. M. Zacharias, P. M. Fauchet, J. Non-Cryst. Solids **227** (1998) 1058.
37. L. Skuja, J. Non-Cryst. Solids **167** (1994) 229.
38. Y. Negishi, S. Nagao, Y. Nakamura, A. Nakajiama, S. Kamei, K. Kaya, J. Appl. Phys. **88** (2000) 6037.
39. E. M. Dianov, V. O. Sokolov, V. B. Sulimov, J. Non-Cryst. Solids **149** (1992) 5.

Lam Research Ex. 1035 - Page 125
Lam Research Corp. v. Inpria Corp.
IPR2024-00033 - U.S. Patent No. 9,823,564

40. V. B. Sulimov, V. O. Sokolov, J. Non-Cryst. Solids **191** (1995) 260.
41. V. B. Sulimov, V. O. Sokolov, B. Poumellec, Phys. Status Solidi B **196** (1996) 175.
42. B. L. Zhang, K. Raghavachari, Phys. Rev. B **55** (1997) 15993.
43. B. B. Stefanov, K. Raghavachari, Phys. Rev. B **56** (1997) 5035.
44. A. S. Zyubin, V. G. Sulimov, Glass Phys. Chem. **25** (1999) 111.
45. G. Pacchioni, L. Skuja and D. Griscom (Eds.), Defects in SiO_2 and Related Dielectrics: Science and Technology, NATO Science Series II, Vol. 2, Kluwer, Dordrecht, 2000.
46. G. Pacchioni, G. Ierano, Phys. Rev. B **57** (1998) 818.
47. L. W. Hobbs, C. E. Jesurum, V. Pulim, B. Berger, Philos. Mag. A **78** (1998) 679.
48. Y. Le Page, L. D. Calvert, E. G. Gabe, J. Phys. Chem. Solids **41** (1980) 721.
49. V. O. Sokolov, V. B. Sulimov, Phys. Status Solidi B **135** (1986) 369.
50. G. Pacchioni, G. Ierano, A. M. Marquez, Phys. Rev. Lett. **81** (1998) 377.
51. G. Pacchioni, M. Vitiello, Phys. Rev. B **58** (1998) 7745.
52. K. Raghavachari, G. Pacchioni, J. Chem. Phys. **114** (2001) 4657.
53. K. Raghavachari, D. Ricci, G. Pacchioni, J. Chem. Phys. **116** (2002) 825.
54. F. Zhou, J. D. Head, J. Phys. Chem. B **104** (2000) 9981.
55. A. S. Zyubin, O. A. Kondakova, S. A. Dembovsky, Glass Phys. Chem. **23** (1997) 58.
56. S. Daprich, I. Komaromi, K. S. Byun, K. Morokuma, M. J. Frisch, J. Mol. Struct. (Theochem) **461** (1999) 1.
57. Yu. D. Glinka, A. S. Zyubin, A. M. Mebel, S. H. Lin, L. P. Hwang, Y. T. Chen, Eur. Phys. J. D **16** (2001) 279.
58. Yu. D. Glinka, A. S. Zyubin, A. M. Mebel, S. H. Lin, L. P. Hwang, Y. T. Chen, Chem. Phys. Lett. **358** (2002) 180.
59. Yu. D. Glinka, A. S. Zyubin, A. M. Mebel, S. H. Lin, L. P. Hwang, Y. T. Chen, J. Chem. Phys. **116** (2002) 281.
60. A. S. Zyubin, A. M. Mebel, S. H. Lin, J. Chem. Phys. **119** (2003) 11408.
61. G. Pacchioni, F. Frigoli, D. Ricci, J. A. Weil, Phys. Rev. B **63** (2000) 054102.
62. H.-J. Werner, P. J. Knowles, J. Chem. Phys. **82** (1985) 5053.
63. P. J. Knowles, H.-J. Werner, Chem. Phys. Lett. **115** (1985) 259.
64. M. E. Casida, C. Jamorski, K. C. Casida, D. R. Salahub, J. Chem. Phys. **108** (1998) 4439.

Lam Research Ex. 1035 - Page 126
Lam Research Corp. v. Inpria Corp.
IPR2024-00033 - U.S. Patent No. 9,823,564

65. H. Nakatsuji, Chem. Phys. Lett. **59** (1978) 362.
66. H. Nakatsuji, Chem. Phys. Lett. **67** (1979) 329.
67. H. Nakatsuji, Chem. Phys. Lett. **67** (1979) 334.
68. K. Hirao, J. Chem. Phys. **79** (1983) 5000.
69. R. J. Buenker, S. D. Peyerimhoff, Theor. Chim. Acta **39** (1975) 217.
70. H.-J. Werner, P. J. Knowles, J. Chem. Phys. **89** (1988) 5803.
71. P. J. Knowles, H.-J. Werner, Chem. Phys. Lett. **145** (1988) 514.
72. K. Andersson, P. A. Malmqvist, B. O. Roos, J. Chem. Phys. **96** (1992) 1218.
73. J. F. Stanton, R. J. Bartlett, J. Chem. Phys. **98** (1993) 7029.
74. R. J. Rico, M. Head-Gordon, Chem. Phys. Lett. **213** (1993) 224.
75. C. Adamo, V. Barone, Chem. Phys. Lett. **314** (1999) 152.
76. S. Hirata, M. Head-Gordon, Chem. Phys. Lett. **302** (1999) 375.
77. S. Hirata, T. J. Lee, M. Head-Gordon, J. Chem. Phys. **111** (1999) 8904.
78. J. Guan, M. E. Casida, D. R. Salahub, J. Mol. Struct. (Theochem) **527** (2000) 229.
79. D. J. Tozer, N. C. Handy, J. Chem. Phys. **109** (1998) 10180.
80. X. Chu, S. I. Chu, Phys. Rev. A **63** (2001) 023411.
81. J. C. Shieh, J. I. Chang, J. C. Wu, R. Li, A. M. Mebel, N. C. Handy, Y. T. Chen, J. Chem. Phys. **112** (2000) 7384.
82. A. S. Zyubin, A. M. Mebel, S. H. Lin, Yu. D. Glinka, J. Chem. Phys. **116** (2002) 9889.
83. N. F. Mott, J. Non-Cryst. Solids **40** (1980) 1.
84. L. S. Cederbaum, N. Domcke, W. von Niessen, J. Phys. B **10** (1977) 2963.
85. W. von Niessen, J. Schirmer, L. S. Cederbaum, Comput. Phys. Rep. **1** (1984) 57.
86. J. V. Ortiz, J. Chem. Phys. **89** (1988) 6348.
87. V. G. Zakrzewski, A. I. Boldyrev, J. Chem. Phys. **93** (1990) 657.
88. A. S. Zyubin, A. M. Mebel, J. Comput. Chem. **24** (2003) 692.
89. A. S. Zyubin, A. M. Mebel, J. Chem. Phys. **119** (2003) 6581.
90. C. Sousa, C. de Graaf, G. Pacchioni, J. Chem. Phys. **114** (2001) 6259.
91. A. M. Mebel, Y.-T. Chen, S. H. Lin, J. Chem. Phys. **105** (1996) 9007.
92. M. Hayashi, A. M. Mebel, K. K. Liang, S. H. Lin, J. Chem. Phys. **108** (1998) 2044.
93. A. M. Mebel, M. Hayashi, K. K. Liang, S. H. Lin, J. Phys. Chem. A **103** (1999) 10674.
94. A. S. Zyubin, A. M. Mebel, S. H. Lin, J. Chem. Phys. **123** (2005) 044701.

Lam Research Ex. 1035 - Page 127
Lam Research Corp. v. Inpria Corp.
IPR2024-00033 - U.S. Patent No. 9,823,564

95. A. A. Bobysev, V. A. Radzig, Fiz. Khim. Stekla (in Russian) **14** (1988) 501.
96. E. J. Friebele, D. L. Griscom, M. Stapelbroec, R. A. Weeks, Phys. Rev. Lett. **42** (1979) 1346.
97. A. S. Zyubin, A. M. Mebel, S. H. Lin, J. Chem. Phys. **125** (2006) 064701.

Lam Research Ex. 1035 - Page 128
Lam Research Corp. v. Inpria Corp.
IPR2024-00033 - U.S. Patent No. 9,823,564

Chapter 5

Density Matrix Treatments of Ultrafast Radiationless Transitions

S.H. Lin[a,b], K.K. Liang[b], M. Hayashi[c], and A.M. Mebel[d]

[a]*Institute of Atomic and Molecular Sciences, Academia Sinica, P.O. Box 23-166, Taipei 106, Taiwan*
[b]*Division of Mechanics, Research Center for Applied Sciences, Academia Sinica, Taipei 115, Taiwan*
[c]*Center for Condensed Matter Sciences, National Taiwan University, Taipei 106, Taiwan*
[d]*Department of Chemistry and Biochemistry, Florida International University, Miami, FL 33199, USA*

1. Introduction . . . 122
2. Density Matrix and Liouville Equation . . . 123
   2.1. Definition of Density Matrix . . . 123
   2.2. Dynamics of Isolated Systems. . . . 126
3. Dynamics of a System Embedded in Heat Bath . . . 132
   3.1. Reduced Density Matrix and its Equation of Motion . . . 134
   3.2. Generalized Master Equations . . . 136
   3.3. Ultrafast Non-Adiabatic Dynamics of Molecular Systems . . . 138
   3.4. Single-Vibronic-Level and Thermal Average Rate Constant. . . . 142
4. Density Matrix Method and Spectroscopies . . . 147
   4.1. Steady State Spectroscopy . . . 147
   4.2. Pump–Probe Experiments . . . 151
5. An Example — Interfacial Electron Transfer in Organic Solar Cells . . . 156
   5.1. Experimental Results and Theoretical Analysis . . . 157
   5.2. Remarks. . . . 172
6. Summary . . . 172
Appendix A. $G_{v_j}(t)$ for Displaced–Distorted Oscillator . . . 173
Appendix B. Derivation of the TCF for the Band-Shape Function . . . 177
References . . . 180

In this chapter, the ultrafast radiationless transition processes are treated theoretically. The method employed is based on the density matrix method, and specifically, a generalized linear response theory is developed by applying the projection operator technique on the Liouville equation so that non-equilibrium cases can be handled properly. The ultrafast molecular

THIN FILMS AND NANOSTRUCTURES, vol. 34
ISSN 1079-4050
DOI: 10.1016/S1079-4050(06)34005-7

© 2007 by Elsevier Inc.
All rights reserved.

Lam Research Ex. 1035 - Page 129
Lam Research Corp. v. Inpria Corp.
IPR2024-00033 - U.S. Patent No. 9,823,564

processes are often monitored experimentally by transient spectroscopic techniques. In order to directly interpret these experimental observations, the susceptibility method is combined with the density matrix method so that linear/non-linear transient spectra of the system under consideration can be calculated. As an example, the interfacial photo-induced electron transfer process in dye-sensitized solar cell system, whose kinetics is often examined by the ultrafast spectroscopic techniques, is studied quantitatively with our methods.

1. Introduction

Conventionally, radiationless transitions refer to electronic relaxation like internal conversion (IC) and intersystem crossing (ISC). In view of the fact that almost all of the non-adiabatic non-radiative processes (e.g., IC, ISC, energy transfer, electron transfer, etc.) can be treated on equal footing, in this chapter, the density matrix method will be introduced which can treat these non-adiabatic processes and provide the theoretical foundation of ultrafast time-resolved spectroscopy used to measure these processes. For this purpose, the so-called femtosecond time-resolved pump–probe experiments are commonly used (see Figure 5.1). From the uncertainty principle, $\Delta E\,\Delta t \approx \hbar/2$, it can be seen that when ultrashort laser pulses are being used, numerous states are pumped simultaneously (or coherently) and thus the probing signal should contain the dynamic information of both populations and coherences (or phases). This indicates that in order to determine the dynamics of populations and coherences, the probing signal experimentally obtained needs to be theoretically analyzed. In this chapter, the density

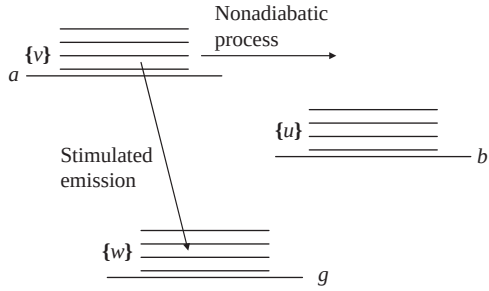


Fig. 5.1. Scheme of the pump–probe observation of non-adiabatic process from a to b by monitoring the stimulated emission from a to the ground state g.

Lam Research Ex. 1035 - Page 130
Lam Research Corp. v. Inpria Corp.
IPR2024-00033 - U.S. Patent No. 9,823,564

matrix method shall be presented for this purpose and it will be shown to be a powerful theoretical method.

2. Density Matrix and Liouville Equation

The density matrix method is useful in treating relaxation processes, linear and non-linear laser spectroscopies and non-equilibrium statistical mechanics. In this chapter, the definition of density matrix and the equation of motion (EOM) it follows are introduced. The projection operator technique, which makes the density matrix method a very powerful tool in non-equilibrium statistical mechanics, is presented.

2.1. DEFINITION OF DENSITY MATRIX

For simplicity, consider a two-state system described by wavefunctions $u_a(q)$ and $u_b(q)$. To describe the dynamics of the system the time-dependent Schrödinger equation has to be solved:

$$\hat{H}\psi(q,t) = i\hbar\frac{\partial\psi(q,t)}{\partial t} \tag{2.1}$$

where

$$\hat{H} = \hat{H}_0 + \hat{H}' \tag{2.2}$$

and

$$\hat{H}_0 u_a = E_a; \quad \hat{H}_0 u_b = E_b \tag{2.3}$$

Using the expansion theorem, it is found that

$$\psi(q,t) = c_a(t)u_a(q) + c_b(t)u_b(q) \tag{2.4}$$

Substituting Eq. (2.4) into Eq. (2.1) results in

$$i\hbar\frac{dc_a}{dt} = (E_a + H'_{aa})c_a + H'_{ab}c_b \tag{2.5}$$

and

$$i\hbar\frac{dc_b}{dt} = H'_{ba}c_a + (E_b + H'_{bb})c_b \tag{2.6}$$

where

$$H'_{aa} = \langle u_a|\hat{H}'|u_a\rangle; \quad H'_{ab} = \langle u_a|\hat{H}'|u_b\rangle \tag{2.7}$$

etc.

Lam Research Ex. 1035 - Page 131
Lam Research Corp. v. Inpria Corp.
IPR2024-00033 - U.S. Patent No. 9,823,564

For the pure system, the density matrix elements are defined by [1–6]

$$\rho_{aa}(t) = c_a(t)c_a(t)^* = |c_a(t)|^2 \tag{2.8}$$

$$\rho_{ab}(t) = c_a(t)c_b(t)^* = \rho_{ba}(t)^* \tag{2.9}$$

$$\rho_{bb}(t) = c_b(t)c_b(t)^* = |c_b(t)|^2 \tag{2.10}$$

where the diagonal elements $\rho_{aa}(t)$ and $\rho_{bb}(t)$ denote the population or probability of the system, while the off-diagonal elements $\rho_{ab}(t)$ and $\rho_{ba}(t)$ describe the coherence or phase of the system. Notice that $\rho_{aa}(t)$, $\rho_{ab}(t)$, $\rho_{ba}(t)$ and $\rho_{bb}(t)$ can be put in a matrix form

$$\hat{\rho}(t) = \begin{pmatrix} \rho_{aa}(t) & \rho_{ab}(t) \\ \rho_{ba}(t) & \rho_{bb}(t) \end{pmatrix} \tag{2.11}$$

which is Hermitian.

Next, consider the property of $\hat{\rho}(t)$. Notice that

$$\begin{aligned} \langle \psi(q,t)|\psi(q,t)\rangle &= |c_a(t)|^2 + |c_b(t)|^2 \\ &= \rho_{aa}(t) + \rho_{bb}(t) = \mathrm{Tr}[\hat{\rho}(t)] = 1 \end{aligned} \tag{2.12}$$

and the quantum mechanical average of a dynamic variable M can be calculated:

$$\begin{aligned} \langle M\rangle &= \langle \psi(q,t)|\hat{M}|\psi(q,t)\rangle \\ &= \rho_{aa}(t)M_{aa} + \rho_{ab}(t)M_{ba} + \rho_{ba}(t)M_{ab} + \rho_{bb}(t)M_{bb} \\ &= \mathrm{Tr}[\hat{M}\hat{\rho}] = \mathrm{Tr}[\hat{\rho}\hat{M}] \end{aligned} \tag{2.13}$$

where, for example

$$M_{ab} = \langle u_a|\hat{M}|u_b\rangle \tag{2.14}$$

To find the EOM for $\hat{\rho}(t)$, notice that

$$\frac{d\rho_{aa}}{dt} = \frac{dc_a}{dt}c_a^* + c_a\frac{dc_a^*}{dt} \tag{2.15}$$

Substituting Eq. (2.5) into Eq. (2.15) yields

$$\frac{d\rho_{aa}}{dt} = -\frac{i}{\hbar}(H'_{ab}\rho_{ba} - \rho_{ab}H'_{ba}) = -\frac{i}{\hbar}[\hat{H},\hat{\rho}]_{aa} \tag{2.16}$$

because

$$[\hat{H}_0,\hat{\rho}] = 0 \tag{2.17}$$

Lam Research Ex. 1035 - Page 132
Lam Research Corp. v. Inpria Corp.
IPR2024-00033 - U.S. Patent No. 9,823,564

Similarly it is found

$$\begin{aligned}\frac{d\rho_{ab}}{dt} &= \frac{dc_a}{dt}c_b^* + c_a\frac{dc_b^*}{dt} \\ &= -\frac{i}{\hbar}[(E_a + H'_{aa}) - (E_b + H'_{bb})]\rho_{ab} + \frac{i}{\hbar}H'_{ab}(\rho_{aa} - \rho_{bb}) \\ &= -\frac{i}{\hbar}[\hat{H}, \hat{\rho}]_{ab} \end{aligned} \tag{2.18}$$

because

$$[\hat{H}_0, \hat{\rho}]_{ab} = (\hat{H}_0\hat{\rho} - \hat{\rho}\hat{H}_0)_{ab} = (E_a - E_b)\rho_{ab} \tag{2.19}$$

In other words, the EOM for $\hat{\rho}(t)$ can be written as

$$\frac{d\hat{\rho}}{dt} = -\frac{i}{\hbar}[\hat{H}, \hat{\rho}] = -i\hat{L}\hat{\rho} \tag{2.20}$$

which is usually called *Liouville* equation (or *von Neumann–Liouville* equation). $\hat{L}$ is usually referred to as the Liouville operator and a super operator.

It should be noted that $\hat{\rho}(t)$ can also be expressed as

$$\hat{\rho}(t) = |\psi(q,t)\rangle\langle\psi(q,t)| \tag{2.21}$$

and that in the above discussion the density matrix $\hat{\rho}(t)$ is for a single system (i.e., a pure system). For an ensemble (i.e., a collection) of systems, the ensemble average is required, i.e.,

$$\rho_{aa}(t) = \langle c_a(t)c_a^*(t)\rangle \tag{2.22}$$

$$\rho_{ab}(t) = \langle c_a(t)c_b^*(t)\rangle = \rho_{ba}(t)^* \tag{2.23}$$

$$\rho_{bb}(t) = \langle c_b(t)c_b^*(t)\rangle \tag{2.24}$$

where $\langle\cdots\rangle$ denotes the ensemble average. This case is often referred to as the *mixed* case; the EOM for $\hat{\rho}(t)$ in this case is also the Liouville equation.

From Eq. (2.20), for a general system the Liouville equation becomes

$$\frac{d\rho_{mn}}{dt} = -\frac{i}{\hbar}\sum_k H_{mk}\rho_{kn} - \rho_{mk}H_{kn} = -i\sum_{m'}\sum_{n'} L_{mn}^{m'n'}\rho_{m'n'} \tag{2.25}$$

where

$$L_{mn}^{m'n'} = \frac{1}{\hbar}(H_{mm'}\delta_{nn'} - H_{n'n}\delta_{m'm}) \tag{2.26}$$

Eq. (2.25) is often referred to as *generalized master equation* (GME). It should be noted that Eq. (2.20) or (2.25) describes the time evolution of an isolated system.

Lam Research Ex. 1035 - Page 133
Lam Research Corp. v. Inpria Corp.
IPR2024-00033 - U.S. Patent No. 9,823,564

2.2. DYNAMICS OF ISOLATED SYSTEMS

To describe the dynamics of an isolated system (for example, how the isolated system relaxes to equilibrium), one often follows the dynamics of the population $\rho_{nn}(t)$ of the system. For this purpose, the *projection operator method* [1,5–7] is employed. A main function of the projection operator $\hat{D}$ is to divide $\hat{\rho}(t)$ into two parts

$$\hat{\rho} = \hat{D}\hat{\rho} + (1 - \hat{D})\hat{\rho} = \hat{\rho}_1 + \hat{\rho}_2 \tag{2.27}$$

where

$$\hat{\rho}_1 = \hat{D}\hat{\rho} \tag{2.28}$$

consists of the diagonal elements $\rho_{nn}(t)$ of $\hat{\rho}(t)$ and

$$\hat{\rho}_2 = (1 - \hat{D})\hat{\rho} \tag{2.29}$$

consists of the off-diagonal elements $\rho_{nm}(t)$ of $\hat{\rho}(t)$.

The operator $\hat{D}$ is a super operator defined by [7]

$$D_{mn}^{m'n'} = \delta_{mm'}\delta_{nn'}\delta_{mn} \tag{2.30}$$

It follows that

$$(\hat{\rho}_1)_{mn} = (\hat{D}\hat{\rho})_{mn} = \sum_{m'}\sum_{n'} D_{mn}^{m'n'}\rho_{m'n'} = \delta_{mn}\rho_{mn} \tag{2.31}$$

and

$$\begin{aligned}(\hat{\rho}_2)_{mn} &= [(1 - \hat{D})\hat{\rho}]_{mn} \\ &= \rho_{mn} - (\hat{D}\hat{\rho})_{mn} \\ &= \rho_{mn} - \sum_{m'}\sum_{n'} D_{mn}^{m'n'}\rho_{m'n'} = (1 - \delta_{mn})\rho_{mn}\end{aligned} \tag{2.32}$$

where δ_{mn} denotes the Kronecker delta.

Taking the Laplace transformation of the Liouville equation

$$\frac{d\hat{\rho}}{dt} = -i\hat{L}\hat{\rho} \tag{2.33}$$

yields

$$p\hat{\tilde{\rho}}(p) - \hat{\rho}(0) = -i\hat{L}\hat{\tilde{\rho}}(p) \tag{2.34}$$

where

$$\hat{\tilde{\rho}}(p) = \int_0^\infty e^{-pt}\hat{\rho}(t)dt \tag{2.35}$$

Lam Research Ex. 1035 - Page 134
Lam Research Corp. v. Inpria Corp.
IPR2024-00033 - U.S. Patent No. 9,823,564

and $\hat{\rho}(0)$ represents the density matrix at $t = 0$. Operating on Eq. (2.34) with $\hat{D}$ and $(1 - \hat{D})$ results in

$$p\hat{\tilde{\rho}}_1(p) - \hat{\rho}_1(0) = -i\hat{D}\hat{L}\hat{\tilde{\rho}}_1(p) - i\hat{D}\hat{L}\hat{\tilde{\rho}}_2(p) \tag{2.36}$$

and

$$p\hat{\tilde{\rho}}_2(p) - \hat{\rho}_2(0) = -i(1 - \hat{D})\hat{L}\hat{\tilde{\rho}}_1(p) - i(1 - \hat{D})\hat{L}\hat{\tilde{\rho}}_2(p) \tag{2.37}$$

This is a set of simultaneous equations for $\hat{\tilde{\rho}}_1(p)$ and $\hat{\tilde{\rho}}_2(p)$. $\hat{\tilde{\rho}}_2(p)$ can be eliminated from Eqs. (2.36) and (2.37) to obtain

$$p\hat{\tilde{\rho}}_1(p) - \hat{\rho}_1(0) = -i\hat{D}\hat{L}\hat{\tilde{\rho}}_1(p) - i\hat{D}\hat{L}\frac{1}{p + i(1 - \hat{D})\hat{L}}\hat{\rho}_2(0) - \hat{\tilde{M}}(p)\hat{\tilde{\rho}}_1(p) \tag{2.38}$$

where $\hat{\tilde{M}}(p)$ represents the memory kernel

$$\hat{\tilde{M}}(p) = \hat{D}\hat{L}\frac{1}{p + i(1 - \hat{D})\hat{L}}(1 - \hat{D})\hat{L} \tag{2.39}$$

Carrying out the inverse Laplace transformation of Eq. (2.38) yields

$$\begin{aligned}\frac{d\hat{\rho}_1}{dt} = & -i\hat{D}\hat{L}\hat{\rho}_1 - i\hat{D}\hat{L}e^{-it(1-\hat{D})\hat{L}}\hat{\rho}_2(0) \\ & - \int_0^t \hat{M}(\tau)\hat{\rho}_1(t - \tau)d\tau\end{aligned} \tag{2.40}$$

Suppose that

$$\hat{\rho}_2(0) = 0 \tag{2.41}$$

which is often referred to as the *random phase approximation* (RPA). Notice that

$$\hat{\rho}_1(t - \tau) = \exp\left(-\tau\frac{d}{dt}\right)\hat{\rho}_1(t) \tag{2.42}$$

Using Eqs. (2.41) and (2.42), Eq. (2.40) can be written as

$$\frac{d\hat{\rho}_1}{dt} = -i\hat{D}\hat{L}\hat{\rho}_1(t) - \hat{K}(t)\hat{\rho}_1(t) \tag{2.43}$$

where $\hat{K}(t)$ is given by

$$\hat{K}(t) = \int_0^t d\tau\hat{M}(\tau)\exp\left(-\tau\frac{d}{dt}\right) = \int_0^t d\tau\hat{M}(\tau)\exp(i\tau\hat{L}) \tag{2.44}$$

Lam Research Ex. 1035 - Page 135
Lam Research Corp. v. Inpria Corp.
IPR2024-00033 - U.S. Patent No. 9,823,564

It is the super operator for the time-dependent relaxation constants. Notice that

$$[\hat{D}\hat{L}\hat{\rho}_1(t)]_{nn} = [\hat{L}\hat{\rho}_1(t)]_{nn} = \sum_m L_{nn}^{mm}\rho_{mm}(t)$$
$$= \frac{1}{\hbar}\sum_m (H_{nm}\delta_{mn} - H_{mn}\delta_{nm})\rho_{mm}(t) = 0 \tag{2.45}$$

and

$$\frac{d\rho_{nn}}{dt} = -\sum_m K(t)_{nn}^{mm}\rho_{mm}(t) \tag{2.46}$$

Another way to express the EOM for $\rho_{nn}(t)$ is to use Eq. (2.40) with RPA, i.e.,

$$\frac{d\rho_{nn}}{dt} = -\sum_m \int_0^t d\tau M(\tau)_{nn}^{mm}\rho_{mm}(t-\tau) \tag{2.47}$$

where

$$M(\tau)_{nn}^{mm} = [\hat{D}\hat{L}e^{-i\tau(1-\hat{D})\hat{L}}(1-\hat{D})\hat{L}]_{nn}^{mm} \tag{2.48}$$

To simplify $M(\tau)_{nn}^{mm}$, it is first shown that

$$\hat{D}\hat{L}_0 = 0; \quad \hat{L}_0\hat{D} = 0 \tag{2.49}$$

by noticing that

$$(\hat{D}\hat{L}_0)_{mn}^{m'n'} = \frac{1}{\hbar}(E_m - E_n)\delta_{mn}\delta_{mm'}\delta_{nn'} = 0 \tag{2.50}$$

and

$$(\hat{L}_0\hat{D})_{mn}^{m'n'} = (\hat{L}_0)_{mn}^{mn}D_{mn}^{m'n'} = \frac{1}{\hbar}(E_m - E_n)\delta_{mn}\delta_{mm'}\delta_{nn'} = 0 \tag{2.51}$$

It follows that

$$M(\tau)_{nn}^{mm} = [\hat{D}\hat{L}'e^{-i\tau(1-\hat{D})\hat{L}}(1-\hat{D})\hat{L}']_{nn}^{mm} \tag{2.52}$$

Now the following relation:

$$\sum_m M(\tau)_{nn}^{mm} = 0 \tag{2.53}$$

Lam Research Ex. 1035 - Page 136
Lam Research Corp. v. Inpria Corp.
IPR2024-00033 - U.S. Patent No. 9,823,564

can be shown by noticing that

$$\sum_m M(\tau)_{nn}^{mm} = \frac{1}{\hbar}\sum_m \sum_{m'} \sum_{m''} A(\tau)_{nn}^{m'm''}(1-\delta_{m'm''})(H'_{m'm}\delta_{mm''} - H'_{mm''}\delta_{m'm})$$

$$= \frac{1}{\hbar}\left\{ \sum_m \sum_{m'} A(\tau)_{nn}^{m'm}(1-\delta_{m'm})H'_{m'm} \right.$$

$$\left. - \sum_m \sum_{m'} A(\tau)_{nn}^{m'm}(1-\delta_{m'm})H'_{m'm} \right\} = 0 \tag{2.54}$$

where

$$\hat{A}(\tau) = \hat{D}\hat{L}' e^{-i\tau(1-\hat{D})\hat{L}} \tag{2.55}$$

Using Eq. (2.53) the master equation (ME) becomes

$$\frac{d\rho_{nn}}{dt} = \sum_m^{m\neq n} \int_0^t d\tau M_{nn}^{mm}(\tau)[\rho_{mm}(t-\tau) - \rho_{nn}(t-\tau)] \tag{2.56}$$

When the memory is short, one can use the Markoff approximation,

$$M_{nn}^{mm}(\tau) = \delta(\tau)k_{mn} \tag{2.57}$$

and

$$k_{mn} = \int_0^\infty d\tau M_{nn}^{mm}(\tau) \tag{2.58}$$

to obtain

$$\frac{d\rho_{nn}}{dt} = \sum_m^{m\neq n} k_{mn}[\rho_{mm}(t) - \rho_{nn}(t)] \tag{2.59}$$

where k_{mn} represents the rate constant for $m \leftrightarrow n$. This is usually called the *Pauli master equation*. At equilibrium, $d\rho_{nn}/dt = 0$ and

$$\rho_{mm} = \rho_{nn} \tag{2.60}$$

That is, states of equal energy are equally probable.

Next, the way to calculate k_{mn} by the perturbation method shall be presented, by regarding $\hat{H}'$ as a perturbation. To the second-order approximation, $M(\tau)^{mm}{}_{nn}$ takes the form

$$M(\tau)_{nn}^{mm} = [\hat{D}\hat{L}' e^{-i\tau(1-\hat{D})\hat{L}_0}(1-\hat{D})\hat{L}']_{nn}^{mm} \tag{2.61}$$

which can easily be simplified:

$$M(\tau)_{nn}^{mm} = -\frac{2}{\hbar^2}|H'_{mn}|^2 \cos\omega_{mn}\tau$$

Lam Research Ex. 1035 - Page 137
Lam Research Corp. v. Inpria Corp.
IPR2024-00033 - U.S. Patent No. 9,823,564

It follows that

$$\begin{aligned} k_{mn} &= \frac{2}{\hbar^2}|H'_{mn}|^2 \lim_{t\to\infty}\frac{\sin\omega_{mn}t}{\omega_{mn}} \\ &= \frac{2\pi}{\hbar^2}|H'_{mn}|^2\delta(\omega_{mn}) \\ &= \frac{2\pi}{\hbar}|H'_{mn}|^2\delta(E_m - E_n) \end{aligned} \tag{2.62}$$

i.e., the Fermi golden rule expression for k_{mn}.

In the above, the principles of how to study the dynamics of an isolated system by using the density matrix method have been shown. However, most experiments are performed for the system (or subsystem) embedded in a heat bath; in this case the isolated system consists of the system plus heat bath. In the following the MEs shall be derived for the system embedded in heat bath. In this case, instead of ρ_{nn}, $\rho_{n_s n_b, n_s n_b}$ will be employed. Here $\{n_\mathrm{s}\}$ and $\{n_\mathrm{b}\}$ describe the system and heat bath, respectively. For the case in which the bath is much larger than the system, it may be assumed that the bath maintains thermal equilibrium and

$$\rho_{n_\mathrm{s}n_\mathrm{b},n_\mathrm{s}n_\mathrm{b}}(t) = \sigma_{n_\mathrm{s}n_\mathrm{s}}(t)\rho^{(\mathrm{b})}_{n_\mathrm{b}n_\mathrm{b}} \tag{2.63}$$

where $\sigma_{n_s n_s}(t)$ describes the population of the system while $\rho^{(\mathrm{b})}_{n_\mathrm{b}n_\mathrm{b}}$ that of the bath [8–10]. In this case, Eq. (2.58) becomes

$$\rho^{(\mathrm{b})}_{n_\mathrm{b}n_\mathrm{b}}\frac{d\sigma_{n_\mathrm{s}n_\mathrm{s}}}{dt} = \sum_{m_\mathrm{s}}\sum_{m_\mathrm{b}} k_{m_\mathrm{s}m_\mathrm{b},n_\mathrm{s}n_\mathrm{b}}(\sigma_{m_\mathrm{s}m_\mathrm{s}}\rho^{(\mathrm{b})}_{m_\mathrm{b}m_\mathrm{b}} - \sigma_{n_\mathrm{s}n_\mathrm{s}}\rho^{(\mathrm{b})}_{n_\mathrm{b}n_\mathrm{b}}) \tag{2.64}$$

or

$$\frac{d\sigma_{n_\mathrm{s}n_\mathrm{s}}}{dt} = \sum_{m_\mathrm{s}} k_{m_\mathrm{s}\to n_\mathrm{s}}\sigma_{m_\mathrm{s}m_\mathrm{s}} - k_{n_\mathrm{s}\to m_\mathrm{s}}\sigma_{n_\mathrm{s}n_\mathrm{s}} \tag{2.65}$$

where

$$\begin{aligned} k_{m_\mathrm{s}\to n_\mathrm{s}} &= \sum_{n_\mathrm{b}}\sum_{m_\mathrm{b}}\rho^{(\mathrm{b})}_{m_\mathrm{b}m_\mathrm{b}}k_{m_\mathrm{s}m_\mathrm{b},n_\mathrm{s}n_\mathrm{b}} \\ &= \frac{2\pi}{\hbar}\sum_{n_\mathrm{b}}\sum_{m_\mathrm{b}}\rho^{(\mathrm{b})}_{m_\mathrm{b}m_\mathrm{b}}|H'_{m_\mathrm{s}m_\mathrm{b},n_\mathrm{s}n_\mathrm{b}}|^2\delta(E_{m_\mathrm{s}m_\mathrm{b}} - E_{n_\mathrm{s}n_\mathrm{b}}) \end{aligned} \tag{2.66}$$

and

$$\begin{aligned} k_{n_\mathrm{s}\to m_\mathrm{s}} &= \sum_{n_\mathrm{b}}\sum_{m_\mathrm{b}}\rho^{(\mathrm{b})}_{n_\mathrm{b}n_\mathrm{b}}k_{m_\mathrm{s}m_\mathrm{b},n_\mathrm{s}n_\mathrm{b}} \\ &= \frac{2\pi}{\hbar}\sum_{n_\mathrm{b}}\sum_{m_\mathrm{b}}\rho^{(\mathrm{b})}_{n_\mathrm{b}n_\mathrm{b}}|H'_{m_\mathrm{s}m_\mathrm{b},n_\mathrm{s}n_\mathrm{b}}|^2\delta(E_{m_\mathrm{s}m_\mathrm{b}} - E_{n_\mathrm{s}n_\mathrm{b}}) \end{aligned} \tag{2.67}$$

Lam Research Ex. 1035 - Page 138
Lam Research Corp. v. Inpria Corp.
IPR2024-00033 - U.S. Patent No. 9,823,564

In obtaining Eq. (2.65), the following relation:

$$\sum_{n_b} \rho^{(b)}_{n_b n_b} = 1 \tag{2.68}$$

has been used. In thermal equilibrium, $\rho^{(b)}_{n_b n_b}$ is given by

$$\rho^{(b)}_{n_b n_b} = \frac{e^{-E_{n_b}/k_B T}}{Q_b(T)} \tag{2.69}$$

where Q_b denotes the partition function of the bath. It can easily be shown that Eq. (2.65) satisfies the principle of detailed balance

$$\begin{aligned} k_{m_s \to n_s} &= \frac{2\pi}{\hbar} \sum_{n_b} \sum_{m_b} \frac{e^{-E_{m_b}/k_B T}}{Q_b} |H'_{m_s m_b, n_s n_b}| \delta(E_{m_s m_b} - E_{n_s n_b}) \\ &= \frac{2\pi}{\hbar} e^{-(E_{n_s} - E_{m_s})/k_B T} \sum_{n_b} \sum_{m_b} \sum \rho^{(b)}_{n_b n_b} |H'_{m_s m_b, n_s n_b}| \delta(E_{m_s m_b} - E_{n_s n_b}) \end{aligned} \tag{2.70}$$

or

$$k_{m_s \to n_s} e^{-E_{m_s}/k_B T} = k_{n_s \to m_s} e^{-E_{n_s}/k_B T} \tag{2.71}$$

It can be seen from the discussion in later sections that vibrational relaxation in dense media plays a very important role in ultrafast phenomena. The dynamics of vibrational relaxation can be described as follows. Let Q be the normal coordinate of the system mode and assume that the system oscillator is linearly coupled to the heat bath [8,11–16], i.e.,

$$\hat{H}' = Q F_b \tag{2.72}$$

For harmonic oscillator, $m_s = n_s \pm 1$. Thus

$$\begin{aligned} \frac{d\sigma_{n_s n_s}}{dt} &= (k_{n_s - 1 \to n_s} \sigma_{n_s - 1, n_s - 1} - k_{n_s \to n_s - 1} \sigma_{n_s, n_s}) \\ &\quad + (k_{n_s + 1 \to n_s} \sigma_{n_s + 1, n_s + 1} - k_{n_s \to n_s + 1} \sigma_{n_s n_s}) \end{aligned} \tag{2.73}$$

or

$$\begin{aligned} \frac{d\sigma_{n_s n_s}}{dt} &= k_{n_s \to n_s - 1} (e^{-\hbar\omega/k_B T} \sigma_{n_s - 1, n_s - 1} - \sigma_{n_s, n_s}) \\ &\quad + k_{n_s + 1 \to n_s} (\sigma_{n_s + 1, n_s + 1} - e^{-\hbar\omega/k_B T} \sigma_{n_s n_s}) \end{aligned} \tag{2.74}$$

Here the relation given by Eq. (2.71) has been used. Notice that

$$k_{n_s \to n_s - 1} = \frac{2\pi}{\hbar} \sum_{m_b} \sum_{n_b} \rho^{(b)}_{n_b n_b} |\langle n_s | Q | n_s - 1 \rangle|^2 |\langle m_b | F_b | n_b \rangle|^2 \delta(E_{m_b} - E_{n_b} - \hbar\omega) \tag{2.75}$$

Lam Research Ex. 1035 - Page 139
Lam Research Corp. v. Inpria Corp.
IPR2024-00033 - U.S. Patent No. 9,823,564

or

$$k_{n_s \to n_s - 1} = n_s k_{1 \to 0} = n_s \left[\frac{\pi}{\omega} \sum_{m_b} \sum_{n_b} \rho^{(b)}_{n_b n_b} |\langle m_b | F_b | n_b \rangle|^2 \delta(E_{m_b} - E_{n_b} - \hbar\omega) \right] \tag{2.76}$$

It follows that

$$\begin{aligned} \frac{d\sigma_{n_s n_s}}{dt} = k_{1 \to 0} [& n_s (e^{-\hbar\omega / k_B T} \sigma_{n_s - 1, n_s - 1} - \sigma_{n_s n_s}) \\ & + (n_s + 1)(\sigma_{n_s + 1, n_s + 1} - e^{-\hbar\omega / k_B T} \sigma_{n_s n_s})] \end{aligned} \tag{2.77}$$

and that at $T = 0$ Eq. (2.77) reduces to

$$\frac{d\sigma_{n_s n_s}}{dt} = k_{1 \to 0} [(n_s + 1)\sigma_{n_s + 1, n_s + 1} - n_s \sigma_{n_s n_s}] \tag{2.78}$$

This model is usually called the *step-ladder model*. According to this model, the vibrational relaxation dynamics of the system depends only on $k_{1 \to 0}$ and vibrational frequency ω.

3. Dynamics of a System Embedded in Heat Bath

In Section 2, the density matrix method is applied to an isolated system. In this section, the system embedded in a heat bath shall be treated; that is, the isolated system shall be divided into two parts, one is referred to as the system which is under observation and the other part the heat bath.

Before presenting a rigorous method to treat this problem, a very useful and simple method, called the *effective Hamiltonian method* [17], shall be discussed as follows.

The two-state system shall be considered as an example for illustration (see Eqs. (2.1)–(2.7)). According to the effective Hamiltonian method, the energies are complex, i.e.,

$$E_a = E_a^0 - \frac{i}{2\hbar}\gamma_a; \quad E_b = E_b^0 - \frac{i}{2\hbar}\gamma_b \tag{3.1}$$

For the case in which $\hat{H}' = 0$, Eqs. (2.5) and (2.6) become

$$i\hbar \frac{dc_a}{dt} = \left(E_a^0 - \frac{i}{2\hbar}\gamma_a \right) c_a \tag{3.2}$$

and

$$i\hbar \frac{dc_b}{dt} = \left(E_b^0 - \frac{i}{2\hbar}\gamma_b \right) c_b \tag{3.3}$$

Lam Research Ex. 1035 - Page 140
Lam Research Corp. v. Inpria Corp.
IPR2024-00033 - U.S. Patent No. 9,823,564

which can be solved,

$$c_{\mathrm{a}}(t) = c_{\mathrm{a}}(0)e^{-(it/\hbar)E_{\mathrm{a}}^{0}-(1/2)\gamma_{\mathrm{a}}t} \tag{3.4}$$

and

$$c_{\mathrm{b}}(t) = c_{\mathrm{b}}(0)e^{-(it/\hbar)E_{\mathrm{b}}^{0}-(1/2)\gamma_{\mathrm{b}}t} \tag{3.5}$$

The density matrix elements for this system are given by

$$\sigma_{\mathrm{aa}}(t) = \sigma_{\mathrm{aa}}(0)e^{-\gamma_{\mathrm{a}}t} \tag{3.6}$$

$$\sigma_{\mathrm{bb}}(t) = \sigma_{\mathrm{bb}}(0)e^{-\gamma_{\mathrm{b}}t} \tag{3.7}$$

and

$$\sigma_{\mathrm{ab}}(t) = \sigma_{\mathrm{ab}}(0)e^{-it\omega_{\mathrm{ab}}-\gamma_{\mathrm{ab}}t} = \sigma_{\mathrm{ba}}(t)^{*} \tag{3.8}$$

where γ_{a} and γ_{b} denote the relaxation rate constants for the a and b states, respectively, while γ_{ab} represents the dephasing constant

$$\gamma_{\mathrm{ab}} = \frac{1}{2}(\gamma_{\mathrm{a}} + \gamma_{\mathrm{b}}) \tag{3.9}$$

From Eqs. (3.6) and (3.7) one can see that γ_{a} and γ_{b} are related to the lifetimes τ_{a} and τ_{b} by

$$\tau_{\mathrm{a}} = \frac{1}{\gamma_{\mathrm{a}}}; \quad \tau_{\mathrm{b}} = \frac{1}{\gamma_{\mathrm{b}}} \tag{3.10}$$

From Eqs. (3.6)–(3.8) one finds that the Liouville equation can be expressed as

$$\frac{d\hat{\sigma}}{dt} = -\frac{i}{\hbar}[\hat{H}_0, \hat{\sigma}] - \hat{\Gamma}\hat{\sigma} \tag{3.11}$$

where $\hat{\Gamma}$ is usually called damping operator with matrix elements

$$(\hat{\Gamma}\hat{\sigma})_{\mathrm{aa}} = \gamma_{\mathrm{a}}\sigma_{\mathrm{aa}} \tag{3.12}$$

$$(\hat{\Gamma}\hat{\sigma})_{\mathrm{bb}} = \gamma_{\mathrm{b}}\sigma_{\mathrm{bb}} \tag{3.13}$$

$$(\hat{\Gamma}\hat{\sigma})_{\mathrm{ab}} = \gamma_{\mathrm{ab}}\sigma_{\mathrm{ab}} \tag{3.14}$$

and $\gamma_{\mathrm{ab}} = \gamma_{\mathrm{ba}}$. One can see that Eq. (3.11) describes the time evolution of a system embedded in a heat bath and $\hat{\Gamma}$ arises from the coupling (or interaction) between the system and the bath. In the next subsection, a rigorous treatment of the dynamics of a system embedded in heat bath shall be presented.

Lam Research Ex. 1035 - Page 141
Lam Research Corp. v. Inpria Corp.
IPR2024-00033 - U.S. Patent No. 9,823,564

3.1. REDUCED DENSITY MATRIX AND ITS EQUATION OF MOTION

Notice that the Hamiltonian of the total (or isolated) system can be expressed as [3–5,18]

$$\hat{H} = \hat{H}_{\mathrm{s}} + \hat{H}_{\mathrm{b}} + \hat{H}' \tag{3.15}$$

where $\hat{H}_{\mathrm{s}}$ and $\hat{H}_{\mathrm{b}}$ represent the Hamiltonians of the system (or subsystem) and heat bath, respectively, while $\hat{H}'$ denotes the interaction between them. The time evolution of the total system is described by the Liouville equation [3–5,18]

$$\frac{d\hat{\rho}}{dt} = -\frac{i}{\hbar}[\hat{H}, \hat{\rho}] = -i\hat{L}\hat{\rho} \tag{3.16}$$

or

$$\frac{d\hat{\rho}}{dt} = -\frac{i}{\hbar}[\hat{H}_{\mathrm{s}}, \hat{\rho}] - \frac{i}{\hbar}[\hat{H}_{\mathrm{b}}, \hat{\rho}] - \frac{i}{\hbar}[\hat{H}', \hat{\rho}] = -i\hat{L}_{\mathrm{s}}\hat{\rho} - i\hat{L}_{\mathrm{b}}\hat{\rho} - i\hat{L}'\hat{\rho} \tag{3.17}$$

where $\hat{\rho}$ is the density matrix of the total system. One has to eliminate the heat bath variables from Eq. (3.17) to obtain the EOM for the system. For this purpose, the density matrix elements shall be expressed as $\rho_{m\alpha,n\beta}$, where (m,n) and (α,β) describe the system and heat bath, respectively [3–5,18].

Let $\hat{\sigma}$ represent the density matrix of the system which is usually referred to as the *reduced density matrix* and is obtained by eliminating the heat bath variables [3–5,18,19]

$$\sigma_{mn} = \sum_{\alpha} \rho_{m\alpha,n\alpha} \tag{3.18}$$

i.e.,

$$\hat{\sigma} = \mathrm{Tr}_{\mathrm{b}}(\hat{\rho}) \tag{3.19}$$

To obtain $\rho_{m\alpha,n\alpha}$ introduce the projection operator $\hat{D}$ so that

$$\hat{\rho}_1 = \hat{D}\hat{\rho}; \quad \hat{\rho}_2 = (1 - \hat{D})\hat{\rho} \tag{3.20}$$

$$\hat{\rho} = \hat{\rho}_1 + \hat{\rho}_2 \tag{3.21}$$

and

$$D^{m'\alpha',n'\beta'}_{m\alpha,n\beta} = \delta_{\alpha\beta}\delta_{mm'}\delta_{nn'}\delta_{\alpha\alpha'}\delta_{\beta\beta'} \tag{3.22}$$

It follows that

$$(\hat{D}\hat{\rho})_{m\alpha,n\beta} = \sum_{m'\alpha'}\sum_{n'\beta'} D^{m'\alpha',n'\beta'}_{m\alpha,n\beta}\rho_{m'\alpha',n'\beta'} = \delta_{\alpha\beta}\rho_{m\alpha,n\beta} \tag{3.23}$$

Lam Research Ex. 1035 - Page 142
Lam Research Corp. v. Inpria Corp.
IPR2024-00033 - U.S. Patent No. 9,823,564

and

$$[(1-\hat{D})\hat{\rho}]_{m\alpha,n\beta} = (1-\delta_{\alpha\beta})\rho_{m\alpha,n\beta} \tag{3.24}$$

To obtain $\hat{\rho}_1$ the Laplace transformation method (see Section 2) can be used, i.e.,

$$\hat{\tilde{\rho}}(p) = \int_0^\infty dt\, e^{-pt}\hat{\rho}(t) \tag{3.25}$$

to obtain [3–5,18,19]

$$p\hat{\tilde{\rho}}(p) - \hat{\rho}(0) = -i\hat{L}\hat{\tilde{\rho}}(p) \tag{3.26}$$

$$p\hat{\tilde{\rho}}_1(p) - \hat{\rho}_1(0) = -i\hat{D}\hat{L}\hat{\tilde{\rho}}(p) \tag{3.27}$$

and

$$p\hat{\tilde{\rho}}_2(p) - \hat{\rho}_2(0) = -i(1-\hat{D})\hat{L}\hat{\tilde{\rho}}(p) \tag{3.28}$$

Solving for $\hat{\tilde{\rho}}_1(p)$ yields (see Section 2)

$$p\hat{\tilde{\rho}}_1(p) - \hat{\rho}_1(0) = -i\hat{D}\hat{L}\hat{\tilde{\rho}}_1(p) - i\hat{D}\hat{L}\frac{1}{p+i(1-\hat{D})\hat{L}}\hat{\rho}_2(0) - \hat{\tilde{M}}(p)\hat{\tilde{\rho}}_1(p) \tag{3.29}$$

where the memory kernel $\hat{\tilde{M}}(p)$ is given by

$$\hat{\tilde{M}}(p) = \hat{D}\hat{L}\frac{1}{p+i(1-\hat{D})\hat{L}}(1-\hat{D})\hat{L} \tag{3.30}$$

It follows that

$$\frac{d\hat{\rho}_1}{dt} = -i\hat{D}\hat{L}\hat{\rho}_1(t) - i\hat{D}\hat{L}\, e^{-it(1-\hat{D})\hat{L}}\hat{\rho}_2(0) - \int d\tau \hat{M}(\tau)\hat{\rho}_1(t-\tau) \tag{3.31}$$

and

$$\frac{d\hat{\sigma}}{dt} = -i\mathrm{Tr}_b[\hat{D}\hat{L}\hat{\rho}_1(t)] - i\mathrm{Tr}_b[\hat{D}\hat{L}\, e^{-it(1-\hat{D})\hat{L}}\hat{\rho}_2(0)] - \int_0^t d\tau \mathrm{Tr}_b[\hat{M}(\tau)\hat{\rho}_1(t-\tau)] \tag{3.32}$$

To simplify Eq. (3.32) which is exact, one needs additional conditions. Suppose that

$$\rho_{m\alpha,n\alpha} = \sigma_{mn}\rho^{(b)}_{\alpha\alpha} \tag{3.33}$$

where $\rho^{(b)}_{\alpha\alpha}$ represents the equilibrium distribution of the heat bath. That is, the heat bath maintains the equilibrium condition during the relaxation of the system. In this case Eq. (3.32) becomes [3–5,18,19]

$$\frac{d\hat{\sigma}}{dt} = -i\bar{L}\hat{\sigma} - \int_0^t d\tau \bar{M}(\tau)\hat{\sigma}(t-\tau) \tag{3.34}$$

Lam Research Ex. 1035 - Page 143
Lam Research Corp. v. Inpria Corp.
IPR2024-00033 - U.S. Patent No. 9,823,564

where

$$\bar{L} = \mathrm{Tr}_{\mathrm{b}}[\hat{D}\hat{L}\hat{\rho}^{(\mathrm{b})}] \tag{3.35}$$

and

$$\bar{M}(\tau) = \mathrm{Tr}_{\mathrm{b}}[\hat{M}(\tau)\hat{\rho}^{(\mathrm{b})}] \tag{3.36}$$

3.2. Generalized Master Equations

From Eq. (3.34), one can obtain the *generalized master equation* (GME), which describes the dynamics of populations and coherences (or phases) of the systems.

$$\frac{d\sigma_{mn}}{dt} = -i\sum_{m'}\sum_{n'}\bar{L}_{mn}^{m'n'}\sigma_{m'n'} - \sum_{m'}\sum_{n'}\int_0^t d\tau \bar{M}(\tau)_{mn}^{m'n'}\sigma_{m'n'}(t-\tau) \tag{3.37}$$

where

$$\bar{L}_{mn}^{m'n'} = \frac{1}{\hbar}(\bar{H}_{mm'}\delta_{nn'} - \bar{H}_{n'n}\delta_{mm'}) \tag{3.38}$$

$$\bar{H}_{mm'} = \sum_{\alpha} H_{m\alpha,m'\alpha}\rho_{\alpha\alpha}^{(\mathrm{b})} \tag{3.39}$$

and

$$\bar{H}_{n'n} = \sum_{\alpha} H_{n'\alpha,n\alpha}\rho_{\alpha\alpha}^{(\mathrm{b})} \tag{3.40}$$

Similarly,

$$\bar{M}(\tau)_{mn}^{m'n'} = \sum_{\alpha}\sum_{\beta} M(\tau)_{m\alpha,n\alpha}^{m'\beta,n'\beta}\rho_{\beta\beta}^{(\mathrm{b})} \tag{3.41}$$

Using the relation

$$\hat{\sigma}(t-\tau) = e^{-\tau(d/dt)}\,\hat{\sigma}(t) \tag{3.42}$$

Eq. (3.34) can be rewritten as

$$\frac{d\hat{\sigma}}{dt} = -i\bar{L}\hat{\sigma} - \hat{\Gamma}(t)\hat{\sigma} \tag{3.43}$$

where

$$\hat{\Gamma}(t) = \int_0^t d\tau \bar{M}(\tau)\, e^{-\tau(d/dt)} = \int_0^t d\tau \bar{M}(\tau)\, e^{\tau(i\bar{L}+\hat{\Gamma}(t))} \tag{3.44}$$

From Eq. (3.43) one can see that due to $\bar{L}$ (see Eq. (3.35) or (3.38)–(3.40)) the energy levels and interactions in the system may be temperature dependent

Lam Research Ex. 1035 - Page 144
Lam Research Corp. v. Inpria Corp.
IPR2024-00033 - U.S. Patent No. 9,823,564

and that $\hat{\Gamma}(t)$ describes the relaxation and dephasing, and energy-level shifts of the system induced by the coupling between the system and the bath.

Using the effective Hamiltonian method, the EOM for the reduced density matrix $\hat{\sigma}$ and the structure of $\hat{\Gamma}$ have been derived. However, how to evaluate $\hat{\Gamma}$ is not provided.

In the following, the perturbation method shall be used to find the GME from Eq. (3.34) by regarding $\hat{H}'$ as the perturbation. Since the derivation is similar to that given in Eqs. (2.44)–(2.61), only the final results will be presented. In the Markoff and second-order approximations, one finds

$$\frac{d\hat{\sigma}}{dt} = -i\bar{L}\hat{\sigma} - \hat{\Gamma}\hat{\sigma} \tag{3.45}$$

$$\frac{d\sigma_{nn}}{dt} = -\sum_{m} \Gamma_{nn}^{mm}\sigma_{mm} = -\sum_{m}^{m\neq n}\left(\Gamma_{nn}^{mm}\sigma_{mm} - \Gamma_{mm}^{nn}\sigma_{nn}\right) \tag{3.46}$$

and

$$\frac{d\sigma_{mn}}{dt} = -(i\omega_{mn} + \Gamma_{mn}^{mn})\sigma_{mn} \tag{3.47}$$

where

$$\Gamma_{nn}^{mn} = -\sum_{m}^{m\neq n} \Gamma_{mm}^{nn} \tag{3.48}$$

$$-\Gamma_{mm}^{nn} = \frac{2\pi}{\hbar}\sum_{\alpha}\sum_{\beta} \rho_{\beta\beta}^{(\mathrm{b})} |H'_{m\alpha,n\beta}|^2 \delta(E_{m\alpha} - E_{n\beta}) \tag{3.49}$$

$$\omega_{mn} = \omega_{mn}^{(\mathrm{s})} + \frac{1}{\hbar}(\bar{H}'_{mm} - \bar{H}'_{nn}) \tag{3.50}$$

and Γ_{mn}^{mn} consists of the real part $\Gamma_{mn}^{mn}(r)$, dephasing rate constant

$$\Gamma_{mn}^{mn}(r) = \frac{1}{2}(\Gamma_{nn}^{nn} + \Gamma_{mm}^{mm}) + \Gamma_{mn}^{mn}(\mathrm{d}) \tag{3.51}$$

and the imaginary part $\Gamma_{mn}^{mn}(i)$ describing the energy-level shifts

$$\Gamma_{mn}^{mn}(i) = \frac{1}{\hbar^2} P \sum_{\alpha}\sum_{\beta}^{\beta\neq\alpha}\sum_{m'}^{m'\neq m} \rho_{\alpha\alpha}^{(\mathrm{b})} \frac{|H'_{m\alpha,m'\beta}|^2}{\omega_{m\alpha,m'\beta}} - \frac{1}{\hbar^2} P \sum_{\alpha}\sum_{\beta}^{\beta\neq\alpha}\sum_{m'}^{m'\neq n} \rho_{\alpha\alpha}^{(\mathrm{b})} \frac{|H'_{n\alpha,m'\beta}|^2}{\omega_{n\alpha,m'\beta}} \tag{3.52}$$

due to the interaction between the system and the heat bath. It should be noted that the dephasing constant can be divided into two parts, the inelastic processes $(\Gamma_{nn}^{nn} + \Gamma_{mm}^{mm})/2$ and the elastic processes $\Gamma_{mn}^{mn}(\mathrm{d})$ called

Lam Research Ex. 1035 - Page 145
Lam Research Corp. v. Inpria Corp.
IPR2024-00033 - U.S. Patent No. 9,823,564

pure dephasing,

$$\Gamma_{mn}^{mn}(\mathrm{d}) = \frac{1}{\hbar}\sum\sum \rho_{\alpha\alpha}^{(\mathrm{b})}\left(H'_{m\alpha,m\beta} - H'_{n\alpha,n\beta}\right)^2 \delta\left(E_\alpha - E_\beta\right) \tag{3.53}$$

From the above one can see that a main difference between the effective Hamiltonian method and the above results is $\Gamma_{mn}^{mn}(\mathrm{d})$. It should be noted that the results given by Eqs. (3.45)–(3.53) can be obtained by using the singular perturbation method [18,20] and other methods [19,21].

3.3. Ultrafast Non-Adiabatic Dynamics of Molecular Systems

In this section, the density matrix method shall be applied to study the ultrafast dynamics of the system embedded in a heat bath. Due to the use of the ultrashort pulse in the pumping lasers the dynamic behaviors of both population and coherence have to be considered [1,19–21].

Consider the non-adiabatic transition $\mathrm{a} \to \mathrm{b}$ shown schematically in Figure 5.2, where a and b may denote the electronic states of D^*A and D^+A^-, respectively. To describe the dynamic processes of the system, one starts with the stochastic Liouville equation

$$\frac{d\hat{\rho}}{dt} = -i\hat{L}_s\hat{\rho} - i\hat{L}'\hat{\rho} - \hat{\Gamma}\hat{\rho} \tag{3.54}$$

where $\hat{L}'$ is responsible for the non-adiabatic processes using the Born–Oppenheimer adiabatic approximation (BOA). Here $\hat{\Gamma}$ denotes the damping operator due to the coupling between the system and the heat bath. The GMEs of the non-adiabatic processes are given by [1,22]

$$\frac{d\rho_{\mathrm{a}v,\mathrm{a}v}}{dt} = -\frac{i}{\hbar}\sum_u \left(H'_{\mathrm{a}v,\mathrm{b}u}\rho_{\mathrm{b}u,\mathrm{a}v} - \rho_{\mathrm{a}v,\mathrm{b}u}H'_{\mathrm{b}u,\mathrm{a}v}\right) - \left(\hat{\Gamma}\hat{\rho}\right)_{\mathrm{a}v,\mathrm{a}v} \tag{3.55}$$

$$\begin{aligned}\frac{d\rho_{\mathrm{a}v,\mathrm{a}v'}}{dt} = & -\left(i\omega_{\mathrm{a}v,\mathrm{a}v'} + \Gamma_{\mathrm{a}v,\mathrm{a}v'}^{\mathrm{a}v,\mathrm{a}v'}\right)\rho_{\mathrm{a}v,\mathrm{a}v'} \\ & -\frac{i}{\hbar}\sum_u \left(H'_{\mathrm{a}v,\mathrm{b}u}\rho_{\mathrm{b}u,\mathrm{a}v'} - \rho_{\mathrm{a}v,\mathrm{b}u}H'_{\mathrm{b}u,\mathrm{a}v'}\right)\end{aligned} \tag{3.56}$$

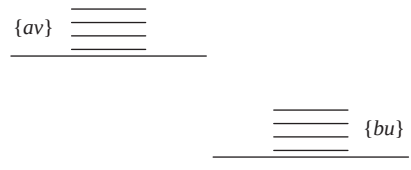


Fig. 5.2. Energy-level scheme for $\mathrm{a} \to \mathrm{b}$.

Lam Research Ex. 1035 - Page 146
Lam Research Corp. v. Inpria Corp.
IPR2024-00033 - U.S. Patent No. 9,823,564

$$\frac{d\rho_{\mathrm{b}u,\mathrm{a}v}}{dt} = -(i\omega_{\mathrm{b}u,\mathrm{a}v} + \Gamma^{\mathrm{b}u,\mathrm{a}v}_{\mathrm{b}u,\mathrm{a}v})\rho_{\mathrm{b}u,\mathrm{a}v} - \frac{i}{\hbar}\left(\sum_{v'} H'_{\mathrm{b}u,\mathrm{a}v'}\rho_{\mathrm{a}v',\mathrm{a}v} - \sum_{u'} \rho_{\mathrm{b}u,\mathrm{b}u'}H'_{\mathrm{b}u',\mathrm{a}v}\right) \tag{3.57}$$

where $\rho_{\mathrm{a}v,\mathrm{a}v}$, $\rho_{\mathrm{a}v,\mathrm{a}v'}$ and $\rho_{\mathrm{b}u,\mathrm{a}v}$ represent the vibronic population, the vibrational coherence (or phase) and the vibronic coherence, respectively.

Eq. (3.57) can be rewritten as

$$\begin{aligned}\frac{d\rho_{\mathrm{b}u,\mathrm{a}v}}{dt} = & -(i\omega_{\mathrm{b}u,\mathrm{a}v} + \Gamma^{\mathrm{b}u,\mathrm{a}v}_{\mathrm{b}u,\mathrm{a}v})\rho_{\mathrm{b}u,\mathrm{a}v} - \frac{i}{\hbar}H'_{\mathrm{b}u,\mathrm{a}v}(\rho_{\mathrm{a}v,\mathrm{a}v} - \rho_{\mathrm{b}u,\mathrm{b}u}) \\ & - \frac{i}{\hbar}\Big(\sum_{v'}^{v'\neq v} H'_{\mathrm{b}u,\mathrm{a}v'}\rho_{\mathrm{a}v',\mathrm{a}v} - \sum_{u'}^{u'\neq u} \rho_{\mathrm{b}u,\mathrm{b}u'}H'_{\mathrm{b}u',\mathrm{a}v}\Big)\end{aligned} \tag{3.58}$$

To the second-order approximation, by using the Laplace transformation method, $\rho_{\mathrm{b}u,\mathrm{a}v}(t)$ can be eliminated from Eq. (3.55):

$$\begin{aligned}\frac{d\rho_{\mathrm{a}v,\mathrm{a}v}}{dt} = & \frac{2}{\hbar}\sum_{u} \mathrm{Im}[H'_{\mathrm{a}v,\mathrm{b}u}\, e^{-t(i\omega_{\mathrm{b}u,\mathrm{a}v}+\gamma_{\mathrm{b}u,\mathrm{a}v})}\rho_{\mathrm{b}u,\mathrm{a}v}(0)] - (\hat{\Gamma}\hat{\rho})_{\mathrm{a}v,\mathrm{a}v} \\ & + \sum_{u}\int_0^t d\tau M(\tau)_{\mathrm{b}u,\mathrm{a}v}[\rho_{\mathrm{b}u,\mathrm{b}u}(t-\tau) - \rho_{\mathrm{a}v,\mathrm{a}v}(t-\tau)]\end{aligned} \tag{3.59}$$

where the memory kernel $M(\tau)_{\mathrm{b}u,\mathrm{a}v}$ is given by

$$M(\tau)_{\mathrm{b}u,\mathrm{a}v} = \mathrm{Im}\left[\frac{2i}{\hbar^2}|H'_{\mathrm{a}v,\mathrm{b}u}|^2\, e^{-\tau(i\omega_{\mathrm{b}u,\mathrm{a}v}+\gamma_{\mathrm{b}u,\mathrm{a}v})}\right] \tag{3.60}$$

In the Markoff approximation Eq. (3.59) reduces to

$$\frac{d\rho_{\mathrm{a}v,\mathrm{a}v}}{dt} = \sum_{u} W_{\mathrm{b}u,\mathrm{a}v}[\rho_{\mathrm{b}u,\mathrm{b}u}(t) - \rho_{\mathrm{a}v,\mathrm{a}v}(t)] - (\hat{\Gamma}\hat{\rho})_{\mathrm{a}v,\mathrm{a}v} \tag{3.61}$$

where $W_{\mathrm{b}u,\mathrm{a}v}$ denotes the rate constant for $\mathrm{a}v \leftrightarrow \mathrm{b}u$,

$$W_{\mathrm{b}u,\mathrm{a}v} = \int_0^\infty dt M(t)_{\mathrm{b}u,\mathrm{a}v} = \frac{2}{\hbar^2}\frac{\gamma_{\mathrm{b}u,\mathrm{a}v}}{\gamma^2_{\mathrm{b}u,\mathrm{a}v} + \omega^2_{\mathrm{b}u,\mathrm{a}v}}|H'_{\mathrm{a}v,\mathrm{b}u}|^2 \tag{3.62}$$

Here it is assumed that $\gamma_{\mathrm{b}u,\mathrm{a}v}$ denotes the real part of $\Gamma^{\mathrm{b}u,\mathrm{a}v}_{\mathrm{b}u,\mathrm{a}v}$ and the imaginary part of $\Gamma^{\mathrm{b}u,\mathrm{a}v}_{\mathrm{b}u,\mathrm{a}v}$ is included in $\omega_{\mathrm{b}u,\mathrm{a}v}$. Similarly,

$$\frac{d\rho_{\mathrm{b}u,\mathrm{b}u}}{dt} = -\sum_{v} W_{\mathrm{b}u,\mathrm{a}v}[\rho_{\mathrm{b}u,\mathrm{b}u}(t) - \rho_{\mathrm{a}v,\mathrm{a}v}(t)] - (\hat{\Gamma}\hat{\rho})_{\mathrm{b}u,\mathrm{b}u} \tag{3.63}$$

Experimentally the dynamics of the product is also often measured.

Lam Research Ex. 1035 - Page 147
Lam Research Corp. v. Inpria Corp.
IPR2024-00033 - U.S. Patent No. 9,823,564

Notice that in $(\hat{\Gamma}\hat{\rho})_{av,av}$ only vibrational relaxation is involved due to the coupling between the system and the heat bath, i.e., [23–25]

$$(\hat{\Gamma}\hat{\rho})_{av,av} = \sum_{v'} \Gamma^{av',av'}_{av,av} \rho_{av',av'} = \Gamma^{av,av}_{av,av}\rho_{av,av} + \sum_{v'}^{v'\neq v} \Gamma^{av',av'}_{av,av} \rho_{av',av'}$$
$$= \sum_{v'}^{v'\neq v} \left(\Gamma^{av',av'}_{av,av} \rho_{av',av'} - \Gamma^{av,av}_{av',av'}\rho_{av,av} \right) \tag{3.64}$$

It follows that

$$\frac{d\rho_{av,av}}{dt} = \sum_{u} W_{bu,av}[\rho_{bu,bu}(t) - \rho_{av,av}(t)]$$
$$- \sum_{v'}^{v'\neq v} \left(\Gamma^{av',av'}_{av,av} \rho_{av',av'} - \Gamma^{av,av}_{av',av'}\rho_{av,av} \right) \tag{3.65}$$

Similarly,

$$\frac{d\rho_{bu,bu}}{dt} = -\sum_{v} W_{bu,av}[\rho_{bu,bu}(t) - \rho_{av,av}(t)]$$
$$- \sum_{u'}^{u'\neq u} \left(\Gamma^{bu',bu'}_{bu,bu} \rho_{bu',bu'} - \Gamma^{bu,bu}_{bu',bu'}\rho_{bu,bu} \right) \tag{3.66}$$

On the right-hand side of Eq. (3.65), the first, second and third terms describe the dynamic behavior of $\rho_{av,av}$ due to the vibronic coherence dynamics, non-adiabatic transitions and vibrational relaxation, respectively. Several cases can be considered. First, if the vibrational relaxation is much faster than electronic processes, then

$$\Gamma^{av',av'}_{av,av} \rho_{av',av'} = \Gamma^{av,av}_{av',av'}\rho_{av,av} \tag{3.67}$$

i.e., principle of detailed balance, and if the heat bath maintains thermal equilibrium, then $\rho_{av,av}$ is related to the Boltzmann distribution P_{av} by

$$\rho_{av,av}(t) = \rho_a(t)P_{av} \tag{3.68}$$

where $\rho_a(t)$ represents the total population of the system in the 'a' electronic state. Similarly,

$$\rho_{bu,bu}(t) = \rho_b(t)P_{bu} \tag{3.69}$$

Using Eqs. (3.68) and (3.69) one can rewrite Eq. (3.65) as [26–29]

$$\frac{d\rho_a}{dt} = W_{b\to a}\rho_b - W_{a\to b}\rho_a \tag{3.70}$$

Lam Research Ex. 1035 - Page 148
Lam Research Corp. v. Inpria Corp.
IPR2024-00033 - U.S. Patent No. 9,823,564

where

$$W_{\mathrm{b}\to\mathrm{a}} = \sum_u \sum_v P_{\mathrm{b}u} W_{\mathrm{b}u,\mathrm{a}v} \tag{3.71}$$

and

$$W_{\mathrm{a}\to\mathrm{b}} = \sum_v \sum_u P_{\mathrm{a}v} W_{\mathrm{a}v,\mathrm{b}u} \tag{3.72}$$

i.e., thermal average rate constants. Here $W_{\mathrm{a}v,\mathrm{b}u} = W_{\mathrm{b}u,\mathrm{a}v}$. Similarly,

$$\frac{d\rho_{\mathrm{b}}}{dt} = -(W_{\mathrm{b}\to\mathrm{a}}\rho_{\mathrm{b}} - W_{\mathrm{a}\to\mathrm{b}}\rho_{\mathrm{a}}) \tag{3.73}$$

Next, if vibrational relaxation is much slower than electronic transition, then

$$\frac{d\rho_{\mathrm{a}v,\mathrm{a}v}}{dt} = -W_{\mathrm{a}v}\rho_{\mathrm{a}v,\mathrm{a}v} + \sum_u W_{\mathrm{b}u,\mathrm{a}v}\rho_{\mathrm{b}u,\mathrm{b}u} \tag{3.74}$$

where $W_{\mathrm{a}v}$ denotes the single-vibronic-level rate constant

$$W_{\mathrm{a}v} = \sum_u W_{\mathrm{a}v,\mathrm{b}u} \tag{3.75}$$

Similarly,

$$\frac{d\rho_{\mathrm{b}u,\mathrm{b}u}}{dt} = -W_{\mathrm{b}u}\rho_{\mathrm{b}u,\mathrm{b}u} + \sum_v W_{\mathrm{a}v,\mathrm{b}u}\rho_{\mathrm{a}v,\mathrm{a}v} \tag{3.76}$$

where

$$W_{\mathrm{b}u} = \sum_v W_{\mathrm{b}u,\mathrm{a}v} \tag{3.77}$$

In condensed phase, $\gamma_{\mathrm{b}u,\mathrm{a}v}$ contains pure dephasing $\Gamma^{\mathrm{b}u,\mathrm{a}v}_{\mathrm{b}u,\mathrm{a}v}(\mathrm{d})$, $\Gamma^{\mathrm{b}u,\mathrm{b}u}_{\mathrm{b}u,\mathrm{b}u}$ and $\Gamma^{\mathrm{a}v,\mathrm{a}v}_{\mathrm{a}v,\mathrm{a}v}$ and it may be very fast so that in the time scale of experiment, the vibronic coherence term may disappear.

The results presented in this section are very general and can be applied to IC, ISC, photo-induced energy transfer (EET) and photo-induced electron transfer (ET) [26,30–36].

The coherence dynamics of products is often observed and will be treated in the following. Consider the electronic levels a and b shown in Figure 5.2. It is found that

$$\begin{aligned}\frac{d\rho_{\mathrm{b}u,\mathrm{b}u'}}{dt} = & -(i\omega_{\mathrm{b}u,\mathrm{b}u'} + \gamma_{\mathrm{b}u,\mathrm{b}u'})\rho_{\mathrm{b}u,\mathrm{b}u'} \\ & -\frac{i}{\hbar}\sum_v \left(H'_{\mathrm{b}u,\mathrm{a}v}\rho_{\mathrm{a}v,\mathrm{b}u'} - \rho_{\mathrm{b}u,\mathrm{a}v}H'_{\mathrm{a}v,\mathrm{b}u'}\right)\end{aligned} \tag{3.78}$$

Lam Research Ex. 1035 - Page 149
Lam Research Corp. v. Inpria Corp.
IPR2024-00033 - U.S. Patent No. 9,823,564

where

$$\frac{d\rho_{\mathrm{a}v,\mathrm{b}u'}}{dt} \cong -(i\omega_{\mathrm{a}v,\mathrm{b}u'} + \gamma_{\mathrm{a}v,\mathrm{b}u'})\rho_{\mathrm{a}v,\mathrm{b}u'} + \frac{i}{\hbar} H'_{\mathrm{a}v,\mathrm{b}u'}\rho_{\mathrm{a}v,\mathrm{a}v} \tag{3.79}$$

and

$$\frac{d\rho_{\mathrm{b}u,\mathrm{a}v}}{dt} \cong -(i\omega_{\mathrm{b}u,\mathrm{a}v} + \gamma_{\mathrm{b}u,\mathrm{a}v})\rho_{\mathrm{b}u,\mathrm{a}v} - \frac{i}{\hbar} H'_{\mathrm{b}u,\mathrm{a}v}\rho_{\mathrm{a}v,\mathrm{a}v} \tag{3.80}$$

It follows that approximately one obtains

$$\frac{d\rho_{\mathrm{b}u,\mathrm{b}u'}}{dt} = -(i\omega_{\mathrm{b}u,\mathrm{b}u'} + \gamma_{\mathrm{b}u,\mathrm{b}u'})\rho_{\mathrm{b}u,\mathrm{b}u'} + \frac{1}{\hbar^2}\sum_v \rho_{\mathrm{a}v,\mathrm{a}v} H'_{\mathrm{b}u,\mathrm{a}v} H'_{\mathrm{a}v,\mathrm{b}u'} \times \left(\frac{1}{i\omega_{\mathrm{a}v,\mathrm{b}u'} + \gamma_{\mathrm{a}v,\mathrm{b}u'}} + \frac{1}{i\omega_{\mathrm{b}u,\mathrm{a}v} + \gamma_{\mathrm{b}u,\mathrm{a}v}}\right) \tag{3.81}$$

Eq. (3.81) can be solved by first solving for $\rho_{\mathrm{a}v,\mathrm{a}v}(t)$ and then substituting the resulting $\rho_{\mathrm{a}v,\mathrm{a}v}(t)$ into Eq. (3.81) to obtain the product coherence $\rho_{\mathrm{b}u,\mathrm{b}u'}(t)$. Another way to create the product vibrational coherence is due to the anharmonic coupling U in the product states

$$\frac{d\rho_{\mathrm{b}u,\mathrm{b}u'}}{dt} = -(i\omega_{\mathrm{b}u,\mathrm{b}u'} + \gamma_{\mathrm{b}u,\mathrm{b}u'})\rho_{\mathrm{b}u,\mathrm{b}u'} - \frac{i}{\hbar} U_{\mathrm{b}u,\mathrm{b}u'}(\rho_{\mathrm{b}u',\mathrm{b}u'} - \rho_{\mathrm{b}u,\mathrm{b}u}) \tag{3.82}$$

3.4. Single-Vibronic-Level and Thermal Average Rate Constant

Figure 5.3 demonstrates the effect of vibrational relaxation on photo-induced ET (PIET) in an ultrashort pulse experiment where more than one vibronic level are coherently pumped and only the single-level rate

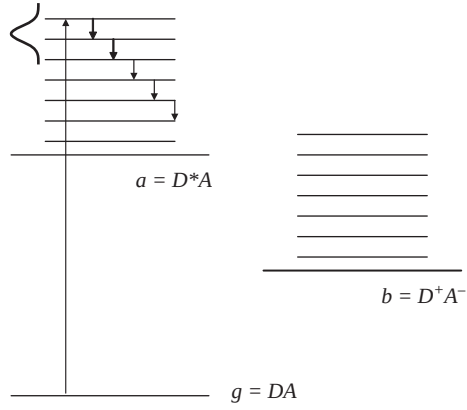


Fig. 5.3. Effect of vibrational relaxation on photo-induced electron transfer.

Lam Research Ex. 1035 - Page 150
Lam Research Corp. v. Inpria Corp.
IPR2024-00033 - U.S. Patent No. 9,823,564

constant plays an important role in ultrafast ET. Although the ET case is used to show the derivation, other electronic processes can be treated similarly.

There are three types of rate constants appearing in Section 3.3, i.e., $W_{\mathrm{b}\vec{u},\mathrm{a}\vec{v}}$, the state-to-state rate constant, $W_{\mathrm{a}\vec{v}}$ (or $W_{\mathrm{b}\vec{u}}$), the single-vibronic-level rate constant, and $W_{\mathrm{a}\to\mathrm{b}}$ (or $W_{\mathrm{b}\to a}$), the thermal average rate constant. However, as will be shown in Section 4, only $W_{\mathrm{a}\vec{v}}$ (or $W_{\mathrm{b}\vec{u}}$) are involved in femtosecond time-resolved measurements (see Figure 5.2). The calculation of $W_{\mathrm{a}\vec{v}}$ (or $W_{\mathrm{b}\vec{u}}$) will be given in this section. In the BOA, the molecular-system wavefunctions $\psi_{\mathrm{a}\vec{v}}$ and $\psi_{\mathrm{b}\vec{u}}$ can be written in terms of the electronic wavefunctions $\Phi_{\mathrm{a}}(\vec{q},\vec{Q})$ and $\Phi_{\mathrm{b}}(\vec{q},\vec{Q})$ and vibrational (ro-vibrational) wavefunctions $\Theta_{\mathrm{a}\vec{v}}(\vec{Q})$ and $\Theta_{\mathrm{b}\vec{u}}(\vec{Q})$. In this case, $H'_{\mathrm{a}\vec{v},\mathrm{b}\vec{u}}$ can be written as

$$H'_{\mathrm{a}\vec{v},\mathrm{b}\vec{u}} = \langle\Theta_{\mathrm{a}\vec{v}}(\vec{Q})|H'_{\mathrm{ab}}|\Theta_{\mathrm{b}\vec{u}}(\vec{Q})\rangle \tag{3.83}$$

where H'_{ab} represents the electronic matrix elements, $H'_{\mathrm{ab}}(\vec{Q})$. In most non-adiabatic processes (except IC), $H'_{\mathrm{ab}}(\vec{Q})$ can be expanded in terms of vibrational coordinates $\{Q_j\}$. For the case in which $H'_{\mathrm{ab}}(\vec{0})$ is non-zero, the first-order term can be neglected, i.e., $H'_{\mathrm{ab}}(\vec{Q}) = H'_{\mathrm{ab}}(\vec{0})$. This is usually called the *Condon approximation*. In this case, one obtains

$$W_{\mathrm{b}\vec{u},\mathrm{a}\vec{v}} = \frac{2\pi}{\hbar^2}|H'_{\mathrm{ab}}(\vec{0})|^2|\langle\Theta_{\mathrm{a}\vec{v}}|\Theta_{\mathrm{b}\vec{u}}\rangle|^2 D(\omega_{\mathrm{b}\vec{u},\mathrm{a}\vec{v}}) \tag{3.84}$$

$$W_{\mathrm{a}\vec{v}} = \frac{2\pi}{\hbar^2}|H'_{\mathrm{ab}}(\vec{0})|^2\sum_{\vec{u}}|\langle\Theta_{\mathrm{a}\vec{v}}|\Theta_{\mathrm{b}\vec{u}}\rangle|^2 D(\omega_{\mathrm{b}\vec{u},\mathrm{a}\vec{v}}) \tag{3.85}$$

$$W_{\mathrm{a}\to\mathrm{b}} = \frac{2\pi}{\hbar^2}|H'_{\mathrm{ab}}(\vec{0})|^2\sum_{\vec{v}}\sum_{\vec{u}}P_{\mathrm{a}v}|\langle\Theta_{\mathrm{a}\vec{v}}|\Theta_{\mathrm{b}\vec{u}}\rangle|^2 D(\omega_{\mathrm{b}\vec{u},\mathrm{a}\vec{v}}) \tag{3.86}$$

$$W_{\mathrm{b}\to\mathrm{a}} = \frac{2\pi}{\hbar^2}|H'_{\mathrm{ab}}(\vec{0})|^2\sum_{\vec{v}}\sum_{\vec{u}}P_{\mathrm{b}\vec{u}}|\langle\Theta_{\mathrm{a}\vec{v}}|\Theta_{\mathrm{b}\vec{u}}\rangle|^2 D(\omega_{\mathrm{b}\vec{u},\mathrm{a}\vec{v}}) \tag{3.87}$$

where $P_{\mathrm{a}\vec{v}}$ and $P_{\mathrm{b}\vec{u}}$ denote the Boltzmann distribution,

$$D(\omega_{\mathrm{b}\vec{u},\mathrm{a}\vec{v}}) = \frac{1}{\pi}\frac{\gamma_{\mathrm{b}\vec{u},\mathrm{a}\vec{v}}}{\gamma^2_{\mathrm{b}\vec{u},\mathrm{a}\vec{v}} + \omega^2_{\mathrm{b}\vec{u},\mathrm{a}\vec{v}}} \tag{3.88}$$

and $|\langle\Theta_{\mathrm{a}\vec{v}}|\Theta_{\mathrm{b}\vec{u}}\rangle|^2$ is the *Franck–Condon factor* (FCF). As $\gamma_{\mathrm{b}\vec{u},\mathrm{a}\vec{v}} \to 0$, $D(\omega_{\mathrm{b}\vec{u},\mathrm{a}\vec{v}})$ reduces to the delta function, $\delta(\omega_{\mathrm{b}\vec{u},\mathrm{a}\vec{v}})$. Notice that the IC case can be treated as follows. If there is only one promoting mode Q_ℓ, then the

Lam Research Ex. 1035 - Page 151
Lam Research Corp. v. Inpria Corp.
IPR2024-00033 - U.S. Patent No. 9,823,564

matrix element $H'_{a\vec{v},b\vec{u}}$ takes the following form [30]:

$$\begin{aligned} H'_{a\vec{v},b\vec{u}} &= \langle \psi_{a\vec{v}} | \hat{H}'_{BO} | \psi_{b\vec{u}} \rangle \\ &= -\hbar^2 \left\langle \Theta_{a\vec{v}} \middle| \left\langle \Phi_a \middle| \frac{\partial}{\partial Q_\ell} \middle| \Phi_b \right\rangle \middle| \frac{\partial \Theta_{b\vec{u}}}{\partial Q_\ell} \right\rangle \\ &\quad -\frac{\hbar^2}{2} \left\langle \Theta_{a\vec{v}} \middle| \left\langle \Phi_a \middle| \frac{\partial^2}{\partial Q_\ell^2} \middle| \Phi_b \right\rangle \middle| \Theta_{b\vec{u}} \right\rangle \end{aligned} \tag{3.89}$$

In Eq. (3.89), the second term on the right-hand side is usually much smaller than that of the first term, and $\hat{H}'_{BO}$ is called the *Born–Oppenheimer coupling*.

To evaluate the rate constants it is necessary to know the potential surfaces of the electronic states a and b. For this purpose, the harmonic surfaces are commonly used,

$$U_a(\vec{Q}) = E_a + \frac{1}{2}\sum_j \omega_j^2 Q_j^2; \quad U_b(\vec{Q}) = E_b + \frac{1}{2}\sum_j \omega_j'^2 Q_j'^2 \tag{3.90}$$

Only the single-vibronic-level rate constants for the displaced surfaces will be given in the following; a more general case is presented in Appendix A. Notice that using the integral representation for the Lorentzian and

$$\Theta_{a\vec{v}} = \prod_j \chi_{av_j}(Q_j); \quad \Theta_{b\vec{u}} = \prod_j \chi_{bu_j}(Q'_j) \tag{3.91}$$

Eq. (3.84) can be written as [32,33]

$$W_{a\vec{v}} = \frac{1}{\hbar^2} |H'_{ab}(\vec{0})|^2 \int_{-\infty}^{\infty} dt\, e^{it\omega_{ba} - \gamma_{ba}|t|} \prod_j G_{v_j}(t) \tag{3.92}$$

where

$$G_{v_j}(t) = \sum_{u_j} |\langle \chi_{av_j} | \chi_{bu_j} \rangle|^2 \exp\left[it \left\{ \left(u_j + \frac{1}{2} \right) \omega_j - \left(v_j + \frac{1}{2} \right) \omega'_j \right\} \right] \tag{3.93}$$

The time-correlation function (TCF) $G_{v_j}(t)$ can be expressed as

$$G_{v_j}(t) = G_{0_j}(t) \sum_{m_j=0}^{v_j} \frac{v_j! [S_j (e^{it\omega_j/2} - e^{-it\omega_j/2})^2]^{v_j - m_j}}{m_j! [(v_j - m_j)!]^2} \tag{3.94}$$

where S_j denotes the *Huang–Rhys factor* $S_j = \omega_j \Delta Q_j^2 / 2\hbar$ and

$$G_{0_j}(t) = \exp[-S_j(1 - e^{it\omega_j})] \tag{3.95}$$

Lam Research Ex. 1035 - Page 152
Lam Research Corp. v. Inpria Corp.
IPR2024-00033 - U.S. Patent No. 9,823,564

In this case for $W_{a\vec{v}}$ it is found that

$$W_{a\vec{v}} = \frac{|H'_{ab}|^2}{\hbar^2}\int_{-\infty}^{\infty} dt\, e^{i\omega_{ba}-\gamma_{ba}|t|-\sum_j S_j(1-e^{it\omega_j})} \times \prod_j \left[\sum_{m_j}^{v_j} \frac{v_j!\{S_j(e^{it\omega_j/2}-e^{-it\omega_j/2})^2\}^{v_j-m_j}}{m_j!\{(v_j-m_j)!\}^2}\right] \tag{3.96}$$

For comparison, the thermal average rate constant is obtained by using $W_{a\vec{v}}$ given by Eq. (3.96):

$$W_{a\to b} = \sum_{\vec{v}} W_{a\vec{v}} = \frac{|H'_{ab}|^2}{\hbar^2}\int_{-\infty}^{\infty} dt\, \exp\Big[it\omega_{ba} - \gamma_{ab}|t| - \sum S_j\{(2\bar{n}_j+1) - (\bar{n}_j+1)e^{it\omega_j} - \bar{n}_j\, e^{-it\omega_j}\}\Big] \tag{3.96A}$$

where $\bar{n}_j = [e^{\hbar\omega_j/k_B T}-1]^{-1}$.

The Marcus equation can be derived by assuming strong vibronic coupling ($\sum_j S_j >> 1$) and high temperature ($\hbar\omega_j/k_B T << 1$). Thus, to the second-order approximation one obtains the Marcus equation:

$$W_T = \frac{|T_{ba}|^2}{\hbar^2}\sqrt{\frac{\pi}{\lambda k_B T}}\exp\left[-\frac{(\Delta G_{ba}+\lambda)^2}{4\lambda k_B T}\right] \tag{3.96B}$$

where $\lambda = \sum_j S_j\hbar\omega_j$ and $\Delta G_{ba} = \hbar\omega_{ba}$. It should be noted that for the thermal average case, the activation energy $\Delta E_a = (\Delta G_{ba}+\lambda)^2/4\lambda$ denotes the energy at the crossing point of the two one-dimensional surfaces and for the multi-mode case, there is more than one crossing point and ΔE_a represents the energy at the minimum crossing point; in other words, in this case the reaction coordinate is defined as the coordinate along the minimum crossing point. For the displaced–distorted oscillator surfaces, the Marcus form of ET rate constant still preserves, but ΔG_{ba} and λ will be more complicated and temperature dependent. However, if there exists a Duschinsky effect between the two surfaces involved in ET, then the Marcus form of ET rate constant will not be valid.

In a previous paper [22], it has been shown that the reaction coordinate is well defined only in the Marcus theory, that is in the classical regime. In this case, the reaction coordinate is along the minimum crossing point in the multi-dimensional potential surfaces (i.e., multi-mode case). In the quantum regime, the reaction coordinate is not well defined especially in the case of the non-relaxed ET like $W_{i\vec{v}}$.

Since the interfacial ET process is faster than the vibrational relaxation, one needs the transition rate from a single molecular vibronic level to the conduction band (or local states coupled to the adsorbed molecule) of the

Lam Research Ex. 1035 - Page 153
Lam Research Corp. v. Inpria Corp.
IPR2024-00033 - U.S. Patent No. 9,823,564

solid surface. Formally, if the initial vibronic state of the adsorbant is labeled by the electronic level i and the vibrational level $\vec{v}$ (there are generally more than one vibrational mode), then the single-level ET rate constant is

$$W_{a\vec{v}} = \frac{|H'_{ab}(0)|^2}{\hbar^2} \int_{-\infty}^{\infty} dt \, \exp\left[-\sum_k S_k(1 - e^{it\omega_k}) + it\omega_{fi} - \gamma_{if}|t| \right] \times \sum_{\vec{n}}^{\vec{v}} \prod_{\ell} \frac{v_\ell!}{(v_\ell - n_\ell)!(n_\ell!)^2} [S_\ell(e^{it\omega_\ell/2} - e^{-it\omega_\ell/2})^2]^{n_\ell} \tag{3.97}$$

where v_ℓ denotes the vibrational state prepared by the pumping laser. Since the final electronic state f is related to the conduction band (or local states coupled to the adsorbed molecule) of the acceptor, a summation over f is required, and since the conduction band (or local states) is considered as a continuum, the summation will be rewritten into an integral:

$$\sum\nolimits_f \to \int g(E)dE \tag{3.98}$$

where $g(E)$ denotes the density of states

$$g(E) = \sum_f \delta(E - E_f) \tag{3.99}$$

If $g(E)$ takes the Gaussian form, then $W_{i\vec{v}}$ becomes

$$W_{i\vec{v}} = \frac{|H'_{fi}|^2}{\hbar^2} \int_{-\infty}^{\infty} dt \, \exp\left[-\sum_k S_k(1 - e^{it\omega_k}) + it\bar{\omega}_{fi} - \frac{D^2t^2}{4} \right] \times \sum_{\vec{n}}^{\vec{v}} \prod_{\ell} \frac{v_\ell!}{(v_\ell - n_\ell)!(n_\ell!)^2} [S_\ell(e^{-it\omega_\ell/2} - e^{-it\omega_\ell/2})^2]^{n_\ell} \tag{3.100}$$

where D represents the width in the Gaussian band-shape. In this case, $g(E)$ plays the role of inhomogeneities. Although in principle, depending on the pumping laser pulse, more than one vibrational mode can be excited, in most cases only one mode is involved in $W_{i\vec{v}}$, i.e.,

$$W_{i\vec{v}} = \frac{|H'_{fi}|^2}{\hbar^2} \int_{-\infty}^{\infty} dt \, \exp\left[-\sum_k S_k(1 - e^{it\omega_k}) + it\bar{\omega}_{fi} - \frac{D^2t^2}{4} \right] \times \sum_{n_\ell}^{v_\ell} \frac{v_\ell!}{(v_\ell - n_\ell)!(n_\ell!)^2} [S_\ell(e^{it\omega_\ell/2} - e^{-it\omega_\ell/2})^2]^{n_\ell} \tag{3.101}$$

In the above discussion the single-vibronic-level and thermal average rate constants have only been calculated using the displaced oscillator surfaces.

Lam Research Ex. 1035 - Page 154
Lam Research Corp. v. Inpria Corp.
IPR2024-00033 - U.S. Patent No. 9,823,564

However, it should be noted that the effect of distortion and mode mixing (i.e., Duschinsky effect) of potential surfaces has been studied [30,37].

4. Density Matrix Method and Spectroscopies

Spectroscopic methods are very useful for determining molecular properties. Time-resolved spectroscopic methods are useful for monitoring the evolution of the molecular properties in real time. Moreover, time-resolved spectroscopic techniques have the best time resolution available among all kinds of time-resolved experimental techniques. Thus, very often time-resolved spectroscopic methods reveal the dynamics of a molecular system in the non-equilibrium regime. In this section, the density matrix method is applied to calculate the spectroscopic properties of molecular systems. These include the linear and non-linear optical processes, in equilibrium or non-equilibrium cases. The approach is based on the susceptibility theory.

4.1. STEADY STATE SPECTROSCOPY

Consider the absorption spectroscopy. To describe the interaction between the system and the radiation field, the dipole approximation is commonly used, i.e.,

$$\hat{V}(t) = -\vec{\mu} \cdot \vec{E}(t) \tag{4.1}$$

where $\vec{\mu}$ denotes the dipole operator and $\vec{E}(t)$ the radiation field

$$\vec{E}(t) = \vec{E}_0 \cos \omega t \tag{4.2}$$

The rate of energy absorption by the system is given by [1,17,38,39]

$$Q = \left\langle \frac{\partial \hat{H}}{\partial t} \right\rangle \tag{4.3}$$

where $\hat{H}$ represents the Hamiltonian of the system in the presence of a radiation field $\vec{E}(t)$. $\hat{H}$ consists of the Hamiltonian of the system $\hat{H}_0$ and its interaction with the radiation field $\vec{E}(t)$

$$\hat{H} = \hat{H}_0 + \hat{V}(t) \tag{4.4}$$

Substituting Eqs. (4.4) and (4.1) into Eq. (4.3) yields

$$Q = -\langle \vec{\mu} \rangle \cdot \frac{d\vec{E}(t)}{dt} = -\vec{P} \cdot \frac{d\vec{E}(t)}{dt} \tag{4.5}$$

Lam Research Ex. 1035 - Page 155
Lam Research Corp. v. Inpria Corp.
IPR2024-00033 - U.S. Patent No. 9,823,564

where $\vec{P}$ denotes the polarization

$$\vec{P} = \langle \vec{\mu} \rangle = \mathrm{Tr}(\hat{\sigma}\vec{\mu}) = \mathrm{Tr}(\vec{\mu}\hat{\sigma}) \tag{4.6}$$

For convenience, write $\vec{E}(t)$ as

$$\vec{E}(t) = \vec{E}(\omega)e^{-it\omega} + \vec{E}(-\omega)e^{it\omega} \tag{4.7}$$

where $\vec{E}(-\omega) = \vec{E}^*(\omega)$. As $\vec{P}(t)$ varies linearly with $\vec{E}(t)$, i.e.,

$$\vec{P}(t) = \vec{P}(\omega)e^{-it\omega} + \vec{P}(-\omega)e^{it\omega} \tag{4.8}$$

where

$$\vec{P}(\omega) = \overleftrightarrow{\chi}(\omega)\vec{E}(\omega) \tag{4.9}$$

and

$$\vec{P}(-\omega) = \overleftrightarrow{\chi}(-\omega)\vec{E}(-\omega) \tag{4.10}$$

or

$$\overleftrightarrow{\chi}(-\omega) = \overleftrightarrow{\chi}(\omega)^* \tag{4.11}$$

Substituting Eqs. (4.7) and (4.8) into Eq. (4.5) one obtains

$$Q = -[\vec{P}(\omega)e^{-it\omega} + \vec{P}(-\omega)e^{it\omega}] \cdot [-i\omega\vec{E}(\omega)e^{-it\omega} + i\omega\vec{E}(-\omega)e^{it\omega}] \tag{4.12}$$

In the *rotating wave approximation* (RWA) (i.e., neglecting the terms $e^{2it\omega}$ and $e^{-2it\omega}$), Eq. (4.12) becomes

$$Q = -(i\omega)[\vec{P}(\omega) \cdot \vec{E}(-\omega) - \vec{P}(-\omega) \cdot \vec{E}(\omega)] \tag{4.13}$$

or

$$Q = -(i\omega)[\overleftrightarrow{\chi}(\omega) - \overleftrightarrow{\chi}(-\omega)]|\vec{E}(\omega)|^2 \tag{4.14}$$

Here the relations described in Eqs. (4.9) and (4.10) have been used. $\overleftrightarrow{\chi}(\omega)$ consists of real part $\overleftrightarrow{\chi}'(\omega)$ and imaginary part $\overleftrightarrow{\chi}''(\omega)$ [17, 39, 40]

$$\overleftrightarrow{\chi}(\omega) = \overleftrightarrow{\chi}'(\omega) + i\overleftrightarrow{\chi}''(\omega) \tag{4.15}$$

It follows that

$$Q = 2\omega \overleftrightarrow{\chi}'(\omega)|\vec{E}(\omega)|^2 \tag{4.16}$$

From the above discussion, one can see that the central problem in linear and non-linear spectroscopies in the susceptibility method is the calculation of $\vec{P}(t)$. In the linear case one has to solve [22, 38, 39]

$$\frac{d\hat{\sigma}}{dt} = -\frac{i}{\hbar}[\hat{H}_0, \hat{\sigma}] - \frac{i}{\hbar}[\hat{V}(t), \hat{\sigma}] - \hat{\Gamma}\hat{\sigma} \tag{4.17}$$

Lam Research Ex. 1035 - Page 156
Lam Research Corp. v. Inpria Corp.
IPR2024-00033 - U.S. Patent No. 9,823,564

perturbatively with respect to $\hat{V}(t)$ to the first-order approximation. That is,

$$\hat{\sigma}(t) = \hat{\sigma}^{(0)}(t) + \lambda\hat{\sigma}^{(1)}(t) + \cdots \tag{4.18}$$

and

$$\vec{P}(t) = \mathrm{Tr}(\hat{\sigma}^{(1)}\vec{\mu}) = \mathrm{Tr}(\vec{\mu}\hat{\sigma}^{(1)}) \tag{4.19}$$

A two-level system (n,m) with $E_n > E_m$ shall be used to illustrate the derivation. In this case, Eq. (4.19) becomes

$$\vec{P}(t) = \sigma_{nm}^{(1)}\vec{\mu}_{mn} + \sigma_{mn}^{(1)}\vec{\mu}_{nm} = 2\mathrm{Re}(\sigma_{nm}^{(1)}\vec{\mu}_{mn}) \tag{4.20}$$

Here for simplicity it is assumed that $\vec{\mu}_{nn} = \vec{\mu}_{mm} = 0$. From Eq. (4.17) one obtains

$$\frac{d\sigma_{nm}}{dt} = -(i\omega_{nm} + \gamma_{nm})\sigma_{nm} + \frac{i}{\hbar}V_{nm}(\sigma_{nn} - \sigma_{mm}) \tag{4.21}$$

where γ_{nm} represents the dephasing constant.

Using the RPA,

$$\sigma_{nm}(t) = \sigma_{nm}(\omega)e^{-it\omega} \tag{4.22}$$

one obtains [22,38,39]

$$\frac{d\sigma_{nm}(\omega)}{dt} = -[i(\omega_{nm} - \omega) + \gamma_{nm}]\sigma_{nm}(\omega) - \frac{i}{\hbar}\vec{\mu}_{nm}\cdot\vec{E}(\omega)(\sigma_{nn} - \sigma_{mm}) \tag{4.23}$$

and

$$\frac{d\sigma_{nm}^{(1)}(\omega)}{dt} = -[i(\omega_{nm} - \omega) + \gamma_{nm}]\sigma_{nm}^{(1)}(\omega) - \frac{i}{\hbar}\vec{\mu}_{nm}\cdot\vec{E}(\omega)(\sigma_{nn}^{(0)} - \sigma_{mm}^{(0)}) \tag{4.24}$$

At steady state, it is found that

$$\sigma_{nm}^{(1)}(\omega) = \frac{i\vec{\mu}_{nm}\cdot\vec{E}(\omega)/\hbar}{i(\omega_{nm} - \omega) + \gamma_{nm}}(\sigma_{mm}^{(0)} - \sigma_{nn}^{(0)}) \tag{4.25}$$

and

$$\vec{P}(t) = \frac{(i/\hbar)\vec{\mu}_{mn}\vec{\mu}_{mn}\cdot\vec{E}(\omega)e^{-it\omega}}{i(\omega_{nm} - \omega) + \gamma_{nm}}(\sigma_{mm}^{(0)} - \sigma_{nn}^{(0)}) + \mathrm{c.c.} \tag{4.26}$$

or

$$\overleftrightarrow{\chi}(\omega) = \frac{(i/\hbar)(\vec{\mu}_{mn}\vec{\mu}_{nm})}{i(\omega_{nm} - \omega) + \gamma_{nm}}(\sigma_{mm}^{(0)} - \sigma_{nn}^{(0)}) \tag{4.27}$$

or

$$\overleftrightarrow{\chi}''(\omega) = \frac{1}{\hbar}(\vec{\mu}_{mn}\vec{\mu}_{nm})\frac{\gamma_{nm}}{(\omega_{nm} - \omega)^2 + \gamma_{nm}^2}(\sigma_{mm}^{(0)} - \sigma_{nn}^{(0)}) \tag{4.28}$$

Lam Research Ex. 1035 - Page 157
Lam Research Corp. v. Inpria Corp.
IPR2024-00033 - U.S. Patent No. 9,823,564

Eq. (4.28) implies that the absorption band-shape for $m \rightarrow n$ is Lorentzian with half-width γ_{nm}. In thermal equilibrium, the Boltzmann distributions can be used for $\sigma_{nn}^{(0)}$ and $\sigma_{mm}^{(0)}$. In this case Eq. (4.28) becomes

$$\overleftrightarrow{\chi}''(\omega) = \frac{\vec{\mu}_{mn}\vec{\mu}_{nm}}{\hbar} \frac{\gamma_{nm}}{(\omega_{nm} - \omega)^2 + \gamma_{nm}^2} \tanh \frac{\hbar\omega_{nm}}{2k_{\mathrm{B}}T} \tag{4.29}$$

For an isotropic system, a random orientational average has to be applied to

$$\overleftrightarrow{\chi}''(\omega)$$

. In this case,

$$\overleftrightarrow{\chi}''(\omega) = \frac{|\vec{\mu}_{nm}|^2}{3\hbar} \frac{\gamma_{nm}}{(\omega_{nm} - \omega)^2 + \gamma_{nm}^2} \left(\sigma_{mm}^{(0)} - \sigma_{nn}^{(0)}\right) \tag{4.30}$$

Conventionally the absorption coefficient $\alpha(\omega)$ is commonly used; the relation between $\alpha(\omega)$ and $\overleftrightarrow{\chi}''(\omega)$ is given by [39]

$$\alpha(\omega) = \frac{4\pi\omega}{c}\chi''(\omega) \tag{4.31}$$

In most cases $\sigma_{mm}^{(0)} >> \sigma_{nn}^{(0)}$, i.e.,

$$\overleftrightarrow{\chi}''(\omega) = \frac{|\vec{\mu}_{nm}|^2}{3\hbar} \frac{\gamma_{nm}}{(\omega_{nm} - \omega)^2 + \gamma_{nm}^2} \sigma_{mm}^{(0)} \tag{4.32}$$

or

$$\alpha(\omega) = \frac{4\pi\omega}{3\hbar c} |\vec{\mu}_{nm}|^2 \frac{\gamma_{nm}}{(\omega_{nm} - \omega)^2 + \gamma_{nm}^2} \sigma_{mm}^{(0)} \tag{4.33}$$

The derivation can be generalized; for the transition between the $\{n\}$ and the $\{m\}$ manifolds, one obtains [17,22,41,42]

$$\alpha(\omega) = \frac{4\pi\omega}{3\hbar c} \sum \sum_{m} \sigma_{mm}^{(0)} |\vec{\mu}_{nm}|^2 \frac{\gamma_{nm}}{(\omega_{nm} - \omega)^2 + \gamma_{nm}^2} \tag{4.34}$$

Next, the calculation of molecular absorption spectra in dense media is presented. For the transition between the two vibronic manifolds $\{\mathrm{a}v\} \rightarrow \{\mathrm{b}u\}$, Eq. (4.34) becomes [41,42]

$$\alpha(\omega) = \frac{4\pi^2\omega}{3a\hbar c} \sum_{v} \sum_{u} P_{\mathrm{a}v} |\vec{\mu}_{\mathrm{b}u,\mathrm{a}v}|^2 D(\omega_{\mathrm{b}u,\mathrm{a}v} - \omega) \tag{4.35}$$

where $D(\omega_{\mathrm{b}u,\mathrm{a}v} - \omega)$ represents the line-shape function and

$$\vec{\mu}_{\mathrm{b}u,\mathrm{a}v} = \langle \psi_{\mathrm{b}u} | \vec{\mu} | \psi_{\mathrm{a}v} \rangle = \langle \Theta_{\mathrm{b}u} \Phi_{\mathrm{b}} | \vec{\mu} | \Theta_{\mathrm{a}v} \Phi_{\mathrm{a}} \rangle = \langle \Theta_{\mathrm{b}u} | \vec{\mu}_{\mathrm{ba}} | \Theta_{\mathrm{a}v} \rangle \tag{4.36}$$

Lam Research Ex. 1035 - Page 158
Lam Research Corp. v. Inpria Corp.
IPR2024-00033 - U.S. Patent No. 9,823,564

In the Condon approximation (i.e., for allowed transitions), it is assumed that [17,41,42]

$$\vec{\mu}_{\mathrm{b}u,\mathrm{a}v} = \vec{\mu}_{\mathrm{ba}} \langle \Theta_{\mathrm{b}u} | \Theta_{\mathrm{a}v} \rangle \tag{4.36a}$$

and

$$\alpha(\omega) = \frac{4\pi^2 \omega}{3ahc} |\vec{\mu}_{\mathrm{ba}}|^2 \sum_v \sum_u P_{\mathrm{a}v} |\langle \Theta_{\mathrm{b}u} | \Theta_{\mathrm{a}v} \rangle|^2 D(\omega_{\mathrm{b}u,\mathrm{a}v} - \omega) \tag{4.37}$$

Here the factor a is introduced to take into account the medium effect and $|\langle \Theta_{\mathrm{b}u} | \Theta_{\mathrm{a}v} \rangle|^2$ denotes the FCF.

$\alpha(\omega)$ given by Eq. (4.37) can be simplified in the same manner as that given in Section 3 for thermal average non-adiabatic rate constant. For displaced oscillator surfaces, $\alpha(\omega)$ is given by [17,22,41–43]

$$\alpha(\omega) = \frac{2\pi\omega}{3ahc} |\vec{\mu}_{\mathrm{ba}}|^2 \int_{-\infty}^{\infty} dt \, \exp\Big[it(\omega_{\mathrm{ba}} - \omega) - \gamma_{\mathrm{ba}}|t| - \sum S_i \{ (2\bar{n}_i + 1) - \bar{n}_i \, e^{-it\omega_i} - (\bar{n}_i + 1) e^{it\omega_i} \} \Big] \tag{4.38}$$

For the strong-coupling case, $\sum_i S_i >> 1$, the short-time approximation can be used; in this case Eq. (4.38) becomes

$$\alpha(\omega) = \frac{2\pi\omega}{3ahc} |\vec{\mu}_{\mathrm{ba}}|^2 (2\bar{n}_i + 1) \left[\frac{2\pi}{\sum_i (2\bar{n}_i + 1) S_i \omega_i^2} \right]^{1/2} \exp\left[- \frac{(\omega_{ba} + \sum_i S_i \omega_i - \omega)^2}{2 \sum_i (2\bar{n}_i + 1) S_i \omega_i^2} \right] \tag{4.39}$$

which has a Gaussian form. Eq. (4.39) indicates that the absorption maximum is $\omega_{\mathrm{ba}} + \sum_i S_i \omega_i$ and independent of T, while the band-width $2[2 \ln 2 \sum_i (2\bar{n}_i + 1) S_i \omega_i^2]^{1/2}$ increases with T.

4.2. PUMP–PROBE EXPERIMENTS

A main feature of ultrafast processes under consideration takes place in the time scale shorter than picoseconds. Thus, it is necessary to employ the laser with pulse-duration ~10 fsec to study these ultrafast processes. From the uncertainty principle $\Delta E \cdot \Delta t \sim \hbar/2$ it can be seen that using this pulse-duration, numerous vibronic states can be coherently pumped (or excited) and thus the probing signal in a pump–probe experiment will contain the information of the dynamics of both population and coherence (or phase). In other words, in order to obtain the information of ultrafast dynamics it is

Lam Research Ex. 1035 - Page 159
Lam Research Corp. v. Inpria Corp.
IPR2024-00033 - U.S. Patent No. 9,823,564

necessary to carefully analyze the probing signal (usually in the form of femtosecond time-resolved spectra). Theoretical description of ultrafast pump–probe experiment is presented in the following by using the *generalized linear response theory* (GLRT) [1,38,44–49].

It has been shown that for the case in which the pumping and probing lasers do not overlap, one can use the GLRT. In this section, it shall be shown how the GLRT can be applied to calculate the ultrafast time-resolved spectra. For this purpose, start from the stochastic Liouville equation to describe the EOM for the density matrix $\hat{\sigma}(t)$ of the system embedded in a heat bath

$$\frac{d\hat{\sigma}}{dt} = -i\hat{L}_0\hat{\sigma} - \frac{i}{\hbar}[\hat{V}(t), \hat{\sigma}] - \hat{\Gamma}\hat{\sigma} = -i\hat{L}_0'\hat{\sigma} - i\hat{L}'\hat{\sigma}; \quad \hat{L}_0' = \hat{L}_0 - i\hat{\Gamma} \tag{4.40}$$

where $\hat{L}_0$, $\hat{V}(t)$ and $\hat{\Gamma}$ represent the Liouville operator of the system, interaction between the system and the probing laser, and the damping operator, respectively. Letting

$$\hat{\sigma} = e^{-it\hat{L}_0'}\hat{\sigma}^{(r)} \tag{4.41}$$

one obtains

$$\frac{d\hat{\sigma}^{(r)}}{dt} = -i\hat{\tilde{L}}'(t)\hat{\sigma}^{(r)} \tag{4.42}$$

where

$$\hat{\tilde{L}}'(t) = e^{it\hat{L}_0'}\hat{L}'(t)e^{-it\hat{L}_0'} \tag{4.43}$$

The EOM of $\hat{\sigma}^{(r)}$ can be formally integrated:

$$\hat{\sigma}^{(r)}(t) = \hat{\sigma}_{\mathrm{i}}^{(r)} - i\int_{t_{\mathrm{i}}}^{t} d\tau\hat{\tilde{L}}'(\tau)\hat{\sigma}^{(r)}(\tau) \tag{4.44}$$

Applying the perturbation method, the first-order solution is given by

$$\hat{\sigma}^{(r)}(t) = e^{-it\hat{L}_0'}\hat{\sigma}^{(r)}(t)^{(1)} = -i\int_{t_{\mathrm{i}}}^{t} d\tau\, e^{-i(t-\tau)\hat{L}_0'}\hat{L}'(\tau)e^{-i(\tau-t_{\mathrm{i}})\hat{L}_0'}\hat{\sigma}_{\mathrm{i}} \tag{4.45}$$

where t_{i} is the initial time of the process and $\hat{\sigma}_{\mathrm{i}} = \hat{\sigma}(t_{\mathrm{i}})$. In our case, the pump and probe pulses do not overlap each other. t_{i} is a moment after the pump pulse completely passed.

Next, the polarization $\vec{P}(t)$ can be calculated. Consider the polarization due to the transitions between the two electronic manifolds $\{\ell\}$ and $\{m\}$, where $\{m\}$ is the upper manifold; to the first order, one obtains

$$\vec{P}(t) = \vec{P}^{(1)}(t) = \mathrm{Tr}[\vec{\mu}\hat{\sigma}^{(1)}(t)] = \sum_{\ell}\sum_{m}\sigma_{\ell m}^{(1)}(t)\vec{\mu}_{m\ell} \tag{4.46}$$

Lam Research Ex. 1035 - Page 160
Lam Research Corp. v. Inpria Corp.
IPR2024-00033 - U.S. Patent No. 9,823,564

where

$$\sigma^{(1)}_{\ell m}(t) = -\frac{i}{\hbar}\int_{t_i}^{t} d\tau\, e^{-i(t-\tau)\omega'_{\ell m}} \times \left\{ \sum_{m'} V(\tau)_{\ell m'} e^{-i(\tau-t_i)\omega'_{m'm}} (\hat{\sigma}_i)_{m'm} - \sum_{\ell'} V(\tau)_{\ell' m} e^{-i(\tau-t_i)\omega'_{\ell\ell'}} (\hat{\sigma}_i)_{\ell\ell'} \right\} \tag{4.47}$$

Here, for example, $\omega'_{mk} \equiv \omega_{mk} - i\gamma_{mk}$ and γ_{mk} is the dephasing constant. Since the system is initially prepared in the $\{\ell\}$ manifold, the first term in the bracket involving $(\hat{\sigma}_i)_{m'm}$ can be removed. In other words,

$$\sigma^{(1)}_{\ell m}(t) = -\frac{i}{\hbar} e^{-it\omega'_{\ell m}} \sum_{\ell'} e^{-it_i\omega'_{\ell\ell'}} (\hat{\sigma}_i)_{\ell\ell'} \int_{t_i}^{t} d\tau\, e^{-i(t-\tau)\omega'_{\ell m}} V(\tau)_{\ell' m} \tag{4.48}$$

The interaction V considered here is the dipole interaction of the system with the applied radiation field of the probing laser, i.e.,

$$V(\tau)_{\ell' m} = -\vec{\mu}_{\ell' m} \cdot [\vec{E}_0(\omega) e^{-i\tau\omega} + \vec{E}_0(-\omega) e^{i\tau\omega}] \tag{4.49}$$

where ω is the frequency of the radiation field. In this case, one obtains

$$\sigma^{(1)}_{\ell m}(t) = -\frac{1}{\hbar} \sum_{\ell'} \sigma(\Delta t)_{\ell\ell'} \frac{\vec{\mu}_{\ell' m}}{\omega + \omega'_{\ell' m}} \cdot \vec{E}_0(-\omega) e^{it\omega} \tag{4.50}$$

where $\Delta t = t - t_i$. The polarization is

$$\vec{P}(t) = \frac{-1}{\hbar} \sum_{\ell} \sum_{\ell'} \sum_{m} \sigma(\Delta t)_{\ell\ell'} \frac{\vec{\mu}_{\ell' m} \vec{\mu}_{m\ell}}{\omega + \omega'_{\ell m} + i\gamma_{\ell m}} \cdot \vec{E}_0(-\omega) e^{it\omega} + \text{c.c.} \tag{4.51}$$

From Eq. (4.51) one can derive the susceptibility

$$\overleftrightarrow{\chi}(\omega) = \frac{-1}{\hbar} \sum_{\ell} \sum_{\ell'} \sum_{m} \sigma(\Delta t)_{\ell\ell'} \frac{\vec{\mu}_{\ell' m} \vec{\mu}_{m\ell}}{\omega + \omega'_{\ell m} + i\gamma_{\ell m}} \tag{4.52}$$

As can be seen from Eq. (4.52), the dynamics of both population (i.e., $\sigma_{\ell\ell}(\Delta t)$) and coherence (i.e., $\sigma_{\ell\ell'}(\Delta t)$ with $\ell' \neq \ell$) is involved in the time-resolved measurement and Eq. (4.52) can be applied to optical absorption and stimulated emission (SE). Furthermore, the ordinary linear response theory is recovered when $\sigma_{\ell\ell'} = 0$ and $\sigma_{\ell\ell}$ represents the Boltzmann distribution.

Next, consider the effect of pumping laser. With a short pulse pumping laser, both population excitation and coherence excitation can be created and the non-adiabatic processes like PIET can take place afterwards. With a similar derivation as that shown in this section one obtains the coherence created by the pumping laser with electric field $\vec{E}_{pu}$ and frequency ω_{pu}

Lam Research Ex. 1035 - Page 161
Lam Research Corp. v. Inpria Corp.
IPR2024-00033 - U.S. Patent No. 9,823,564

as [22,38,44–49]

$$\sigma_{\ell\ell'}(t_{\rm i}) = \frac{\tau_{pu}^2}{\hbar^2}[\vec{\mu}_{\ell g}\cdot\vec{E}^{(0)}_{pu}(\omega_{pu})][\vec{\mu}_{g\ell'}\cdot\vec{E}^{(0)}_{pu}(-\omega_{pu})](\hat{\sigma}_0)_{gg} \tag{4.53}$$

where τ_{pu} denotes the pump–laser pulse-duration. $\hat{\sigma}_0$ is the density matrix of the system before the arrival of the pump pulse. Here it is assumed that initially only the g-state is populated. $\sigma_{\ell\ell}(t_{\rm i})$ is a particular case of $\sigma_{\ell\ell'}(t_{\rm i})$ by setting $\ell' = \ell$.

Eq. (4.53) shows that $\sigma_{\ell\ell'}(t_{\rm i})$, which is involved in $\overleftrightarrow{\chi}(\omega)$ in the GLRT, is proportional to $\vec{E}^{(0)}_{pu}(\omega_{pu})\vec{E}^{(0)}_{pu}(-\omega_{pu})$. This indicates that $\vec{P}(t)$ in the GLRT varies with $\vec{E}_{\rm p}(\omega)$ and $\vec{E}^{(0)}_{pu}(\omega_{pu})\vec{E}^{(0)}_{pu}(-\omega_{pu})$. That is, according to the GLRT (see Eq. (4.53)) the linear susceptibility $\overleftrightarrow{\chi}(\omega)$ due to the probing laser varies with time t through $\sigma_{\ell\ell'}(\Delta t)$ (i.e., the dynamics of the system) which in turn varies with $\vec{E}^{(0)}_{pu}(\omega_{pu})\vec{E}^{(0)}_{pu}(-\omega_{pu})$ of the pumping pulse, and this makes the $\overleftrightarrow{\chi}(\omega)$ change into $\overleftrightarrow{\chi}^{(3)}(\omega, -\omega_{pu}, \omega_{pu})$.

From the above discussion one can see that due to $\sigma_{\ell\ell'}(\Delta t)$ the measurement of $\overleftrightarrow{\chi}(\omega)$ will exhibit quantum beat; the beat frequency is $|\omega_{\ell\ell'}|$ while the beat width is approximately dependent on its dephasing constant. From Eq. (4.53) it can be seen that the ultrafast dynamics of population and coherence appears in $\sigma_{\ell\ell'}(\Delta t)$ in which $\sigma_{\ell\ell'}(t_{\rm i})$ play the role of initial condition, created by the pumping laser.

As one of the alternative methods for treating ultrafast pump–probe experiments [50], the third-order susceptibility method is often used. A main feature of this method is that it can treat the case of the overlapping region between the pump and the probe lasers, but one has to carry out the perturbation calculations to the third-order approximations.

Next, the GLRT shall be applied to analyze the femtosecond time-resolved spectra. Suppose that the probing process corresponds to SE, the relations between the different electronic levels in this case are shown in Figure 5.1. The non-adiabatic process is represented by a → b and SE is from a to g. Notice that in the BOA

$$\psi_{a\vec{v}} = \Phi_a(\vec{q},\vec{Q})\Theta_{a\vec{v}}(\vec{Q}); \quad \Theta_{a\vec{v}}(\vec{Q}) = \prod_j \chi_{av_j}(Q_j) \tag{4.54}$$

and

$$\psi_{g\vec{w}} = \Phi_g(\vec{q},\vec{Q}'')\Theta_{g\vec{w}}(\vec{Q}''); \quad \Theta_{g\vec{w}}(\vec{Q}'') = \prod_j \chi_{gw_j}(Q_j'') \tag{4.55}$$

Lam Research Ex. 1035 - Page 162
Lam Research Corp. v. Inpria Corp.
IPR2024-00033 - U.S. Patent No. 9,823,564

it can be found that

$$\overleftrightarrow{\chi}(\omega,t)=\frac{-1}{\hbar}\sum_{\vec{v}}\sum_{\vec{v}'}\sum_{\vec{w}}\sigma(\Delta t)_{\mathrm{a}\vec{v},\mathrm{a}\vec{v}'}\frac{\vec{\mu}_{\mathrm{a}\vec{v}',\mathrm{g}\vec{w}}\vec{\mu}_{\mathrm{g}\vec{w},\mathrm{a}\vec{v}}}{-\omega+\omega_{\mathrm{a}\vec{v},\mathrm{g}\vec{w}}+i\gamma_{\mathrm{a}\vec{v},\mathrm{g}\vec{w}}} \tag{4.56}$$

Here $\vec{q}$ denotes the electronic coordinates, and $\vec{Q}$ and $\vec{Q}''$ the full sets of nuclear normal coordinates in the photo-excited (a) and ground (g) electronic states. Φ_{a} and Φ_{g} are the electronic wavefunctions. $\Theta_{\mathrm{a}\vec{v}}$ and $\Theta_{\mathrm{g}\vec{w}}$ are the full nuclear wavefunctions of the two different electronic states, each of which can be decomposed into products of single-mode wavefunctions $\chi_{\mathrm{a}v_j}$ and $\chi_{\mathrm{g}w_j}$, respectively. Initially the coherence is created by the pumping process, i.e.,

$$(\hat{\sigma}_{\mathrm{i}})_{\mathrm{a}\vec{v},\mathrm{a}\vec{v}'}=\frac{\tau_{\mathrm{p}u}^2}{\hbar^2}(\vec{\mu}_{\mathrm{a}\vec{v},\mathrm{g}\vec{0}}\cdot\vec{E}_{\mathrm{p}u}(\omega))(\vec{\mu}_{\mathrm{g}\vec{0},\mathrm{a}\vec{v}'}\cdot\vec{E}_{\mathrm{p}u}(-\omega))(\hat{\sigma}_0)_{\mathrm{g}\vec{0},\mathrm{g}\vec{0}} \tag{4.57}$$

From Eq. (4.56) one sees that the observed time-resolved spectra include the contributions from both population $\sigma(\Delta t)_{\mathrm{a}\vec{v},\mathrm{a}\vec{v}}$ and vibrational coherence $\sigma(\Delta t)_{\mathrm{a}\vec{v},\mathrm{a}\vec{v}'}$ where $\vec{v}\neq\vec{v}'$.

It should be noted that due to $\sigma(\Delta t)_{\mathrm{a}\vec{v},\mathrm{a}\vec{v}'}$ the Fourier transform of $\overleftrightarrow{\chi}(\omega,t)$ will yield a Lorentzian band-shape with the band-width determined by the dephasing constant of $\sigma(\Delta t)_{\mathrm{a}\vec{v},\mathrm{a}\vec{v}'}$ and the areas of different Fourier transform bands are approximately proportional to the FCFs $|\langle\Theta_{\mathrm{a}\vec{v}}|\Theta_{\mathrm{g}\vec{0}}\rangle|^2|\langle\Theta_{\mathrm{a}\vec{v}'}|\Theta_{\mathrm{g}\vec{0}}\rangle|^2$. For the single displaced oscillator case, for example, $|\langle\chi_{\mathrm{a}0}|\chi_{\mathrm{g}0}\rangle|^2|\langle\chi_{\mathrm{a}1}|\chi_{\mathrm{g}0}\rangle|^2=S\,e^{-2S}$, where S is the Huang–Rhys factor of this mode.

In the following, the way to calculate the band-shape function of femtosecond time-resolved spectra (i.e., involving the contributions of both population and coherence dynamics) for the displaced harmonic potential surfaces shall be presented. For allowed transitions a $\rightarrow$ n where n is the ground state g in the case of SE and it is a higher excited state in the case of induced absorption, Eq. (4.56) becomes

$$\overleftrightarrow{\chi}(\omega,\Delta t)=-\frac{\vec{\mu}_{\mathrm{an}}\vec{\mu}_{\mathrm{na}}}{\hbar}\sum_{\vec{v}}\sum_{\vec{v}'}\sum_{\vec{u}}\sigma(\Delta t)_{\mathrm{a}\vec{v},\mathrm{a}\vec{v}'}\frac{\langle\Theta_{\mathrm{a}\vec{v}'}|\Theta_{\mathrm{n}\vec{u}}\rangle\langle\Theta_{\mathrm{n}\vec{u}}|\Theta_{\mathrm{a}\vec{v}}\rangle}{\omega_{\mathrm{a}\vec{v},\mathrm{n}\vec{u}}-\omega+i\gamma_{\mathrm{a}\vec{v},\mathrm{n}\vec{u}}} \tag{4.58}$$

which can be rewritten as

$$\overleftrightarrow{\chi}(\omega,\Delta t)=i\frac{\vec{\mu}_{\mathrm{an}}\vec{\mu}_{\mathrm{na}}}{\hbar}\sum_{\vec{v}}\sum_{\vec{v}'}\sigma(\Delta t)_{a\vec{v},a\vec{v}'}\int_0^\infty dt\,e^{-it(\omega-\omega_{\mathrm{an}}-i\gamma_{\mathrm{an}})}\prod_j G_{\mathrm{a}v_j',\mathrm{a}v_j}(t) \tag{4.59}$$

where

$$G_{\mathrm{a}v_j',\mathrm{a}v_j}(t)=\sum_{u_j}e^{it(v_j+1/2)\omega_j}\,e^{-it(u_j+1/2)\omega_j'}\langle\chi_{\mathrm{a}v_j'}|\chi_{\mathrm{n}u_j}\rangle\langle\chi_{\mathrm{n}u_j}|\chi_{\mathrm{a}v_j}\rangle \tag{4.60}$$

Lam Research Ex. 1035 - Page 163
Lam Research Corp. v. Inpria Corp.
IPR2024-00033 - U.S. Patent No. 9,823,564

In Appendix B, the detail of how to compute the TCF $G_{a v'_j, a v_j}(t)$ is shown. The result is

$$G_{a v'_j, a v_j}(t) = (-)^{v_j+v'_j} \sqrt{\frac{v_j! v'_j!}{2^{v_j+v'_j}}} e^{i v_j \omega_j t} \, e^{-S_j(1-e^{-i\omega_j t})} \sum_{m_j=0}^{\min(v_j, v'_j)} \frac{(2e^{-i\omega_j t})^{m_j} \kappa_j^{v_j+v'_j-2m_j}}{m_j!(v_j-m_j)!(v'_j-m_j)!} \tag{4.61}$$

where

$$\kappa_j \equiv \sqrt{\beta_j} d_j (1 - e^{-i\omega_j t}) \tag{4.62}$$

and $\beta_j = \omega_j/\hbar$.

5. An Example — Interfacial Electron Transfer in Organic Solar Cells

In recent years, ET dynamics at the sensitizer–semiconductor nanoparticle interface has been intensively studied [51,52]. In addition to its fundamental importance, understanding the interfacial ET is also crucial to the development of numerous nanoparticle-based devices, such as molecular electronics [53,54] and solar cells based on composites of molecular and nanostructured semiconductor components [55–57].

By using transient absorption spectroscopic techniques, time-resolved measurements of photo-induced interfacial ET with time-constants shorter than 100 fsec have become possible [51,52,58–60]. When ultrashort laser pulses are used in studying PIET, vibrational coherences (or vibrational wave packet) can often be observed and have indeed been observed in a number of dye-sensitized solar cell systems. This type of quantum beat has also been observed in ultrafast PIET in photosynthetic reaction center [22]. It should be noted that when the PIET takes place in the time scale shorter than 100 fsec, vibrational relaxation between the system and the heat bath is slower than PIET; this is the so-called vibrationally non-relaxed ET case, and it will be treated in this section.

To treat PIET, the theoretical framework in which it is regarded as transitions between two potential energy surfaces (PES) shall be employed, and the PESs are obtained by using the BOA. Using this theoretical framework it shall be shown that for the case in which vibrational relaxation between the system and the heat bath is much faster than PIET so that vibrational equilibrium (i.e., thermal equilibrium) is established before PIET

Lam Research Ex. 1035 - Page 164
Lam Research Corp. v. Inpria Corp.
IPR2024-00033 - U.S. Patent No. 9,823,564

takes place, the Marcus equation can be derived under certain approximations. For the case in which PIET is faster than vibrational relaxation, one has to deal with the calculation of the PIET rate originated from the vibronic levels prepared by the pumping laser, i.e., the single-vibronic-level rate constant. It is the purpose of this section to present the calculation of the single-vibronic-level rate constant for PIET.

Thoss et al. [61] have considered the similar kind of system and numerically solved the Liouville equation of the vibronic process via a so-called self-consistent hybrid method (SCH). Their work represents an attempt to consider the vibrational degrees of freedom as well as the electronic degrees of freedom quantum mechanically at the same time. Some other workers have employed the so-called non-adiabatic molecular dynamics method to simulate the effect of nuclear motion on the ET process [62,63]. Willig and coworkers [64–67] employed a model similar to that of Thoss et al. and solved the Schrödinger equation of the system numerically. They did not treat the semiconductor part explicitly like Thoss et al. did, and since it is the Schrödinger equation that they solved, they did not consider the effect of coherence dephasing. Their results are also limited to the one vibrational mode case. Our effort in this section is to provide an analytical expression for the single-vibronic-level electron transfer rate that can be used in different methods of treating PIET, such as the GLRT [22,38] which is based on the density matrix method. Multi-vibrational mode case can be easily studied with this expression.

5.1. Experimental Results and Theoretical Analysis

To show the applications of the theoretical results presented in the previous sections, the DTB-Pe/TiO_2 system shall be used as an example [58]. DTB-Pe (2,5-di-*tert*-butyl-9-perylenyl-methyl-phosphonic acid) is a derivative of perylene in which the perylenyl group works as the chromophore and there are side-groups for preventing the formation of chromophore complex, as well as linker group for chemisorption on TiO_2 surface. From Figure 5.4 one can see that for the electrode to be effective one should choose an organic dye molecule with absorption spectra compatible with the solar spectra and large absorption coefficient. The dye molecules should be chemisorbed on the semiconductor nanoparticle surfaces. To avoid the close contact between dye molecules, alkyl groups are usually introduced into the dye molecule. Another condition that needs to be considered is the relative location of the conduction band of nanoparticles with respect to the excited state of the dye molecule. From the configurations of the electrode shown in

Lam Research Ex. 1035 - Page 165
Lam Research Corp. v. Inpria Corp.
IPR2024-00033 - U.S. Patent No. 9,823,564

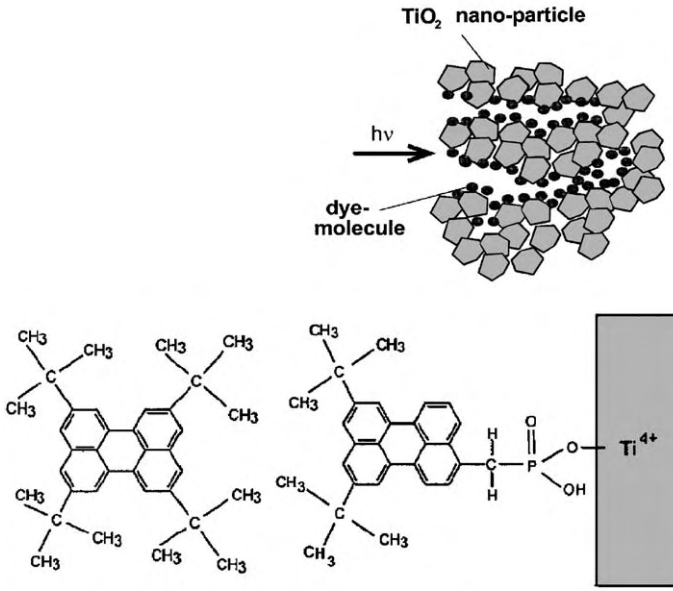


Fig. 5.4. The structure of DTB-Pe, the way it adsorbs on TiO_2 surface and the schematic representation of the structure of the thin film layer of TiO_2 nanoparticles on top of the electrode in a dye-sensitized solar cell, with dye molecules adsorbed on it. (Reprinted with permission from Ref. [58]. Copyright 2001 American Chemical Society.)

Figure 5.4, one can easily understand why the interfacial electron transfer should take place in the 10–100 fsec range because this ET process should be faster than the photo-luminescence of the dye molecules and energy transfer between the molecules. Recently Zimmermann et al. [58] have employed the 20 fsec laser pulses to study the ET dynamics in the DTB-Pe/TiO_2 system and for comparison, they have also studied the excited-state dynamics of free perylene in toluene solution. Limited by the 20 fsec pulse-duration, from the uncertainty principle, they can only observe the vibrational coherences (i.e., vibrational wave packets) of low-frequency modes (see Figure 5.5). Six significant modes, 275, 360, 420, 460, 500 and 625 cm^{-1}, have been resolved from the Fourier transform spectra of ultrashort pulse measurements. The Fourier transform spectrum has also been compared with the Raman spectrum. A good agreement can be seen (Figure 5.5). For detail of the analysis of the quantum beat, refer to Figures 5.5–5.7 of Zimmermann et al.'s paper [58]. These modes should play an important role not only in ET dynamics or excited-state dynamics, but also in absorption spectra. Therefore, the steady state absorption spectra of DTB-Pe, both in

Lam Research Ex. 1035 - Page 166
Lam Research Corp. v. Inpria Corp.
IPR2024-00033 - U.S. Patent No. 9,823,564

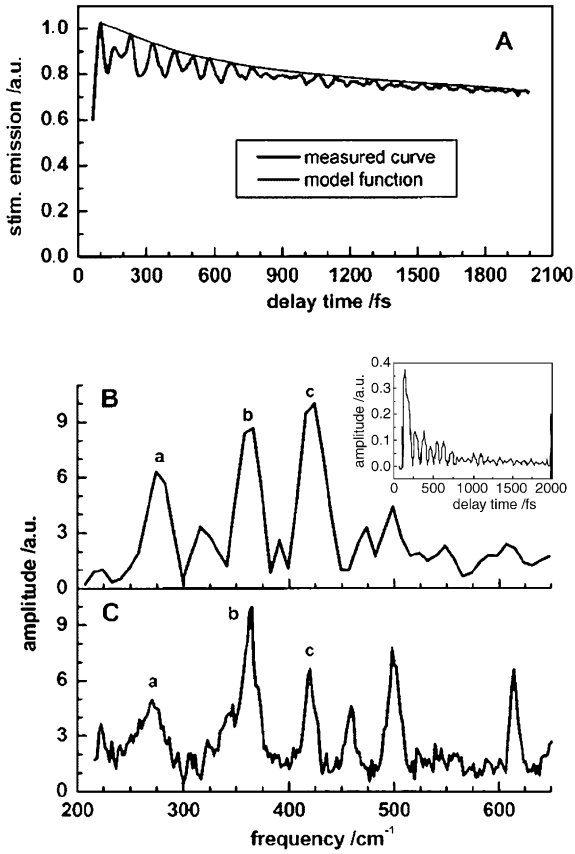


Fig. 5.5. (A) Strong oscillations in the stimulated emission signal at 470 nm due to wave-packet motion in the excited state of perylene (TTB-Pe, $\lambda_{EX} = 435$ nm, measured in toluene). The thin line gives a smooth fit connecting the upper peak values of the oscillations. (B) Fourier transform of the oscillatory part of the emission signal shown in the inset. (C) Raman spectrum of the perylene dye (dry powder). (Reprinted with permission from Ref. [58]. Copyright 2001 American Chemical Society.)

toluene solution and on TiO_2 surface, determine the properties of these vibrational modes. To reduce the number of parameters in the model, however, the modes of 460, 500 and 625 cm^{-1}, which are comparatively weak in the quantum beat amplitude, are grouped into one average mode of frequency 530 cm^{-1}. From the vibronic structures of absorption spectra one can obtain two additional modes, 1500 and 3000 cm^{-1}. Notice that these two modes cannot be observed in the quantum beat in this experiment. Using these modes with their corresponding Huang–Rhys factors shown in

Lam Research Ex. 1035 - Page 167
Lam Research Corp. v. Inpria Corp.
IPR2024-00033 - U.S. Patent No. 9,823,564

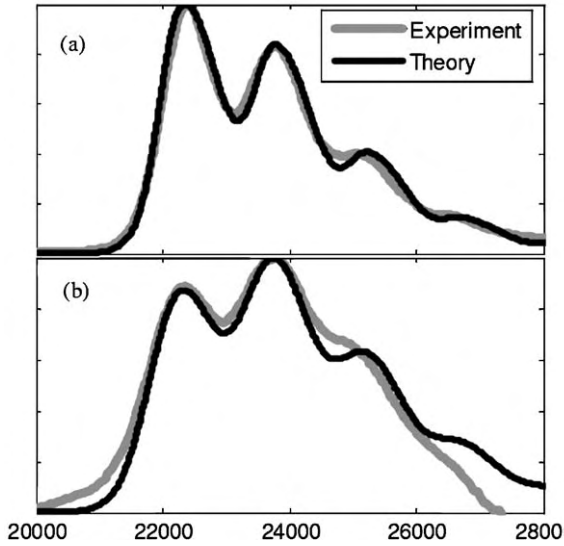


Fig. 5.6. Experimentally observed absorption spectra of DTB-Pe molecule (blue line) and the theoretical fitting (black line) with parameters given in Table 5.1. (a) The result in toluene solution and (b) the result on TiO_2 surface. The 0–0 transition energies are 22,070 cm^{-1} in the toluene solution and 21,950 cm^{-1} on TiO_2 surface.

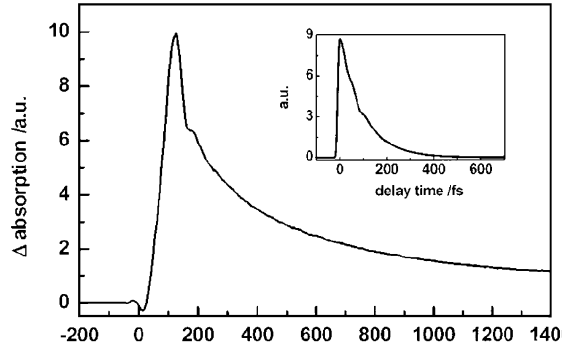


Fig. 5.7. Decay of the excited-state absorption at 715 nm of the perylene chromophore attached to the TiO_2 surface (DTB-Pe, $\lambda_{EX} = 429$ nm). The inset shows a calculated decay curve neglecting a contribution from the absorption of the cation at the probe wavelength. (Reprinted with permission from Ref. [58]. Copyright 2001 American Chemical Society.)

Table 5.1, the absorption spectra of perylene–toluene solution and the perylene–TiO_2 system are reconstructed (see Figure 5.6a and b). The experimental absorption spectra are obtained from those published by Zimmermann in the aforementioned paper.

Lam Research Ex. 1035 - Page 168
Lam Research Corp. v. Inpria Corp.
IPR2024-00033 - U.S. Patent No. 9,823,564

Table 5.1. The parameters of the vibrational modes used in the fitting of the absorption spectra of DTB-Pe molecule in toluene solution and on TiO_2 surface

	Mode							Inhomogeneity (d/cm^{-1})
	1	2	3	4	5	6	7	
	3000[a]	1500[a]	530[a]	420[a]	360[a]	275[a]	30[a]	
S (in toluene)	0.05	0.72	0.3	0.2	0.2	0.2	2.5	250
S (on TiO_2)	0.05	1.0	0.3	0.2	0.2	0.2	3.0	450

Note: The S value is the Huang–Rhys factor, or the (vibronic) coupling constant.
[a]Frequency (cm^{-1}).

The expression of the absorption coefficient from the initial electronic level a to upper electronic level b in the multi-displaced-mode case is [22]:

$$\alpha(\omega) = \frac{2\pi|\vec{\mu}_{ba}|^2\omega}{3\hbar c}\int_{-\infty}^{\infty} dt\ \exp\left\{it(\bar{\omega}_{ba}-\omega) - \frac{d^2t^2}{4} - \sum_j S_j[2\bar{n}_j + 1 - \bar{n}_j\, e^{-it\omega_j} - (\bar{n}_j+1)e^{it\omega_j}]\right\} \tag{5.1}$$

where d describes the width of inhomogeneity distribution and c the light speed in vacuum. The 0–0 transition energy $\bar{\omega}_{ba}$ is 22,070 cm^{-1} in the solution and 21,950 cm^{-1} on TiO_2 surface. The agreement between experimental and calculated spectra is quite reasonable. Note that for the purpose of fitting, we also included a 30 cm^{-1} mode, which displays the effect of all possible low-frequency modes. This 30 cm^{-1} mode is not considered in the computations of ET rates. Recently Wang et al. [68] also analyzed the absorption spectra of a series of DTB-Pe dyes in solution and on TiO_2 surface with different linker groups. To fit the spectra they introduced a single-vibrational mode model with only a 1370 cm^{-1} mode which is assigned to a perylene in-plane C–C stretching mode. In the present work, those vibrational modes below 600 cm^{-1} that are involved in the quantum beat are included. The effect of the 1370 cm^{-1} mode introduced by Wang has a large displacement and it has similar effect on the fitting as the strong-coupling mode 1500 cm^{-1} we use here.

The role of the inhomogeneity d is also important. The effect of the inhomogeneity term is subtly different from other effects such as the strong-coupling low-frequency modes. The values of 250 and 450 cm^{-1} used here for DTB-Pe in solution and DTB-Pe/TiO_2, respectively, were obtained with little ambiguity in the fitting. Therefore, we believe that the increase of d by 200 cm^{-1} from the solution case to the adsorbed case reflects the real order of magnitude of the increase in inhomogeneity on the surface. Such an

Lam Research Ex. 1035 - Page 169
Lam Research Corp. v. Inpria Corp.
IPR2024-00033 - U.S. Patent No. 9,823,564

increase of inhomogeneity, as well as the shift of the absorption band origins, can usually be related to the interaction between the chromophore and the surface. In other words, our fitting indicates that the coupling between the photo-excited state (which is the initial state of the PIET process) and the surface is between 100 and 200 cm^{-1}.

In summary, some information concerning the properties of the vibrational modes relevant to the PIET process as well as the interaction of the dye molecule with the TiO_2 surface is revealed through the fitting of the absorption spectra.

Zimmermann et al. have also performed the femtosecond time-resolved measurements to study the ET of DTB-Pe/TiO_2 system (Figures 5.7 and 5.8). Figure 5.7 shows the studies of the ultrafast PIET process by measuring the decay of the excited-state absorption at 715 nm of the perylene chromophore attached to the TiO_2 surface using $\lambda_{EX} = 429$ nm. Similarly Figure 5.8 shows the studies of the PIET dynamic behavior by measuring the transient absorption at 575 nm of ionized perylene (the product state of ET from the dye molecule to TiO_2) using $\lambda_{ET} = 430$ nm.

To simulate the ET process in the DTB-Pe/TiO_2 system, however, one needs to know the vibrational modes which can be divided into pumping modes and accepting modes. In addition to the eight modes obtained from the analysis of absorption spectra, there may be some high frequency accepting modes participating in ET, but the Huang–Rhys factors for these high frequency modes are usually very small and thus these modes will not be included in our ET rate calculations. In the DTB-Pe/TiO_2 case, even though the initial excited electronic state is well defined, the final charge-transfer state and its density of state distribution are unclear. In this work, a Gaussian distribution of density of states is used to represent the final state. Another functional form of the density of states like

$$g(E) = \frac{\sqrt{E}}{2\pi^2}\left(\frac{2m^*}{\hbar}\right)^{3/2} \tag{5.2}$$

has been used by Anderson and Lian [53].

It should be noted that the ultrafast PIET is usually studied by the pump–probe experiment using ultrashort laser pulses. The probe signals usually include the dynamic information of both coherence and population and to obtain the PIET rate, a theoretical analysis of these signals is required. This has been accomplished for the studies of ultrafast PIET in bacterial photosynthetic reaction centers [22].

Next, we shall present the model calculation of the PIET dynamics as observed through transient spectra. In this process, five different electronic levels are involved, each having a specific potential energy curve. These levels

Lam Research Ex. 1035 - Page 170
Lam Research Corp. v. Inpria Corp.
IPR2024-00033 - U.S. Patent No. 9,823,564

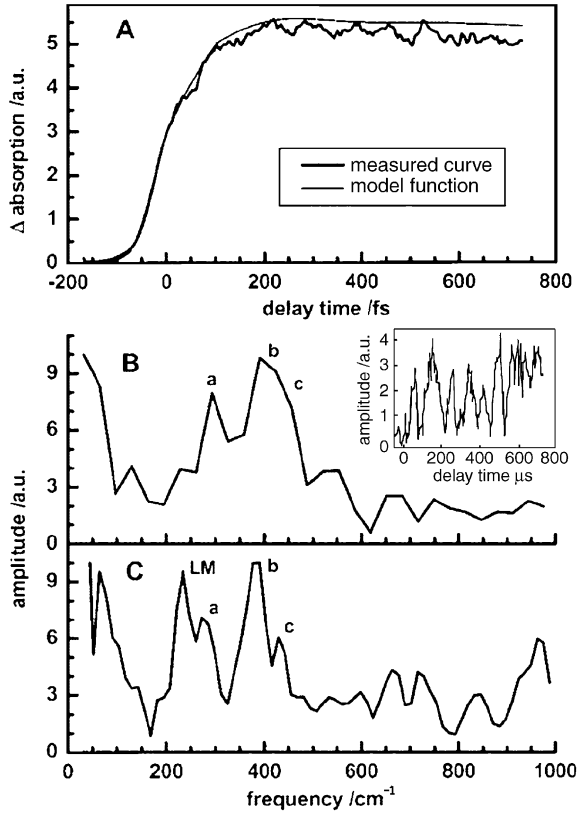


Fig. 5.8. (A) Transient absorption at 575 nm of ionized perylene as product state of electron transfer to TiO_2 (DTP-Pe, $\lambda_{EX} = 430$ nm). The thin line gives a smooth fit connecting the upper peak values of the oscillations. (B) Fourier transform of the oscillatory part of the absorption signal shown in the inset. (C) Fourier transform of the oscillatory part in the transient excited-state absorption at 715 nm of the same dye DTB-Pe in toluene. (Reprinted with permission from Ref. [58]. Copyright 2001 American Chemical Society.)

are: the ground electronic state g; the directly photo-excited-state S_1 (the initial state of the ET reaction) which is assumed to be neutral; the neutral higher excited electronic level S_n which is the final state of the induced absorption from S_1; the charge-separate state CT_1 which is the final state of the ET reaction; and the higher excited charge-separated electronic level CT_n which is the final state of the induced absorption from CT_1. Therefore, numerous parameters are involved in the model. Some of the parameters, such as the PESs of g and S_1, were determined through fitting the steady state spectra. Most of the other parameters are unknown due to the lack of experimental characterization and theoretical studies. We choose to demonstrate the typical

Lam Research Ex. 1035 - Page 171
Lam Research Corp. v. Inpria Corp.
IPR2024-00033 - U.S. Patent No. 9,823,564

behavior of a PIET process by studying a one vibrational mode system instead of using a multi-mode model as that used in fitting the absorption spectra. Hopefully the effect of each parameter will be clearer in the result for us to gain qualitative understanding of the beating phenomenon.

In the calculations, it is assumed that the pumping laser only excites the system from the ground state to the first two vibrational levels of S_1 state. These two levels are coherently excited. Then the Liouville equation of the system is integrated out to obtain the time dependence of the population of the S_1 and CT_1 levels, the coherence within respective levels and the coherence between them. For each moment of time, the band-shape functions of transition between S_1 and S_n and between CT_1 and CT_n together with the density matrix elements of each electronic levels are used to calculate the susceptibility $\chi(\omega, t)$, whose imaginary part is proportional to the absorption spectra (see Section 4). The relative energies of the electronic levels in our calculation are listed in Table 5.2. The energy gaps between S_n and S_1 and those between CT_n and CT_1 only affect the position of the induced spectral features. The energy gap between S_1 and CT_1, instead, strongly influences the PIET dynamics. Therefore, it is changed in the calculation and will be discussed later.

First we use one vibrational mode with frequency $420\,cm^{-1}$ in the calculation. The coupling constants between different electronic PESs are given in Table 5.3. Most of the couplings are very weak. The coupling between the CT_n surface and CT_1 is larger but it only influences the line shape of the induced absorption from CT_1. Weak coupling constants were assumed, first, in accordance with the characteristics of the absorption spectra and, second, to make the trend of the demonstrative calculations simpler. Indeed, strong-coupling cases present more sophisticated dynamics,

Table 5.2. The energy gaps of the transitions

Transition	$S_1 \leftarrow g$	$S_n \leftarrow S_1$	
Energy gap (cm^{-1})	24,850	14,000	17,250

Table 5.3. The coupling constant S between different electronic potential surfaces and the inhomogeneity in calculating the transient absorption spectra

	Transition			
	$S_1 \leftarrow g$	$CT_1 \leftarrow S_1$	$S_n \leftarrow S_1$	$CT_n \leftarrow CT_1$
S	0.3	0.5	0.05	1
Inhomogeneity (cm^{-1})			450	1300

Lam Research Ex. 1035 - Page 172
Lam Research Corp. v. Inpria Corp.
IPR2024-00033 - U.S. Patent No. 9,823,564

and those phenomena are too complicated to be discussed in the length of the present article. It shall be left to be discussed in later articles focusing on specific systems. Besides, later the frequency of the vibrational mode will also be changed, but the parameters of the PESs will be kept constant for simplicity.

As mentioned above, it is assumed that initially only the lowest two vibrational states in the S_1 level are excited. This is equivalent to saying that the pumping energy is kept just above the 0–0 transition from ground state to S_1. In the calculation, it was assumed that there is a single final state of ET reaction (CT_1). The density matrix elements of this state were calculated, and the induced absorption from it to one CT_n state was constructed, and then it was assumed that there is a large inhomogeneity in this level so that a Gaussian inhomogeneity was convoluted with the calculated spectra. By doing this we implicitly assume several things. First, it was assumed that the inhomogeneity at least partly reflects the width of the distribution of the final density of state. More importantly, in this approach it is assumed that the electronic coupling between S_1 and all of these final states is constant. Whether or not this assumption is reasonable has to be examined by detailed studies of the properties of the electronic states of the adsorption system, either through quantum chemistry calculations or by further experiments. Here it is assumed that the molecular orbitals of the chromophore are weakly overlapping with the atomic orbitals of the surface so that the electronic coupling is only determined by the interaction of Hamiltonian matrix elements between the molecular orbitals of the charge-separate state and the photo-excited state of the adsorbent. Second, by doing so it was also assumed that intraband transition in the conduction band of TiO_2 nanoparticle can be ignored in the time scale of our study. That is, for each electronic state inside the distribution of the final states, its density matrix elements of the vibrational states evolve with time independently of the density matrix elements of any other electronic state also inside the final states' distribution. In other words, the population and coherence are not transferred between different final states of ET.

Now we discuss the results of the calculation. First, the calculations of the transient absorption spectra in the range of 10,000–20,000 cm^{-1} right after pumping (time delay equals 0 psec) and 1.6 psec after pumping were performed. The result is plotted in Figure 5.9a. The energy gap between CT_1 state (will be named state b afterwards for brevity) and S_1 state (will be written as state a afterwards), ω_{ba}, is 20 cm^{-1}, i.e., nearly resonant. The ET reaction is efficient despite the weak coupling because of this small energy gap. At time zero, the transient absorption comes from level a, while after 1.6 psec there is obvious absorption from both the reactant state a and the product state b. To get a feeling of how this approximately reproduces the

Lam Research Ex. 1035 - Page 173
Lam Research Corp. v. Inpria Corp.
IPR2024-00033 - U.S. Patent No. 9,823,564

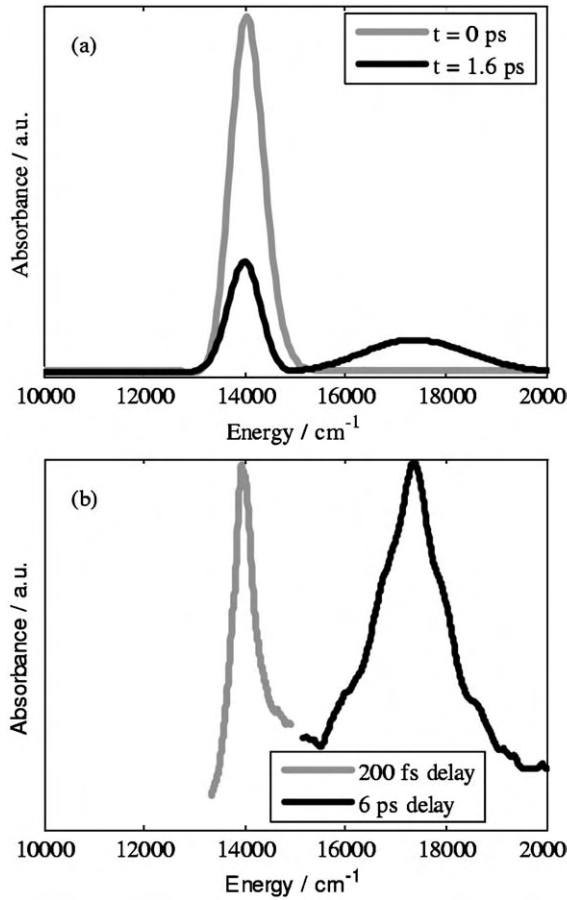


Fig. 5.9. (a) The induced absorption spectra constructed from the theory. At time $t = 0$, the induced absorption is from the reactant state to higher neutral states S_n, while at time $t = 1.6$ psec, contributions from both reactant state and product state appear. (b) In the work of Burfeindt et al. [69], the induced absorption at $t = 200$ fsec is attributed to the reactant induced absorption, while at $t = 6$ psec they concluded that the induced absorption from the product state is observed. (Reprinted with permission from Ref. [69]. Copyright 1996 American Institute of Physics.)

trend of the experiments, in Figure 5.9b, the transient absorption spectra of DTB-Pe on TiO_2 surface at 200 fsec and 6 psec after pumping, observed by Burfeindt et al. [69], are shown.

Experimentally, the transient absorption is observed by measuring the intensity of a probe laser pulse. The observed dynamics is related to the frequency of this pulse (see Section 4). For brevity we refer to the central frequency of the line shape of the probe pulse as the probing frequency.

Lam Research Ex. 1035 - Page 174
Lam Research Corp. v. Inpria Corp.
IPR2024-00033 - U.S. Patent No. 9,823,564

However, presently the shape of the probe pulse is not considered. The transient absorption signal was only calculated at the probing frequency to simulate the probing signal. The result of the simulation on the above model system, probed at the respective peak position of the induced absorption of both the reactant and the product states, is shown in Figure 5.10. Notice that in our simulation the electronic coupling value is $70\,cm^{-1}$, and the ET dynamics is almost as fast as experimentally observed. The experimental result by Zimmermann et al. is shown in Figure 5.11.

For comparison, the same calculation, except changing the vibrational frequency to $275\,cm^{-1}$, is shown in Figure 5.12. The feature of the dynamics is mostly similar, except that the period of the quantum beat is longer. Therefore, hereafter the focus shall only be put on the results for $420\,cm^{-1}$ mode.

Next, the transient absorptions observed at other probing frequencies are shown. Experimentally, the observations are not always made at the peak positions. In Figure 5.13, the probing frequencies are moved $250\,cm^{-1}$ to the red, i.e., to 13,750 and 17,000 cm^{-1}, respectively. The quantum beats of transient absorption in both the reactant and the product states become more pronounced. It can be shown that according to our calculations the quantum beats are more pronounced when the probing frequencies are shifted to either side of the peaks, at least for shifts smaller than $250\,cm^{-1}$.

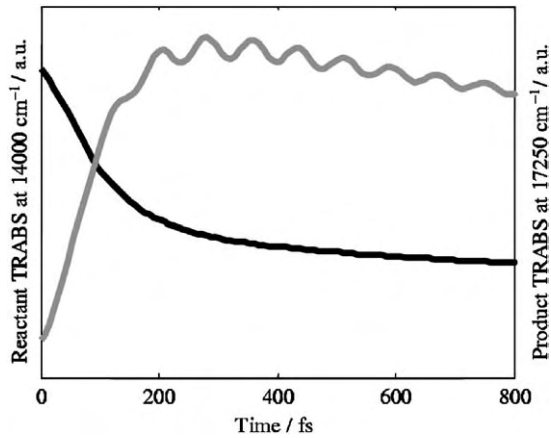


Fig. 5.10. The theoretical calculation of the time trace of transient absorption (TRABS) for a one-mode system. The energy gap is $20\,cm^{-1}$ and the vibrational mode is $420\,cm^{-1}$. The dark curve is the reactant TRABS and the light-gray curve is the product TRABS. The probing frequency is set at respective peak positions of the induced absorption spectra of both reactant state and product state. For discussion see text.

Lam Research Ex. 1035 - Page 175
Lam Research Corp. v. Inpria Corp.
IPR2024-00033 - U.S. Patent No. 9,823,564

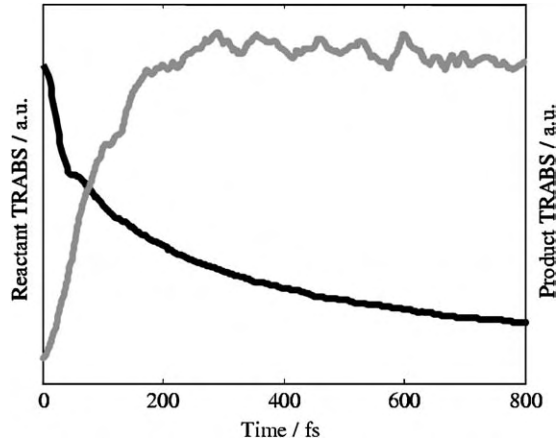


Fig. 5.11. The experimental observation of the reactant TRABS and product TRABS, done by Zimmermann et al. For discussion see text.

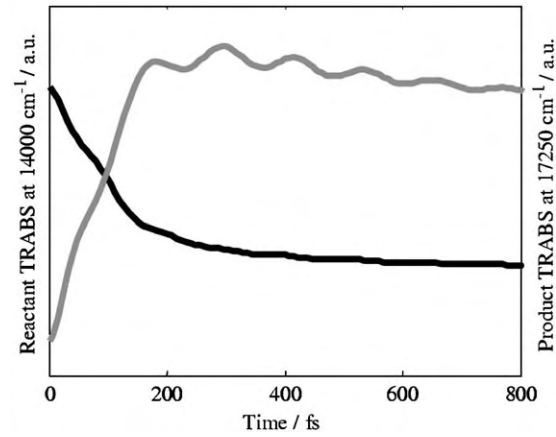


Fig. 5.12. TRABS time trace constructed theoretically for the one-mode model system. Here the frequency of the mode is changed to 275 cm^{-1}. For discussion see text.

The next phenomenon to be discussed here is the energy gap dependence. To demonstrate this effect, the probing frequency is fixed at the peak positions of the induced absorptions to reduce complications from the stronger quantum beats. Shown in Figure 5.14 is the case when the energy gap is increased to 200 cm^{-1}. The ET dynamics is less efficient than the case of 20 cm^{-1} gap. This is reasonable because in the case of single displaced mode, the smaller the energy gap, the better the resonance between the

Lam Research Ex. 1035 - Page 176
Lam Research Corp. v. Inpria Corp.
IPR2024-00033 - U.S. Patent No. 9,823,564

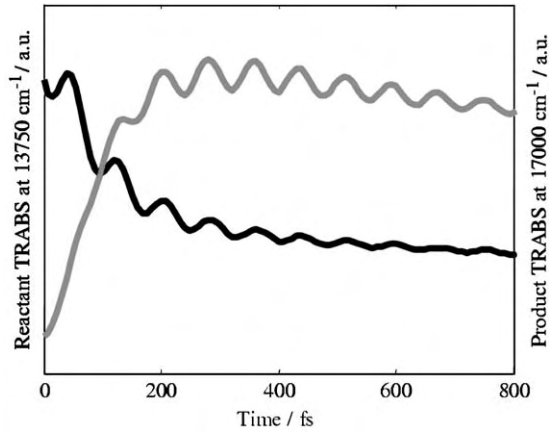


Fig. 5.13. The TRABS dynamics observed at 250 cm^{-1} to the red side of the respective peak positions of the induced absorption spectra of both reactant state and product state. For discussion see text.

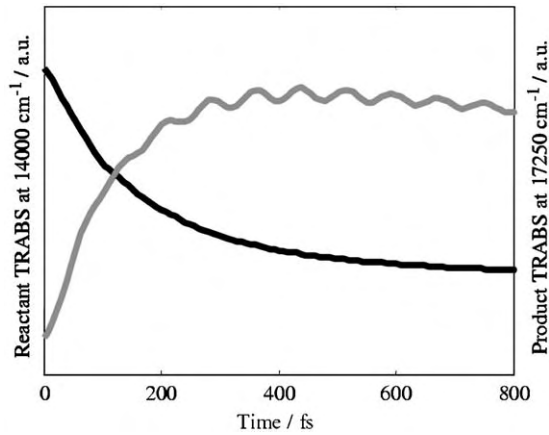


Fig. 5.14. The TRABS dynamics of the model system when the energy gap between reactant and product is increased to 200 cm^{-1}. The other conditions are the same as those in Fig. 5.10. For discussion see text.

initial and the final vibronic levels. In the weak coupling case, the Franck–Condon overlap integral is the largest between $v = 0$ states of initial and final electronic levels. It can be expected that if the pumping energy is close to the bottom of the reactant state so that the $v = 0$ level is efficiently excited, and if at the same time the energy gap between the reactant and the product electronic levels is small, the ET reaction will be

Lam Research Ex. 1035 - Page 177
Lam Research Corp. v. Inpria Corp.
IPR2024-00033 - U.S. Patent No. 9,823,564

much faster than that in other conditions. It is possible that this is the condition satisfied by most of the dye/semiconductor systems having high PIET efficiency. For a pair of one-dimensional displacement-only PESs, the wavefunction of the ground vibrational level of the reactant state, for example, has the greatest overlap with a vibrational level in the product state whose quantum number is closest to the Huang–Rhys factor. In other words, the ET rate is the highest when the energy gap is around $S\hbar\omega$. Thus, when the vibronic coupling is strong, the optimal band gap value may be large. However, since in this case the FCF between the $v = 0$ vibrational level of the reactant electronic state and the $v = n$ vibrational level of the product electronic state is $F_{0n} \approx e^{-S}S^n/n!$, obviously even when the energy gap value is close to the optimal value, the small FCF value still makes the ET rate much smaller than that in the small band gap case with weak vibronic coupling, if the electronic coupling is the same. To design a better system for solar cell, it is desirable to achieve suitable conditions that can enhance ET. This may be one of the directions to consider. On the other hand, one may question how the product state may be close to the reactant state in energy. This has to be studied by more sophisticated experiments that can determine the energy of the product state, or by high-level quantum chemistry computations. However, it is worthy of commenting that, even if the isolated dye molecule (or in solution) may have a relative larger energy gap between these two states, the interaction between the dye with the solid surface may shift the charge-separate state significantly. This is already well understood in the case of hydrogen adsorption to metal surface [70]. Since resonance condition is even stronger than the contribution from FCF, it is indeed interesting to study whether systems with nearly resonant reactant and product electronic states can be discovered. The other problems limiting the efficiency in dye-sensitized solar cells, such as the back electron transfer, may be tackled with other methods [71]. Finally, in Figure 5.15 the case where the energy gap is increased to $420\,\mathrm{cm}^{-1}$ is shown. When all of the other conditions are kept the same, it is seen that the ET dynamics is obviously slowed down. Notice that in this case the initially prepared vibronic states, i.e., the $v = 0$ and 1 states of the initial electronic level, are resonant to the $v = 1$ and 2 states of the final electronic levels, respectively, but the ET efficiency still decreases.

In this section, the golden rule approach has been employed to study ET; for numerical demonstrations the DTB-Pe/TiO_2 system has been chosen and the magnitude of $70\,\mathrm{cm}^{-1}$ has been used for the electronic coupling matrix element which leads to the ET rate in the time scale of 100–200 fsec. The validity and applicability of the golden rule depend on the magnitude of electronic coupling matrix element, electronic energy gap, FCF, density of state and dephasing rate (or damping). The effect of

Lam Research Ex. 1035 - Page 178
Lam Research Corp. v. Inpria Corp.
IPR2024-00033 - U.S. Patent No. 9,823,564

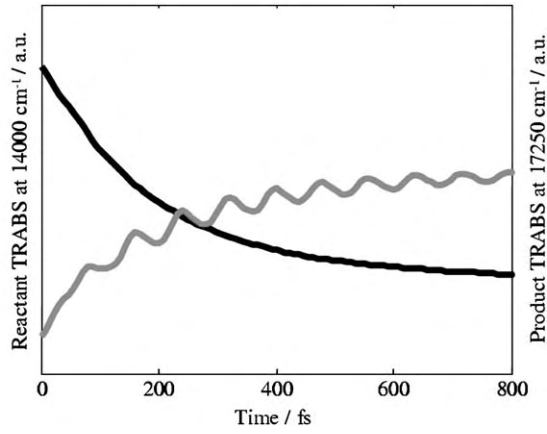


Fig. 5.15. The TRABS dynamics of the model system when the energy gap between reactant and product is increased to 420 cm^{-1}. The other conditions are the same as those in Fig. 5.10. For discussion see text.

higher order approximation has been checked and it was found that the golden rule is applicable under the conditions used in this paper. It should be noted that the golden rule expression given in Section 3 describes the so-called direct ET or ET through space. High-order approximations for calculating ET rate can be investigated by using the Green function method [34] and density matrix method [35]. For the case in which there exists no resonant intermediate electronic state between the initial excited electronic state and the final charge-transfer state, ET can take place through space and also via super exchange (or through bonds), and the Marcus type of ET expression can be obtained in this case. On the other hand, for the case in which there exists a resonant intermediate electronic state, the distance-dependence and temperature-dependence of ET become very complicated. Furthermore, sequential ET can also take place in competition.

From the magnitude of the computed single-level ET rate and the value of electronic coupling chosen for the computation (70 cm^{-1}), it is seen that to achieve ET rate faster than 100 fsec, it is not necessary to have a strong electronic coupling. Rather, the properties of the final state of the ET process are also important factors.

To help completely understand the ultrafast interface ET between dye molecules and semiconductor nanoparticles, it is desirable to experimentally measure the femtosecond time-resolved spectra (i.e., probing signal in the pump–probe experiment) at various pumping wavelengths. Changing laser pulse-durations will also be useful.

Lam Research Ex. 1035 - Page 179
Lam Research Corp. v. Inpria Corp.
IPR2024-00033 - U.S. Patent No. 9,823,564

5.2. REMARKS

In concluding this section, it is desirable to theoretically perform quantum chemistry calculation to study the interactions between adsorbed dye molecule and semiconductor in order to determine the exact location of the charge-transfer state, the final density of states' distribution and the effect of local defects caused by the interaction between the dye molecule and the semiconductor and to obtain the potential surfaces involved in excitation and ET including the interactions between these surfaces. Although Marcus and coworkers [72,73] have performed the tight-binding calculations for the Si/viologen and InP/Me_2Fe systems, higher level calculations are desirable.

In this section, we have shown how the first-principle calculations can be performed to analyze steady state and time-resolved spectra to obtain the rate constants of the processes involved in the experiments and how to employ the *ab initio* potential surfaces and the interactions between these surfaces to calculate these rate constants.

6. Summary

In this chapter, density matrix method has been introduced. It has been shown to be very powerful for treating kinetics or dynamics of a system, whether it is isolated or in contact with the environment. The projection operator method has been introduced to rewrite the Liouville equation so that the EOMs obeyed by the diagonal and off-diagonal matrix elements are separated, though not totally decoupled. GLRT is developed along this line and is very useful for treating non-equilibrium kinetics. The PIET in dye-sensitized solar cell is taken as an example to show how the GLRT can be used to study the transient molecular processes.

Developments in the density matrix method still remain to be done, in both the fundamental aspect and the technical aspect. For example, the properties of the damping operator $\hat{\Gamma}$ are yet poorly known. Usually, only very simple parameters are input by hands. Such approach can help us simplify the process of model setup. However, there might be artifacts in the computation, as will be explained below.

The energy difference between two states $\hbar\omega_{ab} = E_a - E_b$ follows the simple addition rule:

$$\omega_{ab} = \omega_{ac} + \omega_{cb} = \omega_{ax} - \omega_{bc} \tag{6.1}$$

but the diagonal matrix elements γ_{ab} of the damping operator do not follow the same relation. But since we do not have a good model for the algebraic

Lam Research Ex. 1035 - Page 180
Lam Research Corp. v. Inpria Corp.
IPR2024-00033 - U.S. Patent No. 9,823,564

properties of the damping operator, we may simply assume that $\gamma_{ab} = \gamma_a + \gamma_b$ or $\gamma_{ab} = \gamma_a - \gamma_b$. If the dependence of the damping operator on the vibrational states is ignored, i.e., if $\gamma_{av,av} = \gamma_a$, then subtracting the damping constants may result in non-damped terms or long-lasting or long-oscillating dynamics. Fundamental understanding of the properties of the damping operator is an important and difficult problem.

Technically, the density matrix for a molecular system can be very large, especially when many nuclear degrees of freedom are taken into account, or when more than two electronic levels are involved. In the future, to make the density matrix method a realistic tool for large scale problem, computational techniques have to be further developed.

The previous sections of this chapter have been written with more emphasis on the definitions and the mathematical derivations rather than providing a lot of physical discussions. In the following, a few questions are given to guide the readers to think more into the physical meanings of what have been presented:

1. Feynmann pointed out that the wavefunction of a system is not unique, but the density matrix is unique. Discuss the meaning (qualitatively or mathematically) of this statement.
2. What is the RPA? Why is RPA expressed in the way presented in this chapter (Eq. (2.42))?
3. Show that for a pure state the off-diagonal density matrix elements in general do not vanish. *Hint*: Consider, for example, a system whose wavefunction can be expressed by the linear combination of a set of two basis functions $\{\psi_1, \psi_2\}$, i.e., $\Psi = c_1\psi_1 + c_2\psi_2$.
   In terms of this basis set, the off-diagonal density matrix elements ρ_{12} and ρ_{21} do not vanish unless $c_1 = 0$ or $c_2 = 0$. Extend your discussion to the case of basis set of any size.
4. The projection operator method splits the density matrix into diagonal part and off-diagonal part. Discuss why this method is powerful for treating non-equilibrium statistical mechanics?

Appendix A. $G_{v_j}(t)$ for Displaced–Distorted Oscillator

In the present case, we shall write [74]

$$G_{v_j}(t) = e^{\lambda_j(v_j+1/2)} \sum_{u'_j} e^{-\mu'_j(u'_j+1/2)} |\langle \chi_{av_j}(Q_j) | \chi_{bu'_j}(Q'_j) \rangle|^2 \qquad \text{(A.1)}$$

Lam Research Ex. 1035 - Page 181
Lam Research Corp. v. Inpria Corp.
IPR2024-00033 - U.S. Patent No. 9,823,564

where $\lambda_j = -it\omega_j$ and $\mu'_j = -it\omega'_j$. Using the Slater sum, Eq. (A.1) can be written as

$$G_{v_j}(t) = \frac{\sqrt{\beta'_j}\, e^{\lambda_j(v_j+1/2)}}{\sqrt{2\pi\ \sinh\ \mu'_j}} \int_{-\infty}^{\infty}\int_{-\infty}^{\infty} dQ_j d\bar{Q}_j \chi_{av_j}(Q_j)\chi_{av_j}(\bar{Q}_j) \times \exp\left\{-\frac{\beta'_j}{4}\left[(Q'_j+\bar{Q}'_j)^2\ \tanh\frac{\mu'_j}{2} + (Q'_j-\bar{Q}'_j)^2\coth\frac{\mu'_j}{2}\right]\right\} \quad \text{(A.2)}$$

where $\beta'_j = \omega'_j/\hbar$ and

$$\chi_{av_j}(Q_j) = N_{av_j} H_{v_j}\left(\sqrt{\beta_j}Q_j\right) e^{-\beta_j Q_j^2/2} \quad \text{(A.3)}$$

With the contour-integral representation of the Hermite polynomial:

$$H_n(z) = (-)^n \frac{n!}{2\pi i}\oint \frac{e^{-Z^2-2zZ}}{Z^{n+1}}\, dZ \quad \text{(A.4)}$$

it follows that

$$G_{v_j}(t) = K_{v_j}\frac{\sqrt{\beta'_j}\, e^{\lambda_j(v_j+1/2)}}{\sqrt{2\pi\ \sinh\mu'_j}} \times \int_{-\infty}^{\infty}\int_{-\infty}^{\infty} dQ_j d\bar{Q}_j\, e^{-(\beta'_j/4)[(Q'_j+\bar{Q}'_j)^2\ \tanh(\mu'_{j/2})+(Q'_j-\bar{Q}'_j)^2\ \coth(\mu'_{j/2})]} \times e^{-(\beta_j/2)(Q_j^2+\bar{Q}_j^2)}\oint\frac{dZ_1}{Z_1^{v_j+1}}\oint\frac{dZ_2}{Z_2^{v_j+1}} e^{-(Z_1^2+Z_2^2)-2\sqrt{\beta_j}(Z_1Q_j+Z_2\bar{Q}_j)} \quad \text{(A.5)}$$

where $Q'_j = Q_j + d_j$ and

$$K_{v_j} = \left[\frac{(-)^{v_j} v_j! N_{av_j}}{2\pi i}\right]^2 \quad \text{(A.6)}$$

By using the new variables $X = (Q_j + \bar{Q}_j)/\sqrt{2}$ and $Y = (Q_j - \bar{Q}_j)/\sqrt{2}$, Eq. (A.6) can be simplified as

$$G_{v_j}(t) = K_{v_j}\frac{\sqrt{\beta'_j}\, e^{\lambda_j(v_j+1/2)}}{\sqrt{2\pi\ \sinh\ \mu'_j}}\oint\frac{dZ_1}{Z_1^{v_j+1}}\oint\frac{dZ_2}{Z_2^{v_j+1}} e^{-(Z_1^2+Z_2^2)} I_X I_Y \quad \text{(A.7)}$$

Lam Research Ex. 1035 - Page 182
Lam Research Corp. v. Inpria Corp.
IPR2024-00033 - U.S. Patent No. 9,823,564

where

$$I_X = \sqrt{\frac{2\pi}{\beta_j + \beta'_j \tanh(\mu'_j/2)}} \exp\left\{ -\frac{\beta_j \beta'_j \tanh(\mu'_j/2)}{\beta_j + \beta'_j \tanh(\mu'_j/2)} d_j^2 + \frac{\beta_j (Z_1 + Z_2)^2 + 2\sqrt{\beta_j}\beta'_j \tanh(\mu'_j/2) d_j (Z_1 + Z_2)}{\beta_j + \beta'_j \tanh(\mu'_j/2)} \right\} \tag{A.8}$$

and

$$I_Y = \sqrt{\frac{2\pi}{\beta_j + \beta'_j \coth(\mu'_j/2)}} \exp\left\{ \frac{\beta_j (Z_1 - Z_2)^2}{\beta_j + \beta'_j \coth(\mu'_j/2)} \right\} \tag{A.9}$$

It follows that

$$\begin{aligned} G_{v_j}(t) = K_{v_j} & \sqrt{\frac{2\pi\beta'_j}{(\beta_j^2 + \beta'^2_j)\sinh\mu'_j + 2\beta_j\beta'_j \cosh\mu'_j}} e^{\lambda_j (v_j + 1/2)} \\ & \times \exp\left\{ -\frac{\beta'_j \sinh(\mu'_j/2)(\sqrt{\beta_j} d_j)^2}{\beta_j \cosh(\mu'_j/2) + \beta'_j \sinh(\mu'_j/2)} \right\} \\ & \times \oint \frac{dZ_1}{Z_1^{v_j+1}} \oint \frac{dZ_2}{Z_2^{v_j+1}} \\ & \times e^{-(Z_1^2 + Z_2^2) + \frac{\beta_j (Z_1 - Z_2)^2}{\beta_j + \beta'_j \coth\frac{\mu'_j}{2}} + \frac{\beta_j (Z_1 + Z_2)^2}{\beta_j + \beta'_j \tanh\frac{\mu'_j}{2}} + \frac{2\beta'_j \tanh\frac{\mu'_j}{2} \sqrt{\beta_j} d_j (Z_1 + Z_2)}{\beta_j + \beta'_j \tanh\frac{\mu'_j}{2}}} \end{aligned} \tag{A.10}$$

or

$$\begin{aligned} G_{v_j}(t) = \frac{F_{v_j}}{(2\pi i)^2} \oint \frac{dZ_1}{Z_1^{v_j+1}} \oint \frac{dZ_2}{Z_2^{v_j+1}} & \exp\{-A_j (Z_1^2 + Z_2^2) \\ & + B_j (Z_1 + Z_2)\} \exp\{C_j Z_1 Z_2\} \end{aligned} \tag{A.11}$$

where for convenience we have introduced the following notations:

$$D_j = (\beta_j^2 + \beta'^2_j) \sinh \mu'_j + 2\beta_j \beta'_j \cosh \mu'_j \tag{A.12}$$

$$E_j = (\beta'^2_j - \beta_j^2) \sinh \mu'_j \tag{A.13}$$

Lam Research Ex. 1035 - Page 183
Lam Research Corp. v. Inpria Corp.
IPR2024-00033 - U.S. Patent No. 9,823,564

$$A_j = \frac{E_j}{D_j} \tag{A.14}$$

$$B_j = \frac{2\beta'_j \sinh(\mu'_j/2)\sqrt{\beta_j} d_j}{\beta_j \cosh(\mu'_j/2) + \beta'_j \sinh(\mu'_j/2)} \tag{A.15}$$

$$C_j = \frac{4\beta_j \beta'_j}{D_j} \tag{A.16}$$

and

$$F_{v_j} = [(-)^{v_j} v_j! N_{av_j}]^2 \sqrt{\frac{2\pi\beta'_j}{D_j}} \exp\left\{ \frac{\beta'_j \sinh(\mu'_j/2)(\sqrt{\beta_j} d_j)^2}{\beta_j \cosh(\mu'_j/2) + \beta'_j \sinh(\mu'_j/2)} + \lambda_j \left(v_j + \frac{1}{2} \right) \right\} \tag{A.17}$$

Then,

$$\begin{aligned} G_{v_j}(t) &= \frac{F_{v_j}}{(2\pi i)^2} \sum_{n_j=0}^{\infty} \frac{C_j^{n_j}}{n_j!} \oint dZ_1 Z_1^{n_j - v_j - 1} e^{-A_j Z_1^2 + B_j Z_1} \oint dZ_2 Z_2^{n_j - v_j - 1} e^{-A_j Z_2^2 + B_j Z_2} \\ &= F_{v_j} \sum_{n_j=0}^{\infty} \frac{C_j^{n_j}}{n_j!} \left[\frac{1}{2\pi i} \oint dZ Z^{n_j - v_j - 1} e^{-A_j Z^2 + B_j Z} \right]^2 \\ &= F_{v_j} \sum_{n_j=0}^{\infty} \frac{C_j^{n_j} A_j^{v_j - n_j}}{n_j! [(v_j - n_j)!]^2} \left[\frac{(-)^{v_j - n_j} (v_j - n_j)!}{2\pi i} \oint \frac{dZ}{Z^{v_j - n_j + 1}} e^{-z^2 - 2(B_j/2\sqrt{A_j})z} \right]^2 \\ &= F_{v_j} \sum_{n_j=0}^{\infty} \frac{C_j^{n_j} A_j^{v_j - n_j}}{n_j! [(v_j - n_j)!]^2} \left[H_{v_j - n_j} \left(\frac{B_j}{2\sqrt{A_j}} \right) \right]^2 \end{aligned} \tag{A.18}$$

In particular, if $d_j = 0$, then $B_j = 0$ and

$$\begin{aligned} G_{v_j}(t) &= F_{v_j} \sum_{n_j=0}^{v_j} \frac{C_j^{n_j} A_j^{v_j - n_j}}{n_j! [(v_j - n_j)!]^2} \left[\frac{(v_j - n_j)!}{\ell_j!} \delta_{2\ell_j, v_j - n_j} \right]^2 \\ &= F_{v_j} \sum_{n_j=0}^{v_j} \frac{C_j^{n_j} A_j^{v_j - n_j}}{n_j!} \left[\frac{\delta_{2\ell_j, v_j - n_j}}{\ell_j!} \right]^2 \end{aligned} \tag{A.19}$$

where $\delta_{2\ell_j, v_j - n_j}$ denotes the Kronecker delta function. For example,

$$G_{0_j}(t) = F_{0_j}(t) \tag{A.20}$$

Lam Research Ex. 1035 - Page 184
Lam Research Corp. v. Inpria Corp.
IPR2024-00033 - U.S. Patent No. 9,823,564

$$G_{1_j}(t) = F_{1_j}(t)C_j \tag{A.21}$$

$$G_{2_j}(t) = F_{2_j}(t)\left(A_j^2 + \frac{1}{2!}C_j^2\right) \tag{A.22}$$

$$G_{3_j}(t) = F_{3_j}(t)\left(C_j A_j^2 + \frac{1}{3!}C_j^3\right) \tag{A.23}$$

and so on. Eq. (3.94) can be obtained from Eq. (A.18) by setting $\omega_j = \omega_j'$ and $d_j \neq 0$.

Appendix B. Derivation of the TCF for the Band-Shape Function

Continue the derivation starting from Eq. (4.60). Defining the new variables $\lambda_j = -\omega_j t$ and $\mu_j' = \omega_j' t$, the TCF $G_{\mathrm{a}v_j',\mathrm{a}v_j}(t)$ is further written as following:

$$G_{\mathrm{a}v_j',\mathrm{a}v_j}(t) = e^{-i(v_j+1/2)\lambda_j} \sum_{u_j} e^{-i(u_j+1/2)\mu_j'} \langle \chi_{\mathrm{a}v_j'} | \chi_{\mathrm{b}u_j} \rangle \langle \chi_{\mathrm{b}u_j} | \chi_{\mathrm{a}v_j} \rangle \tag{B.1}$$

By using the Mehler's formula in the sinusoidal-function form,

$$\begin{aligned} G_{av_j',av_j}(t) = {} & e^{-i(v_j+1/2)\lambda_j}(-1+i)\sqrt{\frac{\beta_j'}{4\pi \sin \mu_j'}} \\ & \times \int_{-\infty}^{\infty}\int_{-\infty}^{\infty} dQ_j d\bar{Q}_j \chi_{av_j}(Q_j)\chi_{av_j'}(\bar{Q}_j) \\ & \times e^{-(i\beta_j'/4)[(Q_j'+\bar{Q}_j')^2 \tan(\mu_j'/2) - (Q_j'-\bar{Q}_j')^2 \cot(\mu_j'/2)]} \end{aligned} \tag{B.2}$$

Next, consider the displaced oscillator case, i.e., $\omega_j' = \omega_j$, $\beta_j' = \beta_j$ and $\mu_j' = -\lambda_j$. By using the contour-integral representation of the Hermite polynomials (see Eq. (A.4)),

$$\begin{aligned} G_{\mathrm{a}v_j',\mathrm{a}v_j}(t) = {} & (-)^{v_j+v_j'}(-1+i)e^{-i(v_j+1/2)\lambda_j} \sqrt{\frac{\beta_j/\pi}{2^{v_j} v_j! 2^{v_j'} v_j'!}} \sqrt{\frac{\beta_j}{4\pi \sin \mu_j'}} \frac{v_j! v_j'!}{(2\pi i)^2} \\ & \times \oint \frac{dZ_1 e^{-Z_1^2}}{Z_1^{v_j+1}} \oint \frac{dZ_2\, e^{-Z_2^2}}{Z_2^{v_j'+1}} \int_{-\infty}^{\infty}\int_{-\infty}^{\infty} dQ_j d\bar{Q}_j\, e^{-2Z_1\sqrt{\beta_j}Q_j - 2Z_2\sqrt{\beta_j}\bar{Q}_j} \\ & \times e^{-(\beta_j'/4)[(Q_j+\bar{Q}_j)^2 + (Q_j-\bar{Q}_j)^2 + i(Q_j'+\bar{Q}_j')^2 \tan(\mu_j'/2) - i(Q_j'-\bar{Q}_j')^2 \cot(\mu_j'/2)]} \end{aligned} \tag{B.3}$$

where $Q_j' = Q_j + d_j$ and $\bar{Q}_j' = \bar{Q}_j + d_j$; thus, $Q_j' + \bar{Q}_j' = Q_j + \bar{Q}_j + 2d_j$ and

Lam Research Ex. 1035 - Page 185
Lam Research Corp. v. Inpria Corp.
IPR2024-00033 - U.S. Patent No. 9,823,564

$Q_j' - \bar{Q}_j' = Q_j - \bar{Q}_j$. Letting $X = (Q_j + \bar{Q}_j)/\sqrt{2}$ and $Y = (Q_j - \bar{Q}_j)/\sqrt{2}$, we have $dQ_j d\bar{Q}_j = dX dY$ and

$$\begin{aligned} G_{\mathrm{a}v_j', \mathrm{a}v_j}(t) = (-)^{v_j + v_j'}(-1+i)e^{-i(v_j+1/2)\lambda_j} \\ \times \sqrt{\frac{v_j! v_j'!}{2^{v_j+v_j'+2}\pi^2 \sin\mu_j'}} \frac{\beta_j}{(2\pi i)^2} \oint \frac{dZ_1\, e^{-Z_1^2}}{Z_1^{v_j+1}} \oint \frac{dZ_2\, e^{-Z_2^2}}{Z_2^{v_j'+1}} \\ \times \int_{-\infty}^{\infty}\int_{-\infty}^{\infty} dX dY\, e^{-\sqrt{2\beta_j}Z_1(X+Y) - \sqrt{2\beta_j}Z_2(X-Y)} \\ \times e^{-(\beta_j'/2)[X^2+Y^2+i(X+\sqrt{2}d_j)^2 \tan(\mu_j'/2) - iY^2\cot(\mu_j'/2)]} \end{aligned} \tag{B.4}$$

The terms in the exponentials in the integrand can be simplified by observing that

$$\begin{aligned} & -\sqrt{2\beta_j}Z_1(X+Y) - \sqrt{2\beta_j}Z_2(X-Y) \\ & -\frac{\beta_j}{2}\left[X^2 + Y^2 + i(X+\sqrt{2}d_j)^2 \tan\frac{\mu_j'}{2} - iY^2\cot\frac{\mu_j'}{2}\right] \\ = & -\frac{\beta_j}{2}\left(1 + i\tan\frac{\mu_j'}{2}\right)X^2 - \sqrt{2\beta_j}\left(Z_1 + Z_2 + i\sqrt{\beta_j}d_j\tan\frac{\mu_j'}{2}\right)X \\ & -\frac{\beta_j}{2}\left(1 - i\cot\frac{\mu_j'}{2}\right)Y^2 - \sqrt{2\beta_j}(Z_1 - Z_2)Y - i\beta_j d_j^2 \tan\frac{\mu_j'}{2} \end{aligned} \tag{B.5}$$

Thus, one can first carry out the integrals over Y and X:

$$\begin{aligned} & \int_{-\infty}^{\infty} dY \exp\left[-\frac{\beta_j}{2}\left(1 - i\cot\frac{\mu_j'}{2}\right)Y^2 - \sqrt{2\beta_j}(Z_1 - Z_2)Y\right] \\ & = \sqrt{\frac{2\pi}{\beta_j\left(1 - i\cot(\mu_j'/2)\right)}} \exp\left\{\frac{(Z_1 - Z_2)^2}{1 - i\cot(\mu_j'/2)}\right\} \end{aligned} \tag{B.6}$$

and

$$\begin{aligned} & \int_{-\infty}^{\infty} dX \exp\left\{-\frac{\beta_j}{2}\left(1 + i\tan\frac{\mu_j'}{2}\right)X^2 \right. \\ & \left. -\sqrt{2\beta_j}\left(Z_1 + Z_2 + i\sqrt{\beta_j}d_j\tan\frac{\mu_j'}{2}\right)X\right\} \\ & = \sqrt{\frac{2\pi}{\beta_j\left(1 + i\tan(\mu_j'/2)\right)}} \exp\left\{\frac{(Z_1 + Z_2 + i\sqrt{\beta_j}d_j\tan(\mu_j'/2))^2}{1 + i\tan(\mu_j'/2)}\right\} \end{aligned} \tag{B.7}$$

Lam Research Ex. 1035 - Page 186
Lam Research Corp. v. Inpria Corp.
IPR2024-00033 - U.S. Patent No. 9,823,564

Then the TCF can be written as

$$
\begin{aligned}
G_{\mathrm{a}v'_j,\mathrm{a}v_j}(t) = (-)^{v_j+v'_j}\frac{-1+i}{(2\pi i)^2}e^{-i(v_j+1/2)\lambda_j} \\
\times \sqrt{\frac{v_j!v'_j!}{2^{v_j+v'_j}\,\sin\mu'_j\Big(1+i\,\tan(\mu'_j/2)\Big)\Big(1-i\,\cot(\mu'_j/2)\Big)}} \\
\times \oint \frac{dZ_1\, e^{-Z_1^2}}{Z_1^{v_j+1}} \oint \frac{dZ_2\, e^{-Z_2^2}}{Z_2^{v'_j+1}} \\
\times \exp\left\{\frac{(Z_1+Z_2+i\sqrt{\beta_j}d_j\tan(\mu'_j/2))^2}{1+i\,\tan(\mu'_j/2)}+\frac{(Z_1-Z_2)^2}{1-i\,\cot(\mu'_j/2)}\right\} \qquad \text{(B.8)}
\end{aligned}
$$

which can be simplified as

$$
\begin{aligned}
G_{\mathrm{a}v'_j,\mathrm{a}v_j}(t) = \frac{(-)^{v_j+v'_j}}{(2\pi i)^2}e^{-iv_j\lambda_j}\sqrt{\frac{v_j!v'_j!}{2^{v_j+v'_j}}}e^{-S_j(1-e^{i\lambda_j})} \\
\times \oint \frac{dZ_1\, e^{-Z_1^2}}{Z_1^{v_j+1}} \oint \frac{dZ_2\, e^{-Z_2^2}}{Z_2^{v'_j+1}} \exp\{2\,e^{i\lambda_j}Z_1Z_2+\kappa_j(Z_1+Z_2)\} \qquad \text{(B.9)}
\end{aligned}
$$

where κ_j is defined in Eq. (4.62). Next, make the expansion

$$
e^{2Z_1Z_2\,e^{i\lambda_j}} = \sum_{n_j=0}^{\infty}\frac{(2Z_1Z_2\,e^{i\lambda_j})^{n_j}}{n_j!} \qquad \text{(B.10)}
$$

and carry out the contour integrals as follows:

$$
\begin{aligned}
&\frac{1}{(2\pi i)^2}\oint\frac{dZ_1}{Z_1^{v_j+1}}\oint\frac{dZ_2}{Z_2^{v'_j+1}}\sum_{n_j=0}^{\infty}\frac{(2\,e^{i\lambda_j})^{n_j}}{n_j!}Z_1^{n_j}Z_2^{n_j}\,e^{\kappa_jZ_1}\,e^{k_jZ_2} \\
&\quad=\sum_{n_j=0}^{\infty}\frac{(2\,e^{i\lambda_j})^{n_j}}{n_j!}\frac{1}{(2\pi i)^2}\oint\frac{dZ_1\,\exp(\kappa_jZ_1)}{Z_1^{v_j-n_j+1}}\oint\frac{dZ_2\,\exp(\kappa_jZ_2)}{Z_2^{v'_j-n_j+1}} \\
&\quad=\sum_{n_j=0}^{\min(v_j,v'_j)}\frac{(2\,e^{i\lambda_j})^{n_j}}{n_j!}\frac{\kappa_j^{v_j-n_j}}{(v_j-n_j)!}\frac{\kappa_j^{v'_j-n_j}}{(v'_j-n_j)!} \qquad \text{(B.11)}
\end{aligned}
$$

The result in Eq. (B.9) can be rewritten in the form of Eq. (4.61). Notice that we also replace λ_j by $\omega_j t$ in the final representation.

Lam Research Ex. 1035 - Page 187
Lam Research Corp. v. Inpria Corp.
IPR2024-00033 - U.S. Patent No. 9,823,564

References

1. S. H. Lin, R. G. Alden, R. Islampour, H. Ma, A. A. Villaeys, Density Matrix Method and Femtosecond Processes, World Scientific, Singapore, 1991.
2. M. Sargent, III., M. O. Scully, W. E. Lamb, Jr., Laser Physics, Addison-Wesley, Reading, MA, 1974.
3. K. Blum, Density Matrix Theory and Applications, Plenum, New York, 1981.
4. B. Fain, Theory of Rate Processes in Condensed Media, Springer, Berlin, 1980.
5. H. Grabert, Projection Operator Techniques in Nonequilibrium Statistical Mechanics, Springer, Berlin, 1982.
6. W. H. Louisell, Quantum Statistical Properties of Radiation, Wiley, New York, 1973.
7. R. W. Zwanzig, Physica **30** (1964) 1109.
8. S. H. Lin, J. Chem. Phys. **61** (1974) 3810.
9. G. R. Fleming, O. L. J. Gijzeman, S. H. Lin, Faraday Trans. II **70** (1974) 209.
10. S. H. Lin, J. Chem. Phys. **65** (1976) 1053.
11. S. H. Lin, H. P. Lin, D. R. Knittel, J. Chem. Phys. **64** (1976) 441.
12. D. R. Knittel, S. H. Lin, Mol. Phys. **36** (1978) 893.
13. A. Blumen, S. H. Lin, J. Manz, J. Chem. Phys. **69** (1978) 881.
14. S. H. Lin, T. Hays, H. Eyring, Proc. Natl. Acad. Sci. U.S.A. **76** (1979) 3571.
15. S. H. Lin, Chem. Phys. Lett. **70** (1980) 492.
16. S. Yang, J. Shao, J. Cao, J. Chem. Phys. **121** (2004) 11250.
17. K. K. Liang, R. Chang, M. Hayashi, S. H. Lin, Principles of Molecular Spectroscopy and Photochemistry, Chung-Hsin University Press, Taichung, Taiwan, 2001.
18. S. H. Lin, H. Eyring, Proc. Natl. Acad. Sci. U.S.A. **74** (1977) 3105.
19. R. Xu, Y. Mo, P. Cui, S. H. Lin, Y.-J. Yan, Non-Markovian Quantum Dissipation in the Presence of External Fields, in: J. E. Maruani (Ed.), Advanced Topics in Theoretical Chemical Physics, Kluwer, Dordrecht, 2003, pp. 7–40.
20. S. H. Lin, H. Eyring, Proc. Natl. Acad. Sci. U.S.A. **78** (1981) 2013.
21. J. Shao, J. Chem. Phys. **120** (2004) 5053.
22. S. H. Lin, C. H. Chang, K. K. Liang, R. Chang, Y.-J. Shiu, J. M. Zhang, T.-S. Yang, M. Hayashi, F. C. Hsu, Adv. Chem. Phys. **121** (2002) 1–88.

Lam Research Ex. 1035 - Page 188
Lam Research Corp. v. Inpria Corp.
IPR2024-00033 - U.S. Patent No. 9,823,564

23. S. H. Lin, Chem. Phys. Lett. **86** (1982) 533.
24. S. H. Lin, X.-G. Zhang, Z.-D. Qian, X.-W. Li, H. Eyring, Proc. Natl. Acad. Sci. U.S.A. **79** (1982) 1356.
25. T. Ohmae, Y. Fujimura, T. Nakajima, S. H. Lin, J. Mol. Sci. **1** (1983) 33.
26. H. Eyring, S. H. Lin, S. M. Lin, Basic Chemical Kinetics, Wiley, New York, 1980.
27. Y.-J. Yan, R.-X. Xu, Annu. Rev. Phys. Chem. **56** (2005) 187.
28. R.-X. Xu, P. Cui, X.-Q. Li, Y. Mo, Y.-J. Yan, J. Chem. Phys. **122** (2005) 041103.
29. P. Han, R.-X. Xu, B. Li, J. Xu, P. Cui, Y. Mo, Y.-J. Yan, J. Chem. Phys. **110** (2006) 11438.
30. S. H. Lin, J. Chem. Phys. **44** (1966) 3759–3767.
31. S. H. Lin, R. Bersohn, J. Chem. Phys. **48** (1968) 2732.
32. S. H. Lin, J. Chem. Phys. **58** (1973) 5760.
33. W. E. Henke, H. L. Selzle, T. R. Hays, E. W. Schlag, S. H. Lin, J. Chem. Phys. **76** (1982) 1335.
34. S. H. Lin, J. Chem. Phys. **90** (1989) 7103.
35. S. H. Lin, R. G. Alden, C. K. Tang, Y. Fujimura, F. Sugawara, in: J. Jortner, R. Levine, B. Pullman (Eds.), Mode Selective Chemistry — The Jerusalem Symposia on Quantum Chemistry and Biochemistry, Vol. 24, Kluwer, Dordrecht, 1991, pp. 467–484.
36. S. H. Lin, W. Z. Xiao, W. Dietz, Phys. Rev. E **47** (1993) 3698.
37. A. M. Mebel, M. Hayashi, K. K. Liang, S. H. Lin, J. Phys. Chem. A **103** (1999) 10674.
38. B. Fain, S. H. Lin, N. Hamer, J. Chem. Phys. **91** (1989) 4485.
39. Y. R. Shen, The Principles of Nonlinear Optics, Wiley, New York, 1984.
40. S. H. Lin, Y. Fujimura, H. J. Neusser, E. W. Schlag, Multiphoton Spectroscopy of Molecules, Wiley, New York, 1984.
41. S. H. Lin, Theor. Chim. Acta **10** (1968) 310.
42. S. H. Lin, J. Chem. Phys. **62** (1975) 4500.
43. S. H. Lin, J. Chem. Phys. **59** (1973) 4458.
44. S. H. Lin, B. Fain, Chem. Phys. Lett. **155** (1989) 216.
45. B. Fain, S. H. Lin, W. X. Wu, Phys. Rev. A **40** (1989) 824.
46. S. H. Lin, B. Fain, N. Hamer, Adv. Chem. Phys. **79** (1990) 133.
47. S. H. Lin, B. Fain, C. Y. Yeh, Phys. Rev. A **41** (1990) 2718.
48. B. Fain, S. H. Lin, J. Chem. Phys. **93** (1990) 6387.
49. C. Y. Yeh, W. L. Chang, H. Ma, S. H. Lin, Int. J. Quantum Chem. **39** (1991) 356.
50. S. Mukamel, The Principles of Nonlinear Optical Spectroscopy, Oxford University Press, New York, 1995.

Lam Research Ex. 1035 - Page 189
Lam Research Corp. v. Inpria Corp.
IPR2024-00033 - U.S. Patent No. 9,823,564

51. D. F. Watson, G. J. Meyer, Annu. Rev. Phys. Chem. **56** (2005) 119.
52. N. A. Anderson, T. Lian, Annu. Rev. Phys. Chem. **56** (2005) 491.
53. A. Nitzan, M. A. Ratner, Science **300** (2003) 1384.
54. D. M. Adams, L. Brus, C. E. D. Chidsey, S. Creager, C. Creutz, C. R. Kagan, P. V. Kamat, M. Lieberman, S. Lindsay, R. A. Marcus, R. M. Metzger, M. E. Michel-Beyerle, J. R. Miller, M. D. Newton, D. R. Rolison, O. Sankey, K. S. Schanze, Y. James, Z. Xiaoyang, J. Phys. Chem. B **107** (2003) 6668.
55. B. O'Regan, J. Moser, M. Anderson, M. Grätzel, J. Phys. Chem. **94** (1990) 8720.
56. M. K. Nazeeruddin, A. K. Rodicio, R. Humphry-Baker, E. Müller, P. Liska, N. Vlachopoulos, M. Grätzel, J. Am. Chem. Soc. **115** (1993) 6382.
57. A. Hagfeldt, M. Grätzel, Chem. Rev. **95** (1995) 49.
58. C. Zimmermann, F. Willig, S. Ramakrishna, B. Burfeindt, B. Pettinger, R. Eichberger, W. Storck, J. Phys. Chem. B **105** (2001) 9245.
59. D. Kuciauskas, J. E. Monat, R. Villahermosa, H. B. Gray, N. S. Lewis, J. K. McCusker, J. Phys. Chem. B **106** (2002) 9347.
60. J. Kallioinen, G. Benkö, P. Myllyperkiö, L. Khriahctchev, B. Skårman, R. Wallenberg, M. Tuomikoski, J. E. I. Korppi-Tommola, V. Sundström, A. P. Yartsev, J. Phys. Chem. B **108** (2004) 6365.
61. M. Thoss, I. Kondov, H. Wang, Chem. Phys. **304** (2004) 169.
62. W. Stier, O. Prezhdo, J. Phys. Chem. B **106** (2002) 8047.
63. W. Duncan, W. Stier, O. Prezhdo, J. Am. Chem. Soc. **127** (2005) 7941.
64. S. Ramakrishna, F. Willig, V. May, Phys. Rev. B **62** (2000) 16330.
65. S. Ramakrishna, F. Willig, V. May, J. Chem. Phys. **115** (2001) 2743.
66. S. Ramakrishna, F. Willig, V. May, A. Knorr, J. Phys. Chem. B **107** (2003) 607.
67. L. Wang, V. May, J. Chem. Phys. **121** (2004) 8039.
68. L. Wang, R. Ernsforfer, F. Willig, V. May, J. Phys. Chem. B **109** (2005) 9589.
69. B. Burfeindt, T. Hannappel, W. Storck, F. Willig, J. Phys. Chem. **100** (1996) 16463.
70. T. L. Einstein, J. A. Hertz, J. R. Schrieffer, Theory of Chemisorption, in: J. R. Smith (Ed.), Topics in Current Physics, Vol. 19, Springer-Verlag, Berlin, 1980, Chap. 7, pp. 183–235.
71. S. A. Haque, S. Handa, K. Peter, E. Palomares, M. Thelakkat, J. R. Durrant, Angew. Chem. Int. Ed. **44** (2005) 5740.
72. Y. Q. Gao, Y. Georgievskii, R. A. Marcus, J. Chem. Phys. **112** (2000) 3358.
73. Y. Q. Gao, R. A. Marcus, J. Chem. Phys. **113** (2000) 6351.
74. K. K. Liang, C.-K. Lin, H.-C. Chang, M. Hayashi, S. H. Lin, J. Chem. Phys. **125** (2006) 154706.

Lam Research Ex. 1035 - Page 190
Lam Research Corp. v. Inpria Corp.
IPR2024-00033 - U.S. Patent No. 9,823,564

Chapter 6

Ultrafast Radiationless Transitions

M. Hayashi[a], A.M. Mebel[b], and S.H. Lin[c]

[a]*Center for Condensed Matter Sciences, National Taiwan University, Taipei 106, Taiwan*
[b]*Department of Chemistry and Biochemistry, Florida International University, Miami, FL 33199, USA*
[c]*Institute of Atomic and Molecular Sciences, Academia Sinica, P.O. Box 23-166, Taipei 106, Taiwan*

1. Introduction . . . 184
2. Theoretical Approach and Methods . . . 185
   2.1. Non-Adiabatic Processes . . . 186
   2.2. Rate Constants . . . 190
   2.3. Radiationless Transitions . . . 193
3. Photo-Induced Electronic Transfer and Photo-Induced Energy Transfer. . . . 199
   3.1. General Consideration . . . 199
   3.2. Photo-Induced Electron Transfer . . . 200
   3.3. Photo-Induced Energy Transfer . . . 201
4. Applications . . . 204
   4.1. Pump-Probe Time-Resolved Stimulated Emission Spectra . . . 204
   4.2. Bacterial Photosynthetic RCs . . . 211
5. Summary . . . 219
References . . . 222

A microscopic theory for describing ultrafast radiationless transitions; in particular for, photo-induced ultrafast radiationless transitions is presented. For this purpose, one example system that well represents the ultrafast radiationless transaction problem is considered. More specifically, bacterial photosynthetic reaction centers (RCs) are investigated for their ultrafast electronic-excitation energy transfer (EET) processes and ultrafast electron transfer (ET) processes. Several applications of the density matrix method are presented for emphasizing that the density matrix method can not only treat the dynamics due to the radiationless transitions but also deal with the population and coherence dynamics. Several rate constants of the radiationless transitions and the analytic estimation methods of those rate

THIN FILMS AND NANOSTRUCTURES, vol. 34
ISSN 1079-4050
DOI: 10.1016/S1079-4050(06)34006-9

© 2007 by Elsevier Inc.
All rights reserved.

Lam Research Ex. 1035 - Page 191
Lam Research Corp. v. Inpria Corp.
IPR2024-00033 - U.S. Patent No. 9,823,564

constants are also discussed. The uniqueness of the presented theoretical approach allows one to construct a microscopic model to describe ultrafast radiation transitions of large systems to which ordinary *ab initio* and/or density functional theory cannot be applied. For RCs, an excitonic-vibronic model is constructed by analyzing the optical spectra such as the temperature-dependent absorption spectra. To take into account the characteristics of the temperature-dependent absorption spectra, the thermal expansion model is introduced. The radiationless transitions properties of the RCs, i.e., the coupling constants are then deduced.

1. Introduction

Recent rapid developments in ultrashort pulse laser [1–5] make it possible to probe not only the dynamics of population of the system but also the coherence (or phase) of the system. To treat these problems, the density matrix method is an ideal approach. The main purpose of this paper is to briefly describe the application of the density matrix method in molecular terms and show how to apply it to study the photochemistry and photophysics [6–9]. Ultrafast radiationless transactions taking place in bacterial photosynthetic reaction centers (RCs) are very important examples to which the proposed theoretical approach can be applied.

Before presenting the applications, the theoretical background for the density matrix method should be constructed in molecular terms. For this purpose, a detailed definition of the density matrix of the system should be discussed. Let us consider a molecule at position $\vec{R}_\alpha$ interacting with an applied laser field of bandwidth $\delta\omega$ and corresponding wave-vector width $\delta k = \delta\omega/c$. Now, it is assumed that the laser beam spot is similar to δk and a system has only two states described by $|n\rangle$ and $|m\rangle$ with respective energies $\hbar\omega_{n_\alpha}$ and $\hbar\omega_{n_\alpha}$ within $\delta\omega$. In this case, the dynamics of the system can be described as

$$|\Psi(t)\rangle^\alpha = C_{n_\alpha}(t)e^{-it\omega_{n_\alpha}}\, e^{i\vec{k}\cdot\vec{R}_\alpha}|n_\alpha\rangle + C_{m_\alpha}(t)e^{-it\omega_{m_\alpha}}|m_\alpha\rangle\, e^{i\vec{k}\cdot\vec{R}_\alpha}. \tag{1}$$

Here, the phase factor $e^{i\vec{k}\cdot\vec{R}_\alpha}$ is associated with the wave vector of applied laser field and the center of mass (or the center of charge) position of the molecule. The density matrix operator can be then defined as

$$\begin{aligned}\rho^{\alpha\alpha}(t) = |\Psi(t)\rangle^{\alpha\alpha}\langle\Psi(t)| = |C_{n_\alpha}(t)\rangle|^2|n_\alpha\rangle\langle n_\alpha| + |C_{m_\beta}(t)|^2|m_\beta\rangle\langle m_\beta| \\ + C^*_{n_\alpha}(t)C_{m_\alpha}(t)e^{-it\omega_{m_\alpha n_\alpha}}|m_\alpha\rangle\langle n_\alpha| + C_{n_\alpha}(t)C^*_{m_\alpha}(t)e^{-it\omega_{n_\alpha m_\alpha}}|n_\alpha\rangle\langle m_\alpha|,\end{aligned} \tag{2}$$

Lam Research Ex. 1035 - Page 192
Lam Research Corp. v. Inpria Corp.
IPR2024-00033 - U.S. Patent No. 9,823,564

where $\omega_{m_\alpha n_\alpha} = \omega_{m_\alpha} - \omega_{n_\alpha}$. The term $|C_{n_\alpha}(t)|^2$ appearing in the right-hand side of Eq. (2) represents the probability of exciting the molecule to n_α state while the term $C^*_{n_\alpha}(t)C_{m_\alpha}(t)$ is associated with the coherence between n_α and m_α states generated by the applied laser field. One can see that a rapid oscillatory feature can be obviously seen in the time development of the coherence in Eq. (2). One can also notice that there is no space-phase factor in the density operator in Eq. (2). This type of the coherent excitation can be called as intramolecular coherence. A typical example of this type of coherent excitation can be seen in vibrational coherence generation that appears in ordinary femtosecond pump-probe measurements.

For the case in which there are two kinds of molecules; one is at $\vec{R}_\alpha$ and the other at $\vec{R}_\beta$ and each molecule has two states within $\delta\omega$, the dynamics of the system is given by

$$|\Psi(t)\rangle = C_{n_\alpha}(t)e^{-it\omega_{n_\alpha}}\, e^{i\vec{k}\cdot\vec{R}_\alpha}|n_\alpha\rangle + C_{n_\alpha}(t)e^{-it\omega_{m_\alpha}}|m_\alpha\rangle\, e^{i\vec{k}\cdot\vec{R}_\alpha} + C_{n_\beta}(t)e^{-it\omega_{n_\beta}}\, e^{i\vec{k}\cdot\vec{R}_\beta}|n_\beta\rangle + C_{m_\beta}(t)e^{-it\omega_{m_\beta}}|m_\beta\rangle\, e^{i\vec{k}\cdot\vec{R}_\beta}, \tag{3}$$

and the density operator is expressed as

$$\rho(t) = \rho^{\alpha\alpha}(t) + \rho^{\beta\beta}(t) + \rho^{\alpha\beta}(t)e^{i\vec{k}\cdot(\vec{R}_\alpha - \vec{R}_\beta)} + \rho^{\beta\alpha}(t)e^{i\vec{k}\cdot(\vec{R}_\beta - \vec{R}_\alpha)}, \tag{4}$$

where, for example,

$$\rho^{\alpha\beta}(t) = C_{n_\alpha}(t)C^*_{m_\beta}(t)e^{-it\omega_{n_\alpha m_\beta}}|n_\alpha\rangle\langle m_\beta| + C_{m_\alpha}(t)C^*_{n_\beta}(t)e^{-it\omega_{m_\alpha n_\beta}}|m_\alpha\rangle\langle n_\beta|. \tag{5}$$

In Eq. (4), one can see that there are two terms that depend on the space-phase factor. Eq. (5) clearly shows this situation; coherence is generated between the two molecules. This coherent excitation can be called as intermolecular coherence. This type of coherent excitation can be seen in femtosecond pump-probe non-linear coherent optical scattering spectroscopy. This chapter shall only focus on ultrafast radiationless transition as well as the dynamics of the intramolecular coherence and its relaxation.

2. Theoretical Approach and Methods

This section briefly introduces the generalized coupled master equation within the Born–Oppenheimer adiabatic (BOA) approximation. In this case, the non-adiabatic processes are treated as the vibronic transitions between the vibronic manifolds. Three types of the rate constant are then introduced to specify the nature of the transitions depending on whether the electronically excited molecular system achieves its vibrational thermal equilibrium or not. The radiationless transitions can occur between two

Lam Research Ex. 1035 - Page 193
Lam Research Corp. v. Inpria Corp.
IPR2024-00033 - U.S. Patent No. 9,823,564

vibronic states with the same spin multiplicity or between those with different spin multiplicity. Internal conversion (IC) and intersystem crossing (ISC) are then introduced and detailed. All the rate constants are provided with molecular term: all the necessary parameters involved in the rate constants can be easily associated with modern quantum chemistry calculation methods. It is also possible to use these rate constant formulas to deduce some of the molecular parameters from the experimental results.

2.1. Non-Adiabatic Processes

In this section, the general case of non-adiabatic electronic transition is considered. To describe the dynamical processes of the system, the generalized master equation (GME) shall be used [3,10–16]:

$$\frac{d\hat{\sigma}}{dt} = -i\bar{L}_s\hat{\sigma} - i\bar{L}'\hat{\sigma} - \hat{R}\hat{\sigma}, \tag{6}$$

where $\bar{L}'$ is responsible for the non-adiabatic processes. The BOA approximation allows a molecular description of the non-adiabatic electronic transition; especially for the electronic states and with respective vibrational manifolds $\{av\}$ and $\{bu\}$ of a molecule in a condensed phase. Applying the BOA to GME yields the coupled GMEs given by

$$\frac{d\sigma_{av,av}}{dt} = -\frac{i}{\hbar}\sum_u\left(\bar{H}'_{av,bu}\sigma_{bu,av} - \sigma_{av,bu}\bar{H}'_{bu,av}\right) - (\hat{R}\hat{\sigma})_{av,av}, \tag{7}$$

$$\frac{d\sigma_{av,av'}}{dt} = -\left(i\bar{\omega}_{av,av'} + R^{av,av'}_{av,av'}\right)\sigma_{av,av'} - \frac{i}{\hbar}\sum_u \bar{H}'_{av,bu}\sigma_{bu,av'} - \sigma_{av,bu}\bar{H}'_{bu,av'}, \tag{8}$$

$$\begin{aligned}\frac{d\sigma_{bu,av}}{dt} = & -\left(i\bar{\omega}_{bu,av} + R^{bu,av}_{bu,av}\right)\sigma_{bu,av} \\ & -\frac{i}{\hbar}\left(\sum_{v'}\bar{H}'_{bu,av'}\sigma_{av',av} - \sum_{u'}\sigma_{bu,bu'}\bar{H}'_{bu',av}\right),\end{aligned} \tag{9}$$

where $\sigma_{av,av}(t)$, $\sigma_{av,av'}(t)$, and $\sigma_{bu,av}(t)$ represent the vibronic population, the vibrational coherence or phase, and the vibronic coherence, respectively.

Eq. (9) can be written as [1,17–21]

$$\begin{aligned}\frac{d\sigma_{bu,av}}{dt} = & -(i\bar{\omega}_{bu,av} + R^{bu,av}_{bu,av})\sigma_{bu,av} - \frac{i}{\hbar}\bar{H}'_{bu,av}(\sigma_{av,av} - \sigma_{bu,bu}) \\ & -\frac{i}{\hbar}\left(\sum_{v'\neq v}\bar{H}'_{bu,av'}\sigma_{av',av} - \sum_{u'\neq u}\sigma_{bu,bu'}\bar{H}'_{bu',av}\right).\end{aligned} \tag{10}$$

Lam Research Ex. 1035 - Page 194
Lam Research Corp. v. Inpria Corp.
IPR2024-00033 - U.S. Patent No. 9,823,564

To the second-order approximation, it is needed only to consider

$$\frac{d\sigma_{bu,av}}{dt} = -(i\bar{\omega}_{bu,av} + R^{bu,av}_{bu,av})\sigma_{bu,av} - \frac{i}{\hbar}\bar{H}'_{bu,av}(\sigma_{av,av} - \sigma_{bu,bu}). \tag{11}$$

By using the Laplace transformation method [22], $\sigma_{bu,av}(t)$ can be eliminated from Eq. (7)

$$\frac{d\sigma_{av,av}}{dt} = \frac{2}{\hbar}\sum_u \mathrm{Im}[e^{-t(i\bar{\omega}_{bu,av}+\gamma_{bu,av})}\sigma_{bu,av}(0)] - (\hat{R}\hat{\sigma})_{av,av} + \sum_u \int_0^t d\tau M(\tau)_{bu,av}[\sigma_{bu,bu}(t-\tau) - \sigma_{av,av}(t-\tau)]. \tag{12}$$

Here, the memory kernel $M(\tau)_{bu,av}$ is given by

$$M(\tau)_{bu,av} = \mathrm{Im}\left[\frac{2i}{\hbar^2}|(\bar{H}')^2_{av,bu}\, e^{-\tau(i\bar{\omega}_{bu,av}+\gamma_{bu,av})}\right]. \tag{13}$$

In the Markoff approximation, Eq. (7) reduces to

$$\frac{d\sigma_{av,av}}{dt} = \frac{2}{\hbar}\sum_u \mathrm{Im}[e^{-t(i\bar{\omega}_{bu,av}+\gamma_{bu,av})}\sigma_{bu,av}(0)] + \sum_u W_{bu,av}[\sigma_{bu,bu}(t) - \sigma_{av,av}(t)] - (\hat{R}\hat{\sigma})_{av,av}, \tag{14}$$

where $W_{bu,av}$ denotes the rate constant for $av \leftrightarrow bu$

$$W_{bu,av} = \int_0^\infty dt M(t)_{bu,av} = \frac{2}{\hbar^2}\frac{\gamma_{bu,av}}{\gamma^2_{bu,av} + \bar{\omega}^2_{bu,av}}|\bar{H}'_{av,bu}|^2. \tag{15}$$

Here, it is assumed that $\gamma_{bu,av}$ denotes the real part of $R^{bu,av}_{bu,av}$ and the imaginary part is included in $\omega_{bu,av}$. Similarly, the following equation is obtained:

$$\frac{d\sigma_{bu,bu}}{dt} = -\frac{2}{\hbar}\sum_v \mathrm{Im}[e^{-t(i\bar{\omega}_{bu,av}+r_{bu,av})}\sigma_{bu,av}(0)] - \sum_v W_{bu,av}[\sigma_{bu,bu}(t) - \sigma_{av,av}(t)] - (\hat{R}\hat{\sigma})_{bu,bu}. \tag{16}$$

Experimentally the dynamics of the product is also often measured.

Lam Research Ex. 1035 - Page 195
Lam Research Corp. v. Inpria Corp.
IPR2024-00033 - U.S. Patent No. 9,823,564

Notice that in $(\hat{R}\hat{\sigma})_{av,av}$ only vibrational relaxation is involved due to the coupling between the system and the heat bath, i.e.,

$$\begin{aligned}(\hat{R}\hat{\sigma})_{av,av} &= \sum_{v'} R_{av,av}^{av',av'}\sigma_{av',av'} \\ &= R_{av,av}^{av,av}\sigma_{av,av} + \sum_{v'\neq v} R_{av',av'}^{av',av'}\sigma_{av',av'} \\ &= \sum_{v'\neq v} R_{av,av}^{av',av'}\sigma_{av',av'} - R_{av',av'}^{av,av}\sigma_{av,av}. \end{aligned} \tag{17}$$

It follows that

$$\begin{aligned}\frac{d\sigma_{av,av}}{dt} = \frac{2}{\hbar}\sum_{v}\mathrm{Im}[e^{-t(i\bar{\omega}_{bu,av}+\gamma_{bu,av})}\sigma_{bu,av}(0)] + \sum_{v} W_{bu,av}[\sigma_{bu,bu}(t) - \sigma_{av,av}(t)] \\ - \sum_{v'} R_{av,av}^{av',av'}\sigma_{av',av'} - R_{av',av'}^{av,av}\sigma_{av,av}. \end{aligned} \tag{18}$$

Similarly, the following equation is obtained:

$$\begin{aligned}\frac{d\sigma_{bu,bu}}{dt} = &-\frac{2}{\hbar}\sum_{v}\mathrm{Im}[e^{-t(i\varpi_{bu,av}+\gamma_{bu,av})}\sigma_{bu,av}(0)] \\ &- \sum_{v} W_{bu,av}[\sigma_{bu,bu}(t) - \sigma_{av,av}(t)] \\ &- \sum_{u'} R_{bu,bu}^{bu',bu'}\sigma_{bu',bu'} - R_{bu',bu'}^{bu,bu}\sigma_{bu,bu}. \end{aligned} \tag{19}$$

In the right-hand side of Eq. (18), the first term, the second term, and the third term describe the dynamical behaviors of $\sigma_{av,av}$ due to the vibronic coherence dynamics, non-adiabatic transitions [23], and vibrational relaxation, respectively. Several cases can be considered. First, if vibrational relaxation is much faster than electronic processes, then

$$R_{av,av}^{av',av'}\sigma_{av,av} = R_{av',av'}^{av,av}\sigma_{av,av}. \tag{20}$$

If the heat bath maintains thermal equilibrium, then $\sigma_{av,av}$ is related to the Bolzmann distribution P_{av} by

$$\sigma_{av,av}(t) = \sigma_a(t)P_{av}, \tag{21}$$

where $\sigma_a(t)$ represents the total population of the system in the electronic state. Similarly, it is obvious

$$\sigma_{bu,bu}(t) = \sigma_b(t)P_{bu}. \tag{22}$$

Using Eqs. (21) and (22), we can rewrite Eq. (18) as

$$\frac{d\sigma_a}{dt} = \frac{2}{\hbar}\sum_{u}\sum_{v}\mathrm{Im}[e^{-t(i\bar{\omega}_{bu,av}+\gamma_{bu,av})}\sigma_{bu,av}(0)] + (W_{b\to a}\sigma_b - W_{a\to b}\sigma_a). \tag{23}$$

Lam Research Ex. 1035 - Page 196
Lam Research Corp. v. Inpria Corp.
IPR2024-00033 - U.S. Patent No. 9,823,564

Here

$$W_{b\to a} = \sum_u \sum_v P_{bv} W_{bu,av}. \tag{24}$$

and

$$W_{a\to b} = \sum_u \sum_v P_{av} W_{bu,av}. \tag{25}$$

Similarly, the following equation is obtained:

$$\frac{d\sigma_b}{dt} = -\frac{2}{\hbar}\sum_u \sum_v \mathrm{Im}[e^{-t(i\tilde{\omega}_{bu,av}+\gamma_{bu,av})}\sigma_{bu,av}(0)] - (W_{b\to a}\sigma_b - W_{a\to b}\sigma_a). \tag{26}$$

Next, if vibrational relaxation is much slower than electronic transitions then

$$\frac{d\sigma_{av,av}}{dt} = \frac{2}{\hbar}\sum_u \mathrm{Im}[e^{-t(i\tilde{\omega}_{bu,av}+r_{bu,av})}\sigma_{bu,av}(0)] - W_{av}\sigma_{av,av} + \sum_u W_{bu,av}\sigma_{bu,bu}, \tag{27}$$

where W_{av} denotes the single-vibronic level rate constant [24],

$$W_{av} = \sum_u W_{bu,av}. \tag{28}$$

Similarly

$$\frac{d\sigma_{bu,bu}}{dt} = -\frac{2}{\hbar}\sum_v \mathrm{Im}[e^{-t(i\tilde{\omega}_{bu,av}+\gamma_{bu,av})}\sigma_{bu,av}(0)] - W_{bu}\sigma_{bu,bu} + \sum_u W_{bu,av}\sigma_{av,av}, \tag{29}$$

where

$$W_{bu} = \sum_v W_{bu,av}. \tag{30}$$

In condensed phase, $\gamma_{bu,av}$ contains pure dephasing $R^{bu,av}_{bu,av}(d)$, $R^{bu,bu}_{bu,bu}$, and $R^{av,av}_{av,av}$, and may be very fast so that in the time scale of experiment, the vibronic coherence term may disappear. The results presented in this subchapter are very general and can be applied to IC, ISC, photo-induced energy transfer, and photo-induced electronic transfer.

Lam Research Ex. 1035 - Page 197
Lam Research Corp. v. Inpria Corp.
IPR2024-00033 - U.S. Patent No. 9,823,564

2.2. RATE CONSTANTS

There are three types of rate constants appearing in the previous subsection, i.e., $W_{bu,av}$, the state-to-state rate constant, W_{av} (or W_{bu}), the single-vibronic level rate constant, and $W_{a\to b}$ (or $W_{b\to a}$), the thermal average rate constant. In the BOA approximation,

$$\bar{H}'_{av,bu} = \langle \Psi_{av} | \bar{H}' | \Psi_{bu} \rangle \tag{31}$$

and the molecular-system wavefunctions Ψ_{av} and Ψ_{bu} can be written in terms of electronic wavefunctions $\Phi_a(q, Q)$ and $\Phi_b(q, Q)$, and vibrational (ro-vibrational) wavefunctions $\Theta_{av}(Q)$ and $\Theta_{bu}(Q)$, i.e.,

$$\Psi_{av}(q, Q) = \Phi_a(q, Q)\Theta_{av}(Q) \tag{32}$$

and

$$\Psi_{bu}(q, Q) = \Phi_b(q, Q)\Theta_{bu}(Q). \tag{33}$$

In this case, $\bar{H}'_{av,bu}$ can be written as

$$\bar{H}'_{av,bu} = \langle \Theta_{av} | \bar{H}'_{ab} | \Theta_{bu} \rangle, \tag{34}$$

where $\bar{H}'_{ab}$ represents the electronic matrix elements

$$\bar{H}'_{ab} = \langle \Phi_a(q, Q) | \bar{H}' | \Phi_b(q, Q) \rangle = \bar{H}'_{ab}(Q). \tag{35}$$

In most non-adiabatic processes (except IC) [25], $\bar{H}'_{ab}(Q)$ can be expanded in terms of vibrational coordinates Q_ℓ,

$$\bar{H}'_{ab}(Q) = \bar{H}'_{ab}(0) + \sum_\ell \left(\frac{\partial \bar{H}'_{ab}}{\partial Q_\ell} \right)_0 Q_\ell + \cdots. \tag{36}$$

For the case in which $\bar{H}'_{ab}(0)$ is non-zero, the first-order term can be ignored, i.e.,

$$\bar{H}'_{ab}(Q) \approx \bar{H}'_{ab}(0). \tag{37}$$

This is usually called the Condon approximation. In this case, the following three types of the rate constants can be obtained [26,27]:

$$W_{bu,av} = \frac{2\pi}{\hbar^2} |\bar{H}'_{ab}(0)|^2 |\langle \Theta_{av} | \Theta_{bu} \rangle|^2 D(\bar{\omega}_{bu,av}), \tag{38}$$

Lam Research Ex. 1035 - Page 198
Lam Research Corp. v. Inpria Corp.
IPR2024-00033 - U.S. Patent No. 9,823,564

$$W_{av} = \frac{2\pi}{\hbar^2} |\bar{H}'_{ab}(0)|^2 \sum_u |\langle \Theta_{av} | \Theta_{bu} \rangle|^2 D(\bar{\omega}_{bu,av}), \tag{39}$$

and

$$W_{a\to b} = \frac{2\pi}{\hbar^2} |\bar{H}'_{ba}(0)|^2 \sum_u \sum_v P_{av} |\langle \Theta_{av} | \Theta_{bu} \rangle|^2 D(\bar{\omega}_{bu,av}), \tag{40}$$

where

$$D(\bar{\omega}_{bu,av}) = \frac{1}{\pi} \frac{\gamma_{bu,av}}{\gamma_{bu,av}^2 + \bar{\omega}_{bu,av}^2}, \tag{41}$$

$$P_{av} = \frac{e^{-\bar{E}_{av}/k_B T}}{Q_a(T)}, \tag{42}$$

and $|\langle \Theta_{av} | \Theta_{bu} \rangle|^2$ is the Frank–Condon factor. As $\gamma_{bu,av} \to 0$, $D(\bar{\omega}_{bu,av})$ reduces to the delta function

$$\lim_{\gamma_{bu,av}\to 0} D(\bar{\omega}_{bu,av}) = \delta(\bar{\omega}_{bu,av}) = \hbar\delta(\bar{E}_{bu} - \bar{E}_{av}). \tag{43}$$

In this case, $W_{a\to b}$, for example, can be written as

$$W_{a\to b} = \frac{2\pi}{\hbar} |\bar{H}'_{ab}(0)|^2 \rho_{a\to b}, \tag{44}$$

where $\rho_{a\to b}$ denotes the density of states

$$\rho_{a\to b} = \sum_u \sum_v P_{av} |\langle \Theta_{av} | \Theta_{bu} \rangle|^2 \delta(\bar{E}_{bu} - \bar{E}_{av}). \tag{45}$$

The conventional density of states ρ(E) is defined by

$$\rho(E) = \sum_i \delta(E - E_i). \tag{46}$$

To evaluate the rate constants it is necessary to know the potential surfaces of a electronic state and b electronic state. For this purpose, the harmonic surfaces are commonly used,

$$U_a(Q) = \bar{E}_a + \sum_i \frac{1}{2} \omega_i^2 Q_i^2 \tag{47}$$

Lam Research Ex. 1035 - Page 199
Lam Research Corp. v. Inpria Corp.
IPR2024-00033 - U.S. Patent No. 9,823,564

and

$$U_b(Q) = \bar{E}_b + \sum_i \frac{1}{2}(\omega')_i^2 (Q')_i^2. \tag{48}$$

If $\omega_i = \omega'_i$ and $Q_i \neq Q'_i$, the vibrational mode is displaced, if $\omega_i \neq \omega'_i$ and $Q_i = Q'_i$, the vibrational mode is distorted, and if $\omega_i \neq \omega'_i$ and $Q_i \neq Q'_i$, the vibrational mode is displaced distorted. The Duschinsky effect refers to the case where there exists mode mixing.

Only the rate constants for the displaced surfaces will be given in this paper. For $W_{a\to b}$, it becomes [28]

$$W_{a\to b} = \frac{1}{\hbar}|\bar{H}'_{ab}(0)|^2 \int_{-\infty}^{\infty} dt\ \exp[it\bar{\omega}_{ba} - \gamma_{ba}(t)]G_{ba}(t). \tag{49}$$

Here

$$G_{ba}(t) = \prod_{j=1}^{N} g_{ba}^j(t) \tag{50}$$

with

$$g_{ba}^j(t) = \exp[-S_j\{(2\bar{n}_j + 1) - \bar{n}_j\, e^{-it\omega_j} - (\bar{n}_j + 1)e^{it\omega_j}\}], \tag{51}$$

where $\bar{n}_j$ denotes the phonon distribution

$$\bar{n}_j = \frac{1}{\exp(\hbar\omega_j/k_{\mathrm{B}}T) - 1}. \tag{52}$$

Similarly for W_{av} it is found that

$$W_{av} = \frac{1}{\hbar^2}|\bar{H}'_{ab}(0)|^2 \int_{-\infty}^{\infty} dt\ \exp\left[i\bar{\omega}_{ba} - \gamma_{ba}|t| - \sum_j S_j(1 - e^{it\omega_j})\right]$$
$$\times \prod_j \left[\sum_{m'_j}^{v_j} \frac{\{S_j(e^{it\omega_j/2} - e^{-it\omega_j/2})^2\}^{v_j - m'_{ij}}}{m'_j!\{(v_j - m'_j)!\}^2}\right]. \tag{53}$$

Finally, for $W_{bu,av}$ we need to calculate the Frank–Condon factor $|\langle\Theta_{av}|\Theta_{bu}\rangle|^2$ which is given by

$$|\langle\Theta_{av}|\Theta_{bu}\rangle|^2 = e^{-\beta d^2/2}\left|\sum_{m=0}^{u \text{ or } v} \frac{\sqrt{u!v!}(-\sqrt{\beta/2}d)^{v-m}(\sqrt{\beta/2}d)^{u-m}}{m!(v-m)!(u-m)!}\right|^2. \tag{54}$$

It should be noted that W_{av} and $W_{bu,av}$ are usually applicable only to the isolated (i.e., collision-free) molecule case. In this case, the intramolecular vibrational relaxation (IVR) is slow compared with the non-adiabatic

Lam Research Ex. 1035 - Page 200
Lam Research Corp. v. Inpria Corp.
IPR2024-00033 - U.S. Patent No. 9,823,564

process. For the case in which IVR is much faster than the non-adiabatic process under consideration, we have to use the so-called microcanonical rate constant $W_{a\to b}(E)$,

$$W_{a\to b}(E) = \sum_v \sum_u P_{av}(E) W_{bu,av} = \sum_v P_{av}(E) W_{av}, \tag{55}$$

where P_{av} (E) denotes the microcanonical distribution

$$P_{av}(E) = \frac{\delta(E - E_{av})}{\rho_a(E)} \tag{56}$$

and

$$\rho_a(E) = \sum_v \delta(E - E_{av}). \tag{57}$$

It can be shown that $W_{a\to b}(E)$ is related to $W_{a\to b}(T)$ (with $\beta = 1/k_B T$) by

$$W_{ab}(T) = W_{ab}(\beta) = \frac{\int_0^\infty dE \rho_a(E) W_{a\to b}(E) e^{-\beta E}}{\int_0^\infty dE \rho_a(E) e^{-\beta E}}, \tag{58}$$

where

$$Q_a(T) = Q_a(\beta) = \int_0^\infty dE \rho_a(E) e^{-\beta E} \equiv \text{canonical partition function.} \tag{59}$$

Using the method of steepest-descent one can show that approximately

$$W_{a\to b}(E) = W_{a\to b}(\beta). \tag{60}$$

Here, β is to be determined from

$$E = \sum_j \frac{\hbar\omega_j}{e^{\beta\hbar\omega_j} - 1}. \tag{61}$$

Eq. (60) indicates that $W_{a\to b}(E)$ can be obtained from the thermal average rate constant with "temperature" β being determined for Eq. (61).

2.3. RADIATIONLESS TRANSITIONS

In this subsection, the rate constants of IC and ISC are introduced and their structures are detailed. In particular, applying the harmonic potential model to these rate constants provides with practical and applicable theoretical formulas. A numerical evaluation method based on steepest-descent (or saddle-point method) is then demonstrated for the computation.

Lam Research Ex. 1035 - Page 201
Lam Research Corp. v. Inpria Corp.
IPR2024-00033 - U.S. Patent No. 9,823,564

2.3.1. Internal Conversion (IC)

The theory of radiationless transitions (or electronic relaxation) based on the BOA approximation as a basis set was originally proposed by Huang and Rhys [29] and applied to color centers and later modified and extended by Lin and Bersohn [30] to molecular systems in photochemistry and photophysics. Notice that for the IC $a \to b$, the IC rate constant is given by

$$W^{\mathrm{IC}}_{a\to b} = \frac{2\pi}{\hbar^2}\sum_v \sum_u P_{av} |\langle \Psi_{bu}|\hat{H}'_{\mathrm{BO}}|\Psi_{av}\rangle|^2 D(\bar{\omega}_{bu,av}), \tag{62}$$

where $\hat{H}'_{\mathrm{BO}}$ denotes the B–O coupling [24,30]

$$\hat{H}'_{\mathrm{BO}}\Psi_{av} = \hat{H}'_{\mathrm{BO}}[\Phi_a(q,Q)\Theta_{av}(Q)] - \sum_\ell \hbar^2 \frac{\partial \Phi_a}{\partial Q_\ell}\frac{\partial \Theta_{av}}{\partial Q_\ell} - \sum_\ell \frac{\hbar^2}{2}\frac{\partial^2 \Phi_a}{\partial Q_\ell^2}\Theta_{av}. \tag{63}$$

In most cases, the second terms in Eq. (62) are smaller than the first ones. In this approximation, Eq. (63) becomes

$$W^{\mathrm{IC}}_{a\to b}(\ell) = \frac{2\pi}{\hbar^2}\sum_v \sum_u P_{av} \left| \left\langle \Theta_{bu}|R_{ba}(\ell)\left|\frac{\partial \Theta_{av}}{\partial Q_\ell}\right\rangle \right|^2 D(\bar{\omega}_{bu,av}). \tag{64}$$

In this formula

$$R_{ba}(\ell) = -\hbar^2 \left\langle \Phi_b \left| \frac{\partial}{\partial Q_\ell} \right| \Phi_a \right\rangle. \tag{65}$$

The vibrational modes in radiationless transitions have been classified by Lin and Bersohn [30] into promoting modes like Q_ℓ in $R_{ba}(\ell)$ and accepting modes, other vibrational modes participating in accepting the electronic energy $\bar{\omega}_{ba}$ [30–34]. In Eq. (64) for simplicity it is assumed that there is only one promoting mode involved in IC. Suppose

$$\Theta_{av}(Q) = \prod_j \chi_{av_j}(Q_j); \quad \Theta_{bu}(Q) = \prod_j \chi_{bu_j}(Q'_j) \tag{66}$$

and the promoting mode is not displaced and not distorted. Then in the Condon approximation

$$W^{\mathrm{IC}}_{a\to b}(\ell) = \frac{2\pi}{\hbar^2}|R_{ba}(\ell)|^2 [\frac{\omega_\ell \bar{n}_\ell}{2\hbar}\left\{ \prod_{j\neq \ell}\left(\sum_{u_j}\sum_{v_j} P_{av_j}|\langle \chi_{bu_j}|\chi_{av_j}\rangle|^2 \right)\right\} D_-(\bar{\omega}_{bu,av})$$
$$+ \frac{\omega_\ell}{2\hbar}(\bar{n}_\ell + 1)\left\{ \prod_{j\neq \ell}\left(\sum_{u_j}\sum_{v_j} P_{av_j}|\langle \chi_{bu_j}|\chi_{av_j}\rangle|^2 \right)\right\} D_+(\bar{\omega}_{bu,av})] \tag{67}$$

Lam Research Ex. 1035 - Page 202
Lam Research Corp. v. Inpria Corp.
IPR2024-00033 - U.S. Patent No. 9,823,564

If all the accepting modes (usually the totally symmetric modes) are displaced oscillators [24], then

$$W^{\mathrm{IC}}_{a\to b}(\ell) = \frac{1}{\hbar^2}|R_{ba}(\ell)|^2\left\{\frac{\omega_\ell \bar{n}_\ell}{2\hbar}\right\}\int_{-\infty}^{\infty} dt\ \exp[it(\bar{\omega}_{ba}-\omega_\ell)-\gamma_{ba}|t|]G^{\ell}_{ba}(t) + \frac{\omega_\ell(\bar{n}_\ell+1)}{2\hbar}\int_{-\infty}^{\infty} dt\ \exp[it(\bar{\omega}_{ba}+\omega_i)-\gamma_{ba}|t|]G^{\ell}_{ba}(t). \tag{68}$$

where $G^{\ell}_{ba}(t) = \prod_{j\neq\ell}^{N-1} g^{j}_{ba}(t)$ and

$$g^{j}_{ba}(t) = \exp[S_j\{\bar{n}_j\, e^{-it\omega_j} + (\bar{n}_j+1)e^{it\omega_j}\}]. \tag{69}$$

If $(\hbar\omega_\ell)/(k_{\mathrm{B}}T) >> 1$, then Eq. (68) reduces to

$$W^{\mathrm{IC}}_{a\to b}(\ell) = \frac{1}{\hbar^2}|R_{ba}(\ell)|^2\left\{\frac{\omega_\ell}{2\hbar}\right\}\int_{-\infty}^{\infty} dt\ \exp[it(\varpi_{ba}+\omega_i)-\gamma_{ba}|t|]G^{\ell}_{ba}(t). \tag{70}$$

This indicates that the electronic energy gap is reduced by ω_i, one quantum of the promoting mode; i.e., the promoting mode can accept at least one vibration quantum. From Eq. (65) one can see that the symmetry argument can be used to determine the promoting mode. For example, for formaldehyde [35–42] the $\mathrm{n}\to\pi^*$ transition corresponds to $\mathrm{A}_1\to\mathrm{A}_2$ for the $C_{2\mathrm{v}}$ symmetry; in this case the promoting mode for the IC $\mathrm{A}_2\to\mathrm{A}_1$ should possess the A_2 symmetry.

2.3.2. *Intersystem Crossing (ISC)*

Next ISC $a\to b$ is considered. In this case, if the spin–orbit coupling $\hat{H}'_{\mathrm{so}}$ is not large, it can be used as a perturbation for ISC, i.e., [43,44]

$$W^{\mathrm{ISC}}_{a\to b}(T) = \frac{2\pi}{\hbar^2}\sum_u\sum_v P_{av}|\langle\Theta_{bu}|\langle\Phi_b|\hat{H}'_{\mathrm{so}}|\Phi_a\rangle|\Theta_{av}\rangle|^2 D(\bar{\omega}_{bu,av}) \tag{71}$$

and in the Condon approximation Eq. (71) becomes

$$W^{\mathrm{ISC}}_{a\to b}(T) = \frac{2\pi}{\hbar^2}|\langle\Phi_b|\hat{H}'_{\mathrm{so}}|\Phi_a\rangle|^2\sum_u\sum_v P_{av}|\langle\Theta_{bu}|\Theta_{av}\rangle|^2 D(\bar{\omega}_{bu,av}). \tag{72}$$

On the other hand, if the spin–orbit coupling is large and the electronic gap is small, the singlet state and triplet state will strongly mix; these states should be diagonalized and the radiationless fraction can be treated in the IC manner. For the displaced surfaces, Eq. (72) becomes

$$W^{\mathrm{ISC}}_{a\to b}(T) = \frac{1}{\hbar^2}|\langle\Phi_b|\hat{H}'_{\mathrm{so}}|\Phi_a\rangle|^2\int_{-\infty}^{\infty} dt\ \exp[it\bar{\omega}_{ba}-\gamma_{ba}|t|]G_{ba}(t). \tag{73}$$

Lam Research Ex. 1035 - Page 203
Lam Research Corp. v. Inpria Corp.
IPR2024-00033 - U.S. Patent No. 9,823,564

It should be noted that the expressions for IC and ISC cases Eqs. (71) and (72) are quite similar except for the electronic matrix elements and energy gaps. Although the Fourier integral involved in $W^{\mathrm{ISC}}_{a\to b}$ given above can easily be carried out numerically, analytical expressions are often desired; for this purpose, the method of steepest-descent [45–51] (saddle-point method) is commonly used. Take Eq. (73) as an example. $W^{\mathrm{ISC}}_{a\to b}$ will first be written as

$$W^{\mathrm{ISC}}_{a\to b}(T) = \frac{1}{\hbar^2}|\langle\Phi_b|\hat{H}'_{\mathrm{so}}|\Phi_a\rangle|^2 \exp\left[-\sum_j S_j(2\bar{n}_j+1)\right]\int_{-\infty}^{\infty} dt\ \exp[f(t)], \tag{74}$$

where

$$f(t) = it\bar{\omega}_{ba} + \sum_j S_j[\bar{n}_j\, e^{-it\omega_j} + (\bar{n}_j+1)e^{it\omega_j}]. \tag{75}$$

Setting $f'(t^*) = 0$ yields

$$-\bar{\omega}_{ba} = \bar{\omega}_{ab} = \sum_j S_j\omega_j[-\bar{n}_j\, e^{-it^*\omega_j} + (\bar{n}_j+1)e^{it^*\omega_j}]. \tag{76}$$

Here t^* is the saddle-point value of t, and

$$f(t) = f(t^*) + \frac{1}{2}f''(t^*)(t-t^*)^2 + \cdots. \tag{77}$$

Substituting Eq. (77) into Eq. (74) yields

$$W^{\mathrm{ISC}}_{a\to b}(T) = \frac{1}{\hbar^2}|\langle\Phi_b|\hat{H}'_{\mathrm{so}}|\Phi_a\rangle|^2 \exp\left[-\sum_j S_j(2\bar{n}_j+1)\right]\sqrt{\frac{2\pi}{-f''(t^*)}}e^{f(t^*)}. \tag{78}$$

In particular, at $T = 0$ (or $\hbar\omega_j/k_{\mathrm{B}}T \gg 1$, or $\bar{n}_j = 0$) Eq. (76) becomes

$$\bar{\omega}_{ab} = \sum_j S_j\omega_j\, e^{it^*\omega_j}. \tag{79}$$

This equation indicates that it^* is a real number and that when $\overline{\omega}_{ba}/\omega_i$ is large, only the high frequency accepting modes play an important role in radiationless transitions, for example, if one compares the term $e^{it^*\omega_j}$ for $\omega_{\mathrm{j}} = 100\,\mathrm{cm}^{-1}$ and for $\omega_{\mathrm{j}} = 3000\,\mathrm{cm}^{-1}$. To apply this approximation method, it is necessary to first solve Eq. (79) for it^*; this can be accomplished by introducing an average frequency $\tilde{\omega}$ (usually the frequency of major accepting modes) it is then obtained

$$e^{it^*\tilde{\omega}} = \frac{\bar{\omega}_{ab}}{S\tilde{\omega}} \quad \text{or} \quad it^* = \frac{1}{\tilde{\omega}}\ln\left(\frac{\bar{\omega}_{ab}}{S\tilde{\omega}}\right), \tag{80}$$

Lam Research Ex. 1035 - Page 204
Lam Research Corp. v. Inpria Corp.
IPR2024-00033 - U.S. Patent No. 9,823,564

where $S = \sum_j S_j$ and

$$W_{a\to b}^{\mathrm{ISC}}(0) = \frac{1}{\hbar^2}|\langle\Phi_b|\hat{H}'_{\mathrm{so}}|\Phi_a\rangle|^2 \times \sqrt{\frac{2\pi}{\tilde{\omega}\bar{\omega}_{ab}}}\exp\left[-S - \left(\frac{\bar{\omega}_{ab}}{\tilde{\omega}}\right)\left\{\ln\left(\frac{\bar{\omega}_{ab}}{S\tilde{\omega}}\right) - 1\right\}\right]. \tag{81}$$

This is usually referred to as the energy gap expression for radiationless transitions first derived by Engleman and Jortner [52].

Similarly for $T \neq 0$, it follows that

$$f''(t^*) = -\tilde{\omega}\bar{\omega}_{ab}\sqrt{1 + 4\bar{n}(\bar{n}+1)\left(\frac{S\tilde{\omega}}{\bar{\omega}_{ab}}\right)^2} \tag{82}$$

and

$$f(t^*) = -\left(\frac{\bar{\omega}_{ab}}{\tilde{\omega}}\right)\ln\left\{\frac{(\bar{\omega}_{ab}/S\tilde{\omega})\{1 + \sqrt{1 + 4\bar{n}(\bar{n}+1)(S\tilde{\omega}/\bar{\omega}_{ab})^2}\}}{2(\bar{n}+1)}\right\} + \left(\frac{\bar{\omega}_{ab}}{\tilde{\omega}}\right)\sqrt{1 + 4\bar{n}(\bar{n}+1)\left(\frac{S\tilde{\omega}}{\bar{\omega}_{ab}}\right)^2}. \tag{83}$$

For the case of $0 \leq \bar{n} \ll 1$, Eqs. (82) and (83) reduce to

$$f''(t^*) = -\tilde{\omega}\bar{\omega}_{ab}\left[1 + 2\bar{n}(1+\bar{n})\left(\frac{S\tilde{\omega}}{\bar{\omega}_{ab}}\right)^2\right] \tag{84}$$

and

$$f(t^*) = -\bar{\omega}_{ab}/\tilde{\omega}\left[\ln\left(\frac{\bar{\omega}_{ab}}{S\tilde{\omega}}\right) - (1+\bar{n})\right] + \left(\frac{S^2\tilde{\omega}}{\bar{\omega}_{ab}}\right)\bar{n}(1+\bar{n}), \tag{85}$$

respectively. That is,

$$\frac{W_{a\to b}^{\mathrm{ISC}}(T)}{W_{a\to b}^{\mathrm{ISC}}(0)} = \frac{1}{\sqrt{1 + 2\bar{n}(1+\bar{n})(S\tilde{\omega}/\bar{\omega}_{ab})^2}}\exp\left[-\left\{S - \frac{\bar{\omega}_{ab}}{\tilde{\omega}} - \left(\frac{S^2\tilde{\omega}}{\bar{\omega}_{ab}}\right)(1+\bar{n})\right\}\bar{n}\right] \tag{86}$$

and

$$\frac{W_{a\to b}^{\mathrm{ISC}}(T)}{W_{a\to b}^{\mathrm{ISC}}(0)} = \frac{1}{\sqrt{1 + 2\bar{n}(1+\bar{n})(S\tilde{\omega}/\bar{\omega}_{ab})^2}} \times \exp\left[-\left\{S - \frac{\bar{\omega}_{ab}}{\tilde{\omega}} - \left(\frac{S^2\tilde{\omega}}{\bar{\omega}_{ab}}\right)(1+\bar{n})\right\}\bar{n}\right]. \tag{87}$$

Lam Research Ex. 1035 - Page 205
Lam Research Corp. v. Inpria Corp.
IPR2024-00033 - U.S. Patent No. 9,823,564

Another commonly used expression for $W^{\mathrm{ISC}}_{a\to b}$ is derived in the following. Notice

$$W^{\mathrm{ISC}}_{a\to b}(T) = \frac{1}{\hbar^2} |\langle \Phi_b | \hat{H}'_{\mathrm{so}} | \Phi_a \rangle|^2 \int_{-\infty}^{\infty} dt \ \exp[it\bar{\omega}_{ba}] G_{ba}(t). \tag{88}$$

Here, it is noted that

$$\int_{-\infty}^{\infty} dt \ e^{it(\bar{\omega}_{ba} + m\tilde{\omega} - n\tilde{\omega})} = \frac{2\pi}{\tilde{\omega}} \delta\left(\frac{\bar{\omega}_{ba}}{\tilde{\omega}} + m - n\right). \tag{89}$$

Applying Eq. (89) to Eq. (88) leads to

$$W^{\mathrm{ISC}}_{a\to b}(T) = \frac{2\pi}{\hbar^2 \tilde{\omega}} |\langle \Phi_b | \hat{H}'_{\mathrm{so}} | \Phi_a \rangle|^2 \ e^{-S(2\bar{n}+1)} \sum_{m=0}^{\infty} \frac{(S\bar{n})^n (S(\bar{n}+1))^m}{n!m!}, \tag{90}$$

where

$$n = m + \frac{\bar{\omega}_{ba}}{\tilde{\omega}} = m - \frac{\bar{\omega}_{ab}}{\tilde{\omega}}. \tag{91}$$

At $T = 0$, $W^{\mathrm{ISC}}_{a\to b}(T)$ reduces to

$$W^{\mathrm{ISC}}_{a\to b}(0) = \frac{2\pi}{\hbar^2 \tilde{\omega}} |\langle \Phi_b | \hat{H}'_{\mathrm{so}} | \Phi_a \rangle|^2 \ e^{-S} \frac{S^m}{m!}, \tag{92}$$

where $m = \bar{\omega}_{ab}/\tilde{\omega}$. Applying the Stirling's formula $m! \approx m^m \ e^{-m} \sqrt{2\pi m}$ and $x^y = e^{y \ln x}$ to Eq. (92), the energy gap law expression is obtained for $W^{\mathrm{ISC}}_{a\to b}$ which is given by Eq. (81).

Radiationless transitions often show a pronounced deuteration effect. This effect should be discussed. Notice that $\omega_H = \sqrt{2}\omega_D$, and $S_H = S_D/\sqrt{2}$ and that the deuteration effect can be estimated by using the Frank–Condon factor for a displaced oscillator by using the energy law expression. In this case, it is found that

$$I_{H/D} \equiv \frac{W^{\mathrm{ISC}}_{a\to b}(0,H)}{W^{\mathrm{ISC}}_{a\to b}(0,D)} = \frac{1}{2^{1/4}} \exp\left\{ (\sqrt{2}-1) S_H + \frac{\bar{\omega}_{ab}}{\tilde{\omega}_H} (1-\sqrt{2}) \ln S_H \right.$$
$$\left. + \left[\frac{\bar{\omega}_{ab}}{\tilde{\omega}_H} (\sqrt{2}-1) \left(\ln \frac{\bar{\omega}_{ab}}{\tilde{\omega}_H} - 1 \right) \right] \right\}. \tag{93}$$

Suppose that $\bar{\omega}_{ab}/\tilde{\omega}_H = 4$ and $S_H = 0.1$. Then $(W_{a\to b}(H))/(W_{a\to b}(D)) \approx 100$. This result is quite reasonable.

Lam Research Ex. 1035 - Page 206
Lam Research Corp. v. Inpria Corp.
IPR2024-00033 - U.S. Patent No. 9,823,564

Due to recent rapid developments in *ab initio* calculations, it has become possible to perform the first-principle calculations of radiationless transitions.

3. Photo-Induced Electronic Transfer and Photo-Induced Energy Transfer

In many photo-related biosystems such as photosynthetic RCs and/or antenna complexes, photo-induced electronic transfer and photo-induced electronic energy transfer occur. In order to describe these transfer processes, the theoretical formulas for their rate constants are introduced within the BO approximation.

3.1. General Consideration

For photo-induced electron transfer (ET) reactions [53], there exist three cases depending on their mechanism: (1) non-adiabatic, diabatic, or weak coupling case, (2) adiabatic, or strong coupling case, and (3) charge transfer complex case. This section shall focuses on case (1) to which perturbation theory can be applied.

In the previous sections, the expressions for non-adiabatic transitions have been obtained to the first-order approximations. To treat photo-induced energy transfer and photo-induced electronic transfer, to take into account the bridge effect between donor and accepter molecules, the higher order approximations need to be considered. In this case, instead of Eq. (40), the following equation is used:

$$W_{i\to f} = \frac{2\pi}{\hbar^2}|T_{fi}|^2 \sum_v \sum_u P_{iv}|\langle\Theta_{iv}|\Theta_{fu}\rangle|^2 D(\bar{\omega}_{fu,iv}). \tag{94}$$

Here, the electronic matrix element T_{fi} is given by

$$T_{f_i} = \bar{H}'_{fi} + \sum_m \frac{\bar{H}'_{fm}\bar{H}'_{mi}}{\bar{E}_i - \bar{E}_m} + \cdots. \tag{95}$$

The first term in Eq. (95) $\bar{H}'_{fi}$ describes the transfer through space (or the direct transfer), while the second term is usually referred to as the space exchange (or transfer through bonds).

Lam Research Ex. 1035 - Page 207
Lam Research Corp. v. Inpria Corp.
IPR2024-00033 - U.S. Patent No. 9,823,564

For displaced-oscillator surfaces [54–57], Eq. (94) becomes

$$W_{i\to f} = \frac{1}{\hbar^2}|T_{f_i}|^2 \int_{-\infty}^{\infty} dt\ \exp[it\bar{\omega}_{fi} - \gamma_{fi}|t|]G_{fi}(t). \tag{96}$$

3.2. Photo-Induced Electron Transfer

In photo-induced ET the Marcus equation [58–60] is often used and it can be derived from Eq. (96) by using the short-time approximation, i.e., $e^{\pm it\tilde{\omega}} \sim 1 \pm it\tilde{\omega} - (t\tilde{\omega})^2/2$

$$W_{i\to f} = \frac{1}{\hbar^2}|T_{fi}|^2 \int_{-\infty}^{\infty} dt\ \exp\left[it\left(\bar{\omega}_{fi} + \sum_j S_j\omega_j\right)\right] \times \exp\left[-\left(\frac{t^2}{2}\right)\sum_j (2\bar{n}_j + 1)S_j\omega_j^2\right] \tag{97}$$

or

$$W_{i\to f} = \frac{1}{\hbar^2}|T_{f_i}|^2 \sqrt{\frac{2\pi}{\sum_j (2\bar{n}_j + 1)S_j\omega_j^2}} \exp\left[-\frac{(\bar{\omega}_{f_i} + \sum_j S_j\omega_j)^2}{2\sum_j (2\bar{n}_j + 1)S_j\omega_j^2}\right]. \tag{98}$$

In the classical regime $\hbar\omega_j/kT \ll 1$ (or $\bar{n}_j \sim 0$) for all the modes, Eq. (98) reduces to

$$W_{i\to f} = \frac{1}{\hbar^2}|T_{fi}|^2 \sqrt{\frac{\pi}{\lambda kT}} \exp\left[-\frac{(\Delta\bar{E}_{fi} + \lambda)^2}{4\lambda kT}\right]. \tag{99}$$

Here, $\Delta\bar{E}_{fi} = \bar{E}_f - \bar{E}_i = \hbar\bar{\omega}_{fi}$ and λ denotes the so-called reorganization energy $\lambda = \sum_j S_j\hbar\omega_j$. For the case of displaced oscillators $\Delta\bar{E}_{fi} = \Delta G_{fi}$, the free energy changes in a photo-induced ET. Eq. (99) is usually called the Marcus equation [58–60] taking the form of an Arrhenius equation

$$W_{i\to f} = A\, e^{-(E_a/k_B T)}, \tag{100}$$

where

$$A = \frac{1}{\hbar}|T_{fi}|^2 \sqrt{\frac{\pi}{\lambda kT}} \tag{101}$$

and

$$E_a = \frac{(\Delta G_{fi} + \lambda)^2}{4\lambda}. \tag{102}$$

Lam Research Ex. 1035 - Page 208
Lam Research Corp. v. Inpria Corp.
IPR2024-00033 - U.S. Patent No. 9,823,564

It should be noted that in this case the activating energy E_a is related to ΔG_{fi} in a parabolic form. In the single-mode case, E_a represents the energy at the potential energy crossing-point while for the multi-mode case E_a denotes the energy at the minimum crossing-point [61]. In other words, in the classical regime the reaction coordinate is well defined.

From the above discussion, one can see that whether or not the Marcus equation can be used to analyze experimental data, it is important to test its temperature dependence to see if it is of the Arrhenius type.

3.3. PHOTO-INDUCED ENERGY TRANSFER

The Förster [62,63] and Dexter [64] theory in photo-induced energy transfer is discussed. For the singlet–singlet energy transfer [65,66]

$$^1D^*A \rightarrow D^1A^* \tag{103}$$

ignoring the configuration interactions the electronic wavefunctions, $^1D^*A \rightarrow D^1A^*$ can be expressed in terms of Slater determinants as

$$\Phi_i(^1D^*A) = \frac{1}{\sqrt{2}}(|\chi^+_{D^*}\chi^-_D\chi^+_A\chi^-_A| - |\chi^-_{D^*}\chi^+_D\chi^+_A\chi^-_A|) \tag{104}$$

and

$$\Phi_f(D^1A^*) = \frac{1}{\sqrt{2}}(|\chi^+_D\chi^-_D\chi^+_{A^*}\chi^-_A| - |\chi^+_D\chi^-_D\chi^-_{A^*}\chi^+_A|), \tag{105}$$

respectively, where χ_A, χ_{A^*}, χ_D, and χ_{D^*} represent the molecular orbitals of A and D. The perturbation $\hat{H}'$ is due to the two-electron Coulomb interaction between A and D,

$$\hat{H}'_{fi} = \langle\Phi_f\hat{H}'|\Phi_i\rangle = 2\left\langle\chi_D\chi_{A^*}\left|\frac{e^2}{r_{ab}}\right|\chi_{D^*}\chi_A\right\rangle - \left\langle\chi_{A^*}\chi_D\left|\frac{e^2}{r_{ab}}\right|\chi_{D^*}\chi_A\right\rangle. \tag{106}$$

That is, $\hat{H}'_{fi}$ is due to the Coulomb and exchange interactions. Ignoring the exchange interaction and carrying out the multi-pole expansion for the Coulomb interaction yield

$$H'_{fi} = \frac{1}{\varepsilon R^3_{DA}}\left[(\vec{\mu}_A\cdot\vec{\mu}_D) - \frac{3(\vec{\mu}_A\cdot\vec{\mu}_{DA})(\vec{\mu}_{D^*}\cdot\vec{\mu}_{DA})}{R^2_{DA}}\right], \tag{107}$$

where $\vec{\mu}_A$ denotes the transition moment for A

$$\vec{\mu}_A = \sqrt{2}\langle\chi_{A^*}| - e\vec{r}_\alpha|\chi_A\rangle \tag{108}$$

and $\vec{\mu}_D$ denotes the transition moment for D

$$\vec{\mu}_D = \sqrt{2}\langle\chi_{D^*}| - e\vec{r}_\alpha|\chi_D\rangle. \tag{109}$$

Lam Research Ex. 1035 - Page 209
Lam Research Corp. v. Inpria Corp.
IPR2024-00033 - U.S. Patent No. 9,823,564

Here the dielectric constant ε is introduced to take care of the medium effect if R_{DA} is large. $\hat{H}'_{fi}$ is often rewritten as

$$H'_{fi} = \frac{|\vec{\mu}_A||\vec{\mu}_D|}{\varepsilon R_{DA}^3}\Omega_{AD}. \tag{110}$$

Neglecting the super-exchange contribution the thermal average rate constant for the singlet–singlet transfer can be expressed as

$$W_{i\to f} = \frac{2\pi}{\hbar^2}\frac{|\vec{\mu}_A|^2|\vec{\mu}_D|^2}{\varepsilon^2 R_{DA}^6}\Omega_{DA}^2 \sum_v \sum_u P_{iv}|\langle\Theta_{iv}|\Theta_{fu}\rangle|^2\delta(\bar{\omega}_{fu,iv}). \tag{111}$$

Here, for simplicity the dephasing constant $\gamma_{fu,iv}$ is ignored. Using the relations

$$\begin{aligned}\delta(\bar{\omega}_{fu,iv}) &= \delta(\bar{\omega}_{fu}^D + \bar{\omega}_{fu}^A - \bar{\omega}_{iv}^D - \bar{\omega}_{iv}^A) \\ &= \int_{-\infty}^{\infty} d\omega\delta(\bar{\omega}_{fu}^D - \bar{\omega}_{iv}^D + \omega)\delta(\bar{\omega}_{fu}^A - \bar{\omega}_{iv}^A - \omega).\end{aligned} \tag{112}$$

where the nuclear function can be divided a product of the wavefunctions of the acceptor and the donor

$$\Theta_{iv} = \Theta_{iv}^A\Theta_{iv}^D; \quad \Theta_{iv} = \Theta_{fu}^A\Theta_{fu}^D \tag{113}$$

and

$$P_{iv} = P_{iv}^A P_{iv}^D. \tag{114}$$

Eq. (112) becomes

$$\begin{aligned}W_{i\to f} = &\frac{2\pi}{\hbar^2}\frac{|\vec{\mu}_A|^2|\vec{\mu}_D|^2}{\varepsilon^2 R_{DA}^6}\Omega_{DA}^2 \\ &\times \int_{-\infty}^{\infty} d\omega \sum_u \sum_v P_{iv}^A|\langle\Theta_{iv}^A|\Theta_{fu}^A\rangle|^2\delta(\bar{\omega}_{fu}^A - \bar{\omega}_{iv}^A - \omega) \\ &\times \sum_u \sum_v P_{iv}^D|\langle\Theta_{iv}^A|\Theta_{fu}^D\rangle|^2\delta(\bar{\omega}_{fu}^D - \bar{\omega}_{iv}^D - \omega).\end{aligned} \tag{115}$$

Notice that the absorption coefficient $\alpha_{if}(\omega)$ can be expressed as

$$\alpha_{if}(\omega) = \frac{4\pi^2\omega}{3\hbar c\alpha_a}|\vec{\mu}_{fi}|^2 \sum_v \sum_u P_{iv}|\langle\Theta_{fu}|\Theta_{iv}\rangle|^2\delta(\bar{\omega}_{fu,iv} - \omega), \tag{116}$$

where α_a is introduced to correct the medium effect and is a function of refractive index. Similarly the normalized intensity distribution function for

Lam Research Ex. 1035 - Page 210
Lam Research Corp. v. Inpria Corp.
IPR2024-00033 - U.S. Patent No. 9,823,564

emission $i \rightarrow f$ can be expressed as

$$I_{if}(\omega) = \frac{4\alpha_a \omega^3}{3\hbar c^3 A_{if}} |\vec{\mu}_{fi}|^2 \sum_v \sum_u P_{iv} |\langle \Theta_{fu} | \Theta_{iv} \rangle|^2 \delta(\bar{\omega}_{fu,iv} + \omega). \tag{117}$$

In formula (117) A_{if} denotes the radiative rate constant.

Using Eqs. (115) and (116) yields

$$W_{i \rightarrow f} = \frac{9c^4 \alpha_a^A A_{if}^D}{8\pi \alpha_e^D} \frac{\Omega_{DA}^2}{\varepsilon^2 R_{DA}^6} \int_{-\infty}^{\infty} \left(\frac{d\omega}{\omega^4} \right) \alpha^4(\omega) I^D(\omega). \tag{118}$$

This relation was first obtained by Förster and is usually called the Förster theory. Rather than expressing $W_{i \rightarrow f}$ in the spectral-overlap relation, $W_{i \rightarrow f}$ can be expressed in terms of the Franck–Condon factors which can be calculated from the potential surfaces as was done for the photo-induced ET or radiationless transitions.

Next the triplet–triplet energy transfer is considered:

$$^3D^*A \rightarrow D^3A^*. \tag{119}$$

Using the electronic wavefunctions

$$\Phi_i(^3D^*A) = |\, \overset{+}{\chi}_{D^*} \overset{+}{\chi}_D \overset{+}{\chi}_A \overset{-}{\chi}_A \,| \tag{120}$$

and

$$\Phi_f(D^3A^*) = |\, \overset{+}{\chi}_D \overset{-}{\chi}_D \overset{+}{\chi}_{A^*} \overset{+}{\chi}_A \,|, \tag{121}$$

the following equation is obtained:

$$\begin{aligned} H'_{fi} &= \left\langle \overset{-}{\chi}_D \overset{+}{\chi}_{A^*} \middle| \frac{e^2}{r_{ab}} \middle| \overset{+}{\chi}_{D^*} \overset{-}{\chi}_A \right\rangle - \left\langle \overset{-}{\chi}_D \overset{+}{\chi}_{A^*} \middle| \frac{e^2}{r_{ab}} \middle| \overset{-}{\chi}_A \overset{+}{\chi}_{D^*} \right\rangle \\ &= -\langle \chi_D \chi_{A^*} | \frac{e^2}{r_{ab}} | \chi_A \chi_{D^*} \rangle, \end{aligned} \tag{122}$$

i.e., the exchange interaction. In this case, the rate constant is given by

$$\begin{aligned} W_{i \rightarrow f} = \frac{2\pi}{\hbar^2} |H'_{fi}|^2 \int_{-\infty}^{\infty} d\omega \sum_u \sum_v P_{iv}^A |\langle \Theta_{iv}^A | \Theta_{fu}^A \rangle|^2 \delta(\bar{\omega}_{fu}^A - \bar{\omega}_{iv}^A - \omega) \\ \times \sum_u \sum_v P_{iv}^D |\langle \Theta_{iv}^D | \Theta_{fu}^D \rangle|^2 \delta(\bar{\omega}_{fu}^D - \bar{\omega}_{iv}^D + \omega) \end{aligned} \tag{123}$$

in terms of the spectral densities. Eq. (123) can be simplified if one notices that the integration of $\alpha_{if}(\omega)/\omega$ over the light frequency ω yields $|\vec{\mu}_{fi}|^2$, i.e.,

$$\int d\omega \frac{\alpha_{if}(\omega)}{\omega} = \frac{4\pi^2}{3\hbar c \alpha_a} |\vec{\mu}_{fi}|^2. \tag{124}$$

Lam Research Ex. 1035 - Page 211
Lam Research Corp. v. Inpria Corp.
IPR2024-00033 - U.S. Patent No. 9,823,564

For fluorescence intensity, the integration of $I_{if}(\omega)/\omega^3$ over ω is proportional to $|\vec{\mu}_{fi}|^2$. With these relations, the normalized absorption and emission spectra can be defined as being independent of the transition moments $|\vec{\mu}_A|^2$ and $|\vec{\mu}_D|^2$

$$\bar{\alpha}_{if}(\omega) = \frac{\alpha_{if}(\omega)}{\int d\omega(\alpha_{if}(\omega))/(\omega)} = \omega \sum_u \sum_v P_{iv} |\langle \Theta_{iv} | \Theta_{fu} \rangle|^2 \delta(\bar{\omega}_{fu,iv} - \omega) \quad (125)$$

and

$$\bar{I}_{fi}(\omega) = \frac{I_{if}(\omega)}{\int d\omega(I_{if}(\omega))/(\omega^3)} = \omega^3 \sum_u \sum_v P_{iv} |\langle \Theta_{iv} | \Theta_{fu} \rangle|^2 \delta(\bar{\omega}_{fu,iv} + \omega). \quad (126)$$

Applying Eqs. (126) and (127), Eq. (123) reduces to

$$W_{i \to f} = \frac{2\pi}{\hbar^2} |H'_{fi}|^2 \int_{-\infty}^{\infty} d\omega \frac{\bar{\alpha}_{if}^A(\omega) \bar{I}_{fi}^D(\omega)}{\omega^4}. \quad (127)$$

Eq. (127) indicates that it is possible to estimate the energy transfer rate if the absorption spectrum of the acceptor and the fluorescence spectrum of the donor are known. However, the optical properties of the acceptor and donor are not always available; especially for the case in which ultrafast energy transfer takes place. In this case, it is necessary to solve the coupled GMEs with appropriate interactions that account for the energy transfer process.

4. Applications

Ultrafast radiationless transitions are often observed through ultrashort pump-probe time-resolved measurements. In this section, a theoretical formula of the pump-probe time-resolved stimulated emission spectra is briefly introduced and the relationship between the dynamics calculation and the pump-probe spectra are presented. For this purpose, the dynamics of a simple model system with vibrationally non-equilibrated is discussed. For a real application of the theoretical treatment given in this chapter, ultrafast charge transfer taking place in photosynthetic RCs is studied.

4.1. Pump-Probe Time-Resolved Stimulated Emission Spectra

Here a model for the pump-probe time-resolved measurement of a system with two vibronic manifolds $\{n\}$ and $\{m\}$ embedded in a heat bath is considered. The two vibronic manifolds are coupled by the interaction $\hat{H}'$.

Lam Research Ex. 1035 - Page 212
Lam Research Corp. v. Inpria Corp.
IPR2024-00033 - U.S. Patent No. 9,823,564

A pumping laser excites the system from the ground vibronic manifold $\{g\}$ to the excited vibronic manifold {n}. After excitation, a probing laser is applied to induce transitions from the manifold $\{n\}$ to the manifold $\{g\}$ via stimulated emission and/or to higher excited manifolds via induced absorption. This work shall focus on the pump-probe time-resolved stimulated emission experiment. In this case, an expression for the time-resolved profiles is derived in terms of the imaginary part of the transient susceptibility $\overleftrightarrow{\chi}''(\omega_{pu}, \omega_{pr}, \tau)$. In the adiabatic approximation and the Condon approximation, it has been shown that [18,21]

$$\overleftrightarrow{\chi}''(\omega_{pu}, \omega_{pr}, \tau) = -\sum_{n}\sum_{n'} \frac{\vec{\mu}_{ng} \otimes \vec{\mu}_{gn}}{\hbar} \mathrm{Re}\{\rho_{nn'}(\omega_{pu}, \tau) F_{nn'}(\omega_{pr})\}. \tag{128}$$

Here ω_{pu}, ω_{pr}, τ, and $\vec{\mu}_{ng}$ represent the central frequency of the pumping laser, that of the probing laser, the time interval between the two pulses, and the transition dipole moment, respectively and $F_{nn'}(\omega_{pr})$ is the band-shape function associated with the probing optical process. In Eq. (128), $\rho_{nn'}$ is the density matrix element of the molecular system after excitation by the pump pulse.

4.1.1. Relaxation and Coherence Dynamics

The relaxation and coherence dynamics contributions to Eq. (128) within the BOA approximation are considered. For this purpose, $\{g\} = (a, \{u\})$, $\{m\} = (b, \{v\})$, and $\{n\} = (c, \{w\})$ are defined, where, for example, $\{u\}$ represents the vibrational quantum numbers of the vibrational modes of the electronic ground state. For the electronic coupling between the two excited states, it is assumed that the interaction Hamiltonian is given by $\hat{H}' = |c\rangle J_{cb}(Q)\langle b| + \mathrm{h.c.}$ where Q denotes the normal coordinate. The coupled GMEs, for example, for $\rho_{bv,cw}$ can be written as [67]

$$\begin{aligned}\frac{d\rho_{bv,cw}}{d\tau} = & -(i\omega_{bv,cw} + \Gamma_{bv,cw})\rho_{bv,cw} - \sum_{v',w'} \Gamma^{bv',cw'}_{bv,cw} \rho_{bv',cw'} \\ & - \frac{i}{\hbar}\sum_{bv} \langle bv|J_{bc}(Q)|cw\rangle(\rho_{cw,cw} - \rho_{bv,bv}) \\ & - \frac{i}{\hbar}\left(\sum_{cw'=0}^{w'\neq w} \langle bv|J_{bc}(Q)|cw'\rangle \rho_{cw',cw} - \sum_{bv'=0}^{v'\neq v} \rho_{bv,bv'}\langle bv'|J_{bc}(Q)|cw\rangle\right),\end{aligned} \tag{129}$$

where the vibronic dephasing rate constant for the vibronic coherence $bv \leftrightarrow cw$ is given by $\Gamma_{bv,cw} = -\sum_{v'\neq v, w'\neq w} \Gamma^{bv,cw}_{bv',cw'}$. Eq. (129) indicates that the vibronic coherence can be generated from the two contributions: (1) the population difference between $(b,\{v\})$ state and $(c,\{w\})$ state, and (2) the coherence difference between vibrational coherence of $\rho_{bv,bv'}$ and that of $\rho_{cw',cw}$.

Lam Research Ex. 1035 - Page 213
Lam Research Corp. v. Inpria Corp.
IPR2024-00033 - U.S. Patent No. 9,823,564

4.1.2. A Model of Vibrational Relaxation and Dephasing

It has been found that the short-range interaction model can be applied to study the vibrational relaxation of molecules in condensed phases. This model is applied to treat vibrational relaxation and pure dephasing in condensed phases. For this purpose, the secular approximation is employed to Eq. (129). This assumption allows one to focus on several important system–heat bath induced processes such as the vibrational population transition processes, the vibrational coherence transfer processes, and the vibronic processes.

Employing $\hat{V} = |b\rangle F_{1b} Q \exp(-\sum_j \alpha_j q_j)\langle b|$ as the system–heat bath interaction, where q_j denotes the vibrational coordinate of the jth heat bath mode, the vibrational population decay rate constant is obtained as

$$\Gamma_{bv,bv} = \sum_{\Delta=\pm 1} W_{bv,bv+\Delta}, \tag{130}$$

where

$$W_{bv,bv+1} = e^{-\hbar\omega^b_{\text{vib}}/k_{\text{B}}T} W_{bv+1,bv} = (v+1)e^{-\hbar\omega^b/k_{\text{B}}T}\gamma^b_{1\to 0}, \tag{131}$$

and

$$W_{bv,bv-1} = v\gamma^b_{1\to 0}. \tag{132}$$

Here, $\gamma^b_{1\to 0}$ represents the vibrational relaxation rate constant for the transition $v = 1 \to v = 0$ and is given by

$$\gamma^b_{1\to 0} = \frac{F^2_{1b}}{2\hbar\omega^b}\int_{-\infty}^{\infty} dt\ \exp\{-it\omega^b_{\text{vib}}\} \times \exp\left[\sum_j S_j\{(1+2\bar{n}_j) + (1+\bar{n}_j)e^{it\omega_j} + \bar{n}_j\, e^{-it\omega_j}\}\right]. \tag{133}$$

where $\hbar\omega_j$ denotes the one quantum energy of the jth heat bath mode, $S_j = \alpha_j^2/2\beta_j$, $\beta_j = \sqrt{\omega_j/\hbar}$, and $\bar{n}_j = (e^{\hbar\omega_j k_{\text{B}}T} - 1)^{-1}$.

With the same interaction model used in Eq. (130), the vibrational relaxation rate constants associated with the vibrational population transitions $bv+1 \to bv$ and $bv \to bv-1$ are given by

$$-\Gamma^{bv+1,bv+1}_{bv,bv} = (1+v)\gamma^b_{1\to 0} \tag{134}$$

and

$$-\Gamma^{bv-1,bv-1}_{bv,bv} = v\, e^{-\hbar\omega^b_{\text{vib}}/k_{\text{B}}T}\gamma^b_{1\to 0}, \tag{135}$$

respectively.

Lam Research Ex. 1035 - Page 214
Lam Research Corp. v. Inpria Corp.
IPR2024-00033 - U.S. Patent No. 9,823,564

The rate constants of the vibrational coherence dynamics such as vibrational coherence transfer can be derived by using the same interaction model used in Eq. (130). For example, the rate constants of the vibrational coherence transfer processes from $bv+1 \leftrightarrow bv'+1$ to $bv \leftrightarrow bv'$ and from $bv-1 \leftrightarrow bv'-1$ to $bv \leftrightarrow bv'$ are, respectively, given by

$$-\Gamma_{bv,bv'}^{bv+1,bv'+1} = \sqrt{v+1}\sqrt{v'+1}\gamma_{1\to 0}^{b} \tag{136}$$

and

$$-\Gamma_{bv,bv'}^{bv-1,bv'-1} = \sqrt{v}\sqrt{v'}\ \exp\left(\frac{-\hbar\omega_{\text{vib}}^{b}}{k_{\text{B}}T}\right)\gamma_{1\to 0}^{b}. \tag{137}$$

The pure dephasing rate constant can be derived by using the second-order term with respect to the system variable and, for example, assuming $\hat{V} = \sum_{\lambda=b,c}|\lambda\rangle Q^2 F_{2\lambda}(\{q\})\langle\lambda|$ where $F_{2\lambda}(\{q\}) = F_{2\lambda}\ \exp\left(-\sum_j \alpha'_{\lambda j} q_j\right)$ yields the vibronic pure dephasing rate constant $D_{bv,cw}$ which is given by

$$\begin{aligned} D_{bv,cw} = &\left(v+\frac{1}{2}\right)^2 \gamma_b^{(d)} + \left(w+\frac{1}{2}\right)^2 \gamma_c^{(d)} - \left(\frac{v+1/2}{\omega_{vib}^{b}}\right) \\ &\times \left(\frac{w+1/2}{\omega_{vib}^{c}}\right)\pi\hbar \sum_{\ell}\sum_{\ell'} P_\ell \langle\ell|F_b^2(\{q\})|\ell'\rangle\langle\ell'|F_c^2(\{q\})|\ell\rangle\delta(E_{\ell'\ell}) \\ &- \left(\frac{v+1/2}{\omega_{\text{vib}}^{\text{b}}}\right)\left(\frac{w+1/2}{\omega_{\text{vib}}^{\text{c}}}\right)\pi\hbar \sum_{\ell}\sum_{\ell'} P_\ell \langle\ell|F_c^2(\{q\})|\ell'\rangle \\ &\times \langle\ell'|F_b^2(\{q\})|\ell\rangle\delta(E_{\ell'\ell}). \end{aligned} \tag{138}$$

In the case of $\{\alpha'_{bj}\} \approx \{\alpha'_{cj}\}$, it follows that

$$D_{bv,cw} = \left(\frac{v+1/2}{\omega_{\text{vib}}^{b}} - \frac{w+1/2}{\omega_{\text{vib}}^{c}}\right)^2 \pi\hbar \sum_{\ell}\sum_{\ell'} P_\ell |\langle\ell|F_b^2(\{q\})|\ell'\rangle|^2 \delta(E_{\ell'\ell}). \tag{139}$$

In the case in which the vibrational frequencies of the two electronic potentials are same, it is found that

$$D_{bv,cw} = (v-w)^2 \gamma_b^{(d)}, \tag{140}$$

where

$$\begin{aligned} \gamma_b^{(d)} = &\frac{F_2^2}{2(\omega_{\text{vib}}^{b})^2}\int_{-\infty}^{\infty} dt\ \exp\{-it\omega_{\text{vib}}^{b}\} \\ &\times \exp\left[\sum_j S'_j\{(1+2\bar{n}_j) + (1+\bar{n}_j)e^{it\omega_j} + \bar{n}_j\, e^{-it\omega_j}\}\right]. \end{aligned} \tag{141}$$

Lam Research Ex. 1035 - Page 215
Lam Research Corp. v. Inpria Corp.
IPR2024-00033 - U.S. Patent No. 9,823,564

4.1.3. A Single Harmonic Displaced Oscillator Mode System

A model is considered for a system consisting of the ground state manifold $\{au\}$ and the two electronically excited vibronic manifolds $\{bv\}$ and $\{cw\}$. To apply our theory to this system, these two electronically excited vibronic manifolds are coupled via vibronic coupling. It is also assumed that the pumping and probing lasers interact only with the vibronic manifold $\{bv\}$ but not with $\{cw\}$. By applying the Condon approximation to the vibronic coupling terms in Eq. (131) and by applying the secular approximation to the equations, we find

$$\begin{aligned}\frac{d\rho_{bv,bv}}{d\tau} = & -[\{v+(1+v)e^{-\hbar\omega^b_{\rm vib}/k_{\rm B}T}\}\gamma_{1\to 0}+\gamma_b]\rho_{bv,bv} \\ & +(1+v)\gamma_{1\to 0}\rho_{bv+1,bv+1}+v\,e^{-\hbar\omega^b_{\rm vib}/k_{\rm B}T}\gamma_{1\to 0}\rho_{bv-1,bv-1} \\ & -\frac{i}{\hbar}\sum_{cw=0}\{J_{bc}\langle bv|cw\rangle\rho_{cw,bv}-\rho_{bv,cw}J_{cb}\langle cw|bv\rangle\},\end{aligned} \tag{142}$$

$$\begin{aligned}\frac{d\rho_{bv,bv'}}{d\tau} = & -(i\omega_{bv,bv'}+\Gamma_{bv,bv'}+\gamma_b)\rho_{bv,bv'}-\sum_{v'',v'''}\Gamma^{bv'',bv'''}_{bv,bv'}\rho_{bv'',bv'''} \\ & -\Gamma^{bv+1,bv'+1}_{bv,bv'}\rho_{bv+1,bv'+1}-\Gamma^{bv-1,bv'-1}_{bv,bv'-1}\rho_{bv-1,bv'-1} \\ & -\frac{i}{\hbar}\sum_{cw=0}\{J_{bc}\langle bv|cw\rangle\rho_{cw,bv'}-\rho_{bv,cw}J_{bc}\langle cw|bv'\rangle\},\end{aligned} \tag{143}$$

and

$$\begin{aligned}\frac{d\rho_{bv,cw}}{d\tau} = & -\left\{i\omega_{bv,cw}+\Gamma_{bv,cw}+\frac{(\gamma_b+\gamma_c)}{2}\right\}\rho_{bv,cw} \\ & -\Gamma^{bv+1,cw+1}_{bv,cw}\rho_{bv+1,cw+1}-\Gamma^{bv-1,cw-1}_{bv,cw}\rho_{bv-1,cw-1} \\ & -\frac{i}{\hbar}\sum_{bv=0}J_{bc}\langle bv|cw\rangle(\rho_{cw,cw}-\rho_{bv,bv}) \\ & -\frac{i}{\hbar}\left(\sum_{cw'=0}^{w'\neq w}J_{bc}\langle bv|cw'\rangle\rho_{cw',cw}-\sum_{bv'=0}^{v'\neq v}\rho_{bv,bv'}J_{bc}\langle bv'|cw\rangle\right),\end{aligned} \tag{144}$$

where, for example, J_{bc} and $\langle bv|cw\rangle$ represent the electronic coupling and the Franck–Condon overlap integrals, respectively.

Now pump-probe stimulated emission spectra can be determined on the basis of Eqs. (142)–(144). For this purpose, the coupled master equations are numerically solved and then using Eq. (128) pump-probe stimulated emission spectra are computed. For numerical simulation, the Runge–Kutta algorithm with a time step of 4 fsec is employed, and from 7 to 16

Lam Research Ex. 1035 - Page 216
Lam Research Corp. v. Inpria Corp.
IPR2024-00033 - U.S. Patent No. 9,823,564

vibrational states are taken for each electronic state in order to achieve convergence of the numerical calculations.

First the vibronic coupling constant dependence of the pump-probe stimulated emission spectra should be studied. For this purpose, it is set as $\hbar\omega_{\text{vib}} \equiv \hbar\omega^a_{\text{vib}} = \hbar\omega^b_{\text{vib}} = \hbar\omega^c_{\text{vib}} = 100\,\text{cm}^{-1}$ and the Huang–Rhys factors are $S_{ba} = 2.5$ for and $S_{cb} = 1.0$, which are used for the Franck–Condon overlap integrals in Eqs. (142)–(144). The excitation energy is chosen such that it is resonant to the most probable transition. For the pumping and probing optical processes, it is set as $T_{\text{pu}} = T_{\text{pr}} = 80\text{fsec}$ and $\hbar\gamma_{\text{pu}} = \hbar\gamma_{\text{pr}} = 66\,\text{cm}^{-1}$. The temperature is set at 10 K.

Figure 6.1 shows simulation of the population dynamics of the two vibronic manifolds. The populations $\rho_{bv,bv(\tau)}$ and $\rho_{cw,cw(\tau)}$ after excitation are calculated for (a) the weak coupling case and (b) the strong coupling case. Figure 6.1 clearly shows the population transfer between the two electronic states due to the creation of the vibronic coherence.

The energy gap dependence of the pump-probe stimulated emission spectra should be investigated for the non-equilibrium condition in which vibrational equilibrium is not achieved during the observing time. For the

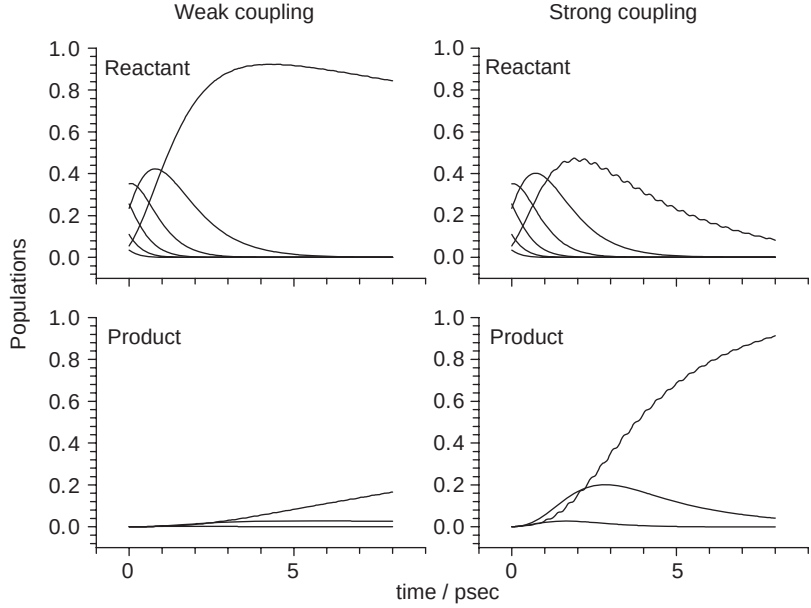


Fig. 6.1. Simulation of the population dynamics of the two vibronic manifolds. The simulations are carried out for the weak coupling case (right panel) and the strong coupling case (left panel).

Lam Research Ex. 1035 - Page 217
Lam Research Corp. v. Inpria Corp.
IPR2024-00033 - U.S. Patent No. 9,823,564

equilibrium condition, Marcus theory predicts that there is a turn over feature in ET rate constants as the energy gap becomes the so-called activationless condition. Therefore, it is interesting to know if one can observe a similar feature for non-equilibrium cases. In Figure 6.2, the spectra are simulated at various energy gaps of the two electronic states b (product state) and c (reactant state), i.e., $\hbar\omega_{bc} - \hbar\omega_{\mathrm{vib}} =$ (a) $-20\,\mathrm{cm}^{-1}$; (b) $-10\,\mathrm{cm}^{-1}$; (c) $0\,\mathrm{cm}^{-1}$; (d) $10\,\mathrm{cm}^{-1}$; (e) $20\,\mathrm{cm}^{-1}$. Figure 6.2 shows that the temporal behavior of each spectrum is almost identical, i.e., the quantum beats appearing within 2 psec result from the vibrational coherence. Thus, they do not depend on the energy gap. However, the long-time behavior of the spectra is quite different and interesting. The dynamics appearing in the calculated spectra depends strongly on the energy gap between the two electronic states. The calculated stimulated emission spectrum at $\hbar\omega_{bc} = 100\,\mathrm{cm}^{-1}$ decreases its intensity most rapidly among the calculated spectra. As the energy gap becomes either larger or smaller than this condition, the intensities decrease slowly. This tendency can be explained in terms of the energy conservation and the Franck–Condon factor. Since for the Huang–Rhys factor $S_{bc} = 1$, the transition occurs most effectively when $\hbar\omega_{bc} = n\hbar\omega_{\mathrm{vib}}$, where $n = 1$. As n increases, the Franck–Condon factor

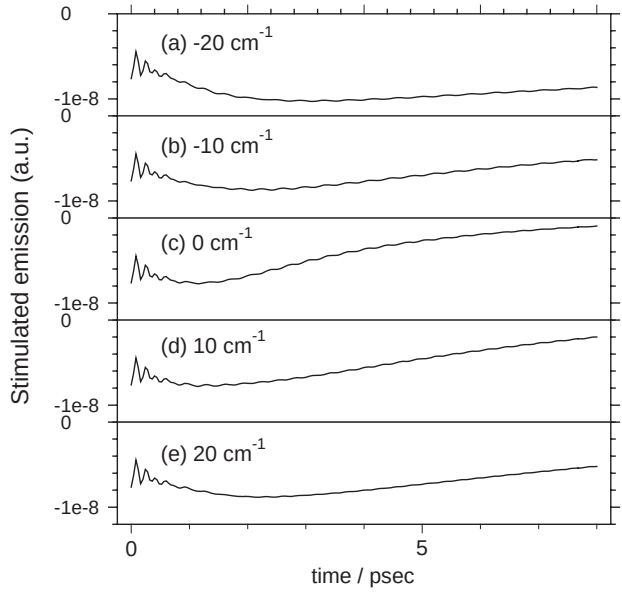


Fig. 6.2. Energy gap dependence calculated for non-vibrationally equilibrium model systems. Pump-probe stimulated emission profiles are calculated for various energy gaps.

Lam Research Ex. 1035 - Page 218
Lam Research Corp. v. Inpria Corp.
IPR2024-00033 - U.S. Patent No. 9,823,564

becomes smaller and the quantum beats due to the vibronic coherence disappear even for the case in which the energy is conserved.

4.2. BACTERIAL PHOTOSYNTHETIC RCs

The spectroscopy and dynamics of photosynthetic bacterial RCs have been one of the important issues for understanding an efficient molecular mechanism of ET and/or electronic excitation energy transfer taking place in bio-systems and considerable experimental attention has been drawn [68–119]. Figure 6.3 shows the schematic representation of the structures of the RC of *Rhodobacter (Rb.) sphaeroides* [104]. Two bacteriochlorophyll *a* (Bchl *a*) molecules together form an electronically coupled pair (P), situated near the periplasmic side of the membrane, through which the RC shows an approximately twofold symmetry forming two branches (L and M). Below P and to each branch are two monomer Bchls *a* (B_L and B_M), two bacteriopheophytin *a* (Bphe *a*) molecules (H_L and H_M), and two ubiquione molecules (Q_L and Q_M). All these pigments are embedded in the protein environment to form a pigment–protein complex. In Figure 6.4, the absorption spectra of the mutant RC of *Rb. sphaeroides* R26 are shown [111]. One can clearly see that the P band has a large blue peak shift as the temperature becomes higher while the peak position of the B band stays but its intensity decreases. In bacterial RCs, rapid ET and/or electronic excitation energy transfer take place upon the excitation of the special pair or

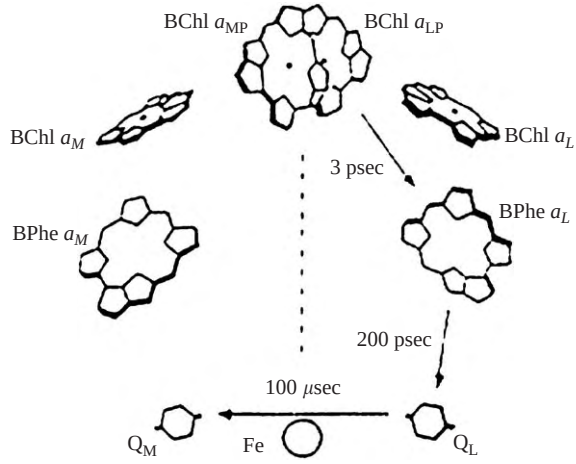


Fig. 6.3. Schematic representation of the structure of the reaction center of *Rhodobacter (Rb.) sphaeroides*.

Lam Research Ex. 1035 - Page 219
Lam Research Corp. v. Inpria Corp.
IPR2024-00033 - U.S. Patent No. 9,823,564

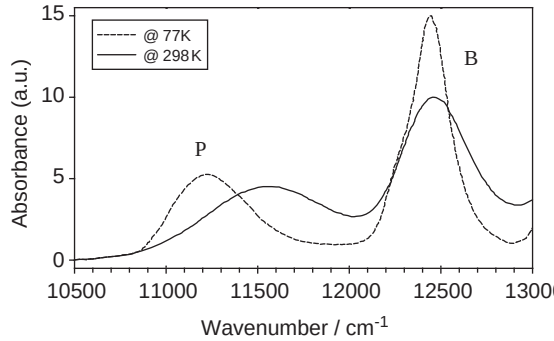


Fig. 6.4. The absorption spectra of the mutant RC of *Rb. sphaeroides* R26. Only P and B bands are shown. The absorption spectrum at 77 K (broken line) and that at 298 K are presented.

bacterial chlorophylls. This is due to the fact that the energy gaps among the electronic states involved in the rapid dynamics are much smaller compared with the first electronic transition energy. In other words, several electronic states exist within $1500\,cm^{-1}$. This congested electronic structure makes it possible to have rapid radiationless processes. In fact, eight electronic states should be needed to treat the rapid radiationless processes in the *Rb. sphaeroides* RC. Since recent experimental measurements have used ultrashort pulses (5–10 fsec), the dynamics of vibrational and vibronic coherences are involved in the observed results.

The RC is an ideal system to test theoretical ideas (memory effect, coherence effect, etc.), fundamental approximations (isolated line approximation, Markov approximation, etc.), and techniques (generalized linear response theory, Förster–Dexter theory, Marcus theory, etc.) for treating ultrafast phenomena. As mentioned above, this ideality is mainly due to the fact that the electronic energy level spacing in RC is small (typically from 200 to $\sim 1500\,cm^{-1}$), and the interactions between these electronic states are weak.

4.2.1. Vibrational Coherence and Relaxation in Photosynthetic Reaction Centers

Let us start with the quantum beats measurements of D_{LL} mutant RCs of *Rb. capsulatus* with 80 fsec pump pulse, which was reported by Matrin et al. [75,76]. This mutant lacks bacterial pheophetines so that ET does not take place in the picosecond time scale. In other words, the quantum beats result from a coherent excitation of vibrational states. In the observed

Lam Research Ex. 1035 - Page 220
Lam Research Corp. v. Inpria Corp.
IPR2024-00033 - U.S. Patent No. 9,823,564

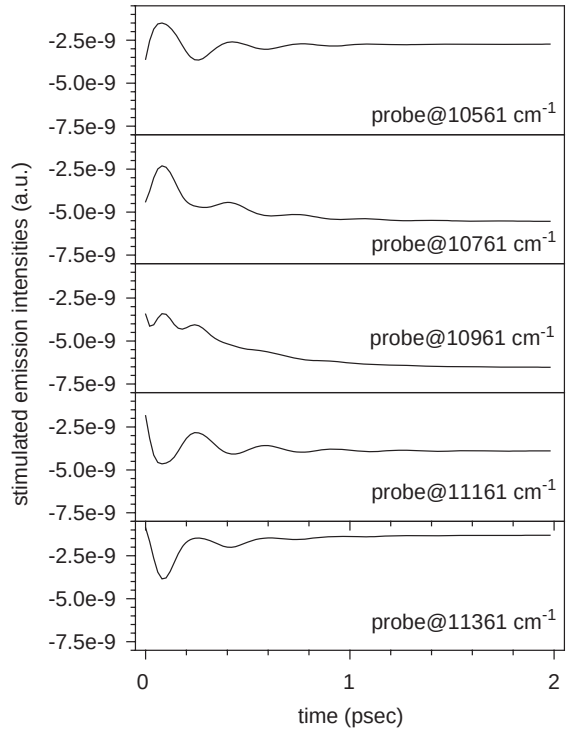


Fig. 6.5. Numerical simulation of quantum beats measurements of D_{LL} mutant RCs of *Rb. capsulatus* with 80 fsec pump pulse. Two vibrational frequencies are included in the simulation. The box with broken line indicates the time region in which the phase evolution of the vibrational quantum beams can be seen clearly.

pump-probed profiles, one can see a clear phase change in quantum beats as the probing wavelength changes. To deal with this problem, Eq. (142) is solved for a closed vibronic system consisting of one electronically excited state with two vibrational modes. Solving the coupled master equations with the two vibrational modes (100 and $30\,cm^{-1}$), the numerical simulation is obtained as shown in Figure 6.5. The vibrational relaxation time is set to 300 fsec. One can see that the phase of the quantum beats is a function of the probing wavelength. In particular, the first large oscillation in quantum beats clearly exhibit the turnover of the phase around the probe wavelength $10{,}961\,cm^{-1}$. In other words, transient Stokes shift appears due to a generation of vibrational coherence. The signals become a plateau as the pump-probe pulse delay time proceeds because no ET takes place in this time region and the plateau feature is due to the vibrational equilibrium.

Lam Research Ex. 1035 - Page 221
Lam Research Corp. v. Inpria Corp.
IPR2024-00033 - U.S. Patent No. 9,823,564

4.2.2. Rapid Electron Transfer in Photosynthetic Reaction Centers

Martin's group has also performed the same type of measurements to wild-type RCs of *Rb. sphaeroides* [77]. A rapid ET takes place upon an excitation of the special pair in this system. Since the bandwidth of the pumping pulse can only cover one electronic state (special pair), quantum beats result from a generation of the vibrational coherence. However, the system also exhibits single-vibronic ET. In this case, the coupled-master equations can be written as

$$\begin{aligned}\frac{\partial \rho_{bv,bv}(t)}{\partial t} = & -\Gamma^{bv,bv}_{bv,bv}\rho_{bv,bv}(t) - W_{c\leftarrow bv}\rho_{bv,bv}(t) \\ & + \Gamma^{bv+1,bv+1}_{bv,bv}\rho_{bv+1,bv+1}(t) + \Gamma^{bv-1,bv-1}_{bv,bv}\rho_{bv-1,bv-1}(t) \end{aligned} \tag{145}$$

and

$$\begin{aligned}\frac{\partial \rho_{bv,bv'}(t)}{\partial t} = & -(i\omega^{b}_{\mathrm{vib}} + \Gamma^{bv,bv'}_{bv,bv'})\rho_{bv,bv'}(t) - \left(\frac{W_{c\leftarrow bv} + W_{c\leftarrow bv'}}{2}\right)\rho_{bv,bv'}(t) \\ & + \Gamma^{bv+1,bv'+1}_{bv,bv'}\rho_{bv+1,bv'+1}(t) + \Gamma^{bv-1,bv'-1}_{bv,bv'}\rho_{bv-1,bv'-1}(t), \end{aligned} \tag{146}$$

where the single-vibronic ET rate constant is given by

$$W_{c\leftarrow bv} = \frac{2\pi}{\hbar}|T_{cb}|^2 \sum_{u=0}^{\infty} |\langle \Theta_{cu}|\Theta_{bv}\rangle|^2 D(E_{cu} - E_{bv}). \tag{147}$$

In the displaced-harmonic surface, Eq. (147) can be written as

$$W_{c\leftarrow bv} = \frac{2\pi}{\hbar}|T_{cb}|^2 \int_{-\infty}^{\infty} d\tau\, e^{i\tau\omega_{cb} - \tau\Gamma_{cb}} \prod_{j=1}^{N} G_{v_j}(\tau), \tag{148}$$

where

$$G_{v_j}(\tau) = \exp\{-S_j(1 - e^{i\tau\omega_j})\} \sum_{n_j=0}^{v_j} \frac{v_j!}{n_j!\{(v_j - n_j)!\}^2} \times \{S_j(e^{i\tau\omega_j/2} - e^{-i\tau\omega_j/2})\}^{v_j - n_j}. \tag{149}$$

The calculated results are shown in Figure 6.6. One can see a probe wavelength-dependent phase in the quantum beats while the signals decay as the time proceeds. In D_{LL} mutant RCs of *Rb. capsulatus*, the phase of the quantum beats shows a turnover feature around the wavelength 10,961 cm^{-1} as discussed in the previous section. In wild-type RCs of *Rb. sphaeroides*, a quite similar turnover feature can also be seen. The turnover indicates that the quantum beats appeared in the early time region are due to vibrational coherence. This numerical simulation suggests that the electronic coupling may not be strong in other RCs if quantum beats show a clear turnover

Lam Research Ex. 1035 - Page 222
Lam Research Corp. v. Inpria Corp.
IPR2024-00033 - U.S. Patent No. 9,823,564

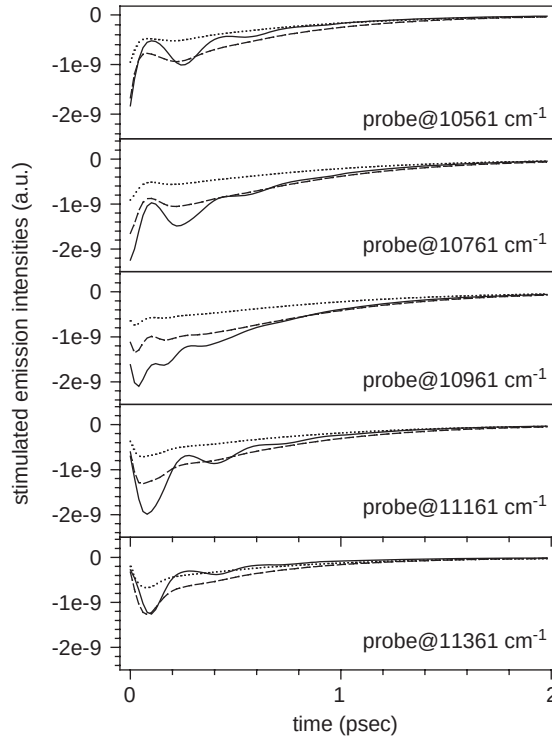


Fig. 6.6. Numerical simulation of quantum beats measurements of wild-type RCs of *Rb. sphaeroides*. The box with broken line indicates the time region in which the RCs can keep a clear phase of the vibrational quantum beams.

feature as a function of the probe wavelength. The temperature dependence is also shown in Figure 6.6. As the temperature increases, the quantum beats due to vibrational coherence disappear quickly and the signal becomes weak in intensity.

4.2.3. Vibronic Coherence in Photosynthetic Reaction Center

Scherer's group has reported 10 fsec pump-probe measurements on mutant RCs of *Rb. sphaeroides* R26 [103]. In this case, at least two electronic states are involved in the pumping process so that the time development of the vibronic coherence should be considered. To perform a numerical simulation on the coupled GMEs (Eqs. (142)–(144)), one has to analyze the absorption spectra of this system first and the energies of the involved electronic states can be determined. The 77 and 298 K absorption spectra

Lam Research Ex. 1035 - Page 223
Lam Research Corp. v. Inpria Corp.
IPR2024-00033 - U.S. Patent No. 9,823,564

and Resonance Raman spectra together with Raman intensity analysis of RCs of *Rb. sphaeroides* R26 were reported by Mathies' group [107–111]. They reported 17 vibrational modes with the fitted coupling constants (Huang–Rhys factors) for the B band and only 14 vibrational frequencies without any coupling constants values for the P band.

To construct a model for the P band, the molecular parameters are adopted from Mathies' results: vibrational frequencies, the coupling constants, the inhomogeneous broadening, and electronic dephasing constant, etc. A microscopic model should contain these molecular parameters. Since

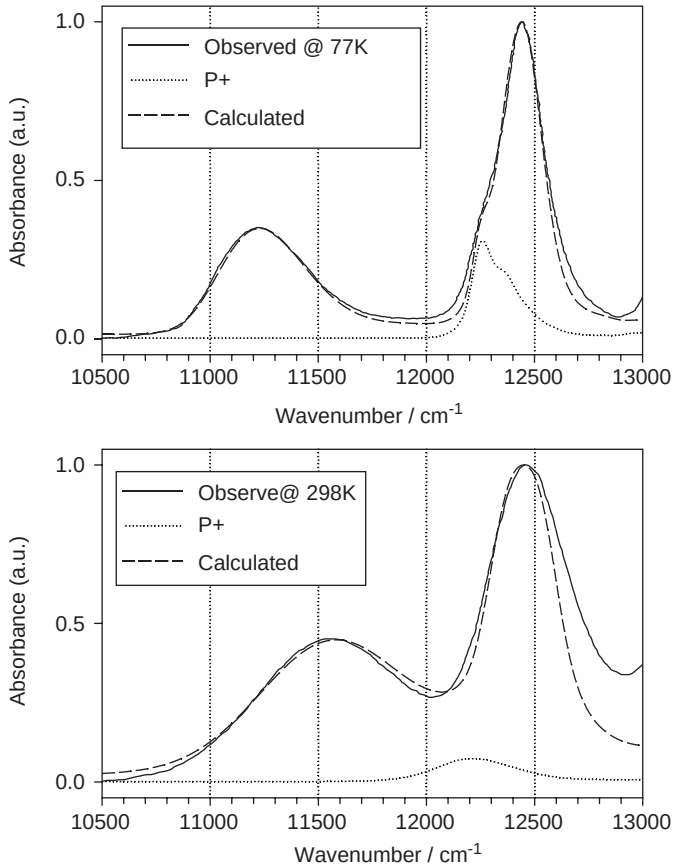


Fig. 6.7. Simulated absorption spectra of mutant RCs of *Rb. sphaeroides* R26. The experimental data are adopted from Refs. [110,121]. The calculated higher excitonic band of the special pair is also shown. Reprinted with permission from [110,121]. Copyright (1997, 2001) American Chemical Society.

Lam Research Ex. 1035 - Page 224
Lam Research Corp. v. Inpria Corp.
IPR2024-00033 - U.S. Patent No. 9,823,564

there are no coupling constant values for the P band, the values can initially be chosen from the B band date for the reason that the special pair also consists of Bchls *a*. Some experimental results provide additional information. For instance, Hochstrasser's group reported that at room temperature the higher excitonic contribution of the special pair is in the red side of 800 nm and the ratio is about 1/10 [88,89]. Scherer et al. showed that the spectra of the lower and higher excitonic contribution of the special pair and B components from the analysis of the wavelength-resolved pump-probe data [103]. In particular, the higher excitonic band absorbs near 810 nm at the low temperature (15 K) and 825 nm at room temperature. Since in the low temperature (4 and 77 K) spectra the P and B bands are far separated, the peak position of the three components can be easily decided. For the B band (containing the higher excitonic band and B components), it is found that the bandwidth of the higher excitonic band is narrower than the lower one. This suggests that the Huang–Rhys factors of the corresponding low frequency modes should be smaller. In addition, the peak intensity ratio of

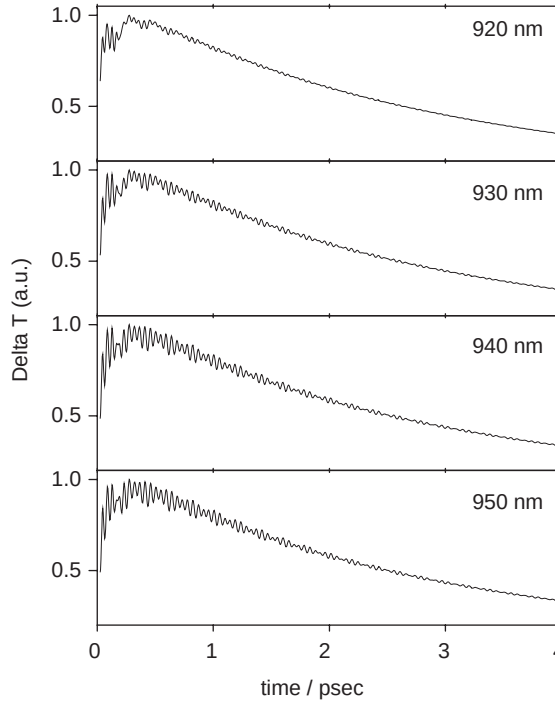


Fig. 6.8. Calculated pump-probe, delta-absorption profiles for mutant RCs of *Rb. sphaeroides* R26.

Lam Research Ex. 1035 - Page 225
Lam Research Corp. v. Inpria Corp.
IPR2024-00033 - U.S. Patent No. 9,823,564

the higher excitonic band to the lower is no longer 1–10 at the temperature lower than room temperature. The simulated absorption spectra are shown in Figure 6.7 [120–122]. The numerical simulation based on the absorption spectra analysis is shown in Figure 6.8. The pump-probe, delta-absorption profiles are calculated for various probe wavelengths. Since the electronic coupling between the lower and upper excitonic bands is not known, the delta-absorption profile should be simulated for various values of the electronic coupling. The best fitting of the quantum beats feature to experimental results is obtained if the electronic coupling between the lower and upper excitonic bands is set to $123\,\mathrm{cm}^{-1}$. For a comparison, a numerical result without the electronic coupling between the involved two electronic states is also shown in Figure 6.9. One can see a rapid rising in the early time region of the simulated profile if the electronic coupling is taken into account. This raising component is due to the radiationless transition between the two electronic states. Radiationless transition from the B band to the higher excitonic band of the special pair is now considered. For this purpose, the three-dimensional pump-probe delta absorption spectra are simulated by changing the value of the electronic coupling between the two relevant electronic states. The best simulation is obtained if the coupling is chosen to $103\,\mathrm{cm}^{-1}$. Figure 6.10 presents the best-simulated delta-absorption spectra.

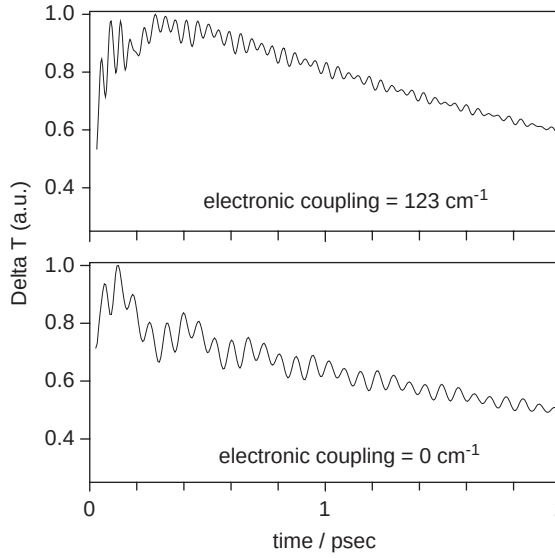


Fig. 6.9. Calculated pump-probe, delta-absorption profiles with and without the electronic coupling between the higher excitonic state and the lower one of the special pair.

Lam Research Ex. 1035 - Page 226
Lam Research Corp. v. Inpria Corp.
IPR2024-00033 - U.S. Patent No. 9,823,564

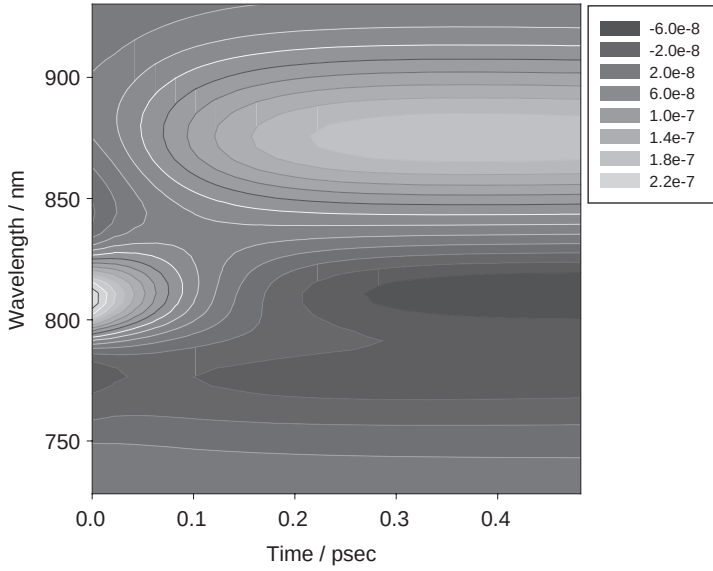


Fig. 6.10. Contour representation of calculated pump-probe delta absorption spectra of mutant RCs of *Rb. sphaeroides* R26. The electronic coupling between the B band and the higher excitonic band of the special pair is included in the simulation.

The presented theoretical approach to large molecular systems such as bacterial photosynthetic RCs can provide microscopic details of ultrafast radiationless transition taking place faster than 100 fsec. In particular, this approach establishes a standard model for treating such ultrafast processes of RCs. It is possible to analyze and provide similar details for wild-type RCs or other mutant RCs; for example, for wild-type RCs of *Rb. sphaeroides* the electronic coupling of radiationless transition from the B band to the higher excitonic band and that from the higher excitonic band to the lower one are found to be 105.5 and 123 cm^{-1}. For R26.Phe-*a* mutant RCs, the former coupling is 105 cm^{-1} and the latter is 123.7 cm^{-1}.

5. Summary

The effects of the vibronic coupling competing with vibrational and/or vibronic relaxation on the femtosecond pump-probe stimulated emission spectra of molecules in condensed phases have been investigated. Taking into account vibronic and vibrational relaxation and vibronic coupling in molecular terms, the coupled master equations have been briefly derived for

Lam Research Ex. 1035 - Page 227
Lam Research Corp. v. Inpria Corp.
IPR2024-00033 - U.S. Patent No. 9,823,564

the vibrational population and vibrational and/or vibronic coherence dynamics. Microscopic expressions of the rate constants for these vibrational and vibronic processes are obtained by employing a short-range interaction model. By simulating the coupled master equations, the effect of vibronic coupling constant, temperature, excitation wavelength, and the energy gap between the relevant electronic states on the transient dynamics appearing in the spectra have been studied.

Although the presented numerical approach to the coupled master equations has shown that a turnover feature can be seen in vibronic dynamics appearing in the calculated pump-probe stimulated emission spectra as a function of the energy gap between the two relevant vibronic states. It is found that vibronic quantum beats cannot be observed when the energy gap becomes larger in which situation it leads to smaller Franck–Condon overlaps between the energy conserved levels.

From the application of the theory performed to bacterial photosynthetic RCs, a characteristic time of vibrational relaxation has been obtained as ~400–500 fsec. Transient Stokes shifts appear due to a generation of vibrational coherence. Vibronic coherence dynamics can be observed if more than two electronic states are coherently excited. Phase relation is very important to identify the origin of the coherence resulting in quantum beats. Our standard model applying to other RCs could provide a physical chemistry approach to the investigation of how the nature arranges the vibronic structure and its dynamics in photosynthetic RCs so that the captured sun light energy can be converted into chemicals very efficiently.

Although a theoretical approach has been desecrated as to how one can apply the generalized coupled master equations to deal with ultrafast radiationless transitions taking place in molecular systems, there are several problems and limitations to the approach. For example, the number of the vibrational modes is limited to less than six for numerical calculations. This is simply just because of the limitation of the computational resources. If the efficient parallelization can be realized to the generalized coupled master equations, the limitation of the number of the modes can be relaxed. In the present approach, the Markov approximation to the interaction between the molecule and the heat bath mode has been employed. If the time scale of the ultrashort measurements becomes close to the characteristic time of the correlation time of the heat bath mode, the Markov approximation cannot be applicable. In this case, the so-called non-Markov treatment should be used. This, in turn, leads to a more computationally demanding task. Thus, it is desirable to develop a new theoretical approach that allows a more efficient algorithm for the computation of the non-Markov kernels. Another problem is related to the modeling of the interaction between the molecule and the heat bath mode. In our model, the heat bath mode is treated as

Lam Research Ex. 1035 - Page 228
Lam Research Corp. v. Inpria Corp.
IPR2024-00033 - U.S. Patent No. 9,823,564

"parameters". This model cannot take into account the temperature dependence of the relaxation rate constants.

Apart from the heat bath mode, the harmonic potential surface model has been used for the molecular vibrations. It is possible to include the generalized harmonic potential surfaces, i.e., displaced-distorted-rotated surfaces. In this case, the mode coupling can be treated within this model. Beyond the generalized harmonic potential surface model, there is no systematic approach in constructing the generalized (multi-mode coupled) master equation that can be numerically solved. The first step to attack this problem would start with anharmonicity corrections to the harmonic potential surface model. Since anharmonicity has been recognized as an important mechanism in the vibrational dynamics in the electronically excited states, urgent realization of this work is needed.

Finally, application of the time-dependent density functional theory (TD-DFT) to the dynamics of the electrons and nucleus of a simple molecule has been realized recently. Although this method is only limited to quite small size of polyatomic systems at present, the approach is promising and has plenty rooms to be improved and extended. Thus, it may be wise to consider an effective combination of TD-DFT and the GME.

The questions below are intended to help the reader in learning the material presented in the chapter.

1. What is the Born–Oppenheimer approximation for?
2. In this chapter, three types of rate constant are introduced. Describe what are the differences among them?
3. What are the couplings that lead to internal conversion and intersystem crossing?
4. Derive Eq. (93) from Eq. (73).
5. Derive Marcus equation from Eq. (97) using the short-time approximation and classical limit.
6. Discuss the so-called turn-over feature in Marcus equation. Draw plots for the temperature and the ΔG_{fi} dependence of Eq. (99), respectively.
7. To solve the generalized coupled master equations such as Eqs. (142)–(144) numerically, what algorism can be used?
8. To observe ultrafast electron transfer taking place in photosynthetic reaction centers, what are the possible experimental techniques?
9. If vibrational coherence is generated in the ultrashort time-resolved experiments, how can one distinguish it from electronic coherence?
10. If quantum chemistry methods cannot be practical to calculate the molecular parameters as potential surfaces of the system, how can one analyze ultrafast phenomena? Is it important to identify the electronic

Lam Research Ex. 1035 - Page 229
Lam Research Corp. v. Inpria Corp.
IPR2024-00033 - U.S. Patent No. 9,823,564

states involved in the ultrafast phenomena? How much important is it to know the vibrational modes of the system?

References

1. M. D. Feit, A. M. Komashko, A. M. Rubenchik, Appl. Phys. A **79** (2004) 1657.
2. X. X. Li, T. Q. Jia, D. H. Feng, Z. Z. Xu, Acta Phys. Sin. **53** (2004) 2154.
3. S. H. Lin, R. Alden, R. Isiampour, H. Ma, A. A. Villaeys, Density Matrix Method and Femtosecond Processes, World Scientific, Singapore, 1991.
4. M. D. Perry, B. C. Stuart, P. S. Banks, M. D. Feit, V. Yanovsky, A. M. Rubenchik, J. Appl. Phys. **85** (1999) 6803.
5. K. Vestentoft, J. A. Olesen, B. H. Christensen, P. Balling, Appl. Phys. A **80** (2005) 493.
6. G. H. Chen, Z. M. Su, Z. W. Shen, Y. J. Yan, J. Chem. Phys. **109** (1998) 2565.
7. S. W. Gao, Phys. Rev. B **55** (1997) 1876.
8. Y. Katashiba, H. Masuda, T. Ohuchi, A. Minoh, M. Tsukakoshi, Jpn. J. Appl. Phys. **42** (2003) 3469.
9. N. J. Turro, Modern Molecular Photochemistry, University Science Books, Sausalito, CA, 1991.
10. K. Blum, Density Matrix Theory and Applications, Plenum Press, New York, 1981.
11. H. Eyring, S. H. Lin, S. M. Lin, Basic Chemical Kinetics, Wiley, New Jersey, 1981.
12. H. Grabert, Projection Operator Techniques in Nonequilibrium Statistical Mechanics, Springer, Berlin, 1982.
13. S. H. Lin, H. Eyring, Proc. Natl. Acad. Sci. U.S.A. **74** (1977) 3623.
14. W. H. Louisell, Quantum Statistical Properties of Radiation, Wiley, New York, 1973.
15. I. Oppenheim, K. E. Shuler, G. H. Weiss, Stochastic Processes in Chemical Physics, The Master Equation, MIT Press, Boston, MA, 1977.
16. R. Xu, Y. Mo, P. Cui, S. H. Lin, Y. J. Yan, Non-Markovian Quantum Dissipation in the Presence of External Fields, in: J. Maruani, R. Lefebvre, E. Brandas (Eds.), Advanced Topics in Theoretical Chemical Physics, Kluwer Academic Publishers, Dordrecht, 2003.

Lam Research Ex. 1035 - Page 230
Lam Research Corp. v. Inpria Corp.
IPR2024-00033 - U.S. Patent No. 9,823,564

17. R. G. Alden, M. Hayashi, J. P. Allen, N. W. Woodnury, H. Murchison, S. H. Lin, Chem. Phys. Lett. **208** (1993) 350.
18. B. Fain, S. H. Lin, N. Hamer, J. Chem. Phys. **91** (1989) 4485.
19. X. Z. Gu, M. Hayashi, S. Suzuki, S. H. Lin, Biochem. Biophys. Acta **1229** (1995) 215.
20. S. H. Lin, R. G. Alden, C. K. Tang, Y. Fujimura, M. Sugawara, Femto-Second Processes and Ultrafast Biological Electron Transfer, in: J. Jortner, R. D. Levine, A. Pullman (Eds.), Mode Selective Chemistry, Proceedings of the Twenty-Fourth Jerusalem Symposium on Quantum Chemistry and Biochemistry held in Jerusalem, Israel, May, Kluwer Academic Publishers, Dordrecht, 1990.
21. S. H. Lin, B. Fain, N. Hamer, Adv. Chem. Phys. **79** (1990) 133.
22. M. Abramowitz, I. A. Stegun, Handbook of Mathematical Functions with Formulas, Graphs, and Mathematical Tables, Dover, New York, 1972.
23. Y. Okuno, S. Mashiko, Int. J. Quantum Chem. **102** (2005) 8.
24. S. H. Lin, J. Chem. Phys. **44** (1966) 3759.
25. Y. Zhao, G. Mil'nikov, H. Nakamura, J. Chem. Phys. **121** (2004) 8854.
26. S. H. Lin, M. Hayashi, R. G. Alden, S. Suzuki, X. Z. Gu, Y. Y. Lin, Ultrafast Electron Transfer and Spectroscopy of Photosynthetic Reaction Centers, in: J. Mantz, L. Wöste (Eds.), Femtosecond Chemistry, VCH, Weihein, 1995.
27. S. H. Lin, M. Hayashi, S. Suzuki, X. Z. Gu, W. Xiao, M. Sugawara, Chem. Phys. **197** (1995) 435.
28. M. Hayashi, R. Islampour, S. H. Lin, Chem. Phys. Lett. **213** (1993) 465.
29. K. Huang, A. Rhys, Proc. Phys. Soc. **A204** (1950) 406.
30. S. H. Lin, R. Bersohn, J. Chem. Phys. **48** (1968) 2732.
31. M. Bixon, J. Jortner, J. Chem. Phys. **48** (1968) 715.
32. G. W. Robinson, R. P. Frosch, J. Chem. Phys. **38** (1963) 1187.
33. W. Siebrand, J. Chem. Phys. **44** (1966) 4055.
34. W. Siebrand, J. Chem. Phys. **46** (1967) 440.
35. J. M. F. Dijk, M. J. H. Kemper, J. H. M. Kerp, H. M. Buck, J. Chem. Phys. **69** (1978) 2453.
36. J. M. F. Dijk, M. J. H. Kemper, J. H. M. Kerp, H. M. Buck, J. Chem. Phys. **69** (1978) 2462.
37. M. J. H. Kemper, J. M. F. Dijk, H. M. Buck, J. Chem. Phys. **70** (1979) 2854.
38. M. J. H. Kemper, L. Lemmens, H. M. Buck, Chem. Phys. **57** (1981) 245.
39. S. H. Lin, Proc. R. Soc. London Ser. A **352** (1976) 57.

Lam Research Ex. 1035 - Page 231
Lam Research Corp. v. Inpria Corp.
IPR2024-00033 - U.S. Patent No. 9,823,564

40. T. Nakajima, S. Kato, J. Chem. Phys. **105** (1996) 5927.
41. F. Pauzat, B. Levy, P. Millie, Mol. Phys. **39** (1980) 375.
42. J. A. Pople, J. W. Sidman, J. Chem. Phys. **27** (1955) 1270.
43. A. C. Albrecht, J. Chem. Phys. **38** (1963) 354.
44. A. C. Albrecht, J. Chem. Phys. **33** (1960) 156.
45. M. R. Hoare, J. Chem. Phys. **52** (1970) 5695.
46. M. R. Hoare, T. W. Ruijgrok, J. Chem. Phys. **52** (1970) 113.
47. K. H. Lau, S. H. Lin, J. Phys. Chem. **75** (1971) 981.
48. S. H. Lin, H. Eyring, J. Chem. Phys. **39** (1963) 1577.
49. S. H. Lin, H. Eyring, J. Chem. Phys. **43** (1963) 2153.
50. S. H. Lin, K. H. Lau, J. Phys. Chem. **75** (1971) 2458.
51. J. C. Tou, S. H. Lin, J. Chem. Phys. **49** (1968) 4187.
52. R. Englman, J. Jortner, Mol. Phys. **18** (1970) 145.
53. S. H. Lin, J. Chem. Phys. **90** (1989) 7103.
54. Z. T. Chu, Y. Y. Lin, S. H. Lin, J. Photochem. Photobiol. A: Chem. **44** (1998) 229.
55. D. Devault, Quantum-Mechanical Tunneling in Biological Systems, Cambridge University, Cambridge, 1984.
56. S. M. Ma, S. H. Lin, H. Eyring, Chem. Phys. Lett. **58** (1978) 159.
57. J. Ulstrup, Charge Transfer Processes in Condensed Media, Springer, Berlin, 1979.
58. R. A. Marcus, J. Chem. Phys. **24** (1956) 966.
59. R. A. Marcus, J. Chem. Phys. **43** (1965) 679.
60. R. A. Marcus, J. Phys. Chem. **72** (1968) 891.
61. S. H. Lin, X. G. Zhang, G. Y. C. Wu, J. Chem. Phys. **85** (1986) 221.
62. T. Förster, Ann. Phys. **2** (1948) 55.
63. T. Förster, Disc. Faraday Trans. **27** (1959) 7.
64. D. L. Dexter, J. Chem. Phys. **21** (1953) 836.
65. S. H. Lin, Proc. R. Soc. London Ser. A **335** (1973) 51.
66. S. H. Lin, Mol. Phys. **21** (1971) 853.
67. M. Hayashi, T.-S. Yang, A. Mebel, C. H. Chang, S. H. Lin, N. F. Scherer, Chem. Phys. **217** (1997) 259.
68. J. Breton, J.-L. Martin, A. Migus, A. Antonetti, A. Orszag, Proc. Natl. Acad. Sci. U.S.A. **83** (1986) 5121.
69. J. Breton, J.-L. Martin, G. R. Fleming, J.-C. Lambry, Biochemistry **27** (1988) 8276.
70. J.-L. Martin, J. Breton, A. J. Hoff, A. Migus, A. Antonetti, Proc. Natl. Acad. Sci. U.S.A. **83** (1986) 957.
71. N. W. Woodbury, M. Becker, D. Middendorf, W. W. Person, Biochemistry **24** (1985) 7516.

Lam Research Ex. 1035 - Page 232
Lam Research Corp. v. Inpria Corp.
IPR2024-00033 - U.S. Patent No. 9,823,564

72. G. R. Fleming, J. L. Martin, J. Breton, Nature **333** (1988) 190.
73. C. Kirmaier, D. Holten, Proc. Natl. Acad. Sci. U.S.A. **87** (1990) 3552.
74. M. H. Vos, J.-C. Lambry, S. J. Robles, D. G. Youvan, J. Breton, J.-L. Martin, Proc. Natl. Acad. Sci. U.S.A. **88** (1991) 8885.
75. M. H. Vos, J.-C. Lambry, S. J. Robles, D. G. Youvan, J. Breton, J.-L. Martin, Proc. Natl. Acad. Sci. U.S.A. **89** (1992) 613.
76. M. H. Vos, F. Rappaport, J.-C. Lambry, J. Breton, J.-L. Martin, Nature **363** (1993) 320.
77. M. H. Vos, M. R. Jones, C. N. Hunter, J. Breton, J.-C. Lambry, J.-L. Martin, Biochemistry **33** (1994) 6750.
78. M. H. Vos, J. Breton, J.-L. Martin, J. Phys. Chem. B **101** (1997) 9820.
79. C.-K. Chan, L. X.-Q. Chen, T. J. DiMagno, D. K. Hanson, S. L. Nance, M. Schiffer, J. R. Norris, G. R. Fleming, Chem. Phys. Lett. **176** (1991) 366.
80. C.-K. Chan, T. J. DiMagno, L. X.-Q. Chen, J. R. Norris, G. R. Fleming, Proc. Natl. Acad. Sci. U.S.A. **88** (1991) 11202.
81. M. Du, S. J. Rosenthal, X. L. Xie, T. J. DiMagno, M. Schmidt, D. K. Hanson, M. Schiffer, J. R. Norris, G. R. Fleming, Proc. Natl. Acad. Sci. U.S.A. **89** (1992) 8517.
82. Z. Y. Wang, R. M. Pearlstein, Y. W. Jia, G. R. Fleming, J. R. Norris, Chem. Phys. **176** (1993) 421.
83. Y. W. Jia, D. M. Jonas, T. H. Joo, Y. Nagasawa, M. J. Lang, G. R. Fleming, J. Phys. Chem. **99** (1995) 6263.
84. D. M. Jonas, M. J. Lang, Y. Nagasawa, T. Joo, G. R. Fleming, J. Phys. Chem. **100** (1996) 12660.
85. M.-L. Groot, J.-Y. Yu, R. Agarwal, J. R. Norris, G. R. Fleming, J. Phys. Chem. B **102** (1998) 5923.
86. S. Maiti, G. C. Walker, B. R. Cowen, R. Pippenger, C. C. Moser, P. L. Dutton, R. M. Hochstrasser, Proc. Natl. Acad. Sci. U.S.A. **91** (1994) 10360.
87. G. C. Walker, S. Maiti, B. R. Cowen, C. C. Moser, P. L. Dutton, R. M. Hoschtrasser, J. Phys. Chem. **98** (1994) 5778.
88. K. Wynne, G. Haran, G. D. Reid, C. C. Moser, P. L. Dutton, R. M. Hoschtrasser, J. Chem. Phys. **100** (1996) 5140.
89. G. Haran, K. Wynne, C. C. Moser, P. L. Dutton, R. M. Hoschtrasser, J. Phys. Chem. **100** (1996) 5562.
90. W. Holzapfel, U. Finkele, W. Kaiser, D. Oesterhelt, H. U. Scheer, W. Zinth, Proc. Natl. Acad. Sci. U.S.A. **87** (1990) 5168.
91. K. Dressler, E. Umlauf, S. Schmidt, P. Hamm, W. Zinth, S. Buchanan, H. Michel, Chem. Phys. Lett. **183** (1991) 270.

Lam Research Ex. 1035 - Page 233
Lam Research Corp. v. Inpria Corp.
IPR2024-00033 - U.S. Patent No. 9,823,564

92. T. Arlt, S. Schmidt, W. Kaiser, C. Lauterwasser, M. Meyer, H. Scheer, W. Zinth, Proc. Natl. Acad. Sci. U.S.A. **90** (1993) 11757.
93. S. Schmidt, T. Arlt, H. Hamm, H. Huber, T. Nägele, J. Wachtveil, M. Meyer, H. Scheer, W. Zinth, Chem. Phys. Lett. **24** (1994) 116.
94. P. Hamm, W. Zinth, J. Phys. Chem. **99** (1995) 13537.
95. P. Hamm, M. Zurek, W. Mäntele, M. Meyer, H. Scheer, W. Zinth, Proc. Natl. Acad. Sci. U.S.A. **92** (1995) 1826.
96. W. Zinth, T. Arlt, J. Wachtveitl, Ber. Bunsenges. Phys. Chem. Chem. Phys. **100** (1996) 1962.
97. I. H. M. van Stokkum, L. M. P. Beekman, M. R. Jones, M. E. van Brederode, R. van Grondelle, Biochemistry **36** (1997) 11360.
98. M. E. van Brederode, M. R. Jones, F. van Mourik, I. H. M. van Stokkum, R. van Grondelle, Biochemistry **36** (1997) 6855.
99. R. J. Stanley, B. King, S. G. Boxer, J. Phys. Chem. **100** (1996) 12052.
100. A. M. Streltsov, T. J. Aartsma, A. J. Hoff, V. A. Shuvalov, Chem. Phys. Lett. **266** (1997) 347.
101. A. M. Streltsov, S. I. E. Vulto, A. Y. Shkuropatov, A. J. Hoff, T. J. Aartsma, V. A. Shuvalov, J. Phys. Chem. B **102** (1998) 7293.
102. S. Sporlein, W. Zinth, J. Wachtveitl, J. Chem. Phys. B **102** (1998) 7492.
103. D. C. Arnett, C. C. Moser, P. L. Dutton, N. F. Scherer, J. Phys. Chem. **103** (1999) 2014.
104. J. W. Lewis, R. A. Goldbeck, D. S. Kliger, X. Xie, R. C. Dunn, J. D. Simon, J. Phys. Chem. **96** (1992) 5243.
105. G. Hartwich, H. Lossau, A. Ogrodnik, M. E. Michel-Beyerle, Slow Charge Separation in a Minority of Reaction Centers Correlated with a Blueshift of the P_{860}-Band in *Rb. sphaeroides*, in: M. E. Michel-Beyerle (Ed.), The Reaction Center of Photosynthetic Bacteria, Springer-Verlag, Berlin, 1996.
106. M. Sugawara, Y. Fujimura, C. Y. Ten, S. H. Lin, J. Photochem. Photobiol. A: Chem. **54** (1990) 321.
107. N. J. Cherepy, A. P. Shreve, L. J. Moore, S. G. Boxer, S. Franzen, R. A. Mathies, Proc. Natl. Acad. Sci. U.S.A. **88** (1991) 11207.
108. N. J. Cherepy, A. P. Shreve, L. J. Moore, S. G. Boxer, R. A. Mathies, J. Phys. Chem. **98** (1994) 6023.
109. N. J. Cherepy, A. R. Holzwarth, R. A. Mathies, Biochemistry **34** (1995) 5288.
110. N. J. Cherepy, A. P. Shreve, L. J. Moore, S. G. Boxer, R. A. Mathies, Biochemistry **36** (1997) 8559.
111. N. J. Cherepy, A. P. Shreve, L. J. Moore, S. G. Boxer, R. A. Mathies, J. Phys. Chem. B **101** (1997) 3250.

Lam Research Ex. 1035 - Page 234
Lam Research Corp. v. Inpria Corp.
IPR2024-00033 - U.S. Patent No. 9,823,564

112. S. G. Johnson, D. Tang, R. Jankowiak, J. M. Hayes, G. J. Small, D. M. Tiede, J. Phys. Chem. **94** (1990) 5849.
113. N. R. S. Reddy, P. A. Lyle, G. J. Small, Photosyn. Res. **31** (1992) 167.
114. N. R. S. Reddy, S. V. Kolaczkowski, G. J. Small, Science **260** (1993) 68.
115. N. R. S. Reddy, S. V. Kolaczkowski, G. J. Small, J. Phys. Chem. **97** (1993) 6934.
116. G. J. Small, J. M. Hayes, R. J. Silbey, J. Phys. Chem. **96** (1992) 7499.
117. P. A. Lyle, S. V. Kolaczkowski, G. J. Small, J. Phys. Chem. **97** (1993) 6924.
118. H. Huber, M. Meyer, H. Scheer, W. Zinth, J. Wachveitl, Photosyn. Res. **55** (1998) 153.
119. S. V. Chekalin, Y. A. Matveetz, A. Y. Shkuropatov, V. A. Shuvalov, A. P. Yartzev, FEBS Lett. **216** (1987) 245.
120. S. H. Lin, C. H. Chang, K. K. Liang, R. Chang, J. M. Zhang, T.-S. Yang, M. Hayashi, Y. J. Shiu, Adv. Chem. Phys. **121** (2002) 1.
121. C. H. Chang, M. Hayashi, R. Chang, K. K. Liang, T.-S. Yang, S. H. Lin, J. Phys. Chem. B **105** (2001) 1216.
122. M. Hayashi, T. S. Yang, K. K. Liang, C. H. Chang, S. H. Lin, J. Chin. Chem. Soc. **47** (2000) 741.

Lam Research Ex. 1035 - Page 235
Lam Research Corp. v. Inpria Corp.
IPR2024-00033 - U.S. Patent No. 9,823,564

Chapter 7

Point Defects on the Silica Surface: Structure and Reactivity

V.A. Radzig

Semenov Institute of Chemical Physics, Russian Academy of Sciences, ul. Kosygina 4, 117977 Moscow, Russia

1. Introduction 233
2. Methods for Creation of Defects on Silica Surface 236
   2.1. Preparation of the Thermo-Activated Silica (TSi) Samples 236
   2.2. Preparation of the Mechano-Activated Silica Samples (MSi) 237
   2.3. Preparation of the "Reactive Silica" (RSi) Samples 238
   2.4. Structure and Concentration of Paramagnetic and Diamagnetic Point Defects on Activated Silica Surface 239
3. Quantum-Chemical Calculations 240
4. Chemical Modification of the Surface Defects 243
   4.1. Preparation of ≡Si-O* Radicals: The System (≡Si* + N_2O) 244
   4.2. Mutual Transformations of the (≡Si-O)$_2$Si: (SC) and (≡Si-O)$_2$Si = O (SG) Groups 248
   4.3. Si = O Bond Strength in the (≡Si-O)$_2$Si = O Group 248
   4.4. Microcalorimetry of the Processes at the SiO_2 and GeO_2 Surfaces 252
5. Interrelation Between the EPR Parameters of the Silicon-Centered Paramagnetic Centers and Their Spatial Structure: Results of Quantum-Chemical Calculations. . . . 253
6. Silicon-Centered Paramagnetic Centers (PCs) in SiO_2 260
   6.1. PC (≡Si_β-O)$_3$$Si_\alpha^\bullet$ on the Surface and in the Bulk of Silica 260
   6.2. PC (≡Si_β-O)$_2$$Si_\alpha^\bullet$-*r*, Where *r* = H(D), OH(OD), NH_2, and CH_3(CD_3) 264
   6.3. Stretching Vibration Frequencies of the Si-H Bonds in the Hydrogenation Products of Silicon-Centered PCs 269
   6.4. Optical Characteristics of the Silicon-Centered PCs 270
7. Paramagnetic Centers ≡Si-O$^\bullet$ on the Silica Surface (Non-Bridging Oxygen Center) 275
8. The (≡Si-O)$_3$Si-O-O* Radicals: Structure and Reactivity 279
9. Diamagnetic Point Defects on Silica Surface 281
   9.1. (≡Si-O-)$_2$Si < O_2 > Si(-O-Si≡)$_2$ Groups (Strained Rings, SRs) on the Silica Surface 282
   9.2. Diamagnetic Sites Containing Two-fold Coordinated Silicon Atoms (≡Si-O-)$_2$Si: (SC): Identification of SC Structure 285
   9.3. Products of High-Temperature Hydration of RSi Samples 288
   9.4. Optical Parameters of SC 290
   9.5. The Mechanism of Singlet–Triplet Conversion of SC 291
   9.6. Silanone Groups (≡Si-O)$_2$Si = O on Silica Surface 292
   9.7. Dioxasilyrane Groups ((≡Si-O)$_2$Si < O_2) 296
   9.8. Reactivity of the > Si < O_2 Groups Toward the Polar X-H (X = OH, NH_2, OCH_3) Molecules 305

THIN FILMS AND NANOSTRUCTURES, vol. 34
ISSN 1079-4050
DOI: 10.1016/S1079-4050(06)34007-0

© 2007 by Elsevier Inc.
All rights reserved.

Lam Research Ex. 1035 - Page 236
Lam Research Corp. v. Inpria Corp.
IPR2024-00033 - U.S. Patent No. 9,823,564

10. Inhomogenity of Physico-Chemical Properties of Surface Defects 309
11. Impurity Centers in Quartz Glass: Carbon in the Silica Structure 314
11.1. ≡Si-$^{\bullet}$CH$_2$, (≡Si-)$_2^{\bullet}$CH, and (≡Si-)$_3$C$^{\bullet}$ Radicals 314
11.2. Reactivity of the (≡Si-)$_3$C$^{\bullet}$ Radicals Toward H_2 Molecules 317
11.3. Increase in the Concentration of Paramagnetic Centers Upon the Thermo Oxidizing Treatment of the RSi Samples 317
12. Nitrogen in Silica 319
12.1. PCs (≡Si-O)$_2$Si*(NH$_2$), (≡Si-O)$_2$Si*-N(Si≡)$_2$, (≡Si-O)$_2$(HO)Si-N*H, and ≡Si-N*-Si≡ 320
12.2. Reactions of ≡Si-N*-H and ≡Si-N*-Si≡ PC With $H_2(D_2)$ 324
12.3. On the Strengths of Si-O and Si-N Bonds in Vitreous Silica 328
13. Surface and Near-Surface Defects in Silica 329
14. Design of Intermediates With Desired Structure on Silica Surface 330
15. Conclusions 335
Questionnaire 339
References 340

Processes (heterogeneous) that occur on the surface of a solid frequently exhibit irreproducibility effects, the dependence on the prehistory of a sample, and other features of the "character" of the surface that leave experimenters at a loss. Often, these qualities are due to a small number of surface active sites (i.e., defects). This is the reason why understanding the mechanisms of such processes requires deciphering the structure of these sites and studying their chemical temperament (i.e., reactivity). For about a decade, we have been solving these problems for silica (amorphous SiO_2), a component most abundant in nature and having very wide applications in various fields, from construction engineering (as a build material) to microelectronics and fiber optics. The first part of this chapter is devoted to the methods for generating of various types (intrinsic or connected with impurity atoms) chemically active sites at the silica surface. The results of experimental studies of the physico-chemical characteristics (EPR, IR, optical spectroscopy, microcalorimetry, and volumetry) of these groups are presented. Quantum-chemical analysis of the corresponding results made it possible to interpret the obtained spectral and kinetic data and relate them to the electronic and geometric structures of these sites. This approach was used to gain information on the physico-chemical characteristics of the main types of defects that can stabilize in the silica structure, and the methods for the direct control of their concentrations were proposed. The closing part of chapter is devoted to the mechanisms of the processes occurring at the silica surface and involving various defects and gas-phase molecules. The pathways and kinetic regularities of the respective individual reaction steps are revealed.

Lam Research Ex. 1035 - Page 237
Lam Research Corp. v. Inpria Corp.
IPR2024-00033 - U.S. Patent No. 9,823,564

1. Introduction

The amorphous SiO_2 (silica) is one of the most-used and extensively studied materials. This is caused by its natural abundance and unique physico-chemical characteristics. Silica was among the first compounds to be prepared in the form of fine-grained powders (nanoparticles) with the specific surface of several hundreds of meter square per gram. The surface characteristics play a leading part in various applications of this material (as a filler or carrier in catalytic systems, as an absorber, etc.) in the fine-grained state. Most studies in this field are associated with a search for the ways of directional modification of the solid surface through the thermal or thermo mechanical treatment, with the object of preparing a material with the desired adsorption characteristics. For instance, to obtain a sample with the hydrophobic surface, one substitutes the $\equiv$Si-O-CH_3, $\equiv$Si-O-Si$(CH_3)_3$, etc. groups for the $\equiv$Si-OH groups. The structure of any group stabilized at the solid surface can be represented as SR, where S is a fragment of the solid surface. In silica, the S group includes a lattice silicon atom, to which the R group is connected, together with its coordination sphere composed of the solid atoms ($\equiv$SiR). The structure of the environment of the lattice atom Si, symbolized by "$\equiv$" or "$>$" (e.g., in the case of the $>Si(OH)_2$ group), is kept in the shade, because it is hard to detect it by the conventional spectral techniques. However, the properties of a surface Si atom involved in the formation of the surface SR fragment are governed just by the structure of its nearest environment. These properties are responsible for the reactivity of this atom and for prerequisites to the formation of SR fragments of the required type. In this work, an attempt is undertaken to discuss the current status of investigations in this field, namely, to demonstrate the progress in determining the physico-chemical characteristics of the structures symbolized by "$\equiv$" or "$>$".

The S groups stabilized at the solid surface can differ in their chemical nature. In the disordered (amorphous) solids, to which silica refers and which are of most practical and theoretical interest, the variations in the spatial structure are inevitable. These variations cause variations in the properties of even those S groups having chemically identical composition of their coordination spheres and give rise to the inhomogeneous line broadening in the spectra of these groups and to their kinetic inequivalence. In this work, special emphasis is placed on the questions associated with these problems.

Particular attention is given to two closely allied problems. The first part of this communication is devoted to the methods for generating S groups of

Lam Research Ex. 1035 - Page 238
Lam Research Corp. v. Inpria Corp.
IPR2024-00033 - U.S. Patent No. 9,823,564

various types at the silica surface. Next, the results of experimental studies of the physico-chemical characteristics (EPR, IR, optical spectroscopy, microcalorimetry, and volumetry) of the groups are presented. Quantum-chemical analysis of the corresponding results made it possible to interpret the obtained spectral and kinetic data and relate them to the electronic and geometric structures of the S groups. This approach was used to gain information on the physico-chemical characteristics of the main types of S defects that can stabilize in the silica structure, and the methods for the direct control of their concentrations were proposed. The closing part of this communication is devoted to the mechanisms of the processes occurring at the silica surface and involving various defects and gas-phase molecules. The pathways and kinetic regularities of the respective individual reaction steps are revealed.

The main factor that allowed this investigation to be carried out was the accessibility of the surface centers to the molecules of the surrounding medium. As a result, these centers can be involved in the reactions with various molecules to chemically modify their structure ($S + R \Rightarrow SR$) and, hence, synthesize (construct) groups of the desired structure at the solid surface. The chemically bonded surface-attached groups are thermally comparatively stable, allowing their spectral parameters and reactivity to be studied in detail. The corresponding data form a necessary basis for determining the mechanisms of the processes occurring at the silica surface. Clearly, two parts of this study are closely related to each other; the first one is devoted to the design of the methods for creating the defects of various types at the solid surface and to the revelation of their structure, while the second part is devoted to the properties and formation mechanisms for these defects and to their use as "growth sites" in the preparation of surface groups with the desired structure.

The problem of structural identification of the S groups can hardly be solved without widespread use of the method for the directional chemical modification of their structure in the reactions with specially chosen gas-phase reactants. This allows structural study of the complexes by using the new experimental techniques whose use was hampered or even impossible for the starting defect. The structural identification of the resulting complexes gains additional information both about the nature of the initial surface center and about its reactivity. For instance, the use of low-molecular free radicals (H, D, and OH atoms, stable nitroxy radicals, and other paramagnetic species) allows the use of the EPR technique in studying the solid diamagnetic defects (paramagnetic probe (spin labeling)):

$$S + r^{\bullet} \rightarrow S^{\bullet} - r.$$

The products of defect hydrogenation accompanied by the S-H(D)-bond formation can be detected by using IR spectroscopy, etc.

Lam Research Ex. 1035 - Page 239
Lam Research Corp. v. Inpria Corp.
IPR2024-00033 - U.S. Patent No. 9,823,564

The material in this chapter is presented with regard to the aforementioned circumstances. Although the chief goal consisted in a detailed discussion of those experimental and computational (quantum-chemical) results forming a basis for the conclusions that could be drawn about the structure and reactivity of the defects of interest, the corresponding sections are not necessarily placed at the beginning of the chapter. For this reason, the data presented in the first sections on the structure and mutual transformations of the defects are not artificial but are the results of special investigations. Experimental and calculated results given in Chapter 7 without references to a literature source constitute unpublished author's finding.

The data on the properties of surface defects in silica are also useful in the structural identification of bulk defects in quartz glass. The use of pure and doped quartz glasses as base materials in fiber optics and new-generation optical devices has provoked growing interest in the structure and properties of the defects in these compounds. However, bulk defects in solids are inaccessible to the majority of molecules of the surrounding medium (hydrogen (deuterium) is an important exclusion for quartz glasses), strongly hampering their structural identification. At the same time, taking into account the structural properties of quartz glass and the "directional" character of the siloxane bond, one can assume that the defects stabilized at the surface and in the bulk of quartz glass can have similar structures. For this reason, the information on the structure and properties of the surface defects is helpful in the determination of the structure of bulk centers [1,2]. One can suggest that some of the point defects that were identified at the silica surface, for example, groups containing the $>Si=O$ bond, play an important role as intermediates in the processes of mutual defect transformations in silica glass, despite the fact that they have not yet been detected experimentally in the bulk of this material.

The obtained experimental data served as a basis for designing the method of directional synthesis of the surface-attached groups with the predetermined chemical composition. This method represents one of the variants of studying the reactionally active intermediates in the commonly used matrix isolation technique. The surface-attached groups are translational immobile, making impossible their mutual encounter, and the role of inert matrix is played by the environmental chemically inactive siloxane bonds. The thermal stability of such groups depends on the activation energies for their intramolecular transformations. In the traditional variant of matrix isolation technique, these energies are much higher than those for the melting of inert matrix. One more advantage of the suggested method is that it provides a possibility for quantitatively studying the reactivity of the synthesized intermediate because of its accessibility to the molecules of surrounding medium.

Lam Research Ex. 1035 - Page 240
Lam Research Corp. v. Inpria Corp.
IPR2024-00033 - U.S. Patent No. 9,823,564

2. Methods for Creation of Defects on Silica Surface

In the most modifications of SiO_2 (excepting stishovite), the silicon atom is bonded to four oxygen atoms, and the oxygen atom is bonded to two silicon atoms. The S group entering into SR, is a surface defect in silica. The use of terms "point" or "extended" for the defect depends on the type of distortions induced in the regular spatial structure of solid. These distortions can be caused by the presence of impurity atoms or local structural distortions in a crystalline solid (vacancy, interstitial atom, etc.). In the case of amorphous solid with short-range order in the atomic spatial arrangement and without long-range order (lack of translational symmetry), the term "defect" is used to demonstrate that the short-range order in the structure of the center is distorted. With such an approach, all those fragments in silica that are not the siloxane bond Si-O-Si should be called the surface defects. The question of the possible existence of defectless (in the above sense) amorphous silica (in its bulk and at its surface) still remains open. On the other hand, one should keep in mind that the siloxane bonds in the silica structure can strongly differ in their characteristics. In the $(\equiv\text{Si-O})_2\text{Si}<\text{O}_2>\text{Si}(\text{O-Si}\equiv)$ groups identified at the surface of dehydrated silica [3,4], the silicon and oxygen atoms entering into a four-member cyclic structure have "proper" coordination numbers. However, because of the uncommon character of chemical bonds in the small ring (the OSiO and SiOSi angles in the four-member ring are close to 90° instead of their standard values of $\cong 109^\circ$ and $\cong 142^\circ$, respectively), this group is chemically highly active (compared with the "ordinary" siloxane bonds) toward the molecules containing the O-H and N-H bonds (water, alcohols, ammonia, etc.).

The surface groups S with the highest free energy should be most efficient in the processes of chemical modification. In this case, one can expect the formation of a great variety of modification products (SR groups). For the compounds with the directional chemical bonds between the neighboring atoms in the main crystalline and amorphous silica modifications, these are the products of bond rupture and/or its rearrangement.

Now let us dwell upon the methods used in this work for the defect generation at the silica surface.

2.1. Preparation of the Thermo-Activated Silica (TSi) Samples

As a rule, the silica surface is covered with a layer of silanol groups ($\equiv$Si-O-H) and adsorbed water, which can be removed by drying at temperatures of ~ 600 K [5,6]. With a rise in temperature, the concentration of silanol

Lam Research Ex. 1035 - Page 241
Lam Research Corp. v. Inpria Corp.
IPR2024-00033 - U.S. Patent No. 9,823,564

groups decreases because of their condensation accompanied by the formation of water molecules and siloxane bridges (≡Si-O-Si≡) [5,6]. At the annealing temperatures above 900 K, new surface groups were found to form. They are responsible for the absorption bands in the silicon IR-transparency window (888 and 908 cm^{-1}) [3,4]. These groups are highly reactive toward the H_2O, CH_3OH, NH_3, etc. molecules. The corresponding reaction products resulting from the insertion of the H-X molecules into the siloxane bond were detected by IR spectroscopy:

$$\equiv \text{Si-O-Si} \equiv + \text{H-X (X} = \text{OH, OCH}_3\text{, NH}_2) \rightarrow \equiv \text{Si-X} + \text{H-O-Si} \equiv .$$

These reactions proceed even at 300 K at a vapor pressure of 10^{-2} Torr. Hence, their activation energies do not exceed few kilocalories per mole.

On the basis of the spectral and kinetic data, these groups were ascribed cyclic four-member structure (≡Si-O)$_2$Si<O$_2$>Si(O-Si≡) [4]. This allows one to refine the structure of the reaction products:

$$(\equiv \text{Si-O})_2\text{Si} < \text{O}_2 > \text{Si(O-Si} \equiv)_2 + \text{H-X (X} = \text{OH, OCH}_3\text{, NH}_2) \rightarrow (\equiv \text{Si-O})_2\text{Si(X)-O-(HO)Si(O-Si} \equiv)_2.$$

The hypothesis for a possible stabilization of such groups at the silica surface was proposed by Perry in 1966 [7].

At the same time, the enhanced reactivity of these groups toward the compounds containing other types of functional groups (saturated and unsaturated hydrocarbons, H_2 and CO_2 molecules, etc.), has not been reported in literature to date. An exception is provided by work [8], where it was found that the strained rings (SRs) disappear upon treating the sample surface by deuterium plasma, although the structure of products and the mechanism of the process were not revealed. Nevertheless, the very fact that deuterium plasma contains chemically active free radical and charged particles indicate that the SRs do not exhibit enhanced reactivity toward the D_2 molecules (as opposed to the HOH or NH_3 molecules). Apart from the SRs, a small amount of terminal hydroxyl groups remains at the silica surface after high-temperature treatment. The stabilization of other chemically active groups in the high-temperature dehydration products of silicon samples has not been reported in literature.

2.2. PREPARATION OF THE MECHANO-ACTIVATED SILICA SAMPLES (MSi)

Silica powder was mechanically treated in a vibrational mill in an inert atmosphere at 300 or 77 K in a quartz vessel with milling balls made from quartz glass. Mechanical treatment of silica [9,10] is accompanied by the

Lam Research Ex. 1035 - Page 242
Lam Research Corp. v. Inpria Corp.
IPR2024-00033 - U.S. Patent No. 9,823,564

destruction of its particles, so that the Si-O bonds intersecting the interface in a three-dimensional SiO_2 network are inevitably disrupted. Some of the disrupted chemical bonds and products of their rearrangement are stabilized at the newly formed (juvenile) surface.

The active centers in silica are generated upon mechanical treatment not only due to the cleavage of the particles of material but also to their mutual contacts (so-called "friction" regime [11–13]). For this reason, the mechanical treatment can be used for generating defects at the surface of high-dispersed silica (aerosol).

The mechanical destruction is one of the efficient methods for preparing and studying the defect structure in doped quartz glasses. The mechanical treatment of such silica samples is accompanied by a drastic increase in their specific surface and, thus, allows a portion of fragments containing impurity atoms to be outcropped at the solid surface in an amount sufficient for recording their spectral parameters and studying their reactivity. It was pointed out above that the advantages of studying properties of the surface defects are caused by the accessibility of the latter to the molecules of surrounding medium. The information obtained by this method on the nature of defects in a nitrogen-doped quartz glass is presented in Section 12.

2.3. Preparation of the "Reactive Silica" (RSi) Samples

Morterra and Low [14,15] have demonstrated that the methoxy groups ($\equiv$Si-OCH_3) can be fully substituted for the surface hydroxyl groups ($\equiv$Si-OH) after treating silica surface in a methanol vapor at 700 K. They found that, upon the subsequent high-temperature pyrolysis of such samples ($T > 1050$ K), a series of chemical reactions proceed, with the following key reaction:

$$\equiv \text{Si-OCH}_3 \Rightarrow \equiv \text{Si-H} + \text{O} = \text{CH}_2.$$

This reaction was named the key reaction because it removes one of the oxygen atoms from the coordination sphere of a surface silicon atom. The resulting $\equiv$Si-H groups are thermally much less stable than the hydroxyl groups. The Si-H bond strength is equal to $\sim$100 kcal/mol [16], whereas the strengths of the H-O and O-Si bonds in the $\equiv$Si-O-H group are 128 [17] and $\sim$140 kcal/mol, respectively. The pyrolysis of the Si-H groups proceeds at temperatures below 1100 K, where the solid retains its stability (the rates of diffusion processes are low), and where this process is accompanied by the decomposition of these groups. As a result, the surface layer of the silica samples thus prepared becomes oxygen deficient and contains a set of chemically active defects. Such sample can chemically adsorb the H_2, CH_4,

Lam Research Ex. 1035 - Page 243
Lam Research Corp. v. Inpria Corp.
IPR2024-00033 - U.S. Patent No. 9,823,564

and other molecules even at room temperature, not to mention oxygen molecules [15], so that the prepared samples were named "reactive silica" (RSi). This term can also be used as a characteristic of the mechanically activated silica samples.

The structure of the centers responsible for the chemisorptions activity of the RSi samples is analyzed in Refs. [18,19] and is discussed in detail in the next sections of this chapter.

The use of the molecules of other (ethyl and heavier) alcohols with this object allows the replacement of the surface hydroxyl groups by the alcohol groups, although the pyrolysis of the latter does not remove oxygen atom. For the groups with a more complicated structure, new transformation channels arise with a higher transformation rate. For example, the thermal decomposition of the surface ethoxy groups follows the scheme

$$\equiv \text{Si-O-CH}_2\text{-CH}_3 \Rightarrow \equiv \text{Si-O-H} + \text{CH}_2 = \text{CH}_2$$

Consequently, the thermal decomposition of the methoxy groups is accompanied by the removal of oxygen atom from the Si-O bond owing not only to a high strength of the C = O bond in the resulting formaldehyde molecule (quantum-chemical calculations give a value of ~60 kcal/mol for the heat effect of this endothermic reaction), but also to the higher activation energies in the other possible decomposition channels of the methoxy group.

2.4. STRUCTURE AND CONCENTRATION OF PARAMAGNETIC AND DIAMAGNETIC POINT DEFECTS ON ACTIVATED SILICA SURFACE

The structures and concentrations of paramagnetic and diamagnetic sites on the surface of TSi, MSi, and thermo chemically activated (RSi) silica is presented in Table 7.1. The data for the RSi sample subjected to the thermo oxidative treatment (see Section 11.3), resulting in an increase in the

Table 7.1. Concentrations of intrinsic defects N (m^{-2}) stabilized on the thermo (TSi), mechanically (MSi), and thermo chemically (RSi) activated SiO_2 surface [9, 10, 15, 18, 19, 52]

N	$\equiv Si^{\bullet}$	$\equiv Si\text{-}O^{\bullet}$	$>Si:$	$>Si=O$	$(\equiv Si\text{-}O)_2Si<O_2>Si(O\text{-}Si\equiv)_2$
1. Tsi	–	–	–	–	1.5×10^{17}
2. Msi	2×10^{16}	2×10^{16}	$(1/5) \times 10^{15}$	$(8/10) \times 10^{16}$	?
3. Rsi	1×10^{15}	–	9×10^{16}	–	1.1×10^{17}
4. RSi[a]	–	2×10^{16}	–	2×10^{16}	1.1×10^{17}

[a]The sample RSi was subjected to thermo oxidative treatment (see Section 11.3).

Lam Research Ex. 1035 - Page 244
Lam Research Corp. v. Inpria Corp.
IPR2024-00033 - U.S. Patent No. 9,823,564

concentration of paramagnetic sites, are presented in the last row. Despite different methods of silica activation, intrinsic defects of two main types in which the silicon atom is bound to three (paramagnetic) or two (diamagnetic) lattice oxygen atoms are stabilized on its surface. The resemblance is more pronounced if we take into account that (1) in the case of mechanically activated silica, the material has a stoichiometric composition and RSi samples are oxygen-deficient and (2) $(\equiv\text{Si-O-})_3\text{Si}^\bullet$, $(\equiv\text{Si-O-})_3\text{Si-O}^\bullet$, $(\equiv\text{Si-O-})_2\text{Si:}$, and $(\equiv\text{Si-O-})_2\text{Si}=\text{O}$ sites are transformed into each other during redox processes (see Section 4).The third type of chemically active sites on silica surface is four-member rings $(\equiv\text{Si-O})_2\text{Si}<\text{O}_2>\text{Si}(\text{O-Si}\equiv)_2$.

The same conclusion follows from the results of structural studies of a hydroxyl cover on SiO_2 [3,6,20]. Several types of hydroxyl groups (terminal $\text{HO-Si(O-Si}\equiv)_3$, geminal $(\text{HO})_2\text{Si(O-Si}\equiv)_2$, and vicinal $(\equiv\text{Si-O})_2\text{Si(OH)-O-Si(OH)(O-Si}\equiv)_2$) were identified at the silica surface. They can be considered as products (SR) of chemical modification of the surface S groups of three different types: paramagnetic (1) $^\bullet\text{Si(O-Si}\equiv)_3$ $(\text{R}=\text{HO}^\bullet)$, diamagnetic (2) $\text{Si(O-Si}\equiv)_2$ $(\text{R}=2(\text{HO}^\bullet))$, and (3) $(\equiv\text{Si-O})_2\text{Si}<\text{O}_2>\text{Si(O-Si}\equiv)_2$ $(\text{R}=\text{H}_2\text{O})$. One can see from the data in Table 7.1 that all listed S groups can be prepared and stabilize, under certain conditions, at the silica surface.

When silica with the developed specific surface ($>100\,\text{m}^2/\text{g}$) is used, the number of active sites per gram of material reaches 10^{18}–10^{19}. This amount is sufficient for their reliable detection by different methods: EPR, IR and optical spectroscopy, microcalorimetry, and adsorption measurements. Using the thermo chemical method, one can activate the surface of powdered and semitransparent film; SiO_2 samples with a thickness of several tens of microns obtained by pressing the high-dispersity silica powder (aerosil). These film samples are suitable for quantitative optical studies in the UV, visible, and IR regions.

3. Quantum-Chemical Calculations

Ab initio quantum-chemical calculations were used in this study for the interpretation of the experimental data (EPR, IR, and optical). The main purpose of the calculations was to elucidate the question of how the geometric factors (spatial structure of the defect) and chemical ones (nature of the substituents) influence the spectral properties of the defects. At present time such calculations can be carried out on acceptable level for systems comparatively small in size. This makes it necessary to use molecular models for calculations of defects in solids.

Lam Research Ex. 1035 - Page 245
Lam Research Corp. v. Inpria Corp.
IPR2024-00033 - U.S. Patent No. 9,823,564

It is surprising that, at first glance, different types of surface defects (paramagnetic and diamagnetic) of silica and their fluorine-substituted low-molecular analogs, for example, $(\equiv\text{Si-O-})_3\text{Si}^\bullet$ and $F_3Si^\bullet$ or $(\equiv\text{Si-O-})_2\text{Si:}$ and F_2Si:, have close physico-chemical characteristics (Table 7.2). This similarity is due to the fact that (i) the electronic states of intrinsic and doped defects under study in SiO_2 are spatially localized and concentrated near the defect atom and (ii) the ≡Si-O- and F-groups as substituents exert a very similar effect on the properties of the silicon atom bound to them. This allows one to use published data on low-molecular fluorine-substituted silicon compounds to predict the parameters of defects in solids. When these data are scarce, the parameters can be obtained by quantum-chemical calculations.

To model defects in solids, a small cluster is usually used, which is cut of a solid structure, and cleaved chemical bonds are ''saturated'' using H atoms or OH groups [24]. As follows from the available experimental data, the F atom is suitable for the saturation of a free valence of the Si atom formed due to the cleavage of the Si-O bond.

Calculations were performed using the Hartree–Fock approximation taking into account electron correlation effects by Meller–Plessett perturbation theory (MP2/6-31G** or UMP2/6-31G** [25]) or density functional theory (DFT, in this work it was used in the B3LYP/6-311G** variant [26,27]). The geometry of molecules or radicals was optimized using both of these methods, which gave close equilibrium parameters of the systems under study. Both isotropic (a_{iso}, using Fermi contact term) and dipolar parts ($b_{1,2,3}$) of the tensors of hyperfine interaction (HFI) of the electron spin with non-zero nuclear spins for PC have been determined at the DFT UB3LYP/6-311G** level. Vibrational spectra were calculated for all of the optimized structures. Transition states (TS) were characterized by a negative eigenvalue of the Hessian matrix. The heat of reactions at 0 K $\Delta H\,(0\,\text{K}) = \Delta E\,(0\,\text{K}) + \Delta(\text{ZPE})$ (here, $\Delta E\,(0\,\text{K})$ and $\Delta(\text{ZPE})$ are differences between the energies and zero-point energies of the initial reactants and products, respectively) were calculated both at the DFT level and at the G2MP2//B3LYP/6-311G(d,p) level [28]. The latter was developed for calculating the heat of the formation of compounds, and it reproduced the thermo chemical characteristics of processes better than DFT did. The enthalpies of compounds at 0 K were calculated from the equation

$$\begin{aligned}\text{E(G2MP2(0 K))} = {} & \text{E(QCISD(T, E4 T)/6-31 1G(d, p))} \\ & + \text{E(MP2/6-311 + G(3df, 2p))} - \text{E(MP2/6-311G(d, p))} \\ & + \text{ZPE} - 0.005\,n(\beta) - 0.0009(n(\alpha) - n(\beta)).\end{aligned}$$

Lam Research Ex. 1035 - Page 246
Lam Research Corp. v. Inpria Corp.
IPR2024-00033 - U.S. Patent No. 9,823,564

Table 7.2. Physico-chemical properties of surface defects of silica and their hydrogen and fluorine-containing low-molecular analogs [22, 23]

1. Structure	a_{iso} (^{29}Si), mT	2. Structure	a_{iso} (^{1}H), mT	3. Structure	ΔH (298 K) kJ/mol	ν (Si-H) cm^{-1}	4. Structure	ν (Si-H) cm^{-1}	5. Structure	ν (Si = O), cm^{-1}	6. Structure	ΔE (X → S_1), eV excitation	ΔE (S_1 → X), eV luminescence	ΔE (T_1 → X), eV luminescence
(≡Si-O)$_3$Si	−47.9	(≡Si-O)$_2$Si-H	7.55	(≡Si-O)$_3$Si-H	418 ± 9	2300	(≡Si-O)$_2$SiH$_2$	2225	(≡Si-O)$_2$Si = O	(1307 ± 1)	(≡Si-O)$_2$Si:	(5.3 ± 0.1)	(4.4 ± 0.1)	(2.75 ± 0.1)
F_3Si	−49.8	F_2Si-H	8.99	F_3Si-H	418	2315	F_2SiH_2	2247	$F_2Si = O$	1309	F_2Si:	$T_{00} = 5.47$	(3.27 ± 0.15)	
H_3Si	−26.6	H_2Si-H	0.8	H_3Si-H	372	2186	H_2SiH_2	2183 2189	$H_2Si = O$	1220	H_2Si:	$T_{00} = 1.93$	(0.2–0.4)	

Lam Research Ex. 1035 - Page 247
Lam Research Corp. v. Inpria Corp.
IPR2024-00033 - U.S. Patent No. 9,823,564

The first term in this expression is the energy of the structure at the QCISD(T,E4 T)/6-311G(d,p) level [29]; the second term is a change in the energy of the system when the size of the basis set (the second parentheses) is increased; the third term is the zero-point energy calculated at the DFT(B3LYP/6-31 1G(d,p)) level; and the other terms are a semiempirical so-called higher level correction [28], in which $n(\beta)$ is the number of β electrons in the system and $(n(\alpha) - n(\beta))$ is the difference between the numbers of α and β electrons. All calculations were carried out with Gaussian 94 [29].

4. Chemical Modification of the Surface Defects

The accessibility of surface sites for molecules of the environment makes it possible to chemically modify the defects in solids on purpose. Some chemical processes involving paramagnetic and diamagnetic defects and CO, N_2O, and O_2 molecules that allow the transform of surface sites from one type into another are presented in Table 7.3. Using the difference in the reactivity of defects, one can prepare silica samples with necessary combinations of paramagnetic and (or) diamagnetic defects stabilized on the surface, for example, ($\equiv$Si-O* + >Si = O), ($\equiv$Si* + >Si<O_2>C = O), or others. If necessary, some of them can be deactivated by transforming into chemically inactive form (e.g., the carbonate form of diamagnetic groups). This is very convenient for the study of some types of point defects. Two examples of such modification are presented in the Sections 4.1. and 4.2.

Table 7.3. Some reactions used for the modification of the structure of surface defects [10, 18, 19, 24, 25]

1. $\equiv Si^{\bullet} + O_2 \rightarrow \equiv$Si-O-$O^{\bullet}$	77K
2. $\equiv Si^{\bullet} + N_2O \rightarrow \equiv$Si-N = N-$O^{\bullet}$[a]	300K
3. $\equiv$Si-N = N-$O^{\bullet} \rightarrow \equiv$Si-$O^{\bullet} + N_2$(g)	450K
4. $\equiv$Si-$O^{\bullet}$ + CO $\rightarrow \equiv$Si-O-$^{\bullet}$C = O	77K
5. $\equiv$Si-O-$^{\bullet}$C = O $\rightarrow \equiv Si^{\bullet} + CO_2$(g)	450K
6. $\equiv$Si-O-$O^{\bullet}$ + 2CO $\rightarrow \equiv Si^{\bullet} + 2CO_2$	500K
7. >Si: + O_2 → >Si<O_2	200K
8. >Si<O_2 + CO → >Si<O_2>C = O	200K
9. >Si<O_2>C = O → >Si = O + CO_2	550K
10. >Si: + CO_2 → >Si = O + CO	650K
11. >Si = O + CO → >Si: + CO_2	650K

[a]Earlier it was supposed [19, 24] that this complex has the other structure - $\equiv$Si-O-N = $N^{\bullet}$.

Lam Research Ex. 1035 - Page 248
Lam Research Corp. v. Inpria Corp.
IPR2024-00033 - U.S. Patent No. 9,823,564

4.1. PREPARATION OF ≡Si-O* RADICALS: THE SYSTEM (≡Si* + N_2O)

The N_2O molecule is a donor of atomic oxygen (the heat of the reaction $N_2O \Rightarrow N_2 + O(^3P)$ is 40 kcal/mol [32]) and it is used to obtain the paramagnetic species like O^- from the F-sites on various oxide surfaces [33,34]:

$$(Me)^{n+} + N_2O \;\Rightarrow\; (Me)^{(n+1)+}\text{-}O^{-1} + N_2(g).$$

However, only for the system ≡Si* + N_2O, the intermediate product of this reaction was registered experimentally [30]:

$$(\equiv \text{Si-O-})_3\text{Si}^* + N_2O \;\Rightarrow\; (\equiv \text{Si-O-})_3\text{Si-N} = \text{N-O}^*.$$

The ESR, IR, and optical methods have been used to register the product of nitrous oxide addition to a silyl-type radical stabilized on the SiO_2 surface [30,31]. The EPR spectrum has three components of the hyperfine structure (hfs) with an intensity ratio close to 1:1:1 and a distance between them of ~36.5 G (Figure 7.1). The apparent hfs of the ESR spectrum is due to the interaction of an unpaired electron with one ^{14}N nucleus ($I = 1$). The formation of radicals is accompanied by the appearance of two new IR bands (Figure 7.1). One of them near 1620 cm^{-1} is very intensive. The second, much less intense band is near 1335 cm^{-1}. The spectrum of optical absorption of the $(\equiv Si\text{-}O)_3Si\text{-}N = N\text{-}O^*$ radical *consists* of three bands with maxima at 3.25, 5.2, and >6 eV (Figure 7.1). The first two of them have comparable intensities, and the intensity of the third band is much higher. The coefficients of extinction of absorption bands are equal to: ε (380 nm) = $(0.8 \pm 0.2) \times 10^{-18}$ cm^2/molecule, ε (238 nm) = $(0.55 \pm 0.2) \times 10^{-18}$ cm^2/molecule. For the short-wave band with the maximum at energies higher than 6 eV, ε (203 nm) = $(2.65 \pm 0.6) \times 10^{-18}$ cm^2/molecule.

When heated above 350 K, the complex is decomposed. Molecular nitrogen is evolved to the gas phase in an amount comparable with the number of decomposed paramagnetic centers (PCs) and the $(\equiv Si\text{-}O\text{-})_3Si\text{-}O^*$ radicals are formed:

$$(\equiv \text{Si-O})_3\text{Si-N} = \text{N-O}^* \;\Rightarrow\; (\equiv \text{Si-O-})_3\text{Si-O}^* + N_2(g).$$

The energy diagram for the $((\equiv Si\text{-}O)_3Si^* + N_2O)$ system constructed on the basis of experimental and calculated data is shown in Figure 7.2 (g). In the calculations, the F_3Si^* radical modeled the paramagnetic center $(\equiv Si\text{-}O\text{-})_3Si^*$. Figure 7.2a shows the structure of the product of nitrous oxide addition to the F_3Si^* radical (C_s symmetry and the $^2A'$ state). All attempts to find the local minimum on the potential energy surface corresponding to the addition of nitrous oxide to the silyl radical via the oxygen atom failed. In this mutual arrangement of the radical center and nitrous

Lam Research Ex. 1035 - Page 249
Lam Research Corp. v. Inpria Corp.
IPR2024-00033 - U.S. Patent No. 9,823,564

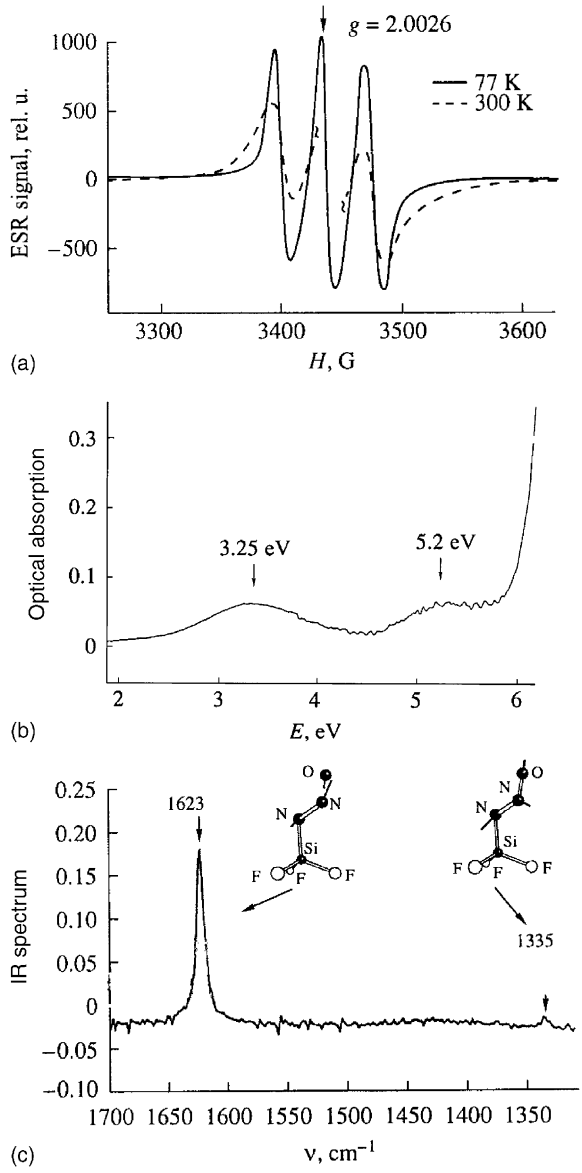
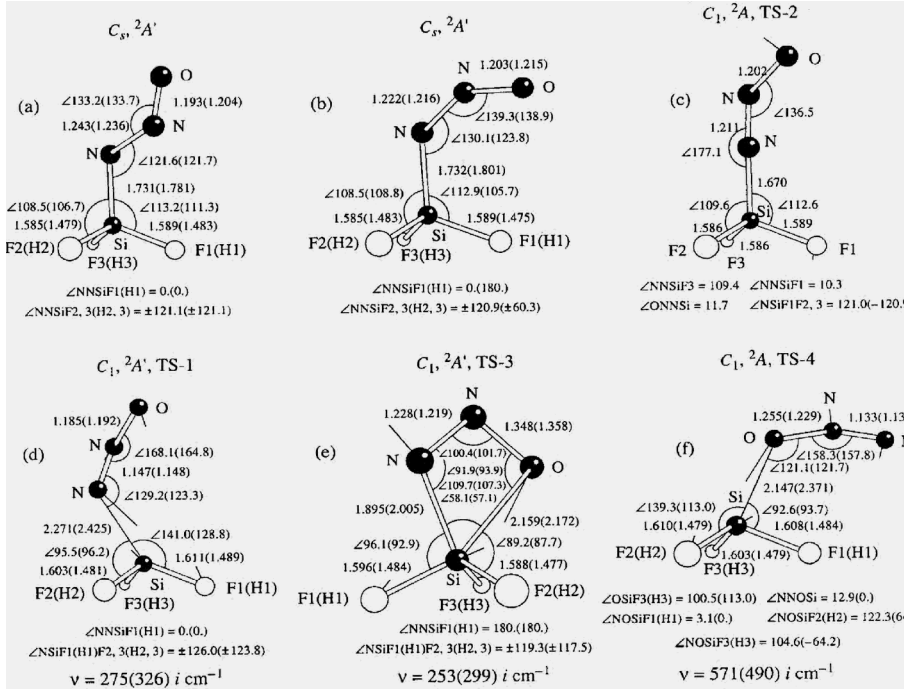


Fig. 7.1. Spectral characteristics of the $(\equiv Si\text{-}O)_3Si\text{-}N = N\text{-}O'$ radical. (a) EPR spectrum (the central component of the spectrum at 300 K is distorted by the superposition of the admixed signal and is not shown; (b) optical absorption spectrum; (c) IR spectrum (calculated form of two normal vibrations of the radical $F_3Si\text{-}N = N\text{-}O^*$ are shown).

Lam Research Ex. 1035 - Page 250
Lam Research Corp. v. Inpria Corp.
IPR2024-00033 - U.S. Patent No. 9,823,564



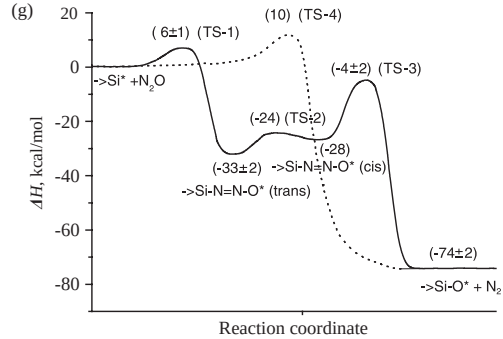


Fig. 7.2. Potential energy diagram (g) for the system (≡Si-O)$_3$Si* + N_2O and geometric characteristics of complexes and transition states (TS) (a–f) for the model systems $F_3Si^* + N_2O$ and $H_3Si^* + N_2O$ (in parentheses). For the TS, characteristic imaginary frequencies are given and atomic shifts that take place when moving along the reaction coordinate are shown. Bond lengths are in angstroms. Torsion angles are in degrees. For experimentally determined values, an error is indicated. The solid line shows the pathway for the formation of products (≡Si-O)$_3$Si-O* + N_2 via an intermediate complex. The dashed line shows the pathway for the direct oxygen abstraction from nitrous oxide.

Lam Research Ex. 1035 - Page 251
Lam Research Corp. v. Inpria Corp.
IPR2024-00033 - U.S. Patent No. 9,823,564

oxide, the O-N bond is elongated and cleaved to form an oxy radical and a nitrogen molecule as the distance between silicon and oxygen atoms becomes close to the length of a chemical bond.

The second minimum on the potential energy surface corresponds to the formation of the complex in the *cis*-configuration of atoms SiNNO (Figure 7.2b). The *trans*-configuration is noticeably stronger: the enthalpy of its formation is lower by 6.5 kcal/mol. This means that, at moderate temperatures, only the *trans*-conformation of the radical is populated. The TS for the *trans–cis* transformation of the radical is shown in Figure 7.1c (TS-2). This TS is formed via opening the valence SiNN angle. The height of the activation barrier is 8.6 kcal/mol (DFT calculation). The activation energy of the reverse reaction is 8.6−6.5 = 2.1 kcal/mol. Figure 7.2d shows the structure of the TS corresponding to the addition of nitrous oxide to the ≡Si* radical (TS-1). In the TS with C_s symmetry, the ONNSi atoms are in the *cis*-configuration. At long distances between Si and N atoms, this configuration has a lower energy than the *trans*-configuration. After passing through the maximum and as the Si and N atoms approach each other, the difference in the full energies of *cis*- and *trans*-configurations decreases and then the latter configuration becomes energetically more favorable and an energetic barrier separates these configurations. Thus, the addition of nitrous oxide results in the formation of the *cis*-configuration, which then transforms into the more stable *trans*-configuration.

In addition to the reverse reaction (the abstraction of nitrous oxide), another possible channel for the transformation of the complex is its isomerization and decomposition resulting in the formation of the oxy radical ≡Si-O* and molecular nitrogen. These products correspond to the absolute minimum on the potential energy surface of the ≡Si* + N_2O system.

Figure 7.2e shows the cyclic TS for isomerization with the decomposition of the ≡Si-N = N-O* radical resulting in the formation of ≡Si-O* + N_2 (TS-3). In the TS, the silicon atom is five-coordinated. The nitrogen atom displaces silicon and the Si-O bond is formed instead of the Si-N bond. As silicon and oxygen atoms approach each other, the N-O bond becomes longer and cleaves. The oxy radical and a nitrogen molecule are the products of this reaction. Note that this TS is possible if the ≡Si-N = N-O* radical is in the *cis*-configuration. According to the calculations, the energy of this TS is lower (8.7 kcal/mol) than the energy of the TS-1 corresponding to the abstraction of nitrous oxide molecule.

Thus, one of the possible channels to the final products of the reaction of silyl-type radicals with nitrous oxide (oxy radical and molecular nitrogen) is the formation of a metastable complex and its further isomerization and decomposition.

Lam Research Ex. 1035 - Page 252
Lam Research Corp. v. Inpria Corp.
IPR2024-00033 - U.S. Patent No. 9,823,564

The second channel for the reaction exists that leads to the same products. This is the direct abstraction of an oxygen atom from N_2O by a silyl radical. Figure 7.2f shows the structure of the transition state (TS-4) corresponding to this channel. According to the calculations, this channel is characterized by high activation energy (10.6 kcal/mol).

4.2. MUTUAL TRANSFORMATIONS OF THE $(\equiv Si\text{-}O)_2Si$: (SC) AND $(\equiv Si\text{-}O)_2Si = O$ (SG) GROUPS

The exposition of a silica sample with stabilized SG at its surface in the CO atmosphere at a temperature of ~600 K is accompanied by the following reaction:

$$>Si = O \; + \; CO \; \Rightarrow \; >Si: \; + \; OCO.$$

The amounts of the reacted CO molecules and formed CO_2 molecules were monitored by volumometry. They proved to be close to each other. The SG $\Rightarrow$ SC was monitored optically (*cf*. Sections 9.4 and 9.6) by recording changes in the band intensities of these centers at 5.65 and 5.3 eV, respectively (in this case, the sample was cooled to 300 K). The rate constants for the reactions were derived from the kinetic curves of the CO molecules consumed at various temperatures. The temperature dependence of the rate constant for this reaction is shown in Figure 7.3a, in the Arrhenius coordinates. The activation energy for the process was found to be 20.7 kcal/mol. Similar method was used to measure the rate constant for the reverse reaction:

$$>Si: \; + \; O = C = O \; \Rightarrow \; >Si = O \; + \; C = O.$$

The temperature dependence of the rate constant for this reaction is shown in Figure 7.3c. The corresponding activation energy was found to be lower and equal to 17.9 kcal/mol.

The structure of the TS for the studied SG $\Leftrightarrow$ SC mutual transformation reactions is shown in Figure 7.3b. The calculations of the activation energies for the forward and reverse reactions yield the values of 20 and 23 kcal/mol, respectively, in a satisfactory agreement with the experimentally measured activation barriers.

4.3. Si = O BOND STRENGTH IN THE $(\equiv Si\text{-}O)_2Si = O$ GROUP

The Si = O bond strength in the SG can be determined from the kinetic data and from the heat effect of the $O = C = O \Leftrightarrow O = C + O(^3P) + 127$ kcal/mol

Lam Research Ex. 1035 - Page 253
Lam Research Corp. v. Inpria Corp.
IPR2024-00033 - U.S. Patent No. 9,823,564

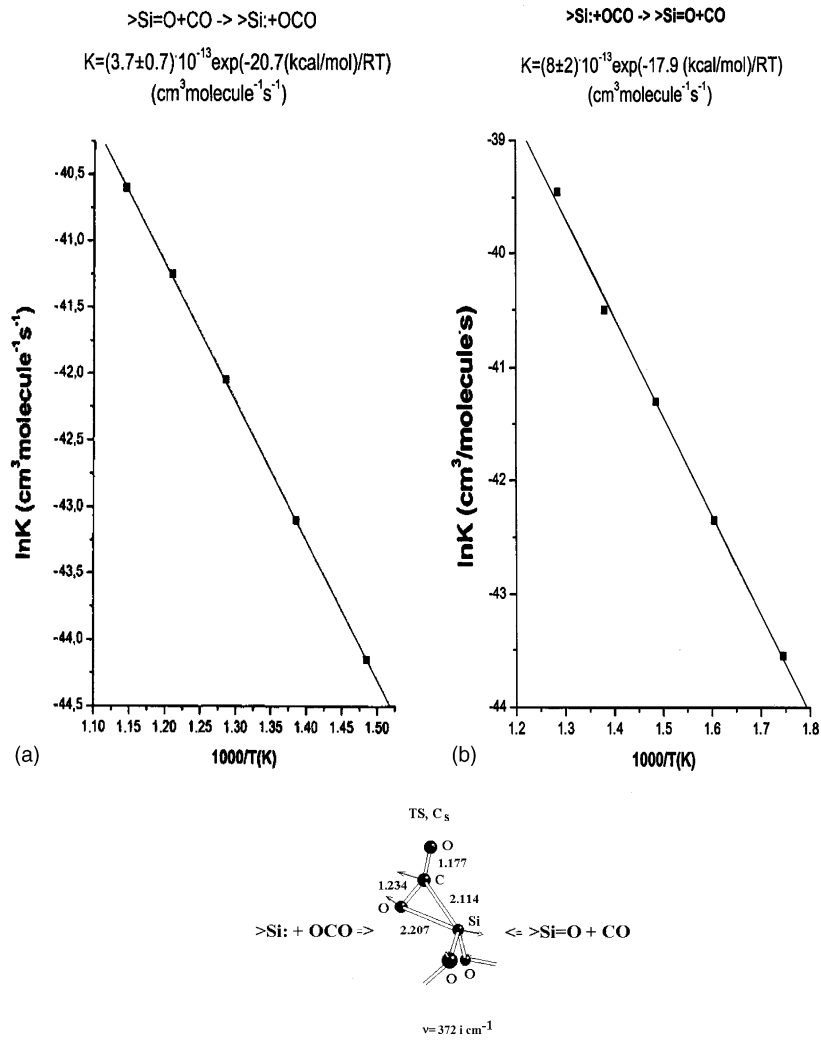


Fig. 7.3. The mutual transformation in system ($>Si=O+CO \leftrightarrow >Si:+CO_2$). (a) The temperature dependence of rate constant for direct reaction; (b) the temperature dependence of rate constant for reverse reaction; (c) the calculated structure of the TS for this reaction.

Lam Research Ex. 1035 - Page 254
Lam Research Corp. v. Inpria Corp.
IPR2024-00033 - U.S. Patent No. 9,823,564

reaction [32]:

$$>\mathrm{Si}=\mathrm{O} \Leftrightarrow >\mathrm{Si}: + \mathrm{O}(^3\mathrm{P}) + (130 \pm 2)\ \mathrm{kcal/mol}.$$

For comparison, we present below the G2(MP2)-calculated heat effects ΔH (0 K) of the Si = O bond rupture for a number of silanone molecules containing different substituents on the silicon atom. The calculations were carried out for the molecules of C_{2v} symmetry, with the spatial geometry of the starting silylene molecules corresponding to the situation where the SiOSiO atoms in the $(H_3Si\text{-}O)_2Si$: and $(F_3Si\text{-}O)_2Si$: molecules are *trans*-positioned, while the HOSiO atoms in the $(HO)_2Si$: molecule are *cis* to each other, and this symmetry is retained upon the formation of the silanone group:

$$H_2Si: + O(^3P) \Rightarrow H_2Si=O - 146\,\mathrm{kcal/mol};$$

$$(H_3Si\text{-}O)_2Si: + O(^3P) \Rightarrow (H_3Si\text{-}O)_2Si=O - 134\,\mathrm{kcal/mol};$$

$$(HO)_2Si: + O(^3P) \Rightarrow (HO)_2Si=O - 131\,\mathrm{kcal/mol};$$

$$(F_3Si\text{-}O)_2Si: + O(^3P) \Rightarrow (F_3Si\text{-}O)_2Si=O - 128\,\mathrm{kcal/mol};$$

$$F_2Si: + O(^3P) \Rightarrow F_2Si=O - 123\,\mathrm{kcal/mol}.$$

Thus, the Si = O bond strength in the silanone group increases with decreasing electronegativity of the substituents at the silicon atom. The bond strength in the surface $(\equiv Si\text{-}O)_2Si=O$ center proved to be intermediate between those obtained for the smallest-size molecular clusters $F_2Si=O$ and $(HO)_2Si=O$ (with the *trans*-arranged O, H, Si, and O atoms). The influence of the spatial position of the β-substituent (in this case, H atom) on the properties of silicon atom is discussed in detail in Section 5.

The silanone group forms a complex with the CO molecule. Optical and IR parameters *of complex* are presented in Figure 7.4 together with the computational results obtained for the $F_2Si=O$ molecule taken as a model of surface center. In the spatial structure of the complex, the C≡O molecule is situated over the silicon atom of silanone group at a distance of 0.207 nm perpendicular to its plane. The formation of such spatial group is evidence that the neighboring lattice atoms in the solid pose no obstacles to the CO molecule in its complexation with the Si_α atom of the $O=Si_\alpha(\text{-}O\text{-}Si_\beta\equiv)_2$ group. This can be the case if the lattice silicon atom (Si_α) of the silanone group is "uplifted" over the surface of the solid, while the O, Si_α, O, and Si_β atoms of the $O=Si_\alpha(\text{-}O\text{-}Si_\beta\equiv)_2$ fragment provide a possibility to form such spatial structure. Examples of such structure are given by the cyclic $O=Si<(O\text{-}Si(O\text{-}Si\equiv)_2)_n>O$ ($n = 2, 3$) structures.

Lam Research Ex. 1035 - Page 255
Lam Research Corp. v. Inpria Corp.
IPR2024-00033 - U.S. Patent No. 9,823,564

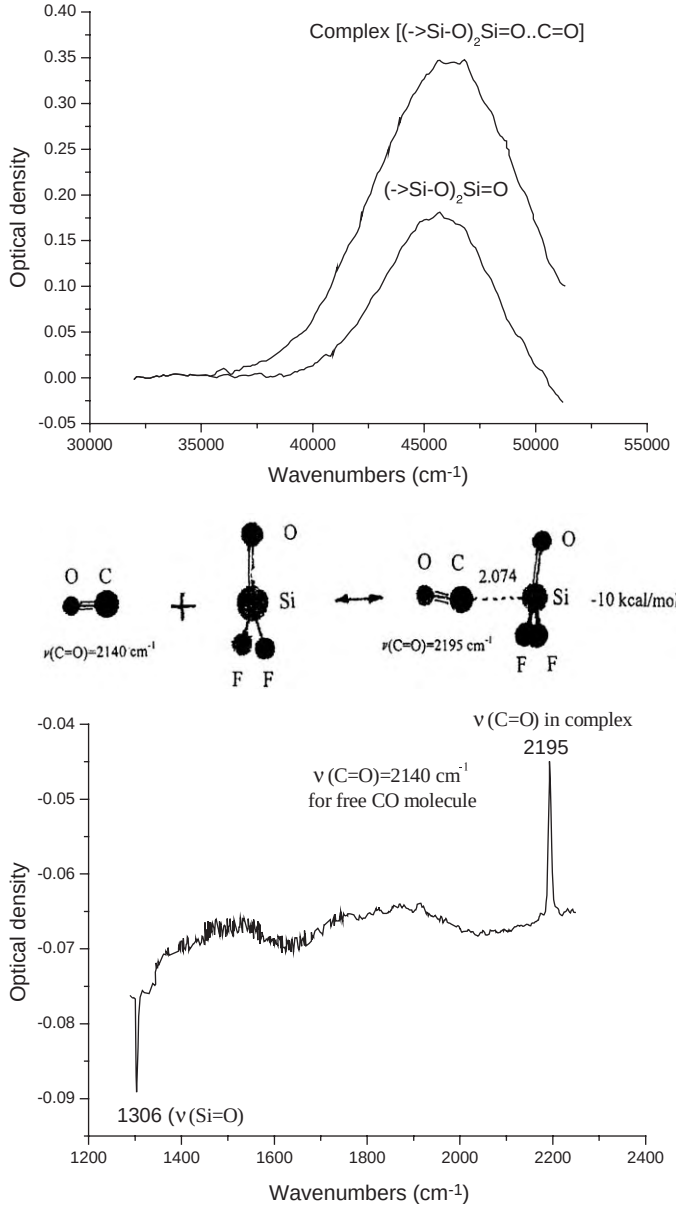


Fig. 7.4. The experimental evidence of the formation of the complexes comprising silanone group and CO molecule, obtained by the optical and IR methods. The calculated structure for model of this complex is given in the same figure.

Lam Research Ex. 1035 - Page 256
Lam Research Corp. v. Inpria Corp.
IPR2024-00033 - U.S. Patent No. 9,823,564

All this is equally related to the spatial structure of the $:Si_{\alpha}(\text{-O-}Si_{\beta}\equiv)_2$ groups that serve as building blocks for the silanone groups.

4.4. MICROCALORIMETRY OF THE PROCESSES AT THE SiO_2 AND GeO_2 SURFACES

The heat effect is one of the main characteristics of every chemical process. The heat effects of the reactions occurring at the solid surface and involving gas-phase molecules can be directly measured. To do this, one must know the amount of heat release during the reaction (microcalorimetry) and the number of absorbed gaseous molecules (volumometry). The heat effects of some reactions proceeding at the surfaces of activated silicon and germanium oxides and accompanied by the modification of the chemical structure of active sites are given in Table 7.4.

On the basis of the obtained data and the literature data on the heat effects of the reactions $N_2O \Rightarrow N_2 + O(^3P) + 40$ kcal/mol, $O_2(^3\sum) \Rightarrow 2O(^3P) + 119$ kcal/mol, and $O=C=O \Rightarrow C\equiv O + O(^3P) + 129$ kcal/mol [38], heat effects were calculated for the other processes, and some bond strengths were determined for the resulting compounds (Table 7.4). In particular, it was shown that the Ge-O bond strength in the compounds of the same type is by 30 kcal/mol lower than for the Si-O bond.

Table 7.4. The heat effects of reactions of point defects on SiO_2 and GeO_2 surface (kcal/mol); the results of calorimetric measurements [35, 36]

Reaction	The heat effect ($\pm 5\%$)
1. $\equiv Si^{\bullet} + O_2 \Rightarrow \equiv Si\text{-}O\text{-}O^{\bullet}$	−60*
2. $\equiv Si^{\bullet} + CO_2 \Rightarrow \equiv Si\text{-}O\text{-}C^{\bullet}=O$	−18*
3. $\equiv Si^{\bullet} + N_2O \Rightarrow \equiv Si\text{-}O^{\bullet} + N_2(g)$	−70*
4. $\equiv Si\text{-}O^{\bullet} + CO \Rightarrow \equiv Si^{\bullet} + CO_2(g)$	−17*
5. $>Si<O_2 + CO \Rightarrow >Si<O_2>C=O$	−90*
6. $>Si=O + N_2O \Rightarrow >Si<O_2 + N_2(g)$	−25*
7. $>Si=O + CO_2 \Rightarrow >Si<O_2>C=O$	−36*
8. $\equiv Ge^{\bullet} + O_2 \Rightarrow \equiv Ge\text{-}O\text{-}O^{\bullet}$	−30*
9. $\equiv Ge\text{-}O^{\bullet} + CO \Rightarrow \equiv Ge^{\bullet} + CO_2(g)$	−44
	Calculated heat effects (using Hess law)
10. $\equiv Si\text{-}O\text{-}O^{\bullet} \Rightarrow \equiv Si\text{-}O^{\bullet} + O(^3P)$	67
11. $\equiv Si\text{-}O^{\bullet} \Rightarrow \equiv Si^{\bullet} + O(^3P)$	112
12. $>Si=O + O(^3P) \Rightarrow >Si<O_2$	–65
13. $\equiv Ge\text{-}O^{\bullet} \Rightarrow \equiv Ge^{\bullet} + O(^3P)$	86
14. $\equiv Ge\text{-}O\text{-}O^{\bullet} \Rightarrow \equiv Ge\text{-}O^{\bullet} + O(^3P)$	67

Lam Research Ex. 1035 - Page 257
Lam Research Corp. v. Inpria Corp.
IPR2024-00033 - U.S. Patent No. 9,823,564

5. Interrelation Between the EPR Parameters of the Silicon-Centered Paramagnetic Centers and Their Spatial Structure: Results of Quantum-Chemical Calculations

The information on the interrelation between the spectral, geometric, and electronic structures of the majority of defects studied in quartz glass is lacking. A considerable amount of experimental data on the paramagnetic defects at the silica surface and silica bulk has been obtained by the EPR technique. Due to the progress of quantum-chemical methods, the possibility arises of revealing this interrelation through the comparison of the values measured experimentally and calculated theoretically for different models of the center. In recent years, the DFT method has found an increasing application in quantum chemistry. The DFT calculations satisfactorily reproduce the equilibrium geometry of molecules and radicals and proved to be efficient in the calculations of their vibrational spectra and EPR parameters. The deviations of the calculated (without using any fitting parameters) HFS constants from their experimental values do not exceed 10% for the radicals of different chemical nature [37].

The use of the smallest-size clusters ($H_3Si^{\bullet}$, $F_3Si^{\bullet}$, $(HO)_3Si^{\bullet}$) and larger clusters ($(H_3Si_{\beta}\text{-}O)_3Si_{\alpha}^{\bullet}$, $(F_3Si_{\beta}\text{-}O)_3Si_{\alpha}^{\bullet}$, and $(HO)_3Si_{\beta}\text{-}O)_3Si_{\alpha}^{\bullet}$) as molecular models of PCs made it possible to gain information on the EPR parameters of the silicon atoms Si_{α} and Si_{β} entering into the defect structure (at present, only these quantities can be measured experimentally). The purpose of the calculations was to reveal the interrelation between the EPR parameters and spatial structure of the PCs. The following geometric parameters were chosen as the characteristics of the defect spatial structure:

1. the degree of "pyramidality" of the center, i.e., the angle $\rho = \angle XSi_{\alpha}F$ (Figure 7.5); it characterizes the displacement of the Si atom from the plane formed by three substituting atoms (hereafter, the symbol X stands for the pseudo atom situated on the symmetry axis of the radical and is used to specify the geometry of the latter);
2. valence (Si_{β}-O-Si_{α}) and dihedral (Si_{β}-O-Si_{α}-X) angles determining the position of the Si_{β} substituent in the coordination sphere of the defect. The experimental data for some silicon-centered PCs are presented in Section 6.

Silicon-centered free radicals have a pyramidal form. Figure 7.5 shows the results of calculations of the dependence of the $F_3Si^{\bullet}$ radical (C_{3v} symmetry) total energy and HFI constant $a_{iso}(^{29}Si)$ on the "degree of its pyramidality", characterized by the value of the ρ angle.

Lam Research Ex. 1035 - Page 258
Lam Research Corp. v. Inpria Corp.
IPR2024-00033 - U.S. Patent No. 9,823,564

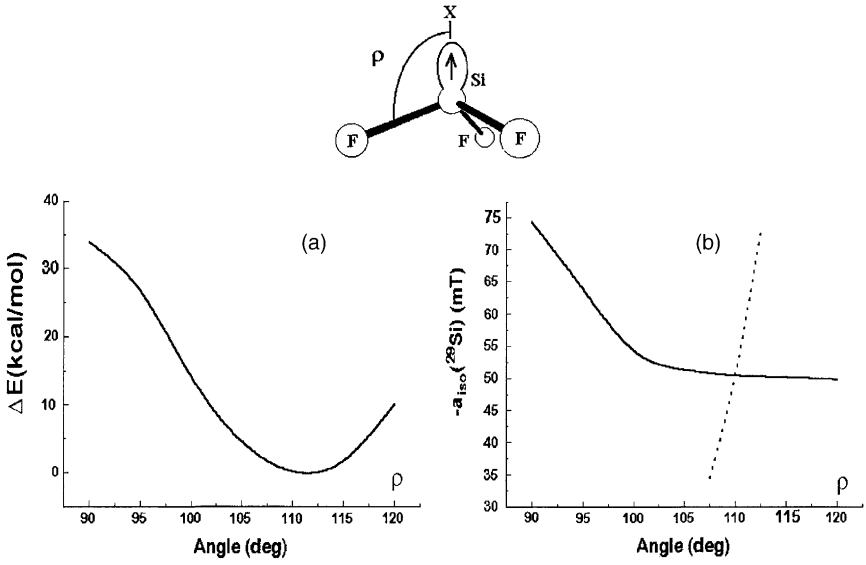


Fig. 7.5. Calculated dependencies of (a) total energy and (b) a_{iso} (^{29}Si) (solid line for the $F_3Si^{\bullet}$ radical (C_{3v} symmetry) on the ρ values (the dashed line represents the dependence described in the text).

The calculation did not show the expected decrease of the value $a_{iso}(^{29}Si)$ as the radical structure approaches the flat form [38,39]. Moreover it turned out that for the flat geometry of this radical the most favorable energetic state is the one in which the unpaired electron is localized not on 3p-AO of Si atom, but on its 3s-AO (when $a_{iso}(^{29}Si) = -743$ G). At deviations of ρ by $\pm 5^{\circ}$ from the equilibrium value the magnitude of $a_{iso}(^{29}Si)$ changed very little. Similar results were obtained also for the radical $(F_3^{29}Si_{\beta}\text{-}O)_3^{29}Si_{\alpha}^{\bullet}$ (the calculations were performed for conformation of the radical with spatial C_{3v} symmetry, $\angle SiOSi = 180^{\circ}$). At small distortions of the radical equilibrium geometry the value $d(a_{iso}(^{29}Si_{\alpha}))/d\rho$ was equal to -1.8 G/degree. Further we will discuss the consequences of these results.

In Ref. [40], tight-binding calculations were carried out to demonstrate that the isotropic constant of HFI $a_{iso}(^{29}Si_{\beta})$ in the $*Si_{\alpha}(\text{-}O\text{-}^{29}Si_{\beta}\equiv)(B)_2$ radical depends on the spatial position of the $^{29}Si_{\beta}$ atom. Similar results were obtained with the more complicated computational schemes (DFT in the 6-311G** basis) [41]. Moreover, it was shown that a change in the spatial position of the β atom is accompanied by the change in the value of the hfs constant $a_{iso}(^{29}Si_{\alpha})$ [41].

The influence of the configuration of β-substituents on EPR parameters of the silyl radicals may already be seen on the example of the $(HO)_3Si^{\bullet}$ radical

Lam Research Ex. 1035 - Page 259
Lam Research Corp. v. Inpria Corp.
IPR2024-00033 - U.S. Patent No. 9,823,564

Table 7.5. The influence of the OH groups configuration on the $(HO)_3Si^{\bullet}$ radical and $(HO)_3$ Si-H molecule properties (the results of DFT calculations, see text for details)[a]

$\phi(^\circ)$	0	90	180
Symmetry	C_{3v}	C_3	C_{3v}
$a_{iso}(^{29}Si)$ (mT)	−26.3	−37.0	−46.7
$a_{iso}(^1H)$ (mT)	−0.10	−0.10	1.95
ν(Si-H) (cm^{-1})	2198	2269	2372
ΔH_0(Si-H) (kcal/mol)	93.2	93.9	99.7

[a]The spatial structure of $(HO)_3Si$ group (C_{3v} or C_3 symmetry) was characterized by the dihedral angle ϕ ($\phi = \angle$XSiOH or $\phi = \angle$HSiOH). For *cis*(*trans*)-configuration of X(H), Si, O, and H atoms ϕ is equal to 0°(180°).

(see also Refs. [41,42]). Transition of OH groups from *cis*- to *trans*-configuration in the radical results in a substantial change in hfs's constants $a_{iso}(^{29}Si)$ and $a_{iso}(^1H)$ (Table 7.5).

A comparison of the $a_{iso}(^{29}Si_\alpha)$ values for the $^{\bullet}Si(OH)_3$ (−470 G (calculation), *trans*-configurated H atoms), $^{\bullet}SiF_3$ (−502 G (calculation) and −500 G (experiment, [43]), and $^{\bullet}Si(O\text{-}Si\equiv)_3$ (−480 G (experiment)) radicals indicates that the order of their influence on the properties of the silicon atom is the following: -O-H(*trans*) < -O-Si≡<-F. This also follows from the values of the Si = O bond strength calculated for the silanone molecules with different substituents (Section 4.3).

Changes of the radical geometry affect their "chemical" properties. Thus, the strength of the Si-H bond (enthalpy (ΔH_0(Si-H)) of process: $(HO)_3Si^{\bullet} + H \Rightarrow (HO)_3Si\text{-}H$) formed upon addition of an H atom to the radical, as well as the frequency (ν(Si-H)) of Si-H valence vibration for $(HO)_3Si$-H molecule depend on the spatial structure of the radical and the product (see Table 7.5). The larger is the $a_{iso}(^{29}Si_\alpha)$ value in the radical, the stronger this bond becomes (the stretching vibration frequency also increases synchronously).

It may be assumed that the reactivity of silyl-type radicals in various chemical processes, which is controlled by the values of the corresponding activation barriers, may also be different for radicals having different spatial structure. According to the semiempirical Polani–Semenov rule the activation energy of single-type chemical reactions decreases when their enthalpies increase. Therefore the reaction $(HO)_3\ Si^{\bullet} + H_2 \Rightarrow (HO)_3Si\text{-}H + H$ will proceed with a higher rate with the participation of those radicals, which are characterized by a larger value of EPR constant $a_{iso}(^{29}Si_\alpha)$. This example clearly illustrates the nature of inhomogeneous broadening effects and differences in reactivity of defects in disordered solids.

Lam Research Ex. 1035 - Page 260
Lam Research Corp. v. Inpria Corp.
IPR2024-00033 - U.S. Patent No. 9,823,564

The XSiOSi dihedral angle value dependence of the HFI constants $a_{iso}(^{29}Si_{\alpha})$ and $a_{iso}(^{29}Si_{\beta})$ for the $(F_3^{29}Si_{\beta}\text{-}O)_3^{29}Si_{\alpha}^{\bullet}$ radical is given in Figure 7.6a and b. The disposition of all three substitutes in the radical was changed in synchronism (the radical retained C_3 symmetry) and the magnitude of the valence angle $Si_{\alpha}OSi_{\beta}$ was fixed.

Thus, the variations in spatial arrangement of β-substituents in radicals of silyl type, for example, of H atom or SiF_3 group in the $(HO)_3Si^{\bullet}$ or $(F_3Si_{\beta}\text{-}O\text{-})_3Si_{\alpha}^{\bullet}$ paramagnetic centers, is accompanied by noticeable changes

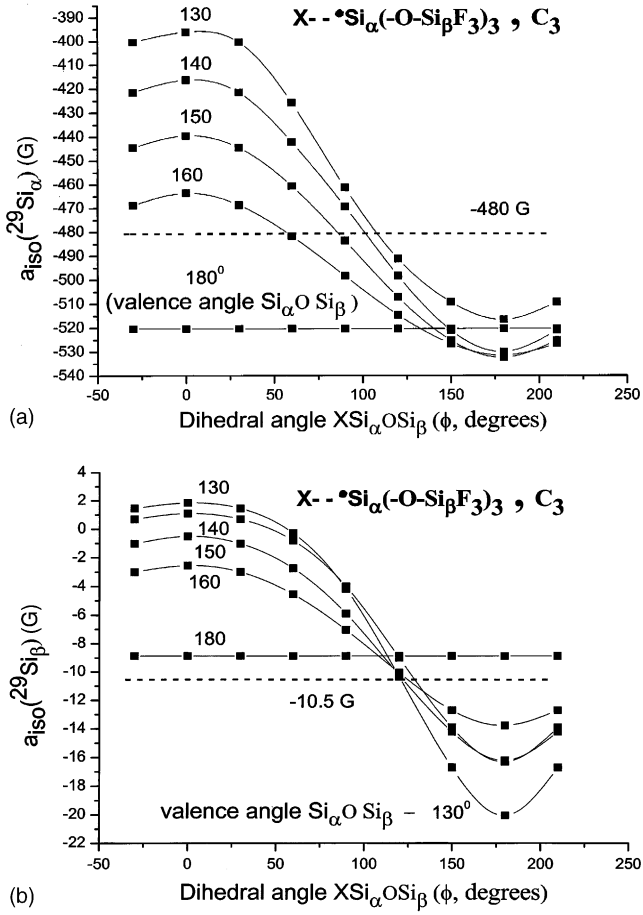


Fig. 7.6. Calculated dependencies (DFT) of the $a_{iso}(^{29}Si_{\alpha})$ (a) and $a_{iso}(^{29}Si_{\beta})$ (b) for $(F_3^{29}Si_{\beta}\text{-}O\text{-})_3^{28}Si_{\alpha}^{\bullet}$ radical on the $XSi_{\alpha}OSi_{\beta}$ dihedral angle θ (see text for details) at the different $Si_{\alpha}OSi_{\beta}$ bond angles (130–180°).

Lam Research Ex. 1035 - Page 261
Lam Research Corp. v. Inpria Corp.
IPR2024-00033 - U.S. Patent No. 9,823,564

Table 7.6. Computed (DFT) isotropic EPR constants $a_{iso}(^{29}Si_{\alpha})$ and $a_{iso}(^{29}Si_{\beta})$ (mT) for $(Y_3Si_{\beta}\text{-}O)_3Si^{\bullet}_{\alpha}$ radicals (Y = H, OH, F)

Y	H	OH B(*cis*)	OH C(*trans*)	F
Symmetry group	C_{3v}	C_3	C_3	C_{3v}
$a_{iso}(^{29}Si_{\alpha})$	−45.25	−44.0	−47.25	−50.6
$a_{iso}(^{29}Si_{\beta})$	−0.39	−0.40	−0.81	−0.87

in constants of HFI between an unpaired electron and α- and β-atoms of ^{29}Si. The maximum values for these constants correspond to the radical configuration in which a β-substituent is out of region with the maximum spin density and the value for dihedral angle X-Si_{α}-O-Si_{β} approach to 180° – "back bond" O-Si_{β} [40].

As calculations show, the values for HFI constants, especially with the Si β-atom noticeably depend on the spatial arrangement of the substituents in the next coordination sphere of PC. Thus, in going from *trans*- to *cis*-configuration of OH groups in the $((HO)_3Si_{\beta}\text{-}O)_3Si_{\alpha}^{\bullet}$ radical, the $a_{iso}(^{29}Si_{\beta})$ constant decreases by 1.7 times (see Table 7.6). The similar although weaker effect is seen for constant $a_{iso}(^{29}Si_{\alpha})$.

Now we will dwell on the problem of influence of chemical nature of substituents on the EPR spectra parameters of the silyl-type radicals. Table 7.6 illustrates the effect of chemical nature of substituents in radicals $^{29}Si_{\alpha}^{\bullet}(\text{-O-}(^{29}Si_{\beta})Y_3)_3$ ($\angle Si_{\alpha}OSi_{\beta} = 180°$, Y = H, F, OH, the *cis*- and *trans*-configurations of OH groups have been considered) on constants $a_{iso}(^{29}Si_{\alpha})$ and $a_{iso}(^{29}Si_{\beta})$. Their structures are presented in Figure 7.7.

The valence angle $\angle Si_{\alpha}OSi_{\beta} = \varphi$ value dependence of the quantities of $a_{iso}(^{29}Si_{\alpha})$ and $a_{iso}(^{29}Si_{\beta})$ for the $^{29}Si_{\alpha}^{\bullet}(\text{-O-}^{29}Si_{\beta}Y_3)_3$ (Y = H, F, OH (*trans*-configurations of OH groups)) radicals possessing the point symmetry C_{3v} are given in Figure 7.8a and b.

Thus, the variations of spatial arrangement of β-substituents, for example, of H atom or $Si_{\beta}Y_3$ group in the radical, influence its spectral parameters in the way similar to the changes in the chemical nature of the substituents at the Si atom. In particular, a hydroxyl group in *trans*-configuration of X-Si-O-H approaches its effect on the Si atom to F atom and in the *cis*-configuration, to H atom.

The results of calculations presented indicate that one has to pay special attention to the spatial structure choosing molecular models for the silica defects. A broad distribution over possible values for the valence (Si-O-Si) and dihedral (Si-O-Si-O) angles is supposed for silica [44]. According to the above-presented results of calculations, changes induced by the variations in spatial structure of radical $(\equiv Si_{\beta}\text{-}O)_3Si_{\alpha}^{\bullet}$ may be expected to be 100–120 G for the $a_{iso}(^{29}Si_{\alpha})$ value and 0–15 G for the $a_{iso}(^{29}Si_{\beta})$ value.

Lam Research Ex. 1035 - Page 262
Lam Research Corp. v. Inpria Corp.
IPR2024-00033 - U.S. Patent No. 9,823,564

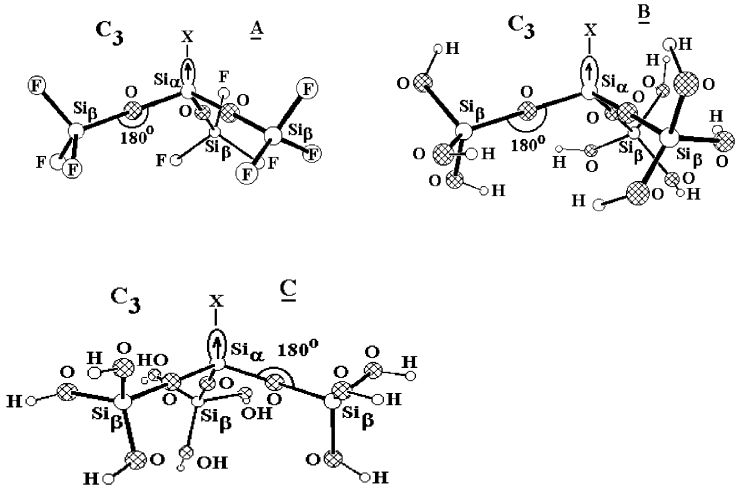


Fig. 7.7. Spatial geometries (DFT) of the radicals which were used for studying the influence of chemical nature of substituents at β-Si atoms on the radical EPR parameters (see Table 7.5).

In conclusion of this section we note that according to the results of calculations the changes of valence and dihedral angles are not associated with large changes of the corresponding radical formation enthalpy. Thus, in the radical $(F_3^{29}Si_\beta\text{-}O)_3^{29}Si_\alpha^\bullet$ opening of the Si_α-O-Si_β angle from 150 to 180° resulted in increase of its energy only by 0.6 kcal/mol (0.03 eV), and the rotation of β-Si atom through 180° (change of *cis*-configuration into *trans*-configuration) demands energy expenditure of only ~0.5 kcal/mol. The total energy changes of the $(F_3Si_\beta\text{-}O)_3Si_\alpha^\bullet$ radical at synchronous variations of the dihedral angles (constrained valence bond angle was equal to 145°) of the three substituents were also found to be small and did not exceed 1.5 kcal/mol. Only in *trans*-configuration of this radical (dihedral angle was equal to 180°) drawing together of three SiF_3 groups led to an increase of the system energy by ~4 kcal/mol. Thus, the results of quantum-chemical calculations are in agreement with the well-known lability of the silica network. Due to the "softness" of the force constants which control the values of valence SiOSi and dihedral XSiOSi angles, the spatial structure of a defect of the type E'-center in silica can easily "adjust" itself to the disposition of β-Si atom entering into the coordination sphere. The disposition of the latter is the main factor, which controls the defect geometry and consequently its spectral properties.

These calculations show that changes in the chemical nature of the substituents and in the spatial structure of the coordination sphere of the Si_β atom (turn of the OH groups) both have an appreciable effect on the EPR

Lam Research Ex. 1035 - Page 263
Lam Research Corp. v. Inpria Corp.
IPR2024-00033 - U.S. Patent No. 9,823,564

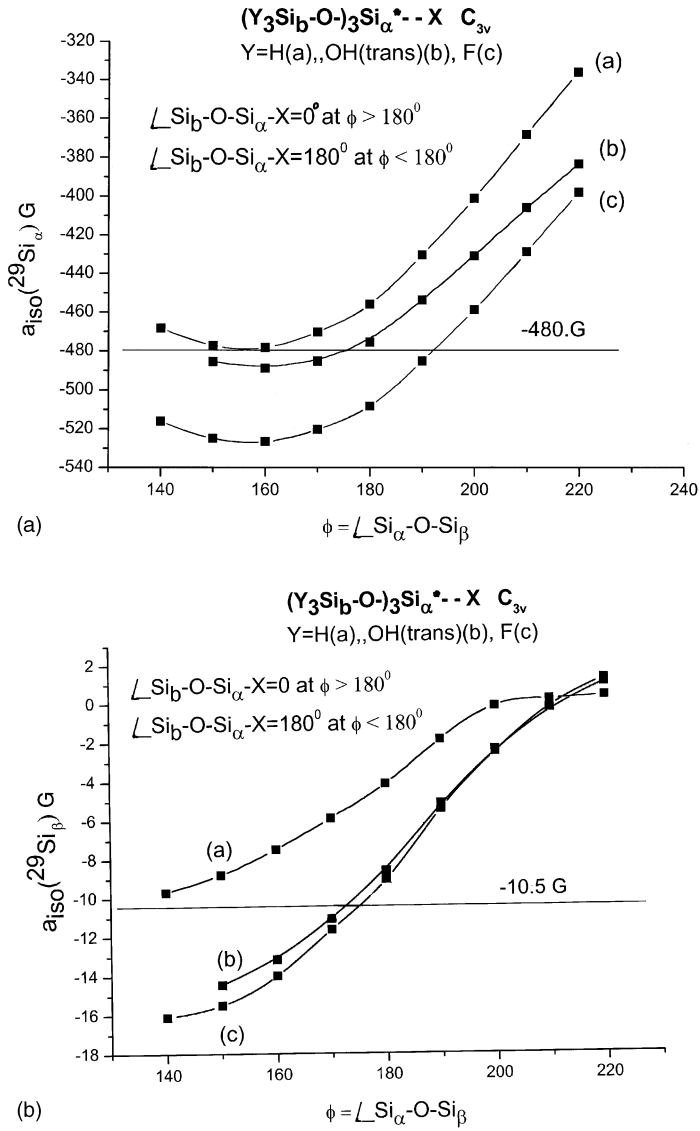


Fig. 7.8. Calculated dependencies (DFT) of the $a_{iso}(^{29}Si_{\alpha})$ (a) and $a_{iso}(^{29}Si_{\beta})$ (b) for $(Y_3^{29}Si_{\beta}\text{-O-})_3^{28}Si_{\alpha}^{\bullet}$ radical (Y = F, H, OH, hydroxyl groups are in *trans*-configuration) on the $Si_{\alpha}OSi_{\beta}$ bond angles. The spatial structure of radicals possessed the point symmetry group C_{3v}.

Lam Research Ex. 1035 - Page 264
Lam Research Corp. v. Inpria Corp.
IPR2024-00033 - U.S. Patent No. 9,823,564

parameters of the PCs, and this is also true for the characteristics of not only the Si_β atom but also of the $^{29}Si_\alpha$ atom separated from it by two chemical bonds. This can only be the case if the intermediate oxygen atom is a good "conductor" for this influence.

Such a behavior is evidence for the lability of the electronic structure of the silicon atom, because it undergoes rearrangement under the action of both chemical and geometric factors. These factors are comparable in their effect: the substitution of the F atom for H brings about almost the same changes in the characteristics of the silicon atom as does the *cis–trans* conversion of the substituent (OH group).

6. Silicon-Centered Paramagnetic Centers (PCs) in SiO_2

Paramagnetic centers were detected by an EPR method at the surface of activated (MSi and RSi) silica [14,45]. Later on, the set of surface PCs with an unpaired electron on the silicon atom was appreciably extended. The method was developed for synthesizing PCs of the type $(\equiv Si_\beta\text{-}O)_2Si_\alpha^\bullet\text{-}r$ on a silica surface, where $r = H$ (D), OH (OD), NH_2 (ND_2) and other low-molecular groups (see Section 6.2). Moreover, in connection with the development of quantum-chemical computing methods, the opportunity appeared for establishing links between experimentally determined radiospectroscopic characteristics of PCs and their electronic and spatial structures. This section presents the results of experimental investigations into radiospectroscopic characteristics of Silicon-centered PCs by the EPR method. Using these data and results of quantum-chemical calculations the analysis of their electronic and geometrical structures is performed.

6.1. PC $(\equiv Si_\beta\text{-}O)_3Si_\alpha^\bullet$ on the Surface and in the Bulk of Silica

The structure of the PCs at the surface of activated silica (MSi) was determined in Ref. [9], where it was shown that they contain three-coordinated silicon atom $\equiv Si_\alpha^\bullet$. This was proved by the observation of the EPR doublet caused by the presence of the ^{29}Si isotope ($I = 1/2$, natural abundance 4.7%) in the sample. The hfs constants from the silicon $^{29}Si_\beta$ atoms entering into the coordination sphere of the defect were determined in further investigations. The EPR spectra of the $(\equiv{}^{29}Si_\beta\text{-}O\text{-})_3^{28}Si_\alpha^\bullet$ radicals stabilized on the surface of silica samples with various concentration of ^{29}Si ($I = 1/2$) are shown on Figure 7.9. The observable hfs is caused by nearly equal interaction of the unpaired electron with the $^{29}Si_\beta$ nuclei. The other fragment of the EPR spectrum of the surface $(\equiv{}^{28}Si_\beta\text{-}O\text{-})_3^{29}Si_\alpha^\bullet$ radical is shown in Figure 7.10

Lam Research Ex. 1035 - Page 265
Lam Research Corp. v. Inpria Corp.
IPR2024-00033 - U.S. Patent No. 9,823,564

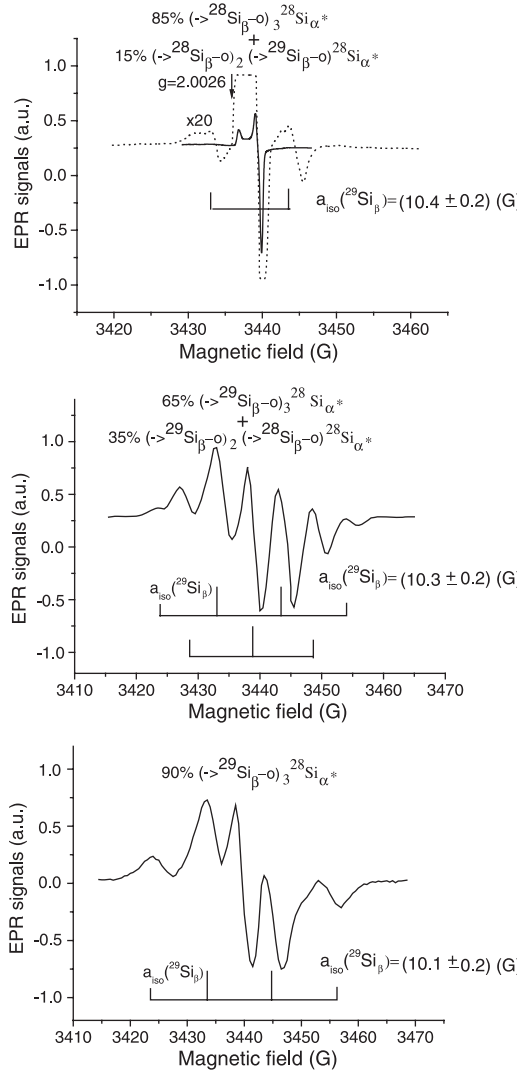


Fig. 7.9. EPR spectra of the surface $(\equiv {}^{29}Si_{\beta}\text{-O-})_3^{28}Si_{\alpha}^{\bullet}$ radicals in the samples of silica with various concentration of ^{29}Si ($I = 1/2$).

(dotted line). The HFI of the unpaired electron with the central silicon atom is characterized by the axially symmetric tensor. These facts, together with the axial symmetry of the g-tensor of a surface center, are testimony that its spatial structure has the local symmetry no less than C_3. The radiospectroscopic parameters of this radical are presented in Table 7.7.

Lam Research Ex. 1035 - Page 266
Lam Research Corp. v. Inpria Corp.
IPR2024-00033 - U.S. Patent No. 9,823,564

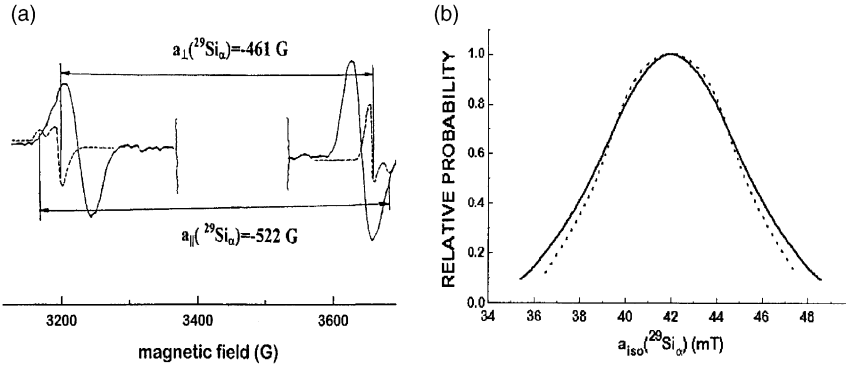


Fig. 7.10. EPR spectra (a) of the $(\equiv^{28}Si\text{-}O\text{-})_3^{29}Si^{\bullet}$ radicals in the bulk (solid line [38]) and on the surface (dashed line) of silica and distribution function (b) for $a_{iso}(^{29}Si_{\alpha})$ values for bulk radicals (solid line – experiment [38], dashed line – calculations, see text for details).

Table 7.7. EPR parameters (mT) of Si- and Ge-centered PC in SiO_2 and GeO_2 [21, 50, 75]

Structure of radical	g_{zz}	g_{xx}	g_{yy}	$a_{iso}(^{29}Si_{\alpha})^a$	b^a	$a_{iso}(^{29}Si_{\beta})$
1. $(\equiv^{29}Si_{\beta}\text{-}O\text{-})_3^{29}Si_{\alpha}^{\bullet}$ (α-quartz)	2.00176	2.00049	2.00029	−41.1	−2.1	0.85; 0.80; 0.08
2. $(\equiv^{29}Si_{\beta}\text{-}O\text{-})_3^{29}Si_{\alpha}^{\bullet}$	2.0018	2.0003	2.0003	−48.1	−2.06	1.05; 1.05; 1.05
3. $(\equiv Ge_{\beta}\text{-}O\text{-})_3^{73}Ge_{\alpha}^{\bullet}$	2.0019	1.9952	1.9952	−24		
4. $(\equiv^{29}Si_{\beta}\text{-}O\text{-})_2^{29}Si_{\alpha}^{\bullet}\text{-}OD(H)$	2.0018	2.0007	2.0002	−41.3	−1.87	0.63; 0.63
5. $(\equiv^{29}Si_{\beta}\text{-}O\text{-})_2^{29}Si_{\alpha}^{\bullet}\text{-}NH_2(ND_2)$	2.0018	2.0011	2.0002	−37.7	−1.86	
6. $(\equiv^{29}Si_{\beta}\text{-}O\text{-})_2^{29}Si_{\alpha}^{\bullet}\text{-}D(H)$	2.0021	2.0017	2.0005	−31.2	−2.09	0.27; 0.27
7. $(\equiv Ge_{\beta}\text{-}O\text{-})_2Ge_{\alpha}^{\bullet}\text{-}H$	2.0017	1.9985	1.9910			
8. $(\equiv^{29}Si_{\beta}\text{-}O\text{-})_2^{29}Si_{\alpha}^{\bullet}\text{-}CH_3$	2.0021	2.0016	2.0005	−30.3	−2.14	
9. $(\equiv Ge_{\beta}\text{-}O\text{-})_2Ge_{\alpha}^{\bullet}\text{-}CH_3$	2.0017	1.9993	1.9910			

[a]The values $a_{iso}(^{29}Si_{\alpha})$ and b are isotropic and anisotropic components of the axially symmetric HFI tensor for the $^{29}Si_{\alpha}$ nucleus. Error in determination of the values of radiospectroscopic parameters for radicals 2, 4, 6 is equal to ±0.0001 for g-tensor components, ±0.06 mT for the $a_{iso}(^{29}Si_{\alpha})$, and b values and ±0.03 mT for the $a_{iso}(^{29}Si_{\beta})$ values. The components of the HFI tensor for D(H) nuclei are equal to: for radical 4–$|a_1| = 0.05(0.34), |a_2| = 0.05(0.32)$, and $|a_3| = 0(0)$ mT ($T = 77$ K), and for radical 6–$|a_1| = 1.25(8.14), |a_2| = 1.205(7.58)$, and $|a_3| = 1.265(8.24)$ mT. Item 6 in the table presents the radiospectroscopic characteristics of the centers of 1′ type (see Section 10 for details).

The computational results presented in Figures 7.6 and 7.8 can be used to visualize the spatial structure of the $(\equiv Si\text{-}O)_3Si^{\bullet}$ radical at the silica surface. The best agreement between the experimental values −480 G ($^{29}Si_{\alpha}$) and −10.5 G ($^{29}Si_{\beta}$) for surface PC and those calculated for the model structures has been obtained for the $^{29}Si_{\alpha}^{\bullet}(\text{-}O\text{-}^{29}Si_{\beta}(OH)_3)_3$ radical possessing the point symmetry C_{3v} with *trans*-configurations of OH groups and the valence angle $\angle Si_{\alpha}OSi_{\beta}$ = (170–180°) and dihedral angle $\angle XSi_{\alpha}OSi_{\beta} = 180°$ (see

Lam Research Ex. 1035 - Page 267
Lam Research Corp. v. Inpria Corp.
IPR2024-00033 - U.S. Patent No. 9,823,564

Figure 7.8). It means that the point symmetry of surface ($\equiv{}^{29}Si_{\beta}\text{-}O)_3Si_{\alpha}^{\bullet}$ PC is closed to C_{3v} group and symmetry axis must be to orient along the normal to the surface. This structure is shown on Figure 7.7c. The spatial arrangement of the substituents ($\equiv Si_{\beta}$) in the coordination sphere of the silicon atom Si_{α} resembles the structure of the silicon coordination sphere in the open modifications of crystalline quartz (tridimite and cristobalite) [46].

All three HFI constants from the Si_{β} atoms in the $(\equiv{}^{29}Si_{\beta}\text{-}O)_3Si_{\alpha}^{\bullet}$ paramagnetic center were measured for crystalline α-quartz (Table 7.7). Using these data, the authors of Ref. [40] have determined the corresponding dihedral angles φ: 150, 147, and 27°, respectively.

Therefore, the spatial structure of the coordination sphere of a paramagnetic center (position and orientation of the nearest-lying Si_{β} atoms) serves as a decisive factor determine the spectral (in this case, EPR) and hence, physico-chemical properties of the defect. The scatter in these characteristics brings about inhomogeneous broadening effects. We illustrate the possible scale of these effects by the example of PCs $(\equiv Si_{\beta}\text{-}O)_3Si_{\alpha}^{\bullet}$ (E'_{γ} centers) [47] stabilized in the bulk of γ-irradiated amorphous SiO_2.

The solid line in Figure 7.10a shows the part of ESR spectra of bulk radicals $(\equiv Si_{\beta}\text{-}O)_3^{29}Si_{\alpha}^{\bullet}$ taken from Ref. [38]. Let us start with the differences in ESR spectrum of surface and bulk centers. At the first glance one could see that inhomogeneous broadening determine the shape of ESR spectrum which is much more pronounced in the case of bulk centers. These experimental findings were quantitatively analyzed in Ref. [38]. Figure 7.10b shows a plot of the distribution function for a number of radicals with given value of isotropic HFI constant.

In Ref. [38] the inhomogeneous broadening of ESR spectra of E'_{γ}-centers was ascribed to differences in degree of pyramidalization of three-coordinated silicon atoms in different radical groups. To calculate a magnitude of this effect the authors assumed that the value of $a_{iso}({}^{29}Si_{\alpha})$ is determined by its deviation from planarity (degree of pyramidalization) through the same relation that was used earlier for the PC of first row elements [48]. The dotted line in Figure 7.5b shows $a_{iso}({}^{29}Si)$ as a function of angle ρ in the $F_3Si^{\bullet}$ radical calculated using this relation. This curve conspicuously disagrees with the results of quantum-chemical calculations. In our opinion it is caused by the failure of the basic assumption of model [48] about the relationship between the radical center configuration and character of the orbital bearing the unpaired electron in case of Si atom.

Thus inhomogeneous broadening of ESR spectra of bulk radicals is caused by different factors. Based on the results of quantum-chemical calculations the observed differences in EPR constants of various groups of radicals could be related to variations in their spatial geometry, namely to different positions of β-Si atoms. We have calculated the distribution

Lam Research Ex. 1035 - Page 268
Lam Research Corp. v. Inpria Corp.
IPR2024-00033 - U.S. Patent No. 9,823,564

function of a number of E'_γ-centers having given value of $a_{iso}(^{29}Si_\alpha)$ using the following assumptions: (1) three dihedral angles, determining orientation of β-substituents in E'_γ-center are independent random values uniformly distributed in the range of 0–180°. (2) Si_α-O-$Si_{\beta(1,2,3)}$ valence angles have equal and constant values. (3) The $a_{iso}(^{29}Si_\alpha)$ value depends on the contributions from three β-substituents, each one determined by the corresponding dihedral angle ($0 \le \phi \le 180°$):

$$-(140 - 20\mathrm{Cos}(\phi))\ (\mathrm{G}).$$

The function used corresponds to the results of calculations (see Figures 7.6 and 7.8) with the coefficients taken from the distribution function describing the inhomogeneous broadening of ESR spectra of PC [38] (Figure 7.10b, solid line). Dotted line shows results of calculations. We see that the experimental and calculated values are in a good agreement. One can also notice that the magnitude of the inhomogeneous broadening observed experimentally (~100 G) approximately fits the differences in HFI constants $a_{iso}(^{29}Si_\alpha)$ obtained from quantum-chemical calculations (see Figures 7.6 and 7.8).

In the case of surface centers, one deals with the PCs characterized by the considerably narrower distribution functions than those typical of the stabilized PCs in the bulk. The isotropic HFI constant between the unpaired electron and the central silicon atom is close to 480 G even in the case where the surface paramagnetic center forms due to the mechanical activation of silica at low (room) temperature, and the material is highly disordered. Although the EPR spectrum of these centers is well resolved, it is, nevertheless, broadened as compared with the spectra of the defects of similar structure stabilized at the surface of the RSi samples (prepared at 1300 K).

To determine $a_{iso}(^{29}Si_\beta)$ values in E'_γ-centers isotopic enriched samples of silica (^{29}Si, 95%) were used [40,49]. This results in broadening of central part of ESR spectrum without appearing of a resolved hfs. According to results of calculations (see Figures 7.2–7.4) EPR constants $a_{iso}(^{29}Si_\alpha)$ and $a_{iso}(^{29}Si_\beta)$ are interrelated. Thus inhomogeneous broadening observed in $^{29}Si_\alpha$ nuclei doublet part of ESR spectrum should also influence central part of the spectrum ($^{28}Si_\alpha$), where $^{29}Si_\beta$ nucleus hfs are directly 'developed'. The absence of resolved structure in this part of the spectrum was explained by inhomogeneous broadening effects [40]. This confirms the conclusion about differences in spatial structure of various groups of bulk E'_γ-centers.

6.2. PC $(\equiv Si_\beta\text{-}O)_2Si_\alpha^\bullet$-$r$, WHERE r = H(D), OH(OD), NH_2, AND $CH_3(CD_3)$

The defects of two types, paramagnetic ($(\equiv Si_\beta\text{-}O)_3Si_\alpha^\bullet$) and diamagnetic ($(\equiv Si\text{-}O)_2Si$: and $(\equiv Si\text{-}O)_2Si = O$), stabilize at the surface of activated silica

Lam Research Ex. 1035 - Page 269
Lam Research Corp. v. Inpria Corp.
IPR2024-00033 - U.S. Patent No. 9,823,564

(MSi and RSi). By involving these centers in the reactions with gas-phase molecules, one can conduct directional chemical modification of their structure (Table 7.3) and quantitatively convert them from one form to the other. This lies at the basis of the method for preparing the surface-stabilized PCs of the type $(\equiv Si_{\beta}\text{-}O)_2Si_{\alpha}^{\bullet}\text{-}r$, where $r = H(D)$, $OH(OD)$, NH_2, $CH_3(CD_3)$, C_2H_5, etc. in silica [18,19]. This method amounts to generating low-molecular mobile radicals $r^{\bullet}$ in the reaction between the surface-stabilized paramagnetic center $S^{\bullet}$ and the gas-phase $r_1{-}r$ molecule:

$$S^{\bullet} + r_1 - r \Rightarrow S - r_1 + r^{\bullet}.$$

This is followed by attaching (accepting) the resulting low-molecular radical to the diamagnetic surface center containing two-coordinated silicon atom:

$$(\equiv \text{Si-O})_2\text{Si} : \; + r^{\bullet} \;\Rightarrow\; (\equiv \text{Si-O})_2\text{Si}^{\bullet} - r.$$

The PCs $(\equiv\text{Si-O})_3\text{Si-O}^{\bullet}$ or $(\equiv\text{Si-O})_3\text{Si}^{\bullet}$) are ordinarily used as a source (generator) of low-molecular radicals, for example, Ref. [50]:

$$(\equiv \text{Si-O})_3\text{Si-O}^{\bullet} \; + \; \text{H-OH} \;\Rightarrow\; (\equiv \text{Si-O})_3\text{Si-O-H} \; + \; {}^{\bullet}\text{OH}; \qquad \text{(I)}$$

$$(\equiv \text{Si-O})_2\text{Si} : \; + \; {}^{\bullet}\text{OH} \;\Rightarrow\; (\equiv \text{Si-O})_2\text{Si}^{\bullet}\text{-OH}. \qquad \text{(II)}$$

The reactivity of the $(\equiv\text{Si-O})_3\text{Si-O}^{\bullet}$ radical in the reactions of H detachment is considerably higher than for the ${}^{\bullet}$OH radicals [51].

Therefore, by using the appropriate molecules, one can generate various low-molecular radicals $r^{\bullet}$ (H, D, OH, OD, CH_3, etc.) and subsequently obtain the silicon-centered radicals containing chemically different substituents. The EPR parameters of some of the PCs obtained by this method are presented in Table 7.7.

The EPR spectra of the $(\equiv Si_{\beta}\text{-}O)_2Si_{\alpha}^{\bullet}\text{-H}$ radicals in the silica samples enriched with the ^{29}Si isotope (95%) are shown in Figure 7.11a. These data were used to gain information on the HFI constants caused by the interaction between the unpaired electron and the Si_{α}, Si_{β} atoms in $(\equiv Si_{\beta}\text{-}O)_2Si_{\alpha}^{\bullet}\text{-H(D)}$. The interaction of the unpaired electron with the $^{29}Si_{\beta}$ nuclei manifests itself in the ill-resolved hfs due to the interaction of the unpaired electron with two magnetically equivalent $^{29}Si_{\beta}$ nuclei: $a(^{29}Si_{\beta 1}) \cong a(^{29}Si_{\beta 2}) = (2.7 \pm 0.3)$ (G).

Figure 7.12 demonstrates the EPR spectra of the $(\equiv Si_{\beta}\text{-}O)_2Si_{\alpha}^{\bullet}\text{-O-H}$ radicals stabilized at the surfaces of silica samples enriched to 4.7, 65, and 95% in the magnetic isotope ^{29}Si. The EPR parameters of this radical are presented in Table 7.7. Two sets of satellite lines corresponding to a doublet with splitting ~400 G and a triplet with splitting ~6.5 G between its lines are caused by the interaction of the unpaired electron with the central (Si_{α}) and two silicon Si_{β} atoms entering into the coordination sphere of the paramagnetic center. The

Lam Research Ex. 1035 - Page 270
Lam Research Corp. v. Inpria Corp.
IPR2024-00033 - U.S. Patent No. 9,823,564

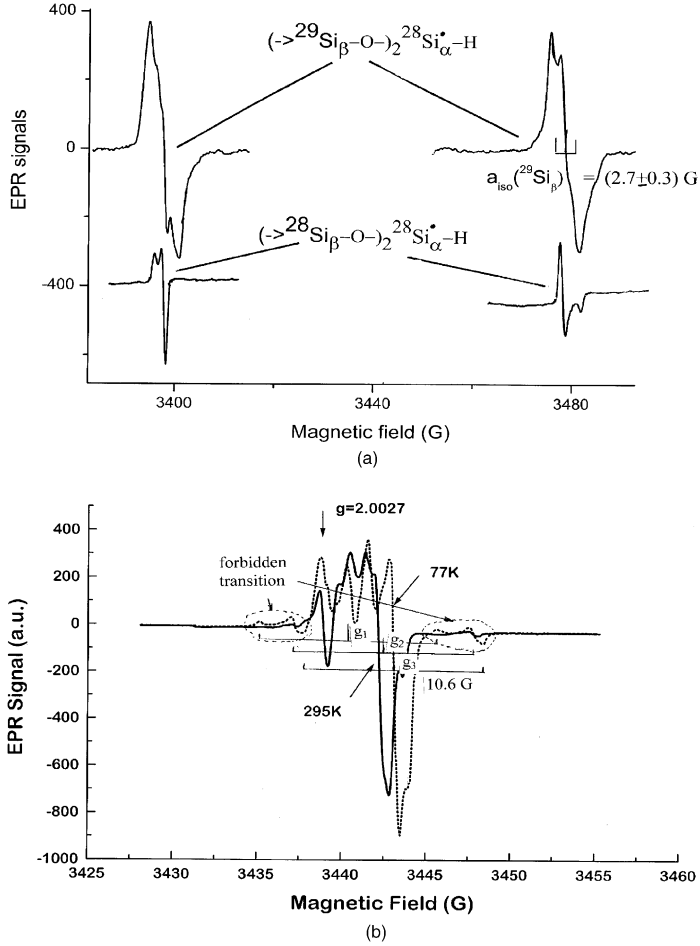


Fig. 7.11. EPR spectra (a) of the ($\equiv^{29}Si_{\beta}$-O-)$_2^{28}Si_{\alpha}^{\bullet}$-H radicals in the sample of silica with 95% concentration of ^{29}Si ($I = 1/2$) and (b) registration of forbidden transition in the ($\equiv^{28}Si_{\beta}$-O-)$_2^{28}Si_{\alpha}^{\bullet}$-OH radicals, caused by the simultaneous electron–nucleus spin flip.

characteristic feature of this paramagnetic center is associated with the presence of the H atom. It shows up in the EPR spectrum (Figure 7.11b) as a forbidden transition caused by the simultaneous electron–nucleus spin flip. The forbidden transition is observed in the EPR spectra of those PCs which contain magnetic nuclei characterized by the anisotropic HFI-tensor components comparable in magnitude to the nuclear (in our case, proton) Zeeman energy in an external magnetic field ($H_0 = 3400$ G and $\Delta H = 10.5$ G). The EPR line shape of the forbidden transition is presented in Figure 7.11b. The

Lam Research Ex. 1035 - Page 271
Lam Research Corp. v. Inpria Corp.
IPR2024-00033 - U.S. Patent No. 9,823,564

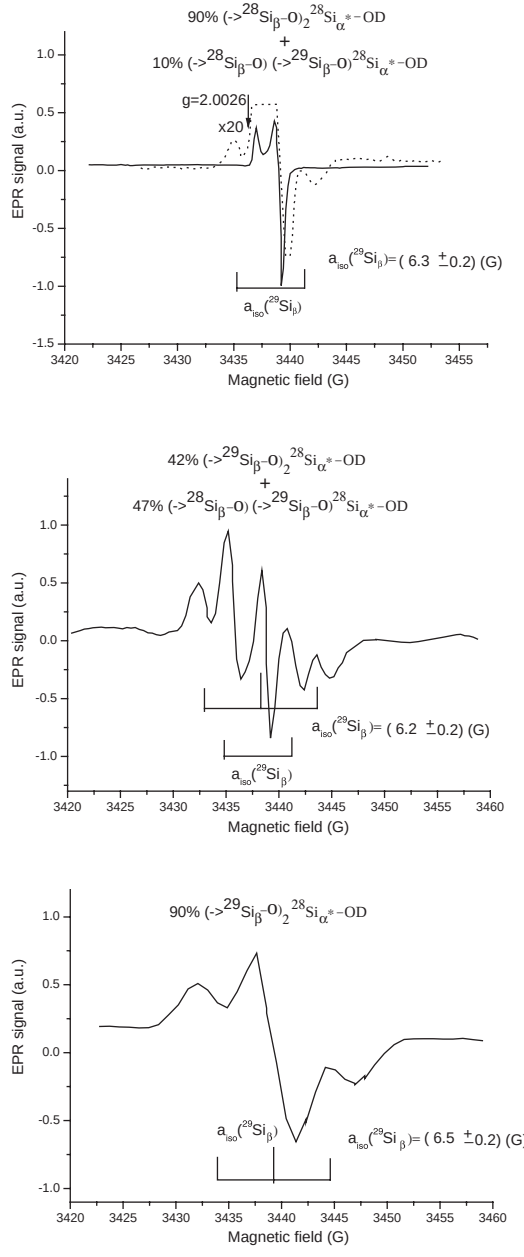


Fig. 7.12. EPR spectra of the surface ($\equiv{}^{29}Si_{\beta}$-O-)$_2^{28}Si_{\alpha}^{\bullet}$-OH radicals in the samples of silica with various concentration of ^{29}Si ($I = 1/2$).

Lam Research Ex. 1035 - Page 272
Lam Research Corp. v. Inpria Corp.
IPR2024-00033 - U.S. Patent No. 9,823,564

spectrum is recorded for a high microwave power in the cavity of a spectrometer, so that the main signal strongly weakens due to saturation, while the signal from the forbidden transition weakens to a much lesser extent. The relative intensity of the forbidden transition increases with lowering temperature. The line shape of this transition is determined by the g-tensor anisotropy of the paramagnetic center, while the forbidden intensity is determined by the magnitude of its anisotropic HFI-tensor components [53]. This allows one to separate the contributions coming to the EPR line shape from the g-tensor anisotropy and from the anisotropy of the HFI tensor due to proton. The observed temperature dependence of the forbidden intensity can be correlated with the temperature dependence of the HFI tensor due to the interaction between the unpaired electron and proton: the anisotropic tensor components determining the intensity of forbidden transition are partly averaged out with increasing temperature because of a rise in the displacement amplitude of the H atom.

The $(\equiv Si\text{-}O)_2Si^{\bullet}\text{-}H$ and $(\equiv Si\text{-}O)_2Si^{\bullet}\text{-}OH$ PCs are the addition products of two different H* and *OH radicals to one and the same diamagnetic SC. The hfs due to the interaction of an unpaired electron with $^{29}Si_{\beta}$ nuclei was detected in EPR spectra of both the radicals (see Table 7.7). In two cases under consideration, these interaction constants are close to each other, i.e., two $^{29}Si_{\beta}$ atoms are magnetically equivalent. Relying on the computed results (see Section 5.3) this implies that the spatial structure of a radical nearest environment possesses the C_s or C_{2v} point group symmetry. Consequently, the diamagnetic SC also exhibits the symmetry whose degree is not lower than that in a radical.

The symmetry of g-tensor reflects the symmetry of PC. From the data reported in Table 7.7 (axially symmetric g-tensor), it follows that the symmetry of paramagnetic center 2 is no lower than C_3 (C_{3v} according discussion in Section 6.1). For PCs 1 and 3, in which the central silicon atom is also coupled to three oxygen atoms, the g-tensor has three different principal values, suggesting that the symmetry of the defect lowers to $\leq C_{2v}$. Thus, even insignificant distinctions in the structures of the second coordination sphere of paramagnetic center show up in its EPR spectrum.

The experimental data in Table 7.7 indicates that the values of two g-tensor components are close for the structurally different PCs. Such is the case for the g_{zz} component, whose value is the closest to the free-electron value $g = 2.0023$. The g_{yy} component also exhibits little changes with changes in the composition of the silicon coordination sphere. This component lies in the symmetry plane of $A\text{-}Si^{\bullet}(O\text{-}Si\equiv)_2$, in which the A-Si bond is located. The third component g_{xx} proves to be most sensitive to the structure of coordination sphere. It is directed perpendicular to the symmetry plane of the paramagnetic center $A\text{-}Si^{\bullet}(O\text{-}Si\equiv)_2$ and, thus, is

Lam Research Ex. 1035 - Page 273
Lam Research Corp. v. Inpria Corp.
IPR2024-00033 - U.S. Patent No. 9,823,564

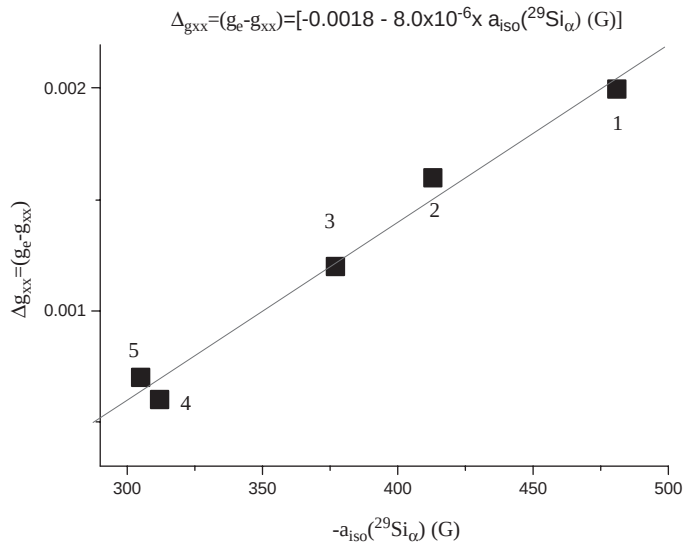


Fig. 7.13. Correlation between Δg_{xx} and the $a_{iso}(^{29}Si_\alpha)$ in the A-Si$^\bullet$(O-Si≡)$_2$ PCs, A = CH_3, H, NH_2, OH, O-Si≡ (see text for details).

particularly sensitive to the changes in the character of those MOs which are responsible for the appearance of new substituent (these MOs include the $3p_y$ AO of the three-coordinate silicon atom). Therefore, the shift of this component is associated with a change in the chemical nature of the A substituent. Figure 7.13 demonstrates the correlation between Δg_{xx} and the $a_{iso}(^{29}Si_\alpha)$ in the A-Si$^\bullet$(O-Si≡)$_2$ PCs.

6.3. Stretching Vibration Frequencies of the Si-H Bonds in the Hydrogenation Products of Silicon-Centered PCs

All known radicals of the silyl type (≡Si-O)$_2$Si$^\bullet-r$ (r = O-Si≡, O-H, NH_2, H, and CH_3) react with the hydrogen molecules even at room temperature. The reaction is accompanied by the disappearance of PCs and formation of the diamagnetic hydrogenation products:

$$(\equiv \text{Si-O})_2\text{Si}^\bullet - r(r = \text{O-Si}\equiv, \text{O-H}, \text{NH}_2, \text{H}, \text{CH}_3) + \text{H}_2 \Rightarrow (\equiv \text{Si-O})_2\text{Si}(r)(\text{H}) + \text{H}^\bullet,$$

$$(\equiv \text{Si-O})_2\text{Si}^\bullet - r(r = \text{O-Si}\equiv, \text{O-H}, \text{NH}_2, \text{H}, \text{CH}_3) + \text{H}^\bullet \Rightarrow (\equiv \text{Si-O})_2\text{Si}(r)(\text{H}).$$

Lam Research Ex. 1035 - Page 274
Lam Research Corp. v. Inpria Corp.
IPR2024-00033 - U.S. Patent No. 9,823,564

Some of these groups can be obtained in other chemical reactions involving surface defects. For instance, the $(\equiv Si\text{-}O)_2Si(OH)(H)$ group can be prepared from the SC in the reaction with water molecule:

$$(\equiv Si\text{-}O)_2Si: + H_2O \Rightarrow (\equiv Si\text{-}O)_2Si(OH)(H).$$

The portions of IR spectra in the Si-H stretching region of the corresponding reaction products are shown in Figure 7.14a. The measured stretching frequencies, together with the results of quantum-chemical calculations performed for the molecular models of surface groups, are given in Table 7.8 [54].

The stretching frequency decreases with a decrease in the HFI constant $a_{iso}(^{29}Si_\alpha)$ of the paramagnetic center. The correlation between these two characteristics of the paramagnetic center and its hydrogenation product is shown in Figure 7.14b. It is close to linear and can be approximated by the expression

$$\nu(Si\text{-}H)(cm^{-1}) = 2067 + 0.48(|a_{iso}(^{29}Si_\alpha)|)(G). \quad (1)$$

This correlation is quite understandable. A decrease in the Si-H stretching frequency is evidence of bond weakening, while the decrease in the value of $a_{iso}(^{29}Si_\alpha)$ points to the fact that the contribution from the silicon 3s AO to the ground-state wave function of paramagnetic center decreases. This, in turn, results in lowering the reactivity of silyl radicals toward the H_2 molecules.

The absorption band corresponding to the Si-H bonds in the bulk of a silica sample subject to the high-temperature hydrogenation is shown in Figure 7.14c by the dashed line [55]. At the long-wavelength edge of the spectrum, it is bounded by a frequency of $2225\,cm^{-1}$ corresponding to the stretching band of the surface $>SiH_2$ groups. The fact that the short-wavelength portion of the spectrum is extended to almost $2350\,cm^{-1}$ is not understood. This value is appreciably higher than the maximal vibrational frequency ($2300–2305\,cm^{-1}$) of the surface groups (Section 10). It follows from relation (1) that such a distribution can be caused by the scatter in the HFI constants $a_{iso}(^{29}Si_\alpha)$ of precursors (silyl radicals) from 300 to 600 G. No data on the HFI constants as large as those have as yet been reported in literature for the central silicon atom in silyl radicals.

6.4. Optical Characteristics of the Silicon-Centered PCs

In this section, the experimental data on the optical absorption spectra of the structurally different silicon-centered PCs stabilized at the surface of quartz glass are reported (see also Ref. [56]), and the question of the possible

Lam Research Ex. 1035 - Page 275
Lam Research Corp. v. Inpria Corp.
IPR2024-00033 - U.S. Patent No. 9,823,564

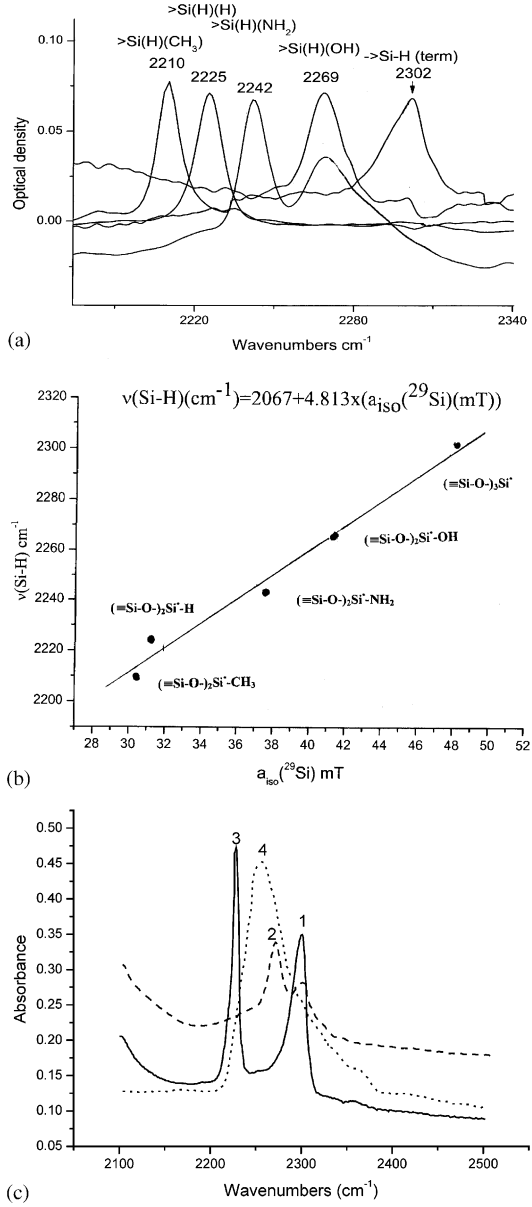


Fig. 7.14. IR spectra (a) of an Si-H groups on the silica surface, correlation diagram (b) between EPR constants ($a_{iso}(^{29}Si_{\alpha})$) for surface silyl radicals and frequencies of Si-H stretching vibrations of the products of their hydrogenation, and (c) the Si-H group absorption band in H_2-loaded silica glass (4) [55], and surface groups ≡Si-H (1), >Si(H)(OH) (2), and >Si(H)(H) (3) [54].

Lam Research Ex. 1035 - Page 276
Lam Research Corp. v. Inpria Corp.
IPR2024-00033 - U.S. Patent No. 9,823,564

Table 7.8. Experimental and calculated (DFT) frequencies of the Si-H and SiO-H stretching vibrations for H-related centers in SiO_2 and their fluorine-containing low-molecular analogs [15, 52, 54]

Structure	ν(exp), cm^{-1}	ν^a(calc), cm^{-1}
$(\equiv Si\text{-}O)_3Si\text{-}H$	2302	
$F_3Si\text{-}H$	2315	2376 (2315)
$(\equiv Si\text{-}O)_3SiO\text{-}H$	3748	
$F_3SiO\text{-}H$		3914 (3749)
$(\equiv Si\text{-}O)_2Si(\text{-}H)(O\text{-}H)$	2269	
	3740	
$F_2Si(\text{-}H)(O\text{-}H)$		2373 (2312)
		3903 (3739)
$(\equiv Si\text{-}O)_2Si^{\bullet}O\text{-}H$	3715	
$F_2Si^{\bullet}O\text{-}H$		3886 (3722)
$(\equiv Si\text{-}O)_2Si^{\bullet}\text{-}H$	2083	
$F_2Si^{\bullet}\text{-}H$		2132 (2077)
$(\equiv Si\text{-}O)_2Si(\text{-}H)(\text{-}H)$	2225	
	2225	
$F_2Si(\text{-}H)(\text{-}H)$	2245	2296 (ν_s) (2237)
	2250	2308 (ν_{as}) (2249)

[a]The calculated data on frequencies of stretching vibrations of Si-H and O-H bonds in fluorine-substituted silicon are presented in this column. The frequencies after using the scaling factors of 0.974 and 0.958 for Si-H and O-H vibrations are given in parentheses.

nature of the corresponding electronic transitions is discussed. The absorption spectra of the $(\equiv Si\text{-}O)_2Si^{\bullet}-r$ ($r = O\text{-}Si\equiv$, O-H, H) PCs are shown in Figure 7.15 (the operating band of the spectrometer was limited by 6.2 eV). The replacement of one of the substituents in a radical is accompanied by increasing the red shift of the low-wavelength absorption edge in the order of $r = O\text{-}Si\equiv$, O-H, H. The excited-state energies of these radicals are no less than 4.5 eV. The absorption spectrum of the $(\equiv Si\text{-}O)_2Si^{\bullet}\text{-}H$ radical is red-shifted relative to the other silicon-centered radicals, allowing the record of a more extended portion of the spectrum. One can see that, after the first broad maximum near 4.9 eV, an appreciable absorption with weak maxima does not end up to 6.2 eV. This experimental result is confirmed by the quantum-chemical calculations of the model systems. The energies of the electron-excited states calculated for the molecular models of the $(\equiv Si\text{-}O)_3Si^{\bullet}$, $(\equiv Si\text{-}O)_2Si^{\bullet}\text{-}H$, and $(\equiv Si\text{-}O)_2Si^{\bullet}\text{-}OH$ radicals by the TD/DFT method in the 6-31 + G(d) basis [57] are given in Table 7.9. The oscillator strengths calculated for these transitions are given in brackets; the letters A and B stand for the transitions of the "electronic" and "hole" types, respectively. According to the calculations, all these radicals have several electron-excited states in the energy range 5–7 eV.

Lam Research Ex. 1035 - Page 277
Lam Research Corp. v. Inpria Corp.
IPR2024-00033 - U.S. Patent No. 9,823,564

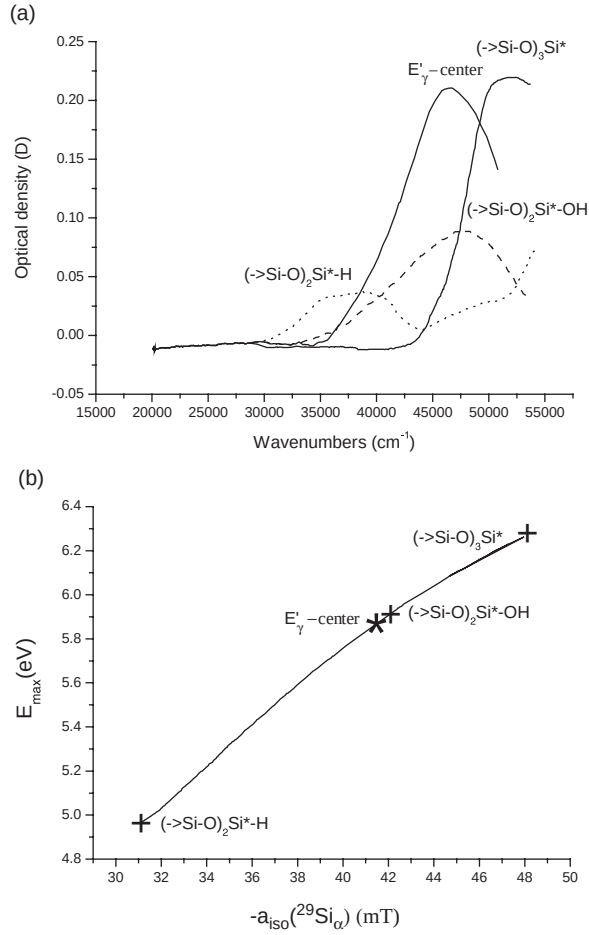


Fig. 7.15. Optical absorption spectra (a) of the surface and the bulk silyl radicals in silica (data for bulk centers adapted from Ref. [46]) and correlation diagram (b) between EPR and optical properties for silyl-type radicals in silica.

The calculations carried out for the $(F_3Si\text{-}O)_3Si^{\bullet}$ radical modeling the paramagnetic center $(\equiv Si\text{-}O)_3Si^{\bullet}$ give a value of 6.2 eV for the energy of the first strong (oscillator strength $2 \times 0.093 = 0.186$; twofold degenerate level) absorption band. These values are close to the experimentally determined parameters of the absorption band of the paramagnetic center $(\equiv Si\text{-}O)_3Si^{\bullet}$: $E = 6.2$ eV and $f = 0.1$–0.2 [56]. The transition of the electronic type is due to the transfer of unpaired electron to the antibonding MOs involved in the bonding of the central silicon atom to the oxygen atom.

Lam Research Ex. 1035 - Page 278
Lam Research Corp. v. Inpria Corp.
IPR2024-00033 - U.S. Patent No. 9,823,564

Table 7.9. Quantum-chemical calculations of the energies (eV) of the lowest electron-excited states for silicon-centered radicals[a]

Radical structure	E_{exc} (eV) (f, A or B)
(F3Si-O)3Si•	5.5 (0.0022,B); 5.8 (0.0013,B); 5.8 (0.0013,B); 5.9 (0.012,A); 6.2 (0.093,A); 6.2 (0.093,A)
$(F_3Si\text{-}O)_2Si^{\bullet}\text{-}H$	4.85 (0.04,A); 4.94 (0.03,A); 5.8 (0.025,AB); 5.85 (0.013,AB)
H-*Si<(O-SiF_2)$_2$>O	4.97 (0.03,A); 5.6 (0.00,B); 5.7 (0.021,A); 5.8 (0.021,A); 6.1 (0.03,A)
$(F_3Si\text{-}O)_2Si^{\bullet}\text{-}OH$	5.0 (0.0015,B); 5.35 (0.047,A); 5.6 (0.044,A); 5.7 (0.014,A); 5.8 (0.08,A); 5.9 (0.02,B)
HO-*Si<(O-SiF_2)$_2$>O	4.91 (0.012,B); 5.39 (0.045,A); 5.52 (0.016,A); 5.58 (0.013,B); 5.62 (0.06,A)

[a]Calculations were performed at TD/6-31+G(d) level. Geometries were optimized at the UB3LYP/6-311G** level. Calculated values of oscillator forces (f) and types of electron excitation (A – "electron", B – "hole" types of electron transitions) are presented in parenthesis.

Let us consider the possible pathways for the transformation of the electronic excitation energy of the silicon-centered PCs. It was experimentally found that this process is not accompanied by luminescence. This means that the electronic excitation energy (>5 eV) is dissipated into the heat and, probably, is partly transferred into the internal energy of photo conversion products. In Ref. [58], it was shown that UV irradiation (77 K, unfiltered light of a mercury high pressure lamp) of a silica sample containing $(\equiv Si\text{-}O)_2Si^{\bullet}\text{-}H$ radicals is accompanied by the effective decomposition of the latter. In this case, the H atoms stabilized in the SiO_2 matrix were detected in the photolysis products. The experimental data on the photo decay of the surface $(\equiv Si\text{-}O)_2Si^{\bullet}\text{-}H$ radicals are presented in Ref. [59]. It was shown that this process proceeds according to the following scheme:

$$(\equiv Si\text{-}O)_2Si^{\bullet}\text{-}H + h\nu \Rightarrow (\equiv Si\text{-}O)_2Si: + H.$$

Thus, in the electronically excited state, the dissociation of the silyl radical is possible which is accompanied by the elimination of one of the substitutes of three-coordinated Si atom (in this case, the H atom). These results agree with the results of the quantum-chemical study of photo conversion of the $H_3Si^{\bullet}$ radicals [60]. In this work it was shown that low-lying electronically excited terms of this radical are dissociation terms, and their relaxation is accompanied by elimination of the H atom.

Low-molecular radicals $^{\bullet}OH$ and $^{\bullet}H$ were also detected under UV-irradiation of the surface $(\equiv Si\text{-}O)_2Si^{\bullet}\text{-}OH$ radicals (our unpublished data). Thus, in this case the decomposition with the production of the low-molecular radical is also typical for the electronically excited state of the

Lam Research Ex. 1035 - Page 279
Lam Research Corp. v. Inpria Corp.
IPR2024-00033 - U.S. Patent No. 9,823,564

$(\equiv Si\text{-}O)_2Si^{\bullet}\text{-}OH$ radical:

$$(\equiv Si\text{-}O)_2Si^{\bullet}\text{-}OH + h\nu \Rightarrow (\equiv Si\text{-}O)_2Si: + {}^{\bullet}OH,$$

$$(\equiv Si\text{-}O)_2Si^{\bullet}\text{-}OH + h\nu \Rightarrow (\equiv Si\text{-}O)_2Si=O + {}^{\bullet}H.$$

In the $(\equiv Si\text{-}O)_2Si^{\bullet}\text{-}OH$ radical, the α-Si atom is already bonded with three oxygen atoms and this PC is chemically similar to the E'_{γ}-center.

In both examples considered it was only possible to detect the primary products of photo decay of the surface defects because they represented low-molecular radicals and could easily leave the place of their "birth" and can be trapped by especially chosen acceptors.

In the case of the $(\equiv Si\text{-}O)_3Si^{\bullet}$ radical, the situation is fundamentally different. One can assume that by absorbing a photon this defect is also transferred into the electronically excited state which is the dissociation state. However, after the Si_{α}-O or O-Si_{β} bond breaking, the dissociation products cannot be spatially separated because of the "cage effect" and, thus, the reverse process proceeds with a high probability, resulting in the reconstruction of the initial radical site:

$$(\equiv Si\text{-}O)_2Si^{\bullet}\text{-}O\text{-}Si\equiv + h\nu \Rightarrow (\equiv Si\text{-}O)_2Si: + {}^{\bullet}O\text{-}Si\equiv \Rightarrow (\equiv Si\text{-}O)_2Si^{\bullet}\text{-}O\text{-}Si\equiv,$$

$$(\equiv Si\text{-}O)_2Si^{\bullet}\text{-}O\text{-}Si\equiv + h\nu \Rightarrow (\equiv Si\text{-}O)_2Si=O + {}^{\bullet}Si\equiv \Rightarrow (\equiv Si\text{-}O)_2Si^{\bullet}\text{-}O\text{-}Si\equiv .$$

Thus, the electronic excitation energy is first spent on a chemical bond breaking (the relaxation of the electronically excited site) and, then, a certain part of the energy is released in the form of the heat during the reconstruction of the disrupted bond. The model proposed may explain the high photo stability of the E'_{γ}-centers in SiO_2.

7. Paramagnetic Centers $\equiv Si\text{-}O^{\bullet}$ on the Silica Surface (Non-Bridging Oxygen Center)

Another type of paramagnetic defects that are attributed to the main intrinsic defects of silica glass, are the so-called non-bridging oxygen hole centers – the $(\equiv Si\text{-}O)_3Si\text{-}O^{\bullet}$ radicals. The EPR spectrum of these radicals, stabilized on the silica surface is presented in Figure 7.16a (conclusions about their existence were made earlier based on the indirect data). The temperature dependence of the intensity of the EPR signal does not obey the Curie law, and the EPR signal can be detected only at $T \leq 100$ K.

Lam Research Ex. 1035 - Page 280
Lam Research Corp. v. Inpria Corp.
IPR2024-00033 - U.S. Patent No. 9,823,564

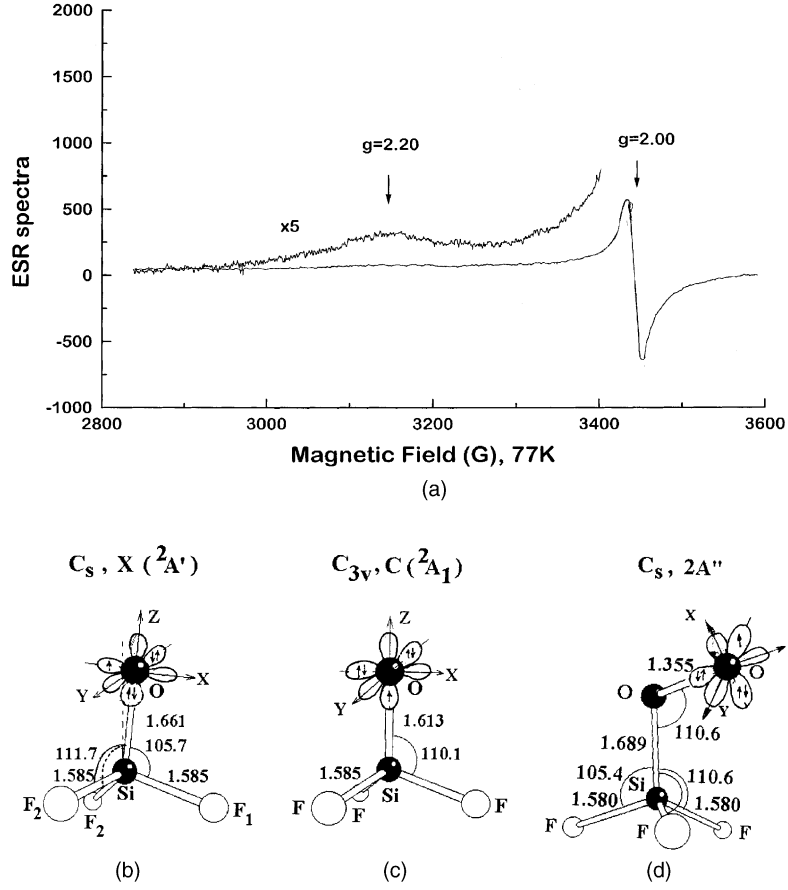


Fig. 7.16. The oxy and peroxy radicals on the silica surface. (a) EPR spectrum of the (≡Si-O)$_3$Si-O$^\bullet$ radical, stabilized on silica surface (77 K); (b, c) optimized structures of the F_3Si-O$^\bullet$ radical in ground (b) and electronically excited (c) states; (d) optimized structure of the F_3Si-O-O$^\bullet$ radical in ground state (Y-axis is perpendicular to the symmetry plane).

The absorption spectrum of surface defects (Figure 7.17) in the range 1.5–6.5 eV consists of two bands with maxima at 2.00 ± 0.02 and 4.9 ± 0.1 eV. The characteristic luminescence with a maximum at 1.95 eV can be excited in both absorption bands [18,19,61].

In order to interpret the observed optical and EPR parameters of the PC, the quantum-chemical calculations of the following model sites were performed: $(HO)_3Si\text{-}O_t^\bullet$ and $F_3Si\text{-}O_t^\bullet$ (see also Refs. [62,63]) (Figure 7.16b and c). In the ground state (X, C_s symmetry, $^2A''$) the Si-O_t bond (the R(Si-O)

Lam Research Ex. 1035 - Page 281
Lam Research Corp. v. Inpria Corp.
IPR2024-00033 - U.S. Patent No. 9,823,564

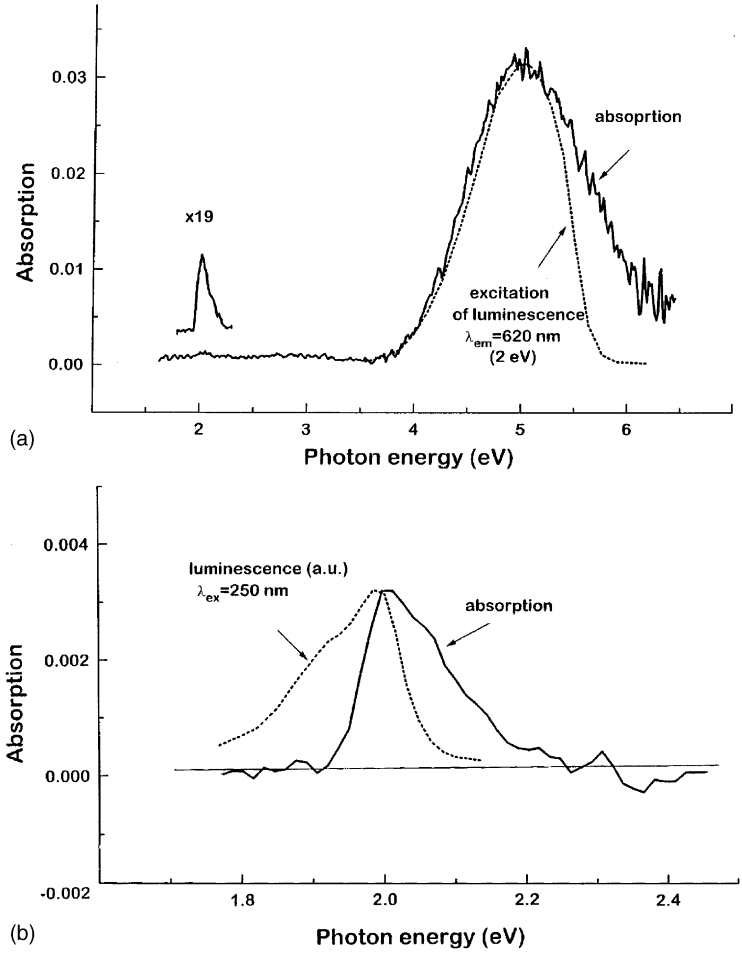


Fig. 7.17. Optical properties of the $(\equiv Si\text{-}O)_3Si\text{-}O^{\bullet}$ radicals. (a) The absorption bands at 2.0.and 4.9 eV and excitation spectrum of the red luminescence; (b) the manifestation of the small Stokes shift for absorption band at 2 eV.

bond −1.67 Å, the Z-axis is directed along this bond) deviates from the axis of symmetry of the F_3Si (or $(HO)_3Si$) fragment by an angle of ~3° results in the removal of an orbital electronic degeneracy in the radical (the Jahn–Teller effect) (Figure 7.16). An unpaired electron occupies the $2p_x$ atomic orbital of the O_t atom (the X-axis is perpendicular to the plane of symmetry). However, the decrease in the system's energy caused by this effect does not exceed 0.1 eV.

Lam Research Ex. 1035 - Page 282
Lam Research Corp. v. Inpria Corp.
IPR2024-00033 - U.S. Patent No. 9,823,564

The first electronically excited state (A, ^{2}A') of the radical is caused by the transition of an electron of the lone pair of the terminal O atom to its $2p_x$ atomic orbital (Figure 7.16b). The energy ΔE of this vertical transition according to the results of the calculations, is equal to ~0.1 eV.The shift of the g_{zz} component of the radical g-tensor from the value 2.0023 (the free-electron value) is connected with this transition. According to Ref. [53], the relation satisfied:

$$\Delta g = (g_{zz} - 2.0023) \sim \lambda/\Delta E \tag{2}$$

where λ is a constant of the spin–orbital interaction for the O atom. The experimental value of Δg is equal to ~0.20. This gives ΔE value equal to 0.15 eV, in a satisfactory agreement with the results of quantum-chemical calculations.

The second electronically excited state (B, ^{2}A') of the radical is related to transition of one of the electrons of the Si-O_t bond to the $2p_x$ atomic orbital of the terminal O atom. In this state, an unpaired electron is to a large extent localized on the $2p_z$ atomic orbital of the terminal O atom (Figure 7.16c).

According to the results of the TD/DFT calculation, the energy of the vertical $X \Rightarrow B$ transition equals to 2.1 eV (oscillator strength $f \cong 2 \times 10^{-4}$). The oscillator strength of this transition has to be small because of a small overlap of the wave functions of the X and B states. The deviation of an O atom from the position coincided with the symmetry axis of the F_3Si fragments (relaxation) is accompanied by a small decrease (0.1 eV) of the energy of the system and a slight reduction (by 0.05 Å) of the length of the Si-O_t bond. The calculated energy of the vertical transition (luminescence) from this excited state to the ground state is equal to ~2 eV. Consequently, as it was experimentally observed, the value of the Stokes shift for the luminescence transition is small. Thus, our analysis of the nature of the excited-electron states of the radical containing the non-bridging oxygen atom do not confirm the model of the electronic transitions in this defect proposed earlier in Ref. [64].

The nature of the electronic transition related to the 4.9 eV absorption band (the C state) of oxy radical is still unknown. It was experimentally found [65] that the quantum yield of the red luminescence (1.95 eV) is equal to 0.5 ± 0.2. Consequently, the nature of this excited state should be so that the transition to the B state will be possible with high probability from this state. This means that the terms corresponding to the C and B states are crossed or converged (come closer to each other) at any arbitrary point of the configurational space.

On the silica surface, the other types of defects of a non-bridging oxygen – $(\equiv Si\text{-}O)_2(HO)Si\text{-}O^\bullet$ and $(\equiv Si\text{-}O)_2(H)Si\text{-}O^\bullet$ have also been obtained. The latter was found to be thermally unstable at 77 K and transformed during

Lam Research Ex. 1035 - Page 283
Lam Research Corp. v. Inpria Corp.
IPR2024-00033 - U.S. Patent No. 9,823,564

intramolecular transfer of the H atom into the $(\equiv Si\text{-}O)_2Si^{\bullet}\text{-}OH$ radical. The substitution of the H atom to the D atom resulted in a substantial decrease in the reaction rate, and the $(\equiv Si\text{-}O)_2(D)Si\text{-}O^{\bullet}$ radical was found to be thermally stable at 77 K. The $(\equiv Si\text{-}O)_2(D)Si\text{-}O^{\bullet} \Rightarrow (\equiv Si\text{-}O)_2Si^{\bullet}\text{-}OD$ reaction starts at the temperature $T \geq 200$ K and has activation energy equal to ~0.6 eV. This means that in the case of the H atom reaction proceeds in accordance with the tunnel mechanism.

8. The $(\equiv Si\text{-}O)_3Si\text{-}O\text{-}O^*$ Radicals: Structure and Reactivity

Peroxy radicals represent one of the reliably identified intrinsic defects in silica. They can be produced on the surface through the oxidation of silyl radicals by molecular oxygen [10]:

$$\equiv Si^{\bullet} + O_2 \Rightarrow \equiv Si\text{-}O\text{-}O^{\bullet}.$$

This reaction readily proceeds already at 77 K, i.e., its activation energy is close to zero. The EPR spectrum of the surface peroxy radical represents an anisotropic line with the following parameters: $g_1 = 2.0025$, $g_2 = 2.0085$, and $g_3 = 2.0718$ [10]. A HFI with the ^{29}Si nucleus ($a_1 = 0.36$ mT, $a_2 = 0.40$ mT, and $a_3 = ?$) was also detected.

In the 1.5–6 eV range only one absorption band was observed for a peroxy radical: $E_{max} = 5.3$ eV, $\Delta E_{1/2} = 1.2$ eV, $\varepsilon_{max} = 140\ m^2/mol$, and oscillator strength $f = (0.06 \pm 0.02)$ (see also Refs. [56,66]). This band is similar to the absorption band of other peroxy radicals ($HOO^{\bullet}$, and $H_3COO^{\bullet}$) and it seems likely that it is also caused by the $\pi \Rightarrow \pi^*$ electronic transition [67].

Optimized structure of the $F_3Si\text{-}O\text{-}O^{\bullet}$ radical in ground state (C_s symmetry), modeling the site in silica, is shown in the Figure 7.16d. The unpaired electron occupies the $2p_x$ atomic orbital of the terminal oxygen atom (the X-axis is perpendicular to the plane of symmetry). The first electronically excited state ($^2A'$) of the radical is related to the electronic transition of the lone pair of the terminal O atom to the $2p_x$ atomic orbital of the same atom. The energy of this vertical transition was found to be equal to $\Delta E = 0.5$ eV.

The shift of one of the components ($g_3 = 2.072$ and $\Delta g_3 = 0.07$) of the g-tensor of a peroxy radical is related to the $(^2A'') \Rightarrow (^2A')$ transition (see the formula (2)). For the $HOO^{\bullet}$ radical, both values have been experimentally determined: $\Delta E = 0.9$ eV and $g_3 = 2.037$ ($\Delta g_3 = 0.035$). The value of ΔE estimated on the basis of these data from expression (2) for a Silicon-centered peroxy radical is 0.45 eV. This value is in a good agreement with the calculated value of 0.5 eV. Thus, a larger value of the g_3 component of a

Lam Research Ex. 1035 - Page 284
Lam Research Corp. v. Inpria Corp.
IPR2024-00033 - U.S. Patent No. 9,823,564

Silicon-centered peroxy radical is explained by a smaller value of the splitting between the ground and first excited state of the radical.

The $\equiv$Si-O-O$^{\bullet}$ radicals stabilized on the solid surface are stable up to the temperature 650 K. During further temperature increase their dissociation starts accompanied by a quantitative formation of the $\equiv$Si-O$^{\bullet}$ radicals and appearance of molecular oxygen in a gas phase. The formation of oxy radicals during this process was controlled by two methods: (1) the EPR method (the appearance of a broad anisotropic signal, see Figure 7.16a; (2) the photoluminescence method (the growth of characteristic red photoluminescence ($E_{max} = 1.95$ eV) under UV irradiation of the sample). Thus, a thermal decomposition of peroxy radicals proceeds according to the scheme:

$$\equiv \text{Si-O-O}^{\bullet} \Rightarrow \equiv \text{Si-O}^{\bullet} + \text{O}(^3\text{P}).$$

The experimental data obtained do not allow one to state that under these conditions the following reaction cannot proceed:

$$\equiv \text{Si-O-O}^{\bullet} \Rightarrow \equiv \text{Si}^{\bullet} + \text{O}_2.$$

However, because a reverse reaction of oxygen addition to a silyl radical proceeds with a high rate, one can state that the formation of the main products of transformation is related to the first process.

The O atom formed during this reaction may either react with the other peroxy radical:

$$\equiv \text{Si-O-O}^{\bullet} + \text{O}(^3\text{P}) \Rightarrow \equiv \text{Si-O}^{\bullet} + \text{O}_2$$

which will lead to the appearance of molecular oxygen in a gas phase, or it will react with the other site on the solid surface. As a result, the number of oxygen atoms formed in a gas phase depends on the state of a solid surface and sharply increases upon the transition from a reduced to oxidized surface (from 0.04 to 0.4).

Thus, for a thermal decomposition of the $\equiv$Si-O-O$^{\bullet}$ radicals the channel of splitting of the O-O bond is possible. This means that in this radical the following inequality of bond strengths are obeyed: (O-O) $\leq$ (Si-O). According to the microcalorimetric results, the heat effect for the reaction of oxygen molecule attachment to the silyl radical (reaction 5 in Table 7.3) is equal to $\sim$60 kcal/mol. Since the O$\equiv$O bond strength is $\sim$120 kcal/mol, this implies that the value of heat effect for the peroxide radical is also close to 60 kcal/mol.

Consider now photochemical properties of $(\equiv\text{Si-O})_3\text{Si-O-O}^{\bullet}$ radicals [56,66,68]. Under the UV irradiation (unfiltered light of a mercury high pressure lamp equipped by a water filter, $T = 300$ K) the following processes were observed: (1) the decrease in the intensity of the EPR signal from peroxy radicals; (2) the formation of $(\equiv\text{Si-O})_3\text{Si-O}^{\bullet}$ radicals whose number

Lam Research Ex. 1035 - Page 285
Lam Research Corp. v. Inpria Corp.
IPR2024-00033 - U.S. Patent No. 9,823,564

is approximately equal to the number of "dead" peroxy radicals (the control was carried out by the EPR method); (3) the appearance of a molecular oxygen in a gas phase.

Thus, the photo transformation of peroxy radicals is accompanied by the formation of the same products as in the case of their thermal decomposition. This means that the main channel of their photo transformation is their photo dissociation accompanied by the elimination of oxygen atom:

$$\equiv \text{Si-O-O}^{\bullet} + h\nu \Rightarrow \equiv \text{Si-O}^{\bullet} + \text{O}(^3\text{P}).$$

Note that theoretical calculations of the surface of a potential energy of electronically excited states of the $HOO^{\bullet}$ radical showed that the states with the excitation energies near 5 eV correspond to dissociative terms from which this radical dissociates with the O-O bond breaking [69].

9. Diamagnetic Point Defects on Silica Surface

The paramagnetic products $(\equiv\text{Si-O})_3\text{Si}^{\bullet}$ and $(\equiv\text{Si-O})_3\text{Si-O}^{\bullet}$ of the homolytic siloxane-bond rupture are fundamental intrinsic defects of the SiO_2 structure. At the surface of activated silica, one can obtain a high (up to several percent of the number of surface atoms) concentration of such centers. They posses a high free energy, so that the decomposition reactions yielding diamagnetic products are quite profitable thermo chemically: the enthalpies of these reactions exceed 50 kcal/mol. What kind of diamagnetic products should be expected to form after the decomposition of these radicals? Clearly, the siloxane bond will be restored. And what happens if two radicals $(\equiv\text{Si-O})_3\text{Si}^{\bullet} + (\equiv\text{Si-O})_3\text{Si}^{\bullet}$ participate in the decomposition event? For a long time, it was believed that only the oxygen vacancy $(\equiv\text{Si-O})_3\text{Si-Si}(\text{O-Si}\equiv)_3$ can be a product of this reaction [46]. Nevertheless, the existence of such defect structure was not proved experimentally.

A new view on this problem arose after the diamagnetic centers with two-coordinate silicon atom were observed at the surface of mechanically activated silica [70]. The subsequent studies of the optical properties of these centers [71] have shown that they are close to those centers that were observed earlier in the bulk of quartz glass but referred to the oxygen vacancies. It has become evident that, apart from the combination reaction of two radicals $(\equiv\text{Si-O})_3\text{Si}^{\bullet}$ and $(\equiv\text{Si-O})_3\text{Si}^{\bullet}$ resulting in the oxygen vacancy, an alternative reaction of their disproportionation with the formation of a center containing two-coordinate silicon and the restoration of one of the siloxane bonds is possible:

$$(\equiv \text{Si-O})_3\text{Si}^{\bullet} + (\equiv \text{Si-O})_3\text{Si}^{\bullet} \Rightarrow (\equiv \text{Si-O})_2\text{Si}: + (\equiv \text{Si-O})_3\text{Si-(O-Si} \equiv).$$

Lam Research Ex. 1035 - Page 286
Lam Research Corp. v. Inpria Corp.
IPR2024-00033 - U.S. Patent No. 9,823,564

The succeeding section is devoted to the structure and reactivity of these diamagnetic groups.

The comparable number of diamagnetic groupings of another type, namely $(\equiv Si\text{-}O\text{-})_2Si < O_2 > Si(\text{-}O\text{-}Si\equiv)_2$ (SRs) (see Section 2.1 and Table 7.1), are also stabilized on the surfaces of RSi samples in addition to SCs. The absorption bands at 888 and 908 cm^{-1} [3,4] in a silica IR transparency window are connected with these groupings. Such centers were registered for the first time on the dehydroxylated surface of silica. Defects of the type considered are characterized by a high reactivity with respect to H_2O, CH_3OH, and NH_3 molecules [3,72]. At the same time, reliable information about the reactivity of SRs with respect to another molecule (e.g., $H_2(D_2)$) is actually lacking. The first part of this section is concerned with a discussion about physico-chemical properties of SRs.

9.1. $(\equiv Si\text{-}O\text{-})_2Si < O_2 > Si(\text{-}O\text{-}Si\equiv)_2$ Groups (Strained Rings, SRs) on the Silica Surface

It was expected that the high reactivity of a ring structure with respect not only to water and ammonia molecules [3,4] but also to another molecules has to show its worth. The results of experimental studies on the $(SRs + D_2)$ system are presented below ($P(D_2) = 11$ Torr). In these experiments, the samples of dehydrated silica were used. The process was controlled with an IR-spectroscopy technique. The SR reaction with deuterium starts for ≥ 1100 K. The process under consideration is accompanied by a decrease in the intensity of SR absorption bands at 888 and 908 cm^{-1}, and by an increase in the intensity of Si-D group absorption bands at 1670 cm^{-1} and SiO-D at 2763 cm^{-1} (see Figure 7.18). In this case $-\Delta N_{SR} \cong \Delta N_{Si-D} \cong \Delta N_{Si-OD}$. The positions of absorption bands characteristic of Si-D and SiO-D bonds being formed testify that they are terminal. Strength vibration frequencies of vicinal groups relating to such a type must be shifted to lower wave numbers. This means that the groups formed under experimental conditions can escape from their own "cage" and become displaced to another place on the surface. Thus, high-temperature hydration of SRs proceeds as follows:

$$(\equiv Si\text{-}O\text{-})_2Si < O_2 > Si(\text{-}O\text{-}Si\equiv)_2 + D_2$$

$$\Rightarrow (\equiv Si\text{-}O\text{-})_2Si(D)\text{-}O\text{-}(DO)Si(\text{-}O\text{-}Si\equiv)_2$$

$$\Rightarrow (\equiv Si\text{-}O)_3Si\text{-}D + DOSi(O\text{-}Si\equiv)_3.$$

Lam Research Ex. 1035 - Page 287
Lam Research Corp. v. Inpria Corp.
IPR2024-00033 - U.S. Patent No. 9,823,564

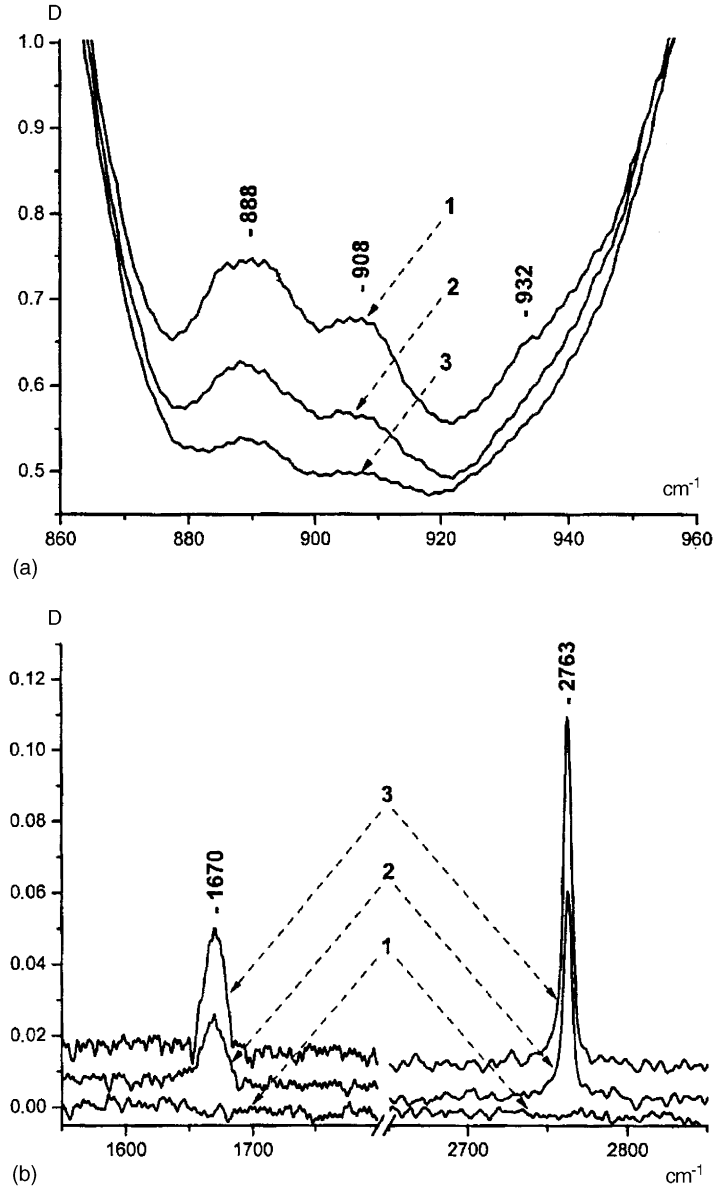


Fig. 7.18. IR spectra of hydrogenation products of SRs, stabilized on the silica surface, by D_2 molecules. (a) The decay of SR (bands at 888 and 908 cm^{-1}); (b) the formation of terminal Si-D (1670 cm) and SiO-D (2763 cm) groups; (1) initial sample; (2) after 20 min at 1173 K ($P(D_2O) = 11$ Torr); (3) after 20 min at 1273 K ($P(D_2) = 20$ Torr).

Lam Research Ex. 1035 - Page 288
Lam Research Corp. v. Inpria Corp.
IPR2024-00033 - U.S. Patent No. 9,823,564

Warming up of a hydrated sample at temperatures above 1100 K was accompanied by the release of molecular deuterium and the restoration of SR absorption bands at 888 and 908 cm^{-1}. Measuring the number of desorbed molecules it was also possible to foresee the number of SRs in the sample.

Table 7.10 lists the results of calculating a number of processes with the participation of a four-member ring. The $F_2Si<O_2>SiF_2$ molecule was taken as a model for this defect. The off-parentheses numbers were obtained at a G2(MP2) level, while those in parentheses at a DFT/UB3LYP//6-311G** level. For the ''ring water molecule'' reaction (3 and 3* reactions in Table 7.10), the calculations of the activation energy and reaction thermal effect were done for two reaction regimes: (1) the reaction between free molecules and (2) the reaction between water molecule and $F_2Si<O_2>SiF_2$ molecule wherein F atoms are fixed in their positions in the free molecule (3* reaction). In this manner we could estimate a possible influence of the solid lattice surrounding the defect on the energy parameters of the reaction studied. As expected, this caused a rise of the activation barrier for the water-molecule addition reaction and a small decrease in the magnitude of the reaction thermal effect.

Table 7.10. Activation energies (E_{act}) and reaction heat ΔH (0 K) (kcal/mol) for processes with participation of the $F_2Si<O_2>SiF_2$ and $F_2Si<O_2>C=O$ groups (for process 3* the F atoms have been fixed at the positions of initial cycle's structure and do not change during next transformations)[a]

Reaction	E_{act} (kcal/mol)	ΔH (0 K) (kcal/mol)
1. $F_2Si<O_2>SiF_2 \Rightarrow$	F_2Si*-O-(*O)SiF_2 ($^3A'$)	111.8 (94.4)
2. $F_2Si<O_2>SiF_2 + H_2O \Rightarrow$	$[F_2Si<O_2>SiF_2 \ldots H_2O]$ (complex)	−11.1
3. $F_2Si<O_2>SiF_2 + H_2O \Rightarrow$	TS + (1.9) $\Rightarrow$ $F_2Si(OH)$-O-(HO)SiF_2	−35.8 (−42.8)
3*. $F_2Si<O_2>SiF_2 + H_2O \Rightarrow$	TS + (7.1) $\Rightarrow$ $F_2Si(OH)$-O-(HO)SiF_2	−42.3
4. $F_2Si<O_2>C=O \Rightarrow$	F_2Si*(O-C(O)-O*) (^3A)	112.1 (95.0)
5. $F_2Si<O_2>C=O \Rightarrow$	F_2Si(O*)(O-*C = O) (^3A)	109.3 (74.7)
6. $F_2Si<O_2>C=O + H_2O \Rightarrow$	$[F_2Si<O_2>C=O \ldots H_2O]$ (complex)	−16.4
7. $F_2Si<O_2>C=O + H_2O \Rightarrow$	TS + 1.9 (7.1) $\Rightarrow$ $F_2Si(OH)$-O-C(O)(OH)	−42.8 (−42.3)
8. $F_2Si<O_2>SiF_2 + CH_3OH \Rightarrow$	$[F_2Si<O_2>SiF_2 \ldots CH_3OH]$ (complex)	−16.4
9. $F_2Si<O_2>SiF_2 + CH_3OH \Rightarrow$	TS (−1.5) $\Rightarrow$ $F_2Si(OH)$-O-$(CH_3O)SiF_2$	−35.5 (−41.8)
10. $F_2Si<O_2>SiF_2 + NH_3 \Rightarrow$	$[F_2Si<O_2>SiF_2 \ldots NH_3]$ (complex)	−16.0 (−19.2)
11. $F_2Si<O_2>SiF_2 + NH_3 \Rightarrow$	TS + 3.4 (−1.6) $\Rightarrow$ $F_2Si(OH)$-O-$(H_2N)SiF_2$	−26.8 (34.4)
12. $F_2Si<O_2>SiF_2 + *H \Rightarrow$	TS + 36.4 (24.2) $\Rightarrow$ $F_2Si(OH)$-O-*SiF_2	−14.2 (−24.9)
13. $F_2Si<O_2>SiF_2 + H_2 \Rightarrow$	TS + 49.3 (45.0) $\Rightarrow$ $F_2Si(OH)$-O-(HO)SiF_2	−9.7 (−18.4)
14. $F_2Si<O_2>SiF_2 + FCH_3 \Rightarrow$	TS + (56.9) $\Rightarrow$ $F_2Si(F)$-O-$(H_3C)SiF_2$	−43.6 (−47.1)
15. $F_2Si<O_2>SiF_2 + CH_3OCH_3 \Rightarrow$	$[F_2Si<O_2>SiF_2 \ldots CH_3OCH_3]$ (complex)	−11.1
16. $F_2Si<O_2>SiF_2 + CH_3OCH_3 \Rightarrow$	TS + (63.1) $\Rightarrow$ $F_2Si(OCH_3)$-O-$(CH_3O)SiF_2$	−38.6

[a]Calculations have been executed at G2(MP2) level or on UB3LYP/6-311G** level (the values in parenthesis).

Lam Research Ex. 1035 - Page 289
Lam Research Corp. v. Inpria Corp.
IPR2024-00033 - U.S. Patent No. 9,823,564

When estimating the strength of the Si-O bond in the ring one may fall back on the results of two calculations for: (1) the heat of formation of the triplet state resulting from the siloxane bond breakage and (2) heat of hydration of the siloxane bond (8 and 9 reactions in Table 7.10). The first estimation gives 112 kcal/mol for the Si-O bond strength in a four-term ring. Assuming that the strengths of Si-H and SiO-H bonds being formed in the hydration product are 100 [16] and 128 kcal/mol [17], respectively (the bond strength in a hydrogen molecule equals 104 kcal/mol); we arrive at a close value of 114 kcal/mol for the ring Si-O bond. This finding is almost 40 kcal/mol less than the Si-O bond strength in a regular silica structure (see Section 12.3).

It is obvious from the results compiled in Table 7.10 that the ring reactivity strongly differs for the compounds with different nature of chemical bonding. In agreement with received experimental data, SRs enter into reactions with polar molecules H_2O, NH_3, and CH_3OH. According to calculated results, all these molecules form relatively strong complexes with SRs. For the most part, a tendency toward complexing makes itself evident in silicon atoms interacting with an electronegative atom of the attacking molecule. However, the reactions involving electroneutral particles, such as H_2 or even H atom, require surmounting of the high activation barrier. In Table 7.10 the results of computations for a number of reactions with the participation of a four-member carbonate structure which can be obtained from SG or DOSG (see 8 and 9 reactions in Table 7.10) are also given. One can readily see the surprising proximity of reactivities for these ring groupings.

9.2. DIAMAGNETIC SITES CONTAINING TWO-FOLD COORDINATED SILICON ATOMS ($\equiv$Si-O-)$_2$Si: (SC): IDENTIFICATION OF SC STRUCTURE

In defects of this type (diamagnetic), the Si atom is linked to two lattice oxygen atoms. SC is related to several diamagnetic defects in which the silicon atom appears in different oxidation states. Currently, silanone ($\equiv$Si-O-)$_2$Si = O [18,19,52] and siladioxirane ($\equiv$Si-O-)$_2$Si$<$O$_2$ groups [18,73,74] are identified in this series.

9.2.1. Identification of the Site Structure

9.2.1.1. Method of paramagnetic spin labeling. The first experimental proof of SC stabilization on the silica surface and, most likely, in quartz glass in general was obtained in Ref. [70], where I applied the paramagnetic probe

Lam Research Ex. 1035 - Page 290
Lam Research Corp. v. Inpria Corp.
IPR2024-00033 - U.S. Patent No. 9,823,564

method to predict the structure of diamagnetic defects on the mechanically activated oxide surface. Low-molecular radical r^* is accepted by a diamagnetic group X, and this process can be accompanied by the formation of a paramagnetic complex:

$$X + r^* \Rightarrow (Xr)^*.$$

The identification of the structure of this complex provides the data on the structure of the X site as well.

H(D) atoms were used in Refs. [70,75] as a paramagnetic probe of the activated silica surface. The structure of complexes formed, $(\equiv Si\text{-}O)_2Si^*\text{-}H(D)$, was found by ESR method. Taking into account the procedure of obtaining these PCs, we may conclude that they are formed due to accepting H(D) atoms by bicoordinated silicon atoms:

$$(\equiv Si\text{-}O)_2Si: \; + H^*(D^*) \; \Rightarrow \; (\equiv Si\text{-}O)_2Si^*\text{-}H(D).$$

This approach, along with the use of H(D) atoms and CH_3 and C_2H_5 radicals as paramagnetic probes, was further applied to reveal the nature of other types of diamagnetic defects stabilized on the SiO_2 surface [18,51,52,73].

9.2.1.2. Products of SC hydrogenation. Another experimental evidence for the fact that SC is stabilized on the activated silica surface was obtained for the hydrogenation of the surface with molecular hydrogen (deuterium). The formation of silyl-hydride bonds during this process were first found by IR spectroscopy in Ref. [15], however, their structure has been identified later [54].

The IR spectra of the products from the chemisorptions of H_2, D_2, and HD molecules by the RSi samples in the region of stretching vibrations of the Si-H and Si-D bonds are presented in Figure 7.19. In the case of hydrogen molecules, a single absorption band was observed at 2225 cm^{-1} (Figure 7.19a) (this band has previously been observed [15]). When D_2 molecules are used as a hydrogenating reagent, the IR spectrum of products has two lines with a comparable intensity at 1608.4 and 1626.4 cm^{-1} (Figure 7.19b). For HD molecules with a minor admixture of D_2, the IR spectrum in the region of Si-D vibrations is a superposition of three bands, two of which (a low-intensity doublet at 1608.4 and 1626.4 cm^{-1}) were also observed in the spectrum of the products of the treatment of RSi with D_2 molecules (see above). The third, high-intensity band is at 1617.5 cm^{-1}, almost exactly in the site between the first two bands (Figure 7.19b). In the region of stretching Si-H vibrations, the position of the absorption band and its width slightly depend on what isotope (H_2 or HD) was used for SC hydrogenation. Thus, absorption bands observed the IR spectrum are related to

Lam Research Ex. 1035 - Page 291
Lam Research Corp. v. Inpria Corp.
IPR2024-00033 - U.S. Patent No. 9,823,564

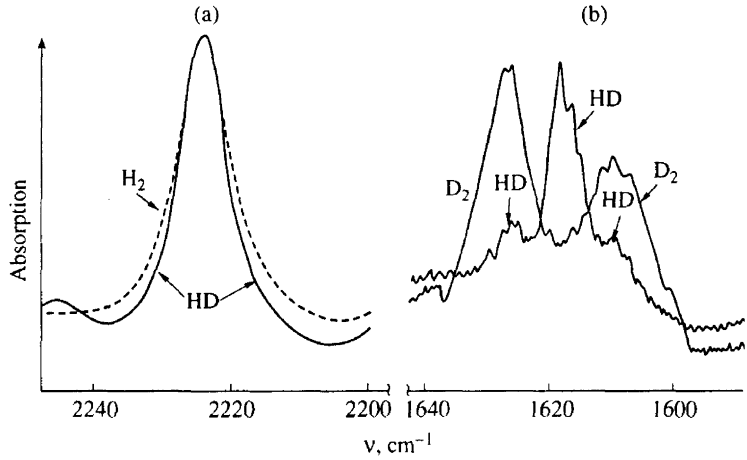


Fig. 7.19. IR spectra of hydrogenation products off SC stabilized on the SiO_2 surface by H_2, HD, D_2 molecules in the region of stretching vibrations of (a) Si-H and (b) Si-D bonds [54].

the $(\equiv Si\text{-}O)_2SiH_2$ (2224.8 cm^{-1}), $(\equiv Si\text{-}O)_2SiHD$ (2224.8 and 1617.5 cm^{-1}), and $(\equiv Si\text{-}O)_2SiD_2$ (1608.4 and 1626.4 cm^{-1}) groups, symmetric and antisymmetric vibrations of the SiD_2 group. For the SiH_2 group, the frequencies of symmetric and antisymmetric stretching vibrations are close, and the IR spectrum contains one band. Therefore, the problem on the structure of products formed during hydrogenation of the surface of RSi samples was solved only using hydrogen isotopes. These experimental findings were confirmed in Ref. [22] by quantum-chemical calculations.

The formation of dihydrosilane groups indicates that they are formed due to SCs hydrogenation:

$$(\equiv Si\text{-}O\text{-})_2Si: + H_2(D_2,\ HD) \Rightarrow (\equiv Si\text{-}O\text{-})_2SiH_2(D_2,\ HD).$$

The formation of the hydrogenation products can proceed following two mechanisms, free radical and molecular. In the presence of free radicals, the hydrogenation process occurs even at room temperature. Typically, the PCs stabilized at the surface of activated silica (MSi, RSi) initiate this process. The initiation of the radical process amounts to generating H(D) atoms through the interaction of the PCs with gaseous molecules, while the subsequent reactions of chain propagation and free-radical decay yield the end products (reaction heat (kcal/mol) are given in brackets):

$$(\equiv Si\text{-}O\text{-})_3Si^* + H_2(D_2) \Rightarrow (\equiv Si\text{-}O\text{-})_3Si\text{-}H(D) + H^*(D^*) + (4 \pm 2);$$

$$(\equiv Si\text{-}O\text{-})_2Si: + H^*(D^*) \Rightarrow (\equiv Si\text{-}O\text{-})_2Si^*\text{-}H(D) - (40 \pm 2);$$

Lam Research Ex. 1035 - Page 292
Lam Research Corp. v. Inpria Corp.
IPR2024-00033 - U.S. Patent No. 9,823,564

$$(\equiv \text{Si-O-})_2\text{Si}^*\text{-H(D)} + \text{H}_2(\text{D}_2) \Rightarrow (\equiv \text{Si-O-})_2\text{SiH}_2(\text{D}_2) + \text{H}^*(\text{D}^*) + (6 \pm 2);$$

$$(\equiv \text{Si-O-})_2\text{Si}^*\text{-H(D)} + \text{H}^*(\text{D}^*) \Rightarrow (\equiv \text{Si-O-})_2\text{SiH}_2(\text{D}_2) - (97 \pm 2).$$

The third reaction in the scheme is the rate-limiting step of this process. The corresponding activation energy is close to 12 kcal/mol [16]. The heat of the hydrogenation reaction is equal to $-(30 \pm 2)$ kcal/mol.

The hydrogenation products are thermally stable up to 750 K. With a further rise in temperature, the dihydrosilane groups begin to decay with the simultaneous quantitative recovery of the SC concentration and release of the corresponding amount of the H_2 molecules:

$$(\equiv \text{Si-O-})_2\text{SiH}_2(\text{D}_2,\ \text{HD}) \Rightarrow (\equiv \text{Si-O-})_2\text{Si}: + \text{H}_2(\text{D}_2,\ \text{HD}).$$

The activation energy for the decay of dihydrosilane groups is equal to (75 ± 3) kcal/mol. If the hydrogenation heat and the activation energy for their decay are known, one can estimate the activation energy for the molecular hydrogenation of SC. It is equal to ~45 kcal/mol. The bimolecular reaction with such activation energy can proceed only at elevated temperatures and hydrogen pressures.

9.3. PRODUCTS OF HIGH-TEMPERATURE HYDRATION OF RSi SAMPLES

The comparable number of $(\equiv\text{Si-O-})_2\text{Si} < \text{O}_2 > \text{Si}(\text{-O-Si}\equiv)_2$ groupings (SRs) are also stabilized at the surfaces of RSi samples in addition to SCs (see Table 7.1). Absorption bands in a silica IR transparency window at 888 and 908 cm^{-1} are connected with these groupings [3,4,72]. Thermal treatment of the RSi surface in 170 Torr of D_2, at which the SC hydration (up to 800 K) proceeds, in no way affects SRs. However, the occurrence of new processes was revealed as the treatment temperature increased. Both SCs and SRs are involved in these reactions. Figure 7.18b portrays the IR spectrum of reaction products after sample's warming up at 1400 K in 170 Torr of D_2 (sample cooling down to room temperature was conducted in a deuterium atmosphere). Thermo chemical treatment brought about the complete decay of SCs (through an optical control) and SRs (through the disappearance of bands in the IR spectrum at 888 and 908 cm^{-1}). Terminal $\equiv$Si-D groups (absorption band at 1670 cm^{-1}) and a small number of hydroxyl terminal $\equiv$SiO-D groupings (absorption band at 2763 cm^{-1}) took the part of major reaction products.

Turning back to the experiment in which high-temperature hydration brought about the "decay" of both the SCs and SRs, and relying on the experimental evidences from SR hydration we succeeded in separating the

Lam Research Ex. 1035 - Page 293
Lam Research Corp. v. Inpria Corp.
IPR2024-00033 - U.S. Patent No. 9,823,564

products associated with SC hydration. The terminal ≡Si-D groupings with an absorption band at 1670 cm^{-1} turned out to be the major product of the reaction. Vacuum pyrolysis of a hydrated RSi sample was accompanied by the D_2 molecules desorption and the reduction of SR (completely) and SC (completely) after warming up at $T = 1400$ K. Thus, the high-temperature SC hydration and high-temperature pyrolysis of their hydration products constitute the forward and reverse processes involving SCs, D_2 molecules, and ≡Si-D groups. In the course of producing RSi, the formation of SCs begins in the stage of pyrolysis of ≡Si-D bonds. Figure 7.20 illustrates the dependence between the amount of hydrogen molecules released from the sample (results of volumetric measurements) and the number of SCs formed in the process (results of optical measurements).

Hence, these processes go on in parallel, although the number of formed SCs makes up only the part of dissociated Si-H groups. Consequently, there exist another "decay" channels for silyl radicals. Most likely they are related to the formation of Si-C bonds in the carbide-like fragments which have been discovered in RSi samples (see Section 11.3). Let us estimate here the activation energy of the reaction of breaking Si-H bonds. This will permit us to judge the relevant reaction mechanism. Homolytic breaking of the ≡Si-H(D) bond with the formation of H(D) atom and ≡Si* radical may serve as one of the reaction channels. The Si-D(H) bond strength ranges

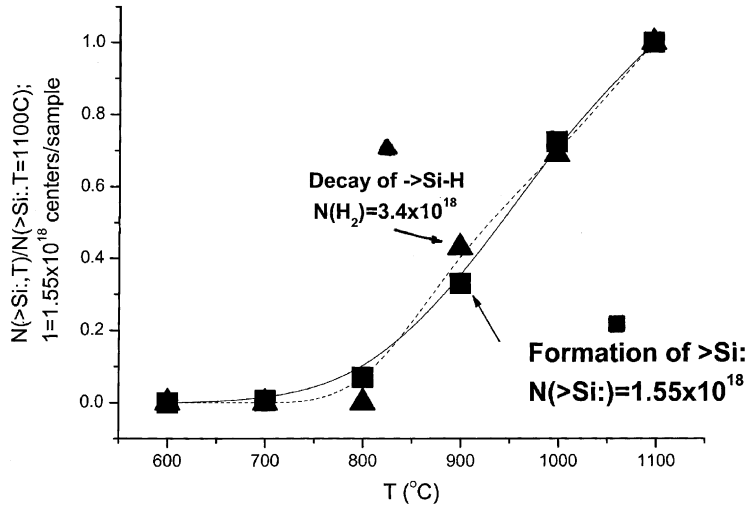


Fig. 7.20. The temperature dependencies of the number of hydrogen molecules released from the sample as a result of the Si-H groups destruction and the number of SCs formed in the process.

Lam Research Ex. 1035 - Page 294
Lam Research Corp. v. Inpria Corp.
IPR2024-00033 - U.S. Patent No. 9,823,564

95–100 kcal/mol [16]. The value of a pre-exponential factor for the reaction of bond breaking with the H-atom formation may be estimated as $10^{16}\,sec^{-1}$ [76]. Therefore, the rate constant of homolytic breaking of this bond at $T = 1100\,K$ (i.e., the temperature at which the Si-H(D) bond breaking starts) will amount to $(1.3–13) \times 10^{-4}\,sec^{-1}$, while the bond breaking lifetime will range 10–100 min. These estimates seem to be reasonable. The SC formation will be considered as a disproportionate reaction of two silicon-centered radicals (see Section 9). Then the reaction schemes for the forward (formation of SCs) and reverse (their transformation to Si-H groups) processes can be given as follows:

$$(\equiv \text{Si-O-})_3\text{Si-H} \Rightarrow (\equiv \text{Si-O-})_3\text{Si}^* + \text{H}^*;\ (\equiv \text{Si-O-})_3\text{Si-H} + \text{H}^* \Rightarrow (\equiv \text{Si-O-})_3\text{Si}^* + \text{H}_2;$$

$$(\equiv \text{Si-O-})_3\text{Si}^* + {}^*\text{Si}(\text{-O-Si} \equiv)_3 \Rightarrow (\equiv \textit{Si-O-})_2\textit{Si}: + (\equiv \text{Si-O-})\text{Si}(\text{-O-Si} \equiv)_3 - (63 \pm 4)\ \textit{kcal/mol}.$$

$$(\equiv \text{Si-O-})_2\text{Si}: + (\equiv \text{Si-O-})\text{Si}(\text{-O-Si} \equiv)_3 \Rightarrow 2 \times (\equiv \text{Si-O-})_3\text{Si}^*;$$

$$(\equiv \text{Si-O-})_3\text{Si}^* + \text{H}_2 \Rightarrow (\equiv \text{Si-O-})_3\text{Si-H} + \text{H}^*;\ (\equiv \text{Si-O-})_3\text{Si}^* + \text{H}^* \Rightarrow (\equiv \text{Si-O-})_3\text{Si-H}.$$

The magnitude of the reaction thermal effect, referred to in the first scheme, was obtained by quantum-chemical computations.

9.4. Optical Parameters of SC

Silylene sites have the optical absorption band with a maximum at 5.2–5.3 eV and two luminescence bands with maxima at 4.35 eV (singlet–singlet transition $S_1 \rightarrow X$) and 2.73 eV (triplet–singlet transition $T_1 \rightarrow X$), both of which being excited in the absorption band of the site (transition $X \rightarrow S_1$) [2,19,37,48,52,71]. The lifetimes of these states at 300 K are equal to 5.1 nsec and 19 msec, respectively [19,42]. The Stokes shifts are 0.8 ± 0.1 eV for the singlet–singlet transition and ~0.5 eV for the triplet–singlet transition ($X \rightarrow T_1$) [64] (estimated on the basis of experimental data).

The F_2Si: [77] and $(R\text{-}O\text{-})_2Si$: [78] molecules in which a silicon atom binds to electronegative substituents (F, O), as in SC, possess similar optical properties. The S_1 and T_1 states of SC are related to the transfer of one of the electrons of the lone pair of the bicoordinated silicon atom ($(MO)_1$ is mainly built of 3s and $3p_y$ AOs of silicon, the y-axis is directed along the

Lam Research Ex. 1035 - Page 295
Lam Research Corp. v. Inpria Corp.
IPR2024-00033 - U.S. Patent No. 9,823,564

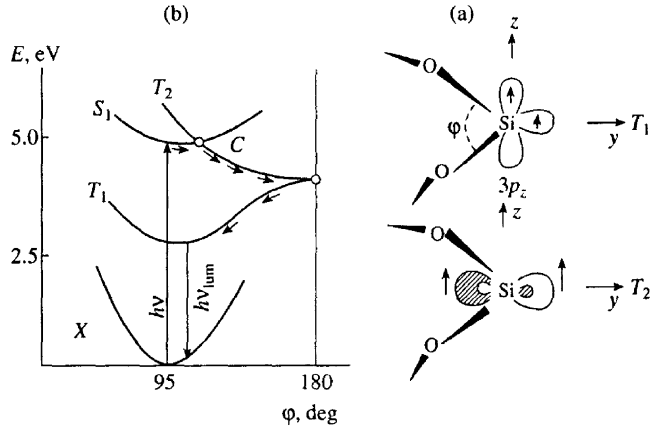


Fig. 7.21. (a) Scheme of triplet states of SC (T_1 and T_2) and (b) dependencies of energies of the ground (X) and lowest electron-excited states (S_1, T_1, and T_2) on the value of bond angle OSiO.

bisector of the OSiO angle) to its vacant $3p_z$ AO ($(MO)_2$, and the z-axis is perpendicular to the plane of OSiO atoms; Figure 7.21b). Under these conditions, unpaired electrons occupy structurally similar molecular orbitals. The energies of the S_1 and T_1 states differ by 1.5–2.0 eV and change in parallel with a change in the bond OSiO angle; i.e., the corresponding terms do not intersect [79].

9.5. The Mechanism of Singlet–Triplet Conversion of SC

The transition of electron-excited SC to the ground state is mainly associated with radiative transitions [42,46,71]. Depending on temperature, the main mechanism of luminescence can be the singlet–singlet (low) or triplet–singlet transition (elevated temperatures). Thus, SC is characterized by a high probability of intercombinational system conversion ($S_1 \rightarrow T_1$). It can occur if the system has an additional term that relates the S_1 and T_1 states; i.e., in certain points of the configurational space of the system, its overlap or quasi-overlap with them takes place. The sites of the silylene type have this term (see Figure 7.21a). According to the results of quantum-chemical calculations, SC has an electron-excited triplet state T_2, which differs from the T_1 state in that one of the electrons of the lone pair of the silicon atom in it is transferred not to its $3p_z$ AO, but to $(MO)_3$, to which 3s and $3p_y$ AOs of silicon mainly contribute as to $(MO)_1$ (see Figure 7.21b). The T_2 term intersects the S_1 term near the energy minimum of the latter [79]. The energy of the T_2 state monotonically decreases with increasing (opening) the bond

Lam Research Ex. 1035 - Page 296
Lam Research Corp. v. Inpria Corp.
IPR2024-00033 - U.S. Patent No. 9,823,564

angle at the bicoordinated silicon atom and has a minimum energy for the linear (or close to linear) arrangement of OSiO atoms.

The adiabatic transition from the T_2 term to the T_1 term is possible in this region of the configurational space. This point is localized in the saddle, and the T_2 and T_1 states in it have the same energies. The energy of the system further decreases as the OSiO angle decreases, but oxygen and silicon atoms are shifted in the plane perpendicular to that in which they moved during the relaxation of the T_2 state. The T_1 state relaxes to its equilibrium geometry, and luminescence transition then occurs from this state. The experimental temperature dependence of the ratio of intensities for singlet and triplet luminescence is determined by the value of the activation barrier for the $S_1 \rightarrow T_1$ transition, which is $\sim$0.1 eV [42].

9.6. SILANONE GROUPS ($\equiv$Si-O)$_2$Si = O ON SILICA SURFACE

The silanone groups ($\equiv$Si-O)$_2$Si = O were experimentally detected on the surface of mechanically activated silica in Ref. [52]. Most likely, this was the first experimental evidence for the stabilization of silanone groups in the silica structure. Then the method for their preparation from SC on the surface of thermo chemically activated silica (RSi) was developed [18,79,80] (see reactions 8–10 in Table 7.3).

The main proof of their existence is based on the following findings: (1) the band of stretching vibrations of the Si = O bond in the silanone group was detected at (1306 ± 1) cm^{-1} by IR spectroscopy [81] (for low-molecular silanones containing electronegative substituents (O, F) at a silicon atom; this band is localized in the 1260–1310 cm^{-1} range [82,83]); (2) the structure of paramagnetic complexes that are formed during accepting low-molecular radicals (H, D, CH_3, CD_3, C_2H_5, cyclo-C_3H_5) by these groups was identified in Refs. [51,52,84] (Table 7.11); and (3) the products of the reaction of silanone groups with H_2 [85], CO_2, N_2O, HC = CH [81,86], and $CH_2 = CH_2$ [87] molecules detected by IR spectroscopy were identified (Table 7.10).

The SGs at the silica surface are responsible for the IR band near 1300 cm^{-1}. The stretching bands of the Si = O bond in the molecules whose silicon atom is bonded to the electronegative substituent (O, F) are seen precisely in this region. The stretching frequency of the Si = O bond in the $F_2Si = O$ molecule was determined experimentally: 1309 cm^{-1} for $F_2Si = {}^{16}O$ and 1276 cm^{-1} for $F_2Si = {}^{18}O$ [88]. The differential IR spectrum corresponding to the transformation of the silanone groups (room temperature)

$$(\equiv \text{Si-O})_2\text{Si} = \text{O} \; + \; \text{O} = \text{N} \equiv \text{N} \; \Rightarrow \; (\equiv \text{Si-O})_2\text{Si} < \text{O}_2\text{N}_2$$

Lam Research Ex. 1035 - Page 297
Lam Research Corp. v. Inpria Corp.
IPR2024-00033 - U.S. Patent No. 9,823,564

Table 7.11. Chemical reactions involving $>Si=O$ groups

1. $(\equiv Si\text{-}O)_2Si=O + {}^{\bullet}H({}^{\bullet}D) \Rightarrow (\equiv Si\text{-}O)_2Si^{\bullet}\text{-}O\text{-}H(D)$
2. $(\equiv Si\text{-}O)_2Si=O + {}^{\bullet}CH_3 \Rightarrow (\equiv Si\text{-}O)_2Si(CH_3)(O^{\bullet}) \Rightarrow (\equiv Si\text{-}O)_2Si(CH_2{}^{\bullet})(OH)$
3. $(\equiv Si\text{-}O)_2Si=O + {}^{\bullet}C_2H_5 \Rightarrow (\equiv Si\text{-}O)_2Si(CH_2\text{-}CH_2{}^{\bullet})(OH)$
4. $(\equiv Si\text{-}O)_2Si=O + c\text{-}({}^{\bullet}CH\text{-}CH_2) \Rightarrow (\equiv Si\text{-}O)_2Si(c\text{-}(CH\text{-}CH^{\bullet}))(OH)$
   CH_2 CH_2
5. $(\equiv Si\text{-}O)_2Si=O + H_2 \Rightarrow (\equiv Si\text{-}O)_2Si(H)(OH)$
6. $(\equiv Si\text{-}O)_2Si=O + CO_2 \underset{\Leftarrow 550K}{\overset{300K \Rightarrow}{\Leftrightarrow}} (\equiv Si\text{-}O)_2Si{<}\,{>}C{=}O$ (O)
7. $(\equiv Si\text{-}O)_2Si=O + N_2O \underset{\Leftarrow 420K}{\overset{280K \Rightarrow}{\Leftrightarrow}} \equiv Si\text{-}O)_2Si{<}$ (O-N ‖ O-N)
8. $(\equiv Si\text{-}O)_2Si=O + HC{\equiv}CH \Rightarrow (\equiv Si\text{-}O)_2Si{<}$ (CH ‖ O) $>CH$
9. $(\equiv Si\text{-}O)_2Si=O + H_2C{=}CH_2 \Rightarrow (\equiv Si\text{-}O)_2Si <$ (CH_2 ‖ O) $> CH_2$

is shown in Figure 7.22a,. The band at 1448 cm^{-1} belongs to the $(\equiv Si\text{-}O)_2Si{<}O_2N_2$ group, and the band at (1306 ± 1) cm^{-1} at the wing of an intense fundamental absorption of silica belongs to the $>Si=O$ group. For the samples with a high concentration of silanone groups, weak band at (2602 ± 1) cm^{-1} (indicated by arrows in Figure 7.22b) in the range 2050–4000 cm^{-1} disappear in the course of this reaction together with the band at 1306 cm^{-1}. The IR spectrum of sample (2), in which, according to the preparation method, the silanone groups with various isotope composition $>Si=^{16}O + >Si=^{18}O$ are expected to appear, is shown in Figure 7.22(c. The silanone groups were obtained by using the ^{18}O-enriched molecular oxygen. In this case, a new band was recorded at 2542 cm^{-1} in addition to the band at 2602 cm^{-1}.

The observed weak bands at 2602 and 2542 cm^{-1} are the first overtones of the stretching $^{28}Si=^{16,18}O$ vibrations in the silanone group. This is indicated by (1) the fact that the bands at 1306 and 2602 cm^{-1} with an integrated-intensity

Lam Research Ex. 1035 - Page 298
Lam Research Corp. v. Inpria Corp.
IPR2024-00033 - U.S. Patent No. 9,823,564

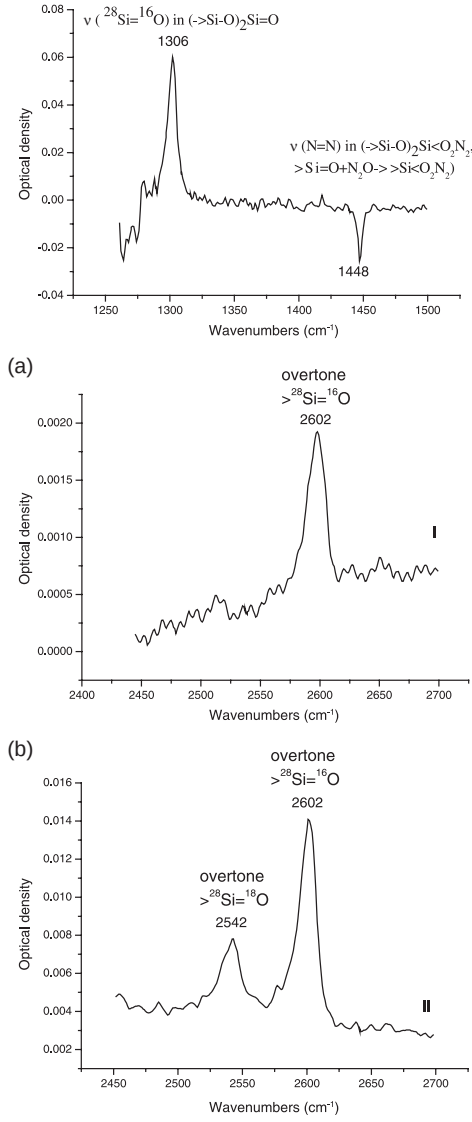


Fig. 7.22. Difference IR spectrum (a) that characterizes the transformation $(\equiv Si\text{-}O)_2Si=O + N_2O \blacktriangleright (\equiv Si\text{-}O)_2Si<O_2N_2$ on the surface of reactive silica, and absorption bands of the first overtone of the Si = O bond stretching vibration in the $(\equiv Si\text{-}O)_2Si=O$ group (b) with different isotopic compositions: $(\equiv Si\text{-}O)_2^{28}Si = {}^{16}O$ (sample I), and $(\equiv Si\text{-}O)_2^{28}Si = {}^{16}O + (\equiv Si\text{-}O)_2^{28}Si = {}^{18}O$ (sample II).

Lam Research Ex. 1035 - Page 299
Lam Research Corp. v. Inpria Corp.
IPR2024-00033 - U.S. Patent No. 9,823,564

($\int D(\nu)d\nu$) ratio of $\sim 1/(450 \pm 100)$ appear and disappear synchronously; (2) the proximity of the transition frequency to a doubled Si = O stretching frequency; and (3) by a value of $(30 \pm 1)\ cm^{-1}$ ($\cong 1/2(2602-2542)\ cm^{-1}$) typical of the isotope effect ($^{16}O \Leftrightarrow {}^{18}O$) in the silanone group [88].

From the data obtained, the Si = O stretching frequency in the silanone group $>{}^{28}Si = {}^{18}O$ at the silica surface can be estimated at $(1276 \pm 2)\ cm^{-1}$. The band at $1306\ cm^{-1}$ is positioned at the wing of the intense fundamental absorption of silica. With a shift of $30\ cm^{-1}$, the $>Si = {}^{18}O$ stretching band is brought into the region where it is hard to record for the samples used. That is why the fundamental absorption band of the silanone group $>Si = {}^{18}O$ was not observed experimentally in Ref. [81].

Quantum-chemical calculations suggest (*cf.* Section 4.3) that the Si = O bond strength in the $X_2Si = O$ molecules decreases with increasing the electronegativity of substituent X. At the same time, the Si = O stretching frequency increases in this sequence. For the $H_2Si = O$ and $F_2Si = O$ molecules, the Si = O bond strength is equal to 146 and 123 kcal/mol, respectively, while the vibration frequencies are 1247 and $1309\ cm^{-1}$. This is one of the rare cases where two molecular characteristics change in opposite directions.

The optical absorption band [52,81] with a maximum at (5.65 ± 0.1) eV and a width at the half-height of 0.9 eV was assigned to silanone groups. The extinction coefficient for the absorption band at a maximum is $\varepsilon(220\ nm) = (3 \pm 0.5) \times 10^{-18}\ cm^2$/molecule, and the oscillator force was $f = 0.045 \pm 0.01$. According to quantum-chemical calculations (TD/DFT) the energies of lowest (intensive) "vertical" transitions in excited states of $F_2Si = O$ molecule are equal to 5.25 eV (excited state $^1B_2$ ($n \rightarrow \sigma^*$), $f = 0.025$), and 5.7 eV (excited state $^1B_1$ ($\sigma \rightarrow \pi^*$), $f = 0.044$) in satisfactory agreement with experimental results.

Unlike the carbonyl group, the silanone group is characterized by a high reactivity, in particular, it is dimerized or oligomerized at a very low temperature. Since it is difficult to obtain and stabilize silanone groups, the experimental data on their reactivity and, especially, the quantitative characteristics of the corresponding processes are limited. Silanone groups are usually assumed to participate in chemical processes as short-lived intermediates. Silanone groups stabilized on the silica surface are thermally stable (up to 850 K) and accessible to gas-phase molecules. This makes it possible to study their reactivity toward various compounds. Table 7.11 presents some examples.

All bimolecular processes studied, except reaction 5, have low activation energies (<4.5 kcal/mol, the reactions were controlled by diffusion). The rate constant of reaction 5 in the Arrhenius form is as follows:

$$k = 1.2 \times 10^{-12} \exp(-13.4(\text{kcal/mol})/RT)\text{cm}^3/\text{molecule sec.}$$

Lam Research Ex. 1035 - Page 300
Lam Research Corp. v. Inpria Corp.
IPR2024-00033 - U.S. Patent No. 9,823,564

It was established that the reaction of the methyl radical with the silanone group occurs via two steps: first it adds to the silicon atom to form the oxy radical, and then the radical is isomerized via a shift of the H atom to oxygen (reaction 2 in Table 7.11). The estimated activation energy of this monomolecular reaction was 16 kcal/mol. This suggests that the addition of other alkyl radicals (reactions 3 and 4) to the silanone groups also occurs via steps. The mechanism of the addition of an H(D) atom to the silanone group remains unclear.

Silanone groups easily undergo the addition to unsaturated molecules (reactions 6–9) to form the corresponding cyclic structures [86,87]. According to the results of quantum-chemical calculations, in these reactions, comparatively stable (~10 kcal/mol) intermolecular complexes are formed, which then yield the final products. The silicon atom of the silanone group mainly participates in complex formation.

9.7. DIOXASILYRANE GROUPS ($(\equiv Si\text{-}O)_2Si<O_2$)

The SCs at the silica surface readily react with molecular oxygen. This reaction is convenient to monitor optically (Figure 7.23a). Oxygen chemisorption is accompanied by the disappearance of the optical absorption band of SCs. The adsorption of one molecule leads to the decay of one SC. Quantum-chemical calculations show that the three-member cyclic symmetric structure (Figure 7.24) is the most stable product of oxygen addition to the SC [74]:

$$(\equiv Si\text{-}O)_2Si: \; + O_2\ (^3\Sigma) \;\Rightarrow\; (\equiv Si\text{-}O)_2Si<O_2.$$

The resulting ground state of the group is a singlet. A characteristic feature of the groups of this type is the presence of a weak O-O bond, whose length, according to the calculations, exceeds the O-O bond length in the peroxide compounds and equals 1.64 Å. Synchronously with the SC decay, two absorption bands appear near 3 and 5 eV (Figure 7.25) and become increasingly intense in the optical spectrum of the sample. The electronic structure of the excited states responsible for the absorption bands at the center near 3 and 5 eV is schematically presented in Figure 7.25b, together with the calculated characteristics of these bands. They are caused by the electronic transition from the π^* or σ MO of the molecule to the σ^* antibonding MO between the ring oxygen atoms.

The rate constant of bimolecular reaction of the oxidation of SC is [18]: $k = (1.8 \pm 0.2) \times 10^{-13} \exp(-(8.0 \pm 0.3)\ (\text{kcal/mol})/RT)\ \text{cm}^3/\text{molecule/sec}$.

The fact that the reaction product occurs in the singlet state in the reaction with the triplet oxygen molecule signifies that the intermediate

Lam Research Ex. 1035 - Page 301
Lam Research Corp. v. Inpria Corp.
IPR2024-00033 - U.S. Patent No. 9,823,564

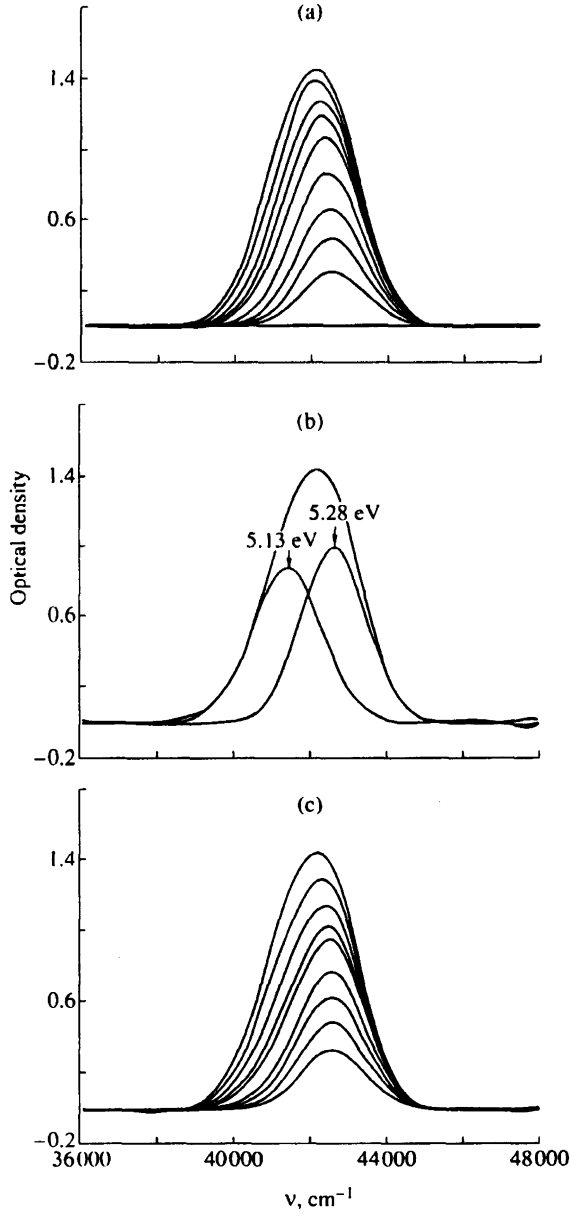


Fig. 7.23. Optical absorption spectra of SC: (a) their changes during reaction of SC with oxygen (a decrease in the intensity correspond to an increase in the reaction time); (b) bimodal nature of the optical absorption spectrum of SC; and (c) the result of modeling of the oxidation of SC.

Lam Research Ex. 1035 - Page 302
Lam Research Corp. v. Inpria Corp.
IPR2024-00033 - U.S. Patent No. 9,823,564

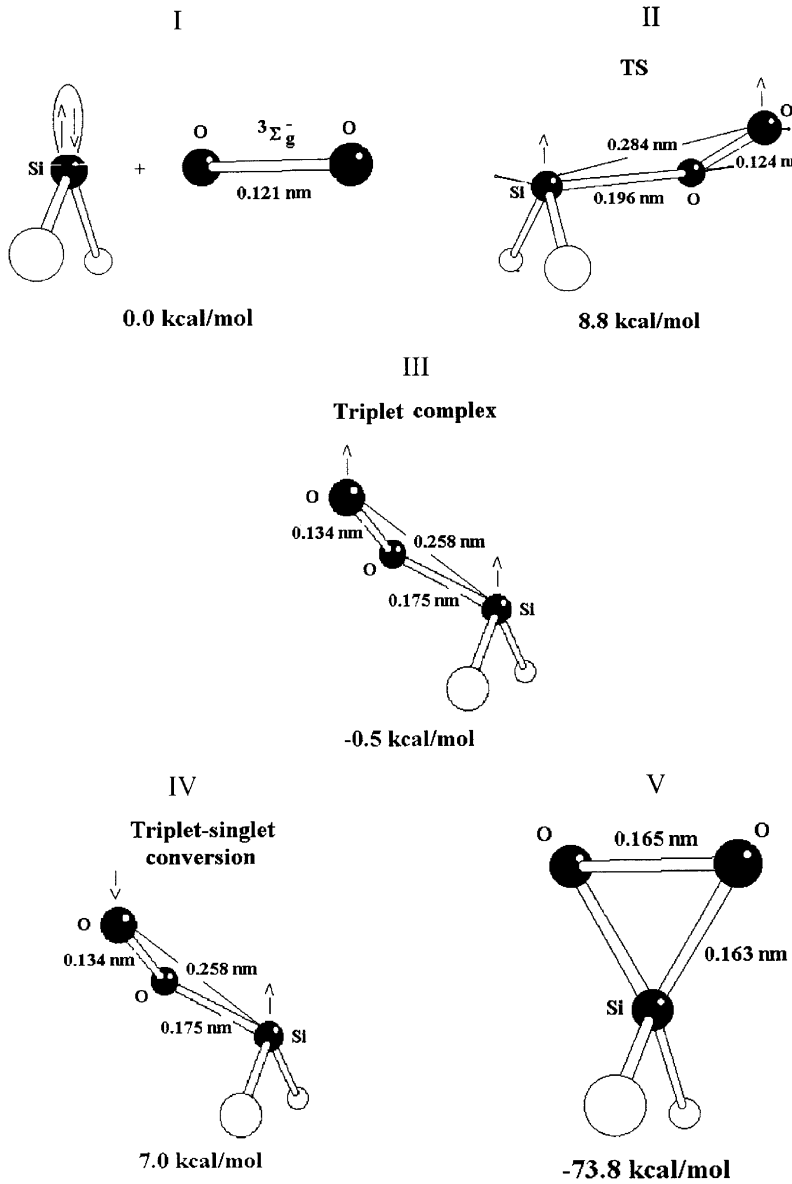


Fig. 7.24. The stage mechanism of formation of DOSG from SC and triplet oxygen molecule.

Lam Research Ex. 1035 - Page 303
Lam Research Corp. v. Inpria Corp.
IPR2024-00033 - U.S. Patent No. 9,823,564

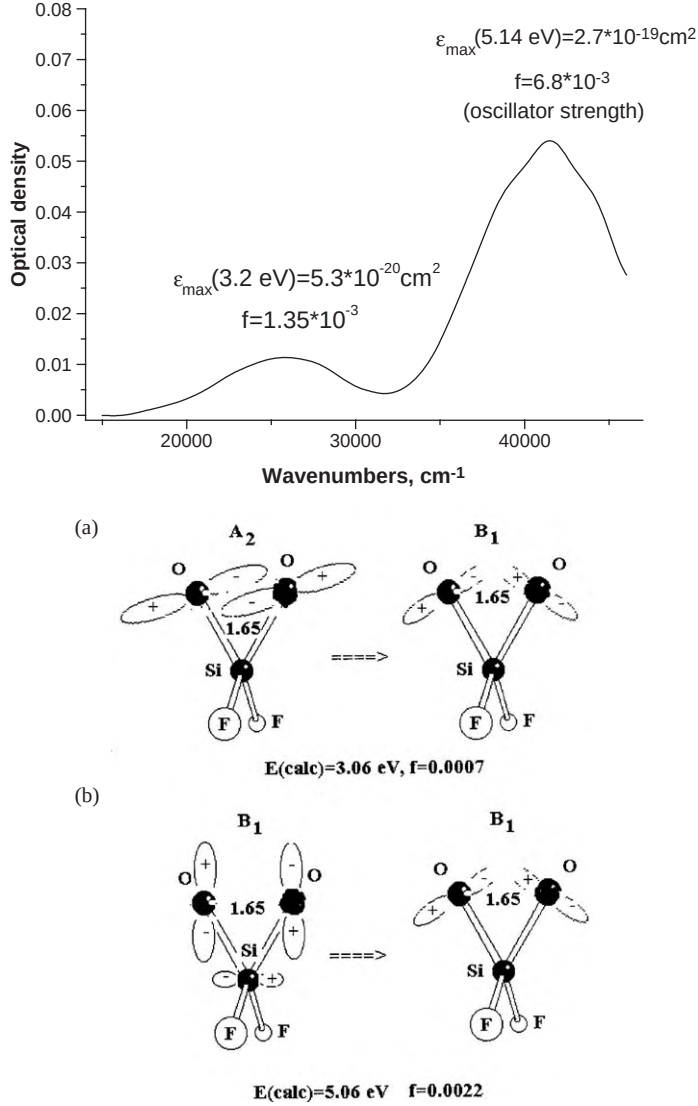


Fig. 7.25. The optical properties of DOSG. (a) The optical absorption bands; (b) the electronic nature of the excited states responsible for the absorption bands of the center near 3 and 5 eV (see text for detail).

Lam Research Ex. 1035 - Page 304
Lam Research Corp. v. Inpria Corp.
IPR2024-00033 - U.S. Patent No. 9,823,564

undergoes triplet–singlet conversion at a certain reaction step. To elucidate the DOSG-formation mechanism, the energy characteristics for the formation of the $F_2Si{<}O_2$ molecule from $F_2Si{:}+O_2$ ($^3\sum$) were calculated quantum-chemically. The optimized structure of a complex formed by the silylene center and a triplet oxygen molecule is shown in Figure 7.24.

The TS with an activation-barrier height of 8.8 kcal/mol separates two triplet states, namely, the initial state and the state of a triplet product of oxygen-molecule addition to the silylene center. The heat of this reaction is small (~1 kcal/mol). Two unpaired electrons in this triplet structure are distanced from each other; one of them is localized on the silicon atom and the other, on the terminal oxygen atom at a distance of ~3 Å. As a result of the subsequent triplet–singlet conversion, the intermediate occurs in the singlet state and relaxes to its ground state (Figure 7.24). In this case, the activation energy for the DOSG formation is the activation energy for the formation of a triplet complex between the oxygen molecule and the SC.

The available experimental data to estimate the heat of the addition reaction between the oxygen molecule and the silylene center (see also reaction 10 in Table 7.4) is used here:

$$>Si:+O_2(^3\Sigma) \Rightarrow >Si:+2O(^3P)+119\ \text{kcal/mol}$$
$$\Rightarrow >Si=O+O(^3P)+[-(130\pm2)+119]\ \text{kcal/mol};$$

$$\Rightarrow >Si{<}O_2 + [(130\pm2)+119-65]\ \text{kcal/mol}$$
$$= >Si{<}O_2-(75\pm3)\ \text{kcal/mol}.$$

In compliance with the experiment, the abstraction of oxygen atom from the $>Si{<}O_2$ group (65 kcal/mol; Table 7.4) requires lesser energy than does the abstraction of the oxygen molecule. A close value for the reaction heat (ΔH (0 K)) has been obtained for a model reaction:

$$F_2Si: + O_2(^3\Sigma) \Rightarrow F_2Si{<}O_2 - 73.6\,\text{kcal/mol}.$$

The same groups can be prepared by a different procedure through the oxidation of the silanone groups with the protoxide molecules [73]:

$$(\equiv Si\text{-}O)_2Si=O + N_2O \Rightarrow (\equiv Si{<}O)_2Si{<}\ O_2 + N_2(g).$$

Below, it is presented the reaction heat calculated for two DOSG reactions that can elucidate the character of the O-O bonding in this group. In the triplet state, the distance between the oxygen atoms in the $F_2Si(O^*)(O^*)$ molecule increases to 2.5 Å; i.e., the chemical bond between these atoms is disrupted. The G2(MP2) energy of the triplet state proved to be

Lam Research Ex. 1035 - Page 305
Lam Research Corp. v. Inpria Corp.
IPR2024-00033 - U.S. Patent No. 9,823,564

24.6 kcal/mol higher than the energy of the ground singlet state of the molecule. Another estimate is based on the calculations of the heat of DOSG hydrogenation:

$$F_2Si{<}O_2 \; + \; {}^*H \; \Rightarrow \; F_2Si(OH)(O^*) \; - \; 106\,\text{kcal/mol};$$

$$F_2Si(OH)(O^*) \; + \; {}^*H \; \Rightarrow \; F_2Si(OH)(OH) \; - \; 124.3\,\text{kcal/mol}.$$

According to the quantum-chemical calculations, the O-H bond strength in the F_3Si-O-H molecule is 128 kcal/mol. The heat of the first reaction can be represented as the sum of two contributions coming from the O-O bond rupture and from the addition of a hydrogen atom to one of the oxy radicals. Since the second value cannot exceed 128 kcal/mol, the ring O-O-bond "strength" thus obtained is $\leq$22 kcal/mol.

The energy of the lowest triplet state of the dioxasilyrane group in which the bond between oxygen atoms of the cycle is broken is only 1 eV higher than that of the ground state [74]. The presence of a weakened O-O bond and the low-lying electron-excited (triplet and singlet) states of the group are indicative of the enhanced DOSG reactivity. In Table 7.12, the pathways of the chemical processes involving this group are shown.

(1) The formation of geminal silanol groups. The hydrogenation of DOSG occurs under rather mild conditions [15,89]. The IR spectra of the hydrogenation products (H_2 and D_2) in the region of the stretching vibrations of O-H and O-D (no other changes were observed in the spectral region from 2000 to 4000 cm^{-1}) are presented in Figure 7.12. Dashed lines in the same figures indicate the absorption bands of isolated terminal hydroxyl groups on the silica surface. The low-frequency shift of the bands indicates that they belong to geminal silanol groups [20], and the overall process of the formation of the hydrogenation products can be described by the following equation:

$$(\equiv \text{Si-O})_2Si{<}O_2 + H_2(D_2) \; \Rightarrow \; (\equiv \text{Si-O})_2Si{<}(OH(D))_2.$$

The surface of silica samples on which mostly geminal silanol groups are stabilized can be prepared by this method. This is convenient for the quantitative study of their physico-chemical properties and reactivity.

The frequencies of the stretching O-H vibrations of terminal and geminal surface silanone groups with different isotopic compositions [89] are presented in Table 7.13.

(2) The reaction of DOSG with CO molecules results in the formation of monodentate carbonate structures detected by IR spectroscopy [15,18] (reaction 1 in Table 7.12). A similar product is formed when

Lam Research Ex. 1035 - Page 306
Lam Research Corp. v. Inpria Corp.
IPR2024-00033 - U.S. Patent No. 9,823,564

Table 7.12. Directions of chemical processes involving $>Si<O_2$ groups

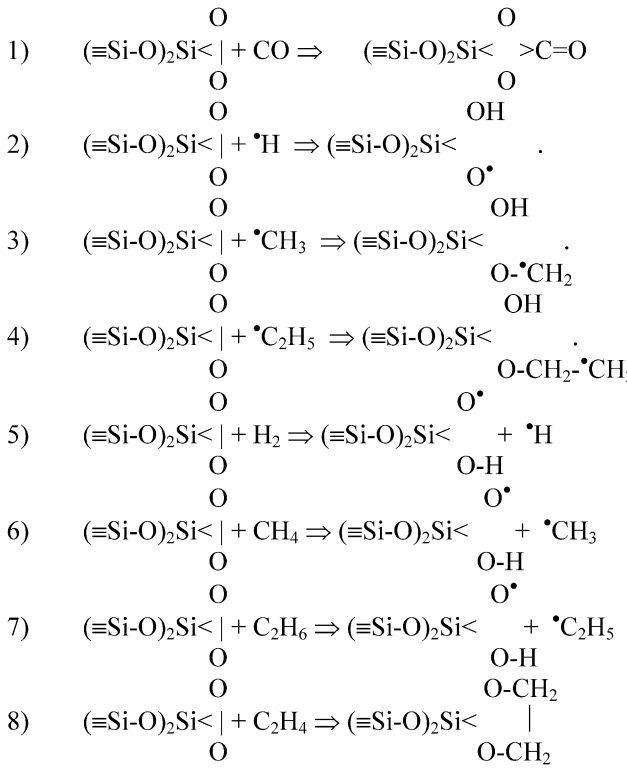


Table 7.13. The frequencies of straight vibrations of the terminal and geminal hydroxyls on silica surface and their isotopic shifts [80, 89]

The structure of hydroxyls	The isotopic shifts of the frequencies of straight vibrations of hydroxyls (cm^{-1})
1. $(\equiv Si\text{-}O)_3Si\text{-}^{16}O\text{-}H(D)$	3748.7 (2763.4)
2. $(\equiv Si\text{-}O)_3Si\text{-}^{18}O\text{-}H(D)$	3736.6 (2746.3)
3. $(\equiv Si\text{-}O)_2HSi\text{-}^{16}O\text{-}H$ $^{16}O\text{-}H(D)$	3741
4. $(\equiv Si\text{-}O)_2Si<$ $^{16}O\text{-}H(D)$ $^{18}O\text{-}H(D)$	3746.4 (2762.0)
5. $(\equiv Si\text{-}O)_2Si<$ $^{18}O\text{-}H(D)$	3734.3 (2744.6)

Lam Research Ex. 1035 - Page 307
Lam Research Corp. v. Inpria Corp.
IPR2024-00033 - U.S. Patent No. 9,823,564

CO_2 undergoes the addition to a silanone group (reaction 7 in Table 7.11) [86,87].

(3) DOSGs are efficient acceptors of low-molecular free radicals [51,73] (reactions 2–4) in Table 7.12). The formation of the corresponding products occurs, most likely, in two steps (except the H atom). The low-molecular radical first adds to one of the oxygen atoms of the cycle, which leads to the cleavage of the O-O bond and the formation of the oxy radical:

$$(\equiv \text{Si-O})_2\text{Si}{<}\text{O}_2 \; + \; {}^{\bullet}r\text{-H} \;\Rightarrow\; (\equiv \text{Si-O})_2\text{Si}\;(\text{O}*)(\text{O-}r\text{-H}),$$

followed by the intramolecular isomerization of the radical complex

$$(\equiv \text{Si-O})_2\text{Si}(\text{O}*)(\text{O-}r\text{-H}) \;\Rightarrow\; (\equiv \text{Si-O})_2\text{Si}(\text{O-H})(\text{O-}r*).$$

The reactions occur at high rates at already 77 K and, hence, their activation energies are close to zero.

The simple procedure for the preparation of the high concentrations of DOSG on the silica surface, their high thermal stability (up to 600 K), and accessibility for molecules from the environment make it possible to study their reactivity toward various compounds.

(4) The ability to generate free radicals in reactions with the molecules of saturated hydrocarbons (CH_4 and C_2H_6) [90] (reactions 6 and 7 in Table 7.12) is an interesting feature of DOSGs, which is due to the presence of a weakened O-O bond in their structure. The reaction of the low-molecular r^* radical with another surface group results in the stabilization of the free radical state (reactions 3 and 4 in Table 7.12). A hydrogen molecule reacts with DOSG via the same mechanism, as in the case of methane and ethane, and this is accompanied by the formation of free radical sites, including atomic hydrogen (reaction 5 in Table 7.12). However, in the case of hydrogen (reaction 2 in Table 7.12), a highly active oxy radical is regenerated, which continues the free radical process (reaction 2), resulting in the hydrogenation of DOSG and the formation of geminal silanol groups. In the case of saturated hydrocarbons (methane and ethane) in a similar process (reactions 6 and 7), grafted hydrocarbon radicals are formed. Their reactivity in reactions with saturated hydrocarbons is much lower than that of oxy radicals. As a result, in the reactions with methane and ethane, free radical sites are stabilized in much higher concentrations on the surface of the oxidized sample than in the case of hydrogen. At the initial stage of these reactions we can obtain $2{>}\text{Si}(r^*)(\text{OH})$ radicals from every 3 DOSG. As a result, the full concentration of free radicals on the silica surface can be increased more than 10 times in this process (see Section 11.3).

Lam Research Ex. 1035 - Page 308
Lam Research Corp. v. Inpria Corp.
IPR2024-00033 - U.S. Patent No. 9,823,564

The rate constants of the reaction of DOSG with methane (250–350 K) and ethane (210–350 K) molecules in the Arrhenius form are [90]:

$$k = (2.2 \pm 0.5) \times 10^{-13} \times \exp(-(9.5 \pm 0.5)\,(\text{kcal/mol})/\text{RT})\ \text{cm}^3/\text{molecule/sec};$$

$$k = (0.9 \pm 0.3) \times 10^{-14} \times \exp(-(4.3 \pm 0.2)\,(\text{kcal/mol})/\text{RT})\ \text{cm}^3/\text{molecule/sec}.$$

Thus, the activation energies of these reactions are low.

DOSGs also react with C_2H_4, C_2H_4O, and CO molecules (300 K); however, these processes are not accompanied by the formation of free radical products [90].

The formation of paramagnetic sites in the reactions of DOSGs with saturated hydrocarbon molecules indicate that, in one of the steps, the system is transformed into the biradical state. The O-O bond of the cycle is the most probable precursor for formation reactive in such processes. It can be assumed that, in both cases, the process occurs through the biradical state. However, in the first case, the low-molecular radical escapes from the reaction zone through the gas phase, and paramagnetic sites are formed. In the second case, the spatial separation of free radical sites is impossible, and they combine or disproportionate to form non-paramagnetic reaction products.

Just as the oxygen vacancy and the SC can be considered as a product of the addition or disproportionation reaction of two silicon radicals (fundamental sources of the oxygen deficiency in SiO_2), so can the peroxide bridge and the DOSG be considered as products of the respective reactions between two oxy radicals (≡Si-O-)$_3$Si-O* (fundamental defects containing excess oxygen in silica):

$$(\equiv \text{Si-O-})_3\text{Si-O}^* + {}^*\text{O-Si}(\text{-O-Si} \equiv)_3 \Rightarrow (\equiv \text{Si-O-})_3\text{Si-O-O-Si}(\text{-O-Si} \equiv)_3;$$

$$(\equiv \text{Si-O-})_3\text{Si-O}^* + {}^*\text{O-Si}(\text{-O-Si} \equiv)_3 \Rightarrow (\equiv \text{Si-O-})_2\text{Si} < \text{O}_2 + (\equiv \text{Si-O-})\text{Si}(\text{-O-Si} \equiv)_3.$$

The quantum-chemical calculations show that the formation of the peroxide bridge is energetically more favorable:

$$(\equiv \text{Si-O-})_3\text{Si-O-O-Si}(\text{-O-Si} \equiv)_3 \Rightarrow (\equiv \text{Si-O-})_2\text{Si} < \text{O}_2 + (\equiv \text{Si-O-})\text{Si}(\text{-O-Si} \equiv)_3 + (35 \pm 5)\,\text{kcal/mol}.$$

The thermal stability of these two groups is comparatively low. The O-O bond strength in the peroxide group is (52 ± 5) kcal/mol, and the heat of the reaction is

$$(\equiv \text{Si-O-})_3\text{Si-O-O-Si}(\text{-O-Si} \equiv)_3 \Rightarrow (\equiv \text{Si-O-})_3\text{Si-O-Si}(\text{-O-Si} \equiv)_3 + \text{O}(^3\text{P}) + (20 \pm 5)\ \text{kcal/mol}.$$

Lam Research Ex. 1035 - Page 309
Lam Research Corp. v. Inpria Corp.
IPR2024-00033 - U.S. Patent No. 9,823,564

The thermal stability of the DOSG is determined by the activation energy for its decay with the pollution of oxygen atom and formation of SG [73]:

$$(\equiv \text{Si-O-})_2\text{Si}{<}\text{O}_2 \Rightarrow (\equiv \text{Si-O-})_2\text{Si}=\text{O} + \text{O}(^3\text{P}) + (65 \pm 3)\ \text{kcal/mol}.$$

This process proceeds at the silica surface at temperatures above 700 K, allowing its activation energy to be estimated at (60–65) kcal/mol. In as much as the reaction heat is calculated for the ground-state products (the energy of the oxygen atom in singlet state is higher by ~47 kcal/mol), this implies that the DOSG decays from the triplet state. The quantum-chemical energy of the lowest triplet level of the $F_2Si{<}O_2$ molecule is only 26 kcal/mol higher than its ground state (see Section 9.7). One can assume that, after the thermally activated rupture of the weak O-O bond, the molecule undergoes transition to the triplet state followed by the decay with the abstraction of an oxygen atom.

9.8. REACTIVITY OF THE $>Si{<}O_2$ Groups Toward the Polar X-H (X = OH, NH_2, OCH_3) Molecules

The enhanced reactivity of the DOSG toward the compounds containing the R-H bonds or the unsaturated bonds of various types (double and triple bonds, CO, and other molecules) is caused by the presence of a weakened O-O bond in the ring. In the reactions with polar X-H (X = OH, NH_2, O-CH_3) molecules, the DOSG exhibits different properties. The reaction with water proceeds at room temperature and at a vapor pressure of $\sim 10^{-3}$ Torr. This process is accompanied by the DOSG decomposition (optical monitoring) and formation of the two new types of hydroxyls that are responsible for the SiO-H and SiOO-H stretching bands at 3743 and 3584 cm^{-1} (Figure 7.26).

The formation of the hydroperoxide Si-O-O-H groups was also detected by the optical method. The DOSG decay is accompanied by an appearance of a structureless wing of a UV band (Figure 7.26b). The position and intensity of this band are nearly the same as in the absorption spectrum of the HOOH molecule in this spectral range.

The reaction mechanism was established in the experiments with isotope-substituted molecules ($H_2^{18}O$ and $>Si{<}^{18}O_2$ ($>Si{:} + {}^{18}O_2 \Rightarrow >Si{<}^{18}O_2$)). The formation of the following products was detected by IR spectroscopy (Figure 7.26a):

$$(\equiv \text{Si-O})_2\text{Si}{<}\text{O}_2 + \text{H}_2{}^{18}\text{O} \rightarrow (\equiv \text{Si-O})_2\text{Si}(^{18}\text{OH})(\text{OOH}).$$

$$(\equiv \text{Si-O})_2\text{Si}{<}{}^{18}\text{O}_2 + \text{H}_2\text{O} \rightarrow (\equiv \text{Si-O})_2\text{Si}(\text{OH})(^{18}\text{O}^{18}\text{OH}).$$

Lam Research Ex. 1035 - Page 310
Lam Research Corp. v. Inpria Corp.
IPR2024-00033 - U.S. Patent No. 9,823,564

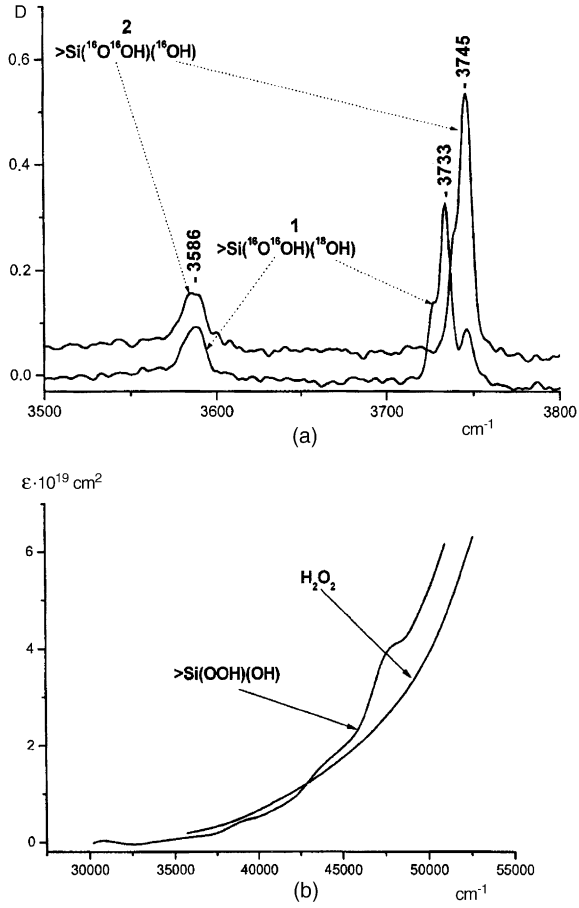


Fig. 7.26. The spectral evidence of the formation of hydroperoxide Si-O-O-H groups in reaction DOSG with water molecules. (a) Registering two new types of hydroxyls that are responsible for the SiO-H and SiOO-H stretching vibration bands at 3743 and 3584 cm^{-1} in the reaction products; (b) appearance of a structureless wing of a UV band whose form is close to that observed in absorption spectrum of the HOOH molecule.

This signifies that the addition of a water molecule to DOSG proceeds through its insertion into one of the Si-O bonds rather than through the reactions involving the O-O bond. Therefore, DOSG exhibits a bifunctional reactivity. The mechanism of this process was established quantum-chemically; it includes (1) the complexation between a water molecule and DOSG (the structure of the complex is given in Figure 7.27a with an energy

Lam Research Ex. 1035 - Page 311
Lam Research Corp. v. Inpria Corp.
IPR2024-00033 - U.S. Patent No. 9,823,564

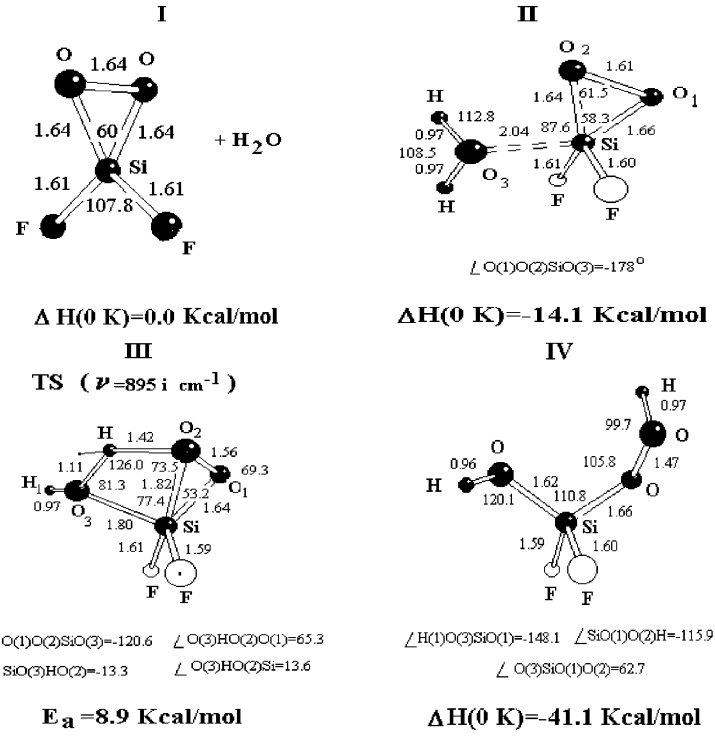


Fig. 7.27. The results of model calculations of stage mechanism of Si-O-O-H group formation.

of ~14 kcal/mol for the complex (G2 calculation) and (2) the decomposition of the complex with the formation of the reaction products. The TS for the decomposition reaction is shown in Figure 7.27b, and the structure of the end product is given in Figure 7.27c. The heat of this process is equal to 44 kcal/mol. The reactions of DOSG with the methanol and ammonia molecules proceed in a similar manner.

Table 7.14 presents the computational results for the heat of some reactions involving hydroperoxide groups, which can be considered as model processes occurring at the silica surface. As compared with the decay channel the rupture of the O-O bond in hydroperoxide and formation of free radicals, the activation energies for the reverse reactions of water and methanol abstraction with the recovery of DOSG are even lower. The pre-exponential factors for these processes are also different. For the O-O bond rupture, its typical value is $10^{(16/17)}\,\mathrm{sec}^{-1}$, whereas for the water abstraction via the cyclic TS it is equal to $10^{11}\,\mathrm{sec}^{-1}$.

Lam Research Ex. 1035 - Page 312
Lam Research Corp. v. Inpria Corp.
IPR2024-00033 - U.S. Patent No. 9,823,564

Table 7.14. The reaction heat (kcal/mol) of the XOOH groups transformation (calculations on G2(MP2) level)

Transformation	Reaction heat (kcal/mol)
$HOOH \Rightarrow HO^* + {}^*OH$	+49.9
$CH_3OOH \Rightarrow CH_3O^* + {}^*OH$	+45.6
$H_3SiOOH \Rightarrow H_3SiO^* + {}^*OH$	+51.3
$H_2FSiOOH \Rightarrow H_2FSiO^* + {}^*OH$	+51.5
$HF_2SiOOH \Rightarrow HF_2SiO^* + {}^*OH$	+54.5
$F_3SiOOH \Rightarrow F_3SiO^* + {}^*OH$	+55.0
$F_2Si(OH)(OOH) \Rightarrow F_2Si(OH)(O^*) + {}^*OH$	+53.3
$F_2Si(OH)(OOH) \Rightarrow F_2Si{<}O_2 + HOH$	+41.1
$F_2Si(OCH_3)(OOH) \Rightarrow F_2Si(OCH_3)(O^*) + {}^*OH$	+53.0
$F_2Si(OCH_3)(OOH) \Rightarrow F_2Si{<}O_2 + CH_3OH$	+42.5
$F_2Si(NH_2)(OOH) \Rightarrow F_2Si(NH_2)(O^*) + {}^*OH$	+51.4
$F_2Si(NH_2)(OOH) \Rightarrow F_2Si{<}O_2 + NH_3$	+31.2

The thermal decomposition of the >Si(OH)(OOH) groups starts at temperatures above 500 K and results in a quantitative formation of the >Si(OH)(OH) groups (geminal hydroxyls). When the process is conducted in a D_2 atmosphere, the >Si(OH)(OD) groups are the main transformation products. This is evident that the thermal decomposition of hydroperoxide groups proceeds following the free-radical mechanism. Another pathway for the formation of the Si-O-D group at temperatures near 600 K is hardly possible. The detection of the paramagnetic particles in the reaction products was a direct proof of the free-radical mechanism of this process. In the experiment, where, in addition to the hydroperoxide groups, silylene centers >Si: were present at the sample surface, the >Si*OH and >Si(O*)(OH) radicals were found in the reaction products by the EPR method, evidencing the formation of low-molecular *OH radicals as hydroperoxide decay products.

A decreasing on 10 kcal/mol (from 44 to 35 kcal/mol) the heat of reaction of ammonia chemisorption, as compared with the water molecule, brought about a change in the mechanism of the process. In this system, the hydroperoxide groups decompose at a temperature more than 100 K lower to form geminal hydroxyls, evidencing the desorption of ammonia molecules. This process is unrelated to the homolytic rupture of the O-O bonds; any attempts at detecting the appearance of free-radical particles in this system went unrewarded. The desorbed ammonia molecules have different ways to react with DOSG. At elevated temperatures, these can be the reactions with the participation of the DOSG O-O bond to yield the geminal hydroxyls $>Si(OH)_2$.

Lam Research Ex. 1035 - Page 313
Lam Research Corp. v. Inpria Corp.
IPR2024-00033 - U.S. Patent No. 9,823,564

10. Inhomogenity of Physico-Chemical Properties of Surface Defects

In disordered solids, of which silica is an example, chemically similar groups may differ in their spectral characteristics. As a rule, a difference in spectral characteristics results in the difference in reactivities. Similar effects appear due to the difference in the spatial arrangement of atoms in the composition of these groups. This is characteristic of amorphous solids. Silylene centers on the silica surface are a convenient object for this experimental study [91].

The changes in the optical absorption spectrum of SC during their oxidation by molecular oxygen are shown in Figure 7.23a. Oxidation is accompanied by a change in the shape of the spectrum, and ''long-wave'' sites react first. As the reaction occurs, its rate decreases. The rate constants of the oxidation of ''long-wave'' and ''short-wave'' sites differ by approximately an order of magnitude. Similar results were obtained for the processes involving SC and other molecules (CH_3OH, $HC{\equiv}CH$ and $H_2C = CH\text{-}CH = CH_2$). In this case, long-wave sites also react first.

These experimental data indicate that the optical absorption band of SG is inhomogeneously broadened due to the sites that differ in both spectral parameters and reactivity.

The difference in the properties of SG appears in the shape of the excitation spectra of singlet ($S_1 \rightarrow X$) and triplet ($T_1 \rightarrow X$) luminescence. The corresponding experimental data are presented in Figure 7.28a. The contribution of the triplet luminescence is noticeably higher for the long-wave fraction of SC, and a decrease in the contribution from the long-wave fraction of SC during oxidation results in a multiple decrease in the contribution of triplet luminescence to the overall luminescence of the sample. The difference in the shapes of the excitation spectra of singlet and triplet luminescence can be attributed to different values of the rate constants of singlet–triplet conversion for particular fractions of SC (see Section 9.5).

Using the difference in reactivity, one can control the content of different SC fractions in the sample and obtain the samples enriched in a short-wave or long-wave SC fraction [66].

In the first study [70], where $(\equiv Si\text{-}O\text{-})_2Si^{\bullet}\text{-}H$ radicals (the products of addition of H atoms to SC) were detected, the EPR spectrum (Figure 7.28b spectrum 1) was reported to be a superposition of two signals with different radiospectroscopic characteristics (the decomposition of the overall signal into two components is shown in Figure 7.28 spectra 1', 1''). Based on the closeness of their radiospectroscopic parameters and chemical properties, Radzig [70] suggested that these signals belonged to chemically identical sites with the same chemical nature.

Lam Research Ex. 1035 - Page 314
Lam Research Corp. v. Inpria Corp.
IPR2024-00033 - U.S. Patent No. 9,823,564

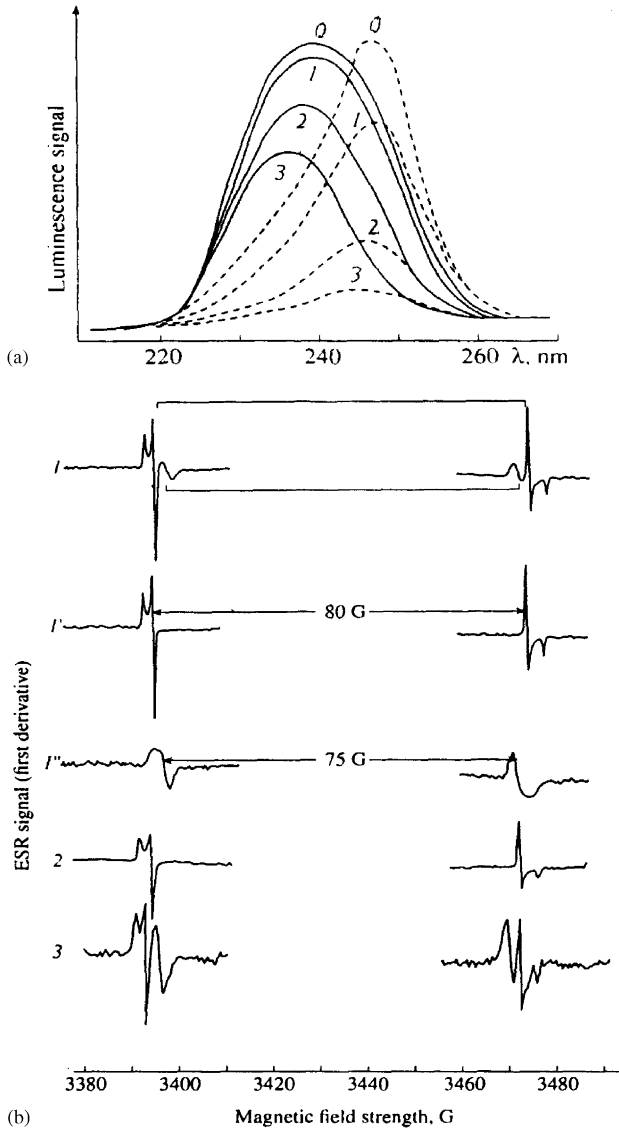


Fig. 7.28. The experimental evidences of a bimodal character of the SC distribution function on the silica surface. (a) Excitation spectra of singlet–singlet (solid line) and triplet–singlet (dashed line) luminescence of SC in the initial silica sample and (1–3) their changes during the oxidation of the sample. Luminescence was detected at 300 K at the wavelength of 285 nm for the singlet–singlet transition and at 455 nm for the triplet–singlet transition; (b) EPR spectra of products of addition of H atom to SS (only lines of $(\equiv{}^{28}\text{Si-O-})_2^{28}\text{Si}^{\bullet}\text{-H}$ is shown): (1) sample A (superposition of EPR spectra *1'* and *1''*); (2) sample B; and (3) sample C (see text for details).

Lam Research Ex. 1035 - Page 315
Lam Research Corp. v. Inpria Corp.
IPR2024-00033 - U.S. Patent No. 9,823,564

Figure 7.28b shows the EPR spectra of the products of probing with atomic hydrogen the surfaces of three samples A, B, and C containing different SC fractions at 300 K. Sample A is the initial sample of RSi, sample B was enriched in the short-wave fraction (type 1'), and sample C had a higher concentration of the long-wave SC fraction (type 1''). For sample A, according to the previous data [70], the EPR spectrum is a superposition of signals of two types with a ratio of intensities close to 1:1 (obtained by comparing the integral intensities of EPR signals). According to the EPR spectrum, sample B almost entirely contains the radicals of type 1', whereas in sample C, ~80% intensity belongs to the sites of type 1''.

Thus, the formation of two types of paramagnetic complexes of atomic hydrogen with silylene sites is related to the difference in the structure of surface SC. For surface SC, whose optical absorption spectrum is shifted to the short-wave region, the addition of the H atom results in the formation of a site of type 1', whereas type 1'' is characteristic of long-wave SC.

It follows from the experimental data that the distribution function of SC is bimodal. The fraction with shorter wavelengths in the optical absorption spectrum is characterized by less pronounced spectral difference between SC in this fraction than that for long-wave SC. The decomposition of the optical absorption spectrum of SC into two fractions and a change in its shape (calculated in this approximation) during oxidation are shown in Figure 7.23b and c, respectively. A satisfactory agreement between the experimental and calculated dependences is observed. The difference in the properties of SCs is certainly associated with their spatial structure; however, it remains unclear what structural features of quartz glass are responsible for the stabilization of two types of sites.

The difference in reactivity was also found for the paramagnetic surface defects $-(\equiv\text{Si-O-})_3\text{Si}^{\bullet}$ radicals [16]. Since the observed effects are due to the difference in the structure of the nearest environment of the surface silicon atom, it is most pronounced when this atom acts as an active site. This difference should cease with an increase in the number of chemical bonds that separate the active site and surface silicon atom of the solid with which it is linked. They are almost absent for the $(\equiv\text{Si-O-})_3\text{Si-CH}_2\text{-}^{\bullet}\text{CH}_2$ radical in which the active site is localized on the terminal carbon atom [16]. For this reason, it is desirable to have a probe in the immediate contact with a lattice silicon atom. The Si-H group fits best these requirements. Such groups can be obtained upon the interaction of the silyl-type radicals with the hydrogen or deuterium molecules (*cf.* Section 6.3). The IR band due to the stretching vibrations of the Si-H bonds obtained upon the hydrogenation of silyl radicals:

$$2\ (\equiv \text{Si-O})_3\text{Si}^{*} \ + \ \text{H}_2(\text{D}_2) \ \Rightarrow \ 2\ (\equiv \text{Si-O})_3\text{Si-H(D)}$$

Lam Research Ex. 1035 - Page 316
Lam Research Corp. v. Inpria Corp.
IPR2024-00033 - U.S. Patent No. 9,823,564

is shown in Figure 7.14. The half-height width of absorption band of the synthesized groups was (16 ± 1) cm^{-1}. We can divide the homogeneous and inhomogeneous contributions from experimental width from the straight vibration of Si-H bonds in the following way. The $(\equiv^{28}Si_{\beta}\text{-}O)_3^{29}Si_{\alpha}^{\bullet}$ radical (precursor of Si-H group) inhomogeneous width of the EPR spectrum lines was (20 ± 2) G (see Figure 7.10). This quantity is determined by the differences in the HFI constants of $^{29}Si_{\alpha}$ atom for individual fractions of PC. As a result, we arrive at inhomogeneous broadening of the IR-band Si-H vibration. According to Eq. (1) in Section 6.3, the value of this broadening equals (9.5 ± 1) cm^{-1} and the homogeneous plus instrumental (2 cm^{-1}) broadenings of this band is (7.5 ± 2) cm^{-1}.

In the above example, we were dealing with comparatively homogeneous fraction of defects involving small amount (less than 1%) of surface atoms. A considerably higher concentration of the Si-H groups (more than 10% of the number of surface silicon atoms) can be achieved by the pyrolysis of the methoxy groups (for the preparation of RSi samples, see Section 2.3). These groups are obtained by the methoxylation of a silica surface, at which various types of surface groups are stabilized: (1) terminal hydroxyls, (2) SRs $(\equiv Si\text{-}O)_2Si < O_2 > Si(O\text{-}Si\equiv)_2$, and (3) siloxane bridges. The changes in the stretching band shapes of the Si-H bonds in the course of their formation upon the decay of methoxy groups are shown in Figure 7.29a, and the same for their decomposition through pyrolysis, in Figure 7.29b. Here, the inhomogeneous broadening effects are much more pronounced.

For comparison, the IR absorption bands corresponding to the Si-H bonds prepared by the hydrogenation of certain types of silicon-centered PCs are also shown in the figures. The frequencies of the greater part of the prepared groups are observed in the range 2300–2250 cm^{-1}. By using correlation relationship (1), we find that these groups are the hydrogenation products of the silicon-centered radicals, for which the HFI constants $a_{iso}(^{29}Si_{\alpha})$ range from 480 G (surface centers $(\equiv Si\text{-}O)_3Si^*$) to 410 G ($(\equiv Si\text{-}O)_2Si^*(OH)$ radicals at silica surface, $(\equiv Si\text{-}O)_3Si^*$ centers in α-quartz; see Table 7.7). The relation between the spectral and kinetic unequivalence of the silyl-hydride bonds is clearly seen from these experimental data. Both the formation and the decomposition of the Si-H groups starts from their low-frequency fraction. This indicates that the methoxy groups bonded to these silicon atoms are thermally less stable. Since the lowering of the stretching frequency is evidence for a lower strength of the formed Si-H bond, one can state that the Si-O bond strength in the corresponding $Si\text{-}OCH_3$ group is also lower.

Lam Research Ex. 1035 - Page 317
Lam Research Corp. v. Inpria Corp.
IPR2024-00033 - U.S. Patent No. 9,823,564

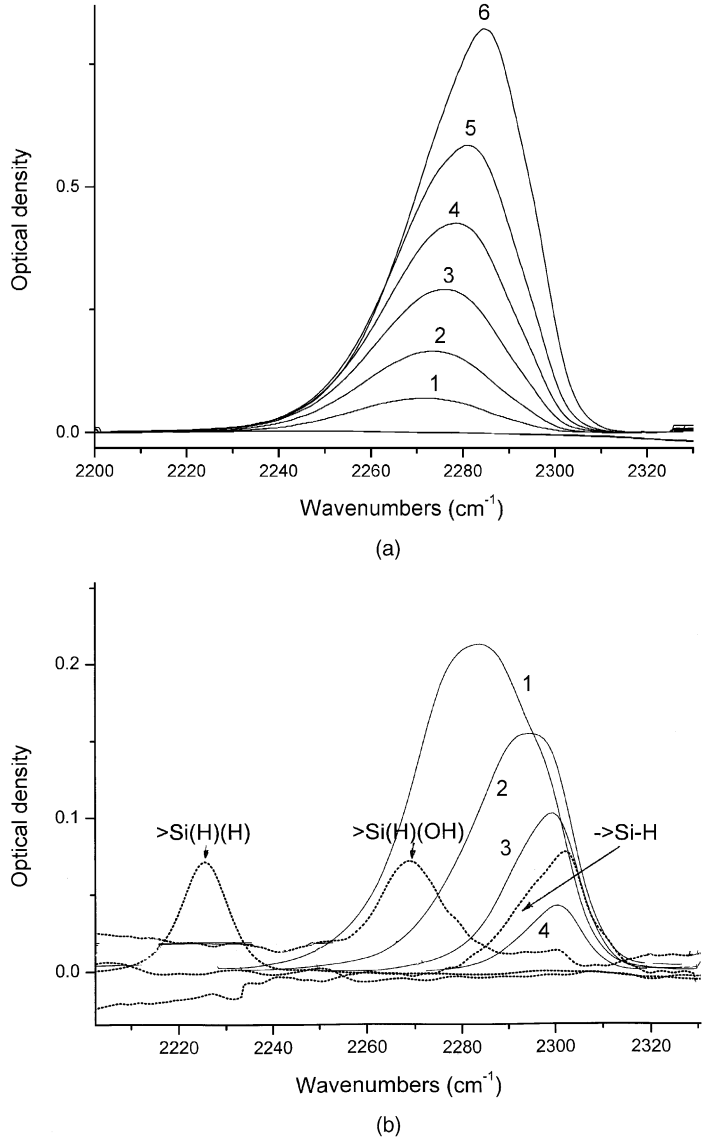


Fig. 7.29. The IR spectra of the Si-H groups on silica surface. (a) Obtained from methoxy groups (see Section 2.3); (1) at 700°C (5 min); (2) at 700°C (10 min); (3) at 700°C (30 min); (4) at 750°C (15 min); (5) at 750°C (30 min); (6) at 800°C (15 min); (b) obtained in the pyrolysis of Si-H groups (see Section 2.3); (1) at 850°C (10 min); (2) at 900°C (10 min); (3) at 950°C (15 min); (4) at 1050°C (15 min); The dashed curve with maximum near 2300 cm^{-1} corresponds to terminal $(\equiv Si\text{-}O)_3Si\text{-}H$ groups.

Lam Research Ex. 1035 - Page 318
Lam Research Corp. v. Inpria Corp.
IPR2024-00033 - U.S. Patent No. 9,823,564

11. Impurity Centers in Quartz Glass: Carbon in the Silica Structure

The physico-chemical characteristics of quartz glass (amorphous SiO_2) are largely determined by the nature of defects in the material. These can be both the intrinsic defects, in which silicon or oxygen atoms have an uncommon coordination, and the groups containing impurity atoms. Defects have a pronounced effect on the spectral characteristics of a material. As a rule, these centers initiate the processes of chemical modification in the structure of quartz glass when designing new devices and equipments, including fiber-optical, on the basis of SiO_2 [92]. In this section, the structure and properties of carbon-containing defects in silica are analyzed.

In the course of RSi formation, some of the carbon atoms fit into the structure of material; heating of the RSi samples in an O_2 atmosphere at temperatures above 800 K is accompanied by the formation of CO_2 [19]. To clarify the mechanism of this process, it is necessary to answer the question of in which way, i.e., via which intermediate states carbon incorporates into the structure of quartz glass and in which forms it stabilizes in glass. Literature information on this point is scarce. In Ref. [14], IR measurements have shown that the formation of the RSi structure is accompanied by the incorporation of hydrocarbon fragments into the silica structure. These are the ≡Si-C≡C-H groups (responsible for the C-H and C≡C stretching bands at 3311 and 2070 cm^{-1}, respectively) and an "unidentified surface group" giving a weak band at 2983 cm^{-1} (2237 cm^{-1} in the deuterated samples) due to the C-H stretching modes. It has now been established that this band belongs to the Si-CH_3 groups.

11.1. ≡Si-$^{\bullet}CH_2$, $(\equiv Si\text{-})_2^{\bullet}CH$, AND $(\equiv Si\text{-})_3C^{\bullet}$ RADICALS

Beginning at 850 K and higher, heating of a methoxylated silica sample is accompanied by the sequential formation of the carbon-centered ≡Si-$^{\bullet}CH_2$ (900 K), ≡Si-$HC^{\bullet}$-Si≡ (1100 K), and $(\equiv Si\text{-})_3C^{\bullet}$ (1300 K) radicals. With a rise in pyrolysis temperature, the concentration of radicals increases. Their EPR spectra parameters are reported in Table 7.15. The answer to the question of the chemical structure of these radicals was obtained in the experiments on samples enriched with magnetic isotopes of the H(D), C(^{13}C), and Si(^{29}Si) nuclei. The $(\equiv Si\text{-})_3C^{\bullet}$ radicals EPR spectra are shown in Figure 7.30.

The EPR signal from the $(\equiv Si\text{-})_3C^{\bullet}$ radicals becomes saturated at a very low microwave power even at 300 K. At the same time, if the paramagnetic oxygen molecules are present in a gas over the sample, the saturation is

Lam Research Ex. 1035 - Page 319
Lam Research Corp. v. Inpria Corp.
IPR2024-00033 - U.S. Patent No. 9,823,564

Table 7.15. Radiospectroscopic characteristics of the carbon-containing paramagnetic centers in silica (1, 4, 6 – experimental results, 2, 3, 5, 7 – results of calculations, b_i – main components of anisotropic part of the HFI tensor, all values are given in G)

Radical structure	Nucleus	a_{iso}	b_1	b_2	b_3	Nucleus	a_{iso}	b_1	B_2	b_3	Nucleus	a_{iso}	b_1	b_2	b_3
1. ≡Si-$^{\bullet}$CH$_2$	^{1}H	−21.0	−5.0	2.5	2.5	^{29}Si	21.0								
2. F$_3$Si-$^{\bullet}$CH$_2$	^{1}H	−20.6	−13.2	−0.8	14.0	^{29}Si	21.3	1.5	0.85	−2.4	^{13}C	22.7	−26.2	−26.1	52.3
3. F$_3$Si-$^{\bullet}$CH$_2$[a]	^{1}H	−20.6	−8.0	4.0	4.0	^{29}Si	21.3	1.5	−0.75	−0.75	^{13}C	22.7	−26.2	13.1	13.1
4. (≡Si-)$_2^{\bullet}$CH	^{1}H	−18.5	−9.8	0.2	9.5										
5. (F$_3$Si-)$_2^{\bullet}$CH	^{1}H	−18.8	−12.5	−0.8	13.3	^{29}Si	18.8	1.1	0.5	−1.6	^{13}C	20.7	−24.9	−24.8	49.7
6. (≡Si-)$_3$C$^{\bullet}$						^{29}Si	16.4	<1.	<1.	<1.	^{13}C	23.2	−23.2	−23.2	46.4
7. (F$_3$Si-)$_3$C$^{\bullet}$						^{29}Si	16.7	0.8	0.3	-1.1	^{13}C	19.4	−23.8	−23.8	47.5

[a]Calculated values for the one-dimensional free rotation of the CH_2 group around Si-C bond in radical.

Lam Research Ex. 1035 - Page 320
Lam Research Corp. v. Inpria Corp.
IPR2024-00033 - U.S. Patent No. 9,823,564

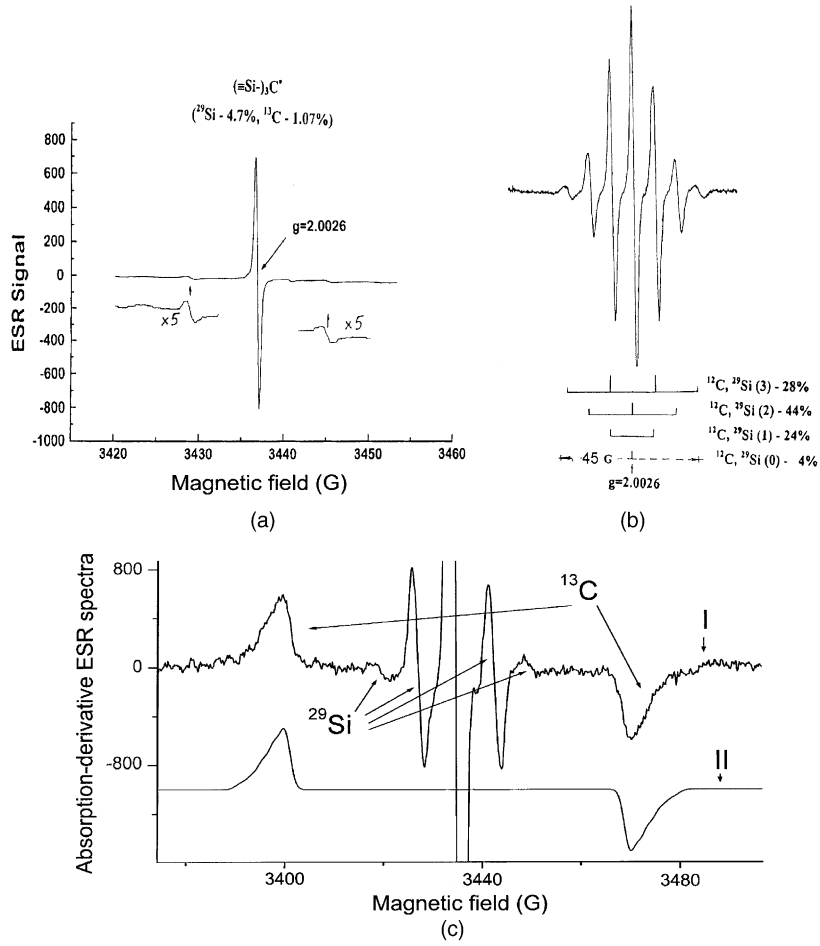


Fig. 7.30. The EPR spectra of the $(\equiv Si\text{-})_3C^{\bullet}$ radicals in samples enriched with magnetic isotopes of the C(^{13}C), and Si(^{29}Si) nuclei. (a) 88% $(\equiv {}^{28}Si\text{-})_3^{12}C^{\bullet} + 12\%$ $(\equiv {}^{29}Si\text{-})_3^{12}C^{\bullet}$; (b) 35% $(\equiv {}^{28}Si\text{-})_3^{12}C^{\bullet} + 65\%$ $(\equiv {}^{29}Si\text{-})_3^{12}C^{\bullet}$; (c) (I) 80% $(\equiv {}^{28}Si\text{-})_3^{13}C^{\bullet} + 16\%$ $(\equiv {}^{28}Si\text{-})_3^{12}C^{\bullet} + 4\%$ $(\equiv {}^{29}Si\text{-})_3^{12}C^{\bullet}$. (II) Result of EPR spectrum simulation of $(\equiv {}^{28}Si\text{-})_3^{13}C^{\bullet}$ radical.

eliminated in part. This signifies that the spin-lattice relaxation time of the center becomes shorter as a result of the collisions with the paramagnetic gas-phase oxygen molecules (spin exchange) and indicates that these radicals are situated in the near-surface silica layer (at a depth of 1 nm and less) [70].

Paramagnetic centers with the EPR parameters analogous to those of the $(\equiv Si\text{-})_3C^{\bullet}$ radicals (a single narrow line with $g = 2.00246$ and two low-intense satellites splitted by 16.4 G) were detected in the oxidized silicon

Lam Research Ex. 1035 - Page 321
Lam Research Corp. v. Inpria Corp.
IPR2024-00033 - U.S. Patent No. 9,823,564

samples [93–95]. These defects were called the EX centers. From the foregoing, one can assert that the EX center in amorphous SiO_2 is the impurity carbon-centered paramagnetic center $(\equiv Si\text{-})_3C^{\bullet}$, whose first coordination sphere is comprised of three magnetically equivalent silicon atoms.

11.2. REACTIVITY OF THE $(\equiv Si\text{-})_3C^{\bullet}$ RADICALS TOWARD H_2 MOLECULES

Recall that the $(\equiv Si\text{-})_3C^{\bullet}$ radicals stabilize in a near-surface layer of the RSi samples, while hydrogen is one of few gases that can dissolve in SiO_2. Annealing of a sample in a H_2 atmosphere at temperatures > 550 K is accompanied by the radical decomposition (EPR monitoring). Heating of the sample in a H_2 atmosphere at 875 K brought about complete disappearance of the EPR signal due to the $(\equiv Si\text{-})_3C^{\bullet}$ radicals. Vacuum heating (with continuous pumping out) of a hydrogenated sample is accompanied by the recovery of the EPR signal from the $(\equiv Si\text{-})_3C^{\bullet}$ radicals as the temperature is successively increased. Heating for 10 min at 1375 K resulted in a complete recovery of the initial EPR intensity for the $(\equiv Si\text{-})_3C^{\bullet}$ radicals. The procedure leading to the radical decomposition in a hydrogen atmosphere and restoration upon high-temperature vacuum heating can be repeated more than once without any noticeable changes in the character of the process.

These experimental data point to the following free-radical chemical processes:

$$(\equiv Si\text{-})_3C^{\bullet} + H_2 \rightarrow (\equiv Si\text{-})_3C\text{-}H + H^{\bullet},$$

$$(\equiv Si\text{-})_3C\text{-}H \rightarrow (\equiv Si\text{-})_3C^{\bullet} + H^{\bullet}.$$

The $(\equiv Si\text{-})_3C^{\bullet}$ radicals in quartz glass are thermally stable at temperatures of the onset of homolytic decomposition of the C-H bonds in the $(\equiv Si\text{-})_3$ C-H groups. Because of this, they can function as "generators" of atomic hydrogen (deuterium) in the H_2 atmosphere.

The C-H bond strength in the $(\equiv Si\text{-})_3C\text{-}H$ group is (100 ± 2) kcal/mol. This estimate is based on the analysis of kinetic data on the formation and decay of these groups and also on the results of quantum-chemical calculations of model systems.

11.3. INCREASE IN THE CONCENTRATION OF PARAMAGNETIC CENTERS UPON THE THERMO OXIDIZING TREATMENT OF THE RSi SAMPLES

The PCs bind only a small portion of carbon atoms that are built into the structure of quartz glass during the preparation of RSi. The EPR-detected

Lam Research Ex. 1035 - Page 322
Lam Research Corp. v. Inpria Corp.
IPR2024-00033 - U.S. Patent No. 9,823,564

carbon-centered free radicals $\equiv$Si-$^{\bullet}$CH$_2$, ($\equiv$Si-)$_2^{\bullet}$CH, and ($\equiv$Si-)$_3$C$^{\bullet}$ are only the visible part of an iceberg. One can assume that these PCs are formed from their diamagnetic precursors $\equiv$Si-CH$_3$, ($\equiv$Si-)$_2$CH$_2$, and ($\equiv$Si-)$_3$CH. The incorporation of carbon into the quartz-glass network starts with the formation of the $\equiv$Si-CH$_3$ groups and proceeds through their subsequent dehydrogenation to ($\equiv$Si)$_4$C. The formation of the $\equiv$Si-CH$_3$ groups in the course of RSi preparation was detected by IR spectroscopy [14]. Along with the silylene centers, the carbide like ($\equiv$Si-)$_4$C fragments comprise a main reservoir, where the oxygen deficiency emerged during the preparation of the RSi samples is "kept." Compared with the stoichiometric silica, the $>$Si: group contains one deficient oxygen atom, and ($\equiv$Si-)$_4$C has four such atoms, of which two go into the formation of CO_2 and another two, to the oxidation of four silicon atoms. A comparison of the amounts of these centers suggests that the number of ($\equiv$Si-)$_4$C fragments in the sample, as derived from the number of the CO_2 molecules collected during the oxidation, comprises (1/2)% of the amount of SCs at the RSi surface. It is conceivable that the carbide-like fragments "cement" the structure of the near-surface layer, thereby enhancing its stability and, hence, favoring the stabilization of the defects of various types at the RSi surface.

The thermo oxidizing treatment of RSi samples in an O_2 (N_2O) atmosphere at temperatures above 750 K [19] is accompanied by oxygen chemisorptions, with the CO_2 molecule being the main low-molecular product of this reaction. The rate of oxygen uptake by the sample manifold increases initially, which is typical of the branched free-radical chain processes. A value of (1.5 ± 0.1) obtained for the ratio between the amounts of the chemisorbed oxygen molecules and the formed CO_2 molecules suggests that the greater part of the collected carbon entered into the silica structure as a stable chemical compound containing the C-Si bonds. The additional oxygen consumption in excess of that necessary for the CO_2 formation should be related to the oxidation of vacancies appearing in solid upon the removal of carbon atoms from it.

The most intriguing fact is that this process is accompanied by a manifold, from 10 to 100 times (up to 10^{13} cm^{-2}), increase in the concentration of PCs (($\equiv$Si-O-)$_3$Si-O$^{\bullet}$ and ($\equiv$Si-)$_3$C$^{\bullet}$ radicals) in the sample. As in the RSi samples, the latter are stabilized in the near-surface silica layers, whereas oxy radicals lie at the silica surface. The oxy radicals produce a characteristic red (620 nm) luminescence excited by the light with a wavelength of 280 nm [64], so that the samples thus prepared emit red light under UV irradiation. Due to a high concentration of the centers in fine-grained silica, this luminescence can be observed even in daylight.

Simultaneously with the increase in the concentration of PCs, the concentration of the defects, whose silicon atoms are bonded to two lattice

Lam Research Ex. 1035 - Page 323
Lam Research Corp. v. Inpria Corp.
IPR2024-00033 - U.S. Patent No. 9,823,564

oxygen atoms, decreases. These are mainly the $>Si=O$ groups. Therefore, these conditions are favorable to the in-depth rearrangement processes in the near-surface silica layer. The formation of numerous PCs in this process indicates that it is a branched free-radical process.

12. Nitrogen in Silica

Nitrogen-doped vitreous silica exhibits a number of properties useful for potential practical applications [96,97]. It is believed that amorphous silicon oxynitride can replace SiO_2 as a gate dielectric in a new generation of nanoscaled MOS devices [98]. Nitrogen-doped vitreous silicas can be used in fiber optic devices and integrated optics [92]; these fibers exhibit enhanced photo refractivity and radiation stability [99,100]. The effect of nitrogen dopant atoms on the spectral characteristics and properties of these glasses should be studied in order to understand the physico-chemical properties of these systems [101].

In doped vitreous silicas, the major portion of nitrogen atoms enters into the glass structure as N-Si$\equiv$ or H-N(Si$\equiv$)$_2$ units, in which the N-Si$\equiv$ and N-H groups replace lattice oxygen atoms (the N-H group and the O atom are isoelectronic systems). The formation of ordinary chemical bonds between nitrogen and oxygen atoms in vitreous silicas is improbable because of the comparatively low strength of the N-O bond in the ($\equiv$Si)$_2$N-O-Si$\equiv$ unit.

In this study, various techniques were used for introducing nitrogen into the composition of vitreous silica. In one of these, nitrogen-doped vitreous silicas SiO_2(N) were prepared using a plasma-chemical SPCVD technology [102,103]. According to the results of elemental analysis, these samples contained 3–5% nitrogen and ~1% chlorine. Paramagnetic centers in the samples of nitrogen-doped vitreous silica were obtained by UV (193 nm) irradiation, y-irradiation, or by the mechanical destruction of the samples in an inert atmosphere. The other technique for the production of nitrogen-containing PCs was based on the chemical modification of defects stabilized on the surface of highly dispersed activated silica (RSi). To obtain nitrogen-containing PCs, NH_3 (ND_3) was used as a modifier molecule. All of the experiments were performed under conditions of a high vacuum or controlled atmosphere.

Paramagnetic centers with an unpaired electron localized on the three-coordinated silicon atom are formed in vitreous silica under exposure to various factors [10,104,105]. In the presence of nitrogen atoms in glass, a portion of these atoms can occur as the ($\equiv$Si-O-)$_2$Si*(-N$<$) structure. However, to the best of the author's knowledge, the occurrence of these centers in

Lam Research Ex. 1035 - Page 324
Lam Research Corp. v. Inpria Corp.
IPR2024-00033 - U.S. Patent No. 9,823,564

nitrogen-doped vitreous silica has never been discussed in the literature. Data on two types paramagnetic defects are reported. At first, unpaired electron localized on the three-coordinated silicon atom connected with nitrogen atom. The ≡Si-N*-Si≡ and ≡Si-N*-H radicals containing a two-coordinated nitrogen atom belong to another type of PCs studied. The ≡Si-N*-Si≡ centers were identified by EPR spectroscopy in sodium silicate glass [106]. More recently, a similarly shaped EPR signal was also observed in nitrogen-doped vitreous silicas by other research groups [107,108]. Centers similar to ≡Si-N*-Si≡ were also obtained on the surface of vitreous silica. This allowed us to study their reactivity toward $H_2(D_2)$ molecules.

12.1. PCs $(\equiv Si\text{-}O)_2Si^*(NH_2)$, $(\equiv Si\text{-}O)_2Si^*\text{-}N(Si\equiv)_2$, $(\equiv Si\text{-}O)_2(HO)Si\text{-}N^*H$, AND ≡Si-N*-Si≡

Radicals $(\equiv Si\text{-}O)_2Si^*(NH_2)$ were obtained as a product of the following two-step process that occurred on the surface of RSi (see Section 9.2 for details):

$$(\equiv Si\text{-}O)_3Si\text{-}O^* + NH_3 \Rightarrow (\equiv Si\text{-}O)_3Si\text{-}O\text{-}H + {}^*NH_2,$$

$$(\equiv Si\text{-}O)_2Si : + {}^*NH_2 \Rightarrow (\equiv Si\text{-}O)_2Si^*(NH_2).$$

The $(\equiv Si\text{-}O)_2(HO)Si\text{-}N^*H$ PC was prepared from $(\equiv Si\text{-}O)_2Si^*\text{-}(NH_2)$ radicals using the following modification steps:

$$(\equiv Si\text{-}O)_2Si^*\text{-}(NH_2) + N_2O \Rightarrow (\equiv Si\text{-}O)_2Si(NNO^*)(NH_2),$$

$$(\equiv Si\text{-}O)_2Si(NNO^*)(NH_2) \Rightarrow (\equiv Si\text{-}O)_2Si(O^*)(NH_2) + N_2$$
$$\Rightarrow (\equiv Si\text{-}O)_2Si(OH)(N^*H).$$

Paramagnetic centers formed in first reaction are stable at room temperature; however, they decompose with the elimination of a nitrogen molecule on heating above 373 K [105]. The resulting oxy radical abstracts an H atom from the amino group to form the above radical centers. The EPR spectrum of this radical was measured at 77 K. At room temperature, we failed to detect the EPR signal of these PCs. This fact suggests a considerable relaxation (reversible) broadening of the signal with temperature. Table 7.16 summarizes the radiospectroscopic characteristics of the $(\equiv Si\text{-}O)_2Si^*\text{-}(NH_2)$ and $(\equiv Si\text{-}O)_2Si(OH)(N^*H)$ radicals.

Figure 7.31 demonstrates the EPR spectra of the samples of nitrogen-doped vitreous silica after mechanical destruction and UV irradiation (RT, $\lambda = 193$ nm). An increase in the UV-radiation dose (to 50 kJ/cm^2) was accompanied by an increase in the concentration of the resulting PC without

Lam Research Ex. 1035 - Page 325
Lam Research Corp. v. Inpria Corp.
IPR2024-00033 - U.S. Patent No. 9,823,564

Table 7.16. Radiospectroscopic characteristics of the nitrogen-containing paramagnetic centers in silica

Radical structure	Main g- and a-tensor values, G[a]			
$>{}^{29}Si^{\bullet}({}^{14}NH_2)$	$g_x = 2.0018 \pm 0.0002$;	$a_x({}^{14}N) = 15.4 \pm 0.2$;	$a_{\parallel}({}^{29}Si) = -414 \pm 2$	
300 K	$g_y = 2.0011 \pm 0.0002$;	$a_y({}^{14}N) = 10.9 \pm 0.2$;	$a_{\perp}({}^{29}Si) = -358.4 \pm 2$	
	$g_z = 2.0002 \pm 0.0002$;	$a_z({}^{14}N) = 12.1 \pm 0.2$;	$a_{\perp}({}^{29}Si) = -358.4 \pm 2$	
	$g_{iso} = 2.0010 \pm 0.0002$;	$a_{iso}({}^{14}N) = 12.8 \pm 0.2$;	$a_{iso}({}^{29}Si) = -377 \pm 2$	
$>Si^{\bullet}\text{-}{}^{14}N(Si\equiv)_2$	$g_{\parallel} = 2.0018 \pm 0.0002$			
300 K	$g_{\perp} = 2.0007 \pm 0.0002$			
	$g_{iso} = 2.0011 \pm 0.0002$;		$a_{iso}({}^{14}N) = 12.5 \pm 0.2$	
$\equiv{}^{29}Si\text{-}{}^{14}N^{\bullet}\text{-}{}^{1}H$	$g_{\parallel} \cong 2.012$;	$a_{\parallel}({}^{14}N) = 0 \pm 1$;	$a_{\parallel}({}^{1}H) \cong -17 \pm 1$	
77 K	$g_{\perp} \cong 2.0043$;	$a_{\perp}({}^{14}N) = 18 \pm 1$;	$a_{\perp}({}^{1}H) \cong -21.5 \pm 1$	
	$g_{\perp} \cong 2.0043$;	$a_{\perp}({}^{14}N) = 18 \pm 1$;	$a_{\perp}({}^{1}H) \cong -21.5 \pm 1$	
	$g_{iso} = 2.0069$;	$a_{iso}({}^{14}N) = 12 \pm 1$;	$a_{iso}({}^{1}H) \cong -20 \pm 1$;	$a_{iso}({}^{29}Si) = 16 \pm 2$
$\equiv Si\text{-}{}^{14}N^{\bullet}\text{-}Si\equiv$*	$g_x = 2.0019$ (2.0039);		a_x (^{14}N) = 36 (36)	
77 K	$g_y = 2.0039$ (2.0026);		$a_y({}^{14}N) \cong 2$ (2)	
	$g_z = 2.0078$–2.0238, (2.006–2.02);		$a_z({}^{14}N) \cong 2$ (2)	

[a]The spin distribution with respect to g_z values consists of five fractions with $g_z = 2.0078$, 2.0118, 2.0158, 2.0198, and 2.0238 which have equal weights. Published data [106] are given in parentheses.

Lam Research Ex. 1035 - Page 326
Lam Research Corp. v. Inpria Corp.
IPR2024-00033 - U.S. Patent No. 9,823,564

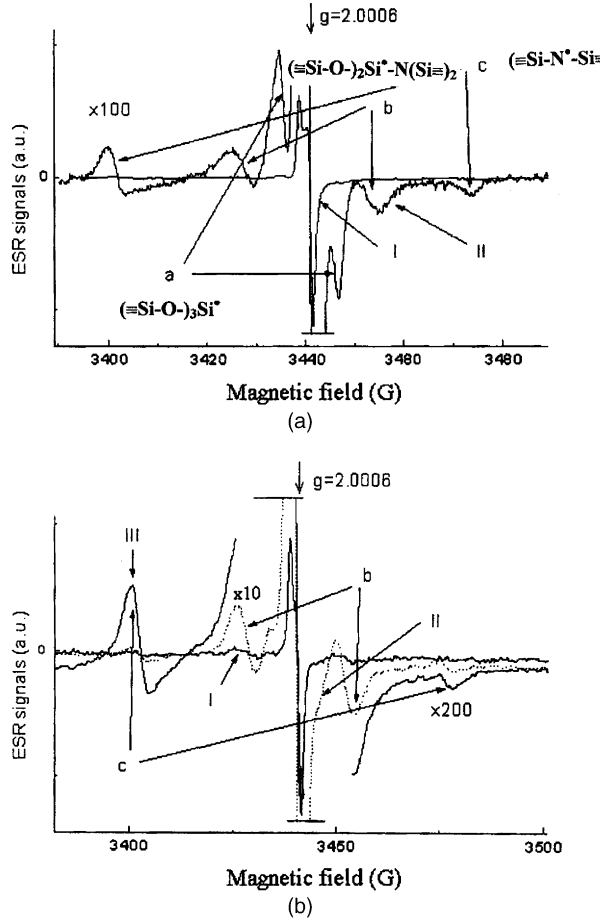


Fig. 7.31. EPR spectra of paramagnetic centers in nitrogen-doped SiO_2 samples: (a) after mechanical treatment at 300 K; arrows indicate lines due to (a) $(\equiv{}^{28}\text{Si-O})_2(\equiv{}^{29}\text{Si-O}){}^{28}\text{Si}^*$; (b) $(\equiv{}^{28}\text{Si-O})_2^{28}\text{Si}^*\text{-}{}^{14}\text{N}<$ and (c) $\equiv{}^{28}\text{Si-}{}^{14}\text{N}^*\text{-}{}^{28}\text{Si}\equiv$ radicals; (b) after UV irradiation ($\lambda = 193$ nm; 300 K); arrows indicate lines due to (b) $(\equiv{}^{28}\text{Si-O})_2^{28}\text{Si}^*\text{-}{}^{14}\text{N}<$, and (c) $\equiv{}^{28}\text{Si-}{}^{14}\text{N}^*\text{-}{}^{28}\text{Si}\equiv$radicals. The spectra were measured at 300 K.

considerable changes in the shape of the signal. The EPR signal of PC formed upon the γ-irradiation of the samples was similar to that shown in Figure 7.31b for UV-irradiated glass. Based on the available published data, the central single anisotropic line in the EPR spectra shown in Figure 7.32 should be assigned to radicals in whom the unpaired electron is localized on the three-coordinated silicon atom. Weeks [104] supposed its structure to be $(\equiv\text{Si-O})_3\text{Si}^*$. In the case of surface centers, the presence of three silicon

Lam Research Ex. 1035 - Page 327
Lam Research Corp. v. Inpria Corp.
IPR2024-00033 - U.S. Patent No. 9,823,564

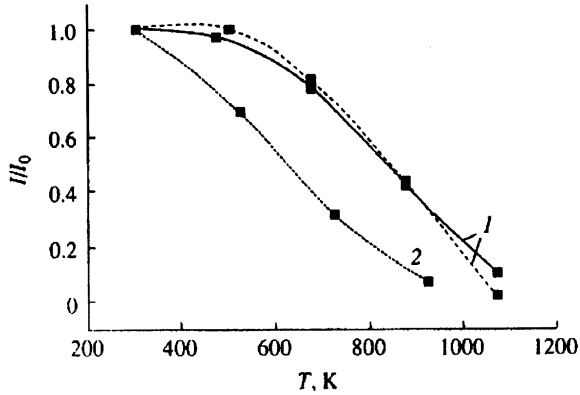


Fig. 7.32. Curves of the thermal annealing of PC in (1) UV- and (2) γ-irradiated SiO_2(N) samples (the exposure time at each temperature was 10 min). I/I_0 is the relative intensity of the EPR signals of PC, where $I_0 = I$ (300 K).

atoms in the coordination sphere of the central (three-coordinated) silicon atom was demonstrated experimentally [41]. Two lines separated by 10.5 G, which are marked "a" in Figure 7.32, are due to the interaction of the unpaired electron with ^{29}Si nuclei ($I \equiv 1/2$, natural abundance of 4.7%) in the coordination sphere of a defect. Relevant data for bulk centers are unavailable.

In all cases, along with the main central signal, the EPR spectra also exhibited two extra lines separated by of 25 G (marked "b" in Figure 7.31). The ratio between the amplitudes of central (due to $(\equiv Si\text{-}O)_3Si^*$ radicals) and side component depended only slightly on the preparation method (irradiation or mechanical treatment). The observed lines are part of a triplet EPR signal with splitting between components of ~12.5 G. This signal is due to the interaction of the unpaired electron with the nitrogen nucleus and belongs to the $(\equiv Si\text{-}O)_2Si^*\text{-}N(Si\equiv)_2$ radical. The central component of this signal is masked by the more intense spectrum of $(\equiv Si\text{-}O)_3$ Si* radicals.

According to the results of calculations, the $SiNSi_2$ fragment in the radical is planar, unlike the $SiNH_2$ group in the $F_2Si\text{-}NH_2$ radical. Thus, the pyramidality of the N atom decreases in the order NH_3, $(\equiv Si\text{-}O)_2Si^*\text{-}NH_2$, $(\equiv Si\text{-}O)_3Si^*$. $NH(Si\equiv)_2$ and $N(Si\equiv)_3$, and the last two members of this series are planar.

Based on the assumption that the EPR signal shown in Figure 7.31 is a superposition of singlet and triplet spectra, the fraction of a triplet signal in the total spectrum was estimated at (15 ± 5)%. According to elemental analysis data, the nitrogen content of glass was (4–5)%. Under the assumption that nitrogen substitutes for an oxygen atom in the coordination

Lam Research Ex. 1035 - Page 328
Lam Research Corp. v. Inpria Corp.
IPR2024-00033 - U.S. Patent No. 9,823,564

sphere of the $(\equiv Si\text{-}O)_3Si^*$ radical in a random fashion, the fraction of nitrogen-containing centers is $3 \times (0.04–0.05) = (0.12–0.15)$, which is consistent with the above result.

The shape of EPR signals in a mechanically activated sample of nitrogen-doped vitreous silica changes after coming into contact with oxygen molecules. The concentration of $(\equiv Si\text{-}O)_3Si^*$ radicals decreased because a portion of these radicals stabilized on the solid surface reacted with oxygen molecules. It is interesting to note that, unlike $(\equiv Si\text{-}O)_3Si^*$ radicals whose concentration decreased more than two times, no changes were detected in the amplitude of lines due to $(\equiv Si\text{-}O)_2Si^*\text{-}N(Si\equiv)_2$ radicals. By this is meant that the major portion of PCs of this type formed upon the mechanical treatment of glass is stabilized in a near-surface layer of the material rather than on the surface. The question as to the reasons for the effect observed are discussed in Section 12.

Figure 7.32 illustrates the thermal decay of PC on the heating of UV- and γ-irradiated samples. The process was not accompanied by considerable changes in the shape of EPR signals; i.e., differences in the structures of the coordination spheres of $(\equiv Si\text{-}O)_3Si^*$ and $(\equiv Si\text{-}O)_2Si^*\text{-}N(Si\equiv)_2$ PC have no effect on the thermal stability. However, note that the thermal stability of PCs in the UV-irradiated sample was much higher.

Based on the characteristic shape of edge components in the EPR spectra of products formed by the mechanical treatment, UV irradiation (see Figure 7.31), or y-irradiation of nitrogen-doped vitreous silica, these components were assigned to $\equiv Si\text{-}N^*\text{-}Si\equiv$ radicals. Mackey et al. [106] recorded an individual EPR spectrum of $\equiv Si\text{-}N^*\text{-}Si\equiv$ radicals in sodium silicate glass.

12.2. REACTIONS OF $\equiv Si\text{-}N^*\text{-}H$ AND $\equiv Si\text{-}N^*\text{-}Si\equiv$ PC WITH $H_2(D_2)$

Molecular hydrogen is one of the few compounds that can be introduced into the bulk of vitreous silica. Chemical processes with the participation of molecular hydrogen are used for modifying the structure of this widely used material. The defects of vitreous silica play an important role in these processes. The exposure of $\equiv Si\text{-}N^*\text{-}H$ radicals to an atmosphere of H_2 at room temperature is accompanied by the chemisorptions of the gas in an amount that is comparable with the number of radicals and by the disappearance of the EPR spectrum of these radicals (radiospectroscopic measurements were performed at 77 K (see Section 12.1)). When diamagnetic centers of the silylene type ($(\equiv Si\text{-}O)_2Si:$) also occurred on the sample surface in addition to the PC $\equiv Si\text{-}N^*\text{-}H$, the decay of radicals in an atmosphere of H_2 was accompanied by the quantitative formation of new PCs: $>Si^*\text{-}H$. The appearance of the $>Si^*\text{-}H$ radicals in the system suggests that H atoms

Lam Research Ex. 1035 - Page 329
Lam Research Corp. v. Inpria Corp.
IPR2024-00033 - U.S. Patent No. 9,823,564

are formed in the course of the reaction of ≡Si-N*-H radicals with H_2 molecules. The H atoms add to silylene groups, which are effective free-radical scavengers [18,19]. The above experimental data demonstrate that the process under consideration occurs in accordance with the following reaction scheme:

$$\equiv \text{Si-N}^*\text{-H} + \text{H}_2(\text{D}_2) \Rightarrow \equiv \text{Si-NH}_2(\text{HD}) + \text{H}^*(\text{D}^*)$$

$$(\equiv \text{Si-O})_2\text{Si} : + \text{H}^*(\text{D}^*) \Rightarrow (\equiv \text{Si-O})_2\text{Si}^*\text{-H(D)}.$$

The reaction of ≡Si-N*-H radicals with deuterium molecules occurs in a similar manner. The rates of both processes are proportional to gas pressure over the sample, and the rate constants of these bimolecular reactions at 301 K are $k(\text{H}_2) = (2.7 \pm 0.3) \times 10^{-17}\,\text{cm}^3/\text{molecule/sec}$ and $k(\text{D}_2) = (5.1 \pm 0.5) \times 10^{-18}\,\text{cm}^3/\text{molecule/sec}$. Thus, the value of the isotope effect of this reaction at room temperature is close to 5.

In reactions with the participation of H atoms, both classical (overbarrier) and quantum (underbarrier, tunneling) modes of overcoming an activation barrier are possible. The value of the isotope effect suggests that the reaction occurs via a classical (overbarrier) path at room temperature. Assuming a normal value of the pre-exponential factor ($10^{-11}\,\text{cm}^3/\text{molecule} \cdot \text{sec}$) for the activation energy of this reaction, we obtain $E = 7.7$ (8.7) kcal/mol (processes with the participation of $H_2(D_2)$ molecules).

Figure 7.33a shows the optimized structure of the TS for the reaction of H abstraction from the hydrogen molecule by the F_3Si-N*-H radical as a low-molecular model of the ≡Si-N*-H surface center. The ≡Si-N*-Si≡ radicals that were stabilized on the surface of mechanically activated SiO_2(N) silica also reacted with H_2 molecules. The process was accompanied by the chemisorptions of the gas in an amount that was comparable to the number of reacted radicals (recall that a portion of these radicals was stabilized in near-surface layers of the material, and they were inaccessible to molecules from a gas phase). The $(\equiv\text{Si-O})_2$Si diamagnetic centers also occurred on the surface of the test sample, and the decay of radicals in an atmosphere of H_2 was accompanied by the formation of new PCs: >Si*-H radicals. Thus, in this case, as well as in the reaction of ≡Si-N*-H radicals with H_2 molecules, the process occurred as follows:

$$\text{H}^{*\cdot} + > \text{Si} : \Rightarrow \; > \text{Si}^*\text{-H}.$$

Figure 7.33c demonstrates the kinetic curve of decay of ≡Si-N*-Si≡ radicals in this process at 301 K, as measured from a decrease in the number of H_2 molecules in a gas phase. However, in this case, unlike the reaction with the participation of ≡Si-N*-H radicals, the rate of bimolecular reaction decreased in the course of the process rather than obeyed the rate law

Lam Research Ex. 1035 - Page 330
Lam Research Corp. v. Inpria Corp.
IPR2024-00033 - U.S. Patent No. 9,823,564

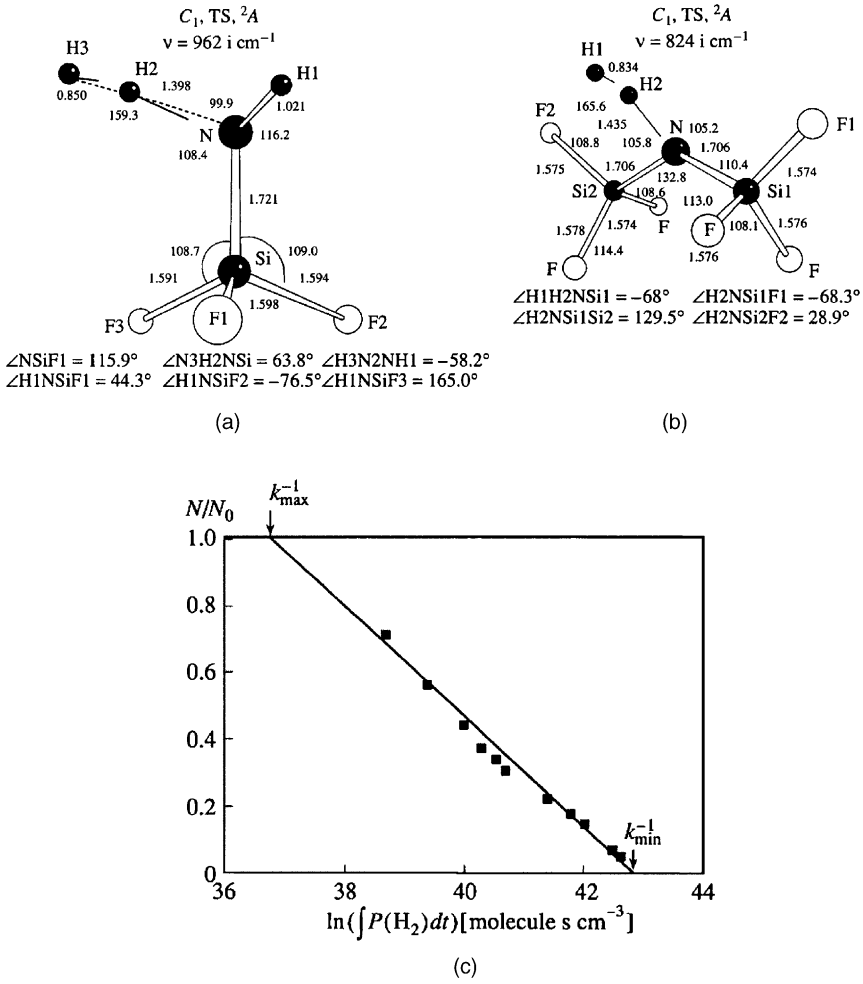


Fig. 7.33. Reactions of the nitrogen-centered radicals ≡Si-*NH and ≡Si-N*-Si≡ with molecular hydrogen: (a) the structure of the TS for the reaction F_3Si-*NH + H_2 → F_3Si-NH_2 + *H; (b) the structure of the TS for the reaction F_3Si-*N-SiF_3 + H_2 → F_3Si-NH-SiF_3 + *H (for both of the TS, characteristic imaginary frequencies are given and atomic shifts that take place when moving along the reaction coordinate are shown); and (c) kinetic curve of the decay of ≡Si-*N-Si≡ radicals in the course of the reaction ≡Si-*N-Si≡ + H_2 → ≡Si-NH-Si≡ + *H at 301 K (for comments, see the text).

Lam Research Ex. 1035 - Page 331
Lam Research Corp. v. Inpria Corp.
IPR2024-00033 - U.S. Patent No. 9,823,564

$dN/dt = kP_{H2}(t)N$. Therefore, the kinetic curve of radical decay was plotted in the $N/N_0 - \ln[\int(P_{H2}\,t)dt]$ coordinates (here, N_0 and N are the initial and current concentrations of ≡Si-N*-Si≡ radicals, respectively, and $\int P_{H2}(t)dt$ is the exposure: a quantity proportional to the number of collisions of gas molecules with a surface center in the time t). The kinetic curve was adequately linearized in these coordinates. The kinetic behavior observed suggests that particular fractions of radicals differ in their reactivity toward hydrogen.

This is typical situation for the processes in disordered (amorphous) solids. In this case the kinetic equation can be presented in the next form: $N(t)/N(0) = \int n(k)\exp(-kt)dk$, $k_{min} \le k \le k_{max}$, where $n(k)$ is the number density of the radicals with a rate constant k. It is the common case when the main part of the kinetic curve are "linearized" in coordinates $([N(t)/N(0)]/\ln t)$ [109–111]. In this case $n(k) \sim 1/k$. Really, $d[N(t)/N(0)]/dt \sim -\int\exp(-kt)dk = (1/t)[\exp(-k_{min}\,t) - \exp(-k_{max}\,t)]$. When the distribution has enough width, $k_{min}t \ll 1 \ll k_{max}t$, for the main time's interval of chemical transformation $d[N(t)/N(0)]/dt \sim (1/t)$ and $N(t)/N(0) \sim \ln t$. It means, that the main part of kinetic curve, $0.9 > [N(t)/N(0)] > 0.1$, we have the linear relation between $[N(t)/N(0)]$ and $\ln(t)$. Extrapolating the linear portion to intersect the axes at $N/N_0 = 0$ and 1, we estimated the values of k_{min} and k_{max}, which characterize the distribution. They were found to be equal 2.5×10^{-19} and 1.1×10^{-16} cm^3/molecule · sec, respectively.

This result might have been expected. It is believed that the observed kinetic non-equivalence of radical centers is due to structural differences (see Section 6.1). A comparison of the range of rate constants k for the reaction of ≡Si-N*-Si≡ radicals with the rate constant of the reaction with the participation of ≡Si-N*-H $k(H_2) = (2.7 \pm 0.3) \times 10^{-17}$ cm^3/molecule · sec demonstrates that one portion of ≡Si-N*-Si≡ radicals exhibits a higher reactivity, whereas the other portion exhibits a lower reactivity in this process. Assuming that the pre-exponential factor for the bimolecular reaction under consideration has a typical value of 10^{-11} cm^3/molecule · sec, we obtain the following activation energies: $E_{max} = 10.5$, $E_{min} = 6.9$, and $E = 7.7$ kcal/mol (E_{min} and E_{max} are the activation energies of reactions that occur with the rate constants k_{min} and k_{min}, respectively). Figure 7.33b shows the structure of the TS for the reaction F_3Si-N*-Si$F_3 + H_2 \Rightarrow F_3$Si-NH-Si$F_3$ + H*. According to calculation data, the activation energy (4.8 kcal/mol) and the heat effect (−11 kcal/mol) of this reaction are lower by 1 kcal/mol and higher by 2.7 kcal/mol, respectively, than those of the reaction F_3Si-N*-H + $H_2 \Rightarrow F_3$Si-NH_2 + H*. Thus, the ≡Si-N*-Si≡ radicals in a free state exhibit a higher reactivity. The higher heat effect of the reaction of H abstraction with the participation of these radicals is indirect evidence for the above conclusion.

Lam Research Ex. 1035 - Page 332
Lam Research Corp. v. Inpria Corp.
IPR2024-00033 - U.S. Patent No. 9,823,564

12.3. ON THE STRENGTHS OF Si-O AND Si-N BONDS IN VITREOUS SILICA

The O atom and the NH group are iso-electronic; this implies a certain similarity between their physico-chemical characteristics. In nitrogen-doped vitreous silicas, the ≡Si-O* and ≡Si-N*-H (≡Si-N*-Si≡) PC can be stabilized, in which an unpaired electron is localized on an electronegative atom (oxygen or nitrogen). Which of these states is thermodynamically more stable? The enthalpies ΔH (0 K) (kcal/mol) of reactions with the participation of fluorine-substituted compounds, which simulated groups in vitreous silica were calculated:

$$F_3Si\text{-}O\text{-}SiF_3 + {}^*NH\text{-}SiF_3 \Rightarrow F_3Si\text{-}NH\text{-}SiF_3 + {}^*O\text{-}SiF_3 + 22.3,$$

$$F_3Si\text{-}N^*\text{-}SiF_3 + F_3Si\text{-}O\text{-}SiF_3 \Rightarrow F_3Si\text{-}N(SiF_3)_2 + {}^*O\text{-}SiF_3 + 23.0.$$

Thus, in this system, the stabilization of a nitrogen-centered paramagnetic center is thermo chemically favorable (by almost 20 kcal/mol). As a result, the equilibrium:

$$\equiv Si\text{-}N^*\text{-}Si \equiv + \equiv Si\text{-}O\text{-}Si \equiv \Leftrightarrow \equiv Si\text{-}N(Si \equiv)_2 + {}^*O\text{-}Si \equiv$$

in nitrogen-doped vitreous silica is shifted to the left (if external conditions permit the establishment of a thermodynamic equilibrium). This result is due to differences in the strengths of Si-O and Si-N bonds in vitreous silica. Consequently, the bond of silicon with oxygen is stronger than that with nitrogen by almost 20 kcal/mol. The results of direct calculations of the strengths of Si-O and Si-N bonds (ΔH (0 K), kcal/mol) in the molecules of $F_3Si\text{-}O\text{-}SiF_3$, F≡Si-N*-Si≡ 3Si-NH-$SiF_3$, and $F_3Si\text{-}N(\text{-}SiF_3)_2$ are given below (the former and latter (in parentheses) figures refer to the results of calculations at the UB3LYP/6-311G(d,p) and G2(MP2//UB3LYP/6-311G(d,p) levels, respectively):

$$F_3Si\text{-}O\text{-}SiF_3 \Rightarrow F_3Si^* + {}^*O\text{-}SiF_3 + 139.7\ (152.6);$$

$$F_3Si\text{-}NH\text{-}SiF_3 \Rightarrow F_3Si^* + {}^*NH\text{-}SiF_3 + 119.0\ (129.1);$$

$$F_3Si\text{-}N(SiF_3)_2 \Rightarrow F_3Si^* + {}^*N(SiF_3)_2 + 118.2.$$

Based on the data obtained, the strengths of Si-O and Si-N bonds in vitreous silica can be estimated at 150 ± 5 and 130 ± 5 kcal/mol, respectively.

Various siloxane bond strengths in vitreous silica have been given in the literature. Silin with coauthors [46,112] reported on a value of 88 kcal/mol, whereas Araujo [113] cited a value of 111 kcal/mol (with no reference to the origin). These are estimated values based on a number of assumptions. Pacchioni and Ierano [114] calculated the strength of the Si-O bond by

Lam Research Ex. 1035 - Page 333
Lam Research Corp. v. Inpria Corp.
IPR2024-00033 - U.S. Patent No. 9,823,564

quantum-chemical methods using a low-molecular cluster containing a siloxane bond (the $Si_2O_7H_6$ molecule calculated at the MP2//HF level) and obtained a value of 126.8 kcal/mol. The value obtained in this work is noticeably higher. In the cited publication, the average strength of the Si-O bond is given, which is equal to a half of the enthalpy of cleavage of two Si-O bonds (in the molecule and the resulting oxy radical):

$$\equiv \text{Si-O-Si} \equiv \Rightarrow \equiv \text{Si}^* + {}^*\text{O-Si} \equiv \Rightarrow \equiv \text{Si}^* + \text{O}(^3\text{P}) + {}^*\text{Si} \equiv .$$

However, the strength of the Si-O bond in glass (the former reaction) is noticeably higher than that in the oxy radical. Moreover, the calculations [114] were performed at another theoretical level.

13. Surface and Near-Surface Defects in Silica

The defects of group B studied in this work "tend" to stabilize not at the silica surface but in a near-surface layer. These centers are inaccessible to the gas-phase O_2 molecules. Among these defects are the PCs $((\equiv\text{Si-O})_3\text{Si})_3\text{C}^\bullet$, $(\equiv\text{Si-O})_2\text{Si}^\bullet\text{-N(Si(O-Si}\equiv)_3)_2$, and the $((\equiv\text{Si-O})_3\text{Si})_3\text{C(Si(O-Si}\equiv)_3)$ group. Oxygen vacancy $(\equiv\text{Si-O})_3\text{Si-Si(O-Si}\equiv)_3$ should also be included in this group. The relevant arguments are advanced in the end of this section. Defects of other types, to which the PCs $(\equiv\text{Si-O})_3\text{Si}^\bullet$, diamagnetic groups $(\equiv\text{Si-O})_2\text{Si:}$, and cyclic structures $(\equiv\text{Si-O-})_2\text{Si} < \text{O}_2 > \text{Si(-O-Si}\equiv)_2$ belong, can (and prefer to) stabilize at the silica surface (group A). After the silica mechanical activation, some of the $(\equiv\text{Si-O})_3\text{Si}^\bullet$ and $(\equiv\text{Si-O})_2\text{Si:}$ defects are situated in the near-surface layer of the material, although they "crop out" at the surface upon sample heating [65].

Below, we endeavor to relate the observed effect to the effect of "geometric" factor. All group B defects contain two or more $(\equiv\text{Si-O})_3\text{Si}$ fragments as substituents. In the configuration corresponding to the lowest "intrinsic" energy of the defect, the symmetry axes of these fragments lie in a common plane. Whether such spatial structure can survive for a defect upon its stabilization at the surface? This can be the case if the symmetry axes of these groups are parallel to the solid surface. However, it is likely that such arrangement is energetically unfavorable. For the paramagnetic center $(\equiv\text{Si-O})_3\text{Si}^\bullet$, representing such fragment, it is more profitable to orient symmetry axis along the normal to the surface rather than parallel to it (see Section 6.1). Because of this, the spatial structure of the group B defect should be distorted upon its outcrop at the surface and become bent instead of planar, which requires an additional expenditure of energy. The "pyramidal" structure of $(\equiv\text{Si-O})_3\text{Si}^\bullet$ is specific only to the surface defects. No

Lam Research Ex. 1035 - Page 334
Lam Research Corp. v. Inpria Corp.
IPR2024-00033 - U.S. Patent No. 9,823,564

such constraints on the spatial structure of the defect coordination sphere exist for the bulk centers (see also Section 6.1).

Oxygen deficiency in pure quartz glasses is ordinarily associated with the presence of the two types of diamagnetic centers in glass: oxygen vacancies $(\equiv Si\text{-}O)_3Si\text{-}Si(O\text{-}Si\equiv)_3$ and SCs $(\equiv Si\text{-}O)_2Si:$. The enthalpy of the equilibrium process:

$$(\equiv Si\text{-}O)_3Si\text{-}Si(O\text{-}Si\equiv)_3 \Leftrightarrow (\equiv Si\text{-}O)_2Si: + (\equiv Si\text{-}O)_2Si(O\text{-}Si\equiv)_2$$

is equal to $\Delta H\,(0\,K) = (\,(25 \pm 5)\,kcal/mol$ (the result of calculation on G2-level using low-molecular model systems, the reactants and products are assumed to be in the thermodynamically most stable states). The formation of RSi terminates at a temperature of 1400 K. If the Boltzmann distribution is established under these conditions, then more than 99% of oxygen deficiency must fall on the oxygen vacancies. In the RSi samples, the SCs stabilize at the surface, whereas the presence of oxygen vacancies at the surface has not been detected experimentally as yet. In any case, the amount of oxygen vacancies at the sample surface does not exceed the number of SCs. With these experimental findings, the expected energy expenditure for the vacancy transfer from the bulk to the surface can be estimated at > 20 kcal/mol.

14. Design of Intermediates With Desired Structure on Silica Surface

Reactive species play an important role in various processes in the gas and condensed phases. Numerous experimental and theoretical studies are devoted to their structure and reactivity. However, to obtain these data, one should usually overcome substantial experimental difficulties. Therefore, the development of new methods for the preparation and stabilization of chemically active species is promising. Of course, these species also include defects stabilized on the activated silica surface. The nature and properties of this surface were the focus of the first section. The set of these species can be more diverse. The accessibility of surface sites (S) for molecules of the environment (P) makes it possible to modify chemically the defects in solids on purpose. The more reactive is site S, the more diverse molecules P can be involved in this process. Point defects that are stabilized on the activated silica surface include a low coordination silicon atom, whose one (paramagnetic $(\equiv Si\text{-}O)_3Si^{\bullet}$ sites) or two (diamagnetic $(\equiv Si\text{-}O)_2Si:$) very strong Si-O bonds are cleaved. Therefore, these defects have excess free energy and they are highly reactive. There are several methods for obtaining grafted

Lam Research Ex. 1035 - Page 335
Lam Research Corp. v. Inpria Corp.
IPR2024-00033 - U.S. Patent No. 9,823,564

intermediates. In one of them, the surface site S undergoes chemical modification, due to which a new group is formed:

$$S + P \Rightarrow SP.$$

If S is a paramagnetic site, for example, $(\equiv Si\text{-}O)_3Si^{\bullet}$ radical, and molecule P is an unsaturated hydrocarbon, the substituted hydrocarbon radical is the reaction product [115]:

$$\equiv Si^{\bullet} + CH \equiv CH \Rightarrow \equiv Si\text{-}CH = {}^{\bullet}CH.$$

Vinyl radicals are one of the most reactive species among hydrocarbon radicals, and this example demonstrates a high chemical activity of PC in the processes of this type. This method was used to obtain substituted hydrocarbon radicals with different structures: $\equiv Si\text{-}O\text{-}CH_2^{\bullet}$, $\equiv Si\text{-}CH_2\text{-}{}^{\bullet}CH(CH_3)$, $\equiv Si\text{-}CH_2\text{-}{}^{\bullet}C(CH_3)_2$, $\equiv Si\text{-}O\text{-}c\text{-}{}^{\bullet}C_6H_6$ [116], fluorine-substituted radicals, $\equiv Si\text{-}O\text{-}CH_2\text{-}{}^{\bullet}CF_2$, $\equiv Si\text{-}CF_2\text{-}{}^{\bullet}CF_2$, and $\equiv Si\text{-}O\text{-}CF_2\text{-}{}^{\bullet}CF(CF_3)$ [117], and other organic radicals [9]. The O_2, CO, CO_2, N_2O (see Table 7.3), and SO_2 [118] molecules can act as modifiers of P. Of course, more complex structures can be designed, successively involving various molecules in the chemical modification of the surface site structure, for example,

$$\equiv Si^{\bullet} + CH \equiv CH \Rightarrow \equiv Si\text{-}CH = {}^{\bullet}CH + CH_2 = CH_2 \Rightarrow$$

$$\equiv Si\text{-}CH = CH\text{-}CH_2 - {}^{\bullet}CH_2 + O_2 \Rightarrow \equiv Si\text{-}CH = CH\text{-}CH_2\text{-}CH_2\text{-}O\text{-}O^{\bullet}.$$

The examples of chemical modification of surface diamagnetic sites are presented in Section 9 (see Tables 7.11 and 7.12). Another method is based on the two-step modification of SC. The diamagnetic sites $(\equiv Si\text{-}O)_2Si$: are efficient acceptors of low-molecular free radicals (see subsection 9.2):

$$(\equiv Si\text{-}O\text{-})_2Si : + r^{\bullet} \Rightarrow (\equiv Si\text{-}O\text{-})_2Si^{\bullet}(r) .$$

This reaction yields the paramagnetic silyl site. When this site is involved in reactions with other molecules, its structure can be modified, and a new paramagnetic complex can be obtained, for example,

$$(\equiv Si\text{-}O\text{-})_2Si^{\bullet}(r) + H_2C = CH_2 \Rightarrow (\equiv Si\text{-}O\text{-})_2Si(CH_2\text{-}CH_2^{\bullet})(r).$$

This method using grafting to one silicon atom of SC makes it possible to approach spatially two chemically different groups r and r_1 and obtain free radical structures of the $(\equiv Si\text{-}O\text{-})_2Si(r_1^{\bullet})(r)$ type. This leads to more diverse intermediates on the solid surface and allows one to study new chemical processes involving these intermediates, including intramolecular reactions between r and r_1 groups. The low-molecular radicals necessary for the first step of SC modification can conveniently be obtained from the saturated H-r molecules, and appropriate defects on the silica surface can be used as

Lam Research Ex. 1035 - Page 336
Lam Research Corp. v. Inpria Corp.
IPR2024-00033 - U.S. Patent No. 9,823,564

their generators. The oxy radicals are most active in substitution reactions [51]:

$$(\equiv \text{Si-O})_3\text{Si-O}^{\bullet} + \text{H} - r \;\Rightarrow\; (\equiv \text{Si-O-})_3\text{Si-O-H} + r^{\bullet}.$$

One of the reasons for that is the high stability of the O-H bond in the newly formed silanol group (125–130 kcal/mol), and H-*r* can be not only a hydrocarbon molecule, but also H-OH, H-NH_2, etc. The diamagnetic dioxasilyrane groups are also the generators of alkyl radicals (see subsection 4.2). Many intermediates can be obtained as the products of thermal or thermo oxidative transformations or photo transformations of other initial structures. For example, vinoxyl radicals were obtained by the photolysis of peroxide radicals of the vinyl type [119]:

$$\equiv \text{Si-CH} = \text{CH-O-O}^{\bullet} + h\nu \;\Rightarrow \equiv \text{Si-}^{\bullet}\text{CH-CH} = \text{O} + \text{O}.$$

Pyrolysis of DOSG results in the formation of silanol groups [73]:

$$> \text{Si} < \text{O}_2 \;\Rightarrow\; > \text{Si} = \text{O} + \text{O}_2.$$

The available experimental data indicate that the intermediates grafted onto the silica surface are matrix stabilized. Even when we deal with reactive intermediates, such as the $(\equiv\text{Si-O-})_3\text{Si-CH}_2\text{-CH}_2^{\bullet}$ radical, their thermal stability is controlled not by chemical processes involving the surrounding matrix, but by the rate constants of the intramolecular isomerization and decomposition reactions:

$$(\equiv \text{Si-O-})_3\text{Si-CH}_2 - {}^{\bullet}\text{CH}_2 \;\Rightarrow (\equiv \text{Si-O-})_3\text{Si-}^{\bullet}\text{CH-CH}_3$$
$$\Rightarrow (\equiv \text{Si-O-})_3\text{Si-CH} = \text{CH}_2 + \text{H}^{\bullet}\ .$$

These reactions occur at temperatures above 450 K, and their activation energies are 35–40 kcal/mol [116]. This implies that the nearest environment of the intermediate does not contain other reactive groups. The siloxane bonds, which are the environment of the surface site, are chemically inert. The concentration of defects on the activated silica surface is $\sim 10^{13}$ site/cm^2, which corresponds (in the case of their random distribution), to the average distance between them of several tens of angstrom. Although the degree of randomness is unknown, no influence of neighbors was observed for the grafted fragments consisting of a few atoms (we mainly deal with these intermediates). These effects should appear at long grafted fragments.

Let us discuss several specific examples to demonstrate the possibility for obtaining various intermediates and study of their reactivity. The next example illustrates another important advantage of the method: possibility for the control of the processes of formation of low-molecular radicals during chemical reactions and obtaining the data on their nature. It was mentioned in Section 4 that one can obtain samples that have diamagnetic groups

Lam Research Ex. 1035 - Page 337
Lam Research Corp. v. Inpria Corp.
IPR2024-00033 - U.S. Patent No. 9,823,564

alongwith the intermediates under study. These groups (D) (of the silylene, silanone, or dioxasilyrane types) are efficient acceptors of low-molecular free radicals (see Sections 9.2, 9.6, and 9.7). Therefore, if low-molecular free radicals ($r^{\bullet}$) are formed in the system during the reaction, they react with these groups to form paramagnetic complexes $(Dr)^{\bullet}$:

$$D + r^{\bullet} \Rightarrow (Dr)^{\bullet}.$$

The identification of the structure of this complex can give the data on the radical $r^{\bullet}$. These data are especially fruitful for the analysis of mechanisms of intramolecular rearrangements of free radicals of different types, in particular, peroxide radicals $(\equiv Si\text{-}O)_2Si(r)(O\text{-}O^{\bullet})$, $r = H$, CH_3, and C_2H_5. The formation of products of peroxide radicals decomposition – H atom or *OH radicals – was detected experimentally.

The majority of processes occurring in the condensed phase are characterized by ''intracellular'' reactions involving the primary products of the transformation. This impedes the isolation of particular elementary steps from the overall process. These difficulties do not arise for an intermediate stabilized on the solid surface. The low-molecular products of the reactions involving this intermediate (atoms, radicals, or molecules) the zone of transformation through the gas phase can leave without hindrance. The occurrence of intracellular reactions is virtually ruled out, which makes it possible to detect primary steps of the corresponding processes.

Defects stabilized on the silica surface that include the two-coordinated silicon atom (SC) and the products of their oxidation (SG and DOSG groups) are of interest primarily from the standpoint of their reactivity. Some data on their reactivity were presented in Section 9. Here we discuss another example. The characteristic luminescence of SC (singlet–singlet and triplet–singlet, see Sections 9.4 and 9.5) in combination with its accessibility to molecules from the environment makes it possible to study experimentally their reactivity in electron-excited states. The presence of gaseous molecules above the sample surface decreases the probability of the radiative deactivation of SC due to the appearance of an additional deactivation channel consisting of photochemical reactions. By monitoring the changes in the luminescence intensity under these conditions, one can determine the rate constants of the corresponding processes and establish their mechanism from the analysis of the product composition. The results of measuring the quenching rate constants of the singlet and triplet luminescence of SC ($\lambda_{exc} = 237$ nm) are presented in Table 7.17. As expected, SCs in electron-excited states are much more reactive than in the ground state.

The reactions of SC in the excited singlet state occur almost without an activation barrier. The reactions of SC in the first triplet state with H_2, N_2O, and CO_2 molecules are characterized by low activation energy.

Lam Research Ex. 1035 - Page 338
Lam Research Corp. v. Inpria Corp.
IPR2024-00033 - U.S. Patent No. 9,823,564

Table 7.17. Quenching rate constants of singlet ($^1(>Si:)^*$) and triplet ($^3(>Si:)^*$) luminescence of SC [41, 59][a]

Reaction	T (K)	K (cm^3/molecule · s)
$^1(>Si:)^* + N_2O$	295	$(2.1 \pm 0.5) \times 10^{-10}$
$^1(>Si:)^* + CO_2$	295	$(1.8 \pm 0.5) \times 10^{-11}$
$^1(>Si:)^* + CO$	295	$(1.8 \pm 0.5) \times 10^{-10}$
$^1(>Si:)^* + H_2$	77	$(1.2 \pm 0.2) \times 10^{-11}$
	295	$(1.7 \pm 0.3) \times 10^{-11}$
$^3(>Si:)^* + CO$	295	$(0.7 \pm 0.1) \times 10^{-10}$
	443	$(0.6 \pm 0.1) \times 10^{-10}$
$^3(>Si:)^* + CO_2$	295–443	$(4.7 \pm 0.2) \times 10^{-12}$ $\exp(-(3.2 \pm 0.2)/RT)$
$^3(>Si:)^* + N_2O$	298–393	$(2.0 \pm 0.8) \times 10^{-12}$ $\exp(-(1.7 \pm 0.2)/RT)$
$^3(>Si:)^* + H_2$	200–400	$(8.4 \pm 1) \times 10^{-13}$ $\exp(-3.6/RT)$
$^3(>Si:)^* + HC{\equiv}CH$	295	$(3.2 \pm 0.2) \times 10^{-10}$
	448	$(3.3 \pm 0.2) \times 10^{-10}$

[a]The activation energy in kcal/mol.

Luminescence quenching is the process of the redistribution of the electron excitation energy. Let us consider the mechanism of the deactivation of triplet excited SC by CO molecules. It has been established experimentally that luminescence quenching of SC in a CO atmosphere is not accompanied by the formation of new chemical compounds. On the other hand, a CO molecule lacks low-lying electron-excited states to consider the electron-excitation energy transfer in this system.

Quantum-chemical calculation of the ($F_2Si: + CO$) system showed that SC in the ground state do not form stable complexes with a CO molecule. Repulsion prevents these molecules in ground states to approach each other. However, SC in the triplet-excited state forms a stable triplet complex of the bi-radical type with a CO molecule ($F_2Si^{\bullet}\text{-}C^{\bullet} = O$). Its heat of formation is ~25 kcal/mol. According to the results of calculation, the singlet term of the repulsion nature crosses the triplet term near the minimum of the energy of the latter. Due to the triplet–singlet conversion, the system is in the singlet state, and the complex decomposes to yield the CO molecule. Thus, the quenching process considered, which is chemical in essence, results in the conversion of the electron excitation energy of SC to the energy of motion of the nuclear subsystem at the stages of relaxation of the triplet complex structure and its decomposition without any chemical transformations in the system. For photoreactions involving other gases (H_2, N_2O, CO_2, and C_2H_2), the decay of SC and the formation of reaction products were

Lam Research Ex. 1035 - Page 339
Lam Research Corp. v. Inpria Corp.
IPR2024-00033 - U.S. Patent No. 9,823,564

observed. For example, the luminescence quenching of SC in the excited singlet (s) and triplet (t) states in a hydrogen atmosphere is related to hydrogen-atom elimination [59]:

$$[(\equiv \text{Si-O})_2\text{Si}:]^*_{s,t} + \text{H}_2 \Rightarrow (\equiv \text{Si-O})_2\text{Si}^{\bullet}\text{-H} + \text{H}^{\bullet}.$$

Let us briefly overview the results of relevant studies. The mechanism of the photolysis of hydrocarbon peroxide radicals of different types was studied [119], and the decomposition of the electron-excited peroxide fragment with an O-O bond cleavage was found to be the primary act of the process. When the reaction is not complicated by the adsorption of molecules on the solid surface, its kinetic parameters can be determined. The rate constants of the reactions of radicals $\equiv\text{Si}^{\bullet}$, $\equiv\text{Si-O-O}^{\bullet}$, $\equiv\text{Si-CH}_2^{\bullet}$, $\equiv\text{Si-O-CH}_2^{\bullet}$, $\equiv\text{Si-CH}_2\text{-CH}_2^{\bullet}$, and $\equiv\text{Si-O-}^{\bullet}\text{C}=\text{O}$ with $\text{H}_2(\text{D}_2)$, CH_4, C_2H_6, and C_3H_8 were measured in Ref. [16].

Paramagnetic centers containing a sulfur atom in different oxidation states, $(\equiv\text{Si-O})_3\text{Si-O-S}^{\bullet}=\text{O}$, $(\equiv\text{Si-O})_3\text{Si-O-S}^{\bullet}\text{O}_2$, $(\equiv\text{Si-O})_3\text{Si-O-SO}_2\text{-O}^{\bullet}$, and $(\equiv\text{Si-O})_3\text{Si-O-SO}_2\text{-O-O}^{\bullet}$, were obtained in Ref. [118]. Their radiospectroscopic parameters were determined, and the mechanism of free radical oxidation of SO_2 molecules in this system was established. The mechanism of the initial steps of free radical polymerization and copolymerization of hydrogen- and fluorine-substituted unsaturated hydrocarbons was studied in Ref. [117]. The pathways were found and the kinetic parameters were determined for reactions of intramolecular H(D) atom transfer between r (CH_3, CD_3, $\text{CH}_2\text{-CH}_3$) and $r_1^{\bullet}$ ($\text{CH}_2\text{-CH}_2^{\bullet}$, $\text{CD}_2\text{-CD}_2^{\bullet}$), in the structure of $(\equiv\text{Si-O})_2\text{Si}(r)(r_1^{\bullet})$ [120].

Thus, the experimental results presented in this section indicate that the chemical modification of surface defects is a convenient and efficient method for the preparation of reactive intermediates with different structures. Using this method, one can synthesize various groups and obtain the data on their spectral parameters and reactivity, pathways and rate constants of thermal, chemical, and photochemical processes involving these groups.

15. Conclusions

The reactivity of a solid surface, particularly, of a broad band-gap insulator such as SiO_2, is controlled by surface defects. These are the intrinsic and impurity paramagnetic and diamagnetic centers. The enhanced reactivity of such centers is caused by the host or impurity atoms entering into the composition of the center in the states with an uncommon coordination mode. Such centers in solids arise under the actions of various types (thermo, mechanical, UV

Lam Research Ex. 1035 - Page 340
Lam Research Corp. v. Inpria Corp.
IPR2024-00033 - U.S. Patent No. 9,823,564

irradiation) and represent the products of bond rupture and subsequent bond rearrangement. The most comprehensive data on the spectral characteristics, structure, and reactivity of a certain type of surface defects can be obtained if they can be prepared (synthesized) selectively at the solid surface.

In recent years, the methods for activating silica surface have been developed in an attempt to obtain samples with a high concentration of point defects. A possibility to thermo chemically activate the surface of a translucent SiO_2 "film" sample prepared by pressing high dispersed silica powder (aerosil) and having a thickness of several tens of microns has been demonstrated. The use of film samples allows the quantitative optical (UV, visible, IR) studies of the spectral properties of surface defects. The structure of intrinsic surface defects has been interpreted for SiO_2. It was established that these defects belong to the two main types, in which the silicon atom entering into the defect composition is bonded, respectively, to three or four lattice oxygen atoms. The PCs $(\equiv Si\text{-}O\text{-})_3Si^{\bullet}$ and, for the mechanically activated samples, $(\equiv Si\text{-}O\text{-})_3Si\text{-}O^{\bullet}$ (with a non-bridging oxygen atom) refer to the first type. In the defects of the second (diamagnetic) type, the Si atom is bonded to two lattice oxygen atoms.

The sequence of paramagnetic defects $(\equiv Si\text{-}O\text{-})_3Si^{\bullet}$, $(\equiv Si\text{-}O\text{-})_3Si\text{-}O^{\bullet}$, and $(\equiv Si\text{-}O\text{-})_3Si\text{-}O\text{-}O^{\bullet}$ is genetically associated with a three-coordinate silicon atom, while the intrinsic diamagnetic defects are represented by the SCs $(\equiv Si\text{-}O\text{-})_2Si$: centers. These centers generate a series of diamagnetic defects, in which the silicon atom occurs in the different oxidation states. To date, the silanone $((\equiv Si\text{-}O\text{-})_2Si = O)$ and dioxasilyrane $((\equiv Si\text{-}O\text{-})_2Si < O_2)$ groups have been identified for this sequence. One more (third) type of defects $(\equiv Si\text{-}O)_2Si < O_2 > Si(O\text{-}Si\equiv)_2$ having a cyclic structure with two silicon atoms and two oxygen atoms should be added to the aforementioned types of defects. These surface groups in silica are high-temperature dehydration products. Based on a study of the chemical properties of the surface defects of different type, the methods have been developed that allow conversion of the centers from one type to the other. These methods can be used to prepare samples containing surface-stabilized point defects of the desired type and in the required proportion. The spectral characteristics allowing the monitoring of the processes of formation and mutual transformation of the surface defects of different type have been determined.

In the disordered (amorphous) solids, the defect structure is inevitably scattered, bringing about inhomogeneous line broadening and kinetic inequivalence of defects. Elucidation of the cause and magnitude of these effects is one of the fundamental problems in the study of amorphous solid state. The role of the sources of inhomogeneous broadening for the surface-stabilized groups bonded to a lattice silicon Si_{α} atom is primarily played by the silicon β atoms comprising its first coordination sphere (on the side of a

Lam Research Ex. 1035 - Page 341
Lam Research Corp. v. Inpria Corp.
IPR2024-00033 - U.S. Patent No. 9,823,564

solid). However, this influence rapidly dies away with an increase in the number of chemical bonds separating "active" center of the defect from the surface Si_α atom. For instance, the manifestations of the β atoms are observed neither in the spectral nor in kinetic characteristics of the $(\equiv Si\text{-}O\text{-})_3Si\text{-}O\text{-}CH_2\text{-}CH_2$* groups, where the active center is localized on the terminal carbon atom.

The form of the distribution function for the characteristics of the particles depends on the sample-preparation procedure. The information on the spectral and kinetic characteristics of a defect can be gained and related to its geometric and electronic structures in those cases where the corresponding distribution functions are comparatively narrow, so that the inhomogeneous broadening does not mask the properties of individual centers. Being equipped with this information, we have a chance of separating the contributions from the homogeneous and inhomogeneous broadening to the spectral band shape or to the shape of kinetic curve. For this reason, the development of the methods for generating comparatively narrow fractions of the defects of different chemical nature and studying their physicochemical characteristics was one of the objectives of this work. The choice of a solid (silica) surface as a subject of investigation proved to be quite suitable for the solution of the posed problem, because the inhomogeneous broadening effects for the surface-stabilized defects are much less pronounced than for the centers in the bulk of a solid.

For the processes occurring in a condensed medium, an important and, often, decisive role is played by the cell effects; to escape from cell, particles must possess a certain mobility. The mobility in a three-dimensional network of siloxane bonds is necessarily associated with the rupture or rearrangement of the chemical bonds between neighboring atoms. Elucidation of the mechanisms of these processes is one of the most intricate and experimentally poorly studied problems of amorphous solids, where the inhomogeneous broadening effects are most pronounced. Figure 7.34 illustrates the curves obtained for the thermal annealing of the SGs stabilized at the MSi (curve I) and RSi (curve II) surfaces. The temperature interval where the transformation occurs is extended by more than 800°. Mutual approach of the $>Si=O$ group and the neighboring $\equiv$Si-O-Si$\equiv$ bond is the rate-limiting step of the process, while the $\equiv$Si-O-Si($<$)-O-Si$\equiv$ group is the reaction product. For free particles, the activation energy for the insertion of SG into the siloxane bond does not exceed several kilocalories per mole. Although such bonds constitute the SG environment, to approach one of them either almost no force should be applied (starting section of curve I) or a barrier of $\sim$80 kcal/mol has to be overcome (high-temperature section of curve II). For a mechanically activated sample, thermal stability of the SGs is appreciably lower, because it is easier for

Lam Research Ex. 1035 - Page 342
Lam Research Corp. v. Inpria Corp.
IPR2024-00033 - U.S. Patent No. 9,823,564

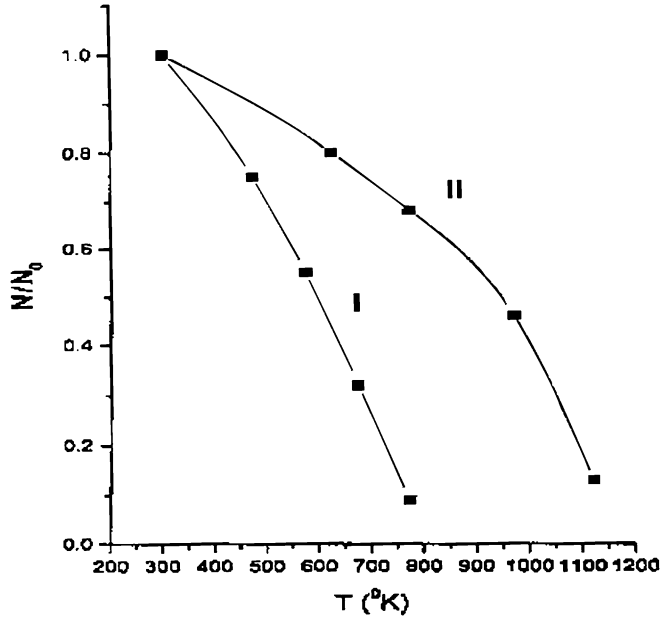


Fig. 34. The curves obtained for the thermal annealing of the $>Si=O$ groups stabilized at the MSi (curve I) and RSi (curve II) surfaces.

them to find an appropriate partner in a disordered material obtained after mechanical treatment.

The silanone group occupies a special place among the intrinsic defects in silica. It is the only diamagnetic defect in the stoichiometric SiO_2. There are strong grounds to believe that this group functions as an intermediate in various chemical processes occurring in SiO_2. It was assumed that the silanone groups appear as intermediate products of the thermal destruction of dimethylcyclosiloxanes [121]. The abstraction of a dimethylsilanone molecule in this process reduces the ring size, whereas the addition to another ring increases it. This process is expected to play an important part also in the transformations of a network of siloxane bonds in amorphous silica, because it consists of the rings differing in size.

The formation of SG as an intermediate species can also be expected for the thermally activated processes of the type

$$(\equiv \text{Si-O-})_3\text{Si}^{\bullet} \rightarrow (\equiv \text{Si-O-})_2\text{Si}=\text{O} + {}^{\bullet}\text{Si} \equiv +(82 \pm 2)\ \text{kcal/mol};$$

$$(\equiv \text{Si-O-})_3\text{Si}^{\bullet} \rightarrow (\equiv \text{Si-O-})_2\text{Si} : +{}^{\bullet}\text{O-Si} \equiv +(88 \pm 2)\ \text{kcal/mol};$$

$$(\equiv \text{Si-O-})_3\text{Si-O}^{\bullet} \rightarrow (\equiv \text{Si-O-})_2\text{Si}=\text{O} + {}^{\bullet}\text{O-Si} \equiv +(72 \pm 2)\ \text{kcal/mol}.$$

Lam Research Ex. 1035 - Page 343
Lam Research Corp. v. Inpria Corp.
IPR2024-00033 - U.S. Patent No. 9,823,564

The values given in this scheme characterize the heat of these processes. The stabilization of the geminal hydroxyls $(\equiv\text{Si-O-})_2\text{Si(OH)}_2$ (with a concentration of $\sim 10^{13}\,\text{cm}^{-2}$) at the surface of SiO_2 points to the fact that some of the surface silicon atoms are bonded to solid via only two lattice oxygen atoms. Thermal decomposition of the surface geminal hydroxyls is accompanied by the formation of the SGs [67]:

$$(\equiv \text{Si-O-})_2\text{Si(OH)}_2 \;\Rightarrow\; (\equiv \text{Si-O-})_2\text{Si} = \text{O} + \text{H}_2\text{O} \;+ (75 \pm 5)\ \text{kcal/mol}.$$

In another method of surface activation to form RSi, the greater part of the reactive centers consists of the $(\equiv\text{Si-O-})_2\text{Si}$: groups, in which the silicon atom is also bonded to only two lattice oxygen atoms. The concentration of these groups is $\sim 10^{13}\,\text{cm}^{-2}$. In this case, the silanone groups can be obtained by the oxidation of silylene centers (see Section 4.2).

High-temperature heating of the hydrated silicon samples is accompanied by the decomposition of hydroxyl groups and formation of the reactive cyclic structures $(\equiv\text{Si-O-})_2\text{Si} < \text{O}_2 > \text{Si}(\text{-O-Si}\equiv)_2$. Their concentration is equal to $\sim 10^{13}\,\text{cm}^{-2}$ [4,72]. These groups can also form through the combination (condensation) of two silanone groups:

$$2(\equiv \text{Si-O-})_2\text{Si} = \text{O} \Rightarrow (\equiv \text{Si-O-})_2\text{Si} < \text{O}_2 > \text{Si}(\text{-O-Si} \equiv)_2 - (125 \pm 5)\ \text{kcal/mol}.$$

Thus, it has become apparent that the processes of formation of, at first glance, dissimilar reactive groups at the solid surface have much in common with each other and that these processes are closely related to the presence of the surface silicon atoms bonded to the lattice via only two oxygen atoms. What is meant by a value of $10^{13}\,\text{cm}^{-2}$ that is almost constant and comprises nearly 2% of the total number of surface atoms? It is not improbable that investigations along this line will furnish a deeper insight into the complicated and intriguing SiO_2 system.

Questionnaire

(1) Let there be the ensemble of particles reacting between themselves under the first-order kinetic law but with differing activation energies of transformation. What will be the shape of the activation energy distribution function of particles if it is known that the distribution function depends on the transformation rate constant according to a hyperbolic law: $n(k) \sim 1/k$ $(k_{\min} \leq k \leq k_{\max})$?

(2) The imperfection in a solid is characterized by: (1) an intense optical absorption band with the energy larger than 5 eV; (2) the luminescence lacking; and (3) the stability with respect to high irradiation doses. Which dissipation channels of electron excitation energy might be suggested and how can they be verified in experiment?

Lam Research Ex. 1035 - Page 344
Lam Research Corp. v. Inpria Corp.
IPR2024-00033 - U.S. Patent No. 9,823,564

(3) Forbidden transitions in an EPR spectroscopy result from simultaneous electron and nucleus spin flips under the action of radio frequency field. For this effect to be observed, the linkage between electron and nucleus spins has to exist. Which interactions between spins are most effective in raising the intensity of a forbidden transition? What is it necessary for the intensities of allowed and forbidden transitions to be compatible in their magnitudes?
(4) Which must be the symmetry of the spatial structure of a paramagnetic center to ensure that its EPR spectrum is characterized by (1) isotropic or (2) axially symmetric g-tensor?
(5) It was established experimentally that the paramagnetic $(\equiv Si\text{-}O)_3Si^*$ center in silica prefers to be stabilized at the surface but not in the bulk of the material. What are the driving forces of this process?
(6) A single absorption band with the maximum at $2225\,cm^{-1}$ is registered in the IR spectrum of $>SiH_2$ groupings in the region of valence vibrations of Si-H bonds. Might it be that only one absorption band in the region of valence vibrations of a Si-D bond will be left over in the case of isotopically-substituted $>SiD_2$ groupings? What can we say about the spatial structure of such a grouping?
(7) When talking about difficulties in interpreting experimental evidences for disordered (amorphous) solids, the researchers often plead the lack of the theory of their matter structure. To what questions about the surface structure of amorphous silica might the theory answer?
(8) Why under changes of the Si-O-Si valence angle does the system's energy vary much less than under changes of the H-O-H valence angle?
(9) Electronically excited state of the $(\equiv Si\text{-}O)_3Si\text{-}O_t^*$ (B, $^2A'$) radical is connected with the transition of one of the σ-electrons of $Si\text{-}O_t$ bond to $2p_x$-AO of the oxygen terminal atom (see Figure 7.16c). An unpaired electron is localized in this state on $2p_z$-AO of the oxygen terminal atom. What is the expected structure of the transient state for the reaction of the radical residing in this excited state with H_2 molecule? Compare this transient state with that for analogous reaction involving a ground-state radical.

References

1. D. L. Griscom, The Natures of Point Defects in Amorphous Silicon Dioxide, in: G. Pacchioni, L. Skuja, D. L. Griscom (Eds.), Defects in

Lam Research Ex. 1035 - Page 345
Lam Research Corp. v. Inpria Corp.
IPR2024-00033 - U.S. Patent No. 9,823,564

SiO_2 and Related Dielectrics: Science and Technology, Vol. 2, Kluwer Academic, Dordrecht, 2000, p. 117.
2. L. Skuja, Optical Properties of Defects in Silica, in: G. Pacchioni, L. Skuja, D. L. Griscom (Eds.), Defects in SiO_2 and Related Dielectrics: Science and Technology, Vol. 2, Kluwer Academic, Dordrech, 2000, p. 73.
3. B. A. Morrow, I. A. Cody, J. Phys. Chem. **80** (1976) 1998.
4. B. C. Bunker, D. M. Haaland, K. J. Ward, T. A. Michalske, W. L. Smith, J. S. Binkley, C. F. Melius, C. A. Balfe, Surf. Sci. **210** (1989) 406.
5. R. K. Iler, The Chemistry of Silica, Wiley, New York, 1979.
6. A. P. Legrand, H. Hommel, A. Tuel, A. Vidal, et al., Adv. Colloid Interface Sci. **33** (1990) 91.
7. J. B. Peri, A. L. Hensley, Jr., J. Phys. Chem. **72** (1968) 2926.
8. A. M. Ferrari, E. Garrone, G. Spoto, P. Ugliengo, A. Zecchina, Surf. Sci. **323** (1995) 151.
9. G. Hochstrasser, J. F. Antonini, Surf. Sci. **32** (1972) 644.
10. V. A. Radtsig, A. V. Bystrikov, Kinet. Katal. **19** (1978) 713.
11. A. N. Streleskii, Proceedings of the 2nd International Conference on Structural Applications of Mechanical Alloing, Vancouver, Canada, 1993, p. 51.
12. V. I. Wettegren, V. J. Korsukov, V. E. Novak, II International Congress of Fracture, Conference Proceedings, Brighton, 1969, p. 545.
13. A. N. Streletskii, P. Yu. Butyagin, Kinet. Katal. **21** (1980) 765.
14. C. Morterra, M. J. D. Low, J. Phys. Chem. **73** (1969) 321.
15. C. Morterra, M. J. D. Low, Ann. N.Y. Acad. Sci. **220** (1972) 135.
16. A. A. Bobyshev, V. A. Radtsig, Kinet. Katal. **31** (1990) 931.
17. V. B. Kazanskii, A. M. Gritskov, V. M. Andreev, Dokladi Acad. Nauk. **235** (1977) 136.
18. V. A. Radzig, Colloids Surf., A: Physicochem. Eng. Aspects **74** (1993) 91.
19. V. A. Radtsig, Chem. Phys. Rep. **14** (1995) 1206.
20. P. Hoffmann, E. Knozinger, Surf. Sci. **188** (1987) 181.
21. R. H. Silsbee, J. Appl. Phys. **32** (1961) 1459.
22. V. A. Radtsig, Kinet. Katal. **37** (1996) 310.
23. V. A. Radtsig, I. V. Berestetskaya, S. N. Kostritsa, Kinet. Katal. **39** (1998) 940.
24. J. Sauer, P. Ugliengo, E. Garrone, V. R. Saunders, Chem. Rev. **94** (1994) 2095.
25. W. J. Hehre, L. Radom, P. v. R. Schleyer, J. A. Pople, Ab Inito Molecular Orbital Theory, Wiley, New York, 1986.

Lam Research Ex. 1035 - Page 346
Lam Research Corp. v. Inpria Corp.
IPR2024-00033 - U.S. Patent No. 9,823,564

26. A. D. Becke, J. Chem. Phys. **98** (1993) 5648.
27. C. Lee, W. Yang, R. G. Pair, Phys. Rev. B: Condens. Matter **37** (1988) 785.
28. L. A. Curtiss, K. Raghavachari, J. A. Pople, J. Chem. Phys. **98** (1993) 1293.
29. M. J. Frisch, G. W. Trucks, H. B. Schlegel, et al., Gaussian 94, Revision D.1, Gaussian, Pittsburgh, 1995.
30. V. A. Radtsig, Kinet. Katal. **20** (1979) 448.
31. V. A. Radtsig, Kinet. Katal. **42** (2001) 696.
32. M. W. Chase, C. A. Davies, J. R. Downey, D. J. Frurip, J. Phys. Chem. Ref. Data **14** (Suppl. 1), (1985) 1.
33. A. J. Tench, T. Lawson, Chem. Phys. Lett. **7** (1970) 459.
34. W. B. Williamson, J. H. Lunsford, C. Nacashe, Chem. Phys. Lett. **9** (1971) 33.
35. V. A. Radtsig, V. A. Khalif, Kinet. Katal. **20** (1979) 705.
36. A. A. Bobyshev, V. A. Radtsig, Kinet. Katal. **22** (1981) 1548.
37. V. Barone, C. Adamo, N. Russo, Int. J. Quantum Chem. **52** (1994) 963.
38. D. L. Griscom, E. J. Friebele, G. H. Sigel, Jr., Solid State Commun. **15** (1974) 479.
39. R. A. B. Devine, J. Arndt, Phys. Rev. B **37** (1987) 9376.
40. D. L. Griscom, M. Cook, J. Non-Cryst. Solids **182** (1995) 119.
41. V. A. Radzig, Defects on Activated Silica Surface, in: G. Pacchioni, G. L. Skuja, D. L. Griscom (Eds.), Defects in SiO_2 and Related Dielectrics: Science and Technology, Vol. 2, Kluwer Academic, Dordrech, 2000, p. 117.
42. V. N. Bagratashvili, S. I. Tsypina, V. A. Radzig, et al., J. Non-Cryst. Solids **180** (1995) 221.
43. M. V. Merritt, R. W. Fessenden, J. Chem. Phys. **56** (1972) 2353.
44. R. L. Mozzi, B. E. Warren, J. Appl. Crystallogr. **2** (1969) 164.
45. P. Yu. Butyagin, A. A. Berlin, A. E. Kalmanson, Vysokomol. Soedin. **1** (1959) 865.
46. A. R. Silin', A. N. Trukhin, Tochechnye defekty i elementarnye vozbuzhdeniya v kristallicheskom i amorfnom SiO_2 (Point Defects and Elementary Excitations in Crystal and Amorphous SiO_2), Zinatne, Riga, Latvia, 1985.
47. R. A. Weeks, C. M. Nelson, J. Am. Ceram. Soc. **43** (1960) 399.
48. A. R. Reinberg, J. Chem. Phys. **41** (1964) 850.
49. D. L. Griscom, Phys. Rev. B **22** (1980) 4192.
50. V. A. Radtsig, S. N. Kozlov, Kinet. Katal. **42** (2001) 62.
51. A. A. Bobyshev, V. A. Radtsig, Kinet. Katal. **31** (1990) 925.

Lam Research Ex. 1035 - Page 347
Lam Research Corp. v. Inpria Corp.
IPR2024-00033 - U.S. Patent No. 9,823,564

52. A. A. Bobyshev, V. A. Radtsig, Kinet. Katal. **29** (1988) 638.
53. A. Carrington, A. D. McLachlan, Introduction to Magnetic Resonance, Harper and Row, New York, 1967.
54. V. A. Radtsig, E. G. Baskir, V. A. Korolev, Kinet. Katal. **36** (1995) 154.
55. Q. Zeng, J. F. Stebbins, A. D. Heany, T. Erdogan, J. Non-Cryst. Solids **258** (1999) 78.
56. A. A. Bobyshev, V. A. Radtsig, Fiz. Khim. Stekla **14** (1988) 501.
57. E. K. U. Gross, J. F. Dobson, M. Petersilka, Density Functional Theory II, in: R. F. Nalewajski (Ed.), Topics in Current Chemistry, Vol. 181, Springer, Berlin, 1996.
58. A. V. Amosov, K. S. Kornienko, I. O. Morozova, et al., Fiz. Khim. Stekla **13** (1), (1987) 126.
59. V. A. Radzig, V. N. Bagratashvili, S. I. Trypina, et al., J. Phys. Chem. **99** (1995) 6640.
60. G. Olbrich, Chem. Phys. **101** (1986) 381.
61. A. N. Streletskii, A. B. Pakovich, Yu. I. Aristov, et al., Khim. Fiz. **1** (1982) 938.
62. V. A. Radzig, I. N. Senchenia, in: Thesis of VII Symposium on Optical and Spectral Properties of Glasses (Vavilov State Optical Institute, Leningrad), (1989) 254.
63. V. A. Radzig, I. N. Senchenia, Khim. Fiz. **10** (1991) 322.
64. L. N. Skuja, J. Non-Cryst. Solids **179** (1994) 51.
65. A. B. Pakovich, Cand. Sci. (Chem.) Dissertation, Moscow Institute of Physics and Technology, Moscow, 1984.
66. A. A. Bobyshev, V. A. Radzig, in: A. R. Silin (Ed.), Spectroscopy of Glass-Forming Systems, Latvian State University, Riga, 1988, p. 85.
67. M. Ia. Mel'nikov, N. V. Fok, Uspehi Khimii **49** (1980) 252.
68. V. A. Radzig, A. A. Bobyshev, I. N. Senchenia, in: Thesis of VII Symposium on Optical and Spectral Properties of Glasses, Vavilov State Optical Institute, Leningrad, 1989, 258.
69. S. R. Langhoff, R. L. Jaffe, J. Chem. Phys. **71** (1979) 1475.
70. V. A. Radtsig, Kinet. Katal. **20** (1979) 456.
71. L. N. Skuja, A. N. Streletsky, A. B. Pakovich, Solid State Commun. **50** (1984) 1069.
72. B. C. Bunker, D. M. Haaland, T. A. Michalske, W. L. Smith, Surf. Sci. **222** (1989) 95.
73. A. A. Bobyshev, V. A. Radtsig, Khim. Fiz. **7** (1988) 950.
74. V. A. Radtsig, I. N. Senchenya, A. A. Bobyshev, V. B. Kazanskii, Kinet. Katal. **31** (1989) 1234.

Lam Research Ex. 1035 - Page 348
Lam Research Corp. v. Inpria Corp.
IPR2024-00033 - U.S. Patent No. 9,823,564

75. V. A. Radtsig, A. A. Bobyshev, Phys. Status Solids B **133** (1986) 621.
76. D. L. Baulch, C. J. Cobos, R. A. Cox, P. Frank, G. Hayman, Th. Just, J. A. Kerr, T. Murrells, M. J. Pilling, J. Troe, R. W. Walker, J. Warnatz, J. Phys. Chem. Ref. Data. **23** (1994) 847.
77. O. M. Nefedov, A. I. Ioffe, L. G. Menchikov, Khimiya karbenov (Chemistry of Carbenes), Khimiya, Moscow, 1990.
78. G. Maier, H. P. Reisenauer, K. Schottler, U. Wessolek-Kraus, J. Organomet. Chem. **366** (1989) 25.
79. B. Wirsam, Chem. Phys. Lett. **22** (1973) 360.
80. V. A. Radtsig, Kinet. Katal. **40** (1999) 764.
81. V. A. Radtsig, I. V. Berestetskaya, S. N. Kostritsa, Kinet. Katal. **39** (1998) 940.
82. H. J. Schnockel, J. Mol. Struct. **65** (1980) 115.
83. R. Withnall, L. Andrews, J. Am. Chem. Soc. **107** (1985) 2567.
84. L. Yu. Ustynyuk, V. A. Radtsig, I. N. Senchenya, Izv. Akad. Nauk. Ser. Khim. **12** (1995) 2409.
85. V. A. Radtsig, I. N. Senchenya, Izv. Akad. Nauk. Ser. Khim. **8** (1996) 1951.
86. V. A. Radtsig, I. V. Berestetskaya, I. V. Kolbanev, Kinet. Katal. **41** (2000) 457.
87. V. A. Radtsig, S. N. Kostritsa, Kinet. Katal. **41** (2000) 267.
88. R. Withnall, L. Andrews, J. Am. Chem. Soc. **108** (1986) 8118.
89. V. A. Radtsig, E. G. Baskir, V. A. Korolev, Kinet. Katal. **36** (1995) 618.
90. V. A. Radtsig, Kinet. Katal. **37** (1996) 302.
91. V. A. Radzig, J. Non-Cryst. Solids **239** (1998) 49.
92. K. Worhoff, P. V. Lambeck, A. Driessen, Lightwave Technol **17** (1999) 1401.
93. A. Stesmans, J. Non-Cryst. Solids **179** (1994) 10.
94. W. E. Carlos, S. M. Prokes, J. Appl. Phys. **78** (1995) 2129.
95. S. M. Prokes, W. E. Carlos, J. Appl. Phys. **78** (1995) 2671.
96. F. H. P. M. Habraken, A. E. T. Kuiper, Mater. Set Eng. R **12** (1994) 123.
97. K. A. Ellis, R. A. Buhrman, IBM J. Res. Dev. **43** (1999) 287.
98. E. P. Gusev, H. C. Lu, E. Garfunkel, T. Gustafsson, M. Green, IBM J. Res. Dev. **43** (1999) 265.
99. E. M. Dianov, K. M. Golant, R. P. Khrapko, A. S. Kurkov, B. Leconte, M. Douay, P. Niay, Electron. Lett. **33** (1997) 236.
100. E. M. Dianov, K. M. Golant, R. P. Khrapko, A. L. Tomashuk, Electron. Lett. **31** (1995) 1490.
101. E. M. Dianov, K. M. Golant, R. P. Khrapko, O. I. Medvedkov, A. L. Tomashuk, S. A. Vasil'ev, Opt. Mater. **5** (1996) 169.

Lam Research Ex. 1035 - Page 349
Lam Research Corp. v. Inpria Corp.
IPR2024-00033 - U.S. Patent No. 9,823,564

102. D. Pavy, M. Moisan, S. Saada, P. Chollet, P. Leprince, J. Marrec, Proceedings of the 12th European Conference on Optical Communications, Barcelona, 1986, p. 19.
103. E. M. Dianov, K. M. Golant, R. P. Khrapko, A. S. Kurkov, A. L. Tomashuk, J. Lightwave Technol. **13** (1995) 1471.
104. R. A. Weeks, J. Non-Cryst. Solids **179** (1994) 1.
105. V. A. Radtsig, Kinet. Katal. **20** (1979) 1206.
106. J. H. Mackey, J. W. Boss, M. Kopp, Phys. Chem. Glasses **11** (1970) 205.
107. J. T. Yount, G. T. Kraus, P. M. Lenahan, D. T. Krick, J. Appl. Phys. **70** (1991) 4969.
108. E. J. Friebele, D. L. Griscom, T. W. Hickmott, J. Non-Cryst. Solids **71** (1985) 351.
109. W. Primak, Phys. Rev. **100** (1955) 1677.
110. A. I. Mikhailov, Ya. S. Lebedev, N. Ya. Buben, Kinet. Katal. **6** (1965) 48.
111. V. A. Radzig, Khim. Fiz. **23** (2004) 70.
112. A. R. Silin, L. A. Lace, J Non-Cryst. Solids **149** (1992) 54.
113. R. Araujo, J. Non-Cryst. Solids **197** (1996) 164.
114. G. Pacchioni, G. Ierano, Phys. Rev. B: Condens. Matter **56** (1997) 7304.
115. E. M. Korol'kova, V. A. Radtsig, M. Ya. Mel'nikov, Dokl. Akad. Nauk. SSSR **331** (1993) 188.
116. V. A. Radtsig, Kinet. Katal. **24** (1983) 173.
117. L. S. Gulyaeva, V. P. Mel'nikov, V. A. Radtsig, Khim. Fiz. **5** (1986) 1405.
118. V. A. Radtsig, Kinet. Katal. **36** (1995) 165.
119. E. M. Korol'kova, V. A. Radtsig, M. Ya. Mel'nikov, Khim. Fiz. **10** (1991) 41.
120. S. N. Kostritsa, V. A. Radtsig, Izv. Akad. Nauk. Ser. Khim. **8** (1997) 1468.
121. L. M. Gusel'nikov, N. S. Nametkin, T. K. Ismailov, A. A. Sobtsov, V. M. Vdovin, Izv. Akad. Nauk. SSSR. Otdelenie Khimicheskih Nauk. **1** (1971) 84.

Lam Research Ex. 1035 - Page 350
Lam Research Corp. v. Inpria Corp.
IPR2024-00033 - U.S. Patent No. 9,823,564

Chapter 8

Atomic-Molecular Kinetic Theory of Physico-Chemical Processes in Condensed Phase and Interfaces

Y.K. Tovbin

Karpov Institute of Physical Chemistry, 10, Vorotsovo Pole Str., Moscow 105064, Russia

1. Introduction . . . 349
2. Gas–Solid Processes . . . 352
   2.1. Gas–Solid Interface . . . 352
   2.2. Lattice-Gas Model and Elementary Processes . . . 357
   2.3. Lateral Interactions . . . 363
   2.4. Quasi-Particle Description of Elementary Rates . . . 364
3. Kinetic Equations for Multistage Processes in Condensed Phase . . . 370
   3.1. Hamiltonian . . . 371
   3.2. Master Equation . . . 372
   3.3. Probabilities of Elementary Reactions . . . 375
   3.4. Kinetic Equations . . . 378
   3.5. Reaction Rates . . . 380
   3.6. Hierarchy of the Kinetic Equations . . . 382
   3.7. Two-Dimensional Model . . . 384
   3.8. Point-Like Models of a Reaction . . . 387
   3.9. Different Mobilities of Reactants . . . 390
4. Surface Processes . . . 391
   4.1. Physical Adsorption and Chemisorption . . . 392
   4.2. Adsorption and Thermodesorption Spectra . . . 395
   4.3. Multistage Processes . . . 399
   4.4. Islands and Two-Dimensional Phases . . . 402
   4.5. Self-Consistency of the Lattice-Gas Model . . . 404
   4.6. Surface Diffusion . . . 409
5. Solid Phase Processes in Solid–Gas Systems . . . 412
   5.1. Interface States . . . 412
   5.2. Diffusion Through Solids . . . 414
   5.3. Phase Transitions and Topochemical Processes . . . 418
6. Physico-Chemical Mechanics Problems . . . 419
   6.1. Rates of Elementary Stages at Solid Deformations . . . 419
   6.2. Hydrogen–Palladium System . . . 421
   6.3. Effective Potential . . . 422
   6.4. Mechanical and Transport Properties of the Pd–H_2 System . . . 423

THIN FILMS AND NANOSTRUCTURES, vol. 34
ISSN 1079-4050
DOI: 10.1016/S1079-4050(06)34008-2

© 2007 by Elsevier Inc.
All rights reserved.

Lam Research Ex. 1035 - Page 351
Lam Research Corp. v. Inpria Corp.
IPR2024-00033 - U.S. Patent No. 9,823,564

7. Numerical Dynamics Investigations 427
7.1. Cellular Automata Technique 427
7.2. Monte-Carlo Technique 429
7.3. Correlation Between Monte-Carlo Simulations and Kinetic Theory 435
8. Summary and Perspectives 438
Appendix A.
Equilibrium Distributions of Particles on Heterogeneous Lattices in Condensed Phases 441
. Cluster Methods 442
. Isotherms of Adsorption 443
. Multiparticles Configurations 445
. Free Energy 446
. Monte-Carlo Method. 446
. Matrix Method 446
. Method of Fragments 447
Appendix B.
Lowering the Dimension of a System of Equations in the Quasi-Chemical Approximation 448
Problems 451
References 452

A unified view of different kinetic problems in condensed phases on basis of the lattice-gas model was developed. Any physico-chemical process in condensed phases should be considered as a multistage process involving various elementary stages of a translational transport of reactive molecules and their chemical conversions. To develop the kinetic equations in condensed phases the master equation was formulated. The master equation is used to generate the kinetic equations for local concentrations and pair correlation functions. The latter set of equations permits consideration of history of formation of the local solid structure as well as its influence on the subsequent elementary stages. The many-body problem and closing procedure for kinetic equations are discussed. The influence of fast and slow stages on a closed system of equations is demonstrated. The multistage character of the kinetic processes in condensed phase creates a problem of self-consistency in describing the dynamics of elementary stages and the equilibrium state of the condensed system. The lattice-gas model is unique one to satisfy solving these problems.

The theory extends the famous Eyring's theory of the absolute reaction rates for elementary stages taking into account a non-ideal behavior of medium. Neighboring atoms and molecules influence the effective potential energetic of the considered reaction and change their activation energy through the potential interactions. A wide circle of experimental data can be described on taking into account a non-ideal behavior of the surrounding medium: adsorption and desorption, catalytic reaction and diffusion, crystal growth and new phase formation, surface and bulk reconstruction, etc.

Lam Research Ex. 1035 - Page 352
Lam Research Corp. v. Inpria Corp.
IPR2024-00033 - U.S. Patent No. 9,823,564

1. Introduction

Surface processes occurring at the gas–solid interface represent both an independent subject of studies and part of studies for a variety of process applications. They met within many heterogeneous catalytic processes, adsorption and membrane methods of gas purification and separation, growth of crystals from the vapor phase and their sublimation as well as deposition of films and their ''dissolution'' in active gaseous environments, and so on [1–3]. Understanding at the atomic-molecular level of these processes calls for a stage-by-stage study of the surface processes and for a development of a theory to describe these processes with account of the major real properties of the investigated systems.

The existence of a solid itself, the solid surfaces, the phenomena of adsorption and absorption of gases are due to the interactions between different components of a system. The nature of the interaction between the particles of a gas–solid system is quite diverse. It depends on the nature of the solid's atoms and the gas-phase molecules. The theory of particle interactions is studied by quantum chemistry [4,5]. To date, one can consider that the prospective trends in the development of this theory for metals and semiconductors [6,7] and alloys [8] have been formulated. They enable one to describe the thermodynamic characteristics of solids, particularly of phase equilibria, the conditions of stability of systems, and the nature of phase transitions [9,10]. Lately, methods of calculating the interactions of adsorbed particles with a surface and between adsorbed particles have been developing intensively [11–13]. But the practical use of quantum-chemical methods for describing physico-chemical processes is hampered by mathematical difficulties. This makes one employ rougher models of particle interaction – model or empirical potentials. Their choice depends on the problems being considered.

The present state of the theories of atomic and molecular processes in condensed phases is characterized by great non-uniformity of its development. Matters are much problematic in the theory of the kinetics of processes at a molecular level. The kinetics of surface processes mainly employs models taking no account of the interaction of the adsorbed particles (the law of masses or surface action) [14–16]. This does not reflect the real properties of a gas–solid interface. There is also a diversity of models when considering the interaction of the particles because various approximations are used (equilibrium is described with a view to the correlation effects, while kinetics ignores them). The problem of approximations is of a fundamental significance in the theory of condensed systems. Interaction between the particles causes all the particles to be bound to

Lam Research Ex. 1035 - Page 353
Lam Research Corp. v. Inpria Corp.
IPR2024-00033 - U.S. Patent No. 9,823,564

one another – a change in the state of a particle affects its neighbors, the latter, in turn, change their influence on their neighbors, and so on. This substantially hinders a description of the state of a system and the solution of the problem on the distribution of the particles.

Exact solution of the problems for many interacting particles are possible in a few cases [17–19]. They include one-dimensional systems and a number of individual cases for two-dimensional systems. In practice, one has to do with approximate methods that make it possible to describe systems within broad regions of a change in the concentrations of particles and the temperature. An important characteristic of an approximation is the appraisal of the extent to which the effects of correlation of the mutual distribution of the particles are taken into account. More accurate approximations take the correlation effects into account more accurately, but the growth in the accuracy is attended by a rapid increase in the intricacy of the model (which makes one finds a reasonable compromise).

The central task of theory is a self-consistent description of the main real factors of a gas–solid system with the aid of a single set of parameters of models for different time intervals including a transition to the equilibrium state if it exists under given external conditions. The problem of the self-consistent description of the evolution of a system is of major significance in the theory of processes in condensed phases, especially when one has in view the simultaneous description of various elementary processes, e.g., the stages of transfer and the stages of chemical transformation. To date, this problem had a positive solution only for models taking no account of particle interaction. Even for processes in non-ideal gases, the fact of the self-consistent description of equilibrium and kinetics must be proved in each specific model. This problem is also of an important practical significance because part of the parameters of a model can be determined independently from the data on the equilibria of individual subsystems and from the kinetics of simpler processes.

This chapter provides a unified view of different kinetic problems in condensed phases on basis of the lattice-gas model. This approach extends the famous Eyring's theory of the absolute reaction rates [20] for wide circle elementary stages: adsorption, desorption, catalytic reaction, diffusion, surface and bulk reconstruction, etc. taking into account a non-ideal behavior of medium. It should be mentioned that Eyring's idea for gaseous phases was intensively developed by Temkin [21] regarding surface processes on the homogeneous surfaces (see also extension of the theory for heterogeneous surfaces in Ref. [22]). This topic was reproduced in famous monograph [23] about the absolute reaction rates.

Section 2 describes condensed phases and interparticle interactions as well as the types of cooperative effects of reagents in condensed phases. Neighboring

Lam Research Ex. 1035 - Page 354
Lam Research Corp. v. Inpria Corp.
IPR2024-00033 - U.S. Patent No. 9,823,564

atoms and molecules influence the effective potential energetic of the considered reaction and change their activation energy through the potential interactions. In general, any chemical reaction in condensed phases should be considered as a multistage process involving various elementary stages of a translational transport of reactive molecules and their chemical conversions.

To develop the kinetic equations in condensed phases the master equation must be formulated. In Section 3 the master equation is used to generate the kinetic equations for local concentrations and pair correlation functions. The latter set of equations permits consideration of history of formation of the local solid structure as well as its influence on the subsequent elementary stages. The many-body problem and closing procedure for kinetic equations are discussed. The influence of fast and slow stages on a closed system of equations is demonstrated. The multistage character of the kinetic processes in condensed phase creates a problem of self-consistency in describing the dynamics of elementary stages and the equilibrium state of the condensed system. This problem is solved within the framework of a lattice-gas model description of the condensed phases.

Section 4 presents a variety of solid–gas surface processes: adsorption, desorption, catalytic reaction, and surface diffusion. Non-ideal behavior of the systems is considered through the effective pair potentials of intermolecular interactions. A wide circle of experimental data can be described on taking into account a non-ideal behavior of the surrounding medium.

A correlation between surface and volume processes is described in Section 5. The atomic-molecular kinetic theory of surface processes is discussed, including processes that change the solid states at the expense of reactions with atoms and molecules of a gas or liquid phase. The approach reflects the multistage character of the surface and volume processes, each stage of which is described using the theory of chemical kinetics of non-ideal reactive systems. The constructed equations are also described on the atomic level description of diffusion of gases through polymers and topochemical processes.

Section 6 describes the use of the kinetic theory for studying physico-chemical mechanics problems. An example of the theory is used to explain the observed properties for hydrogen–palladium systems. It is also used to self-consistently connect the local adsorption and diffusion characteristics of hydrogen atoms with the deformations within the metal membrane.

Section 7 describes the application of numerical techniques (cellular automata and Monte-Carlo (MC)) for dynamical investigation of surface processes. These techniques are alternative approaches for simulations of various multistage processes.

At last, Appendices A and B present equations for equilibrium distributions of particles in condensed phases, and approaches how to

Lam Research Ex. 1035 - Page 355
Lam Research Corp. v. Inpria Corp.
IPR2024-00033 - U.S. Patent No. 9,823,564

reduce the dimensionality of the system of equations in the quasi-chemical approximation.

2. Gas–Solid Processes

Let us consider a volume of space containing a part of the bulk phase of a solid, its surface, and part of the volume of a gas phase. This volume can be divided into three regions. The singled out region of the solid has the same composition and distribution of its components as the remaining part of the solid. Similarly, the singled out region of the gas phase contains components in the same state as in the remaining part of this phase. The second region is one in which the composition and distribution of the particles differs from the other two phases. The molecular interpretation of a phase interface differs from the singling out of the dividing surface between two phases adopted in thermodynamics [24]. It has a finite width, which in the general case can change in time. Let us discuss the main concepts and initial propositions used in the following.

2.1. Gas–Solid Interface

2.1.1. Gas Phase

Let us consider very simple notions of a gas phase as an ideal mixture of molecules [25]. The total pressure P in a gas phase is determined as $P = \sum_{i=1}^{s} P_i$, where P_i, is the partial pressure of the ith component of the gas mixture; $1 \le i \le s$, s is the number of components in the mixture. The partial pressure of a component is related to its concentration c, by the expression

$$P_i = c_i/\beta, \quad \beta = (N_A k_B T)^{-1} = (RT)^{-1}, \quad c_i = N_i/V, \tag{1}$$

where k_B is the Boltzmann constant, N_A the Avogadro constant, R the molar gas constant, T the absolute temperature, N_i the number of molecules of species i, and V the volume of the system.

The molecules of a gas phase are considered to be particles that do not interact with one another, and each of them is a statistically independent system. The statistical sum of a molecule of species i is

$$F_i^0(T) = \sum_n g_{in} \exp\{-\beta E_{in}\}. \tag{2}$$

Here E_{in} is the energy of a molecule of species i in the state n, and g_{in} is the degree of degeneracy of the given state. The energy of a molecule is usually represented as the sum of the relevant contributions of translational,

Lam Research Ex. 1035 - Page 356
Lam Research Corp. v. Inpria Corp.
IPR2024-00033 - U.S. Patent No. 9,823,564

rotational, and vibrational motions (if they can be separated). The calculation of the rotational and vibrational multipliers of the function of states of gas phase molecules is a quantum-statistical problem [26], and one will assume them to be known. The chemical potential of a molecule of species i in the gas phase can be written as follows:

$$\mu_i = \mu_i^0 + \beta^{-1} \ln(\beta P_i / F_i^0), \tag{3}$$

where μ_i^0 determines the reference point. For a free particle in a gas phase, $\mu_i^0 = 0$, while if the adsorbed state is the reference one, then $\mu_i^0 = \varepsilon_i$, where ε_i is the binding energy.

2.1.2. Solid

One will consider that the bulk of a solid is a homogeneous substitutional, interstitial, or mixed-type solution [27]. Also one will treat only the simplest Bravais lattices in which depending on the temperature and concentration of the components their ordered arrangement is possible [28]. The nature of the distribution of the atoms in a solid solution depends on the interaction of its components. It is the simplest to consider the spectrum of possible distributions of the atoms for a binary alloy. One will use the concepts of short- and long-range order for their description. Short-range order characterizes the trend of local distribution of neighboring atoms of an alloy. The atoms of an alloy are said to tend to become ordered if the neighboring location of atoms of different species is more preferable than their chaotic arrangement, and they are said to tend to stratify if the neighboring location of atoms of one species is preferable.

In an equilibrium state, lowering of the temperature in the first case is attended by an ordered arrangement of the alloy atoms, and regular sublattices mainly filled with atoms of one species can be separated from the crystal lattice. The degree of deviation from this arrangement of the atoms characterizes long-range order. In the second case, lowering of the temperature is attended by the separation of a new phase, and the initially homogeneous phase becomes macroinhomogeneous.

In more complicated cases, different combinations of phase transitions of stratification and ordering are possible. For example, a system may pass over to the disordered and ordered phases or to two different ordered phases. The type of the phase transitions and the regions of their realization are determined by the concentrations of the components, the temperature, and the potentials of particle interaction. Similar transitions also occur in multicomponent solutions. An increase in the number of components increases the number of different combinations of the phase transitions [29].

Lam Research Ex. 1035 - Page 357
Lam Research Corp. v. Inpria Corp.
IPR2024-00033 - U.S. Patent No. 9,823,564

2.1.3. Subsurface Region of a Solid

The nature of particle distribution near a surface generally differs from that in the bulk [30,31]. This difference is associated with the absence of a solid phase in the other half-plane. This disturbs the periodicity of the crystalline structure along a normal to the surface and results in a difference in the forces acting on an atom from the side of the other atoms of the alloy surrounding it on the surface and in the bulk (an atom in the bulk has more neighbors than one on the surface). As a result, a different distribution of the atoms ensuring a minimum of the free energy sets in equilibrium. The perturbation produced by a surface affects a subsurface region of a solid. Its width depends on the temperature, concentrations of the solid solution components, and on the potentials of particle interaction.

A very important characteristic of the subsurface region is the surface concentration of the atoms. For alloys, it is customary to speak of the surface segregation of the component whose surface concentration exceeds the bulk one. With an increase in the distance from the surface, the local concentrations of the particles tend to their bulk values. This also relates to the other characteristics of particle distribution determining short- and long-range orders, which in the subsurface region can have a great anisotropy.

How the atoms of a solid are distributed in the subsurface region has a determining influence on all the surface processes: the surface composition determines the properties of the surface on which the gas-phase molecules are adsorbed and the surface reactions proceed, while how the atoms are distributed in the subsurface region governs the dissolution of the adsorbed particles and the rearrangement of the region itself. A much more complicated situation is encountered for a ''frozen'' highly non-equilibrium state of a surface. Under these conditions, the ways of forming the surface are exceedingly important, namely, by splitting-off part of a crystal in vacuum, sputtering onto a support, precipitation from a solution, sintering of a polycrystalline powder, etc. [3], because the procedure employed to prepare a surface and the treatment of a specimen prior to running an experiment affect the state of the surface and the subsurface region first of all.

2.1.4. Adsorption

The surface atoms of a solid have a definite ability of forming bonds with molecules of the gas phase, which increases the concentration of these molecules near the surface [32–34]. A homogeneous surface implies a two-dimensional periodic lattice with equivalent sites. Each site of the

Lam Research Ex. 1035 - Page 358
Lam Research Corp. v. Inpria Corp.
IPR2024-00033 - U.S. Patent No. 9,823,564

surface is composed of an adsorption center, i.e., a region of space where the adspecies is localized. In other words, this is a region of a local potential energy minimum of the adspecies interacting with the solid's atoms. The type of the adsorbed bonds depends on the chemical nature of the gaseous phase molecules and the solid's atoms [11,12]. Conventionally, it is taken to distinguish a physical and a chemical adsorption. In the first case the adsorbent and the adsorbate electrons do not cooperate and in the second one an ordinary chemical bond is formed accompanied by redistribution of these electrons. For homogeneous surface the main role is played by the magnitude of the adsorbent–adsorbate bond. Let ε_i denote the energy of binding of adspecies i with any site on the homogeneous surface. It is accepted that the number of sites (N) remains unaltered during adsorption and each site has z nearest neighbors. The adspecies can be located above the surface atom, the bond between the adjacent atoms or the interstices of the surface lattice. It can found by the corresponding quantum-chemical calculation (*cf.*, e.g., Refs. [13,35,36]). In any case a homogeneous surface represents a regular set of localization regions, although the number of sites depends on the type of the adsorption center. If N_a denotes the number of atoms of the solid's surface, then for the first and the third center types $N = N_a$ and for the bridge bond $N = 2N_a$ (i.e., $N = M$, where M is the number of bonds between the adjacent atoms and equals to $zN_a/2$). The simplest examples of the really existing homogeneous surfaces are the (100) and (111) faces on the cubic crystals ($z = 4$ and $z = 6$, respectively), as well as the basal (0001) faces of graphite and boron nitride [37].

The existence of a surface relief poses, naturally, the problem of the geometrical relations between the localization region and the adspecies size. The latter may be somewhat arbitrarily selected in the range between a gas-kinetic diameter and a first incomplete electronic shell, the bond lengths of the surface molecule in some cases differing from those in the gaseous phase. One uses, as a unit of measure, a lattice site area (σ) defined as $\sigma = S/N$, where S is the area of a homogeneous surface.

Adsorption centers with different bond energies exist on the surface of most solids. Such differences are attributed to discrepancies in the local chemical composition of the surface and geometry of the solid's atoms. These surfaces are called inhomogeneous. Usually these two reasons occur simultaneously. The scale of the inhomogeneities varies greatly from a few Angstroms (point imperfections and impurities) to macrosizes [38,39]. For the inhomogeneous systems one will assume that each type of sites q is characterized by its own size σ_q and the energy ε_q^i of adspecies i bond with such a site, $1 \le q \le t$, where t is the number of site types. For ease of presentation one will restrict to the case when each adspecies occupies one site. The total number of surface sites is made up of the various site

Lam Research Ex. 1035 - Page 359
Lam Research Corp. v. Inpria Corp.
IPR2024-00033 - U.S. Patent No. 9,823,564

types: $N = \sum_{q=1}^{t} N_q$, where N_q is the number of sites q. The function $f_q = N_q/N$ characterizes a fraction of the surface sites belonging to type q (molar fraction) and it is responsible for the surface adsorbent composition. If the number of site types is great, then instead of summation it will be possible to perform integration [38,40]. The problem of determining the function f_q is traditional in the adsorption theory.

2.1.5. *Effect of Adsorbed Particles on the State of a Surface*

If the binding energy of an adsorbed particle to a surface is commensurable with the binding energy between the atoms of the solid, adsorption of molecules may cause substantial changes in the state of the surface. This is largely associated with the adsorbed particles compensating the absence of neighbors at the surface atoms. As a result, the state of the entire subsurface region of the solid may change. This, in turn, will change the number of different adsorption centers on the surface.

As a whole, considerable experimental data have been accumulated in the literature concerning the influence of the gas phase on the surface state of adsorbents and catalysts. The surface state is used specially to preliminarily produce the required surface composition of a catalyst. At the same time, quantitative characteristics of these changes are mainly available only for binary alloys contacting with molecules of H_2, CO, and O_2 [41,42]. Investigations conducted in recent years reveal that the influence of adsorbed particles on the state of a solid surface is apparently more significant than is customarily considered at present. The structural transformations in the surface layers (an example is the rearrangement of the surface layer of platinum in the adsorption of CO and O_2 molecules [43]) and the processes of formation of new phases in them, which are similar to three-dimensional topochemical processes [44], may be of a major significance.

A surface is considered stable or non-rearrangeable if in the course of the adsorption–desorption of the gaseous phase molecules it remains intact, i.e., with the same parameters N, t, and N_q $(1 \leq q \leq t)$ as well as the structural characteristics and adsorption properties of the surface sites. Otherwise, it is regarded as a rearrangeable surface.

2.1.6. *Absorption*

Many solids absorb molecules of the gas phase (H_2, O_2, N_2, etc.) in considerable amounts [45,46]. The dissolved atoms occupy the interstices

Lam Research Ex. 1035 - Page 360
Lam Research Corp. v. Inpria Corp.
IPR2024-00033 - U.S. Patent No. 9,823,564

of the crystal lattices and form interstitial alloys [47]. They also greatly affect the state of the bulk phase of the solid, changing the short- and long-range orders in alloys. With great saturations of the bulk by dissolved atoms, rearrangement of the bulk phase and transitions to multiphase systems are possible. Similar changes are possible in the subsurface region of a solid that alter the state of the surface and affect the surface processes.

2.1.7. Particle Mobility

The components of a phase interface have a wide range of mobilities. The mobility of adsorbed particles exceeds that of the atoms in the bulk of a solid. It is usually considered that the mobility of the adsorbed particles is greater than that of the surface atoms of the solid, and when the state of the solid's atoms changes, the adsorbed particles at each instant are distributed practically in equilibrium. The same relation between the mobilities is presumed for absorbed particles and the atoms of a solid in the bulk. This is apparently not always true. In the general case, each component has its own ratio of the migration activation energies, and cases are possible when the mobilities of the surface atoms of a solid and of the adsorbed particles are commensurable. The mobilities of the atoms of a solid and of absorbed particles may also be commensurable.

In more general cases, the state of a system changes at migrating particles and their participation in reactions. The relations between the reaction rates and the mobilities of the particles may vary within very broad limits. Cases are possible when chemical transformation is the limiting step (the traditional region of chemical kinetics [48]), and when the migration of particles is the limiting factor (diffusion-controlled reactions [49]). As a whole, this leads to various conditions under which processes proceed on a surface and in the subsurface region and determines the diversity of models used to describe them.

2.2. LATTICE-GAS MODEL AND ELEMENTARY PROCESSES

The simplest model of the condensed phase is represented by the lattice-gas model [50]. It reflects two major features of the any species in the condensed phase, viz., their characteristic volume and species interactions. The volume of a crystalline solid is characterized by its natural lattice. With a good approximation, one can consider that the subsurface region of a solid is

Lam Research Ex. 1035 - Page 361
Lam Research Corp. v. Inpria Corp.
IPR2024-00033 - U.S. Patent No. 9,823,564

characterized by the same crystal lattice. When the structure of the surface layers changes in the subsurface region (as occurs in the system CO/Pt(100) [51]) or the lattice parameters of the surface layers change in the subsurface region, the latter can be divided into a number of subregions with different lattice structures.

Consider that the adsorption centers form a surface structure. This assumption is justified even for non-localized adsorption because at low surface coverages the results for a model of localized and non-localized adsorption virtually coincide [52]. When the surface coverage grows, the adsorbed particles behave like a two-dimensional liquid, which a lattice model can be used for [53,54]. Hence, the lattice model is a general one for the condensed phase of a gas–solid system. That the surface and subsurface region structures may differ from the structure of the bulk of the solid is of no significance. This situation fits naturally into the concept of inhomogeneous lattices that is needed at least to take account of the well-known fact of the inhomogeneity of surfaces.

The model system comprises a discrete structure (a lattice) the sites of which accommodate various kinds of adspecies. The discrete arrangement of the particles simplifies the way of describing their position – it is sufficient to set the number of the relevant site. Consider a regular periodic lattice whose constant in its order of magnitude equals the diameter of the particles. For unambiguity, examine a homogeneous solid solution of the substitutional type. Let the number of solution components be s, and the subscript f signify the number of the lattice site, $1 \leq f \leq N$, where N is the number of sites. Every lattice site has z nearest neighbors forming its first coordination sphere (c.s.). For a one-dimensional lattice, one has $z = 2$, for a two-dimensional lattice one has $z = 3$, 4, or 6, and for a three-dimensional lattice one has $z = 4$, 6, 8, or 12. The occupancy of each lattice site is determined by the species of the particle at it. Since at any lattice site there can be a particle of any species, then each specific state of occupancy of site f is a random variable determined [55,56] as follows:

$$\gamma_f^i = 1, \quad \text{if a particle of species } i \text{ is at site } f; \tag{4}$$

$$\gamma_f^i = 0, \quad \text{if a particle of species } j \text{ is at site } j \neq i.$$

So, at any site there must be a particle of one species or another: $\sum_{i=1}^{s} \gamma_f^i = 1$.

First, let us consider the ideal models that take into account a characteristic volume of the adspecies only, and the ideas of the lateral interactions between the adspecies.

Lam Research Ex. 1035 - Page 362
Lam Research Corp. v. Inpria Corp.
IPR2024-00033 - U.S. Patent No. 9,823,564

2.2.1. Elementary Processes and their Models

Changes in the state of the adsorbent–adsorbate system which, at the atomic-molecular level, is described by the lattice-gas model are caused by variations in the occupancy of its individual sites as a result of the elementary processes. The following elementary processes occur on the adsorbent surface: adsorption and desorption of the gaseous phase molecules, reaction between the adspecies, migration of the adspecies over the surface and their dissolution inside the solid. The solid's atoms are capable of participating in the chemical reactions with the gaseous phase molecules, as well as migrating inside the solid or on its surface.

Within the frameworks of the lattice gas model it is reasonable to classify the elementary processes by the number of sites m, which a given process occurs on, i.e., one- and two-site cases. In the first case the changing parameter is the occupancy state of one site. The processes such as these include "isomerization" associated with changes in the internal degrees of freedom of the adspecies ($ZA \rightarrow ZB$, i.e., transition of the adspecies from state A to state B), adsorption–desorption of the atoms and non-dissociating molecules ($A + Z \rightarrow ZA$), reaction according to the collision mechanism ($A + ZB \rightarrow ZD + C$, Eley–Rideal's-type mechanism). It should be remembered that ZA, Z and A denote adspecies A, empty lattice site and species A in the gaseous phase, respectively.

The two-site processes involve a simultaneous change in the occupancy state of both sites. They include reactions between the adspecies ($Z_fA + Z_gB \rightarrow Z_fC + Z_gD$: Langmuir–Hinshelwood's-type mechanism), adsorption–desorption of the dissociating molecules, migration by the vacancy mechanism, reaction of the type $Z_fA + Z_gB + C$, etc. (f and g are the site numbers). The chemical reactions take place between the adspecies located in the neighboring sites, therefore their indices f and g relate to the nearest neighbors. In the general case, if the elementary processes involve the adspecies only, the reaction molecularity coincides with the number of sites m, and if it additionally involves the gaseous phase molecules, the molecularity per unit exceeds m.

The rate of the elementary process is the most important characteristic. If the conditions of the acting masses law are regarded fulfilled, the rate U_A of the mono- ($ZA \rightarrow$ Product) and U_{AB} of the bimolecular ($ZA + ZB \rightarrow$ Product) elementary processes on the homogeneous surface can be written down as follows [58]:

$$U_A = K_A V_A, \quad V_A = \theta_A, \quad U_{AB} = K_{AB} V_{AB}, \quad V_{AB} = \theta_A \theta_B. \qquad (5)$$

Here K_A and K_{AB} are the constants of the mono- and bimolecular reaction, respectively. When writing Eq. (5), it is assumed that the reagents are

Lam Research Ex. 1035 - Page 363
Lam Research Corp. v. Inpria Corp.
IPR2024-00033 - U.S. Patent No. 9,823,564

distributed over the surface in an equilibrated manner, the limiting factor being presented by the chemical conversion process. The θ_i values are macroscopic characteristics representing concentrations of the adspecies i within a reaction space. The concentration component of the reaction rate (V_A or V_{AB}) defines a probability for such an arrangement of the reagents in which they can interact. In the monomolecular process this probability is independent of how the other reagents are arranged, therefore $V_A = \theta_A$. On the other hand, in the bimolecular process the reaction is possible when the reagents are located on two-nearest-neighboring sites, therefore at the random distribution of the reagents the probability of their encounter is $V_{AB} = \theta_A\theta_B$.

The reaction rate constant defines the probability of a reaction at a fixed arrangement of the reagents. For the monomolecular process it relates to each adspecies A irrespective of its arrangement, and for the bimolecular one – to the fixed pair of species A and B located in the neighboring sites. (If the distance between sites f and g is greater than the lattice parameter, the rate constant is equal to zero.) All microlevel features of the elementary process are controlled by the type of the rate constant. In the ideal lattice-gas model, i.e., when ignoring the adspecies interactions, the process rate constant depends only on the occupancy states of one site for a one-site process and on that of both sites for a two-site one. For the oscillational contributions of the adspecies in the lattice sites a similar situation is provided by using Einstein's oscillation model. In doing so, the oscillations of the lattice itself are virtually ignored.

For describing the elementary processes the transition state model (TSM) [20–23,57] is usually used. The TSM gives a clearly defined dependence of the preexponential factor on the type of the energy redistribution over the internal degrees of freedom of the reagents in the activated state. The reaction rate constant yields the following equation [20–23,57]:

$$K_{AB} = K^0_{AB}\exp(-\beta E_{AB}), \quad K^0_{AB} = \kappa F^*_{AB}/(F_A F_B h\beta\sigma), \tag{6}$$

where E_{AB} is the rate activation energy; K^0_{AB} the frequency cofactor or the preexponential rate constant factor; κ the transmission coefficient; h the Planck constant; σ the lattice site area; F^*_{AB}, F_A and F_B are partition functions of the activated complex (AC) and the reagents, respectively.

Let us recall in brief the principal aspects of the TSM, that remain intact when considering the adspecies interactions: (1) the AC is a species with modified properties, one of the oscillational degrees of freedom of which is replaced by a translational motion along the reaction coordinate; (2) the AC is equilibrated with the parent reaction subsystem (this subsystem is formed by the starting reagents only); (3) the volume of the AC is approximately equal to that of the reagents, i.e., the former in the lattice-gas model is equal to the sum of the sites occupied by these reagents; (4) the number of the

Lam Research Ex. 1035 - Page 364
Lam Research Corp. v. Inpria Corp.
IPR2024-00033 - U.S. Patent No. 9,823,564

AC's is few so that any elementary process occurs independently of the other processes and does not affect the distribution pattern of the remaining system's components.

In the general case, the rates of the surface processes ZA → Product and ZA + ZB → Product in the TSM are expressed as follows [58]:

$$U_{\mathrm{A}} = K^*_{\mathrm{A}} V_{\mathrm{A}}, \quad K^*_{\mathrm{A}} = K_{\mathrm{A}} \exp \beta(\Delta\mu_{\mathrm{A}}), \quad K_{\mathrm{A}} = \kappa F^*_{\mathrm{A}}/(F_{\mathrm{A}} h\beta\sigma) \exp(-\beta E_{\mathrm{A}}), \tag{7a}$$

$$\begin{aligned} U_{\mathrm{AB}} &= K^*_{\mathrm{AB}} V_{\mathrm{AB}}, \quad K^*_{\mathrm{AB}} = K_{\mathrm{AB}} \exp \beta(\Delta\mu_{\mathrm{AB}}), \\ K_{\mathrm{AB}} &= \kappa F^*_{\mathrm{AB}}/(F_{\mathrm{A}} F_{\mathrm{B}} h\beta\sigma) \exp(-\beta E_{\mathrm{AB}}), \end{aligned} \tag{7b}$$

Here $\Delta\mu_{\mathrm{A}} = \mu^*_{\mathrm{A}} - \mu_{\mathrm{A}}$ and $\Delta\mu_{\mathrm{AB}} = \mu^*_{\mathrm{AB}} - \mu_{\mathrm{A}} - \mu_{\mathrm{B}}$, here μ^*_{A} and μ^*_{AB} are the chemical potential of the AC for the one- and two-site processes; μ_i are the chemical potentials of the reagents. Here and further on the subscripts in U_i and U_{ij} denote the occupancy state of the sites, which the elementary process occurs on. The chemical potential of the AC is equal to that of the starting reagents; therefore, by substituting their specific values, one has the corresponding expressions for the reaction rates that are equivalent to those reported elsewhere [21,23]. The effective rate constants in Eqs. (7a) and (7b) for the one- and two-site elementary processes coincide with the constants for the corresponding reactions, if the initial reagents are represented by the lattice system components ($K^*_i = K_i$, $K^*_{ij} = K^*_{ij}$, $1 \le i, j \le s$), and are equal to the product of the rate constants and the partial pressures of the gaseous phase molecules "l", if the elementary process involves molecule "l" of this phase $\left(K^*_{i1} = K_{i1} P_1, K^*_{i1} = K_{ij1}\, P_1\right)$.

The more recent theories of chemical conversions [59–61] take into account the fact that the process of overcoming the activation barrier involves a cooperative change of more than one degree of freedom for the starting reagents subsystem. For the surface processes this is expected to lead to a need for considering the dynamics of the solid atom motion and, at least, the model should include information on Debye frequencies for its atoms (see, e.g., Ref. [62]). An additional inconvenience of the models for the elementary surface processes is associated with the fact that the frequencies of the surface atom oscillations differ from those inside the solid. Consideration of the multiphonon contributions to the probabilities that the elementary process can take place results in a significant modification of its rate constant up to the complete disappearance of the activation form of the temperature dependence [63,64].

A considerable contribution to the surface processes that involve hydrogen and helium atoms can be due to tunnel effects at low temperatures. In the approximation, when the rate constant is independent

Lam Research Ex. 1035 - Page 365
Lam Research Corp. v. Inpria Corp.
IPR2024-00033 - U.S. Patent No. 9,823,564

of the solid's oscillations, it has the following form [65,66]:

$$K = v_0 \exp\left(-\frac{2}{h}\int_a^b |p|dx\right). \tag{8}$$

In this formula ν_0 is the frequency of the tunneling species in the potential well, p its impulse, a and b are the coordinates of the potential barrier boundaries. Expressions for the rate constants with account of the lattice oscillations are presented elsewhere [66].

On the inhomogeneous surfaces the reaction rate constants contain additional indices for types of the corresponding sites.

2.2.2. Surface Mobility

The process of migration of adspecies A into the neighboring empty site can be formally written down as follows: $Z_f A + Z_g = Z_f + Z_g A$. Sites f and g are usually taken to lie at the shortest distance.

In the course of migration the AC is equilibrated with the adspecies in site f and empty site g, therefore in Eq. (7b) $\Delta\mu_{AV} = 0$. At $F_V = 1$

$$K_{AV} = K^0_{AV} \exp(-\beta E_{AV}), \quad K^0_{AV} = \kappa F^*_{AV}/(F_A\, h\beta\sigma) \tag{9}$$

where E_{AV} is the energy of migration activation.

On a surface, jumps of particles over various lengths are possible [67]. Their fraction depends greatly on the nature of interaction of a particle with the surface atoms and on the temperature. With an increasing degree of delocalization of adsorption, the fraction of the long jumps grows. On the other hand, an increase in the coverage of the surface reduces the average length of a jump of an adsorbed particle, hence in the following a treatment of migration to neighboring free centers has been considered.

Another important characteristic of the surface processes is a ratio η of the adspecies migration rate constant to those of the surface reaction, adsorption, and desorption rates. At small coverages the parameter η controls the surface process conditions: $\eta \gg 1$ in the kinetic and $\eta \ll 1$ in the diffusion mode. A fast surface mobility of the adspecies and their equilibrium distribution on the surface are the most frequently adopted assumptions. At $\eta \leq 1$ the macroscopic concentrations of adspecies θ_i cannot be used for calculating the process rates, and a more detailed description of their distribution is essential.

Migration of the adspecies deep into the subsurface region results in their dissolution in the solid. The scheme of this process is similar to that when the process occurs on the surface except that sites f and g belong to the localization centers inside the solid. They can be represented either by the

Lam Research Ex. 1035 - Page 366
Lam Research Corp. v. Inpria Corp.
IPR2024-00033 - U.S. Patent No. 9,823,564

interstices of the crystal lattice (for H, O, C, etc.) [45] or by the empty sites of the lattice itself (for Ar, Kr, etc.) [68]. In the first case, the smaller relation between the bond energy for the solid atoms and the migrating adspecies and also between the adspecies themselves, the smaller changes in the solid's state. In the latter case the migration of the dissolved adspecies leads inevitably to the movement of the crystal lattice atoms. In the lattice-gas model the process of adspecies migration over the surface and inside the solid is described similarly. The difference is due to the following factors: (1) the number of the neighboring sites for the adspecies to jump into; (2) the numerical values of the activation energies and the jump rate preexponent constants; and (3) type of the boundary conditions.

2.3. LATERAL INTERACTIONS

The lattice-gas model allows to use it for studying the effect of the lateral interactions between the adspecies on the surface process rate or, in other words, to consider the non-ideality of the reaction system in the surface process kinetics. In the lattice-gas model the interaction of adspecies i and j in sites f and g at the distance r is set by the energy parameter $\varepsilon_{fg}^{ij}(r)$. In the homogeneous lattice systems such distances can be conveniently determined with the use of the numbers of the (c.s.) where site g is located relative to site f. In this case in the parameter $\varepsilon_{ij}(r)$ the index r runs a discrete series of values from 1 to R, where R is the interaction radius; $1 \le r \le R$, $\varepsilon_{ij}(r) = \varepsilon_{ji}(r)$. If $\varepsilon_{ij}(1) \neq 0$ and ε_{ij} $(r > 1) = 0$, one deals with the nearest-neighbors interaction and the index r can be omitted. Note that the number of c.s. does not coincide with that of the individual successive jumps between sites f and g over the shortest path. The interactions of the adspecies with the empty sites (vacancies, $i = V$) are usually taken to be zero: $\varepsilon_{is}(r) \equiv \varepsilon_{iV}(r) = 0$.

The energy parameters describe a mean energy of adspecies interaction for the neighboring adspecies. Such information is rougher than that resulting from the direct use of the dependence of the potential energy on the interadspecies distance; however, this simplifies considerably an account of energy contributions. Depending on the type of the adspecies interaction and distance, these parameters can be both positive and negative. Let us assume that the positive parameters correspond to the attraction of the adspecies while the negative ones – to their repulsion. This is based on the fact that the heat of adsorption for the neighboring attracting (repulsing) adspecies ($R = 1$) increases (decreases) with coverage.

For the physical adsorption purposes it is usually assumed that the adspecies interaction is described by the Lennard–Johns potential [54]

$$U(r) = D[(\sigma/r)^{12} - (\sigma/r)^{6}], \tag{10}$$

Lam Research Ex. 1035 - Page 367
Lam Research Corp. v. Inpria Corp.
IPR2024-00033 - U.S. Patent No. 9,823,564

where D and σ are the constants, σ a size of the molecule hard sphere, and the mean energy ε_{AA} has a positive value. Generally, a sign of the interaction parameter depends on the relation between the potential parameter σ and the lattice constant λ: if $\lambda > \sigma$, then $\varepsilon_{AA} > 0$, and if $\lambda < \sigma$, then $\varepsilon_{AA} < 0$ [69].

If the adsorbate-metal bond is ionic, the interaction between the adspecies will be described by the dipole–dipole repulsion. The interaction energy for the identically oriented dipoles can be described as follows [54]:

$$U(r) = -\mu^2(3\cos^2\varphi - 1)/r^3, \mu = e_0 l. \tag{11}$$

In Eq. (11) μ is the dipole moment; e_0 the elementary charge; l the distance between the dipole charges; φ the angle of the dipole axis orientation to the lines connecting the dipole centers.

In the case of chemisorption the direct exchange repulsion between the closely positioned adspecies may takes place, which decreases exponentially with the distance. There are also reports on the existence of an indirect exchange adspecies interaction through the solid's conduction electrons [70,71]. At great interadspecies distances the energy of this interaction is described as follows:

$$U(r) = C\cos(2k_F r)/r^3, \tag{12}$$

where C is the constant and k_F the electron impulse on the Fermi surface. Gabovich and Pashitsky [70] have shown that depending on the Fermi surface properties the indirect interaction energy can show a slower deceleration: $U(r) \sim r^{-n}$, $1 \le n \le 2.5$. At small interadspecies distances this energy falls off exponentially with distance [71]. At intermediate distances the indirect interaction can be responsible for a change in the potential sign. This corresponds to the attraction of the adspecies located at the second-, third- or fourth-neighbor distances (*cf.* Refs. [72,73]). It has been shown [74] that at small distances one can observe noticeable three-body interactions between the adspecies.

In real systems the interplay of different forces gives rise to a complex dependence of such interactions on the interadspecies distance. Difficulties encountered in the analysis of such interactions have resulted in the appearance of a number of phenomenological theories describing adspecies interaction.

2.4. Quasi-Particle Description of Elementary Rates

The main difference between the occurrence of the elementary processes in the condensed phase and that in the gaseous one consists in a "constant"

Lam Research Ex. 1035 - Page 368
Lam Research Corp. v. Inpria Corp.
IPR2024-00033 - U.S. Patent No. 9,823,564

influence of the environment on the process. In other words, the entire process takes place within the "influence field" produced by the other components of the condensed phase. The initial, intermediate, and final states of the reaction system depend on the interaction of the adspecies participating in the reaction with their neighbors. Calculations of the elementary process rate with the use of the lattice-gas model considering the interaction between all the condensed phase components are based on the principal ideas of the absolute reaction rate theory. Suppose the elementary process takes place on a homogeneous lattice. Its description will take into account the interactions between the nearest neighbors and assume the equilibrated distribution of the adspecies over the lattice sites.

The TSM for elementary processes in condensed systems [58] employs the traditional tenets of Eyring's model [20,23], although it follows from the nature of the condensed state that the driving force of the process is ensured by thermofluctuation excitations of the medium, and not by the translational motion of the particles. In the transition state, an AC reacts with the neighboring particles. The parameter of their interaction ε_{ij}^{*} differs from the parameter of interaction between the initial reactant i which the AC is formed from and the neighboring particle j.

2.4.1. One-Site Reactions

For the rapid surface mobility of adsorbed particles, the expressions for the rates of one-site reactions can be obtained a simple way. Let us illustrate this on the example of the adsorption of non-dissociating molecules for one-component system when $s = 2$ ($i = \mathrm{A}$ – adspecies and $i = \mathrm{V}$ – vacancies). Let $E_i(n)$ and $E_i^{*}(n)$ be the energies of interaction of the central particle i with its neighbors in the ground and transition states, where n is the number of particles of A in the c.s. of particle i. Fig. 8.1 shows the local configuration of adspecies A on the planar lattices with $z = 4$ and $z = 6$. The indexes n and σ characterize the local configuration of the neighboring adspecies in the first c.s. around i, n is the number of adspecies A, and $\sigma(n)$ is the arrangement of n adspecies such as these. For two-body interaction, the index σ can be omitted.

The difference $E_i^{*}(n) - E_i(n)$ determines the change in the magnitude of the activation barrier of desorption ($i = \mathrm{A}$) or adsorption ($i = \mathrm{V}$, one will take the real properties of the vacant sites into consideration in the final expressions) because of interaction of the nearest neighbors in comparison with an ideal system. For two-body interaction one has

Lam Research Ex. 1035 - Page 369
Lam Research Corp. v. Inpria Corp.
IPR2024-00033 - U.S. Patent No. 9,823,564

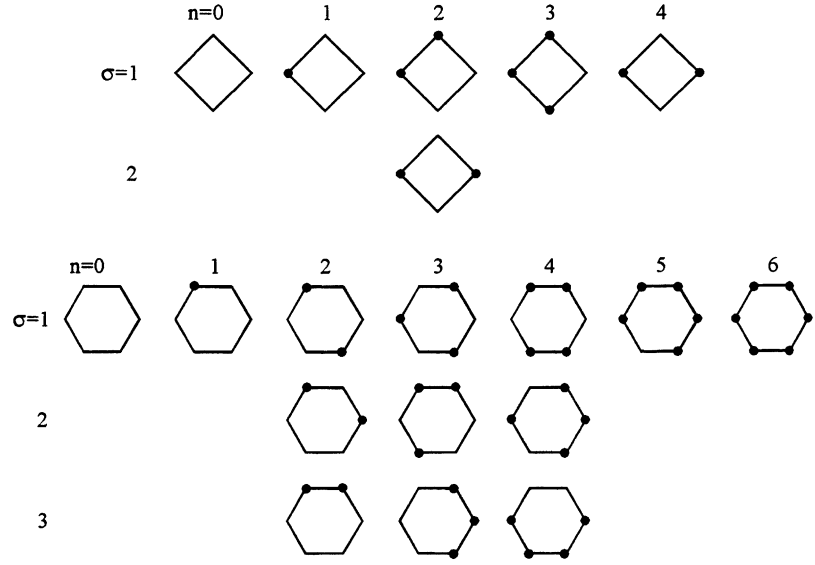


Fig. 8.1. Configurations of the adspecies in the first coordination sphere (c.s.) of the central sites of the two-dimensional lattices with $z = 4$ and 6.

$E_i(n) = n\varepsilon_{i\mathrm{A}} + (z–n)\varepsilon_{i\mathrm{V}}$ and $E^*_i(n) = n\varepsilon^*_{i\mathrm{A}} + (z–n)\varepsilon^*_{i\mathrm{V}}$. The rate of a process at the central site of a cluster containing n particles of A in its c.s. will be written as follows:

$$U_i(n) = K_i^* \theta_i(n) F_i(n), \quad F_i(n) = \exp\{\beta[E_i^*(\ddot{1}) - E_i(\ddot{1})]\}, \tag{13}$$

where K_i^* is the rate constant of an elementary reaction, and its form has been determined in Eqs. (6), (7a), and (7b), while $\theta_i(n)$ is the normalized probability of there being a cluster with n particles of A around the central particle i on the surface.

Expression (13) can be considered as a modified expression for rate of a reaction within the framework of the law of mass action (5), where the place of the rate constant has been taken by the product $K_i^*(n) = K_i^* \exp\{\beta[E_i^*(n) - E_i(n)]\}$, while the place of the concentration of the particles has been taken by the concentration of the quasi-particles, which are the following configurations of the real particles: at the center of a cluster there is particle i, and around it there are n particles of A and $(z–n)$ particles V (the quantity K_i^*(n) can be interpreted as the rate constant for a quasi-particle).

Lam Research Ex. 1035 - Page 370
Lam Research Corp. v. Inpria Corp.
IPR2024-00033 - U.S. Patent No. 9,823,564

Consequently, by going over to larger quasi-particles, one can formally retain the structure of the expressions of the law of mass action, i.e., the product of the rate constant of a reaction and the reactant concentration. But one must have in view that the number of such quasi-particles sharply grows with increasing s and z (and the radius of interaction).

The rate of a reaction relating to a surface as a whole is obtained by the averaging expression (13) over all the local configurations differing in the number of particles of A in the c.s. around particle i:

$$U_i = K_i^* \sum_n U_i(n) = K_i^* \sum_{n=0}^{Z} C_z^n \theta_i(n) \exp\{\beta[n\delta\varepsilon_{iA} - (z-n)\delta\varepsilon_{iV}]\}. \tag{14}$$

Here $\delta\varepsilon_{ij} = \varepsilon_{ij}^* - \varepsilon_{ij}$; C_z^n is the statistical weight of the configuration with n particles of A around the central particle i having the z neighboring sites. The ways of an approximate calculation of the functions θ_i(n) were discussed in Appendix B. In the quasi-chemical approximation, they are expressed in terms of the function θ_i and θ_{ij}, where $\theta_i = N_i/N$, N_i is the number of particles of species i on N total sites, and $\theta_{ij} = (1+\Delta_{ij})N_{ij}/zN$ (N_{ij} is the number of pairs of particles ij).

Insertion of formula $\theta_i(\mathrm{n}) = \theta_i\,(t_{i\mathrm{A}})^n\,(t_{i\mathrm{V}})^{z-n}$, where

$$t_{ij} = \theta_{ij}/\theta_i, \tag{15}$$

into Eq. (14) yields

$$\begin{aligned} U_i &= K_i^* \theta_i \sum_{n=0}^{Z} C_z^n (t_{i\mathrm{A}} \exp \beta\delta\varepsilon_{i\mathrm{A}})^n (t_{i\mathrm{V}} \exp \beta\delta\varepsilon_{i\mathrm{V}})^{z-n} \\ &= K_i^* \theta_i [t_{i\mathrm{A}} \exp \beta\delta\varepsilon_{i\mathrm{A}} + t_{i\mathrm{V}} \exp \beta\delta\varepsilon_{i\mathrm{V}}]^z = K_i^* \theta_I \Lambda_i, \end{aligned} \tag{16}$$

where

$$\Lambda_i = (S_i)^z, \quad S_i = \sum_{j=\mathrm{A}}^{S} t_{ij} \exp \beta\delta\varepsilon_{ij}. \tag{16a}$$

In the formula (16) the function Λ_i describes a non-ideality behavior of the reaction system. In the absence of the lateral interaction, the function $\Lambda_i = 1$ and one returns to the Eq. (5).

Multicomponent reaction systems are considered in a similar way. For these systems, the statistical weights of the configurations of the particles in the c.s. of a cluster are expressed in terms of the polynomial coefficients of the number of combinations of z taken $n_1 \ldots n_{s-1}$ particles of different species at a time (see Appendix A).

Lam Research Ex. 1035 - Page 371
Lam Research Corp. v. Inpria Corp.
IPR2024-00033 - U.S. Patent No. 9,823,564

2.4.2. Two-Site Reactions

The expression for the rate of a bimolecular reaction of adsorbed particles when the latter have a rapid surface mobility can be obtained in the traditional way for chemical kinetics if the law of mass action is used for large quasi-particles. Let us consider the reaction AZ+BZ on a homogeneous surface containing three species of particles ($s = 3$): A, B, and V (the real properties of the vacant sites V are taken into account in the final expressions). Particles of A and B are at neighboring sites of a lattice and enter the c.s. of one another.

As the total number of various adspecies configurations around two central sites with $s = 3$ significantly increases, the Fig. 8.2 illustrates the local configurations of adspecies A for the lattice with $z = 4$ and $s = 2$. Here again, as for Fig. 8.1, the index n is the number of adspecies A around the central adspecies i and j, and index σ their distribution pattern.

Let us assume that total two (z–1) neighboring sites can be divided in two equal parts. Then the (z–1) site around the particle A is surrounded by n_A particles of A, n_B particles of B, and $n_V = z–1–n_A–n_B$ particles of V, while at the (z–1) site around the particle B is surrounded by m_A particles of A, m_B particles of B, and $m_V = z–1–m_A–m_B$ particles V.

Let us denote the energy of interaction of particles of A and B with their neighbors in the ground and transition states by $E_{AB}([nm])$ and $E^*_{AB}([nm])$, where the symbol {[nm]} is an abridged notation of the numbers of neighboring particles of various species $[n_A n_B n_V; m_A m_B m_V]$, while the square

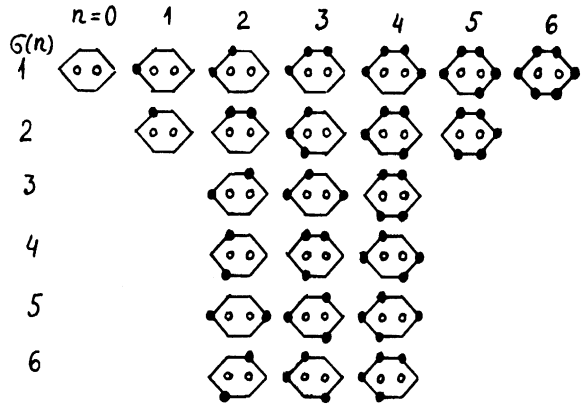


Fig. 8.2. Configurations of adspecies A in the first c.s. around the central adspecies in the square lattice ($s = 2$); the empty circles represent the central adspecies and the black circles – the neighboring adspecies A.

Lam Research Ex. 1035 - Page 372
Lam Research Corp. v. Inpria Corp.
IPR2024-00033 - U.S. Patent No. 9,823,564

brackets signify fixed values of all the numbers. The central A and B particles and their specific set of nearest neighbors {[nm]} form a quasi-particle. Now the rate of an elementary process will be written as

$$U_{AB}(\{[nm]\}) = K^*_{AB}(\{[nm]\})\theta_{AB}(\{[nm]\}), \tag{17}$$

$$K^*_{AB}(\{[nm]\}) = K^*_{AB} \exp \beta[E^*_{AB}(\{[nm]\}) - E^*_{AB}(\{[nm]\})],$$

where K^*_{AB} is the rate constant of the reaction of particles of A and B in the ideal model, $K^*_{AB}(\{[nm]\})$ is the rate constant of the reaction of a quasi-particle, differing from K^*_{AB} in the change in the activation energy of the reaction when the reactant interacts with neighboring particles; $\theta_{AB}(\{[nm]\})$ is the probability of finding neighboring particles of A, B, and V given by the set of values {[nm]} around the reacting A and B particles. On the other hand, the quantity $\theta_{AB}(\{[nm]\})$ is the concentration of the quasi-particles. The rate of a reaction relating to an entire surface is obtained by averaging expression (17) over all the local configurations of the neighboring particles:

$$U_{AB} = \sum_{n_A=0}^{z-1} \sum_{n_B=0}^{z-1-n_A} \sum_{m_A=0}^{z-1} \sum_{m_B=0}^{z-1-m_A} C_{z-1}^{n_A n_B} C_{z-1}^{m_A m_B} K_{AB}(\{[nm]\})\theta_{AB}(\{[nm]\}). \tag{18}$$

Here $C_{z-1}^{n_A n_B}$is the statistical weight of configurations with n_A, n_B particles of A and B around the central particle of A differing in their location at z–1 sites. Analogy $C_{z-1}^{m_A m_B}$ is the statistical weight of configurations with m_A, m_B particles of A and B around the central particle of B. The energies of interaction of particles forming a quasi-particle in the ground and transition states with consideration of paired interaction of the nearest neighbors are:

$$E_{AB}(\{[nm]\}) = \varepsilon_{AB} + \sum\nolimits_{j=A}^{V} \varepsilon_{Aj} n_j + \sum\nolimits_{j=A}^{V} \varepsilon_{Bj} m_j \tag{19}$$

$$E^*_{AB}(\{[nm]\}) = \sum\nolimits_{j=A}^{V} \varepsilon^*_{Aj} n_j + \sum\nolimits_{j=A}^{V} \varepsilon^*_{Bj} m_j.$$

In the first formula, the parameter ε_{AB} reflects the interaction of the reactants in the ground state; this parameter is absent in the second formula because an AC is a single "molecule" and the interaction between fragments of A and B relates to its internal interactions.

To calculate the rate of a reaction, one must use an approximate expression for the concentrations of the quasi-particles $\theta_{AB}(\{[nm]\})$. In the quasi-chemical approximation, the probabilities of all the multiparticle configurations are approximated in terms of the probabilities of two-body configurations. Here it is possible to use the same division into pairs that was employed in the first formula (19) for the energy of two-body

Lam Research Ex. 1035 - Page 373
Lam Research Corp. v. Inpria Corp.
IPR2024-00033 - U.S. Patent No. 9,823,564

interaction, i.e.

$$\theta_{AB}(\{[nm]\}) = \theta_{AB} \prod_{j=A}^{V} \left(t_{Aj}\right)^{n_j} \prod_{j=A}^{V} \left(t_{Bj}\right)^{m_j}. \tag{20}$$

The functions t_{ij} have been defined in Eq. (15), they are found for given values θ_A and θ_B by solving system of equations for equilibrium distribution of species (Appendix A). Inserting expressions (19) and (20) into (18), one obtains:

$$U_{AB} = K^*_{AB} \exp(-\beta\varepsilon_{AB})\theta_{AB}\Phi_A\Phi_B, \tag{21}$$

$$\Phi_i = \sum_{n_A=0}^{z-1} \sum_{n_A=0}^{z-1-n_A} C_{z-1}^{n_A n_A} \prod_{j=A}^{V} [t_{ij} \exp(\beta\delta\varepsilon_{ij})]^{nj} = (S_i)^{z-1}.$$

Here S_i has been defined in Eq. (16a). In the absence of the lateral interaction, the function $\Phi_i = 1$ and one returns to the Eq. (5), as the function $\theta_{AB} = \theta_A\theta_B$.

The conception about quasi-particles in condensed phase gives extension of the absolutely reaction rates in case of a kinetic regime with one limiting stage. In more complex situations the kinetic theory has been used.

3. Kinetic Equations for Multistage Processes in Condensed Phase

The traditional apparatus of statistical physics employed to construct models of physico-chemical processes is the method of calculating the partition function [17,19,26]. The alternative method of correlation functions or distribution functions [75] is more flexible. It is now the main method in the theory of the condensed state both for solid and liquid phases [76,77]. This method has also found an application for lattice systems [78,79]. A new variant of the method of correlation functions – the cluster approach – was treated in the book [80]. The cluster approach provides a procedure for the self-consistent calculation of the complete set of probabilities of particle configurations on a cluster being considered. This makes it possible to take account of the local inhomogeneities of a lattice in the equilibrium and non-equilibrium states of a system of interacting particles. In this section the kinetic equations for wide atomic-molecular processes within the gas–solid systems were constructed.

Lam Research Ex. 1035 - Page 374
Lam Research Corp. v. Inpria Corp.
IPR2024-00033 - U.S. Patent No. 9,823,564

3.1. HAMILTONIAN

As it was defined above the state of occupancy of each site f, $1 \le f \le N$, N is the number of sites, will be characterized by the variable γ_f^i, with $\gamma_f^i = 1$ if the site f contains a particle of kind i and $\gamma_f^i = 0$ if it contains a particle of any other kind. These variables obey the following equations $\gamma_f^i + \ldots + \gamma_f^s = 1$, $\gamma_f^i \gamma_f^j = \Delta_{ij} \gamma_f^i$, where $\Delta_{ij}$is the Kronecker symbol, which states that any site can be occupied by any particle. On the heterogeneous surface the type of the site numbered f will be characterized in the lattice gas model [80,81] by the parameter η_f^q assumed to be known and unvarying during the adsorption process (non-reconstructing surface), with $1 \le q \le t$, where t is the number of types of site. One has $\eta_f^q = 1$ if f is a site of type q and $\eta_f^q = 0$ in the opposite case. The complete set of $\{\eta_f^q\}$, with $1 \le f \le N$, uniquely defines the composition and topography of the surface, which can be of any kind. It is reasonable to assume that lateral interaction is described by a pair potential with an interaction radius R, where R has any given value. Distances will be expressed as the number of c.s. The number of sites in the rth c.s. of a type-q site numbered f will be denoted by $z_f(r)$ [or by $z_q(r)$], with $1 \le r \le R$. The interaction parameter of the species i and j on site of types q and p numbered f and g at a distance r will be denoted by$\varepsilon_{fg}^{ij}(r)$ [or by $\varepsilon_{qp}^{ij}(r)$, since the number of the site and its type are uniquely correlated by the parameters η_f^q].

The Hamiltonian of the adsorption system for a stable (unreconstructed) heterogeneous surface in the grand canonical ensemble is described as follows [80,81]:

$$H = \sum_{f=1}^{N} \sum_{i=1}^{s} h_f^i, \; h_f^i = \left(v_q^i - \frac{1}{2} \sum_{r=1}^{R} \sum_{g_r} \sum_{j=1}^{s} \varepsilon_{qp}^{ij}(r) \gamma_{g_r}^j \eta_{g_r}^p \right) \gamma_f^i \eta_f^q, \qquad (22)$$

$$v_f^i = -\beta^{-1} Ln(Y_q^i), \quad Y_q^i = (a_q^i P_i)^{1/m_i}, \quad a_q^i = (F_q^i)^{m_i} \beta \exp(\beta Q_q^i)/F_i^0.$$

where the subscript g_r numbers the sites around of site f in the rth c.s., a_q^i is the adsorption coefficient of particle i on the site q; F_q^i and F_i^0 are the partition of the adsorbed particle i on site q and of the molecules i in the gas phase; $\beta = (k_B T)^{-1}$; P_i and m_i are the partial pressure and the degree of dissociation of molecule i in gaseous phase (adsorbtive). If $m_i = 1$, one has $Q_q^i = \varepsilon_q^i$, where ε_q^i the energy of the bond between the particle i and the site q, and if $m_i = 2$ one has $Q_q^i = \varepsilon_q^i - D_i$, where D_i is the dissociation energy of the molecule i in the gaseous phase.

The problem in theoretical statistics is to construct closed expressions describing the distribution of the adsorbed particles on the surface. The lateral interaction between these particles makes the state of occupancy of

Lam Research Ex. 1035 - Page 375
Lam Research Corp. v. Inpria Corp.
IPR2024-00033 - U.S. Patent No. 9,823,564

each site dependent on that of its neighbors. At any dynamic processes, including the reconstruction of the solid surface layer and near-surface region one will believe that the variables η_f^q are changed during the considered process as well as the variables γ_f^i for the adsorption layer. So one can restrict to the variables γ_f^i for all site of the gas–solid system and the expression (22) can be rewritten as

$$H = \sum_f \sum_i v_f^i \gamma_f^i - \sum_r \sum_{f,g} \sum_{i,j} \varepsilon_{fg}^{ij}(r) \gamma_f^i \gamma_{g_r}^j, \tag{23a}$$

$$v_f^i = -\beta^{-1} \ln(A_f^i P_i)^{1/m_i}, \quad A_f^i = (F_f^i)^{m_i} \beta \exp(\beta Q_f^i)/F_i^0. \tag{23b}$$

Here v_f^i is the one-particle contribution (or the renormalized chemical potential) of the species i on the site f to full energy of the gas–solid system.

3.2. Master Equation

In Section 1 the rates calculating of the elementary surface processes an assumption on the equilibrium distribution of the reagents over the entire surface of the solid body or in the local macroregion was used. Such an assumption is not always true and the theory of surface processes must reflect the possibility of the existence of a wide spectrum of reagent mobilities. Now, the lattice-gas model is used for describing of the systems which have no equilibrium distribution of their components, i.e., $0 \leq \eta \leq 1$.

The temporal evolution of any system is described by kinetic equations. In the lattice-gas models the evolution of the gas–solid interface is made up of the evolution of occupancies of each of its sites, which can change at the expense of the surface reactions and migration of solid body atoms. The model allows to trace the evolution of all the sites of the system at times τ, $\tau > \tau_m$, where τ_m is the minimum characteristic time interval relating to the most rapid elementary process of changing the occupancy state of the lattice sites.

An increase in the time interval τ is attended by a transition to the region of characteristic time intervals of slower elementary processes, while the description of rapid processes becomes more approximate. The degree of approximation depends on the ratio $\eta = \tau/\tau_m$. Two types of processes are traditionally singled out [48,49]: (1) when the processes of chemical transformation are the limiting ones (the rate of particle migration is much superior to the rate of chemical transformation), and (2) when the processes of particle migration are the limiting ones (the rate of chemical transformation is much superior to the rate of particle migration).

Lam Research Ex. 1035 - Page 376
Lam Research Corp. v. Inpria Corp.
IPR2024-00033 - U.S. Patent No. 9,823,564

In the first case, an increase in η signifies greater mixing of the particles because of their multifold migrations. This is accompanied by a growth in the region of space whose particles are involved in such mixing. This leads to erosion of the initial fluctuations in the density of particle distribution, and the fluctuations do not virtually affect the processes of chemical transformation. With large differences between the rate constants of migration and of chemical transformation, an equilibrium distribution of the components sets in the system. In the second case of diffusion-controlled processes, a growth in η retards the processes of particle mixing and increases the role of the initial fluctuations in the density of reactant distribution.

As a result, the initial statement of the problem, including information on the mechanism of the process (a set of elementary steps of chemical transformations and migrations of the particles), particle interactions, typical times of realization of the elementary processes (they are usually characterized by the rate constants), and the employed way of closing the systems of kinetic equations lead to a hierarchy of the mathematical models differing in the dimension of the system of kinetic equations and the form of their right-hand sides. In inhomogeneous systems, the form of the models is also affected by the nature of the inhomogeneities (which can alter the mechanism of the process, the rate constants of a step, and the particle interactions) and by the external fields. The form of the kinetic equations is simplified if one limits to particular cases of reactant concentrations, e.g., to the region of low concentrations or to an excess of a component.

Each site is occupied by adspecies of one kind ($\gamma_f^i \gamma_f^j = \Delta_{ij} \gamma_f^i$). Let $\mathrm{I} \equiv \gamma_f^1, \ldots, \gamma_f^s$ denote the total set of the γ_f^i values of all the sites of the lattice and $P(\mathrm{I}, \tau)$ denote the probability of finding the system at the time instant τ in a certain state I. The time evolution of the system is described by the master equation [82–84]:

$$\frac{d}{d\tau} P(\{I\}, \tau) = \sum_{\alpha, \{II\}} [W_\alpha(\{\mathrm{II}\} \to \{\mathrm{I}\}) P(\{\mathrm{II}\}, \tau) - W_\alpha(\{\mathrm{I}\} \to \{\mathrm{II}\}) P(P\{\mathrm{I}\}, \tau)], \tag{24}$$

where $W_\alpha(\{\mathrm{I}\} \to \{\mathrm{II}\})$ are the probabilities of realizing the elementary process a from the initial state, denoted as I, to the final state II at the time instant τ. If the elementary process is of one site nature, then the lists of the lattice site occupancies I and II differ only in the γ_f^i values for site f. For the two-site process the lists of site occupancies I and II differ in the occupancies of the two sites. The sum over the occupancies II corresponds to a change in the occupancies of all lattice sites. Interrelation between the occupancies I and II depends on a mechanism of the process which defines a set of elementary stages α. The values $W_\alpha(\{\mathrm{I}\} \to \{\mathrm{II}\})$ correspond to the Marcovian

Lam Research Ex. 1035 - Page 377
Lam Research Corp. v. Inpria Corp.
IPR2024-00033 - U.S. Patent No. 9,823,564

approximation when the probabilities of the elementary transitions are defined only by the current state of the system. In this case the system's memory effects are absent. In order to ensure a correct description of the system in an equilibrium state, these probabilities for a direct and the reverse directions of any stage α must obey the detailed equilibrium condition:

$$W_\alpha(\{\mathrm{II}\} \to \{\mathrm{I}\}) \exp[-\beta H(\{\mathrm{II}\})] = W_\alpha(\{I\} \to \{\mathrm{II}\}) \exp[-\beta H(\{I\})]. \quad (25)$$

Here the Hamiltonian is defined by Eqs. (23a) and (23b).

Except for a number of cases mentioned below a large dimensionality of system (24), which is equal to s^N does not allow to use it for direct integration. In the theory of kinetic equations for describing the evolution of an object, instead of a full function of the distribution $P(\mathrm{I},\tau)$ one uses a reduced technique of its assignment via time correlators which are defined as follows

$$\theta^{i_1 \ldots i_m}_{f_1 \ldots f_m}(\tau) = \langle \gamma^{i_1}_{f_1} \ldots \gamma^{i_m}_{f_m} \rangle = \sum_{i_1=1}^{s} \ldots \sum_{i_N=1}^{s} \Gamma_m P(\{\gamma^i_f\}, \tau), \; \Gamma_m = \prod_{n=1}^{m} \gamma^{i_n}_{f_n}, \quad (26)$$

where a sum over the kinds of adspecies is taken over all the lattice sites. The correlators (26) characterize the probability of finding adspecies i_n in site f_n, $1 \le n \le m$, at the time instant τ and m is the dimensionality of the correlator. In the equilibrium state $P(\{\mathrm{I}\},\tau \to \infty) = \exp(-\beta H(\{\mathrm{I}\}))/Q$, where $H(\{\mathrm{I}\})$ is the total energy of the lattice system in the state I, and Q is the statistical sum of the system. The correlators (26) of varying dimensionality are related to each other by the relations:

$$\theta^{i_1 \ldots i_m}_{f_1 \ldots f_m}(\tau) = \sum_{i_{m+1}=1}^{s} \theta^{i_1 \ldots i_m i_{m+1}}_{f_1 \ldots f_m f_{m+1}}(\tau), \; \sum_{i=1}^{s} \theta^i_f(\tau) = 1. \quad (27)$$

Kinetic equations for the correlators are obtained by multiplying the expressions (23a) and (23b) by Γ_m (26) and by averaging over all the states of the system. The kinds of adspecies in sites f_n, which result in non-zero contributions to a change of the correlators (26) depend on a direction of elementary process α and are determined by the states I or II. This gives the following equations:

$$\frac{d}{d\tau} \theta^{i_1 \ldots i_m}_{f_1 \ldots f_m}(\tau) = \sum_{\alpha, \{II\}} \left[\left\langle \prod_{n=1}^{m} \gamma^{i^*_n}_{f_n} W_\alpha(\{II\} \to \{I\}) \right\rangle - \left\langle \prod_{n=1}^{m} \gamma^{i_n}_{f_n} W_\alpha(\{I\} \to \{II\}) \right\rangle \right], \quad (28)$$

where the kinds of adspecies i^*_n correspond to the occupancies of the lattice sites in state II $\left(i_n \leftrightarrow i^*_n\right)$. A specific form of the right-hand side of Eq. (28) depends on the form of the probabilities W_α.

Lam Research Ex. 1035 - Page 378
Lam Research Corp. v. Inpria Corp.
IPR2024-00033 - U.S. Patent No. 9,823,564

3.3. PROBABILITIES OF ELEMENTARY REACTIONS

Eq. (28) are used initially for obtaining the kinetic equations for condensed phase processes. Let us discuss a fairly general case for the theory of surface processes and assume the lattice to be inhomogeneous and the radius of the adspecies interaction pair potential to be equal to R ($R>1$).

The non-equivalency of the sites is demonstrated in the fact that each site f is characterized by its own set of occupancies s_f, internal degrees of freedom of the adspecies i ($1\le i\le s_f$) which is on site of q-type numbered as f (it determines the reaction rate constants $K_f^{i*}(\alpha)$ and $K_{fg}^{ij*}(\alpha)$) and its own interaction parameters: $\varepsilon_{qp}^{ij}(fg|r)$ and $\varepsilon_{qp}^{ij*}(fg|r)$, where $\varepsilon_{qp}^{ij}(fg|r)$ is the energy parameter between species i and j locating on the sites f and g at the distance r, and $\varepsilon_{qp}^{ij*}(fg|r)$ is the energy parameter between the AC, that arises from adspecies i on the site f, and adspecies j locating on the sites g at the distance r. The interactions of the neighboring adspecies i and j that are positioned in the ground state at the distance r, where $1\le r\le R$, R is the interaction radius. In the general case $\varepsilon_{qp}^{ij*}(fg|r)\neq\varepsilon_{qp}^{ji*}(fg|r)$, if $i\neq j$. The interaction of the AC with the empty site is zero: $\varepsilon_{qp}^{iV*}(fg|r)=0$, however, if this complex is formed above an empty site, as is the case with the adsorption stage $A+Z_f\rightarrow AC_f$, then $\varepsilon_{qp}^{Vj*}(fg|r)\neq 0$, since the AC properties are independent of the elementary process direction. In this case $\varepsilon_{qp}^{Vj*}(fg|r)=\varepsilon_{qp}^{Aj*}(fg|r)$.

As the adspecies i can participate in various elementary reactions in the given total multistage processes, at common case the parameter $\varepsilon_{qp}^{ij*}(fg|r)$ should have the additional indexes of the number α for the selected stage. Such an approach allows to apply an unified approach to considering the inhomogeneity of adspecies distribution, caused by their interaction with the different lattice sites and interaction between each other. (As the number of the site f and its type q are unambiguously related so that the parameters notation can be simplified: $\varepsilon_{fg}^{ij}(r)=\varepsilon_{qp}^{ij}(fg|r)$, $K_q^{i*}(f|\alpha)=K_f^{i*}(\alpha)$, etc).

Let the occupancies of the lattice sites change due to the occurrence of one-site processes $i\leftrightarrow b$ (let Q_f^i denotes their number) and the two-site processes $i+j\leftrightarrow b+d$ (let Q_{fg}^{ij} denotes their number). The probabilities of one-site ($W_f^i(\alpha)$) and two-site ($W_{fg}^{ij}(\chi|\alpha)$ at the distance χ) transitions in TSM will be written as follows [85–87]:

the one-site process $i\rightarrow$ Product

$$W_f^i(\alpha)=\gamma_f^i\exp[-\beta\{\delta H_f^i(\alpha)+\delta F_f^i(\alpha)\}], \tag{29}$$

$$\delta H_f^i(\alpha)=\gamma_f^i\left[v_f^i(\alpha)-v_f^i-\sum_r\sum_{h_r}\sum_m(\varepsilon_{fg}^{im}(\alpha|r))-(\varepsilon_{fg}^{im}(r))\gamma_g^m\right],$$

Lam Research Ex. 1035 - Page 379
Lam Research Corp. v. Inpria Corp.
IPR2024-00033 - U.S. Patent No. 9,823,564

the two-site process $i+j \rightarrow$ Product

$$W_{fg}^{ij}(\chi|\alpha) = \gamma_f^i \gamma_g^j \exp[-\beta\{\delta H_{fg}^{ij}(\chi|\alpha) + \delta F_{fg}^{ij}(\chi|\alpha)\}], \tag{30}$$

$$\delta H_{fg}^{ij}(\chi|\alpha) = (v_{fg}^{ij}(\alpha|\chi) + \varepsilon_{fg}^{ij}(\chi))\gamma_f^i \gamma V - v_f^i \gamma_f^i - v_g^j \gamma_g^j - \sum_r \sum_{\omega_r} \sum_{h_\omega} \sum_m \varepsilon_{fh}^{im}(\alpha|r_1) + \varepsilon_{gh}^{jm}(\alpha|r_2) - \varepsilon_{fh}^{im}(r_1) - \varepsilon_{gh}^{jm}(r_2)\gamma_f^i \gamma_g^j \gamma_h^m,$$

where $\delta H_f^i(\alpha)$ and $\delta H_{fg}^{ij}(\chi|\alpha)$ describe a variation of the potential energy relatively slow variables at realization of the one- and two-sites elementary processes α with a creation of the AC; $\delta F_f^i(\alpha)$ and $\delta F_{fg}^{ij}(\chi|\alpha)$ describe a variation of the free energy relatively rapid variables at realization of the one- and two-sites elementary processes α; $v_f^i(\alpha)$ is the one-particle contribution of the AC for one-site process to the full energy for system under consideration; it is expressed as by the formula (23b); also $v_{fg}^{ij}(\alpha|\chi)$ is the similar one-particle contribution of the AC for two-site process; below one will use the values $\delta\varepsilon_{fg}^{ij}(\alpha|r) = \varepsilon_{fg}^{ij*}(\alpha|r) - \varepsilon_{fg}^{ij}(r)$.

The structure of Eq. (30) about the interactions at $R>1$ of an AC for the two-site elementary process that occupies two adjacent (central) lattice sites with its neighbors should be considered in more detail. Each AC fragment (A and B for the elementary stage $ZA + ZB \rightarrow AC$) is capable of retaining its individuality so that its interaction parameters possess some particular features. To make the numbering of the neighboring adspecies more convenient, it would be appropriate to introduce the concept of a common c.s. of the radius r representing the totality of the sites located at the same distance from the nearest central ones. The position (orientation) of the site in the common rth c.s. will be characterized by an angle between the line l_1 connecting the central sites with the line l_2 connecting a given site with the center of the segment between the central sites. Let π_r denote the number of the various orientations of the neighboring sites in the common rth c.s. and $\kappa(\omega_r)$ is the number of sites with the same orientation ω_r in this sphere ($1 \leq \omega_r \leq \pi_r$), located on the surface of the cone formed by the line l_2 upon rotation around l_1. Shown in Fig. 8.3 is the distribution of the neighboring sites for planar lattices at $R = 2$. Part of the adspecies adjacent the AC is located at such distances r_1 and r_2 from fragments A and B, respectively, that they interact simultaneously with the two initial reagents ($r_1, r_2 \leq R$). In the case of these adspecies the parameter for the interaction of the neighboring adspecies with the AC will be written down as $\varepsilon_{ABj}^*(\omega_r) = \varepsilon_{Aj}^*(r_1) + \varepsilon_{Bj}^*(r_2)$, where ω_r and r_1, r_2 are in one-to-one correspondence. If $r_2 > R$, then $\varepsilon_{ABj}^*(\omega_r) = \varepsilon_{Aj}^*(r_1)$.

Lam Research Ex. 1035 - Page 380
Lam Research Corp. v. Inpria Corp.
IPR2024-00033 - U.S. Patent No. 9,823,564

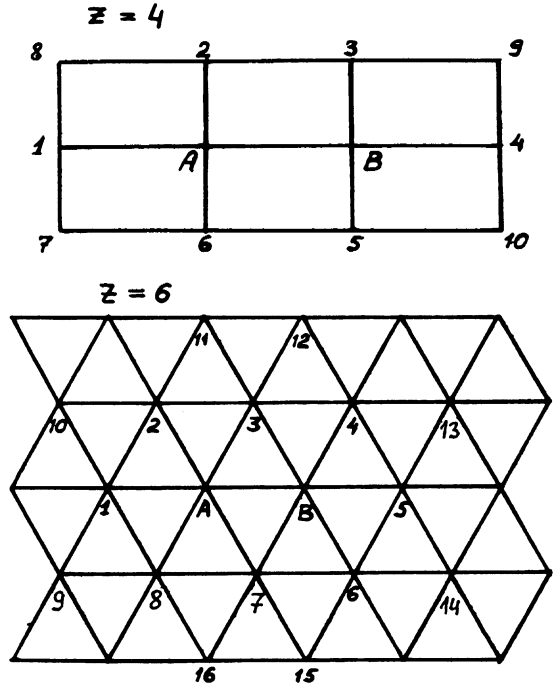


Fig. 8.3. Distribution of the sites of the two-dimensional lattice with $z = 4$ and 6 among the equivalent groups of the first two c.s. For $z = 4$ the first c.s. includes sites 1–6 ($\pi_1 = 4$) and the second one includes – sites 7–10 ($\pi_2 = 2$): site 1 corresponds to $\omega_1 = 1$, sites 2 and 6 – to $\omega_1 = 2$, sites 3 and 5 – to $\omega_1 = 3$, site 4 – to $\omega_1 = 4$, sites 7 and 8 – to $\omega_2 = 1$, and sites 9 and 10 – to $\omega_2 = 2$. For $z = 6$ the first c.s. includes sites 1–8 ($\pi_1 = 5$), and the second one includes – sites 9–16 ($\pi_2 = 4$): site 1 corresponds to $\omega_1 = 1$, sites 2 and 8 – to $\omega_1 = 2$, sites 3 and 7 – to $\omega_1 = 3$, sites 4 and 6 – to $\omega_1 = 4$, site 5 – to $\omega_1 = 5$, sites 9 and 10 – to $\omega_2 = 1$, sites 11 and 16 – to $\omega_2 = 2$, sites 12 and 15 – to $\omega_2 = 3$, and sites 13 and 14 – to $\omega_2 = 4$.

For example when $z = 4$ and $R = 2$ one has $\varepsilon^*_{ABj}(\omega_1 = 1) = \varepsilon^*_{Aj}(1)$; $\varepsilon^*_{ABj}(\omega_1 = 2) = \varepsilon^*_{Aj}(1) + \varepsilon^*_{Bj}(2)$; $\varepsilon^*_{ABj}(\omega_1 = 3) = \varepsilon^*_{Aj}(2) + \varepsilon^*_{Bj}(1)$; $\varepsilon^*_{ABj}(\omega_1 = 4) = \varepsilon^*_{Bj}(1)$; $\varepsilon^*_{ABj}(\omega_2 = 1) = \varepsilon^*_{Aj}(2)$; $\varepsilon^*_{ABj}(\omega_2 = 2) = \varepsilon^*_{Bj}(2)$.

The same simple procedure applies to the construction of the parameters $\varepsilon_{ABj}(\omega_r)$ for the various z and R. If A = B, the symmetrical positions of the common rth c.s. sites relative to the plane passing through the center of and normal to the straight line l_1 are matched by the same $\varepsilon^*_{AAj}(\omega_r)$ values ($1 \leq \omega_r \leq \pi_r/2$) at the doubled values of $\kappa(\omega_r)$.

Expressions (30) correspond to the condition (25). Their substitution into the right-hand side of Eq. (28) yields the appropriate kinetic equations for each site of the lattice (an ensemble of the lattices).

Lam Research Ex. 1035 - Page 381
Lam Research Corp. v. Inpria Corp.
IPR2024-00033 - U.S. Patent No. 9,823,564

3.4. KINETIC EQUATIONS

The first equations (m = 1) of the system are those for θ_f^i which determine the probability of covering site numbered f with adspecies i,

$$\frac{d}{dt}\theta_f^i = \sum_{\alpha}[U_f^b(\alpha) - U_f^i(\alpha)] + \sum_r \sum_h \sum_j \sum_{\alpha}[U_{fh}^{bd}(r|\alpha) - U_{fh}^{ij}(r|\alpha)], \quad (31)$$

$$U_f^i(\alpha) = \langle \gamma_f^i \exp[-\beta\{\delta H_f^i(\alpha) + \delta F_f^i(\alpha)\}]\rangle, \quad (31a)$$

$$U_{fg}^{ij}(r|\alpha) = \langle \gamma_f^i \gamma_g^j \exp[-\beta\{\delta H_{fg}^{ij}(r|\alpha) + \delta F_{fg}^{ij}(r|\alpha)\}]\rangle, \quad (31b)$$

where the first sum relates to the one-site processes and the second one to the two-site processes; $U_f^i(\alpha)$ is the one-site process rate for species i in the stage α ($i \leftrightarrow b$); $U_{fg}^{ij}(r|\alpha)$ is the two-site process rate for species i and j at the distance r in the stage α ($i+j \leftrightarrow b+d$), here $h \in z_f(r)$.

The processes of covering each site depend on the occupancies of the neighboring sites due to (1) the influence of the lateral interactions and the possibility of the central adspecies, (2) reacting with the neighboring ones, or (3) to block the neighboring sites with this adspecies. Therefore in the right-hand side of the Eq. (31) there appear the unknown correlators $\theta_{f_1 \ldots f_m}^{i_1 \ldots i_m}$ with $m = m_1$ and m_2 dimensionality for the one-site and the two-site processes, respectively, ($m_1 = 1 + \sum_{r=1}^{R} z_r$ and $m_2 = 2 + \sum_{r=1}^{R} z_r \sum_{\omega_r=1}^{\pi_r} \kappa(\omega_r)$, where $\kappa(\omega_r)$, is above defined).

By normalizing relations (27) in all the unknown correlators one can exclude the configurations that contain empty sites and order the remaining correlators in a certain way. For example, for the case $s = 2$ one can order the correlators with respect to an increase in the number n_A of adspecies A, $1 \le n_A \le m$; for the case $s = 3$ with respect to the common number $n_{AB} = n_A + n_B$ of the adspecies A and B included in the configuration, $1 \le n_{AB} \le m$, and for a given number n_{AB} one can order the configurations with respect to an increase in the number of adspecies A, $0 \le n_A \le n_{AB}$, etc. In order to find the unknown correlators with the dimensionality 2,3,…,m, it is necessary to use the following (after Eq. (31)) Eq. (28). In each such case expressions (29), (30) bring about in the right-hand side of Eq. (28) the new unknown correlators of higher dimensionality than the correlators of the left-hand side of Eq. (28). The resulting hierarchical sequence of the kinetic equations is unlimited (for the macrosystem), and in order to close, one has to truncate it.

The way of closing depends on the procedure of approximation of the higher correlators via the correlators of lower dimensionality. The simplest method is an approximation of any correlators (26) via the unary

Lam Research Ex. 1035 - Page 382
Lam Research Corp. v. Inpria Corp.
IPR2024-00033 - U.S. Patent No. 9,823,564

correlators θ_f^i. These given approximations have been used in describing the crystal growth process within the framework of the solid-on-solid model at $s = 2$ [87] and $s = 3$ [88].

However this way could not give a self-consistent description between equilibrium and dynamical characteristics for elementary stages [80,89]. The lattice-gas model is the unique one that provides a self-consistent description of the equilibrium distribution of molecules as well as their dynamic behavior if the correlation effects are taken into account. Then the first correlator that provides such self-consistent description of elementary stages is a pair correlator $\theta_{fg}^{ij}(r)$ ($m = 2$) in the quasi-chemical approximation. In the non-equilibrium conditions to calculate the unknown functions $\theta_{fg}^{ij}(r)$ the kinetic Eq. (28) should be used.

The second equations of the kinetic system are those for $\theta_{fg}^{ij}(r)$ which determine the pair probability of covering sites numbered f and g with adspecies i and j at the distance r. With allowance for Eqs. (29) and (30), these equations have the following form:

$$\frac{d}{dt}\theta_{fg}^{ij}(r) = \sum_{\alpha}[U_{fg}^{bd}(r|\alpha) - U_{fg}^{ij}(r|\alpha)] + P_{fg}^{ij}(r) + P_{gf}^{ji}(r), \tag{32}$$

$$P_{fg}^{ij}(r) = \sum_{\alpha}[U_{fg}^{(b)j}(r|\alpha) - U_{fg}^{(i)j}(r|\alpha)] + \sum_{h}\sum_{m}\sum_{\alpha}[U_{hfg}^{(cb)j}(r|\alpha) - U_{hfg}^{(mi)j}(r|\alpha)].$$

In Eq. (32) the second term $P_{gf}^{ji}(r)$ describes the stage $i + m \leftrightarrow b + c$ on the neighboring sites g and h at the distance r. In the right-hand side of the Eq. (32) there appear new terms $U_{fg}^{(i)j}(r|\alpha)$ and $U_{hfg}^{(mi)j}(r|\alpha)$ that reflect an influence of the presence of the neighbor j on rates of the one-site and two-site processes, respectively:

$$U_{fg}^{(i)j}(r|\alpha) = \langle \gamma_f^i \gamma_g^j \exp[-\beta\{\delta H_f^i(\alpha) + \delta F_f^i(\alpha)\}]\rangle, \tag{33}$$

$$U_{hfg}^{(mi)j}(r|\alpha) = \langle \gamma_h^m \gamma_f^i \gamma_g^j \exp[-\beta\{\delta H_{hfg}^{(mi)j}(r|\alpha) + \delta F_{hfg}^{(mi)j}(r|\alpha) + \delta F_{hfg}^{(mi)j}(r|\alpha)\}]\rangle.$$

A presence of the kinetic equations for pair correlators in closed system of equation allows to describe properties about a prehistory of the experimental system (such as the shape and size of spatio-temporal distribution of the reagents along the surface or interface area) and the time of evolution during the considered processes.

More exact than the quasi-chemical approximation (QCA) is the Kirkwood superposition approximation since if takes into account the indirect correlations. The form of the components in the right-hand side of

Lam Research Ex. 1035 - Page 383
Lam Research Corp. v. Inpria Corp.
IPR2024-00033 - U.S. Patent No. 9,823,564

Eqs. (31) and (32) becomes more complicated. The dimensionality of the set of equations, however, coincides with that of the system in the QCA. A more exact description is obtained with the correlators of greater dimensionality $m>2$ (see, e.g., Refs. [90,91]). Of special interest are the one-dimensional systems with $s=2$. Exact solutions for the migrating adspecies on the one-dimensional lattice have been obtained for a small number of sites [92]. In Refs. [93,94] the procedure of numerical analysis of the hierarchical system of equations has been elaborated, which is applicable not only to the one-dimensional [94,95] but also to the two-dimensional lattices [95,96], as well, the interaction with the second neighbors being taken into account ($d=1$) [97]. Also, it should be noted that the expansions (virial or diagrammatic) [98] similar to the common expansion in the equilibrium theory of condensed systems [77] are used for closing the kinetic equations.

3.5. Reaction Rates

Our objective is to derive expressions for one-site ($U_f^i(\alpha)$) (Eq. (31a)) and two-site ($U_{fg}^{ij}(r|\alpha)$) (Eq. (31b)) processes in non-ideal reaction systems. To solve this problem, one should implement averaging over all local configurations of the molecules surrounding the reagents. This procedure takes account of two limiting relations between the representative times of the reaction, τ_r and rearrangement of the medium, τ_m. If $\tau_m \ll \tau_r$ the reaction is slowly and in its course the reagent surrounding has time to be adapted to variations in the state of the reaction subsystem; if $\tau_m \gg \tau_r$ the reaction is rapid and the surrounding has no time to be adjusted to the changes.

To obtain the closed system of kinetic equations one should divide all variables on slow (with the characteristics time τ_m) and rapid (with the characteristics time τ_r) variables with respect to the chosen time interval τ, which is presented in the left sides of the differential Eqs. (31) and (32). As rule, in condensed reaction systems inner degrees of freedoms for reactants can reach the local relaxation state during less time by comparison with rapid variables. In opposite cases, various inner states of reactants should be considered as independent kinds of species.

Angle brackets in Eqs. (31a) and (31b) denote averaging over the whole spectrum of the states of slow variables. Generally, the states of rapid variables depend on those of slow variables, so that $\delta F_f^i(\alpha)$ and $\delta F_{hfg}^{(mi)j}(r|\alpha)$ cannot be taken out of the angle brackets. An expression in the quasi-chemical approximation for the free energy that are needed for calculation of the $\delta F_f^i(\alpha)$ and $\delta F_{hfg}^{(mi)j}(r|\alpha)$ is given in Appendix A.

Lam Research Ex. 1035 - Page 384
Lam Research Corp. v. Inpria Corp.
IPR2024-00033 - U.S. Patent No. 9,823,564

Final formulas for elementary rates have the following forms:
For one-site elementary processes

$$U_f^i(\alpha) = K_f^{i*}(\alpha) V_f^i(\alpha),\ V_f^i(\alpha) = \theta_f^i \prod_{r=1}^{R} \prod_{g \in Z_f} S_{fg}^i(r|\alpha) R_{fg}^i(r|\alpha), \tag{34}$$

where the reaction rate constant $K_f^{i*}(\alpha)$ for molecule i is defined by Eq. (7a) as for the ideal reaction system, $V_f^{i*}(\alpha)$ is the concentration contribution to the one-site reaction rate,

$$S_{fg}^i(r|\alpha) = \sum_m t_{fg}^{im}(r) \exp[\beta\delta\varepsilon_{fg}^{im}(r|\alpha)], \tag{34a}$$

$$R_{fg}^i(r|\alpha) = \prod_k \exp[t_{fg}^{ik}(r) \ln \hat{t}_{fg}^{ik}(r) - \hat{t}_{fg}^{ik*}(r|\alpha) \ln \hat{t}_{fg}^{ik*}(r|\alpha)]. \tag{34b}$$

Here indexes k and m in Eqs. (34a) and (34b) correspond to the rapid and slow variables which correspond to the neighboring species;

$$\hat{t}_{fg}^{ij}(r) = \theta_{fg}^{ij}(r) \exp[-\beta\varepsilon_{fg}^{ij}(r)]/\theta_f^i, \tag{35}$$

$$\hat{t}_{fg}^{ij*}(r|\alpha) = t_{fg}^{ij*}(r|\alpha) \exp[-\beta\varepsilon_{fg}^{ij*}(r|\alpha)];$$

for the two-site elementary processes

$$U_{fg}^{ij}(r|\alpha) = K_{fg}^{ij*}(r|\alpha) V_{fg}^{ij}(r|\alpha), \tag{36}$$

$$V_{fg}^{ij}(r|\alpha) = \theta_{fg}^{ij}(r) \exp[-\beta\varepsilon_{fg}^{ij}(r)] \prod_{r=1}^{R} \prod_{\omega_r=1}^{\pi_r} \prod_{h\omega_r} S_{fgh}^{ij}(\omega_r|\alpha) R_{fgh}^{ij}(\omega_r|\alpha),$$

where the reaction rate constant $K_{fg}^{ij*}(r|\alpha)$ for molecules i and j is defined by Eq. (7b) as for the ideal reaction system, $V_{fg}^{ij}(r|\alpha)$ is the concentration contribution to the two-site reaction rate,

$$S_{fgh}^{ij}(\omega_r|\alpha) = \sum_m t_{fgh}^{ijm}(\omega_r) \exp[\beta\delta\varepsilon_{fgh}^{ijm}(\omega_r|\alpha)], \tag{36a}$$

$$R_{fgh}^{ij}(\omega_r|\alpha) = \prod_k \exp[t_{fgh}^{ijk}(\omega_r) \ln \hat{t}_{fgh}^{ijk}(\omega_r) - t_{fgh}^{ijk*}(\omega_r|\alpha) \ln \hat{t}_{fgh}^{ijk*}(\omega_r|\alpha)]. \tag{36b}$$

In these formulas

$$t_{fgh}^{ijm}(\omega_r) = t_{fh}^{im}(r_1) t_{gh}^{jm}(r_2)/\theta_h^m,\ \ \hat{t}_{fgh}^{ijk*}(\omega_r|\alpha) = t_{fg}^{ijk*}(\omega_r|\alpha) \exp[-\beta\varepsilon_{fgh}^{ijk*}(\omega_r|\alpha)]. \tag{37}$$

To calculate multipliers $R_{fg}^{i*}(r|\alpha)$ and $R_{fgh}^{ij*}(\omega_r|\alpha)$ that are arisen from the contribution of the free energy for rapid variables, it is necessary to solve the set of equations for equilibrium distribution of the system components.

Lam Research Ex. 1035 - Page 385
Lam Research Corp. v. Inpria Corp.
IPR2024-00033 - U.S. Patent No. 9,823,564

The additional components are the ACs, and the distribution of molecules surrounding each complex is described by functions $t_{fg}^{ij}(r|\alpha)$ and $t_{fgh}^{ijk}(\omega_r|\alpha)$ [the latter are related to the former as $t_{fg}^{ij}(r)$ and $t_{fgh}^{ijk}(\omega_r)$ by Eq. (37)]. Taking into account that the number of ACs is small, one can write

$$t_{fg}^{ij*}(r|\alpha) = \theta_{fg}^{ij}(r)\exp[\beta\delta\varepsilon_{fg}^{ij}(r|\alpha)]/\left[\sum_k \theta_{fg}^{ik}(r)\exp[-\beta\delta\varepsilon_{fg}^{ik}(r|\alpha)] + \sum_m \theta_{fg}^{im}(r)\right], \tag{38}$$

where again indexes k and m in the last expression correspond to the rapid and slow variables.

Finally, the formulas for $U_{fg}^{(i)j}(r|\alpha)$ and $U_{hfg}^{(ni)j}(r|\alpha)$ are expressed as

$$U_{fg}^{(i)j}(r|\alpha) = U_f^i(\alpha)\psi_{fg}^{ij}(r|\alpha), \tag{39}$$

$$\psi_{fg}^{ij}(r|\alpha) = t_{fg}^{ij}(r)\exp[\beta\delta\varepsilon_{fg}^{ij}(r|\alpha)]/S_{fg}^{i}(r|\alpha), \tag{39a}$$

$$U_{hfg}^{(ni)j}(r|\alpha) = U_{hf}^{ni}(r|\alpha)\psi_{hfg}^{nij}(\omega_r|\alpha), \tag{40}$$

$$\psi_{hfg}^{nij}(\omega_r|\alpha) = t_{hfg}^{nij}(\omega_r)\exp[\beta\delta\varepsilon_{hfg}^{nij}(\omega_r|\alpha)]/S_{fgh}^{ij}(\omega_r|\alpha), \tag{40a}$$

where index j in Eqs. (39) and (40) corresponds to slow variables.

3.6. Hierarchy of the Kinetic Equations

To obtain macroscopic characteristics, one should pass from the equations operating with local distributions [expressions (34) and (36)] to a rougher description. Such procedure is dependent on physical properties of the considered process. The mathematical models depend on the mobilities of the system's components and on the space–time scale employed to study the relevant process. The choice of the scale depends on the goals and tasks of investigations. The molecular-kinetic theory makes it possible to formulate the general principles of constructing mathematical models, the ways of closing them, and the transition to a specific form of the right-hand sides of the kinetic equations depending on the selected typical value of the time interval for which the time derivative on the left-hand side of the equations is being determined. The description obtained allows to reveal a wide spectrum of local distributions. However, the large dimensionality of the system of equations allows to use such an approach only for a small fragment of the lattice. A size of the area described can be enlarged only if

Lam Research Ex. 1035 - Page 386
Lam Research Corp. v. Inpria Corp.
IPR2024-00033 - U.S. Patent No. 9,823,564

its detailed description is roughened. In this connection various kinetic equations emerge depending on the size of the area considered and the mobility of the adspecies [99].

In the first case one can obtain the following sequence of systems of equations: the three- or the two-dimensional discrete model, the one-dimensional discrete model and the point-like averaged model. The one-dimensional model is obtained by averaging over the sites, which are inside each layer in which the three- or the two-dimensional lattice is split along a certain specified direction (the layer thickness is of the order of an adspecies size). At averaging over all the layers, the point-like averaged model will be obtained. Examples of such a transition are considered for the homogeneous lattices using a process of CO oxidation on platinum catalysts [80,100], and, also, taking account of the formation of the ordered adspecies structures (as an example of a local inhomogeneity of adatoms distribution). In the course of averaging over the sites within the layer or over the entire inhomogeneous lattice the distribution functions appear. For the one-dimensional models the cluster and the averaged distribution functions contain, additionally, the indices for layer numbers where the sites of various types are located [81,101]. The point-like models have no macroflows, therefore for the inhomogeneous lattices such models are apply to for evenly inhomogeneous surfaces only [102]. On its basis one can obtain the kinetic equations for various processes where the QCA is used.

In the second case, if the species mobilities differ greatly, the dimensionality of the system of kinetic equations decreases [103]. Let all the components be divided into two groups of species: a slow (s) and a rapid (r) one. This yields three types of pair functions. For the rapid species the condition of the equilibrium distribution can be considered as satisfied. Then, for the pair functions of types "*sr*" and "*rr*" instead of the kinetic Eqs. (32) algebraic relations in Appendix A apply, whose dimensionality can be lowered using the method of substitution variables according to Appendix B. In this case the kinetic Eqs (31) for the local concentrations and Eq. (32) for the pair functions type "*ss*" do not change. A similar situation remains in passing to the one-dimensional discrete and point-like models.

Let us consider the hierarchy of mathematical model structures describing a process consisting of the stages: (1) $A + Z \leftrightarrow AZ$; (2) $B_2 + 2Z \leftrightarrow 2BZ$; and (3) $AZ + BZ \rightarrow 2Z + C$ proceeding on a flat surface and distinguished by their accuracy of describing the distribution of the reaction system particles. The number of occupation states for any site $s = 3$: $i = A$, B, and V. With a methodological goal in view, one will supplement the process with the stage (4) $BZ + A \rightarrow Z + C$ (for calculations of the real reaction of oxidation of CO molecules on platinum catalysts at low pressures, this step must be omitted).

Lam Research Ex. 1035 - Page 387
Lam Research Corp. v. Inpria Corp.
IPR2024-00033 - U.S. Patent No. 9,823,564

The stages of migration of adsorbed A and B particles are written as (5) $jZ_f + VZ_g \leftrightarrow VZ_f + jZ_g$, where $j = A, B$; f and g are adjacent sites, V is a vacant site (a vacancy). The index α corresponds to the indicated stage numbers. It is enough to consider the interactions of the first and second neighbors in the quasi-chemical approximation. There are two possibilities of the equation constructions: for the distributed two-dimensional model, and for point models. In the last subsection the next question will be discussed – How the form of the systems of equations alters for a great difference in the mobilities of the reactants?

3.7. Two-Dimensional Model

The kinetic equations for the local concentrations of the adsorbed particles that are having comparable migration rates or for initial time interval, have the form

$$\dot{\theta}_f^{\mathrm{A}} = U_f^{\mathrm{V}}(1) - U_f^{\mathrm{A}}(1) - \sum_{g\in z_f}[U_{fg}^{\mathrm{AB}}(3) + U_{fg}^{\mathrm{AV}}(5) - U_{fg}^{\mathrm{VB}}(5)],$$

$$\dot{\theta}_f^{\mathrm{B}} = \sum_{g\in z_f}[U_{fg}^{\mathrm{VV}}(2) - U_{fg}^{\mathrm{BB}}(2) - U_{fg}^{\mathrm{BA}}(3) - U_{fg}^{\mathrm{VB}}(5) + U_{fg}^{\mathrm{VB}}(5)] - U_f^{\mathrm{B}}(4). \qquad (41)$$

All two-site elementary processes are realized on the two nearest neighboring sites f and g. So the index $r = 1$ is omitted in $U_{fg}^{ij}(r|\alpha)$ and below in multipliers $K_{fg}^{ii}(r|\alpha)$. The addends on the right-hand sides of Eq. (41) are the rates of the elementary processes (whose stage numbers α are indicated in parentheses), the particles participating in an elementary process are defined by superscripts, and the site numbers, by subscripts.

The adsorption ($U_f^V(1)$) and desorption ($U_f^A(1)$) rates of A molecules ($\alpha = 1$) are expressed as

$$U_f^{\mathrm{V}}(1) = K_f^{\mathrm{V}}(1)\theta_f^{\mathrm{V}} \prod_{r=1}^{2}\prod_{g\in z_f} S_{fg}^{\mathrm{V}}(r|1), \quad U_f^{\mathrm{A}}(1) = K_f^{\mathrm{A}}(1)\theta_f^{\mathrm{A}} \prod_{r=1}^{2}\prod_{g\in z_f} S_{fg}^{\mathrm{A}}(r|1). \qquad (42)$$

The adsorption ($U_{fg}^{\mathrm{VV}}(2)$) and desorption ($U_{fg}^{\mathrm{BB}}(2)$) rates of B_2 molecules ($\alpha = 2$) are expressed as

$$U_{fg}^{\mathrm{VV}}(2) = K_{fg}^{\mathrm{VV}}(2)\theta_{fg}^{\mathrm{VV}}(1) \prod_{h=1}^{3} S_{fh}^{\mathrm{V}}(2) \prod_{h=4}^{6} S_{gh}^{\mathrm{V}}(2) \prod_{h=7}^{10} S_{fgh}^{\mathrm{VV}}(2),$$

$$U_{fg}^{\mathrm{BB}}(2) = K_{fg}^{\mathrm{BB}}(2) \exp[-\beta\varepsilon_{fg}^{\mathrm{BB}}(1)]\theta_{fg}^{\mathrm{BB}}(1) \prod_{h=1}^{3} S_{fh}^{\mathrm{B}}(2) \prod_{h=4}^{6} S_{gh}^{\mathrm{B}}(2) \prod_{h=7}^{10} S_{fgh}^{\mathrm{BB}}(2). \qquad (43)$$

Lam Research Ex. 1035 - Page 388
Lam Research Corp. v. Inpria Corp.
IPR2024-00033 - U.S. Patent No. 9,823,564

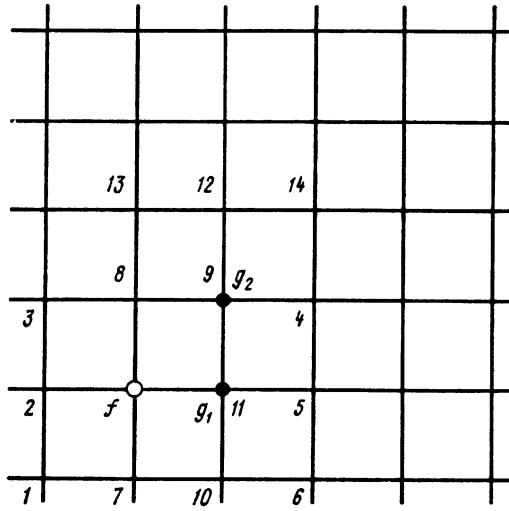


Fig. 8.4. The pairs of sites fg_1 (the number 11) at the distance of the first neighbors (the first neighbors $h = 2, 7, 8, 9, 10, 5$; the second neighbors $h = 1, 3, 4, 6$) and at the distance of the second neighbors fg_2 (the number 9) (the first neighbors $h = 2, 7, 8, 4, 11, 12$; the second neighbors $h = 1, 3, 10, 5, 13, 14$).

The function $\theta_{fg}^{ij}(1)$ contains the index $r = 1$ because the two-site process is occurred on the nearest-neighboring sites. Fig. 8.4 shows neighboring sites h counted from the fixed position of the central sites f and g on which the bimolecular reaction occurs. Sites at which neighboring particles interact either only with a particle at site for only with one at site g correspond to the numbers $h = 1$–6. Sites 2 and 5 are first neighbors, and sites 1, 3, 4, and 6 are second ones. At sites 7–10, the neighboring particles interact with both central particles. In the expressions for the rates of reactions, these site numbers unambiguously determine the distances between interacting particles, therefore the indexes r and ω_r may be omitted in multipliers $S_{fg}^{i}(r|\alpha)$ and $S_{fgh}^{ij}(\omega_r|\alpha)$.

The reactions by the adsorption $(U_{fg}^{\mathrm{AB}}(3), \alpha = 3)$ and collision $(U_{f}^{\mathrm{B}}(4), \alpha = 4)$ mechanisms:

$$U_{fg}^{\mathrm{AB}}(3) = K_{fg}^{\mathrm{AB}}(3)\exp[-\beta\varepsilon_{fg}^{\mathrm{AB}}(1)]\theta_{fg}^{\mathrm{AB}}(1)\prod_{h=1}^{3} S_{fh}^{\mathrm{A}}(3)$$
$$\prod_{h=4}^{6} S_{gh}^{\mathrm{B}}(3)\prod_{h=7}^{8} S_{fgh}^{\mathrm{AB}}(3)\prod_{h=9}^{10} S_{gfh}^{\mathrm{BA}}(3),$$
$$U_{f}^{\mathrm{B}}(4) = K_{f}^{\mathrm{A}}(4)\theta_{f}^{\mathrm{B}}\prod_{r=1}^{2}\prod_{g\in z_f} S_{fg}^{\mathrm{B}}(r|4). \tag{44}$$

Lam Research Ex. 1035 - Page 389
Lam Research Corp. v. Inpria Corp.
IPR2024-00033 - U.S. Patent No. 9,823,564

Migration of adsorbed particles $i = \mathrm{A}, \mathrm{B}$ ($\alpha = 5$):

$$U_{fg}^{i\mathrm{V}}(5) = K_{fg}^{i\mathrm{V}}(5)\theta_{fg}^{i\mathrm{V}}(1)\prod_{h=1}^{3} S_{fh}^{i}(5)\prod_{h=4}^{6} S_{gh}^{\mathrm{V}}(5)\prod_{h=7}^{8} S_{fgh}^{i\mathrm{V}}(5)\prod_{h=9}^{10} S_{gfh}^{\mathrm{V}i}(5) \tag{45}$$

For the reverse direction of a jump of a particle i from site g to the vacant site f, the places of the indices i and V should be exchanged in formula (45).

The system of equations for the local concentrations is supplemented with equations for the probabilities of the two-body configurations $\theta_{fg}^{ij}(r)$ at a distance of r, where $r = 1$ and 2, that obey normalizing relations (27). With a view to these relations for $s = 3$, it is sufficient to write the equations relative to the functions $\theta_{fg}^{ij}(r)$, where $ij = \mathrm{AA}$, AB, BA, and BB. For particles at the distance of first neighbors, the equations have the following form:

For pair "AA"

$$\begin{aligned}\dot{\theta}_{fg}^{\mathrm{AA}}(1) = {} & U_{fg}^{(\mathrm{V})\mathrm{A}}(1|1) - U_{fg}^{(\mathrm{A})\mathrm{A}}(1|1) + U_{fg}^{\mathrm{A}(\mathrm{V})}(1|1) - U_{fg}^{\mathrm{A}(\mathrm{A})}(1|1) \\ & - \sum_{h=7,2,8}[U_{hfg}^{(\mathrm{BA})\mathrm{A}}(1|3) + U_{hfg}^{(\mathrm{VA})\mathrm{A}}(1|5) - U_{hfg}^{(\mathrm{AV})\mathrm{A}}(1|5)] \\ & - \sum_{h=9,5,10}[U_{fgh}^{\mathrm{A}(\mathrm{AB})}(1|3) + U_{fgh}^{\mathrm{A}(\mathrm{AV})}(1|5) - U_{fgh}^{\mathrm{A}(\mathrm{VA})}(1|5)]\end{aligned} \tag{46}$$

for pair "BB"

$$\begin{aligned}\dot{\theta}_{fg}^{\mathrm{BB}}(1) = {} & U_{fg}^{\mathrm{VV}}(2) - U_{fg}^{\mathrm{BB}}(2) - U_{fg}^{(\mathrm{B})\mathrm{B}}(4) - U_{fg}^{\mathrm{B}(\mathrm{B})}(4) - \sum_{h=7,2,8}[U_{hfg}^{(\mathrm{VV})\mathrm{B}}(1|2) \\ & + U_{hfg}^{(\mathrm{BB})\mathrm{B}}(1|2) - U_{hfg}^{(\mathrm{AB})\mathrm{A}}(1|3) - U_{hfg}^{(\mathrm{VA})\mathrm{B}}(1|5) + U_{hfg}^{(\mathrm{BV})\mathrm{B}}(1|5)] \\ & - \sum_{h=9,5,10}[U_{fgh}^{\mathrm{B}(\mathrm{VV})}(1|2) + U_{fgh}^{\mathrm{B}(\mathrm{BB})}(1|2) - U_{fgh}^{\mathrm{B}(\mathrm{BV})}(1|5) \\ & + U_{fgh}^{\mathrm{B}(\mathrm{VB})}(1|5) - U_{fgh}^{\mathrm{B}(\mathrm{BA})}(1|3)]\end{aligned} \tag{47}$$

for pair "AB"

$$\begin{aligned}\dot{\theta}_{fg}^{\mathrm{AB}}(1) = {} & U_{fg}^{(\mathrm{V})\mathrm{B}}(1|1) - U_{fg}^{(\mathrm{A})\mathrm{B}}(1|1) - U_{fg}^{\mathrm{A}(\mathrm{B})}(1|4) - U_{fg}^{\mathrm{AB}}(3) \\ & - \sum_{h=7,2,8}[U_{hfg}^{(\mathrm{BA})\mathrm{B}}(1|3) + U_{hfg}^{(\mathrm{VA})\mathrm{B}}(1|5) - U_{hfg}^{(\mathrm{AV})\mathrm{B}}(1|5)] \\ & + \sum_{h=9,5,10}[U_{fgh}^{\mathrm{A}(\mathrm{VV})}(1|2) - U_{fgh}^{\mathrm{A}(\mathrm{BB})}(1|2) - U_{fgh}^{\mathrm{A}(\mathrm{BA})}(1|3) \\ & - U_{fgh}^{\mathrm{A}(\mathrm{VB})}(1|5) + U_{fgh}^{\mathrm{A}(\mathrm{VB})}(1|5)]\end{aligned} \tag{48}$$

The equation for the pair "BA" is written by changing the places of the superscripts A and B in Eq. (48).

Lam Research Ex. 1035 - Page 390
Lam Research Corp. v. Inpria Corp.
IPR2024-00033 - U.S. Patent No. 9,823,564

When constructing the kinetic equations for the functions $\theta_{fg}^{ij}(r)$ (sites f and $g = 9$ in Fig. 8.4, one must have in view that the state of occupancy of sites f and g cannot change simultaneously because bimolecular reactions occur only on the nearest sites. This leads to the following distinctions in the system of equations for the second neighbors from the system (46)–(48): (1) the addends $U_{fg}^{ij}(\alpha)$ are absent in Eqs. (47) and (48); and (2) summation over h is performed over all the nearest neighbors of sites f and g. For instance, for the pair function $\theta_{fg}^{AB}(2)$ the equation will be written as

$$\begin{aligned}\dot{\theta}_{fg}^{AB}(2) = {} & U_{fg}^{(V)B}(2|1) - U_{fg}^{(A)B}(2|1) - U_{fg}^{A(B)}(1|4) \\ & - \sum_h [U_{hfg}^{(BA)B}(2|3) + U_{hfg}^{(VA)B}(2|5) \\ & - U_{hfg}^{(AV)B}(2|5)] + \sum_h [U_{fgh}^{A(VV)}(2|2) - U_{fgh}^{A(BB)}(2|2) - U_{fgh}^{A(BA)}(2|3) \\ & - U_{fgh}^{A(BV)}(2|5) + U_{fgh}^{A(VB)}(2|5)]. \end{aligned} \tag{49}$$

The addends on the right-hand sides of Eqs. (46)–(49) are expressed in terms of the rates of the elementary processes in accordance with formulas (33). For one-site processes $\alpha = 1$ and 4 no explanations are needed. For two-site processes depending on the distance between sites h and g, one has $U_{hfg}^{(ij)n}(r|\alpha) = U_{hf}^{ij}(r|\alpha)\psi_{hfg}^{ijn}(\omega_r|\alpha)$, where $\psi_{hfg}^{ijn}(\omega_r|\alpha) = \psi_{fg}^{in}(r|\alpha)$, $r_{in} > 2$, $r = 1, 2$; $\psi_{hfg}^{jin}(\omega_r|\alpha) = \psi_{hfg}^{jin}(2|\alpha)$, $r_{in} = 2$, $r = 1$; $\psi_{hfg}^{ijn}(\omega_r|\alpha) = \psi_{hfg}^{jin}(1|\alpha)$, $r_{in} = 1$, $r = 2$. The site $h = 2$ (see Fig. 8.4) corresponds to the distance $r_{in} > 2$, and the sites $h = 7$ and 8 to the distance $r_{in} = 2$ when $r = 1$; when $r = 2$, the sites $h = 2$ and 3 correspond to the distance $r_{in} > 2$, and sites $h = 8$ and 11 to $r_{in} = 1$. The expressions $U_{hfg}^{i(jn)}(r|\alpha)$ are written in a similar way when the particles j and n react.

The constructed system of equations is a closed one. It is solved with the preset initial conditions $\theta_f^i(\tau = 0)$, $\theta_{fg}^{ij}(1, \tau = 0)$, $\theta_{fg}^{ij}(2, \tau = 0)$. The system of equations makes it possible to describe arbitrary distributions of particles on a surface and their evolution in time. The only shortcoming is the large dimension. The minimal fragment of a lattice on which a process with cyclic boundary conditions should be described is 4×4. It is, therefore, natural to raise the question of approximating the description of particle distribution to lower the dimension of the system of equations. In this connection, it is reasonable to consider simpler point-like models.

3.8. POINT-LIKE MODELS OF A REACTION

In point-like models, the averaging procedure is conducted over all the sites of a lattice, therefore diffusion flows are absent in the models. But the effects

Lam Research Ex. 1035 - Page 391
Lam Research Corp. v. Inpria Corp.
IPR2024-00033 - U.S. Patent No. 9,823,564

of particle mobility can be taken into account via the process of their local redistribution that changes the short-range order. This leads to a model considering the restricted mobility of all the reactants and to a model with rapid surface mobility of the reactants.

3.8.1. *Restricted Mobility of the Reactants*

One will characterize the average concentration of particles (θ_σ^i, $\sigma = \delta, \gamma$) and the average fraction of their pairs ($\theta_{\sigma\lambda}^{ij}(r)$) that take into account the ordered distribution $c(2 \times 2)$ of the particles on a surface.

The concentrations of the particles obey the kinetic equations

$$\begin{aligned}\dot{\theta}_\sigma^{\mathrm{A}} &= U_\sigma^{\mathrm{V}}(1) - U_\sigma^{\mathrm{A}}(1) - Z_{\sigma\lambda}(1)[U_{\sigma\lambda}^{\mathrm{AB}}(3) + U_{\sigma\lambda}^{\mathrm{AV}}(5) - U_{\sigma\lambda}^{\mathrm{VA}}(5)],\\ \dot{\theta}_\sigma^{\mathrm{B}} &= -U_\sigma^{\mathrm{B}}(4) + Z_{\sigma\lambda}(1)[U_{\sigma\lambda}^{\mathrm{VV}}(2) - U_{\sigma\lambda}^{\mathrm{BB}}(2) - U_{\sigma\lambda}^{\mathrm{BA}}(3)\\ &\quad - U_{\sigma\lambda}^{\mathrm{BV}}(5) + U_{\sigma\lambda}^{\mathrm{VB}}(5)].\end{aligned} \tag{50}$$

where $z_{\sigma\lambda}(r)$ is the number of neighbors of type λ that are neighbors of a site of type σ at a distance of r for a square lattice, one has $z_{\delta\gamma}(1) = z_{\gamma\delta}(\mathrm{l}) = 4$, and $z_{\delta\delta}(2) = z_{\gamma\gamma}(2) = 4$. The rates of elementary processes in the general form will be written as follows:

$$\begin{aligned}U_\sigma^i(\alpha) &= K_\sigma^i(\alpha)\theta_\sigma^i \prod_{r=1}^{2}\prod_\lambda [S_{\sigma\lambda}^i(r|\alpha)]^{z_{\sigma\lambda}},\\ U_{\sigma\lambda}^{ij}(\alpha) &= K_{\sigma\lambda}^{ij}(\alpha)\theta_{\sigma\lambda}^{ij}(1)\exp[-\beta\varepsilon_{\sigma\lambda}^{ij}(1)]S_{\sigma\lambda}^i(1|\alpha)S_{\lambda\sigma}^j(1|\alpha),\\ &\quad \times [S_{\sigma\sigma}^i(2|\alpha)S_{\lambda\lambda}^i(2|\alpha)S_{\sigma\lambda\lambda}^{ij}(\alpha)S_{\lambda\sigma\sigma}^{ji}(\alpha)]^2.\end{aligned} \tag{51}$$

In the formula (51) the functions $S_{\sigma\lambda}^i(r|\alpha)$ and $S_{\sigma\lambda\lambda}^{ij}(\alpha)$ have the form of Eqs. (34a) and (36a) in which the site numbers have been replaced with the indices of the site types. As previously, the type of a pair of sites is unambiguously related to the distance between them.

The number of equations for two-body probabilities is also sharply reduced. For the first neighbors, four equations relative to $\theta_{\delta\gamma}^{ij}(1)$ are needed, $ij = \mathrm{AA}$, AB, BA, and BB, while for the second neighbors three equations relative to $\theta_{\delta\delta}^{ij}(2)$ are needed, $ij = \mathrm{AA}$, AB, and BB. The normalizing relations have the form

$$\sum_{j=\mathrm{A}}^{\mathrm{V}} \theta_{\sigma\lambda}^{ij}(r) = \theta_\sigma^i, \quad \sum_{i=\mathrm{A}}^{\mathrm{V}} \theta_{\lambda\sigma}^{ji}(r) = \theta_\lambda^j, \quad \sum_{j=\mathrm{A}}^{\mathrm{V}} \theta_\sigma^i = 1. \tag{52}$$

Lam Research Ex. 1035 - Page 392
Lam Research Corp. v. Inpria Corp.
IPR2024-00033 - U.S. Patent No. 9,823,564

The kinetic equations for the functions $\theta^{ij}_{\sigma\lambda}(r)$ are similar to the system (27) in which the site numbers have been replaced with the indices of the site types; the number h has been replaced by γ if h is the nearest site to a type δ site, and by δ if h is the nearest site to a type γ site.

If for the square lattice it is introduced the notation

$$W^{(ij)k}_{\delta\gamma\delta}(1|\alpha) = U^{(ij)k}_{\delta\gamma\delta}(\omega_1 = 1|\alpha) + 2U^{(ij)k}_{\delta\gamma\delta}(\omega_1 = 2|\alpha),$$
$$W^{(ij)k}_{\sigma\sigma\lambda}(2|\alpha) = 2[U^{(ij)k}_{\sigma\sigma\lambda}(\omega_2 = 1|\alpha) + U^{(ij)k}_{\sigma\sigma\lambda}(\omega_2 = 2|\alpha)], \tag{53}$$

where $\omega_1 = 1$ corresponds to a linear arrangement of the sites, when $\omega_1 = 2$ the lines joining the sites form a right angle, while when $\omega_2 = 1$ and they form an obtuse and acute angles, Eqs. (48) and (49), e.g., will be rewritten as follows:

$$\begin{aligned}
\dot\theta^{\mathrm{AB}}_{\delta\gamma}(1) = {} & U^{(\mathrm{V})\mathrm{B}}_{\delta\gamma}(1|1) - U^{(\mathrm{A})\mathrm{B}}_{\delta\gamma}(1|1) - U^{\mathrm{A}(\mathrm{B})}_{\delta\gamma}(1|4) - U^{\mathrm{AB}}_{\delta\gamma}(3) - [W^{(\mathrm{BA})\mathrm{B}}_{\gamma\delta\gamma}(1|3) \\
& + W^{(\mathrm{VA})\mathrm{B}}_{\gamma\delta\gamma}(1|5) - W^{(\mathrm{AV})\mathrm{B}}_{\gamma\delta\gamma}(1|5)] - W^{\mathrm{A}(\mathrm{BB})}_{\delta\gamma\delta}(1|2) + W^{\mathrm{A}(\mathrm{VV})}_{\delta\gamma\delta}(1|2) \\
& - W^{\mathrm{A}(\mathrm{BA})}_{\delta\gamma\delta}(1|3) - W^{\mathrm{A}(\mathrm{BV})}_{\delta\gamma\delta}(1|5) + W^{\mathrm{A}(\mathrm{VB})}_{\delta\gamma\delta}(1|5) \\
\dot\theta^{\mathrm{AB}}_{\sigma\sigma}(2) = {} & U^{(\mathrm{V})\mathrm{B}}_{\sigma\sigma}(2|1) - U^{(\mathrm{A})\mathrm{B}}_{\sigma\sigma}(2|1) - U^{\mathrm{A}(\mathrm{B})}_{\sigma\sigma}(2|4) - [W^{(\mathrm{BA})\mathrm{B}}_{\lambda\sigma\sigma}(2|3) + W^{(\mathrm{VA})\mathrm{B}}_{\lambda\sigma\sigma}(2|5) \\
& - W^{(\mathrm{AV})\mathrm{B}}_{\lambda\sigma\sigma}(2|5) - W^{A(VV)}_{\sigma\sigma\lambda}(2|2) + W^{A(BB)}_{\sigma\sigma\lambda}(2|2) - W^{A(BA)}_{\sigma\sigma\lambda}(2|3) \\
& - W^{A(VB)}_{\sigma\sigma\lambda}(2|5) + W^{A(BV)}_{\sigma\sigma\lambda}(2|5)].
\end{aligned} \tag{54}$$

The addends of equations of type (54) are expressed in terms of the rates of elementary processes (51) by formulas similar to (39) and (40). The system of equations is solved with the given initial conditions for $\theta^{i}_{\sigma}(\tau = 0)$, $\theta^{ij}_{\delta\gamma}(1, \tau = 0)$ and $\theta^{ij}_{\sigma\sigma}(2, \tau = 0)$.

When going over to a model without ordering of the particles, a state of the system is described by variables θ_i, $\theta_{ij}(r)$ and the system (50) is simplified: singling out of sites δ and γ is absent, and the migration contributions between different sublattices are compensated. The system of equations acquires the form

$$\dot\theta_{\mathrm{A}} = U_{\mathrm{V}}(1) - U_{\mathrm{A}}(1) - z(1)U_{\mathrm{AB}}(3),$$
$$\dot\theta_{\mathrm{B}} = -U_{\mathrm{B}}(4) + z(1)[U_{\mathrm{VV}}(2) - U_{\mathrm{BB}}(2) - U_{\mathrm{AB}}(3)]. \tag{55}$$

The probabilities of two-body configurations are determined by solving the kinetic equations relative to $\theta_{ij}(r)$, where $ij = \mathrm{AA}$, AB, or BB, and $r = 1$

Lam Research Ex. 1035 - Page 393
Lam Research Corp. v. Inpria Corp.
IPR2024-00033 - U.S. Patent No. 9,823,564

and 2. As previously, let us consider the equations for $\theta_{AB}(r)$:

$$\begin{aligned}\dot{\theta}_{AB}(1) = {} & U_{(V)B}(1|1) - U_{(A)B}(1|1) - U_{AB}(3) - U_{(A)B}(1|4) + W_{A(VV)}(1|2) \\ & - W_{A(BB)}(1|2) - W_{(BA)B}(1|3) - W_{A(BA)}(1|3) - W_{(VA)B}(1|5) \\ & + W_{(AV)B}(1|5) - W_{A(BV)}(1|5) + W_{A(VA)}(1|5), \\ \dot{\theta}_{AB}(2) = {} & U_{(V)B}(2|1) - U_{(A)B}(2|1) - U_{(A)B}(2|4) + W_{A(VV)}(2|2) \\ & - W_{A(BB)}(2|2) - W_{(BA)B}(2|3) - W_{A(BA)}(2|3) - W_{(VA)B}(2|5) \\ & + W_{(BV)B}(2|5) - W_{A(BV)}(2|5) - W_{A(VB)}(2|5), \end{aligned} \tag{56}$$

where the addends on the right-hand sides are determined by formulas of the previous subsection in which the subscripts of the site numbers or types have been omitted. The system of equations being considered is solved with the given initial conditions $\theta_i(\tau = 0)$, $\theta_{ij}(1,\tau = 0)$, and $\theta_{ij}(2,\tau = 0)$.

3.8.2. *Rapid Mobility of Reactants*

The kinetic system of equations for the concentrations of adsorbed particles coincides with system (50) for ordering of the particles and with system (55) for their disordered distribution. Here the functions $\theta_{ij}(r)$ are determined for the given values θ_i from the solution of algebraic systems that are described in Appendix A. The kinetic equations are solved with given initial conditions $\theta_i(\tau = 0)$, $i = A$ or B.

3.9. Different Mobilities of Reactants

The equations constructed above in the general case hold for any mobilities of the reactants. *A priori* information on great differences in the mobilities of reactants makes it possible to lower the dimension of the system of kinetic equations. Let us consider the case when the stage of migration of one of the components, e.g. A, is rapid, while the other stage have commensurable characteristic times. In the kinetic Eqs. (46), (48) and (49) for $\theta_{fg}^{Ai(r)}$, where $i = A$ or B, and $r = 1$ or 2, the main contribution is made by the addends corresponding to the migration of the A particles, while the remaining addends can be disregarded. As a result, the following four algebraic equations are obtained for the indicated two-body functions ($r = 1$ and 2):

$$\begin{aligned}\theta_{fg}^{VA}(r)\theta_{fg}^{AB}(r) &= \theta_{fg}^{AA}(r)\theta_{fg}^{VB}(r)\exp\{\beta[\varepsilon_{fg}^{VA}(r) + \varepsilon_{fg}^{AB}(r) - \varepsilon_{fg}^{AA}(r) - \varepsilon_{fg}^{VB}(r)]\}, \\ \theta_{fg}^{VV}(r)\theta_{fg}^{AA}(r) &= \theta_{fg}^{AV}(r)\theta_{fg}^{VA}(r)\exp\{\beta[\varepsilon_{fg}^{VV}(r) + \varepsilon_{fg}^{AA}(r) - \varepsilon_{fg}^{AV}(r) - \varepsilon_{fg}^{VA}(r)]\}, \end{aligned} \tag{57}$$

Lam Research Ex. 1035 - Page 394
Lam Research Corp. v. Inpria Corp.
IPR2024-00033 - U.S. Patent No. 9,823,564

(where all interaction parameters of species A and B with vacancy V equal to zero) that are equations of the equilibrium distribution of the particles in the quasi-chemical approximation (Appendix A), but the functions $\theta_{fg}^{BB}(r)$ do not obey this distribution.

For this reason, the local concentrations of the B components will vary and, consequently, the concentrations of the A and V components will also vary. The indicated change in the structure of the system of equations relates to all the levels of the hierarchy. For instance, in a point model with restricted mobility of the B component, the kinetic equation for the function $\theta_{fg}^{BB}(1)$ will be written as follows:

$$\dot{\theta}_{BB}(1) = U_{VV}(1|2) - U_{BB}(1|2) - 2U_{(B)B}(1|4) - 2[W_{(AB)B}(1|3) + W_{(BB)B}(1|2) - W_{(VV)B}(1|2) + W_{(VB)B}(1|5) - W_{B(VB)}(1|5)]. \quad (58)$$

Here the functions $W_{(ij)k}(l|\alpha)$ have been determined in Eq. (53). The system of kinetic equations in a model with a restricted mobility of the B components is solved at the given initial conditions $\theta_i(\tau = 0)$, $i = A, B$; $\theta_{BB}(r,\tau = 0)$, $r = 1$ and 2.

The system of constructed Eqs. (31)–(32) describes the elementary processes at the atomic-molecular level and is a unified interrelated system of equations for the entire inhomogeneous lattice. Its solution allows to determine the sought θ_f^i and $\theta_{fg}^{ij}(r)$ values and calculate the following characteristics: a change in the occupancy of the surface with adspecies i ($\theta_i = \sum_{f=1}^{N} \theta_f^i / N$), the mean number of the neighboring pairs of adspecies ij and any other function estimated via the local functions θ_f^i and $\theta_{fg}^{ij}(r)$. For homogeneous surfaces the system of kinetic equations has an equivalent for any site, therefore these systems give equations constructed simultaneously for the mean macroscopic values on the assumption that the system has no macroflows. In such situations of principal interest are the characteristics of the local adspecies redistribution during the surface processes (changes in the degree of coverage, of the short- and/or long-range order, a number of islands, average characteristics of their perimeter and shape, etc.). In the following sections various application areas that can be investigated by the constructed kinetic systems are described.

4. Surface Processes

This section describes solid–gas surface processes on the surface monolayer: adsorption, desorption, catalytic reaction, and surface diffusion. Non-ideal behavior of the systems is considered through the pair potentials of intermolecular interactions. A wide circle of experimental data can be

Lam Research Ex. 1035 - Page 395
Lam Research Corp. v. Inpria Corp.
IPR2024-00033 - U.S. Patent No. 9,823,564

described on taking into account the lateral interaction between adspecies. An influence the aggregated states of adspecies with forming condensed and ordering phases on surface rates are considered.

4.1. Physical Adsorption and Chemisorption

The nature of the adsorption bond depends on the nature of the solid and the gas-phase molecules. It is customary practice to distinguish physical and chemical adsorption. In the former case, no collectivization of the electrons of the adsorbent and adsorbate occurs, while in the latter case a conventional chemical bond forms with redistribution of the electrons.

At the atomic level, the surface of a monatomic crystal is not homogeneous. It is a distributed system of atoms. The different positions of an adsorbed molecule over the adsorbent atoms are not equivalent energetically. The change in the binding energy when a molecule travels along a surface is shown schematically in Fig. 8.5. In a number of positions, its energy is minimal. Such positions and their environment form regions of localization of adsorbed molecules called adsorption centers of the surface. If the difference E_1–E_2 is large and is much larger than the thermal energy of the adsorbed particles, the latter are predominately in the localization regions, and one has to do with localized adsorption. It generally occurs in chemical adsorption.

If the values of the energies E_1 and E_2 are close and have the order of magnitude of the thermal energy of the adsorbed particles, one has to do with non-localized adsorption. It occurs most frequently in physical adsorption. Here too lowering of the temperature may be attended by a

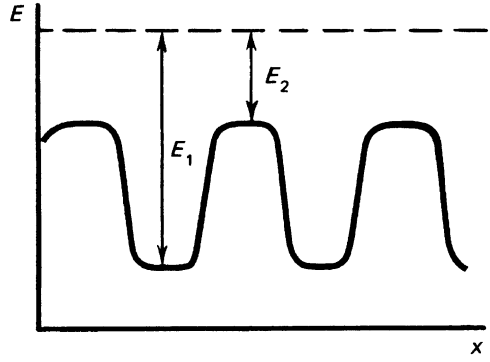


Fig. 8.5. Potential relief of a homogeneous surface. The dashed line depicts the energy of a free particle in a gas; E_1 activation energy of desorption; E_1–E_2 is the activation energy of surface migration.

Lam Research Ex. 1035 - Page 396
Lam Research Corp. v. Inpria Corp.
IPR2024-00033 - U.S. Patent No. 9,823,564

transition from non-localized to localized adsorption (with disregarding of the tunneling effects possible for light particles). The nature of adsorption also depends on the state of the adsorbed particle. With a slow exchange of energy between a particle and the atoms of a solid, the particle may be in excited states [104], which increase the degree of its delocalization.

Most solids have regions of localization of adsorbed particles with different binding energies on their surface. This is due to the different local chemical composition of the surface and a different geometric arrangement of the solid's atoms. Both these factors usually manifest themselves simultaneously. Such surfaces are said to be inhomogeneous. The scale of the inhomogeneities varies within broad limits from point imperfections and impurities to various macroregions [2,38,39].

A type of the adsorption is connected with a type of the phase transition in which adspecies could be involved. The adspecies condensation (the first type of the phase transition) as usually occurs at the physical adsorption, while the adspecies ordering (the second type of the phase transition) occurs at the chemical adsorption. However, more complex phase transitions (ordering with condensation) are quite often realized at the chemical adsorption.

In the condensed phase the AC "permanently" interacts with its neighbors, therefore a change in the local phase composition (as were demonstrated on Figs. 8.1 and 8.2) affects the activation barrier level (Fig. 8.6). Historically the first model used for surface processes is the analogy of the collision model (CM) [23,48,57]. This model uses the molecular-kinetic gas theory [54]. It will be necessary to count the number of the active collisions between the reagents on the assumption that the molecules represent solid spheres with no interaction potential between them. Then the rate constant can be written down as follows (instead of Eq. (6)):

$$K_{AB} = K^0_{AB} \exp(-\beta E_{AB}), K^0_{AB} = P_0 d^2_{AB} \{8\pi(m_A + m_B)/(\beta m_A m_B)\}^{1/2}. \quad (59)$$

In the Eq. (59) P_0 is the steric factor; E_{AB} is the rate activation energy; K^0_{AB} is the frequency cofactor or the preexponential rate constant factor; $d = R_A + R_B$; here R_i and m_i are the radius of the sphere and mass of species i, respectively; $i = A, B$.

In the case of the surface processes it should be taken into account that one of the reagents is represented by the lattice site, therefore for the adsorption rate (U_V (i)) and for the desorption rate (U_i) of molecules i Eq. (59) can be expressed as follows:

$$U_V(i) = s_i P_i/(2\pi m_i \beta^{-1})^{1/2}, s_i = \theta_V \exp[-\beta E_V(i)], \theta_V = 1 - \sum_{i=1}^{s-1} \theta_i$$

$$U_i = v_i \theta_i \exp(-\beta E_i), \quad (60)$$

Lam Research Ex. 1035 - Page 397
Lam Research Corp. v. Inpria Corp.
IPR2024-00033 - U.S. Patent No. 9,823,564

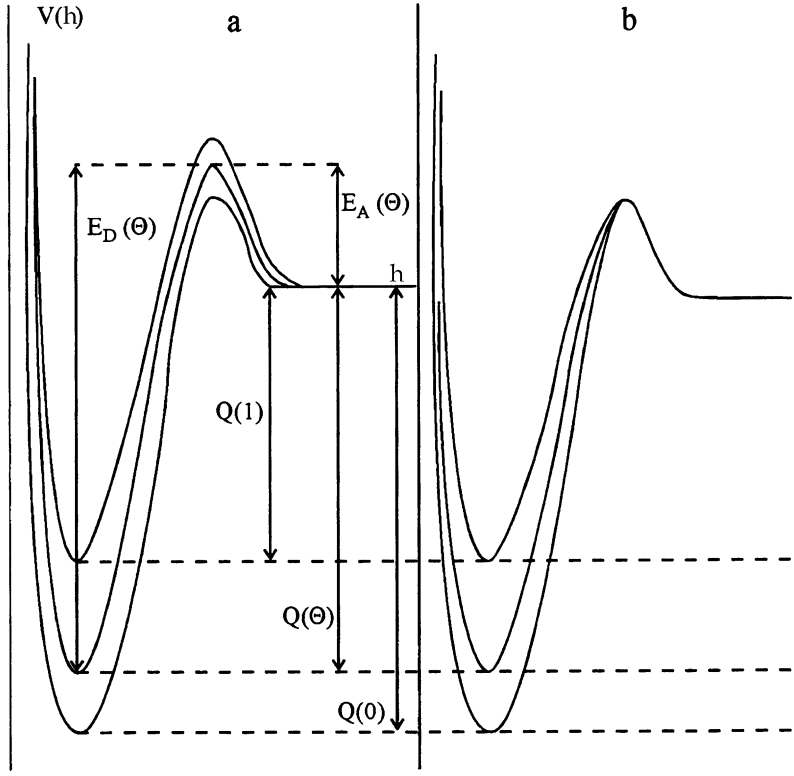


Fig. 8.6. Potential curves of V vs. h in the transitive state model (a) and the collision model (b), where E_A and E_D are the adsorption and desorption activation energies, respectively; Q is the heat of adsorption, h the distance from the surface (horizontal axis of the figure).

where s_i is the sticking coefficient; P_i the partial pressure of molecules i in the gaseous phase; $\theta_V = \theta_s$ the fraction of the empty surface; E_i the activation energy of adspecies i desorption, and for the desorption rate the frequency factor represents a frequency of the adspecies oscillations (ν_i).

A similar interpretation holds for the preexponential factor of the rate constants for the dissociative adsorption, desorption, reaction between the adspecies and their migration. The CM is distinguished by the fact that the preexponential factor is dependent on the properties of the starting reagents only and is independent of the transition state whereas the rate constant depends on the activation barrier height, which is governed by the transition state energy.

For the first time, the collision model including the lateral interaction between adspecies was used by Roberts [105] for adsorption–desorption

Lam Research Ex. 1035 - Page 398
Lam Research Corp. v. Inpria Corp.
IPR2024-00033 - U.S. Patent No. 9,823,564

stages, and then by Toya [106] for explaining the splitting of the thermodesorption spectra (TDS).

The assumption that there is no AC interaction with its neighbors serves the same purpose. Shown in Fig. 8.6 is a difference between the effective adsorption curves in the CM and TSM for the various coverages in the non-ideal system. These curves represent the averaged magnitudes of the similar potential curves belonging to the specific local surroundings of the adspecies (see Figs. 8.1 and 8.2) that participate in the elementary process. From the viewpoint of considering the adspecies interactions in the non-ideal reaction systems, the condition $\varepsilon^* = 0$ is similar to the use of the CM term, irrespective of an elementary process model in the ideal system. Therefore all the models with no AC-neighboring adspecies interactions should be assumed as belonging to the collision-type model. For non-ideal reaction systems, the condition $\varepsilon^* = 0$ is in contradiction with a concept about the transitive state model as the "intermediate" position of the AC between the initial and final reagents. Any quantum chemical calculation of reaction potential reliefs demonstrates correctness of this point of view.

4.2. Adsorption and Thermodesorption Spectra

The stage of adsorption is the simplest elementary process among the other surface processes. It can be both a main process in adsorption and one of the stages of complex interface process. At least one of the adsorption or desorption stage is always presented in any surface process. In the theory of desorption process, the AC was introduced independently for the mono- and bimolecular desorption processes by different authors [107,108] in 1974. In both papers the quasi-chemical approximation has been used. However, actual computations [107] have been performed at $\varepsilon^* = 0$ (the collision model). They have shown that TDS slitting is caused even by a slight repulsion: $|\varepsilon^*| < 0.05 E_{\mathrm{des}}$. The expressions obtained for the desorption rates have been applied to TDS computations for H_2/W(100), CO/W(210), and N_2/W(100) [109,110].

The results of other work [108], concerning the adsorption kinetics processes as well as the desorption process, were published later [111–113]. General expressions for the adsorption and desorption rates, relating to non-dissociating molecules and based on the totality of the neighboring adspecies configurations $\theta_i(n)$ (see Fig. 8.1), have been derived. Depending on how carefully the effects of the correlations between the interacting adspecies are taken into account, different final expressions for the adsorption rates have been obtained. This has made it possible to clarify

Lam Research Ex. 1035 - Page 399
Lam Research Corp. v. Inpria Corp.
IPR2024-00033 - U.S. Patent No. 9,823,564

the effect of the correlations on the rates of all the elementary processes (see also Ref. [114]).

Thus, considering the lateral interactions, it has been possible to explain the empirical Becker–Langmuir dependences [115,116] for the desorption rate ($\ln U_{des} = c_1\theta + c_2$; c_1 and c_2 are "const") and Zeldovich–Roginsky's expressions [117,118] for the adsorption rate ($\ln U_{ad} = c_3\theta + c_4$; c_3, c_4 – const). If $z\beta\delta\varepsilon >> 1$, the region of medium and great coverages with the CA and QCA methods show the presence of power dependences for the desorption rates ($U_{des} \sim \theta^{z+1}$) to provide support for the Bangham–Burt–K-wan expression [119,120]. Varying the adspecies interaction parameters indicates that in systems with a strong adspecies repulsion and at low temperatures ($\beta|\varepsilon| >> 1$) the lateral interactions act as a natural proof of the experimentally known processes of a "fast" and a "slow" chemisorption [121] and the possibility for a unified mechanism of the process to exist despite the presence of a few linear portions on the concentration plots for the process rate logarithms. The latter fact is often regarded as indicating a change in the process mechanism at different surface coverages [121]. Also, an increase in the sticking probability of adsorbed particles with a growth in the coverage at low coverages of a surface can be explained [80,89].

In works [108,111–114] in addition to the lateral interactions, the contributions of the electronic subsystem to the surface electronic gas models have taken into account. For the first time, a quantitative description of the kinetics of the desorption of atoms from the surface of tungsten [122,123] was given by considering both the direct interactions between nearest neighbors and the collective interaction with all the remaining adsorbed molecules. The rates of desorption (Fig. 8.7) obtained from the experimental TDS curves were estimated for 840 K and compared with calculations done using three approximations. That comparison shows [111] that the approximations, after taking account of the effects of correlations (the polynomial approximation in which correlations between interacting adspecies also are presented [80,89]), lead to considerably better agreement with the experimental data than the chaotic approximation that ignoring the correlations.

Some important data concerning the role played by the effects of the correlation and AC interaction with the neighbors on the TDS appearance have been obtained in other work [114]. TDS splitting is due to the correlation effects of the interacting adspecies, therefore the splitting is absent if the mean field approximation (MFA) is used. For the TDS to split, the correlation effects should be supplemented with a sufficient difference between ε^* and ε since no splitting occurs at small differences (as in Ref. [107]). The magnitude of the parameter ε^* is as important as that of ε. The TDS for CO/W(210), CO/Mo(100), Cs/W and CO on a number of metals have been described qualitatively [124,125].

Lam Research Ex. 1035 - Page 400
Lam Research Corp. v. Inpria Corp.
IPR2024-00033 - U.S. Patent No. 9,823,564

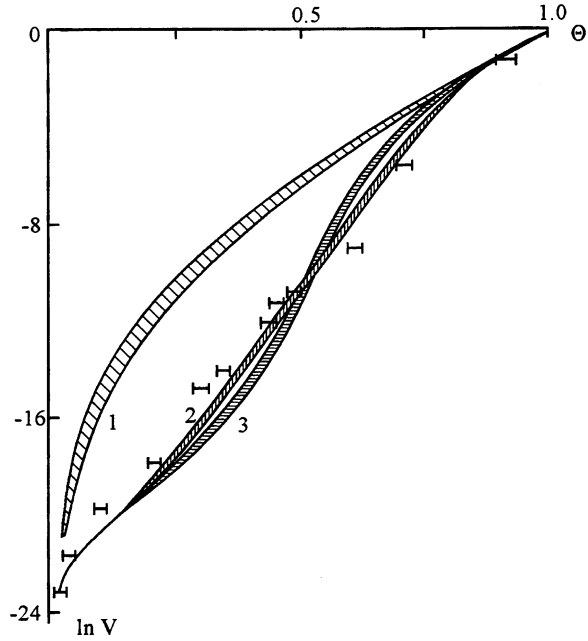


Fig. 8.7. The desorption rates K/W for T = 840 K, calculated for the chaotic (1), polynomial (2), and quasi-chemical (3) approximations [111], where $V = U_{des}(\theta)/U_{des}(\theta = 1)$; symbols denote experimental values of the desorption rates with their errors [122,123].

The importance of considering the correlation effects is a principal for the adsorption and desorption rates in the case of dissociating molecules [126]. If the correlation effects are absent this violates the self-consistent describing of the system's kinetic and equilibrium characteristics.

A question about taking into account the correlation effects is more difficult for heterogeneous surfaces [80,127]. Real adsorbent surfaces are characterized by a large variety of compositions and structures, which depend on the preparation of these materials. Even between nearest neighbors, this involves a complex analysis of the whole adsorption system. The state of occupancy of any lattice site (denoted as "f") depends on the type of the site, as well as on the occupancy of its nearest neighbors, which depend in turn on the type and state of occupancy of the more distant neighbors h, including also the lattice site f, from which the consideration began. As a result, the probability of localization of a molecule on a particular site depends not only on the type of this site, but also on the types of the vicinal sites. Then, depending on the required accuracy of the evaluation of the effect of the distribution of vicinal sites upon the local filling at each lattice site, different approaches to the description of

Lam Research Ex. 1035 - Page 401
Lam Research Corp. v. Inpria Corp.
IPR2024-00033 - U.S. Patent No. 9,823,564

the equilibrium distribution of the particles and the kinetics of adsorption will be required. On a homogeneous surface, the distribution of the adparticles depends on the structure of the surface and the potential of intermolecular interaction. On heterogeneous surfaces an additional effect is observed that is connected with different adsorption and kinetic features for different lattice sites as well as their spatial distribution on the surface. Changing the spatial character of the distribution of different lattice sites (at a fixed number), yields surfaces differing in their adsorption and kinetic characteristics.

The kinetic theory of interface processes, including the adsorption one, on heterogeneous surfaces was constructed in Refs. [80,85,89]. An example of an application of the theory taking into account both lateral interactions and surface heterogeneity is the TDS for H_2 on Ir(110)-2 × 1 described in Refs. [127,128]. The elementary lattice consists of three sites (Fig. 8.8): one "strong" (site of the first type) and two "weak" (sites of the second and third types). The sites of the third type are separated only formally for an easier presentation of the distribution function – the molecular characteristics of these sites are the same as those of the sites of second type.

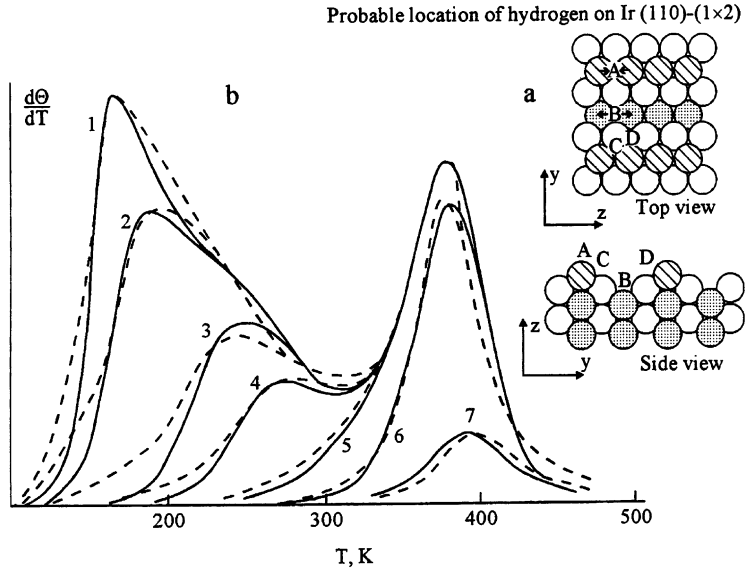


Fig. 8.8. (a) Probable locations of the hydrogen on Ir(110)-2 × 1. Part (b) shows the TDS curves for H_2 on Ir(110)-2 × 1, calculated for various initial coverages. Broken lines – experiment [129] with $\theta_0 = 0.99$ (curve 1), 0.86 (2), 0.61 (3), 0.48 (4), 0.37 (5), 0.27 (6), 0.068 (7). It was assumed that adsorption occurs at position B (sites with strong adsorption bonding) and C (sites with weak bonding).

Lam Research Ex. 1035 - Page 402
Lam Research Corp. v. Inpria Corp.
IPR2024-00033 - U.S. Patent No. 9,823,564

The lateral interactions considered are limited to three coordination shells $R = 3$. All parameters related to lateral interactions for the third coordination shell are assumed to be zero except $\varepsilon_{11}(3)$ and $\varepsilon^*_{11}(3)$. The curves presented in Fig. 8.8 show reasonable agreement. This model describes all the peculiarities of the experimental TDC: splittings of the peaks, correlations between the intensities and the areas under the low and high temperature maxima, the nature of the peak shifts along the temperature axis due to increases of the initial coverage, the broadening of the low temperature maxima, etc. The features related to the splittings of the peaks are determined by the heterogeneity of the Ir(110)-2 × 1 edge and the features of the self-peak are determined by the lateral interactions. Among these features one should emphasize a typical broadening of the low temperature peak as well as the fact that the position of the low temperature maximum is shifted to lower temperature (second-order desorption) whereas the position of the maximum of the high temperature peak does not change (first-order desorption).

This suggests the existence of strong repulsions between adsorbed atoms localized on ''weak'' sites and a strong attraction between atoms on ''strong'' sites. Because the ''strong'' sites are isolated, the attraction between adsorbed atoms localized on these sites involves only the third coordination shell. It should be noted that the authors reporting the experimental TDS [129] have commented upon these curiosities of peak evolution and have drawn some conclusions about the lateral interactions. However, they have not arrived at any quantitative estimates.

4.3. Multistage Processes

For occurring the chemical reaction more then one component should be presented in the reaction volume. So, for describing multistage chemical process the theory should describe the multicomponent mixtures. A theory of the absolute rates of reactions on homogeneous surfaces for multicomponent system has been developed in Ref. [130]. General expressions for the rates of elementary processes occurring on one site and two neighboring sites together with the associated expressions in the approximations have been obtained. This has made it possible to ''reproduce'' all the previously known models as well as to illustrate their interrelations and differences. Problems concerning the self-consistent description of the forward and reverse reaction rates for each stage and the reaction system equilibrium have been considered (see below Subsection 3.5). At the first time, the self-consistent properties for the lattice-gas model have been proved [130]. Later similar results for pair potential with any radius of interactions and on

Lam Research Ex. 1035 - Page 403
Lam Research Corp. v. Inpria Corp.
IPR2024-00033 - U.S. Patent No. 9,823,564

heterogeneous surfaces have been extended [89]. Lateral interactions affect the magnitude of each elementary reaction rate. This manifests itself through the functions S_{ij} ($S_{ij} = 1$, if $\delta\varepsilon_{ij} = 0$) in Eqs. (16a) and (21), and change in the probability of the reagents encounter θ_{ij} (21) ($\theta_{ij} \neq \theta_i\theta_j$) for a bimolecular reaction to occur. Changes of the rate in a non-ideal adsorption system as compared with that in an ideal one show up in the dynamic dependences of $\theta_i(\tau)$, where τ denotes the time.

It is natural that non-ideality of the adsorption system produces a strong effect on the way the multistage process occurs, viz., on its intermediate regimes and the number of stationary states, existence of self-oscillations, etc. (The dynamic modes are also characterized in Ref. [131].)

The simplest example of how the adsorption system non-ideality affects the number of its elementary stages has been discussed in Ref. [132] (see also Ref. [89]). The stages ($\alpha = 1$) $A + Z \leftrightarrow ZA$, and ($\alpha = 2$) $B + ZA \rightarrow Z + C$, in the absence of interaction involves one stationary state. The kinetic equation describing time variations of the surface coverage with the adspecies A is written down as follows:

$$d\theta_A/d\tau = P(q) = U_{ad} - U_r;\ U_r = K^*_{AB}(2)\theta_A[S_A(2)]^z, \tag{61}$$

$$U_{ad} = K^*_V(1)(1 - \theta_A)[S_V(1)]^z - K_A(1)\theta_A[S_A(1)]^z.$$

The summands of Eq. (61) correspond to the elementary stages of adsorption, desorption, and the reaction, respectively. The rate constants and the functions $S_i(\alpha)$ contain an additional index α which denotes stage number. This allows to distinguish between the elementary processes where adspecies i can be involved. Thus adspecies A is capable of being desorbed or reacting with molecule B, and the properties of the AC resulting from these elementary processes will be different ($F^*_A(\alpha = 1) \neq F^*_A(\alpha = 2)$ and $\varepsilon^*_{AA}(\alpha = 1) \neq \varepsilon^*_{AA}(\alpha = 2)$). Thus, considering the non-ideality increases the number of the stationary states as compared with that for the ideal systems. Note that addition of the third linear stage that involves another adspecies makes it necessary to examine the self-oscillation process (*cf.* a similar situation reported by Bykov and Yablonsky [133]). The study conducted [132] has revealed that the multiplicity of the stationary states, associated with the non-monotonous dependence of the rates of the first or the second stages on coverage is observed for the parameters $|\beta\varepsilon_{AA}| < 3 \div 5$. The relationship $|\varepsilon^*_{AA}(\alpha = 2)| > |\varepsilon_{AA}|$ for the negative parameters suggests the presence of steric hindrances during AC formation.

The relationship $|\varepsilon^*_{AA}(\alpha = 2)| < |\varepsilon_{AA}|$ implies that the interaction of the AC with the adspecies is weaker than that of one adspecies with another. This fact is readily attributed to the AC being moved away from the surface and matches the real situation. A similar relationship for the first stage

Lam Research Ex. 1035 - Page 404
Lam Research Corp. v. Inpria Corp.
IPR2024-00033 - U.S. Patent No. 9,823,564

corresponds to the non-monotonous dependence of the adsorption rate on coverage. The attraction of the adspecies promotes the acceleration of adsorption to the point when the reduction of the number of empty sites with coverages becomes a predominant factor. Experimentally the adsorption rate was observed to increase with coverage at small θ, followed by its drop during the adsorption of the N molecules and the Ar atoms on tungsten [134], as well as the adsorption of the CO and O molecules on Pt(111) [135]. In systems in which adspecies are attracted at temperatures below the critical ones the first-order phase transition is possible, again with an increase in the number of the stationary states.

Out of all catalytic processes the lattice-gas model has been most often used for describing CO oxidation on platinum metals. Actually, this reaction is the one that serves to develop various theoretical approaches. The simplest model is based on the idea of a homogeneous surface of a metal face that undergoes no rearrangement during the catalytic process. The kinetic equations of the three-stage mechanism have the form [136]:

$$\dot{\theta}_1 = U_3(1) - U_1(1) - zU_{12}(3), \dot{\theta}_2 = z[U_{33}(2) - U_{22}(2) - U_{12}(3)], \qquad (62)$$

where the indices $i = 1$, 2, and 3 stand for ZCO, ZO, and Z, respectively; $\alpha = 1$, 2, and 3 correspond to the adsorption–desorption stage of CO molecules, the adsorption–desorption stage of O_2 molecules, and reaction between ZCO and ZO, respectively.

The rates of elementary stages are expressed as

$$U_3(1) = K_3^*(1)\theta_3[S_3(1)]^z; \quad U_1(1) = K_1(1)\theta_1[S_1(1)]^z; \qquad (62a)$$

$$U_{ij}(\alpha) = K_{ij}^*(\alpha)\exp(-\beta\varepsilon_{ij})[S_i(\alpha)S_j(\alpha)]^{2(z-1)}, \alpha = 2 \text{ and } 3. \qquad (62b)$$

For the first time the reaction of CO oxidation was considered in Refs. [137,138]. However, the equations for two-site processes differ from corrected Eq. (62b) due to using in these works a different definition for the bimolecular reaction activation energy: the term with ε_{ij} was absent in the reaction activation energy. Actually calculations were performed with simplified assumption about $\varepsilon_{ij}^* = 0$ (the collision model). The theoretical curves have given a qualitative agreement with experiment data.

A complete model for the stationary CO oxidation on platinum according to Eq. (62) with the use of the QCA and TSM has been discussed in Ref. [136]. Its parameters were determined independently from the TDS of CO and O_2 on the Pt(111) face [135]. The experimental evidence [139] for the stationary CO oxidation on a polycrystalline sample with a predominant orientation of the (111) faces ($\geq 90\%$) are described adequately. The numerical analysis of the model indicates that the parameters $\varepsilon_{ij}^* = (3)$ produce a strong effect on the activation barrier height and cannot be

Lam Research Ex. 1035 - Page 405
Lam Research Corp. v. Inpria Corp.
IPR2024-00033 - U.S. Patent No. 9,823,564

regarded as minor perturbations. The model according to Eq. (62) provides a qualitative description of the stationary CO oxidation rate on polycrystalline platinum [140], and at a pressure around 1 Torr it predicts the existence of two peaks on the oxidation rate-temperature plot (instead of the only one at low pressures) as detected experimentally elsewhere [141].

At present, various surface reactions are considered by simply employing the MC method (see Section 7.1). However, a question about self-consistent description of the proposed schemes for reaction mechanism as rules still is open.

4.4. Islands and Two-Dimensional Phases

The above surface process models are based on the assumption of a uniform distribution of the adspecies over surface. As the temperatures of the systems lower, the interactions between the adspecies are capable of leading to the disturbance of this condition. Their attraction is likely to result in adlayer separation to yield a rarefied and a dense phase whereas the repulsion may promote an ordering process. In the former case the initially homogeneous phase converts to a heterogeneous one. Each of these phases occupies a macroscopic region of the surface while retaining its homogeneity within each phase. In the latter case the distribution of the adspecies becomes locally non-uniform so that the occupations of the nearest sites differ greatly. Now one is going to consider the effect of adspecies separation on the surface process kinetics.

Forming the two-dimensional phases means that surface migration of all adspecies is significantly faster than the elementary processes of adsorption–desorption or catalytic reactions. Calculation of the coexisting phases can be performed by using the equalities for the chemical adspecies potentials in the different phases and the expansion pressures in the two phases [142]. In another way, computations of coverages for the coexisting phases can be performed by using the Maxwell rule [17]. As a result, the entire region is broken into three portions: $0 \le \theta \le \theta_{1c}$, $\theta_{1c} \le \theta \le \theta_{2c}$, $\theta_{2c} \le \theta \le 1.0$. In the first and the third portions the elementary process rates are expressed through usual equations for one-phase system and in the second portion such rates relating to the surface as a whole – through the rates of the individual phases and a fraction of the surface occupied by the dense phase (σ) which is related to the total coverage θ via the lever rule $\sigma = (\theta - \theta_{1c})/(\theta_{2c} - \theta_{1c})$, i.e., $U_i(\theta) = \sigma U_{i}\,\theta_{2c}) + (1-\sigma) U_i(\theta_{1c})$.

This problem seems to be treated by Benziger and Schoofs for the first time within the frameworks of the lattice-gas model in 1984 [143]. The main difference between the works advocating the separation process and those

Lam Research Ex. 1035 - Page 406
Lam Research Corp. v. Inpria Corp.
IPR2024-00033 - U.S. Patent No. 9,823,564

[144,145], where the attraction of these adspecies is taken into account, lies in the fact that the former additionally consider the regions where the rarefied and the dense phases exist. To do so [143], the conditions based on the equalities of the chemical adspecies potentials in the different phases and the expansion pressures in the two phases have been adopted [142].

In studies of HCOOH decomposition: (1) $HCOOH + 2Z \rightarrow ZHCOO + ZH$, (2) $ZHCOO + Z \rightarrow ZH + ZCO$, (3) $2ZH \leftrightarrow 2Z + H$, and (4) $ZCO \rightarrow Z + CO$, in steady-state conditions on a Ni surface Benziger and Schoofs [143] have revealed that the process rate is likely to depend on the pressure of formic acid and CO and slightly on that of hydrogen. The lateral interactions have been useful in explaining the non-monotonical dependences observed for the process rate on HCOOH and CO pressure on the assumption that the adspecies separate in the adsorption layer. The attraction between the intermediate adspecies HCOO–HCOO is not strong enough to cause separation but this is also assisted by the CO adspecies. A state diagram for a ternary mixture (ZCO–ZHCOOH-empty sites) at 548 K has been computed and the experimental conditions have been shown to give rise to the first-order phase transition (the ZH adspecies are responsible for a small fraction).

The role of interactions of the AC with its neighbors for two-phase systems has been studied in Ref. [146]. In the case of the physical adsorption, if $\varepsilon^* > \varepsilon$, the inclusion of condensation leads to higher desorption rates as compared with the case when such an inclusion is absent, and the rates always increase with θ in the two-phase region (increasing ε^* enhances the desorption rates). If $\varepsilon^* < \varepsilon$, the inclusion of condensation reduces these rates that otherwise pass through a maximum, and in the two-phase region one can observe a possible decrease in $U_A(\theta)$ with lower ε^*. The effective monoatomic desorption energies fall off (rise) monotonically at $\varepsilon^* > \varepsilon$ ($\varepsilon^* < \varepsilon$).

Multilayer adsorption models have been used by Asada [147,148] to account for the zero-order desorption kinetics. The two layers are equilibrated. Desorption goes from the rarefied phase only. This model has been generalized [148] for an arbitrary number of layers. The filling of the upper layer was studied with allowance for the three neighboring molecules being located in the lower one. The desorption frequency factor (CM) was regarded as being independent of the layer number. The theory has been correlated with experiment for the Xe/CO/W system [149]. Analysis of the two-layer model has been continued in Ref. [150], to see how the ratios of the adspecies flows from the rarefied phases of the first and the second layers vary if the frequency factors for the adspecies of the individual layers differ from one another. In the thermodynamic equilibrium conditions these flows were found to be the same at different ratios of the above factors.

Lam Research Ex. 1035 - Page 407
Lam Research Corp. v. Inpria Corp.
IPR2024-00033 - U.S. Patent No. 9,823,564

4.5. Self-Consistency of the Lattice-Gas Model

The parameters of the models, which include the equilibrium constants, the rate constants of elementary processes, and the interaction potentials, differ when the same experimental data are described by using different approximations. This is why the description of complicated processes requires that all the subsystems be considered with one level of accuracy, i.e., with the employment of the same approximation. For this purpose, it is essential that the physical and chemical fundamentals introduced into a mathematical model correspond to the real conditions within a broad range of variations of the external conditions. Now the parameters of models found from an analysis of individual subsystems can also be used when describing a process as a whole.

The developed theory allows to construct mathematical models that would satisfy different limiting states of a system and the joint influence of real factors with an identical accuracy of their consideration. This point of view in a certain sense is opposite to the traditional situation when a single factor is taken as the basis, and the contributions of all other factors are ignored. To take into account the real properties of surface systems, the competition of the contributions of various factors must be considered.

This necessity also follows from the requirement of the simultaneous description of various experimental characteristics. In recent years, a complex procedure of measuring various characteristics becomes usual. Illustrative in this respect is the studying of the adsorption of nitrogen molecules on the face (110) of nickel [151] – to establish how matters stand as seven different procedures were compared. The use of simplified models for describing individual characteristics does not guarantee the description of other characteristics of a system with their aid. For instance, the adsorption isotherms are often described by the Langmuir isotherm, although the heat of adsorption changes with the coverage.

An importance of the self-consistent description of the equilibrium and kinetic properties demonstrated two examples, which based on explicit taking into account the correlation effects between desorbed species with their changing the phase states.

As shown in previous subsection, the activation energy of desorption coincides with the adsorption heat if there is no lateral interaction of the activated desorption complex and its surrounding, $\varepsilon^* = 0$. This is the model that Jones and Perry invoked [144,145] to describe thermal desorption in the Hg/W(100) system. They were able to reproduce the experimental data, taking $K_0(\theta) \equiv K_0 = \text{const}$, and $E_{ef}(\theta) \equiv Q(\theta)$; the adsorption heat $Q(\theta)$ was calculated with the quasi-chemical approximation for a homogeneous surface. The calculated and experimental spectra were found to be in a

Lam Research Ex. 1035 - Page 408
Lam Research Corp. v. Inpria Corp.
IPR2024-00033 - U.S. Patent No. 9,823,564

satisfactory accordance at the following molecular parameters: $K_0 = 10^{16}$ sec^{-1}, $\varepsilon_{H_gH_g} = 5.85$ kJ/mol, and $E(0) = 172$ kJ/mol. However, the fitted strength $\varepsilon_{H_gH_g}$ of lateral attractions is not enough to be responsible for the two-dimensional condensation from Hg atoms at the observed temperatures, although the same authors experimentally established this fact when measuring the equilibrium isotherms and then supported it by a MC simulation [144].

So, this is an example of such theoretical treatment when thermodynamic and kinetic characteristics are not self-consistent with each other. The theoretical failure above occurred due to the desorption equation used, that does not allow for the real distribution of the Hg atoms, i.e., the macroscopic equation used does not describe the two-dimensional adspecies condensation appearing in the experiment. It should be taken into account that adspecies are in two coexisting phases, so the total desorption rate is a sum of the desorption rates from these phases [146,152].

The coverage of each phase is calculated from the two-dimensional phase diagram at fixed total coverage; and the share of each phase in desorption follows from the rule of a level, imposed onto the two-dimensional phase diagram. Authors obtained an excellent accordance with experimental TDS (Fig. 8.9) for the following molecular parameters: $K_0 = 10^{13}$ sec^{-1}, $E(0) = 136.5$ kJ/mol, $\varepsilon_{H_gH_g} = 10.4$ kJ/mol, and $\varepsilon^*_{H_gH_g}/\varepsilon_{H_gH_g} = 0.55$. The only difference between calculated and experimental results is observed at $\theta_0 \sim 1$, and this is perhaps due to the formation of the second layer of adspecies that was neglected in this calculations. The values of lateral interaction constants found are quite reasonable: the strength of lateral attraction, $\varepsilon_{H_gH_g}$, is sufficiently large to be responsible for the two-dimensional condensation at the experimental temperature range, therefore, the anomalously high K_0, that was obtained before, takes an usual magnitude. Another result is a considerable decrease of the activation desorption energy $E(0)$.

The another example is connected with TDS in system CO/Ru(001) [153]. There were many attempts to describe the experimental data, however, even rather non-physical assumptions could not give acceptable results (see detail in Ref. [128]).

The adsorbed CO molecules are under strong lateral repulsion, in particular, adsorption of these molecules on the Ru(001) face leads to an appearance of the R($\sqrt{3} \times \sqrt{3}$) ordered structures in LEED patterns [153]. This means absence of an uniform occupation of every adsoprtion site by the CO molecules; the CO molecules are accommodated in the different sublattices non-uniformly, and this is the typical case when lateral interactions are responsible for a non-uniform adspecies distribution on a homogenous surface. Splitting of the experimental spectra is a signal of the

Lam Research Ex. 1035 - Page 409
Lam Research Corp. v. Inpria Corp.
IPR2024-00033 - U.S. Patent No. 9,823,564

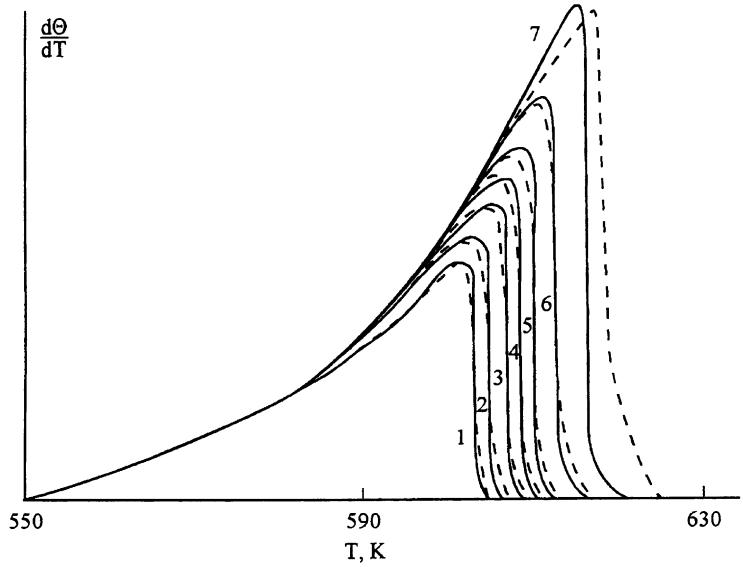


Fig. 8.9. The TDS curves for the system Hg/W(100) coincide with experimental data (broken lines) when calculated with $\theta_0^1 < \theta_0 < \theta_0^2$ (1–6), where $\theta_0^1 \sim 0.45$ and $\theta_0^2 \sim 0.8$ [144], they deviate from the experimental data at $\theta_0 = 0.99$ [152].

$R(\sqrt{3} \times \sqrt{3})$ ordering; therefore, a kinetic molecular model to describe such spectra should be able to predict properly an adspecies ordering.

An account of the adspecies ordering is of the main importance for the model to reproduce the experimental results of the CO/Ru(001) system. Insertion in Fig. 8.10 shows a division of the hexagonal lattices into sublattices to take $R(\sqrt{3} \times \sqrt{3})$ ordering into account. To stress this fact, Fig. 8.10 shows the coverages of different sublattices as a function of the temperature. The saturation coverage is around $\theta_0 = 0.66$; this refers to the case when α-sublattice, θ_α, is filled totally, and γ-sublattice, θ_γ, is empty. As temperature increases, the total coverage θ of the surface decreases, and, at $\theta = 0.5$, one can see the beginning of the low temperature peak and inversion of the sublattices. Below $\theta = 0.5$, energetically more favorable is the configuration when α-sublattice is empty and γ-sublattice is filled. During this inversion, one observes the low temperature peak, and then, the desorption rate quickly drops down; and this is reflected in the TDS splitting. The further rise of the temperature at first increases the probability for the elementary act of desorption, and then destroys the $R(\sqrt{3} \times \sqrt{3})$ ordered configuration. Both factors lead to the second peak in the TDS, and, at the top of this peak, a difference in the coverages of the sublattices

Lam Research Ex. 1035 - Page 410
Lam Research Corp. v. Inpria Corp.
IPR2024-00033 - U.S. Patent No. 9,823,564

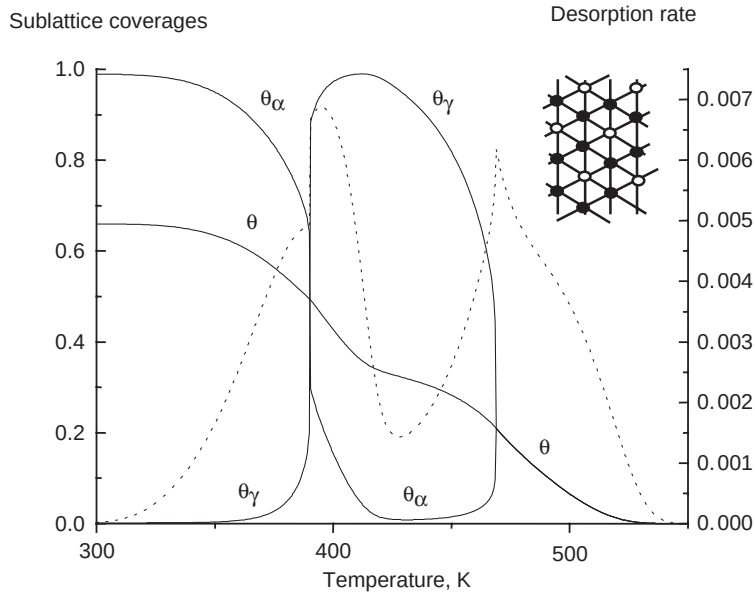


Fig. 8.10. For the CO/Ru(001) system, sublattices coverages as a function of temperature, and relevant spectrum (dots). Insert is a sketch of hexagonal lattice divided in such a way to include R($\sqrt{3} \times \sqrt{3}$) ordering, closed circles – α and open – γ sublattices [128].

vanishes totally, thus, one can see the characteristic flexure in the high temperature peak.

Fig. 8.11a gives results with R($\sqrt{3} \times \sqrt{3}$) ordering included as compared with experimental data in Fig. 8.11b [153]. The molecular parameters found describing the experimental spectra are quite reasonable: the first neighbors are under repulsion, $\varepsilon(1) = -6.3$ kJ/mol, and the second – under attraction, $\varepsilon(2) = 3.15$ kJ/mol; $\varepsilon^*(r)/\varepsilon(r) = -0.5$ for $r = 1$ and 2. Such strengths of the lateral interactions provide a difference in the coverage of the sublattices (see Fig. 8.10); so one can reproduce all the experimental features, including the TDS splitting and shape of the high temperature peak as well. Differences at large initial coverages are evidently because one used the simples variant of the model taking care about R($\sqrt{3} \times \sqrt{3}$) ordering; there are evidently more far lateral interactions that are of importance at such coverages. In contrast to the above picture, the model without ordering gives a simple splitting at $\theta = 0.5$ (see Fig. 8.11c), and this is a qualitatively wrong picture for the experimental data where the splitting begins at $\theta = 0.33$.

So, the values of the parameters found with the transition state theory for reactions in condense matter do lead to a consistency in thermodynamic and

Lam Research Ex. 1035 - Page 411
Lam Research Corp. v. Inpria Corp.
IPR2024-00033 - U.S. Patent No. 9,823,564

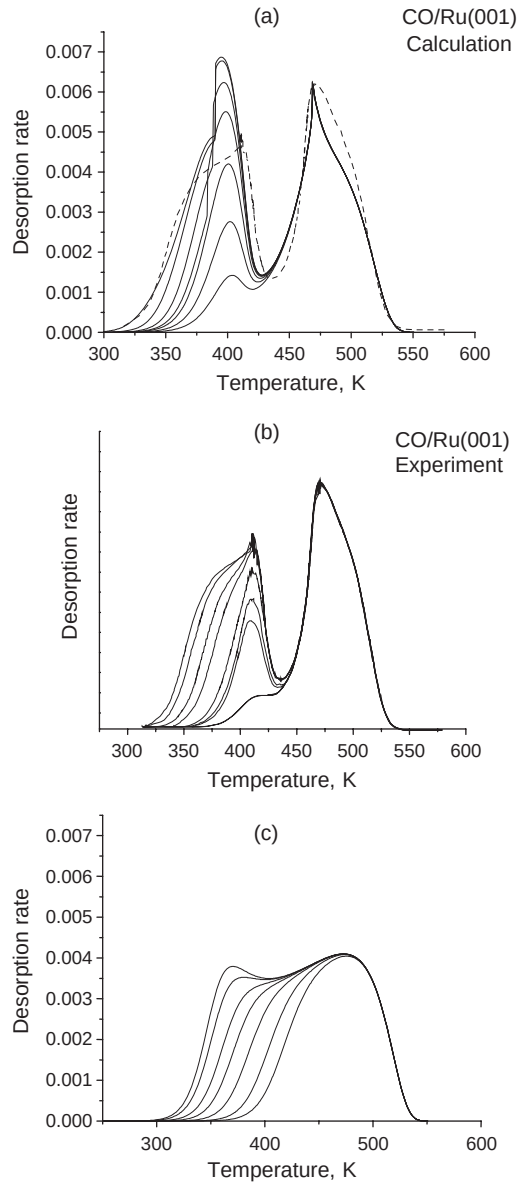


Fig. 8.11. CO/Ru(001) TDS found in the work [128] with including ordered structures (a), experimental data [153] (b), and without $R(\sqrt{3} \times \sqrt{3})$ ordering (c). The parameters of calculated spectra are: $K_D = 10^{13}$ sec^{-1}, $E_D = 132$ kJ/mol, $\varepsilon(1) = -6.3$, $\varepsilon(2) = 3.15$ kJ/mol, $\varepsilon^*(r)/\varepsilon(r) = -0.5$; $\theta_0 = 0.38, 0.43, 0.49, 0.54, 0.58, 0.63, 0.66$ [128].

Lam Research Ex. 1035 - Page 412
Lam Research Corp. v. Inpria Corp.
IPR2024-00033 - U.S. Patent No. 9,823,564

kinetic adsorption properties. Other systems of self-consistency of kinetic equations constructed with the lattice model are presented in Refs. [80,89]. Since the lattice model is self-consistent, hence, with this model, both equilibrium and kinetic characteristics can be found on the basis of the same set of the molecular parameters. Thus, to reduce the number of unknown parameters involved in the lattice model from kinetic data, the independent experimental data are to be used. This especially refers to the data on equilibrium adsorption properties, in order to estimate the heterogeneous distribution function and lateral interaction constants.

4.6. SURFACE DIFFUSION

The transfer of the adspecies within macrodistances is described with the aid of diffusion equations. The concentrations of the adspecies therein is characterized by the local degrees of lattice coverage $\theta(x)$ with adspecies i in the vicinity of the point with the coordinates x. In the absence of external fields the diffusion equation for each component has the form [154,155]:

$$d\theta(x)/d\tau = \mathrm{div}\left[\sum_{j=1}^{s-1} D_{ij}\mathrm{grad}\theta_j(x)\right] + I_i(x), 1 \le i \le s-1, \qquad (63)$$

where D_{ij} is the diffusion coefficient of adspecies i under the effect of the adspecies j gradient; $I_i(x)$ is the reaction contribution to the change in the number of adspecies in the vicinity of the point x. The diffusion coefficients are local characteristics of the transfer process. To obtain their relation with the unit jumps of the adspecies, it would be most convenient to use a kinetic approach based on estimating the local flow of the adspecies between two neighboring planes. Thus it will be possible to obtain expressions for both the diffusion and the self-diffusion coefficients.

The migration of the adspecies is largely governed by a vacancy mechanism, i.e., their jump into the neighboring empty site. The theory of the interacting adspecies diffusion according to this mechanism in lattice systems has been initiated by studies on three-dimensional diffusion of alloy components (*cf.* Section 5 dealing with the rearrangement of a subsurface solid region). One of the main differences between the surface and three-dimensional diffusion of the adspecies lies in the fact that their density changes in very broad regions. Therefore, understanding the concentration dependences of the diffusion coefficients is essential for describing the process of substance mass transfer. Experimental data suggest that the surface adspecies transfer depends on a variety of factors such as structure and composition of a substance, chemical nature of the adspecies, and their

Lam Research Ex. 1035 - Page 413
Lam Research Corp. v. Inpria Corp.
IPR2024-00033 - U.S. Patent No. 9,823,564

aggregation state, system's temperature, etc. [156,157]. One principal factor governing the dependence $D(\theta)$ consists in the lateral interaction between the adspecies.

The temporal evolution of the concentration profiles of the adspecies with allowance for their interaction seems to have been studied for the first time by Bowker and King [158]. Initially, the distribution of the adspecies density has been given up in the form of a "step" (this technique is often applied to surface diffusion studies). Consideration has been given to the concentration profiles in the case of attraction and repulsion of the adspecies to conclude that they can be used to estimate the lateral interactions. The applicability of the model to the description of diffusion in the O/W (110) system [159] is discussed.

The TSM has been applied in computing the concentration dependences for the self-diffusion and diffusion coefficients [160–162]. General expressions for $D^*(\theta)$ and $D(\theta)$, that are specified in the various approximations, have been derived. The theory gives possibility to explain a change of sign for the diffusion coefficient in case of strong attraction between molecules. Such a trend indicates a new phase to be formed (as a result of a two-dimensional condensation). It should be remembered that the adspecies flow direction is responsible for the gradient of the chemical potential rather than that of the concentration. The flow is directed toward a lower free energy side. For the non-interacting adspecies the main contribution is due to the entropy factor resulting in the spreading of the adspecies ensemble so that $D>0$. In the case of a strong interaction the energy contribution may play the deciding role. More exhaustive information on adspecies transfer can be obtained if the process is described not with the use of the total local density θ (since the system turns heterogeneous) but instead with discrimination between the local distributions of the low- and the high-density phases. The calculations [162] enable one to obtain a satisfactory agreement between the diffusion data for the O/W(110) system [159].

The effect of the collective jumps of the adspecies on their surface transfer (QCA, CM) has been treated by Tarasenko and Chumak [163]. The motion of the dimers and trimers on lattices with $z = 4$ and 6 was discussed. The dimer motion consists of the following steps: (1) a jump of one of the adspecies with the associated change in the dimer orientation; (2) a parallel transfer of the dimer relative to the line connecting its adspecies in the initial position, and (3) a longitudinal displacement of the dimer along the line connecting its atoms (l). On a lattice with $z = 6$ the first type of motion breaks into two cases: (1) the distance between the dimer adspecies in the terminal state remains the same as that in the initial one, or (2) this distance increases. If the frequencies of the different jumps are similar to one another, then even a minor attraction between the adspecies results in a

Lam Research Ex. 1035 - Page 414
Lam Research Corp. v. Inpria Corp.
IPR2024-00033 - U.S. Patent No. 9,823,564

smaller contribution of the collective trimer jumps. The number of dimers increases with θ together with their contribution to the overall transfer process but this involves a parallel heightening of the potential barriers, which have to be overcome by the adspecies. As the attraction grows, the energy barrier becomes a predominant factor. In addition, a particular case of adspecies jumps on the anisotropic (110) face has been explored [164]. Generally, it is believed that along with the jumps of the individual adspecies one should take into account the collective dimer motion whereas the collective jumps of the larger number of adspecies can be ignored.

In the general case, for a multicomponent system at an arbitrary radius of interaction between the adspecies in a one-step approximation in time a similar treatment gives the following expression for the diffusion coefficients in the transfer equations:

$$D_{ij} = z^* \lambda^2 U_{i\mathrm{V}} \partial\{\ln(\chi_i \exp(\beta\mu_1)\}/\partial\theta_j, \chi_i = \theta_{\mathrm{VV}}(1)/[t_{i\mathrm{V}}(1)]^2, \qquad (64)$$

where $U_{i\mathrm{V}}$ is the rate of adspecies i jumps into the neighboring empty sites and μ_i is the chemical potential of adspecies i. In particular, as indicated by surface transfer computations, the concentration dependence of the diffusion coefficients depends on how such interactions are approximated.

The presence of the cofactor χ_i serves as "a hint" of a need for the presence of a correlation cofactor f_c which is bound to appear during a more detailed kinetic derivation of the expression for the diffusion coefficient due to changes in the functional relation between the local density and the probabilities of multibody configurations, the relation being controlled by the adspecies concentration gradient. This factor has been considered in the case of binary alloys [155,165] (see Subsection 5.2):

$$D(\theta) = z^* \lambda^2 U_{i\mathrm{V}} f_c \partial(\beta\mu_1)/\partial\theta_j. \qquad (65)$$

It should be mentioned, cofactor f_c cannot follow from any thermodynamic constructions.

The developed theory was also used for investigation of the diffusion coefficients on heterogeneous surfaces [166]. Concentration dependences of self-diffusion coefficients and mass transfer of atoms adsorbed on heterogeneous surfaces are investigated within the entire range of monolayer coverage. Hops of atoms to the neighboring free adsorption sites within the monolayer and lateral interactions between the nearest neighbors are taken into account in the quasi-chemical approximation. Model surfaces of various topography – patch-wise, chaotic, and ordered of the $c(2 \times 2)$ type containing two sorts of adsorption sites and also an amorphous TiO_2 (rutile) surface with a great number of adsorption site types – are considered. The peculiarity of Ar adsorption on amorphous rutile is Ar atom blocking of several neighboring adsorption sites. To allow for this fact, one uses a

Lam Research Ex. 1035 - Page 415
Lam Research Corp. v. Inpria Corp.
IPR2024-00033 - U.S. Patent No. 9,823,564

quasi-one-site model based on dividing the area occupied by an atom with a finer lattice. The feasibility of predicting the concentration dependences of self-diffusion and diffusion coefficients using equilibrium data on heats and isotherms of adsorption is discussed.

The real-space renormalization-group (RSRG) technique has been used analysis of atom diffusion on square and honeycomb lattices with blocks of different size and symmetries [167,168]. It has been shown that the precision of the method depends strongly not only on the number of sites in the block but also on its symmetry. In general, the accuracy of the method increases with the number of sites in the block. The most accurate results have been obtained for the largest cluster containing 34 sites ($z = 4$) and 42 ($z = 3$). Authors concluded that the RSRG method can be applied at least for the systems with simple symmetry to characterize the thermodynamic and kinetic properties of interacting adsorbates.

The accuracy of calculations is found to be a non-monotonic function of the size of a cluster, and to depend strongly on its symmetry. The phase diagram of the Ising antiferromagnetic spin model and of the corresponding lattice-gas model is constructed with high accuracy. The ordered phase in the lattice system is shown to appear in the very narrow density interval, $0.447 < \theta < 0.553$. In addition, the coverage dependence of the chemical diffusion coefficient and mean-square density fluctuations are studied at temperatures below the critical one. Both quantities are demonstrated to exhibit singularities at the critical coverages. The type of singularities, in particular, the critical slowdown of diffusion is in agreement with the predictions of the scaling theory.

5. Solid Phase Processes in Solid–Gas Systems

Section 5 describes a correlation between surface and volume processes for solid samples and how to use the kinetic theory for reflecting changes in solid at the expense of reactions with atoms and molecules of a gas or liquid phase. The approach includes the multistage nature of the surface and volume processes, each stage of which is described by using the non-ideal reactive system theory.

5.1. Interface States

The kinetic equations under consideration describe the evolution of the gas–solid interface state. Up to now one has not considered in detail the

Lam Research Ex. 1035 - Page 416
Lam Research Corp. v. Inpria Corp.
IPR2024-00033 - U.S. Patent No. 9,823,564

external conditions where the solid body finds itself and how the solid body state changes upon its formation. In both cases the kinetic equations for the surface processes should be supplemented with the equations that relate the evolution of the interface and the volume phases. The kinetic equations for the surface processes represent boundary conditions with respect to the kinetic equations pertaining to the volume processes. They describe the rates of surface conversions (catalytic reactions), motion of the phase interface (growth or sublimation (etching) of the solid body) and the processes of mass transfer if adspecies are dissolved in the body.

The kinetic equations for the volume gas phase are of the gas dynamic type [169,170]. When they are used, the equations of the surface processes considered above should be supplemented with those for the impulse and energy transfer. Earlier it has been implicitly assumed that the heat effects of the surface processes at all stages do not play any role, i.e., the resulting heat of reaction is instantly absorbed in the volume of the solid body (a reservoir of an unlimited capacity), and all the processes proceed at a constant temperature. In the general case it is not so, especially with the catalytic processes [171] and with small of solid body volumes.

The specific properties of the gaseous phase molecules and a set of the physico-chemical processes which take place therein are extremely diverse (excitation of the oscillational degrees of freedom, dissociation, chemical reactions, etc.) and call for special consideration (see, e.g., Ref. [170]). Also, of great importance is the geometry of the surface in the gas flow [172]. All these questions are beyond the scope of this discussion.

The kinetic equations for the volume phase of the solid body are equations of the diffusion type (63). Much attention has been given to them in the literature [154,155], therefore here will be reminded only those aspects of the theory of mass transfer for which the lattice-gas model has been used. These are problems involved in the construction of expressions for the diffusion the coefficients and boundary conditions of the diffusion equations.

The problem of boundary conditions during the species mass transfer through the solid has been disclosed in much detail elsewhere [49]. The problem consists essentially in determining the number k' $(1 \le k' \le \kappa)$ of the layer in the subsurface region of width κ for which it can be taken that $d(\theta_k^i)/d\tau = 0$, then

$$\sum_{j=1}^{s-1} D_{ij} d\theta_j/dx + z_{kk-1}(U_{kk-1}^{iV} - U_{kk-1}^{Vi}) = 0, x = \lambda(k - k'), \qquad (66)$$

where D_{ij} is the diffusion coefficient of species i under the effect of the species j gradient; U_{kk-1}^{iV} is the rate of the species i jump from layer k into layer k–1.

Lam Research Ex. 1035 - Page 417
Lam Research Corp. v. Inpria Corp.
IPR2024-00033 - U.S. Patent No. 9,823,564

For $k > k'$ the adspecies mass transfer process is described by the diffusion Eq. (63). If the species migration in the subsurface region and the exchange with the gaseous phase occur fast, then $k' = 1$, therefore the boundary condition comprises the 3rd kind condition. Otherwise, it would be necessary to take into account the temporal evolution of the species in subsurface layers k', and the kinetic equations for these layers can contain the time derivatives. Most works devoted to mass transfer problems and also to the surface segregation of the alloy components [155,173]. The boundary conditions in the non-ideal systems are discussed in Ref. [174]. They require the use of equations for the pair functions of the type $d(\theta_{kq}^{ij})/d\tau = 0$. When describing the interphase boundary motion, the 3rd kind boundary conditions are also possible, although the 1st and the 2nd kind conditions are used more often. The latter are mainly applied to the description of many problems with species redistribution in the closed volume [175].

5.2. Diffusion Through Solids

The lattice-gas model has been traditionally applied to the construction of the diffusion coefficient concentration dependencies. The diffusion and the self-diffusion coefficients for the interstitial atom migration in ordered and disordered alloys with *bcc* and *fcc* lattices have been obtained by Krivoglaz and Smirnov [176,177]. Generally, the $\ln D$–β dependence is non-linear even for disordered alloys. At the ordering point this dependence has a bend and a jump for the *bcc* and the *fcc* lattices, respectively. The ordering of the alloy atoms results in a higher effective energy of diffusion activation. Another subject of this works cited is the effect of the interstitial atoms on the self-diffusion of the atoms of the pure metal and those of the disordered and the ordered alloys as well as the effect of the interaction on the self-diffusion coefficients in the disordered substitution alloys (the vacancy mechanism of atom migration, *bcc*, $s = 2$ and 3). Even a small amount of impurity B produces a sharp effect on the self-diffusion coefficient of atom A. The diffusion of the interstitial atoms has been described in much detail by Smirnov [177]. They do not take into account the effects of the migrating atom temporal correlation.

A more rigorous approach to calculating the diffusion coefficients has been adopted by Kikuchi [165]. A binary substitution alloy ($s = 3$) has been considered with the vacancy mechanism of atom migration. He was the first to take account of the temporal correlations and to obtain expressions for the correlation cofactor f_c in the non-ideal systems. The derived coefficients satisfy Onsager's reciprocal relations.

Lam Research Ex. 1035 - Page 418
Lam Research Corp. v. Inpria Corp.
IPR2024-00033 - U.S. Patent No. 9,823,564

In a particular case for the self-diffusion of atoms A in a pure metal (equilibrium vacancy concentration, $s = 2$, $\theta_B = 0$) his expression for f_c coincides with that obtained earlier by Lidiard [178] who has considered atom displacement into the nearest-neighboring sites; therefore these expressions differ from the exact f_c values (Campaan and Haven [179] and Schoen and Lowen [180]).

Other work [181] deals with the dependencies of the diffusion coefficients in the alloy-ordering region on the jump rate constants for the different atoms, interatomic parameter interactions and temperatures ($s = 4$). The importance of considering the correlation effects in the multicomponent alloys has been stressed. When using the fitting interaction parameters obtained from the phase diagram, the dependencies $D(\theta)$ provide a qualitative agreement with the experimental data [182] for β-Ag–Mg alloy and T within 500–700 K. The effect produced by temperature and species ordering on the characteristics of cationic diffusion and ionic conduction in solid electrolytes as exemplified by β''- and β-aluminates has been studied by Sato and Kikuchi [183]. In the former structure all the sites are equivalent and in the latter they are broken into two groups of equivalent sites. The correlation factors for cationic diffusion and cation motion in the external field have been shown to heavily depend on the cationic sublattice composition; however, their relation is only dependent on the lattice geometry.

Amandykov and Gurov [155,184] have extended Kikuchi's approach to the case when the TSM is used (QCA, $R = 1$). According to these authors, the expression for the correlation cofactor depends on the parameter of the AC interaction with the neighboring species. Therefore, this behavior exerts a significant effect on the concentration dependence of the diffusion coefficients. The potential of atoms interaction at any distances has been applied to the construction of the kinetic equation describing the diffusion decomposition of solid solutions [185].

A general theory of the diffusion of molecules in solid has been constructed for consideration of a transport process in the glass-type polymeric membranes [186–189]. The influence of non-homogeneities in the properties of membrane matrices on the permeability of membranes is an important aspect of the theory of transfer of low-molecular substances in membranes. Microheterogeneity of a membrane is associated with its molecular structure and the nature of interactions with diffusant molecules. In the case of inorganic membranes, non-uniformities are associated with the presence of different-type interstices in crystal lattices and the imperfections of the lattices. In the case of organic membranes, non-uniformities are due to different interaction energies of diffusant molecules with different functional groups of polymer chains and to differences in the morphology of their packing.

Lam Research Ex. 1035 - Page 419
Lam Research Corp. v. Inpria Corp.
IPR2024-00033 - U.S. Patent No. 9,823,564

Fundamentals of a method for developing models of mass transfer of low-molecular substances in non-reconstructing microheterogeneous membranes were formulated. The local properties of membranes differ in sorbability with respect to species and in the probability for a species to jump from one sorption site to another. Because of this, the permeability of a membrane depends on the amounts of different-type sites, their mutual arrangement, mutual influence of adjacent molecules, and the probabilities of jumps between different sites. The probabilities of occupation of different sorption sites are described by kinetic equations, which take into account the interactions between species. The atomic-molecular discrete and continuous models of mass transfer for thin and thick films are constructed.

Developing approach has given an explanation at what conditions the matrices with macroscopic non-uniformities (e.g., lamellar systems, heterogeneous inclusion phases, etc.) and with effective macroscopic diffusion coefficients; in the latter case, a matrix is considered as a homogeneous one and when the phenomenological model of double sorption, which operates with sorption sites of two types could be used [190–192].

Discrete and continuum models of transfer of molecules over various sorption sites of a microheterogeneous membrane were considered for systems with weak intermolecular interactions and membranes with constant composition and structure. An equation for estimating size effects on permeability coefficient Π of microheterogeneous membranes was derived [188], and the possibility of applying the continuum model to calculate the Π value in thin films of thickness L is numerically analyzed. The effect of the composition and structure of a uniformly microheterogeneous membrane on the permeability coefficients Π was studied. The dependence of Π on the composition is a convex function if the migration between different sorption sites proceeds more quickly than between identical sites and a concave one in the opposite case [189].

It was shown that if the rate constants of desorption of molecules from the surface and migration of molecules in the bulk are of the same order of magnitude, then homogeneous films are correctly described by the continuum model at $L_{\text{hom}} \geq 300\lambda$, where λ is the mean diffusion jump length ($\lambda \sim 0.5\,\text{nm}$). For heterogeneous films, the L range where the continuum model is applicable depends on the composition and the structure of the membrane, and $L_{\text{het}} < L_{\text{hom}}$. The effects of the difference in the sorption capacities of ''weak'' and ''strong'' sites and of a pressure drop between outside membrane surfaces on the permeability coefficient of the membrane were studied [188].

The sorption isotherms and concentration dependences of Π for CO_2 molecules in glassy substituted polycarbonates are described by considering

Lam Research Ex. 1035 - Page 420
Lam Research Corp. v. Inpria Corp.
IPR2024-00033 - U.S. Patent No. 9,823,564

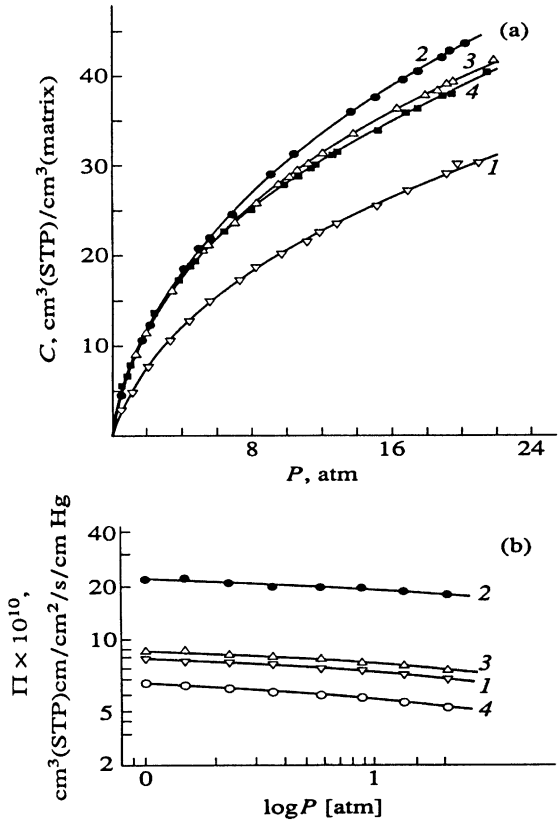


Fig. 8.12. Sorption isotherms (a) and the permeability coefficients (b) for CO_2 sorption by (1) bisphenol A polycarbonate, (2) tetramethyl polycarbonate, (3) tetrachloropolycarbonate, and (4) tetrabromopolycarbonate at 35°C [189].

the individual contribution from each type of substituents [189]. The experimental values [193] and theoretical curves are presented in Fig. 8.12. As can be seen, they are in close agreement.

The lattice model of mass transfer gives self-consistent expressions for sorption isotherms and permeability coefficients for microheterogeneous membranes of variable thickness at an arbitrary degree of filling. The parameters of the lattice model can be related to the molecular structure of a matrix and to the parameters of the interaction between diffusant and matrix [191]. The lattice model can serve as a basis to construct phenomenological models, which are capable of describing the features of a molecular system "diffusant-membrane matrix".

Lam Research Ex. 1035 - Page 421
Lam Research Corp. v. Inpria Corp.
IPR2024-00033 - U.S. Patent No. 9,823,564

5.3. Phase Transitions and Topochemical Processes

Usually phase transition in a gas–solid system is described by the topochemical models [44,194]. Such models assuming chaotic or regular configurations of the islands or nuclei of the new phase – disks or squares for the two-dimensional and sphere for the three-dimensional reaction systems. The reaction rate depends on the duration of aggregation (on the initial distribution and configuration of the islands) and that of the reaction itself. Its value is much lower than that taking place in the chaotic distribution of the adspecies.

A new phase formation inside solid connects with a creation of solid–solid interfaces. A total process is controlled by a diffusion transport of the absorbed species to these interfaces. At these interfaces similar Eq. (66) should be used

$$\sum_{j=1}^{s-1} D_{ij} d\theta_j/dx + U^i_{gh} = 0, \tag{67}$$

where the diffusion description refers to one of the coexisting solid phases through which the transport is occurred, while the another term is described possible surface reactions of species i between the both surface layers of the phases g and h. This equation presents an equality of the species flows by the transport and reaction stages at stationary regimes. So, the kinetic description of the topochemical processes by traditional models consists in using the above-mentioned equations.

A fixed form of the nuclei simplifies a description of the diffusion processes. From physical point of view it corresponds to the time interval when initial stage was finished. For small initial times another model can be used [195]. The formation of a new phase is described by the rate of formation of new phase nuclei at an arbitrary membrane point, and the rate of growth of the new phase, with the use of balance equations for transition of atoms from the interphase boundary to the new phase without specifying the shape and size of the new phase region. The occurrence of metal atoms in the phases and the interphase boundary (coherence of phases) is taken into account by the structure of the reaction cluster within which an elementary reaction occurs with the use of the pair correlation functions θ_{ij}, that have been mentioned at non-ideal behavior of the lateral interaction between reagents. Using the pair correlation functions extends a possibility for description of the processes with new phase formation. This approach was used for analysis of the transport process of hydrogen through palladium membranes [195].

Lam Research Ex. 1035 - Page 422
Lam Research Corp. v. Inpria Corp.
IPR2024-00033 - U.S. Patent No. 9,823,564

6. Physico-Chemical Mechanics Problems

Using the kinetic theory for studying physico-chemical mechanics problems is briefly discussed in this section to explain the observed properties of the hydrogen–palladium system. It is also used to self-consistently connect the absorption and diffusion characteristics of hydrogen atoms with the deformations within the metal membranes.

6.1. Rates of Elementary Stages at Solid Deformations

An extension of the kinetic theory on cases when a mechanical pressure interacts with kinetic processes inside solid volume and on interfaces has wide application interests. The elastic deformations in solid are presented from influence of external forces and from presence of internal defects of crystal structure: point defects (vacancy, intersite atoms, complexes of atoms, etc.), extended defects (dislocations and inner interfaces in polycrystals), and three-dimensional defects (heterophases crystals, polycrystals).

A description of a kinetic evolution for point defects can be carried out directly through above specified kinetic schemes and equations for elementary processes which were employed regarding the absorbed species. For describing a kinetic evolution of two- and three-dimensional macrodefects, it is necessary to construct models for connection of elementary processes with a change of structural macrodefects [196].

In the description how atomic distributions in solid are changed, it is natural to consider that mechanical deformations occur much faster than all atomic processes, and the mechanical deformations are possibly found in a condition of the mechanical balance: For any atom with the number f inside the solid one has the following macroscopic equation [197]

$$\partial\sigma_{ik}(f)/\partial\chi_k = -G_i(f), \tag{68}$$

where σ_{ik} is the component of the tensor for internal strain, $G_i(f)$ is the i component of volume forces. Similar for surface atom f one has:

$$\sigma_{ik}(f)n_k = P_i + F_i(f). \tag{69}$$

Here $F_i(f)$ is the i component of external forces, n_i is the i component of normal vector to surface [197].

The lattice-gas model provides effective ways on atomic-molecular level for allowing the mechanical equilibrium of all solid atoms and adsorbed particles on any (flat or structural-rough) surface if one expresses

Lam Research Ex. 1035 - Page 423
Lam Research Corp. v. Inpria Corp.
IPR2024-00033 - U.S. Patent No. 9,823,564

interparticle distances through the parameter of interactions between species. It is natural to use the same parameters that define a non-ideal behavior of considered reaction systems. As a result, a microscopic interpretation of dependences for rate of elementary stages as well as mechanical properties should be taken into account through the same effective potentials of intermolecular interactions. As usual the effective pair potentials are used for such tasks because the problem is rather difficult for numerical realizations.

A deviation of interatomic distances changes the energy interaction and the value of activation barrier. As a result, the magnitudes $K_{fg}^{ij}(\alpha)$ and $\varepsilon_{fg}^{ij}(\alpha)$ are changed.

The lattice-gas model permits to estimate the traditionally used empirical Zhurkov's expression for break of elastic-strain bonds (see, e.g. Ref. [198])

$$k = k_0 \exp\{-\beta(E_a - \sigma V^{\#})]\}. \tag{70}$$

In the formula (70) k_0 and E_a are the preexponential factor and the activation energy for thermal process of bond breaking, $\sigma V^{\#}$ is the work made by elastic pressure during the elementary process (σ is the strain, $V^{\#}$ is the activation volume).

The other formulas for the rate constant at various phenomenological models have also been suggested (e.g., see Ref. [199]):

$$k = k_0 \exp\{-E_a/(A_0 + kT)]\}, \text{ or } k = k_1 + k_2(\eta E_a/kT)\exp\{-\beta E_a\}, \tag{71}$$

where the parameter A_0 is expressed via frequencies of the molecular oscillations and the parameters of reaction potential barrier; η the coefficient of friction that characterizes interactions of the active oscillator with environments; k_1 the constant for activation dissociation rate of actively oscillator; and k_2 the constant for direct mechanical perturbations that could initiate the direct dissociation of active oscillator.

Application of the kinetic theory for condensed phases shows that given expressions (70) and (71) have macroscopic character and do not concern separate intermolecular bond (and correspond with a particular elementary stage), but to a macrosample as a whole. Local rates of elementary reactions in condensed environment have "a usual view" (without the term of types $\sigma V^{\#}$ or A_0, and so on), however all energetic characteristics concerning current magnitudes of local mutual arrangements of "reagents" differ from similar magnitudes in the absence of mechanical strains. It changes the energetic characteristics of the reagent interaction with neighboring molecules. For reception of observable average values of elementary reaction rates it is necessary to conduct averaging over coordinates of all neighboring molecules. The averaging function depends on the particular mechanism of the total process, covering all elementary processes in

Lam Research Ex. 1035 - Page 424
Lam Research Corp. v. Inpria Corp.
IPR2024-00033 - U.S. Patent No. 9,823,564

vicinities of considered elementary volume, and from characteristic time scale, on which averaging is carried out.

6.2. Hydrogen–Palladium System

In the hydrogen–palladium system, local concentrations θ_H of hydrogen may vary in a wide range – from zero to one hydrogen atom per metal atom [200–202]. At temperatures below $T = 565\,K$, this factor results in a change in the phase composition of the membrane matrix: α and β phases appear. The two-phase state of the metal gives rise to internal stresses; it is also responsible for hysteresis effects in the flux characteristics of the membrane and a scatter in experimental data [200–202]. Although the strong influence of interstitial hydrogen on the mechanical, and correspondingly, sorption and transport properties of Pd membranes has been demonstrated in many studies, the measurements were unsystematic, so it is impossible to unambiguously relate the phase composition of the matrix to these properties. A negative role is played by the fact that the physico-chemical and mechanical characteristics of materials are studied separately, although interatomic interactions underlie all observed phenomena.

A theory that would describe changes in the properties of a palladium membrane as a function of the characteristics of the hydrogen flow and would take into account the mutual influence of various thermodynamic, transport, and mechanical characteristics of the Pd–H_2 system in a self-consistent manner, has been developed in Ref. [195]. The kinetic systems of equations describing the transfer of interstitial atoms in homogeneous and microheterogeneous metal alloys, without taking into consideration phase rearrangements and mechanical stresses [80,174], were generalized in Ref. [195] in order to take into account mechanical stresses and changes in the properties of the microheterogeneous matrix during phase rearrangements. The equations deduced in Ref. [195] are rather complicated and need a numerical analysis. So, an average version of the atomistic theory proposed in Ref. [195], which demonstrated that the atomistic model self-consistently predicts various concentration-dependent characteristics of membranes was developed [203]. In particular, one estimated the effect of dissolved hydrogen atoms on the mechanical properties of palladium based on the thermodynamic characteristics and the concentration dependence of the lattice constant for Pd–H alloys, including the Peierls force (it is known that the presence of dislocations influences sorption and transport characteristics [204]). The sorption characteristics and the intensity of the hydrogen flux through a membrane can be expressed through the potential of interatomic interactions [195]. On the other hand, the mechanical characteristics of a

Lam Research Ex. 1035 - Page 425
Lam Research Corp. v. Inpria Corp.
IPR2024-00033 - U.S. Patent No. 9,823,564

solid can be expressed through the constants characterizing the elasticity, which are determined by the same potential of interatomic interactions [205,206].

6.3. Effective Potential

The form of the potential for the system under study was discussed in many publications [28,202,207,208]. Effective pair potentials are widely used in theoretical estimates and numerical calculations. When a many-particle interatomic potential is taken into account, the quantitative description of experimental data improves. For example, the consideration of three-body interactions along with two-particle interactions made it possible to quantitatively describe the stratification curve for interstitial hydrogen in palladium [209]. Let us describe the pair interaction of all the components (hydrogen and metal atoms in the α and β phases) by the Lennard–Jones potential: $\varphi_{ij}(r_{ij}) = 4\ \varepsilon_{ij}\ [(\sigma_{ij}/r_{ij})^{12}-(\sigma_{ij}/r_{ij})^{6}]$, where ε_{ij} and σ_{ij} are the parameters of the corresponding potentials. All the distances r_{ij}, are considered within c.s. of radius r ($1 \le r \le R$), where R is the largest radius of the radii of interaction R_{ij} between atoms i and j).

The interstitial sublattice comprises interstitial hydrogen atoms and free internodes (vacancies V), whereas the metal lattice is composed of palladium atoms and vacancies V. The potential energy of the system can be presented as [195]

$$U = U_{\mathrm{MM}} + U_{\mathrm{MH}} + U_{\mathrm{HH}}, \tag{72}$$

where the summands describe the metal–metal, metal–hydrogen, and hydrogen–hydrogen interatomic interactions, respectively.

The distances between atoms appearing in the potentials can be expressed through the lattice constants for nearest neighbors λ^{k}_{fh}, where $k = x, y, z$ are the components of the vectors between nearest neighbors; f and h are the number of atoms at various distances. Thus, the total potential energy of the system can be expressed through the parameters λ^{k}_{fh} and minimized with respect to them:

$$dU/d\lambda^{k}_{fh} = 0. \tag{73}$$

As a result, one can obtain relations that determine changes in all the lattice constants and the total energy of the system at a given arrangement of the palladium and hydrogen atoms. Solving this system of equations yields a set of $\{\lambda^{k*}_{fh}\}$ values, which are then used to calculate the energetic parameters of the lattice $\varepsilon^{ij}_{fg}(r) = \varphi_{ij}(r_{fg}|\{\lambda^{k*}_{fh}\})$ at given distributions of hydrogen and metal atoms. The parameters $\varepsilon^{ij}_{fg}(r)$ characterize the average energy of interaction between species i and j located at sites f and g separated by a

Lam Research Ex. 1035 - Page 426
Lam Research Corp. v. Inpria Corp.
IPR2024-00033 - U.S. Patent No. 9,823,564

distance r. The energies of interaction of H and Pd with vacancies in the lattice and sublattice were assumed to be equal to zero.

To simplify the description of the Pd–H system, one roughened the hydrogen atom distribution over nodes in the model developed in Ref. [195] by introducing an intermediate (corresponding to 2–3 distances between palladium atoms) scale. This scale makes it possible to consider an averaged distribution of hydrogen atoms over intermodes; at the same time, it is much smaller than typical distances considered in the macroscopic theory of elasticity [28,205,206]. In addition, one introduced a number of other simplifications. Potential function (72) takes into account the presence of vacancies in the metal lattice. At relatively low temperatures, the contribution from these vacancies can be disregarded. One also used the correction function $S_{n,m}$ proposed by Mie [210,211] to calculate the contributions from the second-nearest and more remote neighbors. The modified pair Lennard–Jones potential can be written as $\varphi_{ij}(r_{ij}) = 4\ \varepsilon_{ij}\ \psi_{ij}$, where $\psi_{ij} = S_{12}(\sigma_{ij}/r_{ij})^{12} - S_6\ (\sigma_{ij}/r_{ij})^6$, therefore, it is possible to limit the description to the contribution from the nearest neighbors. Finally, one introduced an average constant of the *fcc* metal lattice and reduced the problem to an effective one-dimensional lattice under the assumption that hydrogen atoms yield an averaged contribution to the potential curve for the interaction between palladium atoms. In doing so, one unambiguously related the average distance between the centers of the internodes with the constant of the *fcc* lattice; in order to take into account the resultant change in the lattice constant, one replaced the parameter σ_{MM} by the function $\sigma_{\mathrm{MM}}(\theta_{\mathrm{H}})$. Then the effective potential ε_{ef} for the interaction between palladium atoms (located at site f and around it: $g \in z_f$) can be written after averaging the local distributions of hydrogen atoms around the given metal atom, one introduced their average concentration $\theta = \sum_{g \in zf} \theta_g^{\mathrm{H}} / z_f$, as next

$$\varepsilon_{ef} = 4(\varepsilon_{\mathrm{MM}}\psi_{\mathrm{MM}} + \theta_{\mathrm{H}}\varepsilon_{\mathrm{MH}}\psi_{\mathrm{MH}}/2 + z_f\theta_{\mathrm{HH}}\varepsilon_{\mathrm{HH}}\psi_{\mathrm{HH}}/2). \tag{74}$$

The function $\theta_{\mathrm{HH}}(\theta_{\mathrm{H}})$ should be calculated by using actual approximations. To calculate the thermodynamic and kinetic characteristics of the system in a self-consistent manner, it is necessary to use the quasi-chemical approximation, because it takes into account nearest-order correlations (which are absent in the mean-field approximation) [80].

6.4. MECHANICAL AND TRANSPORT PROPERTIES OF THE Pd–H_2 SYSTEM

Formula (74) yields an averaged description of the mean energy of the Pd–H_2 system, which refers to local uniform regions of the membrane. Based on the averaged version of the atomistic model for the Pd–H_2 system,

Lam Research Ex. 1035 - Page 427
Lam Research Corp. v. Inpria Corp.
IPR2024-00033 - U.S. Patent No. 9,823,564

the effect of interstitial hydrogen atoms on the local thermodynamic, transport, and mechanical properties of palladium membranes was considered. Local deformations caused by the presence of interstitial atoms were taken into account. The model makes it possible to estimate the shear modulus of palladium as a function of the interstitial hydrogen concentration from experimental data on the lattice constant and various thermodynamic properties of the Pd–H system, such as the enthalpy of sublimation of palladium, heat capacity, hydrogen sorption, and stratification characteristics. Expressions for estimating the compression and Young module, the Poisson coefficient, and the Peierls activation barrier for the motion of edge dislocations were also obtained [203]. The model qualitatively describes the available data on the thermodynamic and mechanical characteristics of the membrane matrix and predicts its behavior under non-equilibrium conditions.

To reduce the number of unknown parameters of the model, it was assumed [203] that the dependence $\sigma_{MM}(\theta_H)$ can be determined from existing experimental data [200,212]. Fig. 8.13 compares the shear modulus for two limiting states of the membrane matrix: equilibrium (η) and non-equilibrium (η^*). The model proposed qualitatively agrees with few reliable experimental data on the effect of dissolved hydrogen on the mechanical modules. It correctly predicts the decrease in both Young's modulus and sheer modulus during the saturation of the metal with hydrogen in a wide

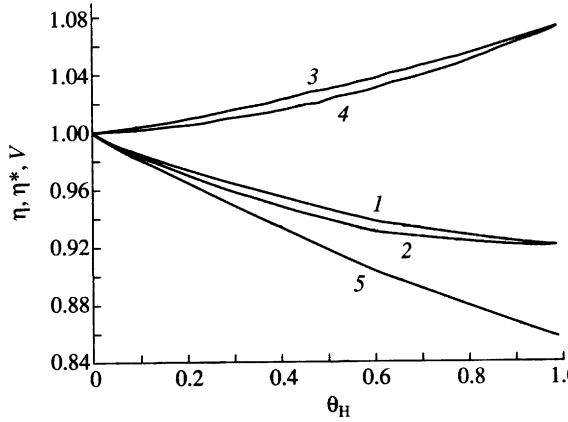


Fig. 8.13. Concentration dependences of the relative change in the sheer modulus (1, 2) $\eta(\theta_H)$ for the equilibrium state of the system and (3, 4) $\eta^*(\theta_H)$ for the non-equilibrium state and (5) a relative change in the volume per palladium atom $V(\theta_H)$ at $T = 300$ K. Curves 1 and 3 are constructed in the quasi-chemical approximation; curves 2 and 4 are in the mean field approximation [213].

Lam Research Ex. 1035 - Page 428
Lam Research Corp. v. Inpria Corp.
IPR2024-00033 - U.S. Patent No. 9,823,564

range of concentration. At small hydrogen densities, it gives a linear decrease in Young's modulus (as in Ref. [214]) and particularly, up to $\theta_H \sim 0.014$, it decreases to 0.65 and 0.70% in the QCA and MFA, respectively, while experiment [214] shows a decrease to 1.1%. At the density $\theta_H = 0.63$, the model predicts a decrease in the sheer modulus by 6.3 and 7.0% in the QCA and MFA, respectively, while the experimental value of Ref. [215] was 4%. Furthermore, as was tentatively estimated in Ref. [216] in the MFA at $\theta_H \sim 0.6$, dynamic Young's modulus in the Pd–H_2 system should increase to 8% at the high hydrogen concentrations when the mutual effects of included hydrogen atoms become substantial. This conclusion well agrees with an increase in η^* by 7.4% according to the calculations shown in Fig. 8.13a if one assumes that "the dynamic character of Young's modulus" is determined by the non-equilibrium state of the local bulk part of the metal. The latter case is realized for some local regions of the phase, in which palladium cannot be converted into the β phase because of an external compression [28].

Theoretical formulas show that the self-diffusivity of interstitial metal atoms decreases with an increase in the concentration of included hydrogen, which blocks free interstitial sites. A calculation of the coefficient of self-diffusion in the QCA is presented in Fig. 8.14. To calculate concentration dependences of the self-diffusivity, authors used $\varepsilon_{HH} = 0.6$ kcal/mol [217]. The curves are normalized to a self-diffusivity of 2.9×10^{-3} sm/sec at $\theta_H = 0$ [218]. As can be seen, the character of curves 1–3 and 5 substantially depends on the value of $\alpha_H = \varepsilon^*_{HH}/\varepsilon_{HH}$, which reflects the difference between

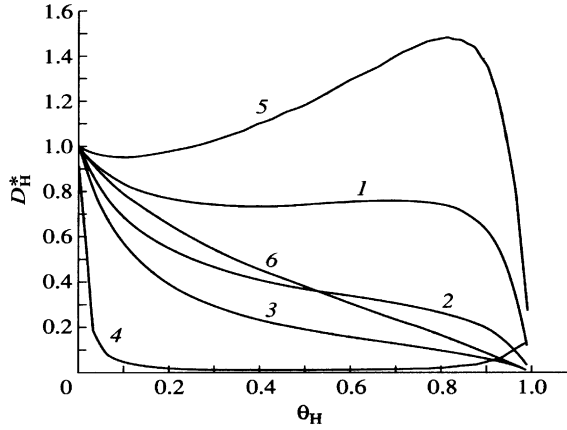


Fig. 8.14. Normalized concentration dependences of the self-diffusivity of hydrogen in palladium at $T = 300$ K and $\alpha_H = 0.50$ (3), 0.56 (2, 4, 6), 0.62 (1), and 0.66 (5) [213].

Lam Research Ex. 1035 - Page 429
Lam Research Corp. v. Inpria Corp.
IPR2024-00033 - U.S. Patent No. 9,823,564

the interaction of the included atom with its neighbors in the transition state (ε^*_{HH}) and in the ground state (ε_{HH}). Curve 2 corresponds to the experimental value of the self-diffusivity measured with NMR technique at $\theta_H = 0.7$ [219]. For, this value, the change in the t_{HV} function, which characterizes the part of free neighbor interstitial sites, where included atoms may jump, is shown as curve 6. When the correlation effects are taken into account, this function differs from the linear ($1–\theta_H$) function typically used in the MFA. For comparison, at the same α_H value, curve 4 for D^*_H at $\varepsilon_{HH} = 1.63$ kcal/mol is given. At a large occupation, D^*_H has a maximum and goes to zero at $\theta_H = 1$. For the parameters of the model corresponding to curve 4, the dependence of t_{HV} on the concentration of dissolved hydrogen practically coincides with curve 3 and it is not shown in Fig. 8.14.

6.4.1. Effect of Lattice Deformation on the Properties of Membranes

The developed theory allows to estimate the effect of lattice deformation for a palladium membrane on its sorption and transport properties by calculating changes in the φ_{MH} and φ_{HH} values. For large degrees of membrane filling, one compared the values of the potentials φ_{MH} and φ_{HH} corresponding to the above-mentioned equilibrium and non-equilibrium states of the membrane. This estimation gives that φ_{MH} and φ_{HH} may change by values as high as 11 and 15%. These changes produce a very strong effect on the energetic characteristics of the system, because the quantity φ_{HH} enters into expressions for the isotherm, heat, and heat capacity with a coefficient of $z = 12$. Also this quantity enters into expressions for the rate of migration with a coefficient (z–1). As a result, the deformation of the membrane strongly affects all its equilibrium and transport characteristics. In addition, the model predicts that, the lattice constant of the β phase increases with the hydrogen concentration, resulting in an increase in the rate of hydrogen migration, in agreement with the data reported in Ref. [220].

Thus, changes in the phase composition of a membrane as a result of its operation may substantially alter local mechanical characteristics, a process that should be taken into account and controlled when analyzing experiments in which intense flows of hydrogen pass through a palladium membrane. The model also makes it possible to relate independent experimental data on equilibrium, transport, and mechanical properties of palladium membranes. The estimates obtained are in close agreement with a large numbers of experimental data [200–202] on the behavior of various characteristics of palladium membranes with different prehistories and under different condition of hydrogen transport.

Lam Research Ex. 1035 - Page 430
Lam Research Corp. v. Inpria Corp.
IPR2024-00033 - U.S. Patent No. 9,823,564

7. Numerical Dynamics Investigations

Except the kinetic equations, now various numerical techniques are used to study the dynamics of surfaces and gas–solid interface processes. The cellular automata and MC techniques are briefly discussed. Both techniques can be directly connected with the lattice-gas model, as they operate with discrete distribution of the molecules. Using the distribution functions in a kinetic theory *a priori* assumes the existence of the total distribution function for molecules of the whole system, while all numerical methods have to generate this function during computations. A success of such generation defines an accuracy of simulations. Also, the well-known molecular dynamics technique is used for interface study. Nevertheless this topic is omitted from our consideration as it requires an analysis of a physical background for construction of the transition probabilities. This analysis is connected with an oscillation dynamics of all species in the system that is absent in the discussed kinetic equations (Section 3).

7.1. CELLULAR AUTOMATA TECHNIQUE

Nearly three decades ago for describing the dynamic surface processes, the so-called ''cellular automata'' approach was suggested [221–223]. In this numerical technique the considered process develops on a discrete lattice each site (cell) of which can be located in a discrete state. All the cells are taken on the corresponding time step in random succession. The evolution of the occupancy state for each cell on the given time step is controlled by the specified rules of coupling this state with the corresponding states of the neighboring cells on a previous step. The rules represent analogs of the transition probabilities that have been discussed in Sections 2. However, as rule, the transition probabilities do not connect directly with certain intermolecular interactions or molecular pictures. A main attention during simulations addresses to spatial distribution of molecules or a local organization of the cells in the chosen states. Depending of the situation, each cell can match either a site (a microscopic level) or a certain region (a meso- or a macroscopic level) of the surface. If during the process one traces the spatial arrangement of the cells with the same occupancy state, it will be possible to follow the formation and the distribution of the two-dimensional phases, spatial and temporal self-organization, etc.

The transition probabilities can be strictly determinated or stochastic. In the latter case the cellular automata noise plays the role of temperature in

Lam Research Ex. 1035 - Page 431
Lam Research Corp. v. Inpria Corp.
IPR2024-00033 - U.S. Patent No. 9,823,564

the equilibrium systems, and it is essential for phase formation in the non-equilibrium conditions [224]. At present the method is finding a growing application to studies of the kinetic phase transitions from the viewpoint of the dynamic system theory, description of dendrite crystals [225], biological systems [226], and other samples [223].

The cellular automata technique has been used by Moller et al. [227] for describing CO oxidation on Pt(100). The transition probabilities are described by data on the elementary process rates in the case of CO and O adsorption and desorption, reaction (ZCO + ZO), and surface rearrangement. The process of the redistribution of the adspecies in the course of their ordering has been omitted. Surface rearrangement occurs on a few neighboring empty (structure $1 \times 1 \rightarrow$ hex) or CO-occupied (hex $\rightarrow 1 \times 1$) sites. The simulation results represent qualitatively all the observed dependences of CO oxidation. The effect of periodic perturbations of oxygen pressure and temperature on the kinetic oscillations of the CO/Pt(100) oxidation rate has been studied by Schmankner et al. [228]. In this case it has been possible to observe the transitions of the aperiodic autonomous oscillations to a regular behavior under the action of the external perturbations. The spatial distribution of the various surface regions correlate with the oscillation type.

The CO oxidation rate on the Pt(210) and (111) faces with respect to the partial CO and O pressures and temperature has been discussed in Ref. [229]. The numerical studies have been made for the various sets of the elementary processes: (1) without the elementary processes of CO and desorption and migration, as in other work [230], and (2) considering all these stages. The latter variant leads to a substantially better agreement with experiment. The computations take into account the lateral interactions. The surfaces are regarded as being stable. The effect of each of the additional stages of the second variant on the poisoning conditions of the surface with the CO molecules has been discussed. Moreover, the type of the adsorption bond for CO (above the Pt atom or the interatomic Pt bond) has been found to be not important, although the phase transition point becomes somewhat displaced. Another subject has been the effect of CO ordering and heat of reaction on the catalyst poisoning conditions.

A macrolevel cell can be exemplified by the cellular model [231] and [232] when the cell is incorporated into a system of the strongly bonded Pt crystallites applied to a zeolite. The model allows to describe the complex oscillations of the CO oxidation rate. A heavy dependence of the reaction rates to be computed on the way the coupling rules for the neighboring cells are selected is shown. By varying these rules, it is possible to simulate the various experimental conditions.

Lam Research Ex. 1035 - Page 432
Lam Research Corp. v. Inpria Corp.
IPR2024-00033 - U.S. Patent No. 9,823,564

Now cellular automata technique is widely used in various applications. Rather complete reviews including common non-equilibrium properties of the dynamic processes are given in Refs. [233–235].

7.2. Monte-Carlo Technique

At present the MC method is a traditional numerical technique of statistical physics. It seriously competes with the theory of kinetic equations since the difficulty of their solution drastically increases when adspecies distribution is described in detail. Algorithms of the MC method are rather simple, and allow to obtain solutions with no supplementary conditions inevitable in case the cluster approaches are applied. It is especially important for the system with high interaction, therefore the MC methods are successfully used in all regions, including the critical ones. Today a volume of the system can change in areas of 10^4–10^7 sites. In many cases, however, the difference between the solutions obtained and that in the case of the thermodynamic limit is rather small that they, as some investigators believe, can be considered as exact.

The method itself has been first used in statistical physics by Metropolis et al. [236] for calculating the equilibrium state of the gaseous phase. Later on it has been widely applied in investigating the equilibrium state of the gas–solid interface [237]. These studies widely used the lattice-gas model that appreciably simplifies the calculations of realized adspecies configurations. On its basis many theoretical principles of the early theories have been tested [238] and the parameters of adspecies interaction have been determined from the LEED data [239]. Such publications are not discussed here. This section presents a short discussion on the application of the MC method in studying the surface processes kinetics. Technical problems are given in the relevant literature [240,241]. The MC method is successfully applied to those aspects of the surface process kinetics, which go beyond the scope of the lattice-gas model.

Now the MC simulation is the most popular technique for studying the surface and gas–solid interface processes, so one restricts by briefly listing the first papers in this area and discusses a correlation between MC and theoretical results (the next Subsection 7.3).

7.2.1. Adsorption Processes and Surface Reactions

For the first time the MC method seems to have been applied to the surface process kinetics in the description of the C_2N_2 molecule desorption from the

Lam Research Ex. 1035 - Page 433
Lam Research Corp. v. Inpria Corp.
IPR2024-00033 - U.S. Patent No. 9,823,564

Pt(110) surface [242]. It has been shown that considering the anisotropy involved in the adspecies interaction in the (001) and (110) directions, except when $\varepsilon_{110} \sim \varepsilon_{001}$, the process of desorption from the surface can be viewed as the one occurring independently on the various chains. The dissociative NO/Co(0001) [243,244] adsorption kinetics has been described by the same authors. The description of the TDS and the sticking coefficient suggests that the nitrogen and oxygen atoms undergo a weak attraction and the former are also capable of forming islands, therefore the order of the N_2 desorption rate is variable in the presence of oxygen. The adspecies desorption from the islands in the absence of equilibrium between the dense and the rarefied phases have also been studied [91].

The MC simulation has been used for analysis of the TDS for the interacting adspecies on the inhomogeneous surfaces [245–247]. Analysis [245,246] has been given to lattices with two types of sites and various patterns of their discrete and Gauss distributions relative to each other. The number of peaks during TDS splitting depends on both adspecies interactions and type of the surface inhomogeneity. The model has been applied to the CO/MgO TDS description to conclude that for this system the lateral interaction contribution is small.

The attraction of the adspecies has been shown to give a narrowed peak, and desorption occurs at higher temperatures [247]. The repulsion of the adspecies causes TDS splitting. It has been found that the interaction between the different adspecies ($s = 3$) affects only the spectrum of the adspecies with a lower desorption energy, and the two kinds of adspecies undergo desorption together under the specified conditions only. Generally, the effect of the lateral interactions on the desorption kinetics is great so that one can obtain a dissimilar behavior for the different adspecies. Also, a layer-by-layer desorption has been treated [247] (three layers, $R = 1$, $s = 2$). The process occurs if one atom is not overhung by any other.

In the simplified model of CO surface oxidation [248,249] it was accepted that any collision of the CO and the O_2 gas molecules leads to adsorption, and any two neighboring CO and O atoms react immediately (the adspecies are immobile). Also the model has been used in studies of the effect of adspecies clustering on the rate of each of the three-oxidation stages (a comparison with the chaotic reagents distribution) and that of the oxidation rate constant on the stationary coverages θ_{CO} and θ_O. The same reaction has been considered in Ref. [250] including an influence of the lateral interaction.

Some aspects of CO oxidation on the Pt surface have been studied in Refs. [251,252]. The computations performed [251] suggest the clustering of the CO molecules and the fact that the reaction rate is proportional to the island perimeter. The clustering increases a difference between the reaction

Lam Research Ex. 1035 - Page 434
Lam Research Corp. v. Inpria Corp.
IPR2024-00033 - U.S. Patent No. 9,823,564

rates computed by the MC method and the ideal model. Consideration [252] has been given to the formation of the Pt atoms islands as the surface passes from the hex to the 1×1 structure. The excess Pt atoms pass to the upper layer (over the (100) face) to form differently sized islands due to migration. The large islands appear only in the narrow temperature region since at the high temperatures the mean size of the islands is small and at the low temperatures the formation of large islands is prevented by kinetic hindrances.

7.2.2. Surface Diffusion and Phase Formation

The MC method has been applied in computing the concentration dependence of the surface diffusion coefficient [253]. The $D(\theta)$ curves have a symmetrical maximum at $\theta = 0.5$ that becomes more pronounced when considering the second-neighbors interaction. The computational results match qualitatively the experimental evidence O/W(110). For the same system at $T < T_c$, where T_c is the critical ordering temperature, a $c(2 \times 2)$ adspecies superstructure has been produced [254]. The dependence $D(\theta)$ at $\theta = 1/2$ has a sharply pronounced maximum. Analysis of the process leading to the formation of the $c(2 \times 2)$ phase due to the surface adspecies diffusion indicates [255] that at $T < T_c$ the phase grows as a result of a nucleation-type mechanism and the input of the material can be described by a diffusion equation. At $T > T_c$ the long-range order disappears but the short-range one remains intact, which promotes island formation at $\varepsilon(2) > 0$. Also, the process of establishing the long-range order due to domain coalescence with the ordered $c(2 \times 2)$ structure has been studied. The inclusion of the oxygen atom diffusion on the W(110) face points to the fact [256] that the displacement of the adspecies along the one-dimensional row of the tungsten atoms is much faster than that occurring transverse to it, and at $T < T$ and $\theta \sim 0.5$ there appears the $p(2 \times 1)$ phase. The dependence $D(\theta)$ can have three maxima.

More complex potential including pair and ternary interactions of the nearest neighbors has been used for analysis of oxygen and hydrogen [257]. For the oxygen atoms the computed data have been shown to coincide and for the hydrogen atoms not to coincide with the experiment, which in the latter case suggests the existence of a different jump mechanism. For the surface migration of the H, D, and T atoms toward W(100) the major role is played by the tunneling effect. Computations by the MC method allowing for the effect of the lateral interactions on the height of the activation barrier and its tunneling penetration have been performed by Tringides and Gomer [65].

Lam Research Ex. 1035 - Page 435
Lam Research Corp. v. Inpria Corp.
IPR2024-00033 - U.S. Patent No. 9,823,564

The competitive contributions of the surface inhomogeneity and the lateral interactions complicate determinations of each of them. Surface inhomogeneity depends on a number of factors, and their detailed characterization is related to the individual properties of the system under study. Thus, for the H/Ru (001) system analysis of the dependence $D(\theta)$ indicates [258] that the interactions of the adspecies play practically no role although the TDS evidence suggests the existence of a strong dependence of the effective activation energy with a coverage θ. In this case the most influential factor is represented by the non-equivalent distribution of the hydrogen atoms over three ruthenium atoms, depending on the presence or the absence of the ruthenium atom in the second surface layer.

The general analysis of the dependences $D(\theta)$ without lateral interactions on the inhomogeneous surfaces has been performed [259]. As θ grows, the random walk of the adspecies in the external field on a lattice with the chaotic sites distribution first causes their increasing and then (on further θ growth) decreasing active displacement. If the external field is absent or the number of traps is small, this effect is not observed. The dependence $D(\theta)$ has been computed for different fractions of the casually blocked regions and the variously distributed traps [259].

The phase conversions are mainly studied using the MC method. It allows to derive a wide range of domain characteristics such as their average size, perimeter and shape of the islands, the function of their distribution by size, etc., using various ways for changing the state of the system (adsorption, desorption, reactions, temperature variations, etc.) [260,261]. In studies of the phase formation processes the principal attention is paid to the late stages of domain growth. In this case the characteristic mean domain size L changes in time as $L \sim \tau^n$, and the main problem consists in finding a value of n and revealing the factors that affect this quantity. This value has been established in Ref. [262] depending on the process mechanism: $n = 0.35$ for Kawasaki dynamics and $n = 0.5$ for the Glauber dynamics whereas the analytical result [263] gives $n = 0.5$.

In studies of the (3×1) domain growth for the O/Pd(111) system (Kawasaki dynamics), considering the interaction anisotropy for all points of the phase diagram, it has been found in Ref. [264] that $n = 0.5$. The same result has been obtained later for the Glauber dynamics, as well [265]. Despite strong domain growth anisotropy in this system, the generalized anisotropic scaling is obtained rather accurately. A universal dependence $L \sim \tau^n$ for the two-dimensional Potts model (multicomponent systems, $s = 2$, 3, 4) has been derived [266]. The value $n \sim 0.46$ corroborates the feasibility of the dynamic generalization of the "weak universality" hypothesis proposed by Zuzuki [267].

Lam Research Ex. 1035 - Page 436
Lam Research Corp. v. Inpria Corp.
IPR2024-00033 - U.S. Patent No. 9,823,564

Interesting possibilities of studying the effect of the process mechanism on the n values have been considered [268]. It is taken that surface migration occurs through the preadsorption state, and adspecies migration from this state to the chemisorbed one depends on the local configuration of the chemisorbed adspecies. The n value has been found to depend on the adspecies transition from the preadsorbed to the chemisorbed state. If this rate is high, the n value approximates those typical of closed systems (the Kawasaki dynamics). For the low rate this value resembles those encountered in open systems (the Glauber dynamics) although the total number of adspecies remains the same. A modification of the computational model has been proposed in Ref. [269] for thermally excited processes using the MC method. The surface adspecies diffusion coefficients and the n values when the ordered domains grow have been computed.

7.2.3. Crystal Growth

The MC method has been widely applied to crystal growth studies [270–272]. The possibility of establishing various mechanisms of thin film growth has been discussed by Nieminen and Kaski [273]. In doing so, it is proposed to use the correlations between the time coverage dependences, root-mean-square deviations of the coverage, estimates of the number of the clusters in the substrate, and the pattern type for the various growth mechanisms. The computations take into account the effect of the substrate on the processes occurring in the overlying layers. Along with the layer-by-layer and the island-type mechanisms, the authors have managed to identify an intermediate multilayer growth process, which is interpreted as a kinetically limited case of the layer-by-layer growth.

The MC method has been actively used for Si films in describing the process of clustering and nucleation [274], thin film growth [275,276]), etching [277], etc. The effect produced by bombardment of the films with energetic Si atoms and Ar^+ ions on the structure of the resulting α-Si film has been treated [278]. The bombardment with these ions has been found to be responsible for the α-Si structure coalescence. The growth of the Si(100) crystal and its surface reconstruction in the course of the molecular-beam epitaxy have been studied [279]. The model accounts of the deposition of the Si atoms, their surface migration, formation, and reorientation of the surface Si dimers. The dimers have been shown to play an important role in determining the crystal growth nature. Conditions responsible for the surface roughness and formation of the ordered series of dimeric pairs

Lam Research Ex. 1035 - Page 437
Lam Research Corp. v. Inpria Corp.
IPR2024-00033 - U.S. Patent No. 9,823,564

have been established. An explicit consideration of the lattice anisotropy due to dimeric reconstruction [280] gives rise to a pseudobilayer growth mechanism.

The growth of the saturated and the unsaturated films in the Ising model has been discussed [281]. If the process starts with the oversaturated volumes, the film growth obeys completely the Lifshits–Slezov theory ($h \sim \tau^{1/3}$). In the unsaturated volume case the film thickness grows as τ^m, where m is the small value depending on the adsorbate – substrate interaction in the middle field regime and $m = 1/8$ in the fluctuation regime. On the large times the thickness approaches to the equilibrium values as $\tau^{-1/2}$.

7.2.4. Complex Processes

Now possibilities of the MC simulation allow to consider complex surface processes that include various stages with adsorption and desorption, surface reaction and diffusion, surface reconstruction, and new phase formation, etc. Such investigations become today as natural analysis of the experimental studying. The following papers [282–285] can be referred to as corresponding examples. Authors consider the application of the lattice models to the analysis of oscillatory and autowave processes in the reaction of carbon monoxide oxidation over platinum and palladium surfaces, the turbulent and stripes wave patterns caused by limited CO_{ads} diffusion during CO oxidation over Pd(110) surface, catalytic processes over supported nanoparticles as well as crystallization during catalytic processes.

These models consider the mechanisms of formation of oscillations: a mechanism involving the phase transition of planes Pt(100): (hex) (1×1) and a mechanism with the formation of surface oxides Pd(110). The models demonstrate the oscillations of the rate of CO_2 formation and the concentrations of adsorbed reactants. These oscillations are accompanied by various wave processes on the lattice that models single crystalline surfaces. The effects of the size of the model lattice and the intensity of CO_{ads} diffusion on the synchronization and the form of oscillations and surface waves are studied. It was shown that it is possible to obtain a wide spectrum of chemical waves (cellular and turbulent structures and spiral and ellipsoid waves) using the lattice models developed [283]. Also, the influence of the internal parameters on the shapes of surface concentration waves obtained in simulations under the limited surface diffusion intensity conditions has been studied [284]. The hysteresis in oscillatory behavior has been found under step-by-step variation of oxygen partial pressure. Two different oscillatory regimes could exist at one and the same parameters of the reaction. The parameters of oscillations (amplitude, period, and the

Lam Research Ex. 1035 - Page 438
Lam Research Corp. v. Inpria Corp.
IPR2024-00033 - U.S. Patent No. 9,823,564

shape of spatio-temporal patterns on the surface) depend on the kinetic prehistory of the system. The possibility for the appearance of the cellular and turbulent patterns, spiral, ring, and stripe oxygen waves on the surface in the cases under study has been shown [284].

An interpretation of the results for catalytic reaction kinetics on active supported nanoparticles on the scale down to ~10 nm has been obtained by the MC technique [285]. The technique allows the peculiarities of the reaction performance on the nanometer scale, including the inherent heterogeneity of metal crystallites as well as spontaneous and adsorbate-induced changes of the shape and degree of dispersion of supported catalysts.

7.3. CORRELATION BETWEEN MONTE-CARLO SIMULATIONS AND KINETIC THEORY

In the review information only about the first steps of MC simulation is given as today this method is dominant by comparison with the kinetic theory. The calculations based on the dynamic MC methods for the lattice-gas model are carried out using the master equation (24). The calculation results depend appreciably on the way of assigning the probabilities of transitions W_α. This was repeatedly pointed out in applying both the cluster methods (Section 3) and the MC method (see, e.g. Ref. [269]). Nevertheless, practically in all the papers of Section 7 the expressions (29) and (30) do not take into account the interaction between AC and its neighbors (i.e., the collision model was used). It means $\varepsilon_{ij}^*(r) = 0$, whereas analysis of the cluster simulations demonstrated important influence of the parameter $\varepsilon_{ij}^*(r)$ (that restricts obtained MC results).

In the beginning there were enough considerations about comparisons between MC and theory results. In the surface processes the concentration of the adspecies varies in wide ranges and in many situations the path of the concentration changes intersects of the regions of their different phases. Naturally, a problem arises as to the accuracy of the cluster methods that provide a rough description of the critical regions of the phase transitions in the description of the kinetic processes. The feasibility of such checking is ensured by correlating these methods with the MC approach. Such correlation has been made by many authors, and in this work one will limit with a few examples. It is natural that the correlation assumes the use of the same transition probabilities W_α in both methods.

The two methods have been shown to give the same general principles for the temporal evolution of the smeared adspecies profiles for the different interaction parameters [158] ($R = 1$, CM, QCA). However, there are some differences in the middle coverage region ($\theta \sim 0.5$). For $\varepsilon > 0$ the MC

Lam Research Ex. 1035 - Page 439
Lam Research Corp. v. Inpria Corp.
IPR2024-00033 - U.S. Patent No. 9,823,564

method gives a feeble minimum, which is absent in the QCA approach on the dependence $D(\theta)$. For the strong adspecies repulsion a numerical difference exists at $z = 2$. The results obtained by the MC method [158] agree well with those reported in Ref. [286]. In the disordered region the MFA and the MC methods give practically the same results, whereas in the region where the 2×1 adspecies structure is formed, which is distinguished by strong diffusion anisotropy, they show some differences. A similar conclusion follows from other works [287] ($R = 1$, QCA). A correlation of the analytical expressions reported by Loring et al. [288] with those produced by the MC method [259] for the diffusion of the non-interacting adspecies on an inhomogeneous lattice (part of the sites being blocked) also yields a high degree of accuracy.

A conclusion about a good agreement follows from the comparison of desorptions for the C_2N_2 molecules [243], obtained by these methods ($R = 1$) and for the irreversible adsorption of the dissociating diatomic molecules in the absence of the surface adspecies mobility [91] ($R = 1$). Note also that all features of the TDS computed by the QCA [114] and the MC [289] methods for any ε agree completely at $R = 1$. However, the effects of clustering or disordering deteriorate the agreement (*cf.*, e.g. Refs. [290,291]).

Comparison of the data obtained in the crystal growth studies using the MC method and in the solution of the kinetic equations indicates a satisfactory quantitative agreement [272,292]. Such an agreement relates not only to one crystallization characteristic (dependence of the growth rate on temperature, surface roughness, concentration profile of the transition region, etc.) but to their combination, as well. The same is true of the appearance of the kinetic phase diagrams. Note that a good correlation has been obtained with the use of the QCA approach only. Similar computations with the kinetic MFA equations ensure but a qualitative agreement since the numerical values show fairly large differences. Nevertheless, a satisfactory correlation between the MFA and the MC methods have been observed in nucleation and growth (at $d = 2$) studies in a system with two stable phases [293].

Let us discuss in more detail the reason for differences in the computational results obtained by the MC methods in the case of the first- and the second-order transitions. In all such comparisons formulas has been used considering the non-ideality of the system but ignoring changes in the type of an adspecies distribution characteristic of a given phase transition. In the first- and the second-order transitions the system becomes macro- and microinhomogeneous, respectively. Therefore, if this factor is ignored, the results obtained by the equations for homogeneous surfaces cannot be compared with those derived by the MC method. Thus, considering the existence of different adspecies phases is expected to markedly diminish a

Lam Research Ex. 1035 - Page 440
Lam Research Corp. v. Inpria Corp.
IPR2024-00033 - U.S. Patent No. 9,823,564

discrepancy between the dynamic characteristics computed by the cluster and the MC methods in the entire concentration region except for the critical ones. To improve the theory within critical areas, the scaling theory and, in particular, the RSRG method have to be used [294]. Also in papers [295,296] an alternative method, based on the exact statistical results, has been suggested.

Moreover, as the system of Eq. (24) is a starting point for the cluster-type approach and the MC method, therefore in principle the two methods can be used in combination. It has been proposed by Hood et al. [297] to write down the kinetic equations for describing variations in the occupancy state of each lattice site, i.e., to abandon consideration of the lattice ensemble, and to solve the system of the equations with the dimension equal to the number of sites. The system of the connected equations has been solved numerically. In each time interval the desorption probability for a given molecule is determined by the random sampling and then the general adsorbate change found. The combination approach allows to trace the adlayer structure and to construct a correlation between the structural and the kinetic behavior of the process. Such an approach has been applied to the N_2/Ru(001) system to obtain a qualitative agreement with experiment [298].

Another alternative for the combination utilization of the MC and the cluster methods has been proposed by Silverberg and Ben-Shaul [291,299]. If the mobilities of the different adspecies are very much dissimilar, the rejection procedure in the standard MC method becomes little efficient and the computations take a lot of time. Therefore, to save time, the slow phases have been proposed to be described by the MC and the fast ones by the cluster method ($R = 1$, TSM).

Although very often one can conclude that the MC method allows to obtain exact solutions, nevertheless it does not eliminate incorrect results, either. Thus an additional peak has been observed between two ''main'' peaks in the ordering region on the TDS curve with the use of this method [300], which is absent if the equations reported in other work [301] are used. The peak is attributed to the absence of an equilibrium distribution of the adspecies within the adlayer (the phenomenon of metastability). The absence of such a peak has been confirmed by computations using the transition matrix technique [302].

Similarly, the computational results obtained by the MC method [266] do not provide support for the already found dependence of the index n in equation $L \sim \tau^n$ on the number of the system's components ($s > 2$, MC) [303].

On heterogeneous surfaces, the probability of metastable states increases due to local inhomogeneities. Therefore, the adsorption parameters calculated by MC should be always checked against the results obtained by other methods.

Lam Research Ex. 1035 - Page 441
Lam Research Corp. v. Inpria Corp.
IPR2024-00033 - U.S. Patent No. 9,823,564

A practical cause for all MC incorrect results is not enough due to statistics for averaging that overestimate the different non-equilibrium states during dynamic processes. However this question, as a rule, is not discussed for multistages processes because of the absence of standard reliable data that could be obtained only by the kinetic theory.

8. Summary and Perspectives

The development of the kinetic theory made it possible to obtain a solution of the problem on the self-consistent description in time and in an equilibrium state of the distributions of interacting species between the sites of homogeneous and inhomogeneous lattices. This enables one to solve a large number of matters in the practical description of processes at a gas–solid interface. The studied examples of simple processes, namely, adsorption, absorption, the diffusion of particles, and surface reactions, point to the fundamental role of the cooperative effects due to the interaction between the components of the reaction system in the kinetics of these processes.

Non-ideal models of surface processes made it possible to explain the following facts:

(1) Splitting of the TDS for homogeneous surfaces as a result of repulsion of the nearest chemisorbed particles.
(2) The empirical laws of adsorption processes of Becker–Langmuir, Roginsky–Zeldovich, and Benham–Barta–Kwan, but unlike these laws, the constructed models also describe the processes correctly when $\theta \to 0$ and when $\theta \to 1$.
(3) The varying order of magnitude of the rate of desorption including its zero value that is associated with the existence of two or more phases of the adsorbed molecules on a surface.
(4) An increase in the sticking probability of adsorbed particles with a growth in the coverage at low coverages of a surface.
(5) The phenomenon of adsorbed particle ordering and the change in the rates of the surface processes in ordered systems; the relation of the characteristics of these processes to data on low-energy electron diffraction.
(6) Jumps, breaks, and peak-like behavior of the concentration dependences of the diffusivity in structural phase transitions.
(7) The negative values of the diffusivities in processes of particle aggregation and a change in the rates of processes under conditions of stratification of the adsorption system.

Lam Research Ex. 1035 - Page 442
Lam Research Corp. v. Inpria Corp.
IPR2024-00033 - U.S. Patent No. 9,823,564

(8) The strong mutual influence of adsorbed particles of various species on the rates of elementary processes.
(9) The dependence of the kinetic characteristics of processes on the conditions of formation of the initial states of the reaction system (on a prehistory of the system).
(10) The plurality of steady states of the reaction systems and isothermal self-oscillating modes of proceeding of reactions. And so on.

It is quite natural that in more involved processes too the role of the cooperative effects is substantial, and they must be considered correctly. As a result of employing the molecular-kinetic theory of processes in condensed phases it is necessary that all the real properties of a system would "appear" in a natural way on the basis of knowledge of the potentials of interaction between particles.

The theory of surface processes constructed on the basis of the cluster approach considers all the indicated factors. It uses a common principle for describing all the components of a system, namely, the adsorbed particles and particles (atoms or ions) of the solid. The distinctions associated with the nature of the various components are reflected only in the energies of their interactions with the other components. This manifests itself in their rate constants of migration and chemical transformation (in terms of the energies of interaction of the elementary processes) that are traditionally considered in ideal models, and in taking account of the contributions resulting from the non-ideal nature of the reaction system.

The general circle of kinetic models of an atomic and molecular level covered by the theory reflects the basic factors of experimental systems: interactions between particles and the state of aggregation of the components, surface inhomogeneity, a different mobility of the particles, and reorganization of the subsurface region of a solid, as well as prehistory properties of the experimental system (the shape and size of spatio-temporal distribution of the reagents along the surface) and how they change during the considered processes. The models of a molecular level operate with the states of occupancy of individual sites, and the phase, a site belongs to, must be determined additionally from macroscopic conditions. It should be noted that the form of the systems of kinetic equations, in addition to the indicated factors, depends on the approximations used to consider interaction and on the interaction potential.

Equations of the kinetic theory make it possible to describe processes of particle redistribution between the layers of the subsurface region and of the change in their state of aggregation in each layer. This reflects most of the possible mechanisms of the reorganization processes, including the change in the structure (symmetry) and the lattice parameters (recall that the

Lam Research Ex. 1035 - Page 443
Lam Research Corp. v. Inpria Corp.
IPR2024-00033 - U.S. Patent No. 9,823,564

equations are constructed on an arbitrary type of inhomogeneous lattices). It is natural that subsequently the models describing processes on non-reorganizing inhomogeneous and on reorganizing surfaces will acquire widespread application. The same can be said with respect to the joint consideration of various real factors and their applications to multistep processes, including practically important catalytic processes, because matters relating to the change in the activity of catalysts (thermal stability, sintering, poisoning, etc.) can be investigated on their basis. Close problems arise when studying the nature of the surface segregation of alloys in vacuum and in the gas phase, in the growth of crystals from the gas phase and their sublimation, in the formation and removal of protective films, in etching of a surface and acting on it with streams of particles varying in energy and so on.

In addition to a broad range of applied questions, the set out theory of processes at a gas–solid interface contains great "internal" reserves.

The more accurate consideration of the correlation effects also plays an important role in the kinetics of elementary processes. It is reasonable to note the possibility of the correlated appearance of "ACs" of a reaction in the critical and subcritical regions. It was shown [304] that the consideration of such correlation gives a different value for the rate of a reaction. This situation is not unexpected. Though traditionally every elementary process is described independently of other elementary processes, the fact of conjugated chemical transformations is well known [48,305,306].

This phenomenon is explained for gases by the presence of intermediate compounds formed during the main reaction that stimulate accompanying reactions [305]. In a condensed phase, conjugation effects are possible as a result of the particle interaction when a particle passes from the ground state to a transition one, and their role can be quite appreciable. General expressions have been obtained for the rates of reactions on homogeneous and inhomogeneous surfaces for rapid mobility of the reactant when correlation between the ACs has been taken into account [58,80,89]. Such effects may cause local heating in highly exothermal reactions.

More accurate consideration of the geometry of the bond between adsorbed particles and atoms of the solid was in the development of the theory [307]. Here questions appear as to how to consider the orientation of the adsorbed particles (this problem is solved by a method described herein if each orientation of the particles is characterized by its own molecular parameters and is treated as a separate species of particles) and the blocking by large particles of several surface atoms.

A close but still more involved problem appears if an adsorbed particle and surface atoms are considered to form several types of adsorption centers (several localization regions at distances of the order of the lattice constant).

Lam Research Ex. 1035 - Page 444
Lam Research Corp. v. Inpria Corp.
IPR2024-00033 - U.S. Patent No. 9,823,564

Quantum-chemical calculations make it possible to specify these types of adsorbent–adsorbate bonds more precisely. For instance, on the faces (100) and (111) of single crystals, three types of bonds are singled out that differ in the arrangement of an adsorbed particle: (1) a particle over an atom of the solid; (2) a particle over the bond between adjacent atoms; and (3) a particle over an interstice of atoms of the solid. The coexistence of adsorbent–adsorbate bonds is considered by a transition to an auxiliary inhomogeneous lattice whose constant is smaller than that of the lattice of the solid's atoms and to the distribution thereon of larger particles.

It also seems natural to reject the traditional assumption in the kinetics of surface processes that all the parameters of particle interaction in the system adsorbed particles-atoms of the solid do not depend on their internal degrees of freedom. Account of the indicated relation leads to a temperature dependence of the interaction parameters [308], which corresponds to a real situation.

Finally, the considered theory can be generalized for charged adsorbed or absorbed particles and the redistribution of the charges in the solid associated with their presence. Consideration of the charges requires the addition of equations relating to the distribution of the charges to the constructed systems of equations for the distribution functions and their simultaneous solution. Though the mathematical difficulties involved in solving such a problem grow quite appreciably, the theory can have a great significance for describing processes on the surfaces of many insulators and semiconductors.

Appendix A. Equilibrium Distributions of Particles on Heterogeneous Lattices in Condensed Phases

If N_a molecules distributed over N surface sites, are at equilibrium, their normalized distribution function is specified as [80,309,310]

$$\theta_N^k(\{\gamma_f^i\}) = \frac{1}{Q}\exp[-\beta E_k(\{\gamma_f^i\})], \qquad Q = \sum_{k=1}^{\mathrm{B}} \exp[-\beta E_k(\{\gamma_f^i\})], \tag{A.1}$$

where k labels some specific configuration of N_a molecules on the surface; this configuration is defined by a list of adsorption statuses γ_f^i, $1<f<N$; $\beta = (k_{\mathrm{B}}\mathrm{T})^{-1}$; i is the molecule type, $1 \le i \le s$ (s is the number of different adsorption statuses); $\gamma_f^i = 1$, if a site is occupied by a molecule of the ith type, otherwise $\gamma_f^i = 0$; $E_{\mathrm{k}}(\{\gamma_f^i\})$ is the total energy of the system with configuration k (the total number of configurations equals $B = s^N$); Q is the

Lam Research Ex. 1035 - Page 445
Lam Research Corp. v. Inpria Corp.
IPR2024-00033 - U.S. Patent No. 9,823,564

partition function of the system;

$$E_k(\{\gamma_f^i\}) = E_k^1(\{\gamma_f^i\}) + E_k^2(\{\gamma_f^i\}), \quad E_k^1(\{\gamma_f^i\}) = -\sum_{f,i} \beta^{-1} \ln(a_f^i p_i)^{1/m_i}$$
$$E_k^2(\{\gamma_f^i\}) = \frac{1}{2} - \sum_{f,g} \sum_{i,j} \varepsilon_{fg}^{ij}(r), \quad a_f^i = \frac{1}{F_i^0}(F_f^i)^{m_i} \beta \exp(\beta Q_f^i). \tag{A.2}$$

Here $E_k^1(\{\gamma_f^i\})$ stands for the single-particle contribution to the total energy, allowing for molecule interaction with the surface; Q_f^i is the heat released in adsorption of molecules i on the fth site; F_f^i the internal partition function for the ith molecules adsorbed on the fth site; F_i^0 the internal partition function for the ith molecule in the gas phase; m_i the dissociation degree of the ith molecule, and a_f^i the Henry local constant for adsorption of the ith molecule on the fth site. Lateral interaction is modeled by $E_k^2(\{\gamma_f^i\})$, and $\varepsilon_{fg}^{ij}(r)$ allows for interaction between the ith and jth particles adsorbed on the fth and gth sites spaced r apart. In the lattice gas model, separations are conveniently measured in coordination-sphere numbers, $1 \leq r \leq R$. For a homogeneous surface, molecular parameters a_f^i and $\varepsilon_{fg}^{ij}(r)$ are independent of the site nature, while for heterogeneous, they may depend on it.

Cluster Methods

The main idea of the cluster method (CM) lies in the analysis of local configurations of molecules on some "central" surface fragment and its surroundings. The entire surface is divided into three domains, central domain (incorporating the central cluster), intermediate one (involving the nearest surroundings of the central cluster) of width R, and the other surface that does not interact with the central molecules. The central domain is commonly chosen to include one or two sites. The probability of configuration, such that the central sites of the cluster are in state k_c and the surroundings, in state k_s, is given in the CM by expression

$$\theta(k_c, k_s) = \frac{1}{Q} \text{const}(k_0) \exp[-\beta E(k_c, k_s)]. \tag{A.3}$$

In this formula $E(k_c,k_s)$ is the total energy of the central cluster, comprises single-particle contributions of the central molecules and their later interactions with one another and with the molecules of the surroundings. These contributions are specified by the appropriate terms in Eq. (A.2) where subscript f pertains to the central sites of the cluster, and g to the sites interacting with the central sites (interaction of the central sites with one another is also taken into account, if of course, their number is ≥ 2). Quantity const k_0, in Eq. (A.3) is independent of the central cluster state,

Lam Research Ex. 1035 - Page 446
Lam Research Corp. v. Inpria Corp.
IPR2024-00033 - U.S. Patent No. 9,823,564

which in fact enables one to eliminate unknowns Q and const k_0, from Eq. (A.3) and to relate $\theta(k_c,k_s)$ to energies $E(k_c,k_s)$. To do this, it is necessary to specify Eq. (A.3) at different k_s, for every k_c. Finally, one obtains an exact, yet, non-closed set of equations for the functions appearing in Eq. (A.3). Then all surface sites are sequentially treated as central, and the sets of equations for all sites are closed in some unique manner to obtain a unique set of equations for the entire surface. This method describes any type of surface inhomogeneity [80,309,310].

When deducing approximations it is important to account for (a) correlation between laterally interacting molecules and (b) the effect of surface site disposition on the distribution of these molecules. The first factor appears in many-body problems, while the second is inherent solely in heterogeneous systems. Pair distribution functions fail to account for the surface topology accurately, and therefore it was suggested to use the cluster distribution functions and divide heterogeneous surfaces into fragments. The cluster method simulates the local lattice topology at $r < R$ more or less adequately, however, at $r > R$, the lattice connectivity is lost completely. When a surface is modeled by a fragment, the lattice topology within the fragment is described adequately, however, the fragment size is limited by the available means of solving a huge closed set of equations in one or another approximation (say, quasi-chemical or mean field). A fragment may incorporate hundreds or thousands of sites that reflect many types of heterogeneous surfaces.

ISOTHERMS OF ADSORPTION

The concentration of molecules is usually assumed to equal the number of these molecules N_i in unit volume, $c_i = N_i/V$. In the lattice-gas model, the concentration of the component i is characterized by the $\theta_i = N_i/N$ value, which is the ratio between the actual number of particles in some volume and the maximum possible number of the same particles closely packed in the same volume. So, one then has $\theta_i = c_i\, v_0$, where $v_0 = V/N$.

The local density of particles i in cell f will be denoted by θ_f^i. Obviously,

$$\sum_{i=1}^{s-1} \theta_f^i + \theta_f^s = 1. \tag{A.4}$$

The average partial fluid concentration θ_i and the total average system filling θ can be written in terms of local concentrations as

$$\theta_i(\{P\}) = \sum_{f=1}^{t} F_f \theta_f^i(\{P\}), \quad \theta(\{P\}) = \sum_{i=1}^{s-1} \theta_i(\{P\}), \tag{A.5}$$

Lam Research Ex. 1035 - Page 447
Lam Research Corp. v. Inpria Corp.
IPR2024-00033 - U.S. Patent No. 9,823,564

where F_f is the fraction of sites of type f. The $\{P\}\equiv P_1, \ldots, P_{s-1}$ symbol is used to denote the set of all partial pressures of mixture components P_i, $1 \le i \le s-1$. Every cell f is characterized by its own interaction energy Q_f^i between molecules of kind i and surface site f and, accordingly, its own Henry constant a_f^i. All lattice sites can be divided into groups with equal properties according to this parameter. The number of such groups will be denoted by t. The local Henry constant is $a_f^i = a_f^{i0}\exp(\beta Q_f^i)$, where $\beta = (kT)^{-1}$ and $a_f^{i0} = \beta F_i/F_i^0$, here a_f^{i0} is the preexponential factor of the Henry constant; F_i and F_i^0 are the partition functions of molecules i in the lattice system and outside it (in the gas phase), respectively; $1 \le f \le t$.

The normalization condition for sites of various types has the form

$$\sum_{f=1}^{t} F_f = 1. \tag{A.6}$$

The local partial adsorption isotherms $\theta_f^i(\{P\})$ of various adsorption centers, which are needed for Eq. (A.5), are calculated by the system of equations from Refs. [80,89]. These equations take into account energetic non-uniformity of lattice sites and intermolecular interactions at a distance of R c.s.,

$$a_f^i P_i = \frac{\theta_f^i \Lambda_f^i}{\theta_f^v} \tag{A.7}$$

Here the Λ_f^i function describes non-ideality of the adsorption system; the quasi-chemical approximation (QCA)

$$\Lambda_f^i = \prod_r \prod_g \left(1 + \sum_{j=1}^{s-1} x_{fg}^{ij}(r) t_{fg}^{ij}(r)\right)^{z_{fg}(r)}, \quad x_{fg}^{ij}(r) = \exp(-\beta\varepsilon_{fg}^{ij}(r)) - 1, \tag{A.8}$$

the chaotic approximation

$$\Lambda_f^i = \prod_r \prod_g \left(1 + \sum_{j=1}^{s-1} x_{fg}^{ij}(r)\theta_g^j(r)\right)^{z_{fg}(r)}, \tag{A.9}$$

and

the mean field approximation (MFA)

$$\Lambda_f^i = \exp\left\{-\beta \sum_r \sum_g z_{fg}(r) \sum_{j=1}^{s-1} \varepsilon_{fg}^{ij}(r)\theta_g^j(r)\right\}. \tag{A.10}$$

where $z_{fg}(r)$ is the number of neighboring sites in layer g at distance r from the site under consideration f. It indicates that the lateral interaction

Lam Research Ex. 1035 - Page 448
Lam Research Corp. v. Inpria Corp.
IPR2024-00033 - U.S. Patent No. 9,823,564

parameter $\varepsilon_{fg}^{ij}(r)$ between neighboring molecules i and j separated by r c.s. may be a function of temperature and local composition around sites f and g, whereas interactions of all molecules ($i = s-1$) with vacancies ($j = s$) as well as between vacancies ($i, j = s$) are zero. Index g runs over all neighbors $z_f(r)$ of site f at distance $r \leq R$ within the pore, where R is the radius of the interaction potential.

The $t_{fg}^{ij}(r) = \theta_{fg}^{ij}(r)/\theta_f^i$ functions in QCA describe the conditional probabilities of the presence of a neighboring particle j in a site of type g at distance r from the central particle i in a site of type f, whereas the $\theta_{fg}^{ij}(r)$ functions describe similar full probabilities. These last functions satisfy the equations

$$\theta_{fg}^{ij}(r)\theta_{fg}^{ss}(r) = \theta_{fg}^{is}(r)\theta_{fg}^{sj}(r)\exp[\beta\varepsilon_{fg}^{ij}(r)], \tag{A.11}$$

which are solved using the normalization conditions

$$\sum_{j=1}^{s}\theta_{fg}^{ij}(r) = \theta_f^i, \quad \sum_{i=1}^{s}\theta_{fg}^{ij}(r) = \theta_g^j, \tag{A.12}$$

together with the Eq. (A.4).

The equilibrium distribution of particles over sites of various types was found from system (A.4)–(A.12) by any iterative method (as rule, the Newton method is preferable) for selected $\{\theta_i\}$ or $\{P_i\}$ sets.

MULTIPARTICLES CONFIGURATIONS

Expressions for the probabilities of multiparticle configurations through the lower correlations are written as the QCA

$$\theta_{f(g_1\cdots g_z)^R}^{i(j_1\cdots j_z)^R} = \theta_f^i\prod_{r=1}^{R}\prod_{g=1}^{z}\prod_{j=1}^{s}[t_{fg}^{ij}]^{n_{fg}^j(r)}, \tag{A.13}$$

where the functions θ_f^i and $t_{fg}^{ij}(r) = \theta_{fg}^{ij}(r)/\theta_f^i$ are determined from a solution of the system of Eqs. (A.7), (A.8), (A.11), (A.12), here $1 \leq i$ and $j \leq s$, $1 \leq r \leq R$; the under symbol $f(g_1 \ldots g_z)R$ denote full list of the sites on the heterogeneous lattice with the fixed arrangements of all sites within R c.s. around of the central site f (the cluster $f(g_1 \ldots g_z)R$); the upper symbol $(j_1 \ldots j_z)R$ denote full list of the species on the given cluster $f(g_1 \ldots g_z)R$ of the heterogeneous lattice around of the central species i; $n_{fg}^j(r)$ is the number of species j on pairs of types fg at distance r in the rth c.s.around central species i, where $\sum_{j=1}^{s} n_{fg}^j(r) = z_{fg}(r)$; the mean field and chaotic

Lam Research Ex. 1035 - Page 449
Lam Research Corp. v. Inpria Corp.
IPR2024-00033 - U.S. Patent No. 9,823,564

approximations

$$\theta^{i(j_1\cdots j_z)^R}_{f(g_1\cdots g_z)^R} = \theta^i_f \prod_{r=1}^{R} \prod_{g=1}^{z} \prod_{j=1}^{s} [\theta^j_g]^{n^j_{fg}(r)} \tag{A.14}$$

Free Energy

Free energy of multicomponent mixture at equilibrium distribution in the QCA is in the following form:

$$F = \frac{1}{N} \sum_{f=1}^{N} \sum_{i} M^i_f \theta^i_f = \sum_{f=1}^{t} \sum_{i} F_f M^i_f \theta^i_f \tag{A.15}$$

$$M^i_f = v^i_f + \sum_{r=1}^{R} \sum_{g_r} \varepsilon^{ii}_{fg}(r) t^{ii}_{fg}(r) + \beta^{-1} \ln \theta^i_f - \frac{1}{2} \beta^{-1} \sum_{r=1}^{R} \sum_{g_r} Ln \left(\frac{\theta^{ii}_{fg}(r) \theta^{ik}_{fg}(r)}{(\theta^i_f)^2 \theta^{ki}_{fg}(r)} \right). \tag{A.16}$$

Monte-Carlo Method

MC method admits of studying surface fragments with the number of sites N_{MC} ranging from 10^4 to 10^7. Even though this number is far from macroscopic, it is large enough to provide for reasonably accurate results. At the aforesaid values of N_{MC}, many types of heterogeneous surfaces are simulated adequately.

Matrix Method

For simplicity, hereinafter one considers single-component adsorption where $s = 2$, $i = \mathrm{A}$ (a site is occupied), $i = v$ (a site is free), and $a^v p_v = 1$. The matrix method (MM) [17,19] may serve to either confirm or impugn the results obtained by MC. MM is based on a generally plausible assumption that the surface fragment with N_{MM} sites can recur periodically along some direction. The MM analog of partition function (A.1) is

$$\begin{gathered} Q = \sum_{\delta_1} (P_{\delta_1 \delta_1})^m = Sp(P_{\delta_1 \delta_1})^m, P_{\delta_k \delta_{k+1}} = \exp[-\beta(E_{\delta_k} + E_{\delta_k \delta_{k+1}})], \\ E_{\delta_k} = -\sum_{f,i} \beta^{-1} \ln(a^i_f p_i)^{1/m_i} - \tfrac{1}{2} \sum_{f,g} \sum_{i,j} \varepsilon^{ij}_{fg}(r), E_{\delta_k \delta_{k+1}} = -\tfrac{1}{2} \sum_{f,g} \sum_{i,j} \varepsilon^{ij}_{fg}(r), \end{gathered} \tag{A.17}$$

where δ_i is the number of the configuration of the kth fragment; $P_{\delta_k \delta_{k+1}}$ the matrix element of the transition between configurations of recurring

Lam Research Ex. 1035 - Page 450
Lam Research Corp. v. Inpria Corp.
IPR2024-00033 - U.S. Patent No. 9,823,564

fragments, each involving $L = N/m$ rows (m is the number of recurring fragments in a strip containing N sites; in the macroscopic limit, $m \to \infty$). At $s = 2$, the number of configurations equal $B = 2^N$, $1 \leq \delta_k \leq B$, and $\delta_{m+1} = \delta_1$. Symbol $\mathrm{Sp}P^m$ signifies the sum of diagonal elements of the transition matrix, raised to the power of m, E_{δ_k} is the total energy of the kth fragment having configuration δ_k, subscripts f and g number the sites of the kth fragment; $E_{\delta_k \delta_{k+1}}$ is the energy of lateral interaction between molecules residing at the adjacent sites k (subscript f) and $k+1$ (subscript g) with configurations δ_k and δ_{k+1}. The MM accounts for both inhomogeneity of surface sites and lateral interaction of adsorbate molecules. The ways of solving this problem are considered in Ref. [310] as the number of configurations B rapidly increases with the fragment size, which considerably complicates calculation of the maximum eigenvalue of the transition matrix.

To refine calculations of adsorption on heterogeneous surfaces with different topologies some enhancing capabilities of the matrix technique was suggested by paper [310]. One has to (a) widen the range of topologies adequately described by MM and (b) elucidate whether the correlation effects taken into account in the method of fragments (MFs) are sufficient. Early desorption rates were calculated in Ref. [302] by MM, assuming that interaction between the AC and the neighboring molecules was negligibly weak. Actually it was a limitation by the collision model for the desorption rate as the energy $\varepsilon_{fg}^{ij*}(r) = 0$. There is no such a constraint in CM. The modifications of the MM capabilities: widening of heterogeneous – system range to which MM applies, removing the restrictions from $\varepsilon_{fg}^{ij*}(r) = 0$, and increasing the fragment size by combining MM with CM, were performed [309,310].

METHOD OF FRAGMENTS

An alternative approach for surface fragments larger than in MM, which accounts for correlation effects more accurately than CM (MFs) was suggested [310]. This method rests on the CM concepts of fragments, and therefore, is called here the MFs. MF was intended to eliminate the necessity for using approximations when closing the set of equations for cluster functions (A.3). At $\mathrm{const}(k_0) = 1$ in Eq. (A.3), the probability to find the ith configuration of molecules on the fragment assumes the form $\theta_i = \exp(-\beta E_k)/Q$, where E_k is the total energy of molecules to be calculated from Eq. (A.2) where f and g label the sites of the fragment. At $\mathrm{const} = 1$, two situations are possible: (a) a given fragment has fixed surroundings and, in particular, it breaks all bonds linking it to the lattice

Lam Research Ex. 1035 - Page 451
Lam Research Corp. v. Inpria Corp.
IPR2024-00033 - U.S. Patent No. 9,823,564

and (b) the adsorption statuses of the surrounding sites are related to those of the central sites by the periodic boundary conditions. In case (b), the fragment simulates a macroscopic surface with periodic topology (there are N/N_f fragments on the surface, where N_f is the number of sites on the fragment). A fragment may have an arbitrary internal topology. If every configuration of molecules on a surface fragment is brought in correspondence with some type of a quasi-particle, denoted by $k(k \leftrightarrow \{\gamma_f^i\})$ the full configuration spectrum may be treated as a mixture of quasi-particles (the number of quasi-particle types equals $B = 2^{N_f}$). The quasi-particle concentration can be specified as

$$\theta_k = \left[\sum_{n=1}^{B} \exp\{\beta[E_n - E_k]\}\right]^{-1}, \quad \sum_{k=1}^{B} \theta_k = 1. \tag{A.18}$$

This implies that the mixture of quasi-particles is ideal, and all thermodynamic and kinetic functions are calculated by the equations for ideal mixtures. Probabilities of any local configurations of adsorbed molecules $\theta([\gamma_f^i])$ (where $i_1 \ldots i_m$ are the adsorption statuses of m sites $f_1 \ldots f_m$, of the fragment; $m \leq N_f$) are calculated from total probabilities (A.18) by summing over adsorption statuses of the other sites ($h_1 \ldots h_p$, $m+p = N_f$) of the fragment. Denoting the number of occupied sites with the kth configuration by n_k the probability of totally occupied surface assumes the form [309–312]

$$\theta = \sum_{k=1}^{B} n_k \theta_k. \tag{A.19}$$

The method yields an exact solution to the problem on adsorbed – molecule distribution over a finite number of fragment sites. The maximum number of surface sites is limited from above and equals the number of fragment sites. A full set of topologies of a given fragment consists of all possible arrangements of dissimilar sites.

Appendix B. Lowering the Dimension of a System of Equations in the Quasi-Chemical Approximation

A closed system of equations in the quasi-chemical approximation consists of next equations relative to the functions θ_f^i and $\theta_{fg}^{ij}(r)$, where $1 \leq i$ and $j \leq s$:

$$\theta_{fg}^{in}\theta_{fg}^{vv} = \theta_{fg}^{iv}\theta_{fg}^{vn} \exp[-\beta\varepsilon_{fg}^{in}(r)], \quad 1 \leq r \leq R, \tag{B.1}$$

Lam Research Ex. 1035 - Page 452
Lam Research Corp. v. Inpria Corp.
IPR2024-00033 - U.S. Patent No. 9,823,564

$$\sum_{j=1}^{s} \theta_{fg}^{ij}(r) = \theta_f^i, \quad \sum_{i=1}^{s} \theta_f^i = 1. \tag{B.2}$$

This system describes the particle distribution for considering the interaction of the given number of neighbors R on inhomogeneous and homogeneous (at $\theta_{fg}^{ij}(r) = \theta_{ij}(r)$ and $\theta_f^i = \theta_i$) lattices.

An increase in the number of components of a system raises the dimension of the system of equations. The number of equations for θ_f^i grows linearly with increasing s, while that of the equations for two-body functions $\theta_{fg}^{ij}(r)$ even for a homogeneous lattice at $R = 1$ increases as $s(s-1)/2$. A growth in R and in the number of site types in a lattice increases the dimension of a system of equations still more.

It was already noted in early publications [165,184] (similar procedure is traditionally used in the QCA for describing various properties: thermodynamic, phase interfaces, diffusion processes, kinetics of reactions) that for $R = 1$ the dimension of a system of equations can be lowered sharply if one goes over from equations in the variables θ_i and θ_{ij}, to new variables X_i with the aid of the following relation:

$$\theta_{ij} = a_{ij} X_i X_j, \quad a_{ij} = \exp(\beta \varepsilon_{ij}). \tag{B.3}$$

In this case Eq. (B.1) transform into identities $1 \equiv 1$. Then instead of the functions θ_i, the functions X_i are the unknown ones. Their number is s, i.e., the same as in the mean field approximation or in the absence of interaction. If the quantities θ_{i} are considered to be given

$$\theta_i = X_i \sum_{j=1}^{s} a_{ij} X_j, \tag{B.4}$$

the unknown X_i's are found by solving the system of Eq. (B.4). In the general case, the choice of the coefficients a_{ij} is ambiguous, e.g., $a_{ij} = \exp(\beta \varepsilon_{ij}/2)$.

The condition of normalizing the functions θ_i enables us to express one of them in terms of the others, i.e., in terms of the functions θ_i the system of equations has the dimension $(s-1)$. A similar lowering of the dimension of a system is also possible for the system (B.4), if from the functions X_i one goes over to the functions

$$Y_i = a_{is} X_i \Big/ \sum_{j=1}^{s} a_{js} X_j \tag{B.5}$$

or to the functions

$$Y_i^* = X_i / X_s. \tag{B.6}$$

Lam Research Ex. 1035 - Page 453
Lam Research Corp. v. Inpria Corp.
IPR2024-00033 - U.S. Patent No. 9,823,564

The replacement of the variables in (B.5) is symmetrical relative to the values of the quantities X_i, but leads to cumbersome expressions. The asymmetry of the replacement in (B.6) yields unnormalized values of the functions Y_i^*, but leads to simpler equations. Its use is preferable if it is known that the concentration of the component s (vacant surface sites or a "solvent" in a solution) is not very small. As a result, the system of equations with the dimension $s(s+1)/2$ is reduced to the system of equations of the dimension $(s-1)$.

In the general case, the structure of Eq. (B.1) also makes it possible to substantially lower the dimension of the system of equations to $(s-1)Rt$, where R is the interaction radius and t is the number of site types. This is achieved by converting the system of equations for the two-body functions into the identities $1 \equiv 1$ with the aid of the substitution

$$\theta_{fg}^{ij}(r) = a_{fg}^{ij}(r) X_f^i(r) X_g^j(r), a_{fg}^{ij}(r) = \exp[\beta \varepsilon_{fg}^{ij}(r)]. \tag{B.7}$$

Here the new variables $X_f^i(r)$, where $1 \leq i \leq s$ and $1 \leq q \leq t$, are determined by solving the isothermal equations of system or by solving the following system of equations

$$\theta_f^i = X_f^i(r) \sum_{j=1}^{s} a_{fg}^{ij}(r) X_g^j(r). \tag{B.7a}$$

The further lowering of the dimension of a system of equations is associated with the natural generalization of expressions (B.5) and (B.6):

$$Y_f^i(r) = a_{fg}^{is}(r) X_f^i(r) / \sum_{j=1}^{s} a_{fg}^{is}(r) X_g^j(r), \quad Y_f^i(r)^* = X_f^i(r) / X_f^s(r). \tag{B.8}$$

In conclusion it should be noted that the indicated lowering of the dimension of the system of equations in the quasi-chemical approximation can be used not only in problems describing the equilibrium and kinetics of surface processes for the rapid surface mobility of particles in steady-state conditions, but also in non-steady conditions. In the latter case, the derivatives of the functions $Y_f^i(r)$ or $Y_f^i(r)*$ on the left-hand sides of the equations are linearly related to one another, and for integration of the system of equations with respect to time they must be determined preliminarily from the relevant system of equations. Notwithstanding this circumstance, the indicated replacement of the variables noticeably diminishes the calculation difficulties in solving the problem.

Lam Research Ex. 1035 - Page 454
Lam Research Corp. v. Inpria Corp.
IPR2024-00033 - U.S. Patent No. 9,823,564

Problems

The questions below will help to the reader to fix the facts of this chapter.

(1) What conditions are taken into consideration while deriving equations for the chemical kinetics of non-ideal reaction systems (the law of acting masses)?
(2) Show that the equations for mean field approximation could be derived from equations of the quasi-chemical approximation under condition of $\beta\varepsilon \to 0$.
(3) Show that the one- and two-site rates of reactions taking into account a non-ideal behavior of the system in the quasi-chemical approximation at the small density ($\theta_i \to 0$) transform to equations of the law of acting masses.
(4) Show that the equality of adsorption and desorption rates for dissociating molecules, derived in the mean field and chaotic approximations for interacting the nearest neighbors, do not satisfy the equations of isotherms in similar approximations (this means the absence of a self-consistency between description of the equilibrium and dynamic characteristics of the system). Check out, that the discussed self-consistency property is fulfilled for equations in the quasi-chemical approximation.
(5) Derive the expressions in the context of quasi-particles concept for the rates of adsorption and desorption of dissociating molecules on the (111) face with $z = 6$. Compare expressions found with the general formulas of Section 3.
(6) Consider a basic distinction between the transitive state model and the collision model for the adsorption rate $U_{ad}(\theta)$. What types of curves could be obtained taking into account the interaction between nearest neighbors and additional contributions from the second neighbors.
(7) What factors influence on splitting up of curves of thermo-desorption spectra?
(8) What types of potential interactions answer the presence of condensed phases, ordered phases, and condensed phases with ordering of components in reaction systems?
(9) Compose a system of kinetic equations for the four-stage process [143]: (1) $HCOOH + 2Z \to ZHCOO + ZH$, (2) $ZHCOO + Z \to ZH + ZCO_2$, (3) $2ZH \leftrightarrow 2Z + H_2$, and (4) $ZCO_2 \to Z + CO_2$, in case of rapid mobility of all surface particles using the transitive state model.

Lam Research Ex. 1035 - Page 455
Lam Research Corp. v. Inpria Corp.
IPR2024-00033 - U.S. Patent No. 9,823,564

(10) Compose a kinetic scheme of the process of hydrogen absorption inside a volume of a metal with a detailed description of elementary migration stages of atoms near to a surface of the metal.
(11) To compose a kinetic scheme of process how to change the concentration profile of atoms in multicomponent alloys in vicinity of the flat surface in comparison with the similar alloy profile in vacuum at the process of an interaction of this alloy with gaseous molecules. Explain the cause of such concentration profile reorganization.
(12) To compose equations for adsorption of the O_2 molecules with an allowance for the slow surface mobility of adsorbed particles along a surface. Compose the similar equations for adsorption of the CO molecules at low temperatures, when the surface mobility of adsorbed molecules needed be taken into account.
(13) In what way is a prehistory of a sample formation taken into account by using the distributed and point-like mathematical models of kinetic processes?
(14) Why the calculation based on the kinetic equations and the Monte-Carlo dynamic method should give identical results. What are the practical causes of differences between these methods? What are the ways to reduce these differences?
(15) Which parameters of the lattice-gas model change under influence of the oscillations of the (a) adsorbed atoms and (b) atoms of substrate?
(16) What functions to describe a distribution of adsorption centers on non-uniform surfaces are needed for calculation of adsorption isotherm, the adsorption and desorption rates of dissociating molecules, for allowing the lateral interaction between the nearest neighbors?
(17) Derive the following expression for the function $\theta_{fg}^{AA}(r)$:

$$\theta_{fg}^{AA}(r) = \frac{2\theta_f^A \theta_g^A}{d_{fg}(r) + b_{fg}(r)}, \quad \text{where } b_{fg}(r) = [(d_{fg}(r))^2 + 4x_{fg}(r)\theta_f^A \theta_g^A]^{1/2},$$

$$d_{fg}(r) = 1 + x_{fg}(r)(1 - \theta_f^A - \theta_g^A), \quad x_{fg}(r) = \exp[-\beta\varepsilon_{fg}^{AA}(r)] - 1,$$

from equations of the quasi-chemical approximation for $s = 2$ on a non-uniform surface (B.1), which in an explicit form gives the expression for pair functions via unitary functions and considerably accelerates calculations.

References

1. M. W. Roberts, C. S. McKee, Chemistry of the Metal–Gas Interface, Clarendon Press, Oxford, 1978.

Lam Research Ex. 1035 - Page 456
Lam Research Corp. v. Inpria Corp.
IPR2024-00033 - U.S. Patent No. 9,823,564

2. G. A. Somorjai, Chemistry in Two-Dimension Surface, Cornell University Press, Ithaca, NY, 1981.
3. R. Laudise, The Growth of Single Crystals, Prentice-Hall, Englewood Cliffs, NJ, 1970.
4. J. C. Slater, The Self-Consistent Field for Molecules and Solids, McGraw-Hill, Inc., New York, 1974.
5. I. G. Kaplan, Introduction to the Theory of Intermolecular Interactions, Nauka, Moscow, 1982.
6. A. Animalu, Intermediate Quantum Theory of Crystalline Solids, Prentice-Hall, Englewood Cliffs, NJ, 1977.
7. I. M. Thdilkovsky, The Band Structure of Semiconductors, Nauka, Moscow, 1978.
8. H. Ehrenreich, L. Schwartz, The Electronic Structure of Alloys, Academic Press, New York, 1976.
9. V. A. Gubanov, A. L. Ivanovsky, M. V. Ryzhkov, Quantum Chemistry in the Science of Materials, Nauka, Moscow, 1987.
10. V. E. Panin, Yu. A. Khon, I. I. Naumov, S. G. Psakhye, A. I. Landa, E. V. Chulov, The Theory of Phases in Alloys, Nauka, Moscow, 1984.
11. L. A. Bolshov, A. P. Napartovich, A. O. Naumovets, A. G. Fedorus, Russ. Phys. Rev. **122** (1977) 125.
12. J. Smith (Ed.), Theory of Chemisorption, Springer, Berlin, 1980.
13. H. Dunken, V. Lygin, Quantenchemie der Adsorption an estkorperoberflachen, VEB Deutscher Verlag fur Grundstoffindustrie, Leipzig, 1978.
14. S. L. Kiperman, Fundamentals of Chemical Kinetics in Heterogeneous Catalysis, Khimiya, Moscow, 1979.
15. A. Ya. Rozovsky, Heterogeneous Chemical Reactions: Kinetics and Macrokinetics, Nauka, Moscow, 1980.
16. G. S. Yablonsky, V. I. Bykov, A. N. Gorban, Kinetic Models of Catalytic Reactions, Nauka, Novosibirsk, 1983.
17. K. Huang, Statistical Mechanics, Wiley, New York, 1963.
18. V. E. Shneider, J. Exp. Theor. Phys. **66** (1974) 638.
19. R. J. Baxter, Exactly Solved Models in Statistical Mechanics, Academic Press, London, 1982.
20. H. Eyring, J. Chem. Phys. **3** (1935) 107.
21. M. I. Temkin, Russ. J. Phys. Chem. **11** (1938) 169.
22. M. I. Temkin, Russ. J. Phys. Chem. **15** (1941) 296.
23. S. Glasstone, K. Laidler, H. Eyring, The Theory of Rate Processes, Princeton University, NY, 1941.
24. J. W. Gibbs, Collected Works, Vols. 1 and 2, Longmans Green, New York, 1928.

Lam Research Ex. 1035 - Page 457
Lam Research Corp. v. Inpria Corp.
IPR2024-00033 - U.S. Patent No. 9,823,564

25. I. Prigogine, R. Defay, Chemical Thermodynamics. Trans. by D. H. Everett, Longmans Green, London, 1954.
26. L. D. Landau, E. M. Lifshits, Statistical Physics, 2nd edition, Vol. 5, Nauka, Moscow, 1964.
27. C. Kittel, Introduction to Solid State Physics, 4th edition, Wiley, New York, 1976.
28. A. G. Khachaturian, The Theory of Phase Transformations and Structure of Solid Solutions, Nauka, Moscow, 1974.
29. Yu. M. Gufan, Structural Phase Transitions, Nauka, Moscow, 1982.
30. V. Kymar, D. Kymar, S. K. Joshi, Phys. Rev. B **19** (1979) 1954.
31. J. L. Moran-Lopez, L. M. Falicov, Phys. Rev. B **18** (1978) 2542.
32. A. Adamson, The Physical Chemistry of Surfaces, Wiley, New York, 1976.
33. S. R. Morrison, The Chemical Physics of Surfaces, Plenum Press, New York, 1977.
34. O. V. Krylov, V. F. Kiselev, Adsorption and Catalysis on Transition Metals and Their Oxides, Khimiya, Moscow, 1981.
35. T. H. Upton, W. A. Goddard III, Phys. Rev. Lett. **42** (1979) 472.
36. G. M. Zhidomirov, I. D. Mikheikin, Advances in Sciences and Technology. Molecular Structure and the Chemical Bond, Vol. 9, VINITI, Moscow, 1984.
37. N. N. Avgul, A. V. Kiselev, D. P. Poshkus, Adsorption of Gases and Vapor on Homogeneous Surfaces, Khimiya, Moscow, 1975.
38. S. Z. Roginsky, Adsorption and Catalysis on Nonuniform Surfaces, Izd. Akad. Nauka SSSR, Moscow-Leningrad, 1948.
39. V. Danning, in: E. A. Flood (Ed.), The Solid–Gas Interface, Marcel Dekker, Inc., New York, 1967, p. 271.
40. S. Z. Roginsky, O. M. Todes, Problems of kinetics and catalysis, Izd. Nauka, Moscow, **8** (1949) 339.
41. T. Wang, L. D. Schmidt, J. Catal. **71** (1981) 411.
42. J. Sedlacek, L. Hilaire, P. Legare, et al., Surf. Sci. **115** (1982) 541.
43. K. Griffiths, T. E. Jackman, J. A. Davies, et al., Surf. Sci. **138** (1984) 113.
44. A. Ya. Rozovsky, The Kinetics of Topochemical Reactions, Khimiya, Moscow, 1974.
45. J. D. Fast, Interaction of Metals and Gases, Kinetics and Mechanisms, Vol. 2, Macmillan, London, 1971.
46. P. V. Geld, R. A. Ryabov, L. P. Mokhracheva, Hydrogen and the Physical Properties of Metals and Alloys: Hydrides of the Transition Metals, Nauka, Moscow, 1985.

Lam Research Ex. 1035 - Page 458
Lam Research Corp. v. Inpria Corp.
IPR2024-00033 - U.S. Patent No. 9,823,564

47. A. A. Smirnov, The Theory of Interstitial Alloys, Nauka, Moscow, 1979.
48. N. M. Emanuel, D. T. Knorre, Course in Chemical Kinetics, 4th edition, Vysshaya Shkola, Moscow, 1984.
49. A. A. Ovchinnikov, S. F. Timashev, A. A. Belyi, Kinetics of Diffusion-Controlled Chemical Processes, Khimiya, Moscow, 1986.
50. T. L. Hill, Statistical Mechanics, McGraw-Hill, New York, 1956.
51. G. Ertl, Surf. Sci. **152/153** (1985) 328.
52. W. A. Steele, in: E. A. Flood (Ed.), The Solid–Gas Interface, Chapter 10, Vol. 1, Marcel Dekker, New York, 1967, p. 307.
53. Yu. K. Tovbin, Russ. J. Phys. Chem. **79** (2005) 2140.
54. J. Hirschfelder, C. Curtiss, R. Bird, Molecular Theory of Gases and Liquids, Wiley, New York, 1954.
55. B. Ya. Balagurov, V. G. Vaks, R. O. Zaitsev, Solid State Phys. **16** (1974) 2302.
56. Yu. K. Tovbin, Kinet. Catal. **19** (1978) 1453.
57. K. J. Laidler, Chemical Kinetics, McGraw-Hill Book Company, New York, 1965.
58. Yu. K. Tovbin, Russ. J. Phys. Chem. **55** (1981) 284.
59. P. J. Robinsen, K. A. Holbrook, Unimolecular Reactions, Wiley, London, 1972.
60. E. E. Nikitin, Theory of Elementary Atomic and Molecular Processes in Gases, Khimiya, Moscow, 1971.
61. H. Eyring, S. H. Lin, S. M. Lin, Basic Chemical Kinetics, Wiley, New York, 1980.
62. Z. W. Gortel, H. J. Kreuzer, R. Teshima, Phys. Rev. B **22** (1980) 512.
63. V. M. Fain, Phys. Stat. Sol. B **63** (1974) 411.
64. V. M. Fain, Theory of Rate Processes in Condensed Media, Lecture Notes in Chemistry, Vol. 20, Springer-Verlag, Berlin, 1980.
65. M. Tringides, R. Gomer, Surf. Sci. **166** (1986) 440.
66. V. I. Gol'dansky, L. I. Trakhtenberg, V. N. Flerov, Tunneling Phenomena in Chemical Physics, Gordon and Breach, NY, 1989.
67. A. S. Prostnev, M. A. Kozhushner, B. R. Shub, Russ. Chem. Phys. **5** (1986) 85.
68. C. F. Melius, W. D. Wilson, C. L. Bisson, Radiat. Eff. **153** (1980) 111.
69. V. K. Fedyanin, Russ. J. Phys. Chem. **47** (1973) 1287.
70. A. M. Gabovish, E. A. Pashitsky, Phys. Solid State **18** (1976) 377.
71. T. Einstein, J. R. Schriffer, Phys. Rev. B **7** (1973) 3629.
72. J. -P. Muscat, Prog. Surf. Sci. **25** (1987) 191.
73. N. H. March, Prog. Surf. Sci. **25** (1987) 229.

Lam Research Ex. 1035 - Page 459
Lam Research Corp. v. Inpria Corp.
IPR2024-00033 - U.S. Patent No. 9,823,564

74. T. Einstein, Phys. Rev. B **16** (1977) 3411.
75. N. N. Bogolyubov, Problems of the Dynamic Theory in Statistical Physics, OGIZ, Moscow, 1946.
76. I. P. Bazarov, The Statistical Theory of the Crystal State, Moscow State University Press, Moscow, 1972.
77. C. A. Croxton, Liquid State Physics. A Statistical Mechanical Introduction, Cambridge University Press, Cambridge, 1974.
78. V. K. Fedyanin, in: N. N. Bogolyubov (Ed.), Statistical Physics and the Quantum Theory of a Field, Nauka, Moscow, 1973, p. 241.
79. V. L. Kuzmin, Russ. J. Math. Phys. **28** (1976) 389.
80. Yu. K. Tovbin, Theory of Physical Chemistry Processes at Gas–Solid Interface, Izd. Nauka, Moscow, 1990; CRC Press, Boca Raton, FL, 1991.
81. Yu. K. Tovbin, Langmuir **13** (1997) 979.
82. L. van Hove, Physica **23** (1957) 441.
83. R. Balesku, in: M. Biel and G. Rae (Eds.), Irreversibility in the Many-Body Problem, Plenum Press, New York, 1972.
84. Yu. K. Tovbin, Dokl. Phys. Chem. **262** (1982) 929.
85. Yu. K. Tovbin, Dokl. Phys. Chem. **277** (1984) 917.
86. Yu. K. Tovbin, Russ. J. Phys. Chem. **70** (1996) 1655.
87. J. D. Weeks, G. H. Gilmer, K. A. Jackson, J. Chem. Phys. **65** (1976) 712.
88. D. E. Temkin, Kristallographiya **23** (1978) 1151.
89. Yu. K. Tovbin, Prog. Surf. Sci. **34** (1990) 1.
90. L. A. Vlasova, V. E. Shneider, Phys. Solid State **20** (1978) 3463.
91. J. W. Evans, H. Pak, Surf. Sci. **199** (1988) 28.
92. D. J. W. Geldart, H. J. Kreuzer, F. S. Rys, Surf. Sci. **176** (1986) 284.
93. J. W. Evans, D. K. Hoffman, J. Stat. Phys. **36** (1984) 65.
94. R. S. Nord, D. K. Hoffman, J. W. Evans, Phys. Rev. A **31** (1985) 3820.
95. J. W. Evans, R. S. Nord, Phys. Rev. A **31** (1985) 3831.
96. J. W. Evans, R. S. Nord, Phys. Rev. B **31** (1985) 1759.
97. J. W. Evans, D. R. Burgess, J. Chem. Phys. **79** (1983) 5023.
98. J. W. Evans, Physica A **123** (1984) 297.
99. Yu. K. Tovbin, Dokl. Phys. Chem. **302** (1988) 385.
100. Yu. K. Tovbin, Surf. Phys. Chem. Mech. **5** (1989) 5.
101. Yu. K. Tovbin, Russ. J. Phys. Chem. **64** (1990) 865.
102. Yu. K. Tovbin, Kinet. Catal. **21** (1980) 1165.
103. Yu. K. Tovbin, Dokl. Phys. Chem. **302** (1988) 385.
104. O. V. Krylov, B. R. Shub, Nonequilibrium Processes in Catalysis, Khimiya, Moscow, 1990.

Lam Research Ex. 1035 - Page 460
Lam Research Corp. v. Inpria Corp.
IPR2024-00033 - U.S. Patent No. 9,823,564

105. J. K. Roberts, Some Problems of Adsorption, Cambridge University Press, Cambridge, 1939.
106. T. Toya, J. Vac. Sci. Technol. **9** (1972) 890.
107. D. L. Adams, Surf. Sci. **42** (1974) 12.
108. Yu. K. Tovbin, Adsorption on a ideal regular structure with interaction between the adatms, Ph.D. Thesis, NIFKhI im. L. Ya. Karpova, Moscow, 1974.
109. D. L. Adams, L. H. Germer, Surf. Sci. **23** (1970) 419.
110. D. L. Adams, L. H. Germer, Surf. Sci. **32** (1972) 205.
111. Yu. K. Tovbin, V. K. Fedyanin, Phys. Solid State **17** (1975) 1511.
112. Yu. K. Tovbin, V. K. Fedyanin, Kinet. Catal. **19** (1978) 989.
113. Yu. K. Tovbin, V. K. Fedyanin, Kinet. Catal. **19** (1978) 1202.
114. Yu. K. Tovbin, Kinet. Catal. **20** (1979) 1226.
115. I. Langmuir, J. Am. Chem. Soc. **54** (1932) 2798.
116. T. A. Becker, Trans. Am. Electrochem. **55** (1929) 153.
117. Ya. B. Zeldovich, Acta Phys. Chim. USSR **1** (1934) 449.
118. S. Z. Roginsky, Ya. B. Zeldovich, Acta Phys. Chim. USSR **1** (1934) 554.
119. D. M. Bangham, F. F. Burt, Proc. R. Soc. Lond. A **105** (1924) 481.
120. T. Kwan, J. Phys. Chem. **60** (1956) 1033.
121. M. I. Low, Chem. Rev. **60** (1960) 267.
122. L. D. Schmidt, R. Gomer, J. Chem. Phys. **42** (1965) 3573.
123. L. D. Schmidt, R. Gomer, J. Chem. Phys. **45** (1966) 1605.
124. T. E. Felter, P. J. Estrup, Surf. Sci. **76** (1978) 464.
125. B. E. Nienwehuys, G. A. Somorjai, Surf. Sci. **72** (1978) 8.
126. Yu. K. Tovbin, V. K. Fedyanin, Phys. Solid State **22** (1980) 1559.
127. Yu. K. Tovbin, in: W. Rudzinski, W. A. Steele, G. Zgrablich (Eds.), Equiliblia and Dynamics of Gas Adsorption on Heterogeneous Solid Surfaces, Elsevier, Amsterdam, 1997, p. 201.
128. Yu. K. Tovbin, E. V. Votyakov, Langmuir **15** (1999) 6070.
129. D. E. Ibbotson, T. S. Witting, W. H. Wheinberg, J. Chem. Phys. **72** (1980) 4885.
130. Yu. K. Tovbin, Russ. J. Phys. Chem. **55** (1981) 284.
131. C. A. Pikos, D. Luss, Chem. Eng. Sci. **32** (1977) 191.
132. Yu. K. Tovbin, A. V. Cherkasov, Theor. Exp. Chem. **20** (1984) 507.
133. V. I. Bykov, G. S. Yablonsky, React. Kinet. Catal. Lett. **16** (1981) 377.
134. B. V. Filippov, I. L. Sorokin, G. V. Berezin, in: V. V. Struminski (Ed.), Molecular Gasodynamics, Nauka, Moscow, 1982, p. 120.
135. H. Steininger, S. Lehwald, H. Ibach, Surf. Sci. **123** (1982) 1, 264.
136. G. G. Elenin, A. V. Sinilo, Yu. K. Tovbin, Kinet. Catal. **27** (1986) 960.

Lam Research Ex. 1035 - Page 461
Lam Research Corp. v. Inpria Corp.
IPR2024-00033 - U.S. Patent No. 9,823,564

137. V. P. Zhdanov, Surf. Sci. **123** (1982) 106.
138. V. P. Zhdanov, Surf. Sci. **137** (1984) 515.
139. V. L. Tataurov, V. P. Ivanov, in Nonstationary Processes in Catalysis, Izd. Inst. Katal. Sib. Otd. Akad. Nauk SSSR, Novosibirsk, 1979, Part 2, p. 170.
140. N. Pacia, A. Cassuto, A. Pentenero, B. J. Weber, J. Catal. **41** (1976) 455.
141. G. K. Hori, L. D. Schmidt, J. Catal. **38** (1975) 335.
142. S. Sunderesan, Proceedings at the Annual Meeting of the American Institute of Chemical Engineers, Los Angeles, CA, 1982, paper 59B.
143. J. B. Benziger, G. R. Schoofs, J. Phys. Chem. **88** (1984) 4439.
144. R. C. Jones, D. L. Perry, Surf. Sci. **71** (1978) 59.
145. R. C. Jones, D. L. Perry, Surf. Sci. **82** (1979) 540.
146. Yu. K. Tovbin, O. A. Kuznetsova, Russ. J. Phys. Chem. **64** (1990) 426.
147. H. Asada, J. Res. Inst. Catal. Hokk. Univ. **30** (1982) 55.
148. H. Asada, J. Res. Inst. Catal. Hokk. Univ. **31** (1983) 1.
149. R. Opila, R. Gomer, Surf. Sci. **112** (1981) 1.
150. H. Asada, M. Masuda, Surf. Sci. **207** (1989) 517.
151. M. Goize, M. Grunze, W. Unerti, Progr. Surf. Sci. **22** (1986) 101.
152. Yu. K. Tovbin, E. V. Votyakov, Russ. J. Phys. Chem. **67** (1993) 141.
153. H. Pfnur, P. Feulner, D. Menzel, J. Chem. Phys. **79** (1983) 2400, 4613.
154. R. Haase, Thermodynamik der irreversiblen prozesse, Dr. Dietrich Steinkopff Verlag, Darmstaadt, 1963.
155. K. P. Gurov, V. A. Kartashkin, Yu. E. Ugaste, Interdiffusion in Multiphase Metallic Systems, Izd. Nauka, Moscow, 1981.
156. H.P. Bonzel, in: J.M. Blakely (Ed.), Surface Physics of Materials, Academic Press, New York, 1975, p. 279.
157. G. Ehrlich, K. Stolt, Ann. Rev. Phys. Chem. **31** (1980) 603.
158. M. Bowker, D. A. King, Surf. Sci. **71** (1978) 583.
159. R. Butz, H. Wagner, Surf. Sci. **63** (1977) 448.
160. Yu. K. Tovbin, V. K. Fedyanin, Russ. J. Phys. Chem. **54** (1980) 3127.
161. Yu. K. Tovbin, V. K. Fedyanin, Russ. J. Phys. Chem. **54** (1980) 3132.
162. E. M. Gohman, Yu. K. Tovbin, V. K. Fedyanin, in Physics of Interphase Phenomena, Izd. Kabardino-Balkar. Gos. Univer., Nal'chik, 1981, p. 145.
163. A. A. Chumak, A. A. Tarasenko, Surf. Sci. **91** (1980) 694.
164. A. A. Tarasenko, A. A. Chumak, Surf. Phys. Chem. Mech. **3** (1983) No. 2, p. 35.
165. R. Kikuchi, J. Phys. Chem. Solids, **20** (1961) 17.
166. V. V. Gvozdev, Yu. K. Tovbin, Chem. Phys. Rep. **18** (1999) 179.

Lam Research Ex. 1035 - Page 462
Lam Research Corp. v. Inpria Corp.
IPR2024-00033 - U.S. Patent No. 9,823,564

167. A. A. Tarasenko, L. Jastrabik, F. Nieto, C. Uebing, Phys. Rev. B **59** (1999) 8252.
168. A. A. Tarasenko, L. Jastrabik, C. Uebing, Phys. Rev. B **57** (1998) 10166.
169. C. Cercignani, Theory and Application of the Boltzmann Equation, Scottish Academic Press, Edinburgh, London, 1975.
170. B. V. Alekseev, Mathematical Kinetics of Reacting Gases, Izd. Nauka, Moscow, 1982.
171. B. Halpern, D. E. Rosier, JCS Farad. Trans. Part 1, **74** (1978) 1883.
172. J. D. Waskiewicz, A. L. Mirray, C. H. Lewis, A. I. A. A. J. **16** (1978) 189.
173. S. Kristyan, J. Gilber, Surf. Sci. **224** (1989) 476.
174. Yu. K. Tovbin, Russ. Chem. Rev. **57** (1988) 929.
175. J. Crank, The Mathematics of Diffusion, Clarendon Press, Oxford, 1956.
176. A. M. Krivoglaz, A. A. Smirnov, Theory of Ordered Alloys, Gos. Izd. Fiz. Mat. Lit., Moscow, 1958.
177. A. A. Smirnov, Molecular-Kinetic Theory of Metals, Izd. Nauka, Moscow, 1966.
178. A. B. Lidiard, Phil. Mag. **46** (1955) 1218.
179. K. Campaan, Y. Haven, Trans. Farad. Soc. **52** (1956) 786.
180. A. H. Schoen, R. W. Lowen, Bull. Am. Phys. Soc. (Series 2) **5** (1960) 280.
181. R. Kikuchi, H. Sato, J. Chem. Phys. **51** (1969) 161.
182. H. A. Dumian, H. I. Aaronson, Trans. A.I.M.E. **230** (1964) 44.
183. H. Sato, R. Kikuchi, J. Chem. Phys. **55** (1971) 677–702.
184. K. K. Amandykov, K. P. Gurov, Phys. Metals Metallog. **38** (1974) 903, 1307.
185. A. Yu. Zakharov, E. I. Pipka, Phys. Solid State **23** (1981) 3159.
186. Yu. K. Tovbin, Dokl. Phys. Chem. **312** (1990) 1423.
187. Yu. K. Tovbin, Russ. J. Phys. Chem. **71** (1997) 1454.
188. E. V. Votyakov, Yu. K. Tovbin, Russ. J. Phys. Chem. **71** (1997) 676.
189. E. V. Votyakov, Yu. K. Tovbin, Russ. J. Phys. Chem. **71** (1997) 858.
190. H. L. Frisch, S. A. Stern, Crit. Rev. Solid. State Mater. Sci. **11** (1983) 123.
191. I. N. Bekman, in: A. P. Zakarov (Ed.), Hydrogen Interaction with Metals, Nauka, Moscow, 1988, p. 143.
192. A. E. Chalykh, Diffusion in Polymer Systems, Khimiiya, Moscow, 1987.
193. N. Muruganandam, W. I. Koros, D. R. Paul, J. Polym. Sci., Part B: Polym. Phys. **25** (1987) 1999.

Lam Research Ex. 1035 - Page 463
Lam Research Corp. v. Inpria Corp.
IPR2024-00033 - U.S. Patent No. 9,823,564

194. P. Barret, Kinetics of Heterogeneous Processes, Gauthier Villars, Paris, 1973.
195. E. V. Votyakov, N. F. Vasyutkin, M. M. Senyavin, Yu. K. Tovbin, Russ. J. Phys. Chem. **73** (1999) 1924.
196. H. Engelke, in: J. A. Simmons, R de Wit, R. Bullough (Eds.), Fundamental Aspects of Dislocation Theory, Nat. Bur. Stand. Spec. Publ., **II**, No.317, 1970, p. 1137.
197. L.D. Landau, E.M. Lifshits, Theory of Elasticity, 4th edition, Vol. 7, Nauka, Moscow, 1987.
198. V. R. Regel, A. I. Slutsker, E. E. Tomachevski, Kinetical Nature of Solid Body Stability, Nauka, Moscow, 1974.
199. S. F. Timashev, L. I. Trakhtenberg, Yu. K. Tovbin, Russ. J. Phys. Chem. **68** (1994) 2144.
200. G. Alefeld, J. Voelkl (Eds.), Hydrogen in Metals, Vols. 1 and 2. Springer, New York, 1978.
201. H. Frieske, E. Wicke, Ber Bunsen-Ges. Phys. Chem. **77** (1973) 50.
202. H. Brodowsky, Ber Bunsen-Ges. Phys. Chem. **72** (1968) 1055.
203. Yu. K. Tovbin, E. V. Votyakov, Russ. J. Phys. Chem. **75** (2001) 721.
204. R. M. Gabidullin, Fiz.-Khim. Mekh. Mater. **12** (1976) 52.
205. A. M. Kosevich, Physical Mechanics of Imperfect Crystals, Naukova Dumka, Kiev, Ukraine, 1981.
206. G. Leibfried, Bestrahlungseffekte in Festkorperneine Einfuhrung in die Theorie, Teubner, Stuttgart, 1965.
207. A. P. Zakharov (Ed.), in: Hydrogen Interaction with Metals, Nauka, Moscow, 1987.
208. G. Alefeld, J. Voelkl (Eds.), in: Hydrogen in Metals, Vol. 1, Springer, New York, 1978, p. 16.
209. E. V. Votyakov, Yu. K. Tovbin, Russ. J. Inorg. Chem. **44** (1999) 987.
210. V. M. Danilenko, Models of Imperfect Crystals, Naukova Dumka, Kiev, 1983.
211. E. A. Moelwyn-Hughes, Physical Chemistry, Pergamon, London, 1961.
212. P. V. Gel'd, R. A. Ryabov, L. P. Mokhracheva, Hydrogen and the Physical Properties of Metals and Alloys, Nauka, Moscow, 1985.
213. E. V. Votyakov, N. F. Vasyutkin, M. M. Senyavin, Yu. K. Tovbin, Protection of Metals **37** (2001) 33.
214. R. J. Farrago, R. B. McLellan, J. Phys. Chem. Solids **39** (1978) 781.
215. J. M. Rove, J. Phys. (Paris) **8** (1978) 7.
216. L. I. Smirnov, V. A. Gol'tsov, Phys. Metals Metallog. **84** (1997) 47.
217. E. Wicke, H. Brodowsky, in: G. Alefeld, J. Voelkl (Eds.), Hydrogen in Metals, Vol. 2, Springer, New York, 1978, p. 91.

Lam Research Ex. 1035 - Page 464
Lam Research Corp. v. Inpria Corp.
IPR2024-00033 - U.S. Patent No. 9,823,564

218. J. Voelkl, G. Alefeld, in: G. Alefeld, J. Voelkl (Eds.), Hydrogen in Metals, Vol. 1, Springer, New York, 1978, p. 379.
219. A. F. W. Seymour, R. I. Cotts, Phys. Rev. Lett. **35** (1975) 165.
220. D. N. Jewett, A. C. Makrides, Trans. Faraday Soc. **61** (1965) 932.
221. R. Vollmar, Algorithmen in zellurlarautomaten, Teubner Studienbucher Informatik, Stuttgart, 1979.
222. S. Wofram, Rev. Mod. Phys. **55** (1983) 601.
223. D. Farmer, T. Toffoli, S. Wolfram (Eds.), Cellular Automata, North-Holland, New York, 1984.
224. K. Kaneko, Y. Akutsu, J. Phys. A **19** (1986) L69.
225. J. S. Langer, Rev. Mod. Phys. **52** (1980) 1.
226. R. Rosen, Prog. Theor. Biol. **6** (1981) 161.
227. P. Moller, K. Wetzl, M. Eiswirth, G. Ertl, J. Chem. Phys. **85** (1986) 5328.
228. R. J. Schmankner, M. Eiswirth, P. Moller, K. Wetzl, G. Ertl, J. Chem. Phys. **87** (1987) 742.
229. M. Ehsasi, M. Matloch, O. Frank, J. H. Block, K. Christmann, F. S. Rys, W. Hirschwald, J. Chem. Phys. **91** (1989) 4949.
230. R. M. Ziff, E. Gulari, Y. Barshad, Phys. Rev. Lett. **56** (1986) 2553.
231. A. Dress, M. Gerhardt, N. I. Jaeger, P. J. Plath, H. Schuster, in: Temporal Order, Springer Series in Sinergetics, Springer-Verlag, Berlin, 1985, p. 67.
232. N. I. Jaeger, K. Moller, P. J. Plath, Ber. Bunsenges. Phys. Chem. **89** (1985) 633.
233. Patent Formation and Lattice-Gas – automata, A. T. Lawniczakand, R. Kapral (Eds.), Field Institute Communications, Vol. 6, 1996.
234. P. Bak, How Nature Works. The Science of Self-Organized Criticality, Oxford University Press, Oxford, 1997.
235. S. Wolfram. A New Kind of Science, Wolfram Media, 2002, p. 1196.
236. M. Metropolis, A. W. Rosenbluth, M. N. Rosenbluth, A. N. Teller, E. Teller, J. Chem. Phys. **21** (1953) 1087.
237. D. Nicholson, N. G. Parsonage, Computer Simulation and the Statistical Mechanics of Adsorption, Academic Press, New York, 1982.
238. F. F. Abraham, G. M. White, J. Appl. Phys. **41** (1970) 1841.
239. G. Ertl, J. Kuppers, Surf. Sci. **21** (1970) 61.
240. K. Binder (Ed.), Monte Carlo Methods in Statistical Physics, Topics in Current Physics, vol. 7, Springer-Verlag, Berlin, 1979.
241. K. Binder (Ed.), Application of the Monte Carlo in Statistical Physics, Topic in Current Physics, vol. 36, Springer-Verlag, Heidelberg, 1984.
242. M. E. Bridge, R. M. Lambert, Surf. Sci. **63** (1977) 315.

Lam Research Ex. 1035 - Page 465
Lam Research Corp. v. Inpria Corp.
IPR2024-00033 - U.S. Patent No. 9,823,564

243. M. E. Bridge, R. M. Lambert, Proc. R. Soc. Lond. A **370** (1980) 545.
244. M. E. Bridge, R. M. Lambert, Surf. Sci. **94** (1980) 469.
245. J. L. Sales, G. Zgrablich, Surf. Sci. **187** (1987) 1.
246. J. L. Sales, G. Zgrablich, Phys. Rev. B **35** (1987) 9520.
247. D. Gupta, C. S. Hirtzel, Surf. Sci. **210** (1989) 322.
248. M. Dumont, P. Dufour, Comput. Phys. Commun. **41** (1986) 1.
249. A. Sadiq, K. Yaldram, J. Phys. A **21** (1988) L207.
250. H. -P. Kaukonen, R. M. Nieminen, J. Chem. Phys. **91** (1989) 4380.
251. P. Arayo, W. Porod, R. Sant, E. E. Wolf, Surf. Sci. **208** (1989) L80.
252. A. E. Reynolds, D. Kaletta, G. Ertl, R. J. Behm, Surf. Sci. **218** (1989) 452.
253. M. Bowker, D. A. King, Surf. Sci. **72** (1978) 208.
254. E. Murch, Phil. Mag. A **43** (1981) 871.
255. A. Natori, H. Ohtsubo, Surf. Sci. **184** (1987); **289** (1987).
256. A. Sadig, K. Binder, Surf. Sci. **128** (1983) 350.
257. M. Tringides, R. Gomer, Surf. Sci. **166** (1986) 419.
258. C. H. Mak, J. L. Brand, B. G. Kochler, S. M. George, Surf. Sci. **191** (1987) 108.
259. C. H. Mak, H. C. Andersen, S. M. George, J. Chem. Phys. **88** (1988) 4052.
260. J. W. Evans, R. S. Nord, J. A. Rabaey, Phys. Rev. B **37** (1988) 8598.
261. E. T. Gawlinski, M. Grant, J. D. Gunton, K. Kaski, Phys. Rev. B **31** (1985) 281.
262. S. Sadig, K. Binder, J. Stat. Phys. **35** (1984) 517.
263. I. M. Lifshits, V. V. Slyozov, J. Phys. Chem. Solids **19** (1961) 35.
264. T. Ala-Nissila, J. D. Gunton, in: M. Grunze, H. J. Kreuzer (Eds.), Kinetics of Interface Reactions, Springer-Verlag, Berlin, 1987, p. 253.
265. T. Ala-Nissila, J. D. Gunton, Phys. Rev. B **38** (1988) 11418.
266. S. Tang, D. P. Landau, Phys. Rev. B **36** (1987) 567.
267. M. Zuzuki, Prog. Theor. Phys. **51** (1974) 1992.
268. H. C. Kang, W. H. Weinberg, Phys. Rev. B **38** (1988) 11543.
269. H. C. Kang, W. H. Weinberg, J. Chem. Phys. **90** (1989) 2824.
270. Y. Saito, H. Muller-Krumbhaar, J. Chem. Phys. **70** (1979) 1078.
271. H. Muller-Krumbhaar, Monte Carlo Methods in Statistical Physics: K. Binder, (Ed.), Topics in Current Physics, Vol. 7, Springer-Verlag, Berlin, 1979.
272. T. A. Cherepanova, J. Cryst. Growth, Part 1, **52** (1981) 319
273. J. A. Nieminen, K. Kaski, Surf. Sci. **185** (1987) L489.
274. J. Salik, Phys. Rev. B **32** (1985) 1824.
275. K. H. Muller, J. Vac. Sci. Technol. A **3** (1985) 2089.

Lam Research Ex. 1035 - Page 466
Lam Research Corp. v. Inpria Corp.
IPR2024-00033 - U.S. Patent No. 9,823,564

276. J. Salik, J. Appl. Phys. **57** (1985) 5017.
277. G. E. Blonder, Phys. Rev. B **33** (1986) 6157.
278. J. Ferron, R. R. Koropecki, R. Arce, Phys. Rev. B **35** (1987) 7611.
279. S. A. Barnett, A. Rockett, Surf. Sci. **198** (1988) 133.
280. M. R. Wilby, S. Clarke, T. Kawamura, D. D. Vvedensky, Phys. Rev. B **40** (1989) 10617.
281. Z. Jiang, C. Ebner, Phys. Rev. B **39** (1989) 2501.
282. V. I. Elokhin, A. V. Myshlyavtsev, E. I. Latkin, E. D. Resnyanskii, D. E. Sheinin, B. S. Bal'zhinimaev, Kinet. Catal. **39** (1998) 264.
283. V. I. Elokhin, E. I. Latkin, A. V. Matveev, V. V. Gorodetskii, Kinet. Catal. **44** (2003) 692.
284. A. V. Matveev, E. I. Latkin, V. I. Elokhin, V. V. Gorodetskii, Chem. Eng. J. **107** (2005) 181.
285. V. I. Elokhin, A. V. Myshlyavtsev, Dekker Encyclopedia of Nanoscience and Nanotechnology, Marcel Dekker, New York, 2004, p. 621.
286. A. A. Chumak, A. A. Tarasenko, Surf. Sci. **91** (1980) 694.
287. D. A. Reed, G. Ehrlich, Surf. Sci. **105** (1981) 603.
288. F. R. Loring, H. G. Andersen, M. D. Fayer, J. Chem. Phys. **80** (1983) 5731.
289. D. Gupta, C. S. Hirtzel, Chem. Phys. Lett. **149** (1988) 527.
290. M. Stiles, H. Metiu, Chem. Phys. Lett. **128** (1986) 337.
291. M. Silverberg, A. Ben-Shaul, Chem. Phys. Lett. **134** (1987) 491.
292. T. A. Cherepanova, A. S. Koziejowska, Phys. Stat. Sol. A **77** (1983) 35.
293. R. M. Bradley, P. N. Strenski, Phys. Rev. B **40** (1989) 8967.
294. Shang-keng Ma, Modern Theory of Critical Phenomena, W. A. Benjamin, Inc., London, 1976.
295. Yu. K. Tovbin, A. B. Rabinovich, E. V. Votyakov, Russ. Chem. Bull. **51** (2002) 1531.
296. Yu. K. Tovbin, A. B. Rabinovich, Langmuir **20** (2004) 6041.
297. E. S. Hood, B. H. Toby, W. H. Weinberg, Phys. Rev. Lett. **55** (1985) 2437.
298. D. Menzel, H. Phnur, P. Feulner, Surf. Sci. **126** (1983) 374.
299. M. Silverberg, A. Ben-Shaul, Surf. Sci. **214** (1989) 17.
300. J. L. Sales, G. Zgrablich, V. P. Zhdanov, Surf. Sci. **209** (1989) 208.
301. Yu. K. Tovbin, S. Yu. Surovtsev, Kinet. Catal. **26** (1985) 1181.
302. A. V. Myshlyavtsev, V. P. Zhdanov, Chem. Phys. Lett. **162** (1989) 43.
303. S. Sahni, G. S. Grest, M. P. Anderson, D. J. Srolovitz, Phys. Rev. Lett. **50** (1983) .
304. Yu. K. Tovbin, V. K. Fedyanin, Russ. J. Phys. Chem. **54** (1980) 3127.

Lam Research Ex. 1035 - Page 467
Lam Research Corp. v. Inpria Corp.
IPR2024-00033 - U.S. Patent No. 9,823,564

305. V. N. Kondratyev, E. E Nikitin, Chemical Processes in Gases, Nauka, Moscow, 1981.
306. D. A. Frank-Kamenetsky, Diffusion and Heat Transfer in Chemical Kinetics, Academy of Science USSR, Moscow, 1967.
307. Yu. K. Tovbin, Russ. Chem. Bull. **46** (1997) 458.
308. B. Hellsing, A. Mallo, Surf. Sci. **144** (1984) 336.
309. Yu. K. Tovbin, Chem. Phys. Rep. **15** (1996) 231.
310. Yu. K. Tovbin, Russ. J. Phys. Chem. **70** (1996) 700.
311. Yu. K. Tovbin, T. V. Petrova, Russ. J. Phys. Chem. **70** (1996) 870.
312. Yu. K. Tovbin, T. V. Petrova, Russ. J. Phys. Chem. **71** (1997) 123.

Lam Research Ex. 1035 - Page 468
Lam Research Corp. v. Inpria Corp.
IPR2024-00033 - U.S. Patent No. 9,823,564

Chapter 9

Integrated Approach to Dielectric Film Growth Modeling: Growth Mechanisms and Kinetics

A.A. Bagatur'yants[a,b], M.A. Deminskii[a,c], A.A. Knizhnik[a,c], B.V. Potapkin[a,c], and S.Y. Umanskii[a,d]

[a]*Kinetic Technologies Ltd., pl. Akademika Kurchatova 1, Moscow 123182, Russia*

[b]*Photochemistry Center, Russian Academy of Sciences, ul. Novatorov 7a, Moscow 119421, Russia*

[c]*Russian Research Center, Kurchatov Institute, pl. Akademika Kurchatova 1, Moscow 123182, Russia*

[d]*Semenov Institute of Chemical Physics, Russian Academy of Sciences, ul. Kosygina 4, Moscow 119991, Russia*

1. Introduction . . . 468
2. Quantum-Chemical Modeling . . . 470
3. Gas–Surface Reactions Proceeding via a Strongly Adsorbed Precursor . . . 471
   3.1. Description of the Model . . . 471
   3.2. Master Equation and Macroscopic Rate Constants . . . 472
   3.3. Macroscopic Rate Constant of a Barrierless Adsorption–Desorption Reaction 477
4. Simulation Methods . . . 479
   4.1. Molecular Dynamics . . . 479
   4.2. Monte Carlo Method . . . 483
   4.3. Kinetic Monte Carlo Method . . . 483
   4.4. Lattice and Dynamic Versions of Kinetic Monte Carlo . . . 485
   4.5. Kinetic Monte Carlo Method with Dynamic Relaxation (KMC-DR) . . . 486
   4.6. Reactor Modeling of Thin-Film Deposition . . . 488
5. Modeling of the Deposition of Thin Dielectric Films . . . 493
   5.1. Molecular Dynamics Modeling of Precursor Interaction With Surface . . . 493
   5.2. Kinetic Mechanism of Zirconium and Hafnium Oxide Film Deposition . . . 494
   5.3. Reduction of the Kinetic Mechanism of $Zr(Hf)O_2$ Film Growth . . . 502
   5.4. Kinetic Monte Carlo and Molecular Dynamics Modeling of ZrO_2 Film Roughness in an ALD Process . . . 503
   5.5. Modeling of the ZrO_2 Film Composition Using the Monte Carlo Method . 508
   5.6. Modeling of the $SiZrO_2$ Interface Structure Using the KMC-DR Method . 512
6. Conclusions and Outlook . . . 516
Questions and Problems . . . 516
References . . . 517

THIN FILMS AND NANOSTRUCTURES, vol. 34
ISSN 1079-4050
DOI: 10.1016/S1079-4050(06)34009-4

© 2007 by Elsevier Inc.
All rights reserved.

Lam Research Ex. 1035 - Page 469
Lam Research Corp. v. Inpria Corp.
IPR2024-00033 - U.S. Patent No. 9,823,564

Theoretical methods currently used and developed for the description of the epitaxial growth of dielectric and semiconductor thin films are considered. A multiscale approach to film growth modeling is formulated. This approach includes *ab initio* calculations of the main gas-phase and surface reactions, estimation of the rate constants using transition state or RRKM theory, and kinetic modeling using the kinetic Monte Carlo (KMC) method or formal chemical kinetics. General aspects of quantum-chemical modeling are briefly discussed. Methods for calculating microscopic rate constants of gas–surface and surface reactions based on the transition state or RRKM theory are described in detail. The main aspects of atomistic simulation methods, such as molecular dynamics, Monte Carlo, and KMC in both the lattice and the dynamic versions, are discussed. A KMC method is supplemented with a dynamic relaxation procedure (KMC-DR) in the cases when it is necessary to model irregular growth (defect or amorphous films). Specific technical details of KMC and KMC-DR methods are discussed. A formal kinetic approach to the simulation of film growth is also given. As an example of the specific application of the multiscale techniques, the problem of ZrO_2 ALD on an Si(100) substrate is considered. The simulation of ZrO_2 film growth successfully predicts the structure and composition of the growing film, the formation of defects and accumulation of impurities in the growing film, and the ZrO_2/Si(001) interface structure.

1. Introduction

Thin semiconductor films (and other nanostructured materials) are widely used in many applications and, especially, in microelectronics. Current technological trends toward ultimate miniaturization of microelectronic devices require films as thin as less than 5 nm, that is, containing only several atomic layers [1]. Experimental deposition methods have been described in detail in recent reviews [2–7]. Common thin-film deposition techniques are subdivided into two main categories: physical deposition and chemical deposition. Physical deposition techniques, such as evaporation, molecular beam epitaxy, or sputtering, involve no chemical surface reactions. In chemical deposition techniques, such as chemical vapor deposition (CVD) and its most important version, atomic layer deposition (ALD), chemical precursors are used to obtain chemical substances or their components deposited on the surface.

The structure, properties, and deposition mechanism of thin films cannot be understood well without modeling at an atomic level. It is very important for technological applications that the results of such atomistic modeling

Lam Research Ex. 1035 - Page 470
Lam Research Corp. v. Inpria Corp.
IPR2024-00033 - U.S. Patent No. 9,823,564

will be directly connected with macroscopic characteristics. On the other hand, processes and structures essential for thin-film growth involve various time and spatial scales. Therefore, the problem of thin-film simulation is a typical example when the use of so-called multiscale (or mesoscale) simulation is of key importance. Various strategies of multiscale modeling as applied to various film growth processes have recently been described in Refs. [8–17].

In this chapter, we present a general strategy for the multiscale simulation of thin-film growth that starts from *ab initio* (first-principles) calculations of elementary steps and structures and eventually leads to the level of reactor modeling [18–20]. We will mostly refer to chemical deposition methods, which are more general from the viewpoint of modeling, because these methods involve both chemical and physical processes (see, for example, a recent review [21]). When considering a CVD process, one should take into account gas-phase reactions of reaction components in the CVD reactor and gas–surface reactions. In addition, it is necessary to describe film growth on a realistic time and spatial scale, that is, as a sequence of elementary gas–surface and surface reactions (including surface diffusion, if necessary) on a relatively large surface area.

In more detail, our approach can be briefly summarized as follows: gas-phase reactions, surface structures, and gas–surface reactions are treated at an *ab initio* level, using either cluster or periodic (plane-wave) calculations for surface structures, when appropriate. The results of these calculations are used to calculate reaction rate constants within the transition state (TS) or Rice–Ramsperger–Kassel–Marcus (RRKM) theory for bimolecular gas-phase reactions or unimolecular and surface reactions, respectively. The structure and energy characteristics of various surface groups can also be extracted from the results of *ab initio* calculations. Based on these results, a chemical mechanism can be constructed for both gas-phase reactions and surface growth. The film growth process is modeled within the kinetic Monte Carlo (KMC) approach, which provides an effective separation of fast and slow processes on an atomistic scale. The results of Monte Carlo (MC) simulations can be used in kinetic modeling based on formal chemical kinetics.

This approach was successfully used in modeling the CVD of silicon nitride (Si_3N_4) films [18, 19, 22, 23]. Alternatively, molecular dynamics (MD) simulations can be used instead of or in combination with the MC approach to simulate kinetic steps of film evolution during the growth process (see, for example, a study of ZrO_2 deposition on the Si(100) surface [24]). Finally, the results of these simulations (overall reaction constants and film characteristics) can be used in the subsequent reactor modeling and the detailed calculations of film structure and properties, including defects and impurities.

Lam Research Ex. 1035 - Page 471
Lam Research Corp. v. Inpria Corp.
IPR2024-00033 - U.S. Patent No. 9,823,564

2. Quantum-Chemical Modeling

The main purpose of quantum-chemical modeling in materials simulation is to obtain necessary input data for the subsequent calculations of thermodynamic and kinetic parameters required for the next steps of multiscale techniques. Quantum-chemical calculations can also be used to predict various physical and chemical properties of the material in hand (the growing film in our case). Under quantum-chemical, we mean here both molecular and solid-state techniques, which are now implemented in numerous computer codes (such as Gaussian [25], GAMESS [26], or NWCHEM [27] for molecular applications and VASP [28], CASTEP [29], or ABINIT [30] for solid-state applications).

While quantum-chemical calculations related to gas-phase reactions or bulk properties have become now a matter of routine, calculations of local properties and, in particular, surface reactions are still a matter of art. There is no simple and consistent way of adequately constructing a model of a surface impurity or reaction site. We will briefly consider here three main approaches: (1) molecular models, (2) cluster models, and (3) periodic slab models.

In molecular models, a surface site is modeled using an analogous molecular reaction. This is the simplest approach, which requires the least amount of computational resources. The selection of a molecule that can more or less adequately reproduce the properties of the surface site under study determines the success or failure of the approach. This approach was used in Ref. [20] in the multiscale simulation of zirconium and hafnium oxide film growth.

In cluster models, a surface site is modeled using a surface fragment (cluster) that contains the surface site of interest and its nearest environment. The further procedure depends on the substrate type.

In the case of covalently bonded materials, boundary cluster atoms have so-called dangling bonds that connect the cluster with the remaining part of the crystal. Normally, these dangling bonds are saturated with hydrogen atoms to avoid spurious boundary unbound states. As a result, stoichiometric, covalently bonded clusters are obtained. Then, the boundary cluster atoms can be treated in two ways: (1) their positions can be fixed at some experimental (or calculated) crystalline positions or (2) their positions can be fully relaxed in calculations of various surface structures (local minima and TSs). In the second way, the cluster is treated as a free (gas-phase) supermolecule, so that this kind of the cluster approximation resembles molecular models with the only difference that such a cluster has commonly no experimental analogs. Clusters of this type have been used in modeling film growth processes in the case of such materials as Si, Si_3N_4, SiGe, Al_2O_3, and SiO_2 [22–24, 31–40].

Lam Research Ex. 1035 - Page 472
Lam Research Corp. v. Inpria Corp.
IPR2024-00033 - U.S. Patent No. 9,823,564

In the case of ionic materials, the cluster simulating a surface site must be embedded in the surrounding matrix. The problem of embedding has been discussed in numerous papers, and many embedding recipes and techniques have been proposed [41–48].

As to periodic slab models, their application is rather straightforward, but poses many problems in the cases when the activation energy should be found for a surface reaction at a bulky surface group. On the other hand, this is probably the best approach to determine the structural properties of an active site and the interaction energies between an active site and the reacting species.

3. Gas–Surface Reactions Proceeding via a Strongly Adsorbed Precursor

Once the thermodynamic parameters of stable structures and TSs are determined from quantum-chemical calculations, the next step is to find theoretically the rate constants of all elementary reactions or elementary physical processes (say, diffusion) relevant to a particular overall process (film growth, deposition, etc.). Processes that proceed at a surface active site are most important for modeling various epitaxial processes. Quantum-chemical calculations show that many gas–surface reactions proceed via a surface complex (precursor) between an incident gas-phase molecule and a surface active site. Such precursors mostly have a substantial adsorption energy and play an important role in the processes of dielectric film growth. They give rise to competition among subsequent processes of desorption, stabilization, surface diffusion, and chemical transformations of the surface complex.

Available calculated *ab initio* quantum-chemical data are not sufficient for a purely *ab initio* calculation of the rates of all participating processes. Therefore, a model approach is desirable that incorporates the available quantum-chemical data and depends on a small set of physically reasonable parameters. The model must describe the competing processes of adsorption, desorption, chemical transformations, and energy relaxation into the bulk. A possible model of this type will be described below.

3.1. DESCRIPTION OF THE MODEL

Quantum-chemical calculations show that the reaction path profiles $U_{rp}(q_r)$ (where q_r is a reaction coordinate) for exothermic reactions of a gas molecule B with a surface center A/s/ via a surface precursor AB/s/ with the formation of a gas molecule D and a new surface center C/s/ have

Lam Research Ex. 1035 - Page 473
Lam Research Corp. v. Inpria Corp.
IPR2024-00033 - U.S. Patent No. 9,823,564

qualitative forms, examples of which are shown in Figures 9.1 and 9.2. TC_{ad} and TC_f are transition complexes for precursor AB/s/ decomposition back to the reagents and forward to the products.

The following set of macroscopic reactions corresponds to the reaction path profiles presented in Figures 9.1 and 9.2:

$$B + A/sB + A/s \underset{k_r^-}{\overset{k_r^+}{\rightleftarrows}} D + C/s/;D + C/s/; \quad (1)$$

$$B + A/sB + A/s \underset{k_{des}}{\overset{k_{ads}}{\rightleftarrows}} AB/s/;AB/s/; \quad (2)$$

$$AB/sAB/s \underset{k_d}{\overset{k_f}{\rightleftarrows}} D + C/s/.D + C/s/. \quad (3)$$

The following model is assumed for the reaction center A/s/: cluster A containing N_A neighboring atoms is embedded in the substrate bulk. The bulk produces two effects: (1) it restricts the $3N_A$ degrees of freedom of A to vibrations or internal rotations and (2) it induces relaxation of the internal energy of A into the bulk. Gas-phase molecule B containing N_B atoms is adsorbed at center A/s/ without activation energy, forming precursor AB/s/. The precursor can decay through either the desorption of B or a chemical transformation with the desorption of product molecule D and the formation of a new surface center C/s/. The precursor AB/s/ can also exchange energy with the bulk. The surface diffusion of C/s is neglected in the simplest model considered here.

The evaluation of macroscopic rate constants of adsorption (k_{ads}) and direct reactions (k_r^+, k_f) involves the following steps:

(1) formulation and simplification of the microscopic master equation that takes into account the coupled processes of chemical transformations and energy exchange with the bulk;
(2) evaluation or estimation of the microcanonical (microscopic) rates of chemical transformations and energy transfer entering into the master equation;
(3) solution of the master equation.

The rate constants of desorption (k_{des}) and reverse reactions (k_r^-, k_d) are calculated using the detailed balance relations.

3.2. Master Equation and Macroscopic Rate Constants

Generally speaking, gas–surface reactions via a precursor (with the reaction path profiles shown in Figures 9.1 and 9.2) cannot be treated in the

Lam Research Ex. 1035 - Page 474
Lam Research Corp. v. Inpria Corp.
IPR2024-00033 - U.S. Patent No. 9,823,564

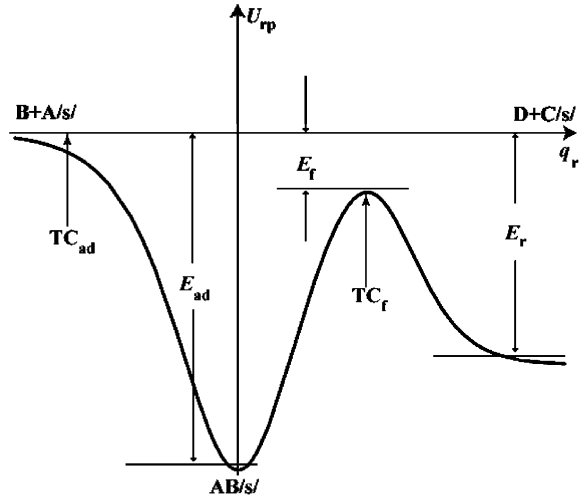


Fig. 9.1. Reaction path profile of an exothermic gas–surface reaction without activation energy via a precursor.

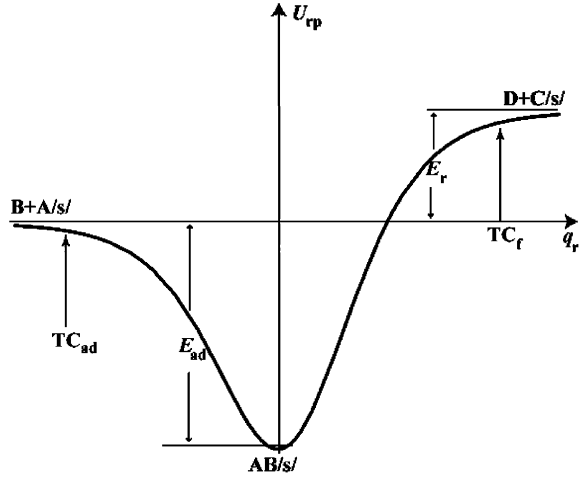


Fig. 9.2. Reaction path profile of an endothermic gas–surface reaction via a precursor.

framework of the standard canonical transition state theory (CTST). The reason for that is as follows. When a molecular system appears in the potential well, energy is rapidly (during 10^{-11} to 10^{-12} sec) redistributed from the reaction coordinate to other internal degrees of freedom of the precursor AB/s/(E) (stable surface center corresponding to the compound

Lam Research Ex. 1035 - Page 475
Lam Research Corp. v. Inpria Corp.
IPR2024-00033 - U.S. Patent No. 9,823,564

system AB/s/ in the potential well (see Figures 9.1 and 9.2) with the total energy E). During this redistribution, the system completely loses all the memory of its initial state (conditions of its formation) except for the conservation of the total energy E (from here on, the zero of E coincides with the ground-state energy level of AB/s/). If this is the case, all the internal states of AB/s/ with the same values of E are dynamically equivalent.

In such a situation, it is sufficient to characterize the state of AB/s/ by the distribution function $f(E)$ over E, which can also depend on time t. This distribution function is formed by energy transfer processes that proceed in the complex AB/s/(E) with the total energy E. These processes include its decomposition back to reagents and forward to products. Processes of AB/s/(E) formation, its decomposition to reagents and products, and energy exchange with the bulk are assumed to be dynamically independent. However, these processes are coupled kinetically. In fact, the average energy of noninteracting X and Y/s is much higher (by the value of the order of the adsorption energy E_{ad}; see Figures 9.1 and 9.2) than the internal thermal energy of AB/s/. Therefore, AB/s/ formed from thermal B and A/s/ initially has a strongly nonthermal internal energy distribution. However, subsequent AB/s/(E) energy exchange with the bulk and decomposition to reagents and products modify this distribution.

As mentioned above, it is assumed that the system is sufficiently far from chemical equilibrium, so the reverse reactions between D and C/s/ can be neglected. In this case, the behavior of Ab/s/(E) can be described by the following kinetic scheme:

$$\{\mathrm{B}+\mathrm{A/s/}\}(E)\{\mathrm{B}+\mathrm{A/s/}\}(E)\underset{k^{-}(E)}{\overset{\delta k_{ad}(E)}{\rightleftarrows}}\mathrm{AB/s/}(E);\mathrm{AB/s/}(E); \quad (4)$$

$$\mathrm{AB/s/}(E)\xrightarrow{k^{+}(E)}\{\mathrm{D}+\mathrm{C/s/}\}(E); \quad (5)$$

$$\mathrm{AB/s/}(E)\mathrm{AB/s/}(E)\underset{k_b(E\leftarrow E')}{\overset{k_b(E\rightarrow E')}{\rightleftarrows}}\mathrm{AB/s/}(E').\mathrm{AB/s/}(E'). \quad (6)$$

Here, $\{\mathrm{B}+\mathrm{A/s/}\}(E)$ and $\{\mathrm{D}+\mathrm{C/s/}\}(E)$ are pairs of reagents and products with the total energy E, $\delta k_{ad}(E)$ the partial rate constant of AB/s/(E) formation, $k^{-}(E)$ and $k^{+}(E)$ the microcanonical rate constants of the decomposition of the complex to reagents and products, and $k_b(E\rightarrow E')$ ($k_b(E\leftarrow E')$) the rate constant of energy exchange between AB/s/(E) (AB/s/(E')) with the bulk. The bulk is assumed to be in thermal equilibrium with temperature T. Therefore, the energy-exchange rate constants satisfy the following detailed balance relations:

$$k_b(E\rightarrow E')f_{eq}(E)=k_b(E\leftarrow E')f_{eq}(E'), \quad (7)$$

Lam Research Ex. 1035 - Page 476
Lam Research Corp. v. Inpria Corp.
IPR2024-00033 - U.S. Patent No. 9,823,564

where

$$f_{\text{eq}}(E) = \frac{1}{Q}\rho(E)\ \exp\left(-\frac{E}{k_{\text{B}}T}\right) \tag{8}$$

is the equilibrium internal distribution function of AB/s/, Q the partition function of the fixed surface center AB/s/, and $\rho(E)$ the density of quantum states of vibrations and internal rotations of AB/s/.

The master equation corresponding to the scheme given by Eqs. (4)–(6) and governing the time variation of the AB/s(E) surface concentration $n_{\text{AB/s/}}(E, t)$ has the form

$$\frac{dn_{\text{AB/s/}}(E,t)}{dt} = -\int_0^\infty dE' K(E,E') n_{\text{AB/s/}}(E',t) + F(E,t), \tag{9}$$

where

$$K(E,E') = [k_{\text{b}}^{(\text{tot})}(E)\delta(E-E') - k_{\text{b}}(E \leftarrow E')] + [k^+(E) + k^-(E)]\delta(E-E'), \tag{10}$$

and

$$k_{\text{b}}^{(\text{tot})}(E) = \int_0^\infty dE' k_{\text{b}}(E \rightarrow E') \tag{11}$$

is the overall rate constant of internal energy relaxation from AB/s/ to the bulk, and the source term $F(E, t)$ describes the increase of $n_{\text{AB/s/}}(E, t)$ due to adsorption of B on the surface center A/s/.

Using the principle of detailed balancing for the processes of adsorption (rate constant $\delta k_{\text{ad}}(E)$) and AB/s/(E) decomposition back to reagents (rate constant $k^-(E)$) $F(E, t)$ can be represented in the form

$$F(E,t) = \frac{k^-(E)}{K(T)} f_{\text{eq}}(E) n_{\text{B}}(t) n_{\text{A/s/}}(t). \tag{12}$$

Here,

$$K(T) = \frac{Q_{\text{B}}(T) Q_{\text{A/s/}}(T)}{Q(T)}\ \exp\left(-\frac{E_{\text{ad}}}{k_{\text{B}}T}\right) \tag{13}$$

is the equilibrium constant for the adsorption–desorption reaction B + A/s/ $\leftrightarrow$ AB/s/, Q_{B} the partition function of gas molecules B per unit volume, $Q_{\text{A/s/}}$ the partition function of the fixed surface center A/s/, and $n_{\text{B}}(t)$ and $n_{\text{A/s/}}(t)$ the volume and the number densities of B and A/s/ at time instant t.

Thus, in the framework of the model under consideration, the most important effect of the bulk on the gas–surface reaction via the precursor is the relaxation of the internal energy of AB/s/. This relaxation is governed by the bulk thermal conductivity and the relaxation time τ_{rel} can be estimated from

Lam Research Ex. 1035 - Page 477
Lam Research Corp. v. Inpria Corp.
IPR2024-00033 - U.S. Patent No. 9,823,564

the data for metal oxides reported in Ref. [49]. Such estimates give that

$$\tau_{rel} \sim 10^{-11} - 10^{-12} c. \tag{14}$$

The vibrationally excited precursor AB/s/(E) can decay not only via energy transfer to the bulk but also via a chemical transformation (desorption of B and reaction with the formation of D and C/s/). These chemical processes can be characterized by the "chemical" lifetime τ_{ch}, which can be estimated in the framework of the statistical RRKM theory (see, e.g., Refs. [50, 51]) using the reaction parameters of reagents B and A/s/, precursor AB/s/, and transition complexes determined based on the results of quantum-chemical calculations. Such estimates were performed for many reactions of interest for the growth of metal oxide films [20]. It appeared that in the wide temperature range

$$\tau_{ch} \tilde{>} 10^{-10} \text{ sec}. \tag{15}$$

Thus, typically

$$\tau_{rel} << \tau_{ch}, \tag{16}$$

and, therefore, the vibrationally excited AB/s/(E) complex relaxes to attain the Boltzmann energy distribution before the chemical transformation occurs. This fact leads to two consequences:

(1) direct reaction (1) proceeding without the formation of an intermediate adsorption complex is suppressed by energy relaxation and can be excluded from the kinetic scheme;
(2) reaction (2) of the formation and reverse decomposition of the adsorption complex, and reaction (3) of its transformation to the products proceed at thermal equilibrium.

Therefore, the rate constants k_{ads}, k_{des}, and k_f (see Eqs. (2) and (3)) can be calculated using the transition state theory (TST) (see, e.g., Refs. [50–52]). If the reaction needs to overcome a potential barrier (e.g., the formation reaction of the products C/s/ + D with the energy path profile shown in Figure 9.1), the transition complex is well defined (rigid transition complex Tc_f) and the standard TST can be used. If the potential barrier is absent (both reactions in Figure 9.1 and adsorption–desorption in Figure 9.2), the position of the transition complex cannot be fixed on the potential energy surface (PES). In this case, the reaction proceeds through a loose transition complex, and the variational TST should be used to find the structure of the transition complex and to calculate the rate constants (see Refs. [50, 51]).

Lam Research Ex. 1035 - Page 478
Lam Research Corp. v. Inpria Corp.
IPR2024-00033 - U.S. Patent No. 9,823,564

3.3. MACROSCOPIC RATE CONSTANT OF A BARRIERLESS ADSORPTION–DESORPTION REACTION

For definiteness, consider barrierless adsorption–desorption reaction (2). In the variational TST, the position $q_r^{\neq}$ of transition complex TC_{ad} in the reaction path (see Figures 9.1 and 9.2) corresponds to a maximum of the Helmholtz free energy $a^{\neq}(q_r)$ of the trial transition complex $TC_{ad}(q_r)$ considered as a function of the reaction coordinate.

Following Refs. [52–55], it is assumed that surface complex AB/s/ can be represented as two fragments (escaping molecule B and surface center A/s/; see Figure 9.3) interacting along the reaction coordinate q_r through the Morse potential

$$U(q_r) = D\{1 - \exp[-\alpha(q_r - q_{re})]\}^2. \tag{17}$$

Here, D is the classical desorption energy, q_{re} the equilibrium distance, and α an adjustable parameter. The classical desorption energy is given by:

$$D = E_{ad} + \varepsilon_z - \varepsilon_{z,B} - \varepsilon_{z,A/s/}, \tag{18}$$

where ε_z, $\varepsilon_{z,B}$, and $\varepsilon_{z,A/s/}$ are the zero-point vibrational energies of AB/s/, B, and A/s/, respectively. Calculations have shown that α does not differ significantly from $2\,\text{Å}^{-1}$.

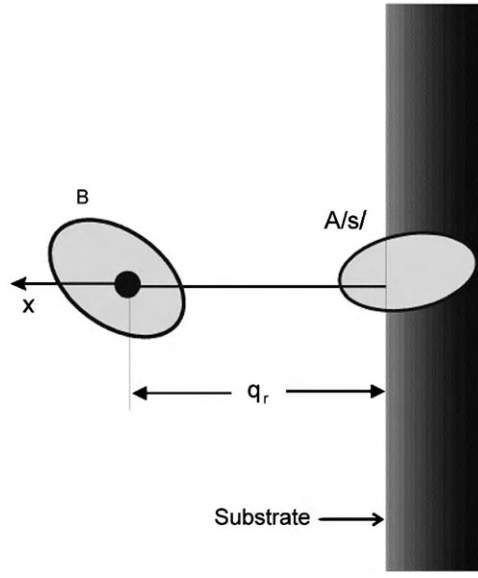


Fig. 9.3. Model of a loose transition complex.

Lam Research Ex. 1035 - Page 479
Lam Research Corp. v. Inpria Corp.
IPR2024-00033 - U.S. Patent No. 9,823,564

The Helmholtz free energy $a^{\neq}(q_r)$ is defined by the following equations:

$$a^{\neq}(q_r) = a_{th}^{\neq}(q_r) + U(q_r) + \varepsilon_z^{\neq}(q_r), \tag{19}$$

$$a_{th}^{\neq}(q_r) = -k_B T \ln Q^{\neq}(q_r), \tag{20}$$

where $Q^{\neq}(q_r)$ is the partition function and $\varepsilon_z^{\neq}(q_r)$ the zero-point vibrational energy of the transition complex $TC_{ad}(q_r)$.

It is assumed that the degrees of freedom of TC_{ad} include $s^{\neq}$ vibrations that are close to the vibrations of the noninteracting B and A/s/, two surface-restricted rotations corresponding to the "soft" rocking vibrations of B in AB/s/, and r_B free rotations similar to the rotations of free B as a whole, where

$$r_B = \begin{cases} 2, & \text{if B is linear} \\ 3, & \text{if B is nonlinear.} \end{cases} \tag{21}$$

For the calculation of $\varepsilon_z^{\neq}(q_r)$ and the free energy of the internal degrees of freedom $a_{th}^{\neq}(q_r)$, the following interpolation equations are used [52]:

$$\varepsilon_z^{\neq}(q_r) = \left(\varepsilon_z - \frac{\hbar\omega_r}{2} - \varepsilon_{z,roc} - \varepsilon_{z,B} - \varepsilon_{z,A/s/}\right) \exp[-\gamma(q_r - q_{re})] + \varepsilon_{z,B} + \varepsilon_{z,A/s/}, \tag{22}$$

$$a_{th}^{\neq}(q_r)[a + k_B T \ln Q_{1v}^{(r)} - a_{roc} - a_B - a_{A/s/}]exp[-\gamma(q_r - q_{re})] - k_B T \ln Q_{r,rest}(q_r) + a_B + a_{A/s/}. \tag{23}$$

Here, $\varepsilon_{z,roc}$ is the zero-point energy of the two "soft" rocking vibrations mentioned above; ω_r the frequency of the normal mode of AB/s/ corresponding to the reaction coordinate; a, $a_{A/s/}$, and a_B the Helmholtz free energies of the internal degrees of freedom of AB/s/, A/s/, and B; a_{roc} the Helmholtz free energy of the two "soft" rocking vibrations mentioned above.

The parameter γ determines the distance at which the free energy of AB/s/ transforms to that of noninteracting B and A/s/. Numerous calculations in Refs. [52–55] have shown that, with a satisfactory accuracy, it can be accepted that

$$\gamma = 0.75\left(\frac{\alpha}{2}\right). \tag{24}$$

Partition functions are given by standard formulas, e.g., the partition function of the normal mode of AB/s/ corresponding to the reaction coordinate

$$Q_{1v}^{(r)} = \frac{1}{1 - \exp(-(\hbar\omega_r)/(k_B T))}, \tag{25}$$

Lam Research Ex. 1035 - Page 480
Lam Research Corp. v. Inpria Corp.
IPR2024-00033 - U.S. Patent No. 9,823,564

and that for two equivalent surface-restricted rotations

$$Q_{\mathrm{r,rest}}(q_{\mathrm{r}}) = \frac{k_{\mathrm{B}}T}{B_{\mathrm{eff}}(q_{\mathrm{r}})}. \tag{26}$$

$$B_{\mathrm{eff}}(q_{\mathrm{r}}) = \frac{2q_{\mathrm{r}}}{q_{\mathrm{r}} - R_{\mathrm{B}}} \frac{\hbar^2}{2m_{\mathrm{B}}q_{\mathrm{r}}^2}, \tag{27}$$

where m_{B} is the mass of B and R_{B} its van der Waals radius.

Given the parameters α and γ and the necessary characteristics of AB/s/, A/s/, and B, the maximum Helmholtz free energy of the transition complex $a^{\neq}_{\max} = a^{\neq}(q^{\neq}_{\mathrm{r}})$ can be found numerically, and k_{des} can be calculated using the equation

$$k_{\mathrm{des}} = \frac{k_{\mathrm{B}}T}{2\pi\hbar} \exp\left(-\frac{a^{\neq}_{\max} - a}{k_{\mathrm{B}}T}\right). \tag{28}$$

The adsorption rate constant k_{ads} is calculated using k_{des} given by Eq. (28) and the detailed balancing principle.

4. Simulation Methods

The main goal of simulation methods is to obtain information on the spatial and temporal behavior of a complex system (a material), that is, on its structure and evolution. Simulation methods are subdivided into atomistic and phenomenological methods. Atomistic methods directly consider the evolution of the system of interest at the atomic level with regard to the microscopic structure of the substance. These methods include classical and quantum MD and various modifications of the MC technique. Phenomenological methods are based on macroscopic equations in which the atomistic nature of the material is not directly taken into account. Within the multiscale approach, both groups of methods mutually complement each other, which permits the physicochemical system under study to be described most comprehensively.

4.1. Molecular Dynamics

The MD technique permits thin films to be investigated under both equilibrium and nonequilibrium conditions. Therefore, in addition to equilibrium properties, such as structure, density, etc., MD predicts the nonequilibrium behavior of thin films, for example, energy relaxation for an ion interacting

Lam Research Ex. 1035 - Page 481
Lam Research Corp. v. Inpria Corp.
IPR2024-00033 - U.S. Patent No. 9,823,564

with the surface. We will present here the basics of MD implementation and consider the problem of choosing proper energy functionals for MD simulations.

4.1.1. Equation of Motion

In ordinary classical MD, classical equations of motion for a many-particle system

$$\frac{d}{dt}\left(\frac{\partial L}{\partial \dot{q}_i}\right) = \frac{\partial L}{\partial q_i} \tag{29}$$

are solved numerically [56]. Here, $L = K - U$ is the Lagrange function of the system (K and $U(q)$ are the kinetic and potential energies of the system, respectively), q_i the generalized coordinates of the system, and q the set of all generalized coordinates.

The potential energy of the system $U(q)$ can be determined from the solution of the corresponding quantum-mechanical problem for electrons (in this case, it is called first-principles MD), or by using empirical energy functionals (they will be discussed in detail below).

The numerical integration of dynamic Eq. (29) is carried out using an approximation by finite-difference expressions. There are several finite-difference approximations of Eq. (29), which differ in their approximation accuracy. The popular velocity method by Verlet [57]

$$q^{n+1} = q^n + dt \cdot v^n + \tfrac{dt^2}{2} a^n,$$
$$v^{n+1} = v^n + \tfrac{dt}{2}(a^n + a^{n+1}),$$

where v^n and a^n are, respectively, velocities and accelerations at the time t^n, and dt the time step, has an approximation accuracy of order $O(dt)$ for the velocity. More accurate equations were suggested for the integration of system (29) [58]. The time step of integration dt is determined by the largest vibrational frequency in the system and is $\sim 10^{-15} c$.

The Langrage function of the system L can be generalized to describe the effective interaction of the system with a thermostat or the isobaric behavior of the system. For example, for the system connected with a thermostat, one can use the Langrage function by Nosé [59]:

$$L = \sum_i \frac{m_i s^2 \dot{q}_i^2}{2} - U(q) + \frac{Q}{2}\dot{s}^2 - T \ln s,$$

where the Lagrangian contains an additional degree of freedom s with the effective mass Q and the potential energy determined by the desired

Lam Research Ex. 1035 - Page 482
Lam Research Corp. v. Inpria Corp.
IPR2024-00033 - U.S. Patent No. 9,823,564

temperature T. A modification of this method leads to the equation of motion by Nose–Hoover [60]

$$m_i\ddot{q}_i = -\nabla_i U - \varsigma\dot{q}_i,$$
$$\dot{\varsigma} = \frac{1}{Q}\left(\sum_i \frac{m_i\dot{q}_i^2}{2} - T\right).$$

In this type of equations the forces depend on not only the coordinates of atoms, but also their velocities (as effective friction force); therefore, numerical integration of equation of motion should be performed self-consistently, since $a^{n+1} = a^{n+1}(v^{n+1})$.

4.1.2. *Energy Functional for MD*

At present, simulations with the MD method using a first-principles energy functional can be performed for relatively small systems that contain several hundreds of atoms. Therefore, for the simulation of larger systems, one should use empirical energy functionals.

For species with strong polar bonds (e.g., metal oxides or halides) the interaction between ions can be described as the sum of Coulomb and short-range pair interactions. The latter is usually written in the Born–Mayer form

$$V_{ij}(r_{ij}) = A\ \exp\left(-\frac{r}{\rho_{ij}}\right) - \frac{C}{r_{ij}^6},$$

where the first term describes repulsion at short distances, while the second term gives van der Waals attraction between atoms. In periodic systems, for calculation of long-range Coulomb interaction one should use special methods, such as the Ewald method or the multipole method (fast multipole method, FMM) [61]. Ion charges can be fixed (e.g., equal to the formal charges of elements in the given material) or varied, depending on the local environment. For example, in the electronegativity equilibration method (QEq) [62], charges in the given configuration are determined by minimizing the functional

$$E_{\mathrm{QEq}} = \sum_i \left[\eta_i q_i + \frac{1}{2}\chi_i q_i^2\right] + \sum_{i<j}\frac{q_i q_j}{r_{ij}},$$

where constants η_i and χ_i are determined from the electron affinity and ionization energies of each element.

In systems with more strong covalent chemical bonds, it is necessary to take into account the attraction of atoms due to the exchange interaction, which strongly depends on the orientation. The orientational dependence of

Lam Research Ex. 1035 - Page 483
Lam Research Corp. v. Inpria Corp.
IPR2024-00033 - U.S. Patent No. 9,823,564

covalent bonds can be allowed for by using three-body interactions of the form

$$V_{ijk} = k(\cos\ \theta_{ijk} - \cos\ \theta_0)^2.$$

For atoms with sp^3 hybridization (e.g., Si in SiO_2), the parameter $\cos\theta_0 = -1/3$ corresponds to the angle in the tetrahedron. The three-body term with an angular dependence is also used in the Stillinger–Weber potential [63] for systems with the diamond lattice

$$E = \sum_{i<j} A_{ij}\ \exp\left(\frac{\rho}{r_{ij} - r_{\max}}\right)\left(\frac{B}{r_{ij}^4} - 1\right) + \sum_{i<j<k} k_{ijk}(\cos\ \theta_{ijk} - \cos\ \theta_0)^2\ \exp\left(\frac{\rho}{r_{ij} - r_{\max}}\right)\ \exp\left(\frac{\rho}{r_{ik} - r_{\max}}\right),$$

where the interaction vanishes for $r > r_{\max}$.

In systems where atoms can change their hybridization and coordination, one should take into account the dependence of the bond energy on the presence and orientation of other bonds (that is, on the bond order). For covalent systems, such a dependence was suggested by Abell [64]

$$V_{ij} = V_{ij}^{\mathrm{R}}(r_{ij}) - b_{ij} V_{ij}^{\mathrm{A}}(r_{ij}),$$

where the interaction between atoms i and j is subdivided into the repulsive (V_{ij}^{R}) and attractive (V_{ij}^{A}) terms, while the contribution of the latter is determined by the existence and orientation of other atoms via coefficient b_{ij}. The expression for b_{ij} suggested by Tersoff [65] for Si, Ge, and C atoms has the following form:

$$b_{ij} = (1 + (\beta\xi_{ij})^n)^{-1/2n},$$
$$\xi_{ij} = \sum_{k \neq i,\, j} f_{\mathrm{c}}(r_{ik}) g(\theta_{ijk})\ \exp(\lambda^3 (r_{ij} - r_{ik})^3),$$
$$g(\theta) = 1 + \frac{c^2}{d^2} - \frac{c^2}{d^2 + (h - \cos\theta)^2},$$

where $f_c(r) = 0$ for $r > r_{\max}$. A similar form of the energy functional was used by Brenner [66, 67] in the empirical potential for hydrocarbons. Bond-order-based potentials were also derived for oxide systems [68].

For systems with metallic bonds, the empirical embedded atom method (EAM) suggested by Daw and Baskes [69] is widely used. In this method, the bond energy is expressed as a function of the density at the site of

Lam Research Ex. 1035 - Page 484
Lam Research Corp. v. Inpria Corp.
IPR2024-00033 - U.S. Patent No. 9,823,564

atom location

$$E = \sum_i F(\rho_i) + \sum_{i<j} V_{ij}^{\mathrm{R}}(r_{ij}),$$
$$\rho_i = \sqrt{\sum_j \rho_{ij}^2(r_{ij})},$$

where the second term in the equation for energy describes the short-range pair repulsion. In spite of the difference in functional forms, it was shown [70, 71] that the EAM functional can be reduced to the bond-order formalism. The difference between EAM and bond-order methods in the Tersoff form is that the coefficient b_{ij} in the Tersoff functional depends on the angle between bonds. The angular dependence for density was introduced in the modified embedded atom method (MEAM). This functional form was used for both metallic and oxide systems [72, 73].

4.2. MONTE CARLO METHOD

The MC method [56, 61] is used for the determination of equilibrium distributions and calculations of equilibrium properties. The method uses a Markovian sequence of stochastic steps in the phase space, and each step is characterized by some probability of occurrence. One of the possible methods for calculation of step probability is Metropolis method, in which the probability of transition from the state i to the state j is equal to:

$$P_{i\to j} = \begin{cases} 1, & \Delta E_{ij} < 0, \\ \exp\left(-\frac{\Delta E_{ij}}{T}\right), & \Delta E_{ij} > 0. \end{cases}$$

Unlike the MD technique, the MC method does not describe the dynamic properties of a system but rather gives only information on the distribution function in the phase space. For the calculation of the energy change as a result of a transition, one can use the same energy functionals as those in MD. The length of the step in the phase space is usually adjusted to achieve the required average probability of step occurrence.

4.3. KINETIC MONTE CARLO METHOD

On the one hand, the KMC method is a version of the standard MC method in which a set of specific transitions in the phase space corresponding to chemical transformations (reactions) is used instead of arbitrary steps in the

Lam Research Ex. 1035 - Page 485
Lam Research Corp. v. Inpria Corp.
IPR2024-00033 - U.S. Patent No. 9,823,564

phase space of the system. In fact, the KMC method deals only with transitions from one local minimum on the PES to another one and does not describe motions in the vicinity of each minimum, that is, local vibrations. Thus, the KMC method can explore more efficiently PES than the standard MC method.

On the other hand, the KMC method can describe not only equilibrium systems, but also nonequilibrium ones, including evolution processes and relaxation to an equilibrium state. The relation of the KMC with evolution processes in real time is carried out by creating a table of all possible reactions at a given instant of time together with their rates $\{r_i, k_i\}$. The probability of process i will be determined by the ratio

$$P_i = \frac{k_i}{\sum\limits_j k_j}.$$

It was shown [74] that if, after a completed MC step selected in accordance with the above formula for the probability, the time is increased by an increment

$$\Delta t = -\frac{\ln \xi}{\sum\limits_j k_j}, \tag{30}$$

where ξ is a random number $0 < \xi < 1$, then the average values derived from KMC correspond to the solution of the kinetic equations. Thus, KMC can be considered as a stochastic method of solving the differential kinetic equations. In this case, the system of kinetic equations is commonly written in the mean-field approximation, that is, with the neglect of fluctuations and correlations in the distribution of substances. However, it has been shown [75] that such fluctuations and correlations in certain cases are important for the kinetics of transformations. Moreover, the occurrence of such processes as the blocking of active sites, the lateral interaction of adsorbates, and phase separation requires an extension beyond the limits of the mean-field approximation. Thus, the KMC method has been proved to be a powerful tool for studying complex heterogeneous processes [76].

For heterogeneous systems, the set of reactions includes adsorption, dissociation, surface diffusion, desorption, and other processes. In this case, the rates of processes can differ by many orders of magnitude. In accordance with Eq. (30), the time step is determined by the fastest process in the system. This condition strongly restricts the maximum real time in the simulation and prevents modeling of rare processes. One of the ways of overcoming this problem can be to exclude all fast processes from the table of reactions and use equilibrium distributions for these processes. For example,

Lam Research Ex. 1035 - Page 486
Lam Research Corp. v. Inpria Corp.
IPR2024-00033 - U.S. Patent No. 9,823,564

in the case of fast surface diffusion, one can take this process into account by the randomization of reagent positions after each reaction step [77].

4.4. LATTICE AND DYNAMIC VERSIONS OF KINETIC MONTE CARLO

The KMC method requires that a certain set of reactions be specified. This set includes transformations from reagents to products that correspond to local minima on the PES. Therefore, in the general case, to construct the table of reactions in KMC method, one should determine local minima on the PES and then determine the rate constants of transitions between them. Since PES is modified after each reaction, the process of searching for local minima should be dynamically performed in the course of the KMC run. This implementation of the KMC method is called dynamic KMC, since the set of all possible reactions at a given time is determined dynamically during the run rather than specified before calculations. Therefore, to implement dynamic KMC, it is required to specify an energy functional for the calculation of PES, methods of searching for local minima, and methods for the calculation of rate constants for transitions between local minima.

As in the MD method, PES for KMC can be derived from first-principles methods or using empirical energy functionals described above. However, the KMC method requires the accurate evaluation of the PES not only near the local minima, but also for transition regions between them. The corresponding empirical potentials are called reactive, since they can be used to calculate parameters of chemical reactions. The development of reactive potentials is quite a difficult problem, since chemical reactions usually include the breaking or formation of new bonds and a reconfiguration of the electronic structure. At present, a few types of reactive empirical potentials can semi-quantitatively reproduce the results of first-principles calculations: these are EAM and MEAM potentials for metals and bond-order potentials (Tersoff and Brenner) for covalent semiconductors and organics.

The search for local minima in the neighborhood of a given local minimum is usually performed by the excitation of the system from this state followed by the relaxation of the system. If the relaxation of the excited system results in a state different from the initial state (and explored earlier), then a new local minimum is found, otherwise the evolution of the excited system is continued. The ways of moving out of the initial state can be different: in temperature accelerated dynamics (TAD) by Sorensen and Voter [78], MD is used at high temperatures; in the activation–relaxation technique (ART) by Mousseau and Barkema [79] and the local activated Monte Carlo method (LAMC) [80], the system evolves along the direction opposite to the direction of the force; in the long-scale kinetic Monte Carlo

Lam Research Ex. 1035 - Page 487
Lam Research Corp. v. Inpria Corp.
IPR2024-00033 - U.S. Patent No. 9,823,564

(LSKMC) method [81], the search for saddle points in the vicinity of a given local minimum by the dimer method was used [82]. For the found new local minima, the rate constants of transitions are calculated based on the TST

$$k = \frac{Z^{\neq}}{Z_{\text{reag}}} \exp\left(-\frac{E^{\neq}}{T}\right),$$

where $Z^{\neq}$ and Z_{reag} are the partition functions of the TS and the reagent, respectively, and $E^{\neq}$ the energy of the TS (activation energy) with respect to reagents. In ART, LAMC, and LSKMC methods, a harmonic approximation to the TST is usually used, that is, preexponential factors are calculated using vibrational frequencies. In the TAD method, the preexponential factor is determined directly using the escape time from the local minimum calculated by MD

$$v_0 = \frac{1}{t_{\text{escape}}} \exp\left(\frac{E^{\neq}}{T}\right).$$

To estimate the activation energy ($E^{\neq}$) for the given reagents and products, one can use methods for searching of saddle points for given stationary points, such as the nudged elastic band method (NEB) [83].

In dynamic KMC, the major part of the time is spent to search for local minima and transition paths between them. In particular cases, the positions of local minima on PES are known *a priori*. For example, for a growing crystalline film, the stationary positions of deposited atoms will very likely coincide with the positions of atoms in the crystal lattice. Thus, sometimes it is possible to strongly simplify the KMC method, assuming that particles occupy only the positions in the lattice known in advance and all the transitions take place only between these positions. This simplified KMC method is called the lattice kinetic MC method. Thus, in the framework of the lattice KMC, there is no need to specify an energy functional for the interaction between atoms, and only kinetic parameters of possible reactions must be specified instead. The corresponding reactions are investigated in advance with model systems usually using quantum-mechanical calculations. In lattice KMC, a lattice site can be occupied by one or several atoms (groups), and a chemical group at one site can shield neighboring sites (see, e.g., Ref. [84]) or change the reaction energies at neighboring sites [85].

4.5. Kinetic Monte Carlo Method with Dynamic Relaxation (KMC-DR)

The KMC-DR was suggested in Ref. [24] as a hybrid of lattice and dynamic KMC. Just as in the lattice KMC method, possible chemical reactions in this

Lam Research Ex. 1035 - Page 488
Lam Research Corp. v. Inpria Corp.
IPR2024-00033 - U.S. Patent No. 9,823,564

method are specified in advance based on the results of separate quantum-chemical calculations, while the structure is relaxed after each reaction step using a given energy functional. Thus, KMC-DR uses an energy functional only to relax the system to a local minimum rather than to calculate rate constants of reactions; that is, KMC-DR does not need reaction potentials. The construction of a table of all possible reactions at a given instance of time is performed based on an analysis of the graph of chemical bonds in the system and a search for possible configurations of reagents in this graph and distances between the reagents. Since this procedure of constructing the graph and searching in it is significantly faster than searching for the neighboring local minima in dynamic KMC, the KMC-DR method is faster than dynamic KMC.

Taking into account the dependence of rate constants on the local chemical environment is the main difficulty in the KMC-DR method. It was suggested to take into account this dependence in the framework of the KMC-DR method in two ways: (1) using *a priori* dependence on the distances and the coordination numbers of reagent atoms and (2) using an analysis of the distribution of product atoms (PA) in the given configuration. The second way verifies the possibility of the distribution of reaction products for the given configuration and gives initial positions for the relaxation of the system. This is carried out by the relaxation of the system with a simplified set of interatomic potentials: spring potentials for chemical bonds and repulsive Buckingham potentials for unbound atoms.

In general, the product distribution algorithm works in the following way. At the first step, the products of the reaction are distributed in accordance with predefined coordinates with respect to reagent coordinates. After that, the algorithm determines NA to the PA based on some maximum distance. All other atoms are treated as bulk atoms (BA), being fixed during the distribution of PAs. The reason for such a subdivision is to perform the local relaxation of the nearest atoms but to prevent large-scale expansion during the distribution of products. Interactions are set according to the following scheme: (1) spring bonds are set for each bond in PA, between NA and NA, NA and BA, and NA and PA for each PA that has a corresponding reagent atom; (2) all other interactions are described as repulsive using Buckingham potentials. Then, PA and NA are relaxed, and, if their final energy is larger than some threshold value, the reaction is rejected and the initial coordinates of all atoms are restored. Otherwise, the reaction is accepted and the system is relaxed using a more accurate energy functional. Since simple interatomic potentials are used in the product distribution algorithm, this step does not require large resources.

Lam Research Ex. 1035 - Page 489
Lam Research Corp. v. Inpria Corp.
IPR2024-00033 - U.S. Patent No. 9,823,564

4.6. Reactor Modeling of Thin-Film Deposition

The main physicochemical processes in thin-film deposition are chemical reactions in the gas phase and on the film surface and heat–mass transfer processes in the reactor chamber. Laboratory deposition reactors have usually a simple geometry to reduce heat–mass transfer limitations and, hence, to simplify the study of film deposition kinetics and optimize process parameters. In this case, one can use simplified gas-dynamics reactor such as well stirred reactor (WSR), calorimetric bomb reactor (CBR, batch reactor), and plug flow reactor (PFR) models to simulate deposition kinetics and compare theoretical data with experimental results.

The model of a deposition reactor describes the following phases: gas phase, surface phase, condensed phase, reactor walls, and external ambient (see Figure 9.4).

Simplified reactor models of a deposition process can be classified by

(1) reagent and product mixing conditions (CBR corresponds to instantaneous mixing in the closed system, WSR corresponds to instantaneous mixing in the presence of external substance sources and sinks, and PFR corresponds to instantaneous mixing in each section and the absence of mixing along the reactor coordinate);
(2) external thermodynamics parameters (PT corresponds to a constant pressure at a given temperature, VT corresponds to a constant volume at a given temperature, VU corresponds to a constant volume at a given internal energy, and PH corresponds to a constant volume at a given enthalpy);

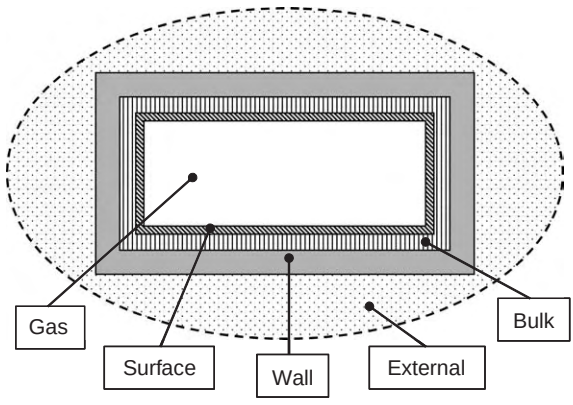


Fig. 9.4. Main phases in a deposition reactor.

Lam Research Ex. 1035 - Page 490
Lam Research Corp. v. Inpria Corp.
IPR2024-00033 - U.S. Patent No. 9,823,564

(3) heat exchange (''environment–thermostat'' model, in which gas, surface, condensed phase, and reactor walls are a uniform system with temperature differing from the environment temperature, while environment is considered as a thermostat $T_{gas} = T_{bulk} = T_{surf} = T_{wall} \neq T_{ext}$; and the model, in which reactor wall, surface phase, condensed phase, and environment are uniform thermostats $T_{gas} \neq T_{bulk} = T_{surf} = T_{wall} = T_{ext}$).

Generally, the gas-phase concentrations N_k are described by a set of master equations of chemical kinetic (equations for active masses at the source/sink of the kth substance in the chemical reactions W_k)

$$W_k^{gas} = \sum_{gas\ reaction} \Delta v_{ki} q_i^{gas}, \tag{31}$$

where Δv_{ki} is the net stoichiometric coefficient of the kth component in the ith reaction.

Surface component concentrations X_k are also described by a set of formal kinetic equations in the framework of the surface site formalism. In this formalism, a set of surface centers (sites) Γ_n is defined for each condensed phase (n). Each site is characterized by a set of surface substances (j) that are present at this site (Figure 9.5).

In this case, the source/sink for the surface and condensed-phase component concentrations are as follows:

$$S_{j(n)}^{surf/bulk} = \sum_{surface\ reaction} \Delta v_{j(n)i} q_i^{surf}, \tag{32}$$

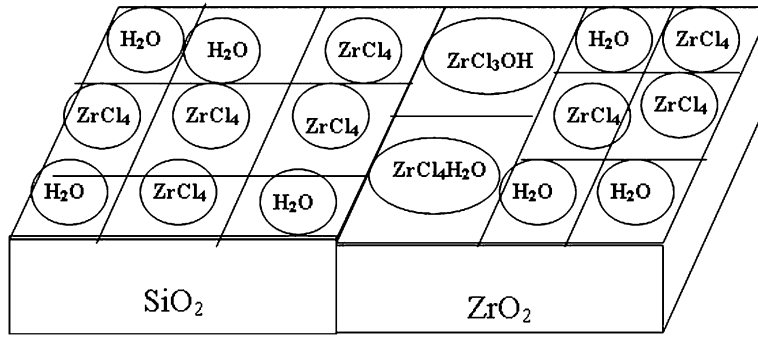


Fig. 9.5. Surface sites and surface substances.

Lam Research Ex. 1035 - Page 491
Lam Research Corp. v. Inpria Corp.
IPR2024-00033 - U.S. Patent No. 9,823,564

the site concentration is defined as

$$\Gamma_n = \sum_{\text{surf},\, n-\text{phase}} \sigma_{j(n)} X^{\text{surf}}_{j(n)}, \tag{33}$$

and the surface reaction rate is defined as

$$q_i^{\text{surf}} = k_i^{\text{f}} \left(\prod_{\text{gas, surf, bulk}} (X_k)^{v_{k_i}^-} - K_{\text{c}i}^{-1} \prod_{\text{gas, surf, bulk}} (X_k)^{v_{k_i}^+} \right),$$

$$K_{\text{c}i} = K_{\text{p}i} \left(\frac{P_{\text{atm}}}{RT} \right)^{\sum_{\text{gas}} \Delta v_{k_i}} \prod_{\text{surf}} (\Gamma_n^{\text{o}})^{\sum_{\text{surf},\, n-\text{phase}} \Delta v_{k_i}} \prod_{\text{surf}} \left(\frac{1}{\sigma_{k(n)}} \right)^{\sum_{\text{surf},\, n-\text{phase}} \Delta v_{k_i}},$$

$$K_{\text{p}i} = \exp\left\{ \frac{1}{RT} \sum_{\text{gas, surf, bulk}} \Delta v_{k_i} (T \cdot s_i - h_i) \right\}.$$

Here, k_{i}^{f} is the rate constant; $v_{k_i}^{+,-}$ the stoichiometric coefficients of the kth component in the ith reaction of reagents and products, correspondingly; K_i the equilibrium constants; $\sigma_{j(n)}$ the number of sites occupied by surface substance j of condensed phase n; Γ_n^{o} the surface site density in the nth phase standard state; and h_k and s_k the enthalpy and the entropy of the kth substance.

The composition of the condensed phase and the film thickness are determined by balance between the film formation and the substance consumption rates

$$\frac{dm_{i(n)}^{\text{bulk}}}{dt} = \frac{\mu_{i(n)}^{\text{bulk}}}{N_{\text{A}}} A_{\text{r}} S_{i(n)}^{\text{bulk}}, \tag{34}$$

where A_{r} is the area of the active reactor surface and $S_{i(n)}{}^{\text{bulk}}$ the formation rate of the ith bulk substance due to surface reactions.

The Arrhenius form is usually used for rate constants

$$k = A \times \left(\frac{T}{300} \right)^n \exp\left(\frac{-E_a}{RT} \right).$$

It is well known that the rate constant of surface reactions depends on the local environment. Although the kinetic methods work in the mean-field approach, the local environment dependence is considered approximately by including the dependence of the effective activation energy and the pre-exponential factor on the average composition of the entire surface or on the specific surface in the given reactor section

$$A = f(X_i), \qquad E_{\text{a}} = f(X_i). \tag{35}$$

Lam Research Ex. 1035 - Page 492
Lam Research Corp. v. Inpria Corp.
IPR2024-00033 - U.S. Patent No. 9,823,564

For the description of nonstationary processes in a periodic reactor, the CBR is used. The equations for gas-phase and surface component concentrations are described by the ODE system.

The number of gas-phase molecules varies according to the following law:

$$\frac{dN_k^{\text{gas}}}{dt} = V_{\text{r}} W_k^{\text{gas}} + A_{\text{r}} S_k^{\text{gas}}, \tag{36}$$

$$\frac{dA_{\text{r}} X_{j(n)}^{\text{surf}}}{dt} = A_{\text{r}} S_{j(n)}^{\text{surf}}, \tag{37}$$

where $N_k{}^{\text{gas}}$ is the number of molecules of the kth type in the gas phase and V_{r} the reactor volume.

The equation for temperature depends on the model type:

(I) T-type reactor:

$$T = \Theta(t).$$

(II) Q-type reactor:

$$\frac{dU}{dt} = -Q \quad \text{at constant volume;}$$

$$\frac{dH}{dt} = -Q \quad \text{at constant pressure.}$$

Here, Q is the heat loss in the reactor.

The internal energy of the reactor is $U = H - P^{\text{gas}} V_{\text{r}}$, where the reactor enthalpy is the sum of the enthalpies of reactor parts

$$H = H^{\text{gas}} + H^{\text{surf}} + H^{\text{bulk}}, \tag{38}$$

$$H^{\text{gas}} = M^{\text{gas}} h^{\text{gas}} = \rho^{\text{gas}} V_{\text{r}} \sum_{\text{gas}} \frac{N_k^{\text{gas}}}{M_{\text{gas}} N_{\text{A}}} h_k(T), \tag{39}$$

$$H^{\text{surf}} = \sum_{\text{surf}} \frac{N_{j(n)}^{\text{surf}}}{N_{\text{A}}} h_{j(n)}(T), \qquad H^{\text{bulk}} = \sum_{\text{bulk}} \frac{m_{i(n)}^{\text{bulk}}}{\mu_{i(n)}} h_{i(n)}(T). \tag{40}$$

If the reactor operates in the regime of intense mixing of gas-phase substances, the WSR reactor model should be used. The equations for the surface and condensed-phase component concentrations are the same as those in the CBR equations, and the equations for the gas-phase component

Lam Research Ex. 1035 - Page 493
Lam Research Corp. v. Inpria Corp.
IPR2024-00033 - U.S. Patent No. 9,823,564

concentrations are modified with an additional term for the source/sink

$$\frac{dN_k^{\text{gas}}}{dt} = V_{\text{r}} W_k^{\text{gas}} + A_{\text{r}} S_k^{\text{gas}} + F^{\text{in}} C_k^{\text{in}} - F^{\text{out}} C_k^{\text{gas}}, \tag{41}$$

where F^{in} is the absolute inlet mass flow, $F^{\text{out}} = M^{\text{gas}}/\tau$ the absolute outlet mass flow, $C_k{}^{\text{gas}} \equiv X_k{}^{\text{gas}}/\rho^{\text{gas}} = N_k{}^{\text{gas}}/(\rho^{\text{gas}} V_{\text{r}}) = N_k{}^{\text{gas}}/M^{\text{gas}}$, and $\tau = M^{\text{gas}}|_{t=0}/F^{\text{in}}$ the average residence time in the reactor.

The equation for temperature is derived from the energy conservation law

$$\frac{dH}{dt} = -Q + F^{\text{in}} h^{\text{in}} - F^{\text{out}} h^{\text{gas}},$$

where the enthalpy is given by Eqs. (38)–(40), and $h^{\text{in}} = (1/N_{\text{A}}) \sum_{\text{gas}} C_k{}^{\text{in}} h_k(T^{\text{in}})$.

This model allows one to determine the steady-state concentrations of gas and surface substances, the composition of the condensed phase, and the steady-state film growth rate.

A reactor for thin-film deposition can have a tubular structure with a flowing chemically active gas. In this case, the PFR model can be used. This one-dimensional model uses the assumption of a uniform component distribution in a reactor section. This means that the boundary layer formation processes are not taken into account.

This model is applicable if the thickness of the boundary layer $\delta x \sim 2(Dt)^{1/2}$ is small as compared to the distance between the reactor walls (where t is the residence time in the reactor and D the diffusion coefficient). In this case, component concentration equations are obtained from the mass and momentum conservation laws and the continuity equation

$$\frac{\partial \rho u S C_k^{\text{gas}}}{\partial x} = S W_k^{\text{gas}} + a S_k^{\text{gas}}, \tag{42}$$

$$\frac{\partial \rho u S}{\partial x} = a \sum_{k_{\text{gas}}} S_{k_{\text{gas}}} \frac{\mu_{k_{\text{gas}}}}{N_{\text{A}}}, \tag{43}$$

$$\frac{\partial u}{\partial t} + u \frac{\partial u}{\partial x} + \frac{1}{\rho} \frac{\partial P}{\partial x} = F_{\text{bulk}} + F_{\text{surface}}, \tag{44}$$

where x is the coordinate along the reactor axis, a the surface area per reactor length unit, S the cross-sectional area at point x of the reactor, ρ the gas density, P the pressure, and $F_{\text{bulk/surface}}$ the forces determined by the gas interaction with the condensed and surface phases. Forces F can be put to zero with the same accuracy as the neglect of viscosity in Eq. (44).

Lam Research Ex. 1035 - Page 494
Lam Research Corp. v. Inpria Corp.
IPR2024-00033 - U.S. Patent No. 9,823,564

The equation for temperature can be obtained from the energy conservation law for the flow

$$\frac{\partial(u \cdot \{E + PS\})}{\partial x} = -Q,$$

where

$$E = U + \frac{\rho S}{2} u^2,$$

$$U = H - P^{\text{gas}} S,$$

$$H = \frac{1}{N_A} \left(\rho S \sum_{\text{gas}} C_k^{\text{gas}} h_k(T) + \sum_{\text{surf}} N_{j(n)}^{\text{surf}} h_{j(n)}(T) \right).$$

5. Modeling of the Deposition of Thin Dielectric Films

This section deals with the application of the techniques described above to one of the most important problems for current microelectronics, namely the epitaxial growth of a thin high-k dielectric film on a silicon surface. For a recent review, see, for example, Ref. [86]. Here, the growth of a ZrO_2 film from $ZrCl_4$ and H_2O as metal and oxygen precursors will be considered in detail.

5.1. MOLECULAR DYNAMICS MODELING OF PRECURSOR INTERACTION WITH SURFACE

Quantum-mechanical calculations of the interaction of metal chloride precursors with the metal oxide surface show that adsorption occurs via the formation of a stable intermediate complex with a binding energy of ~20 kcal/mol as a result of the formation of a donor–acceptor bond (see Ref. [20]). The existence of a deep well in the reaction path leads to an acceleration of the colliding particle, which results in a deviation of the kinetic energy distribution from equilibrium. Therefore, nonequilibrium processes can take place during adsorption, such as nonequilibrium diffusion on the surface [87]. The importance of these nonequilibrium processes for film growth kinetics is determined by the ratio of the characteristic time of energy relaxation of the nonequilibrium particle to the time of the chemical transformation of the adsorbed complex.

To estimate the relaxation time of the adsorbed complex, MD modeling of $ZrCl_4$ adsorption on the hydroxylated ZrO_2 surface was performed. The

Lam Research Ex. 1035 - Page 495
Lam Research Corp. v. Inpria Corp.
IPR2024-00033 - U.S. Patent No. 9,823,564

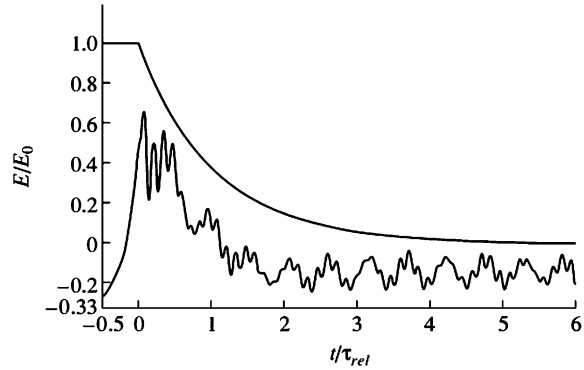


Fig. 9.6. Evolution of the kinetic and total energy of $ZrCl_4$ precursor during adsorption on the ZrO_2 surface.

empirical potential for the oxide substrate was taken from Ref. [88]. The empirical potential for $ZrCl_4$ was derived by fitting to the optimized stricture and the matrix of second derivatives calculated from first principles. The Coulomb interaction was described with fixed formal ion charges ($Q_{Zr} = 4$, $Q_O = -2$, $Q_{OH} = -1$, $Q_{Cl} = -1$). The potential for the interaction of $ZrCl_4$ with the surface was fitted to the first-principles data, such as the optimized structure of $ZrCl_4$ surface complex and the adsorption energy of $ZrCl_4$.

A periodic model of the zirconia surface was used in MD modeling. It consisted of 2×2 elementary ZrO_2 cells, and $ZrCl_4$ precursors incident perpendicular to the surface. The ZrO_2 surface was connected with a thermostat with a temperature of 600 K, and the initial velocities of the $ZrCl_4$ precursor corresponded to a temperature of 600 K.

The total and kinetic energies of $ZrCl_4$ precursors were recorded during the MD run (see Figure 9.6). It is seen from the figure that the variation of the total energy of $ZrCl_4$ precursor is described by an exponential law. The calculated relaxation time is $\tau_{rel} = 2.6 \times 10^{-12}$ sec. Similar calculations performed at temperatures $T = 500$–800 K have shown that the relaxation time does not change significantly in this temperature interval. This time is notably smaller than the time of the chemical transformation of $ZrCl_4$ in the products; hence, the rate constant of this transformation can be calculated by assuming an equilibrium distribution.

5.2. Kinetic Mechanism of Zirconium and Hafnium Oxide Film Deposition

The basic kinetic regularities of film growth must be considered to build the film deposition kinetic mechanism. In the case of ZrO_2 film growth from

Lam Research Ex. 1035 - Page 496
Lam Research Corp. v. Inpria Corp.
IPR2024-00033 - U.S. Patent No. 9,823,564

zirconium chloride, the experimental features can be summarized as follows [89–94]:

(a) the ZrO_2 film growth rate (mass or thickness increment per cycle) on hydroxylated surfaces is much higher than that on bare metal oxide surfaces;
(b) the maximum amount of the deposited oxide (film mass increment) per cycle is 30–50% of ZrO_2 monolayer (ML);
(c) the average film mass and thickness increments per ALD cycle decrease with increasing temperature;
(d) the Cl:M ratio (x) in the chemisorbed MCl_x surface groups at the surface of a growing film varies from $x = 2(MCl_2)$ at low temperature (200°C) to 3–4 at high temperature (600°C);
(e) the residual chlorine concentration in the film decreases from ~5% to <1% as temperature increases from 200°C to 600°C.

These features can be used to recover the elementary mechanism and reaction parameters.

In accordance with these features, the film deposition mechanism presented in Figure 9.7 was suggested. To explain the decrease in the film growth rate and the variation of the composition of chemisorbed MCl_x surface groups with temperature, it was assumed that the concentration of surface OH groups is controlled by the dehydroxylation (water desorption) reaction (Figure 9.8).

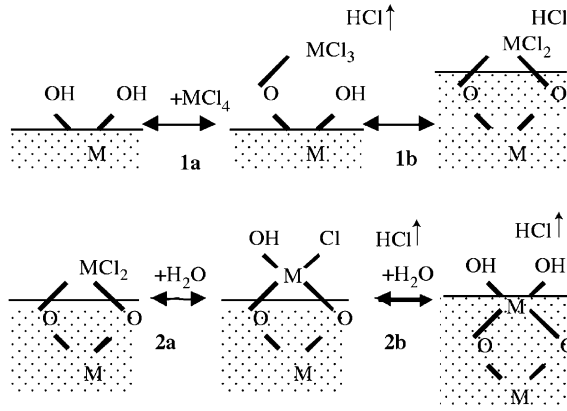


Fig. 9.7. ZrO_2 film growth: (1a) chemical adsorption, (1b) $ZrCl_2$ formation, (2a) the first stage of hydrolysis, and (2b) the second stage of hydrolysis.

Lam Research Ex. 1035 - Page 497
Lam Research Corp. v. Inpria Corp.
IPR2024-00033 - U.S. Patent No. 9,823,564



Fig. 9.8. Water desorption from the surface.

To describe the surface of the growing film within formal kinetics, we introduced various groups of surface sites (see Figures 9.7 and 9.8):

(a) sites that describe the varying degree of surface hydroxylation: $M(OH)_2/s/$ (hydroxylated surface site) and $MO/s/$ (dehydroxylated surface site);
(b) sites that describe the physical adsorption of a metal precursor: $MCl_4M(OH)_2/s/$;
(c) sites that describe the chemical adsorption of a metal precursor on hydroxylated sites: $MOM(OH)Cl_3/s/$ and $MO_2MCl_2/s/$;
(d) sites that describe the physical adsorption of water: $MO_2MCl_2H_2O/s/$ and $MO_2MClOHH_2O/s/$;
(e) sites that describe the products of water treatment: $MO_2MClOH/s/$.

The elementary stages of this mechanism are presented in Table 9.1.

The rate coefficients of reactions (15)–(27) were taken from the results of *ab initio* calculations. Reactions (28) and (29) describe the process of surface dehydroxylation/hydroxylation. We used a value of 10^{13} sec^{-1} as an estimation of the preexponential factor (this value corresponds to the characteristic frequency of internal vibrations of the reaction center) for the desorption reaction. To describe the experimental dependence of the growth rate vs. temperature adequately, we considered that the water adsorption energy is a linear function of the hydroxylation degree β

$$E_{ad} = \begin{cases} E^0_{ad} - \Delta\varepsilon \cdot (2\beta - 1); & 1/2 < \beta < 1 \\ E^0_{ad}; & \beta < 1/2 \end{cases}.$$

The mechanism (15)–(29) was implemented in a nonsteady-state PFR model. The goal of the simulations was to determine the remaining adjustable parameters based on the available experimental data. The following experimental data were used to adjust the reactor parameters: the dependence of the film growth rate on the process temperature, the time dependence of the film mass increment during the MCl_4 pulse, the ratio of the total film mass increment attained in an ALD cycle m_0 to the mass increment during the MCl_4 pulse m_1, the Cl:M ratio (x) in the chemisorbed MCl_x

Lam Research Ex. 1035 - Page 498
Lam Research Corp. v. Inpria Corp.
IPR2024-00033 - U.S. Patent No. 9,823,564

Table 9.1. Kinetic scheme and parameters of rates of ZrO_2 film growth in the framework of the "minimum" mechanism

Reaction: $k = A \times T^n \exp(-E_a/RT)$ ($[k] = cm^3/sec$; cm^2/sec; sec^{-1}; $[E_a] =$ kcal/mol, $[T] = K$)	ZrO_2 mechanism		
	log(A)	n	E_a
Reactions of MCl_4 adsorption on the hydroxylated surface			
$MCl_4 + M(OH)_2/s/ \rightarrow MCl_4M(OH)_2/s/$ (15)	−13.00	0.86	−0.22
$MCl_4M(OH)_2/s/ \rightarrow M(OH)_2/s/ + MCl_4$ (16)	13.70	0.00	23.00
$MCl_4M(OH)_2/s/ \rightarrow MOM(OH)Cl_3/s/ + HCl$ (17)	10.30	0.50	16.30
$MOM(OH)Cl_3/s/ + HCl \rightarrow MCl_4M(OH)_2/s/$ (18)	−13.70	1.00	4.73
$MOM(OH)Cl_3/s/ \rightarrow MO_2MCl_2/s/ + HCl$ (19)	10.32	0.50	16.31
$MO_2MCl_2/s/ + HCl \rightarrow MOM(OH)Cl_3/s/$ (20)	−13.70	1.00	4.73
Reactions of H_2O with the chlorinated surface, new $M(OH)_2$ layer formation			
$H_2O + MO_2MCl_2/s/ \rightarrow MO_2MCl_2H_2O/s/$ (21)	−12.79	0.96	−0.17
$MO_2MCl_2H_2O/s/ \rightarrow H_2O + MO_2MCl_2/s/$ (22)	13.20	0.00	15.10
$MO_2MCl_2H_2O/s/ \rightarrow MO_2MClOH/s/ + HCl$ (23)	13.70	0.00	18.80
$MO_2MClOH/s/ + HCl \rightarrow MO_2MCl_2H_2O/s/$ (24)	−13.04	0.97	−0.02
$H_2O + MO_2MClOH/s/ \rightarrow MO_2MClOHH_2O/s/$ (25)	−12.79	0.96	−0.17
$MO_2MClOHH_2O/s/ \rightarrow H_2O + MO_2MClOH/s/$ (26)	13.20	0.00	15.10
$MO_2MClOHH_2O/s/ \rightarrow MO_2/b/ + M(OH)_2/s/ + HCl$ (27)	13.70	0.00	18.80
Reactions of surface (de)hydroxylation			
$M(OH)_2/s/ \rightarrow MO/s/ + H_2O$ (28)	13.00	0.00	34.5–57 33−53[a]
$MO/s/ + H_2O \rightarrow M(OH)_2/s/$ (29)	−13.00	0.00	10.00

[a]Values for the extended mechanism.

Lam Research Ex. 1035 - Page 499
Lam Research Corp. v. Inpria Corp.
IPR2024-00033 - U.S. Patent No. 9,823,564

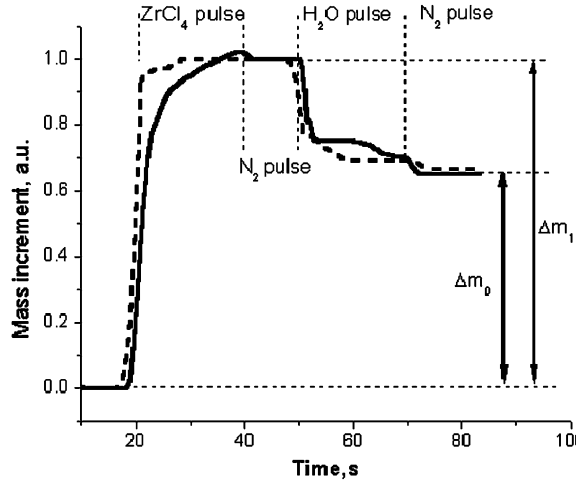


Fig. 9.9. Film mass increment during one cycle. Comparison of modeling results (dashed line) with the experimental data. Modeling conditions correspond to experimental conditions in Ref. [93].

surface groups as a function of temperature, and the chlorine concentration in the film. Modeling conditions correspond to the experimental conditions [89–94]. The modeling results are shown in Figures 9.9 and 9.10.

The best agreement with the experimental data was achieved with the next values of unknown model parameters:

the number density of available surface metal atoms of $6 \times 10^{14}\,\mathrm{cm}^{-2}$ for the growing ZrO_2 surface;

$$E_{\mathrm{ad}}^{0} = E_{\mathrm{a}}(28) - E_{\mathrm{a}}(29) = 47\ \mathrm{kcal/mol};$$

$$\Delta\varepsilon = 22.5\ \mathrm{kcal/mol}.$$

Though the mechanism (15)–(29) describes satisfactorily the experimental temperature dependence of the growth rate, it does not consider some of the important physical processes and meets difficulties in the description of other experimental dependences. First, this minimum mechanism neglects surface diffusion processes, which may be important in the water desorption mechanism. Indeed, at low coverages, dehydroxylation is controlled by the OH surface diffusion rate. Second, the minimum mechanism cannot explain the experimental fact that the Cl:Zr ratio in the chemisorbed $ZrCl_x$ surface groups changes from 2 to 3 with increasing temperature, because it operates with a single type of hydroxylated sites, namely $Zr(OH)_2$.

Lam Research Ex. 1035 - Page 500
Lam Research Corp. v. Inpria Corp.
IPR2024-00033 - U.S. Patent No. 9,823,564

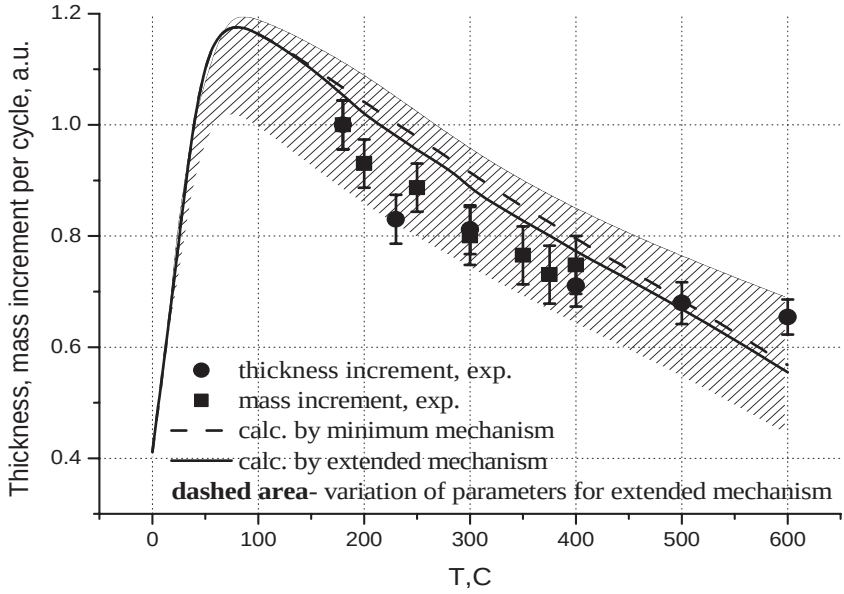


Fig. 9.10. Film mass and thickness increments per cycle as a function of the process temperature. Dashed and solid lines correspond to the calculated results by the minimum (15)–(29) and extended (15)–(54) mechanisms. The dashed area corresponds to sensitivity analysis. Circles correspond to the calculation of the mass increment from experimental data and squares correspond to direct mass increment measurement [93].

Because of the reasons discussed above, the minimum scheme (15)–(29) was extended. We introduced the following additional groups of surface sites (see Figure 9.11):

(a) sites that describe the variable degree of surface hydroxylation: 50% dehydroxylated site M(OH)O(OH)M/s/ and 75% dehydroxylated site M(OH)OMOMO(OH)M/s/;
(b) sites that describe the physical adsorption of a metal precursor on partially dehydroxylated sites: M(OH)O(OH)MMCl_4/s/, MCl_4M-(OH)O(OH)MMCl_4/s/, and MCl_4M(OH)OMOMCl_3/s/;
(c) sites that describe the chemical adsorption of a metal precursor on hydroxylated sites: M(OH)OMOMCl_3/s/, Cl_3MOMOMOMCl_4/s/, and Cl_3MOMOMOMCl_3/s/;
(d) sites that describe the products of water treatment: M(OH)OMOM-(OH)Cl_2/s/, Cl_3MOMOMOM(OH)Cl_2/s/, Cl_2(OH)MOMOMOM-(OH)Cl_2/s/, and Cl_2(OH)MOMOM(OH)/s/.

Lam Research Ex. 1035 - Page 501
Lam Research Corp. v. Inpria Corp.
IPR2024-00033 - U.S. Patent No. 9,823,564

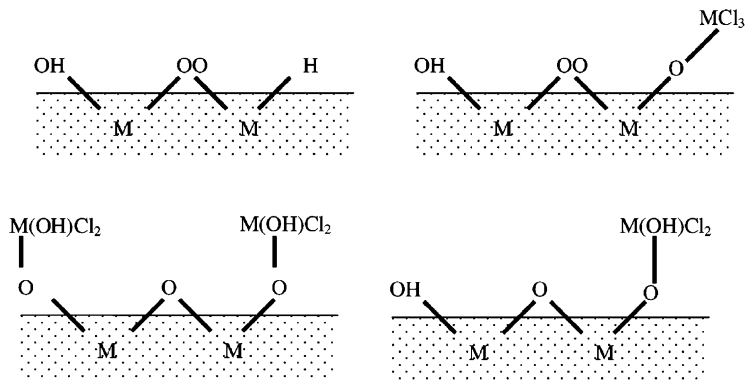


Fig. 9.11. Additional types of surface complexes on a partially hydroxylated surface.

It is reasonable to assume that the area occupied by a surface site is proportional to the number of metal atoms in this site. The elementary stages additional to the mechanism (15)–(29) are shown in Table 9.2.

Reactions (30)–(34) describe dehydroxylation/hydroxylation in the case of control by the diffusion-assisted reaction of hydroxyl groups. The preexponential factor of the rate constant of this reaction is of the same order of magnitude as the preexponential factor of the surface diffusion coefficient, $\sim 10^{-2}\,\mathrm{cm}^2/\mathrm{sec}$. Just as in the case of reaction (28), it was considered that the activation energy of reaction (32) depended on the coverage. Reactions (35)–(54) describe film growth on partially dehydroxylated surfaces. Because there is no information on the kinetic parameters of these reactions, these parameters were estimated or were taken by analogy with reactions (15)–(27) of the minimum mechanism. The results of simulations are shown in Figure 9.10. Since there was some arbitrariness in the choice of the rate parameters of the extended mechanism, these results are presented as areas in the figures. These areas correspond to the variation of the preexponential factors of reactions (30)–(54) by one order of magnitude and the variation of the activation energies of dehydroxylation reactions (28), (30), and (32) over the range ± 3 kcal/mol.

The best agreement with the experimental data was obtained with

$$E_{\mathrm{ad}} = E_{\mathrm{a}}(28) - E_{\mathrm{a}}(29) = 43\ \mathrm{kcal/mol},$$

$$E_{\mathrm{ad}} = E_{\mathrm{a}}(32) - E_{\mathrm{a}}(34) = 43\ \mathrm{kcal/mol},$$

and

$$\Delta\varepsilon = 20\ \mathrm{kcal/mol}.$$

Lam Research Ex. 1035 - Page 502
Lam Research Corp. v. Inpria Corp.
IPR2024-00033 - U.S. Patent No. 9,823,564

Table 9.2. Extension of the "minimum" mechanism

Reaction: $k = A \times T^n \exp(-E_a/RT)$ ($[k]$ = cm^3/sec; cm^2/sec; sec^{-1}; $[E_a]$ = kcal/mol, $[T]$ = K)	ZrO_2 mechanism		
	log(A)	n	E_a
Reactions of surface (de)hydroxylation			
$MO/s/ + M(OH)_2/s/ \rightarrow M(OH)O(OH)M/s/$ (30)	−2.00	0.00	20.00
$M(OH)O(OH)M/s \rightarrow MO/s/ + M(OH)_2/s/$ (31)	13.00	0.00	10.00
$2\,M(OH)O(OH)M/s/ \rightarrow M(OH)OMOMO(OH)M/s/ + H_2O$ (32)	−2.00	0.00	33–53
$M(OH)OMOMO(OH)M/s/ \rightarrow M(OH)O(OH)M/s/ + MO_2M/s/$ (33)	13.00	0.00	20.00
$MO_2M/s/ + H_2O \rightarrow M(OH)O(OH)M/s/$ (34)	−13.00	0.00	10.00
MCl_4 precursor adsorption/desorption on the partially dehydroxylated surface			
$M(OH)O(OH)M/s/ + MCl_4 \rightarrow M(OH)O(OH)MMCl_4/s/$ (35)	−13.04	0.86	−0.22
$M(OH)O(OH)MMCl_4/s/ \rightarrow M(OH)O(OH)M/s/ + MCl_4$ (36)	13.70	0.00	23.00
$M(OH)O(OH)MMCl_4/s/ + MCl_4 \rightarrow MCl_4M(OH)O(OH)MMCl_4/s/$ (37)	−13.04	0.86	−0.22
$MCl_4M(OH)O(OH)MMCl_4/s/ \rightarrow M(OH)O(OH)MMCl_4/s/ + MCl_4$ (38)	13.70	0.00	23.00
$M(OH)O(OH)MMCl_4/s/ \rightarrow M(OH)OMOMCl_3/s/ + HCl$ (39)	10.32	0.50	16.31
$M(OH)OMOMCl_3/s/ + HCl \rightarrow M(OH)O(OH)MMCl_4/s/$ (40)	−13.7	1.00	4.73
$MCl_4M(OH)O(OH)MMCl_4/s/ \rightarrow Cl_3MOMOMOMCl_4/s/ + HCl$ (41)	10.32	0.50	16.31
$Cl_3MOMOMOMCl_4/s/ + HCl \rightarrow MCl_4M(OH)O(OH)MMCl_4/s/$ (42)	−13.7	1.00	4.73
$Cl_3MOMOMOMCl_4/s/ \rightarrow Cl_3MOMOMOMCl_3/s/ + HCl$ (43)	10.32	0.50	16.31
$Cl_3MOMOMOMCl_3/s/ + HCl \rightarrow MCl_3M(OH)O(OH)MMCl_4/s/$ (44)	−13.7	1.00	4.73
$M(OH)OMOMCl_3/s/ + MCl_4 \rightarrow MCl_4M(OH)OMOMCl_3/s/$ (45)	−13.04	0.86	−0.22
$MCl_4M(OH)OMOMCl_3/s/ \rightarrow M(OH)OMOMCl_3/s/ + MCl_4$ (46)	13.7	0.00	23.00
$MCl_4M(OH)OMOMCl_3/s/ \rightarrow Cl_3MOMOMOMCl_3/s/ + HCl$ (47)	10.32	0.5	16.31
$Cl_3MOMOMOMCl_3/s/ + HCl \rightarrow MCl_4M(OH)OMOMCl_3/s/$ (48)	−13.7	1.00	4.73
Reactions of H_2O			
$M(OH)OMOMCl_3/s/ + H_2O \rightarrow M(OH)OMOM(OH)Cl_2/s/ + HCl$ (49)	−13.00	0.00	10.00
$M(OH)OMOM(OH)Cl_2/s/ + H_2O \rightarrow M(OH)O(OH)M/s/ + MO_2/b/ + 2HCl$ (50)	−13.00	0.00	10.00
$Cl_3MOMOMOMCl_3/s/ + H_2O \rightarrow Cl_3MOMOMOM(OH)Cl_2/s/ + HCl$ (51)	−13.00	0.00	10.00
$Cl_3MOMOMOM(OH)Cl_2/s/ + H_2O \rightarrow Cl_2(OH)MOMOMOM(OH)Cl_2/s/ + HCl$ (52)	−13.00	0.00	10.00
$Cl_2(OH)MOMOMOM(OH)Cl_2/s/ + H_2O \rightarrow Cl_2(OH)MOMOM(OH) + 2HCl + MO_2/b/$ (53)	−13.00	0.00	10.00
$Cl_2(OH)MOMOM(OH) + H_2O \rightarrow M(OH)O(OH)M/s/ + MO_2/b/ + 2HCl$ (54)	−13.00	0.00	10.00

Lam Research Ex. 1035 - Page 503
Lam Research Corp. v. Inpria Corp.
IPR2024-00033 - U.S. Patent No. 9,823,564

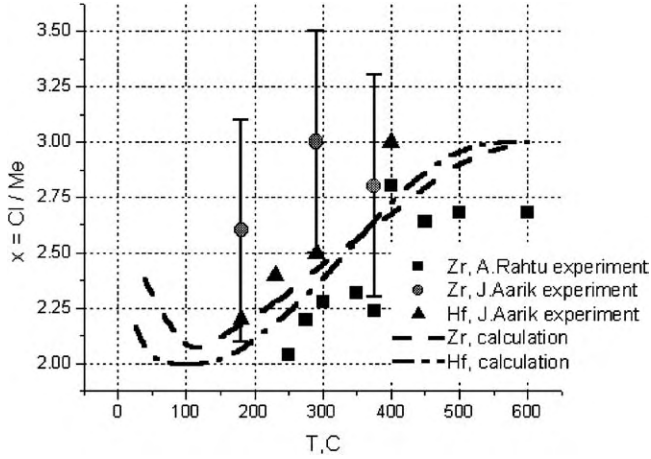


Fig. 9.12. Dependence of the Cl:Zr ratio on the temperature in surface complexes.

The mechanism describes the change in the Cl:Zr ratio with temperature (Figure 9.12). At $T > 200^{\circ}C$, the film growth rate essentially decreases due to the recombination of OH/s/ surface groups. In this case, the formation of a new layer proceeds through precursor reactions with a partially dehydroxylated surface. This leads to a change in the Cl:Zr ratio in the chemisorbed $ZrCl_x$ surface groups from 2 to 3. In the low-temperature region $T < 150^{\circ}C$, where experimental points are absent, the results of our simulations predict that the film growth rate decreases with the process temperature. It was emphasized above that this behavior is explained by the stabilization of the adsorption complex at low temperatures. In accordance with quantum-chemical calculations, adsorption complexes have a sufficiently deep potential well and block the next stages of the film growth.

5.3. Reduction of the Kinetic Mechanism of $Zr(Hf)O_2$ Film Growth

The kinetic mechanism developed from first-principles calculations can be used for the atomistic modeling of films in the framework of the KMC and similar methods. However, for practical applications in KMC, a kinetic mechanism taking into account specific system features should be adopted. As it was stated above, the time step of KMC is determined by the fastest process in system. For the processes of the chemical deposition of ZrO_2 films, the essential feature is the formation of a stable intermediate complex due to the formation of donor–acceptor bonds. It was shown above that these intermediate complexes have high mobility, which results in fast

Lam Research Ex. 1035 - Page 504
Lam Research Corp. v. Inpria Corp.
IPR2024-00033 - U.S. Patent No. 9,823,564

Table 9.3. The reduced kinetic mechanism for the lattice KMC model of ZrO_2 film growth in ALD process

(R1)	$ZrCl_4(g) + Zr(OH)_2O = ZrCl_2OZrO_2 + 2HCl(g)$
(R2)	$Zr(OH)_2O = ZrO_2 + H_2O(g)$
(R3)	$ZrO_2 + H_2O(g) = Zr(OH)_2O$
(R4)	$ZrCl_2OZrO_2 + 2H_2O = Zr(OH)_2OZrO_2 + 2HCl(g)$

diffusion processes of these complexes on the surface. Therefore, for practical calculations with the KMC method, the intermediate complexes should not be directly included in the KMC model and effective models should be used instead. This can be done by reducing the derived kinetic mechanism in order to eliminate intermediate stages related to intermediate complexes.

Different methods of mechanism reduction can be used, depending on the reaction path of precursor–surface interactions. If the energy barrier for the transformation of the intermediate adsorbed complex in the products is significantly smaller than the desorption energy from this complex, then product formation processes are faster than desorption processes. In this case, it is possible to use a quasi-steady-state approximation for the concentration of the intermediate complex if the duration of the adsorption pulse is longer than the characteristic time of complex transformation. If the energy barrier for the transformation of the intermediate complex in the products is larger than the desorption energy from this complex, then the desorption processes of the intermediate complex are faster than processes of its transformation in the products. One should note that, since desorption proceeds via a ''loose'' transition complex and the transformation reaction usually proceeds via a rigid TS, the rate of the desorption process will be larger than the rate of the transformation process for equal energy barriers. In this case, it is possible to use a quasi-equilibrium approximation for the concentration of the intermediate complex.

The kinetic mechanism for ZrO_2 film growth in the ALD process reduced from the detailed scheme is shown in Table 9.3.

5.4. KINETIC MONTE CARLO AND MOLECULAR DYNAMICS MODELING OF ZrO_2 FILM ROUGHNESS IN AN ALD PROCESS

Based on the kinetic mechanism of film deposition, it is possible to construct some KMC models of film growth, depending on the problem and the required details of elaboration.

A rather simple model of film growth can be used for an investigation of the roughness of a growing film in the ALD process. It is possible to

Lam Research Ex. 1035 - Page 505
Lam Research Corp. v. Inpria Corp.
IPR2024-00033 - U.S. Patent No. 9,823,564

consider in this model that the film consists of ZrO_2, $ZrO(OH)_2$, and $ZrCl_2O$ groups located at face-centered cubic lattice sites (these sites correspond to cations in cubic ZrO_2). Based on the quantum-chemical calculations, the metallic precursor is adsorbed on $ZrO(OH)_2$ groups only, that is, on hydroxylated sites.

In the framework of this model, the next effects of the dependence of reaction rates on the local environment will be considered:

(a) the dependence of the water adsorption energy on the surface hydroxylation degree $E_a = E_a^0 - \Delta E_{OH} \cdot N_{OH}$, where E_a^0 is water desorption energy from isolated site, ΔE_{OH} the adjustable parameter, and N_{OH} the number of nearest OH groups.
(b) the dependence of the adsorption energy of precursors on their surface coverage $E_a = E_a^0 - \Delta E_{Cl} \cdot N_{ZrCl_x}$, where E_a^0 is the activation energy for $ZrCl_x$ adsorption on an isolated site, ΔE_{Cl} the adjustable parameter, and N_{ZrCl_x} the number of the nearest $ZrCl_x$ groups.

The first effect describes the dependence of the hydroxylation degree on the temperature; hence, it determines the temperature dependence of the film growth rate. The second effect restricts the maximum coverage of the oxide surface by metallic precursors and determines the maximum growth rate. For the dependence of the kinetic parameters on local environment, we used the following values:

$$\Delta E_{Cl} = 120\ \text{kJ/mol} \quad \text{and} \quad \Delta E_{OH} = 20\ \text{kJ/mol}.$$

Fast proton diffusion at the surface was modeled by the random exchange of ZrO_2 and $ZrO(OH)_2$ groups over the entire growing film.

The simulation of the film profile was carried using 30×30 cells of ZrO_2 ($100\ \text{Å} \times 100\ \text{Å}$). It was verified that the film roughness does not depend on the size of the simulated film.

First, it was verified how the reduced kinetic mechanism with adjustable parameters ΔE_{Cl} and ΔE_{OH} describes the ALD saturation of the surface coverage as a function of temperature. The calculated coverage of the flat (001) ZrO_2 surface by $ZrCl_4$ precursors is given in Figure 9.13. It is necessary to note that, at 500°C, the surface hydroxylation is less than 50% and OH diffusion somewhat increases the thickness increment per cycle. The calculated results are in good agreement with the available experimental results for ALD: there is a maximum of the surface coverage of ~0.4 ML at a temperature of ~200°C, and, at higher temperatures, the surface coverage smoothly decreases due to the desorption of water from the ZrO_2 surface.

Lam Research Ex. 1035 - Page 506
Lam Research Corp. v. Inpria Corp.
IPR2024-00033 - U.S. Patent No. 9,823,564

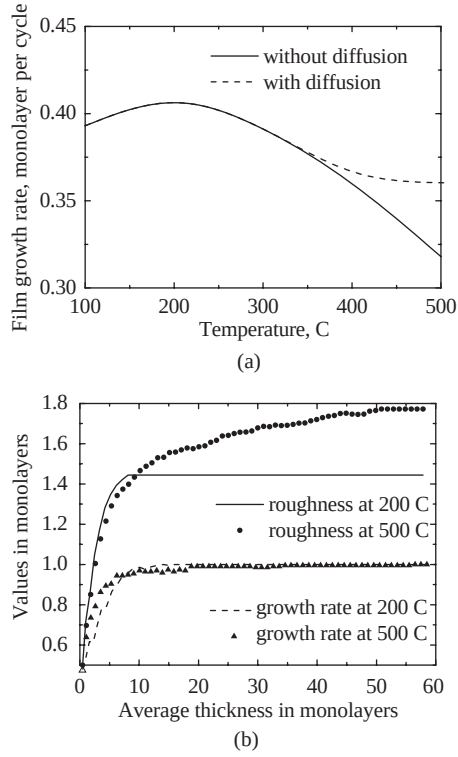


Fig. 9.13. (a) Calculated coverage of the flat (001) ZrO_2 surface at various process temperatures; (b) calculated growth rate and roughness evolution at various process temperatures.

The dependence of the film growth rate and the film roughness for two characteristic temperatures (200°C and 500°C correspond to fully and partly hydroxylated surfaces) is shown in Figure 9.13b. As it was already mentioned, the average ALD film growth rate is ~0.5 ML per cycle. In the case under consideration, the film growth rate rapidly increases up to 1 ML per cycle (Figure 9.13b) and its roughness, up to 1.4–1.8 ML. With further growth, the surface shape and roughness do not change. At a rise in temperature (up to 500°C), the maximum rate is reached later, which is connected with an appreciable reduction of the amount of the adsorbed water at the surface. Therefore, in principle, the ALD method should ensure precise control of film thickness if the repulsion between precursors is the only reason for submonolayer coverage.

Such an increase in the growth rate up to 1 ML per cycle is explained by the mutual repulsion of $ZrCl_4$ molecules on the surface only between the nearest neighbors; hence, the neighboring columns, having a difference in

Lam Research Ex. 1035 - Page 507
Lam Research Corp. v. Inpria Corp.
IPR2024-00033 - U.S. Patent No. 9,823,564

height more than one site, will be filled by the precursor without local restrictions, and nothing interferes with growth of such columns on the surface. The roughness is limited by the ALD process to a finite value. One should note that the surface coverage with respect to the local surface normal is still less than 50%, as was determined by the restrictions for the local environment.

For more realistic modeling, it is necessary to consider the surface relaxation of the growing film due to the diffusion of the deposited particles. This process is not a specific feature of ALD and can be considered independently in the model in the same way as in PVD modeling: similarly to the surface tension in liquids, selective diffusion [95] is introduced leading to the relaxation of the surface and the reduction of its area.

The characteristic time of this diffusion was estimated by carrying out the molecular dynamic relaxation of the film surface within the limits of the above model at 500°C. In MD calculations, the pair interaction energy between atoms is approximated by the Buckingham pair potential (Zr–O, O–O) (see Table 9.4). To describe covalent bonds more correctly, a three-body O–Zr–O term in the Stillinger–Weber form was introduced in addition to the Coulomb term.

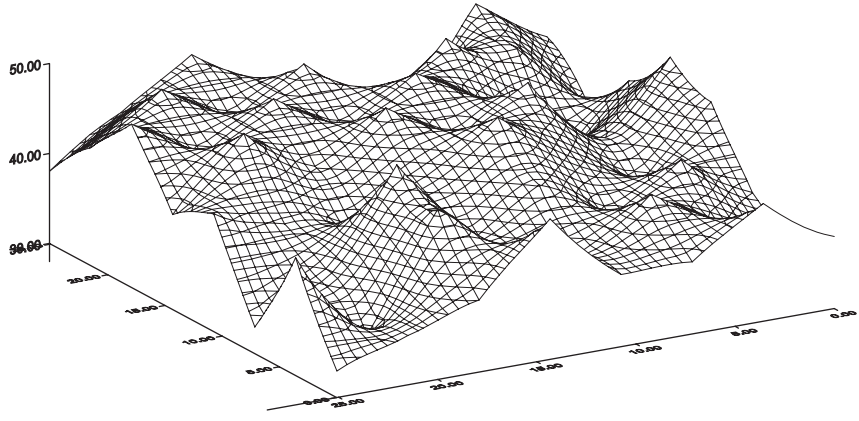
The sample of size 30 Å × 30 Å had an initial roughness of 1.8 ML. After a molecular dynamic relaxation run above 2000 K, the film roughness decreased by 20–30% (up to 1.2 ML) within tens of picoseconds. Thus, the smoothing of a film happens due to the resolving of surface peaks (see Figure 9.14). After the corresponding recalculation, the estimation of the characteristic time of a jump for the range 100–500°C gives tens of nanoseconds.

In the framework of the MC model, relaxation can be replaced effectively by restricted "diffusion" of ZrO_2 groups at a finite distance. This distance is a model parameter and is determined by the correspondence of the obtained roughness to the roughness obtained in molecular dynamic simulations. "Diffusion" is carried out as a jump to an empty position of one of the nearest neighbors, and the position with the greatest number of neighbors is most preferable. The dependence of the "diffusion" rate of the ZrO_2 group on the local environment is introduced through the activation barrier for

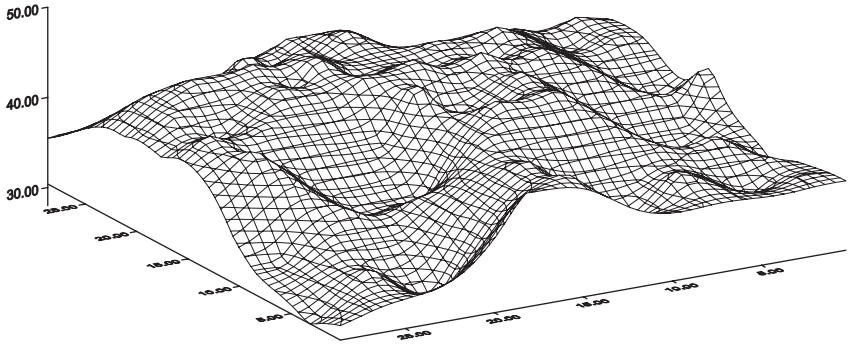
Table 9.4. Interatomic potentials parameters for ZrO_2

Parameter	Zr–O	O–O	Parameter	O–Zr–O
A	9353.3 eV	117673.1 eV	k	19.65 eV
r_0	0.213466 Å	0.187901 Å	r_0	1.80531 Å
C	14.15 eV Å^6	64.87 eV Å^6	θ_0	80.34°
r_{min}	1.00000 Å	0.800000 Å	r_{max}	2.60136 Å

Lam Research Ex. 1035 - Page 508
Lam Research Corp. v. Inpria Corp.
IPR2024-00033 - U.S. Patent No. 9,823,564



(a)



(b)

Fig. 9.14. Influence of surface diffusion on the film roughness. Surface (a) before molecular dynamic relaxation and (b) after molecular dynamic relaxation.

diffusion: $E_a = \Delta E_{ZrO_2} \cdot N_{neigh}$, where ΔE_{ZrO_2} is an adjustable parameter and N_{neigh} the number of the nearest neighbors.

The modeling of a growing film with regard to surface relaxation gives the stationary film growth rate in good accordance with experiment (Figure 9.15a). The values of roughness (~0.9 ML) are within the limits of experimental data before the onset of crystallization. As well as for PVD modeling, the roughness slightly decreases with increasing temperature. However, because crystallization begins early at high temperatures, direct comparison with experiment is impossible.

Lam Research Ex. 1035 - Page 509
Lam Research Corp. v. Inpria Corp.
IPR2024-00033 - U.S. Patent No. 9,823,564

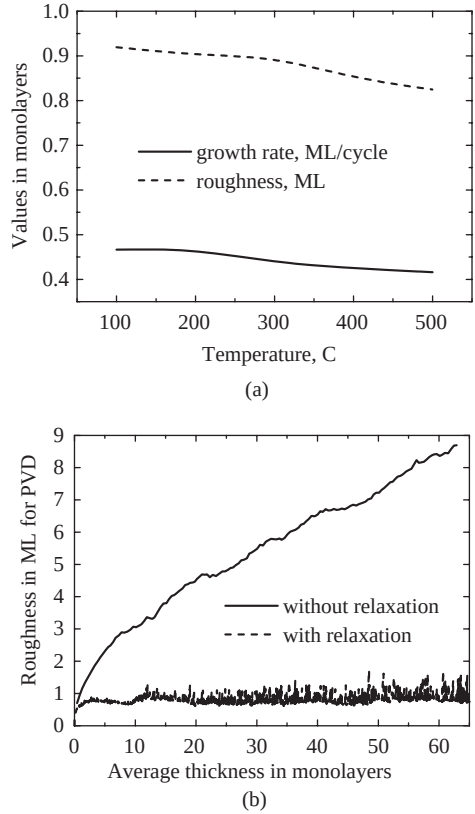


Fig. 9.15. (a) Growth rate of an ALD (001) ZrO_2 film and its surface roughness as functions of the process temperature with regard to surface relaxation; (b) surface roughness of a PVD film without and with regard to relaxation (~1 ML).

Notice that taking into account the diffusion of hydrogen does not essentially change the results of growth for all temperatures and only slightly increases the average film growth rate. This fact becomes noticeable at high temperatures (above 400°C), where the surface is less than half hydroxylated and the diffusion contribution increases (Figure 9.13a).

5.5. Modeling of the ZrO_2 Film Composition Using the Monte Carlo Method

For the practical use of thin films, it is necessary to control the defect concentration in the deposited film. Therefore, defect formation during film

Lam Research Ex. 1035 - Page 510
Lam Research Corp. v. Inpria Corp.
IPR2024-00033 - U.S. Patent No. 9,823,564

growth must be considered. In the case of ZrO_2 film deposition from zirconium chlorides and water, the residual chlorine atoms and hydroxyl groups are the basic defects. To model the ZrO_2 film composition, it is necessary to use a more detailed model of film growth than the model examined above for the investigation of the growing film shape. In the given model, the filling of anion sites in the ZrO_2 lattice is considered directly. This approach allows one to define directly the possible diffusion paths of impurities (H, Cl) and vacancies in the anion sublattice and take into account the dependence of the reactivity of impurities on their local chemical environment. Hence, the lattice MC model was developed in which cation sites were filled by zirconium atoms and anion sites were filled by oxygen atoms, hydroxyl groups, and chlorine atoms.

In this lattice, the zirconia atoms deposited from metal precursors occupy their inherent cation positions in the crystal lattice. In accordance with experiment [89–94] and quantum-chemical calculations [20, 33], the adsorption of water molecules on the *t*-ZrO_2 (001) surface results in the formation of two dibridged hydroxyl groups whose oxygen atoms are located close to the oxygen anion sublattice sites previously unoccupied in the crystal lattice. Therefore, in this lattice KMC model, it was assumed that the adsorbed oxygen atoms occupy the available anion sites on the surface of tetragonal zirconia. The hydrogen atoms were not considered explicitly, and the chemisorbed hydroxyl groups were considered as single entities. It was also assumed that chlorine atoms occupy oxygen positions in the crystal lattice (substitutional chlorine impurity). This suggestion is based on the fact that the Zr–Cl bond length in the $ZrCl_4$ precursors $r_{Zr-Cl} \approx 2.35$ Å falls well within the range 2.05–2.45 Å of the Zr–O bond distances in bulk *t*-zirconia.

The effect of the inhomogeneous chemical environment was modeled using the following two rules:

(a) a cation lattice site is unavailable for the adsorption of a $ZrCl_x$ group if at least one of the neighboring anion lattice sites is already occupied by a chlorine atom;
(b) a chlorine atom in the film must have at least one Zr vacancy in its nearest neighborhood, because the chlorine ionic radius $r_{ion}(Cl) \approx 1.84$ Å is much larger than the oxygen ionic radius $r_{ion}(O) \approx 1.2$ Å.

Rule (a) states that an adsorbed $ZrCl_x$ ($x = 1$–3) group prevents the chemisorption of $ZrCl_4$ with the formation of $ZrCl_x$ groups on the nearest neighboring sites. This rule results in the maximum surface coverage by $ZrCl_x$ groups of 50% for the regular structure on the planar fully hydroxylated surface (staggered adsorption) and ~35% coverage for random

Lam Research Ex. 1035 - Page 511
Lam Research Corp. v. Inpria Corp.
IPR2024-00033 - U.S. Patent No. 9,823,564

adsorption on the surface. The fulfillment of rule (b) leads to the formation of zirconium vacancies in the growing zirconia film together with residual chorine impurities.

The dissociative adsorption of water proceeds on a surface M–O pair with the formation of two neighboring OH groups on the surface. It was assumed that the energy of the reversible dissociative adsorption of water depends on the chemical environment of the corresponding surface lattice sites

$$E_{\mathrm{ad}} = E_{\mathrm{ad}}^{0} - \Delta E_{\mathrm{ad}} \cdot N_{\mathrm{OH}}$$

where N_{OH} is the total number of the neighboring hydroxyl groups for the two specified surface sites.

In addition to the dependences of the reaction constants on the local environment examined above, the dependence of the activation energy of Zr–Cl bond hydrolysis on the chemical environment of the chlorine atom was taken into account. This effect was considered to be responsible for the increased introduction of chlorine atoms into the growing film and was used for the explanation of the temperature dependence of the chlorine concentration in the deposited film.

It was assumed that the chlorine atoms could be removed from the film if a continuous diffusion path connecting the chlorine atom with the surface through oxygen vacancies existed. Here, when the diffusion path was determined, rule (b) was taken into account: a chlorine atom can occupy the site in the anion sublattice if there is at least one cation vacancy in its coordination shell.

The chemical reactions discussed above are sufficient in the case of an ideal film. However, in the case of real films with impurities and structural defects (e.g., lattice vacancies), it is necessary to supplement the set of chemical reactions with the physical processes of diffusion and relaxation (healing of defects). Therefore, we added surface and bulk diffusion processes for zirconium, chlorine, oxygen, and hydrogen atoms; hydroxyl groups; and $ZrOH_yCl_x$/s/ surface species. Within the rigid lattice model, the diffusion of atoms and groups proceeds only through vacant lattice sites (note the above definition of the free diffusion path for chlorine atoms based on rule (b)). The diffusion of hydrogen atoms proceeds via jumps from one oxygen atom to another. The mobility of a zirconium group bearing a chlorine atom was also limited by rule (b). Unfortunately, information available in the literature on the diffusion coefficients in zirconia films is very scarce. However, under real experimental conditions (gas pressure and process temperature), the processes of diffusion over vacant lattice sites must be much faster than all gas–surface chemical reactions. In our KMC simulations, this fact was taken into account by setting the rates of all

Lam Research Ex. 1035 - Page 512
Lam Research Corp. v. Inpria Corp.
IPR2024-00033 - U.S. Patent No. 9,823,564

diffusion processes 10 times greater than the rates of typical gas-phase reactions.

In this way, we generated ~30,000 chemical events for each pulse of an ALD cycle. The initial substrate contained 5×5 cells of t-ZrO_2 oriented along the [001] direction.

For model verification, the maximum coverage of the fully hydroxylated zirconia surface with $ZrCl_4$ was investigated. The calculated coverage of the fully hydroxylated (001) surface of t-ZrO_2 averaged over a set of simulations is ~35%. In film growth simulations, it has been found that the growing film thickness is proportional to the number of ALD cycles, and the maximum film growth rate is ~0.4 ML per ALD cycle. This value is in reasonable agreement with experimental results reported in Ref. [96] (~0.4 ML per ALD cycle) and Ref. [90] (~0.6 ML per ALD cycle). Moreover, the temperature dependence of the film growth rate is similar to that in Figure 9.10 obtained within the formal kinetic approach: there is a maximum of the film growth rate at low temperatures (~200°C) and a slow decrease in the film growth rate at higher temperatures. Here, the best fit was obtained for $E_{ad}^0 = 42$ kcal/mol and $\Delta E_{ad} = 2.4$ kcal/mol. These values are in adequate agreement with the corresponding values obtained in the formal kinetic simulations. Indeed, with regard to the normalization of ΔE_{ad} to one OH group in KMC and one surface site in formal kinetics, $\Delta\varepsilon = \Delta E_{ad} N = 14.4$ kcal/mol, where $N = 6$ is the number of the neighboring OH/s/ groups per one dissociatively adsorbed water molecule.

Next, we investigated the dependence of the chlorine atom concentration in the growing film on the process conditions. To take into account the effect of the local chemical environment of a surface chlorine atom on the probability of its reaction with a water molecule, we used the following dependence of the activation energy of this reaction on the number of the nearest neighboring Zr atoms in the chlorine coordination shell:

$$E_a = E_a^0 + \Delta E_a \cdot N_{Zr},$$

where N_{Zr} is the number of zirconium neighbors. Taking into account this dependence for the reaction probability, we calculated the residual chlorine concentration in the as-deposited zirconia film (see Figure 9.16). The results in Figure 9.16 were obtained with $E_a^0 = 2.5$ kcal/mol and $\Delta E_a = 1.2$ kcal/mol, which corresponds to the best fit to experimental data. Thus, the relatively weak dependence of the activation energy on the chemical environment of the chlorine atom can explain the chlorine concentration observed experimentally in the as-deposited film.

Lam Research Ex. 1035 - Page 513
Lam Research Corp. v. Inpria Corp.
IPR2024-00033 - U.S. Patent No. 9,823,564

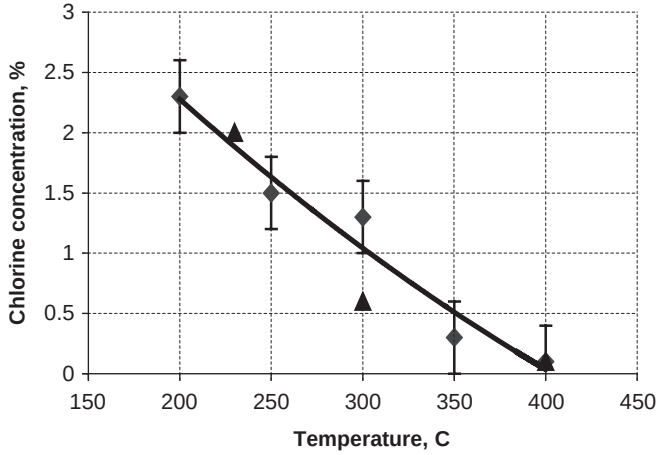


Fig. 9.16. Temperature dependence of the residual chlorine concentration in the growing film; triangles are experimental points and diamonds are simulation results.

5.6. Modeling of the Si/ZrO_2 Interface Structure Using the KMC-DR Method

The model of film growth presented above permits one to investigate the dependence of the film growth rate on the process parameters, the profile of the growing film, and its composition. Nevertheless, the structure of the deposited films cannot be determined with these models, since they are based on the lattice KMC model. However, the structure of the growing film is often not known in advance, for example, due to a mismatch between the crystal structures of the film and the substrate. This effect takes place for the deposition of ZrO_2 on the Si(001) substrate, where as-deposited thin films are obtained in an irregular form because of the mismatch. To describe these cases, one should go beyond the lattice KMC method and use dynamic variants of KMC. Therefore, the KMC method with dynamic relaxation [24] was used to investigate the formation of a ZrO_2 film on the Si substrate.

The initial structure for the simulation of film growth was taken from first-principles investigations of $ZrCl_4$ adsorption kinetics on the Si(001) substrate and the formation of the first layer of zirconium oxide [33]. It was shown that $ZrCl_4$ precursors are adsorbed as a $ZrCl_3$ complex and then can form $ZrCl_2$. The oxidation of dimers on the Si(001) surface significantly simplifies the formation of $ZrCl_2$ groups between dimer rows; the activation energy in this case is only 17.5 kcal/mol. With this activation energy, the rate of transformation $ZrCl_3 \rightarrow ZrCl_2$ at $T = 300^{\circ}C$ will be $> 10^6\,sec^{-1}$, which is significantly larger than the adsorption rate for ALD conditions

Lam Research Ex. 1035 - Page 514
Lam Research Corp. v. Inpria Corp.
IPR2024-00033 - U.S. Patent No. 9,823,564

($\sim 10^5\,\mathrm{sec}^{-1}$). Thus, one can expect that, during the first ALD cycle, $ZrCl_2$ groups will form between dimer rows on the hydroxylated silicon surface.

Therefore, the Si(001) surface covered with $ZrCl_2$ groups between dimer rows was taken as the initial structure for the simulation of zirconia film growth. The following set of chemical reactions was used as kinetic mechanism for film growth:

$$\mathrm{ZrOH} + \mathrm{ZrCl_4(g)} \rightarrow \mathrm{ZrOZrCl_3} + \mathrm{HCl(g)}, \tag{1'}$$

$$\mathrm{ZrOH} + \mathrm{ZrCl} \rightarrow \mathrm{ZrOZr} + \mathrm{HCl(g)}, \tag{2'}$$

$$\mathrm{ZrOHZrOH} \rightleftarrows \mathrm{ZrOZr} + \mathrm{H_2O(g)}, \tag{3'}$$

$$\mathrm{ZrOH} + \mathrm{ZrOH} \rightleftarrows \mathrm{ZrOZr} + \mathrm{H_2O(g)}, \tag{4'}$$

$$\mathrm{ZrCl} + \mathrm{H_2O(g)} \rightarrow \mathrm{ZrOH} + \mathrm{HCl(g)}. \tag{5'}$$

The rate constants for reactions (1′) and (5′) were taken from the reduced kinetic mechanism developed based on the detailed first-principles kinetic mechanism. The rate constant of reaction (2′) was taken to be three times larger than the rate constant of reaction (1′) for the given process parameters. It was assumed that dehydration is negligible during the purge pulse and the metal precursor pulse. Moreover, it was assumed that the adsorption of oxygen and metal precursors proceeds until the complete saturation of the surface. Although this degree of saturation can hardly be achieved in experiment, this model is a good approximation of the ideal ALD process.

The relaxation of the structure in the KMC-DR method was done using an approach based on the density functional theory and linear combination of atomic orbitals implemented in the Siesta code [97]. The minimum basis set of localized numerical orbitals of Sankey type [98] was used for all atoms except silicon atoms near the interface, for which polarization functions were added to improve the description of the SiO_x layer. The core electrons were replaced with norm-conserving Troullier–Martins pseudopotentials [99] (Zr atoms also include 4p electrons in the valence shell). Calculations were done in the local density approximation (LDA) of DFT. The grid in the real space for the calculation of matrix elements has an equivalent cutoff energy of 60 Ry. The standard diagonalization scheme with Pulay mixing was used to get a self-consistent solution. In the framework of the KMC-DR method, it is not necessary to perform an accurate optimization of the structure, since structure relaxation is performed many times.

The proposed kinetic mechanism was used to model zirconia film growth in the ALD process in the framework of the KMC-DR method. The structures of the zirconia film after first, second, third, and fourth ALD cycles are

Lam Research Ex. 1035 - Page 515
Lam Research Corp. v. Inpria Corp.
IPR2024-00033 - U.S. Patent No. 9,823,564

shown in Figure 9.17a–d. The general picture of ZrO_2 film deposition on the Si(100) surface can be summarized as follows: at the first ALD cycle, $ZrCl_4$ precursors occupy sites between dimers (interdimer) and form bridged Zr–Cl–Zr bonds (see Figure 9.17a). Since the distance between the $ZrCl_2$ groups in the direction perpendicular to dimer rows is rather large (distance Cl–Cl is ~5 Å), at the next ALD cycle, the $ZrCl_4$ precursor cannot fill the gap on the Si–O–Si dimer but rather forms $ZrCl_2$ or $ZrCl_3$ groups on the top of the previous precursors (see Figure 9.17b). The maximum surface coverage is determined by the repulsion of chlorine ions. The formation of continuous films begins in the third ALD cycle (see Figure 9.17c). This process is initiated by the formation of bridged Zr–Cl–Zr bonds between

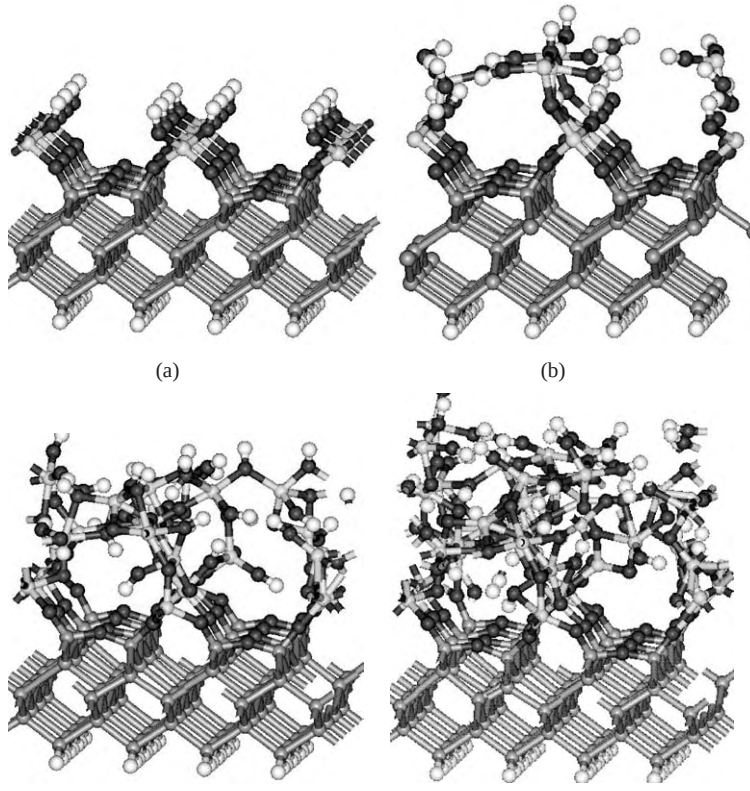


Fig. 9.17. Simulated structures of a ZrO_2 film after (a) one ALD cycle, (b) two ALD cycles, (c) three ALD cycles, and (d) four ALD cycles. Black balls are O, dark gray balls are Si, light gray balls are Zr, and white balls are H atoms.

Lam Research Ex. 1035 - Page 516
Lam Research Corp. v. Inpria Corp.
IPR2024-00033 - U.S. Patent No. 9,823,564

dimer rows, in which the bond length of one bond r_1(Zr–Cl) is ~2.4 Å, while the length of the other bond r_2(Zr–Cl) is ~2.6 Å.After the hydrolysis of chlorine ligands, these bridged bonds transform into ordinary Zr–O–Zr bonds, in which the distance r(Zr–O) is ~2.1–2.4 Å, so that film densification begins at this stage. Thus, on the one hand, chlorine ligands limit the maximum surface coverage, but, on the other hand, they initiate the formation of a continuous film via the formation of bridged bonds. In the subsequent ALD cycles, the formation of a continuous film is continued simultaneously with film densification.

The dependence of the surface coverage on the number of ALD cycles is shown in Figure 9.18. The average film growth rate is ~0.6 ZrO_2 monolayer/ALD cycle, which is in good agreement with the experimental film growth rate [100]. From this result, it is seen that the surface coverage at each ALD cycle is lower than monolayer due to the repulsion between chlorine atoms of the precursor. The densification of the film proceeds simultaneously with film deposition. This process describes the transformation from the 4-coordinated zirconium in the metal precursor to 7(8)-coordinated zirconium in the zirconia bulk. In fact, as it is seen from Figure 9.18, the average coordination number of a zirconium atom reaches 6 after four ALD cycles. This relatively small value of the Zr coordination number means that the deposited film is still of low density after four ALD cycles. It is seen from Figure 9.17d that the film is still not fully uniform at this moment.

From the results of this modeling, another important result can be seen: due to a mismatch between the Si(001) and the ZrO_2 lattices one should

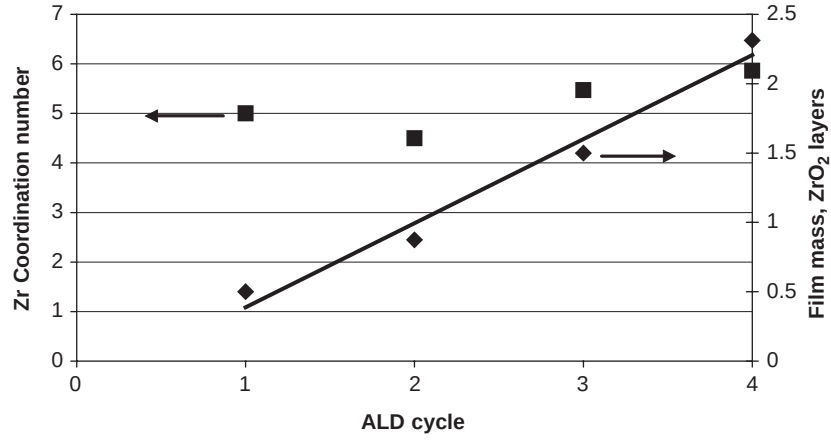


Fig. 9.18. Dependence of ZrO_2 film mass and the Zr average coordination number on the number of ALD cycles.

Lam Research Ex. 1035 - Page 517
Lam Research Corp. v. Inpria Corp.
IPR2024-00033 - U.S. Patent No. 9,823,564

expect the formation of residual terminal Zr–OH groups near the interface. In fact, such groups were observed in the simulation (see, e.g., Figure 9.17c), as $ZrCl_4$ groups fill the space on the oxidized silicon dimers.

6. Conclusions and Outlook

The presented results demonstrate that theoretical multiscale simulation methods can be successfully used for the description of the epitaxial growth of dielectric and semiconductor thin films. The multiscale approach to film growth includes *ab initio* calculations of the main gas-phase and surface reactions, estimation of the rate constants using transition state or RRKM theory, and kinetic modeling using MD, KMC, and formal chemical kinetics methods. The KMC method is a very promising tool for the atomistic simulation of thin-film growth, while irregular growth (formation of defect or amorphous films and accumulation of impurities) can be described by the KMC-DR. The example of the specific application of the multiscale technique to the problem of ZrO_2 ALD on an Si(100) substrate demonstrates the potential of the approach. The simulation of ZrO_2 film growth successfully predicts the film structure and composition of the growing film, the formation of defects and accumulation of impurities in the growing film, and the ZrO_2/Si(001) interface structure.

The development of multiscale simulation techniques that involve the atomistic modeling of various structures and processes still remains at its early stage. There are many problems to be solved associated with more accurate and detailed description of these structures and processes. These problems include the development of efficient and fast methods for quantum calculations at the atomistic level, the development of transferable interatomic potentials (especially, reactive potentials) for molecular dynamic simulations, and the development of strategies for the application of multiscale simulation methods to other important processes and materials (optical, magnetic, sensing, etc.).

Questions and Problems

1. Explain the difference between constructing a cluster model for covalent and ionic crystals.
2. Describe the main processes that proceed at an active surface site; describe the typical potential energy curve for a surface adsorbed complex.

Lam Research Ex. 1035 - Page 518
Lam Research Corp. v. Inpria Corp.
IPR2024-00033 - U.S. Patent No. 9,823,564

3. Write expressions for the adsorption and desorption rate constants.
4. Write and explain the equation of motion by Nosé–Hoover.
5. Describe the main approaches to the construction of empirical force fields for molecular dynamic simulations. Describe the difference between ordinary and reactive force fields.
6. Write the time increment for the KMC method.
7. Describe the difference between the lattice and dynamic versions of the KMC method.
8. Describe the main reactor types used in reactor modeling.

References

1. The International Technology Roadmap for Semiconductors, Semiconductor Industry Association, San Jose, CA, 1999, http://public.itrs.net/files/1999_SIA_Roadmap/Home.htm.
2. P. R. Willmott, Prog. Surf. Sci. **76** (2004) 163.
3. J. Musil, P. Baroch, J. Vlcek, K. H. Nam, J. G. Han, Thin Solid Films **475** (2005) 208.
4. U. Helmersson, M. Lattemann, J. Bohlmark, A. P. Ehiasarian, J. T. Gudmundsson, Thin Solid Films **513** (2006) 1.
5. B. D. Fahlman, Curr. Org. Chem. **10** (2006) 1021.
6. H. Kim, P. G. McIntyre, J. Korean Phys. Soc. **48** (2006) 5.
7. Z. H. Barber, J. Mater. Chem. **16** (2006) 334.
8. S. T. Rodgers, K. F. Jensen, J. Appl. Phys. **83** (1998) 524.
9. K. F. Jensen, S. T. Rodgers, R. Venkataramani, Curr. Opin. Solid State Mater. Sci. **3** (1998) 562.
10. T. P. Merchant, M. K. Gobbert, T. S. Cale, L. J. Borucki, Thin Solid Films **365** (2000) 368.
11. H. N. G. Wadley, X. Zhou, R. A. Johnson, M. Neurock, Prog. Mater. Sci. **46** (2001) 329.
12. G. Valente, C. Cavallotti, M. Masi, S. Carra, J. Cryst. Growth **230** (2001) 247.
13. A. Nakano, M. E. Bachlechner, R. K. Kalia, E. Lidorikis, P. Vashishta, G. Z. Voyiadjis, T. J. Campbell, S. Ogata, F. Shimojo, Comput. Sci. Eng. **3** (2001) 56.
14. R. M. Nieminen, J. Phys.: Condens. Matter **14** (2002) 2859.
15. A. Dollet, Surf. Coat. Technol. **177–178** (2004) 245.
16. C. Cavallotti, M. Di Stanislao, D. Moscatelli, A. Veneroni, Electrochim. Acta **50** (2005) 4566.
17. D. D. Vvedenskii, J. Phys.: Condens. Matter **16** (2004) R1537.

Lam Research Ex. 1035 - Page 519
Lam Research Corp. v. Inpria Corp.
IPR2024-00033 - U.S. Patent No. 9,823,564

18. A. A. Bagatur'yants, A. Kh. Minushev, K. P. Novoselov, A. A. Safonov, S. Ya. Umanskii, A. S. Vladimirov, A. Korkin, Predictive Simulation of Semiconductor Processing Status and Challenges, in: J. Dabrowski, E. R. Weber (Eds.), Springer Series in Materials Science, Vol. 72, Springer, Berlin, 2004.
19. A. A. Bagatur'yants, A. A. Korkin, K. P. Novoselov, L. L. Savchenko, S. Ya. Umanskii, in: C. R. A. Catlow, E. Kotomin (Eds.), Computational Materials Science, IOS Press, Amsterdam, 2003.
20. M. Deminsky, A. Knizhnik, I. Belov, S. Umanskii, E. Rykova, A. Bagatur'yants, B. V. Potapkin, M. Stoker, A. A. Korkin, Surf. Sci. **549** (2004) 67.
21. Y. Kajikawa, S. Noda, Appl. Surf. Sci. **245** (2005) 281.
22. A. A. Bagatur'yants, K. P. Novoselov, A. A. Safonov, L. L. Savchenko, J. V. Cole, A. A. Korkin, Mater. Sci. Semicond. Process. **3** (2000) 23.
23. A. A. Bagatur'yants, K. P. Novoselov, A. A. Safonov, J. V. Cole, M. Stoker, A. A. Korkin, Surf. Sci. **486** (2001) 213.
24. A. A. Knizhnik, A. A. Bagaturyants, I. V. Belov, B. V. Potapkin, A. A. Korkin, Comput. Mater. Sci. **24** (2002) 128.
25. M. J. Frisch, G. W. Trucks, H. B. Schlegel, G. E. Scuseria, M. A. Robb, J. R. Cheeseman, J. A. Montgomery, Jr., T. Vreven, K. N. Kudin, J. C. Burant, J. M. Millam, S. S. Iyengar, J. Tomasi, V. Barone, B. Mennucci, M. Cossi, G. Scalmani, N. Rega, G. A. Petersson, H. Nakatsuji, M. Hada, M. Ehara, K. Toyota, R. Fukuda, J. Hasegawa, M. Ishida, T. Nakajima, Y. Honda, O. Kitao, H. Nakai, M. Klene, X. Li, J. E. Knox, H. P. Hratchian, J. B. Cross, V. Bakken, C. Adamo, J. Jaramillo, R. Gomperts, R. E. Stratmann, O. Yazyev, A. J. Austin, R. Cammi, C. Pomelli, J. W. Ochterski, P. Y. Ayala, K. Morokuma, G. A. Voth, P. Salvador, J. J. Dannenberg, V. G. Zakrzewski, S. Dapprich, A. D. Daniels, M. C. Strain, O. Farkas, D. K. Malick, A. D. Rabuck, K. Raghavachari, J. B. Foresman, J. V. Ortiz, Q. Cui, A. G. Baboul, S. Clifford, J. Cioslowski, B. B. Stefanov, G. Liu, A. Liashenko, P. Piskorz, I. Komaromi, R. L. Martin, D. J. Fox, T. Keith, M. A. Al-Laham, C. Y. Peng, A. Nanayakkara, M. Challacombe, P. M. W. Gill, B. Johnson, W. Chen, M. W. Wong, C. Gonzalez, J. A. Pople, Gaussian 03, Revision C.02, Gaussian, Inc., Wallingford, CT, 2004, http://www.gaussian.com/; J.B. Foresman, Æ. Frisch, Exploring Chemistry with Electronic Structure Methods, 2nd edition, Gaussian, Inc. Pittsburgh, PA, 1996.
26. http://www.msg.ameslab.gov/GAMESS/GAMESS.html; M.W. Schmidt, K.K. Baldridge, J.A. Boatz, S.T. Elbert, M.S. Gordon, J.H. Jensen, S. Koseki, N. Matsunaga, K.A. Nguyen, S.J. Su, T.L. Windus,

Lam Research Ex. 1035 - Page 520
Lam Research Corp. v. Inpria Corp.
IPR2024-00033 - U.S. Patent No. 9,823,564

M. Dupuis, J.A. Montgomery, J. Comput. Chem. **14** (1993) 1347; M.S. Gordon, M.W. Schmidt, Advances in Electronic Structure Theory: GAMESS A Decade Later, in: C.E. Dykstra, G. Frenking, K.S. Kim, G.E. Scuseria, (Eds.), Theory and Applications of Computational Chemistry, The First Forty Years, Elsevier, Amsterdam, 2005.

27. http://www.emsl.pnl.gov/docs/nwchem/nwchem.html; E. Aprà, T.L. Windus, T.P. Straatsma, E.J. Bylaska, W. de Jong, S. Hirata, M. Valiev, M. Hackler, L. Pollack, K. Kowalski, R. Harrison, M. Dupuis, D.M.A. Smith, J. Nieplocha, V. Tipparaju, M. Krishnan, A.A. Auer, E. Brown, G. Cisneros, G. Fann, H. Fruchtl, J. Garza, K. Hirao, R. Kendall, J. Nichols, K. Tsemekhman, K. Wolinski, J. Anchell, D. Bernholdt, P. Borowski, T. Clark, D. Clerc, H. Dachsel, M. Deegan, K. Dyall, D. Elwood, E. Glendening, M. Gutowski, A. Hess, J. Jaffe, B. Johnson, J. Ju, R. Kobayashi, R. Kutteh, Z. Lin, R. Littlefield, X. Long, B. Meng, T. Nakajima, S. Niu, M. Rosing, G. Sandrone, M. Stave, H. Taylor, G. Thomas, J. van Lenthe, A. Wong, Z. Zhang, NWChem, A Computational Chemistry Package for Parallel Computers, Version 4.7, Pacific Northwest National Laboratory, Richland, WA, USA; 2005; R.A. Kendall, E. Apra, D.E. Bernholdt, E.J. Bylaska, M. Dupuis, G.I. Fann, R.J. Harrison, J. Ju, J.A. Nichols, J. Nieplocha, T.P. Straatsma, T.L. Windus, A.T. Wong, Comput. Phys. Commun., **128** (2000) 260.

28. http://cms.mpi.univie.ac.at/vasp/vasp/vasp.html; G. Kresse, J. Furthmüller, Phys. Rev. B **54** (1996) 11169; G. Kresse, J. Furthmüller, Comput. Mater. Sci. **6** (1996) 15; G. Kresse, J. Hafner, Phys. Rev. B **47** (1993) 558.

29. http://www.castep.org/; M. D. Segall, P. L. D. Lindan, M. J. Probert, C. J. Pickard, P. J. Hasnip, S. J. Clark, M. C. Payne, J. Phys.: Condens. Matter **14** (2002) 2717.

30. http://www.abinit.org; X. Gonze, J.-M. Beuken, R. Caracas, F. Detraux, M. Fuchs, G.-M. Rignanese, L. Sindic, M. Verstraete, G. Zerah, F. Jollet, M. Torrent, A. Roy, M. Mikami, Ph. Ghosez, J.-Y. Raty, D. C. Allan, Comput. Mater. Sci. **25** (2002) 478; X. Gonze, G.-M. Rignanese, M. Verstraete, J.-M. Beuken, Y. Pouillon, R. Caracas, F. Jollet, M. Torrent, G. Zerah, M. Mikami, Ph. Ghosez, M. Veithen, J.-Y. Raty, V. Olevano, F. Bruneval, L. Reining, R. Godby, G. Onida, D. R. Hamann, D. C. Allan, Zeit. Kristallogr. **220** (2005) 558.

31. Y. Widjaja, C. B. Musgrave, Surf. Sci. **469** (2000) 9.

32. I. M. Iskandarova, A. A. Knizhnik, E. A. Rykova, A. A. Bagatur'yants, B. V. Potapkin, A. A. Korkin, Microelectron. Eng. **69** (2003) 587.

Lam Research Ex. 1035 - Page 521
Lam Research Corp. v. Inpria Corp.
IPR2024-00033 - U.S. Patent No. 9,823,564

33. V. V. Brodskii, E. A. Rykova, A. A. Bagaturyants, A. A. Korkin, Comput. Mater. Sci. **24** (2002) 278.
34. Y. Widjaja, C. B. Musgrave, Appl. Phys. Lett. **80** (2002) 3304.
35. Y. Widjaja, J. H. Han, C. B. Musgrave, J. Phys. Chem. B **107** (2003) 9319.
36. K. Raghavachari, M. D. Halls, Mol. Phys. **102** (2004) 381.
37. C.-L. Cheng, D.-S. Tsai, J.-C. Jiang, Jpn. J. Appl. Phys. **44** (2005) 7625.
38. W. Chen, D. W. Zhang, J. Ren, H.-L. Lu, J.-Y. Zhang, M. Xu, J.-T. Wang, L.-K. Wang, Thin Solid Films **479** (2005) 73.
39. J.-H. Wang, M. C. Lin, Surf. Sci. **579** (2005) 197.
40. Z. Hu, C. H. Turner, J. Phys. Chem. B **110** (2006) 8337.
41. Z. Barandiaran, L. Seijo, J. Chem. Phys. **89** (1988) 5739.
42. V. B. Sulimov, P. V. Sushko, A. H. Edwards, A. L. Shluger, A. M. Stoneham, Phys. Rev. B **66** (2002) 024108.
43. E. R. Batista, R. A. Friesner, J. Phys. Chem. B **106** (2002) 8136.
44. L. Kantorovich, O. Danyliv, J. Phys.: Condens. Matter **16** (2004) 2575.
45. A. A. Sokol, S. T. Bromley, S. A. French, C. R. A. Catlow, P. Sherwood, Int. J. Quantum Chem. **99** (2004) 695.
46. M. L. Sushko, A. Y. Gal, A. L. Shluger, J. Phys. Chem. B **110** (2006) 4853.
47. N. C. Hernándeza, C. M. Zicovich-Wilson, J. Chem. Phys. **124** (2006) 194105.
48. P. Huang, E. A. Carter, J. Chem. Phys. **125** (2006) 084102.
49. A. Goldsmith, L. E. Waterman, L. E. Hirschhorn, Handbook of Thermophysical Properties of Solid Materials, Pergamon Press, Oxford, 1961.
50. R. G. Gilbert, S. C. Smith, Theory of Unimolecular and Recombination Reactions, Blackwell, Oxford, 1990.
51. K. A. Holbrook, M. J. Pilling, S. H. Robertson, Unimolecular Reactions, Wiley, New York, 1996.
52. M. Quack, J. Troe, J. Ber. Buns. Phys. Chem. **81** (1977) 329.
53. J. Troe, J. Phys. Chem. **83** (1979) 114.
54. J. Troe, J. Chem. Phys. **75** (1981) 226.
55. J. Troe, J. Chem. Phys. **79** (1983) 6017.
56. M. P. Allen, D. J. Tildesley, Computer Simulation of Liquids, Clarendon Press, Oxford, 1987.
57. L. Verlet, Phys. Rev. **165** (1967) 201.
58. D. Beeman, J. Comp. Phys. **20** (1976) 130.
59. S. Nosé, Mol. Phys. **52** (1984) 255.
60. W. G. Hoover, Phys. Rev. A **31** (1985) 1695.

Lam Research Ex. 1035 - Page 522
Lam Research Corp. v. Inpria Corp.
IPR2024-00033 - U.S. Patent No. 9,823,564

61. D. Frenkel, B. Smit, Understanding of Molecular Simulation: From Algorithms to Applications, Academic Press, San Diego, 2002.
62. A. K. Rappe, W. A. Goddard, III, J. Phys. Chem. **95** (1991) 3358.
63. F. H. Stillinger, T. A. Weber, Phys. Rev. B **31** (1985) 5262.
64. G. C. Abell, Phys. Rev. B **31** (1985) 6184.
65. J. Tersoff, Phys. Rev. Lett. **56** (1986) 632; Phys. Rev. B **37** (1988) 6991.
66. D. W. Brenner, Phys. Rev. B **42** (1990) 9458.
67. D. W. Brenner, O. A. Shenderova, J. A. Harrison, S. J. Stuart, B. Ni, S. B. Sinnot, J. Phys.: Condens. Matter **14** (2002) 783.
68. T. Watanabe, I. Ohdomari, Thin Solid Films **343–344** (1999) 370.
69. M. S. Daw, M. I. Baskes, Phys. Rev. B **29** (1984) 6443.
70. D. Brenner, Phys. Rev. Lett. **63** (1989) 1022.
71. K. Albe, K. Nordlund, R. S. Averback, Phys. Rev. B **65** (2002) 195124.
72. X. W. Zhou, H. N. G. Wadley, J.-S. Filhol, M. N. Neurock, Phys. Rev. B **69** (2004) 035402.
73. T. P. Swiler, R. E. Loehman, Acta Mater. **48** (2000) 4419.
74. K. A. Fitchthor, W. H. Weinberg, J. Chem. Phys. **95** (1990) 1090.
75. V. N. Kuzovkov, E. Kotomin, Rep. Prog. Phys. **51** (1988) 1479.
76. R. M. Nieminen, A. P. J. Jansen, Appl. Catal. A **160** (1997) 99.
77. M. R. Radeke, E. A. Carter, Phys. Rev. B **55** (1997) 4649.
78. M. R. Sorensen, A. F. Voter, J. Chem. Phys. **112** (2000) 9599.
79. N. Mousseau, G. T. Barkema, Phys. Rev. E **57** (1998) 2419.
80. M. Kaukonen, J. Perajoki, R. M. Nieminen, G. Jungnickel, T. Frauenheim, Phys. Rev. B **61** (2000) 980.
81. G. Henkelman, H. Jónsson, J. Chem. Phys. **115** (2001) 9657.
82. G. Henkelman, H. Jónsson, J. Chem. Phys. **111** (1999) 7010.
83. G. Henkelman, H. Jonsson, J. Chem. Phys. **113** (2000) 9978.
84. C. C. Battaile, D. J. Srolovits, J. E. Butler, J. Cryst. Growth **194** (1998) 353.
85. A. P. J. Jansen, Phys. Rev. B **69** (2004) 035414.
86. J. Robertson, Rep. Prog. Phys. **69** (2006) 327.
87. S. Ya. Umanskii, I. V. Belov, B. V. Potapkin, private communication.
88. P. J. Wilde, C. R. A. Catlow, Solid State Ionics **112** (1998) 173.
89. J. Aarik, A. Aidla, A.-A. Kiisler, T. Uustrate, V. Sammelselg, Thin Solid Films **340** (1999) 110.
90. J. Aarik, A. Aidla, H. Mandar, T. Uustrate, K. Kukli, M. Schuisky, Appl. Surf. Sci. **173** (2001) 15.
91. J. Aarik, A. Aidla, H. Mandar, T. Uustrate, V. Sammelselg, J. Cryst. Growth **220** (2000) 105.
92. H. Siimon, J. Aarik. J. Phys. D: Appl. Phys. **30** (1997) 1725.

Lam Research Ex. 1035 - Page 523
Lam Research Corp. v. Inpria Corp.
IPR2024-00033 - U.S. Patent No. 9,823,564

93. J. Aarik, A. Aidla, H. Mandar, T. Uustrate, V. Sammelselg, Thin Solid Films **408** (2002) 97.
94. A. Rahtu, Mikko Ritala, J. Mater. Chem. **12** (2002) 1484.
95. F. Family, Physica A **266** (1999) 173.
96. M. Ylilammi, Thin Solid Films **279** (1996) 124.
97. http://www.uam.es/siesta.
98. O. F. Sankey, D. J. Niklewski, Phys. Rev. B **40** (1989) 3979.
99. N. Troullier, J. L. Martins, Phys. Rev. B **43** (1991) 1993.
100. V. Sammelselg, E. Rauhala, K. Arstila, A. Zakharov, J. Aarik, A. Kikas, J. Karlis, A. Tarre, A. Seppälä, J. Asari, I. Martinson, Mikrochim. Acta **139** (2002) 165.

Lam Research Ex. 1035 - Page 524
Lam Research Corp. v. Inpria Corp.
IPR2024-00033 - U.S. Patent No. 9,823,564

Chapter 10

Vapor Deposited Composite Films Consisting of Dielectric Matrix with Metal/Semiconductor Nanoparticles

G.N. Gerasimov[a], and L.I. Trakhtenberg[b]

[a]*Karpov Institute of Physical Chemistry, 10, Vorotsovo Pole Str., Moscow, 105064, Russia*

[b]*Semenov Institute of Chemical Physics, Russian Academy of Sciences, Kosygina Str. 4, Moscow, 117977, Russia*

1. Introduction . . . 524
2. Features of Metal and Semiconductor Nanoparticles . . . 526
   2.1. Metal Nanocrystals . . . 526
   2.2. Semiconductor Nanocrystals. . . . 531
3. Methods of Preparation and Structure of Nanocomposite Films . . . 536
   3.1. M/SC Nanoparticle Deposition on a Surface of Dielectric Substrate . . . 537
   3.2. Co-Deposition of M/SC and A Dielectric Material. . . . 544
4. Physico-Chemical Properties of Nanocomposite Films . . . 554
   4.1. Conductivity and Photoconductivity . . . 554
   4.2. Sensor Properties. . . . 557
   4.3. Dielectric Properties . . . 562
   4.4. Catalytic Activity . . . 566
5. Conclusions . . . 571
Acknowledgments . . . 574
References . . . 574

This chapter concerns composite films prepared by physical vapor deposition (PVD) method. These films consist of dielectric matrix containing metal or semiconductor (M/SC) nanoparticles. The structure of films is considered depending on their formation by deposition of M/SC onto dielectric substrates as well as by layer-by-layer or simultaneous deposition of M/SC and dielectric vapor. Data on mean size, size distribution, and arrangement of M/SC nanoparticles in so obtained different composite films are given and discussed in relation to M/SC nature and matrix properties. Some models of nucleation and growth of M/SC nanoparticles by the diffusion of M/SC atoms/molecules over a surface or in volume of dielectric matrix are proposed and analyzed in connection with experimental data.

THIN FILMS AND NANOSTRUCTURES, vol. 34
ISSN 1079-4050
DOI: 10.1016/S1079-4050(06)34010-0

© 2007 by Elsevier Inc.
All rights reserved.

Lam Research Ex. 1035 - Page 525
Lam Research Corp. v. Inpria Corp.
IPR2024-00033 - U.S. Patent No. 9,823,564

Properties of films including dark- and photo-induced conductivity, sensor properties, dielectric characteristics, and catalytic activity are presented in dependence on film structure. The main attention is drawn to physical and chemical effects that resulted from the electron transfer processes in composite films containing M/SC nanoparticles. This short review discusses mechanism of conductivity in nanocomposite films via tunnel electron transfer between M/SC nanoparticles as well as the nature of sensor effects, which are due to changes of conductivity under influence of substances penetrated in films from environment and adsorbed on M/SC nanoparticles. The review also describes special low-frequency dielectric responses caused by metal nanoparticles contained in dielectric media having different properties. Various models of these responses based on electron transfer processes in this system are examined. The catalytic properties of M nanoparticles in composite films are considered in relation to charging of nanoparticles resulting from electron transfer between the particles and environment, as well as from redistributions of electrons between the particles of the various size. Presented data show that the charging of M nanoparticles leads to a sharp increase in their catalytic activity and to changes of catalytic reactions direction.

In conclusion, perspective directions for investigation of PVD-produced composite films with M/SC nanoparticles and possible areas for their practical applications are presented.

1. Introduction

The composite films containing metal or semiconductor (M/SC) nanoparticles in various dielectric matrices, draw much attention in connection with fundamental scientific problems and technological applications [1–3]. Specific properties of such films are determined by both individual characteristics of immobilized nanoparticles and interaction of particles with a matrix. Moreover, the new important effects caused by interaction between M/SC nanoparticles appear in composite films at the high M/SC contents [2,3].

M/SC nanoparticles in size from 1 to 10 nm are of greatest interest because their electronic structure depends markedly on the particle size [4–6]. There are now a lot of methods for a deposition of M/SC and dielectric on solid substrates from liquid or gaseous phase to produce composite films containing M/SC nanoparticles inside or on a surface of a dielectric matrix. Liquid-phase technique uses colloidal solutions of M/SC nanoparticles. Such solutions are formed by chemical reactions of various precursors in the presence of stabilizers, which are adsorbed on the surface of nanoparticles and preclude their aggregation. But it is necessary to take into account, that

Lam Research Ex. 1035 - Page 526
Lam Research Corp. v. Inpria Corp.
IPR2024-00033 - U.S. Patent No. 9,823,564

stabilizers can influence essentially the surface structure of formed particles and, accordingly, their physical and chemical characteristics. Besides at the liquid-phase chemical synthesis there is a danger to incorporate various impurities, in particular, ions in a lattice of M/SC nanoparticles [7]. At the same time the deposition of atomic or molecular beams from gaseous phase on an appropriate substrate gives films containing M/SC nanoparticles without impurities and any coverings screened a nanoparticle surface. Moreover, such gas-phase technique allows producing complex film systems, which cannot be made by a liquid-phase synthesis. Necessary atomic or molecular beams can be created by sputtering of corresponding targets or by chemical reaction in a gas phase.

This review is concerned to vapor deposition of M/SC dielectric nanostructured composite films as well as to their structure and physico-chemical properties. Only physical processes of M/SC nanoparticle formation (without participation chemical precursors) on a surface or inside a dielectric matrix are considered. In Section 2, the basic features of electronic structure of nanosized M/SC particles are specified. Further in Section 3, various methods of physical vapor deposition (PVD) are briefly presented. Also the structure of deposited films is considered in relation to properties of a dielectric matrix and conditions of M/SC nanoparticle formation. Along with experimental data some models of nucleation and growth of particles on a substrate surface and inside a matrix are submitted. Some physico-chemical properties of PVD-prepared solid composite films containing immobilized M/SC nanoparticles are described and discussed in Section 4. Subsection 4.1 deals with dark- and photo-induced conductivity of composite films, which is governed by tunnel electron transfer between M/SC nanoparticles. Sensor properties of films caused by change of their conductivity as a result of adsorption of molecules from an environment on M/SC nanoparticles are considered in Subsection 4.2. Dielectric characteristics of composite films with M nanoparticles in low-frequency electromagnetic field are examined in Subsection 4.3. Unlike high-frequency dielectric characteristics ε' and ε'' originated from specific electron plasma oscillations in M nanoparticles, values of ε' and ε'' in the low-frequency range are determined mainly by processes of electron transfer across a film. The possible models for low-frequency dielectric characteristics of composite films with M nanoparticles are presented. Subsection 4.4 deals with catalytic activity of films with M/SC nanoparticles, which depends both on the electron structure of nanoparticles and interaction between them and surrounding matrix. The special attention is drawn to specific catalytic effects arising at high concentration of particles in a film and resulted most probably from electron transfer between particles. A practical implementation of composite films with M/SC nanoparticles is discussed in final section.

Lam Research Ex. 1035 - Page 527
Lam Research Corp. v. Inpria Corp.
IPR2024-00033 - U.S. Patent No. 9,823,564

2. Features of Metal and Semiconductor Nanoparticles

First of all, electronic structure of nanoparticles was discussed. The influence of the size of particle on its electronic structure is determined by the nature of bonds in the particle lattice. In the lattice of molecular crystal intermolecular bonds cause only minor alterations in an electronic structure of molecules and are localized between the nearest neighbors in such lattice. In the lattice of inorganic crystal with purely ionic bonds the interaction of ion with medium is also localized in small space of the several coordination spheres surrounding an ion in the lattice. The transition of ion in the excited state gives essential disturbance of ionic lattice only in this space.

Thus, the interaction between structural entities of molecular and ionic crystals does not lead to appreciable delocalization of electrons strongly bonded to these entities. Therefore, the electronic structure of molecular and ionic crystals is practically not influenced by the size of such crystals. Size effects arise only in M/SC crystals with covalent (or at least partly covalent) bonds and depend on a relationship between the crystal size a and the length ξ of delocalization (or, otherwise, electronic correlation) for valent electrons in a lattice.

2.1. Metal Nanocrystals

The idealized polyacetylene chain of CH groups connected to one another by bonds of identical length and each having one p_z electron (represented in Figure 10.1 by black dots) can serve as the simplest one-dimensional model of metal [6, 8–10]. In such system because of the exchange interaction

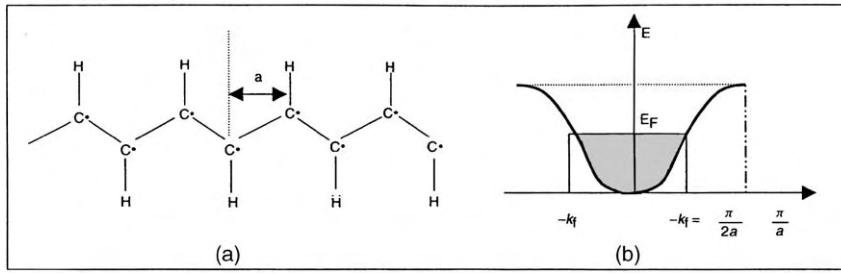


Fig. 10.1. One-dimensional metal model of interacting $2p_z$-electrons in polymer chain from C–C- bonds of equal length [9]: (a) the configurations of chain with repeat union (a). $2p_z$-electrons are indicated by black dots; (b) energy band scheme for $2p_z$-electrons; E_F: Fermi energy.

Lam Research Ex. 1035 - Page 528
Lam Research Corp. v. Inpria Corp.
IPR2024-00033 - U.S. Patent No. 9,823,564

between p_z electrons they occupy delocalized molecular π orbitals. Usually, to exclude edge effects, a linear chain of N atoms is replaced with cyclic system (in this case, as an example, the system with even N is taken). Twice degenerated energy levels $E(j)$ of this system are defined according to Huckel approximation as [10]

$$E(j) = \alpha + 2\beta \cos\left(\frac{2\pi j}{N}\right), \quad j = 0, \pm 1, \ldots, \pm\frac{N}{2},$$

where α is a p_z-electron level in isolated C atom and β the integral characterizing exchange interaction between next p_z electrons (exchange integral). Because two π orbitals with numbers $\pm j$ have the same energy level j and each orbital has two electrons, N of p_z electrons fill only the bottom half first band of levels (Figure 10.1), and the top half of this band remains free. The energy scheme of π orbital band is shown in Figure 10.1 as function of wave number $k = 2j\,\pi/Na$, where a is the bond length. The distance between the next levels $\Delta E_1 = E\,(j) - E\,(j \pm 1)$ at $N \gg 1$ is equal to

$$\Delta E_1 = \pm 4\beta \sin\left[\frac{(2j \pm 1)\pi}{N}\right] \sin\left(\frac{\pi}{N}\right). \tag{1}$$

The boundary between bands with the filled and empty levels in this model is similar to Fermi level in band structure of metal. Close to this boundary at $j = N/4$ or $k = \pi/2a$ (Fig. 10.1) and $N \gg 1$ the value $\Delta E_1 = \Delta E_F \approx \pm 4\beta\pi/N$. Thus, in the given one-dimensional model of metal energy gap ΔE_F between filled and empty electron levels is inversely proportional to the chain length. Analogous consideration of simple three-dimensional models (for example, cubic model with s electrons) [9] shows that in the three-dimensional system of delocalized bonds with identical length the value ΔE_F, as a first approximation, is inversely proportional to volume of a crystal and quickly reduces to zero with increasing of crystal size. Transition of system in the metal state depends on temperature and proceeds at $\Delta E_F \leq kT$. According to calculations and experimental data [5, 11–13] particles containing more than 500 atoms of metal (the size more than 2 nm) are in the metal state already at room temperature (kT~0.25 meV). The internal electronic structure of such particles practically does not differ from that of bulk metal.

However, transition from discrete to a continuous spectrum of levels does not mean full disappearance of quantum dimensional effects. It has been shown [14] that even in rather large metal nanocrystals in the size 5–10 nm it is necessary to take into account the direct influence of crystal boundaries on density of the crystal electronic levels that leads to the dependence of Fermi energy on the crystal size. The Fermi energy correction for a spherical crystal caused by crystal surface is inversely proportional to radius of crystal

Lam Research Ex. 1035 - Page 529
Lam Research Corp. v. Inpria Corp.
IPR2024-00033 - U.S. Patent No. 9,823,564

R [15]. For particles Ag with $R = 5\,\text{nm}$ this correction lifts Fermi level to 0.22 eV in comparison with level for bulk metal [15]. The surface-determined size effect for Fermi energy of metal nanoparticles results in mutual charging of nanoparticles of different sizes by the tunnel electron transfer between nanoparticles. Such charging processes, as it will be shown below (Subsection 4.4), greatly influence catalytic reactions induced by assembly of metal nanoparticles with size distribution immobilized in solid dielectric matrix.

There are two more size effects playing the important role in properties of composite films with metal nanoparticles: influence of the size of particle on its optical characteristics and on electron work function W. The increase of W with decreasing the particle size is due to the rise of potential of the positive charge remaining on nanoparticle after electron release. For spherical nanoparticle with radius R the dependence of W (eV) on R (Å) according to work [5] looks like

$$W(R) = W_\infty + \frac{(3/8)e^2}{R}, \tag{2}$$

where W_∞ is the work function for bulk metal and e the electron charge. The relation (2) holds good for nanoparticles of various metals in the wide range of R down to 0.5 nm, i.e., also in the field of quantum particles [5]. Dependence of W on R essentially influences the conductivity of composite films with M nanoparticles and, in particular, is the cause for so-called Coulomb blockade (see work [15] and Subsection 5.1 of Chapter 11). The matter is that the electron transfer from a massive electrode to M nanoparticle of radius R in the environment with dielectric constant ε is accompanied by increase in electron energy on value $e^2/\varepsilon R$ [15]. So the electron transfer does not proceed if the potential difference between an electrode and a particle is less than this value. Characteristic example is the tunnel current in the system consisting of two aluminum electrodes, divided by film Al_2O_3 containing Sn nanoparticles; because of Coulomb blockade the current in this system sharply falls at reduction of a potential difference between electrodes below some critical value [15].

Size effects in optics of M nanocrystals are caused by influence of a crystal surface on movement of conductivity electrons in alternating electromagnetic field. Under action of a field with frequency ω oscillations of conductivity electrons, which unlike valent electrons are not bonded to cations of M crystal, are determined by the Eq. (3) [14]

$$m\left(\frac{d^2x}{dt^2}\right) + mr\left(\frac{dx}{dt}\right) = eE_{\text{ext}}\ \exp\{-i\omega t\}. \tag{3}$$

In this equation m and x are the mass and displacement of electron, respectively and E_{ext} an intensity of an external electric field. The term

Lam Research Ex. 1035 - Page 530
Lam Research Corp. v. Inpria Corp.
IPR2024-00033 - U.S. Patent No. 9,823,564

$mr(dx/dt)$ characterizes electromagnetic energy losses by electron friction, which approximately are proportional to the rate dx/dt of the electron movement [14]. Coefficient of friction (r) is a characteristic constant of the energy dissipation at electron oscillations in given metal. This constant $r = v_f/R_m$, where v_f is speed of electrons with energy Fermi and R_m is free-pass length for electron in given metal.

The solution of this equation looks like [14]

$$x = a\ \exp\{-i\omega t\},$$

where

$$a = \frac{e}{m} E_{ext} \left[\frac{-1}{\omega^2 + r^2} + \frac{ir\omega}{\omega^2(\omega^2 + r^2)} \right].$$

Polarization of the metal due to displacement of these electrons under action of a field is

$$P = exN_c = \omega_p^2 E \left[\frac{-1}{\omega^2 + r^2} + \frac{ir\omega}{\omega^2}(\omega^2 + r^2) \right]. \tag{4}$$

Here, N_c is the number of conductivity electrons containing in unit of volume, $\omega_p = (N_c e^2/m)^{1/2}$ the plasma frequency of metal, and $E = E_{ext}$ $\exp\{-i\omega t\}$. The real part of coefficient at E in the formula (4) is the part of dielectric permeability ε_c' caused by conductivity electrons ($\varepsilon_c' = -\omega_p^2/\omega^2 + r^2$). Total dielectric permeability ε' is equal to

$$\varepsilon' = \varepsilon_\infty - \frac{\omega_p^2}{\omega^2 + r^2}. \tag{5}$$

In expression (5), ε_∞ is the high-frequency dielectric constant of metal caused by interband transitions. The value ε_∞ in the first approximation can be taken to be equal to 1 [16]. The imaginary part of coefficient at E in the formula (4) represents dielectric losses ε_c'' from conductivity electrons

$$\varepsilon_c'' = \frac{\omega_p^2 r\omega}{\omega^2(\omega^2 + r^2)}. \tag{6}$$

Usually $\omega >> r$ and $\varepsilon_c'' = \omega_p^2 r/\omega^3$ [16]. Absorption of radiation energy by conductivity electrons is [14]

$$Q_c \approx \frac{E^2 \omega_p^2 r}{\omega^2}. \tag{7}$$

The absorption spectrum of continuous thin film Ag is compared to that of Ag nanocrystals of much the same sizes as thickness of the film [17]. At high energy of radiation both spectra are practically identical, because absorption of such radiation results from interband transitions in metal [17].

Lam Research Ex. 1035 - Page 531
Lam Research Corp. v. Inpria Corp.
IPR2024-00033 - U.S. Patent No. 9,823,564

Features of nanocrystals optics are shown in visible and near UV spectrum where absorption is determined by behavior of conductivity electrons [16, 17].

According to the formula (7) absorption spectrum for conductivity electrons in bulk metal should be a smooth curve down to $\omega \to 0$. Ag film in the near UV range demonstrates spectrum of such type. Appearance of a near UV absorption peak in a spectrum of M nanocrystal is caused by the surface charges that resulted from displacement of conductivity electrons under action of an external field. These charges create in a nanocrystal the internal field directed against external one [16]. For conductivity electrons this internal field plays a role of quasi-elastic bonds between valent electrons and cations in a crystal lattice.

As is specified in work [17], the system of conductivity electrons in a nanocrystal is similar to the resonator. Thereof electromagnetic field in a crystal can give rise to collective electronic excitations [17], which refer to as surface plasmons as they are caused by charges on a nanocrystal surface in dielectric [16]. At $\omega < \omega_p$ dielectric permeability $\varepsilon'(\omega)$ according to the formula (5) is negative. It means that conductivity electrons in a nanocrystal oscillate out of phase with electric oscillations of an external field [16].

Optical absorption in M nanocrystals embedded in dielectric matrix depends on characteristics of matrix and interface between matrix and nanocrystals. In the classical model of Mie only macroscopical dielectric permeability of environment ε_2' is taken into account [16]. In this model charges at the M nanocrystal surface are determined by ε_2' and so frequency ω_a corresponding to a peak of resonant absorption is defined from a relation [18].

$$\varepsilon'(\omega) = -2\varepsilon_2'. \tag{8}$$

The classical model considers optical absorption of isolated nanocrystals with $2R \ll \lambda$ (light wave length) when light induces a dipolar excitation of the whole particle. In this case the position of plasmon absorption peak depends only on an environment and material of nanocrystal but not on a crystal size [16–18]. However, as is specified in work [17], in particles with $2R > \lambda$ light also induces multipole excitations that result in strong broadening of absorption band and their extension to the low-energy range of spectrum. Similar effects are caused the interaction between particles at their optical excitation in a system with high particle concentration [17]. All this leads to gradual transition from a spectrum of surface plasmons in nanocrystals to spectrum of bulk metal. This matter is examined thoroughly in work [17].

The considered classical model allows the explanation of the basic features of optical absorption for M nanocrystal in dielectric matrix at low nanocrystals content [18]. In particular, half-width ($\Delta_{1/2}$) of the plasmon

Lam Research Ex. 1035 - Page 532
Lam Research Corp. v. Inpria Corp.
IPR2024-00033 - U.S. Patent No. 9,823,564

band for nanocrystals in dielectric matrix does not depend on ε_2' and increases proportionally to $1/2R$ because in small particles characteristic constant r of the electron energy dissipation is determined by inelastic scattering of electrons on the particle borders [16, 18].

At the same time the classical model Mie considers a particle as a metal drop and does not describe the effects caused by structure of nanocrystal. As is shown in work [8], experimental data on $\Delta_{1/2}$ of the plasmon band in many cases essentially differ from forecasts of classical model owing to inelastic electron scattering on internal and surface defects of nanocrystals. The kind and concentration of defects depend on a way of nanocrystal formation. Also, this model does not provide an explanation for the important effects resulted from chemosorption of various ligands on a nanocrystals surface. Chemisorbed ligand gives new resonant state in the conductivity band of nanocrystal above the Fermi level [19]. The interaction of plasmons with electronic levels of a chemisorbed ligand leads to the additional plasmon dissipation resulting in broadening of plasmon absorption band. The value of such broadening depends on the position of these levels [19]. The interaction between plasmons and electronic levels of chemisorbed molecules is also the cause for a sharp increase of peaks in the Raman spectrum of these molecules. Such effects are used in optical sensors for detection of various compounds and biological objects [5].

2.2. SEMICONDUCTOR NANOCRYSTALS

The chain of conjugated C–C bonds of identical length a with completely delocalized π electrons (Figure 10.1) considered above as a one-dimensional model of metal is unstable. Calculation has shown that the overall energy of this system is lowered as a result of so-called Peierls deformation at which one of two next bonds is compressed, and another is stretched, so the general length of chain remains constant. So the chain of identical bonds a transforms to the one-dimensional lattice alternated bonds with period $a_1 = 2a$ (Figure 10.2) [9]. After this deformation the energy levels of π orbitals in cyclic system with even number N of dimer units of the length a_1 in Huckel approximation are defined as [9]

$$E(k) = \alpha \pm (\beta_1^2 + \beta_2^2 + 2\beta_1\beta_2 \cos ka_1)^{1/2}. \quad (9)$$

Here, as in metal model wave number $k = 2\pi j/Na_1$ ($j = 0, \pm 1, \ldots, .N/2$), β_1, and β_2 are exchange integrals for short and long bonds in the lattice dimer unit, respectively, and it was obvious that $\beta_1 > \beta_2$. As is shown in Figure 10.2 π orbital levels form two bands divided by the band gap ΔE. The minimal value of gap ΔE (ΔE_0) between highest occupied molecular orbitals

Lam Research Ex. 1035 - Page 533
Lam Research Corp. v. Inpria Corp.
IPR2024-00033 - U.S. Patent No. 9,823,564

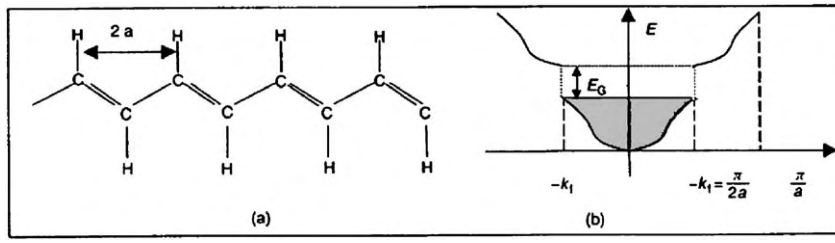


Fig. 10.2. One-dimensional semiconductor model of interacting $2p_z$-electrons in polymer chain from C–C- bonds of alternating length (π-electron system of polyacetylene) [9]: (a)-the configurations of chain with repeat union 2a; (b)-energy band scheme for $2p_z$-electrons; E_G: the gap between valent and conduction bands.

(HOMO) and lowest unoccupied molecular orbitals (LUMO) at $k = \pi/a_1$ does not depend on N and $\Delta E_0 = 2(\beta_1 - \beta_2)$ [6, 9]. Another approach based on taking into account π electron correlation was developed in the work [8].

In this system with even number N of dimer units a_1 orbitals HOMO and LUMO are nonbonding with zero overlap [9]. Therefore, the photo-induced electron transition between these orbitals is forbidden. The first electron transition with lowest energy in optical spectrum of this system proceeds between HOMO and unoccupied molecular orbital next to LUMO [6]. Simple calculations based on formula (9) give the energy ΔE_1 of this transition at $N \gg 1$ as

$$\Delta E_1 = \Delta E_0 + \frac{2\pi^2 \beta_1 \beta_2}{N^2(\beta_1 - \beta_2)}. \tag{10}$$

This relationship describes correctly the main features of dimensional effects in semiconductors:

(1) the increase in a difference $\Delta E_1 - \Delta E_0$ with decrease of ΔE_0 [6];
(2) the proportionality between $\Delta E_1 - \Delta E_0$ and $1/N^2$ at small values $\Delta E_1 - \Delta E_0$ [20].

Estimations [21] give $\beta_1 \approx 3.7$ eV and $\beta_2 \approx 2.8$ eV. In view of these estimations according to expression (10) the difference $\Delta E_1 - \Delta E_0$ reaches value 0.1 eV at decrease of the polymer chain length ($N \to \infty$) down to value $N_{0.1}$ equal, ~40 dimer units or 80 bonds C–C. At the same time, experimental data for polyenes give the value $N_{0.1} \approx 20$ bonds C–C [22]. Thus, the model of noninteracting molecular orbitals delocalized along the whole chain overestimates increase ΔE with reduction of length of a chain.

Consideration of dimensional effect for the one-dimensional π-electron polymeric semiconductor with use of the Eq. (9) is based on classical Huckel

Lam Research Ex. 1035 - Page 534
Lam Research Corp. v. Inpria Corp.
IPR2024-00033 - U.S. Patent No. 9,823,564

model. According to this model alternation of bonds with various lengths in a polymer chain caused by Peierls deformation leads to alteration of all molecular π orbitals. But, as is stated in work [23], influence of Peierls deformation on dispersion curve $E(k)$ is essential only for orbitals near to borders of energetic bands. For such orbitals the de Broglie wavelength of electron, which is equal to the distance between wave function nodes, is close to the lattice period $a_1 = 2a$ as with the result that electron diffract on the lattice. Alteration of energetic band is revealed in the interval $\xi^{-1} = (\beta/\delta\beta)\bar{a}$ ($\bar{a}$ is average length of bonds in a chain and $\delta\beta$ is the value of modulation for exchange integral β between neighboring p_z electrons, caused by alternation of bonds), close to the band borders. Outside this interval the dispersion $E(k)$ is similar to that of the above-considered one-dimensional metal model of identical conjugated π bonds C–C without Peierls deformation [23]. The parameter ξ characterizes the delocalization length (or electron correlation length) of electrons in one-dimensional system with alternated π bonds [23].

In polymer organic semiconductors with conjugated π bonds $\delta\beta$ is mostly $\sim 0.2\beta - 0.1\beta$ so according to work [23] $\xi \sim 5\bar{a} - 10\bar{a}$. Other calculations of polarizability for polyene and polyacetylene chains give $\xi \sim 20\bar{a} - 40\bar{a}$ [24]. Calculation of ΔE for the semiconductor demands the adequate description of the electron-excited states arising at transition of electron from the filled (valent) band to free band (conductivity band). For electron-excited states it is necessary to take into account configuration interaction of molecular orbitals in the intervals ξ^{-1} of the energy spectrum close to borders of valent and conductivity bands [23, 25]. This interaction results in formation of localized wave functions, describing electron in conductivity band and positively charged hole in valent band. These quasi particles (electron and hole) are connected together by the exchange interaction and Coulomb forces and so form a new quasi particle that is an electron–hole pair [6]. Exchange interaction caused by overlapping of wave functions for electron and hole plays a decisive role in electron–hole pairs for a one-dimensional semiconductors, in particular, in polymers with conjugated π bonds [23, 24, 26]. These interactions govern the localization length of an electron–hole pair, which can be considered as a charge transfer exciton. It has been shown that in polymer chain with conjugated π bonds the localization length of electron–hole pair does not practically depend on the Coulomb interaction between electron and hole [24].

In inorganic semiconductor crystals with three-dimensional system of conjugated bonds (for example, for the system of sp^3 bonds in crystals with tetrahedral cells [27]) delocalization of electron/hole wave functions sharply increases and, accordingly, exchange interaction between these particles decreases. A distance between electron and hole in such bulk crystals, which

Lam Research Ex. 1035 - Page 535
Lam Research Corp. v. Inpria Corp.
IPR2024-00033 - U.S. Patent No. 9,823,564

characterizes the exciton size, is determined by the screened Coulomb interaction between these nanoparticles. This exciton (exciton Wanier) can be considered as hydrogen-like atom. The exciton size a_{EX} in the ground state with lowest energy in the absent of steric hindrances is equal to the Bohr exciton radius a_B [20]

$$a_{EX} = a_B = \frac{\hbar^2 \varepsilon}{(1/\mu_e + 1/\mu_h)e^2}.$$

Here μ_e and μ_h are effective masses of electron and hole, respectively. Near to bottom of conductivity band and near to top of valent band where dependence E from k is close to parabolic, electron and hole move under action of a field as particles with effective masses $\mu_e = \hbar^2/(d^2E_c(k)/dk^2)$ and $\mu_h = -\hbar^2/(d^2E_v(k)/dk^2)$ [6]. In particular, in above-considered one-dimensional polymer semiconductor $\mu_e = \mu_h = \hbar^2\Delta E_0/2\beta_1\beta_2\bar{a}^2$ [6]. As a first approximation, it is possible to present nanocrystal as a sphere with radius R, which can be considered as a potential well with infinite walls [6]. The value of ΔE in such nanocrystal is determined by the transition energy between quantum levels of electron and hole, with the account Coulomb interaction between these nanoparticles.

$$\Delta E = \Delta E_0 + \frac{\hbar^2\pi^2}{2R^2}\left[\frac{1}{\mu_e} + \frac{1}{\mu_h}\right] - \frac{1.8e^2}{R\varepsilon}. \tag{11}$$

According to selection rules [20], interband transitions are possible only between levels with identical quantum numbers.

The formula (11) in view of relations for μ_e and μ_h describes above-mentioned basic features of size effects in semiconductor crystal. It is important that as against metals, semiconductors show appreciable quantum dimensional effects at the sizes of particles from 3 to 10 nm (depending on electronic structure of the semiconductor and sizes of ΔE_0) [20]. Such nanoparticles are usually formed at synthesis of nanocomposite films.

In particular, photocatalytic reactions on the surface of different inorganic SC nanoparticles depend on the energy of light generated electron–hole pairs [29]. Unlike polyene chain with conjugated C–C bonds, inorganic SC particles demonstrate asymmetric shift of electron and hole levels relative Fermi level of SC under change of the particle size. As is specified in work [29], in many inorganic SC nanoparticles the rise of electron level in conductivity band with decreasing of particle size is essentially more than lowering of hole level in valent band [29].

Lam Research Ex. 1035 - Page 536
Lam Research Corp. v. Inpria Corp.
IPR2024-00033 - U.S. Patent No. 9,823,564

Therefore, size effects for such SC nanoparticles are rather appreciable in processes with participation of the electronic centers, in particular, in the oxygen photoreduction resulting from the electron transfer from photo-excited SC nanoparticle to oxygen molecules adsorbed on its surface [29]. It should be noted that the relative part of surface atoms in SC nanoparticles is very high: for example, in CdS crystals of size 5 nm this part is ~15% [6]. As a result, initially formed exciton Wanier during very short time (about several picoseconds) is captured by various (mainly shallow) traps or adsorbed molecules on SC nanoparticle surface [6]. It has been established [29] that photoreduction of oxygen, which does not proceed on a surface of macroscopical SC crystal MoS_2 (as it is impossible by thermodynamic criteria), is realized on a surface MoS_2 nanocrystals of size ~2.5 nm. The further reduction of nanocrystals size leads to sharp increasing rate constant of this photoreaction [29].

Beside, the above-mentioned asymmetry of size-depended shifts of electron and hole levels for light-produced Wannier excitons can lead to the photo-induced mutual charging of SC nanoparticles with different sizes in composite film with high SC content. Such process for SC nanoparticles of different electron structure has been noticed in work [29]. It has been shown that the photo-induced mutual charging of SC nanoparticles can increase their photocatalytic activity [29].

It is believed that surface localized electron–hole pairs produced under light in SC nanoparticles participate in photo-induced processes of charge transfer between nanoparticles. These processes most probably of quantum tunnel type determine photoconductivity of composite films containing SC nanoparticles in a dielectric matrix. The photocurrent response time in this case should correspond to the lifetime τ_p of such pairs, which is of the order nanosecond and even more [6]. This rather long τ_p makes photo-induced tunnel current in composite film possible.

The electron and hole centers generated by light and localized on a surface of SC nanoparticle influence the coefficient of light absorption by such particle [6, 30, 31]. In a local electric field of these centers absorption of light results in formation of a deformed exciton with decreasing overlap of wave functions for electron and hole that means reduction of the dipole moment (or the moment of higher order) for electron transition giving this exciton and the increase of the exciton radiation life time [6, 30]. Such effects serve a base for nonlinear optical properties, in particular, high hyperpolarizability of the third order $\chi^{(3)}$ characteristic for SC nanoparticles, immobilized on a surface or inside a dielectric matrix [31]. It should be noted that value $\chi^{(3)}$ as well as other nonlinear optical characteristics in this case depends on lifetime of surface stabilized electron–hole pairs in SC nanoparticles. This lifetime is substantially influenced by properties (mainly, dielectric permeability) of a matrix surrounding SC nanoparticles [30].

Lam Research Ex. 1035 - Page 537
Lam Research Corp. v. Inpria Corp.
IPR2024-00033 - U.S. Patent No. 9,823,564

3. Methods of Preparation and Structure of Nanocomposite Films

To produce gas-phase atoms or molecules of M/SC and dielectric substances aimed at PVD of composite films following methods are used [28, 32, 33]:

(1) *Thermal vacuum evaporation.* This method is used for evaporation and the subsequent deposition of various metals. Rather volatile metals such as Ag, Au, Cu, and Pd can be evaporated from heated containers. Evaporation of less volatile metals, in particular, Ti or Mo, occurs by electrical heating of metal filaments or bands [32]. In certain conditions chemical active gases, such as oxygen, sulfur vapors, and others, introduced in evaporation zone react with metal atoms giving semiconductor compounds (for example, oxides, sulfides).

Simultaneous evaporation of metal with organic and inorganic substances followed by vapor deposition on a substrate allows the production of composite films containing M nanoparticles stabilized in various dielectric matrices [2, 28]. The use of monomer molecules in this process polymerizing during deposition or as a result of the subsequent reactions yields polymeric nanocomposite films with metal inclusions [2, 3, 28, 37]. The new low-temperature synthesis of polymeric nanocomposite films has been elaborated recently. This synthesis is based on the deposition of M/SC and monomers vapors at temperature ~80 K followed by low-temperature solid-state polymerization of obtained films in conditions of ''frozen'' thermal movement of molecules (cryochemical synthesis) [2]. This synthesis has important features, which will be considered further.

(2) *Pulse laser sputtering.* Such method allows sputtering substances with extremely low volatility, which cannot be turned into a gaseous state in the simple thermal way. With the help of a laser method it is possible to vaporize as refractory metals and dielectrics. Laser sputtering with the subsequent condensation of obtained vapors was used, in particular, for preparing nanoparticles of TiO_2 [35] and Si [34]. Under action of a laser pulse the local dense cloud of atoms or molecules of volatilized substance is formed [34] to give a possibility to attain high concentration of nanoparticles at vapor deposition on a rather small-sized area. For detailed descriptions of laser dispergating for metals see Chapter 15.

(3) *Sputtering of a metal electrode in plasma of the arc discharge.* Usually a radio-frequency discharge is used in the presence of background inert gas (for example, xenon [32]) at low pressures (in the range 0.05–1 mmHg [32]). The discharge produces positively charged ions of background gas, which are accelerated by electric field and bombard a metal target. Atoms or small clusters taking off from a target are deposited on a substrate. Methodic

Lam Research Ex. 1035 - Page 538
Lam Research Corp. v. Inpria Corp.
IPR2024-00033 - U.S. Patent No. 9,823,564

described in work [36] provides introducing of organic compound vapors in the discharge zone. Polymerization of such compounds under action of high-energy ions on (or near to) substrate surface simultaneously with metal deposition leads to formation of polymer composite films filled by M nanoparticles. [36]. The use of oxygen or other chemical active gases as background gases in the charge plasma can give semiconductor metal compounds [33].

(4) *Magnetron method of metal cathode sputtering under action of heavy ions.* This method uses magnetic field directed parallel to cathode surface that allows rise in efficiency of ionization for background inert gas by electrons emitted from cathode [38]. Arising ions of gas concentrate near to the cathode resulted in intensifying of the cathode sputtering. The stream of the sputtered substance goes to a substrate situated outside a magnetic trap [32, 38]. The important feature of this method is the absence of radiation damages of a substrate. Addition of oxygen to background inert gas, which is mainly argon, results in formation of semiconductor oxides [32, 38].

This chapter concerns two types of nanocomposite films M/SC dielectric: (a) composite films produced by the vapor deposition of M/SC onto a surface of dielectric substrate or by layer-by-layer deposition of M/SC and dielectric on a substrate, (b) composite films formed as a result of simultaneous deposition of M/SC and dielectric.

3.1. M/SC Nanoparticle Deposition on a Surface of Dielectric Substrate

Nanostructured films are mainly produced by sputtering and the subsequent deposition of M/SC in vacuum at residual pressure of gas no more than 10^{-2} mmHg. In this case the free flight time of sputtered atoms (in general initial sputtered particles can be molecules or small clusters) l_f is no less than 5 cm [39]. This value of l_f is comparable to usual distance between M/SC target and substrate in experiments on PVD film preparing. In such conditions atoms reach a substrate surface almost without collisions with molecules of gas. Thus, nuclei of a new phase are formed heterogeneously by aggregation of adsorbed atoms on a substrate surface [39–41]. With increasing gas pressure l_f sharply decreases (at pressure ~0.1 mmHg the value l_f ~0.05 cm [39]). This leads to energy losses of sputtered atoms at their collisions with molecules of gas resulting in homogeneous condensation of atoms with formation of M/SC nanoparticles. Then nanoparticles are deposited on a substrate surface as a nanostructured film.

Heterogeneous and homogeneous processes give particles with different morphology. The work [40] shows that the deposition of Ag, sputtered by

Lam Research Ex. 1035 - Page 539
Lam Research Corp. v. Inpria Corp.
IPR2024-00033 - U.S. Patent No. 9,823,564

magnetron method, on a carbon substrate in high vacuum gives film containing nanoparticles of irregular form. Films obtained in an argon stream at pressure $\sim 10^{-2}$ mmHg and higher, when homogeneous condensation of atoms prevails, consist of nanoparticles of form close to spherical. The average size of nanoparticles ($\bar{d}$) in such film is less, than that of nanoparticles in the film resulted from heterogeneous process [40].

At magnetron Au sputtering $\bar{d}$ of nanoparticles deposited on a Si substrate, at argon pressure higher than 0.05 mmHg, i.e., at homogeneous formation of nanoparticles in gaseous phase, does not depend on argon pressure. At the same time the intensity of metal sputtering increases with argon pressure [41]. Apparently, at homogeneous process the value $\bar{d}$ corresponds to the average critical size of metal particles, precipitated from a gas phase in given conditions on a substrate surface. In this case the precipitated particles do not grow further on a substrate surface because atoms or small clusters of M/SC capable to diffuse over a surface and to coalesce with particles do not reach a substrate. Therefore, the increase in intensity of M/SC deposition leads to the rise of the surface concentration of particles instead of $\bar{d}$ value. Particles combine in rather large aggregates making a film only at high degrees of surface filling by M/SC.

Quasi-spherical form of crystalline Ag nanoparticles ($\bar{d} \sim 4$ nm), prepared by homogeneous gas-phase condensation in work [40], is characteristic of isolated small metal particles [11]. It is necessary to take into account that in such very small particles because of a high relative part of surface atoms there can be distortions of the ordered structure in surface layers. Such distortions reveal especially near to edges of crystal lattices that smoothes the form of particles. Larger metal particles ($\bar{d} \sim 20$ nm), formed in a gas phase by magnetron sputtering of Mo at argon pressure ~ 0.15 mmHg look already as faceted monocrystals [39].

The growth of nanoparticles on substrate surface proceeds by collisions of the deposited atoms migrating on a surface with growing nuclei of a new phase. Usually, such growth of nuclei is considered as completely chaotic process. However, actually diffusion of atoms to nuclei can be influenced by a structure of substrate surface around growing nuclei. Therefore, on a nonuniform carbon surface with various extended defects one can expect the formation of irregular shaped particles as it is in work [40]. Formation of M/SC particles from the atoms adsorbed on a substrate surface occurs by two ways depending on the surface energy of substrate (γ_B) and M/SC phase (γ_A) as well as on the interfacial energy for the boundary M/SC substrate (γ^*) [42, 43]. At $\gamma_A + \gamma^* \geq \gamma_B$ three-dimensional nuclei are formed on a substrate surface from the outset followed by their growth and aggregation to yield an island film (3D process). In particular, films from M/SC nanoparticles grow on organic polymer surfaces by such a way. In another case

Lam Research Ex. 1035 - Page 540
Lam Research Corp. v. Inpria Corp.
IPR2024-00033 - U.S. Patent No. 9,823,564

$\gamma_A + \gamma^* \leq \gamma_B$ two-dimensional islands of M/SC phase arise originally. Then, these islands coalesce in two-dimensional layer, on which the following layer of M/SC phase grows in the same way (2D process). Processes of this type are characteristic for deposition of M vapors on metal substrates and SC vapors on semiconductor substrates or on dielectrics with lattice structure and physical and chemical properties similar to that of deposited SC [42, 43].

Aggregation of atoms deposited on a substrate surface can be divided into three stages:

(1) Nucleation of new phase: as the surface concentration N_s of nanoparticles and their size d increase during deposition of M/SC vapors at this stage.
(2) Stationary growth of M/SC particles: N_s reaches limiting value. This is the result of increase in a surface of particles and reduction of distance between them so that practically all deposited atoms join growing particles. In these conditions the probability of formation of new nuclei is close to zero.
(3) Coagulation of particles by connection of the neighboring particles during growth or as a result of diffusion-governed collisions of particles on a substrate surface. The first process (static coagulation) becomes appreciable when at uniform filling of a substrate surface with M/SC particles the average distance $d_i \sim N_s^{1/2}$ between them decreases so that it becomes comparable with d [44]. It occurs at a degree of filling of ~30% [45], so at an initial stage of deposition static coagulation can be neglected. The second process, usually designated as dynamic coagulation, depends on the size of particles and their interaction with a matrix, i.e., from value γ^*.

Works [46, 47] specify marked diffusion of small clusters Si (of size up to 2.5 nm) and the platinum metal clusters consisting of 20 atoms on a surface of amorphous carbon at room temperature. At the same time, clusters of transition and platinum metals do not diffuse on surface of Si and Al_2O_3 even at high temperatures [46]. Apparently, at small values γ^*, for example, at deposition of noble metals on polytetrafluorethylene or amorphous carbon, small mobile clusters, arising right at the beginning of process, can coagulate forming immobilized nuclei for M/SC particle growth.

The scheme of nucleating and growth of particles at deposition of M/SC from gaseous phase on a substrate is submitted in work [43]. The atoms adsorbed from a gas phase (adatoms) diffuse over a surface. During diffusion adatoms are partly desorbed and in part are stabilized on a surface, forming nuclei of a new phase. Such nuclei arise by collision of diffusing adatoms and their aggregation into stable primary clusters or as a result of

Lam Research Ex. 1035 - Page 541
Lam Research Corp. v. Inpria Corp.
IPR2024-00033 - U.S. Patent No. 9,823,564

adatom capture by surface defects. For a single isolated atom the adsorption residence time τ_s is determined by the rate of desorption so that

$$\tau_s = \frac{1}{\nu}\exp\left\{\frac{E_{des}}{kT}\right\},$$

where ν is a vibration frequency of bond between atom and substrate surface ($\sim 10^{13}\,sec^{-1}$) and E_{des} the atom desorption energy [42]. On an average, during τ_s adatom displaces on the surface over the distance that is

$$X_D = (D_s t_s)^{1/2}.$$

Here D_s is the coefficient of two-dimensional diffusion of adatoms, which is equal to

$$D_s = \left(\frac{\nu_d a_o^2}{4}\right)\exp\left\{\frac{-E_D}{kT}\right\}.$$

In this expression ν_d is a frequency of adatom vibration over the surface, a_o the jump distance, of the order of the surface lattice parameter, and E_D the activation energy of adatom diffusion [42]. Thus,

$$X_D = a_o\left(\frac{\nu_d}{\nu}\right)\exp\left\{\frac{E_{des} - E_D}{kT}\right\}.$$

Because usually $E_{des} \gg kT$ and $E_D \ll E_{des}$ (see, for example, [42]), adatoms in absence of special restrictions can migrate over rather large distances. During surface migration adatoms collide with each other and aggregate yielding small clusters (in the simplest case, dimers), which lose mobility and are fixed on a substrate surface. Such clusters serve as M/SC phase nuclei. In this variant the nucleation and the growth of M/SC nanoparticles occur randomly on whole surface. It is supposed that heterogeneity of surface and surface defects influence only the value of D_s but do not alter the random character of diffusion-governed processes. Such random formation of a nanostructured film is realized at deposition of Au vapors on a surface of amorphous carbon at room temperature [48].

Figure 10.3 demonstrates the time dependence for N_s and degree of a surface covering (θ) by Au particles in their monolayer on the amorphous carbon surface at PVD of Au vapors at room temperature [49]. It should be noted that at an initial stage of deposition, i.e., $\theta \sim 0.05-0.1$, the N_s value quickly reaches a maximum, and then is reduced up to a certain limit at $\theta \geq 0.2$. In the given system at $\theta \sim 0.1$ the average size of particles Au is only 1–2 nm [48].

As noted above, such small Au clusters on a surface of amorphous carbon are most likely mobile. It is believed that as θ increases, initial small mobile clusters coagulate into larger immobilized centers for growth of M/SC

Lam Research Ex. 1035 - Page 542
Lam Research Corp. v. Inpria Corp.
IPR2024-00033 - U.S. Patent No. 9,823,564

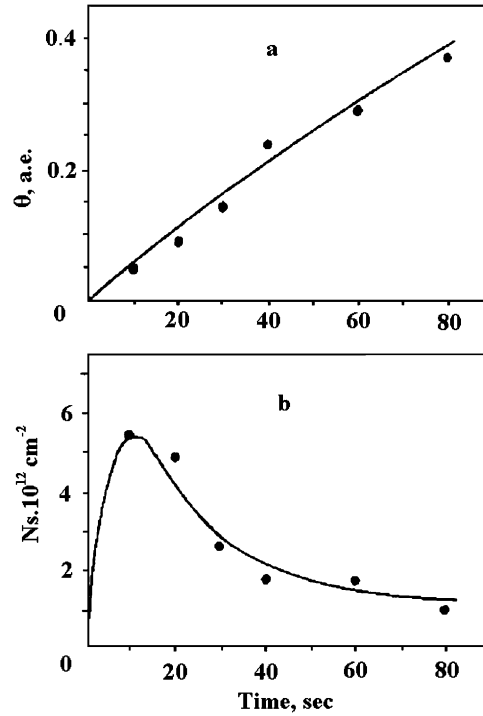


Fig. 10.3. The time dependence of an Au coverage θ (a) and a surface concentration of Au nanoparticles N_s (b) for PVD of Au monolayer on a surface of amorphous carbon at room temperature.

particles. As a consequence, N_s decreases down to a certain limiting value (Figure 10.3b) corresponding to stationary or so-called aggregative process of M/SC deposition when, as mentioned above, all atoms deposited on a substrate join growing particles. The $\bar{d}$ value of Au particles grows approximately proportionally to time of vapor deposition in spite of the fact that the free surface of a substrate is reduced [48, 50]. Apparently, the diminishing of atom arrival to growing particles from M/SC adsorbed on a substrate is compensated by deposition of atoms on particles directly from gaseous phase. This process is accompanied by displacement of atoms over Au particle [50] with increase in its area and corresponding rise of energy of interaction between the particle and the amorphous carbon substrate.

The model of Au deposition onto amorphous carbon in works [48–50] does not take into account the influence of Au atom desorption on the particle formation. It is allowable if E_{des} is so great that the mean time of nucleation is much less than τ_s even at low θ values. However, at PVD of

Lam Research Ex. 1035 - Page 543
Lam Research Corp. v. Inpria Corp.
IPR2024-00033 - U.S. Patent No. 9,823,564

M/SC on many, in particular, polymer substrates the desorption of adatoms should be taken into consideration. In this case the probability of M/SC phase nucleation at PVD, usually designated as condensation coefficient C, is defined by a competition between desorption of adatoms and their irreversible fixing on a substrate surface. Irreversibility of M/SC atom fixing is provided either by its aggregation with other atoms or by immobilization on surface defect which can be surface steps, outputs of dislocations, vacancies, etc. [42].

Nucleation of M/SC particles on defects is typical for systems with weak interaction between adsorbed atoms and substrate lattice. At nucleation on defects coefficient C is the probability for adatom to be captured by defect. As a first approximation, one can assume that defects immobilized diffusing adatoms are uniformly distributed on a surface and their surface concentration is equal to N_m. In this case C is determined by the relationship between X_D and the mean interval $đ_m$ separating defects of such type ($đ_m = N_m^{-1/2}$): $C = X_D/đ_m$ at $X_D < đ_m$ and $C = 1$ at $X_D \geq đ_m$ [51].

Nucleation and growth of nanoparticles at PVD of metals onto different polymers were thoroughly investigated in works [44, 52, 53]. Coefficient C is defined as the ratio of the number of atoms immobilized on a polymer surface to the total number of atoms arriving at this surface during given time. This ratio was measured by radiotracer method and X-ray photoelectron spectroscopy. Measurements are carried out at very low values of θ when the addition of deposited atoms to metal particles and small clusters can be neglected. Therefore, these measurements allowed determining the true coefficient C caused by only the interaction of adatoms with polymer substrate. PVD for Ag, Au, and Cu was investigated with the use of films prepared from polymer solutions [44, 52, 53]. This circumstance is essential because C can change depending on conditions of the polymer substrate preparation.

It has been stated that the nucleation of M particles at PVD of these metals on polymers having high surface energy, such as polyimides containing highly polar groups, occurs randomly over all substrate surface via dimerization of adatoms and $C \approx 1$ [44]. Maximal value of N_s (N_s^{max}), which is attained at stationary (aggregative) mode of deposition, increases with the rise of W_{dep} as $N_s^{max} \sim (W_{dep}/D_s)^{1/3.5}$ [44]. This relationship is in accordance with the theory of random nucleation elaborated in works [42, 43]. PVD of metals on the polyimide surface proceeds in the same manner as the above considered PVD of Au on amorphous carbon except that immobilized nuclei of Au particles on amorphous carbon surface are not dimers but larger nuclear clusters.

The decrease of polymer surface energy, in particular, with lowering of polymer polarity (when employing as substrates polystyrene, polycarbonate, and Teflon with incorporated C–O–C groups [53]) leads to the reduction of

Lam Research Ex. 1035 - Page 544
Lam Research Corp. v. Inpria Corp.
IPR2024-00033 - U.S. Patent No. 9,823,564

C. The nucleation on such substrates occurs on surface defects. It has been shown that C depends on the metal nature [44]: judging from obtained data [44] C raises with increasing of capability of deposited atoms to complexation with polymer functional groups. Unlike N_s^{max} at PVD on polyimide, in this case N_s^{max} does not depend on W_{dep} but is determined by the concentration of defects [53]. The creation of surface defects by irradiation of the Teflon and polystyrene films with Ar ions of high energy leads to a sufficient increase of C. With increasing of the irradiation dose the value of the coefficient C is approaching unity when the average distance between the defects becomes comparable with the X_D.

It has been shown [44, 53] that when the temperature is sufficiently lower than the glass transition temperature (T_g) of a polymer, metal atoms deposited from the gaseous phase do not penetrate inside the polymer and produce nanoparticles, which are localized exclusively on its surface. The heating of the resulting system up to temperatures higher than T_g leads to a gradual incorporation of these particles into the polymer layers adjacent to the surface. Therefore, varying components of system to be deposited and the deposition procedure one can form PVD-layered systems with a predetermined specific structure and properties. Thus, the layers of magnetic Ni nanoparticles in the Teflon wrapping were obtained as a result of the layer-by-layer deposition of Ni vapor and the sputtered Teflon fragments on a Teflon substrate [53].

The multilayer nanocomposite films containing layers of quasi-spherical Fe nanoparticles ($\bar{d} = 5.8$ nm) separated by dielectric layers from boron nitride (BN) are synthesized by the repeated alternating deposition of BN and Fe onto a silicon substrate [54]. In this work the authors managed to realize the correlation in the arrangement of Fe nanoparticles between the layers: the thin BN layer deposited on the Fe layer has a wave-like relief, on which the disposition of Fe nanoparticles is "imprinted"; as a result, the next Fe layer deposited onto BN reproduces the structure of the previous Fe layer. Thus, a three-dimensional ordered system of the nanoparticles has been formed on the basis of the initial ordered Fe nanoparticle layer deposited on silicon substrate [54]. The analogous three-dimensional structure composed of the Co nanoparticles layers, which alternate the layers of amorphous Al_2O_3, has been obtained by the PVD method [55].

The sequential deposition of carbon and Ge vapors, produced by the ion-assisted spraying of these substances at the room temperature, gives a film, where Ge sheets located between carbon layers are in the amorphous state [56]. In this system it is possible to "control" the size of nanocrystals forming in Ge sheets by changing the sheet thickness (d_{sh}). The annealing of so produced film at 870 K results in crystallization of the Ge sheets with $d_{sh} > 3$ nm only. In sheets of d_{sh} from 3 to 30 nm the $\bar{d}$ value of prepared Ge

Lam Research Ex. 1035 - Page 545
Lam Research Corp. v. Inpria Corp.
IPR2024-00033 - U.S. Patent No. 9,823,564

nanocrystals is proportional to d_{sh} as $\bar{d} = 0.9d_{sh}$. In the Ge sheets with $d_{sh} > 30$ nm the influence of the "shell" from carbon layers surrounding Ge sheet on the $\bar{d}$ of Ge nanocrystals after sheet crystallization reduces sharply and practically vanishes at $d_{sh} > 70$ nm, when $\bar{d} \sim 40$ nm [56].

The problem of the particle-size distribution obtained at the PVD of M/SC on a substrate is discussed in the paper [57]. The distribution is modeled for isotropic particle growth of adatoms on the ideal smooth surface provided that all particles consisting of two and more adatoms are immobilized, and the addition of a diffusing adatom to the growing particle is irreversible. At this modeling, the authors took into account the correlation of the growth of neighboring particles of the system as well as the increase of the rate constant for the capture of adatoms by the growing particle according to the increase of its diameter.

Results of this modeling that give an asymmetric distribution curve (earlier presented in the paper [43]) are in good agreement with experimental date obtained at Co-deposition on a Ru-monocrystal face [59]. However, usually it is observed that a Gauss-type size distribution for deposited particles [54, 60] is stipulated by chaotic distortions of the structure in different parts of the real surface as well as the corresponding changes of the parameters that determine the particle growth. At high values θ when the coagulation of neighboring growing particles becomes noticeable, the size distribution can acquire a bimodal character [43].

3.2. Co-Deposition of M/SC and A Dielectric Material

For synthesis of composite films with M/SC nanoparticles distributed in the volume of a dielectric matrix, method PVD is used as co-deposition of M/SC and dielectric material vapors. A comparison of films produced by co-deposition and layer-by-layer deposition PVD methods has been made on the example of BN-Fe nanocomposite films [57]. Unlike the above considered film from alternating layers of Fe and BN, which has ordered structure, co-deposited BN-Fe nanocomposite films consist of amorphous completely disorder matrix BN containing a chaotic system of immobilized Fe nanoparticles. At the same time, these particles in contrast to those of layered film have much smaller size ($\bar{d} = 2.3$ nm) since in this case the metal atoms are inside a matrix which slowdowns the diffusion process of atoms aggregation.

If the arising dielectric matrix is very rigid, the deposition process gives a film of solid M/SC solution in dielectric material. Such solution is formed, in particular, by co-deposition of CdS and SiO_2, sputtered under the action of ionic plasma [61]. Semiconducting crystals of CdS in amorphous matrix

Lam Research Ex. 1035 - Page 546
Lam Research Corp. v. Inpria Corp.
IPR2024-00033 - U.S. Patent No. 9,823,564

SiO_2 are formed as a result of thermal treatment of supersaturated solid solution. At the first stage of this process critical nuclei of a new phase are formed only. The value $\bar{d}$ and size distribution of these nuclei do not depend on CdS concentration but are governed by thermodynamic properties of system. The rate of nucleus formation sharply falls with decreasing of a solution supersaturation and reduces practically to zero at certain limiting CdS concentration c_c, at which crystallization process passes to the second stage of diffusion controlled nucleus growth. At this stage the number of growing particles remains constant, and $\bar{d}$ increases proportionally to $[(c_c - c_e)D\tau_a]^{1/2}$, where c_e is the equilibrium CdS concentration in the solution, τ_a the annealing time, and D the diffusion coefficient for CdS in amorphous SiO_2 matrix [61].

At the co-deposition of nanocomposite components formation of M/SC particles proceeds simultaneously with formation of a dielectric matrix, and the relationship between these processes determines the nanocomposite structure. This problem has been in detail investigated for the case of M/SC nanoparticles formation in polymer matrices. Synthesis of nanocomposite films by simultaneous PVD of polytetrafluoroethylene (PTFE) and Au has been carried out in works [62–64]. Polymer and metal were sputtered under action of Ar ions and then the obtained vapors were deposited on substrates (quartz, glass, silica, mica, etc.) at various temperatures. Here, it is necessary to note that polymer sputtering cannot be considered as only physical process: PFTE polymer chains destruct under action of high-energy ions, and formed chemically active low-molecular fragments are then deposited and polymerized on a substrate surface.

Because all procedure of films preparing takes place in high vacuum, polymerization of PFTE fragments and aggregation of metal atoms, as it was noted above, proceed heterogeneously on surface of a substrate or of a growing film. Using transmission electronic microscopy (TEM) values $\bar{d}$ and N_s for Au nanoparticles inside PTFE composite film of thickness 10 nm deposited at a room temperature were measured depending on a volume fraction (φ) of Au in obtained film [62, 63]. The results of measurements are given in Table 10.1. It is easy to see that with increase of φ from 0.05 to 0.3 the value $\bar{d}$ first grows insignificantly, but then sharply rises at increase of φ from 0.2 to 0.3. At the same time N_s appreciably decreases with growth φ [62,63]. Such φ dependence of N_s for co-deposited PFTE-Au film differs from results [44, 52, 53] obtained at metal deposition on a Teflon surface (see higher) when N_s is determined only by surface defects and does not depend on the rate of metal deposition.

In the case of co-deposition nucleation and growth of metal nanoparticles are influenced by the process of a polymer matrix formation from deposited low-molecular fragments (TFE) of PTFE. At the initial stages the deposited

Lam Research Ex. 1035 - Page 547
Lam Research Corp. v. Inpria Corp.
IPR2024-00033 - U.S. Patent No. 9,823,564

Table 10.1. Average diameter $\bar{d}$ and surface numeric concentration N_s of Au nanoparticles in cut-off of composite Au-PTFE films produced by co-deposition of Au and floor-organics vapors in dependence on Au volume content φ [62]

φ	$\bar{d}$ (nm)	N_s (cm^{-2})
0.05	2.0 ± 0.6	6.63×10^{12}
0.15	2.7 ± 0.7	4.98×10^{12}
0.20	3.6 ± 1.5	2.37×10^{12}
0.3	7.8 ± 3.5	7.70×10^{11}

layer contains rather high percent of polymerizing low-molecular fragments. In such layer with low viscosity not only Au atoms, but also dimers and small clusters of Au coagulate as it takes place at deposition of Au onto amorphous carbon (see above and Ref. [48]). The confirmation of such assumption is a sharp decrease of N_s and corresponding growth of $\bar{d}$ at increase φ from 0.2 to 0.3. At high φ a coagulation of even rather large and slowly moving clusters becomes possible already at beginning of deposition in low-viscous layer due to reducing of distances between Au clusters with a rise of φ (Table 10.1).

The model of polymer nanocomposite formation as a result of co-deposition of M/SC and monomer vapors onto substrate is developed [51, 58]. It is supposed that the deposition onto cooled substrate gives monomer layer with randomly distributed atom/molecules of M/SC. At the heating of layer the diffusion of M/SC atoms/molecules followed by their aggregation and formation of M/SC nuclei proceeds simultaneously with monomer polymerization. The diffusion of M/SC atoms/molecules to nuclei results in growth of M/SC particles. Polymerization is accompanied by decreasing of free volume of organic matrix and corresponding fall of diffusion rate for M/SC atoms/molecules. In accordance with data of works [52, 53] it was supposed that diffusion of M/SC atoms/molecules stops at full conversion of a monomer in polymer. So in the model the time for the growth of M/SC particles is limited to process of the matrix polymerization, which is almost not influenced by the presence of M/SC. The number of atoms, which have a time to achieve a growing nucleus before monomer matrix completely transforms to a polymer one, is approximately the same for all nuclei. This leads to rather narrow size distribution for M/SC particles. The solution of the kinetic equation with variable coefficient of diffusion leads to analytical expression for limiting radius of nanoparticles [58].

The diffusion of M/SC atoms/molecules to nuclei results in growth of M/SC particles. To illustrate the experimental data given in Table 10.1 let us consider a thin layer of mixture of TFE and Au that have been deposited at a substrate surfaces in time, which is much less than time required for

Lam Research Ex. 1035 - Page 548
Lam Research Corp. v. Inpria Corp.
IPR2024-00033 - U.S. Patent No. 9,823,564

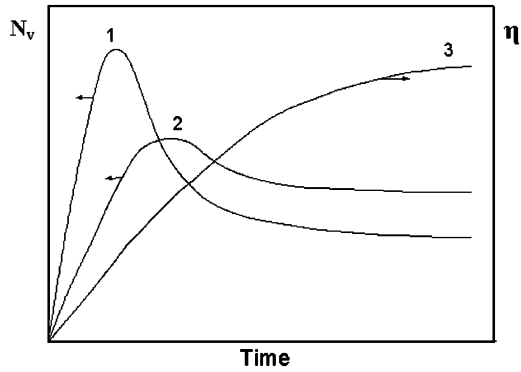


Fig. 10.4. Supposed model for the time dependence of volume concentration N_v of M/SC nanoparticles during polymerization of co-deposited M/SC organics layers with different M/SC contents φ_1 (curve 1) and φ_2 (curve 2) at $\varphi_1 > \varphi_2$. Curve 3 characterizes the increase in layer viscosity during polymerization.

aggregation of Au and polymerization of TFE. In this case the time dependence of N_s for two various φ after layer formation can be presented with curves 1 and 2, given in Figure 10.4 together with a curve 3 characterizing the change of a layer viscosity during the polymerization. At high value φ concentration of small mobile metal clusters quickly reaches a maximum and then falls as a result of coagulation even until the polymerization begins to retard markedly this process. At small φ the concentration of metal clusters increases slowly, and their coagulation occurs, for the most part, already at high viscosity of a polymerizing layer when the rate of this process is sharply reduced. It is necessary to note that with reduction of free volume of system and corresponding increase of viscosity, the rate of the clusters' coagulation falls much more strongly than the rate of the atom addition to growing particles. These reasons allow explaining the increase of N_s for particles immobilized in a final polymer layer with decrease of φ.

PTFE films containing Au nanoparticles have been prepared by deposition of Au sputtered by radio-frequency discharge in the presence of gas mixtures C_3F_8–Ar or C_2F_4–Ar [36, 65]. The discharge leads to polymerization of these fluoro-organic monomers. Apparently, reaction proceeds in part in a gas phase with formation of "heavier" fluoro-organic intermediates, which were deposited and polymerized onto a substrate simultaneously with deposition of Au. In this system the value $\bar{d}$ of Au nanoparticles at $\varphi = 0.16$ is close to that of particles in above considered films of works [61, 62]. It shows that preparing Au-containing composite films by ion-assisted Teflon sputtering and a discharge plasma polymerization method follows the same physical and chemical processes.

Lam Research Ex. 1035 - Page 549
Lam Research Corp. v. Inpria Corp.
IPR2024-00033 - U.S. Patent No. 9,823,564

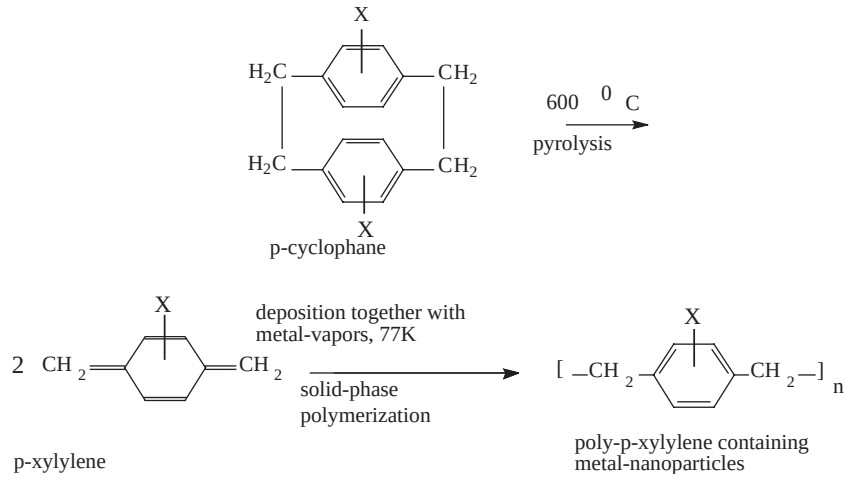
At the same time, in the films formed in plasma the increase φ from 0.16 to 0.62 results only in insignificant growth $\bar{d}$ [36]. Probably, solidification of films during the discharge-induced polymerization of deposited low-molecular compounds occurs faster than solidification of films from sputtered Teflon fragments. It should be taken into account that polymerization in discharge plasma gives the cross-linked polymer matrix, which especially strongly holds the metal inclusions and prevents coagulation of large metal nanoparticles. In agreement with data of X-ray and electronic diffraction Au crystallites formed in this system at room temperature are textured. The reasons of the crystallite texturation in a glass-like polymer matrix are not clear, taking into account the fact that interaction of Au with Teflon is very weak and at deposition of Au onto Teflon surface the texturation of obtained nanocrystal was not observed [44, 53]. Close to 160°C there is a transition of cross-linked polymer matrix in a high-elastic state. The movement of small crystallites, which aggregate with formation of larger nanoparticles, is defrozen only in the temperature range over the transition temperature [36].

As mentioned above, the new method of cryochemical synthesis of polymer nanocomposite films has been developed based on co-deposition of M/SC and monomer vapors at temperature ~80 K and subsequent low-temperature solid-state polymerization of monomer matrix ([2] and works cited herein). It has been established that a number of monomers (acrylonitrile, formaldehyde, *p*-xylylene and its derivatives) polymerize in solid state in absence of thermal movement of molecules owing to own specific supra-molecular structure. When reaction is initiated by γ- or UV-radiation the formation of a polymer matrix occurs even at the temperatures close to temperature of liquid helium [66–69].

p-Xylylene (PX) compounds containing different substituents are the most suitable monomers for cryochemical synthesis of metal containing polymers because they polymerize at low temperatures completely without use of any foreign substance, in particular, initiators or sensitizers. By varying of substituents one can modify physico-chemical properties of obtained poly-*p*-xylylene (PPX) matrix in rather wide range. PX compounds arise by pyrolysis of corresponding [2,2]-*para*-cyclophanes [70]. Scheme 1 shows preparation of PX-compounds and their polymerization in deposited metal containing films. Under UV–vis radiation polymerization was realized at temperatures down to 77 K. While heating deposited monomer its thermal polymerization proceeds quickly around 160–170 K [71] that is ~50° below fusion temperature of monomer [72].

Cryochemical synthesis of Ag–PPX systems and their structures were studied in Ref. [73–76]. The simultaneous vapor deposition of PX and mono-substituted chloro-PX (Cl-PX) and cyano-PX (CN-PX) with Ag at

Lam Research Ex. 1035 - Page 550
Lam Research Corp. v. Inpria Corp.
IPR2024-00033 - U.S. Patent No. 9,823,564



Scheme 1. Preparation of p-xylylene monomers and their polymerization after deposition together with metal vapors

77 K does not lead to complexation or the formation of any organometallic compounds [73, 75]. In the case of PX and Cl-PX such deposition proceeds without polymerization. The co-deposition of CN-PX with Ag is accompanied by the partial polymerization of monomer. The initial condensates at 77 K contain a small amount of Ag nanocrystals which can be revealed and characterized using UV–vis spectroscopy because such crystals (as it has been shown in Subsection 2.1) have the specific absorption band of surface electron plasmons ~430 nm [77]. UV irradiation of these condensates at 77 K leads to total conversion of monomers to corresponding polymers (PPX, ClPPX, and CNPPX). However, intensity (D_{cr}), maximum position (λ_{max}) and half-width ($\Delta_{1/2}$) of the nanocrystals plasmon band do not practically change in the course of cryopolymerization (Table 10.2) [73, 75, 80]. Thermal polymerization close to 170 K leads to only very insignificant increase in D_{cr}.

Because D_{cr} is proportional to the content of Ag nanocrystals and $\Delta_{1/2}$ is in inverse proportion to their mean size d [77, 78], one may conclude that the state and amount of Ag nanocrystals were not affected by the cryopolymerization. Sharp growth of D_{cr} at heating of obtained metal-polymer films specifies that the main part of Ag at 77 K is in a form of small noncrystalline Ag_n clusters, which aggregate with formation of nanocrystals under action of thermal relaxation processes in polymer matrix. According to data in work [79], in UV–vis spectra of PPX films on a background of the PPX absorption only absorption bands of Ag_n with $n > 15$ could be observed in "open" range of PPX spectrum at $\lambda > 320$ nm. Because in this spectral range

Lam Research Ex. 1035 - Page 551
Lam Research Corp. v. Inpria Corp.
IPR2024-00033 - U.S. Patent No. 9,823,564

Table 10.2. Spectral characteristics and content of Ag nanocrystals in the solid system during the synthesis of Ag–PPX nanocomposite

System	λ_{max} (nm)[a]	$\Delta_{1/2}$ (nm)[a]	D_{cr} (at λ_{max})[a]	Content of Ag nanocrystals (at.%)
PX–Ag at 77 K	430	93	0.24	4.2
PPX–Ag at 77 K	430	93	0.24	4.2
PPX–Ag at 298 K	435	96	0.28	5.0
PPX–Ag at 320 K	443	98	1.10	16.3
PPX–Ag at 373 K	443	98	1.22	18.0

[a]Designations are given in the text.

there are no absorption bands except for absorption band of Ag nanocrystals, it may be concluded that clusters stabilized in obtained films contain less than 15 atoms [73, 80].

Solid polymer matrix hinders the aggregation of cryochemically prepared Ag clusters so that substantial part of Ag in the prepared Ag–PPX systems remains in noncrystalline form at ambient and even higher temperatures. As was stated in Refs. [73, 75, 80], Ag introduced into the investigated PPX matrices transforms fully to nanocrystals after annealing at 373 K. Therefore, the ratio of D_{cr} in a spectrum of an examined film to $(D_{cr})_0$ in a spectrum of the same film annealed at 373 K characterizes a degree of the cluster crystallization (Table 10.2). Spectral data show that the position of plasmon band for nanocrystals in Ag–PPX films heated from 77 to 293 K shifts to the long wavelength range and then does not change at heating from 293 to 373 K (Table 10.2).

The same effect was observed for Ag–ClPPX films [73, 80].

It should be noted that, unlike Ag nanocrystals of Ag–PPX nanocomposites with λ_{max} of plasmon band in the range 430–445 nm, nanocrystals prepared by reduction of Ag^+ ions in solution of poly (N-vinylpyrrolidone) [81] as well as nanocrystals formed by introducing Ag vapors into liquid polybutadiene [77] have plasmon band with λ_{max} around 410 nm. As is specified in Ref. [81], the UV–vis spectrum of nanocrystals depends on their size and form as well as on the surrounding matrix. The plasmon band of Ag nanocrystals [77, 81] coincides with that of modeling spherical nanoparticles with a smooth ideal surface, which were theoretically treated from different points of view in Ref. [82, 83].

The nanocrystals of such type form in various liquid media, such as organic solution [77, 81] or the softened quasi-liquid glass [82, 83], where there are no steric hindrances for the growth of equilibrium crystals without surface defects. At the same time, barriers for aggregation of clusters or atoms to metal nanocrystals in solid system that arises during the cryochemical solid-state synthesis favor the formation of crystals with structural defects,

Lam Research Ex. 1035 - Page 552
Lam Research Corp. v. Inpria Corp.
IPR2024-00033 - U.S. Patent No. 9,823,564

especially on the crystal surface. This increases the surface diffuseness of such nanocrystals resulted to the red wavelength shift of the surface plasmon resonance [84]. The defreezing of polymer matrix and corresponding alteration of the metal–dielectric interface can explain the further increase of λ_{max} of plasmon band.

The formation of Ag nanocrystals from small Ag clusters is greatly influenced by the structure of polymer matrix. In cryochemically synthesized films Ag–PPX and Ag–CNPPX small Ag clusters are more stable than those in similar films Ag–ClPPX [3, 80]. The rather high stability of clusters in Ag-containing PPX can be explained by features of the PPX amorphous phase where clusters are mainly localized. Due to absence of substituents in PPX chains this phase differs probably from similar phase of substituted PPX in higher density and consequently hinders the cluster aggregation in the greater degree. In CNPPX (as compared with ClPPX) there is probably the enhanced interaction between electron-donating Ag clusters and highly polar electrophilic CN groups of polymer environment that provides high stability of clusters.

According to UV–vis spectra [75,80] and X-ray diffraction [73] data the d value of Ag nanocrystals embedded in PPX and ClPPX films by cryochemical synthesis is ~5 nm. At the same time X-ray diffraction pattern of a layered Ag–ClPPX system obtained by successive deposition of monomer and Ag at 77 K, followed by cryopolymerization and annealing at 293 K, has shown the value d ~12 nm [73]. So d of Ag nanocrystals in a polymerized co-condensate is determined mainly, by steric restrictions on the crystal growth in the interior of solid matrix.

The Ag-containing PPX was investigated also by TEM. The TEM pattern demonstrates globular particles of sizes between 2 and 12 nm quite homogeneously dispersed within the polymeric matrix [75]. Histogram of the particle size distribution shows that the main particle size is between 4 and 6 nm that is in good agreement with the results of X-ray and spectral measurements for Ag–ClPPX.

Similar histograms were determined by TEM for Pb-, Zn-, and Cd-containing nanocomposite PPX films prepared by vapor deposition cryochemical synthesis [85]. The value d of metal nanocrystals in these films is also ~5 nm. The same approximately size d (~4.5 nm) has been evaluated from $\Delta_{1/2}$ of X-ray diffraction peak for semiconductor PbS nanocrystals in PbS–PPX nanocomposite [71]. It should be particularly emphasized that d value of M/SC nanocrystals embedded by cryosynthesis in PPX and ClPPX matrices does not depend on M/SC content as for low loading (0.2–2 vol.% for Ag in PPX and ClPPX [75, 80] and 0.01–1 vol.% for Pb in PPX [85]) and for high loading (5–11 vol.% for PbS in PPX [3, 71, 86]) systems.

Lam Research Ex. 1035 - Page 553
Lam Research Corp. v. Inpria Corp.
IPR2024-00033 - U.S. Patent No. 9,823,564

Besides, as can be seen from the cited data, this value is almost one and the same irrespective of the nature of M/SC so that it is determined by only structure and properties of a polymeric matrix. In this connection it should draw attention to the fact that according to spectral data [80] the $\bar{d}$ value of Ag nanocrystals in films Ag–CNPPX is much less than that of Ag nanocrystals in films Ag–PPX and Ag–ClPPX. As was specified above, it is possible to expect essential interaction between Ag particles with strongly polar CN substituents of PPX that hinders the growth of Ag nanocrystals.

The more detailed study of the crystallite size distribution and crystallite arrangement in PPX matrix was carried out for cryochemically synthesized nanocomposite PbS–PPX films in the range of PbS content from 4.7 to 10.2 vol.%. The distribution curves obtained from analysis of wide-angle X-ray scattering (WAXS) data is presented in Figure 10.5 [71, 86]. The curve for nanocomposite with 4.7 vol.% of PbS differs a little from histograms of the crystallite size distribution determined by TEM for nanocomposite films Ag–PPX and Pb–PPX with low metal content [75, 80]. It means that, as the average size of crystals, distribution in the sizes almost does not depend on nature of M/SC incorporated in polymer as a result of cryochemical synthesis.

PbS–PPX nanocomposite with 4.7 vol.% of PbS was investigated also by small angle X-ray scattering (SAXS) method, which characterizes different

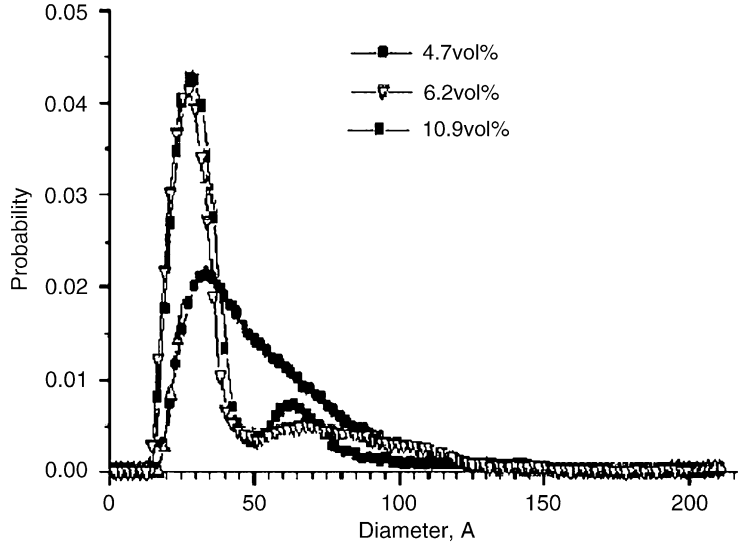


Fig. 10.5. Size-distribution of PbS crystallites in dependence of PbS concentration in the PPX-PbS composite [86].

Lam Research Ex. 1035 - Page 554
Lam Research Corp. v. Inpria Corp.
IPR2024-00033 - U.S. Patent No. 9,823,564

PbS inclusions in PPX matrix regardless of their internal structure. The size distribution of PbS inclusions calculated from SAXS data are similar to the WAXS crystallite size distribution in Figure 10.5. This result signifies that PbS nanoparticles do not aggregate in matrix but are distributed in PPX mostly as small crystallites [71].

It has been shown that the arrangement of nanocrystals in composite films is determined by PPX supramoleculare structure. The SAXS curve at relatively small PbS content of 4.7 vol.% has broad maximum, which specifies some order in an arrangement of PbS nanocrystals. In this case PPX matrix retains still semicrystalline structure [71]. In such matrix the nucleation and subsequent growth of inorganic nanocrystals takes place mostly in amorphous regions where there is enough free volume. It is possible that the observed SAXS maximum corresponds to an average periodicity between PbS nanocrystal assemblies in different amorphous regions separated by PPX lamellar crystallites. The characteristic parameter of this supramolecular periodicity is ~25 nm that approximately coincides with thickness of PPX lamellas [71].

An increase in concentration of PbS leads to the change of the crystal size distribution, which acquires a bimodal form. Recently, it was shown that such bimodal crystal size distribution takes place not only in PPX–PbS samples, but also in PPX containing Ag nanocrystals [87]. Unlike other analogous systems, the composites obtained by the cryochemical solid-state synthesis demonstrate a marked increase in the percentage of small crystals with increasing content of inorganic component (M/SC) incorporated in polymer. Figure 10.5 shows that the contribution of PbS crystallites of ~3 nm size increases from 20 to 80% with an increase in the overall PbS content from 4.7 to 10 vol.%. At the same time, the high PbS loading favors the formation of rather large crystals in the 70–120 Å size range. For this reason the crystal mean size determined from the half-width of the X-ray diffraction line does not change significantly and remains in the range 4–5 nm.

It should be taken into consideration that at the cryochemical synthesis of M/SC–PPX systems M/SC particles grow in a solid polymer matrix with microheterogeneous grained structure. In such matrix the growth of M/SC particles is determined by a local environment of growing particle. Nuclei of a new M/SC phase are formed most probably in extended defects of matrix between solid grains. The further growth of nuclei fixed in the solid polymer matrix is governed by the diffusion atom/molecule flow to a growing nuclei lengthways of extended defects.

As has been noted above the $\bar{d}$ value and the size distribution of M/SC nanoparticles in cryochemically synthesized M/SC–PPX does not depend on either concentration or a kind of particles. This suggests that in a solid

Lam Research Ex. 1035 - Page 555
Lam Research Corp. v. Inpria Corp.
IPR2024-00033 - U.S. Patent No. 9,823,564

medium (at least, in the investigated PPX matrixes) there can be limitations on the size of growing particles caused only by structure and properties of a medium. It should take into account that the growth of nucleus is accompanied by increasing of local strains in a surrounding area of matrix. It is believed that at a certain critical level of stains the solid environment of a growing particle is rearranged in such a manner that closes access of atoms to a particle and stops its further growth.

The reasons for unusual change of the crystal size distribution curve with increasing metal content are unclear now. Preliminary data show [86] that an increase in the content of M/SC inclusions decreases the polymer matrix crystallinity and polymer crystal size. It is believed that this process is accompanied by the formation of a large number of local defected sites. This facilitates reorganization of strained matrix that stops the growth of M/SC particle. At the same time an increase in M/SC content can lead to formation of large spatial defects with high free volume where nanocrystals have a possibility to coagulate giving rather large crystalline clusters. It may be supposed that such defects arise under strains accompanying nucleation at high loading.

4. Physico-Chemical Properties of Nanocomposite Films

PVD solid-state synthesis can produce composites with high (close to percolation threshold) content of stable metal particles of varying size, trapped inside different polymer matrices. Due to the high-metal content obtained nanocomposites get important valuable properties. First, the effects caused by the local behavior of isolated particles are sharply amplified (for example, the density of magnetic data recording in composite containing ferromagnetic monodomain nanoparticles). Besides, in nanocomposites with high-metal content one should take into account the interaction between nanoparticles, which determines cooperative behavior of the system of metal nanoparticles immobilized in polymer matrix. This interaction manifests itself mainly as charge transfer processes between nanoparticles. In particular, these processes substantially influence electrophysical and dielectric properties as well as catalytic activity of metal–polymer materials synthesized by PVD technique.

4.1. Conductivity and Photoconductivity

The effect of M content on electrical resistance R_{el} of M containing nanocomposite film has been studied using as an example films of Teflon with Au

Lam Research Ex. 1035 - Page 556
Lam Research Corp. v. Inpria Corp.
IPR2024-00033 - U.S. Patent No. 9,823,564

nanoparticles, produced by a plasma method of PVD [36]. When M/SC particles are isolated in polymer so that the interaction between them can be neglected, R_{el} of composite film practically coincides with that of polymer matrix. In such composites M/SC nanoparticles can only inject carriers into polymer but do not influence substantially the conductivity process [88]. The conductivity of such type is observed usually in composite films containing M/SC nanoparticles in amounts less than 4–5 vol.% [89]. With an increase in concentration N_v of particles, R_{el} gradually decreases and at certain critical value $(N_v)_c = p_c$ (percolation threshold) sharply falls down to R_{el} close to that of metal film. This transition is caused by formation of an infinite percolation cluster of particles – a filament consisting of connected particles and penetrating the whole film.

Percolation threshold p_c corresponding transition to metal conductivity in composite films from Teflon with Au nanoparticles is ~30 vol.% [36]. The similar transition to semiconductor conductivity in films of polyvinyl alcohol containing nanocrystals CuS takes place at p_c ~15–20 vol.% [88]. In cryochemically synthesized films PPX with Ag nanocrystals conductivity of metal type is achieved already in films with Ag content ~7 vol.%: conductivity of these composite films increases with the lowering temperature proportional to $(1+\alpha T)^{-1}$ similarly to that of block metals, but coefficient α is ~2.5 times less than value α_0, characteristic for block silver [86].

Unusually small value of p_c in this system speaks that the true concentration of Ag in the areas of a film, where Ag nanocrystals are formed, strongly differs from the average concentration determined in experiment. Systems with concentration of M/SC nanoparticles close to p_c are of special interest. In such systems the essential increase in conductivity as compared to that of pure polymer results from processes of tunnel electron transfer between nanoparticles. Conductivity of composite system with regard to electron tunneling between M/SC nanoparticles has been considered in work [88] on the basis of the following model. In the model, the spherical particle of radius R_q is surrounded with the sphere of radius R_d describing the delocalization for conductivity electrons of the particle and partial transition of electronic density in an environment (Figure 10.6a).

The change of electronic conductivity $G(r)$ over diameter of such two-sphere model composition as element in a system of contacting particles is shown in a Figure 10.6b. The transfer of electron across this composition consists of three stages: electron tunneling over the interspace $R_d - R_q$ is replaced by the M/SC conductivity across a particle with subsequent electron tunneling over the further interspace $R_d - R_q$. The probability of electron tunneling falls down exponentially with increase in distance from the surface of particle.

According to this model the tunnel current arises due to formation of the infinite percolation cluster of contacting external spheres with R_d. The

Lam Research Ex. 1035 - Page 557
Lam Research Corp. v. Inpria Corp.
IPR2024-00033 - U.S. Patent No. 9,823,564

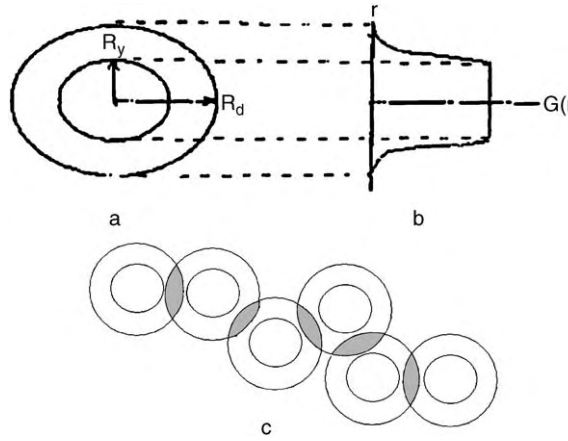


Fig. 10.6. Percolation cluster model of tunnel current in composite film containing M/SC nanoparticles: (a) two-sphere model of spherical M/SC nanoparticle of radius R_q surrounded by outer sphere (radius R_d) that is defined by a degree of electron delocalization extending the nanoparticle and characterizes electron tunneling (see text); (b) the distribution of conductivity $G(r)$ over the two-sphere particle; (c) two-dimensional pattern of cluster from overlapping two-sphere particles (overlapping areas of outer spheres are shown).

occurrence of tunnel current precedes transition to metal conductivity provided by infinite cluster from contacting particles of radius R_q. Reduction of R_{el} with growth of particle concentration is caused not only by increase in number of ways for tunnel current but also by rise of electron tunneling probability in consequence of decrease in distances between particles (in the model, external spheres unlike inner ones are permeable, Figure 10.6c) [88]. Calculations by a Monte Carlo method have shown that such model well describes character of conductivity dependence on concentration of M/SC particles in composite film [88].

The question arises, naturally, about the limiting size of external sphere in the considered model. This size can be estimated, recognizing that a tunnel current should exceed thermionic one. Therefore, value R_d depends on temperature and height of a barrier for tunnel electron transfer. Comparison of tunnel and thermionic currents has shown that at room temperature and a barrier of height ~1 eV the tunnel current will prevail over the thermionic one at a spacing between particles no more than 5–6 nm, i.e., at values $R_d - R_q \leq$ 2–3 nm [90].

The current(I)–voltage(U) relationship (IVR) for tunnel current depends on intensity of field F. At not so strong fields ($<$50,000 V/cm) IVR looks mostly like $\ln I \sim U^{1/2}$ [90]. Such IVR was stated for conductivity in PPX films containing 5–10 vol.% of PbO nanoparticles [89]. Such particles have

Lam Research Ex. 1035 - Page 558
Lam Research Corp. v. Inpria Corp.
IPR2024-00033 - U.S. Patent No. 9,823,564

been produced by oxidation on air of Pb nanocrystals in cryochemically synthesized Pb–PPX composite films. At the same time, in similar PPX films containing Pd nanocrystals the tunnel current I is proportional to U according to classical Ohm law [91].

Different IVR for PPX films with PbO and Pd nanoparticles can be probably caused by the difference in the work functions for PbO and Pd. Besides, nanoparticles PbO and Pd most likely have a various surface, and a field around charged nanoparticle depends on surface distortions. It is believed that unlike M nanoparticles of Pd, SC nanoparticles PbO resulted from Pb oxidation contains essential surface defects, for example, bulges where the density of a charge increases. Such defects cause local amplification of electric field in a interspace between the charged and neutral particles of a film. As a result, the effect of field on barrier of electron tunneling increases leading to deviation IVR from classical ohmic dependence.

PPX-composite films containing semiconductor nanocrystals of PbO (formed by oxidation of Pb nanocrystals) and PbS show photoconductivity [71, 89]. In the PbO–PPX films the photocurrent value (I_{ph}) in the wavelength range 250–350 nm does not depend on wavelength and the ratio between I_{ph} and dark current is close to 10^4. Then I_{ph} is gradually reduced to zero at increase of wavelength to 450 nm [89].

In the PPX films containing semiconductor PbS nanocrystals of mean size $\sim$45 Å the photoconductivity has been found even at 630 nm. This wavelength is close to the long-wave edge of the electron absorption of nanocrystals determined from UV–vis of the films [71]. I_{ph} in PbS–PPX is proportional to 0.8–1 power of the light intensity and the activation energy of photoconductivity is 10^{-1}–10^{-2} eV. The energy of light quantum at wavelength 630 nm is $\sim$2 eV, whereas the electronic work function of PbS nanocrystal is higher than 4 eV. This circumstance has led to a conclusion that observed photoconductivity is caused by the photo-induced tunnel electron transfer [71]. The photocurrent response time is 0.2–0.5 sec [71]. Such rather high (for the electron photo detachment) value of the response time suggests that photocurrent proceeds with participation of intermediate long-lived electron–hole pairs generated by light in semiconductor nanocrystals and localized presumably on their surface defects as it was discussed above in Section 2.

4.2. SENSOR PROPERTIES

The conductivity of films containing M/SC nanoparticles is influenced (and in many cases very strongly) by chemisorption of chemical compounds on the nanoparticles surface and the subsequent reactions with participation of

Lam Research Ex. 1035 - Page 559
Lam Research Corp. v. Inpria Corp.
IPR2024-00033 - U.S. Patent No. 9,823,564

chemisorbed molecules. The reason is that such chemical processes on surfaces of M/SC nanoparticles in the nanostructured film lead to changes in number of current carriers (mainly, electrons) and/or the potential barriers for the carrier transfer between the particles [92, 93]. This phenomenon is used in conductometric sensors for detecting various substances in an atmosphere. Sensors based on semiconducting metal oxides, especially SnO_2, are the most widespread and used for detecting the contents of such gases reducers, as H_2, CO, CH_4, etc., in an atmosphere [92].

The work of a metal-oxide sensor can be considered by the example of SnO_2 film. The minimal band gap ΔE_0 between the top of valent band E_v and the bottom of conductivity band E_c in SnO_2 crystals ranges, for various data, from 3.5 to 4 eV. Therefore, the generation of carriers by thermal interband transitions is highly improbable. The conductivity in these crystals is due to the thermal ionization of donor defects in SnO_2 lattice, for the greatest part, oxygen vacancies which electron levels are situated near to conductivity band of SnO_2 [93]. At temperatures higher than 100°C practically all electrons pass from vacancies in conductivity band of SnO_2 [93]. However, on air conduction electrons are in great part captured by the surface electron-acceptor oxygen centers arising as a result of oxygen chemisorption on the semiconductor surface. Such capture results in falling conductivity.

At the same time chemical reaction of reducing agents with the oxygen centers ''liberates'' electrons and gives an increase in conductivity. Thus, conductivity of a film consisting of SnO_2 particles is determined by equilibrium between redoxy reactions and the chemisorption processes on a surface of semiconducting particles. For a CO sensor at working temperatures (200–400°C), when electron-acceptor centers are O atoms [93], this equilibrium looks as (e^-: electron in a conductivity zone of SnO_2, the index ''ad'' means a particle adsorbed on SnO_2 surface) [94–96]:

$$O_2 \rightleftarrows 2O_{ad}$$

$$O_{ad} + e^- \rightleftarrows (O^-)_{ad}$$

$$CO \rightleftarrows (CO)_{ad}$$

$$(CO)_{ad} + (O^-)_{ad} \rightleftarrows e^- + (CO_2)_{ad} \rightarrow CO_2.$$

The capture of conduction electrons by adsorbed oxygen atoms results in depletion of near-surface SnO_2 layer of width Λ with electrons and occurrence of positive charge in this layer [93–95]. Such change in band structure can be caused by repulsing of conductivity electrons from negatively charged centers on SnO_2 surface. As a result, near to the surface of SnO_2

Lam Research Ex. 1035 - Page 560
Lam Research Corp. v. Inpria Corp.
IPR2024-00033 - U.S. Patent No. 9,823,564

particle there is a potential barrier V, which has the form of well-known relation [95]

$$V(x) = V_s \exp\left(\frac{-x}{L_D}\right), \tag{12}$$

where x is the distance from surface into SnO_2-particle, V_s the barrier height at surface ($x = 0$), and L_D the Debay's length of charge screening, which characterizes the barrier width Λ and is equal to

$$L_D = \left(\frac{\varepsilon kT}{e^2 n_v}\right)^{1/2}.$$

Here, n_v is the concentration of conductivity electrons in volume of the crystal, which equals to concentration of completely ionizing donor centers in SnO_2 lattice and ε is the SnO_2 dielectric permittivity [93]. The height V_s is proportional to eN_s^2 [97], where N_s is the concentration of adsorbed oxygen ions. The value

$$\Delta V(x) = V_s - V(x) = V_s\left[1 - \exp\left(\frac{-x}{L_D}\right)\right]. \tag{13}$$

The critical parameter for work of a nanostructured sensor is the value $x = x_c$ at which $\Delta V(x)$ equals kT. According to formula (13) the value $x_c = L_D kT/V_s$.

Conductivity is caused by the transfer of electrons over percolation cluster of semiconducting particles (Figure 10.7) and depends on ratio between diameter of particles d and x_c. At $d \gg x_c$ the electron transfer requires to overcome significant barriers on borders between particles. Reactions of reducing agents, in particular CO, with adsorbed oxygen, causes a decrease of N_s and, as a consequence, reduction of V_s and Λ, accompanying with the growth of conductivity. At the same time, the values E_c and n_v, characterizing inner areas of particles outside the layer Λ, remain constant. So, in a sensor with large particles only rather small part of a sensor material takes part in the sensor response (Figure 10.7a). In a percolation cluster of particles with $d \leq x_c$ barriers between particles are $\leq kT$ [98]. It means that conductivity electrons move freely between nanoparticles. Thus, electronic perturbations in any particle of percolation cluster practically instantly delocalize in its volume, causing respective change in E_c and n_v in whole cluster (Figure 10.7b) [93]. In result, at $d \leq x_c$ all electrons in conductive band of percolation cluster are involved in sensoring process.

The sensoring effect, i.e., sensor sensitivity S_c, grows at increase of the ionization degree of adsorbed oxygen, caused by equilibrium $O_{ad} + e^- \rightleftarrows (O^-)_{ad}$ [96], which is shifted to the right with increase of number of electrons, participating in the ionization reaction. Thus, in a cluster of

Lam Research Ex. 1035 - Page 561
Lam Research Corp. v. Inpria Corp.
IPR2024-00033 - U.S. Patent No. 9,823,564

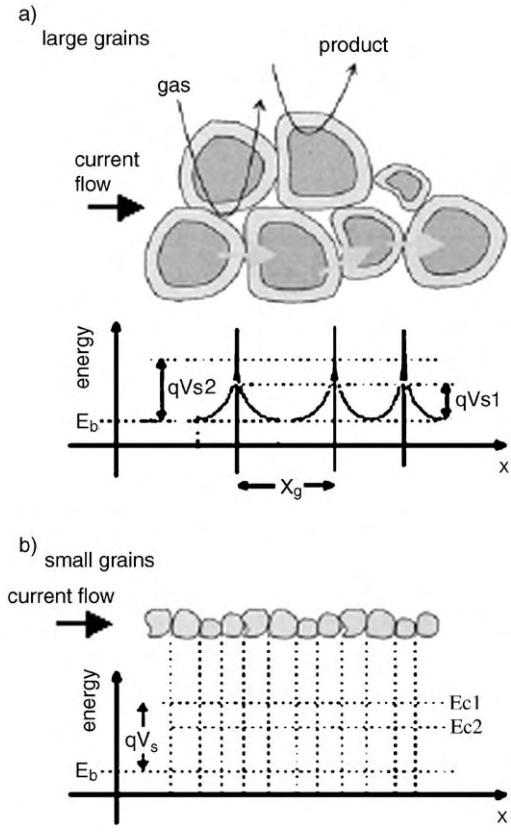


Fig. 10.7. Structural and energy band model of grained SnO_2-sensor [93]. a) Large grain sensor: grain diameter $d \equiv x_g \gg$ charge depletion layer x_c (see text). qV_s1 is surface potential barrier for electron (q) transfer in a system of large grain with adsorbed O^--centres, qV_s2 is such potential barrier in the presence of reducing gas reacting with O^--centres. b) Small grain sensor: $d \equiv x_g \leq x_c$ (see text). Ec1 and Ec2 - positions of conduction band with adsorbed O^- centres in the absence and in the presence of reducing gas, respectively.

nanoparticles having $d \leq x_c$ the maximal degree of ionization O_{ad} and the maximal value S_c are achieved at given specific (related to unit of a cluster volume) concentration $(O_{ad})_{sp}$. Further increase S_c at reduction d is caused by the growth of $(O_{ad})_{sp}$ due to increase in the specific surface of a nanoparticle cluster [99].

In films considered sensoring effects arise owing to change of carrier (in this case, electron) concentration in a cluster of contacting SC nanoparticles, which penetrates all film and provides the passage of a current.

Lam Research Ex. 1035 - Page 562
Lam Research Corp. v. Inpria Corp.
IPR2024-00033 - U.S. Patent No. 9,823,564

Conductometric sensoring effects of other sort have been found out in the composite PPX films with rather low contents of M/SC nanoparticles, where conductivity, as has been shown above (Subsection 4.1), is determined by processes of tunnel electron transfer between the particles. PPX film containing Pd nanocrystals demonstrates sensor response on low hydrogen pressures at ambient temperature [91]. The electrical resistance of the film increases under influence of hydrogen presumably because of dissociative adsorption of hydrogen molecules on Pd nanocrystals that leads to the rise of the electron work function for these nanocrystals [100] and correspondingly to the increase of barrier to the tunnel electron transfers between nanocrystals. After removal of hydrogen the film resistance returns to its initial value within 30–60 sec [91] so that such films can be used as a reversible sensor on hydrogen.

It should be noted that the influence of hydrogen on the resistance of Pd–PPX films depends on voltage. The tunnel conductivity of initial film in the absence of hydrogen has the linear IVR but under action of hydrogen this relationship gets strongly nonlinear character and follows the low $\ln I \sim U^{1/2}$ (see above). Hydrogen penetrating in the film disrupts the ways of tunnel current of initial film. At the same time, it is known that the absorption of hydrogen by Pd particles leads to a distortion of Pd lattice and can give essential surface roughness of particles. As was pointed out above, in this case electric field between nanoparticles can rise very strongly exceeding on some orders average intensity of a field in the film. This leads to an increase of the field effect on the tunnel conductivity and to the appearance of new ways for tunnel current. Therefore, the fall of conductivity under action of hydrogen is replaced by increase in conductivity already at rather low voltages [91].

Composite PPX–PbO films produced by PVD cryochemical synthesis are sensitive sensors on humidity. The conductivity of the PPX film containing ~10 vol.% of PbO nanoparticles sharply increases with the rise of air humidity. The influence of water vapors on the film conductivity is reversible: at replacement of humid air on dry one the conductivity comes back quickly to an initial value for dry air and direct and reverse response times are ~10–15 sec [89].

The IVR at various values of air humidity testifies to the tunneling mechanism of the conductivity [89]. It is believed that the adsorption of water, most probably as a dimer complexes $(H_2O)_2$ typical for water vapors, on the boundary between semiconductor PbO and PPX matrix gives localized positively charged states such as $H_3O^+ \cdots H_2O$ in the intervals between PbO particles that favors the interparticle electron transfer. Similar effects are considered in work [101]. Such process results in substantial increase of conductivity provided that water complexes fill if not all but the

Lam Research Ex. 1035 - Page 563
Lam Research Corp. v. Inpria Corp.
IPR2024-00033 - U.S. Patent No. 9,823,564

majority of intervals between PbO nanoparticles in percolation cluster. It becomes possible because such PbO cluster, as it has been marked above, is located in extended defects of a polymeric matrix where the water molecules penetrating into polymer are also localized near to PbO nanoparticles of cluster.

It should be noted that the given sensor is much more sensitive than a sensor based on composite films CuS–polyvinyl alcohol prepared by a classical liquid-phase method [88]. In these films the sensor effect is caused by increase in probability of tunnel transitions between CuS semiconducting particles owing to increase in macroscopical dielectric permeability of a hydrophilic matrix absorbing water from the surrounding atmosphere [88].

PPX films containing PbO nanocrystals also show increase in their conductivity under action of small quantities of ammonia and ethanol vapors from gaseous environment [89, 102, 103]. This effect takes place in the presence of water vapors only and so, most probably, is due to the formation of ionized or highly polarized molecular complexes $NH_3 \cdots H_2O$ and $C_2H_5OH \cdots H_2O$. The responses of conductivity to ammonia and ethanol are also reversible: the film conductivity returns to its initial value after the removal of these substances from the surrounding atmosphere.

The sensor effect for ammonia is especially strong and is revealed even in the films containing ~5 vol.% PbO. At the same time the appreciable increase in conductivity of composite films under action of ethanol vapors is appeared at PbO content ~15 vol.% [103]. It is believed that the influence of H_2O, NH_3, and C_2H_5OH on tunnel electron transfer between PbO particles depends on potential and radius of action of the intermediate positively charged centers formed by the molecules of these substances penetrating in interspaces of polymer matrix between these particles. Apparently, NH_4^+ centers arising from dissociation of $NH_3 \cdots H_2O$ adsorbed on PbO exert the most influence on electron tunneling even at long distances whereas the introduction of C_2H_5OH gives effect only at small distance between particles PbO in the films with the high contents of PbO particles.

4.3. Dielectric Properties

Films of pure PPX and PPX composites with nanoparticles of various metals resulted from cryochemical solid-state synthesis were studied by the dielectric spectroscopy method [104]. Dielectric spectroscopy has proven very useful for studying the structure and dynamics of polymer materials as well as the transport mechanism of charge carriers. To study features of the polymer structure dielectric test methods were used due to their high sensitivity to morphological changes.

Lam Research Ex. 1035 - Page 564
Lam Research Corp. v. Inpria Corp.
IPR2024-00033 - U.S. Patent No. 9,823,564

In the temperature interval of −70 to 0°C and in the low-frequency range, an unexpected dielectric relaxation process for polymers is detected. This process is observed clearly in the sample PPX with metal Cu nanoparticles. In sample PPX + Zn only traces of this process can be observed, and in the PPX + PbS as well as in pure PPX matrix the process completely vanishes. The amplitude of this process essentially decreases, when the frequency increases, and the maximum of dielectric losses have almost no temperature dependence [104]. This is a typical dielectric response for percolation behavior [105]. This process may relate to electron transfer between the metal nanoparticles through the polymer matrix. Data on electrical conductivity of metal containing PPX films (see above) show that at metal concentrations higher than 5 vol.% there is an essential probability for electron transfer from one particle to another and thus such particles become involved in the percolation process. The minor appearance of this peak in PPX + Zn can be explained by oxidation of Zn nanoparticles.

Based on conceptions of work [105] the specific dielectric relaxation in PPX with M nanoparticles is supposed to be connected with reorientation of dipoles in polymer environment of M nanoparticles that accompanies the electron transfer between M nanoparticles of percolation cluster. Dipole centers in PPX are *cis*-units of polymer chains on a surface of lamellar PPX crystallites. Such centers are characteristic, in particular, for extended polymer defects (dislocations, grain boundaries, interfaces between amorphous and crystalline areas) where, most probably, M nanoparticles are formed.

The simplest illustrative model considers a percolation cluster as a straight line of M nanoparticles adsorbed on a polymer surface. The localization of electron charge on a nanoparticle initiates local reorganization of dipoles near to a charged particle with a rate constant $\sim 1/\tau_1$, where τ_1 is the mean characteristic time of this rearrangement for dipoles on polymer surface close to adsorbed particle. After a particle loses electron as a result of its transfer on neighboring particle of cluster, dipoles in an environment of discharged particle comes back in an initial completely unordered state with a rate constant $\sim 1/\tau_2$, where τ_2 is, correspondingly, the characteristic time of reverse rearrangement. The residence time for electron on a particle of cluster is determined by characteristic time τ_t of the tunnel electron transfer between neighboring particles in cluster. It should be noted that the elementary act of tunnel electron transfer proceeds in a time of order 10^{-14} sec, and $\tau_t \sim 1/P_t$, where P_t is a probability of electron transfer in unit of time.

If total number of dipoles μ surrounded M nanoparticle is equal to C, the number of dipoles C_{dt} oriented toward particle in a time τ_t after localization of electron on a particle can be, in the first approximation, presented as $C_{dt} = C[1 - \exp(-\tau_t/\tau_1)]$. According to the proposed model this rearrangement of molecular dipoles creates in a nearest environment of particle dipole

Lam Research Ex. 1035 - Page 565
Lam Research Corp. v. Inpria Corp.
IPR2024-00033 - U.S. Patent No. 9,823,564

moment $M_1 = m\mu C_{dt}$, directed perpendicular to polymer surface. Here m is coefficient, which depends on a distribution of dipoles on polymer surface. Reduction of number C_d of oriented dipoles as a result of a relaxation after leaving of electron from particle presumably can be described for the first particle of cluster as $C_{d1} = C_{dt} \exp[-(t-\tau_t)/\tau_2]$, because relaxation begins after the time interval τ_t. Correspondingly for the second particle $C_{d2} = C_{dt} \exp[-(t-2\tau_t)/\tau_2]$ and for jth particle $C_{dj} = C_{dt} \exp[-(t-j\tau_t)/\tau_2]$. Taking into account that $t = N\tau_t$, summation over j from 1 to N gives the total number of oriented dipoles $(C_{dt})_{tot}$ after tunnel electron transport lengthways of cluster from N nanoparticles

$$(C_d)_{tot} = C_{dt} \frac{1 - \exp(-N\tau_t/\tau_2)}{1 - \exp(-\tau_t/t_2)}.$$

Assuming that coefficient m is the same for all M particles of cluster the total dipole moment M in cluster is

$$M = \frac{m\mu C[1 - \exp(-\tau_t/\tau_1)][1 - \exp(-N\tau_t/\tau_2)]}{1 - \exp(-\tau_t/\tau_2)}. \tag{14}$$

If $\tau_1 >> \tau_t$, the rearrangement of dipoles is "frozen" and M is close to zero. In the opposite case, when the relaxation rate is very high and $\tau_2 << \tau_t$, the value $M = m\mu C_{dt}$. It can be supposed that $\tau_1 << \tau_2$ because ion–dipole interaction of charged particle with environment can accelerate reorganization of environment around such particle. It should be taken into account that structural element that participates in a rearrangement of polymer surface near to charged particle is, most probably, not a single *cis*-unit of PPX chain but a group of units such as fold on PPX surface. In this case μ is the dipole of such group and can be much more than that of single unit.

If $\tau_1 \sim \tau_t$ and $\tau_2 >> \tau_1$ and τ_t, the transport of electron lengthways of percolation cluster of M particles leads to a correlated rearrangement of dipoles so that M considerably increases. The intensity of dielectric losses is proportional to M, which in the considered model rises with increasing N as is shown in Eq. (14) up to a limiting value

$$M_{lim} = \frac{m\mu C[1 - \exp(-\tau_t/\tau_1)]}{1 - \exp(-\tau_t/\tau_2)}.$$

Because the time of electron transit over a cluster from N particles is $t_N = N\tau_t$ it is easy to understand that in this model intensity of losses grows with reduction of a field frequency ν down to value $\nu_{lim} \sim 1/2\tau_2$ and then remains constant. The temperature range for these dielectric losses is determined by a relationship between τ_1, τ_2, and τ_t and does not depend on a frequency of the electromagnetic field that is in accordance with experimental data.

Lam Research Ex. 1035 - Page 566
Lam Research Corp. v. Inpria Corp.
IPR2024-00033 - U.S. Patent No. 9,823,564

The considered model of a straight line of M nanoparticles illustrates only general features of dielectric losses caused by an M nanoparticle cluster in polymer matrix. Actually such cluster is a complex fractal system. Analysis of dielectric relaxation parameters of this process allowed the determination of fractal properties of the percolation cluster [104]. The dielectric response for this process in the time domain can be described by the Kohlrausch–Williams–Watts (KWW) expression

$$\Psi\left(\frac{t}{\tau}\right) \sim \exp\left[\left(\frac{t}{\tau}\right)^{\nu}\right],$$

where Ψ is the dipole correlation function, τ the average relaxation time, and ν the stretched parameter, $0 < \nu \leq 1$. It was shown [107] that in complex fractal systems, for the relaxation caused by the charge transfer along the ramified path, the stretched parameter ν could be related to the fractal dimension D_f of the percolation cluster, $\nu = D_f/3$.

For the sample PPX + Cu the calculated fractal dimension D_f is equal to 2.609 [104]. It should be noted that the above-mentioned size distribution of metal nanoparticles leads to the mutual charging of such particles in the percolation cluster. This effect is discussed in the Section 4.4 in connection with catalysis by nanoparticles. As is stated in Ref. [70], the specific low-temperature peak of dielectric losses in the synthesized composite samples PPX + Cu can probably be due to the interaction of electromagnetic field with mutually charged Cu nanoparticles immobilized in the PPX matrix. It should be noted that the mutual charging of M nanoparticles caused by a size distribution of particles is not static: electron tunneling between nanoparticles lead to a migration of charges in a system because difference in Fermi energy for particles which differ little in size $\leq kT$.

The high-temperature relaxation process is typical for amorphous polymers and can be assigned to the α-relaxation that appears in the whole frequency range and in the temperature interval from 50 to 100°C. This process is well observed for all samples. It corresponds to the glass–rubber transition of the amorphous phase.

The peak of the dielectric loss of this process reflects its viscoelastic nature by obeying the time–temperature superposition principle, wherein the peak is shifted to higher temperatures for shorter times (higher frequencies) and vice versa. This process has been described by the Havriliak–Negami empirical formula [106, 108]

$$\varepsilon^*(\omega) \sim \frac{\Delta\varepsilon}{[1 + (i\omega\tau')^{\alpha}]^{\beta}}.$$

Here, $\Delta\varepsilon$ is the dielectric strength and τ the mean relaxation time. The parameters α and β describe the symmetric and asymmetric broadening of

Lam Research Ex. 1035 - Page 567
Lam Research Corp. v. Inpria Corp.
IPR2024-00033 - U.S. Patent No. 9,823,564

the relaxation process. The temperature dependencies of the relaxation times of the observed α relaxation process for pure PPX, PPX + Cu, and PPX + Zn samples demonstrate an Arrhenius behavior with the energies of activation 196, 187, and 201 kJ/mol, respectively, and correlate with the activation energies of the α process in most known polymer materials.

Along with metal–polymer films, nanocomposites from the boron-silicate porous glass containing 4–6 wt.% of Pd recently have been investigated as well [109]. These nanocomposites have been characterized by electron microscopy and X-ray diffraction. Microelectronic photos of nanocomposite samples have shown pores with diameters $\sim$30 nm. According to data of small-angle X-ray diffraction the mean diameter of Pd particles is $\sim$30 nm that coincides with diameters of glass pores.

Real and imaginary parts of dielectric permittivity of nanocomposites have been measured in dependence on temperature and frequency of electromagnetic field for temperatures from -120 to 300°C and in the frequency range from 0.1 to 10^5 Hz. Comparison of dielectric spectra of Pd containing nanocomposite with similar spectra of porous glass without Pd nanoparticles has shown specific dielectric losses related to metal nanoparticles in glass matrix [110]. It should be noted that in this system, unlike metal–PPX composites, effect of metal nanoparticles on dielectric properties of nanocomposite reveals at low metal contents. To elucidate the nature of these dielectric losses and the mechanism of the electron transport in a composite with metal nanoparticles, the theory of dielectric permittivity has been developed for a system of metal nanoparticles embedded in dielectric matrix containing electron traps. Such traps are characteristic for inorganic glasses from metal oxides or metal salts.

It is supposed that a medium contains a great number of traps, a small part from which is filled by electrons as a result of electron transfer from metal nanoparticles to traps. The energy levels of electrons in such traps lie below the conduction band of medium but above Fermi level of metal nanoparticle. The theory considers interaction of electrons with charged and neutral nanoparticles. The function for electron distribution in medium has been determined with the low-frequency electromagnetic field present. This allowed obtaining expressions for real and imaginary parts of dielectric permittivity. On this stage the conducted theoretical treatment reproduces qualitatively features of dielectric spectra of metal containing nanocomposites in inorganic glass matrix.

4.4. Catalytic Activity

The study of atomic clusters in a gas phase have shown that high-specific catalytic activity is characteristic for ''quantum'' clusters, containing less

Lam Research Ex. 1035 - Page 568
Lam Research Corp. v. Inpria Corp.
IPR2024-00033 - U.S. Patent No. 9,823,564

than 20–30 metal atoms, while clusters having the greater size behave as usual metal catalysts [111]. In Ref. [112], it was revealed that the chemisorption of benzene occurs at Rh clusters containing no more than 18 atoms whereas for particles of the greater size there is only physical benzene adsorption as on the surface of bulk metal. Surface of small clusters with discrete electronic levels is characterized by broken or deformed quasi-chemical bonds, which are essentially more localized and, hence, more active in comparison with bonds located on a surface of bulk metal.

Thus, the size effects for catalytic reactions of metal atom clusters in a gas phase are manifested only in very small, essentially "quantum" clusters, which are in essence nonmetal particles. Another situation takes place in films, containing a set of nanoparticles immobilized at a surface or inside of a dielectric matrix. In this case the influence of M nanoparticle size on catalytic activity and structure of products formed is observed for considerably larger already "classical" particles of sizes from 2 ($\sim$150 atoms) to 20–30 nm ($\sim 10^5$ atoms) [113, 114]. It is necessary to note that catalytic properties of M nanoparticles in composite systems are determined substantially by their interaction with a matrix, which depends on the size of particles.

The main reaction product of tetrachloroethylene hydrogenation catalyzed by Pd particles of average size 20–40 nm immobilized on the oxide substrate is thichloroethylene. At the same time, catalytic reaction with the use of black palladium deposited on the same substrate gives mainly the saturated compounds [113]. It has also been established that Pd particles of sizes $\sim$2.5 nm deposited on Al_2O_3 catalyze the dissociation of CO whereas the larger particles in the size $\sim$27 nm as well as a continuous film of metal Pd are inactive in this process [115].

The size effect in reactions catalyzed by nanoparticles of platinum metals (Pd, Pt, and Rh) deposited on a surface of oxide substrates is associated with interaction between these particles and substrates. The cycle opening hydrogenation of methylcyclopentane under action of Pt nanoparticles deposited on Al_2O_3 [114] is an example of such effect. It has been shown that decrease in the size of particles from 10 to 2 nm leads to the reduction of a ratio between branched (the sum 2-methyl- and 3-methylpentane) and linear hydrocarbons (*n*-hexane) in the reaction products down almost 1, i.e., the reaction loses a selectivity. The specificity of reaction in this system is a partial transfer of electrons from M nanoparticles to an oxide substrate. As a result of this transfer areas of the particles adjoining to a substrate surface acquire a positive charge [114]. At the same time reaction on the charged centers of metal, unlike reaction on not charged metal, is not selective. A decrease of the particle size results in increase of contact area between particles and substrate surface that leads to corresponding rise of the relative

Lam Research Ex. 1035 - Page 569
Lam Research Corp. v. Inpria Corp.
IPR2024-00033 - U.S. Patent No. 9,823,564

contents of charged centers in the particles deposited on the Al_2O_3 surface. In turn, this reduces selectivity of catalytic reactions [114].

Influence of a charge on catalytic properties of M nanoparticles is the reason of the effects, which have been discovered in work [115] at the investigation of CO dissociation catalyzed by Pd nanoparticles in sizes 2.5 nm (see above). Such particles deposited by PVD method on thin film (1.6 nm) of Al_2O_3 lose completely catalytic activity, when this Al_2O_3-film with Pd nanoparticles is situated on a layer of metal Al. In this case there is only physical adsorption of CO on Pd [108]. It is possible to assume that reaction in this system is suppressed due to the tunnel electron transfer from Al to Pd nanoparticles through thin dielectric Al_2O_3 film, separating them from a layer of metal Al. Such process interferes the formation of the active positively charged centers on Pd nanoparticles [115].

The considered works concern systems where the substrate plays an active role in catalytic reactions with participation of M nanoparticles located on its surface. This role shows itself not only in modification of the catalytic properties of particles by a charge transfer between them and a substrate, but also in formation of triple complexes, in which the reacting molecule is connected both with a substrate and with an M nanoparticle [114]. Meanwhile, specific increased catalytic activity of M nanoparticles has been found out also in cryochemically synthesized nanocomposite PPX films, in which nonpolar polymer matrix only weakly interacts with M nanoparticles.

Catalytic isomerization of 3,4-dichlorobutene catalyzed by Pd nanoparticles of Pd–PPX film was studied at 100°C [91]. The ratio of *trans*- to *cis*-1, 4-dichlorobutene for the reaction in this system with low concentration of Pd nanoparticles is ~10, and coincides with the ratio obtained for the reaction with the usual palladium catalyst. But the selectivity of the reaction decreases with increasing of Pd concentration: the yield of *trans*-l,4-dichlorobutene decreases while the yield of *cis*-l,4-dichlorobutene remains constant. This result shows that the change in the catalytic properties of the composite is determined by interactions between nanoparticles rather than by the size effects. At catalytic reaction catalyzed by Pd–PPX films, where the volume content of Pd nanoparticles is close to percolation threshold, the *trans*-to-*cis* ratio for produced isomers of l,4-dichlorobutene is ~2.9 that is close to equilibrium value of this ratio.

Specific catalytic properties of synthesized Pd–PPX nanocomposites have been explained by the tunnel charge transfer between nanoparticles. As mentioned in Section 2, the energy of Fermi level of small metal particle depends on its size [14]. At the same time, M nanoparticles immobilized in PPX matrix have rather wide size distribution in the range 2–8 nm (Section 3). Electron transfer between particles of different size results in their mutual charging that leads to equalization of their electrochemical potentials [15].

Lam Research Ex. 1035 - Page 570
Lam Research Corp. v. Inpria Corp.
IPR2024-00033 - U.S. Patent No. 9,823,564

This process should greatly affect catalytic isomerization of 3,4-dichlorobutene: this reaction on positively charged Pd nanoparticles proceeds, most probably, via intermediate carbonium ions and gives the mixture of l,4-dichlorobutene isomers close to the equilibrium one [91].

Another example of specific catalytic action of nanocomposite film with M nanoparticles (Cu–PPX) is the reaction of the C–Cl bonds metathesis

$$CCl_4 + C_{10}H_{22} = CHCl_3 + C_{10}H_{21}Cl, \quad \text{(I)}$$

catalyzed by Cu nanoparticles in Cu–PPX films. This reaction was studied at 180°C in the mixture of *n*-decane with CCl_4 and molar ratio CCl_4/*n*-decane = 4:1 [116]. The values of specific catalytic activity (*Y*), which is defined as the number of molecules of chlorodecanes produced per one Cu atom of the nanocomposite film during 1 h of the reaction, are presented in the Table 10.3 along with the data on the electrical resistance (*R*) of the composite films.

At very small concentration of Cu (X_{Cu}) around 1 vol.%, *R* of composite film is close to that of pure PPX. In this case Cu nanoparticles in matrix are fully isolated and so do not practically interact with one another and do not influence the composite conductivity. The *Y* value for such Cu nanoparticles in PPX (Table 10.3) is very small. The sharp fall of *R* with increasing X_{Cu}, which is caused by the tunnel electron transfer between Cu nanoparticles, leads to the strong rise of *Y* for Cu–PPX composite films (Table 10.3). *Y* reaches the maximal value in the range 5–10 vol.% of Cu. Based on above presented considerations it may be suggested that in such composite the relative share (fraction/part) of Cu nanoparticles involved in tunnel electron transfer processes greatly increases due to formation of tunnel percolation clusters. But the further increase of X_{Cu} up to 14% gives rise to explosive aggregation of nanoparticles resulting in formation of isolated large-scale metal inclusions: this process accompanied by the substantial decrease of

Table 10.3. Dependence of conductivity and catalytic activity of nanocomposites Cu–PPX on Cu content

Content of Cu (vol.%)	Electrical resistance at 77 K (Ω)	Electrical resistance at 298 K (Ω)	Yield of chlorodecanes (mol.%)	Specific catalytic activity
1.3	∞	∞	Traces	Traces
3.5	7.0×10^8	3.5×10^8	4	130
5.0	10.2×10^3	8.3×10^3	15	500
7.0	3.3×10^3	645	20	650
10.3	66	29	35	1150
14	16.2×10^3	3.1×10^3	14	450

Lam Research Ex. 1035 - Page 571
Lam Research Corp. v. Inpria Corp.
IPR2024-00033 - U.S. Patent No. 9,823,564

number of metal nanoparticles and the corresponding rise of R results in the fall of Y (Table 10.3).

The maximal Y value for Cu–PPX catalyst is 1150 [116]. It is much more than the activity of all known catalysts of this reaction. For comparison, the same reaction of C–Cl bond metathesis was investigated on the special prepared catalyst containing 1 mass% of high-dispersed metallic Cu deposited on silica. In conditions analogous to those of the reaction with the nanocomposite Cu–PPX film, Y for this catalyst was 4. Moreover, it has low selectivity: in this case the formation of by-products from condensation processes takes place along with the main reaction, whereas Cu–PPX catalyst gives monochlorosubstituted decanes only [116].

The increase in catalytic activity with the rise of metal content can be explained by the mutual charging of Cu nanoparticles by tunnel electron transfer between particles of different size. Presumably, negative charged particles formed in this case, among positively charged ones, facilitate initiation of the chain reaction (I) via dissociation of CCl_4.

$$CCl_4 \rightarrow CCl_3 + Cl. \qquad \text{(II)}$$

Electron affinity E_a of molecule CCl_4 ($(E_a)_{CCl_4}$) is $\sim$2 eV. Therefore, the adsorption of this molecule on negatively charged Cu nanoparticle is accompanied by the capture of electron so that reaction (II) proceeds as

$$(CCl_4)^-_{ad} \rightarrow (CCl_3)_{ad} + (Cl)^-_{ad}, \qquad \text{(IIa)}$$

where the index "ad" designates an adsorbed particle. As a first approximation, if not to take into account adsorption bonds, it is possible to assume that amount of energy necessary for CCl_4 dissociation in reaction (IIa) is less than that in gas-phase reactions (II) on $\Delta E_a = (E_a)_{Cl} - (E_a)_{CCl_4}$, where $(E_a)_{Cl}$ is the electron affinity of Cl equal to 3.6 eV, i.e., ΔE_a is 1.6 eV. Consequently, one would expect the increase of the rate of CCl_4 dissociation, which is the initial act of the chain metathesis reaction (I).

The same dependence between concentration of M nanoparticles (N_s) on a surface of a dielectric substrate and their catalytic activity has been also found out in the investigation of an amorphous films of M nanoparticles [117], prepared by laser electrodispersion technique and deposited on SiO_2 dielectric surface layer of thermally oxidized Si (see Chapter 15). It has been shown that in various reactions of chlorinated hydrocarbons catalyzed by so prepared nanostructured Cu film with growth N_s the value of Y increases firstl, reaches a maximum at $N_s \sim 4 \times 10^{12}$ particles/cm^2, and then quickly falls.

Probably, in these reactions as well as in reaction under action of Cu–PPX film [116], catalytic activity increases due to appearance of negatively charged Cu nanoparticles formed by the tunnel transfer of electrons between

Lam Research Ex. 1035 - Page 572
Lam Research Corp. v. Inpria Corp.
IPR2024-00033 - U.S. Patent No. 9,823,564

particles of different size in the deposited film. It should be noted that the dependence of Y on N_s changes dramatically, when SiO_2 film, isolating Cu nanoparticles from Si, is such thin that makes possible a tunnel electron transfer between Cu nanoparticles and Si. In this case smooth reduction of Y is observed as N_s grows [117].

It is important also that at small N_s the value of Y in this case essentially exceeds Y for the reaction taking place on SiO_2 layer fully isolating Cu nanoparticles from Si [117]. It is possible to assume that tunnel electron transfer between Si substrate and Cu nanoparticles through thin SiO_2 film gives negatively charged Cu nanoparticles as $(E_a)_{Cu}$ is higher than $(E_a)_{Si}$. However, with increase of N_s the degree of the Cu film charging falls because of repulsion between negative charges located on nanoparticles.

5. Conclusions

The given review concerns the following problems:

(1) *Influence of the M/SC particle size on its electronic structure (so-called size- effect).* In classical *M*/SC particles, which determine the properties of PVD-produced composite films, this effect is caused by interaction of conductivity electrons with an interface between a particle and an environment. It results in occurrence of surface potentials and redistribution of electronic density in a particle.

(2) *Formation and structure of PVD-prepared composite films that consist of dielectric matrix containing M/SC nanoparticles.* Depending on conditions of PVD of M/SC on a substrate the M/SC nanoparticles are formed either by homogeneous condensation of substances in a gas phase with the subsequent deposition on a substrate or by aggregation of the atoms (molecules) adsorbed on a substrate surface (heterogeneous condensation). In case of heterogeneous condensation the structure of M/SC nanostructured film is caused by interaction between deposited substance and a substrate that allows influencing this structure, choosing a substrate with the account on the nature of a deposited substance.

At co-deposition of dielectric and M/SC the structure of a nanocomposite film depends on a relationship between the rate of formation of M/SC particles and the rate of making of a solid dielectric matrix. Models of such deposition are discussed. The special attention is paid to new low-temperature processes of nucleating and growth of nanoparticles in a solid polymeric matrix containing the inclusions of

Lam Research Ex. 1035 - Page 573
Lam Research Corp. v. Inpria Corp.
IPR2024-00033 - U.S. Patent No. 9,823,564

atoms and small clusters of M/SC. It is supposed that in this case the average size and size distribution of the nanoparticles are governed by deformations in the solid polymeric matrix connected with growth of M/SC particles.

(3) *Physical and chemical properties of PVD-produced composite films with M/SC nanoparticles including dark- and photo-induced conductivity, conductometric sensoring properties, dielectric characteristics, and catalytic activity*.

Experimental data relating to the conductivity of composite films with M/SC nanoparticles are described by the classical percolation model in terms of tunnel processes. Chemisorption of chemical compounds on the surface of M/SC nanoparticles in films and the subsequent reactions with participation of chemisorbed molecules change the concentration of conducting electrons and/or barriers for their tunnel transfer between the nanoparticles with the result of strong influence on the film conductivity. Such films are used as conductometric sensors for detecting various substances in an atmosphere.

The specific low-frequency dielectric losses are found out in composite films, containing M nanoparticles. It is assumed that these losses are caused by interaction of an electromagnetic field with the dipoles' reorientation in the environment connected with tunnel electrons 'transfer between the nanoparticles or traps of the environment.

The catalytic properties of M nanoparticles in composite films are considered in relation to charging of nanoparticles result from electron transfer between the particles and the environment, as well as from redistributions of electrons between the particles of various sizes. The last factor is the most probable reason for a sharp increase in catalytic activity of M nanoparticles and a change of direction of catalytic reactions induced by M nanoparticles with increasing of their concentration in a composite film.

The most perspective directions of investigation in the area of PVD-produced composite films with M/SC nanoparticles are the following ones:

- The investigation of the structure of PVD-prepared composite films depending on the nature of M/SC, properties of a dielectric matrix and the method of film deposition. Systematic researches in this area practically were not carried out early.
- Theoretical and experimental studying of the tunnel electrons' transfer in relation to the size distribution of nanoparticles in a film and to mutual charging of particles of various sizes.
- The investigation of adsorption and chemisorption of various substances on M/SC nanoparticles in PVD-prepared films

Lam Research Ex. 1035 - Page 574
Lam Research Corp. v. Inpria Corp.
IPR2024-00033 - U.S. Patent No. 9,823,564

depending on the nature and size of the nanoparticles and properties of a matrix as well. These processes underlie the catalytic and sensoring effects in films so such research is very important for understanding these effects.

- Elucidation of the mechanism of new low-frequency dielectric effects in PVD-prepared films with M nanoparticles by widespread investigations of these effects depending on the nature and concentration of nanoparticles embedded in matrices with different dielectric characteristics.

In summary, it is necessary to note that PVD-prepared composite films with M/SC nanoparticles are of great practical interest. These films are sensitive and selective conductometric sensors, suitable for detecting various substances in an atmosphere. Method PVD opens prospects for creation of new sensor composite films, containing M/SC nanoparticles of various electronic structures that can improve essentially performance characteristics of sensors. Besides in such systems one would expect substantial growth of photocatalytic activity of SC nanoparticles that is of interest for various applications, in particular, for photocatalytic decomposition of water [29]. The PVD method allows creating composite films with preset nonuniform distribution of electron donating and electrophilic SC nanoparticles in a dielectric matrix. In such way it is possible to produce nanostructured films having the valuable photovoltaic properties. Composite films containing M and SC nanoparticles demonstrate also marked nonlinear optic effects caused by surface plasmon resonance of M nanoparticles and specific two-photon absorption in SC nanoparticles [31].

To help readers in the fixation of this chapter material some questions are given below:

1. What is the correlation between the electron work function for spherical metal particle and its radius?
2. What is the dependence of the gap between the energy bands in semiconductor nanocrystals on its size?
3. What methods are used for evaporation and sputtering of substances to obtain nanocomposite films by PVD method?
4. What is the difference between the homogeneous and the heterogeneous formation of nanoparticles in the process of the film deposition from gaseous phase?
5. What is the dependence of the nucleation of metal particles on the polymer surface from the interaction energy of metal atoms with polymer?
6. What are the peculiarities of the M/SC nanoparticle formation at the co-deposition of M/SC and dielectrics in the process of PVD?

Lam Research Ex. 1035 - Page 575
Lam Research Corp. v. Inpria Corp.
IPR2024-00033 - U.S. Patent No. 9,823,564

7. What is the dependence of the mean size and the size distribution of M/SC nanoparticles on the concentration and nature of M/SC in the process of the solid-state low-temperature synthesis of polymer composite films by PVD method?
8. What is the sensor response on hydrogen for polymer films with palladium nanocrystals? What is the possible reason of this response?
9. How the catalytic activity of M nanoparticles depends on their concentration in composite film?

Acknowledgments

The authors would like to thank RFBR (project 06-08-00545) for financial support and Prof. Vladimir Gromov, Dr. Antonina Kozachenko, and Mrs. Raisa Eveleva for help in preparing the manuscript.

References

1. A. N. Shipway, E. Katz, I. Willner, Chem. Phys. Chem. **1** (2000) 18.
2. L. I. Trakhtenberg, G. N. Gerasimov, Metal-Containing Polymers: Cryochemical Synthesis, Structure and Physicochemical Properties, in: G. Carotenuto, L. Nicolais (Eds.), Metal/Polymer Nanocomposites, Wiley, New York, 2005, p. 37.
3. L. I. Trakhtenberg, G. N. Gerasimov, E. I. Grigoriev, Russ. J. Phys. Chem. **73** (1999) 209.
4. E. Shumacher, Chimia **42** (1988) 357.
5. A. P. Alivisatos, Science **271** (1996) 933.
6. Y. Wang, N. Herron, J. Phys. Chem. **95** (1991) 525.
7. U. Kreibig, Z. Phys. **B31** (1978) 39.
8. I. A. Misurkin, A. A. Ovchinnikov, Russ. Chem. Rev. **46** (1977) 1835.
9. A. Moliton, R. C. Hiorns, Polym. Int. **53** (2004) 1397.
10. J. K. Burdett, Proc. Solid State Chem. **15** (1984) 174.
11. K. Sattler, The Energy Gap of Clusters, Nanoparticles and Quantum Dots, in: H. S. Nalwa (Ed.), Handbook of Thin Films Materials, Academic Press, San Diego, CA, 2002, p. 62.
12. A. I. Frenkel, C. W. Hills, R. C. Nuzzo, J. Phys. Chem. **105** (2001) 12689.
13. S. Di Nardo, L. Lozzi, M. Passacantando, P. Picozzi, S. Santuchi, M. De Crescenzi, Surf. Sci. **307** (1994) 922.

Lam Research Ex. 1035 - Page 576
Lam Research Corp. v. Inpria Corp.
IPR2024-00033 - U.S. Patent No. 9,823,564

14. C. A. Wert, R. M. Thomson, Physics of Solids, McGraw-Hill Book Company, New York, 1964.
15. E. L. Nagaev, Sov. Phys. Uspekhi **162** (1992) 49.
16. P. Muivaney, Langmuir **12** (1996) 788.
17. U. Kreibig, Z. Phys. D: At. Mol. Clusters **3** (1986) 239.
18. L. Genzel, T. P. Martin, U. Kreibig, Z. Phys. **B21** (1975) 339.
19. B. N. J. Persson, Surf. Sci. **281** (1993) 153.
20. A. L. Efros, M. Rosen, Ann. Rev. Mater. Sci. **30** (2000) 475.
21. A. J. Heeger, S. Kivelson, W.-P. Su, Rev. Mod. Phys. **60** (1988) 782.
22. M. J. Dewar, J. Chem. Soc. (1952) 3544.
23. S. Abe, Excitonic Effects in the Linear and Nonlinear Optical Properties of Conjugated Polymers, in: N. S. Sariciftci (Ed.), Primary Photoexcitations in Conjugated Polymers, World Scientific, Singapore, 1997, p. 115.
24. D. Lu, G. Chen, W. A. Goddard III, J. Chem. Phys. **101** (1994) 4920.
25. M. J. S. Dewar, The Molecular Orbital Theory of Organic Chemistry, McGraw-Hill Book Company, New York, 1969.
26. M. Rohlfing, St. G. Louie, Phys. Rev. Lett. **82** (1999) 1959.
27. M. G. Bawendi, M. L. Steigerwald, L. E. Brus, Ann. Rev. Phys. Chem. **41** (1990) 477.
28. A. D. Pomogailo, A. S. Rozenberg, I. Ye. Uflyand, Nanoparticles of Metals in Polymers, Khimia, Moscow, 2000.
29. R. F. Khairutdinov, Russ. Chem. Rev. **67** (1998) 125.
30. Y. Wang, A. Suna, J. McHugh, E. F. Hilinski, P. A. Lucas, R. D. Johnson, J. Chem. Phys. **92** (1990) 6927.
31. G. Banfi, V. Degiorgio, D. Ricard, Adv. Phys. **47** (1998) 447.
32. M. Moskovits and G. A. Ozin (Eds.), Cryochemistry, Wiley, New York, 1976.
33. M. T. Swihart, Curr. Opin. Colloid Interface Sci. **8** (2003) 127.
34. Y. Nakata, J. Muramoto, T. Okada, M. Maeda, J. Appl. Phys. **91** (2002) 1640.
35. A. Harano, K. Shimada, T. Okubo, M. Sadakata, J. Nanopart. Res. **4** (2002) 215.
36. E. Kay, Zeit. Phys. D: At. Mol. Clusters **3** (1986) 251.
37. M. P. Andrews, G. A. Ozin, J. Phys. Chem. **90** (1986) 2922.
38. F. K. Urban III, A. Hosseini-Tehrani, P. Griffiths, A. Khabari, Y. -W. Kim, I. J. Petrov, J. Vac. Sci. Technol. **B20** (2002) 995.
39. G. M. Chow, C. L. Chien, A. S. Edelstein, J. Mater. Res. **6** (1991) 8.
40. C. N. R. Rao, V. Vijayakrishnan, H. N. Aiyer, G. U. Kulkarni, G. N. Subbanna, J. Phys. Chem. **97** (1993) 11157.

Lam Research Ex. 1035 - Page 577
Lam Research Corp. v. Inpria Corp.
IPR2024-00033 - U.S. Patent No. 9,823,564

41. P. Ayub, R. Chandra, P. Taneja, A. K. Sharma, R. Pinto, Appl. Phys. A **73** (2001) 67.
42. J. A. Venables, Surf. Sci. **299/300** (1994) 798.
43. J. A. Venables, G. D. T. Spiller, M. Hanbűcken, Rep. Prog. Phys. **47** (1984) 399.
44. V. Zaporojtchenko, K. Behnke, A. Thran, T. Strunskus, F. Faupel, Appl. Surf. Sci. **144–145** (1999) 335.
45. J. A. Blackman, Physica A **220** (1995) 85.
46. P. Moriarty, Rep. Prog. Phys. **64** (2001) 297.
47. A. Galdikas, Thin Solid Films **418** (2002) 112.
48. S. Xu, B. L. Evans, D. I. Flynn, C. En, Thin Solid Films **238** (1994) 54.
49. S. Muzard, C. Templier, J. Delafond, J. C. Girard, D. Thiaudiere, L. Pranevicius, A. Galdikas, Surf. Coat. Technol. **100–101** (1998) 98.
50. G. Jasinskas, A. Galdikas, Mater. Sci. (Medžiagotyra) **10** (2004) 211.
51. H. Song, O. J. Ilegbusi, L. I. Trakhtenberg, Thin Solid Films **476** (2005) 190.
52. V. Zaporojtchenko, T. Strunskus, K. Behnke, C. V. Bechtolsheim, A. Thran, F. Faupel, Microelectron. Eng. **50** (2000) 465.
53. V. Zaporojtchenko, J. Zekonyte, A. Biswas, F. Faupel, Surf. Sci. **532–535** (2003) 300.
54. D. Babonneau, S. Camelio, T. Girardeau, M. Jaouen, O. Lyon, J. Appl. Cryst. **36** (2003) 430.
55. D. Babonneau, F. Petroff, J.-L. Maurice, F. Fettar, A. Vaure's, A. Naudon, Appl. Phys. Lett. **76** (2000) 2892.
56. T.-M. John, P. Veit, R. Anton, T. P. Drüsedeau, Thin Solid Films **296** (1997) 69.
57. F. Family, M. Popescu, J. G. Amar, Physica A **306** (2002) 129.
58. L. I. Trakhtenberg, A. B. Rabinovich, V. A. Kaminskii, G. N. Gerasimov, Chem. Phys. Rep. **21** (2002) 69.
59. M. C. Bartelt, A. K. Schmid, J. W. Evans, R. Q. Hwang, Phys. Rev. Lett. **81** (1998) 1901.
60. F. Fettar, J.-L. Maurice, F. Petroff, L. F. Schelp, A. Vaurès, A. Fert, Thin Solid Films **319** (1998) 120.
61. O. Lublinskaya, S. Gurevich, A. Ekimov, I. Kudryavtsev, A. Osinskii, M. Gandais, Y. Wang, J. Cryst. Growth **184/185** (1998) 360.
62. N. Cioffi, I. Losito, L. Torsi, I. Farella, A. Valentini, L. Sabbatini, P. G. Zambonin, T. Bleve-Zacheo, Chem. Mater. **14** (2002) 804.
63. N. Cioffi, I. Farella, L. Torsi, A. Valentini, A. Tafuri, Sensor. Actuat. **B84** (2002) 49.
64. H. Takele, U. Schürmann, H. Greve, D. Paretkar, V. Zaporojtchenko, F. Faupel, Eur. Phys. J. Appl. Phys. **33** (2006) 83.

Lam Research Ex. 1035 - Page 578
Lam Research Corp. v. Inpria Corp.
IPR2024-00033 - U.S. Patent No. 9,823,564

65. J. Perrin, B. Despax, E. Kay, Phys. Rev. **B32** (1985) 719.
66. G. N. Gerasimov, S. M. Dolotov, A. D. Abkin, Radiat. Phys. Chem. **15** (1980) 405.
67. G. N. Gerasimov, A. D. Abkin, Chem. Phys. Rep. **3** (1984) 170.
68. E. S. Mansueto, Ch. A. Wight, J. Am. Chem. Soc. **111** (1989) 1900.
69. L. M. Alexandrova, L. V. Shundina, G. N. Gerasimov, I. Ye. Kardash, Polym. Sci. (Russia) **35** (1993) 361.
70. L. Alexandrova, R. Vera-Graziano, Poly-*p*-Xylylenes, in: J. C. Salamone (Ed.), Polymeric Materials Encyclopedia, CRC Press, Boca Raton, FL, 1996, p. 7180.
71. E. V. Nikolaeva, S. A. Ozerin, A. E. Grigor'ev, E. I. Grigor'ev, S. N. Chvalun, G. N. Gerasimov, L. I. Trakhtenberg, Mater. Sci. Eng. **C8–9** (1999) 217.
72. G. Treiber, K. Boehlke, F. Weits, B. Wunderlich, J. Polym. Sci., Polym. Phys. Ed. **11** (1973) 1111.
73. G. N. Gerasimov, V. A. Sochilin, S. N. Chvalun, L. V. Volkova, I. Ye. Kardash, Macromol. Chem. Phys. **197** (1996) 1387.
74. G. Sergeev, V. Zagorsky, M. Petrukhina, J. Mater. Chem. **5** (1995) 31.
75. L. Alexandrova, E. Sansores, E. Martinez, E. Rodrigez, G. Gerasimov, Polymer **42** (2001) 273.
76. L. I. Trakhtenberg, G. N. Gerasimov, L. N. Aleksandrova, V. K. Potapov, Radiat. Phys. Chem. **65** (2002) 479.
77. M. P. Andrews, G. A. Ozin, Chem. Mater. **1** (1989) 174.
78. K. P. Charle, F. Frank, W. Schulze, Ber. Bunsenges. Phys. Chem. **88** (1984) 350.
79. M. P. Andrews, G. A. Ozin, J. Phys. Chem. **90** (1986) 2922.
80. G. N. Gerasimov, E. V. Nikolaeva, E. I. Smirnova, V. A. Sochilin, L. I. Trakhtenberg, Dokl. Phys. Chem. **380** (2001) 184.
81. C. Carotenuto, G. P. Pepe, L. Nicolais, Eur. Phys. J. **B16** (2000) 11.
82. U. Kreibig, C. V. Fragstein, Z. Phys. **224** (1969) 307.
83. L. Genzel, T. P. Martin, U. Kreibig, Z. Phys. **B21** (1975) 339.
84. P. Apell, A. Ljungbert, Solid State Commun. **44** (1982) 1367.
85. G. B. Bushueva, V. V. Zagorskii, G. M. Zinenkova, M. A. Petrukhina, O. V. Revokatov, G. B. Sergeev, Russ. Phys. Bull. **61** (1997) 1871.
86. S. A. Ozerin, M. D. Thesis, Moscow Physical Technical Institute, Moscow, 1999.
87. L. I. Trakhtenberg, Yu. F. Krupyanskii, G. N. Gerasimov, Chem. Phys. Reports **26** (2007), in press.
88. D. Yu. Godovski, Adv. Polymer Sci. **119** (1995) 81–122.
89. G. N. Gerasimov, E. I. Grigoriev, A. E. Grigoriev, P. S. Vorontsov, S. A. Zavialov, L. I. Trakhtenberg, Chem. Phys. Rep. **17** (1998) 1247.

Lam Research Ex. 1035 - Page 579
Lam Research Corp. v. Inpria Corp.
IPR2024-00033 - U.S. Patent No. 9,823,564

90. J. G. Simmons, J. Appl. Phys. **35** (1964) 2472.
91. P. S. Vorontsov, E. N. Golubeva, E. I. Grigor'ev, S. A. Zavyalov, L. M. Zavyalova, L. I. Trakhtenberg, Russ. J. Phys. Chem. **72** (1998) 1912.
92. D. Kohl, J. Phys. D: Appl. Phys. **34** (2001) R125–R149.
93. M. E. Franke, T. J. Koplin, U. Simon, Small **2** (2006) 36.
94. K. D. Schierbaum, U. Weimer, W. Göpel, R. Kowalkowski, Sensor. Actuat. **B3** (1991) 205.
95. W. Göpel, K. D. Schierbaum, Sensor. Actuat. **B26–27** (1995) 1.
96. V. Brynzari, G. Korotchenkov, S. Dmitriev, Sensor. Actuat. **B61** (1999) 143.
97. G. Bläser, T. Rühl, C. Diehl, M. Ulrich, D. Kohl, Physica. **A266** (1999) 218.
98. N. Barsan, U. Weimar, J. Electroceram. **7** (2001) 143.
99. G. -J. Li, X. -H. Zhang, S. Kawi, Sensor. Actuat. **B60** (1999) 64.
100. P. D. Cobden, B. E. Nieuwenhuyas, V. V. Gorodetskii, Appl. Catal. **A188** (1999) 69.
101. R. M. Hill, ERA Res. Rep. No. **5232** (1967) 1.
102. G. Sergeev, V. Zagorsky, M. Petrukhina, S. Zav'yalov, E. Grigor'ev, L. Trakhtenberg, Anal. Commun. **34** (1997) 113.
103. L. I. Trakhtenberg, E. Axelrod, G. N. Gerasimov, A. E. Grigoriev, E. I. Grigoriev, S. A. Zav'yalov, Yu. Feldman, Sci. Isr.: Technol. Adv. **1** (1999) 572.
104. L. I. Trakhtenberg, E. Axelrod, G. N. Gerasimov, E. V. Nikolaeva, E. I. Smirnova, J. Non-Cryst. Solids **305** (2002) 190.
105. Y. Feldman, A. Puzenko, Y. Ryabov, Chem. Phys. **284** (2002) 139–168.
106. Yu. Feldman, N. Kozlovich, I. Nir, N. Garti, Phys. Rev. **E51** (1995) 478.
107. A. Gutina, E. Axelrod, A. Puzenko, E. Rysiakiewicz-Pasek, N. Kozlovich, Yu. Feldman, J. Non-Cryst. Solids **302** (1998) 235.
108. Yu. Feldman, N. Kozlovich, Yu. Alexandrov, R. Nigmatullin, Ya. Ryabov, Phys. Rev. **E54** (1996) 5420.
109. L. Trakhtenberg, G. Gerasimov, E. Axelrod, Yu. Feldman, 3rd International Conference on Broadband Dielectric Spectroscopy and its Applications, BDS 2004, Delft, Netherland, August 23–26, 2004, p. 199.
110. A. Gutina, T. Antropova, E. Rysiakiewicz-Pasek, K. Virnik, Yu. Feldman, Microporous Mesoporous Mater **58** (2003) 237.
111. M. Boudart, J. Mol. Cat. **30** (1985) 27.

Lam Research Ex. 1035 - Page 580
Lam Research Corp. v. Inpria Corp.
IPR2024-00033 - U.S. Patent No. 9,823,564

112. C. Berg, M. Beyer, T. Scindler, G. Niedner-Shattenburg, V. E. Bondybey, J. Chem. Phys. **104** (1996) 7940.
113. G. A. Martin, Catal. Rev. Sci. **30** (1998) 519.
114. K. Hayek, R. Kramer, Z. Zaál, Appl. Catal. **A162** (1997) 1.
115. V. Johánek, I. Stará, N. Tsud, K. Veltruská, V. Matolìn, Appl. Surf. Sci. **162–163** (2000) 679.
116. L. I. Trakhtenberg, G. N. Gerasimov, E. I. Grigoriev, S. A. Zav'yalov, O. V. Zagorskaya, V. Yu. Zufman, V. V. Smirnov, Nanoheterogeneous Metal-Polymer Composites as a New Type of Effective and Selective Catalysts, in: A. Corma, F. V. Melo, S. Mondioroz, J. L. G. Fierro (Eds.), Studies in Surface Science and Catalysis, Elsevier, Amsterdam, 2000, p. 941.
117. T. N. Rostovshchikova, V. V. Smirnov, V. M. Kozhevin, D. A. Yavsin, M. A. Zabelin, I. N. Yassievich, S. A. Gurevich, Appl. Catal. **A296** (2005) 70.

Lam Research Ex. 1035 - Page 581
Lam Research Corp. v. Inpria Corp.
IPR2024-00033 - U.S. Patent No. 9,823,564

Chapter 11

Transport and Magnetic Properties of Nanogranular Metals

B.A. Aronzon, S.V. Kapelnitsky, and A.S. Lagutin

Russian Research Center, Kurchatov Institute, Moscow 123182, Russia

1. Introduction 582
2. Production of Nanocomposite Films 585
3. Structure of Granular Metals (Nanocomposites) 589
4. Magnetic Properties of Granular Magnetic Metals 595
   4.1. General Statements and Magnetization at Low Temperatures 597
   4.2. Magnetization at High Temperatures (Paramagnetic Region) 599
   4.3. Magnetization of Granular Ferromagnetic Metals with Non-Spherical Granules 601
   4.4. A Relaxation of Magnetization and Nanocomposite as Cluster Spin Glass . 604
5. Magnetotransport Properties of the Granular Metals 607
   5.1. Conductivity Dependence on a Metal Granules Fraction: The Percolation Threshold 608
   5.2. Temperature Dependence of Conductivity 612
   5.3. Magnetoresistance: Field Dependence of Conductivity 614
   5.4. Hall Effect 621
6. Quantum-Size Effects in Granular Metals Near the Percolation Threshold 627
7. Conclusions 631
8. Questions for Readers 632
References 633

Physical properties of solids containing metal granules of several nanometers, embedded into a dielectric matrix, are described in this chapter. The ion-beam sputtering (IBS), electron-beam sputtering (EBS) and magnetron sputtering (MS) with subsequent annealing are considered as main methods for such materials production. Magnetic, electrical and galvanomagnetic properties of nanogranular metals differ drastically from those of homogeneous materials. They are strongly dependent on metal volume fraction and show very peculiar features in the vicinity of the percolation threshold. The unique properties of nanogranular metals make them prospective candidates for a wide range of possible applications.

The magnetic properties are described as a function of magnetic grain sizes and shapes; different possible states such as ferromagnetic, superparamagnetic and cluster glass as well as transition between them are discussed.

THIN FILMS AND NANOSTRUCTURES, vol. 34
ISSN 1079-4050
DOI: 10.1016/S1079-4050(06)34011-2

© 2007 by Elsevier Inc.
All rights reserved.

Lam Research Ex. 1035 - Page 582
Lam Research Corp. v. Inpria Corp.
IPR2024-00033 - U.S. Patent No. 9,823,564

Special attention is paid to transport properties (resistance and Hall effect) because they are very sensitive to external parameters being the base for working mechanisms in many types of sensors and devices. The magnetic field and temperature dependences of resistance and Hall effect are considered in the framework of the percolation theory. Various types of magnetoresistances such as giant and anisotropic ones as well as their mechanisms are under discussion.

The influence of the various types of quantum effects and, in particular, of the quantum-size effect on the electronic transport in granular metals is described in the vicinity of the percolation transition.

1. Introduction

To find out how popular and actual the terms ''nanocomposite'' and ''granular materials'' are, it is enough to enter any of the Internet search sites and type these words. The quantity of the corresponding links will easily exceed a million, but one will be convinced soon that different investigators mean under these terms a huge set of diversified materials. It is assumed commonly that composite materials represent themselves as solids consisting of two or more substances with legible boundaries between its components. However, this definition appears to be too wide because it covers many absolutely different materials. This chapter is devoted to the description of properties of solids containing metal granules, embedded into a dielectric matrix. Mainly, electric and magnetic properties of the magnetic granulated metals will be discussed, in which metal granules are magnetic. Interest in these materials has been invoked in the 70th year after pioneer work of Abeles et al. [1]. The study of granular metals has experienced several peaks of activity, and nowadays is again extremely relevant and popular (see, for example, reviews [2–4] and books [5–11]).

A permanent interest in this class of artificial materials is caused by the fact that physical properties of such solids can be well controlled and varied in very wide limits by changing matrix and metal materials, as well as granular concentration and shape. In particular, it is possible to get a material with any preset conductivity in the range from a good metal to a good dielectric. Namely, electric properties of the granulated metals were the focus of investigations in the 70th year. Later the mainstream of researches was shifted to studying its optical properties and to the creation of coatings with largely varied dielectric and magnetic permeabilities. Special interest began to invoke in the 90th year of the study of magnetic properties of the granular metals (see, for example, the review [12]) due to the tendency

Lam Research Ex. 1035 - Page 583
Lam Research Corp. v. Inpria Corp.
IPR2024-00033 - U.S. Patent No. 9,823,564

of increasing the magnetic record density and the discovery of the giant magnetoresistance (GMR) effect [13]. The GMR effect appeared extremely promising for development of read heads of hard drives and elements of non-volatile memory such as magnetic random access memory (MRAM).

Interest in these materials is now increasing extraordinarily. In the first place, it is connected with technological advances (see, for example, [7–11]) and with the transition to very small granules, whose sizes are less than 100 nm.Secondly, it is caused by the demands of development of new information technologies and by the technological progress in general. These reasons on the threshold of a new millennium have led to a conclusion by the US Government Commission that prospects of nanotechnologies are brilliant. The decision is based on recommendations of the World Technology Evaluation Center. As a result, the US National Program for development of nanotechnologies has been accepted, which seems to be an initial push of the nanotechnological boom all over the world. It is really hard to imagine now our world without mobile phones, in which functions are extending regularly but their weight and dimensions are decreasing permanently, without microchips, including ones which could be implanted in a human body [14], and without microcomputers.

All of these require the creation of nanodimensional structures, which are the only ones that can provide the solution of goals to be sought and, in particular, can provide the required increment of the operation rates and the memory of computer systems keeping its geometrical sizes on the same level. Indeed, the record density on magnetic media is growing up at high speed: approximately 100% per year, within last two decades, but the basic restrictions of this huge growth have been outlined already. A simple reduction of the size of magnetic domains leads to a sharp increase of magnetic disorder and the influence of thermal fluctuations. In result, a reduction of magnetic memory reliability takes place, the quantity of read/write errors increases and the storage time of information falls down. This restriction can be overcome if one uses for recording the structured media consisting of magnetic nanoparticles with identical shapes and sizes. Each nanoparticle will be attributed to one bit of information. Some other obligatory conditions, which these particles should fulfill, are discussed in Section 4.

One could estimate the importance of development of nanotechnologies from the fact that next year after signing National Nanotechnological Initiative, the US Government allocated for this purpose 500 million dollars.

The terms ''nanoscience'' and ''nanotechnology'' are formed from the rather general concepts ''science'' and ''technology'' together with the prefix ''nano'', specifying the size of objects. One nanometer corresponds to

Lam Research Ex. 1035 - Page 584
Lam Research Corp. v. Inpria Corp.
IPR2024-00033 - U.S. Patent No. 9,823,564

1 millionth part of a millimeter or 10^{-9} m. Thus, when one is speaking about nanocomposites or about nanogranular metals, it means the material consisted of metal granules with sizes equal to several nanometers or less than 100 Å, as mentioned above.

The characteristic sizes of nanogranules already are approaching the atomic range, and the next stage of the substance fragmentation is a molecule or atom. It is impossible to determine the legible boundary between nanogranules and molecules in sense of the object size. A metal nanogranule with the reference size of 1 nm contains ~25 atoms while there are a lot of inorganic molecules containing many more atoms, and one does not tell about huge organic molecules. Some rather indistinct difference between nanogranules and molecules is possible to be defined in such a way: when one is speaking about nanogranules, it nevertheless means an object formed from relatively large number of identical atoms (from 10^2 up to 10^6).

The physical properties of nanogranules essentially differ from those of macroscopical pieces of the same substance, and the main difference is their dependence on the size of nanoparticle. The relative part of atoms, located on the surface of nanogranule, is very large and strongly depends on the grain size. The fraction of the surface atoms of a granule grows in inverse proportion to its linear size. This is clear from the fact that the granule volume is proportional to the cube of its size, while surface is its square function. When the size of the granule becomes comparable to the distance between granule atoms, practically all atoms become located on the granule surface. The surface atoms and those in the granule volume show quite different behavior and properties. The fact is that the surrounding and forces, as well as the energy bonds with other atoms, for these two cases are significantly different. If at least in one dimension the size of studied object becomes less than 100 nm, its properties, as a rule, become size-dependent.

Another distinguishing feature between properties of nanogranules and macroscopical grains is the quantum effects observed in nano-objects. Energy of electron in such granules quantizes similar to the quantization of the electron energy in atoms. To be more precise, the difference of energies between the electron levels becomes big enough and quantum effects begin to manifest in the temperature range where the experiment is carried out (for details see Section 6). The properties of nanocomposites depend on the granule size even more strongly than those of separate granules. Essential part of the nanocomposite volume is attributed to the inter-granular boundaries. As a result, along with common current in granules there is a chance for electron tunneling between the adjacent granules [5,15], for interference of electrons passing through different ways [5] and for mutual effects of electrical fields, created by some granules, on the energy levels of electrons in other granules (effects of the Coulomb's blockade, single

Lam Research Ex. 1035 - Page 585
Lam Research Corp. v. Inpria Corp.
IPR2024-00033 - U.S. Patent No. 9,823,564

electron transistor [5,7]). More comprehensively, these phenomena will be discussed in Section 6.

Possibilities of practical usage of nanogranular metal composites spread from already mentioned optical coatings and magnetic memory up to new areas of electronics and optoelectronics, including quantum computer, quantum dot[1] lasers, single electron transistor, quantum switches and many other devices, whose principles of work could be found in books dedicated to nanotechnology, for example in [7–11], sensors for gases (chemical sensors) and sensors for different physical values (temperature, pressure, magnetic field). But area of their possible use is so wide that this consideration requires special discussion, which is beyond the scope of this chapter.

2. Production of Nanocomposite Films

The studies of metal–dielectric nanocomposites and methods of their manufacture also have a long history (see review [1]). Recently, the technological progress has ensured the development of a wide collection of new methods and techniques suitable for production of nanoparticles and nanomaterials, including nanocomposites. It is possible to classify these methods as the following:

- crunching in various mills with subsequent pressing and/or sintering [7];
- chemical methods, which consist of coating of granules by ligands or inorganic molecules and forming the materials from granules covered by insulating material [16,17];
- implantation of granules into monomers with subsequent polymerization actively discussed in this book; oxidation by the tip of atomic force microscope [18–20];
- filling pores of various porous materials, such as zeolites, opals, porous silicon and aluminum, with metals or semiconductors or use of these materials as a mask for nanostructure preparation [21,22];
- radiative methods, such as implantation and selective removal of atoms [23,24];
- imprinting (printing by nanostructured die) [25];
- various lithographic methods: laser interference photolithography, ultraviolet photolithography and electronic lithography [26].

[1]Quantum dots are objects with sizes in all three directions equal to few nanometers. Such systems resemble molecules and the energy levels of electrons in them quantize. Energies of the transitions between these levels depend on quantum dots material and size, and those transitions are the base for the quantum dots laser radiation.

Lam Research Ex. 1035 - Page 586
Lam Research Corp. v. Inpria Corp.
IPR2024-00033 - U.S. Patent No. 9,823,564

Detailed description of all mentioned material processing tools can be found in special literature and handbooks[2] [7–11]. In this chapter, only the most popular method of composite production – the method of a material sputtering on a substrate [4,27] – will be discussed.

The most popular method of granular metal preparation is heating and sputtering of material from composed target, containing both components of a composite, or from two different targets. Typical grain size in materials prepared by this method is in the range from 3 to 100 nm.Dispersion of the granule size can be minimized down to a value less than 10% [28,29]. One can manage to form regular enough two-dimensional lattice of practically mono-dispersed granules [30–32] using the self-organizing methods (see, for example, [7]). Self-organization means the spontaneous formation of three-dimensional order in a system. It is widely used in different methods of nanotechnology to prepare regular structures. Self-organization is caused by the influence of the surface tension forces and different other interactions between granules (in particular, the Coulomb's interaction), but also between metal granules and a dielectric matrix.

The ion-beam sputtering (IBS), the electron-beam sputtering (EBS) and the magnetron sputtering (MS) are most popular methods for granular metal production [28], but one of the most universal method is IBS, indeed. Each of these methods has its own advantages and disadvantages [4], some of which are discussed below. Production of composite films by the IBS and EBS methods is based on knocking out atoms, molecules and ions from the target surface, made from depositing material or its components with the subsequent precipitation of material ions on the substrate surface. Control of ion beam is performed by means of voltage applied to elements of the IBS (EBS) facility. Typical scheme of the IBS facility is shown in Figure 11.1. Often an additional ion-beam source, not shown in this figure, is placed in the sputtering chamber with the aim to clean the substrate surface.

The ion beam is created by electric field in the ion gun (marked 3 in Figure 11.1) from plasma-forming gas atmosphere usually residual or added oxygen (usually argon is used). The degree of ionization of the plasma-forming gas increases in the presence of argon under the pressure $\sim 10^{-4}$ bar and decreases the pressure under which discharge becomes stable. Electric field draws out ions from plasma, creating current of the high-energy particles which fall on the target and pulverize it. Low operating pressure is provided by argon supply in the vicinity of anode. Mainly, neutral atoms flow out from target; the parts of ions and clusters are insignificant. The quantity of

[2]To get brief imagination about many of the shown methods, we recommend to see site http://isis.ku.dk/kurser/blob.aspx?feltid=7516.

Lam Research Ex. 1035 - Page 587
Lam Research Corp. v. Inpria Corp.
IPR2024-00033 - U.S. Patent No. 9,823,564

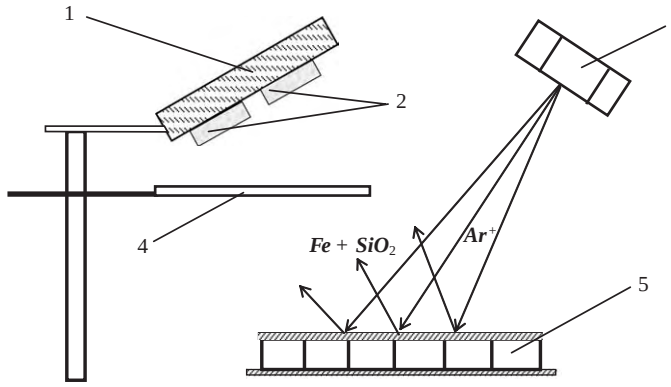


Fig. 11.1. The scheme of the setup for composite film deposition by ion-beam sputtering of the compound target: (1) substrate holder with heater; (2) substrate; (3) ion-beam source; (4) shutter.

atoms drawn out from target after impact with one ion is called the sputtering factor. Diverse materials have different sputtering factors that lead to metal concentration dependence on the target type at the prepared nanocomposite.

Parameters that allow to control the processes of film growth are as follows: the accelerating voltages, the plasma-forming gas pressure, discharge current, the distance from target to substrate, the speed of pumping out, the value of electric potential that is applied to target and substrate and temperature of substrate.

The main disadvantage of the IBS is the low speed deposition: no more than 200 Å per minute. This is ten times less than the deposition speed for the MS process. Another disadvantage is some etching of growing film by discharge ions and the capture of those ions by a film, which leads to imperfections in the nanocomposite film. Advantages of this method are as follows:

- High speed of cooling of the deposit material during the process of film formation, sufficient for the preparation of metal films in metastable or amorphous state (usually these states appeared when the kinetic energy of the depositing atoms was higher than 10 eV).
- Possibility for the preparation of multi-component alloys with concentrations of elements much higher than their equilibrium values. This is due to the fact that the film composition is mainly determined by the relative contents of components in the stream of sputtered atoms and by the adhesion factor, but is not defined by thermodynamic equilibrium.

Lam Research Ex. 1035 - Page 588
Lam Research Corp. v. Inpria Corp.
IPR2024-00033 - U.S. Patent No. 9,823,564

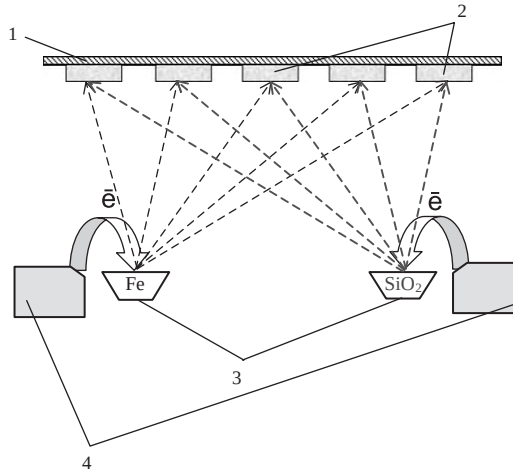


Fig. 11.2. The scheme of the setup for composite film preparation with separate sputtered targets and a multiple hearth electron-beam source: (1) substrate holder; (2) substrates; (3) water-cooled copper crucibles; (4) electron-beam guns.

- Versatility of process, which expresses itself in the possibility to sputter practically any material.

In some cases, the IBS installation shown in Figure 11.2 is used. Contrary to the scheme presented in Figure 11.1, this method uses sputtering with two ion-beam or electron-beam sources and two different targets. This modification of the IBS or EBS facility gives the possibility to get at once a set of samples with different metal contents, which permits to investigate the concentration dependences of nanocomposite properties. The additional advantages of this method (EBS) are the high deposition speed and the high purity of process.

For the granular nanocomposite processing, the non-wettabillity and insolubility of all its components is required, in order to avoid mixing of separate materials that compose the nanocomposite. In particular, one should avoid the mixing and solubility of granules and matrix materials. Just by fulfilling these conditions, metal atoms will collect themselves into granules during the deposition process.

Principal scheme of the MS facility is presented in Figure 11.3. The MS method differs from above-described IBS and EBS methods, in that the target of sputtering material is a cathode. In this case, the electrical discharge in crossed electric and magnetic fields is also used. Plasma is located in the vicinity of target that provides high density of the charged particle

Lam Research Ex. 1035 - Page 589
Lam Research Corp. v. Inpria Corp.
IPR2024-00033 - U.S. Patent No. 9,823,564

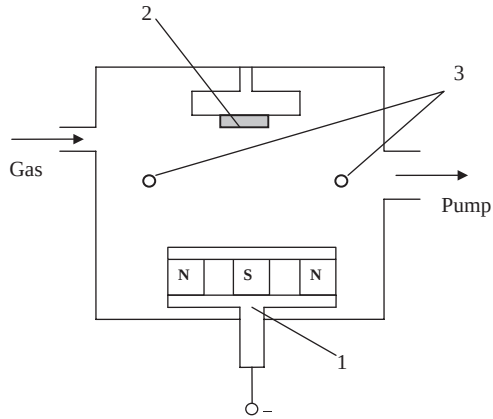


Fig. 11.3. The scheme of the magnetron sputtering setup: (1) cathode; (2) target; (3) anode.

current and high speed of material deposition. Selection and acceleration of ions of plasma along with the material sputtering is managed by application of high negative potential to cathode–target. Negative electrical offset voltage additionally provides the substrate cleaning.

The granule sizes, its forms and orientation are distributed widely enough in case of MS, but recently some papers appeared, where the methods of producing the mono-dispersed granules are described [29–32] (see also Chapter 15 of this handbook).

3. Structure of Granular Metals (Nanocomposites)

It is natural that physical properties of nanocomposites depend on their structure. It should be reminded that only granular metals, composed from granules of a metal, embedded into insulating matrix, will be discussed in this chapter. One can highlight the following structure parameters, which determine properties of these materials: size and shape of grains, their concentration and character of their arrangement in the matrix (it can be periodic, regular or random). Only materials with nanogranules will be considered and none of the effects connected with the periodical ordering of granules will be taken into account. It should be mentioned that theoretical description of materials with periodical arrangements of nanogranules can be made using the results of solid state theory, developed for crystals, due to the fact that nanoparticles also manifest the quantization of electron energy,

Lam Research Ex. 1035 - Page 590
Lam Research Corp. v. Inpria Corp.
IPR2024-00033 - U.S. Patent No. 9,823,564

similar to atoms. The possibility of producing such materials opens the prospect of preparing materials with any predefined properties, but it is the next day of the material science.

As it was already pointed out, the transition from micro- to nanogranules results in a drastic change of granular metal properties: almost all of them become strongly dependent on the granule size. The range in which grains could be considered as nanoparticles is restricted by two limits. The upper limit is determined by the value when it becomes comparable with the characteristic length of any transport process (like the length of an electron free path) or with the dimension at which quantum effects or any other physical phenomenon associated with nanophysics start to be not actual (for instance, a quantization of the electron energy). All these limitations are about few tens of nanometers, and that is the reason why the upper limit in nanoscale physics is conditionally equal to 100 nm.Below this limit, many other properties of the metal granules (mechanical, magnetic, etc.) undergo significant changes: the hardness is increased and magnetic granules become single-domain magnets. The bottom limit of the nanoparticle size is evident: these are crystal lattice parameters of the nanogranule material (the crystal cell sizes), which typically are around few nanometers. Below this limitation, the crystal symmetry of the granule material will be lost, and one will obtain a matrix doped by atoms instead of the granular metal.

The dependence of nanogranular metal properties on the grain size is connected, first of all, with the quantization of energy of electron in the granule volume. As the energy distance between these levels depends on the size of granule, so the energy of the optical transitions as well as the energy of thermal excitation and transitions between granules should be determined by this size. The above energies in turn are responsible for all optical properties of granular metals together with their transport properties, in particular conductivity (for details see Section 6). Energy of magnetic field, stored in a granule, also depends on its size together with the coercive fields (see Section 4).

Another reason for the size-dependent properties in granular metals is not manifestation of quantum effects, but the rise of the surface state fraction. If one considers a metal granule as a sphere with diameter D and thickness of the surface layer h_s, it is clear that the interface portion depends on the granule size and its relative contents are described by the following equation:

$$\frac{\Delta V}{V} = \left[\frac{\pi}{6}D^3 - \frac{\pi}{6}(D - h_s)^3\right]\left(\frac{\pi}{6}D^3\right)^{-1} = \frac{6h_s}{D} \tag{1}$$

where V is the total volume of a composite and ΔV the interface volume. This ratio partially explains observed size dependencies of electro-physical,

Lam Research Ex. 1035 - Page 591
Lam Research Corp. v. Inpria Corp.
IPR2024-00033 - U.S. Patent No. 9,823,564

magnetic, optical and mechanical (strength, hardness, elasticity) properties of granular metals. For instance, up to 50% of the granule volume relates with the surface states when the thickness of interface h_s is equal to 3–4 atomic monolayers (0.5–1.5 nm) and diameter D reaches few nanometers. Moreover, the states of the surface atoms differ from those of internal atoms. Basically, this is caused by the difference of an environment and, so, by the value of the binding energy of atoms, the surface energy and the character of interactions between the granule surface and a matrix material.

Small size of granule leads to the structural changes of its material. It is favorable for defects of crystal structure (like vacancies, dislocations, defects of packing) to diffuse from the granule volume to its surface, because every defect brings an additional energy into granule and the energy of ideal crystal lattice is minimal. The diffusion of defects improves crystal structure of small granules, being an additional reason for appearance of the size-dependent properties of granular metals.

The concentration of granules is another parameter which effectively affects properties of granular metals. For the first approximation, the structure of granular metal can be described by two parameters: diameter of granule D and volume part of metal x, which can vary in the range from 0 to 1 (this approach is applicable in case of spherical granules).

At low x values, granules are isolated from one another and electric properties of this composite are close to insulator. With increase in the value of x, granules begin to stick together, forming an uninterrupted chain, and further – a macroscopic network, which provides metallic conductivity of a composite. The critical volume contents of granules, x_c, at which the metallic clustering begins infinitely is called the percolation threshold. For samples of a limited size, the percolation threshold x_c is determined as x at which the size of metallic cluster reaches that of a sample. Evolution of the material structure with increase of x_c is illustrated in Figure 11.4 [12]. The description of electrical and magnetic properties of a system near the threshold of percolation is carried out in the frame of the theory of percolation, which is presented in reviews and books [34,35], and is applied directly to granular metals in [5,36,37] (see also Section 5.1). If parameters x and D are known, then the quantity of granules in the volume unit is given by the ratio $n \cong (2x/D^3)$ and the average distance between granules is equal to $r \cong D(2/x)^{1/3}$.

A simple consideration of granular metals in the framework of the classic percolation theory when granules are treated as metal balls, embedded into insulating material, appears to be very limited. Taking into account quantum effects and, first of all, possibility of the tunnel transitions between nanogranules leads to the change in parameters of the percolation theory and even to diminishing of the percolation threshold [15,38,39]. Even in

Lam Research Ex. 1035 - Page 592
Lam Research Corp. v. Inpria Corp.
IPR2024-00033 - U.S. Patent No. 9,823,564

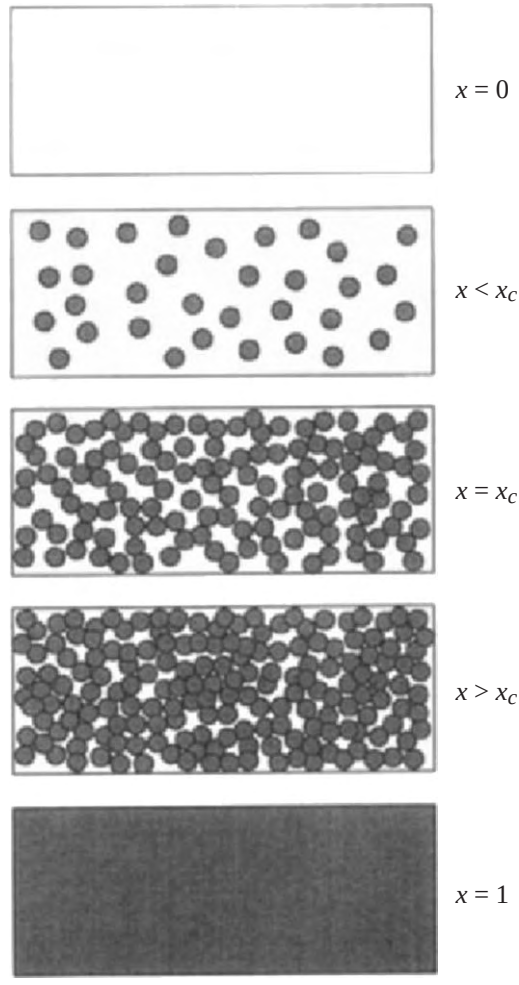


Fig. 11.4. Schematic sketch of granular metal structure depending on metal volume fraction x. Volume fraction corresponding to the percolation threshold is denoted as x_c.

the framework of classic theory, it is necessary to take into account non-sphericity of the granule shape and parameters of a matrix additionally to consideration of the electron tunnel transitions between granules.

Shape of granules essentially affects the properties of granular metal. Concerning the nanocomposite structure, it is possible to outline fibrous and laminate composites together with grain nanocomposites, in which shape of granules is close to spherical. In fibrous composites, sizes of inclusions in

Lam Research Ex. 1035 - Page 593
Lam Research Corp. v. Inpria Corp.
IPR2024-00033 - U.S. Patent No. 9,823,564

one dimension significantly surpass sizes in other dimensions and laminate composites consist of flat layers of components. The presence of significant differences in properties of composites caused by the composite structure is evident. Moreover, properties of grain materials depend significantly on the granule shape. The anisotropy of granule shape leads to the anisotropy of electro-physical properties, and the current flow conditions differ for different directions. The granule shape anisotropy influences magnetic properties even much more, leading to the appearance of additional term in the Hamiltonian, in other words, to additional energy of a composite (see Section 4). The internal anisotropy of granule material (crystallographic anisotropy) affects properties of granular metal in similar way. The usage of inclined sputtering or coating of sample in the presence of magnetic field can help sometimes to control the anisotropy of materials.

It is necessary to note that the morphology of granular materials is extremely varied and it is defined by characteristics of materials, from which nanocomposite is composed, as well as by technological parameters of the manufacturing method and by the substrate properties.

The deposited metal atoms move diffusively and are gathering into small granules. The diffusion coefficient of metal atoms depends on temperature and that is why the grain size depends on temperature of a substrate. The granule size in Fe/SiO_2 films is around 4 nm at the substrate temperature T_s of up to 400 K; it approaches 6 nm during the temperature rise of up to 575 K and reaches 15 nm at $T_s = 775$ K [40]. Moreover, with increase in the ratio between metal and dielectric components, granules grow up and combine with each other forming granules of larger size (often non-spherical) depending on conditions of the deposition process. Annealing acts in a similar way and is often used for manufacturing nanocomposite films. The effectiveness of annealing is demonstrated in Figure 11.5, where electron microscope images of films, containing FePt granules in an SiO_2 matrix ($x = 0.25$), prepared at different annealing temperatures are presented. The nanocomposite structure also depends strongly on properties of materials, used as its components. Obligatory conditions for the formation of granular metal are non-wettability and insolubility of its components into each other [4]. This prevents mixing of components and leads to the formation of granular material.

All listed effects have an influence on the granule size and shape as well as on the distances between granules. This helps in understanding why experimental values of the critical volume fraction of metal granules x_c strongly differ from the calculated ones in the framework of classical percolation theory [35], in particular, for In granules on top of an SiO_2 surface $x_c = 0.82$ [5]. However, the shape of metal granules does not strongly differ from spherical one for significantly large number of metal–insulator granular

Lam Research Ex. 1035 - Page 594
Lam Research Corp. v. Inpria Corp.
IPR2024-00033 - U.S. Patent No. 9,823,564

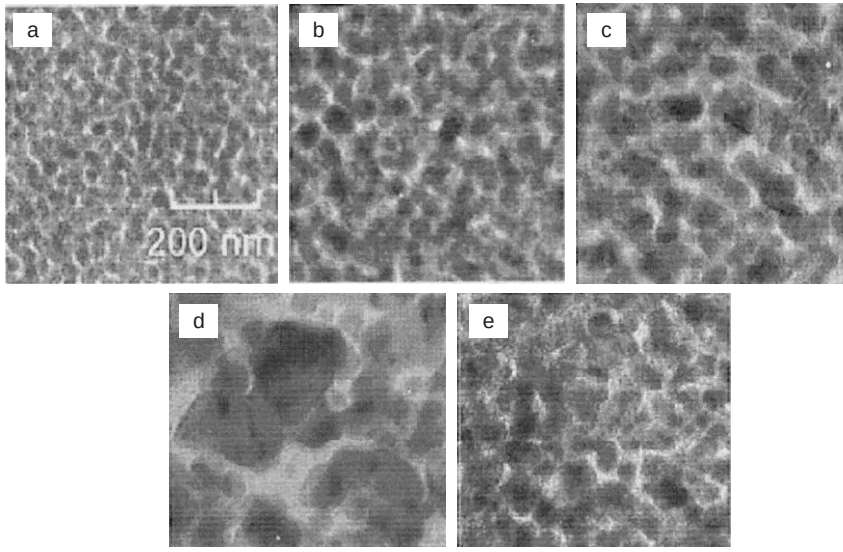


Fig. 11.5. Annealing effect on structure of the granular metal (FePt)/SiO_2 [39]. TEM images (a)–(e) correspond to annealing temperatures 500°C, 525°C, 550°C, 575°C and 600°C, respectively.

nanocomposites: the aspect ratio of granule is not more than 2, the x_c value is in the range 0.5–0.6 and the granule sizes are in the range 3–10 nm.This relates to, most often mentioned in literature, granular metals like Fe, Co, Au, Cu in an SiO_2 or Al_2O_3 matrix.

The important parameters, which determine properties of granular metal, are the granular dispersions over size and shape, or in other words the width of corresponding distributions. The peaks of these distributions determine properties of granular metals, while if the above distributions are too wide the size and shape dependences of granular metal properties and hence the possibility to control the material properties disappear. As a rule, the distribution of granules over sizes is quite narrow. An example of the size distribution of granules in a Fe/SiO_2 nanocomposite is presented in Figure 11.6. The special techniques open the possibility to realize above-mentioned self-organization processes and to get practically mono-dispersed granules (see Section 2).

Practically all methods of producing nanomaterials are non-equilibrium; accordingly, the materials prepared are far away from thermodynamic equilibrium. Large number of interface areas and boundary conditions, residual tensions and crystal structure defects lead to possibility of implementation of several processes, changing the material structure during

Lam Research Ex. 1035 - Page 595
Lam Research Corp. v. Inpria Corp.
IPR2024-00033 - U.S. Patent No. 9,823,564

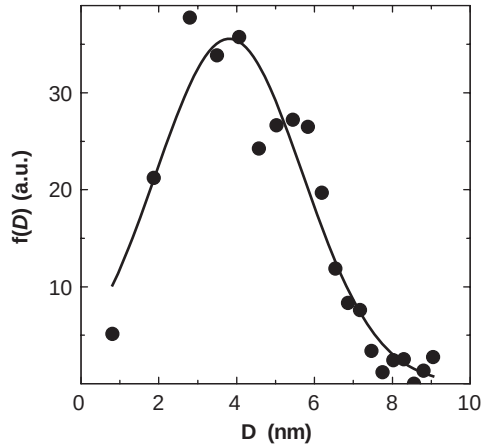


Fig. 11.6. Grain size distribution function $f(L)$ defined by TEM image of $Fe_x(SiO_2)_{1-x}$ thin films. Solid line is the Gaussian fit $f(L) \propto \exp[-(L - \langle L \rangle)^2/2\sigma_L^2]$ with the average value $\langle L \rangle = 3.8$ nm and the dispersion $\sigma_L = 1.9$.

thermal, deformational treatment and other impacts. Among them, there are crystallization and amorphization, homogenization and segregation, agglomeration, etc. All of these processes, of course, affect the physical properties of granular metals.

4. Magnetic Properties of Granular Magnetic Metals

At the time, it is difficult to imagine industrial and household devices that do not use magnetic sensors, magnetic devices or elements of magnetic memory. Because of this, it is quite clear that interest in magnetic properties of materials and, in particular, granular metals is actual and permanent one.

It is necessary to introduce some definitions before discussing magnetic properties of granular metals. Ferromagnet is a material in which practically all magnetic moments of atoms are ordered in the same direction at temperatures lower than the so-called Curie temperature (T_c). The T_c value is specific for each material. Magnetic moment per volume unit is called magnetization M. Bulk ferromagnetic materials, used in practice, possess high T_c and large values of a saturated magnetization M_s (M_s is the maximal magnetization of a material at a given temperature), for instance, for iron $M_s \approx 1700$ gauss at $T = 300$ K and $T_c = 769^\circ$C. Magnetic ordering in ferromagnets below T_c is caused by the exchange interaction, which tends to

Lam Research Ex. 1035 - Page 596
Lam Research Corp. v. Inpria Corp.
IPR2024-00033 - U.S. Patent No. 9,823,564

align magnetic moments of atoms parallel to each other even in the absence of the external magnetic field. The appropriate magnetic energy is called magneto-static and increases proportionally to the sample volume. In order to minimize this energy, large ferromagnetic samples divide themselves into separate areas called domains; inside each of them all magnetic moments of atoms are aligned in the same direction, but magnetic moments of distinct domains are oriented differently. As a result, total magnetic moment of a sample disappears in the absence of the external magnetic field that leads to reduction in magnetic energy. Usually, sizes of domains in ferromagnets are of the order of 10^{-4}–10^{-2} cm.

Typical magnetization curve of ferromagnetic material (the field dependence of magnetization) is demonstrated in Figure 11.7. Arrows show directions of the sweep of the external magnetic field H. The given magnetization curve corresponds to initially non-magnetized material and goes out from the beginning of coordinates. The point corresponding to the intersection of the curve with the ordinate axis gives a value of the residual magnetization M_r, and the point of intersection of the curve with the abscissa characterizes the half-width of the hysteresis loop and is called "the coercive force" (H_c). This parameter determines the strength of the external magnetic field necessary for reducing the residual magnetization down to zero.

Another important parameter of bulk ferromagnetic material is the constant of magnetocrystalline anisotropy K_c, which characterizes the dependence of magnetization on its direction relatively to the crystallographic axes. This value has dimensionality of the energy density, and it characterizes the energy necessary for reverse magnetization of single-domain particle. Value of K_c for pure iron is small, and bulk iron samples possess small coercive force $H_c \approx 10$ Oe.Materials with small coercive force are

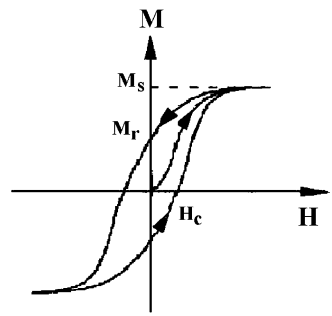


Fig. 11.7. The granular ferromagnetic metal magnetization M as a function of an external magnetic field H at temperatures below the blocking temperature. Arrows indicate the direction of the field sweep. M_r: remnant magnetization, M_s: saturation magnetization, H_c: coercivity.

Lam Research Ex. 1035 - Page 597
Lam Research Corp. v. Inpria Corp.
IPR2024-00033 - U.S. Patent No. 9,823,564

called magneto-soft materials and they are widely used in devices, in which the reverse of magnetization should happen often.

4.1. GENERAL STATEMENTS AND MAGNETIZATION AT LOW TEMPERATURES

Nanocomposites consisting of grains of ferromagnetic metal, embedded in insulating matrix, is the topic of this chapter and its magnetic properties are the subject of this section. They are determined mainly by the volume fraction (x) of ferromagnetic granules. At $x > x_c$, granules form the ferromagnetic cluster by threading the whole volume of a sample, and magnetic properties of nanocomposite in this case become similar to magnetic properties of a bulk ferromagnet. It is necessary to mention that there are two x_c values. First of them is related to the sample conductivity and second to the magnetically ordered cluster. These two x_c values are different because the magnetic interaction between granules has a long-range component (the dipole–dipole interaction), while for the current flow particles should contact (touch) each other or at least be at the tunneling distance. However, this difference is relatively small at common temperatures (above $T_c/10$) and will not be taken into account in this chapter.

Granules in a composite are completely separated at $x < x_c$ and weakly interact with one another. In this case, the nanogranular metals behave as a set of independent granules. Nanograins are always single-domain particles. The reason is that the creation of the domain structure is possible only in big enough samples, in which sizes exceed the critical one. This size is called ''the single-domain limit'' and typically is about a few tens of nanometers. This value is determined by the following balance. The loss of magneto-static energy caused by division of a sample volume into set of domains[3] should exceed the energy of creation of domain walls separating the adjacent domains. Thus, at $x < x_c$ each nanogranule at temperature below T_c will behave as a separate magnetic particle with magnetic moment proportional to its volume, if one disregards interactions between granules.

Such particles possess very high magnetic moment (10^3–10^6 μ_B [41]) in comparison with a separate atom, and this behavior of the whole set of non-interacting particles in magnetic field is called ''superparamagnetism''. The term means that the assemblage of granules shows the same magnetic field and temperature dependences as a gas of paramagnetic atoms. The only difference is that in the last case magnetic field changes the orientation of atoms themselves, but in motionless single-domain granules the orientation

[3]Magneto-static energy is proportional to sample volume multiplied by the averaged magnetization. When sample breaks into set of domains with randomly oriented magnetic moments, the averaged magnetization diminishes that results in lowering of magneto-static energy.

Lam Research Ex. 1035 - Page 598
Lam Research Corp. v. Inpria Corp.
IPR2024-00033 - U.S. Patent No. 9,823,564

of their magnetic moments varies. If material of granule is isotropic, there is no preferable direction for orientation of its magnetic moment. Under action of strong enough magnetic field, magnetic moments of all granules align along the field and magnetization reaches its maximum called the saturation magnetization M_s. Subsequent reduction of magnetic field down to zero will lead to the randomization of magnetic moments of granules: orientations of all these moments become randomly distributed and the total magnetic moment of the sample vanishes (for more details see Section 4.3).

Shape of granules usually differs from spherical, and a material of granule has its own crystal structure, which is isotropic very rarely. These two factors cause appearance of the preference direction for magnetic moment in a granule, which is called the axis of easy magnetization or simply speaking "easy axis". Magnetic moment of a particle is oriented along this axis in the absence of magnetic field that relates to the minimum of magnetic energy of a granule. Deepness of this minimum is equal $E_A = KV_g$, where K is the constant of magnetic anisotropy of the granule, and V_g is the granule volume. Physical sense of E_A could be expressed in the following way: in order to change orientation of the magnetic moment of granule by the angle θ, it is necessary to overcome potential barrier, which is determined by the energy $E_A(\theta) = KV_g \sin^2 \theta$.[4] There are two contributions to K value. They are magnetocrystalline anisotropy K_c and magnetic shape anisotropy K_s, linked with the particle shape, which usually appears to be more essential for granular materials. The presence of anisotropy leads to the fact that preliminarily magnetized sample partially keeps its magnetization after vanishing of the external magnetic field. Residual magnetization in zero magnetic field M_r is equal to $M_s/2$, because magnetic moments of granules are aligned along the easy axis at low temperatures, but only in the one direction (from two possible ones), where the external magnetic field refers to. In other words, the space distribution of magnetic moments represents semi-sphere, i.e. average value of the space angle, in which magnetic moments of granules are spread is equal to 1/2. Magnetization curve of a granular metal has a hysteresis loop (Figure 11.7) and looks similar to magnetization curve of bulk ferromagnetic metal.

To reverse the orientation of granule magnetization, it is necessary to overcome the energy of magnetic anisotropy. Above the temperature $T_b = E_a/k_B$ (k_B is the Boltzmann constant), magnetic moments of granules are oriented randomly, M_r turns into zero and magnetic hysteresis disappears. This temperature is called the temperature of blockade ($T_b \approx KV/k_B$), because at $T < T_b$ magnetic moments of granules still keep their orientations: this is a state with so-called "frozen moments". If the temperature is above

[4]Here, approximation of the single-axis anisotropy is used.

Lam Research Ex. 1035 - Page 599
Lam Research Corp. v. Inpria Corp.
IPR2024-00033 - U.S. Patent No. 9,823,564

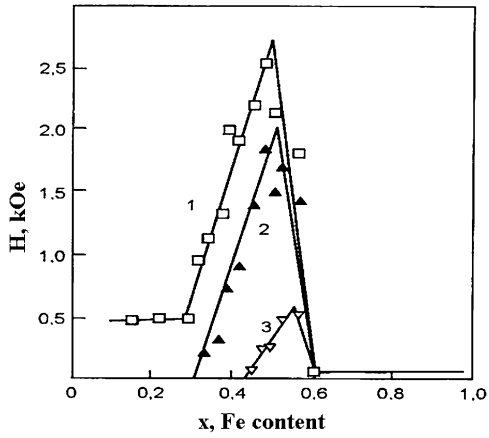


Fig. 11.8. Coercive field of the granular metal $Fe_x(SiO_2)_{1-x}$ vs. composition. The curves (1–3) correspond to 2 K, 77 K and 300 K, respectively [4].

T_b, then the direction of the magnetic moment of a nanogranule is affected by the thermal fluctuations. Temperature decrease leads to monotonic increase of M_r and H_c approaching maximum at $T = 0$ K.

It is clear that H_c noticeably increases with decreasing temperature, because temperature fluctuations sharply decrease in this case and magnetic moments of granules are aligned mainly along the easy axis, which relates to minimum energy. Value H_c strongly depends on temperature and concentration of nanoparticles (see Figure 11.8). As it is seen from this figure, H_c sharply increases while approaching the percolation threshold from dielectric side ($x \rightarrow x_c$, with $x < x_c$) and reaches values ~500 Oe at room temperature and 2500 Oe at $T = 2$ K. When concentration of iron granules exceeds x_c, the coercive force essentially decreases down to values, which are typical for bulk iron, and does not depend on x above x_c. The last takes place, because the percolation cluster is already formed in whole volume of sample. Thus, H_c has a sharp maximum in the vicinity of the percolation threshold [4].

4.2. MAGNETIZATION AT HIGH TEMPERATURES (PARAMAGNETIC REGION)

Previous paragraph was dedicated to the description of spontaneous magnetization of granular metal nanocomposite. In this section, behavior of this material at paramagnetic state ($T > T_b$) will be discussed. Magnetic moment of a granular metal in this temperature range is induced by the external

Lam Research Ex. 1035 - Page 600
Lam Research Corp. v. Inpria Corp.
IPR2024-00033 - U.S. Patent No. 9,823,564

magnetic field. Magnetization curve of a nanocomposite above the blocking temperature T_b is described by the Langeven function [42,43]:

$$M = M_s L\left(\frac{\mu H}{k_B T}\right) = M_s\left[\coth\left(\frac{\mu H}{k_B T}\right) - \frac{k_B T}{\mu H}\right]. \quad (2)$$

Here, M and M_s are the magnetization and the saturated magnetization of a sample, respectively, μ the magnetic moment of a granule, and H the strength of magnetic field. It is convenient to express the saturated magnetization of a sample in terms of that value for a granule material m_s, using relations $M_s = xm_s$ and $\mu = m_s V_g$, where V_g is the average volume of a granule:

$$M = xm_s\left[\coth\left(\frac{\mu H}{k_B T}\right) - \frac{k_B T}{\mu H}\right]. \quad (2')$$

The ratio (2′) is valid for non-interacting isotropic granules (here the term "isotropic" means spherical granules of a homogeneous material). At high temperatures, it is possible to get from Eq. (2′) the following expression for magnetic susceptibility [6]:

$$\chi = \frac{xVm_s^2}{3k_B(T - T_0)}. \quad (3)$$

Relation (3) looks similar to the Curie–Weiss law for paramagnetic materials. According to this law, the inverse susceptibility $1/\chi$ linearly depends on temperature. The corresponding line crosses the abscissa axis at the temperature T_c, which is called Curie–Weiss temperature [41]. In common, the temperature T_0 for granular systems also could be defined in a similar way as a temperature at which $1/\chi(T)$ reverts to zero. Comparing the experimentally found dependence $\chi(T)$ with the formula (3), one can get the temperature dependence of M_s. The very high magnetic fields need to achieve full saturation of a granular magnetic metal at $T >> T_b$ because a granule magnetic moment μ is small and K_s is large (e.g. the shape anisotropy of granules is rather essential). So, it is unreal in normally used magnetic fields (1–10 kOe). As it has already been mentioned, similar behavior is named superparamagnetism. The formation of superparamagnetic state can be detected experimentally by vanishing of a magnetic hysteresis and observation of the magnetization curve in the form of expression (2). The last means that experimental values of magnetization measured at various temperatures and in different magnetic fields should fit to one curve in the coordinates M and H/T.

Above-mentioned relations are rough approximations, because they were obtained under assumptions that all granules have the same size and are isotropic and non-interacting. Usually, these assumptions are rather bad

Lam Research Ex. 1035 - Page 601
Lam Research Corp. v. Inpria Corp.
IPR2024-00033 - U.S. Patent No. 9,823,564

match to the real granular metal. The most important is that these relations do not take into account the size dispersion of granules. For spherical granules, the size dispersion (distribution of granules over sizes) is described by function $f(D)$

$$f(D) = (2\pi \ln \sigma_D)^{-1} \exp\left[\frac{-(D - \langle D\rangle)^2}{2\sigma_D^2}\right], \tag{4}$$

and the nanocomposite magnetization could be estimated by the following relation [44]:

$$M = x m_s \int_0^\infty L\left(\frac{m_s V H}{k_B T}\right) f(D) dD. \tag{5}$$

It is necessary to note that the Langeven function L depends on variable D, over which the integration is conducted, $V_g = \pi D3/6$. Using this ratio and experimental dependence $M(H)$, it is possible to get experimental size dispersion and then compare it with results of electron microscopy measurements. In the case when deviation of the granule shape from spherical is insignificant, such comparison testifies the applicability of the given model [45] (see also Section 6).

4.3. MAGNETIZATION OF GRANULAR FERROMAGNETIC METALS WITH NON-SPHERICAL GRANULES

To describe the properties of granular ferromagnetic metals, sometimes the consideration taking into account the dispersion of granules only over sizes is insufficient. It is so especially when the concentration of granules is close to the percolation threshold. The description of such nanocomposite magnetization within the framework of the Langeven model (Eqs. (2), (4) and (5)) is not adequate for its temperature dependence. According to experimental results, their magnetization slightly depends on temperature in contradiction with the above equations. In particular, magnetization of a $Fe_x(SiO_2)_{1-x}$ composite with $x = 0.5$ is practically temperature independent [46] (the percolation threshold for given material $x_c = 0.56$).

One of the reasons of the specified contradiction is the presence of the shape anisotropy of granules and dissimilarity of their forms. The influence of anisotropy on magnetic properties of nanocomposites was considered in Refs. [47,48] on the basis of experimental results [46,48], obtained for granular metal $Fe_x(SiO_2)_{1-x}$. In Ref. [48], the magnetization of a $Fe_{0.5}(SiO_2)_{0.5}$ nanocomposite was studied in the temperature range 4.2–300 K under action of magnetic fields up to 25 T. For that, the Kerr effect measurements

Lam Research Ex. 1035 - Page 602
Lam Research Corp. v. Inpria Corp.
IPR2024-00033 - U.S. Patent No. 9,823,564

and the direct measurements of magnetization were used. It has been shown that magnetization changes with the temperature increase no more than by 15% in the whole used range of magnetic fields. The granular ferromagnetic metal magnetization could be temperature independent, if the anisotropy energy $E_A = KV_g$ exceeds the thermal energy k_BT. It is because this energy keeps the magnetic moment of a granule in a certain position. The constant of magnetocrystalline anisotropy (K_c) for iron is $\sim 10^5$ erg/cm^3, and for granules of the size $\sim$10 nm one could get $E_A \sim 10^3$ K. The energy related to the shape anisotropy is determined by the constant $K_s \approx M_s v$, where v is difference of the demagnetization factors for various directions [41]. Under reasonable assumptions concerning the shape of granules (ellipsoids of rotations with eccentricity 2–10), this energy could be estimated as $\sim 10^4$ K. Both estimations essentially exceed temperature of experiment [46] that explains weak temperature dependence of granular metal magnetization.

For magnetic field in which magnetization of a granular metal begins to saturate, $H_A = E_A/M_sV_g$. H_A is $\sim$1 kOe for magnetocrystalline anisotropy and approaches 10 kOe in case of the shape anisotropy. Experimental values for this field obtained in measurements described in Ref. [48] are close to 10 kOe; however, full saturation of magnetization was not reached in these experiments even at fields up to 250 kOe. So, the magnetic anisotropy caused by non-spherical shape of grains appears to be more essential and, namely, it defines the field dependence of magnetization of the granular metal.

To describe the magnetization dependence on magnetic fields for such materials, some assumptions on granule shape are needed. In materials produced by sputtering (see Section 2), granules could be considered as extended ellipsoids with axes $a > b = c$. The aspect ratio (''the greatest size/the smallest size'') varies in the limits from 1 up to 10. Magnetic moment of a granule in the absence of magnetic field is aligned along the easy axis corresponding to the large axis of ellipsoid. The external magnetic field aspires to turn this moment along its direction. As a result, the granule magnetic moment occupies a certain intermediate position between the field direction and the large axis of ellipsoid. This position is determined by the balance of two energies. First of them is the energy of interaction of the granule magnetic moment with an external magnetic field, and second is the energy of magnetic anisotropy of a granule. According to Refs. [47,49], full energy E of the elliptical granule in magnetic field is equal to:

$$E = V\left(\frac{1}{2}M_s^2 v \sin^2(\beta - \gamma) - HM_s \cos \gamma\right). \tag{6}$$

Here, the first term in big brackets is energy of anisotropy per volume unit, γ the angle between magnetic moment of a granule and direction of the

Lam Research Ex. 1035 - Page 603
Lam Research Corp. v. Inpria Corp.
IPR2024-00033 - U.S. Patent No. 9,823,564

external magnetic field, β the angle between direction of the external magnetic field and the big axis of ellipsoid, the term $\beta - \gamma$ corresponds to angle between magnetic moment of a granule and the big axis of ellipsoid, and v the difference of the demagnetization factors of ellipsoid along axes a and b. The second term in Eq. (6) is attributed to energy of interaction of magnetic moment of a granule and the external magnetic field H.

The equilibrium orientation of the magnetic moment corresponds to a value of that angle at which the energy E has minimal value. It can be found out from the Eq. (6) by minimization of the right part of this equation over parameter γ. For a single granule or in case of equally oriented granules, this direction depends on the external magnetic field and is defined by following equation [48]:

$$\frac{\sin\ 2(\beta-\gamma)}{\sin\ \gamma} = \frac{2H}{M_s v}. \tag{7}$$

If all granules have the identical shape ($v = \text{constant}$) and directions of their big axes are distributed in space uniformly, the field dependence of magnetization of a granular ferromagnetic metal can be written down as

$$\frac{M}{M_s} = \frac{1}{\pi}\int_0^{\pi} \cos\ \gamma\left(\frac{2H}{M_s v}, \beta\right) d\beta. \tag{8}$$

For a real system, it is necessary to take into account the distinction of the form of granules or, in other words, the distribution of granules over parameter v, whose value is determined by function $f(v)$. Then, for $M(H)$ dependence one has [31]

$$\frac{M}{M_s} = \frac{1}{\pi}\int_{v_{\min}}^{v_{\max}} \int_0^{\pi} \cos\gamma\left(\frac{2H}{M_s v}, \beta\right) f(v) d\beta\ dv. \tag{9}$$

Here, limits of integration are defined by the range in which shapes of grains are distributed. It appears that even the homogeneous distribution of granules $f(v) = (v_{\max} - v_{\min})^{-1}$ is sufficient to describe well experimental findings for magnetization curves of a $Fe_x(SiO_2)_{1-x}$ nanocomposite [46]. The formula (9) is difficult for practical use; therefore, one can use simplified relations obtained in the limits of weak (the initial part of the magnetization curve) and strong magnetic fields (the case of magnetic saturation) [47]

$$M = \frac{1}{2} H \langle v^{-1} \rangle \quad \text{(weak fields)}, \tag{10}$$

Lam Research Ex. 1035 - Page 604
Lam Research Corp. v. Inpria Corp.
IPR2024-00033 - U.S. Patent No. 9,823,564

$$M = M_s\left[1 - \langle v^2\rangle\left(\frac{M_s}{4H}\right)^2\right] \quad \text{(strong fields)}. \tag{11}$$

These relations provide the possibility to get information on the size distribution of granules in nanocomposites on the basis of magnetization curve only. On the other hand, with the help of these formulas one is able to calculate magnetization curve for a material if the grain distribution over shapes is known. This possibility is important for applications, because magnetic nanocomposites and, in particular, the ferromagnetic granular metals can be used in systems for magnetic record of information and in systems for magnetic electronics, where magnitudes of the residual magnetic moment, the magnetic moment at the saturation and the coercive force as well as a knowledge of magnetization curve are extremely essential. Recently, the great interest is caused by systems with a regular arrangement of granules; magnetic properties of these systems were studied, in particular, in Refs. [2,50,51].

4.4. A Relaxation of Magnetization and Nanocomposite as Cluster Spin Glass

For applications, it is important to know the time response of system under variations of the external magnetic field (switching on, turning off). Relaxation of magnetization of a single granule or of a set of identical granules was considered in a number of papers (see, for example, Ref. [41] or [12] and references there). It is shown that characteristic relaxation time of magnetization τ_r is described by the Arrhenius law:

$$\tau_r = \tau_0 \exp\left(\frac{E_A}{k_B T}\right), \tag{12}$$

where τ_0 is the period of precession of the magnetic moment. This ratio could be used to experimentally find τ_0 and E_A values. Indeed, applying various experimental techniques for measurements of magnetization (Superconducting Quantum Interference Device (SQUID) magnetometer, vibrating magnetometer, measurement of susceptibility, neutronography and study of the Messbauer effect) makes it possible to vary the duration and the temperature of measurements that is necessary for independent definition of τ_0 and E_A. The values of τ_0 derived in this manner from different measurements lie in a very wide range, and this indicates the limited applicability of Eq. (12) [12]. However, it is valid only for single or identical granules, because this formula does not take into account distribution of granules

Lam Research Ex. 1035 - Page 605
Lam Research Corp. v. Inpria Corp.
IPR2024-00033 - U.S. Patent No. 9,823,564

over sizes and shapes. The values of τ_0 are in the range from 10^{-9} to 10^{-13} sec; for iron particularly, τ_0 is $\sim 10^{-10}$ sec [52].

Let's consider in detail the magnetization relaxation for the ferromagnetic granular metal $Fe_x(SiO_2)_{1-x}$ with $x = 0.5$ to reveal a role of the grain distributions over sizes and shapes. It will be assumed that all granules are ellipsoids (see Section 4.3). Experiment shows that in this material the magnetization varies with time after switching off magnetic field (relaxes, coming back to the value, which was found initially in the absence of magnetic field) in a logarithmic manner [49,53]. Similar processes with logarithmic time dependence, contrary to common exponent-like dependence, usually are referred as long-term processes.

A single-domain, extended granule of nanocomposite represents itself as the two-level system, because due to the magnetic anisotropy it can have two stable states for the magnetic moment orientation relative to the easy axis of magnetization (the big axis of an ellipsoid). These two stable states correspond to two possible projections of the magnetic moment on this axis. Hence, the granular metal with anisotropic particles can be considered as a substance consisting of a set of microscopic subsystems with two energy states. Transitions between these states are limited by energy barrier and could occur by means of the over-threshold activation and/or by tunneling. This model, known as the model of two-level systems, is widely used for description of glasses of various origins. The type of the transition, i.e. activation or tunneling, is defined by the ratio between temperature and the height of the energy barrier. In this chapter, magnetic nanogranules are under consideration, so transitions between states related to two possible orientations of the grain magnetic moment projection to its easy axis are taken into account.

The two-level nature of non-spherical granule is shown in Figure 11.9. This figure presents the dependence of granule energy in the external magnetic field as a function of an angle γ between this field and the granule magnetization. The curves presented in Figure 11.9 are calculated according to Eq. (6) for different external magnetic fields expressed in normalized values $h_v = (2H/M_s v)$.

It is evident that the dependence $E(\gamma)$ has two minima at low values of magnetic fields ($h_v \ll 1$) and there is only one minimum for strong fields ($h_v > 1$). Only transitions between the states corresponding to two energy minima in weak fields cause the relaxation of magnetization. In fact, just at the moment when a strong enough magnetic field is switched off, all magnetic moments of granules are still revolved in one side and $M_r = M_s/2$ (see Section 4.1). After that, there are two minima for $E(\gamma)$ dependence (upper curve in Figure 11.9). The magnetization relaxes by transitions between these two states to the value related to the equilibrium state for a zero

Lam Research Ex. 1035 - Page 606
Lam Research Corp. v. Inpria Corp.
IPR2024-00033 - U.S. Patent No. 9,823,564

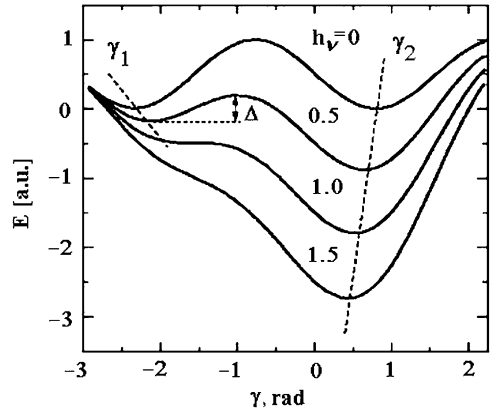


Fig. 11.9. The magnetic energy E of an ellipsoidal granule vs. γ-angle between the granule magnetic moment and an external magnetic field. The external field is directed at angle $\beta = 3\pi/4$ with ellipsoid's large-axis direction [47].

magnetic field, when there is no preferred orientation for the moments of granules. Commonly, times of transitions between these states are distributed randomly in large enough range that is due to a wide distribution of energy barriers over their heights and is a principal reason of long-term (non-exponent-like) relaxation of the corresponding physical parameter [54]. All above-stated facts point to the glass-like nature of nanocomposites.

The results of calculations shown in Figure 11.9 are obtained for the case, when the external magnetic field is oriented at the angle $3\pi/4$ relative to the big axis of a granule. Similar picture can be obtained at $\beta = \pi/4$. Let us consider the behavior of the system after a weak magnetic field is switched on at $T = 0\,\mathrm{K}$. If initial (at $H = 0$) magnetic moment is directed under a sharp angle to a magnetic field ($\beta = \pi/4$), it will be kept in the right energy minimum (see Figure 11.9). Thus, the equilibrium angle of the orientation of the magnetic moment γ monotonously aspires to zero with increase of the magnetic field. If an initial angle is blunt ($\beta = 3\pi/4$), γ changes with abrupt reversal of its sign, apparently from the data shown in Figure 11.9. That relates with the jump of magnetic moment from the "left" energy minimum to the "right" one. The simple way to study experimentally relaxation processes in a granulated ferromagnet [49] follows from here and is described below.

Let us place a sample in a strong enough magnetic field satisfying the condition $h_v > 1$ (for iron granules, this field is $\sim$10 kOe). Thus, magnetic moments of the majority of granules appear in the only one minimum of energy (for definiteness, in the right one), being aligned along the external

Lam Research Ex. 1035 - Page 607
Lam Research Corp. v. Inpria Corp.
IPR2024-00033 - U.S. Patent No. 9,823,564

magnetic field. Then, the strength of magnetic field needs to be reduced up to a value corresponding to the presence of two minima of an angular dependence of the granule energy and, finally, one should invert magnetic field (change its direction to the opposite). At the initial moment, the magnetic moments of granules will be located in the right minimum. However, this state is out of equilibrium, because the right minimum of energy is higher than the left one. The transition to the left minimum is energetically favorable, but for this purpose the system should overcome the energy barrier ΔE between these two minima. This transition to equilibrium state will be accompanied by the relaxation of the magnetic moment. To define the characteristic times of this relaxation, it is possible to use Eq. (12) with the following modification: the term E_A (the energy of magnetic anisotropy) should be replaced by the height of energy barrier ΔE. The reason is that the external magnetic field directed under angle to the granule axis has changed the anisotropy of the system. Under the action of an external magnetic field, the height of this barrier depends on the angle β between magnetic field and the big axis of the granule. So, E_A coincides with ΔE only in the case when the external magnetic field is directed along the granule axis. As a result, one could obtain [49,53]:

$$\tau_r = \tau_0 \exp\left(\frac{\Delta E}{k_B T}\right). \tag{13}$$

Thus, as ΔE depends on angle β, the system of randomly oriented but identical grains shows strong enough spreading of the relaxation times and the relaxation of its magnetization depends on time in essentially non-exponent-like manner (long-term relaxation). The detailed analysis, however, shows that to get the logarithmic type of relaxation it is obligatory to take into account the size dispersion of granules [49]. Calculations based on the framework of the suggested model and the above-described experiment [49,53] have shown a good qualitative agreement. This result specifies that the magnetic condition of a nanocomposite is satisfactorily described in the model of cluster spin glass.

5. Magnetotransport Properties of the Granular Metals

The devices, based on variation of electronic transport properties (mainly, resistance and Hall effect) under action of an external magnetic field, are very popular now and their production is one of the most successful areas of the modern instrument-making industry. In this area, many types of micro

Lam Research Ex. 1035 - Page 608
Lam Research Corp. v. Inpria Corp.
IPR2024-00033 - U.S. Patent No. 9,823,564

and nanostructures are created and issued for various applications. Among them, there are reading heads for magnetic memory, elements of non-volatile memory (MRAM, for example), sensors of a magnetic field and a current, the galvanic decoupling elements and various switches. These are called magnetoresistive devices (elements) and very often they have considerably improved characteristics and expanded functionalities in comparison with devices based on other effects. Magnetoresistive nanostructures promise new applications, which are even much more attractive. The logic gates, spin transistors and microprocessors are now under development. The list of probable scopes for such devices is very wide: the computer industry, medical, space, motor industry, instrument making, etc. The market of magnetoresistive nanodevices is one of the most intensively growing. In 2004, the sales volume reached 4.3 billion dollars, and in 2009, it will reach 12 billion dollars at an annual growth of 23%.

In this chapter, the conductivity and the Hall effect (see Section 5.4) in granular metals will be discussed.

5.1. Conductivity Dependence on a Metal Granules Fraction: The Percolation Threshold

The description of transport properties of the granulated metals is usually carried out within the framework of the percolation theory [33,34] and theory of an effective media [55]. This approach is applicable only for granules of the big enough, classical sizes. Progress dictates transition to nanoscale that leads to necessity to take into account the electron tunneling between separate grains. The possibility of tunneling shifts the percolation threshold toward lower metal fractions [38,39,56] (the quantum percolation threshold). At low enough temperatures, consideration must be given to quantum effects in the conductivity [57–59], quantization of conductivity in nanocontacts [60,61], size quantization of an electron energy within a granule [62] and Coulomb blockade [5] (see Sections 6 of this chapter and 2.1 of Chapter 10 of this handbook). Here, the quantum effects in the conductivity mean corrections to the conductivity caused by electron interference and renormalization of electro-electron interaction [57–59].

According to the classical percolation theory, there is a critical concentration of the volume fraction of granules x_c at which the infinite conducting cluster is formed from the metallic grains. At concentration of granules higher than the critical, $x > x_c$, the material conductivity is of a metallic type. At $x < x_c$, the material behaves as an insulator and its conductivity is defined by the hopping of electrons between granules, through the energy barriers insulating them from each other. It is so-called hopping mechanism of

Lam Research Ex. 1035 - Page 609
Lam Research Corp. v. Inpria Corp.
IPR2024-00033 - U.S. Patent No. 9,823,564

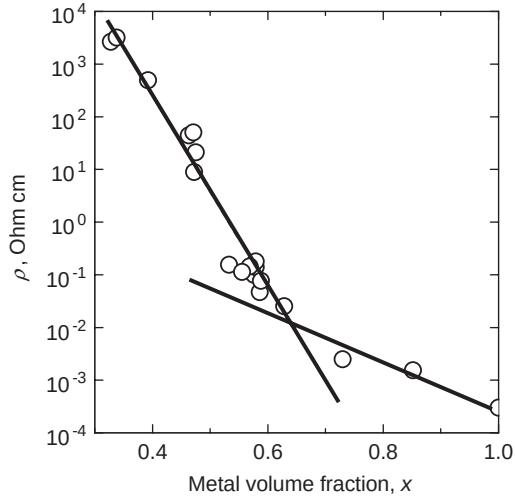


Fig. 11.10. Room-temperature resistivity of $Fe_x(SiO_2)_{1-x}$ nanocomposite as a function of iron volume fraction.

conductivity [34]. The concentration dependence of the nanocomposite resistance is presented in Figure 11.10, where the experimental results for the Fe/SiO_2 granular metal with grains of 4 nm size are shown. Methods of these sample production and the grain distribution over size have been discussed earlier (see Figure 11.6 and Sections 2 and 3). From the data presented in Figure 11.10, it is seen that in the given material critical concentration $x_c \approx 0.6$. It should be stressed that at $x > x_c$ the granular metal resistivity ρ depends on temperature weakly, while at $x < x_c$ this dependence is an exponential one. Such strong difference in temperature dependences of ρ serves as a method of x_c detection.

The properties of the granular ferromagnetic metals which depend on a magnetic field are the main subject of this section. The resistance in the case is a tensor value because under magnetic field action it is anisotropic. It will be assumed that an external magnetic field or a vector of the sample magnetic moment is directed along z-axis. The resistivity in a plane perpendicular to the magnetic field (transversal resistance), $\rho_{xx} = (E_x/J_x)$, will differ from the longitudinal one, $\rho_{zz} = (E_z/J_z)$; the voltage arises in a direction perpendicular to both the current and the magnetic field. This is the Hall effect and the corresponding resistance, $\rho_{xy} = (E_y/J_x)$, is called the Hall resistance. Here, J_i is an electric current along an axis i and E_j an electric field in j-direction. So, these components of the resistivity tensor and the corresponding conductivity tensor $\hat{\sigma}$ will be discussed. At x values far above

Lam Research Ex. 1035 - Page 610
Lam Research Corp. v. Inpria Corp.
IPR2024-00033 - U.S. Patent No. 9,823,564

or much lower than the critical value x_c, properties of the system are close to those of metal or insulator. In the vicinity of the percolation transition, strong amplification of several effects (for example, Hall effect, non-linearity of the current–voltage characteristic, strain dependence of resistivity, non-linearity of optical properties, harmonics of the reflected or transmitted signal of radiation, etc.) was observed. Such materials are suitable for production of various sensors and other practical applications. Therefore, the main attention will be paid to the behavior of the granular metals just at the percolation threshold.

According to the classical percolation theory, when a metal fraction tends to the critical x_c the resistivity follows the power law:

$$\rho_{xx} \propto \left[\frac{x - x_c}{x_c}\right]^{-t}, \tag{14}$$

$$\rho_{xy} \propto \left[\frac{x - x_c}{x_c}\right]^{-g}. \tag{15}$$

The similar law is for the concentration dependence of the correlation length of the percolation cluster (that is the size at which a self-crossing of current paths occurs or the effective radius of the percolation net):

$$\xi_p \propto \left[\frac{x - x_c}{x_c}\right]^{-v}. \tag{16}$$

Critical indexes are given by $t \approx 2$, $g \approx 0.5$, $v \approx 0.88$ for three-dimensional objects [34,63,64]. Usually, critical indexes at $x < x_c$ and $x > x_c$ are assumed to be identical. Within the framework of the classical theory for objects of dimension d, critical indexes fit the following equation:

$$g = 2[t - (d - 1)v]. \tag{17}$$

Value $t = 2$ for the granular metals has been confirmed experimentally in several papers (see, for example, Ref. [1]); however, for $Ni_x(SiO_2)_{1-x}$ nanocomposite with granules of nanometer size it was found $t \approx 2.7$, $g \approx 2$ [65]. It rather essentially differs from the classical theory predictions. Also, the noticeable differences of the experimental values of critical indexes from the theoretical ones have been found in papers [66,67]. Authors of these papers attributed the discrepancy between the experimental data and results of the classical percolation theory to the quantum effects, which lead to the Anderson localization of charge carriers [57,58].

It is well accepted by many physicists that the interplay of localization and percolation plays an essential role near the percolation threshold. The

Lam Research Ex. 1035 - Page 611
Lam Research Corp. v. Inpria Corp.
IPR2024-00033 - U.S. Patent No. 9,823,564

reason is that the percolation describes systems with the long-range spatial disorder (classical scale), while the Anderson localization considers systems with the short-range (quantum) disorder. At the same time, near the percolation threshold and close to Anderson transition, the corresponding effective lengths (correlations and localizations) tend to infinity and the difference of scales vanishes.

Attempts to take into account both localization and percolation or, in other words, to allow for quantum effects in percolation go back to Khmelnitskii's pioneer paper [68]. The experimental attempts to study quantum effects in conductivity close to the percolation threshold have been undertaken in Refs. [69–71]. The physical sense of these results is stated in Ref. [71] and could be described as follows. The percolation cluster is non-uniform; it includes both big conductive regions (''lakes'') and small regions (weak links or bottlenecks) which connect lakes to each other. On approaching the percolation threshold from the metallic side of the transition, these weak links become thinner and longer, and at $x = x_c$ the cluster breaks or tears into pieces just in such areas. As a result, exactly these conditions start to be sufficient for the electron localization. Thus, a percolation provokes an Anderson localization in bottlenecks of the percolation cluster. Sheng and collaborators [36,37,72] tried to take into account the influence of tunneling on conductivity for systems in the vicinity of the percolation transition. Similar attempts have been made in papers [38,56]. The obtained results prove that the possibility of tunneling shifts the percolation threshold toward smaller x values and affects material properties in its vicinity.

However, for the adequate description of nanogranular metal near to the percolation threshold with account for quantum effects or, in other words, of the interplay of percolation and localization one should consider the set of all of these above-mentioned effects, including tunneling, interference, electron–electron (e–e) interaction, size quantization of electron energy, because it is impossible to choose one from them. Complexity or sophistication of the problem is related to the absence of a small parameter and the adequate mathematical apparatus. That restrained the progress of these studies for a long time. Only in the last few years was the progress outlined due to results of the group of Efetov and Loh (see the review [3]). Nevertheless, the problem is still far enough from the solution and the theory is too complicated and well developed to be discussed in the given edition.

Let us notice, at last, that x_c in the granular metals often essentially exceeds the values given by the classical percolation theory (0.2–0.3), and it appears $\sim$0.5–0.6 [5,46,53,65]. This discrepancy is connected not to the quantum effects, but more likely with technological procedure of the nanocomposite preparation, by interaction between metallic granules and a

Lam Research Ex. 1035 - Page 612
Lam Research Corp. v. Inpria Corp.
IPR2024-00033 - U.S. Patent No. 9,823,564

matrix and/or between the sample and a substrate and has been discussed in Section 3.

In magnetic nanocomposites (the granular metals with magnetic grains), another peculiar feature taking place in the vicinity of percolation transition is of great importance. At metal fractions close to $x = x_c$, the maximum value of the GMR is observed. The magnetoresistance (change of resistance under a magnetic field action) in ferromagnetic granular metals will be considered in Section 5.3.

5.2. Temperature Dependence of Conductivity

The galvanomagnetic properties of nanocomposites and their conductivity, in particular, near the percolation transition can be described within the two-component model developed for the case by Efros and Shklovskii [73] on the basis of Dykhne theory [74]. This theory was developed just for the description of materials containing two different components with sharp distinction for conductivity values (Dykhne media) and describes well the concentration dependence of the effective conductivity in the case of the classical grain sizes and so in the absence of quantum effects. However, even if quantum effects do not play an essential role, the adequate description of the conductivity dependence on temperature has not been elaborated till now. The reason is that numerous experimental results for granules, with the metal contents $x < x_c$, follow well-known $T^{-1/2}$:

$$\sigma(T) \propto \exp\left\{\frac{-T_0}{T^{1/2}}\right\}. \tag{18}$$

Here, T_0 is the parameter whose value depends on x and equals to 0 at $x = x_c$. The analysis of the experimental data for the temperature dependence of the nanocomposites conductivity is presented in Sheng and Adkins reviews [72,75] and also in the recent paper of Zvyagin and Keiper [76]. Studies of conductivity in the granular metal Fe/SiO_2 [77,78] also are in a good agreement with Eq. (18). The given dependence was not found only in experimental results obtained by Gurevich et al. [29,32]. Probably, the reason for that is the very narrow grain distribution over sizes in samples used in these measurements contrary to other experiments.

Eq. (18) is usually attributed to the variable-range hopping conductivity in presence of the Coulomb gap [34]. However, the analysis [72,75,76] shows that it is unrealistic explanation for the case of nanocomposites, because to fit experimental value on the basis of this theory one has to assume that the length of a single hop is less than the size of granules D and the electron

Lam Research Ex. 1035 - Page 613
Lam Research Corp. v. Inpria Corp.
IPR2024-00033 - U.S. Patent No. 9,823,564

wavelength is much greater than that given by the material structure. Furthermore, contrary to semiconductors in granular metals an electron hops between grains but not atoms. Grains have sizes which are comparable with inter-grain distance and so granules could block electron's way that prevents the long-distance hops. For hops between nearest neighbors, Eq. (18) could be obtained under assumption of some correlation between the size of granules D and the inter-grain distance L. Sheng [79] assumed $D/L = \text{constant}$. However, the analysis of experimental data presented by Adkins [75] does not show any correlation between D and L. Meilikhov [80] has obtained Eq. (18) under weaker assumption $\partial D/\partial L = \text{constant}$. The experimental data presented in Figure 11.11 [77,78] are in qualitative agreement with Eq. (18) and so with Sheng and Meilikhov calculations; moreover, the temperature dependence of the ρ_{xy} is also in accordance with Eq. (18) [81]. It should be noted that these data are unique because it is the only paper dealing with temperature dependence of both ρ_{xx} and ρ_{xy}. However, weakness of the Sheng [79] model marked by Adkins [75] could be attributed to Meilikhov [80] in full measure. The reason is that, as marked above, the experiment does not show presence of any correlation between the size of granules and the distance between them (for the detailed analysis see [76]).

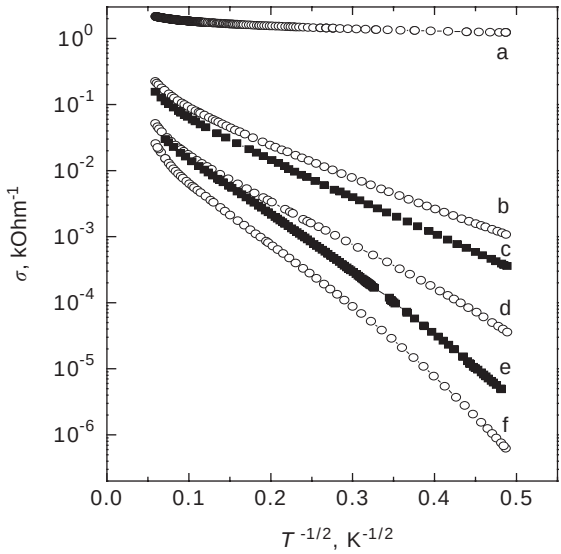


Fig. 11.11. Conductance vs. temperature for $Fe_x(SiO_2)_{1-x}$ nanocomposite in metallic state (curve a, $x \approx 0.7$) and in the series of dielectric samples (curves b–f, x in the range of 0.56 to ~0.4). T_0 values calculated from $\sigma(T) \propto \exp(-T_0/T^{1/2})$ law are 140 K, 185 K, 255 K, 410 K and 550 K for b–f curves, respectively [78].

Lam Research Ex. 1035 - Page 614
Lam Research Corp. v. Inpria Corp.
IPR2024-00033 - U.S. Patent No. 9,823,564

There is lack of the universal, commonly accepted explanation of the conductivity–temperature dependence in nanocomposites at $x < x_c$. The most interesting and reliable is the Zvyagin and Keiper model [76]. According to this model, the main mechanism of conductivity is the variable-range hopping between grains located far away from each other. To make such hops real, they suggested the electron path for the single transition from an initial granule to the final that, in addition to tunneling between grains, also includes electrons transportation through virtual states in intermediate granules (in granules located between initial and final ones). The assumption of the possibility of transitions through virtual states is the main idea of Zvyagin and Keiper [76], which opens the possibility for variable-range hopping. Similar transitions through real states are extremely improbable due to the big difference between energies of these states, so for such a transition an electron should get quite high energy. That means the temperature at which such transitions could be possible many times over exceeds the temperature of measurements.

The main restriction of Efros and Shklovskii [73] and Dykhne [74] results is the lack of consideration of quantum effects. Taking into account the quantum corrections to conductivity [57–59] leads to the following temperature dependence at metal fractions above the percolation threshold:

$$\sigma(T) \propto T^{1/2}. \tag{19}$$

In dirty metals at low temperatures, similar dependence is observed everywhere; for nanocomposites also it has been reported in a few papers [82–85]. It is specific for nanocomposites that, as it was demonstrated in papers [66,82,85], this dependence could be observed up to very high (room) temperatures. This is due to the small mean free path of electrons in granular metals caused by the strong disorder which are natural for such material. Let us recall that the equation $k_B T \sim \hbar/\tau$ determines the limiting temperature up to which quantum corrections due to an electron interference are actual and the dependence (19) is fair. Here, t is the electron moment relaxation time. However, in some cases at low temperatures the unexpected deviation of experimental data from the dependence (19) was observed [66,82,85]. Discussion of this surprising effect will make a part of the contents of the Section 6.

5.3. Magnetoresistance: Field Dependence of Conductivity

The variation of a material resistivity under action of an external magnetic field is called magnetoresistance. For its quantitative characterization, usually scientists use the $\Delta\rho/\rho$ value, where $\Delta\rho = \rho(H) - \rho(0)$ is the change of

Lam Research Ex. 1035 - Page 615
Lam Research Corp. v. Inpria Corp.
IPR2024-00033 - U.S. Patent No. 9,823,564

resistance in magnetic field and $\rho = \rho(0)$ is its value in zero field. Magnetoresistance is positive ($\Delta\rho/\rho > 0$) if resistance increases in magnetic field and negative otherwise. There are a lot of physical mechanisms resulting in magnetoresistance and some of them are discussed below.

Classical magnetoresistance [58] takes place in all metals and semiconductors (magnetic and non-magnetic). The nature of this effect is the curvature of the charge carriers (electrons) trajectory due to the Lorentz force caused by the action of magnetic field. The ratio between the radius of the electron orbit in magnetic field in the absence of collisions (the Larmour radius) and its mean free path serves as a measure of this curvature. In granular metals with an insulating matrix, electrons move as free particles only inside the metallic cluster at $x > x_c$ or within granules. In both cases, the electron mean free path is very small, being $\sim$1 nm.This is because these materials contain much more defects than pure metals and grain sizes are usually $<$10 nm.As a result, the classical magnetoresistance of granular metals is very weak and can be neglected compared to other mechanisms of magnetoresistance considered below.

Similar statement can be attributed to the magnetoresistance under the hopping mechanism of conductivity and it is also true for both magnetic and non-magnetic materials. This is *the hopping magnetoresistance* [34]. This mechanism of magnetoresistance is due to the shortage of the electron wave function under the influence of magnetic field. Probability of the electron tunneling from one granule into another, and so the hopping conductivity, is determined by the overlapping of electron wave function "tails" beyond a metal granule. The electron effective mass in metal (m) is large enough and consequently the change of electron energy in magnetic field $\hbar(eH/mc)$ is insignificant, especially in comparison with the height of the energy barrier in the insulating matrix ($\sim$10 eV). The ratio of these values defines the influence of magnetic field on the decay length of electron wave function in insulator, surrounding a granule. This length is typically small (some nanometers). Therefore, the influence of magnetic field on the hopping conductivity in granular metals appears to be weak and usually it should not be taken into account.

If *the quantum corrections to conductivity are* actual *the magnetoresistance* related to the influence of the magnetic field on these corrections takes place [57–59]. The interference of electrons passing the closed part of trajectory in clockwise and counter-clockwise directions causes the so-called corrections to the conductivity. The phases of the electron wave functions in this case are equal and so this interference is constructive. Therefore, the probability for electrons to come back to the initial point doubles. This leads to the interference corrections which increase the classical resistance. The external magnetic field breaks the "left–right" symmetry, and the phases collected by the electron wave function while it passes trajectory in clockwise and

Lam Research Ex. 1035 - Page 616
Lam Research Corp. v. Inpria Corp.
IPR2024-00033 - U.S. Patent No. 9,823,564

counter-clockwise directions appear different. The interference vanishes and the resistance diminishes, which is negative magnetoresistance.

Similar effect appears due to the quantum corrections of conductivity caused by the renormalization of the e–e interaction in materials with the strong enough electron scattering. These corrections also are influenced by the magnetic field and this is one more reason for magnetoresistance. However, in normal metals, both these mechanisms of magnetoresistance are essential at very low temperatures only, typically below $T = 10\,\mathrm{K}$. In granular metals, these effects can be observed even at higher temperatures [82], but in magnetic granular metals other mechanisms of magnetoresistance are much more essential, and they will be considered below.

Classical and hopping mechanisms lead to positive magnetoresistance (PMR), but mechanism connected with the quantum corrections can cause both: positive and negative magnetoresistance (NMR). The above-listed mechanisms of magnetoresistance are essential for any granular metal, while in magnetic materials other specific mechanisms take place. These specific mechanisms are much more important for magnetic nanocomposites and they are the basis for the magnetoresistive devices; therefore, they will be in focus in the following sections.

The so-called *anisotropic magnetoresistance* is responsible for the main contribution to the magnetic field dependence of resistance in ferromagnetic materials. Magnitude of this effect and even its sign depend on orientation of the magnetization with respect to the direction of current. If the directions of the current and magnetization coincide, magnetoresistance ($\rho\|$) is positive, while it becomes negative if magnetization is perpendicular to the direction of the current ($\rho_\perp$). The physical sense of anisotropic magnetoresistance can be understood using the following rather simplified consideration. Magnetic properties of a material are defined by magnetic ions having *d*-electrons in the outer electronic shell. Wave function of *d*-electron represents a rosette in the plane perpendicular to the direction of the ion magnetic moment. The magnitude of the cross-sectional scattering of electron on this ion is less if electron meets the rosette sideways, in comparison with the case when the rosette plane is perpendicular to the electron velocity. It is evident that if orientation of magnetic moments of ions coincides with direction of the electron velocity, the scattering of electrons and so the resistance are maximal. These parameters are minimal in the opposite case, when the magnetization is perpendicular to the electron movement. The external magnetic field aspires to turn the magnetic moments of ions along this direction and, consequently, resistance decreases at $\vec{H} \perp \vec{j}$ with increase of the external magnetic field and it increases at $\vec{H} || \vec{j}$. Anisotropic magnetoresistance was many times observed in layered structures. The $\Delta\rho/\rho$ value could be several percents; however, it is enough for the functioning of

Lam Research Ex. 1035 - Page 617
Lam Research Corp. v. Inpria Corp.
IPR2024-00033 - U.S. Patent No. 9,823,564

reading heads for magnetic record of information. Hysteresis of the magnetization results also in that of anisotropic magnetoresistance, which appears as a shift of the resistivity minimum or maximum from zero magnetic field aside to negative or positive magnetic fields depending on the direction of its sweep.

Giant magnetoresistance was discovered in 1988 by Babich et al. [13] in multi-layered ferromagnetic structures Fe/Cr. Later, this phenomenon was observed in lots of other structures and, in particular, in granular metals. The nature of this phenomenon is connected with the spin-dependent scattering or spin-dependent tunneling. It means that if the orientation of electron spin coincides with the orientation of the magnetic moment of impurity, the scattering amplitude is much less than in case of opposite orientations. Similarly for the hopping conductivity, energy of the electron state with its spin aligned opposite to the magnetic moment of a granule is larger than energy of this state when they are parallel to each other. As soon as at the tunnel transition between granules electron keeps its spin, the tunneling demands additional energy and the probability of those transitions is less in the first case (opposite orientations). In a granular metal with the hopping mechanism of conductivity ($x < x_c$), the magnetic moments of superparamagnetic nanogranules are oriented randomly at $H = 0$ and the conductivity of this material is rather small. With increase of the external magnetic field, the magnetic moments of granules arrange in parallel and conductivity grows up. This is NMR.

Due to the symmetry, magnetoresistance cannot depend on the sign of magnetic field and, consequently, it is the even function of the magnetic moment. In the first approximation, it is possible to express the field dependence of magnetoresistance as follows:

$$\rho(H) - \rho(H_s) \propto 1 - \left(\frac{M}{M_s}\right)^2, \tag{20}$$

where M_s is the magnetic moment at saturation and H_s the saturation field. Commonly, the ratio (20) describes well the experimental dependences (see Figure 11.12), but in some cases for the exact fitting of the experimental results it is necessary to take into account terms of the fourth order [12]. The GMR is isotropic in contrast with the anisotropic magnetoresistance and is always negative. In nanocomposites of the type ''ferromagnetic metal in a non-magnetic metallic matrix'', value of this magnetoresistance is determined by the spin-dependent scattering, but in case of a dielectric matrix it exists due to the tunneling of electrons between granules. Usually, its magnitude $\Delta\rho/\rho \approx 5\%$, while the tunneling magnetoresistance can reach several tens of percents.

Lam Research Ex. 1035 - Page 618
Lam Research Corp. v. Inpria Corp.
IPR2024-00033 - U.S. Patent No. 9,823,564

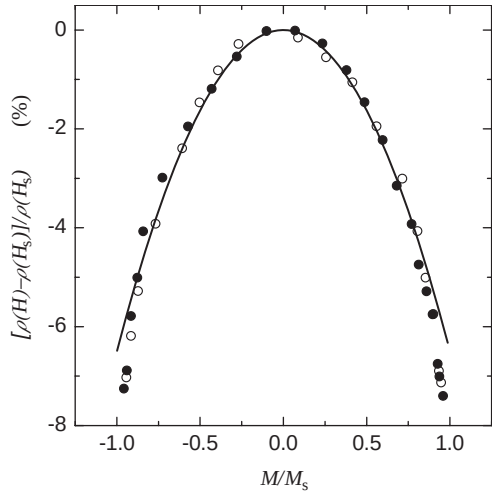


Fig. 11.12. Magnetoresistance vs. magnetization. The solid curve represents the dependence $\Delta\rho/\rho = -0.065(M/M_s)^2$ [4].

Anisotropic magnetoresistance takes place mainly at $x > x_c$, when ferromagnetic cluster is formed. In contrast, the GMR usually is observed at $x < x_c$ in granular metals. These statements could be supported by experimental results on studies of the magnetoresistance in a Fe/SiO_2 nanocomposite, presented in Figure 11.13 [78]. These measurements were carried out in magnetic field lying in the plane of a sample parallel to the current. Under such conditions, the anisotropic magnetoresistance is positive. It is clearly seen from the curves shown in Figure 11.13 that at the metallic side of the percolation transition PMR is observed (curve a, $x \approx 0.7$); similar result was obtained in Ref. [87]. At the same time, in samples with $x < x_c$ (curves b–d) NMR is observed that corresponds to prevailing role of the GMR. The NMR value in the case achieves 5%; it is much more than that for a Ni/SiO_2 system [88] and is close to value obtained in Ref. [87] for a Co/SiO_2 system (4.5%). The results presented in Figure 11.13 also testify that in the vicinity of the percolation transition, the magnetoresistance dependence on composition of a material is extremely strong. The maximum of magnetoresistance $\Delta\rho/\rho(x)$ relates to the x value at which a metallic cluster, penetrating a whole sample volume, is not formed yet. It corresponds to values of x close to the percolation threshold, but still smaller than x_c. The transition from the anisotropic magnetoresistance to GMR (crossover from positive to NMR) under diminishing metal fraction x and the composition dependence of the $\Delta\rho/\rho(x)$ maximum position are well illustrated by results shown in

Lam Research Ex. 1035 - Page 619
Lam Research Corp. v. Inpria Corp.
IPR2024-00033 - U.S. Patent No. 9,823,564

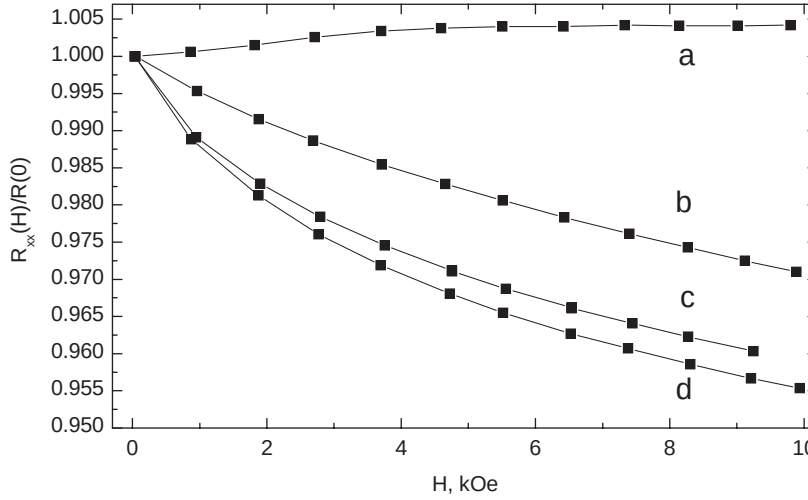


Fig. 11.13. Field dependence of conductance at $T = 77$ K for $Fe_x(SiO_2)_{1-x}$ nanocomposite in metallic state ($x \approx 0.7$, curve a) and in the series of "dielectric" samples (curves b–d) having activation energies, meV: (b) 1.0; (c) 1.25; (d) 2.83 [78].

Figure 11.14. The above-mentioned conclusions are proven to be true by experimental studies [86–90] and by Monte-Carlo simulations [91].

The magnetoresistance of magnetic granular metals with an insulating matrix has been discussed above. The magnetoresistance dependence on composition for nanocomposites with ferromagnetic grains embedded in a non-magnetic metallic matrix behaves in a similar manner. Similarly, the $\Delta\rho/\rho(x)$ functions for both types of matrixes are clearly demonstrated in Ref. [87] and evidently illustrated in Figure 11.15. The change of the granule material, for example substitution of Ni by Co, does not qualitatively affect the magnetoresistance behavior under variation of the ferromagnetic metal content. Also, this substitution causes analogous changes of the magnetoresistance for materials based on both insulating and metallic matrixes. These statements were concluded and proven experimentally by Gerber et al. [87] (see Figure 11.15). Taking into account all these circumstances, the authors of this paper have stated that both phenomena, the spin-dependent scattering and the spin-dependent tunneling, are defined by the energy difference of electronic states in magnetic nanoparticle for different alignments of the electron spin.

Till now, the direct tunneling of electrons from one granule into another has been under consideration. Probability of the spin-dependent tunneling transitions is increasing and the corresponding magnetoresistance substantially grows, if these transitions occur through the intermediate states in an

Lam Research Ex. 1035 - Page 620
Lam Research Corp. v. Inpria Corp.
IPR2024-00033 - U.S. Patent No. 9,823,564

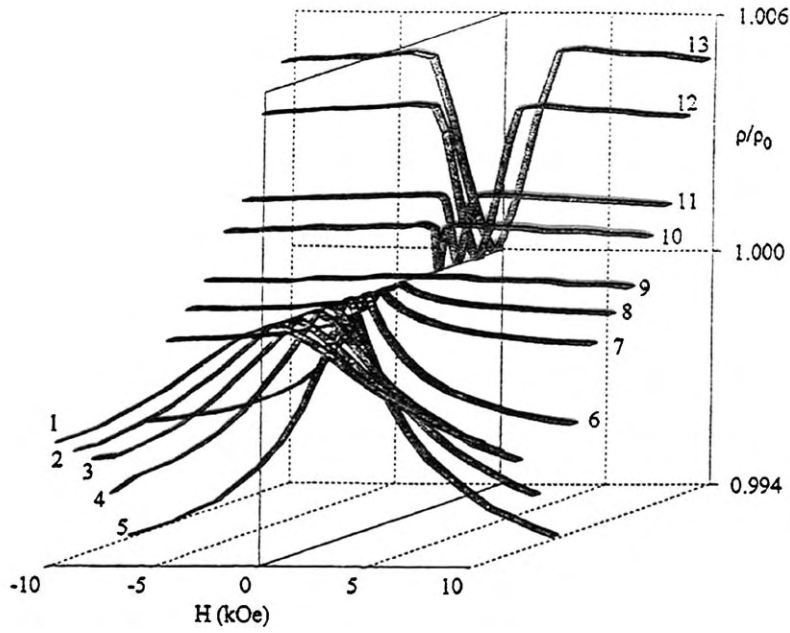


Fig. 11.14. Normalized magnetoresistance of $Ni_x(SiO_2)_{100-x}$ granular metal measured at room temperature. Magnetic field is applied parallel to the current flow, ρ_0 is the zero-field resistivity [88]. Various curves correspond to different metal fraction: (1) 40.6%; (2) 41.4%; (3) 42.2%; (4) 43.1%; (5) 44.7%; (6) 45.9%; (7) 47.8%; (8) 48.4%; (9) 60.0%; (10) 83.5%; (11) 84.8%; (12) 88.3%; (13) 91.3%.

insulating matrix [92,93]. This process is referred to as the high-order tunneling and takes place under a strong influence of the Coulomb blockade effects. Also, in nanocomposites with a metallic matrix, the presence of small particles containing few atoms together with relatively large magnetic nanogranules leads to increase of $\Delta\rho/\rho$ by several orders at decreasing temperature. This is because, due to the presence of fine particles, which are difficult to magnetize, the magnetic moment of a nanocomposite grows when the temperature falls down to the helium value even in strong magnetic fields. This statement is supported by experimental results of the Co/Ag nanocomposite studies and by phenomenological calculations [94]. In these simulations, the electron scattering by nanogranules and fine particles was taken into account.

Taking into account the non-spherical shape of granules leads to deviation of the $\Delta\rho/\rho(H)$ dependence from the square law, which becomes logarithmic in high magnetic fields. This is similar to the superparamagnetic behavior of magnetization. The parametrical dependence $\Delta\rho/\rho \propto (H/T^{8/3})$

Lam Research Ex. 1035 - Page 621
Lam Research Corp. v. Inpria Corp.
IPR2024-00033 - U.S. Patent No. 9,823,564

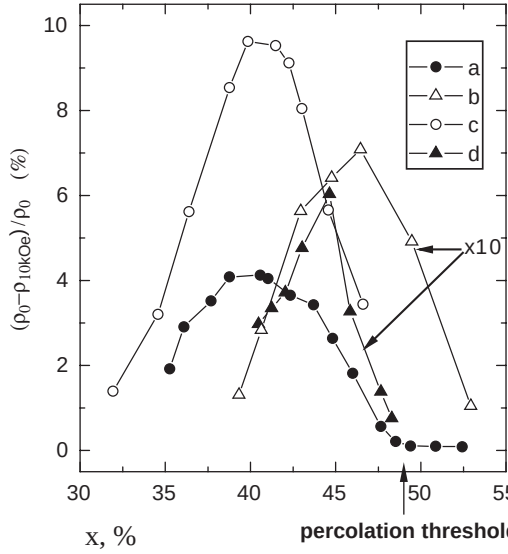


Fig. 11.15. Normalized magnetoresistance as a function of the ferromagnetic metal fraction x: (a) –Co–SiO_2; (b) –Ni–Ag; (c) –Co–Ag; (d) –Ni–Sio_2. The results for Ni-samples are multiplied by 10 [87].

for the case was obtained theoretically and supported by experimental results [95].

5.4. HALL EFFECT

Magnetic field acts on moving electrons by the Lorentz force directed perpendicularly to both the electron velocity and magnetic field. This leads to the appearance of non-diagonal components of the conductivity tensor. Namely, these components cause an electric field perpendicular to both the current flowing through a sample and to the external magnetic field:

$$E = j \times B.$$

The development of the electric field in the direction perpendicular to the current is called Hall effect. At $x \gg x_c$, i.e. under conditions when the metallic cluster is big and well formed running through the whole sample volume, behavior of the Hall effect is similar to that in bulk, homogeneous metals [96,97]. The only difference is that the cluster volume, through which the current flows, fills only a part of the sample volume. The Hall

Lam Research Ex. 1035 - Page 622
Lam Research Corp. v. Inpria Corp.
IPR2024-00033 - U.S. Patent No. 9,823,564

component of the resistivity tensor in magnetic field or, in other words, the Hall resistivity $\rho_{xy} = (E_y/J_x)$ is an important parameter. Here, J_x is electric current along x-axis, and E_y the electric field in the y-direction. Following Ref. [98], it is possible to write:

$$\rho_{xy} = \frac{\rho_{xym}\sigma_m^2 + \rho_{xyd}\sigma_d^2}{(\sigma_m + \sigma_d)^2} \approx \rho_{xym} + \rho_{xyd}\left(\frac{\sigma_d}{\sigma}\right)^2. \quad (21)$$

Here, index m refers to a metal and d to a dielectric phase of the material. It is assumed that the conductivity of the metallic phase is much more than it is for dielectric phase, i.e. $\sigma_m >> \sigma_d$, because the nanocomposite is considered with metallic gains embedded in an insulating matrix. At $x >> x_c$, the conductivity σ_m approximately equals that of the whole sample σ. The difference of the Hall resistance in metal and dielectrics is even stronger than the difference of corresponding resistances for the same materials and, consequently, at $x >> x_c$ in rough approximation the Hall resistance of a nanogranular metal practically coincides with that of the metal, from which granules are formed ($\rho_{xy} = \rho_{xym}$). From the physical point of view, that is because the reduction of the volume fraction giving contribution to the Hall effect is compensated by increase of the density of the current flowing though it. The approximate Eq. (21) could also be used at $x << x_c$, at the dielectric side of the percolation transition far away from it. However, the Hall effect practically is not measurable in this case and the related experimental results are not known. That is the reason why the behavior of the Hall effect only in the vicinity of the percolation threshold will be discussed below.

There are only a few publications on studies of the Hall components of the conductivity tensor near the percolation threshold contrary to its diagonal components (resistance). It is due to difficulties in getting reliable experimental data on the Hall effect (HE) under the hopping conductivity, i.e. at the insulator side of the percolation transition. The majority of experimental results were obtained on studies of semiconductors and they, in many respects, are inconsistent (see Refs. [99,100] and references there). The theoretical calculations and analysis of experimental data were performed by Galperin et al. [100] in 1992; however, since that time the situation practically has not changed. The general opinion is that the hopping Hall effect is much weaker than that at usual band conductivity. The hopping HE is so weak that it makes its measurements very difficult due to the presence of a lot of parasitic voltages exceeding the Hall voltage significantly. The main contribution to these parasitic effects are connected with non-equipotential arrangement (asymmetry) of the Hall probes [96] and with the contribution of the non-coherent mesoscopic effects, caused by the

Lam Research Ex. 1035 - Page 623
Lam Research Corp. v. Inpria Corp.
IPR2024-00033 - U.S. Patent No. 9,823,564

non-uniformity of the percolation cluster on scales smaller than its correlation length.

In ferromagnetic materials, including the granular metals, the Hall resistivity follows the equation:

$$\rho_{xy} = R_0 B + R_s 4\pi M. \tag{22}$$

There are two contributions to ρ_{xy} and so two terms in Eq. (22): the first one (normal HE) is caused by the Lorentz force and is proportional to magnetic induction B; the second one (anomalous HE) is proportional to magnetization M (R_0 and R_s are coefficients of normal and anomalous Hall effects, respectively). The second term is related to the influence of the spin–orbital interaction (SOI) on the scattering of the spin-polarized electrons and essentially exceeds the normal component [97].

In particular, it is established for a granular system $(NiFe)_x/(SiO_2)_{1-x}$ [101–104] that in this case R_s is two orders of magnitude larger than R_0 and can exceed upto four orders of magnitude from R_s obtained in case of a homogeneous metal ($x = 1$). However, despite the high value of the Hall coefficient in these materials, experiments till now were performed mainly at the metallic side of the percolation transition [101–104].

The discussion of Eq. (21) is still correct even for magnetic granular metals, where the Hall effect has the anomalous nature [81], and its behavior at $x >> x_c$ is similar to that in bulk ferromagnetic metals. The only distinction is related to the difference between volumes of a sample and a cluster.

As it was already noted, the HE measurements are especially difficult under the regime of the hopping conductivity and in the vicinity of the percolation transition, where several mechanisms contribute to the Hall effect having almost equal activation energies. In the common semiconductors, the band conductivity is most essential mechanism of the Hall effect, because the electron activation energy for the band and the hopping conductivity are close, and the hopping contribution to the Hall effect is negligible compared to the band contribution. This problem does not exist in case of granular metals, where the activation energy for the band conductivity ($\sim$10 eV) exceeds the activation energy for the hopping process by many orders of magnitude. In magnetic nanocomposites, the anomalous character of the Hall effect makes the hopping HE even more measurable, and the related results are more reliable [97,105]. However, even for granular metals [106] and for analogous materials with magnetic metals [101–105] almost all measurements are limited to the metallic side of the percolation transition. Only a few papers present results of Hall effect studies under hopping conductivity in magnetic nanocomposites [100,107] and these results are discussed below.

Lam Research Ex. 1035 - Page 624
Lam Research Corp. v. Inpria Corp.
IPR2024-00033 - U.S. Patent No. 9,823,564

In semiconductors, the transition to the hopping conductivity is accompanied by the change of mechanism of the Hall effect, and so it is reasonable to expect the analogous change of the mechanism of the anomalous Hall effect (AHE). It is well known that the probability of the tunneling between two centers does not contain terms linear with magnetic field. Therefore, as it was obtained by Holstein [107] to describe the Hall effect, it is necessary to consider at least three centers and to take into account the possibility of the indirect tunnel transitions. As a result, correlations between the Hall and longitudinal resistances become weaker: $\rho_h \propto (\rho_{xx})^m$, where $m<1$. In particular, it is predicted that $m = 0.35$ for the variable-range hopping conductivity and $m = 0.5$ for conductivity with a constant activation energy [100], which is remarkably less compared to the common band conductivity ($m = 1$).

The tunneling in magnetic nanocomposites also does not contain terms, linear with magnetic field. However, there are no detailed theoretical studies of AHE under these conditions. One needs to outline paper [108], in which the case of the strong scattering of the *d-electrons* in ferromagnetic metals including hopping was theoretically considered. Thus, it has been shown that the Hall effect in both magnetic and non-magnetic materials is due to correlated variations (under action of spin–orbit interaction) of probabilities of the transitions between triple states.

There are only very few experimental data on the Hall effect in magnetic nanocomposites at $x<x_c$. The lack of the more detailed studies is caused by the high level of noise inherent to systems with the percolation type of conductivity and by parasitic voltages due to asymmetry of the Hall probes amplified by the strong GMR effect in the case. However, using the special technique for reducing the Hall probes asymmetry and the digital filtration of a signal, the authors of paper [96] succeeded in detecting AHE in films of the Fe/SiO_2 granular metal under the hopping regime of conductivity at the level of 10^{-2}% of the asymmetry voltage.

The Hall effect measurements were carried out in magnetic fields up to 10 kOe at temperatures in the range 77–300 K. There were simultaneously registered voltage V_y between the Hall probes and current I_x flowing through a sample at positive and negative values of the external magnetic field H. The Hall resistance R_h was derived as the difference between transversal resistances $R_{xy} = V_y/I_x$, obtained for positive (R^+_{xy}) and negative (R^-_{xy}) signs of magnetic field: $R_h = (R^+_{xy} - R^-_{xy})/2$. The sign of the Hall effect was detected by a comparison with signal of the reference sample. The HE appeared positive for all samples studied, as well as for single-crystal iron [109].

As already demonstrated, in the given structures at $x<x_c \approx 0.6$ the conductivity is of the hopping type (see Figure 11.11). It confirms that these observations of the HE were carried out under the hopping conductivity.

Lam Research Ex. 1035 - Page 625
Lam Research Corp. v. Inpria Corp.
IPR2024-00033 - U.S. Patent No. 9,823,564

Temperature dependence of the Hall resistivity is described by the same "–1/2" law:

$$\rho_h \propto \exp\left(\frac{T_h}{T}\right)^{1/2}, \tag{23}$$

in which, however, the characteristic temperature T_0 (see Eq. (18)) should be replaced by T_h. That favors the hopping nature of the Hall effect. To prove its anomalous nature and to extract the AHE contribution to the Hall voltage, i.e. with the second term in Eq. (22), two identical samples were prepared with $T_0 = 150$ K. First was served to study the field dependence $\rho_h(H)$; another was used to measure magnetization by means of magneto-optical Kerr effect. Results of these measurements at $T = 77$ and 300 K are shown in Figure 11.16. From this figure, it appears that the field dependences $\rho_h(H)$ and $M(H)$ coincide in ferromagnetic metals as well. One should note that the coefficient of AHE $R_s = \rho_h(H)/M(H)$ achieves 1.6×10^{-7} Ω-cm/G at $T = 77$ K (see inset in Figure 11.16) that exceeds the R_s value in bulk iron by five orders of magnitude [109]. Such strong amplification could not be explained, if one considers only contribution to the Hall voltage from the Hall effect inside separated granules [101–103].

Let us address the parametrical dependence of the Hall resistance on longitudinal resistance (the parameter is temperature) for the above samples with $x < x_c$. It is clear that R_h increases with growth R_{xx} for all samples, i.e. when the temperature is lowered. By fitting this curve with an exponential function ($R_h \propto R_{xx}^m$), it was found that the exponent m varies from 0.44 to

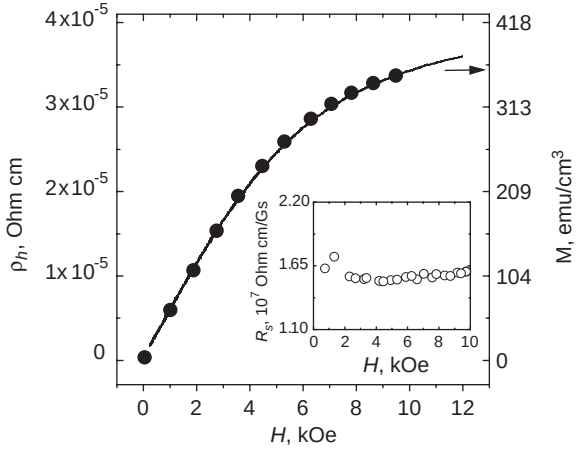


Fig. 11.16. The magnetic field dependence of the Hall resistivity ρ_h (solid circles) and magnetization M (line) at $T = 300$ K. The inset plots extraordinary Hall coefficient R_s at $T = 77$ K [46].

Lam Research Ex. 1035 - Page 626
Lam Research Corp. v. Inpria Corp.
IPR2024-00033 - U.S. Patent No. 9,823,564

0.59 and its average value is $m \approx 0.5$. This is remarkably less than what follows from the models for AHE in ferromagnetic metals [97], where the band conductivity is the main mechanism ($m = 1$ at asymmetric scattering or $m = 2$ for the side jump model). However, these results are in accordance with the predictions for the hopping conductivity in semiconductors [100] and are the reason for the following consideration.

As it was shown [108], the main contribution to the Hall conductivity comes from triangular configurations of granules. It is possible to suggest that there is an optimal size grain a_h and triangles of such grains are responsible for the main contribution to the Hall resistivity. This assumption reminds slightly of the model elaborated by Shklovskii and Efros for the description of the conductivity in semiconductors and for that case proven by a lot of experiments. If triangular configurations of an optimal grain contribute mainly to the Hall resistance, then one should consider the triangles with side of length l_h. The length l_h is approximately equal to the average distance between granules of size a_h. In this approximation, the Hall resistance ρ_h can be expressed as [110]:

$$\rho_h \propto \frac{\rho_{ip}\rho_{pj}\rho_{ji}}{\rho_{ip} + \rho_{pj} + \rho_{ji}} W_{ipj}, \tag{24}$$

where

$$\rho_{ip} \propto \exp\left(\frac{2l_h}{\lambda} + \frac{w_h}{kT}\right) \tag{25}$$

is the resistance of the tunneling transition $i \to p$, λ the characteristic length of the electron wave decay in an insulating matrix, $W_{ipj} \propto \exp(-3l_h/\lambda - w_h/kT)$ the amplitude of interference in unit of magnetic field and $w_h = (e^2/\varepsilon a_h)[1 - (x/x_c)^{1/3}]$ the activation energy for the electronic transition between two originally neutral granules. Thus,

$$\rho_h \propto \exp\left(\frac{l_h}{\lambda} + \frac{w_h}{kT}\right). \tag{26}$$

Consideration of a system with widespread granule sizes shows that in the case when the temperature dependence of resistance of a nanocomposite is described by the "–1/2 "law, the characteristic temperature $T_0 \propto \lambda^{-3/2}$. The temperature dependence of the Hall resistance is described by the same law (see Eq. (18)):

$$\rho_h \propto \exp\left(\frac{T_h}{T}\right)^{1/2}, \tag{27}$$

Lam Research Ex. 1035 - Page 627
Lam Research Corp. v. Inpria Corp.
IPR2024-00033 - U.S. Patent No. 9,823,564

in which, however, T_h substitutes T_0 and $T_h = 2^{-3/2}T_0 \approx T_0/3$. It leads to the scaling relation $\rho_h \propto \rho_{xx}^m$ with $m \approx 0.6$, which is in agreement with experimentally found values.

6. Quantum-Size Effects in Granular Metals Near the Percolation Threshold

As it was mentioned above, even if at least one of the metal particle sizes is of nanometer range, the electron energy quantization could affect the physical properties of the nanogranular metal. The influence of the quantum-size effects (QSE) on the electronic transport in granular metals is especially pronounced in the vicinity of the percolation threshold [85] and it is the main subject of the present section.

Also, there are some other quantum effects additional to the size quantization of an electron energy in the grain which should be taken into account for discussion of conductivity in granular metals near the percolation threshold. One of them is related to the renormalization of e–e interaction in dirty metals [57–59]. The nature of this effect is due to the possibility of two interacted electrons to meet each other once more in a short time. The interference of these two interactions associated with repeated e–e collisions makes the e–e interaction stronger. The reproducibility of e–e collisions is determined by a large number of defects which scatter electrons that randomize their trajectories. The temperature dependence of conductivity for samples with $x > x_c$, but close to x_c, is usually determined by e–e interaction corrections to conductivity and follows the famous law $\sigma(T) \propto \sqrt{T}$ in a wide range of temperatures [82–85]. However, it was found surprisingly that for nanogranular metals with granule concentration very close to x_c the temperature dependence of conductivity deviates from the above law at temperatures below critical one ($T_t \approx 70\,\mathrm{K}$) to a higher resistivity [66,85].

This very surprising result was attributed to the effect of QSE on percolation transition [85]. The scheme of percolating channel very close to percolation threshold is shown in Figure 11.17a. The main feature of the conducting channels is the existence of bottlenecks constituting bridges between larger metallic parts. Those weak links correspond to geometrical constrictions of iron particles in contact. The smallest bridge is the single grain with dimensions determined by size distribution presented in Figure 11.6 for the particular case. Because its size is ~3–4 nm, the QSE should be very actual for such granule at temperatures less than $\approx 100\,\mathrm{K}$. QSE, induced by the confinement of the electron motion, results in the electronic level splitting within the constriction which induces an energy barrier Δ for

Lam Research Ex. 1035 - Page 628
Lam Research Corp. v. Inpria Corp.
IPR2024-00033 - U.S. Patent No. 9,823,564

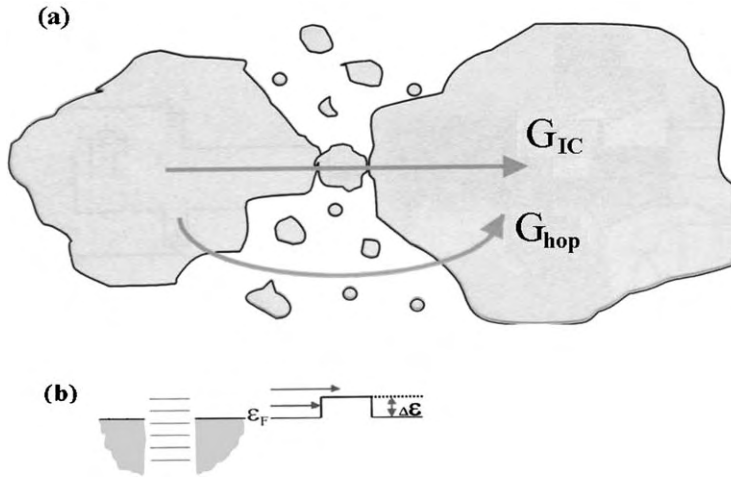


Fig. 11.17. (a) Scheme of percolating channel in the vicinity of a weak link between larger metallic regions. $G_{IC}(T)$ is the conductance through the percolating cluster and $G_{hop}(T)$ corresponds to the hopping conductance over separated granules; (b) energy levels splitting owing to QSE and barrier Δ for conduction electrons within the constriction.

conduction electrons (see Figure 11.17b). The height of such barrier could be estimated as $\Delta = 1/[N(\varepsilon_F)\, L^3] \sim \varepsilon_F/(k_F L)^3$, where $N(\varepsilon_F) \propto m^{3/2}\varepsilon_F^{1/2}/h^3$ is the electronic density of state at the Fermi level and L is granule size acting as a constriction. If L is $\sim$3 nm for barrier height, one has $\Delta = 10$ meV that corresponds with the T_t value.

At temperatures above T_t, electrons pass this barrier freely while at lower temperature conductivity through the barrier is due to electron tunneling. So, raising the temperature results in a crossover from tunneling to metal-type conduction. Thus, temperature induces insulator–metal transition in the same way as a metallic fraction variation near x_c. This transition was cold QSE transition.

Now, let us discuss the temperature dependence of the conductivity. The electron overcoming the barrier has a wavelength $\lambda_\Delta \sim h/(2m\varepsilon_\Delta)^{1/2}$, much longer than the value $\lambda_F \sim h/(2m\varepsilon_F)^{1/2}$, characteristic for the infinite cluster "lakes" (big regions of the cluster). For small enough ε_Δ-values, i.e. $\lambda_\Delta >> l \sim L$, where l is the electron mean free path, electrons in the constriction are localized. This mechanism gives rise to Anderson localization near the percolation threshold and was observed in Pd_xC_{1-x} granular metallic films [66] with structure similar to the system $Fe_{x\approx x_c}-SiO_2$.

Following the Shklovskii model [98], the conductivity of granular metal was analyzed as the sum of two distinct conductances $G_{IC}(T)$ and $G_{hop}(T)$ contributing to the electronic transport. Here, $G_{IC}(T)$ is the conductance related

Lam Research Ex. 1035 - Page 629
Lam Research Corp. v. Inpria Corp.
IPR2024-00033 - U.S. Patent No. 9,823,564

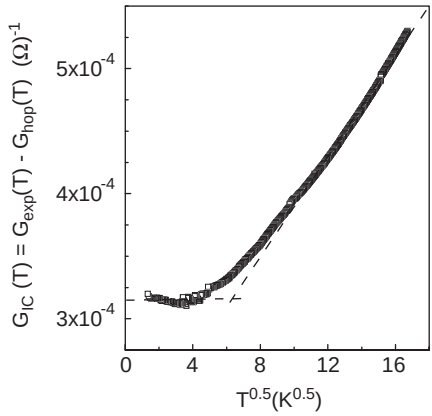


Fig. 11.18. Temperature dependence of the metallic conductance of the infinite cluster $G_{IC}(T)$ deduced from the difference between the experimental conductance and that corresponding to the hopping regime (see text): $G_{IC}(T) = [G_{exp}(T) - G_{hop}(T)]$. The dashed lines are guides for eyes [85].

to the current passing through the infinite cluster and $G_{hop}(T)$ corresponds to the hopping regime over separated granules, $G_{hop}(T) \propto \exp(-\sqrt{T_0/T})$. From the conductivity data, the temperature dependences of these two contributions to sample conductance were deduced. The T_0 value is estimated to be $\sim$12 K and $G_{IC}(T)$ is inferred from the $[G(T) - G_{hop}(T)]$ difference and is shown in Figure 11.18. The temperature dependence of $G_{IC}(T)$ (see Figure 11.18) reveals a drastic crossover at $T \approx 60$ K. That could be considered as a method to determine the T_t value, which is close to the above-mentioned value. At low temperatures, $G_{IC}(T)$ is practically temperature independent and dominates the overall conductivity. Well above 60 K, $G_{IC}(T)$ roughly follows the $\sqrt{T}$ law in accordance with the predictions of the theory of quantum corrections to the metallic conductivity.

The occurrence of the two clearly defined conductivity regimes was interpreted by the predominant role of QSE at low temperature ($T < T_t$) leading to sizeable energy barriers in the smallest granules which contact clusters of bigger size. For $T > T_t \approx \Delta$, the barriers are smeared out by the temperature, the conductivity is metallic, while at low temperatures, electrons can tunnel through the barrier and the conductivity is temperature independent like the barrier transmittance.

The tunnel conductance $g(T)$ of the constriction is defined by thermal-activated tunnel transitions [62]:

$$g(T) \propto \frac{\exp(-L/\lambda_\Delta)(\pi kT/\varepsilon_L)}{\sin(\pi kT/\varepsilon_L)}, \tag{28}$$

Lam Research Ex. 1035 - Page 630
Lam Research Corp. v. Inpria Corp.
IPR2024-00033 - U.S. Patent No. 9,823,564

where $\lambda_\Delta \sim h/(2m\Delta)^{1/2}$, and $\varepsilon_L = \Delta(\lambda_\Delta/L) \sim h^2/mL^2(k_F L)^{1/2}$. The cited relation is valid at $kT/\varepsilon_L < 1$.

At low temperatures, the constriction conductance has minimal value and can be considered as a "switched off" one. However, starting from the temperature $T \sim T_L = \varepsilon_L/k$, the conductance of the constriction rises. Formally, $g \to \infty$ at $T \geq T_L$, so the energy $\varepsilon_L \propto L^{-5/2}$ corresponds to activation energy for the constriction of size L. It means that, at a given temperature, only the contacts with $L > L_T$, where $L_T \sim K_F^{-1}(\varepsilon_F/kT)^{2/5}$ are "switched on". In the "switched on" constriction, the conductance is defined by the above-mentioned renormalization of e–e interaction in dirty metals and depends on temperature as follows: $g = g_0 + \text{constant} \cdot \times T^{1/2}$, where the parameter g_0 is determined by the condition $g(T_L) = 0$, that is $g(T) \propto (T^{1/2} - T_L^{1/2})$. All constrictions of smaller sizes are switched "off" at this temperature.

The temperature-dependent part G_T of the conductivity through the metallic cluster is calculated as the sum of conductances of "open" constrictions. The distribution $f(\varepsilon_L)$ of constrictions over the activation energies can be evaluated from the relevant part of the conductance G_T [85]:

$$f(\varepsilon_L) \propto \left.\frac{\partial[\sqrt{T}(\partial G_T/\partial T)]}{\partial T}\right|_{T=\varepsilon_L/k}. \tag{29}$$

The inferred distribution $f(\varepsilon_L)$ is shown in Figure 11.19 (small circles). The distribution is finally approximated by a log–norm function (solid line in Figure 11.19):

$$f(\varepsilon_L) \propto \exp\left(\frac{-\ln^2(\varepsilon_L/\varepsilon_0)}{2\sigma^2}\right) \tag{30}$$

with $\varepsilon_0 = 1.35\,\text{meV}$ and $\sigma = 1$. It means that the average constriction activation energy is equal to $\langle \varepsilon_L \rangle = \varepsilon_0 \exp(3\sigma^2/2) = 6\,\text{meV}$, i.e. 70 K, which is the transition temperature and is in accordance with T_t. On the same plot, the grains distribution $f(1/L^3)$ over their reciprocal volumes (large circles), which are proportional to the activation energies ε_L, is shown. This distribution of iron grain over size was estimated from the transmission electronic microscopic (TEM) images and is presented in Figure 11.6. Excellent agreement between these two distribution functions is evident. The energy $\langle \varepsilon_L \rangle = 6\,\text{meV}$ corresponds to an average grain size $(\langle L^{-3} \rangle)^{-1/3}$ of 3 nm in accordance with the theoretical estimation. These results provide the evidence that in the very close vicinity of the percolation threshold, the temperature effects may induce insulator–metal transition called the "quantum-size effect transition" (resulting in a crossover from the tunneling

Lam Research Ex. 1035 - Page 631
Lam Research Corp. v. Inpria Corp.
IPR2024-00033 - U.S. Patent No. 9,823,564

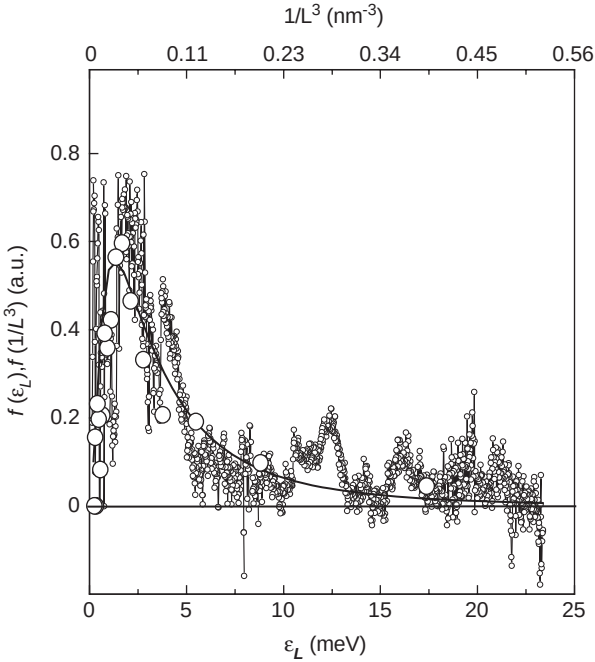


Fig. 11.19. Distribution function $f(\varepsilon_L)$ of tunnel barriers (associated with constrictions of the metallic cluster) over their activation energies (small circles) and distribution function $f(1/L^3)$ of grains over their reciprocal volumes (large circles) [85]. Solid line is the fit of experimental curve by the log–norm function $f(\varepsilon_L) \propto \exp[-\ln^2(\varepsilon_L/\varepsilon_0)/2\sigma^2]$ with $\varepsilon_0 = 1.35\,\text{meV}$ and $\sigma = 1$.

to the metallic-type conductivity) in the same way as a metallic fraction variation near x_c does.

7. Conclusions

The main conclusion is that granular metals produced by sputtering are good candidates for artificial materials with any desirable properties. Nanograins act as atoms in solids forming the material structure and assigning its properties; they are controlled by the materials of grain and matrix, size of granules and inter-granular distance. The advantages of granular materials compared to quantum dots array are the following: grains could be prepared practically from any metal and for matrix almost any insulator could be used, while quantum dots up to now could be grown only epitaxially from very restricted set of semiconductor material. In other words, there are no

Lam Research Ex. 1035 - Page 632
Lam Research Corp. v. Inpria Corp.
IPR2024-00033 - U.S. Patent No. 9,823,564

strong limitations on materials from which granular metals could be obtained by sputtering. Second advantage is that the sputtering is much less expensive than the molecular beam or other epitaxial methods.

To achieve the goal of creating materials with programmable properties, one needs to overcome the problems of getting the granular metal with an identical grain size, shape and inter-grain distance, which means to form the pattern media from the metal granules in an insulator matrix. On the basis of the modern sputtering technology, several groups succeeded to produce metal grains with very sharp size distribution. However, producing the pattern media is the task to be performed. It is clear that self-organization methods could be effective for that, but it is for future job. For the first step on this way, one has to study self-organization processes in more details.

Nevertheless, the above-mentioned goal is not achieved yet; nanogranular materials are widely used for magnetic storage, as an optical media and coating. In this chapter, it was shown that nanogranular metals cover wide ranges of parameters and properties. Their electrical resistance ranges from that typical for good metal up to insulator one, magnetization from ferromagnetic behavior to superparamagnetic and so on.

New very promising possibilities have opened by recently observed quantum effects in nanogranular metals described partly in Section 6. But much more detailed knowledge is needed for their use, so studies on these effects should be continued. Also, some problems known to be unsolved for a long time, such as the temperature dependence of electrical conductivity and a reason for the Hall effect, are also looking for their solution. The affect of shape distribution on magnetic, electrical, optical and relaxation processes is not clear today in detail; the task appears to be too sophisticated but it should be solved at least by computer simulation.

8. Questions for Readers

What is the typical grain size for nanogranular metals?
What are the limitations for materials to produce granular materials by sputtering?
What does x_c mean?
What does superparamagnetism mean?
At what point does ferromagnetic transition occur?
Is domain structure actual for nanogranular metals?
Does Langeven function describe well magnetic field dependence of magnetization? Is it true for temperature dependence?

Lam Research Ex. 1035 - Page 633
Lam Research Corp. v. Inpria Corp.
IPR2024-00033 - U.S. Patent No. 9,823,564

What should be taken into account to describe well the temperature dependence of magnetization?
How does the granular metal conductivity depend on composition?
What is the difference between the temperature dependencies of conductivity for $x > x_c$ and $x < x_c$?
What is the difference between the anisotropic and giant magnetoresistances?
At what range of the granular metal composition is the giant magnetoresistance actual?
How much could be an anisotropic magnetoresistance?

References

1. B. Abeles, P. Sheng, M. D. Coutts, Y. Arie, Adv. Phys. **24** (1975) 407.
2. J. S. Denardin, M. Knobel, L. S. Dorneles, L. F. Schelp, J. Magn. Magn. Mater. **294** (2005) 206.
3. I. S. Beloborodov, A. V. Lopatin, V. M. Vinokur, K. B. Efetov, arXiv:cond-mat, 0603522 (20 March 2006).
4. I. V. Zolotuhin, Ju. E. Kalinin, O. V. Stogney, Novye Napravlenija Fizicheskogo Materialovedenija (in Russian), Voronezh State Vniversity, Voronezh, 2000, p. 360.
5. V. F. Gantmakher, Electrons and Disorder in Solids (translated from Russian by L. I. Man), International Series of Monographs on Physics 130, Oxford University Press, New York, 2005, p. 225.
6. H. Gleiter, Acta Mater. **48** (2000) 1.
7. C. P. Poole, Jr., F. J. Owens, Introduction to Nanotechnology, John Wiley and Sons, Hoboken, NJ, 2003.
8. B. Bushan (Ed.), Springer Handbook of Nanotechnology, Springer, Berlin, 2004, p. 1500.
9. Goddard, et al. (Ed.), Handbook of Nanoscience, Engineering and Technology, CRC Press, Boca Raton, FL, 2002, p. 848.
10. N. S. Halwa (Ed.), Encyclopedia of Nanoscience and Nanotechnology, ASP, Los Angeles, 2004.
11. P. M. Ajayan, L. S. Shadler, P. V. Braun, Nanocomposite Science and Technology, Wiley–VCH, Weinheim, 2003, p. 230.
12. C. L. Chien, Annu. Rev. Mater. Sci. **25** (1995) 129.
13. M. N. Babich, J. M. Broto, A. Fert, F. Nguen Van Dau, F. Petroff, P. Etienne, G. Creuzet, A. Friedrich, J. Chazelas, Phys. Rev. Lett. **61** (1988) 2472.

Lam Research Ex. 1035 - Page 634
Lam Research Corp. v. Inpria Corp.
IPR2024-00033 - U.S. Patent No. 9,823,564

14. R. E. Micher, Biomed. Microdevices **3** (2001) 119.
15. V. I. Goldanskii, L. I. Trakhtenberg, V. N. Flerov, Tunneling Phenomena in Chemical Physics, Gordon and Breach Science Publishers, New York, 1989.
16. C. Murray, C. Kagan, M. Bawendi, Annu. Rev. Mater. Sci. **30** (2000) 545.
17. A. D. Pomogailo, Russ. Chem. Rev. **69** (2000) 53.
18. C. A. Mirkin, MRS Bull **26** (2001) 535.
19. U. Kunze, Superlattices Microstruct. **31** (2000) 3.
20. E. Meyer, H. J. Hug, R. Bennewitz, Scanning Probe Microscopy. The Lab on a Tip, Springer, Berlin, 2003, p. 211.
21. H. Chik, J. M. Xu, Mater. Sci. Eng. R **43** (2004) 103.
22. L. E. Rehn, B. J. Kestel, P. M. Baldo, et al., Nucl. Instrum. Methods Phys. Res. **206** (2003) 490.
23. Yu. N. Parkhomenko, A. I. Belogorokhov, N. N. Gerasimenko, A. V. Irzhak, M. G. Lisachenko, Semiconductors **38** (2004) 572.
24. B. A. Gurovich, D. I. Dolgii, E. A. Kuleshova, E. P. Velikhov, E. D. Ol'shanskii, A. G. Domantovskii, B. A. Aronzon, E. Z. Meilikhov, Physics-Uspechi **44** (2001) 1.
25. S. Y. Chou, Nano-imprint lithography and lithographically induced self-assembly, MRS Bull **26** (2001) 512.
26. P. Rai-Choudhury, Handbook of Microlithography, Micromashining and Microfabrication, SPIE, Bellingham, 1997.
27. M. Sedova, Ph. D. Thesis, in Russian, Moscow, 2002.
28. T. N. Rostovshikova, V. V. Smirnov, S. A. Gurevich, V. M. Kozhevin, D. A. Yavsin, S. M. Nevskaya, S. A. Nikolaev, E. S. Lokteva, Catal. Today **105** (2005) 344.
29. D. A. Zakheim, I. V. Rozhanskii, I. P. Smirnova, S. A. Gurevich, JETP **91** (2000) 553.
30. X. Lin, H. M. Jaeger, C. Sorensen, K. Klabunde, J. Phys. Chem. B **105** (2001) 3353.
31. D. Yu, C. Wang, B. L. Wehrenberg, P. Guyott-Sionnest, Phys. Rev. Lett. **92** (2004) 216802.
32. D. A. Zakheim, I. V. Rozhansky, S. A. Gurevich, Nanotechnology **14** (2003) 366.
33. W. Essam, Rep. Prog. Phys. **43** (1980) 833; D. Stauffer, A. Aharony, Introduction to the Percolation Theory, 2nd edition, Taylor and Francis, London, 1992.
34. B. I. Shklovskii, A. L. Efros, Electronic Properties of Doped Semiconductors, Springer, Berlin, 1984.
35. B. Abeles, H. L. Pinch, J. L. Gittelmann, Phys. Rev. **35** (1975) 247.
36. P. Sheng, Phys. Rev. Lett. **45** (1988) 60.

Lam Research Ex. 1035 - Page 635
Lam Research Corp. v. Inpria Corp.
IPR2024-00033 - U.S. Patent No. 9,823,564

37. Z.-Q. Zhang, P. Sheng, Phys. Rev. B **44** (1991) 3304.
38. D. Toker, D. Azulay, N. Simoni, I. Balberg, O. Millo, Phys. Rev. B **68** (2003) 041403(R).
39. T. Saito, O. Kitakami, Y. Shimada, J. Magn. Magn. Mater. **239** (2002) 310.
40. Z. Zhang, C. Li, S. Ge, J. Magn. Magn. Mat. **198–199** (1999) 30.
41. A. H. Morrish, Physical Principles of Magnetism, Wiley, NY, 1965; S. V. Vonsovskii, Modern Theory of Magnetism (in Russian), Moscow, 1952 or any other textbook on magnetism.
42. S. Honda, T. Okada, M. Nawate, M. Takumoto, Phys. Rev. B **56** (1997) 14556.
43. E. F. Ferrari, F. C. S. da Silva, M. Knobel, Phys. Rev. B **56** (1997) 6086.
44. E. Z. Meilikhov, JETP Lett. **69** (1999) 623.
45. G. Xiao, C. L. Chien, J. Appl. Phys. **67** (1987) 3308.
46. B. A. Aronzon, D. Yu. Kovalev, A. N. Lagarkov, E. Z. Meilikhov, V. V. Rylkov, M. A. Sedova, N. Negre, M. Goiran, J. Leotin, JETP Lett. **70** (1999) 90.
47. E. Z. Meilikhov, JETP **89** (1999) 1184; E. Z. Meilikhov, JETP **90** (2000) 987.
48. N. Negre, B. Raquet, M. Goiran, et al., Physica B **298** (2001) 515.
49. V. V. Rylkov, B. A. Aronzon, A. B. Davydov, D. Yu. Kovalev, E. Z. Meilikhov, JETP **94** (2002) 779.
50. J. Escrig, P. Landeros, J. C. Retamal, D. Altbir, J. d'Albequerque e Castro, Appl. Phys. Lett. **82** (2003) 3478.
51. E. Z. Meilikhov, R. M. Farzetdinova, Microlectron. Eng. **69** (2003) 288.
52. F. Bodker, S. Morup, M. S. Pedersen, et al., J. Magn. Magn. Mater. **177–181** (1998) 925.
53. B. Aronzon, A. Davydov, D. Kovalev, E. Meilikhov, V. Rylkov, M. Sedova, J. Leotin, J. Magn. Magn. Mater. **242–245** (2002) 631.
54. W. A. Phillips, Rep. Prog. Phys. **50** (1987) 1657.
55. S. Kirkpatrik, Rev. Mod. Phys. **45** (1973) 574.
56. A. K. Sarychev, F. Brouers, Phys. Rev. Lett. **73** (1994) 2895.
57. B. L. Altshuler, A. G. Aronov, in: A. L. Efros, M. Pollak (Eds.), Electron–Electron Interaction in Disordered Systems, North-Holland, Amsterdam, 1985.
58. A. A. Abrikosov, Fundamentals of the Theory of Metals, North-Holland, Amsterdam, 1988.
59. P. A. Lee, T. V. Ramakrishnan, Rev. Mod. Phys. **57** (1985) 287.
60. R. Landauer, Z. Phys. **68** (1987) 217.
61. M. Buttiker, Phys. Rev. B **41** (1990) 7906.
62. C. B. Duke, in: E. Burstein, S. Lundqvist (Eds.), Tunneling Phenomena in Solids, Plenum, New York, 1969.

Lam Research Ex. 1035 - Page 636
Lam Research Corp. v. Inpria Corp.
IPR2024-00033 - U.S. Patent No. 9,823,564

63. D. J. Bergman, D. Straud, Solid State Commun. **46** (1992) 149.
64. M. Sahimi, Application of Percolation Theory, Taylor and Francis, Bristol, PA, 1994.
65. A. B. Pakhomov, X. Yan, Phisica A **229** (1996) 402; A. B. Pakhomov, X. Yan, Solid State Commun. **99** (1996) 139.
66. A. Carl, G. Dumpich, E. F. Wassermann, Phys. Rev. B **50** (1994) 4802.
67. X. X. Zhang, Chuncheng Wan, H. Liu, Z. Q. Li, P. Sheng, Phys. Rev. Lett. **86** (2001) 5562.
68. D. E. Khmelnitskii, JETP Lett. **32** (1980) 248.
69. A. G. Aronov, M. E. Gershenzon, Yu. E. Zhuravlev, Sov. Phys. JETP **60** (1984) 554; M. E. Gershenzon, P. M. Echetrnach, H. M. Bozler, A. L. Bogdanov, B. Nilsson, Phys. Rev. Lett. **74** (1995) 446.
70. B. A. Aronzon, N. K. Chumakov, T. Dietl, J. Wrobel, JETP **78** (1994) 216.
71. B. A. Aronzon, N. K. Chumakov, A. A. Snarskii, J.-M. Broto, H. Rakoto, J. Leotin, Proceedings of the 24th Conference on the Physics of Semiconductors, World Scientific, Singapore, 1998, p. 43.
72. P. Sheng, Philos. Mag. B **65** (1992) 357.
73. A. L. Efros, B. I. Shklovskii, Phys. Status Solidi B **76** (1976) 475.
74. A. M. Dykhne, Sov. Phys. JETP **32** (1971) 63.
75. C. J. Adkins, J. Phys.: Condens. Matter. **1** (1989) 1253; C. J. Adkins, in: P. P. Edwards, C. N. R. Rao (Eds.), Metal–Insulator Transitions Revisited, Taylor & Francis, London, 1996.
76. I. P. Zvyagin, R. Keiper, Philos. Mag. B **81** (2001) 9; I. P. Zvyagin, R. Keiper, Phys. Status Solidi B **230** (2002) 151.
77. B. Aronzon, A. A. Likalter, V. V. Ryl'kov, A. K. Sarychev, M. A. Sedova, A. M. Varfolomeev, Phys. Status Solidi B **205** (1998) 151.
78. B. A. Aronzon, A. E. Varfolomeev, D. Yu. Kovalev, A. A. Likalter, V. V. Rylkov, M. A. Sedova, Phys. Solid State **41** (1999) 857.
79. P. Sheng, B. Abeles, Y. Arie, Phys. Rev. Lett. **31** (1973) 44.
80. E. Z. Meilikhov, JETP **88** (1999) 819.
81. B. A. Aronzon, E. Z. Meilikhov, V. V. Rylkov, A. N. Lagarkov, M. A. Sedova, I. A. Evstuhina, D. Yu. Kovalev, N. Negre, M. Goiran, J. Leotin, Physica B **284–288** (2000) 1980.
82. A. Carl, G. Dumpich, D. Hallfarth, Phys. Rev. B **39** (1989) 3015.
83. N. Savvides, S. P. McAlister, C. M. Hurd, I. Shiozaki, Solid State Commun. **42** (1982) 143.
84. Y. Koike, M. Okamura, T. Fukase, J. Phys. Soc. Jpn. **54** (1985) 3018.
85. B. Raquet, M. Goiran, N. Negre, J. Leotin, B. Aronzon, V. Rylkov, E. Meilikhov, PRB **62** (2000) 17144.
86. B. A. Aronzon, A. Granovskii, D. Kovalev, E. Meilikhov, V. Rylkov, M. Sedova, JETP Lett. **71** (2000) 469.

Lam Research Ex. 1035 - Page 637
Lam Research Corp. v. Inpria Corp.
IPR2024-00033 - U.S. Patent No. 9,823,564

87. A. Milner, A. Gerber, B. Groisman, M. Karpovsky, A. Gladkih, Phys. Rev. Lett. **76** (1996) 475.
88. J. L. Gitelman, Y. Goldstein, S. Bozovski, Phys. Rev. B **5** (1972) 3609.
89. A. Gerber, A. Milner, G. Deutcher, M. Karpovsky, A. Gladkih, Phys. Rev. Lett. **78** (1997) 4277.
90. K. Yakushiji, S. Matani, K. Takanashi, J.-G. Ha, H. Fujimori, JMMM **212** (2000) 75.
91. C. Xu, P. M. Hui, Z. Y. Li, J. Appl. Phys. **90** (2001) 365.
92. S. Matani, S. Takanashi, K. Takanashi, K. Yakushiji, S. Maekawa, H. Fujimori, Phys. Rev. Lett. **81** (1998) 2799.
93. T. Zhu, Y. J. Wang, Phys. Rev. B **60** (1999) 11918.
94. Y. Lu, C. Xu, Z.-Y. Li, JMMM **223** (2001) 267.
95. E. Z. Meilikhov, B. Raquet, JETP **92** (2001) 816.
96. C. M. Hurd, The Hall Effect in Metal and Alloys, Plenum, NY, 1972; L. Berger, G. Bergmann, in: C. L. Chien, C. R. Westgate (Eds.), The Hall Effect and Its Applications, Plenum, NY, 1980; E. V. Kuchis, Gal'vanomagnitnye effecty i methody ih issledovaniya (Galvanomagnetic effects and methods of their studies) (in Russian), Radio i Svyaz', Moscow, 1990.
97. A. V. Vedyaev, A. B. Granovskiĭ, O. A. Kotel'nikova, Kineticheskie Yavleniya v Neuporyadochennykh Ferromagnitnykh Splavakh (Kinetic Phenomena in Disordered Ferromagnetic Alloys) (in Russian), Moscow State University, Moscow, 1992.
98. B. Shklovskii, Sov. Phys. JETP **45** (1977) 152.
99. N. F. Mott, E. A. Devis, Electron Processes in Non-Crystalline Materials, Clarendon Press, Oxford, 1979.
100. Yu. M. Galperin, E. P. German, V. G. Karpov, Sov. Phys. JETP **72** (1991) 193.
101. A. B. Pakhomov, X. Yan, Y. Xu, Appl. Phys. Lett. **79** (1996) 6140.
102. A. B. Pakhomov, X. Yan, Solid State Commun. **99** (1996) 139.
103. A. B. Pakhomov, X. Yan, N. Wang, et al., Physica A **241** (1997) 344.
104. A. B. Pakhomov, X. Yan, B. Zhao, Appl. Phys. Lett. **67** (1995) 3497.
105. X. X. Zhang, C. Wan, H. Liu, Z. Q. Li, P. Sheng, Phys. Rev. Lett. **86** (2001) 5562.
106. X. N. Ying, N. Wang, A. B. Pakhomov, et al., Phys. Rev. B **53** (1996) 14032.
107. T. Holstein, Phys. Rev. **124** (1961) 1329.
108. A. V. Vedyaev, A. B. Granovskii, Sov. Phys. Solid State **28** (1986) 2310.
109. I. S. Grigoriev, E. Z. Meilikhov (Eds.), Handbook of Physical Quantities, CRC Press, Boca Raton, FL, 1997, p. 902.
110. M. Gruenewald, H. Mueller, P. Thomas, D. Wuertz, Solid State Commun. **38** (1981) 1011.

Lam Research Ex. 1035 - Page 638
Lam Research Corp. v. Inpria Corp.
IPR2024-00033 - U.S. Patent No. 9,823,564

Chapter 12

Organized Organic Thin Films: Structure, Phase Transitions and Chemical Reactions

S. Trakhtenberg

Center for Green Chemistry, University of Massachusetts Lowell, One University Avenue, Lowell, MA 01854, USA

1. Introduction . . . 640
2. Preparation and Structure of Langmuir–Blodgett Films . . . 645
   2.1. Langmuir Monolayers . . . 646
   2.2. Film Transfer . . . 648
   2.3. Structure of Langmuir–Blodgett Films . . . 649
3. Temperature-Induced Phase Transitions in Langmuir–Blodgett Films . . . 650
   3.1. Order–Disorder Transitions . . . 651
   3.2. Effect of Phase Transitions on the Reactivity of Langmuir–Blodgett Films . . . 652
4. Self-Assembled Films . . . 654
   4.1. Covalently Bonded Silane Monolayers . . . 655
   4.2. Stability of Self-Assembled Silane Films . . . 656
   4.3. Self-Assembled Silane Multilayers . . . 657
5. Conclusions . . . 659
Acknowledgments . . . 661
References . . . 661

This chapter describes two types of organized organic thin films, namely Langmuir–Blodgett (LB) films and self-assembling films. These films are interesting both fundamentally as ordered two-dimensional systems and practically due to their applications as proxy systems for biological membranes and atmospheric aerosols and for their potential usefulness in microelectronics and non-linear optics. In the first section, the historical account of research on organized organic thin films is presented, and both LB and self-assembly techniques are introduced. The second section discusses films on air–water interface (Langmuir films) and their transfer onto solid support, resulting in LB films. The third section deals with temperature-induced phase transitions in LB films. The fourth section describes self-assembled films and focuses on silane mono- and multilayers. The fifth section describes the use of organized organic thin films as proxies for atmospheric surfaces and also presents some thoughts on possible future directions and potential opportunities for these systems.

THIN FILMS AND NANOSTRUCTURES, vol. 34
ISSN 1079-4050
DOI: 10.1016/S1079-4050(06)34012-4

© 2007 by Elsevier Inc.
All rights reserved.

Lam Research Ex. 1035 - Page 639
Lam Research Corp. v. Inpria Corp.
IPR2024-00033 - U.S. Patent No. 9,823,564

1. Introduction

The effects of spreading oil on the surface of water were known already to mariners in antiquity [1]. They carried casks of oil on their ships to be dumped into the water in case of storm, which had a soothing effect on the waves. This practice was not forgotten through Dark Ages, and was mentioned, for example, in the Venerable Bede's *Ecclesiastical History of the English Nation* [2], and even survived into modern times.

What is of interest for us now is not the storm-soothing mechanism (belonging to the field of fluid mechanics and hydrodynamics), but the ability of a relatively small amount of oil to spread over large areas of water surface, or, to be more precise, to form thin film on the air–water interface.

In the 18th century, Benjamin Franklin [3] was experimenting with spreading oil on the surface of Clapham Pond (Pennsylvania) and found out that just one teaspoon of oil is enough to cover half an acre of water. Later an interest arose in films consisting not of oils but of surfactants. The word "surfactant" means surface-active; namely surfactants are the substances for which it is energetically most favorable to occupy an interface between two phases [4]. Normally surfactant molecules are amphiphilic. They consist of two parts, namely a polar, hydrophilic "head" group and a non-polar, hydrophobic "tail". Some amphiphilic molecules have two tails, and sometimes the terminal group (farthest from the "head") is considered as a separate entity, but in general, any amphiphilic molecule has polar and non-polar regions.

In the early 20th century, Langmuir [5] prepared ordered films of amphiphilic molecules on air–water interface and systematically studied their structure. In his experiments solutions of water-insoluble amphiphiles in a volatile organic solvent were prepared. A drop of solution has to be carefully placed on the air–water interface. After a few minutes the solvent evaporates, and the non-volatile amphiphilic molecules remain on the surface. The hydrophilic heads of the molecules (and the first methylene group of the tail, closest to the head) are immersed in water, while the tails are prevented from getting into the water phase by their hydrophobic nature.

The structure of the films can be controlled by changing the area occupied by the amphiphilic molecules [6]. Langmuir troughs are equipped with a movable barrier and pressure sensor. When no external pressure is applied, the Langmuir films are usually described as a two-dimensional gas. Like gas molecules, the amphiphiles are spread on the entire available interface so that the average area per molecule is significantly larger than the molecular cross-sectional area. The "gas phase" Langmuir film consists of totally disordered molecules not interacting with each other, as schematically presented in Figure 12.1A.

Lam Research Ex. 1035 - Page 640
Lam Research Corp. v. Inpria Corp.
IPR2024-00033 - U.S. Patent No. 9,823,564

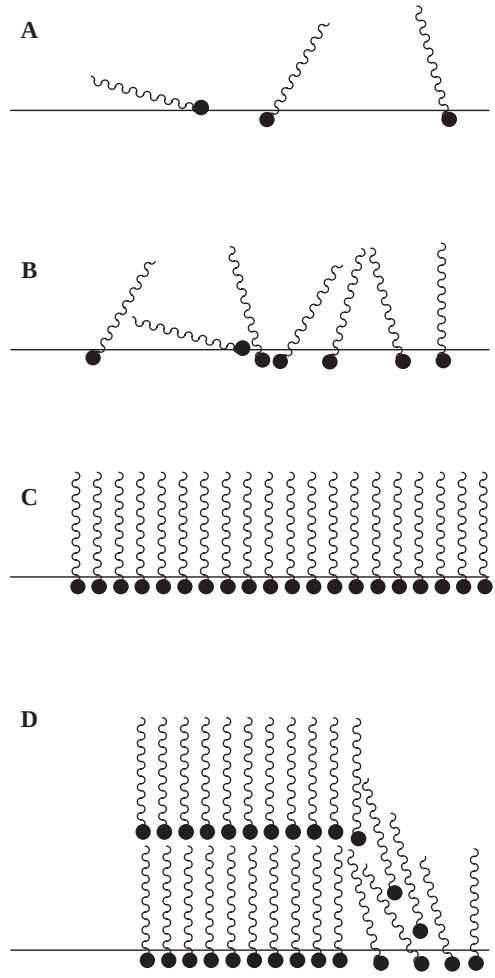


Fig. 12.1. Structure of Langmuir film: (A) gas phase; (B) liquid phase; (C) solid phase; (D) collapse.

As the barrier moves, the area available to the amphiphilic molecules decreases. This automatically causes the average area per molecule as well as the average distance between the molecules to decrease. Initially, it does not affect the interaction between the molecules (or domains), since they are still far away from each other. In this situation, the pressure is inversely proportional to the area per molecule, according to the two-dimensional ideal gas law. Eventually, however, the intermolecular distances are short enough that the intermolecular interactions can no longer be neglected, and the film

Lam Research Ex. 1035 - Page 641
Lam Research Corp. v. Inpria Corp.
IPR2024-00033 - U.S. Patent No. 9,823,564

behavior becomes non-ideal. This is described as a ''liquid'' phase, which is depicted schematically in Figure 12.1B. The pressure rises with decreasing area faster than is the case for the ''gas'' films.

Eventually, the decrease of the available area causes the molecules to minimize the space they occupy, which, as in three dimensions, results in the film becoming ''solid'', i.e. acquiring order, where the individual molecules are aligned with each other as shown in Figure 12.1C. At this point the intermolecular distances are close to the molecular diameter, and steric repulsion is significant. Therefore, any minute change in the area per molecule causes dramatic increase in pressure. Finally, the area per molecule becomes too small. This causes the film to collapse, forming multilayers as shown in Figure 12.1D. As a result, the pressure undergoes a sharp drop.

The pressure represented as function of the surface area is referred to as pressure–area or π–A isotherm. A schematic representation of a pressure–area isotherm is presented in Figure 12.2, with the dotted vertical lines separating the different phases and the regions where phases coexist. It is important to take into account that the actual form of the isotherm depends on a variety of factors, such as temperature, pH and the nature of the amphiphilic molecule.

The ''solid'' films on the air–water interface, while fundamentally interesting, do not seem to have any obvious potential practical applications. On the other hand, the importance of organic films on solid substrates cannot be overestimated. Apart from applications in electronics, optics, protective coatings, etc., organized organic thin films are an excellent model system for

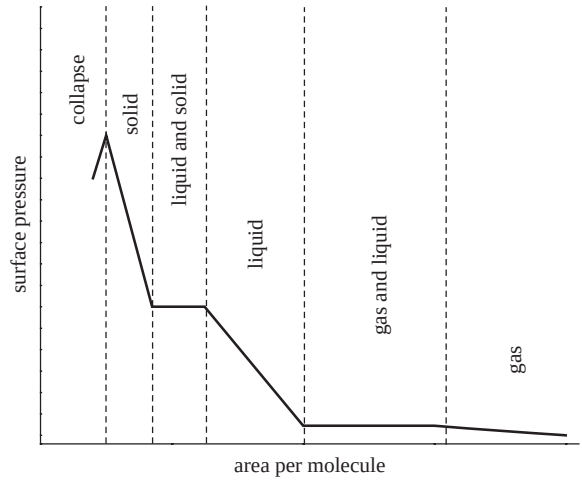


Fig. 12.2. Pressure–area (π–A) isotherm of a Langmuir film.

Lam Research Ex. 1035 - Page 642
Lam Research Corp. v. Inpria Corp.
IPR2024-00033 - U.S. Patent No. 9,823,564

oriented basic research. Due to the tendency of surfaces to adsorb contaminants in the process of lowering free energy, almost all "real life" surfaces are fully or partially covered with organic materials. Hence, it is important to investigate organic surfaces. However, in order to study these interactions properly, well-defined organic surfaces should be chosen, and methods of preparing such surfaces reproducibly are essential.

In 1934, Langmuir's trainee, Blodgett [7], built the first trough for transferring the films from air–water interface onto a solid substrate, and the first LB films were prepared. The transfer is represented schematically in Figure 12.3. First a Langmuir film is prepared on the air–water interface. The film is compressed until it becomes solid, after which the pressure is maintained constant. Next a vertically oriented hydrophilic substrate is slowly immersed into water. The hydrophobic tails of the amphiphiles do not have a

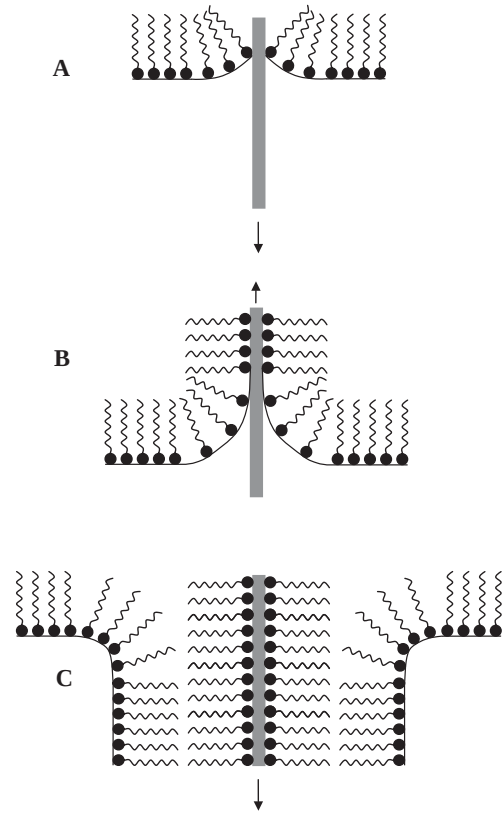


Fig. 12.3. Langmuir–Blodgett film transfer: (A) first downstroke, (B) upstroke and (C) subsequent downstrokes.

Lam Research Ex. 1035 - Page 643
Lam Research Corp. v. Inpria Corp.
IPR2024-00033 - U.S. Patent No. 9,823,564

strong affinity for the substrate, and therefore the transfer does not occur at this stage. Finally, the immersed substrate is slowly pulled up from the water through the film, while pressure is still maintained constant. Due to the affinity between the hydrophilic heads and the hydrophilic substrate as well as the constant pressure applied by the movable barrier, the film is transferred from the surface of water onto the substrate while maintaining its structure.

If preparation of thicker films is desirable, this process can be repeated. It should be noted, however, that on the subsequent immersions of the substrate, its surface is hydrophobic; therefore, the film is going to be transferred on both inwards and outwards trips. This results in the number of layers in a Langmuir–Blodgett (LB) film typically being odd. If, for some reason, a film with an even number of layers is required, then a hydrophobic substrate should be chosen, which enables transfer of the film during the first immersion as well.

In the 1940s, it was demonstrated in the pioneering work of Zisman and coworkers [8] that the LB technique is not the only way to create an organized organic monolayer on a solid substrate. It was demonstrated that when a compatible substrate is exposed to a solution of an amphiphilic compound, the dissolved molecules form a self-assembled monolayer on the substrate surface. Such films maintain their structural integrity after they are removed from solution. The most common examples of such films are organosulfur films on gold substrates [9] and alkyltrichlorosilane films on silicon dioxide substrates [10]. Compared with the LB films, the self-assembled films are somewhat less ordered. On the other hand, these films are easier to prepare, since they do not require special instrumentation and can easily be deposited on both planar and non-planar substrates. Also, in many cases the amphiphilic molecules which make the self-assembled film are chemisorbed on the substrate. Such films are more stable when heated or exposed to solvents than are typical LB films, which are held to the substrate by non-covalent interactions.

While preparation of multilayers by the self-assembly method is less straightforward than that by the LB method, it still can be accomplished [11–13]. The amphiphilic molecule should have a functionalized terminal group. In order to avoid either uncontrolled multilayer deposition or the simultaneous attachment of both head and terminal groups to the substrate, the terminal group should be protected. After the first monolayer is deposited, the sample should be removed from the solution, the terminal groups should be deprotected and the sample should be returned to the solution for deposition of the second layer. Subsequent deprotections and reimmersions allow one to coat the desired number of layers onto the substrate.

Thus far, methods of organizing small molecules into mono- and multilayers have been discussed. However, both LB and self-assembly techniques allow deposition of polymer films as well. Two approaches to preparing polymer films by LB method have been described. An amphiphilic polymer film can be

Lam Research Ex. 1035 - Page 644
Lam Research Corp. v. Inpria Corp.
IPR2024-00033 - U.S. Patent No. 9,823,564

created on air–water interface and transferred onto the solid substrate by the conventional LB technique [14]. Amphiphilic polymers typically have a hydrophilic backbone, such as polyvinyl alcohol or polyethylene oxide, and hydrophobic side groups. LB films prepared from polymers with hydrophilic side groups attached to a hydrophobic backbone have also been reported. The transfer of polymer films onto a solid substrate is technically more complicated than that of monomer films, due to the higher viscosity of the former [6]. However, modifications in the polymer structure, such as the introduction of spacers into the backbone, allow additional methods of controlling the structure of the resulting films [15]. Another method of polymer film formation by the LB method is to prepare films from polymerizable monomers, such as cinnamic acid derivatives [16]. These films can be subsequently polymerized when already on solid support, thus avoiding the difficulties of transferring the polymer films from air–water interface. The LB technique allows arrangement of monomers into highly ordered structures prior to polymerization, which allows one to obtain polymers with improved electrical [17] and optical [18] properties. However, in many cases polymerization, while producing improved thermal and mechanical stability, is accompanied by changes in intermolecular distances which disrupt the order of the film and create multiple defects [19].

The self-assembly method of forming multilayer polymer films, commonly referred to as ''layer-by-layer deposition'', has gained tremendous popularity in recent years. In this method, a precleaned substrate is repeatedly immersed in aqueous solutions of anionic and cationic polymers with a brief rinse between immersions. At each immersion, a monolayer of polymer is deposited onto the surface, bearing the opposite charge of that acquired at the previous immersion. Rinsing steps remove the excess polymer, ensuring that not more than one monolayer is deposited at each immersion. This process can be repeated a number of times, resulting in robust films of desired thickness held together by electrostatic interactions between neighboring polycationic and polyanionic layers [20].

As can be seen from the above description, the field of organized organic thin films is rather broad. This chapter therefore should be taken as a sparse survey that to some extent reflects particular topics of interest to the author. Detailed coverage of this area can be found in more comprehensive monographs [6,21,22] and reviews [23–29].

2. Preparation and Structure of Langmuir–Blodgett Films

The preparation of LB films consists of two distinct steps. First, an ordered film, referred to as Langmuir monolayer, is prepared on an air–liquid

Lam Research Ex. 1035 - Page 645
Lam Research Corp. v. Inpria Corp.
IPR2024-00033 - U.S. Patent No. 9,823,564

interface. Then the film is transferred onto a solid support. The resulting film, referred to as LB film, is also ordered; however, its structure is generally different from that of the Langmuir monolayer.

2.1. LANGMUIR MONOLAYERS

The apparatus used for preparing the films is referred to as a trough. Troughs are equipped with pressure and temperature sensors and one or more movable barriers, allowing the surface area of the trough to be changed. They are usually made from easy-to-clean materials such as Teflon. While cleanliness is crucially important, it is necessary to avoid the use of surfactants, traces of which can incorporate into Langmuir films; therefore, only inorganic detergents should be used. Cleaning the trough should be concluded by rinsing with large amounts of pure water.

The clean trough is filled by the liquid on the surface of which the films will be prepared. This liquid is referred to as the subphase. Usually the subphase is either pure water or a dilute aqueous solution of an inorganic salt, typically with a divalent cation, such as cadmium. The nature of the cation and its concentration, as well as the pH and temperature of the subphase, were found to play an important role in the structure and stability of the films.

The dilute solution ($\sim 10^{-2}$ M) of the amphiphilic substance, most commonly a long-chain fatty acid, should be prepared in a volatile organic solvent immiscible with the subphase, such as chloroform. The required amount of solution should be carefully transferred dropwise onto the air–subphase interface. It is important not to allow the drops to sink into the subphase, since on one hand it will result in contaminating the subphase, and on the other hand the "drowned" amphiphile molecules will not become part of the film, thus introducing error into the calculations of area per molecule. The drops of solution should be placed on the surface at large distances from each other, in order to allow the liquid to spread unobstructed.

As the solvent evaporates, the amphiphilic molecules remain on the air–subphase interface. Their hydrophilic heads are immersed into the aqueous subphase while the hydrophobic tails are protruding in the air. While the surface concentration of the molecules and the surface pressure are sufficiently low, the system can be treated as a two-dimensional gas, which can be described by the following equation of state:

$$\pi A = k_B T \tag{1}$$

where π is the surface pressure, A the area per molecule, k_B the Boltzmann constant and T the temperature [4]. At room temperature (20°C) and surface pressure of 0.1 mN/m, at which conditions a typical Langmuir film is in gas

Lam Research Ex. 1035 - Page 646
Lam Research Corp. v. Inpria Corp.
IPR2024-00033 - U.S. Patent No. 9,823,564

phase, the corresponding area per molecule can be estimated from Eq. (1) to be of $\sim$4000 Å^2.

As the movable barriers compress the surface, decreasing the area per molecule, the surface pressure rises until the vapor-to-liquid phase transition occurs [30–33]. At this stage the two-dimensional gas (vapor) coexists with two-dimensional aggregates (liquid). The transition surface pressure, as well as area per molecule in both gas and liquid regions, is temperature dependent. For example, for *n*-pentadecanoic acid monolayers prepared on surface of 0.01 M HCl at 20°C, the transition surface pressure was found to be 0.132 mN/m, area per molecule in the two-dimensional vapor phase was 1500 Å^2, and area per molecule in the two-dimensional liquid phase was 41.5 Å^2 [32]. As the temperature increases, transition pressure and area per molecule in the liquid phase increase too, while the area per molecule in the coexisting vapor phase decreases. It should be noted here that, as in three-dimensional systems, the first-order vapor-to-liquid phase transition can be observed only over limited range of temperatures, i.e. only at temperatures above the triple point but below critical temperature. In a typical preparation of LB films, relatively large amounts of the amphiphilic substance are used, so that initial area per molecule is usually $\sim$50 Å^2, which corresponds to the state in which the two-dimensional vapor and liquid phases coexist.

As the compression of the surface continues, the vapor phase disappears and the film is in the liquid state, also referred to as liquid expanded (LE, E or L_1) state. The area per molecule in this state is in the range of 25–40 Å^2 for fatty acid films, which is intermediate between those in gaseous and solid (i.e. condensed) states. The surface pressure increases as the area per molecule decreases. The molecules in the liquid expanded state interact strongly with each other but are not closely packed. Defects, such as *gauche* conformations, can be found in the alkyl tails of the molecules.

When the area per molecule approaches the cross-sectional area of the molecule, the new condensed phase starts to form [34]. Initially it coexists with the expanded phase, resulting in the second plateau on the isotherm, characteristic of a first order phase transition. The new phase is referred to as liquid condensed (LC or L_2). Although called ''liquid'' for historical reasons, this phase is characterized by long range order and close packing of the molecules. In this phase, molecules are packed in a centered rectangular lattice, so that each molecule has six nearest neighbors forming a slightly distorted hexagon. The molecules are tilted with respect to the surface normal in the direction of the nearest neighbor along the short side of the unit cell. The tilt angle is of $\sim$30° for long-chain fatty acids [35]. As the area per molecule continues to decrease, the tilt angle decreases, and the surface pressure increases until the next phase transition occurs, when the direction

Lam Research Ex. 1035 - Page 647
Lam Research Corp. v. Inpria Corp.
IPR2024-00033 - U.S. Patent No. 9,823,564

of the tilt changes. In the new phase, referred to as L'_2, the chains are tilted toward the next nearest neighbor. As the compression of the film continues, the tilt angle decreases farther until the chains' orientation becomes normal to the surface. The lattice may be hexagonal (superliquid or LS phase) [36] or centered rectangular (solid S and close-packed solid CS phases) [35]. If the compression of the film continues, the pressure rises abruptly until the film collapses due to formation of multilayer structures, accompanied by a drop in surface pressure [6].

It is possible to control the pressures at which the phase transitions occur by fine tuning the strength of intermolecular interactions between the amphiphilic molecules. The interactions between the hydrophobic tails depend on temperature [37], while the interactions between the hydrophilic heads depend on the chemical composition of the subphase, namely its pH and ionic strength [4]. For example, the fatty acid molecules in films prepared on subphase with high pH and high concentration of divalent salt, such as $CaCl_2$ or $CdCl_2$, are normal to the surface, i.e. are in "solid" state, even at low pressures. Pressure–area isotherms of such films are "featureless"; compressed films are stable and easy to transfer [38].

2.2. FILM TRANSFER

After the desired pressure is reached, the film is typically left for a while in the compressed state in order to ensure pressure equilibration throughout the system. If maintaining the constant pressure does not cause significant decrease in the average area per molecule over time, the film is considered stable and can be transferred onto the substrate.

Film transfer is achieved by moving the vertically oriented substrate through the surface of the film, alternately in down and up directions, while maintaining constant surface pressure. For hydrophilic substrates (which are typically used) three scenarios can be distinguished, namely the first downstroke, upstrokes and subsequent downstrokes. At the first downstroke, the hydrophilic substrate is interacting with the hydrophobic outer surface of the film. Since the affinity between the two is low, the film stays unchanged while the substrate passes through the film as shown in Figure 12.3A. During the upstroke the hydrophilic substrate interacts with hydrophilic inner surface of the film. Due to constant pressure being maintained by the barriers, the film is being transferred onto the substrate as the substrate passes through the air–subphase interface. The hydrophilic heads of the amphiphilic molecules are situated on the substrate surface, while the hydrophobic tails are dangling in the air, rendering the substrate hydrophobic as represented in Figure 12.3B. At the subsequent downstrokes,

Lam Research Ex. 1035 - Page 648
Lam Research Corp. v. Inpria Corp.
IPR2024-00033 - U.S. Patent No. 9,823,564

the hydrophobic film on the substrate surface interacts with the hydrophobic outer surface of the film on the air–subphase interface. This interaction also results in the transfer of film onto the substrate surface. Here the hydrophobic tails of the newly deposited film form a bilayer with the hydrophobic tails of the film deposited during the previous upstroke, while the hydrophilic heads are situated on the substrate–subphase interface, because of which the substrate is rendered hydrophilic again as shown in Figure 12.3C. This process allows one to obtain hydrophobic mono- or multilayers composed of odd number of layers. If the substrate is hydrophobic rather than hydrophilic, the film transfer occurs at the first downstroke as well and the number of layers in the resulting multilayers will be even. Regardless of the substrate nature, the mode of deposition described above is most common; it usually results in stable films and is referred to as Y-deposition [39].

Other deposition modes were observed as well, namely X-deposition, when the film transfer occurs only at downstrokes [39], and Z-deposition, when the film transfer occurs only at upstrokes [6]. X- or Z-mode deposition occurs more commonly in the films consisting of amphiphilic molecules where either the head group is only weakly polar (such as ester) or the terminal group of the hydrophobic tail is not a methyl.

2.3. Structure of Langmuir–Blodgett Films

It is common to consider the film deposition process within the framework of the "carpet deposition" model [23,24,40]. This model implies that as the Langmuir monolayer is being transferred from the horizontal air–subphase interface onto the vertical substrate surface, it mainly preserves its identity and general structure, by analogy with a carpet preserving its identity, structure and pattern whether it is being rolled, unrolled, laid on a floor or hung on a wall. A number of general experimental observations support the "carpet deposition" view. During the film transfer, the so-called transfer ratio is monitored at each of the strokes. Transfer ratio is defined as the ratio between the decrease in the Langmuir film area (determined from the barrier positions before and after the stroke) and the area of the substrate. Carpet deposition predicts transfer ratio of 1 at each stroke where deposition is expected, and, indeed, transfer ratios outside of the 0.95–1.05 range indicate poor quality of the resulting LB film. Further, the thickness of the LB multilayer films has been demonstrated by a variety of experimental methods to be proportional to the number of deposition cycles [23,39,41].

While true in general, the carpet deposition model does not take into account the different nature of interactions between the monolayer and

Lam Research Ex. 1035 - Page 649
Lam Research Corp. v. Inpria Corp.
IPR2024-00033 - U.S. Patent No. 9,823,564

subphase on one hand and the monolayer and substrate or monolayer and the underlying monolayer on the other hand, and this model is therefore not reliable when the finer details of the LB film structure are considered. Thus, the tilt angles of the carboxylic acid molecules in the LB films deposited from L'_2 phase were found to be lower (closer to normal) than those of the molecules forming the Langmuir monolayer prior to deposition [23,42,43]. Moreover, the tilt angle may not be uniform throughout the multilayer film, being higher in the layer adjacent to the substrate and decreasing in the subsequent layers. Also, the ordering of the molecules in the LB films may depend on the number of layers. The most studied system is the LB films of fatty acids and their salts, especially those with divalent cations as counterions. For example, monolayers of Cd arachidate were reported to have hexagonal structure with area per molecule of 19.7 $Å^2$, while in the multilayers, the molecules are forming a crystal structure with orthorhombic unit cell and area per molecule of 18.2 $Å^2$, lower than that observed in the monolayer [44]. The tilt angle of arachidic acid molecules in LB multilayer films was found to depend on the pressure which was maintained in the corresponding Langmuir monolayer during the deposition process [45]. The films deposited at relatively low pressures consist of tilted molecules, whereas when deposition occurs at higher pressures, the molecules are oriented normally to the substrate. Films of Cd arachidate have been reported to consist of untilted molecules [46,47].

3. Temperature-Induced Phase Transitions in Langmuir–Blodgett Films

Temperature-induced changes in the LB films' structure have been studied extensively [44,48–61]. In earlier studies Fourier transform infrared (FTIR) spectrometry in grazing angle mode was used to detect thermally induced disorder in the alkyl chains. In the perfectly ordered untilted all-*trans* alkyl chains, all the methylene groups are oriented parallel to the substrate. Since the vibrations of the methylene groups do not have a component orthogonal to the substrate, they cannot be detected. However, when the alkyl chain becomes disordered and loses its all-*trans* character due to *gauche* defects, the methylene vibrations acquire a component perpendicular to the substrate, which can easily be detected [48,49]. In later studies, more detailed information on the structural changes in LB films was obtained using X-ray diffraction and other techniques such as atomic force microscopy (AFM).

Lam Research Ex. 1035 - Page 650
Lam Research Corp. v. Inpria Corp.
IPR2024-00033 - U.S. Patent No. 9,823,564

3.1. Order–Disorder Transitions

Langmuir–Blodgett films are ordered systems. On one hand, the molecules comprising the film are aligned in the direction normal (or tilted at some constant angle) to the substrate surface. On the other hand, the head groups form two-dimensional lattice. As the temperature increases, some defects may appear in these ordered structures. The possible defects include the deviations from all-*trans* character of the individual chains, such as *gauche* conformations. Alternatively, the chain orientation – either tilt angle or the plane in which the carbon atoms are located – can change. Finally the intermolecular distances, i.e. the parameters of the lattice, can be affected by temperature changes.

Temperature-induced order–disorder phase transition in LB films was first reported by Naselli et al. in 1985 [48]. The multilayers of Cd arachidate (seven layers thick) were deposited on silver substrate, and their infrared spectra were taken at various temperatures. A two-step melting process was observed. As the temperature increased from room temperature to ~60°C, no changes in the film structure were detected. In the temperature range between 65°C and 100°C, the intensities of the CH_2 stretching bands started to increase, while the intensities of the CO_2 stretching bands remained unchanged. This was attributed to progressive disorder of the alkyl tails, while the head groups remained ordered. On cooling, the intensities of the CH_2 stretching bands returned to their original values, indicating that the order–disorder transition was reversible. When the films were heated to 125°C, which is above Cd arachidate bulk melting temperature (110°C), the disordering of the alkyl tails becomes irreversible. Moreover, the ordering of the head groups appeared to be irreversibly disrupted as well. Subsequent Raman spectroscopy studies clarified the nature of the observed chain disorder. It was demonstrated that *gauche* defects appear only above 90°C. Thus, the chain disorder between 65°C and 90°C is due to chain tilting, especially near defects, such as voids or domain boundaries.

Cohen et al. [49] studied temperature-induced order–disorder phase transitions in LB monolayers on Cd arachidate deposited on silver and aluminum substrates using FTIR spectroscopy. Similarly to the multilayer films, monolayers undergo reversible disordering at temperatures above 60°C and become irreversibly disordered if heated above the bulk melting point.

Thermal behavior of Cd stearate, Cd arachidate and Cd behenate monolayers was studied by Riegler [53] using electron diffraction. This study confirmed the previous observations on the disordering of the monolayers starting well before the melting temperature. The relationship between the length of the alkyl chain and the temperature at which the alkyl

Lam Research Ex. 1035 - Page 651
Lam Research Corp. v. Inpria Corp.
IPR2024-00033 - U.S. Patent No. 9,823,564

chains become disordered was established. The onset of disorder was detected at 35°C in Cd stearate monolayers, 55°C in Cd arachidate monolayers and 75°C in Cd behenate monolayers. Each of the monolayers had hexagonal structure at room temperature. On heating, the overall hexagonal geometry did not change; however, expansion of the lattice was observed.

The temperature-induced changes in the structure of LB multilayer films of Cd arachidate were further studied by Tippman-Krayer et al. [44] using X-ray diffraction. The room temperature structure, an orthorhombic lattice with unit cell dimensions of $a = 4.85$ Å, $b = 7.50$ Å, $c = 56$ Å, remains unchanged on heating until ~60°C. As the temperature continues to increase, the position and intensity of the (0 2) diffraction peak change, indicating the increase in the b dimension of the unit cell. When the temperature reaches 100°C, the lattice becomes hexagonal, similar to that of a Cd arachidate monolayer. This corresponds to an increase of the area per molecule from 18.2 Å^2 at room temperature to 19.7 Å^2 at 103°C. The transition is reversible, i.e. on cooling, the hexagonal lattice rearranges back into the orthorhombic lattice. However, if the temperature is raised above 110°C, an irreversible melting occurs. Order–disorder phase transition of Cd arachidate multilayer is schematically presented in Figure 12.4.

3.2. Effect of Phase Transitions on the Reactivity of Langmuir–Blodgett Films

Reaction between LB films of Cd arachidate and ground state atomic oxygen, O(^{3}P), was investigated at various temperatures using FTIR spectroscopy [55,56]. Intensity of the CH_2 stretching infrared band was monitored in a transmission mode and was found to decrease in the course of the reaction due to disappearance of the CH_2 groups.

For multilayer films (five monolayers thick), the depletion of the CH_2 band was found to depend linearly on temperature in the range between −30°C and 120°C, with a change of slope occurring at ~60°C. The observed linear dependence was attributed to the reactivity being controlled by the penetration of O(^{3}P) atoms between the vibrating Cd arachidate chains, while the chain vibrations are described by two-dimensional harmonic potential

$$f\langle(\Delta r)^2\rangle = k_B T \tag{2}$$

where f is the effective harmonic force constant and Δr the change of the radius of the channel between the Cd arachidate chains due to vibrations.

Lam Research Ex. 1035 - Page 652
Lam Research Corp. v. Inpria Corp.
IPR2024-00033 - U.S. Patent No. 9,823,564

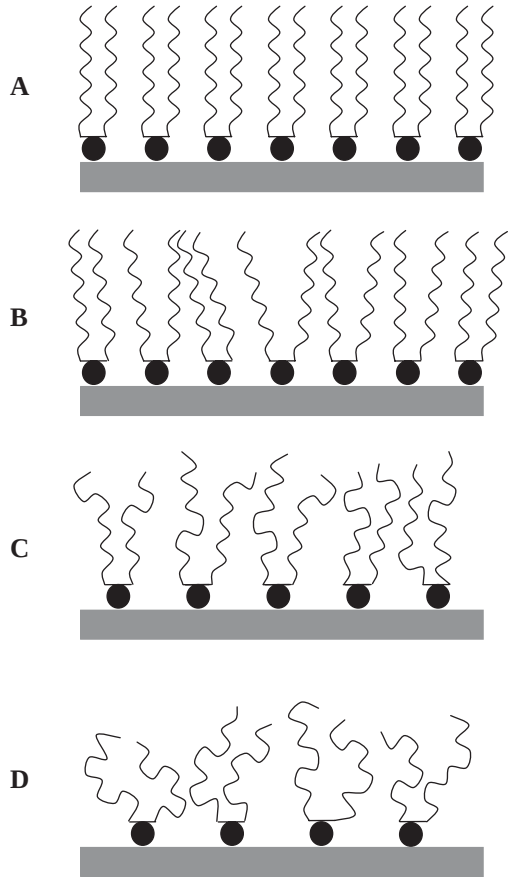


Fig. 12.4. Order–disorder transition in Cd arachidate multilayers: (A) 20°C – chains are normal to the surface; (B) 70°C – chains are tilted randomly; (C) 95°C – chains acquired *gauche* defects and distances between head groups increased; (D) 110°C – chains are completely disordered and distances between head groups increased further.

The reaction cross-section σ in this case is linearly dependent on both temperature T and the inverse of the effective harmonic force constant of the interchain vibrations f.

$$\sigma = \frac{\pi k_B T}{f} + \text{constant} \tag{3}$$

The change in slope was explained by decrease of the effective harmonic force constant due to the temperature-induced expansion of the lattice observed in earlier studies.

Lam Research Ex. 1035 - Page 653
Lam Research Corp. v. Inpria Corp.
IPR2024-00033 - U.S. Patent No. 9,823,564

For monolayer films, the temperature dependence of reactivity was somewhat more complicated than that for the multilayer films. Three temperature ranges could be distinguished. Below 20°C and above 60°C, the reactivity dependence on the temperature was similar to that observed for the multilayer films. However, between 20°C and 60°C, no dependence of reactivity on temperature was observed. This observation was rationalized by considering the two opposing effects that the temperature increase has on the molecular vibrations. On one hand, the increase in temperature causes an increase of the reaction cross-section; on the other hand, increase in temperature causes an increase of the amount of defects in the chains, such as kinks and bends. These defects are responsible for the decrease in the free space between the chains and for the increased repulsion between the chains, which cause an increase of the force constant f. This effect was not observed in the multilayer films, since they are more organized than monolayers, and the defects such as kinks and bends occur in multilayers only at significantly higher temperatures.

4. Self-Assembled Films

Self-assembled monolayers were first prepared by Zisman and coworkers in 1946 [8] due to serendipity. In the course of experiments with solutions of long-chain aliphatic alcohol in a non-polar solvent, it was noticed that the walls of the glass flask in which the experiments were performed were not wetted by the solutions, i.e. they became oleophobic. This observation triggered detailed investigation, in the course of which it was demonstrated that a close-packed film similar to LB monolayers can be formed when a compatible substrate is immersed in a dilute solution of an appropriate amphiphilic substance. It was believed initially that the film might be first forming on the air–solution interface and then "picked" by the substrate in the process of immersion and reimmersion. However, since tightly packed films could be obtained from very dilute solutions, where only gaseous film on the air–solution interface could be expected, it was concluded that the film formation occurs in solution or more precisely on the solvent–substrate interface. Self-assembled films were successfully prepared from long-chain aliphatic alcohols, monocarboxylic acids, primary amines and some esters. It was demonstrated that the alkyl chain length plays the major role in determining the film-forming ability of the amphiphilic molecule. This can be explained by considering the role of the interchain interactions. Since the strength of van der Waals interaction between two parallel rods is proportional to the rod's length, the chains should be long enough to allow for sufficiently strong interaction. On the other hand, the longer the chain is, the

Lam Research Ex. 1035 - Page 654
Lam Research Corp. v. Inpria Corp.
IPR2024-00033 - U.S. Patent No. 9,823,564

more likely it is to have defects such as *gauche* conformations, which distort the rod-like shape of the molecules and disrupt their close packing. A wide variety of non-polar solvents, such as long-chain alkanes (C8–C16) and bicyclohexyl, and substrates, such as platinum, glass, nickel, iron, copper and aluminum, were tested and found suitable for formation of self-assembled films. The fundamental importance of this pioneering work cannot be underestimated. For the first time, it was demonstrated that close-packed monolayer films can be obtained by spontaneous assembly from solution. However, this technique did not become widely utilized until more than 30 years later, probably because the only advantage of the new films over the traditional LB films was the relative simplicity of preparation. For example, it was shown that the films could be subsequently dissolved in low molecular weight organic solvents such as benzene or petroleum ether. This observation can be rationalized by considering that the interactions between the film and the substrate are not specific and do not involve formation of covalent bonds. Thus, the self-assembly method at that time did not result in films that were more stable or robust than LB films. Also, the area per molecule reported for the self-assembled films was of $\sim 30\,\text{Å}^2$, which is significantly higher than $\sim 20\,\text{Å}^2$, which is characteristic of LB films, and this higher area per molecule indicates a higher degree of disorder. Finally, the self-assembly method did not allow for the preparation of multilayers. Another factor which could indirectly contribute to the lack of immediate popularity of self-assembled monolayers was the state of surface analysis techniques at the time, which for the most part could not obtain sufficient information on the structure of nanometer-thick coatings.

4.1. COVALENTLY BONDED SILANE MONOLAYERS

The breakthrough in the field of self-assembled monolayers occurred in 1980s, when a number of robust well-ordered monolayer systems were introduced. The conceptual difference between the new studies and the one described before was in the specific nature of the interaction between the amphiphilic molecule and the substrate. Namely, the film-forming amphiphile and the substrate were chosen in such a way so as to allow for formation of a covalent bond between the substrate and the head group of the amphiphilic molecule. The most popular pairs include, but are not limited to, alkyltrichlorosilanes on SiO_2 substrates reported by Sagiv in 1980 [10], and organosulfur compounds on Au introduced by Allara and coworkers in 1983 [9,62].

Although it was postulated earlier that silane monolayers covalently bound to substrates possessing dangling OH groups could be formed by the

Lam Research Ex. 1035 - Page 655
Lam Research Corp. v. Inpria Corp.
IPR2024-00033 - U.S. Patent No. 9,823,564

self-assembly method [63], it was Sagiv [10] who first prepared the true monolayers of octadecyltrichlorosilane (OTS). The film formation was initially believed to proceed in three steps. First, the $SiCl_3$ head groups are completely or partially hydrolyzed into silanols by the traces of water present in the system. Then the silanol groups form hydrogen bonds with the substrate and silanol groups belonging to other nearby molecules. Finally, condensation occurs, resulting in the formation of covalent bonds between the silane molecules and the substrate as well as between neighboring silane molecules, resulting in the formation of a two-dimensional siloxane network. The main impediment to successful formation of a monolayer film is the presence of excessive moisture in the system resulting in hydrolysis and condensation of OTS in solution rather than on the surface. To avoid this, it is important to use anhydrous solvents and ensure that the only traces of water in the system are adsorbed on the substrate. In this case hydrolysis of the silane groups will occur on the substrate surface and will be followed by adsorption.

The mechanism of formation of OTS films was studied extensively [26,27,64–72]. Two pathways were proposed: uniform growth and island growth [64]. The uniform growth model involves adsorption of individual OTS molecules at random. At low coverages, the molecules will be tilted at various angles and generally disordered. As the coverage increases, the decreased area per molecule would cause the decrease of tilt angles and increased close packing. The island growth model implies that at low coverages, individual islands are formed separated by areas of bare substrate. The ordering of OTS molecules in each island is similar to that in the complete monolayer. A number of experimental studies included evidence in favor of either the uniform growth [64–66,70] or the island growth [67–69,71,72] models. This contradiction can be attributed to the differences between experimental methods utilized by various research groups and minor differences in experimental conditions such as temperature and relative humidity [26]. Recent studies have demonstrated that the formation of monolayer occurs in a two-step process [71]. First, comparatively large islands are adsorbed on the substrate. The molecules in the islands are oriented perpendicularly to the surface, i.e. their organization is essentially the same as that in the full monolayer. The subsequent, slower step involves adsorption of monomers into the gaps between the islands.

4.2. Stability of Self-Assembled Silane Films

Comparing OTS films to either self-assembled or LB films of carboxylic acids it should be noted that OTS films are significantly more stable. OTS

Lam Research Ex. 1035 - Page 656
Lam Research Corp. v. Inpria Corp.
IPR2024-00033 - U.S. Patent No. 9,823,564

films cannot be dissolved in water or organic solvents [73]. Also, OTS films can be heated to higher temperatures (140°C) than films consisting of carboxylic acids of comparable length without causing irreversible changes or even significant disorder [49]. This increased stability results from strong interactions between neighboring OTS molecules and between OTS molecules and the substrate. In the "ideal" case, each OTS molecule will participate in three covalent bonds: one with the substrate and two with neighbors as shown in Figure 12.5. Since the distances between the active hydroxyl sites on the substrate do not necessarily match the optimal distances between the OTS molecules it is possible for some molecules to participate in only one or two covalent bonds while the free hydroxyl groups may be hydrogen bonded to either the substrate or the nearby OTS molecule also possessing a free hydroxyl. This flexibility allows formation of robust films on nearly any hydroxylated substrate, such as SiO_2, Al_2O_3, polyvinyl alcohol and oxidized polyethylene. Moreover, the optimal distance between OTS molecules is hard to define, because the distance between close-packed alkyl chains is higher than the distance between the Si atoms connected by a siloxane Si–O–Si link. Thus, for the tails not to overlap, they have to be splayed, which in turn decreases the coverage [74]. However, there is no experimental evidence of significant tilt in OTS films. The OTS molecules form close-packed hexagonal structure (possibly somewhat distorted) with average area per molecule of $\sim 21\ \text{Å}^2$, which is only slightly higher than that in close-packed LB films [73]. This apparent difficulty led some authors to doubt the siloxane bonding in monolayers at full coverage [74]. Alternatively, the structure of alkyltrichlorosilane monolayer as a siloxane network in the state of dynamic equilibration, i.e. with continuous breaking and reforming of siloxane bonds, was proposed [13]. This model is consistent with experimental observations of both stability and robustness of OTS and of other similar films, as well as the significant surface–solution exchange between alkyltrichlorosilane molecules in solution and those attached to the surface and forming otherwise insoluble monolayers.

4.3. Self-Assembled Silane Multilayers

The ability to use the LB technique for forming not only monolayer but also multilayer structures presented an additional challenge to the developers of the self-assembling films. OTS and its homologues possessed excellent film-forming ability, but the resulting monolayers were chemically inert, which prevented the build-up of additional layers. Using bifunctional molecules with trichlorosilane group on one end and a hydroxyl group on the other end would not be feasible, since such compounds would most likely be

Lam Research Ex. 1035 - Page 657
Lam Research Corp. v. Inpria Corp.
IPR2024-00033 - U.S. Patent No. 9,823,564

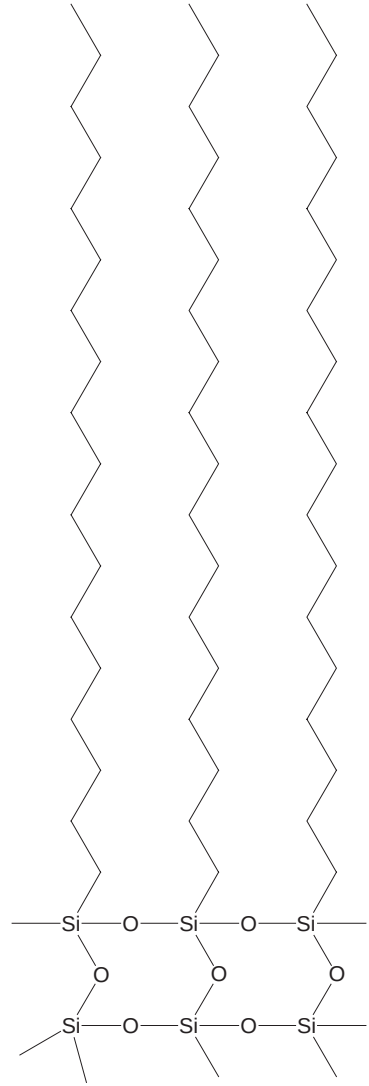


Fig. 12.5. OTS monolayer on silicon dioxide substrate.

unstable due to either intra- or intermolecular reaction between the two terminal groups. Also, the build-up of the second and subsequent layers would start before the first layer formation would be finalized, thus resulting in a highly disordered multilayer assembly. A number of systems were designed in order to overcome this difficulty. The molecules used had the

Lam Research Ex. 1035 - Page 658
Lam Research Corp. v. Inpria Corp.
IPR2024-00033 - U.S. Patent No. 9,823,564

trichlorosilane group on one end and an inert group that could be turned into a hydroxyl when desired on the other end. The first study [11] involved films of 15-hexadecenyltrichlorosilane (HTS) self-assembled on silicon substrate. After the good quality monolayers were prepared, the terminal alkene groups were selectively converted into alcohols by hydroboration and hydrogen peroxide oxidation. The resulting hydroxyl-terminated film was exposed to the HTS solution and the second HTS layer was chemisorbed. The resulting multilayer (up to three layers) films were less ordered than the OTS monolayer, which was attributed to the lower length of the former's hydrocarbon chain. Nevertheless, the feasibility of forming multilayer structures via self-assembly was successfully demonstrated. Subsequent study [12] which utilized methyl 23-(trichlorosilyl)tricosanoate resulted in successful preparation of ordered multilayers up to 25 monolayers thick. After deposition of each layer the terminal ester groups were reduced to alcohols by exposure to $LiAlH_4$ in tetrahydrofuran, thus allowing for the deposition of the next layer. An alternative method of preparation of ordered multilayer structures via self-assembly of trichlorosilanes results in a system where the neighboring layers are connected via hydrogen bonds [13]. The first step involves deposition of an alkene-terminated trichlorosilane monolayer on silicon substrate. Next, the terminal alkene groups are converted to carboxylic acid groups by exposure to potassium permanganate. Subsequently, the next layer of alkene-terminated trichlorosilanes is deposited on the carboxylic acid-functionalized surface. FTIR measurements demonstrated that the carboxylic acids of the underlying layer form hydrogen bonds with silanol groups of the newly deposited upper layer. Then the procedure can be repeated, i.e. the terminal groups of the top layer can be oxidized and the new alkene-terminated layer can be deposited on top of it, until the desired multilayer thickness is reached. Although the hydrogen bonds are not as strong as covalent bonds, the resulting multilayer systems are stable in both organic and aqueous media. Moreover, the flexibility of hydrogen bonded structure allows for incorporation of various guest species between the siloxane layers.

5. Conclusions

The research on organized organic thin films extends back for more than a century [75]. However, since 1980s, the interest in these systems has increased dramatically due to the development of new methods of preparation of such systems and advances in scientific instrumentation. Langmuir and LB films are of great fundamental interest as low-dimensionality systems.

Lam Research Ex. 1035 - Page 659
Lam Research Corp. v. Inpria Corp.
IPR2024-00033 - U.S. Patent No. 9,823,564

Self-assembled films, especially those containing functionalities other than the head groups, are potentially suitable for technological applications.

The versatility of both methods allows for constructing well-defined systems with tailorable properties. Ordered films consisting of biologically relevant molecules, such as DNA, can be prepared [76]. Ordered organic–inorganic composites can be prepared by incorporating metal or semiconductor nanoparticles into the films [77]. Organized organic thin films are of interest for their potential usefulness in non-linear optics [78] and molecular electronics [79] applications.

Recently, a number of studies have appeared where the organized organic thin films were used as proxies for atmospheric organic aerosols [80]. It was suggested by Ellison et al. [81] that formation of organic coated sea-salt aerosols includes spontaneous organization of long-chain amphiphilic molecules on the liquid surface into an inverted micelle-like structure. Organic monolayers, either LB or self-assembled, serve as suitable laboratory proxies for such systems, being easy to prepare in a reproducible manner, well defined and easily characterized by available instrumental methods. Such studies included adsorption of water on organic surfaces, where alkene-terminated octenyltrichlorosilane monolayer, saturated OTS monolayer and corrugated mixed monolayer of alkyltrichlorosilanes of different lengths (C18 and C22) were exposed to water vapors [82,83]. Reaction of ozone with organic aerosols was investigated using alkene-terminated octenyltrichlorosilane [84,85] and allyltrichlorosilane [85] monolayers. Hydroxyl radical uptake was studied on allyltrichlorosilane monolayer [86] and OTS monolayer [86,87]. Interactions of other atmospherically relevant gas phase species, including halogen radicals [88], with organic monolayers were also studied.

To summarize, organized organic thin films is a fascinating, rapidly developing field attracting the attention of a diverse pool of researchers with interests ranging from theoretical physics to materials science and from biochemistry to atmospheric chemistry. While these techniques have not yet attained widespread industrial application, research toward that goal is promising.

The questions below are intended to help the reader in learning the material presented in the chapter:

1. Estimate the area per molecule (in Å^2) in Franklin's experiment on Clapham pond.
2. Explain what is meant by a two-dimensional gas.
3. What is the temperature of order–disorder phase transition in LB monolayers of cadmium arachidate? Is it reversible?
4. What structure does the LB monolayer of cadmium arachidate have before and after phase transition?

Lam Research Ex. 1035 - Page 660
Lam Research Corp. v. Inpria Corp.
IPR2024-00033 - U.S. Patent No. 9,823,564

5. What is the temperature of phase transition in a LB multilayer of cadmium arachidate? Is it reversible?
6. What structure does the LB multilayer of cadmium arachidate have before and after phase transition?
7. Why are traces of water necessary for formation of OTS monolayers?

Acknowledgments

The author would like to thank SAPPI Fine Paper for financial support and Mr. Mark Gordon for help in preparing the manuscript.

References

1. Pliny, Natural History, Harvard University Press, Cambridge, MA, 1979.
2. Bede, Historical Works, Harvard University Press, Cambridge, MA, 1979.
3. B. Franklin, W. Brownrigg, Mr. Farish, Philos. Trans. **64** (1774) 445.
4. J. Israelachvili, Intermolecular and Surface Forces, Academic Press, Boston, MA, 1992.
5. I. Langmuir, J. Am. Chem. Soc. **39** (1917) 1848.
6. A. Ulman, An Introduction to Ultrathin Organic Films: From Langmuir–Blodgett to Self-Assembly, Academic Press, Boston, MA, 1991.
7. K. B. Blodgett, J. Am. Chem. Soc. **56** (1934) 495.
8. W. C. Bigelow, D. L. Pickett, W. A. Zisman, J. Colloid Sci. **1** (1946) 513.
9. R. G. Nuzzo, D. L. Allara, J. Am. Chem. Soc. **105** (1983) 4481.
10. J. Sagiv, J. Am. Chem. Soc. **102** (1980) 92.
11. L. Netzer, J. Sagiv, J. Am. Chem. Soc. **105** (1983) 674.
12. N. Tillman, A. Ulman, T. L. Penner, Langmuir **5** (1989) 101.
13. R. Maoz, J. Sagiv, D. Degenhardt, H. Möhwald, P. Quint, Supramol. Sci. **2** (1995) 9.
14. S. J. Mumby, J. F. Rabolt, J. D. Swalen, Macromolecules **19** (1986) 1054.
15. H. Ringsdorf, G. Schmidt, J. Schneider, Thin Solid Films **152** (1987) 207.
16. H. Koch, A. Laschewsky, H. Ringsdorf, K. Teng, Makromol. Chem. **187** (1986) 1843.
17. M. Ozaki, Y. Ikeda, I. Nagoya, Synth. Met. **28** (1989) C801.

Lam Research Ex. 1035 - Page 661
Lam Research Corp. v. Inpria Corp.
IPR2024-00033 - U.S. Patent No. 9,823,564

18. B. Tieke, D. Bloor, Makromol. Chem. **180** (1979) 2275.
19. A. Laschewsky, H. Ringsdorf, Macromolecules **21** (1988) 1936.
20. Y. Lvov, G. Decher, H. Möhwald, Langmuir **9** (1993) 481.
21. G. L. Gaines, Insoluble Monolayers at Liquid–Gas Interfaces, Wiley, New York, 1966.
22. M. C. Petty, Langmuir–Blodgett Films: An Introduction, Cambridge University Press, Cambridge, 1996.
23. I. R. Peterson, J. Phys. D: Appl. Phys. **23** (1990) 379.
24. D. K. Schwartz, Surf. Sci. Rep. **27** (1997) 241.
25. V. M. Kaganer, H. Möhwald, P. Dutta, Rev. Mod. Phys. **71** (1999) 779.
26. F. Schreiber, Prog. Surf. Sci. **65** (2000) 151.
27. D. K. Schwartz, Annu. Rev. Phys. Chem. **52** (2001) 107.
28. N. Sandhyarani, T. Pradeep, Int. Rev. Phys. Chem. **22** (2003) 221.
29. F. Schreiber, J. Phys.: Condens. Matter **16** (2004) R881.
30. G. A. Hawkins, G. B. Benedek, Phys. Rev. Lett. **32** (1974) 524.
31. M. W. Kim, D. S. Cannell, Phys. Rev. A **13** (1976) 411.
32. N. R. Pallas, B. A. Pethica, J. Chem. Soc. Faraday Trans. 1 **83** (1987) 585.
33. S. J. Collins, A. Dhathathreyan, T. Ramasami, J. Colloid Interface Sci. **203** (1998) 249.
34. N. R. Pallas, B. A. Pethica, Langmuir **1** (1985) 509.
35. R. M. Kenn, C. Böhm, A. M. Bibo, I. R. Peterson, H. Möhwald, J. Als-Nielsen, K. Kjaer, J. Phys. Chem. **95** (1991) 2092.
36. J. Pignat, J. Daillant, L. Leiserowitz, F. Perrot, J. Phys. Chem. B **110** (2006) 22178.
37. F. Jähnig, J. Chem. Phys. **70** (1979) 3279.
38. M. C. Shih, T. M. Bohanon, J. M. Mikrut, P. Zschack, P. Dutta, J. Chem. Phys. **96** (1992) 1556.
39. K. B. Blodgett, J. Am. Chem. Soc. **57** (1935) 1007.
40. J. A. Spink, J. Colloid Interface Sci. **23** (1967) 9.
41. N. J. Geddes, W. G. Parker, J. R. Sambles, D. J. Jarvis, N. R. Couch, Thin Solid Films **168** (1989) 151.
42. A. Bonnerot, P. A. Chollet, H. Frisby, M. Hoclet, Chem. Phys. **97** (1985) 365.
43. W. L. Barnes, J. R. Sambles, Surf. Sci. **183** (1987) 189.
44. P. Tippman-Krayer, R. M. Kenn, H. Möhwald, Thin Solid Films **210/211** (1992) 577.
45. S. A. Evenson, J. P. S. Badyal, C. Pearson, M. C. Petty, J. Phys. Chem. **100** (1996) 11672.

Lam Research Ex. 1035 - Page 662
Lam Research Corp. v. Inpria Corp.
IPR2024-00033 - U.S. Patent No. 9,823,564

46. J. D. Swallen, Thin Solid Films **152** (1987) 151.
47. D. L. Allara, J. D. Swallen, J. Phys. Chem. **86** (1982) 2700.
48. C. Naselli, J. F. Rabolt, J. D. Swallen, J. Chem. Phys. **82** (1985) 2136.
49. S. R. Cohen, R. Naaman, J. Sagiv, J. Phys. Chem. **90** (1986) 3054.
50. J. P. Rabe, J. D. Swallen, J. F. Rabolt, J. Chem. Phys. **86** (1987) 1601.
51. C. Böhm, R. Steitz, H. Riegler, Thin Solid Films **178** (1989) 511.
52. Y. Okahata, K. Kimura, K. Ariga, J. Am. Chem. Soc. **111** (1989) 9190.
53. J. E. Riegler, J. Phys. Chem. **93** (1989) 6475.
54. Y. Sasanuma, Y. Kitano, A. Ishitani, H. Nakahara, K. Fukuda, Thin Solid Films **199** (1991) 359.
55. Y. Paz, S. Trakhtenberg, R. Naaman, J. Phys. Chem. **97** (1993) 9075.
56. Y. Paz, S. Trakhtenberg, R. Naaman, J. Phys. Chem. **98** (1994) 13517.
57. K. Taniike, T. Matsumoto, T. Sato, Y. Ozaki, K. Nakashima, K. Iriyama, J. Phys. Chem. **100** (1996) 15508.
58. J. B. Peng, G. J. Foran, G. T. Barnes, I. R. Gentle, Langmuir **13** (1997) 1602.
59. A. Haran, D. Dimitrov, S. Trakhtenberg, R. Naaman, J. Chem. Phys. **113** (2000) 7571.
60. J. B. Peng, G. J. Foran, G. T. Barnes, I. R. Gentle, Langmuir **19** (2003) 4701.
61. S. Morita, K. Nichogi, Y. Ozaki, J. Phys. Chem. B **108** (2004) 7871.
62. M. D. Porter, T. B. Bright, D. L. Allara, C. E. D. Chidsey, J. Am. Chem. Soc. **109** (1987) 3559.
63. W. A. Zisman, Ind. Eng. Chem. Prod. Res. Dev. **8** (1969) 98.
64. S. R. Wasserman, G. M. Whitesides, I. M. Tidswell, B. M. Ocko, P. S. Pershan, J. D. Axe, J. Am. Chem. Soc. **111** (1989) 5852.
65. I. M. Tidswell, B. M. Ocko, P. S. Pershan, S. R. Wasserman, G. M. Whitesides, J. D. Axe, Phys. Rev. B **41** (1990) 1111.
66. I. M. Tidswell, T. A. Rabedeu, P. S. Pershan, S. D. Kosowsky, J. P. Folkers, G. M. Whitesides, J. Chem. Phys. **95** (1991) 2854.
67. K. Bierbaum, M. Grunze, A. A. Baski, L. F. Chi, W. Schrepp, H. Fuchs, Langmuir **11** (1995) 2143.
68. R. Banga, J. Yarwood, A. M. Morgan, B. Evans, J. Kells, Langmuir **11** (1995) 4393.
69. T. Komeda, K. Namba, Y. Nishioka, J. Vac. Sci. Technol. A **16** (1998) 1680.
70. T. Vallant, J. Kattner, H. Brunner, U. Mayer, H. Hoffmann, Langmuir **15** (1999) 5339.
71. R. Resch, M. Grasserbauer, G. Friedbacher, T. Vallant, H. Brunner, U. Mayer, H. Hoffmann, Appl. Surf. Sci. **140** (1999) 168.

Lam Research Ex. 1035 - Page 663
Lam Research Corp. v. Inpria Corp.
IPR2024-00033 - U.S. Patent No. 9,823,564

72. A. G. Richter, C.-J. Yu, A. Datta, J. Kmetko, P. Dutta, Phys. Rev. E **61** (2000) 607.
73. S. R. Wasserman, Y.-T. Tao, G. M. Whitesides, Langmuir **5** (1989) 1074.
74. M. J. Stevens, Langmuir **15** (1999) 2773.
75. A. Pockels, Nature **43** (1891) 437.
76. S. G. Ray, S. S. Daube, G. Leitus, Z. Vager, R. Naaman, Phys. Rev. Lett. **96** (2006) 036101.
77. A. Samokhvalov, R. W. Gurney, M. Lahav, S. Cohen, H. Cohen, R. Naaman, J. Phys. Chem. B **107** (2003) 4245.
78. R. Popovitz-Biro, K. Hill, E. M. Landou, M. Lahav, L. Leiserowitz, J. Sagiv, H. Hsiung, G. R. Meredith, H. Vaherzeele, J. Am. Chem. Soc. **110** (1988) 2672.
79. M. C. Petty, M. R. Bryce, D. Bloor, An Introduction to Molecular Electronics, Oxford University Press, New York, 1995.
80. Y. Rudich, Chem. Rev. **103** (2003) 5097.
81. G. B. Ellison, A. F. Tuck, V. Vaida, J. Geophys. Res. Atmos. **104** (1999) 11633.
82. E. Thomas, Y. Rudich, S. Trakhtenberg, R. Ussyshkin, J. Geophys. Res. Atmos. **104** (1999) 16053.
83. Y. Rudich, I. Benjamin, R. Naaman, E. Thomas, S. Trakhtenberg, R. Ussyshkin, J. Phys. Chem. A **104** (2000) 5238.
84. T. Moise, Y. Rudich, J. Geophys. Res. Atmos. **105** (2000) 14667.
85. Y. Dubowski, J. Vieceli, D. J. Tobias, A. Gomez, A. Lin, S. A. Nizkorodov, T. M. McIntire, B. J. Finlayson-Pitts, J. Phys. Chem. A **108** (2004) 10473.
86. A. K. Bertram, A. V. Ivanov, M. Hunter, L. T. Molina, M. J. Molina, J. Phys. Chem. A **105** (2001) 9415.
87. M. J. Molina, A. V. Ivanov, S. Trakhtenberg, L. T. Molina, Geophys. Res. Lett. **31** (2004) L22104/1.
88. T. Moise, Y. Rudich, Geophys. Res. Lett. **28** (2001) 4083.

Lam Research Ex. 1035 - Page 664
Lam Research Corp. v. Inpria Corp.
IPR2024-00033 - U.S. Patent No. 9,823,564

Chapter 13

Non-Catalytic Photo-Induced Immobilization Processes in Polymer Films

S. Trakhtenberg, A.S. Cannon, and J.C. Warner

Center for Green Chemistry, University of Massachusetts Lowell, One University Avenue, Lowell, MA 01854, USA

1. Introduction 666
2. Photo-Induced Processes in Natural Polymers – DNA 671
3. Photopolymers and Photoresists Containing DNA Bases 676
4. Light-Induced Immobilization of Crosslinkable Photoresists 679
5. Reverse Processes 687
6. Conclusions 690
Acknowledgments 691
References 691

This chapter describes non-catalytic photo-induced immobilization processes in polymer films. These processes are fundamental to a variety of applications such as microelectronics, imaging, and release mechanisms. The main focus of this chapter is on photopolymers containing thymine, a DNA base. In the first section, the historical account of applications of photoresist polymers is presented, and the processes of thymine photodimerization and its reversal are introduced. The second section discusses the mechanism of ultraviolet (UV) light-induced photodimerization of thymine. Concerted reaction resulting in the formation of cyclobutane rings is discussed in the context of Woodward–Hoffmann Frontier Molecular Orbital theory. The third section deals with synthetic polymers that incorporate thymine moieties as pendant groups. In this section examples are given of both organic- and water-soluble photopolymers, which can be immobilized by photo-induced crosslinking, and the applications of those polymers. The fourth section focuses on soluble polymers that are immobilized as result of exposure to irradiation, such as UV light. The kinetics of immobilization is described in the context of Flory's theory of network formation. The fifth section describes various methods known to trigger the reverse crosslinking process, resulting in the re-solubilization of photo-immobilized films. The sixth section presents some thoughts on possible future directions and potential opportunities for this technology.

THIN FILMS AND NANOSTRUCTURES, vol. 34
ISSN 1079-4050
DOI: 10.1016/S1079-4050(06)34013-6

© 2007 by Elsevier Inc.
All rights reserved.

Lam Research Ex. 1035 - Page 665
Lam Research Corp. v. Inpria Corp.
IPR2024-00033 - U.S. Patent No. 9,823,564

1. Introduction

In the year 2000, the Nobel Prize in Physics was shared by three scientists: Zhores I. Alferov and Herbert Kroemer, developers of semiconductor heterostructures used in high-speed- and opto-electronics and Jack St. Clair Kilby, inventor of integrated circuits. Integrated circuits changed the face of both scientific research and everyday life in more ways than even their inventor could have imagined back in 1958 [1]. Everyday consumer electronics from personal computers to microwave ovens were made possible and affordable by integrated circuits. The list of applications for integrated circuits is extensive, and even today the list continues to expand.

The field of electronics started with the invention of the vacuum tube, a device that allowed for the control of electron flow. Used for signal amplification in audio and other devices, vacuum tubes made radio broadcasting possible in the 1920s, followed by TV broadcasting in 1930s. In the mid-20th century there were attempts to use vacuum tubes for constructing computers. The fastest computer in the world at the time, ENIAC of 1946, was able to perform about 5000 arithmetic operations per second, contained 19,000 vacuum tubes of 16 different types, weighed over 30 tons and occupied 1800 square feet [2]. It became obvious at that time that in order to develop new, faster computers an alternative to vacuum tubes had to be found. The computers assembled from vacuum tubes were too large, consumed too much energy and moreover, being built from hundreds of thousands of individual components, were expensive and unreliable. The ENIAC's average trouble-free operating time was only about 100 h per week [2].

The first breakthrough came in 1948 when semiconductor transistors were invented [3]. It was demonstrated that the way electric current flows through these miniature solid-state devices could be altered by selecting the nature, amounts and locations of impurities (dopants). For example, adding arsenic to germanium causes it to conduct current via free electron flow (n-type), while adding gallium to germanium causes it to conduct current via electron deficiencies or holes (p-type) [4]. Early transistors consisted of neighboring areas with different conductivity types through selective doping. Substituting vacuum tubes with solid-state transistors allowed for miniaturization of electronics. However, large amounts of individual components still had to be assembled together. Moreover, the components of different types were made from different materials by different technologies.

In May of 1958, Jack Kilby was hired by Texas Instruments to work on miniaturization of electronic products [1]. He had no specified project and could develop his own ideas. His freedom was further enhanced in that

Lam Research Ex. 1035 - Page 666
Lam Research Corp. v. Inpria Corp.
IPR2024-00033 - U.S. Patent No. 9,823,564

historic summer by a trivial circumstance: as a newly hired employee he was not eligible for the organized "mass vacation", which was enjoyed by over 90% of the Texas Instruments employees. Nearly alone in his laboratory he was left to his thoughts and formulated an idea which later became known as "The Monolithic Idea", namely that if all components of an electric circuit could be made from the same material they also could be included in a single chip. First, Kilby had to demonstrate that not only transistors – but each individual component of an electronic circuit, such as capacitors or resistors – could technically be made from the same material, such as silicon. When this was achieved, the next step was to build a true integrated circuit, where all the components were made within a single piece of semiconductor material. The success was announced in March 1959 when working integrated circuits, both silicon- and germanium-based, were presented. As is common with new, breakthrough ideas, the electronics community was initially unreceptive to Kilby's inventions. However, when the new technology was successfully used in the Apollo moon mission, acceptance began to spread quickly as many companies began incorporating integrated circuits into their products. To help popularize integrated circuits Texas Instruments developed the first handheld electronic calculator.

The technology most often used to make integrated circuits is referred to as photolithography [5]. This word is derived from Greek and means "writing on stone with light." As the name implies, it is the process by which optical methods are used to transfer the circuit patterns from master images, called masks or reticles, to substrates, typically silicon wafers. In order to create the patterns, wafers are coated with a photosensitive material called photoresist, which changes its solubility upon exposure to light. Since the photoresists in most cases do not adhere well to silicon-based surfaces, the wafers are prepared by cleaning, followed by a pretreatment to promote adhesion of the photoresist to the wafer with materials such as hexamethyldisilazane (HMDS) [6].

The wafers are then coated with photoresist by a procedure referred to as spin coating [7]. A small amount of dilute solution of the resist in a volatile solvent is applied to the center of the wafer. The wafer then is spun at a high rate (usually above 1000 rpm) and the solution is spreading over the wafer. As the solvent evaporates, the thin layer of the resist remains on the surface. The resulting thickness of the photoresist layer depends on a variety of factors, namely resist solution concentration and viscosity, rate of spinning, temperature, and solvent volatility, and is typically in the range of 0.1–2 μm. The resist is then heated in a "soft-bake" process at a relatively low temperature (100°C) to drive off excess solvent and to densify the resist layer [5]. The coated wafer is then exposed to light through the appropriate mask to pattern the surface of the resist. The masks are made from sheets of glass

Lam Research Ex. 1035 - Page 667
Lam Research Corp. v. Inpria Corp.
IPR2024-00033 - U.S. Patent No. 9,823,564

(or quartz for UV-sensitive resists) on which there is a pattern of a UV opaque material, usually metal, such as chromium. This allows the selective irradiation of only the desired areas of the photoresist-coated wafer in order to transfer the pattern from the mask onto the wafer. The photoresists are classified as positive or negative depending on the effect of their exposure to light. Positive photoresists become soluble upon exposure, while negative photoresists become insoluble. Upon exposure to light the resist-coated wafer is exposed to a developing solution, usually a strong aqueous base [8]. Developing solution selectively removes the resist layer either from exposed areas (in case of positive resists) or from unexposed areas (in case of negative resists). The development stage results in the wafer with the semiconductor surface partially protected by the resist, which repeats the pattern on the mask. In the subsequent steps, the unprotected areas are altered, for example by chemical etching, while protected areas remain intact. Finally, the remaining photoresist is stripped off the wafer, which now features the pattern identical to the one on the mask. Since the integrated circuits consist of a number of the patterned layers, the process described above is repeated several times, using different masks [5].

As indicated in the preceding description, photoresists play a major role in the formation of integrated circuits. However, the applications of photoresists are not limited to microelectronics and the use of photoresist materials has been dated back to ancient times. It is believed that in ancient Egypt, the linen cloths used in wrapping a mummy were hardened by dipping the linens in a lavender oil solution of high molecular weight bitumen of Judea mined near the Dead Sea and exposing them to sunlight to photocure [9–11], although the accuracy of this information is currently under discussion [12]. The same natural photosensitive resin was successfully used in the first experiments on photolithography in France [9]. Joseph Nicefore Niepce, inventor and amateur Egyptologist, experimented with glass coated with bitumen [13]. In 1822 he exposed a glass plate coated with bitumen to sunlight through an oiled engraving. Oil made the clear portions of the engraving transparent and the bitumen under those areas hardened, while the bitumen under the dark areas of the engraving remained intact. After a few hours of exposure the images were developed in lavender oil, which resulted in the negative image of the original engraving. Niepce named the process, he invented, ''heliography'', namely sun writing. He later extended his experiments to pewter plates. After developing the image in lavender oil he exposed the substrate to acid. Areas coated by hardened bitumen were protected from the acid, while the areas from which the bitumen was rinsed were etched by the acid, thus enhancing the quality of the plate. Niepce was quite possibly the first to experiment with photoresist and etching processes.

Lam Research Ex. 1035 - Page 668
Lam Research Corp. v. Inpria Corp.
IPR2024-00033 - U.S. Patent No. 9,823,564

Although the structure of natural bitumen is quite complex, it is believed that its behavior as a photoresist material is caused by crosslinking between individual molecules [9]. Similarly, a large number of synthetic negative photoresist polymers are designed to incorporate functional groups, which are able to undergo photocrosslinking. An example of such photoresist polymer is poly(vinyl cinnamate) synthesized around 1945 by Louis Minsk in Eastman Kodak laboratories [14,15]. When exposed to light, the unsaturated carbon–carbon bonds of pendant cinnamate groups undergo a cycloaddition reaction, covalently linking the individual polymer chains into a three-dimensional network.

A wide range of high molecular weight biological molecules also contain functional groups which are able to undergo photoreactions. Proteins and nucleic acids are the most photoactive natural polymers [16]. Nucleic acids are especially interesting in that regard, because on one hand all nucleic acid residues (bases) are good UV absorbers and moreover, due to the rigid DNA or RNA structure, the bases are aligned parallel to each other, permitting overlap of the electronic orbitals. In contrast, neither phosphate nor sugar moieties and the backbone of nucleic acids are UV absorbers [17]. The structures of DNA and RNA bases are presented in Figure 13.1.

It was first reported in 1941 that DNA can be damaged by exposure to UV light, which was initially attributed to depolymerization [18,19]. Only in the 1960s was it recognized that dimerization of adjacent thymine bases in the DNA strands via photocycloaddition is a major factor in biological inactivation of exposed DNA [17]. As a result of this photoreaction the double carbon–carbon bonds in thymine moieties cyclizes with an adjacent thymine forming so-called cyclobutane thymine dimer as shown in Figure 13.2. The thymine photodimer was first isolated and analyzed in 1960 by Beukers and Berends [20] who experimented with frozen aqueous solutions of thymine.

Thymine photodimerization reaction causes bends in the DNA strand rendering it unable to replicate. In human skin, exposure to sunlight can cause formation of significant numbers of cyclobutane thymine dimers, also referred to as (T< >T) lesions [21]. There is a mechanism of repairing the (T< >T) lesions in human skin. Typically, when the cyclobutane photodimer is detected, an *excisionase* enzyme replaces the damaged region of the DNA with fresh material using the complementary DNA strand as a template [22]. Defects of the excision-repair mechanism have been linked to skin cancer [23]. Some organisms such as *Escherichia coli* have another, more elegant way, to repair the photodamage to its DNA. They produce a different enzyme, *DNA photolyase*. It binds to the thymine photodimers, restores them to their original form, ''unzipping'' the cyclobutane linkage, and then dissociates [24].

Lam Research Ex. 1035 - Page 669
Lam Research Corp. v. Inpria Corp.
IPR2024-00033 - U.S. Patent No. 9,823,564

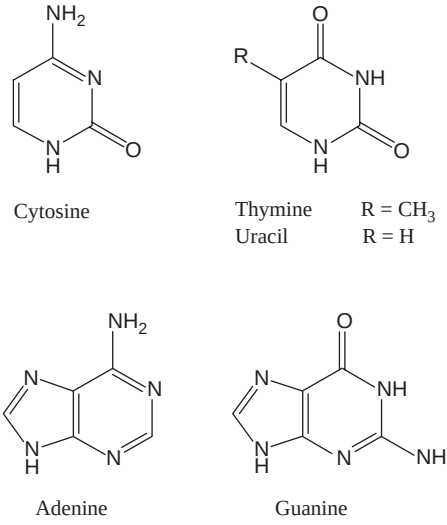


Fig. 13.1. Structures of nucleic acid bases. Cytosine, adenine, and guanine are found in both DNA and RNA. Thymine is a DNA base and uracil is an RNA base.

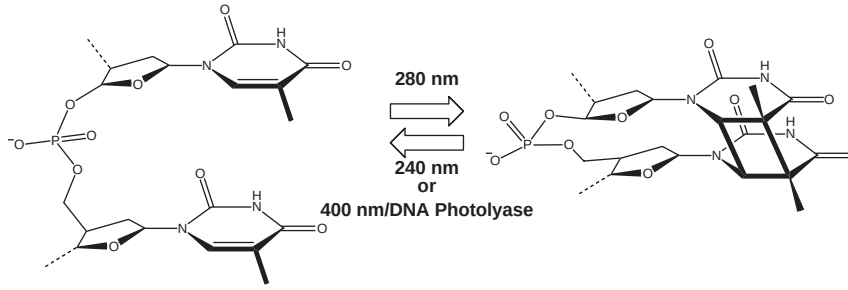


Fig. 13.2. Photodimerization of thymine moieties in a DNA strand.

Reports on photoreactivity of DNA bases led to creating a family of bio-inspired synthetic photoactive polymers that incorporated these functional groups [25]. Among them the polymers with pendant thymine groups [26–34] are especially interesting due to their ability to photocrosslink, allowing for their use in photoresist applications [26,35,36]. When exposed to UV light, thymine-containing polymers undergo a transition from individual linear polymer chains, soluble in a suitable solvent, to an insoluble crosslinked network where the polymer chains are connected to each other through thymine cyclobutane photodimers. Existence of natural mechanisms to reverse the photodimerization and to restore the polymers to their

Lam Research Ex. 1035 - Page 670
Lam Research Corp. v. Inpria Corp.
IPR2024-00033 - U.S. Patent No. 9,823,564

original state provides exciting opportunities to create fully recyclable photoresist materials [37].

2. Photo-Induced Processes in Natural Polymers – DNA

It has been long established that exposure to UV light causes damage to living organisms. It was first demonstrated nearly 130 years ago [38]. Since then, numerous studies were performed to elucidate the mechanism of the effect. The genetic material, DNA, appears to be a primary target due to its biological importance and because it is a good UV absorber. Indeed, the action spectra of many UV effects strongly resemble the absorption spectra of the corresponding nucleic acids [39]. Since the nucleic acid bases, purines (adenine and guanine) and pyrimidines (thymine and cytosine) are the main contributors to the UV absorption of the DNA, it is logical to assume that their photochemistry is mainly responsible for the DNA inactivation by UV light. Nearly 100 years after the initial work on the germicidal effect of light, it was demonstrated that the biological inactivation of DNA should be primarily attributed to the formation of thymine dimers [40]. Other events, such as breaking of the DNA strands or cross-links between two DNA strands, did not occur in numbers sufficient to cause any biological effects as result of exposure to biologically relevant irradiation doses.

A number of studies on photochemistry of the nucleic acid bases in aqueous solutions demonstrated that while uracil undergoes reversible hydration under exposure to UV irradiation, the other bases (thymine, adenine, and guanine) were stable [41,42]. However, the sensitivity of dissolved thymine to UV irradiation can be significantly increased if the solution is rapidly frozen [43]. In 1960 the thymine photoproduct was isolated from irradiated frozen aqueous solution of thymine. Elemental analysis, molecular weight measurements, powder X-ray diffraction, NMR and IR spectroscopy confirmed that the most likely photoproduct is a thymine dimer [20]. Similar photoproduct was obtained by hydrolysis of irradiated DNA. Its formation was attributed to reaction between two adjacent thymine groups on the same DNA chain [44]. Independently an identical compound was isolated from DNA of UV-irradiated bacteria [45].

Since the thymine photodimer was first isolated, its structure and the mechanism of the photodimerization reaction were studied extensively. Four different isomers of cyclobutane thymine dimer were proposed, but NMR spectroscopy was demonstrated to be insufficient to distinguish between them [46]. The structures of thymine photodimers are presented in Figure 13.3. A few years later the structure of thymine photodimers

Lam Research Ex. 1035 - Page 671
Lam Research Corp. v. Inpria Corp.
IPR2024-00033 - U.S. Patent No. 9,823,564

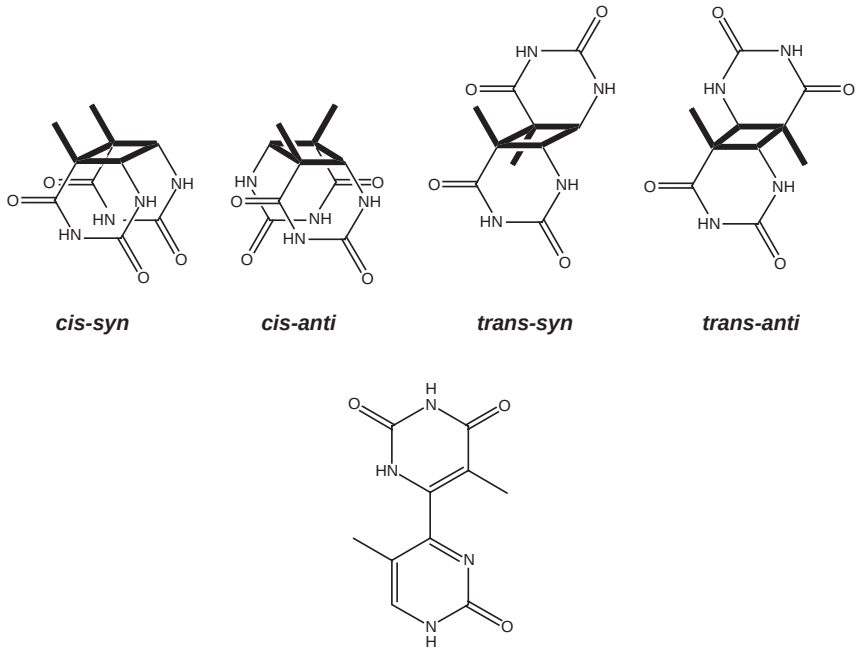


Fig. 13.3. Structures of thymine photodimers: four stereoisomers of thymine cyclobutane dimer and the (6-4) photoadduct.

obtained from either frozen aqueous solutions of thymine exposed to UV irradiation [47] or irradiated DNA [48] was determined to be predominantly the *cis–syn* isomers. In addition, the identity of the major thymine photoproducts from both studies was confirmed by co-crystallizing ^{14}C-labeled DNA-derived thymine photoproduct with unlabeled frozen solution-derived thymine photoproduct and subjecting the co-crystals to a stereospecific rearrangement reaction in ^{18}O-enriched solvent. The product of the rearrangement reaction was consistent with the *cis–syn* structure of the reagents [49]. The abundance of the *cis–syn* thymine photodimers obtained from DNA can be attributed to the prevalence of photoreactions between adjacent thymine groups on the same DNA strand, rather than interstrand cross-links which would result in either *cis–anti* or *trans–anti* products [46]. Indeed, UV irradiation of DNA under biologically relevant conditions rarely results in cross-linking of the DNA strands [50]. However, when dry DNA films were prepared and irradiated by UV light, the solubility of the films decreased dramatically upon irradiation, in a way similar to a typical

Lam Research Ex. 1035 - Page 672
Lam Research Corp. v. Inpria Corp.
IPR2024-00033 - U.S. Patent No. 9,823,564

negative photoresist behavior [51,52]. In this case crosslinking between the DNA strands could be responsible for the insolubilization of the DNA [51] possibly due to thymine photodimerization.

The mechanism of formation of thymine cyclobutane dimer was investigated both theoretically [53–56] and experimentally [57–65]. The theoretical investigations usually consider the thymine photodimerization as a 2 + 2 cycloaddition discussed in the context of Woodward–Hoffmann Frontier Molecular Orbital theory [66]. This theory describes concerted reactions, which proceed without a transition state while breaking and creating bonds occur simultaneously. In order for a reaction to proceed in a concerted manner it has to be ''symmetry allowed'', namely the symmetries of the reactant and product frontier molecular orbitals (HOMO and LUMO) should match-up. Symmetry allowed reactions usually proceed readily under mild reaction conditions, while symmetry forbidden reactions do not proceed at all or proceed through other non-concerted pathways. Symmetry allowed reactions could be further classified as thermally allowed and photochemically allowed. In thermally allowed reactions the symmetries of reagents and products highest occupied molecular orbitals should match while both reagents and products are in the ground state. In photochemically allowed reactions reagent(s) can be promoted to the excited state by absorption of a photon, thus changing the symmetry of the highest occupied molecular orbital (corresponding to the lowest unoccupied molecular orbital in the ground state) in such a way that the symmetries of the reagents' and product's orbitals match. It should be pointed out here that even symmetry allowed reactions in some cases are associated with relatively high energy barriers. However, those are not due to symmetry but due to other changes such as bond lengths, angles, hybridizations, etc. A popular example of 2 + 2 cycloaddition is dimerization of ethylene resulting in cyclobutane. Formally, this reaction is thermally allowed when two ethylene molecules approach each other orthogonally, in a so-called *supra–antara* process. However, calculations on multicomponent self-consistent field (MC-SCF) level demonstrated that even for the symmetry allowed process the energy of the transition state is very high and the reaction occurs through a non-concerted mechanism involving formation of a diradical intermediate [67]. The process with a different *supra–supra* reaction geometry, namely when two ethylene molecules approach each other with their double bonds in the same plane, is thermally forbidden, but photochemically allowed. When a ground-state ethylene molecule approaches an ethylene molecule in its first excited state the combined symmetry of the reagents orbitals matches that of cyclobutane in its first excited state and the reaction proceeds readily.

In a recent report [54], the potential energy curves for both thermal and photo-induced dimerization of thymine resulting in the *cis–syn* dimer were

Lam Research Ex. 1035 - Page 673
Lam Research Corp. v. Inpria Corp.
IPR2024-00033 - U.S. Patent No. 9,823,564

calculated. It was demonstrated that concerted thermal thymine cycloaddition is unlikely since it would require activation energy of more than 80 kcal/mol. Photochemical cycloaddition requires absorption of a photon (E~4.5–4.7 eV; λ~264–276 nm) by one of the thymines, which causes $S_1 \leftarrow S_0$ transition. Under irradiation the dimerization occurs readily. The reverse photoreaction, namely splitting of the thymine dimer into two thymines, requires irradiation with a shorter wavelength of light (E~4.9–5.0 eV).

It should be noted here that thymine photodimerization may occur by a non-concerted mechanism, involving free radical intermediates. Indeed, photoproducts other than *cis–syn* dimer, such as the next most abundant thymine dimer, so-called 6–4 adduct, were observed in irradiated DNA. However, the quantum yield of *cis–syn* photodimer formation (ϕ ~0.02) is more than an order of magnitude higher than that of the 6–4 adduct (ϕ ~0.0013) which in turn is an order of magnitude higher than the quantum yields for other thymine isomers [68]. This specificity can lead to the conclusion that the thymine photodimerization occurs predominantly via concerted 2 + 2 cycloaddition mechanism. A time-resolved study of thymine dimer formation demonstrated that thymine cyclobutane dimers are formed on a timescale of less than 200 nsec, while the 6–4 adduct is formed on a timescale of few milliseconds [69]. The delay in the formation of the latter was attributed to the mechanism of its formation through a reactive intermediate.

A number of experimental studies were carried out to elucidate the mechanism of thymine photodimerization. Although it was generally acknowledged that the thymine photodimerization in both DNA and frozen aqueous solutions proceeds from the excited singlet state via excited dimers [57,58] the role of excited triplet states was intriguing. It was demonstrated [59] that thymine photodimerization in frozen aqueous solution does not involve any triplet precursors. However, it was pointed out that the lifetime of the thymine excited singlet is of about 10^{-12} sec. This is of the same order of magnitude as the period of intermolecular vibrations in the condensed phase, but a few orders of magnitude lower than the time needed by an excited thymine molecule and a ground-state thymine molecule to diffuse towards each other in solution. The implications of these observations are that on one hand solution photodimerization most likely involves triplet precursors, but on the other hand the observations of solution photodimerization proceeding necessarily through triplet precursors should not be generalized to photodimerization in crystals or polymers. Studies on photodimerization of thymine pendant groups attached to a polymer backbone proved that in a polymer strand the photodimerization proceeds via singlet precursors [60]. Also low molecular weight ester derivatives of thymine entrapped in

Lam Research Ex. 1035 - Page 674
Lam Research Corp. v. Inpria Corp.
IPR2024-00033 - U.S. Patent No. 9,823,564

poly(vinyl acetate) thin solid film undergo photodimerization via the singlet state [60]. On the other hand irradiation of thymine solution in acetonitrile [61] demonstrated that thymine undergoes photodimerization through triplet precursors, which was proved by adding isoprene to the solution. In the presence of isoprene, a triplet quencher, the thymine photodimerization did not occur; while in absence of isoprene thymine photodimerization occurred readily. It should be noted, however, that the thymine photoproduct formed under those conditions (*trans–anti* isomer) was different from that produced by irradiation of DNA or frozen aqueous solution of thymine (*cis–syn* isomer). A later study of thymine photodimerization in acetonitrile solution [62] revealed that all four isomers of thymine cyclobutane dimers are present among the products. It was also shown that, although adding a triplet quencher pentadiene resulted in almost complete quenching of thymine photodimerization, some thymine photodimers were formed nevertheless, which was attributed to the singlet state reaction pathway.

A number of studies on sensitization of thymine photodimerization in DNA such as, for example, using acetophenone [63], pyridopsoralenes [64], and 2-(4-acetylphenyl) isoindolin-1-one [65], demonstrated that the triplet energy transfer from the excited state of the sensitizer to the ground state of the thymine results in formation of the triplet thymine which undergoes photodimerization with another ground-state thymine. These studies demonstrate the feasibility of thymine photodimer formation in DNA via triplet precursors. The thymine photodimerization pathway involving triplet intermediate states was explored theoretically, and the following mechanism was proposed for the formation of the *cis–syn* photodimer. First, an excited singlet state is formed when a photon ($\lambda \sim 264$–276 nm) is absorbed by the thymine. The excited triplet state is then formed via intersystem crossing. This is followed by a C5 attack to C5′ of the second thymine, and then a C6–C6′ crosslink is formed between the two molecules resulting in formation of a diradical. Alternatively, a C5–C5′ crosslink is being formed following the C6 attack on C6′ also resulting in a diradical, but this path is somewhat less favorable energetically. However, in both cases there is a very high energy barrier ($\sim$60 kcal/mol) preventing formation of thymine cyclobutane dimer from the triplet diradical. The reaction nevertheless may proceed since there is an opportunity for the intersystem crossing back to the singlet potential energy curve. Taking into account the solvent effects makes this path even more favorable. The photodimerization involving triplet precursors is demonstrated to be slower than the concerted reaction proceeding via singlet state. The determining factor will be the possibility of the intersystem crossing from the excited singlet into the excited triplet state before the excited thymine singlet has a chance to undergo concerted photodimerization.

Lam Research Ex. 1035 - Page 675
Lam Research Corp. v. Inpria Corp.
IPR2024-00033 - U.S. Patent No. 9,823,564

3. Photopolymers and Photoresists Containing DNA Bases

All four DNA bases are heterocyclic aromatic compounds, and therefore all of them absorb UV very efficiently, which makes them suitable components of a synthetic (as well as natural) photoreactive system. In general, purines are about an order of magnitude less photosensitive than pyrimidines [16], most likely due to higher degree of conjugation in the former, which stabilizes the double bonds. High photosensitivity allows for the use of lower doses of irradiation and results in the photoresist exhibiting inherently higher selectivity. These considerations make photopolymers with incorporated purines less advantageous than those with incorporated pyrimidines.

The photochemistry of pyrimidines is well known and described in detail in the previous section. Upon irradiation with UV light, both thymine and cytosine undergo $2+2$ dimerization. The 5,6 double bonds of adjacent pyrimidine molecules break and the cyclobutane ring is formed connecting the two molecules into a dimer. Other photodimers, such as 6–4 adduct were observed as well, but the cyclobutane dimer is the major product. However, while the formation of thymine photodimer is accompanied by the disappearance of the UV absorption band centered at $\lambda \sim 270$ nm, the cytosine photodimer does absorb the UV light in that region. Therefore, cytosine photodimerization can be reversed by exposure to UV light of the same frequency as that which was used to create it; whereas the reversal of thymine photodimerization requires photons with significantly lower wavelength ($\lambda \sim 240$ nm). This results in the higher equilibrium monomer to dimer ratio for cytosine relative to that for thymine. Therefore, the photodimerization of cytosine is less efficient than that of thymine [70]. It is also important to note the differences between the photoreactivity of pyrimidines in aqueous systems. Under exposure to UV light cytosine is susceptible to hydrolytic deamination, resulting in cytosine being converted to a uracil [71]. When uracil is irradiated in the presence of water, hydration occurs with a water molecule being added at the 5,6 double bond. This reaction is somewhat reversible [72], but nevertheless it is competing with the photodimerization. However, when thymine is irradiated (even in presence of water) the stable thymine cyclobutane photodimer is the main product. Although it has been found that uracil-based photoresists will form stable cyclobutane photodimers upon UV irradiation with high quantum efficiency [73], thymine-based photoresists are of primary interest for designing photosensitive polymers, especially if aqueous processing is required.

Since 1970s extensive systematic research was done on designing synthetic polymers containing nucleic acid bases [25]. Thymine pendant groups were successfully attached to a variety of polymer backbones, including

Lam Research Ex. 1035 - Page 676
Lam Research Corp. v. Inpria Corp.
IPR2024-00033 - U.S. Patent No. 9,823,564

polymethacrylates [26], polyethyleneimines [27], polystyrene [28], and many other polymer backbones. The photochemistry of thymine pendant groups incorporated in a synthetic polymer, namely intramolecular and intermolecular photodimerization of thymine moieties, has been studied extensively both in solution and in polymer films [29–32]. It was demonstrated that thymine-containing polymers are more photoreactive than thymine monomers or dimers, and that thymine polymers are more photoreactive in films than they are in solutions. This phenomenon has been attributed to the different mechanisms of thymine photodimerization [60]. As mentioned earlier, the photodimerization of thymine dimers in solution proceeds via triplet excited states, while the thymine pendant groups in polymers photodimerize via both singlet and triplet precursors. Also, in a dimer the excited thymine moiety has only one ground-state thymine to react with, while in the polymer each thymine (except for the terminal ones) has at least two neighbors. As the stacking interactions between the thymine bases become stronger, the ratio of singlet to triplet states of the photodimerization precursor increases [33]. In the condensed phase the photodimerization proceeds mainly through singlet precursors [60].

Two different approaches were used in the design of thymine-based negative photoresist materials [35]. One approach includes the photopolymerization of bis-thymine derivatives where upon irradiation low molecular weight compounds form polymers with thymine dimers in the main chain. These polymers are not soluble in the solvent suitable for the corresponding bis-thymine monomers (hence photoresists). A second approach involves photodimerization of thymine pendant groups in linear polymer chains. Photodimerization occurs between two thymine groups attached to two different chains (intermolecular photodimerization) and the two chains become crosslinked. After a certain number of these crosslinking events, all the chains in the polymer become part of one crosslinked network. These transitions (from individual chains to one crosslinked system) are generally associated with a variety of changes in the polymer physical properties, such as elasticity and tensile strength [74]. A property which changes dramatically upon crosslinking is solubility. Polymers consisting of separate chains usually can be dissolved in a suitable solvent. However, a crosslinked polymer network, being effectively one macromolecule with ''infinite'' (compared to that of one polymer chain) molecular weight is normally insoluble.

The need for an inexpensive, stable and versatile system, which incorporates thymine moieties in the polymer backbone led to design of the vinylbenzylthymine (VBT) monomer [34]. Its structure is presented in Figure 13.4. This monomer can be synthesized in one step from thymine and vinylbenzyl chloride. The monomer contains several built-in functionalities.

Lam Research Ex. 1035 - Page 677
Lam Research Corp. v. Inpria Corp.
IPR2024-00033 - U.S. Patent No. 9,823,564

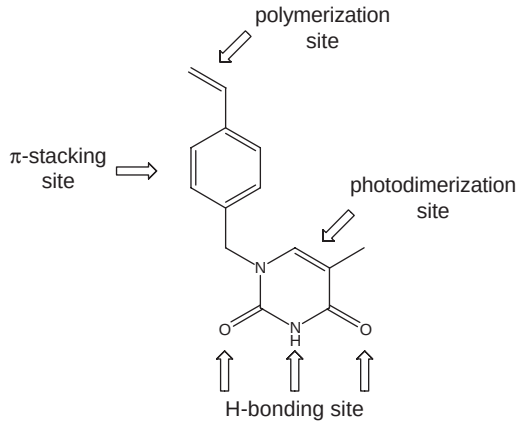


Fig. 13.4. Structure of vinylbenzylthymine (VBT) monomer.

First, the vinyl group allows for polymerization (or co-polymerization). By varying the nature of comonomer(s) and the VBT-to-comonomer(s) ratio the properties of the polymer can be fine-tuned. Second, the benzyl group serves as a link between the polymer backbone and the pendant thymine. It has the advantage of being chemically stable (unlike ester groups which are prone to hydrolysis) yet provides the thymine with enough distance from the backbone to allow limited rotational freedom. Third, the benzyl ring and the imide functional group (–CONHCO–), allow for enhanced intermolecular interactions, namely π-stacking and hydrogen bonding, respectively. The hydrogen-bonding pattern can be disrupted (if desired) by alkylating the imide nitrogen at the N-3 position. Finally, the 5,6 unsaturated bond in thymine allows for the photodimerization reaction and is responsible for the photoresist properties of the polymer.

Homogeneous free-radical polymerization of VBT with styrene, methyl methacrylate, or other similar comonomers results in an organic-soluble photoresist. Alternatively, aqueous-soluble photoresists can be prepared by copolymerization of VBT with either cationic or anionic substituted styrenes, such as vinylbenzyltriethylammonium chloride (VBA) or vinylphenyl sulfonate (VPS). The resulting copolymers can be dissolved in the suitable solvent (defined by the copolymer) and cast onto a compatible substrate. After allowing the solvent to evaporate (annealing at elevated temperature might be desirable) the VBT-containing copolymer can be rendered insoluble via exposure to UV light.

The versatility of VBT makes it an attractive research platform, since the balance between photoreactivity, solubility, and non-covalent interactions can be fine-tuned for a variety of applications. Copolymers of VBT and VPS

Lam Research Ex. 1035 - Page 678
Lam Research Corp. v. Inpria Corp.
IPR2024-00033 - U.S. Patent No. 9,823,564

were demonstrated to serve as a viable template for enzymatic synthesis of conductive polyaniline, allowing for surface patterning with a conductive polymer under mild conditions [75]. Copolymers of VBT and VBA can be used to create surfaces with bacteriostatic properties [76]. Block copolymers of VBT and VPS form micelles in aqueous solutions, and their stability could be either increased by photocrosslinking the thymine groups or decreased by methylating the thymine, thus disrupting the hydrogen bonding [77]. The VBT-based micelles have potential applications in drug delivery due to the unique ability to control their stability. Copolymers of VBT with dodecylmethacrylate have been demonstrated to form supramolecular self-assembled structures, which were identified as vesicles [78]. These vesicles were held together by hydrogen bonding between thymine groups and consequently could be decomposed by adding a complementary monomer vinylbenzyl adenine.

4. Light-Induced Immobilization of Crosslinkable Photoresists

Photoresists contain photoactive components, which absorb light of a specific wavelength and upon absorption undergo chemical transformation. As a result of such transformations, the extinction coefficient of the active ingredient changes. In addition, photoresists typically contain other components which may or may not absorb light, but do not undergo chemical reactions as result of exposure and whose extinction coefficients are therefore constant.

Let us consider frontal exposure of a crosslinkable photoresist film deposited on a non-reflective substrate. During exposure in this situation, the regions of the photoresist film close to the bottom of the film, i.e., to photoresist-substrate interface, will receive lower exposure dose than the regions at the top of the film. This is because part of the light is absorbed by the photoresist at the top of the film and never reaches the bottom. Since the amount of remaining photoactive ingredients at any specific depth depends on the exposure dose, upon exposure the composition of the photoresist will become non-uniform, changing with the distance from the top of the film. As the exposure dose increases the number of crosslinks connecting the polymer chains increases too. Initially, it results only in the increase in the molecular weight of the polymer, which does not strongly influence solubility. Eventually, however, the density of the crosslinks reaches the critical point, when an ''infinite'' molecular weight networks are formed from a large number of crosslinked polymer chains. Such networks constitute the insoluble fraction of the crosslinked polymer which is referred to as *gel*. This

Lam Research Ex. 1035 - Page 679
Lam Research Corp. v. Inpria Corp.
IPR2024-00033 - U.S. Patent No. 9,823,564

is as opposed to the soluble fraction *sol*, consisting of separate polymer chains and crosslinked fragments of "finite" molecular weight.

Prior to irradiation and at low irradiation doses the photoresist film consists only of *sol*, which can be fully solubilized during the development stage. As the irradiation dose increases, *gel* will start forming at the top of the film. If the photoresist is developed at this stage, the bottom layers consisting only of *sol* will be solubilized and both *sol* and *gel* fractions of the photoresist film will be rinsed off the substrate during the development step. Thus, in order to create an image, i.e., to ensure that the irradiated polymer stays on the substrate after development, the amount of irradiation should be sufficient to allow formation of *gel* in the bottom layer of the photoresist film. Taking into account that the onset of *gel* formation in the bottom layer occurs after the onset of *gel* formation in the top layers, it is expected that the resulting insoluble layer would have considerable thickness already at the lowest exposure dose allowing for the image formation. Alternatively, if the photoresist layer were irradiated from the bottom, through a transparent substrate, such as quartz, *gel* would first form at the bottom of the film. Thus, the minimal irradiation dose required to obtain images will be lower, but the thickness of the corresponding insoluble layer will also be low. As the irradiation dose increases, the *gel* will form at the top layers of the photoresist film, thus increasing the image thickness upon development. It is important to note that in both cases the difference between irradiation doses received by top and bottom layers is significant only for thick photoresist films with high extinction coefficients. If the photoresist film is thin and its extinction coefficient is low, the amount of irradiation absorbed by the film is negligible, and therefore the top and bottom layers of the film are exposed to about the same irradiation dose. These photoresist films can be treated as "uniformly crosslinked systems", which behave in accordance with the theory of *gel* formation developed by Flory [79–81] and further generalized by Stockmayer [82,83] and Charlesby [84]. The theory is based on the two following assumptions. First, it is postulated that no intramolecular reactions leading to formation of cyclic structures can occur. This assumption was later confirmed experimentally for a number of photocrosslinkable polymers [85]. Second, each crosslinkable moiety is assumed to be equally reactive, regardless of its surroundings and the length of the polymer chain to which it belongs. This assumption is accurate for a number of polymer systems [82].

Let us consider a system consisting of A_0 polymer chains of varying length. The polymer chains are built from identical crosslinkable units, and the total number of units in the system is A_1. If we define N_s as the number of *s*-meric chains in the system (for example, N_1 is the number of monomers, N_2 is the number of dimers, etc.) the number of polymer chains A_0 will be

Lam Research Ex. 1035 - Page 680
Lam Research Corp. v. Inpria Corp.
IPR2024-00033 - U.S. Patent No. 9,823,564

given by

$$A_0 = \sum_s N_s \tag{1}$$

and the total number of units in the system A_1 will be given by

$$A_1 = \sum_s sN_s. \tag{2}$$

Then the number-average size λ_n and the weight average size λ_w are given by

$$\lambda_n = \frac{\sum sN_s}{\sum N_s} \tag{3}$$

and

$$\lambda_w = \frac{\sum s^2 N_s}{\sum sN_s} \tag{4}$$

respectively. Also, the weight fraction of s-meric chains, w_s is given by

$$w_s = \frac{sN_s}{\sum sN_s}. \tag{5}$$

Since we are considering the simplest case where each unit has one crosslinkable moiety, w_s is also a fraction of the crosslinkable groups in the s-meric chains.

If the system is exposed to irradiation dose r, a fraction of units α ($0 \leq \alpha \leq 1$) undergoes photocrosslinking. α is referred to as crosslinking density. Thus, the total number of crosslinked units is $\alpha A_1 = \alpha \sum sN_s = \alpha \lambda_n \sum N_s$. Since the total number of chains is $A_0 = \sum N_s$, the average number of crosslinked units per chain γ, referred to as the crosslinking index, is given by

$$\gamma = \frac{\alpha \lambda_n \sum_s N_s}{\sum_s N_s} = \alpha \lambda_n. \tag{6}$$

As the crosslinking density α increases, the probability of the appearance of "infinitely large" molecules increases. In order to find the critical value of α, i.e., the *gel* point, consider a randomly chosen chain with at least one crosslink. According to the first assumption, the crosslink connects the chain with some other chain. According to the second assumption all the units have the same reactivity regardless of the length of the chain to which they belong. Therefore, the probability that the other chain (crosslinked to the first one) is s-meric is equal to the weight fraction of s-meric chains, w_s, which is also the fraction of the crosslinkable groups in the s-meric chains.

Lam Research Ex. 1035 - Page 681
Lam Research Corp. v. Inpria Corp.
IPR2024-00033 - U.S. Patent No. 9,823,564

Since the crosslinking density α is the probability of any unit to be crosslinked, the number of additional crosslinked units on an s-meric chain, crosslinked to the first chain, is expected to be equal to α multiplied by the number of remaining crosslinkable groups $(s-1)$. Thus, the expected number of additional chains crosslinked to the s-meric chain, which is crosslinked to the first randomly chosen chain, is $\alpha(s-1)$. Averaging over all chain sizes will give the average expectance of additional chains ν.

$$\nu = \sum w_s \alpha(s-1) = \alpha\left(\sum w_s s - \sum w_s\right) = \alpha(\lambda_w - 1). \tag{7}$$

An average expectance of additional chains ν, which is greater than unity allows for a non-zero probability of the randomly selected crosslinked chain belonging to an infinitely large system [79,83]. This gives the critical value of crosslinking density α_c corresponding to the *gel* point.

$$\alpha_c = \frac{1}{\lambda_w - 1} \approx \frac{1}{\lambda_w}. \tag{8}$$

The corresponding critical value of crosslinking index γ_c at *gel* point is given by

$$\gamma_c = \alpha_c \lambda_n \approx \frac{\lambda_n}{\lambda_w}. \tag{9}$$

It is interesting to note that the Eq. (9) is also valid for random copolymer systems consisting of both crosslinkable and non-crosslinkable units [83].

Prior to the *gel* point, all the polymer is soluble; i.e., it belongs to the *sol* fraction. When the *gel* point is reached, some of the polymer becomes insoluble (*gel*) due to formation of an "infinitely" large system. As the crosslinking density α increases, the amount of *gel* increases (and the amount of *sol* decreases). The partition between *sol* and *gel* fractions depends on the crosslinking density as well as on the primary distribution of the polymer chain sizes. It can be calculated in the following way [86]. The probability φ_{sol} is defined as the probability for the randomly chosen non-crosslinked unit to belong to the *sol* fraction. A randomly chosen crosslinked unit will belong to the *sol* fraction if and only if in absence of the crosslink both the unit itself and the unit to which it is crosslinked would both belong to the *sol* fraction. Thus, the probability of a crosslinked unit to be part of the *sol* is ϕ_{sol}^2. Since the probability for a randomly selected unit to be crosslinked equals α, the probability of the unit to be crosslinked and to belong to the *sol* is $\alpha\phi_{sol}^2$, while the probability of the unit not to be crosslinked and to belong to the *sol* is $(1-\alpha)\varphi_{sol}$. The probability of the unit to belong to the *sol*, whether crosslinked or not, W_{sol} is therefore

$$W_{sol} = (1-\alpha)\varphi_{sol} + \alpha\varphi_{sol}^2 = \varphi_{sol}[1 - \alpha(1-\varphi_{sol})]. \tag{10}$$

Lam Research Ex. 1035 - Page 682
Lam Research Corp. v. Inpria Corp.
IPR2024-00033 - U.S. Patent No. 9,823,564

It should be noted here that W_{sol} is also the weight fraction of *sol*, and $W_{gel} = 1 - W_{sol}$ is the weight fraction of *gel*.

The probability that an *s*-meric polymer chain has *p* crosslinked units is given by

$$P_s(p) = \frac{s!}{(s-p)!p!}\alpha^p(1-\alpha)^{s-p} \tag{11}$$

and the probability that this chain belongs to *sol*, which is calculated as the probability of all *p* of its partners belonging to *sol* in absence of all of the *p* crosslinks, is ϕ_{sol}^p. Therefore, the probability that an *s*-meric chain with *p* crosslinks is part of the *sol* fraction is given by

$$R_s(p) = P_s(p)\varphi_{sol}^p = \frac{s!}{(s-p)!p!}\alpha^p(1-\alpha)^{s-p}\varphi_{sol}^p \tag{12}$$

and the probability for a randomly chosen *s*-meric chain to be part of the *sol* fraction is then

$$R_s = \sum_p P_s(p)\varphi_{sol}^p = [1-\alpha(1-\varphi_{sol})]^s. \tag{13}$$

Since the weight fraction of *s*-meric chains is w_s, the weight fraction of *sol*, W_{sol} is given by

$$W_{sol} = \sum_s w_s R_s = \sum_s w_s[1-\alpha(1-\varphi_{sol})]^s. \tag{14}$$

For low crosslinking density α, most of the units in the system are not crosslinked and $\varphi_{sol} \cong W_{sol}$. This leads to the following expression for W_{sol}

$$W_{sol} = \sum_s w_s[1-\alpha(1-W_{sol})]^s \tag{15}$$

which can be solved numerically if the initial distribution w_s is known.

Since the primary interest for photoresist applications is the *gel* fraction rather than the *sol* fraction, the Eq. (15) can be rewritten in a following form:

$$1 - W_{gel} = \sum_s w_s[1-\alpha W_{gel}]^s. \tag{16}$$

Eqs. (8) and (16) allow calculation of the crosslinking density at the *gel* point and the weight fraction of *gel* after the *gel* point is reached as functions of crosslinking density for a polymer with known molecular weight distribution. Therefore, the next step is to find the relationship between crosslinking density and the time and intensity of the incident irradiation, i.e., exposure conditions. In order to solve this problem analytically, the simplified system was considered where the irradiation is monochromatic and the active

Lam Research Ex. 1035 - Page 683
Lam Research Corp. v. Inpria Corp.
IPR2024-00033 - U.S. Patent No. 9,823,564

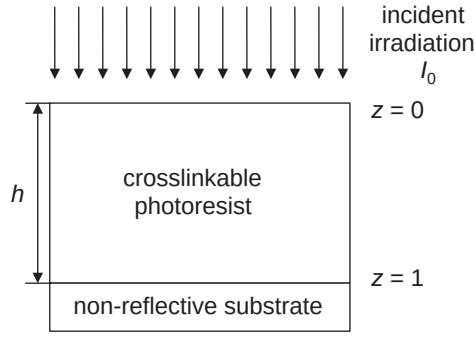


Fig. 13.5. Frontal irradiation of photoresist film coated on a non-reflective substrate.

(crosslinkable) ingredients are the only species absorbing at the wavelength of irradiation while the absorbances of both inactive ingredients and crosslinked products are low enough to be neglected [87–89].

Figure 13.5 shows a diagram of photoresist film coated on a non-reflective substrate and irradiated from the front. The thickness of the photoresist is h. It is convenient to introduce a dimensionless variable z measuring the position in the film, with $z = 0$ on the top of the film and $z = 1$ on the photoresist/substrate interface. The photoresist with density ρ consists of crosslinkable units with molecular weight M_0, molar absorptivity ε, and concentration m. At the onset of irradiation, concentration of the crosslinkable units is uniform through the film, $m = m_0 = \rho/M_0$, and the initial optical density of the film is D_0, which is given by

$$D_0 = \varepsilon m_0 h \tag{17}$$

As the irradiation progresses, m becomes a function of time t and position z due to photocrosslinking resulting from irradiation intensity I, which is a constant, at the top of the film $I = I_0$, but becomes a function of t and z at the underlying layers.

The rate of change of the concentration of crosslinkable units m is

$$\frac{\partial m(z,t)}{\partial t} = -2.303\varepsilon\phi m(z,t)I(z,t) \tag{18}$$

where ϕ is the quantum efficiency of photocrosslinking, i.e., number of crosslinked groups per absorbed quantum of irradiation (in the absence of chain reactions, 2 is the maximum value ϕ can reach). The reduction in intensity of the irradiation as it penetrates into the resist film is

$$\frac{\partial I(z,t)}{\partial z} = -2.303\varepsilon h m(z,t)I(z,t) \tag{19}$$

Lam Research Ex. 1035 - Page 684
Lam Research Corp. v. Inpria Corp.
IPR2024-00033 - U.S. Patent No. 9,823,564

After substituting the exposure time t for a dimensionless variable τ, where

$$\tau = \frac{I_0 \phi t}{m_0 h} \tag{20}$$

the solution to the system of partial differential Eqs. (18) and (19) can be thus written in a form

$$m(z,\tau) = \frac{m_0}{1 + \dfrac{10^{D_0 \tau} - 1}{10^{D_0 z}}} \tag{21}$$

$$I(z,\tau) = \frac{I_0}{1 + \dfrac{10^{D_0 z} - 1}{10^{D_0 \tau}}} \tag{22}$$

The image is formed at irradiation doses high enough to cause gelation of the photoresist adjacent to the substrate ($z = 1$). In order to achieve crosslinking density α_c the concentration of crosslinkable groups should decrease from m_0 to $(1-\alpha_c)m_0$. Substituting $m(z, \tau) = (1-\alpha_c)m_0$ and $z = 1$ in Eq. (21) and solving for τ gives the dimensionless exposure time τ_c required to produce an image

$$\tau_c = \frac{1}{2.303 D_0} \log\left[1 + \frac{\alpha_c \times 10^{D_0}}{1 - \alpha_c}\right]. \tag{23}$$

The corresponding minimal exposure dose $E_G = I_0 t_c$ is referred to as speedpoint of the photoresist and is a reciprocal of photosensitivity. It can be found from (20) and (23)

$$E_G = \frac{m_0 h}{2.303 \phi D_0} \log\left[1 + \frac{\alpha_c \times 10^{D_0}}{1 - \alpha_c}\right]. \tag{24}$$

Substituting $m_0 = \rho / M_0$, and $\alpha_c = 1/\lambda_w = M_0/M_w$, where M_w is the weight average molecular weight of the polymer and taking into account that $\alpha_c \ll 1$, Eq. (24) can be presented in the form

$$E_G = \frac{\rho h}{2.303 \phi M_0 D_0} \log\left[1 + \frac{\alpha_c \times 10^{D_0}}{1 - \alpha_c}\right] \approx \frac{\rho h}{2.303 \phi M_w} \frac{10^{D_0}}{D_0}. \tag{25}$$

For optically thin resist films, where $D_0 \ll 1$, the speedpoint is given by

$$E_G = \frac{\rho}{2.303 \varepsilon m_0 \phi M_w}. \tag{26}$$

At exposure doses exceeding the speedpoint, gelation occurs throughout the resist layer and a fraction of resist is immobilized on the substrate. The total amount of the immobilized resist is controlled by the overall

Lam Research Ex. 1035 - Page 685
Lam Research Corp. v. Inpria Corp.
IPR2024-00033 - U.S. Patent No. 9,823,564

crosslinking density in the layer. The crosslinking density $\alpha(z, \tau)$ can be found from the concentration of remaining crosslinkable units

$$\alpha(z,\tau) = 1 - \frac{m(z,\tau)}{m_0} = \frac{10^{D_0\tau} - 1}{10^{D_0 z} + 10^{D_0\tau} - 1} \tag{27}$$

and the overall crosslinking density $\alpha(\tau)$ can be found by integrating (27) over all values of z.

$$\alpha(\tau) = \frac{1}{2.303 D_0} \log \frac{10^{D_0(\tau+1)}}{10^{D_0\tau} + 10^{D_0} - 1} \tag{28}$$

Finally, for a resist with known molecular weight distribution, Eq. (16) can be applied, and the fraction of immobilized resist W_{gel} can be found as function of exposure time τ.

A plot of the *gel* fraction versus exposure is referred to as a characteristic curve of the resist. The contrast of a resist film is defined as the slope of the characteristic curve, dW_{gel}/dE at speedpoint, where $E = E_G$, and it can be presented as

$$\frac{dW_{gel}}{dE} = \frac{dW_{gel}}{d\alpha}\frac{d\alpha}{dE}. \tag{29}$$

It was demonstrated [89] that if the polymer molecular weight is distributed lognormally with dispersity (half width) β, the derivative $dW_{gel}/d\alpha$ at speedpoint is given by

$$\frac{dW_{gel}}{d\alpha} = 2\lambda_w e^{-\beta^2}. \tag{30}$$

The derivative $d\alpha/dE$ at speedpoint can be easily found from (8) and (26).

$$\frac{d\alpha}{dE} = \frac{2.303 \varepsilon m_0 \phi M_0}{\rho} \tag{31}$$

and the resist contrast is given by

$$\frac{dW_{gel}}{dE} = 2\lambda_w e^{-\beta^2} \frac{2.303 \varepsilon m_0 \phi M_0}{\rho} = \frac{2e^{-\beta^2}}{E_G}. \tag{32}$$

The predictive value of the theoretical treatment described above was verified experimentally [88,90]. The experimental results were in excellent agreement with the calculated speed point and characteristic curve of crosslinking photoresist.

Lam Research Ex. 1035 - Page 686
Lam Research Corp. v. Inpria Corp.
IPR2024-00033 - U.S. Patent No. 9,823,564

5. Reverse Processes

Incorporating thymine moieties into synthetic polymers allowed for the design of a family of photocrosslinkable polymers with the properties of negative photoresists [26,34–36]. As mentioned earlier, under exposure to UV light thymine groups undergo a photodimerization reaction. [20] In cases when the two thymine groups forming a photodimer belong to different polymer chains, the dimer becomes the crosslink. When enough crosslinks are formed, most of the polymer chains are covalently connected, becoming effectively one macromolecule of "infinite" molecular weight. Such crosslinked systems are typically insoluble [74]. A reverse process, where the thymine photodimers can be effectively "unzipped" would be highly beneficial.

There are two main reasons why the reversal of thymine photodimerization is of interest for a designer of photopolymers. First, in most applications, photoresists are being used to protect specific areas of the substrate only temporarily. After exposing the unprotected areas to desired levels of etching or other agents, the need for a photoresist is eliminated, and the photoresist is typically stripped off the substrate, allowing for the next step of the photoresist coating and image formation [5]. The ability to reverse the photocrosslinking, i.e., to resolubilize the cured photoresist, would greatly simplify the photoresist stripping step. Moreover, when the photodimerization is reversed, the polymer returns to its original form and may be collected and reused in subsequent applications. Apart from traditional photoresist applications, the ability to reverse photocrosslinking allows for the design of recyclable plastics, where a crosslinked product in the end of its useful life can be decomposed to the initial state of separate polymer chains, from which a new product can be formed. A second reason why the reversal of thymine photodimerization is of interest is in the design of positive photoresists containing thymine dimers in the backbone [35]. Photosplitting of the dimers results in chain scission and therefore increased solubility.

There are two different methods of splitting a thymine dimer: photochemical and enzymatic. In the photochemical method, the sample containing thymine dimers is irradiated with UV light. Splitting of the thymine cyclobutane dimer follows the same symmetry rules as its formation: it is thermally forbidden but photochemically allowed. When a dimer absorbs a photon of suitable wavelength ($\lambda \sim 240$ nm), it reacts with a quantum yield of nearly 100% forming two thymines [60]. In the enzymatic method an enzyme recognizes thymine dimers and repairs them. It may require the absorption of a photon, or it may happen in the dark.

Lam Research Ex. 1035 - Page 687
Lam Research Corp. v. Inpria Corp.
IPR2024-00033 - U.S. Patent No. 9,823,564

In nature, the most common way to remove thymine dimers (T< >T lesions) from DNA is excision repair [24], as was described briefly earlier. This pathway is not specific to thymine dimers; it is the mechanism for removal from DNA of any covalently modified nucleotides. First a sequence of nucleotides, including the damaged one(s) is removed from the DNA strand by an enzyme *excision nuclease* (also referred to as *excisionase*). Then the new nucleotide sequence, identical to the one removed, is synthesized with help of an enzyme *polymerase*. Here, the complementary DNA strand serves as a template for the nucleotide sequence synthesis. Finally, the newly synthesized repair patches are ligated into the DNA strand, restoring it to its original state using the enzyme *ligase*. This pathway is least relevant to photopolymer systems, and the authors are not aware of any study where *excisionase* enzymes were used on man-made polymers containing photodimers of nucleic acid bases.

Photoreactivation, i.e., the reversal of photo-induced biological inactivation upon subsequent exposure to visible or UV light, has been known since at least the 1930s when Hausser and von Oehmcke found out that banana peels darkening due to exposure to UV light can be prevented if they were subsequently irradiated with near UV and visible light [91]. Later, in the 1960s, when thymine photodimerization in DNA was discovered, and it became evident that biological inactivation is largely due to the formation of thymine dimers in DNA, the connection between photoreactivation and thymine chemistry was established [92]. It was demonstrated that the photoreactivating enzyme from baker's yeast, capable of repairing UV-induced damage to bacterial transforming DNA, is also able to remove thymine dimers from UV-irradiated DNA. Irradiation of a DNA-yeast enzyme mixture with long wave UV light ($\lambda \sim 370$ nm) resulted in the removal of more than 90% of the thymine photodimers. Since irradiation of thymine dimers with long wave UV light in absence of the enzyme does not cause disappearance of the dimers, the enzyme had to play the major role in the photoreactivation mechanism. It was proved later [93] that the combined action of yeast enzyme and light causes splitting of the thymine dimers, rather than their excision from DNA. In the following years enzymes responsible for photoreactivation (*DNA photolyases*) were found in a number of species, but not in humans (or placental mammals in general) [94]. The mechanism of the *DNA photolyase* action is as follows [24,95,96]. First, the enzyme binds to the thymine photodimer. Then the photodimer is flipped out of the DNA double helix structure and transferred into the enzyme's active site. This step can occur in the dark, since it does not involve absorption of a photon. The next step, however, requires irradiation. The optimal wavelength depends on the nature of the light absorbing chromophore (photoantenna) incorporated into

Lam Research Ex. 1035 - Page 688
Lam Research Corp. v. Inpria Corp.
IPR2024-00033 - U.S. Patent No. 9,823,564

the specific enzyme. *DNA photolyases* from *E. coli*, yeast and some other organisms demonstrate maximum activity at wavelength of ~380 nm.These are folate-type enzymes with MTHF as a photoantenna chromophore. Enzymes demonstrating maximum activity at wavelength of ~440 nm belong to the deazaflavin type and contain 8-HDF as a photoantenna chromophore. Absorption of the photon by the enzyme's photoantenna is followed by energy transfer to $FADH^-$, a chromophore present in both types of *DNA photolyase* and located in close proximity to the active site of the enzyme. The excited $^1(FADH^-)^*$ in turn transfers an electron to the thymine dimer converting the latter into a radical anion. Due to symmetry considerations, 2 + 2 cycloreversion of either the thymine dimer or the thymine dimer radical anion are thermally forbidden. However, while the thymine dimer is stable even at elevated temperatures, the energy barrier for the splitting of the thymine dimer radical anion into a thymine and a thymine radical anion is relatively low (~10 kcal/mol), and the reaction proceeds readily at ambient temperatures via a non-concerted pathway. Finally, the newly produced thymine radical anion is converted to thymine by transferring an electron back to FADH, thus completing the cycle. The thymines are restored to their original locations in the DNA strand, and the enzyme disengages.

Enzymatic photoreversal of thymine (and in general pyrimidine) dimerization have a wide range of potential practical applications. It was reported, for example, that topical treatment of UVB-irradiated human skin with *DNA photolyase* from *Anacystis nidulans* accompanied by exposure to long wavelength (340–450 nm) photoreactivating light prevented erythema, sunburn-cell formation, and UV-induced immunosuppressive effects [97]. On the other side of the spectrum, *DNA photolyase* from *E. coli* was demonstrated to reverse photocrosslinking in thymine-containing negative photoresist allowing easy stripping and subsequent recycling [37].

Non-enzymatic photoreversal of thymine dimerization by short-wave UV (~240 nm) was used to design positive photoresists [26]. Alternatively an image can be obtained by photodecoupling of crosslinks in preirradiated thymine-containing negative photoresists. Since the quantum efficiency of thymine dimer splitting is significantly higher than that of thymine dimer formation, this approach may result in a positive resist system with high sensitivity. Another interesting application of photoreversibility of thymine dimerization was reported recently [98]. It was demonstrated that the wettability of a thymine-terminated self assembled monolayer changes upon thymine photodimerization. Subsequent photocleavage of the dimers results in the reversal of the wettability change to the original contact angle values. This allows for the design of photoresponsive surfaces with reversible wetting properties.

Lam Research Ex. 1035 - Page 689
Lam Research Corp. v. Inpria Corp.
IPR2024-00033 - U.S. Patent No. 9,823,564

6. Conclusions

The significance of thymine photodimerization in UV-induced biological inactivation is evident by the vast amount of information on its structure and chemistry already accumulated in the literature. Ongoing research has been inspired in part by the recent awareness of increasing levels of UV radiation at the Earth's surface due to ozone depletion [99]. Thymine-containing polymers and supramolecular structures are bio-inspired systems which recently gained much attention due to their photosensitivity and molecular recognition patterns [35,60,78,98,100–104]. Extending the knowledge gained from studying the natural phenomena associated with thymine reactivity and intermolecular interactions has generated a diapason of potential practical applications ranging from photoresists [35,36] and organic–inorganic hybrid devices [100] to antibacterial coatings [76], drug delivery systems [77,101], and recyclable plastics [37].

Copolymerizing VBT with either cationic or anionic substituted styrenes allowed us to obtain a fully water-processable photoresist [36]. Extension of polymeric structures is possible through backbone and side-chain modifications, especially terpolymers. Three-component systems containing the photoreactive monomer, the solubilizing monomer, and a "functional" monomer open the door to a virtually infinite set of physical and chemical parameters to be exploited and optimized.

With increasing attention given to the environmental and toxicological implications associated with commercial materials, thymine-based polymeric systems offer a Green Chemistry platform [105]. Such systems can be designed that are consistent with the principles of Green Chemistry. These systems can be water soluble, require low energies for processing, derived from renewable feedstocks, and be biodegradable and non-toxic.

From an intellectual perspective, these systems offer insight into physiologically relevant processes while at the same time providing commercially relevant opportunities in materials science. This synergy is somewhat unique in scientific endeavor and will undoubtedly provide new knowledge and materials that have not yet been imagined.

The questions below are intended to help the reader in learning the material presented in the chapter.

1. What is a photoresist? What are their applications?
2. In the heliography experiments described in the *Introduction* was bitumen acting as a positive or as a negative photoresist?
3. What is the difference between the structure of the thymine dimer in DNA irradiated *in vivo* and in dry films? What would you expect to be the structure of thymine dimers in crosslinked VBT photoresist?

Lam Research Ex. 1035 - Page 690
Lam Research Corp. v. Inpria Corp.
IPR2024-00033 - U.S. Patent No. 9,823,564

4. What is the difference between singlet and triplet states of the excited thymine molecule? Why do triplet precursors play a more important role in thymine dimerization in solutions than in films?
5. What makes the copolymers of VBT with VPS water soluble?
6. Draw two VBT molecules hydrogen bonded to each other.
7. Draw a graph of the *gel* fraction W_{gel} as function of crosslinking density for a polymer consisting of chains of equal length of (a) 10, (b) 30, (c) 100 crosslinking units. For each curve show on the graph the critical crosslinking density α_c. What crosslinking density is required in each case to insolubilize 99% of the polymer?
8. What photoresist polymer would you expect to have the best contrast? (a) High M_w, large β, (b) low M_w, large β; (c) high M_w, small β; (d) low M_w, small β.
9. What wavelength of light is required to split thymine photodimers (a) in presence of *DNA photolyase*; (b) in absence of *DNA photolyase*? Why is the former process biologically significant, while the latter is not?

Acknowledgments

Authors would like to thank SAPPI Ltd. for financial support, Mr. Mark Gordon for assistance in preparing the manuscript, and Dr. Roger A. Boggs for fruitful discussions.

References

1. J. Kilby, Chem. Phys. Chem. **2** (2001) 482.
2. K. Kempf, Electronic Computers Within the Ordnance Corps, U.S. Army Ordnance Corps, 1961.
3. W. Shockley, Circuit Element Utilizing Semiconductor Material, US Patent 2, 569, 347, 1951.
4. J. Bardeen, Semiconductor Research Leading to the Point Contact Transistor, in: Nobel Lectures, Physics 1942–1962, Elsevier Publishing Company, Amsterdam, 1964.
5. H. J. Levinson, Principles of Lithography, SPIE The International Society for Optical Engineering, 2001.
6. C. G. Khan Malek, S. S. Das, J. Vac. Sci. Technol. B **16** (1998) 3543.
7. S. Middleman, A. K. Hochberg, Process Engineering Analysis in Semiconductor Device Fabrication, McGraw-Hill, New York, 1993.
8. M. J. Bowden, A Perspective on Resist Materials for Fine-Line Lithography, in: L. F. Thompson, C. G. Willson, J. M. J. Frechet (Eds.),

Lam Research Ex. 1035 - Page 691
Lam Research Corp. v. Inpria Corp.
IPR2024-00033 - U.S. Patent No. 9,823,564

Materials for Microlithography. Radiation-Sensitive Polymers, ACS, Washington DC, 1984.
9. K. Horie, Introduction to Photopolymers and Microelectronics, in: K. Horie, T. Yamashita (Eds.), Photosensitive Polyimides, Technomic Publishing Company, Inc., Lancaster, PA, 1995.
10. J. Rullkotter, A. Nissenbaum, Naturwissenschaften **75** (1988) 618.
11. P. G. Bahn, Nature **356** (1992) 109.
12. S. A. Buckley, R. P. Evershed, Nature **413** (2001) 837.
13. J. Towler, The Silver Sunbeam, Joseph H. Ladd, New York, 1864.
14. L. M. Minsk, J. G. Smith, V. P. Van Deusen, J. F. Wright, J. Appl. Polymer Sci. **2** (1959) 302.
15. L. M. Minsk, W. P. Van Deusen, E. M. Robertson, Printing-Plate Resists of Cinnamic Acid Esters of Polyvinyl Alcohol and Cellulose, US Patent 2, 610, 120, 1952.
16. J. Jagger, Introduction to Research in Ultraviolet Photobiology, Prentice Hall, Inc., Englewood Cliffs, NJ, 1967.
17. A. D. McLaren, D. Shugar, Photochemistry of Proteins and Nucleic Acids, Pergamon Press, New York, 1964.
18. A. Hollaender, J. P. Greenstein, W. V. Jenrette, J. Nat. Canc. Inst. **2** (1941) 23.
19. J. P. Greenstein, W. V. Jenrette, Cold Spring Harb. Symp. Quant. Biol. **9** (1941) 236.
20. R. Beukers, W. Berends, Biochim. Biophys. Acta **49** (1961) 181.
21. J. Cadet, P. Vigny, Photochemistry of Nucleic Acids, in: H. Morrisson (Ed.), Bioorganic Photochemistry, Wiley, New York, 1990.
22. P. C. Hanavalt, S.-C. Liu, C. S. Parsons, J. Invest. Dermatol. **77** (1981) 86.
23. R. B. Setlow, Nature **71** (1978) 713.
24. A. Sancar, Chem. Rev. **103** (2003) 2203.
25. K. Takemoto, J. Polym. Sci. Polym. Symp. **55** (1976) 105 and references cited therein.
26. Y. Inaki, M. J. Moghaddam, K. Takemoto, Pyrimidine Derivatives as Lithographic Materials, in: E. Reichmanis (Ed.), Polymers in Microlithography: Materials and Processes, ACS, Washington DC, 1989.
27. C. G. Overberger, Y. Inaki, J. Polym. Sci. Polym. Chem. Ed. **17** (1979) 1739.
28. K. Kondo, T. Sato, Y. Inaki, K. Takemoto, Die Makromolekulare Chemie **176** (1975) 3505.
29. Y. Kita, Y. Inaki, K. Takemoto, J. Polym. Sci. Polym. Chem. Ed. **18** (1980) 427.

Lam Research Ex. 1035 - Page 692
Lam Research Corp. v. Inpria Corp.
IPR2024-00033 - U.S. Patent No. 9,823,564

30. Y. Kita, T. Uno, Y. Inaki, K. Takemoto, J. Polym. Sci. Polym. Chem. Ed. **19** (1981) 1733.
31. Y. Inaki, Y. Suda, Y. Kita, K. Takemoto, J. Polym. Sci. Polym. Chem. Ed. **19** (1981) 2519.
32. Y. Kita, T. Uno, Y. Inaki, K. Takemoto, J. Polym. Sci. Polym. Chem. Ed. **19** (1981) 2437.
33. Y. Kita, T. Uno, Y. Inaki, K. Takemoto, J. Polym. Sci. Polym. Chem. Ed. **19** (1981) 477.
34. C. M. Cheng, M. J. Egbe, M. J. Grasshoff, D. J. Guarrera, R. P. Pai, L. D. Taylor, J. C. Warner, J. Polym. Sci. Part A: Polym. Chem. **33** (1995) 2515.
35. Y. Inaki, Polymer News **17** (1992) 367.
36. S. Trakhtenberg, J. C. Warner, R. Nagarajan, F. F. Bruno, L. A. Samuelson, J. Kumar, Chem. Mater. **18** (2006) 2873.
37. J. R. Whitfield, A. Morelli, J. C. Warner, J. Macromol. Sci. A **42** (2005) 1541.
38. A. Downes, T. P. Blunt, Proc. R. Soc. Med. **26** (1877) 488.
39. B. Rajewsky, H. Bucker, H. Pauli, Arch. Biochem. Biophys. **82** (1959) 229.
40. R. B. Setlow, Molecular Changes Responsible for Ultraviolet Inactivation of the Biological Activity of DNA, in: Mammalian Cytogenetics and Related Problems in Radiobiology, Pergamon Press, Long Island City, NY, 1964.
41. R. L. Sinsheimer, R. Hastings, Science **110** (1949) 525.
42. D. Shugar, K. L. Wierzchowski, Postepi Biochimii **4** (1958) 243.
43. R. Beukers, J. Ijlstra, W. Berends, Rec. Trav. Chim. **77** (1958) 729.
44. R. Beukers, J. Ijlstra, W. Berends, Rec. Trav. Chim. **79** (1960) 101.
45. A. Wacker, H. Dellweg, D. Weinblum, Naturwissenschaften **47** (1960) 477.
46. D. L. Wulff, G. Fraenkel, Biochim. Biophys. Acta **51** (1961) 332.
47. G. M. Blackburn, R. J. H. Davies, J. Chem. Soc. C **23** (1966) 2239.
48. G. M. Blackburn, R. J. H. Davies, Biochem. Biophys. Res. Commun. **22** (1966) 704.
49. G. M. Blackburn, R. J. Davies, J. Am. Chem. Soc. **89** (1967) 5941.
50. R. B. Setlow, W. L. Carrier, J. Mol. Biol. **17** (1966) 237.
51. D. Shugar, J. Baranowska, Nature **185** (1960) 33.
52. R. W. Kaplan, Naturwissenschaften **42** (1955) 184.
53. S. K. Srivastava, P. C. Mishra, Int. J. Quant. Chem. **16** (1979) 1051.
54. B. Durbeej, L. A. Eriksson, J. Photochem. Photobiol. A **152** (2002) 95.
55. B. Durbeej, L. A. Eriksson, Photochem. Photobiol. **78** (2003) 159.

Lam Research Ex. 1035 - Page 693
Lam Research Corp. v. Inpria Corp.
IPR2024-00033 - U.S. Patent No. 9,823,564

56. R. B. Zhang, L. A. Eriksson, J. Phys. Chem. B **110** (2006) 7556.
57. A. A. Lamola, J. Eisinger, Proc. Natl. Acad. Sci. U.S.A. **59** (1968) 46.
58. P. J. Wagner, D. J. Bucheck, J. Am. Chem. Soc. **90** (1968) 6530.
59. J. Eisinger, R. G. Shulman, Proc. Natl. Acad. Sci. U.S.A. **58** (1967) 895.
60. Y. Inaki, Reversible Photoimerization of Pyrimidine Bases, in: W. M. Horspool, F. Lenci (Eds.), CRC Handbook of Organic Photochemistry and Photobiology, 2nd Edition, CRC Press, Boca Raton FL, 2004.
61. A. A. Lamola, J. P. Mittal, Science **154** (1966) 1560.
62. P. J. Wagner, D. J. Bucheck, J. Am. Chem. Soc. **92** (1970) 181.
63. A. A. Lamola, T. Yamane, Proc. Natl. Acad. Sci. U.S.A. **58** (1967) 443.
64. A. Moysan, A. Viari, P. Vigny, L. Voituriez, J. Cadet, E. Moustacchi, E. Sage, Biochemistry **30** (1991) 7080.
65. V. Lhiaubet-Vallet, J. Trzcionka, S. Encinas, M. A. Miranda, N. Chouini-Lalanne, J. Phys. Chem. B **108** (2004) 14148.
66. R. B. Woodward, R. Hoffmann, Angew. Chem. **8** (1969) 781.
67. F. Bernardi, A. Bottoni, M. A. Robb, H. B. Schlegel, G. Tonachini, J. Am. Chem. Soc. **107** (1985) 2260.
68. T. Douki, M. Court, S. Sauvaigo, F. Odin, J. Cadet, J. Biol. Chem. **275** (2000) 11678.
69. S. Marguet, D. Markovitsi, J. Am. Chem. Soc. **127** (2005) 5780.
70. D. J. Fenick, H. S. Carr, D. E. Falvey, J. Org. Chem **60** (1996) 624.
71. K. Takasawa, C. Masutani, F. Hanaoka, S. Iwai, Nucleic Acids Res. **32** (2004) 1738.
72. R. J. Boorstein, T. P. Hilbert, R. P. Cunningham, G. W. Teebor, Biochemistry **29** (1990) 10455.
73. Y. Inaki, S.-I. Fukunaga, Y. Suda, J. Polym. Sci. Polym. Chem. **24** (1985) 119.
74. A. Charlesby, Atomic Radiation and Polymers, Pergamon Press, New York, 1960.
75. S. Trakhtenberg, Y. Hangun-Balkir, J. C. Warner, F. F. Bruno, J. Kumar, R. Nagarajan, L. A. Samuelson, J. Am. Chem. Soc. **127** (2005) 9100.
76. R. F. El-Hayek, K. Dye, J. C. Warner, J. Biomed. Mater. Res.: Part A **79A** (2006) 874.
77. K. Saito, L. Ingalls, J. C. Warner, Polymer Preprints **47** (2006) 829.
78. J. F. Lutz, A. F. Thunemann, R. Nehring, J. Polym. Sci. Part A: Polym. Chem. **43** (2005) 4805.
79. P. J. Flory, J. Am. Chem. Soc. **63** (1941) 3083.

Lam Research Ex. 1035 - Page 694
Lam Research Corp. v. Inpria Corp.
IPR2024-00033 - U.S. Patent No. 9,823,564

80. P. J. Flory, J. Am. Chem. Soc. **63** (1941) 3091.
81. P. J. Flory, J. Am. Chem. Soc. **63** (1941) 3096.
82. W. H. Stockmayer, J. Chem. Phys. **11** (1944) 45.
83. W. H. Stockmayer, J. Chem. Phys. **12** (1944) 125.
84. A. Charlesby, Proc. R.. Soc. Med. **A222** (1954) 542.
85. A. Reiser, P. L. Egerton, Macromolecules **12** (1979) 670.
86. P. J. Flory, Principles of Polymer Chemistry, Cornell University Press, Ithaca, NY, 1953.
87. A. Reiser, E. Pitts, Photogr. Sci. Eng. **20** (1976) 225.
88. A. Reiser, J. Chim. Phys. **77** (1980) 469.
89. A. Reiser, E. Pitts, J. Photogr. Sci. **29** (1981) 187.
90. N. J. H. Parham, E. Pitts, A. Reiser, Photogr. Sci. Eng. **21** (1977) 145.
91. R. D. Ley, Proc. Natl. Acad. Sci. U.S.A. **90** (1993) 4337.
92. D. L. Wulff, C. S. Rupert, Biochem. Biophys. Res. Commun. **7** (1962) 237.
93. J. K. Setlow, Photochem. Photobiol. **3** (1964) 405.
94. E. C. Friedberg, G. C. Walker, W. Siede, R. D. Wood, R. A. Schultz, T. Ellenberger, DNA Repair and Mutagenesis, ASM Press, Washington DC, 2006.
95. P. F. Heelis, R. F. Hartman, S. D. Rose, Chem. Soc. Rev. **24** (1995) 289.
96. T. Langenbacher, X. Zhao, G. Bieser, P. F. Heelis, A. Sancar, M.-E. Michel-Beyerle, J. Am. Chem. Soc. **119** (1997) 10532.
97. H. Stege, L. Roza, A. A. Vink, M. Grewe, T. Ruzicka, S. Grether-Beck, J. Kruttmann, Proc. Natl. Acad. Sci. U.S.A. **97** (2000) 1790.
98. S. Abbott, J. Ralston, G. Reynolds, R. Hayes, Langmuir **15** (1999) 8923.
99. J. S. Seinfeld, S. N. Pandis, Atmospheric Chemistry and Physics: From Air Pollution to Climate Change, Wiley, New York, 1997.
100. Y. Imai, T. Ogoshi, K. Naka, Y. Chujo, Polym. Bull. **45** (2000) 9.
101. Y. Dahman, J. E. Puskas, A. Margaritis, Z. Merali, M. Cunningham, Macromolecules **36** (2003) 2198.
102. D. J. Duffy, K. Das, S. L. Hsu, J. Penelle, V. M. Rotello, H. D. Stidham, J. Am. Chem. Soc. **124** (2002) 8290.
103. O. Uzun, V. M. Rotello, J. Am. Chem. Soc. **126** (2004) 14773.
104. H. Xu, R. Hong, T. Lu, O. Uzun, V. M. Rotello, J. Am. Chem. Soc. **128** (2006) 3162.
105. P. Anastas, J. C. Warner, Green Chemistry: Theory and Practice, Oxford University Press, Oxford, 1998.

Lam Research Ex. 1035 - Page 695
Lam Research Corp. v. Inpria Corp.
IPR2024-00033 - U.S. Patent No. 9,823,564

Chapter 14

Formation of Unconventional Compounds and Catalysts in Magnesium-Containing Organic Films

V.V. Smirnov, L.A. Tyurina, and I.P. Beletskaya

Chemistry Department, Lomonosov Moscow State University, Leninskie Gory, Moscow 119992, Russia

1. Introduction: Reactions in the Films Obtained by Co-Condensation of Metal Vapor with Organic Compounds 697
2. Synthesis of Magnesium-Containing Films by Co-Condensation of Reagents 701
3. Synthesis of RMg_4X Compounds in Thin Films of Co-Condensates 703
4. Mechanism of the Processes in Organic Magnesium-Containing Films and the Nature of the Magic Number Four. 705
5. Competition between the Aggregation of Magnesium Atoms and the Generation of Radicals in Mg–RX Films 710
6. Structure and Reactivity of Unconventional Organomagnesium Compounds Obtained in Co-Condensate Films 712
7. Catalytic Reactions in Mg–RH Films 714
8. Synthesis of Catalysts in Multicomponent Films Containing Magnesium and a Transition Metal 717
9. Conclusions 719
References 720

Low-temperature synthesis in metal-containing films is an original and promising field of organometallic chemistry. A classical Grignard reaction in Mg–RX films turned out to yield novel compounds of composition RMg_nX. The use of cluster Grignard reagents and their hydride analogues considerably extends the range of objects and processes in the chemistry of organomagnesium compounds and makes it possible to observe catalytic transformations of hydrocarbons.

1. Introduction: Reactions in the Films Obtained by Co-Condensation of Metal Vapor with Organic Compounds

Low-temperature synthesis in thin films obtained by co-condensation of metals and organic compounds on a cooled surface is an original and promising field of organometallic chemistry. Works dealing with low-temperature

THIN FILMS AND NANOSTRUCTURES, vol. 34
ISSN 1079-4050
DOI: 10.1016/S1079-4050(06)34014-8

© 2007 by Elsevier Inc.
All rights reserved.

Lam Research Ex. 1035 - Page 696
Lam Research Corp. v. Inpria Corp.
IPR2024-00033 - U.S. Patent No. 9,823,564

reactions in metal-containing films were pioneered in the 1920s under the leadership of N.N. Semenov, a Nobel laureate in chemistry [1]. These works disclosed that explosive reactions took place in films obtained by condensation of cadmium and sulfur vapors on a surface cooled with liquid air. It was later found that acrylic monomers underwent rapid polymerization in films of their co-condensates with magnesium [2]. These investigations have been greatly advanced by the development of the matrix isolation method, which makes it possible to identify and study compounds unstable under usual conditions [3, 4]. Since the pioneering works of the 1970s (see, e.g., Refs. [5–10]), a multitude of reactions of metals with different substrates in cooled thin films have been studied. They have been surveyed in numerous papers, monographs, and reviews (see, e.g., Refs. [11–13]).

One major reason for the great interest in the processes of thin metal-containing films is that reactions on the surface of small metal clusters can be studied. Indeed, prior to the development of thin-film chemistry, reactions of similar particles were studied only in the gas phase at rather high temperatures. Under these conditions, most of the primary products are unstable and decompose in the course of further reaction, which is nonselective. As a result, the information obtained on the routes and mechanisms of reactions of disperse metals appears to be scarce, while the use of such reactions in synthesis is inexpedient. Conversely, low-temperature reactions in the films of co-condensates are very promising from the standpoint of determining the detailed reaction mechanism, as well as for synthesis of previously unknown complexes and organometallic compounds. It is important that atoms of only a few metals react with organic compounds immediately at the instant of their contact on the cooled substrate. Rather often, atoms and/or small (molecular) clusters are first stabilized in the film, and then their transformations are observed.

In some cases, polymerization of organic compounds, for example, paraxylylene, a product of pyrolysis of paracyclophane, in metal-containing films yields samples stable at ambient or elevated temperatures [14–16] (see also Chapter 10 of this handbook). However, it is a more common practice to use organic compounds that are liquid at room temperature as a matrix (the component that is in excess with respect to the metal). The further fate of the resulting films depends on the proportion between the metal aggregation rate and the reaction rate of the metal with the matrix. Figure 14.1 shows the general scheme of transformations that occur in co-condensate films as they warm up. In one limiting case (route A, Figure 14.1) when the matrix is inert with respect to the metal and the aggregation rate is high, an increase in the mobility of atoms and small clusters leads to the formation of metal microcrystallites and, eventually, massive metal samples. Naturally, such a metal differs in properties from bulk metal. Its structure is, as a rule,

Lam Research Ex. 1035 - Page 697
Lam Research Corp. v. Inpria Corp.
IPR2024-00033 - U.S. Patent No. 9,823,564

rich in defects. Even if the most inert organic compounds, such as, say, alkanes, are used as a matrix, the resulting metal powder contains from a few tenths of a percent to a few percent of organic matter as fragments of matrix molecules. These films are highly disperse, have a loose structure, and are devoid of the surface oxide layer; therefore, they are of interest as potential catalysts, acceptors of hydrogen and other gases, and reagents for organometallic synthesis. Let us give only one example for the metal that is dealt with in this chapter. As is known, magnesium is not among efficient hydrogen acceptors, which include platinum group metals and lanthanides. However, after condensation with an organic component and removal of the latter, magnesium can be used for hydrogen storage. Materials capable of accumulating hydrogen can also be obtained based on two metals: magnesium with nickel or magnesium with copper. Co-condensation of these pairs of metals with organic compounds followed by removal of volatile components yields metal composites that efficiently store hydrogen [17–19].

A different situation arises when the affinity of the matrix substance for a metal is higher than that of, say, alkanes but is insufficient for common chemical reactions to take place resulting in stable products. In this case, as the matrix softens, the process can stop halfway through when metal particles range from a few nanometers to hundreds of nanometers in size. This pathway is shown by route B in Figure 14.1. The nascent nanoclusters

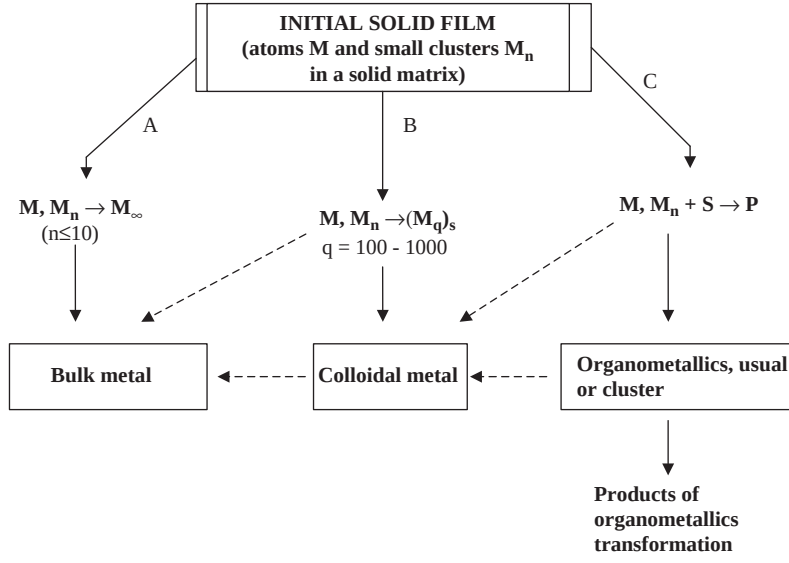


Fig. 14.1. The general scheme of transformations that occur in co-condensate Mg–organic films at their warming up.

Lam Research Ex. 1035 - Page 698
Lam Research Corp. v. Inpria Corp.
IPR2024-00033 - U.S. Patent No. 9,823,564

have the major properties of a conventional metal but are not quite identical to it.

The chemistry and physics of such particles represent a separate, rapidly developing field. The consideration of this field (even if brief) is beyond the scope of this review. From the standpoint of this review, of most interest is the fact that melting of similar films often produces stable colloid solutions of metals in non-aqueous media. Early works in this field were summarized in review [19]. Among later results, noteworthy is the stabilization of metal nanoparticles in tertiary amines, which appear to be a unique medium for formation of stable colloid solutions of a wide variety of metals [20, 21]. Metal colloids stable for, at least, several years were obtained through the intermediate formation of thin films of co-condensates of metals with amines.

If the reactivity of the matrix is high, reactions dominate over aggregation as the film warms up and, thus, stable chemical compounds are formed (route C, Figure 14.1). Chemical reactions in the films obtained by co-condensation offer excellent possibilities for synthesis of metal derivatives, both the already synthesized ones and the as yet unsynthesized and otherwise inaccessible compounds. This strategy made it possible to obtain for the first time unusual metal carbonyls ($Cu(CO)_3$, $Ag(CO)_3$, $Pt(CO)_4$, etc.), previously unknown metal bisarene complexes, lithium dichloride, divalent aluminum compounds, and many others [22–24]. An important feature of reactions in low-temperature films is that they involve small (molecular) metal clusters forming at the initial stage of aggregation. This property of the films made it possible to synthesize for the first time cluster organomagnesium compounds, which were found to have unique and very interesting properties.

The chemistry of organomagnesium compounds, which owes its emergence to Victor Grignard [25], has recently celebrated its 100th anniversary. Grignard reagents remain the most important metal-containing reagents in synthetic organic chemistry, providing a methodological basis for synthesis. This class of compounds allows one to deal with the major challenge of organic synthesis, i.e., to form new carbon–carbon bonds. As early as in 1950, 1400 pages of the fundamental monograph by Kharasch [26] were devoted to the description of only major synthetic applications of the Grignard reaction. Organomagnesium synthesis involves the nucleophilic addition of Grignard reagents to the carbon–carbon multiple bond and the nucleophilic substitution at the carbon atom. These fundamental chemical reactions make organomagnesium compounds indispensable in both preparatory chemistry and commercial synthesis, for example, in production of drugs and food additives. Large-scale applications of Grignard reagents can be exemplified by the production of the anticancer drug tamoxifen, its

Lam Research Ex. 1035 - Page 699
Lam Research Corp. v. Inpria Corp.
IPR2024-00033 - U.S. Patent No. 9,823,564

hydroxy derivative droloxifene (Pfizer), which is currently under development for the treatment of osteoporosis, and numerous Analgetics [27].

It is not a surprise, therefore, that, by 1975, more than 40,000 publications had addressed the synthesis and application of Grignard reagents [28]. No exact data are currently available; however, there is no doubt that the number of publications has increased manifold since then. The studies of formation of organomagnesium compounds and their properties, reactions, and structures are currently continued. Advances in this field have been reviewed, e.g., in Refs. [29–31]. Nevertheless, an entire field of organomagnesium chemistry – the chemistry of organic magnesium clusters – has remained unknown until recently. It was taken for granted that the stoichiometry of the classical Grignard reaction is expressed by the equation

$$RX + Mg \rightarrow RMgX, \tag{1}$$

where X is a halogen and R is an organic radical (most often, alkyl). It has of course long been recognized that reaction (1) is complicated by the participation of solvent molecules (most often, tetrahydrofuran or diethyl ether), RMgX compounds can associate and are in mobile equilibrium with R_2Mg and MgX_2, and so on. However, the reaction itself was believed to occur according to Eq. (1); i.e., one atom of magnesium reacts with one molecule of an organic halide. Only studies of reactions in the films of magnesium co-condensates with organic halides (and some hydrocarbons) have revealed new facets of this process, associated with the existence of small metal clusters, which are our main concern in this review.

Thus, reactions in metal-containing films are of interest from the standpoint of producing small metal clusters and studying the specific features of their formation and interaction with organic components. In the following sections, these questions will be surveyed as applied to the classical reaction of magnesium with organic halides in films of their co-condensates.

2. Synthesis of Magnesium-Containing Films by Co-Condensation of Reagents

All three limiting cases shown in Figure 14.1 can take place, either separately or in parallel, in the films of magnesium co-condensates with organic compounds. Route A can be realized in films obtained by co-condensation of magnesium with *n*-alkanes and some oxygen-containing compounds when no chemical reaction occurs. The metal thus obtained contains some amount of fragments of organic molecules, has a developed surface, and is

Lam Research Ex. 1035 - Page 700
Lam Research Corp. v. Inpria Corp.
IPR2024-00033 - U.S. Patent No. 9,823,564

extremely reactive. Magnesium resulting from the co-condensation of its vapor with the above compounds has been suggested for use as a dihydrogen absorber of high capacity [17, 18] or in reaction (1) with organic halides that do not react with common magnesium turnings [32].

Attempts to put into practice route B failed for a long time. The co-condensation of magnesium vapor with functional organic compounds leads only sometimes to the formation of unstable colloid solutions [33]. Only the use of tertiary amines as matrices made it possible to obtain properly stable solutions of zero-valent magnesium [20, 21]. These solutions turned out to be excellent initiators of radical reactions with participation of carbon tetrachloride [34]. However, the above routes of transformation are an exception rather than a rule for magnesium. The high activity of magnesium atoms and clusters leads to that; even at low temperatures (and often prior to the melting of co-condensate films), these particles react with organic compounds to give quite unexpected products.

Organomagnesium synthesis in films of co-condensates of magnesium and organic halide vapors codeposited on the surface at liquid-nitrogen temperature was pioneered by Skell and Girard [35]. They observed the solid-phase reaction of magnesium (atomic as was believed at that time) with propyl halides. The reaction products were not isolated, and their composition was judged by the composition of the reaction mixture after hydrolysis. The works by Sergeev et al. [36–38] represented an important milestone in the study of magnesium reactions. In these works, the specific features of reactions in magnesium-containing organic films were revealed. In particular, the reaction of magnesium with unreactive molecules, such as fluorobenzene and CCl_4, which do not react with magnesium under common conditions, was carried out for the first time.

Sergeev et al. [36–38] were the first to use ESR (Electron Spin Resonance) for studying the mechanism of reactions in films containing magnesium and organic halides. At low temperatures, the spectra showed a singlet assigned to a radial ion pair, the precursor of an organomagnesium compound. At the same time, the spectra showed the signals due to the corresponding organic (alkyl and aryl) radicals. The fact that the yield of organomagnesium compounds strongly depends on the metal content of the films suggested that organic halides might react with magnesium aggregates, rather than with atoms, to form radical ion pairs presumably involving metal clusters. At the same time, the authors assumed that the end reaction products form only after atomization of the metal clusters and are classical non-solvated Grignard reagents:

$$RX + Mg_n \rightarrow (RX^{\bullet -})Mg_n^{\bullet +} \rightarrow RMgX + Mg_{n-1}.$$

Lam Research Ex. 1035 - Page 701
Lam Research Corp. v. Inpria Corp.
IPR2024-00033 - U.S. Patent No. 9,823,564

Klabunde et al. [39–41] carried out co-condensation of magnesium (and calcium) with methyl halides by codepositing their vapors with a noble gas excess at helium temperatures. This method made it possible to prepare and spectrally identify not only magnesium atoms but also small magnesium clusters in a noble gas matrix, as well as to study the transformations of these clusters as the film warms up. Under the matrix isolation conditions at ~10 K, magnesium atoms were found to be totally inert, whereas small magnesium clusters reacted with methyl halides. This observation allowed the assumption that, at low temperatures, cluster analogues of Grignard reagents, for example, RMg_2X and RMg_3X, were first to form and that their further interaction with a methyl halide excess leads to the formation of common methylmagnesium halides CH_3MgX. The latter process is thermodynamically very favorable. Later on, these results were revised. It was stated in Ref. [42] that, at helium temperatures, neither magnesium atoms nor magnesium clusters react with methyl halides. Moreover, the formation of cluster Grignard reagents, even as intermediate products, seemed questionable in the light of computational results (see, e.g., Ref. [43]), which showed that an increase in the number of Mg atoms in the RMg–Mg···–X chain destabilized the system. This finding, while irreproachable from the computational standpoint, was caused by an incorrect choice of the initial model: as was shown later, the cluster core in such compounds should have a compact structure.

Thus, early theoretical and experimental studies of low-temperature reactions in the magnesium–organic halide films allowed one to formulate the problem of obtaining cluster Grignard reagents inaccessible for classical organometallic synthesis but provided no actual evidence of their formation and stabilization.

3. Synthesis of RMg_4X Compounds in Thin Films of Co-Condensates

Direct evidence of the existence of organomagnesium compounds with a cluster metal core has been obtained by matrix-assisted laser desorption/ionizaiton time-of-flight mass spectrometry (MALDI-TOF MS). This method allows one to record the spectra of molecular ions $[MH]^+$ of protonated molecules M. The major advantage of this method is that the use of volatile matrices makes it possible to measure the mass spectra of compounds that hardly transform to the gas phase under other conditions. This is true in full measure for organomagnesium compounds. The method does not provide detailed information on the geometry of corresponding

Lam Research Ex. 1035 - Page 702
Lam Research Corp. v. Inpria Corp.
IPR2024-00033 - U.S. Patent No. 9,823,564

molecules, but clearly shows their individuality and makes it possible to determine their composition. This is possible because protonation to form quasi-molecular ions $[MH]^+$ is a typical (and under definite conditions, unique) way of ionization provided by this mass spectrometry technique. The uniqueness of the empirical formula found by this method is ensured by the fact that, in addition to the major mass peaks, the spectra show the peaks caused by the presence of the isotopes of the elements constituting a molecule. The consistency between the peak intensity ratio and the natural abundance of the corresponding isotopes ensures an unambiguous assignment of the spectrum to a particular molecule.

This technique is applicable, first of all, because some organic compounds interact with magnesium to give solid adducts stable not only at low temperatures but also at room temperature. In other words, reactions with an organic component excess resulting in the decay of cluster derivatives by no means always take place. In some cases, the excess of the organic component can be removed without destroying an organometallic compound. This is the case, in particular, for low-temperature films formed by magnesium and an excess of chloro- or, even better, fluorobenzene [44]. The mass spectrum of the product of the low-temperature reaction of magnesium with fluorobenzene. The spectrum consists of four peaks with $m/z = 193$–196 Da (m/z is the ratio of the molecular mass to the charge of the ion; for H^+, $m/z = 1$; Da stands for Dalton, an atomic mass unit) of the quasi-molecular ions of protonated phenyltetramagnesium fluoride molecules. The ratio of the integrated intensities of these peaks is consistent with the theoretical composition $C_6H_5Mg_4F$ for this molecule. The spectral pattern remains unaltered when the reagent ratio in the films varies, which is another piece of evidence supporting the individuality of this compound. Elemental analysis of fine-crystalline solid samples gives the same empirical formula [45]. It is worth noting that recrystallization of solid phenyltetramagnesium fluoride samples has no effect on the composition of the organomagnesium clusters. This points to the formation of individual chemical compounds, stable both in solution and solid states at room temperature. Thus, the reaction product in fluorobenzene–magnesium films is $C_6H_5Mg_4F$.

The reaction with fluorobenzene is not an exception. Analogously, phenyltetramagnesium chloride $C_6H_5Mg_4Cl$ has been obtained in solid co-condensate films. As for other organic halides, the situation is not so simple. Solutions obtained after warming of the films of magnesium co-condensates with bromo- and iodobenzene contain, in addition to $C_6H_5Mg_4X$, classical non-solvated Grignard reagents C_6H_5MgX. In the case of alkyl halides, after keeping the resulting solution for a few hours, magnesium black is deposited so that the solution contains only a classical Grignard reagent. Finally, the most active halides react with magnesium immediately

Lam Research Ex. 1035 - Page 703
Lam Research Corp. v. Inpria Corp.
IPR2024-00033 - U.S. Patent No. 9,823,564

when the film is deposited to yield only conventional compounds RMgX [46, 47].

As already mentioned, the co-condensation of magnesium and alkane vapors does not lead to organometallic compounds. Benzene and some other hydrocarbons exhibit the same behavior. The situation changes radically when polynuclear hydrocarbons with mobile hydrogen atoms are used. Anthracene, indene, and isomeric methylindenes react with magnesium to form solid adducts displaying high stability upon long-term storage at room temperature [48, 49]. The product obtained upon co-condensation of anthracene and magnesium differs in composition and properties from the known magnesium–anthracene complex obtained from tetrahydrofuran solutions [50, 51].

Elemental analysis, studies of hydrolysis products, and MALDI-TOF MS measurements unambiguously show that all derivatives have four magnesium atoms per organic molecule [52]. For anthracene, the $C_{14}H_{10}Mg_8$ compound was identified in some experiments. None of the organic halides or hydrocarbons was found to form an adduct with two, three, or five metal atoms. Thus, there is a rather representative set of uncommon organomagnesium compounds containing four magnesium atoms per organic molecule. For anthracene, the adduct containing $8 = 2 \times 4$ metal atoms is also known. This is quite natural since the anthracene molecule has two identical sites with activated hydrogen atoms in the 9- and 10-positions.

Hence, the number four can be treated as the magic one for organic magnesium clusters: stable adducts of uncommon composition are formed only when magnesium is taken in a four-fold excess over the organic component. The question of the nature of this magic number is intriguing and deserves special attention. This nature can be elucidated by considering the specific features of low-temperature processes in the films of magnesium co-condensates with organic compounds.

4. Mechanism of the Processes in Organic Magnesium-Containing Films and the Nature of the Magic Number Four

Formation of metal–organic compound co-condensates presents a peculiar problem, which is difficult to study. Most experimental methods are inapplicable to the study of the processes that take place at the instant of co-condensation. This brings to the fore theoretical approaches. The state of the art of computational quantum-chemical methods makes it possible to adequately describe the structure of organometallic compounds and estimate their stability and, sometimes, reactivity.

Lam Research Ex. 1035 - Page 704
Lam Research Corp. v. Inpria Corp.
IPR2024-00033 - U.S. Patent No. 9,823,564

A growing co-condensate film can be, to a first approximation, divided into two zones. The lower part, which is in contact with a cooled (as a rule, to ~80 K) substrate, is a solid crystalline or, more often, glassy matter. Diffusion in this zone is extremely hindered and any chemical transformation is very slow. The upper part of the film continuously receives energy released upon condensation of an organic substance and hot metal atoms. It can be considered as a pseudoliquid layer. The mobility of particles in this layer can be compared to the mobility in a viscous liquid but their lifetime should not be long: contact with the cold lower layer and shielding with newly deposited molecules will lead to a decrease in the kinetic energy of the particles and to their "freezing" into the existing solid film of the condensate. This description is likely applicable only to thin films, for which the surface is large as compared to the thickness, and under the condition of slow supply of substances from the gas phase. Only in this case, the content of substances in the surface layer and their lifetime may be sufficient for three competing processes to take place:

(a) chemical interaction of atoms and clusters with an organic substance (matrix) in the pseudoliquid layer,
(b) association of atoms and small clusters to form larger particles, and
(c) stabilization of atoms and clusters in the solid part of the film.

Processes (b) and (c) are limited by diffusion and heat removal. The activation energies of these processes are low. Process (a) involves common chemical reactions and is improbable at low temperatures (~80 K). Indeed, as already mentioned, only the most active organic halides with weakened carbon–halogen bonds react with magnesium immediately in the course of condensation. Therefore, only the aggregation and stabilization processes are actually important. Let us consider them in the light of quantum-chemical calculations.

"Bare" magnesium clusters represent one of the favorite objects of study for experts in the field of metal cluster calculations. Figure 14.2 shows the structures of lowest molecular magnesium clusters calculated in Ref. [53] by the DFT (Density Functional Theory) method with the use of the "Priroda" program package [54] and by conventional *ab initio* methods. Analogous results have been reported in other works [55–60]. Although direct experimental data on the structures of clusters have hitherto been absent, the consistency of the results obtained with the use of very different computational schemes gives confidence that their geometries were determined rather reliably. The same is true for the cluster stabilization energies: all works, except for [61] (where, in calculations at the DFT level, a function not quite suitable for the description of clusters was used), give similar

Lam Research Ex. 1035 - Page 705
Lam Research Corp. v. Inpria Corp.
IPR2024-00033 - U.S. Patent No. 9,823,564

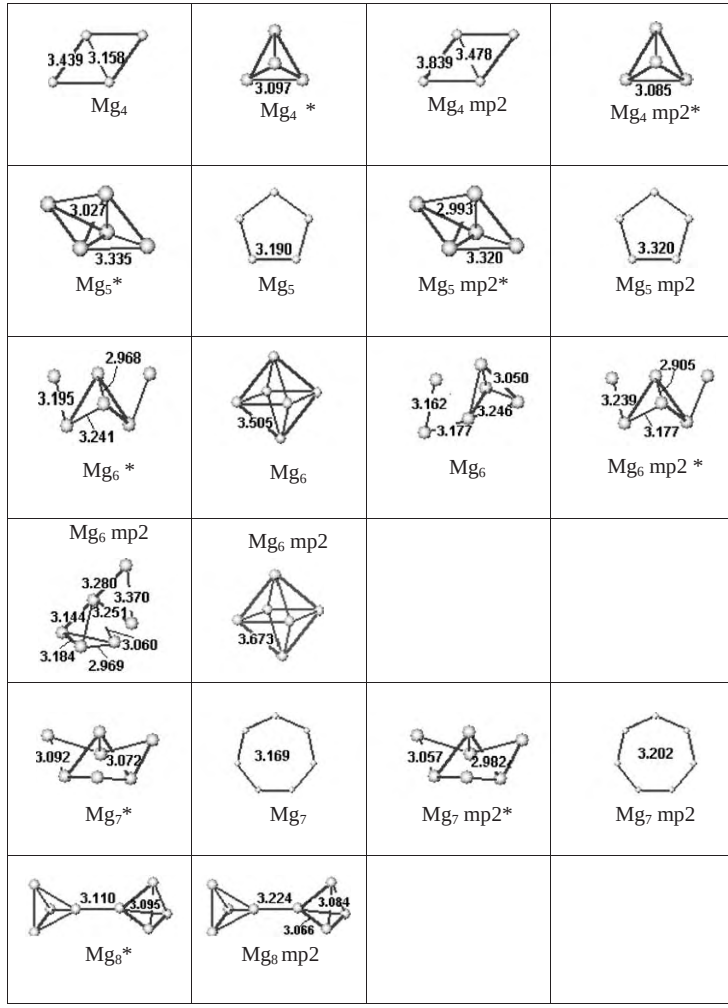


Fig. 14.2. The structures of bare magnesium clusters (* – the most stable isomers).

results. Let us consider the energies released as a magnesium atom is attached to clusters of different nuclearity. The energies (based on the data of several works) of the reactions $Mg_{(n-1)} + Mg \rightarrow Mg_n$ are listed below.

n	2	3	4	5	6
E, kcal/mol	2 – 3	8 – 9	18 – 20	7 – 8	8 – 10

Lam Research Ex. 1035 - Page 706
Lam Research Corp. v. Inpria Corp.
IPR2024-00033 - U.S. Patent No. 9,823,564

The high energy gain upon the formation (and, hence, the stability) of the tetranuclear cluster sharply differs from the data for other particles. The extremal character of formation energy as a function of nuclearity is evident: tetranuclear clusters are the most stable. This indicates that Mg_4 clusters can predominantly accumulate even in the as-deposited film.

Analysis of the potential energy surfaces (PESs) of the interacting magnesium atoms and clusters shows that all processes of magnesium association are activationless. Then, the proportion between clusters of different composition would seem to be determined only by the lifetime of particles in the mobile layer and by the deposition rate from the gas phase. At first glance, there are no reasons for the predominant accumulation of more stable particles. The situation is different if the entropy factor is taken into account.

Let the lifetime of particles in the surface layer be sufficiently long for equilibrium in activationless association processes to be established. For this, not very strict, approximation, the concentration of any particle is estimated based on the Gibbs energy. The latter can be extracted from quantum-chemical calculations. These calculations allow one to determine the moments of inertia and vibrational frequencies and, hence, not only the internal energy but also the enthalpy and entropy of a system.

Under reasonable assumptions about the structure of the film surface layer, the concentrations of different clusters in the pseudoliquid layer can be assessed based on the corresponding free energies. The computational results are shown in Figure 14.3. According to these data, under the typical experimental conditions of co-condensation (overall metal amount, $\sim 1 \times 10^{-5}$ mol; liquid phase volume, 0.1 ml; overall metal concentration $[Mg]_0$, ~0.1 M), the concentration of Mg_5 at 80 K should be six orders of magnitude lower than that of Mg_4. At 120 K, this difference is four orders of magnitude.

The contribution of other clusters is even lower. It is evident that, as the lifetime of mobile particles in the surface layer increases, higher clusters may accumulate through the successive addition of atoms to Mg_5 to eventually form giant clusters and massive metal.

As a rule, the formation of the massive metal is not experimentally observed. Thus, the lifetime of particles in the mobile state is too short for the formation of bulky clusters and the process terminates at the level of Mg_4 particles. The preferable accumulation of definite clusters seems to be the major reason for the selective formation of compounds with the Mg_4 cluster core.

The same composition of the magnesium cluster adducts with halides and hydrocarbons confirm the above conclusion that the composition of primary condensation products is determined by the competition between

Lam Research Ex. 1035 - Page 707
Lam Research Corp. v. Inpria Corp.
IPR2024-00033 - U.S. Patent No. 9,823,564

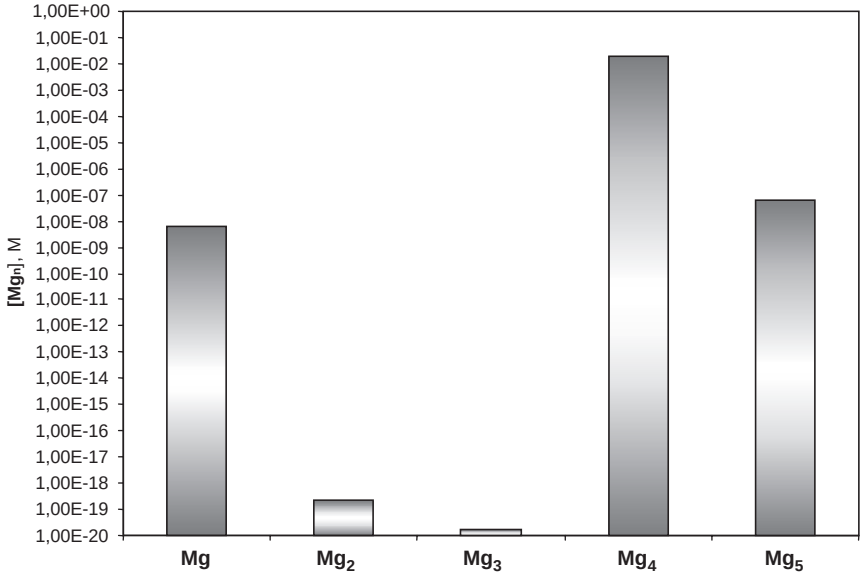


Fig. 14.3. Calculated concentrations of various magnesium clusters in a codeposite film.

association of atoms and stabilization of small clusters. However, further stabilization of the clusters in these systems proceeds differently.

The compositions and stabilities of organomagnesium derivatives based on different organic compounds have already been considered above. The correlation of the selectivity of cluster insertion with the bond strength in an organic halide or hydrocarbon is quite noticeable.

Compounds with the strongest bonds (C–H, C–halogen in chloro- and fluorobenzenes) selectively form derivatives of the Mg_4 cluster. Bromobenzene, in which the carbon–halogen bond is weaker, reacts with magnesium to form a mixture of a tetramagnesium derivative and a classical Grignard reagent. Solutions formed on melting the films based on alkyl halides are initially a mixture of products and contain only a conventional mononuclear Grignard reagent shortly after the melting. Finally, allyl halides and other derivatives with very weak C–halogen bonds form a conventional Grignard reagent immediately in the course of co-condensation with magnesium.

The reasons behind the existence of this correlation are considered in the next section. Before proceeding to the analysis of these reasons, let us formulate the major conclusion of Section 4: the magic number of nuclearity is a result of the optimal proportion between the energy and entropy factors in tetranuclear magnesium clusters.

Lam Research Ex. 1035 - Page 708
Lam Research Corp. v. Inpria Corp.
IPR2024-00033 - U.S. Patent No. 9,823,564

5. Competition between the Aggregation of Magnesium Atoms and the Generation of Radicals in Mg–RX Films

As already mentioned, only the most active halohydrocarbons react with magnesium in the course of vapor codeposition. However, even in this case, the process is not merely the insertion of the metal atom into the C–X or C–H bond. Quantum-chemical calculations (see, e.g., Ref. [62]) predict that the activation energy of such a process is so high that it is improbable not only at low temperatures but also at room temperature. This conclusion is supported by the experiments on gas-phase reactions. Under the conditions of these experiments, magnesium atoms are actually not inserted into carbon–halogen bonds at any temperature [63]. Under these conditions, compounds with strong carbon–halogen bonds do not react with magnesium at all. In the case of organic halides with weak carbon–halogen bonds, free radicals are formed by the reaction

$$RX + Mg \rightarrow R^{\bullet} + MgX^{\bullet}. \quad (2)$$

Recombination of the particles formed by reaction (2) yields a classical Grignard reagent. Processes in films are analogous. It is clear that the stronger the bond in an initial organic halide, the lower the probability of reaction (2). Therefore, only rather active halides generate radicals when reacting with magnesium atoms and, eventually, form RMgX compounds. Magnesium atoms do not interact with very strong C–F and C–Cl bonds in halobenzenes at low temperatures; therefore, Mg atoms are aggregated to form the Mg_4 cluster, which is inserted into these bonds. This ensures the selective synthesis of organomagnesium clusters on further warming of the films. The reactions with PhBr and PhI represent the intermediate case when the synthesis of organomagnesium compounds is accompanied by reactions of the corresponding organic radicals. Therefore, it is natural that, in these systems, phenyltetramagnesium bromide is formed together with phenylmagnesium bromide and the byproducts of phenyl radical transformations: benzene (in the absence of hydrolysis) and diphenyl. In this case, the radical is identified experimentally by ESR.

The interactions in magnesium-containing films follow a clear pattern: *when organic tetramagnesium clusters are formed, radicals are absent; and when radicals and the products of their transformation are present, organomagnesium clusters are formed, if at all, together with classical RMgX compounds and other products derived from radicals.*

The proposed scheme of interactions in films is supported by the reaction of organopolymagnesium halides and organopolymagnesium hydrides with organic halides. Indeed, the concept of competition between the molecular

Lam Research Ex. 1035 - Page 709
Lam Research Corp. v. Inpria Corp.
IPR2024-00033 - U.S. Patent No. 9,823,564

insertion of a magnesium cluster into the C–X bonds and the generation of radicals implies that the stabilized Mg_4 cluster from RMg_4X can be inserted into other C–X′ bonds of an organic halide RX′ added to RMg_nX. The selectivity of Mg_4 insertion in RX–Mg films and in RX′–RMg_4X systems should be analogous. This is actually the case. In the organomagnesium cluster–organic halide systems, various transmetallation reactions occur [64, 65], for example,

$$PhMg_4F + PhCl \rightarrow PhMg_4Cl,$$
$$C_9H_8Mg_4 + PhF \rightarrow PhMg_4F,$$
$$C_{14}H_{10}Mg_4 + PhF \rightarrow PhMg_4F,$$
$$C_9H_8Mg_4 + PhCl \rightarrow PhMg_4Cl,$$
$$C_{14}H_{10}Mg_4 + PhCl \rightarrow PhMg_4Cl,$$
$$C_9H_8Mg_4 + PhBr \rightarrow PhMg_4Br + PhMgBr(+Ph-Ph + PhH), \text{etc.}$$

(where C_9H_8 is indene and $C_{14}H_{10}$ is anthracene). Transmetallation for conventional organomagnesium compounds is unknown. In this case, this reaction allows one to separate the stages of stabilization of the Mg_4 cluster and those of its insertion into C–X bonds. It is possible, for example, that the clusters stabilized upon insertion into the C–F bond in the films at low temperatures are then inserted into weaker C–Cl or C–Br bonds in a solution at room temperature. Moreover, the Mg_4 cluster in the solution can be inserted even into the C–Cl bonds of alkyl halides [64]. As already mentioned, direct synthesis in films containing alkyl halides does not yield cluster derivatives; rather, the generation of radicals dominates, and the reaction yields conventional alkylmagnesium halides. At the same time, in solutions containing preliminarily formed tetranuclear derivatives, cluster compounds are obtained in good yield.

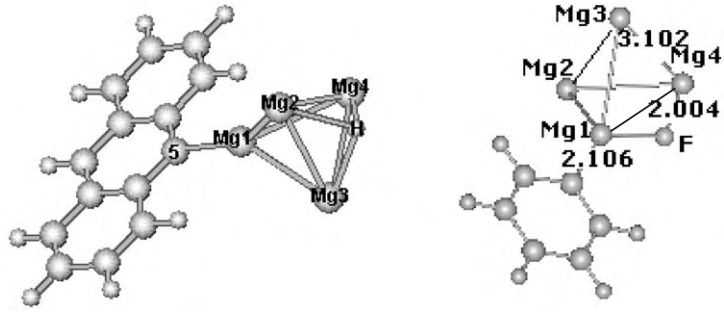
The following specific features of formation of organomagnesium clusters in the films obtained by codeposition of magnesium and organic compound vapors can be formulated:

1. Magnesium clusters formed in the films and inserted into C–H and C–X bonds are tetranuclear.
2. Selective synthesis of tetranuclear organomagnesium clusters occurs only through their insertion into the strongest chemical bonds C–X and C–H. Insertion of the clusters into weaker bonds is accompanied by recombination of organic radicals both in the Mg–RX films and in the course of transmetallation.
3. The tetranuclear magnesium cluster is rather stable, which makes it possible to obtain by transmetallation cluster alkyl Grignard reagents inaccessible by direct synthesis in the films of reagents.

Lam Research Ex. 1035 - Page 710
Lam Research Corp. v. Inpria Corp.
IPR2024-00033 - U.S. Patent No. 9,823,564

6. Structure and Reactivity of Unconventional Organomagnesium Compounds Obtained in Co-Condensate Films

The structure of RMg_4X particles is of great interest. The specific features of synthesis in films, the high reactivity, the presence of an excess of the initial organic compounds, and the air and moisture sensitivity of the products prevent the use of conventional methods of structure determination. This gap can be filled by the use of quantum-chemical calculations. The calculation in Ref. [53] predicts the existence of a large number of isomers closely lying on the energy scale. These isomers differ from one another in structural details of the cluster core and in the location of the halogen (or hydrogen in the case of hydrides) atom with respect to this core. Figure 14.4 shows the structures of the most stable isomers of cluster fluorides and hydride for anthracene and fluorobenzene. One feature in common is a compact structure of the cluster core, whereas the halogen (or hydrogen) atom acts as a bridge between two or three atoms of the metal core. The cluster core is a distorted tetrahedron. Solvation can play a definite role in the stabilization of Mg_4 clusters. Calculations show that all organic compounds under consideration are able to form complexes with both bare clusters and cluster organomagnesium derivatives. The stability of such complexes increases as the number of magnesium atoms in the cluster increases from 1 to 4; then, the stability ceases to increase. Among the associates with an Mg:RX(RH) ratio more than 1:1, the most energetically favorable is the formation of associates for tetranuclear clusters [53].



A B

Fig. 14.4. The structures of the organomagnesium compounds: (A) Mg–anthracene adduct, (B) Mg–fluorobenzene adduct.

Lam Research Ex. 1035 - Page 711
Lam Research Corp. v. Inpria Corp.
IPR2024-00033 - U.S. Patent No. 9,823,564

Let us consider a possible mechanism of formation of cluster organomagnesium compounds. Calculations of the PES of cluster–organic halide (or hydrocarbon) systems by the dynamic reaction path method permit the assumption that the insertion of Mg_4 into C–X or C–H bonds requires some rearrangement of the associates (complexes) of organomagnesium clusters with RX (RH) molecules. The Mg_4 insertion activation energy is estimated at 10–17 kcal/mol. For example, the insertion of Mg_4 into the C–H bond of allylbenzene is characterized by the activation energy of 12.3 kcal/mol [66]. At the same time, for the insertion of a magnesium atom, the activation energy is 40–50 kcal/mol. In addition, the cluster insertion products can be a result of rearrangement in more complicated associates. For example, in the complex of Mg_4 with two allylbenzene molecules, the calculated insertion activation energy decreases to 10.1 kcal/mol.

As already mentioned, the C–H bond strength determines stabilization patterns of cluster organomagnesium compounds. In just the same way and for analogous reasons, the character of transformation of organopolymagnesium derivatives depends on the bond strength in the molecules that are allowed to interact with organic magnesium clusters. In particular, in the presence of active halides RX (e.g., allyl halides), radical processes leading to the decay of the metal cluster are dominant. Therefore, the properties of the $PhMg_4F$–PhF and $PhMg_4Cl$–PhCl systems differ from those of the $PhMg_4Br$–PhBr and $PhMg_4I$–PhI systems, in which radicals are readily generated. Reactions related to the presence of the metal cluster are typical, first of all, for fluoro- or chlorobenzenes, which are unable to generate phenyl radicals.

The Table 14.1 summarizes the chemical reactions of cluster Grignard reagents obtained in co-condensate films. As follows from the Table 14.1, cluster Grignard reagents enter into various reactions. Among these reactions, only the cross-coupling reaction is known for conventional RMgX reagents. The other transformations are not typical of conventional organomagnesium compounds. It is worth noting that all these reactions can be carried out in a catalytic mode. Halogen exchange can proceed as a reaction catalyzed by cluster Grignard reagents both in the solid

Table 14.1. Reactions of Cluster Grignard Reagents

Cross-coupling	$PhMg_nBr + C_3H_5Br \rightarrow PhC_3H_5\ (+ Mg_nBr_2)$
Halogen exchange	$PhMg_4Cl + C_3H_5Br \rightarrow PhMg_4Br + C_3H_5Cl$
Catalytic halogen exchange	$PhF + C_7H_{15}Cl \xrightarrow{PhMg_4F} PhCl + C_7H_{15}F$
Transmetallation	$PhMg_4F + C_7H_{15}Cl \rightarrow PhF + C_7H_{15}\ Mg_4Cl$
Catalytic isomerization of Alkylhalides	$n\text{-}C_7H_{15}Cl \xrightarrow{PhMg_4F} i\text{-}C_7H_{15}Cl$

Lam Research Ex. 1035 - Page 712
Lam Research Corp. v. Inpria Corp.
IPR2024-00033 - U.S. Patent No. 9,823,564

magnesium–organic halide films at low temperatures and in solutions at room temperature [67]:

$$RF + R'Cl \xrightarrow{RMg_4X} RCl + R'F$$

Yet another example of catalysis by cluster Grignard reagents is isomerization of alkyl halides. It turned out that, in the presence of these reagents, *n*-chloroalkanes undergo partial isomerization to produce a mixture of secondary chloroalkanes. The catalytic turnover number is as large as 20.

Thus, as distinct from conventional Grignard reagents, their cluster congeners exhibit catalytic properties. This phenomenon is of great interest for a main group organometallic compound.

Nevertheless, the range of reactions catalyzed by cluster organomagnesium halides is rather limited. Catalytic applications of organopolymagnesium hydrides, which have become accessible due to the interaction of magnesium with hydrocarbons in the films of their co-condensates, are considerably more diverse.

7. Catalytic Reactions in Mg–RH Films

The range of catalytic reactions of unsaturated compounds in the films of their co-condensates with magnesium is very wide, and the catalytic turnover number in them is orders of magnitude higher than in reactions over cluster Grignard reagents. According to the scheme in Figure 14.5, the

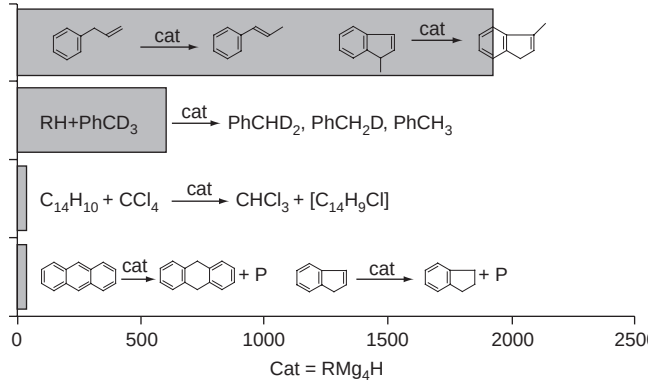


Fig. 14.5. The turnover number in catalytic reactions on cluster organomagnesium compounds.

Lam Research Ex. 1035 - Page 713
Lam Research Corp. v. Inpria Corp.
IPR2024-00033 - U.S. Patent No. 9,823,564

catalyzed reactions are very diverse and include self-hydrogenation, allyl isomerization, deuterium–hydrogen exchange, and hydrodehalogenation of polyhalomethanes [68–71]. All these reactions conventionally occur in solutions or in the gas phase in the presence of transition metal catalysts under rather severe conditions. In films, they can be carried out even at 100 K.

Indeed, let us consider, for example, olefin self-hydrogenation. This is generally a multistage process beginning with disproportionation of a pair of olefin molecules to the corresponding alkane and a polyunsaturated compound (diene or alkyne), which rapidly polymerizes to form high-molecular-weight products P:

$$2C_nH_{2n} \xrightarrow{\text{catalyst}} C_nH_{2n+2} + P \qquad (3)$$

It turned out that this reaction occurs in solid magnesium–olefin films at 100–130 K with yields of alkanes of up to 80% (based on magnesium). Until recently, self-hydrogenation reactions over catalysts containing main group metals were unknown. Similar results were obtained for Ni- or Pd-based catalysts but at temperatures hundreds of degrees higher [72]. Reaction (3) in magnesium-containing films was first observed for 1-alkenes [69]. The efficiency of catalysis in films increases even more for self-hydrogenation of indene or anthracene [70].

Self-hydrogenation is only one of the processes that occur in magnesium-containing films. Both H–D exchange, for example,

$$PhCD_3 + C_{14}H_{10} \rightarrow PhCD_2H,\ PhCDH_2,\ PhCH_3 + \text{deuterated anthracenes},$$

and allyl isomerization proceed at a very high rate [68, 71]. Both reactions are well known; previously, they were catalyzed only by transition metals and their compounds.

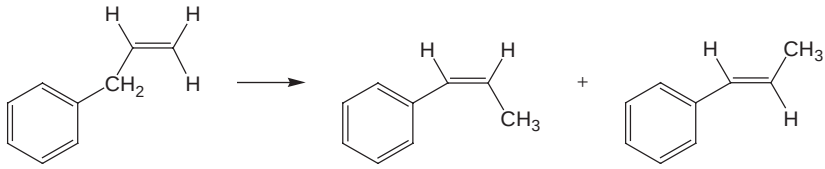
Hence, there are strong grounds to state that *compounds with the tetranuclear cluster magnesium core formed in Mg–RH films have catalytic properties similar to those of transition metal complexes. The catalytic activity of organomagnesium clusters can be very high.*

Among the reactions on organomagnesium clusters, allyl isomerization of olefins seems to be the best-understood one at the present time. In the films containing magnesium and olefins, such as allylbenzene and 1-methylindene, multiple bond migration proceeds in very high yields.

Isomerization of allylbenzene in magnesium-containing films begins even in the solid phase. Allylbenzene completely converts into β-methylstyrene in

Lam Research Ex. 1035 - Page 714
Lam Research Corp. v. Inpria Corp.
IPR2024-00033 - U.S. Patent No. 9,823,564

the course of melting of the film:



The turnover number is as large as 5000. This number is limited only by the amount of allylbenzene introduced into the reaction and can likely be much larger. Taking into account that the reaction is completed in the course of mixing the reagents, which lasts no longer than 1–2 min, the allyl isomerization rate in Mg–RH films at low temperatures is very high. For comparison, in the presence of supported Pt or Pd at 150°C, the turnover number per hour for the isomerization of 1-butene is no more than 400 mol/mol h [73].

The isomerization of 1-methylindene to 3-methylindene proceeds analogously. The reaction starts in the solid film at 120–130 K, and the conversion of the initial reagent is completed at 230 K. It is evident that the specific features of the reactions of unsaturated compounds in the films of their co-condensates with magnesium point to a quite unique character of these processes, which combine an unconventional nature of the active site, high performance, and mild reaction conditions.

Magnesium–allylbenzene films were comprehensively studied by infrared (IR) spectroscopy at 77–160 K. Their spectrum at 77–120 K is identical to the spectrum of neat allylbenzene; no bands that could be assigned to an organomagnesium compound or the products of olefin transformation were observed. At ~120 K, new absorption bands appear at 1480–1490, 2733, and 1284 cm^{-1} typical of *trans*-β-methylstyrene; i.e., isomerization begins at this temperature, well before the melting point of the solid sample is reached. Accumulation of the isomerization product proceeds with stepwise kinetics: a warming of the film to a definite temperature leads to the formation of some amounts of the product, and the reaction stops shortly after this temperature is established. For example, as the temperature increases to 150 K, a certain amount of *trans*-β-methylstyrene gradually accumulates; after this temperature is reached and the heating is stopped, the reaction continues for another 5 min and then is terminated. When the sample melts, the reaction proceeds to completion in a matter of seconds. This course of solid-phase reactions is rather typical of binary systems, but, as far as is known, has not been previously reported for catalytic reactions.

Thus, the courses of reactions of unsaturated compounds in the films of their co-condensates with magnesium point to a quite unique character

Lam Research Ex. 1035 - Page 715
Lam Research Corp. v. Inpria Corp.
IPR2024-00033 - U.S. Patent No. 9,823,564

of these processes, which combine high performance and mild reaction conditions.

An unsaturated compound in the course of its isomerization in magnesium-containing films performs two functions: (i) it forms a catalyst when the Mg_4 cluster is inserted into the activated C–H bond, and (ii) it acts as a reaction substrate. The stages of the synthesis of the catalyst and isomerization can be separated. For example, anthracenyltetramagnesium hydride can be preliminarily obtained in anthracene–magnesium films, and then it can be used as a catalyst. The introduction of this cluster compound into a solution of allylbenzene or methylindene at room temperature ensures high yields of multiple bond migration products.

Let us consider the mechanism of catalysis on organomagnesium clusters for the isomerization of allylbenzene as an example. For this reaction, detailed quantum-chemical calculations of stationary points of the PES corresponding to stable compounds and their complexes, as well as of the entire reaction path, were performed. The calculation [66] shows that the tetrahedral magnesium cluster interacts with allylbenzene to form molecular complexes of moderate stability in which the cluster is located either near the benzene ring (the complex stabilization energy is $E_{st} = -3.6$ kcal/mol) or near the multiple bond ($E_{st} = -3.3$ kcal/mol). The energy barrier to cluster reorientation in the complexes is close to zero. It is likely that the cluster jumps between the two positions. It is inserted into the C–H bond in the methylene group of allylbenzene. It is worth noting that, although the process at the early stage involves the carbon atom adjacent to the aromatic nucleus, in its further course, the double bond migration and the reorientation of the cluster to the terminal carbon atom in the side chain are barrierless and occur without formation of new adducts. Thus, the resulting adduct is not an allylbenzene derivative; rather, it is a derivative of the allylbenzene isomer, methylstyrene. In other words, isomerization in the cluster adduct is an activationless process and occurs almost instantaneously. The insertion of the magnesium cluster into the C–H bond of allylbenzene and the migration of the double bond in it occur synchronously in one stage.

8. Synthesis of Catalysts in Multicomponent Films Containing Magnesium and a Transition Metal

The above examples clearly demonstrate unusual catalytic properties of the products synthesized in magnesium-containing organic films. However, binary magnesium–organic compound systems do not exhaust the possibilities of such synthesis. The range of magnesium catalysts synthesized in films

Lam Research Ex. 1035 - Page 716
Lam Research Corp. v. Inpria Corp.
IPR2024-00033 - U.S. Patent No. 9,823,564

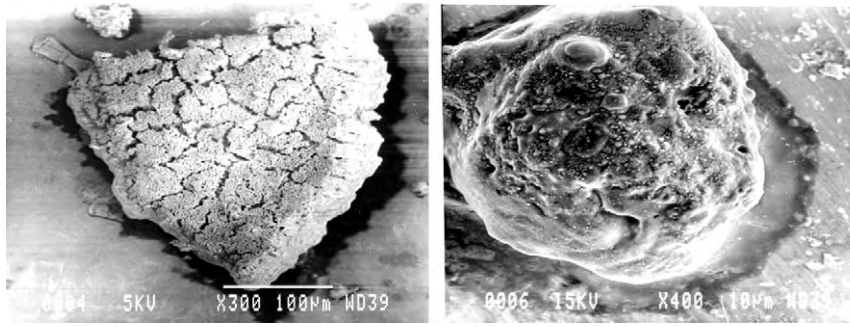


Fig. 14.6. The microphotographs of the structures of $TiCl_4$–Mg–RH codeposite particles: (1) RH = benzene, (2) RH = pentane.

can be extended by introducing transition metal compounds into co-condensation. For example, synthesis in bimetallic films $TiCl_4$–Mg–RH (where RH is an aliphatic or aromatic hydrocarbon) makes it possible to obtain catalysts of different transformations of α-olefins (from propylene to dodecene inclusive), including oligo- and polymerization [69, 74].

Depending on the nature of hydrocarbon RH, different structures can be obtained in bimetallic films $TiCl_4$–Mg–RH. The microphotographs of these structures are shown in Figure 14.6. Catalyst 1 was obtained in $TiCl_4$–Mg–benzene films, and catalyst 2 was obtained in $TiCl_4$–Mg–pentane films. As is seen, the particles of the catalysts differ in size, shape, and porosity of their constituting fragments. In particular, catalyst 2 has pores 300–500 nm in size and contains spherical particles with a smooth surface. Catalyst 1 consists of smaller particles combined in columnar associates. The catalytic properties of the systems obtained in these films are also sharply different. The interaction in the $TiCl_4$–Mg–benzene films gives nanometer particles with a rather high catalytic activity in polymerization of propylene and other olefins. The activity of the catalysts depends on the $TiCl_4$:Mg ratio and is a maximum for the equimolar composition. In these films, alkylation of $TiCl_4$ occurs, which compares it to the classical titanium–magnesium catalysts of polymerization. At the same time, there are significant differences between these catalysts. In particular, classical Ziegler–Natta catalysts of polymerization are active only in the presence of organoaluminum compounds. In our case, the latter are not only unnecessary but also are catalytic poisons. Conventional catalysts catalyze the polymerization of lower olefins (especially, propylene) much more readily than that of higher olefins. The catalyst obtained in the films shows the opposite tendency. Thus, low-temperature synthesis in films yields original catalytic systems. Their structures and mechanism of their action are yet to be studied.

Lam Research Ex. 1035 - Page 717
Lam Research Corp. v. Inpria Corp.
IPR2024-00033 - U.S. Patent No. 9,823,564

It is impossible to consider here all transformations that occur in the films containing magnesium cluster derivatives or are catalyzed by the products of synthesis in these films. Very interesting reactions involving carbon oxides, carbonyl compounds, etc., remained beyond the scope of this review. However, beyond question is a unique character of the processes in which reactions typically catalyzed by transition metals occur at a high rate in the presence of main group clusters and, as a rule, under very mild conditions. This allows us to believe that the organic magnesium clusters that form in the films obtained by condensation are candidates for use as basis for designing novel types of catalysts.

9. Conclusions

In summary, it is worth noting that this chapter deals with original objects whose existence was proved quite recently. Organomagnesium clusters as a new class of cluster compounds owe their appearance to the classical Grignard reaction carried out in films of the co-condensates of the reagents, magnesium, and organic halides. The competition between the aggregation of metal atoms and the insertion of the resulting clusters into C–X and C–H bonds in the Mg–RX and Mg–RH films turns out to ensure the selective synthesis of tetranuclear magnesium clusters.

Cluster derivatives for magnesium were unknown until recently, as distinct from other metals. The reactivity of organomagnesium clusters and the direction of the processes involving these clusters differ considerably from those typical of conventional organomagnesium compounds. It is natural that the notions expounded above are tentative and will be refined, as information will be amassed. It is unquestionable that studies of the films obtained by vapor codeposition of organic compounds with main group metals (or simultaneously with main group and transition metals) will make it possible to synthesize novel, as yet unknown cluster compounds. Despite specific difficulties associated with the use of the co-condensation method, it cannot be ruled out that the unique chemical properties of these clusters will find practical use. First of all, this can apply to catalysis. In addition, this strategy can be used to obtain new reagents for fine organic and organometallic synthesis, high-sensitivity sensors, storage cells for light gases (especially, for hydrogen), and other interesting materials, in particular, drugs.

Below are the questions that will help the reader better understand the material in this chapter.

1. How does the stabilization energy of Mg_n clusters change with an increase in their nuclearity from $n = 2$ to $n = 5$?

Lam Research Ex. 1035 - Page 718
Lam Research Corp. v. Inpria Corp.
IPR2024-00033 - U.S. Patent No. 9,823,564

2. How does the entropy of formation of Mg_n clusters change in going from $n = 4$ to $n = 5$?
3. What are the processes in magnesium–organic halide films that lead to stabilization of tetranuclear magnesium clusters?
4. What are the reactions known for both cluster Grignard reagents and their classical analogues: halogen exchange, catalytic halogen exchange, catalytic isomerization of *n*-chloroalkanes, or cross-coupling?
5. What is the nature of the catalytic activity of organomagnesium clusters?

References

1. N. N. Semenov, A. I. Shal'nikov, Zh. Russk. Fiz.-Khim. O-va. **60** (1928) 303.
2. V. A. Kargin, V. A. Kabanov, Zh. Vses. Khim. O-va im. D. I. Mendeleeva **9** (1964) 602.
3. I. Norman, G. Porter, Nature **174** (1954) 508.
4. E. Whittle, D. A. Dows, G. C. Pimentel, J. Chem. Phys. **22** (1954) 1943.
5. R. L. DeKokh, Inorg. Chem. **10** (1971) 1205.
6. J. L. Slater, R. K. Sheline, K. C. Lin, W. Weltner, Jr., J. Chem. Phys. **55** (1971) 5129.
7. J. K. Burdett, J. J. Turner, J. Chem. Soc. Chem. Commun. (1971) 885.
8. J. H. Darling, J. S. Ogden, Inorg. Chem. **11** (1972) 666.
9. H. Huber, E. P. Kündig, M. Moskovits, G. A. Ozin, Nat. Phys. Sci. **235** (1972) 98.
10. E. P. Kündig, M. Moskovits, G. A. Ozin, New Synth. Meth. **3** (1975) 151.
11. M. Moskovits, G. A. Ozin, Cryochemistry, Wiley, New York, 1976.
12. K. J. Klabunde, Free Atoms, Clusters and Nanosized Particles, Academic Press, San Diego, 1994.
13. K. J. Klabunde (Ed.), Nanoscale Materials in Chemistry, Wiley, New York, 2001.
14. G. N. Gerasimov, V. A. Sochilin, S. N. Chvalun, Macromol. Chem. Phys. **197** (1996) 1387.
15. L. I. Trakhtenberg, G. N. Gerasimov, Metal-Containing Polymers: Cryochemical Synthesis, Structure and Physico-Chemical Properties, in: G. Carotenuto, L. Nicolais (Eds.), Metal/Polymer Nanocomposites, Wiley, New York, 2005.
16. L. I. Trakhtenberg, E. Axelrod, G. N. Gerasimov, E. V. Nikolaeva, E. I. Smirnova, J. Non-Cryst. Solids **305** (2002) 190.

Lam Research Ex. 1035 - Page 719
Lam Research Corp. v. Inpria Corp.
IPR2024-00033 - U.S. Patent No. 9,823,564

17. H. Imamura, Y. Murata, S. Tsuchiya, J. Less Common Met. **123** (1986) 59.
18. H. Imamura, T. Nobunaga, M. Kawahigashi, S. Tsuchiya, J. Less Common Met. **135** (1987) 277.
19. S. C. Devis, K. J. Klabunde, Chem. Rev. **82** (1982) 153.
20. S. E. Kondakov, V. V. Smirnov, Bull. Soc. Chim. Belg. **103** (1994) 131.
21. S. E. Kondakov, V. V. Smirnov, A. Yu. Olenin, Bull. Soc. Chim. Belg. **104** (1995) 369.
22. P. L. Timms, J. Chem. Soc., Chem. Commun. **18** (1969) 1033.
23. K. J. Klabunde, Chemistry of Free Atoms and Particles, Academic Press, New York, 1980.
24. P. S. Skell, J. E. Girard, J. Am. Chem. Soc. **94** (1972) 5518.
25. V. Grignard, Ann. Chim. **24** (1901) 433.
26. M. S. Kharasch, O. Reinmuth, Grignard Reactions of Nonmetallic Substances, Prentice-Hall, New York, 1954.
27. F. R. Bush, D. M. Antonis, Grignard Reagents – Industrial Applications and Strategy, in: H. G.Richey, , Jr. (Ed.), Grignard Reagents. New Developments, Wiley, Chichester, 2000.
28. J. S. Thayer, Adv. Organomet. Chem. **13** (1975) 1.
29. H. G. Richey, Jr. (Ed.), Grignard Reagents. New Developments, Wiley, Chichester, 2000.
30. G. S. Silverman and P. E. Rakita (Eds.), Handbook of Grignard Reagents, Marcel Dekker, New York, 1996.
31. B. J. Wakefield, Organomagnesium Methods in Organic Synthesis, Academic Press, New York, 1995.
32. K. J. Klabunde, H. F. Efner, L. Satek, W. Donley, J. Organomet. Chem. **71** (1974) 309.
33. K. Kimura, Bull. Soc. Chem. Jpn. **60** (1987) 3093.
34. S. E. Kondakov, V. V. Smirnov, L. A. Tyurina, Dokl. Akad. Nauk SSSR. **325** (1992) 536.
35. S. Skell, J. E. Girard, J. Am. Chem. Soc. **94** (1972) 5518.
36. G. B. Sergeev, V. V. Smirnov, F. Z. Badaev, J. Organomet. Chem. **224** (1982) 29.
37. G. B. Sergeev, V. V. Smirnov, V. V. Zagorsky, J. Organomet. Chem. **201** (1980) 9.
38. G. B. Sergeev, V. V. Zagorsky, F. Z. Badaev, J. Organomet. Chem. **243** (1983) 123.
39. Y. Imizu, K. J. Klabunde, Inorg. Chem. **23** (1984) 3602.
40. Y. Tanaka, S. C. Davis, K. J. Klabunde, J. Am. Chem. Soc. **104** (1982) 1013.
41. K. J. Klabunde, A. Whetten, J. Am. Chem. Soc. **108** (1986) 6529.

Lam Research Ex. 1035 - Page 720
Lam Research Corp. v. Inpria Corp.
IPR2024-00033 - U.S. Patent No. 9,823,564

42. N. Solov'ev, N. A. Nemukhin, G. B. Sergeev, S. K. Burt, I. A. Topol', J. Phys. Chem. **101** (1997) 8625.
43. Q. Jasien, C. E. Dykstra, J. Am. Chem. Soc. **105** (1983) 2089.
44. L. A. Kombarova, L. A. Tyurina, V. V. Smirnov, Metalloorg. Khim. **5** (1992) 1038.
45. L. A. Tjurina, V. V. Smirnov, G. B. Barkovskii, E. N. Nikolaev, S. E. Esipov, I. P. Beletskaya, Organometallics **20** (2001) 2449.
46. A. M. Egorov, A. V. Anisimov, Vest. Mosk. Univ., Ser. 2, Khim. **40** (1999) 209.
47. A. M. Egorov, A. V. Anisimov, Appl. Organomet. Chem. **9** (1995) 285.
48. L. A. Tyurina, V. V. Smirnov, G. B. Barkovskii, Vest. Mosk. Univ., Ser. 2, Khim. **34** (1993) 55.
49. L. Tjurina, G. Barkovskii, D. Potapov, V. Smirnov, I. Beletskaya, Low Temperature Chemistry: 3rd International Conference, Nagoya University, Japan, 1999, p. 99.
50. B. Bogdanovič, S.-T. Liao, R. Mynott, K. Schlichte, U. Westeppe, Chem. Ber. **117** (1984) 1378.
51. B. Bogdanovič, Acc. Chem. Res. **21** (1988) 261.
52. L. A. Tjurina, V. V. Smirnov, G. B. Barkovskii, S. E. Esipov, I. P. Beletskaya, Physical Organic Chemistry: 15th IUPAC Vonference, Goteborg, Sweden, 2000, p. 99.
53. I. P. Gloriozov, V. V. Smirnov, L. A. Tyurina, Zh. Fiz. Khim. **78** (2004) 1635.
54. D. N. Lajkov, Chem. Phys. Lett. **281** (1997) 151.
55. C. W. Bauschlicher, P. S. Bagus, B. N. Cox, J. Chem. Phys. **77** (1982) 4032.
56. J. Acola, K. Rytkxnen, M. Manninen, Eur. Phys. J. **16** (2001) 21.
57. T. J. Lee, A. P. Rendell, P. R. Taylor, J. Chem. Phys. **93** (1990) 6636.
58. C. W. Bauschlicher, H. Partridge, Chem. Phys. Lett. **300** (1999) 364.
59. W. Klopper, J. Almlof, J. Chem. Phys. **99** (1993) 5167.
60. J. Jellinek, P. H. Acioli, J. Phys. Chem. A **106** (2002) 10919.
61. P. C. Jasien, J. A. Abbondondola, J. Mol. Struct. **671** (2004) 111.
62. S. R. Davis, J. Am. Chem. Soc. **113** (1991) 4145.
63. N. Shafizadech, J. Rostas, G. Taich, B. Bourguignon, M. Prisant, Chem. Phys. **142** (1990) 111.
64. L. A. Tjurina, V. V. Smirnov, D. A. Potapov, S. A. Nikolaev, S. E. Esipov, I. P. Beletskaya, Organometallics **23** (2004) 1349.
65. L. A. Tyurina, V. V. Smirnov, I. P. Beletskaya, Mendeleev Commun. **12** (2002) 108.
66. I. P. Gloriozov, V. V. Smirnov, D. A. Potapov, L. A. Tyurina, Russ. J. of Phys. Chem. **80** (2006) 702.

Lam Research Ex. 1035 - Page 721
Lam Research Corp. v. Inpria Corp.
IPR2024-00033 - U.S. Patent No. 9,823,564

67. L. A. Tjurina, V. V. Smirnov, I. P. Beletskaya, J. Mol. Catal. **182–183** (2002) 395.
68. V. V. Smirnov, I. P. Beletskaya, L. A. Tyurina, G. B. Barkovskii, A. N. Kashin, I. G. Tarkhanova, Kinet. Katal. **39** (1998) 885.
69. I. G. Tarkhanova, V. V. Smirnov, N. S. Kulikov, L. A. Tyurina, Neftekhimiya **4** (1992) 303.
70. L. A. Tyurina, V. V. Smirnov, D. A. Potapov, Kinet. Katal. **44** (2003) 1.
71. D. A. Potapov, L. A. Tyurina, V. V. Smirnov, Izv. Ross. Akad. Nauk, Ser. Khim. **6** (2005) 1155.
72. V. M. Gorelik, I. A. Kop'eva, I. A. Oreshkin, B. A. Dolgoplosk, Kinet. Katal. **33** (1992) 121.
73. B. Wells, G. R. Wilson, J. Catal. **9** (1967) 70.
74. I. G. Tarkhanova, V. V. Smirnov, V. I. Tsetkova, L. A. Tyurina, Izv. Ross. Akad. Nauk, Ser. Khim. **5** (1999) 900.

Lam Research Ex. 1035 - Page 722
Lam Research Corp. v. Inpria Corp.
IPR2024-00033 - U.S. Patent No. 9,823,564

Chapter 15

Charge Effects in Catalysis by Nanostructured Metals

S.A. Gurevich[a], V.M. Kozhevin[a], I.N. Yassievich[a], D.A. Yavsin[a], T.N. Rostovshchikova[b], and V.V. Smirnov[b]

[a]*Ioffe Physico-Technical Institute of RAS, Polytekhnicheskaya 26, St. Petersburg 194021, Russia*

[b]*Chemistry Department, Lomonosov Moscow State University, Leninskie Gory, Moscow 119992, Russia*

1. Introduction . . . 726
2. Catalyst Fabrication and Structural Properties . . . 729
   2.1. Catalyst Fabrication by Laser Electrodispersion of Metals . . . 729
   2.2. Structural Properties of the Catalyst Coatings . . . 732
3. Charge State of Metallic Nanostructures . . . 735
4. Effect of Nanoparticle Charging on the Catalytic Properties . . . 741
   4.1. Analytical Estimates . . . 742
   4.2. Experimental Results and Discussion . . . 744
5. Summary . . . 750
References . . . 752

The catalyst structures, which are thin granulated films consisting of Cu, Ni, or Pd nanoparticles, were fabricated by means of laser electrodispersion technique. This technique allows producing nearly monodispersive and amorphous metal nanoparticles (the particle sizes are 5.0 nm for Cu, 2.5 nm for Ni, and 2.0 nm for Pd; the size dispersion is less than 10%). These particles were deposited on dielectric (thermally oxidized silicon) or semiconductor (naturally oxidized Si) supports and the resulting particle surface densities were closely controlled by the time of deposition. The most important common feature of the fabricated catalysts is their unusually high (up to 10^5 product mole per metal mole per hour) specific catalytic activity measured in several chlorohydrocarbon conversions (Cu, Ni) and hydrogenation (Ni, Pd) reactions. In all the reactions, strong dependencies of the specific catalytic activity on the particle surface density and solution polarity have been observed. The nature of the support affected the activity as well, for instance, different activities were measured when using p- or n-doped Si supports. These experimental facts are explained assuming that, along with

THIN FILMS AND NANOSTRUCTURES, vol. 34
ISSN 1079-4050
DOI: 10.1016/S1079-4050(06)34015-X

© 2007 by Elsevier Inc.
All rights reserved.

Lam Research Ex. 1035 - Page 723
Lam Research Corp. v. Inpria Corp.
IPR2024-00033 - U.S. Patent No. 9,823,564

the small size and amorphous state of the particles, particles charge fluctuations (resulting from inter-particle or particle–support tunnel electron transitions) determine the catalytic activity of these structures. A theoretical model is developed providing means for calculating the number of the charged particles in case when the structure is deposited on a dielectric or on a conducting support. The speculations on the mechanism of tunnel electron transfer from the charged nanoparticle to the chemisorbed reagent molecule show that, for the reactions proceeding with the electron transfer, nanoparticle charging may result in substantial reduction of the reaction activation energy. Combining these two models allows quantitative estimation of the effect of the particle charge on the catalytic activity. Estimations made on this basis are in good agreement with the experimental results. Utilization of the described phenomenon of particle interaction (related with their charging) opens up a new way for managing the catalytic properties of immobilized metallic nanoparticles.

1. Introduction

Recently, a profound interest in studies of properties of granulated metals, structures constituted by metallic nanoparticles, has been aroused. Problems associated with the application of these structures in the development of new nanoelectronic devices [1], devices for ultrahigh-density magnetic recording [2], new functional coatings [3], and high-efficiency solid-state catalysts [4] are widely discussed in the literature. This chapter is concerned with catalytic properties of metallic nanostructures.

Catalysis by metallic nanoparticles is a highly important area of the modern science of catalysis. In most of the presently used catalysts, the active substance is deposited onto a support in the form of nanoparticles, which, in the first place, makes large the surface area of a catalyst and thereby provides a significant increase in its capacity. For example, quite a number of large-tonnage techniques for processing of hydrocarbon raw materials (hydrogenation and dehydrogenation, not to mention the fine organic synthesis) employ metal nanoparticles and metal compounds fixed on various, mostly oxide or carbon supports [5–7]. A successful strategy of development of this area is passing from determination of properties of nanosize catalysts to their prognostication and, further, to synthesis of catalysts with optimal properties.

In the development of nanostructured metal catalysts, one should take into account their principal distinctive feature, the dependence of the catalytic activity and/or selectivity on the particle size. This dependence, or the size effect, is due to the simple relationship between the catalyst surface area and

Lam Research Ex. 1035 - Page 724
Lam Research Corp. v. Inpria Corp.
IPR2024-00033 - U.S. Patent No. 9,823,564

the particle size: the smaller the particles, the larger the effective surface area of the catalyst. There are, however, two other, and even more important, reasons. First, the energy parameters of metal nanoparticles are known to be dependent on their size. The second is that the surface structure of a particle changes with its size. In particular, the surface curvature, the appearance of different crystal planes on the surface, and the presence of surface defects may all strongly depend on the particle size [8–11]. Combined, these factors most frequently lead to an increase in the catalytic activity upon a decrease in the particle size (direct size effect). In some cases, however, the activity of a catalyst may decrease as particles become smaller (inverse size effect) or reach its maximum value at a certain particle size. The reasons why the size-related properties are manifested in catalysis have been analyzed in detail in the literature [12]. Most frequently, dramatic changes in physical and catalytic properties occur at particle sizes of several nanometers to several tens of nanometers. The properties of such nanoparticles containing hundreds and thousands of atoms are fundamentally different from those of bulk metals, on one hand, and from the properties of isolated atoms and small clusters, on the other. It is particles of this kind that are used in real catalytic processes, and these particles are the subject of present chapter.

It is important to emphasize that an adequate understanding of the mechanisms of catalytic processes that involve nanoparticles requires not only the properties of individual particles, but also those of the whole macroscopic system comprising a large number of particles (ensemble) and the support. This concept was first formulated in the late 1990s in Refs. [13–15] and was further developed by other authors [16–18]. An analysis of the properties of a catalytic system constituted by particles and a support requires that interaction between its separate components should be taken into account. In doing so, it is necessary to consider both the interaction of particles with one another within the ensemble and the interaction of the particles with the support. The nature of such an interaction may vary, being associated with local electric or magnetic fields, charge or mass transfer, etc. For example, it will be seen from what follows that charge transfer between particles in the ensemble or between the particles and the support may occur under certain conditions, which leads, in the end, to charging of the system of particles and markedly changes their energy state. Depending on the fabrication technology, and on properties of particles and the support, particle ensembles of various densities and varied type of particle arrangement on the support surface can be obtained. All these factors affect the catalytic activity and it is necessary to take them into account when designing a catalytic system [4,19,20].

This chapter is focused on charge-related effects in catalysis on metallic nanoparticles. The role of these effects was first discussed in the already mentioned studies [13–15] and was reviewed in Ref. [21], but it has not been

Lam Research Ex. 1035 - Page 725
Lam Research Corp. v. Inpria Corp.
IPR2024-00033 - U.S. Patent No. 9,823,564

conclusively elucidated until now. At the same time, it can be stated that analysis of charge effects in the catalysis by metal nanoparticles is one of the main research areas, which may prove to have key importance in the development of new highly effective catalytic techniques.

When considering the charge effects, it is necessary to keep in mind their relationship with structure properties of a catalyst. There exist various methods for producing metallic nanoparticles and structures on their base, which can be conditionally divided into two large groups. In the first of these, nanoparticles are formed via aggregation of atoms (or small clusters), and in the second, as a result of dispersion of bulk metals. Methods based on aggregation of atoms into nanoparticles include thermal evaporation and condensation [22], reduction from solutions and that in microemulsions [23], and cryochemical synthesis [24] (see also Chapter 10 of this handbook). To the second group should be referred, e.g., the technology described in [25], in which nanoparticles were obtained by thermal evaporation of an overheated metal. Most of the methods described above can produce metallic particles 3–100 nm in size, which have, in certain cases, rather narrow size scatter.

However, a common disadvantage of most of the mentioned techniques (except cryochemical synthesis) is that they cannot give structures with high particle density on the support surface. At the same time, structures of just this type exhibit most clearly charge effects, which lead in many cases to a significant rise in catalytic activity. One of the main difficulties is due to the fact that nanoparticles, which have a large specific surface area, tend to coagulate into larger aggregates and this tendency is particularly noticeable in high-density structures. The appearance of coarse aggregates leads to loss of the unique properties of separate nanoparticles. For this reason, a search for methods that can improve the coagulation stability of the metallic nanostructures is the task whose accomplishment governs the development of new promising areas in catalysis.

In Section 2 of this chapter, a method for synthesis of high-density nanostructured catalyst is discussed. This method is based on the technique of laser electrodispersion of metals, developed at the Ioffe Physico-Technical Institute, Russian Academy of Sciences [26]. The same section discusses structural properties of the catalysts fabricated. It is demonstrated that these catalysts are composed of metallic nanoparticles of a strictly specified size, which, in addition, have amorphous structure. A consequence of the amorphous state of the particles is that they do not coagulate on coming in contact and retain their unique physico-chemical properties even in densely packed multilayer coatings. Section 3 is devoted to processes of tunnel charge transfer in a system of densely packed metallic nanoparticles and to effects of particle interaction with the support, which give rise to specific charge states of a catalyst. Owing to this effect, and also to structural

Lam Research Ex. 1035 - Page 726
Lam Research Corp. v. Inpria Corp.
IPR2024-00033 - U.S. Patent No. 9,823,564

features of nanoparticles, high-density coatings produced by laser electrodispersion exhibit an extremely high catalytic activity in quite a number of different catalytic processes.

2. Catalyst Fabrication and Structural Properties

This section describes the method of laser electrodispersion of metals, which was used to synthesize all the catalysts whose properties are discussed in this chapter. This method proved to be exceedingly promising both for synthesis and study of model catalytic systems and for fabrication of catalysts that exhibit a record-breaking high catalytic activity.

2.1. Catalyst Fabrication by Laser Electrodispersion of Metals

The method of laser electrodispersion is based on laser ablation, which occurs when a target is irradiated by a high-power pulsed laser. Previously, the laser ablation has been widely used for deposition of metallic coatings. However, under the usual process conditions the target material was primarily converted into the vapor phase. Accordingly, the coatings obtained on a substrate were either homogeneous metallic films, or thin island-type films. Characteristic for laser ablation is also the formation at the target surface (and further deposition on a substrate) of fine micrometer- or submicrometer-size metallic drops. This was regarded as an adverse effect and attempts were made to minimize it. The distinctive feature of our approach consists in that this adverse effect is made useful and the formation of microdrops becomes a predominant process. In the process developed, the initially generated liquid metallic microdrops are then divided into a large number of nanometer-size drops, which very rapidly cool down to solidification. The resulting nanoparticles are deposited on a substrate surface. This process is accomplished on turning the laser ablation to more severe target irradiation conditions characterized by a high temperature of laser torch plasma.

Liquid metal drops coming from the target surface proceed into the laser torch plasma produced by optical breakdown of the evaporated target material. Entering plasma area, these drops become negatively charged (as any isolated body placed in plasma would do). At a plasma temperature of 20–30 eV, the charge of microdrops reaches the critical value, at which they become unstable and start to split into smaller drops. This process of drop fission, which results from the development of a capillary instability of charged liquid drops, has been analyzed in a number of studies [27]. The

Lam Research Ex. 1035 - Page 727
Lam Research Corp. v. Inpria Corp.
IPR2024-00033 - U.S. Patent No. 9,823,564

simple reason for the appearance of this instability is that the Coulomb repulsion force exceeds the surface tension. An estimate of the instability threshold, which makes it possible to determine the corresponding amount of charge, was first obtained by Rayleigh [28]:

$$Q \geq 8\pi(\varepsilon_0 \alpha R^3)^{1/2}. \quad (1)$$

In this expression, Q and R are the drop charge and radius, α the surface tension of a molten material, and ε_0 the permittivity of free space. It is well known that the drop charge Q is proportional to the electron temperature of the plasma (T_e) [29]. With this fact taken into account, it is readily clear that T_e is to be raised to bring microdrops in the fission mode.

The development of the capillary instability of drops commonly involves two stages. First, on exceeding the instability threshold, the drop loses its spherical shape and its fission starts, with a large number of finer (daughter) drops ejected from the prominence on the surface of the maternal drop. Analysis shows that daughter drops are also unstable. Accordingly, the drop fission process has a cascade nature (see Figure 15.1), with the drop size decreasing by approximately a factor of 10 at each stage of the cascade.

A new feature, on which the laser electrodispersion method is based, consists in that the process of cascade fission terminates after the daughter drops reach a nanometer size. As charged drops immersed in plasma become smaller, the electric field on their surface increases, which results in a dramatic increase in the field emission of electrons. After the size of the daughter drops decreases to several nanometers, the flow of electrons emerging from the drop surface starts to exceed that coming in from the plasma. In this case, the drops discharge and become stable, so that the fission terminates. Thus, fission of micrometer and submicrometer drops in the laser torch plasma yields a tremendous number of nanometer drops with narrow size dispersion and a small amount of residues of maternal drops that had not enough time for total fission.

The scheme by which nanostructures are formed by laser electrodispersion is shown in Figure 15.2. In accordance with this scheme, a laser pulse causes

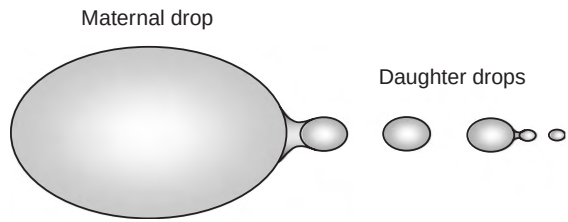


Fig. 15.1. Scheme of the cascade fission of a charged liquid drop.

Lam Research Ex. 1035 - Page 728
Lam Research Corp. v. Inpria Corp.
IPR2024-00033 - U.S. Patent No. 9,823,564

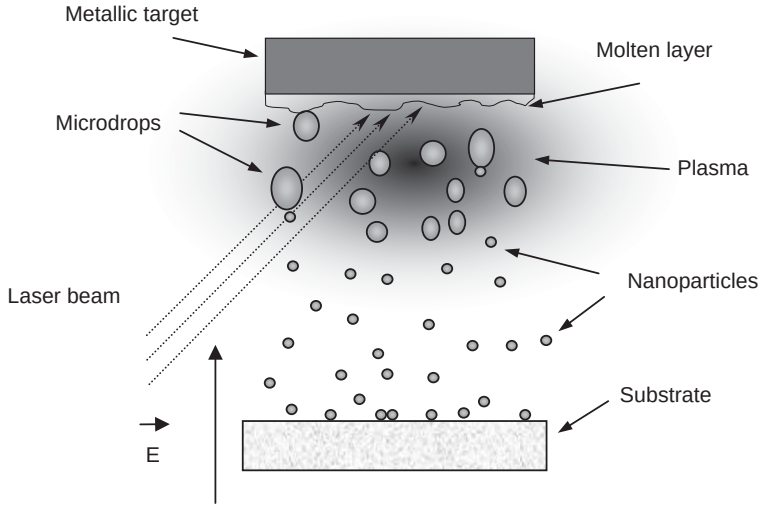


Fig. 15.2. Schematic of the nanostructure formation process.

melting of the target surface and creates the laser torch plasma near the surface. Microdrops of molten metal, which escape from the target and arrive into the plasma, are charged and their fission occurs to give nanosize drops.

Estimates show that nanosize drops formed in the plasma fly apart at a velocity of $\sim 10^4$ cm/sec, whereas the velocity of expansion of the plasma cloud exceeds 10^6 cm/sec. Accordingly, a microsecond after the laser pulse terminates the expanding plasma moves away from the target and charged nanodrops continue their movement in a vacuum, cool down to solidification, and the resulting nanoparticles finally arrive to the substrate surface.

The motion trajectory of charged nanoparticles can be corrected with electric field. This opportunity was used to separate the charged nanoparticles from the residues of maternal drops that had not enough time for separation. For this purpose, a steady voltage was applied to the gap between the target and the substrate, so that the corresponding electric field was concentrated near the substrate. The electric field strength was chosen so as to direct nanosize particles to the substrate without disturbing the motion of larger drops.

In case of deposition on a dielectric substrate, the trajectories of arriving nanoparticles are additionally disturbed (in the vicinity of the surface) by the Coulomb interaction with nanoparticles deposited in the preceding pulses. As a result, nanoparticles occupy vacant places on the surface and, at short film deposition times, their distribution over the substrate is virtually uniform. At longer deposition, as well as in the case of conducting substrate, particle arrangement on the surface may be more sophisticated, that is

Lam Research Ex. 1035 - Page 729
Lam Research Corp. v. Inpria Corp.
IPR2024-00033 - U.S. Patent No. 9,823,564

specific particle self-organization can be observed. Depending on the deposition time and type of substrate, structures composed of sparsely arranged or aggregated particles, densely packed single- or multilayer coatings can be obtained on the substrate.

It is also worth noting that laser electrodispersion can produce nanostructured alloy coatings and composite coatings composed of particles of different metals. For these purposes, alloyed targets are used and targets made of different materials are alternately irradiated.

2.2. STRUCTURAL PROPERTIES OF THE CATALYST COATINGS

Direct experimental observation of the drop fission in the laser torch plasma would be exceedingly difficult. The main obstacles are associated with the short duration of the fission process (< 100 nsec) and the small size and high velocity of the particles. In addition, it should be taken into account that the charging and division of particles occur in high-density and hot laser torch plasma and the presence of this plasma complicates the problem to an even greater extent. Accordingly, the validity of the process scheme we suggested can be only confirmed by indirect data. One of the results indicating that the process of microdrop fission occurs was obtained in an experiment in which the substrate was mounted in a close vicinity of the target surface. As can be seen in Figure 15.3, the surface of the substrate placed near the target is covered with submicrometer particles. It is also to note that part of these

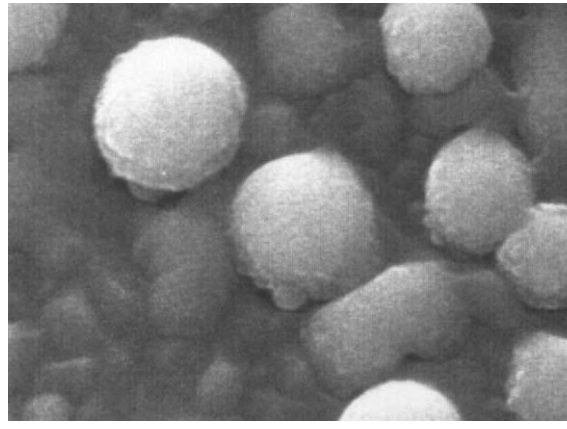


Fig. 15.3. Submicrometer metallic particles on the surface of a substrate mounted near the copper target.

Lam Research Ex. 1035 - Page 730
Lam Research Corp. v. Inpria Corp.
IPR2024-00033 - U.S. Patent No. 9,823,564

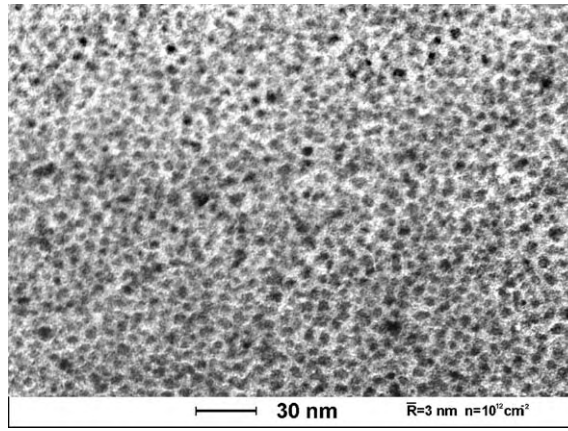


Fig. 15.4. TEM micrograph of a copper nanostructure on a substrate placed at a distance of 5 cm from the target. Deposition time: 1 min.

particles have projections whose size is approximately 10 times smaller than that of the main particles. The presence of such particles with projections can be interpreted as a consequence of rapid cooling and deposition onto the substrate of drops that are in the initial stage of fission.

Figure 15.4 shows a transmission electron microscopy (TEM) micrograph of a granulated copper film deposited by laser electrodispersion. The substrate onto which the structure was deposited was placed at a distance of ~5 cm from the target. It is important to note that only nanoparticles of average size equal to 5 nm are seen on the substrate surface, and there are no coarse particles (residues of drops that had not enough time to disintegrate). Additional studies demonstrated that coarse particles of size 100–200 nm also exist, but can only be observed by scanning over a larger substrate area because their number is exceedingly small, about one coarse particle per 10^6 nanoparticles. This fact can serve as additional evidence in favor of the nanoparticles formation process described above.

It can also be seen in Figure 15.4 that, at a comparatively low surface density, the structure is composed of isolated Cu nanoparticles uniformly distributed over the surface. In this film, the particle surface density is on the order of $10^{12}\,\mathrm{cm}^{-2}$. If the deposition time is raised from 1 to 5 min, nanoparticles are grouped into ensembles (Figure 15.5), within which particles are in contact with one another. The highest packing density of particles in a single-layer coating is reached at a deposition time of 5 min.At even longer deposition times, a second layer of particles starts to be formed, and particles of the second layer tend to occupy places over gaps between particles of the first layer.

Lam Research Ex. 1035 - Page 731
Lam Research Corp. v. Inpria Corp.
IPR2024-00033 - U.S. Patent No. 9,823,564

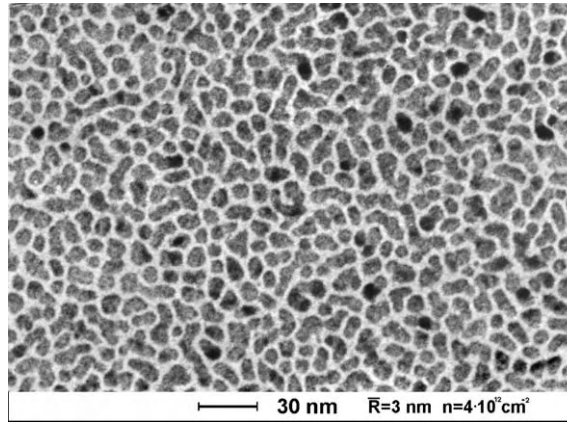


Fig. 15.5. TEM micrograph of a copper nanostructure. Deposition time: 5 min.

By now, the possibility of deposition of granulated Cu, Ni, Pd, Pt, and Au films by laser electrodispersion has been experimentally verified. The structural parameters of the films being formed were studied by various diagnostic techniques, with the most informative results obtained with TEM, atomic-force microscopy (AFM), and X-ray photoelectron spectroscopy (XPS).

TEM micrographs of the structure of Ni and Pd films are shown in Figure 15.6. It can be seen that the arrangement of particles of all the three metals on the substrate is strongly disordered. At the same time, a close comparison of Figures. 15.5 and 15.6 shows that the structures formed by, e.g., Cu and Ni nanoparticles are somewhat different. For example, Cu nanoparticles combine into isolated islands composed of 3–6 particles, while Ni structures exhibit a tendency toward ordering of nanoparticles into chains containing up to 15–20 particles.

As shown by the results of processing of the TEM images of the structures, the relative size dispersion of nanoparticles formed by all the metals studied does not exceed 10% and their average size is only determined by the material of which the particles are composed. For example, the average sizes of Ni and Pd particles are 2.5 and 2 nm, respectively.

Important data on the structure of the films were obtained in an analysis of electron diffraction patterns recorded directly in the transmission electron microscope. In all cases, the diffraction patterns had the form of diffuse halos, which indicate that nanoparticles are in the amorphous state [30]. The fact that the nanoparticles are amorphous is in all probability due to the exceedingly fast cooling of nanometer drops after the expansion of the plasma cloud. Estimates of the cooling rate of nanodrops at the instant of their hardening give values of up to 10^7 K/sec.

Lam Research Ex. 1035 - Page 732
Lam Research Corp. v. Inpria Corp.
IPR2024-00033 - U.S. Patent No. 9,823,564

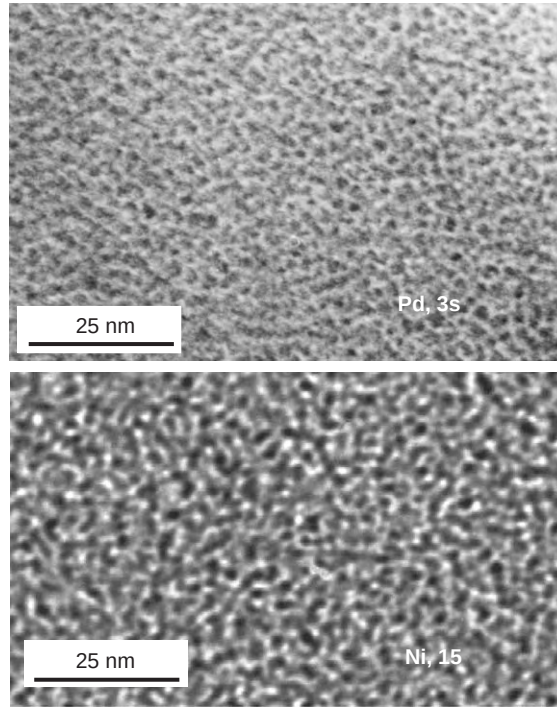


Fig. 15.6. TEM micrographs of Ni and Pd structures.

A feature common to all the metals is that nanoparticles do not coagulate on coming in contact with each other. Presumably, this feature is a consequence of the amorphous state of the metal in the particles. It is worth noting that a transition from the amorphous to the polycrystalline state was observed only in copper structures upon heating to above 150°C, with the particles coagulating to form larger polycrystalline grains. Nanoparticles of Ni and Pd demonstrated a considerably higher stability against coagulation, no transition to the polycrystalline state occurred even upon heating to above 400°C. The absence of coagulation under normal conditions makes it possible to deposit densely packed and multilayer coatings composed of separate nanoparticles of the same size.

3. Charge State of Metallic Nanostructures

As shown by the results of numerous experiments, the catalytic activity of nanostructured metals, in quite a number of chemical reactions, is closely

Lam Research Ex. 1035 - Page 733
Lam Research Corp. v. Inpria Corp.
IPR2024-00033 - U.S. Patent No. 9,823,564

associated with their electrical properties. In turn, the electrical properties of metallic nanostructures depend on a number of structural parameters, such as the size and mutual position of the particles, material of the support (insulator, semiconductor, or metal), etc. Taking into account that the size dispersion of nanoparticles formed by laser electrodeposition is less than 10%, it may be thought, when analyzing the charge state of structures of this kind, that all the particles are identical. We should also take into consideration the fact that, at the instant of time when the structure is formed, nanoparticles tend to be uniformly distributed over the surface because of mutual Coulomb repulsion. This makes it possible to characterize the positions of particles by only a single parameter, surface density of particles on the substrate.

At a low surface density of particles, when the average distance between them exceeds 4–5 nm, exchange of electrons between neighboring particles is unlikely. Accordingly, nanoparticles can be charged in this case only via exchange of electrons either with the support, if this is a metal or a semiconductor, or with some external conductor, e.g., with the tip of a tunnel microscope. If such sparse structures are deposited onto an insulator, the density of charged particles is low and the conductivity of the coating is virtually zero.

Raising the particle density leads to a decrease in the width of interparticle gaps and to a pronounced increase in the probability of electron tunneling from one particle to another. If, in this case, a structure is deposited onto a dielectric substrate, the number of charged particles and the conductivity of the coating increase dramatically. The conductivity of coatings of this kind is in many regards similar to the hopping conductivity in semiconductors: e.g., the temperature dependence of the conductivity obeys the same law in both cases.

Further increase in the density of nanoparticles leads to formation of close contacts between them, which leads to collectivization of electrons in ensembles of contacting particles. In the high-density limit, when each nanoparticle is in contact with all of its neighbors, the nanostructure becomes similar in its electrical properties to a thin metallic film and is characterized by a metallic type of conduction.

As shown below, nanostructures with an intermediate density are the most interesting as regards the search for materials with the highest catalytic activity. On one hand, particles in these structures are separated from one another and charge is localized on isolated particles, and, on the other hand, they are situated sufficiently closely for the charge exchange between neighboring particles to become possible.

In structures of this kind, the probability of electron tunneling depends on the particle size, height and width of tunneling barriers, and ambient

Lam Research Ex. 1035 - Page 734
Lam Research Corp. v. Inpria Corp.
IPR2024-00033 - U.S. Patent No. 9,823,564

temperature [31]. In this case, the ensemble-averaged stationary concentration of charges is primarily determined by the energy spectrum of various charge states and the ambient temperature. Let us first consider the situation in which nanoparticles are deposited onto a dielectric support. At a not-too-high particle density, when the effects of mutual electrostatic polarization are not important yet, the average number N_z of charged particles with charge Ze (e is the elementary charge) is given by the expression [32]:

$$\frac{N_Z}{N} = \frac{\exp(-Z^2e^2/r\varepsilon kT)}{\sum\limits_{Z=-\infty}^{\infty} \exp(-Z^2e^2/r\varepsilon kT)}, \tag{2}$$

where N is the total number of nanoparticles in the system, r the radius of nanoparticles, and ε and T the dielectric constant and ambient temperature. This expression gives a time-averaged number of charged particles, whereas the true charge distribution in the system fluctuates with a period on the order of the electron tunneling time. The exponent of the exponential function in formula (2) includes the ratio of the charging energy, $Z^2e^2/r\varepsilon$, i.e., the electrostatic energy of an isolated charged particle, to the thermal energy kT. It is also to note that, according to Eq. (2), the average numbers of negatively and positively charged particles with charges of equal magnitudes are the same, i.e., the system of nanoparticles remains, on the whole, electrically neutral. As follows from Eq. (2) for the case of room temperature and $\varepsilon \approx 1$ (i.e., in air or in a vacuum), the fraction of charged particles in nanostructures composed of particles of size 2–5 nm is small, $\sim 10^{-3}$, with the particles only singly charged. As the polarity of the environment increases to $\varepsilon \approx 10$–20, a value characteristic of liquid media, the situation changes cardinally. There appear a large number of doubly and triply charged particles, and the fraction of neutral particles does not exceed 40%.

To perform a more rigorous calculation of the concentration of charged particles with account of their mutual polarization, which plays a particularly important role in dense structures, a model based on the Monte-Carlo procedure has been developed. In this model, electron transitions between particles are taken in accordance with the calculated probabilities of these transitions [33,34]. Figure 15.7 compares the results of such calculations with the data obtained using expression (2). It is to note that the model [34] has been specially developed for describing the charge state of structures composed of identical nanoparticles. The dependences in Figure 15.7 are qualitatively similar for both the models; however, quantitative differences are strong, especially in calculating the densities of doubly and triply charged granules.

Lam Research Ex. 1035 - Page 735
Lam Research Corp. v. Inpria Corp.
IPR2024-00033 - U.S. Patent No. 9,823,564

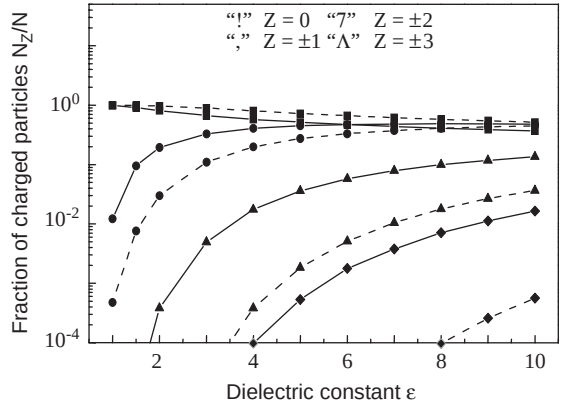


Fig. 15.7. Fraction of charged particles vs. the dielectric constant of the medium. Dashed lines, calculation by formula (2); solid lines, numerical simulation.

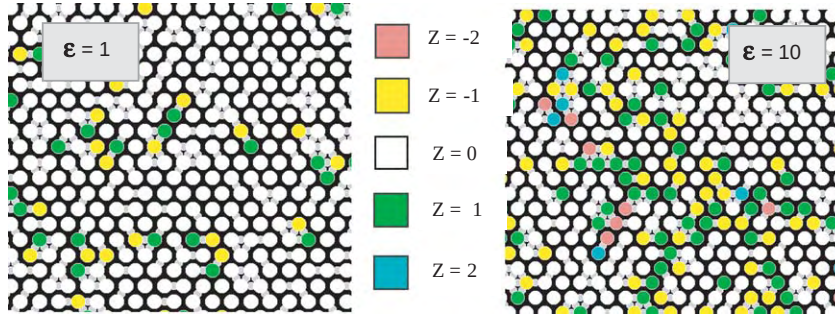


Fig. 15.8. Distribution of charged particles in dense single-layer coating composed of monodisperse nanoparticles (numerical simulation for dielectric constants $\varepsilon = 1$ and $\varepsilon = 10$, $T = 100°C$). Z is the charge multiplicity of nanoparticles.

The calculations also demonstrate that charged granules are mostly arranged in dipoles. Figure 15.8 illustrates this tendency. It can be seen that, at both high and low polarities of the medium, neighboring particles most frequently carry charges of opposite signs. Accordingly, the electric field created by these charges is mainly concentrated in the inter-particle gaps. Because the distances between particles are exceedingly small, the electric field strength is very high: depending on the particle size and polarity of the medium, it varies from 10^6 to 4×10^6 V/cm.

The models considered give results that account for a large body of experimental data obtained in measurements of the conductivity of nanostructures composed of various metals, deposited onto dielectric substrates

Lam Research Ex. 1035 - Page 736
Lam Research Corp. v. Inpria Corp.
IPR2024-00033 - U.S. Patent No. 9,823,564

[35]. However, these models are inapplicable to analysis of the charge state of structures deposited on the surface of a metal or a semiconductor. For example, in the case of a metallic substrate, it is necessary to take into account two additional factors: effect of the conducting substrate on the self-capacitance and mutual capacitance of nanoparticles and the possibility of exchange of electrons between the nanoparticles and the substrate. In this case, the charge state of the system very strongly depends on whether or not an oxide layer is present between a particle and the substrate. In the absence of an oxide layer, the surfaces of particles and substrate are equipotential and charge densities on the surface of particles and substrate are zero. If an oxide layer exists, and just this case most frequently occurs in practice, a charge may be localized on particles and electron transport occurs via tunneling across the oxide layer. In this case, the charge state of the system at a low surface density of particles is described by an expression similar to (2):

$$\frac{N_Z}{N} = \frac{\exp(-(Z - Z_{\text{eff}})^2 e^2 / r\varepsilon kT)}{\sum_{Z=-\infty}^{\infty} \exp(-(Z - Z_{\text{eff}})^2 e^2 / r\varepsilon kT)}. \tag{3}$$

Here, $Z_{\text{eff}} = \Delta\phi r\varepsilon / e^2$ is the average charge of the system of nanoparticles, determined by the difference of the work functions of the metals constituting particles and the substrate ($\Delta\phi$). Accordingly, the charge state of such a nanostructure becomes dependent on $\Delta\phi$ and differs from the charge state of a structure deposited onto a dielectric substrate.

Figure 15.9 presents the results of calculations of the charge state of Ni nanostructures on metallic substrates with different work functions. It can

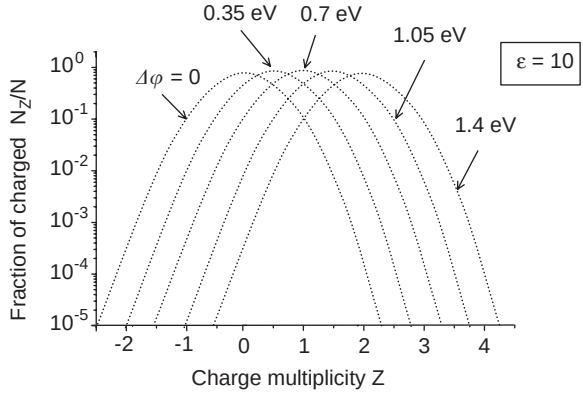


Fig. 15.9. Fraction of charged Ni particles vs. their charge multiplicity at a varied difference of the work functions of Ni and of the substrate material.

Lam Research Ex. 1035 - Page 737
Lam Research Corp. v. Inpria Corp.
IPR2024-00033 - U.S. Patent No. 9,823,564

be seen that, for some substrates, the number of charged particles may be large: e.g., at $\Delta\phi \approx 0.7\,\text{eV}$, the fraction of singly charged particles is as large as 70%, with the rest of the particles being either neutral or doubly charged. Thus, the charge state of nanostructures can be controlled by an appropriate choice of the materials of a catalyst and a support.

When describing the charge state of nanostructures deposited on a semiconducting substrate, it is necessary to take into account that, in contrast to a metal substrate, the charge in a semiconductor is distributed in a relatively thick depletion layer near the surface, and the process of charge exchange between the semiconductor and nanoparticles is largely determined by the state of the semiconductor surface. Let us consider as an example the charge effects that occur in metallic nanostructures deposited on the surface of doped silicon of p- and n-type. It is worth noting that, under common conditions, a 1–2 nm-thick layer of the natural oxide SiO_2 is formed on the silicon surface and this layer is tunnel-transparent for electrons.

Figure 15.10 shows near-surface band diagrams of p- and n-type silicon with nickel particles deposited onto its surface. A characteristic feature of these diagrams is band bending near the semiconductor surface, which is determined by the so-called pinning of the Fermi level, i.e., by fixation of its energy position at the surface. It is well known that the pinning is due to the formation of specific surface states and the position of the Fermi level at the surface is fixed at $\delta = 0.4\,\text{eV}$ from the top of the valence band at any type of doping. The values of energy gap E_g of silicon, electron affinity χ and Ni work function ϕ(Ni) are also shown in Figure 15.10. It can be seen that the Fermi level in nickel particles deposited onto p-type silicon lies $\Delta = 0.67\,\text{eV}$ above the Fermi level in silicon (here, we neglect the difference between the position of the Fermi level and valence band edge, which is a good

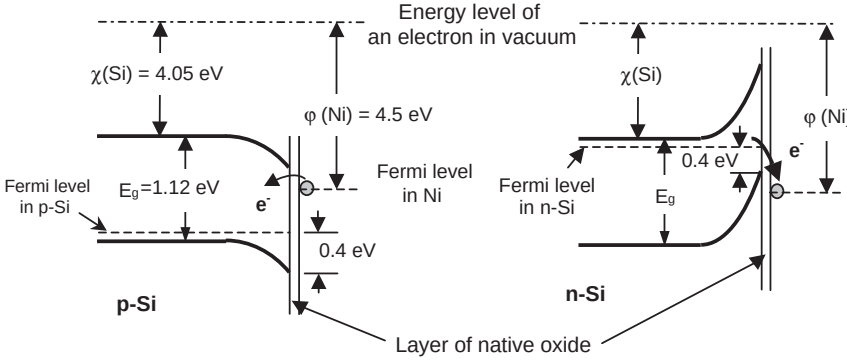


Fig. 15.10. Band diagrams illustrating the effect of charging of Ni nanoparticles on the surface of silicon. Ni particles are charged positive on p-type silicon and negative on n-type Si.

Lam Research Ex. 1035 - Page 738
Lam Research Corp. v. Inpria Corp.
IPR2024-00033 - U.S. Patent No. 9,823,564

approximation in most cases). This quantity is on the order of the charge energy of nickel particles carrying one or two extra electrons. Since $\Delta > 0$, the attainment of equilibrium in the system constituted by silicon and Ni particles will be accompanied by electron flow from nickel particles into silicon (as shown by the arrow in Figure 15.10). After the thermodynamic equilibrium in the system is attained, nickel particles will be *positively charged*, with, on average, one or two lacking electrons per particle.

Similarly, the band diagram of n-type Si shows that, in this case, the deposited nickel nanoparticles will be negatively charged on reaching the equilibrium in the system. Thus, the sign and amount of charge appearing on Ni particles depend on the type of doping of the semiconductor.

It is to mention that the model considered is valid in the case of relatively low concentration of metallic particles on the semiconductor surface. The point is that the characteristic surface density of built-in charges on the surface of Si is $\sim 10^{12}\,\mathrm{cm}^{-2}$. If the density of the deposited particles of a catalyst is considerably higher than $10^{12}\,\mathrm{cm}^{-2}$, equilibrium in the semiconductor–nanoparticles system will be attained in another way. In this case, a nanostructured film can be regarded as continuous and the situation is closer to that in the so-called Schottky contact, in which there is a thin oxide layer between a semiconductor and metal, but the *electric capacitance of the metal is obviously high*. As a result, in attainment of equilibrium by charge redistribution, the potential of the metallic layer remains virtually unchanged.

A characteristic feature of the systems of nanoparticles deposited on a conducting substrate is that the electric field generated by charged particles is mostly concentrated in the gaps between the particles and the substrate. However, the electric field strength is about the same in both the cases considered (metal and semiconductor substrates) and varies from 10^6 to $4 \times 10^6\,\mathrm{V/cm}$.

We considered above processes of charge transfer in monodisperse structures composed of identical nanoparticles. If there is a considerable particle size scatter, the description of charge state of such structures becomes much more complicated. This issue has been the subject of several studies (see, e.g., Refs. [35,36]).

4. Effect of Nanoparticle Charging on the Catalytic Properties

This section describes a simple model that enables evaluation of the influence of charge effects on the catalytic activity of metallic nanostructures. Also, the results of experiments performed with nanostructured catalysts synthesized by laser electrodispersion are discussed. These results demonstrate a relationship between the catalytic activity and charge density in the

Lam Research Ex. 1035 - Page 739
Lam Research Corp. v. Inpria Corp.
IPR2024-00033 - U.S. Patent No. 9,823,564

catalyst structure: in quite a number of reactions, an increase in the charge density leads to a significant rise in the catalytic activity.

4.1. Analytical Estimates

Nanoparticle charging can affect the rate of a catalytic reaction for two reasons. The first is that charged particles create an electric field. As mentioned above, this field is concentrated in gaps between nanoparticles or between the nanoparticles and the substrate. In both cases, the gap width varies within the range 1–3 nm. Because the electric field strength in the gap is $\sim 10^6$ V/cm, the potential difference across the molecules of size on the order of 1 nm, present in these gaps, may reach values of 0.1 V. Accordingly, the molecules in the gaps can be excited with a transition to higher energy levels, ~0.1 eV above the ground state. The appearance of excited molecules may lead to a significant increase in the rate of chemical reactions [12].

The second charge effect that can affect the catalytic activity of nanostructures is observed for reactions involving electron transfer between the reactant molecules and nanoparticles. If the key stage of the reaction is electron transfer from a metal nanoparticle to an adsorbed molecule, then the presence of a negative charge on the nanoparticle makes the electron transfer energetically more favorable. Owing to this, the catalytic reaction can be accelerated. It is worth noting that, in most of real structures, thin oxide sheaths are formed on the surface of metallic nanoparticles. Therefore, charge transfer should occur via electron tunneling through the potential barrier associated with the presence of an oxide on the surface. It is also to note that the alternative process, transfer of an electron with its excitation into the continuous spectrum, is considerably less probable, because in this case the electron has to overcome a very high potential barrier equal to the work function of the metal.

Let us compare the probabilities of tunnel electron transfer from singly and doubly charged metallic nanoparticles ($Z = -1$ and $Z = -2$) to an adsorbed molecule. In the general case, tunnel electron transfer occurs in three stages: (i) thermal activation of an electron in the metal, (ii) tunneling of the electron through the barrier to a molecular level, and (iii) transformation of the adiabatic potential of the molecule.

If a metallic nanoparticle is singly negatively charged (has one extra electron), the electron leaves behind, upon tunneling through the barrier, a *neutral* particle, i.e., the tunneling occurs in a zero electric field, as shown in Figure 15.11a. As a result of the tunnel transfer, the electron must find itself at the molecular affinity level (E_A), whose energy position is determined by processes of chemisorption of the reactant molecule on the surface of the

Lam Research Ex. 1035 - Page 740
Lam Research Corp. v. Inpria Corp.
IPR2024-00033 - U.S. Patent No. 9,823,564

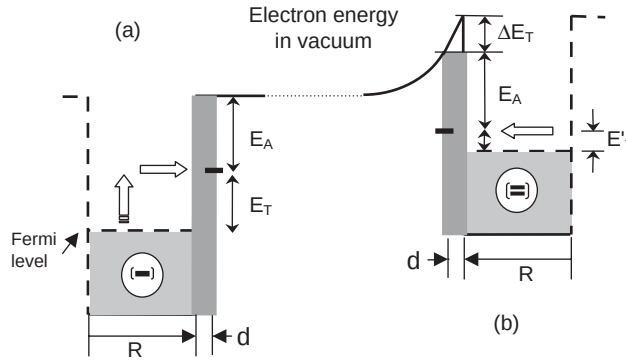


Fig. 15.11. Band diagrams illustrating electron transfer from the surface of negatively charged nanoparticle to adsorbed molecules of the reactant: (a) singly charged particle, and (b) doubly charged particle.

oxide sheath. It can be seen in the figure that, for charge transfer to occur, it is necessary that an electron in the metal should be thermally activated. In this case, an electron at the Fermi level must acquire an additional energy equal to E_T, and this value is the activation energy of this process.

In case the nanoparticle is doubly negatively charged, an electron tunnels through the potential barrier to a molecule, leaving behind *one extra electron*, i.e., the tunneling occurs in a repulsive electric field (Figure 15.11b). Let us now assume that the electric field of charged particle does not affect the molecule affinity E_A (energy E_A is reckoned from the potential level at the particle surface). Then, it can be seen from the figure that the electron activation energy decreases by a value equal to the potential drop across the oxide sheath. This value can be readily estimated to be [37]:

$$\Delta E_T = \frac{e^2}{\varepsilon_d R}\frac{d}{R+d}. \tag{4}$$

Here, ε_d and d are the dielectric constant and the thickness of the oxide sheath of the metal, and R the radius of a metallic core of nanoparticle.

Similar analysis can be made for particles with an arbitrary initial charge multiplicity Z. If, in particular, a particle is originally neutral, tunneling will occur in an attractive electric field. It can be readily seen that, in the general case, the activation energy is $E_T+(Z+1)\Delta E_T$. The assumption that the molecular affinity E_A is independent of the electric field of charged particles is quite reasonable, because at $|Z| \leq 3$ this field is still considerably weaker than the local electric fields associated with the chemisorption process.

Let us now evaluate the influence exerted by the particle charge on the specific (per unit mass of the metal) catalytic activity of nanostructures. Let

Lam Research Ex. 1035 - Page 741
Lam Research Corp. v. Inpria Corp.
IPR2024-00033 - U.S. Patent No. 9,823,564

us compare the specific activity of low-density structures, in which the charge effects are unimportant, with that of high-density structures, in which a considerable part of particles is charged (N_Z/N is the fraction of particles with a charge Z). To obtain the estimate of interest, it is necessary to take into account that the catalytic activity exponentially depends on the activation energy. Further, to account for the contribution of particles with different original charges, it is necessary to take a sum of exponentials with different activation energies dependent on Z, i.e., to sum over charge multiplicities Z. Thus, the ratio of the specific activity of a high-density structure (A) to that of a sparse structure (A_0) is equal to

$$\frac{A}{A_0} = \sum_Z \frac{N_Z}{N} \exp\left[-\frac{E_T + (Z+1)\Delta E_T}{kT}\right]. \tag{5}$$

In a particular case of copper nanostructures, nanoparticles have the form of metallic nuclei of radius $R = 1.7$ nm coated with a Cu_2O sheath of thickness $d = 0.7$ nm with $\varepsilon_d \approx 4$ [38]. For structures of this kind, the dependence of the fraction of charged particles on the dielectric constant of the solution is presented in Figure 15.7. Substitution of these values in expression (5) gives $A/A_0 \approx 10$. This value is in reasonable agreement with the experimental data presented below.

It should be emphasized once more that, in addition to the average number of charged particles, an important characteristic of the system is the lifetime of the ''instantaneous'' distribution of charges or the existence time of dipoles formed by neighboring charged particles. Estimates show that this time is $\sim 10^{-10}$ sec for copper nanostructures composed of 5 nm particles. This time is considerably longer than the characteristic time of a chemical reaction and, more so, than that of tunnel transfer of an electron from particles to reactant molecules. Thus, in analysis of the catalytic activity of nanostructures the charge distribution and the electric fields created by charged particles can be regarded as stationary.

4.2. Experimental Results and Discussion

Originally, the effect of charge state of nanostructures on their catalytic activity was recognized from analysis of the experimental data on the catalytic properties of metallic nanoparticles immobilized in the matrix of a polyparaxylylene polymer [13–15,24]. It was found that the dependence of the catalytic activity (and, in some cases, of the selectivity) of copper, palladium, and iron nanoparticles on the metal content of these structures has a maximum. This maximum exists not only for the specific (related to unit weight) activity, but also for the absolute activity. More specifically, for copper and

Lam Research Ex. 1035 - Page 742
Lam Research Corp. v. Inpria Corp.
IPR2024-00033 - U.S. Patent No. 9,823,564

palladium nanocomposites used as catalysts in isomerization of chloro-olefins the maximum of catalytic activity was attained at an average distance between neighboring particles equal to several nanometers. This distance is small enough to permit tunnel electron transfer between metal nanoparticles. It was also shown that a steep rise in the conductivity of these structures occurs at the same metal content at which the activity is at a maximum. This coincidence qualitatively confirmed the assumption that charge redistribution between nanoparticles affects their catalytic properties. However, a more rigorous analysis of these effects requires a model catalytic system in which the size, shape, and composition of particles would remain unchanged on widely varying the degree of surface coverage (or volume filling) by these particles. Nanostructures formed by laser electrodispersion considered above proved to be the most appropriate for this purpose.

In fabrication of the catalysts by laser electrodispersion, thermally oxidized silicon wafers with a thickness of SiO_2 oxide layer of $\sim$1 μm were used as a substrate. A substrate with so thick an oxide layer can be regarded as an insulator. In some cases, wafers of crystalline (1 0 0) Si were used, which had on their surface only a thin (1–2 nm) layer of a natural oxide. This layer is tunnel-transparent for electrons, and, therefore, charge exchange between supported nanoparticles and silicon is possible.

In the study, a certain type of chemical reaction, sensitive to the charge state of a catalyst, was chosen. As test reactions for copper and nickel films, the following chlorohydrocarbons conversions were selected [30,34,39]:

- allyl isomerization of 3,4-dichlorobutene-1 into *trans*-1,4-dichlorobutene-2:

$$CH_2Cl - CHCl - CH = CH_2 \rightleftarrows CH_2ClCH = CHCH_2CL;$$

- addition of carbon tetrachloride at the double bond of octane-1:

$$CCl_4 + CH_3(CH_2)_5CH = CH_2 \rightarrow CH_3(CH_2)_5CHCl\text{-}CH_2(CCl_3);$$

- joint metathesis of C–H and C–Cl bonds in decane and carbon tetrachloride:

$$RH + CCl_4 \rightarrow RCl + CHCl_3,$$

where $R = C_{10}H_{21}$. Active ion–radical or radical intermediates of these processes are formed upon electron transfer from catalyst particles to the reactant [40]:

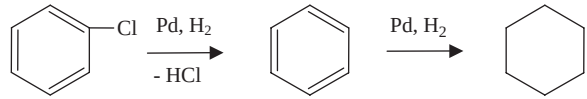
$$M_n + RCl \rightarrow M_n^+ + RCl^{\bullet} \rightarrow M_n^+(Cl^-) + R^{\bullet}.$$

Lam Research Ex. 1035 - Page 743
Lam Research Corp. v. Inpria Corp.
IPR2024-00033 - U.S. Patent No. 9,823,564

This key stage of catalysis is exceedingly sensitive to the charge state of the catalyst.

The catalytic activity of nickel and palladium films was studied in hydrogenation of nonene-1 and chlorobenzene [41]:

$$C_9H_{18} + H_2 \rightarrow C_9H_{20};$$



The reactions mentioned above can also be of practical importance, e.g., as model reactions for processing of organochlorine wastes.

All the metallic nanostructures deposited by laser electrodispersion on both types of silicon substrates were found to be exceedingly active in the above processes. The activity was orders of magnitude higher than that of typical supported catalysts prepared by the standard techniques. Such a high activity is presumably due not only to the small size and amorphous state of nanoparticles, but also to the influence exerted by the charge effects discussed above.

Let us first consider the case of substrates of thermally oxidized silicon (dielectric support). Figure 15.12 shows several examples of how the specific catalytic activity of copper nanoparticles produced by laser electrodispersion depends on the particle density in the above three reactions involving chlorohydrocarbons. It can be seen that, in all cases, the catalytic activity has a maximum at virtually the same particle density of $3–4 \times 10^{12}\,cm^{-2}$. Here, the presence of the maximum cannot be due to the ordinary size effect in which a dependence on the particle size is manifested because all the films are composed of metal particles of the same size and shape. The presence of such a maximum can hardly be attributed to anything other than interparticle interaction. It is important to note that the maximum catalytic activity is observed at the surface particle densities at which there occurs a steep rise in the film conductivity (by nine orders of magnitude!) and a film passes from the dielectric state to the conducting state. In our opinion, the data obtained can serve as clear evidence in favor of the existence of a *size effect of the second kind*, which consists in that the properties of the structures vary with the surface particle density or average width of the gap between neighboring particles. In this case, the size effect of the second kind is, in the end, manifested in that the catalytic properties of a nanostructure strongly depend on its charge state.

An even more clearly pronounced manifestation of the influence exerted by the charge of nanoparticles on their catalytic properties was observed in a

Lam Research Ex. 1035 - Page 744
Lam Research Corp. v. Inpria Corp.
IPR2024-00033 - U.S. Patent No. 9,823,564

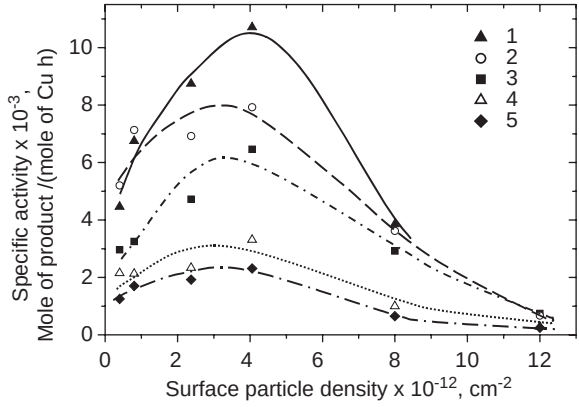


Fig. 15.12. Specific catalytic activity vs. surface density of copper nanoparticles on thermally oxidized silicon in reactions involving chlorohydrocarbons: (1) $CCl_4 + C_8H_{16}$ at 150°C, (2) the same at 130°C and $\varepsilon = 10$, (3) isomerization of dichlorobutenes at 110°C, (4) isomerization of dichlorobutenes at 130°C, and (5) $CCl_4 + C_{10}H_{22}$ at 130°C.

study of the activity of Cu nanoparticles in the reaction of dichlorobutene isomerization at different dielectric constants of a solvent. Analysis of the dependences obtained (see Figure 15.13) shows that at a low surface particle density $n = 1.6 \times 10^{11}\,\mathrm{cm}^{-2}$, when charge exchange between nanoparticles is virtually impossible, the rate of the catalytic reaction is independent of the solvent polarity. An increase in the particle density to $n = 8 \times 10^{11}\,\mathrm{cm}^{-2}$, accompanied by a decrease in the width of gaps between nanoparticles to 1.5–2.5 nm, leads to a strong dependence of the activity on the solvent polarity. This result is not unexpected and is in good agreement with the estimates made above. Indeed, raising the solvent polarity leads to an increase in the fraction of charged nanoparticles (see Figure 15.7), which, in turn, causes, in accordance with formula (5), a rise in the gain coefficient of catalytic activity, A/A_0.

As can be seen in Figure 15.13, the ten-fold increase in activity is attained at a particle density $n = 4 \times 10^{12}\,\mathrm{cm}^{-2}$ and $\varepsilon = 10$, which is in good agreement with the above estimate $A/A_0 \approx 10$.

Another specific feature of the catalytic behavior of the structures under study consists in that the chemical nature of a metal becomes a factor less important for catalysis as the surface nanoparticles density increases. This is well seen in Figure 15.14, which shows the results obtained in measurements of the activity of copper- and nickel-based catalysts in the reaction of carbon tetrachloride addition to olefins. Presented in this figure are the activities of catalysts prepared by laser electrodispersion and the conventional deposition techniques. Two important features are worth noting. First, the activity

Lam Research Ex. 1035 - Page 745
Lam Research Corp. v. Inpria Corp.
IPR2024-00033 - U.S. Patent No. 9,823,564

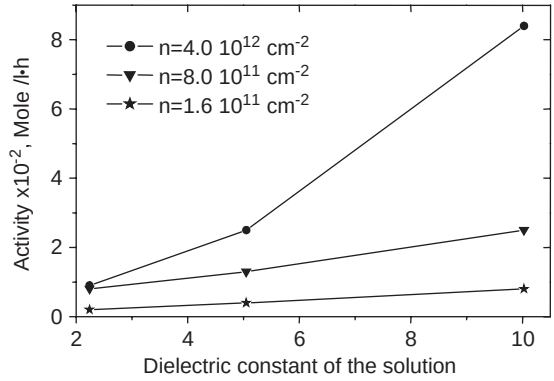


Fig. 15.13. Activity of Cu nanoparticles in the reaction of dichlorobutene isomerization vs. the dielectric constant of the solvent at different nanoparticle densities.

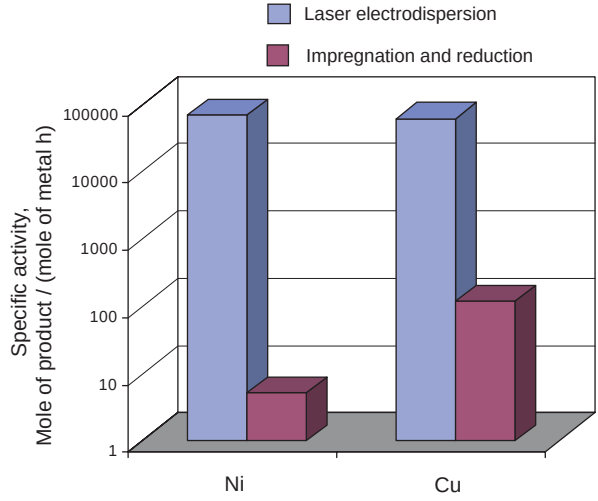


Fig. 15.14. Comparison of specific catalytic activities of Ni and Cu nanoparticles deposited onto a thermally oxidized silicon by laser electrodispersion ($n \approx 5 \times 10^{12}\,\mathrm{cm}^{-2}$) with those of catalysts prepared by the method of impregnation and reduction (1% Ni/SiO_2, 1% Cu/SiO_2). Reaction of carbon tetrachloride addition to olefins.

of the conventional catalysts is many orders of magnitude lower than that of films prepared by laser electrodispersion. Second, and exceedingly important, is that the conventional nickel-based catalysts are considerably less active in the given reaction than those based on copper. At the same time, equally high activities are observed at close surface particle densities for

Lam Research Ex. 1035 - Page 746
Lam Research Corp. v. Inpria Corp.
IPR2024-00033 - U.S. Patent No. 9,823,564

copper and nickel structures deposited by laser electrodispersion. The highly active catalysts synthesized by this method also exhibited unusually low effective activation energy of carbon tetrachloride addition to olefins. The value of 50 kJ/mol, obtained for the reaction with octane-1, is substantially lower than the commonly observed activation energies of 80–100 kJ/mol [42]. The possible reason is that the appearance of highly active charged states in a catalyst makes different metals closer in their catalytic properties.

Passing to conducting substrates markedly changes the situation. Figure 15.15 shows dependences of the catalytic activities of copper nanoparticles on the particle density, measured in the reaction of isomerization of dichlorobutenes with the particles deposited onto the surface of oxidized and unoxidized silicon. Similar results were obtained with nickel nanostructures under the identical process conditions. On both types of substrates, the activity of nanoparticles is exceedingly high, but the dependence of the catalytic activity on the particle density exhibits fundamentally different types of behavior. In deposition of particles onto a dielectric substrate (thermally oxidized silicon), this dependence shows a sharp maximum. At the same time, in the case of deposition onto a conducting substrate, a gradual decrease in activity is observed as the degree of coverage of the support surface with particles increases. Again, this behavior is in good agreement with the results obtained in modeling of the charge state of nanostructures. Calculations show that the maximum density of charged copper particles is reached on the dielectric substrate at a density $n \approx 4 \times 10^{12}\,\mathrm{cm}^{-2}$, at which the catalytic activity is the highest. On conducting substrates, the density of charged Cu particles is virtually constant

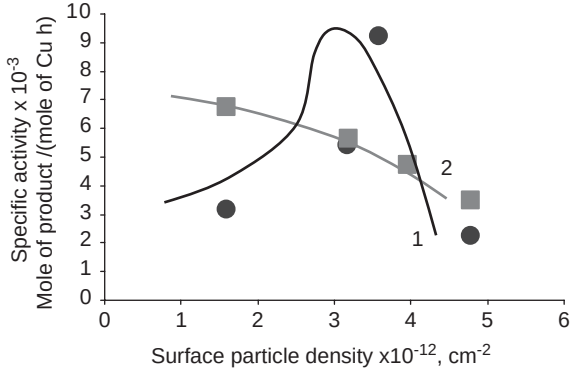


Fig. 15.15. Specific catalytic activity vs. surface density of copper nanoparticles in dichlorobutene isomerization at $T = 110°C$: (1) oxidized silicon support and (2) silicon support.

Lam Research Ex. 1035 - Page 747
Lam Research Corp. v. Inpria Corp.
IPR2024-00033 - U.S. Patent No. 9,823,564

at $n < 3 \times 10^{12}\,\mathrm{cm}^{-2}$ and decreases as the density increases further, i.e., the run of this dependence is similar to that of curve 2 in Figure 15.15.

The dissimilarities between the charge states of nickel nanostructures deposited onto substrates of well-conducting p- and n-type silicon (unoxidized) were manifested in different catalytic activities in the reaction of carbon tetrachloride addition to olefins. It was shown that negatively charged nanoparticles on an n-type Si substrate have a two times higher activity, compared with positively charged particles on a p-type Si substrate (see Figure 15.10).

The specific property of nickel nanoparticles deposited onto silicon substrates of different types of doping was also clearly manifested in another reaction we studied, hydrogenation of multiple bonds. It is known that the optimal situation for catalysis of processes of this kind is presence of a positive charge on metallic particles [43]. This can be achieved upon deposition of Ni nanoparticles onto p-type silicon. Indeed, experiments did show that the activity of Ni nanoparticles onto p-type silicon exceeds by nearly two orders of magnitude the activity of catalysts based on ultra-dispersed platinum and palladium, prepared by other methods.

Application of charge effects in catalysis may also prove highly useful in practical regard. As an example of this kind can serve the results obtained in a study of the catalytic activity and stability of palladium nanoparticles produced by laser electrodispersion in a practically important process of hydrodechlorination of chlorobenzene. It was shown that using a catalyst with the optimal degree of surface coverage makes it possible to raise the activity by three orders of magnitude, compared with the conventional catalyst. It is also important that the catalyst deposited by laser electrodispersion retains its high activity during a sufficiently long time. The operational stability of a catalyst is a difficultly solved problem of key importance in processes of hydrodechlorination in the gas phase. It is worth noting that catalytic hydrodechlorination is the only truly ecologically safe technique for elimination of toxic polyorganochlorine wastes of technological origin. This method has not found wide use solely because of the high expenditure of the precious metal and low stability of the catalysts. Here, an opportunity to tackle with these problems can be foreseen.

5. Summary

Considered in this chapter are specific features of the catalytic behavior of metallic nanostructures of new type, produced by laser electrodispersion of metals. This method makes it possible to obtain Cu, Ni, or Pd nanoparticles whose sizes are specific to each particular metal, with the relative particle size scatter being exceedingly narrow, $\leq 10\%$. An important distinctive

Lam Research Ex. 1035 - Page 748
Lam Research Corp. v. Inpria Corp.
IPR2024-00033 - U.S. Patent No. 9,823,564

feature of these catalysts consists in that metallic particles are amorphous. A consequence of the amorphous state of the metal is the high stability of nanoparticles against coagulation. This made it possible to form catalytic coatings with high particle density on the support surface, including those in which neighboring particles are in close contact with one another. Experiments show that the catalytic activity of these structures in quite a number of reactions of chlorohydrocarbon conversion is exceedingly high and surpasses that of the conventional catalysts by orders of magnitude. Also, a strong dependence of the catalytic activity on the particle density in a structure was observed. These dependences were found to be fundamentally different for coatings deposited onto various, conducting (e.g., p- and n-type silicon) and dielectric substrates. These new manifestations of the catalytic behavior of nanostructured metallic catalysts are, in all probability, due to specific charge effects, which are the most important in high-density structures. It was shown that charge fluctuations in high-density structures, which occur owing to tunnel transitions of electrons between particles, result in, at temperatures close to room temperature, a considerable fraction of nanoparticles in the structure being charged. The quantitative estimate of this effect is in good agreement with the experimental data.

The results obtained, as well as the developed concept of the influence of nanoparticle density on the catalytic activity (size effect of the second kind), may be the most useful in the following cases:

- in development of catalysts based on precious and rare metals, when the content of such a metal can be lowered by orders of magnitude without changing the basic parameters of a catalyst;
- in obtaining the necessary selectivity, when the process temperature can be lowered without any loss of catalytic activity, with milder conditions of the process thereby provided;
- in intensifying the already existing technologies, with the working load on a catalyst substantially raised at the same apparatus volume, without any decrease in the conversion of reactants.

It is to note that some of the issues touched upon in this chapter still require a more detailed experimental study and theoretical interpretation. In particular, the model considered above, which makes it possible to relate an increase in the catalytic activity to appearance of charge on nanoparticles, undoubtedly needs refinement and a more thorough experimental verification. A clear understanding of the important issue of how the electrical properties of conducting supports affect the catalytic activity of deposited structures requires that, in the first place, experiments with a larger number of reactions and a wide variety of metallic and semiconducting substrates

Lam Research Ex. 1035 - Page 749
Lam Research Corp. v. Inpria Corp.
IPR2024-00033 - U.S. Patent No. 9,823,564

should be performed. It is also necessary to develop a model that could describe the dependence of the catalytic activity of metallic nanostructures on the strength of the electric fields that exist in the gaps between charged nanoparticles or in those between the particles and the support.

It is beyond any doubt, however, that the concepts concerning the influence exerted by the charge state of metallic nanostructures on their catalytic activity and the role of the support in catalysis can be used in purposeful development of new catalytic systems and in optimization of the properties of the existing catalysts. These opportunities open up new prospects for technological catalysis.

These are the questions for repeating the content of the chapter:

1. Estimate the temperature of laser torch plasma corresponding to the threshold of capillary instability of liquid 100 nm copper drop. This estimate can be done using the instability threshold condition (1) rewritten in the form:

$$kT_e > 0.4 \times e\left(\frac{\alpha R}{\varepsilon_0}\right)^{1/2} \frac{R_D}{R + R_D},$$

   where k is the Boltzmann's constant, e the electron charge, R_D the Debye radius in laser torch plasma. The value of surface tension of copper is $\alpha = 1.3\,\mathrm{N/m}$ and Debye radius is $R_D = 100\,\mathrm{nm}$.
2. Estimate the surface density of 5 nm Cu particles tightly packed in one layer covering on smooth support surface. Make this estimation for cubic and hexagonal particle arrangement.
3. Using the expression (2), calculate the ratio of the numbers of singly and doubly charged 5 nm copper particles taking the dielectric constant $\varepsilon = 10$ and ambient temperature $T = 300\,\mathrm{K}$.
4. Using formula (4), compare the value of the potential drop across the oxide sheath of copper nanoparticle with the thermal energy kT. In calculation, use the value of copper nuclei radius $R = 1.7\,\mathrm{nm}$, the thickness of Cu_2O sheath $d = 0.7\,\mathrm{nm}$, and the dielectric constant of the sheath $\varepsilon_d \approx 4$.

References

1. Y. Naveh, K. Likharev, Superlattices Microstruct. **27** (2000) 1.
2. P. Zhang, F. Zuo, F. K. Urban, III, A. Khabari, P. Griffths, A. Hosseini-Tehrani, J. Magn. Magn. Mater. **225** (2001) 337.
3. K.-H. Yoo, J. W. Park, J. Kim, K. S. Park, J. J. Lee, J. B. Choi, Appl. Phys. Lett. **74** (1999) 2073.

Lam Research Ex. 1035 - Page 750
Lam Research Corp. v. Inpria Corp.
IPR2024-00033 - U.S. Patent No. 9,823,564

4. A. Yu. Stakheev, L. M. Kustov, Appl. Catal. **188** (1999) 3.
5. O. V. Krylov, Heterogeneous Catalysis: Textbook, M.PTC, Akademkniga, Moscow, 2004.
6. V. I. Bukhtiyarov, M. G. Slin'ko, Russ. Chem. Rev. **70** (2001) 147.
7. J. D. Aiken, R. G. Finke, J. Mol. Catal. A **145** (1999) 1.
8. B. Coq, F. Figueras, Coord. Chem. Rev. **178–180** (1998) 1753.
9. C. R. Henry, Appl. Surf. Sci. **164** (2000) 252.
10. M. Boudart, Adv. Catal. **20** (1969) 153.
11. G. A. Somorjai, Langmuir **7** (1991) 3176.
12. A. L. Buchachenko, Russ. Chem. Rev. **72** (2003) 375.
13. P. S. Vorontsov, G. N. Gerasimov, E. N. Golubeva, E. I. Grigor'ev, S. A. Zavyalov, L. M. Zav'yalova, L. I. Trakhtenberg, Russ. J. Phys. Chem. **72** (1998) 1742.
14. L. I. Trakhtenberg, G. N. Gerasimov, E. I. Grigor'ev, S. A. Zavyalov, O. V. Zagorskaya, V. Yu. Zufman, V. V. Smirnov, Nanoheterogeneous Metal–Polymer Composites as a New Type of Effective and Selective Catalysts, in: B. Delmon, J. T. Yates (Eds.), Studies in Surface Science and Catalysis, Adv., 130 12th ICC, Part B, Elsevier, Amsterdam, 2000.
15. L. I. Trakhtenberg, G. N. Gerasimov, E. I. Grigor'ev, S. A. Zavyalov, O. V. Zagorskaya, V. Yu. Zufman, V. V. Smirnov, Russ. J. Phys. Chem. **74** (2000) 846.
16. I. P. Suzdalev, P. I. Suzdalev, Russ. Chem. Rev. **70** (2001) 177.
17. H. Colfen, S. Mann, Angew. Chem. Int. Ed. **42** (2003) 2350.
18. I. W. Hamley, Angew. Chem. Int. Ed. **42** (2003) 1692.
19. A. Yu. Stakheev, Yu. M. Shulga, N. A. Gaidai, N. S. Telegina, L. M. Kustov, K. M. Minachev, Mendeleev Commun. **11** (2001) 186.
20. D. E. Ramaker, M. Teliska, Y. Zhang, A. Yu. Stakheev, D. C. Koningsberger, Phys. Chem. Chem. Phys. **5** (2003) 4492.
21. L. I. Trakhtenberg, G. N. Gerasimov, E. I. Grigor'ev, Russ. J. Phys. Chem. **73** (1999) 209.
22. S. Tohno, M. Itoh, S. Aono, H. Takano, J. Colloid Interface Sci. **180** (1996) 574.
23. H. Herrig, R. Hempelmann, Mater. Lett. **27** (1996) 287.
24. L. I. Trakhtenberg, G. N. Gerasimov, Metal Containing Polymers: Cryochemical Synthesis, Structure and Physico-Chemical Properties, in: G. Carotenuto, L. Nicolais (Eds.), Metal/Polymer Nanocomposites, Wiley, New York, 2005.
25. K. Deppert, L. Samuelson, Appl. Phys. Lett. **68** (1996) 1409.
26. V. M. Kozhevin, D. A. Yavsin, V. M. Kouznetsov, V. M. Busov, V. M. Mikushkin, S. Yu. Nikonov, S. A. Gurevich, A. V. Kolobov, J. Vac. Sci. Technol. B **18** (2000) 1402.

Lam Research Ex. 1035 - Page 751
Lam Research Corp. v. Inpria Corp.
IPR2024-00033 - U.S. Patent No. 9,823,564

27. A. I. Grigorev, S. O. Shiryaeva, Sov. Phys. Tech. Phys. **36** (1991) 258.
28. L. Rayleigh, Philos. Mag. **14** (1882) 182.
29. Yu. P. Raizer, Physics of Gas Discharge, Springer-Verlag, Berlin, 1991.
30. T. N. Rostovshchikova, V. V. Smirnov, V. M. Kozhevin, D. A. Yavsin, M. A. Zabelin, I. N. Yassievich, S. A. Gurevich, Appl. Catal. A: Gen. **296** (2005) 70.
31. B. Abeles, P. Sheng, M. D. Coutts, Y. Arie, Adv. Phys. **24** (1975) 407.
32. E. Z. Meilikhov, JETP **93** (2001) 625.
33. D. A. Zakheim, I. V. Rozhansky, I. P. Smirnova, S. A. Gurevich, JETP **91** (2000) 553.
34. V. M. Kozhevin, T. N. Rostovshikova, D. A. Yavsin, M. A. Zabelin, V. V. Smirnov, S. A. Gurevich, I. N. Yassievich, Dokl. Phys. Chem. **387** (2002) 324.
35. V. I. Kozub, V. M. Kozhevin, D. A. Yavsin, S. A. Gurevich, JETP Lett. **81** (2005) 226.
36. E. L. Nagaev, Sov. Phys. Uspekhi **35** (1992) 747.
37. V. A. Saranin, Phys. Uspekhi **42** (1999) 385.
38. H. Wieder, W. Czanderna, J. Appl. Phys. **37** (1966) 184.
39. T. N. Rostovshchikova, V. V. Smirnov, V. M. Kozhevin, D. A. Yavsin, S. A. Gurevich, Kinet. Catal **44** (2003) 555.
40. T. N. Rostovshchikova, V. V. Smirnov, A. I. Kokorin, J. Mol. Catal. A: Chem. **129** (1998) 141.
41. T. N. Rostovshchikova, V. V. Smirnov, S. A. Gurevich, V. M. Kozhevin, D. A. Yavsin, S. M. Nevskaya, S. A. Nikolaev, E. S. Lokteva, Catal. Today **105** (2005) 344.
42. W. J. Bland, R. Davis, J. L. A. Durrant, J. Organomet. Chem. **280** (1985) 397.
43. A. Yu. Stakheev, L. M. Kustov, Appl. Catal. **188** (1999) 3.

Lam Research Ex. 1035 - Page 752
Lam Research Corp. v. Inpria Corp.
IPR2024-00033 - U.S. Patent No. 9,823,564

Chapter 16

Synthesis of Crystalline C-N Thin Films

H. Song, and O.J. Ilegbusi

Department of Mechanical, Materials and Aerospace Engineering, University of Central Florida, Orlando, FL 32816, USA

1. Introduction . . . 756
2. Synthesis . . . 758
3. Theoretical Models . . . 761
   3.1. Thermodynamic Models. . . . 761
   3.2. Molecular Dynamics Simulation . . . 765
   3.3. Thermal Spike Model . . . 766
4. Characterization . . . 770
   4.1. Microstructure: XRD and TEM . . . 770
   4.2. Chemical State: EELS and XPS . . . 771
   4.3. Composition: AES and RBS . . . 773
5. Potential Applications of CN Films . . . 774
6. Closure . . . 774
Acknowledgement . . . 775
Questions . . . 775
References . . . 775

This chapter describes the physico-chemical phenomena underlying the synthesis of crystalline carbon nitride (C-N) thin films. In section 1, the status of current research on C-N films is briefly reviewed as well as its benefits. Section 2 describes the experimental techniques employed to produce C-N films. These techniques include laser ablation of graphite targets in an atomic nitrogen ambience, dual ion beam assisted deposition, reactive sputtering of pure graphite target with pure N_2, rf-plasma-assisted hot filament chemical vapor deposition (cvd) and ion implantation. The theoretical models are described in section 3 for predicting the thermal stability and formation of C-N films. These models include thermodynamics, molecular dynamics, and thermal spike. In section 4, some characterization techniques are described including X-ray diffraction (XRD) and transmission electron microscopy (TEM) for microstructure, rutherford backscattering (RBS) and auger electron spectroscopy (AES) for composition, and electron energy loss spectroscopy (EELS) and X-ray photoelectron spectroscopy (XPS) for chemical state. Some characterization results are also

THIN FILMS AND NANOSTRUCTURES, vol. 34
ISSN 1079-4050
DOI: 10.1016/S1079-4050(06)34016-1
© 2007 by Elsevier Inc.
All rights reserved.

Lam Research Ex. 1035 - Page 753
Lam Research Corp. v. Inpria Corp.
IPR2024-00033 - U.S. Patent No. 9,823,564

presented. The prospects for practical application of C-N films are summarized in the concluding section 5. Some diagnostic questions are provided at the end to reinforce the materials discussed in the chapter.

1. Introduction

Carbon nitride (C-N) thin films have generated considerable interest recently as a result of theoretical evidence of their potentially attractive properties. These properties, which derive largely from the short covalent bonding of the compounds, include high values of wear and corrosion resistance, thermal conductivity and electrical resistance, and electron field emission. These properties make C-N films ideal materials for electronic packaging and laser-source, and for applications in which high property-to-mass ratio is desired as in space vehicles, lightweight, and high-performance materials.

Liu and Cohen [1] were the first to propose C-N materials from theoretical studies. The studies predicted such materials have superior properties due to their unique bonding structure. By means of an empirical model and *ab-initio* calculation they predicted as illustrated in Figure 16.1 that C-N with the β-C_3N_4 structure could have low compressibility comparable to diamond. Using a typical C−N bond length of 1.47–1.49 Å, this empirical formula suggests that a tetrahedral-bonded C−N solid material would have bulk modulus of 461–483 GPa, larger than any other known material. Moreover, *ab-initio* calculations have shown that several other structures may form stable C-N in addition to β-C_3N_4. Two possible structures have been proposed for hypothetical C-N, namely, a defect zinc-blended cubic structure and a defect graphite rhombohedral structure [2,3].

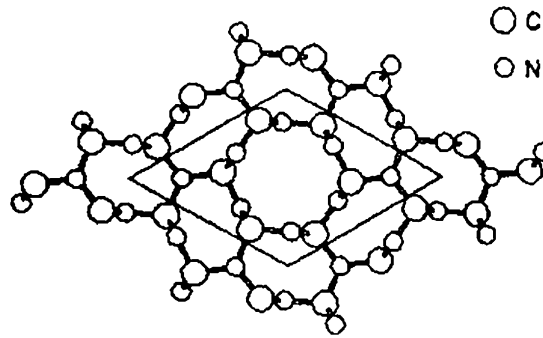


Fig. 16.1. Hypothetical β-C_3N_4 crystal structures [1].

Lam Research Ex. 1035 - Page 754
Lam Research Corp. v. Inpria Corp.
IPR2024-00033 - U.S. Patent No. 9,823,564

Cote and Cohen [4] investigated eight possible C-N structures with 1:1 stoichiometry and found the rhombohedral and GaAs structures to be most energetically favorable. In addition to the uncertainty of the most favorable structure for C_3N_4 C-N, several metastable C-Ns with different compositions such as C_4N_3, CN, and C_2N have also been proposed from other theoretical calculations [4,5]. More recently, *ab-initio* tight-bonding molecular dynamics method has been used to study amorphous C-N structures [6]. It was found that for high-density amorphous C-N, nitrogen incorporation strongly favors trigonal carbon coordination, thus counteracting the formation of low-compressibility tetrahedral-bonded phases. These studies primarily attempts to provide possible explanation for the wide range of nitrogen concentrations observed experimentally in polycrystalline C-N films.

The theoretical studies have raised considerable interest in the synthesis of hard C-N materials, and have elucidated the potentially enormous complexity in the phase diagram of C-N materials. Many novel experimental techniques have been employed to synthesize the crystalline C-N solids including reactive sputtering [7–9], enhanced CVD [10,11], laser ablation of carbon with a reactive nitrogen source [12–14], ion-beam deposition or implantation [15–19], RF-plasma-assisted hot filament CVD [20], electron impact ionization [21,22], inductively coupled technique [23–25], and other reactive techniques [26–29]. Despite these efforts no conclusive evidence has yet been reported for the synthesis of any crystalline C-N material. There have been many claims [12,30–34] that crystalline β-C_3N_4 grains were observed. However, these claims could not demonstrate sufficient characteristics to provide a reasonable level of confidence. It was not possible to measure the bulk modulus of the materials produced in these studies because the observed β-C_3N_4 grains were too small and embedded in the matrix of amorphous thin films. For example, the grain size of crystallites was less than 10 nm in the works of Niu et al. [12] and Song et al. [30]. The crystallites produced by Yu et al. [31] had dimensions of approximately 0.5 μm and occupied less than 5% of the film volume. Although there was evidence from electron diffraction studies that nanocrystalline β-C_3N_4 was synthesized by pulsed laser deposition and reactive sputtering, the diffraction data was incomplete and the nanocrystalline C-N was less than 10% of the overall product. The overall nitrogen stoichiometry in reported C-N solids has always been much lower than that expected for C_3N_4. In addition, in most of the reported C-Ns, whether there has been electron diffraction or not, the local bonding of carbon is almost 100% sp^2 hybridization. In spite of these previous efforts, there is still no credible and consistent experimental evidence of the existence of β-C_3N_4 phase in the films produced.

Lam Research Ex. 1035 - Page 755
Lam Research Corp. v. Inpria Corp.
IPR2024-00033 - U.S. Patent No. 9,823,564

The main product of these synthesis attempts has been amorphous C-Ns with a range of properties and compositions. The mechanical and electrical properties of the amorphous C-Ns largely depend on the composition, bonding character, and structures. The amorphous C-Ns still exhibited attractive characteristics such as exceptionally high values of hardness and electrical resistivity [35]. It was suggested that C-N thin films could be an attractive diamond-like coating material for thermal management in multi-chip modules and micro-scale devices [35]. A study of the field-emission properties of C-N thin films indicated enhancement in the emitted current density [36]. Walters et al. [37] predicted that this material would, as a consequence, have a wide range of potential applications, such as in electronic packaging and wear protective coatings for magnetic storage devices.

2. Synthesis

A number of experimental techniques has been employed to produce crystalline C-Ns since Liu and Cohen [1] first predicted the possibility of synthesizing diamond-like covalent β-C_3N_4 solid. The preparation of β-phase C-N is a complex process that is controlled by a variety of factors. These factors include the type, energy, and chemical status of reactants that provide the carbon and nitrogen sources as well as the deposition environments. The vast majority of current experimental efforts have concentrated on thin-film deposition from sources of highly energetic or reactive carbon and atomic nitrogen, hoping to provide sufficient energy for formation of tetrahedral C−N bonding structures.

There are two strategies to promote the formation of such bonding structure. One is the activation of nitrogen and subsequent promotion of the bonding between carbon and nitrogen. A very reactive nitrogen source such as ionized or atomic nitrogen is used to promote direct bonding with carbon. Another is to pre-mix them in a high-energy state such as a plasma which is then rapidly quenched on a substrate at low temperature. Coupled with the essential rapid solidification process, the large degrees of freedom in bonding and stoichiometry exhibited by nitrogenous carbon species produce an amorphous material. Experiments have also shown that there are three types of bonding states (C = N, C≡N, and C−N) in the films. As a result of this diversification, complexity, and the limited knowledge base, previous attempts have succeeded in producing only amorphous films.

The laser ablation technique was first used to synthesize C-Ns by Niu et al. [12] wherein high-energy fragments react with nitrogen atoms generated independently by an RF-plasma discharge. This technique attained a

Lam Research Ex. 1035 - Page 756
Lam Research Corp. v. Inpria Corp.
IPR2024-00033 - U.S. Patent No. 9,823,564

high nitrogen content of up to 50 atm.%. Although the product was largely amorphous, small crystallites were observed. Analysis of the laser ablation yield distribution showed that the nitrogen composition was determined by the overall growth rate. This result suggests that a surface reaction between reactive carbon and nitrogen species plays a key role in the formation of C-N compounds. However, the C-N materials synthesized by this technique were unstable. Annealing of laser ablated thin films leads to an initial loss of a more volatile sp-bonded nitrogen component at 550°C, and then a more complete loss of nitrogen above 900°C.

Marton et al. [38] used three different techniques to deposit C-N films: low-energy ion beam deposition, dc magnetron sputtering, and e-beam evaporation of carbon with electron cyclotron resonance nitrogen source. Although crystalline α-C_3N_4 grains were observed in local regions of films, all samples had similar constituent compositional features.

The dual ion-source system is widely considered to have great potential for depositing C-N thin films. Figure 16.2 illustrates a practical embodiment of this technique. This system has four major components: vacuum generator, dual ion-sources with power-control units, ionizer, and deposition chamber. The vacuum generator comprises a mechanical pump, diffusion pump, thermocouple gauge, ionization gauge, and appropriate valves to connect these parts together. The power-control units enable the energy and beam current density of bombarding ions to be adjustable over a broad range to simultaneously bombard the deposited carbon films. The deposition chamber is equipped with broad-beam Kaufman ion sources, a rotating water-cooled substrate holder and a rotating water-cooled target holder. The substrate holder is used to diffuse the heat produced from substrates during deposition.

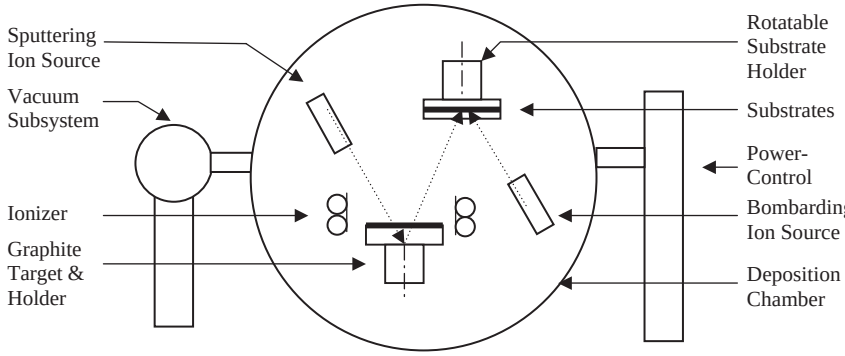


Fig. 16.2. Schematic of the dual ion-source deposition system.

Lam Research Ex. 1035 - Page 757
Lam Research Corp. v. Inpria Corp.
IPR2024-00033 - U.S. Patent No. 9,823,564

The sputtering source operated with argon can produce high-energy beam currents say up to 1.5 keV.The ions are extracted through a two-electrode multiple aperture system, allowing low pressure to be maintained inside the deposition chamber. The predominantly neutral carbon particles from the sputtering yield are ionized locally. The voltage required for acceleration of reactants is supplied to the substrates as self-bias to increase their kinetic energy.

This method has some advantages that evidently are more beneficial to the formation of diamond-like coatings than other methods. It can provide a variety of ions or clusters over relatively broad ranges of energy and beam current density. The technique has been used to prepare tiny crystallites identified to be β-C_3N_4 immersed in amorphous matrix [38]. A magnet deflector was employed in the experimental system to distinguish various particles. Clusters of NCN radical were incorporated into the films by bombardment. In the experiments, tetrahedral bonded C−N was established prior to film deposition. Large crystallites of β-C_3N_4 with a dimension of 0.4 μm were observed locally in some areas of the thin films thus produced with a high nitrogen concentration.

CVD technique is also used to synthesize crystalline C-Ns since it offers high purity at low temperature. It has been successful in depositing highly crystalline diamond in combination with the reactive plasma, which preferentially etches amorphous carbon and graphite. High temperature of up to 750°C still resulted in the formation of pure diamond even with feed gas of high N/C ratio up to 0.4. Above 600°C, nitrogen etching and thermal decomposition are observed to be significant as a result of the high relative stability and volatility of CN and HCN-containing components. These results indicate that there exists an upper limit below which the CN materials could be formed by CVD techniques and otherwise only carbon materials are produced.

The CVD technique has also been used to produce hydrogen-containing C-N materials as a consequence of the diversity of nitrogen-containing organic species. Several studies have reported that hydrogenated films of amorphous C-N can be synthesized under RF-plasma discharge through a feedstock of N_2 and hydrogenated carbons on substrates at temperatures in the range of 300–700°C [39–41]. These films suffer, however, from the large quantity of hydrogen (12–43 atm.%), moderate to low quantities of nitrogen (4–18 atm.%), and a significant amount of oxygen (9 atm.%), the latter attributed to *ex-situ* absorption. There exists no convenient way to remove the hydrogen that profoundly influences the bonding character and other properties. Thus they represent a distinct set of materials from pure C-Ns.

Lam Research Ex. 1035 - Page 758
Lam Research Corp. v. Inpria Corp.
IPR2024-00033 - U.S. Patent No. 9,823,564

3. Theoretical Models

The difficulty of synthesizing C-N films makes it crucial to develop and apply theoretical models principally to guide and optimize the design of experimental methods for this purpose. The most widely applied models can be classified into three – thermodynamic, molecular dynamics, and thermal spike models. These models are described below.

3.1. THERMODYNAMIC MODELS

To date nearly all experimental efforts have produced amorphous C-Ns, indicating that C-Ns do not have high-temperature stability. Therefore, it is fundamentally important to study the kinetics and thermodynamic stability of C-Ns. Such a study would explain the metastability of C-N and guide the strategies for production of stable crystalline C-N film. In addition, C-N materials suffer from nitrogen etching and thermal decomposition, which are significant below C_3N_4 stoichiometry, as well as a tendency to form amorphous products. Considerable theoretical efforts have, therefore, been devoted to the relative stability of C_3N_4 structure, CN structure, and amorphous materials.

The enthalpy of formation for C-Ns can be estimated from the sum of the enthalpy contribution of the bonds in the solid, using empirical bond-enthalpy values derived from molecular species. This method has been used to estimate the free energy of formation of β-C_3N_4 structure between the range of 588 and 816 kJ/mol [42]. Stevens [43], in a similar fashion, estimated that the enthalpy of formation for paracyanogen and graphitic–C_3N_4 ranges from 270 to 350 kJ/mol and from 281 to 401 kJ/mol, respectively. Ilegbusi and Song [44] estimated the enthalpy and entropy of formation for amorphous C-Ns. Using a Debye model, Odintsov and Pepekin [45] underestimated the formation enthalpy of β-C_3N_4 as 18.7 kJ/mol, assuming β-C_3N_4 was the only binary material.

Nitrogen etching and thermal decomposition phenomena lead to significant nitrogen loss during C-N synthesis. The kinetics of these phenomena is, therefore, crucial to successful synthesis of C-N films. Theoretical studies [46] have shown that the formation of N_2 dimers becomes increasingly important as nitrogen content increases in amorphous C-Ns. It was postulated that this molecular nitrogen formation is an intrinsic barrier in the dynamic growth process, leading to an upper limit in the nitrogen composition. N_2 formation and desorption constitute a significant source of nitrogen loss

Lam Research Ex. 1035 - Page 759
Lam Research Corp. v. Inpria Corp.
IPR2024-00033 - U.S. Patent No. 9,823,564

much greater, for instance, than C-N formation, and places an upper limit on the nitrogen content, estimated to be approximately 45% atomic composition for ion beam deposition techniques [47].

Several synthesis techniques can induce the formation of two nitrogen-containing volatile compounds namely, molecular nitrogen and cyanogens. The nitrogen molecule is suggestive of a favorable and simple decomposition pathway to nitrogen loss in low temperature and pressure [48]. The kinetics of decomposition and diffusion of nitrogen atoms in the synthesis of C-N films are strongly dependent on the local temperature. The energized bombarding nitrogen ions provide the kinetic energy to the deposited atoms by collision and thus increase the local temperature. Qualitatively, the decomposition rate (k) and the diffusion coefficient (D) can be expected to follow the Arrhenius rate law:

$$k = v \exp\left(\frac{-\Delta G^*}{k_B T}\right) \tag{1}$$

$$D = D_0 \exp\left(\frac{-Q}{k_B T}\right) \tag{2}$$

where v is a mean collision frequency of the nitrogen atoms, ΔG^* the activation energy for the decomposition reaction, k_B the Boltzmann's constant, T the absolute temperature at the deposition interface, D_0 a material constant, and Q the activation energy for diffusion of nitrogen atoms in the films.

The kinetics-dependence of the nitrogen to carbon composition ratio, $[N/C]$, in C-N films can, therefore, be described by the following semi-empirical equation:

$$\left[\frac{N}{C}\right] = \left[\frac{N}{C}\right]_0 \left(1 - \exp\left(-\frac{\Delta G^* + Q}{k_B T}\right)\right) \tag{3}$$

where $[N/C]_0$ is the arrival ratio. We introduce the reduced activation energy ε, defined as $\varepsilon \equiv (\Delta G^* + Q)/k_B T$, which merges the contributions both of the decomposition reaction and the diffusion of nitrogen at the deposition interface. It is noted that nitrogen decomposition is a non-equilibrium thermal activation process during ion bombardment, which suggests that the parameters ΔG^*, Q, and T, are strongly dependent on the bombarding energy. However, it is possible to characterize the nitrogen decomposition process using only the reduced activation energy ε. Figure 16.3 shows the experimental nitrogen-to-carbon ratios as a function of the kinetic energy of bombarding nitrogen beam [48].

Lam Research Ex. 1035 - Page 760
Lam Research Corp. v. Inpria Corp.
IPR2024-00033 - U.S. Patent No. 9,823,564

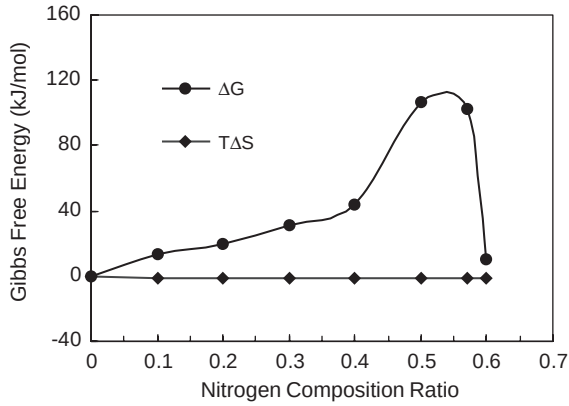


Fig. 16.3. Calculated free energy of formation of amorphous carbon nitrides as a function of nitrogen composition ($T = 300\,\mathrm{K}$)

The thermophysical properties necessary for the growth of tetrahedral bonded films could be estimated with a thermal statistical model. These properties include the thermodynamic sensible properties, such as chemical potential μ, Gibbs free energy G, enthalpy H, heat capacity C_p, and entropy S. Such a model could use statistical thermodynamic expressions allowing for translational, rotational, and vibrational motions of the atom.

The free energy of formation of amorphous C-N of varying nitrogen concentration was calculated using the thermochemical coordinate technique [44]. The enthalpy of formation was formulated using the cohesive energy and the entropy of reaction by assuming an ideal mixing. The enthalpy comprised two components: a chemical component due to electronic redistribution in forming the amorphous phase, and an elastic component arising from the difference in size between solute and solvent atoms. The contribution of the latter component was ignored in the study. This simplification could be justified by the lack of periodic structure in the amorphous phase, ensuring that the constituent atoms are not constrained to a specific volume.

The thermodynamic functions of one mole of compound consisting of N_0 identical molecules in standard state are related to the partition function and its derivatives, thus [44]:

$$\mu(T) = RT \ln\left(\frac{N_0}{Q(T)}\right) \tag{4}$$

$$H(T) = H(0) + RT^2 \frac{\partial \ln Q(T)}{\partial T} \tag{5}$$

Lam Research Ex. 1035 - Page 761
Lam Research Corp. v. Inpria Corp.
IPR2024-00033 - U.S. Patent No. 9,823,564

$$S(T) = R\ln\frac{Q(T)}{N_0} + RT\frac{\partial \ln Q(T)}{\partial T} \tag{6}$$

$$C_P(T) = RT^2\frac{\partial \ln^2 Q(T)}{\partial T^2} + 2RT\frac{\partial \ln Q(T)}{\partial T} \tag{7}$$

$$G(T) = H(T) - TS(T). \tag{8}$$

Here $H(0)$ is the enthalpy of compound for $T = 0$, N_0 the Avogadro's number, H the enthalpy, S the entropy, C_p the specific heat, and G the Gibbs free energy. $Q(T)$ is the production of the partition function of different modes of motion, thus,

$$Q(T) = \prod_i Q_i(T) \tag{9}$$

where

$$Q_i(T) = \sum_j \exp\left(-\frac{\varepsilon_{ij}}{kT}\right). \tag{10}$$

The parameter ε_{ij} is the discrete energy at energy level j associated with a certain motion mode i. The following expressions give the energy levels for translation, rotation, and vibration modes, respectively:

$$\varepsilon_t = \frac{h^2}{8mV^{2/3}}(n_x^2 + n_y^2 + n_z^2) \tag{11}$$

$$\varepsilon_r = j(j+1)h^2/8\pi^2 I, \quad j = 0, 1, 2... \tag{12}$$

$$\varepsilon_{\text{vib}} = \left(v + \frac{1}{2}\right)h\omega, \quad v = 0, 1, 2... \tag{13}$$

In these formulas h is the Planck's constant, m the molecular mass, V molar volume, n_x, n_y, and n_z are the numbers of particles per quantum level in the three coordinate directions, I is the moment of inertia of compound, j is the rotational quantum number, ω is the vibration frequency of molecules of the compound, and v is the vibration state.

Figure 16.4 shows the predicted variation of free energy of formation of amorphous C-N films with composition of nitrogen [44]. The results confirm that the synthesis of CN films will definitely require energized reactants to

Lam Research Ex. 1035 - Page 762
Lam Research Corp. v. Inpria Corp.
IPR2024-00033 - U.S. Patent No. 9,823,564

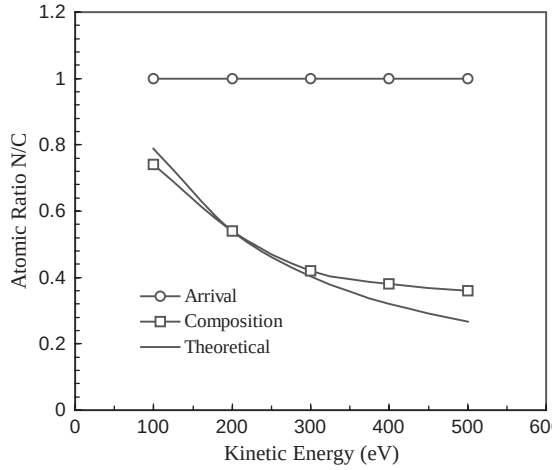


Fig. 16.4. Experimental and predicted atomic N/C ratios as a function of kinetic energy of bombarding ions.

overcome the high kinetic energy barrier associated with the modification of bonding structures.

3.2. MOLECULAR DYNAMICS SIMULATION

Molecular dynamics simulation has been used to study the relative cohesive energy for amorphous C-Ns [6,49]. The simulations were conducted with supercells of 140 atoms at varying densities and five compositions from pure carbon to C_3N_4. These efforts determined the lowest energy configurations for various stoichiometries of C-Ns. The bonding arrangement for high nitrogen composition models indicated a disposition toward the linear and planar bonding found in paracyanogen. The difference between the calculated cohesive energy of amorphous and crystalline C-N states was less than the difference between that of amorphous and crystalline carbon states. Since amorphous carbon is readily and preferentially synthesized over crystalline carbon under lightly energetic conditions, this explains why amorphous C-Ns are found as the only products of reactive deposition techniques.

Another important consideration in the theoretical description of C-N materials is the bonding configuration for the carbon and nitrogen atoms, which make up the solid. The crystalline structures, which employ tetrahedral sp^3 carbon bonding have dramatically larger calculated bulk moduli

Lam Research Ex. 1035 - Page 763
Lam Research Corp. v. Inpria Corp.
IPR2024-00033 - U.S. Patent No. 9,823,564

and densities than the structures, which have planar or sp^2 carbon bonding. The electronic and mechanical properties of the amorphous structures are strongly dependent on the predominant bonding configuration of the constituent atoms.

We illustrate the molecular dynamics technique by application to the ion beam deposition technique. Molecular dynamics could be used to investigate the effect of deposition conditions on the microstructure of the growing film. The microstructural characteristics of interest include film roughness and porosity.

Newton's classical equation of motion is first integrated in time to obtain the trajectory of each particle (ion) thus:

$$\frac{d2r_i(t)}{dt^2} = \sum_{i<j} F_i(r_{ij})/m \tag{14}$$

where i denotes specific atom, r_i the displacement, r_{ij} the distance between particles i and j, F_i the interaction force between particles i and j, and m the atomic mass. The force F_i is computed from the gradient of the potential energy of the system with respect to the position of each particle.

The simulation is initiated with a layer of prescribed structure that has the thickness of a single stationary atom. The calculation could investigate separately, initial states of pure amorphous phase (uniform atomic distribution) and a tetrahedral crystalline structure. The system could be simplified by assuming that the reactants are uniform with minimal interaction before arriving at the substrates. This assumption is consistent with the requirement that particles be of identical chemical state (such as C sp^3 and N sp^2 hybridization) to enhance the formation of the β-phase structure. Subsequent particle positions are then tracked in time to provide a detailed picture of the film growth. The growth rate and film structure, including roughness and porosity, are predicted as a function of kinetic energy (E) of ions, ratio of reactants, deposition angle, and substrate temperature. The final structure is evaluated relative to the initiating phase structure.

3.3. Thermal Spike Model

The kinetic energy of the reactants plays a significant role in determining the bonding characteristics and property of the deposited films [50,51]. For example, the composition and bonding configuration of constituent atoms in C-N films prepared by the ion-beam deposition technique are strongly dependent on the energy of the bombarding ions. Thus, this technique has become popular providing the kinetic energy to reactants for formation of

Lam Research Ex. 1035 - Page 764
Lam Research Corp. v. Inpria Corp.
IPR2024-00033 - U.S. Patent No. 9,823,564

the desired phase. In particular, ion bombardment can induce atomic rearrangement and thus, the transient modification of bonding and structure of films through collision cascade and energy dissipation. From a thermodynamic point of view, the phase transition is an activated process in which the lattice atoms concerned must rearrange themselves for formation of a new phase. Therefore, describing the fraction of rearranged target atoms provides a possible means of identifying the influence of experimental conditions such as ion energy, on the bonding character and properties of the deposited films.

Although molecular dynamics [52] has several advantages for describing the film growth process, a major drawback is the difficulty of addressing the effect of a variety of processing parameters. Other analytic models consider the ion bombardment as a point-like energy deposition process, which suggests a stress-induced mechanism for formation of diamond-like carbon. However, the predicted ion energy dependence in the high-energy region often does not accord with the experimental results due to significant diffusion and collision cascade of deposited carbon [53]. These effects lead to a decrease in the sp^3 fraction of DLC films. Thermal spike model provides an estimate of the time scale, critical dimensions, relevant energy densities, and number of thermally activated rearrangement processes. In effect, this technique involves describing the film growth process as a sequence of individual ion impact events well separated in space and time.

Although the effect of chemical bonding on energy dissipation in chemical systems is not included [54,55], the cylindrical thermal spike model takes into account the specific features of an ion-beam bombardment process such as energy loss and collision cascade. In particular, the individual ion bombardment will induce an initial energy deposited in a finite volume through collision cascades as illustrated in Figure 16.5.

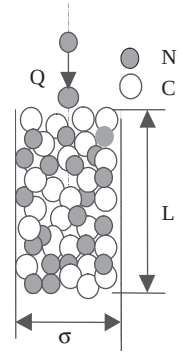


Fig. 16.5. Schematic of thermal spike for ion-beam deposition.

Lam Research Ex. 1035 - Page 765
Lam Research Corp. v. Inpria Corp.
IPR2024-00033 - U.S. Patent No. 9,823,564

In this finite volume, a number of target atoms will be rearranged through collision and thermal activation before the energy dissipates via phonon collision. In this model, it is assumed that the ion energy is deposited uniformly along the ion's path with constant stopping power dE/dx. If the number of rearranged atoms is comparable to the total number of atoms present within the finite volume, a significant modification of local film bonding and structure can be expected. Therefore, it is important to develop an analytic expression for the fraction of rearranged target atoms as a function of ion bombarding energy. This ratio is used to describe the ability of an ion impact event to induce the modification of local bonding and structure of the thin film. A cylindrical thermal spike model is used to calculate this ratio for a C-N film deposited using ion beam deposition. The essential assumption of the cylindrical thermal spike model is that a portion of the energy transmitted to the lattice by an incident particle could reappear in the form of lattice vibrations (or phonon excitation) in such a line concentrated way that the local temperatures would be sufficiently high to induce Fourier's law. For simplicity, it is assumed that local energy density rather than temperature describes the dissipation of thermal energy. Within this framework, the dissipation of energy by the transport equation can be given by

$$J_E = -D\text{grad}\rho_E \tag{15}$$

where J_E is the energy flux, D the energy diffusion constant, and ρ_E the time- and space-dependent energy density. The energy diffusion constant D is relative to the velocity of sound and the phonon mean path in C-N materials, and has a typical value of $5 \times 10^{11}\,\text{nm}^2/\text{sec}$.

The parameter N_T/N_S is calculated, representing the ratio of total number of rearranged atoms to number of atoms in the synthesized volume. This ratio effectively describes the ability of a given ion-target combination to achieve complete rearrangement of the spike volume. The total number N_T of rearranged target atoms taking place within the duration of a cylindrical spike can be given by:

$$N_T = 2\pi LNv_0 \int_0^\infty dt \int_0^\infty u \cdot \exp\left(-\frac{E'}{Q} \cdot N(4\pi LDt) \cdot \exp\left(+\frac{u^2}{4Dt}\right)\right) du. \tag{16}$$

For a finite initial width σ of the energy density distribution, the lower limit of the integral is replaced by $t_0 = \sigma^2/2D$ and we find an approximate

Lam Research Ex. 1035 - Page 766
Lam Research Corp. v. Inpria Corp.
IPR2024-00033 - U.S. Patent No. 9,823,564

solution for the number of rearrangement processes of the form:

$$N_T(Q,\sigma) \approx \left(\frac{Q}{E'}\right)^2 \frac{v_0}{4\pi NLD} \exp\left(-\frac{\sigma^2}{\sigma_C^2}\right). \tag{17}$$

Here σ_c is the characteristic width defined by $\sigma_c = (Q/2\pi E' NL)^{1/2}$. The ratio N_T/N_S can be obtained from the relation

$$\frac{N_T}{N_S} = \frac{Q}{LE'} \frac{e \cdot v_0}{4\pi ND} \exp\left(-\frac{\sigma^2}{\sigma_C^2}\right). \tag{18}$$

Equation (18) indicates that N_T/N_S decreases exponentially with increasing initial width σ. The initial width itself increases with increasing ion energy due to significant energy transfer from the primary ion to recoil atoms, leading to a large collision cascade volume. Therefore, it will eventually decrease significantly at high ion energies.

Figure 16.6 shows the predicted N_T/N_S ratio and measured Knoop hardness as a function of nitrogen ion bombarding energy for C-N film [48]. The prediction is in good agreement with the available experimental data [18,56,57]. The result from this model can provide the optimum condition for formation of sp^3 bonding configuration. In effect, the model will allow us to obtain the range of ion energy for which each atom within a specific

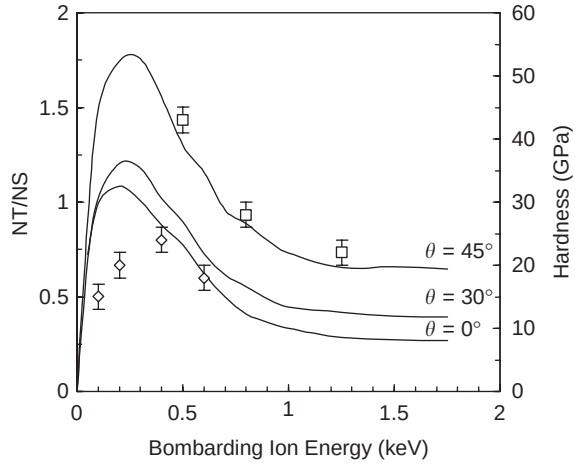


Fig. 16.6. Predicted N_T/N_S ratio (solid curve) for three incident angles and measured Knoop hardness as a function of nitrogen ion bombarding energy for carbon nitride film [56]. Hardness data ◇ and □ obtained from References [18] and [57], respectively.

Lam Research Ex. 1035 - Page 767
Lam Research Corp. v. Inpria Corp.
IPR2024-00033 - U.S. Patent No. 9,823,564

volume (thermal spike volume) will be rearranged at least once, suggesting the possibility of forming a stable bond configuration and film microstructure. The results could be used to relate the microstructure and bond character of deposited film to the bombarding ion energy to guide the design of experiments.

4. Characterization

Many techniques have been used to characterize C-N materials including X-ray diffraction (XRD) and transmission electron microscopy (TEM) for structure, X-ray photoelectron spectroscopy (XPS) and electron energy loss spectroscopy (EELS) for bonding character, and Auger electron spectroscopy (AES) and Rutherford backscattering spectrometry (RBS) for composition. The vast majority of synthesis attempts have resulted in amorphous C-Ns of varying composition and properties. Although properties such as resistivity or hardness have been readily measured, there has been a great deal of difficulty in accurately determining composition, bonding character, and structure for these amorphous materials.

4.1. Microstructure: XRD and TEM

All the claims of successful synthesis of crystalline C-N to date have been made on the basis of X-ray and electron diffraction data showing diffraction peaks similar or related to one or more expected structure. Partial matching of significant diffraction peaks is nothing more than the identification of a possible relationship.

Figure 16.7 depicts the typical patterns of C-N films deposited with the ion beam technique with bombarding energy of 100, 300, and 500 eV [48]. The films are observed to have only two broad scattering peaks centered at 28° and 69°. This characteristic at least identifies the films as nanocrystaliine possibly embedded in an amorphous matrix. A similar behavior was also observed using electron diffraction of a C-N thin film [30]. The diffraction peak centered at 69° corresponds to an intermediate spacing of 1.44 Å.This value is close to the sum of the atomic radii of carbon and nitrogen. Although the diffraction intensity is nearly independent of the bombarding energy of nitrogen ions, the diffraction peak at 28° becomes increasingly intense and converges to a graphite-like spacing at 3.3 Å as the bombarding energy decreases. This result is probably induced by the increase of disordered configuration of the graphite-like layered structure as the

Lam Research Ex. 1035 - Page 768
Lam Research Corp. v. Inpria Corp.
IPR2024-00033 - U.S. Patent No. 9,823,564

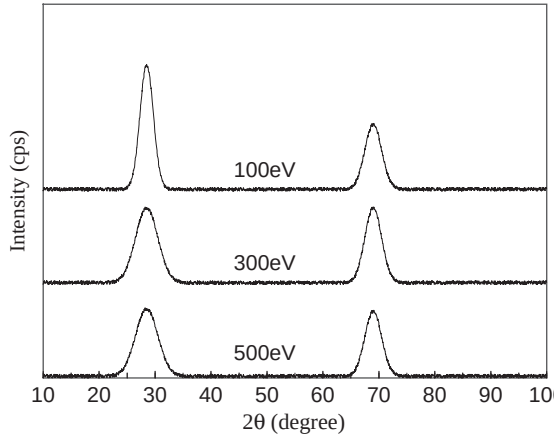


Fig. 16.7. XRD pattern of films as a function of the bombarding energy.

bombarding energy decreases. This phenomenon was also observed in the formation of amorphous carbon [58].

4.2. CHEMICAL STATE: EELS AND XPS

The most commonly used techniques for assessing bonding character are XPS, AES, and EELS. Since the first two are surface- and the latter bulk-spectroscopic techniques, the latter gives more accurate estimates of the bonding character. Although the general character of the bonding configuration of the bulk can be suggested by XPS, this technique is unreliable for carbon and nitrogen materials because the high energy of dangling bonds at a surface lead to a high probability of surface reconstruction. Thus, XPS may underestimate the sp^3 bonding character of the bulk. However, if hydrogen is available the sp^3 bonding character can be overestimated since hydrogen stabilizes sp^3 bonding at the surface. Synthesis studies in which the bonding character has been thoroughly investigated using EELS have demonstrated that all C-N materials have predominantly sp^2 character.

The EELS and RBS methods are generally considered to be the most reliable for relative carbon and nitrogen composition given the bulk nature of the measurement and similarity in the atomic number and ionization cross-section. XPS composition data has been shown to agree with RBS data with a slight overestimate of nitrogen content: XPS data is 5–6% higher than RBS at low N-content (20 atm.%) and 3–6% higher at higher N-content (42 atm.%). XPS can also severely underestimate the nitrogen content if the surface has a higher level of oxygen contamination.

Lam Research Ex. 1035 - Page 769
Lam Research Corp. v. Inpria Corp.
IPR2024-00033 - U.S. Patent No. 9,823,564

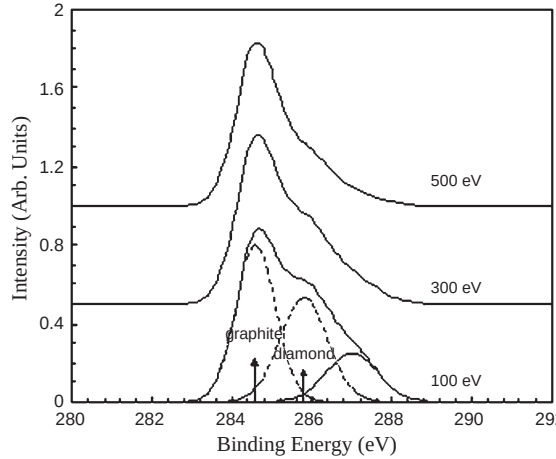


Fig. 16.8. XPS of C 1 s electrons as a function of nitrogen ion bombarding energy.

Studies utilizing these characterization techniques to identify the bonding state of both carbon and nitrogen atoms in C-N thin films include XPS [59], EELS [60], RS [61], and FT-IR absorption spectrum [62,63]. These studies have collectively demonstrated the existence of various chemical bonding states such as C–N, C = N, and C≡N, indicating that a C-N film is not a pure homogeneous phase.

Figure 16.8 shows a series of X-ray photoelectron spectra for the C 1 s state from films deposited at 100, 300, and 500 eV nitrogen ion bombardment [48]. The corresponding results for N 1 s state are presented in Figure 16.9. An AES depth profile indicated an approximately 7 atm.% of absorbed oxygen at the surface of the sample. Thus the spectra shown were obtained from a depth of 100 Å beneath the surface layer. The binding energy values corresponding to diamond (285.8 eV), graphite (284.6 eV), and nitrogen (399.0 eV) are noteworthy in the figures. The peak location for graphite was determined under similar conditions to those of the CN films. The XPS for C 1 s and N 1 s can be deconvoluted into Gaussian components. For all the three samples investigated, there were three contributions in C 1 s spectrum and two in N 1 s spectrum. For the carbon atoms, the major peak at 284.6 eV could be attributed to the C–C bonding in the graphite layer and possibly to surface carbon, which had lost its nitrogen neighbors due to surface exposure [64]. The peak at 285.8 eV was attributed to both the tetrahederal sp^3 C–C bonding and the sp^2 tridiagonal C–N bonding, while the peak at 287.0 eV was due to the sp^3 tetrahederal C–N bonding. For nitrogen, the peak at 398.8 eV was associated with the bonding characteristic with sp^3 hybridized carbon, while the peak at 400.2 eV with the bonding with sp^2 hybridized

Lam Research Ex. 1035 - Page 770
Lam Research Corp. v. Inpria Corp.
IPR2024-00033 - U.S. Patent No. 9,823,564

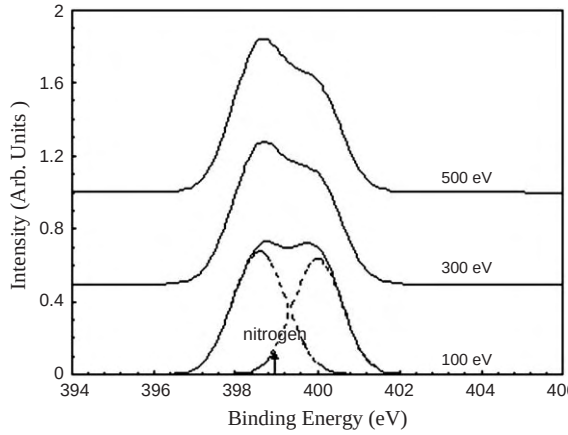


Fig. 16.9. XPS of N 1 s electrons as a function of nitrogen ion bombarding energy.

carbon. The bonding peaks at 288.1 eV for C = O bonding and at 396.8 eV for N–O bonding made minimal contributions to the XPS spectrum. This result was attributed to the decrease of oxygen contamination in the films that were produced by high-vacuum deposition.

The relative quantity of each bonding component can be estimated from the area it covers normalized by the total area for C 1 s and N 1 s spectra. Holloway et al. [65] used this approach to demonstrate that XPS data dramatically overestimates the sp^3-bonded component. This observation can, however, reflect the influence of the nitrogen bombarding energy on the bonding characteristics of C-N films. As the bombarding energy increases, the contribution of C–N bonds (sp^2 tridiagonal and sp^3 tetrahedral) to C 1 s significantly decreases. This trend is consistent with the variation of the nitrogen concentration with bombarding energy. In C–N bonds, the ratio of sp^2 to sp^3 decreases significantly with increase in bombarding energy of the nitrogen ions. Analysis of the N 1 s spectrum also supports this result.

4.3. COMPOSITION: AES AND RBS

Two important factors need to be controlled in the preparation of β-phase C-N thin films: nitrogen concentration and β-C_3N_4 composition. There has so far been only limited success in producing films with total N content approaching the 57 atm.% required for β-C_3N_4 phase. Studies that claim to produce β-C_3N_4 structure [29–34] report nitrogen concentrations of lower than 45 atm.%, indicating non-uniform distribution of nitrogen in the thin films. Fernandez et al. [51] obtained C-N films with nitrogen concentration

Lam Research Ex. 1035 - Page 771
Lam Research Corp. v. Inpria Corp.
IPR2024-00033 - U.S. Patent No. 9,823,564

of 44 atm.% using dual ion beam sputtering. Zhang et al. [61] prepared C-N thin films containing up to 50% nitrogen by reactive laser ablation of carbon with atomic nitrogen.

Figure 16.3 presented earlier shows the variation of the N/C atomic composition ratio obtained from AES as a function of the bombarding kinetic energy of the N ion beam with the ion beam deposition technique [48]. Also shown in the figure are the prescribed N/C arrival ratio as well as that predicted using theoretical activation model. As the bombarding energy increases, the difference between the N/C composition ratio and the arrival ratio progressively increases non-linearly. This result implies that a high bombarding energy produces a significant decrease in the N concentration of the films. This phenomenon has been attributed to chemically enhanced preferential sputtering and reflection by nitrogen ion beam bombardment [17].

There is however, no reliable explanation for the non-linear characteristics exhibited by the deviation of the N/C composition ratio from the arrival ratio with the bombarding energy. It may be postulated that spontaneous decomposition reaction is always present at the deposition interface of C-N films. This process leads directly to the formation of nitrogen molecules within the C-N matrix near the deposition interface by the reaction of two nitrogen atoms. The molecules produced diffuse out of the films, resulting in a loss of nitrogen content. Figure 16.3 also shows that as the bombarding energy increases, the larger deviation predicted between the N/C composition ratio and the arrival ratio accords with the experimental data.

5. Potential Applications of CN Films

C-N thin films could be an attractive diamond-like coating material for thermal management in multi-chip modules and micro-scale devices [35]. The field-emission properties of C-N thin films were studied, and indicated an enhancement in the emitted current density [36]. It has been predicted that this material would, as a consequence, have a wide range of potential applications, such as in electronic packaging and wear protective coatings for magnetic storage devices [37].

6. Closure

This chapter has highlighted some of the complexities of synthesizing crystalline C-N films. Due to these complexities, there is yet no credible proof

Lam Research Ex. 1035 - Page 772
Lam Research Corp. v. Inpria Corp.
IPR2024-00033 - U.S. Patent No. 9,823,564

that crystalline β-C_3N_4 has been successfully synthesized to any significant extent. Specifically, the intrinsic bias toward sp^2 hybridization at high nitrogen content makes it difficult to produce the desired tetrahedral-bonded structures of β-C_3N_4 using existing synthesis techniques. This chapter has, however, provided guidance and suggestions on the most promising techniques to achieve this objective, aided by theoretical models and characterization techniques. In summary, β-C_3N_4 thin film promises to be an important material in the coming decades. Comprehension of the fundamental mechanism of bond formation and film growth, as well as the development of appropriate synthesis technology, is critical to exploiting its potential qualities.

Acknowledgement

The work was partially supported by the USA National Science Foundation, Grant No. DMI 9977316.

Questions

1. What crystalline structure for C-Ns is predicted to have the highest bulk modulus over existing materials? What is the predicted value of bulk modulus?
2. Discuss the strengths and weaknesses of three experimental techniques that have been used to synthesize C-N materials? List three techniques.
3. What is the basis for the claims that crystalline β-C_3N_4 C-Ns have been observed in some experimental efforts? Can these claims be justified by the available data presented?
4. Explain why is that the nitrogen content in synthesis experiments cannot be sufficiently high to the stoichiometry of C_3N_4?
5. What is the primary assumption underlying the application of the thermal spike model to ion-beam assisted deposition of C-N materials?

References

1. A. Y. Liu, M. L. Cohen, Science **245** (1989) 841; Phys. Rev. **B42** (1990) 10727.
2. A. Y. Liu, R. M. Wentzcovitch, Phys. Rev. **B50** (1994) 10362.

Lam Research Ex. 1035 - Page 773
Lam Research Corp. v. Inpria Corp.
IPR2024-00033 - U.S. Patent No. 9,823,564

3. D. M. Teter, R. J. Hemley, Science **271** (1996) 53.
4. M. Cote, M. L. Cohen, Phys. Rev. **B55** (1997) 5684.
5. T. Hughbanks, Y. Tian, Solid State Commun. **96** (1995) 321.
6. F. Weich, J. Widany, T. Frauenheim, Phys. Rev. Lett. **78** (1997) 3326.
7. M. Y. Chen, D. Li, X. Lin, V. P. Dravid, J. Vac. Sci. Technol. **A11** (1993) 521.
8. H. W. Lu, X. R. Zou, J. Q. Xie, J. Phys. D Appl. Phys. **31** (1998) 363.
9. C. W. Ong, X. A. Zhao, Y. C. Tsang, J. Mater. Sci. **32** (1997) 2849.
10. A. Bousetta, M. Lu, A. Bensaoula, A. Schultz, Appl. Phys. Lett. **65** (1994) 696.
11. Y. Chen, L. Guo, F. Chen, E. G. Wang, J. Phys. Condens. Matter **8** (1996) L685.
12. C. Niu, Y. Z. Lu, C. M. Lieber, Science **261** (1993) 334.
13. Z. Zhang, S. Fan, C. M. Lieber, Appl. Phys. Lett. **66** (1995) 3582.
14. Z. Ren, Y. Du, Z. Ying, Y. Qiu, X. Xiong, J. Wu, F. Li, Appl. Phys. Lett. **65** (1994) 1361.
15. X. W. Su, H. W. Song, F. Z. Cui, W. Z. Li, J. Phys. Condens. Matter **7** (1995) L517.
16. K. J. Boyd, D. Marton, S. S. Todorov, A. H. Al-Bayati, J. Kulik, R. A. Zuhr, J. W. Rabalais, J. Vac. Sci. Technol. **A13** (1995) 2110.
17. X. W. Su, H. W. Song, F. Z. Cui, W. Z. Li, H. D. Li, Surf. Coat. Technol. **84** (1996) 388.
18. K. Ogata, J. F. D. Chubaci, F. Fujimoto, J. Appl. Phys. **76** (1994) 3791.
19. N. Tsubouchi, Y. Horino, B. Enders, Appl. Phys. Lett. **72** (1998) 1412.
20. Y. F. Zhang, Z. H. Zhou, H. L. Li, Appl. Phys. Lett. **68** (1996) 634.
21. J. Hopwood, F. Qian, J. Appl. Phys. **78** (1995) 758.
22. M. Dickson, J. Hopwood, J. Vac. Sci. Technol. **A15** (1997) 2307.
23. A. Kolitsch, W. Moller, Th. Malkow, S. J. Bull, V. Magula, M. Domankova, Surf. Coat. Technol. **128–129** (2000) 126.
24. Y. Kusano, J. E. Eretts, I. M. Hutching, Thin Solid Films **343–344** (1999) 250.
25. D. Li, S. Lopez, Y. W. Chung, M. S. Wong, W. D. Sproul, J. Vac. Sci. Technol. **A13** (1995) 1063.
26. M. Chhowalla, I. Alexandrou, C. Kiely, G. A. J. Ameratunga, R. Aharonov, R. F. Fontana, Thin Solid Films **290–291** (1996) 103.
27. Z. M. Ren, Y. C. Du, Z. F. Ying, F. M. Li, J. Lin, Y. Z. Ren, Z. F. Zong, Appl. Phys. **A64** (1997) 327.
28. D. G. McCulloch, A. R. Merchant, Thin Solid Films **290–291** (1996) 99.

Lam Research Ex. 1035 - Page 774
Lam Research Corp. v. Inpria Corp.
IPR2024-00033 - U.S. Patent No. 9,823,564

29. J. Kouvetakis, A. Bandari, M. Todd, B. Wilkens, Chem. Mater. **6** (1994) 811.
30. H. W. Song, F. Z. Cui, X. M. He, W. Z. Li, H. D. Li, J. Phys. Condens. Matter **6** (1994) 6125.
31. K. M. Yu, M. L. Cohen, E. E. Haller, W. L. Hansen, A. Y. Liu, I. C. Wu, Phys. Rev. **B49** (1994) 5034.
32. D. Li, Y. W. Chung, M. S. Wong, W. D. Sproul, J. Appl. Phys. **74** (1993) 219.
33. S. Kumar, T. L. Tansley, Solid State Commun. **88** (1993) 803.
34. Y. Li, Z. Zhang, S. Xie, G. Yang, Chem. Phys. Lett. **247** (1995) 253.
35. Z. J. Zhang, S. Fan, J. L. Huang, C. M. Lieber, Appl. Phys. Lett. **68** (1996) 2639.
36. S. R. Silva, G. A. J. Ameratunga, J. R. Barnes, Appl. Phys. Lett. **71** (1997) 1477.
37. J. K. Walters, M. Kuha, C. Spaeth, E. Dooryhee, R. J. Newport, J. Appl. Phys. **83** (1998) 3529.
38. D. Marton, K. J. Boyd, A. H. Al-Bayati, S. S. Todorov, J. W. Rabalais, Phys. Rev. Lett. **4** (1994) 118.
39. H. X. Han, B. J. Feldman, Solid State Commun **65** (1988) 921.
40. M. Ricci, M. Trinquecoste, F. Auguste, R. Canet, P. Delhaes, J. Mater. Res. **8** (1993) 480.
41. G. Mariotto, F. L. Freire, Jr., C. A. Achete, Thin Solid Films **241** (1994) 255.
42. V. Badding, D. C. Nesting, Chem. Mater. **8** (1996) 535.
43. A. J. Stevens, The stability of carbon nitride materials, Harvard University, Ph.D. Thesis, 1998.
44. O. J. Ilegbusi, H. Song, J. Mater. Process. Manuf. Sci. **8** (2000) 34.
45. V. Odintsov, V. Pepekin, 26th International Annual Conference of I.C.T., 1995.
46. S. S. Todorov, D. Marton, K. J. Boyd, A. H. Al-Byati, J. W. Rabalais, J. Vac. Sci. Technol. **A12** (1994) 3192.
47. Z. Ren, Y. Du, Z. Ying, Y. Qiu, X. Xiong, J. Wu, F. Li, Appl. Phys. Lett. **65** (1994) 1361.
48. H. Song, O. J. Ilegbusi, Thin Solid Films **388** (2001) 114.
49. Th. Frauenheim, G. Jungnickel, P. Stich, M. Kaukonen, F. Weich, J. Widany, D. Porezag, Diam. Relat. Mater. **7** (1998) 348.
50. M. Hakovirta, J. Salo, R. Lappalainen, A. Anttila, Phys. Lett. **A205** (1995) 287.
51. A. Fernanez, P. Prieto, C. Quirs, J. M. Sans, J. -M. Martin, B. Vacher, Appl. Phys. Lett. **69** (1996) 764.

Lam Research Ex. 1035 - Page 775
Lam Research Corp. v. Inpria Corp.
IPR2024-00033 - U.S. Patent No. 9,823,564

52. N. A. Marks, D. R. Mckenzie, B. A. Pailthorpe, M. Bernasconi, M. Parinello, Phys. Rev. **B54** (1996) 5703.
53. C. A. Davis, Thin Solid Films **226** (1993) 30.
54. N. E. Dodson, S. Satpathy, Z. Pawlowska, Phys. Rev. **B36** (1987) 1032.
55. J. Polanyi, J. Appl. Phys. **77** (1989) 4750.
56. H. Song, O. J. Ilegbusi, J. Mater. Process. Manuf. Sci. **10** (2002) 229.
57. M. Kohzaki, A. Matsumuro, T. Hayashi, M. Muramatsu, K. Yamaguehi, Thin Solid Films **308–309** (1997) 239.
58. H. Holsaas, C. M. Sebastian, H. Feldermann, R. Merk, C. Ronning, in: M. P. Segal, W. J. Milner, J. E. Jaskie (Eds.), Symposium Proceedings, Covalently Bonded Disordered Thin Film Materials, Vol. 498, Boston, USA, December 2–4, Materials Research Society, 1997, p. 129.
59. M. Tabbal, P. Merel, S. Moisa, M. Chaker, A. Ricard, M. Moisan, Appl. Phys. Lett. **69** (12) (1996) 1698.
60. G. A. J. Ameratunga, M. Chhowalla, C. J. Kiely, I. Alexandrou, R. Aharonov, R. M. Devenish, Nature **383** (1996) 321.
61. Z. J. Zhang, S. Fan, C. M. Lieber, Appl. Phys. Lett. **66** (1995) 3582.
62. E. J. Chi, J. Y. Shim, H. K. Baik, Appl. Phys. Lett. **71** (1997) 324.
63. L. C. Chen, T. R. Lu, C. T. Kuo, D. M. Bhusari, J. J. Wu, K. H. Chen, T. M. Chen, Appl. Phys. Lett. **72** (1998) 3449.
64. Z. Wu, Y. Yu, X. Liu, Appl. Phys. Lett. **68** (1996) 1291.
65. B. C. Holloway, D. K. Shuh, M. A. Kelly, W. Tong, J. A. Carlisle, I. Jimenez, D. G. J. Sutherland, L. J. Terminello, P. Pianetta, S. Hagstrom, Thin Solid Films **290–291** (1996) 94.

Lam Research Ex. 1035 - Page 776
Lam Research Corp. v. Inpria Corp.
IPR2024-00033 - U.S. Patent No. 9,823,564

Subject Index

ab initio calculations 67, 76, 83
absorption coefficient 150, 157, 161
absorption 147, 150–151, 153, 155–169
adiabatic 199
adiabatic approach 10
adiabatic transitions 9
amorphous metal nanoparticles 725
Anderson localization 610–611, 628
Arrhenius equation 200
atomic layer deposition (ALD) 468, 495–496, 503–506, 508, 511–516
atomistic simulation 468, 516

band-shape 146, 150, 155, 164, 177
Born–Oppenheimer approximation (BOA) 2, 138, 143, 154, 156
bridge effect 38

carbon nitride 755–756, 763, 769
catalysis 714–715, 717, 719, 725–728, 746–747, 750, 752
catalytic activity 568, 572, 574
catalytic activity of M-nanoparticles 566
catalytic properties 1
catalytic reactions 402, 413
cellular automata technique 427–429
charge effect 725, 727–729, 731, 733, 735, 737, 739–741, 743–747, 749–751, 753
charge transfer complex 199
chemical vapor deposition films 4
chemical vapor deposition (CVD) 468–469, 755
chemisorption 364, 392, 396
chlorohydrocarbon 5
chlorohydrocarbon conversion 725, 751
cluster 1, 5, 697–698, 700–715, 717, 719–720
cluster methods 435, 437, 442
cluster spin glass 604, 607
coercive force 596, 599, 604
coherence effect 3, 212
condensed phase 2, 4, 347–351, 357–358, 364–365, 370, 375, 393, 420, 439–441, 451
Condon approximation 143, 151, 190, 205, 208
conductivity and photoconductivity 554–557
coupled-master equations 214
covalent bonding 5
crossing-point 201
Cryochemical synthesis
  of M/SC-polymer nanocomposite films 553
  mean size and size distribution of nanoparticles 553–554
crystal medium 38

density matrix 121, 123–125, 127, 132–134, 137–138, 147, 152, 154, 157, 164–165, 171, 173
density matrix method 2–3, 121–123, 130, 132, 138, 147, 157, 171–173, 183
dephasing 133, 137–138, 141, 149, 153–155, 157, 170
diamagnetic characteristics 3
diamond-like coating 758, 760, 774
dielectric properties 1
dielectric properties of M-nanoparticles 562
diffusion through solids 414
dipole approximation 147
displaced 192
displaced distorted 192
displaced-oscillator surfaces 200
displacement of equilibrium positions 10
distorted 192
Duschinsky effect 192

effective reorganization energy 38
electrical properties 4
electrodispersion technique 5

Lam Research Ex. 1035 - Page 777
Lam Research Corp. v. Inpria Corp.
IPR2024-00033 - U.S. Patent No. 9,823,564

electronic coupling 208
electronic spectra 2
electronic structure 526–531
electron transfer (ET) 2–3, 59, 122, 141–143, 145–146, 156–158, 161–163, 165–172
electron tunneling amplitude 37
electronic transition 67, 70–72, 76, 78, 80–81, 86, 103–104, 107–109, 113–115
energy gap expression for radiationless transitions 197
energy transfer 122, 141, 158
epitaxial growth 4
excited states 281, 295–296, 299
excitonic-vibronic 184
Eyring theory 4

Förster–Dexter theory 3, 212
femto-second time-resolved spectra 2
Film Growth 467–471, 492–497, 499, 502–505, 507–509, 511–513, 515–516
Frank–Condon factor (FCF) 3, 143, 151, 155, 170, 191
Franck–Condon overlap 208

gas–solid interface 349, 352, 372, 412, 427, 429, 438, 440
gas–surface reactions 469, 471–472
generalized linear response theory (GLRT) 3, 152, 154, 157, 172, 212
generalized master equation (GME) 125, 136–138, 186
Germania 67–68, 72, 99, 114–116
giant magnetoresistance 583, 617, 633
Green Chemistry 665, 690
Green function 2
Grignard reaction 5

Hall effect 582, 607–610, 621–625, 632
heat bath 130–135, 137–138, 140, 152, 156
high-performance materials 756
hydrogen–palladium system 351, 419, 421
hydrogenation 5, 725–726, 746, 750

Induced 137, 155, 163–169
interfacial phenomena 1
intermediate particles 37
internal conversion (IC) 122, 141, 143, 186, 189
internal conversion theory 3
intersystem crossing (ISC) 122, 141, 186, 189
intramolecular vibrational relaxation 192
ion beam deposition 757, 759, 762, 766–768, 774
isolated line approximation 212

kinetic equations 348, 351, 370, 372–375, 377–380, 382–384, 387–391, 401, 409, 412–414, 416, 427, 429, 436–437, 439, 451–452
kinetic Monte Carlo (KMC) method 4, 468–469, 483, 485–486, 503
kinetic properties 1

Langmuir–Blodgett 4, 639, 643–645, 649–652
laser electrodispersion films 4
lattice-gas model 348, 350–351, 357, 359–360, 363, 365, 371–372, 379, 399, 401–402, 412–414, 419–420, 427, 429, 435, 442–443, 452
Liouville equation 121, 123, 125–126, 133–134, 138, 152, 157, 164, 172
Liouville operator 125, 152

M/SC nanoparticles growth 554
M/SC nanoparticles nucleation 554
magnetoresistance 582, 612, 614–621, 633
magnesium 698–699, 701–717, 719–720
magnetic properties 1
magnetization curve 596, 598, 600, 603–604
Marcus equation 200
Marcus theory 3, 212
Markov approximation 187, 212
master equation 348, 351, 372–373, 435
matrix method 446
mean size and size distribution 545, 549, 552–553
mean size and size distribution of M/SC nanoparticles 557, 565
media reorganization 3
melting point 1
memory effect 3, 212
Metal nanocrystal 526–531
method of fragments 447
methods of preparation by PVD 554
microscopy 755, 770
mode mixing 192

Lam Research Ex. 1035 - Page 778
Lam Research Corp. v. Inpria Corp.
IPR2024-00033 - U.S. Patent No. 9,823,564

modeling of deposition 536–537, 544, 548
modeling of PVD 554
molecular dynamics 468–469, 479, 493, 503, 755, 757, 761, 765–767
multiscale simulation 469–470, 516
multistage processes 351, 370, 375, 399
multi-vibrational electron transitions 29

nanogranules 584, 589–591, 605, 617, 620
nanoparticle 67–72, 80–81, 83, 89, 99
non-radiative processes 122
nucleation 542

order–disorder transitions 651
organized organic thin films 639, 641–643, 645, 647, 649, 651, 653, 655, 657, 659–661, 663

pair correlation functions 4
paramagnetic characteristics 3
percolation threshold 581–592, 599, 601, 608, 610–611, 614, 618, 622, 627–628, 630
phase transitions 349, 353, 393, 418, 428, 435, 438
photoabsorption 3, 67–68, 70, 72, 95, 99, 114–116
photodimerization 5
photo-induced electronic energy transfer 199
photo-induced electronic transfer (PIET) 142, 153, 156–157, 162, 164, 170, 189, 199, 200
photo-induced energy transfer 189
photo-induced transfer 2
photoluminescence 3, 67–68, 83, 95, 99, 108
photopolymers 5, 665, 676, 687
physical adsorption 363, 392–393, 403
physical vapor deposition (PVD) 537, 544–545
physico-chemical mechanics 351, 419
point defects 3, 67, 69–73, 76, 81, 83, 89–90, 99–100, 107, 113, 115–116, 231, 235, 239, 243, 281, 330, 336
polar media 9
polarization 148, 152–153
polycrystalline films 757
pump–probe experiment 122, 151–152, 154, 162, 171

quantum chemistry 253
quantum corrections to conductivity 614–616
quantum-size effects 627

radiationless transitions 2–3, 6
random phase approximation (RPA) 127, 128, 149, 173
rate constant 129, 133, 137, 139, 141–146, 151, 157, 172
reaction rates 348, 350, 357, 361, 370, 380, 399, 420, 428, 431
relaxation 122–123, 128, 131–133, 135, 137, 140–142, 145, 156–157
reorganization energy 9, 200
Rice–Ramsperger–Kassel–Marcus (RRKM) theory 4, 468–469, 476, 516
rotating wave approximation (RWA) 148
Runge–Kutta 208

saddle-point method 193
secular approximation 208
self-assembly 639, 644–645, 655–656, 659
self-assembly techniques 5
self-consistency of the lattice-gas model 404
semiconductor nanocrystal electronic structure 231–236
sensor 1, 4
sensor properties 525, 557
shift of the frequencies 11
short-time approximation 200
silica 3, 67–76, 80, 83–84, 89, 93–94, 114–116
singlet–singlet energy transfer 201
single-vibronic level rate constant 190
single-vibronic-level 141–144, 146, 157
spectroscopy 232, 234, 237, 240, 286, 292, 301, 305, 318, 320, 340
spillover of Born–Oppenheimer approach 37
spin-dependent tunneling 617, 619
steepest-descent 193
strong coupling 199
sub-barrier scattering 37
surface diffusion 351, 391, 409–410, 431, 434
susceptibility 122, 147–148, 153–154, 164, 205

thermal average 141–143, 145–146, 151
thermal average rate constant 190
thermal spike model 761, 766–768, 775
thermodesorption spectra 395

Lam Research Ex. 1035 - Page 779
Lam Research Corp. v. Inpria Corp.
IPR2024-00033 - U.S. Patent No. 9,823,564

thermodynamic properties 4
thin films 4–5, 468, 479, 508, 512, 516, 755–756, 758–760, 772–774
thymine 665, 669–679, 687–691
thymine-containing polymers 5
time-correlation function (TCF) 144, 156, 177, 179
topochemical processes 351, 356, 418
transient 205
transient absorption (TRABS) 167–169, 171
transition probability 10
transition state theory 473, 476
transmitted energy 10
transport properties 4
triplet–triplet energy transfer 203
tunnel current and percolation threshold 568
tunnel electron transfer between M/SC nanoparticles 561–562, 569–571
tunneling 584, 597, 605, 608, 611, 614–615, 617, 619–620, 624, 626, 628, 630, 642

ultrafast electron transfer processes 183
ultrafast electronic-excitation energy transfer 183
ultrafast radiationless transitions 183

vacuum magnetron sputtering films 4
variable range hopping 612, 614, 624
vibrational coherence dynamics 207
vibrational coherence transfer 207
vibrational population transitions 206
vibrational relaxation rate constants 206
vibrational relaxation techniques 3
vibrational thermal equilibrium 185
vibronic coupling 208
vibronic coupling terms 208
vibronic transitions 185

Lam Research Ex. 1035 - Page 780
Lam Research Corp. v. Inpria Corp.
IPR2024-00033 - U.S. Patent No. 9,823,564

Recent Volumes In This Series

Maurice H. Francombe and John L. Vossen, *Physics of Thin Films*, Volume 16, 1992.

Maurice H. Francombe and John L. Vossen, *Physics of Thin Films*, Volume 17, 1993.

Maurice H. Francombe and John L. Vossen, *Physics of Thin Films, Advances in Research and Development, Plasma Sources for Thin Film Deposition and Etching*, Volume 18, 1994.

K. Vedam (guest editor), *Physics of Thin Films, Advances in Research and Development, Optical Characterization of Real Surfaces and Films*, Volume 19, 1994.

Abraham Ulman, *Thin Films, Organic Thin Films and Surfaces: Directions for the Nineties*, Volume 20, 1995.

Maurice H. Francombe and John L. Vossen, *Homojunction and Quantum-Well Infrared Detectors*, Volume 21, 1995.

Stephen Rossnagel and Abraham Ulman, *Modeling of Film Deposition for Microelectronic Applications*, Volume 22, 1996.

Maurice H. Francombe and John L. Vossen, *Advances in Research and Development*, Volume 23, 1998.

Abraham Ulman, *Self-Assembled Monolayers of Thiols*, Volume 24, 1998.

Subject and Author Cumulative Index, Volumes 1-24, 1998.

Ronald A. Powell and Stephen Rossnagel, *PVD for Microelectronics: Sputter Deposition Applied to Semiconductor Manufacturing*, Volume 26, 1998.

Jeffrey A. Hopwood, *Ionized Physical Vapor Deposition*, Volume 27, 2000.

Maurice H. Francombe, *Frontiers of Thin Film Technology*, Volume 28, 2001.

Maurice H. Francombe, *Non-Crystalline Films for Device Structures*, Volume 29, 2002.

Maurice H. Francombe, *Advances in Plasma-Grown Hydrogenated Films*, Volume 30, 2002.

Vladimir Agranovich and Franco Bassani, *Electronic Excitations in Organic Based Nanostructures*, Volume 31, 2003.

Alexey Kavokin and Guillaume, *Cavity Polaritons*, Volume 32, 2003.

Alexander V. Khomchenko, *Waveguide Spectroscopy of Thin Films*, Volume 33, 2005.

Lam Research Ex. 1035 - Page 781
Lam Research Corp. v. Inpria Corp.
IPR2024-00033 - U.S. Patent No. 9,823,564